

nature



THE INTERNATIONAL WEEKLY JOURNAL OF SCIENCE

What NASA's New Horizons probe will find when it reaches Pluto **PAGES 40 & 45**

GEARING UP FOR THE FLY-BY

GENE EDITING

THE CRISPR REVOLUTION

Promise and perils of the new DNA engineering

PAGE 20

MEDICAL ETHICS

TESTING TIMES

Optimal prenatal diagnosis — for mother and child

PAGE 29

PARTICLE PHYSICS

LHC RAISES THE STANDARD

Detection of B meson decays favours standard model

PAGES 42 & 60

NATURE.COM/NATURE

4 June 2015 £10

Vol. 522, No. 7554



THIS WEEK

EDITORIALS

PLUTO The planetary dance at the edge of the Solar System **p.6**

WORLD VIEW Cheer up chemists, the public is on your side **p.7**

INCOGNITO Female songbirds dressed down for travel **p.9**



Health plan

Proposals to improve the international emergency response to disease outbreaks in the wake of the Ebola epidemic should be implemented — but local solutions are the best defence.

As West Africa starts to recover from the worst of the Ebola epidemic, how can scientists, health experts and politicians ensure that the world is better prepared next time? The global failure to respond quickly and effectively to the epidemic has prompted much soul searching, and already ideas about what needs to change are emerging. The danger is that the political will to realize such solutions — including better-tailored research agendas and streamlined clinical-trials regulation — will be harder to find as Ebola fades from the headlines and public concern moves on.

It is good news, then, that plans to improve global disease response are in the pipeline, and could be announced as soon as this weekend. Prepared under the leadership of Germany's Chancellor Angela Merkel, the proposals are expected to be presented at the annual summit of the G7 group of leading industrialized countries, due to take place in Elmau, Germany, on 7–8 June. The package of measures is a promising sign that politicians at the highest level take the threat of infectious disease seriously, and it lays out some sensible suggestions.

Surveillance is key. Ebola first emerged in West Africa in December 2013, but was not identified until the following March, a delay that allowed it to spread out of control. The new proposals aim to boost surveillance systems by providing low- and middle-income countries with US\$12 million to \$15 million annually. That might not sound much, but experience in poorer countries shows that a little money can go a long way in building capacity, such as a trained workforce. In many countries, new investments can also piggyback on existing networks.

Another lesson of Ebola is the dire need for modern tools such as diagnostics, drugs and vaccines. Yet the world's biomedical research and development system is simply not geared towards generating products for which there is little or no market.

BE PREPARED

The G7 plan is expected to address this, initially with a survey of potential threats and an audit of available candidate drugs and vaccines. A funding pool of \$50 million to \$100 million annually would then take the most promising candidates through to phase I clinical trials to test their safety. This would mean that, in the event of an outbreak, they could be taken directly into clinical trials to test their efficacy in the field. This is a sensible proposal. One of the most frustrating aspects of the Ebola epidemic was that several potential drugs and vaccines existed but had not undergone phase I trials.

Public–private partnerships created over the past 15 years have encouraged the research and development of products to address neglected diseases and others that do not have large markets. They can also serve as a hub for coordinating research and attracting further funds. In principle, therefore, if similar partnerships were aimed at potential threats, they could accelerate product development. Research agencies must not only step up support for work on such threats, but also translate this into medical countermeasures (see page 18).

Another welcome proposal is to speed up trials by developing protocols and experimental designs before outbreaks occur, and to have these pre-approved by regulators, so that when there is an outbreak, trials could start immediately. For Ebola, such trials were agreed by researchers, regulatory authorities and affected countries only after the epidemic was under way. (To their credit, everyone involved pulled out all the stops to cooperate and fast-track the process. They agreed on protocols and experimental designs in a matter of months, a procedure that normally takes years.)

“The ultimate goal must be functional health systems in every country.”

The proposals also call for \$150 million to \$200 million per year to create a reserve force of 10,000 scientists and health-care workers who can be rapidly deployed during an outbreak — a sort of United Nations ‘Blue Helmets’ for health. The oft-touted idea has merit, but

should not distract from the more fundamental need to expand the global workforce of disease researchers and health-care workers.

Who would be in charge of such a force? Indeed, who would coordinate the other measures if they are approved? And how will they sit with existing initiatives, such as the US-led Global Health Security Agenda coalition of several dozen countries and organizations that was launched in February last year?

The new proposals call for the creation of a \$40-million-a-year multilateral organization that would be responsible for global outbreak response. Housed within the World Health Organization (WHO), the unit would be autonomous enough to avoid WHO bureaucracy. It would have a mandate to link to UN agencies, the World Bank and other organizations — including non-governmental organizations, industry and philanthropies. Such inclusiveness has too often been insufficient.

The G7 and other countries should back the suggested moves. Governments and organizations should find the cash required. But all involved should remember that international systems for responding to outbreaks are only part of the picture — as starkly exposed by Ebola. What is most important is having robust health systems on the front line.

At the World Health Assembly, the annual meeting of the health ministers of WHO member states, which was held last month in Geneva, Switzerland, Merkel rightly said that the ultimate goal must be functional health systems in every country. That was the explicit aim of the revised International Health Regulations, adopted in 2007 by 196 countries, including WHO member states, which committed to targets for surveillance and emergency-response infrastructure.

Yet most countries missed the 2012 deadline for achieving these targets, with only 64 countries reporting being up to speed as of this year. At the Geneva meeting, the deadline for the remainder was extended yet again, to 2016. In the current flurry of interest in emergency initiatives, society should not forget that what is needed most is long-term investment in research and health-care systems in all countries, so that they can better respond to disease threats themselves. ■

Misplaced faith

The public trusts scientists much more than scientists think. But should it?

British chemists are a diffident and self-conscious bunch. A poll by the Royal Society of Chemistry (RSC) has revealed that its members are pessimistic about their status in society. The general public, said the chemists, thinks that chemistry is boring and of little value. Worse, they said, the public thinks chemists are unapproachable. Such negative views have shaped the way that British chemists have promoted themselves and their research; they have focused on counteracting a negative and damaging stereotype about chemistry and chemicals.

Yet as RSC science communicator Chiara Ceci writes in a World View on page 7, the British public does not think these things at all. In another part of the poll, most members of the public were generally positive about chemistry, if a little hazy on its specific benefits and exactly what chemists do. The strongest reaction to the central science was not fear or confusion, but simple indifference. That can be useful. It creates what public-relations experts call a void in the collective consciousness — one that they can fill with positive images.

If the British public likes chemistry — at least more than the chemists believed — then it is positively glowing about science in general. Survey respondents described it with words such as ‘welcoming’, ‘sociable’ and ‘fun’. And a separate poll by Ipsos MORI this year showed that scientists are among the most trusted professionals in Britain; some nine in ten people said that they trust scientists to follow all of the research rules and regulations relevant to them.

How many scientists would say the same? Not many, probably, of the

attendees at this week's 4th World Conference on Research Integrity in Rio de Janeiro, Brazil. As we report on page 14, attendees at the week-end discussed the latest high-profile case of scandal, fraud allegations and retraction. The attention drawn by the paper in question — discussing how views on same-sex marriage can be changed — prompted *The New York Times* to publish an editorial titled ‘Scientists who cheat’. That will not help to fill any void with positive images.

Some scientists do cheat, of course, just as some scientists drive too fast, take drugs and are unfaithful to their spouses. The reasons are complex and varied. With some exceptions, scientific organizations

do not engage with the issue of misconduct as seriously as they should. Why would they, when public confidence and (moral and financial) support remains so high?

Media coverage of the same-sex-marriage retraction was laced with portentous language, claiming that faith and trust in science had been profoundly shaken. Yet, as researchers who follow misconduct issues will know, faith

and trust in science have survived worse in recent years.

That should not be taken as an excuse to ignore the problem of research misconduct or to minimize its importance. And although high-profile fraud makes headlines, a broader and more common set of unappealing behaviours — from corner-cutting to data-juggling — lie under the surface. Convention says that a tiny minority of scientists cheats, yet academics and researchers frequently make the case that irregularities are widespread. A 2014 survey of hundreds of economists, for example, found that 94% admitted to having engaged in at least one “unaccepted” research practice (*S. Necker Res. Policy* **43**, 1747–1759; 2014).

Just like with British chemistry, it seems that the wider public's view of science and research is rosier than that of many people who are directly involved. For how long can this continue? ■

“Nine in ten people trust scientists to follow the rules. How many scientists would say the same?”

To Pluto

The coming months promise to shed new light on the Solar System's underworld.

Pluto has always had something of a raw deal. In classical mythology, while Zeus got sovereignty of heaven and Poseidon mastery of the seas, their brother Pluto (former name, Hades) was lumbered with the underworld and its legions of the dead. Pluto the planet had its discovery delayed by a decade-long legal battle, and then barely made it into the textbooks of the twenty-first century before astronomers decided to strip away its full planetary status. Its classification of dwarf planet is still contested by some. To others, it is the first example of the plutoid category of trans-Neptunian objects.

And then there are its moons. When the fourth of Pluto's satellites was discovered in 2011, a campaign headed by *Star Trek* actor William Shatner proposed the name Vulcan. Preferring to maintain the underworld theme, astronomers chose Cerberus, after the dominion's three-headed guard dog — although because that is already the name of an asteroid, they had to settle on the Greek spelling, Kerberos.

The other minor moons, Styx (gloomy river and one-time plunge pool for the infant Achilles), Hydra (many-headed serpentine sentinel) and Nix (a variant spelling of Nyx, goddess of the night) are joined by a large moon about half the size of Pluto called Charon (ferryman of the Styx and son of Nyx). Charon, some astronomers say, forms with Pluto the Solar System's only binary planet. Or perhaps that should be double plutoid system.

In other words, nothing about this corner of our Solar System has been straightforward. And as the NASA spacecraft New Horizons

hurtles towards it for the first close-up look at these bodies, astronomers this week pose new questions about the heavenly body formerly known as the planet Pluto. The answers, some of which might come when New Horizons flies past the dwarf planet in mid-July, could help researchers to understand how planets and their moons form in the first place.

Little is known about Pluto's creation, but astronomers had assumed that it formed from the remains of a collision between proto-Pluto and a proto-Charon. The smaller moons may have then come together from bits among the swirling impact debris. The 2012 discovery of Styx was already something of a surprise, because studies had suggested the other three smaller moons were packed so closely together that there was no room for another.

On page 45 of this issue, planetary scientists Mark Showalter and Douglas Hamilton describe how they analysed Hubble Space Telescope images to build up a picture of the orbital configurations and brightnesses of Pluto's small moons. They find that Styx, Nix and Hydra are locked together in what astronomers call three-body resonance, a phenomenon that links the timing of their orbits and usually makes their movements stable.

They also suggest that Kerberos is a little out of place. Although Nix and Hydra have bright surfaces similar to that of Charon, Kerberos appears as dark as coal, and this raises questions about how this mixed satellite system might have formed. (Pluto is the brightest of the lot, with a reflectivity roughly that of sea ice.) Their findings are discussed in a News & Views article on page 40.

The mythological name of Hades for the god of the underworld was replaced because Pluto has a more positive spin: it associated the ruler with the mineral wealth found underground. The next few weeks promise a revival of interest in Pluto, and a polishing of its image too. It deserves its time in the (dim and distant) Sun. ■

➔ **NATURE.COM**
To comment online,
click on Editorials at:
go.nature.com/xhunqv

Misplaced faith

The public trusts scientists much more than scientists think. But should it?

British chemists are a diffident and self-conscious bunch. A poll by the Royal Society of Chemistry (RSC) has revealed that its members are pessimistic about their status in society. The general public, said the chemists, thinks that chemistry is boring and of little value. Worse, they said, the public thinks chemists are unapproachable. Such negative views have shaped the way that British chemists have promoted themselves and their research; they have focused on counteracting a negative and damaging stereotype about chemistry and chemicals.

Yet as RSC science communicator Chiara Ceci writes in a World View on page 7, the British public does not think these things at all. In another part of the poll, most members of the public were generally positive about chemistry, if a little hazy on its specific benefits and exactly what chemists do. The strongest reaction to the central science was not fear or confusion, but simple indifference. That can be useful. It creates what public-relations experts call a void in the collective consciousness — one that they can fill with positive images.

If the British public likes chemistry — at least more than the chemists believed — then it is positively glowing about science in general. Survey respondents described it with words such as ‘welcoming’, ‘sociable’ and ‘fun’. And a separate poll by Ipsos MORI this year showed that scientists are among the most trusted professionals in Britain; some nine in ten people said that they trust scientists to follow all of the research rules and regulations relevant to them.

How many scientists would say the same? Not many, probably, of the

attendees at this week's 4th World Conference on Research Integrity in Rio de Janeiro, Brazil. As we report on page 14, attendees at the week-end discussed the latest high-profile case of scandal, fraud allegations and retraction. The attention drawn by the paper in question — discussing how views on same-sex marriage can be changed — prompted *The New York Times* to publish an editorial titled ‘Scientists who cheat’. That will not help to fill any void with positive images.

Some scientists do cheat, of course, just as some scientists drive too fast, take drugs and are unfaithful to their spouses. The reasons are complex and varied. With some exceptions, scientific organizations

do not engage with the issue of misconduct as seriously as they should. Why would they, when public confidence and (moral and financial) support remains so high?

Media coverage of the same-sex-marriage retraction was laced with portentous language, claiming that faith and trust in science had been profoundly shaken. Yet, as researchers who follow misconduct issues will know, faith

and trust in science have survived worse in recent years.

That should not be taken as an excuse to ignore the problem of research misconduct or to minimize its importance. And although high-profile fraud makes headlines, a broader and more common set of unappealing behaviours — from corner-cutting to data-juggling — lie under the surface. Convention says that a tiny minority of scientists cheats, yet academics and researchers frequently make the case that irregularities are widespread. A 2014 survey of hundreds of economists, for example, found that 94% admitted to having engaged in at least one “unaccepted” research practice (*S. Necker Res. Policy* **43**, 1747–1759; 2014).

Just like with British chemistry, it seems that the wider public's view of science and research is rosier than that of many people who are directly involved. For how long can this continue? ■

“Nine in ten people trust scientists to follow the rules. How many scientists would say the same?”

To Pluto

The coming months promise to shed new light on the Solar System's underworld.

Pluto has always had something of a raw deal. In classical mythology, while Zeus got sovereignty of heaven and Poseidon mastery of the seas, their brother Pluto (former name, Hades) was lumbered with the underworld and its legions of the dead. Pluto the planet had its discovery delayed by a decade-long legal battle, and then barely made it into the textbooks of the twenty-first century before astronomers decided to strip away its full planetary status. Its classification of dwarf planet is still contested by some. To others, it is the first example of the plutoid category of trans-Neptunian objects.

And then there are its moons. When the fourth of Pluto's satellites was discovered in 2011, a campaign headed by *Star Trek* actor William Shatner proposed the name Vulcan. Preferring to maintain the underworld theme, astronomers chose Cerberus, after the dominion's three-headed guard dog — although because that is already the name of an asteroid, they had to settle on the Greek spelling, Kerberos.

The other minor moons, Styx (gloomy river and one-time plunge pool for the infant Achilles), Hydra (many-headed serpentine sentinel) and Nix (a variant spelling of Nyx, goddess of the night) are joined by a large moon about half the size of Pluto called Charon (ferryman of the Styx and son of Nyx). Charon, some astronomers say, forms with Pluto the Solar System's only binary planet. Or perhaps that should be double plutoid system.

In other words, nothing about this corner of our Solar System has been straightforward. And as the NASA spacecraft New Horizons

hurtles towards it for the first close-up look at these bodies, astronomers this week pose new questions about the heavenly body formerly known as the planet Pluto. The answers, some of which might come when New Horizons flies past the dwarf planet in mid-July, could help researchers to understand how planets and their moons form in the first place.

Little is known about Pluto's creation, but astronomers had assumed that it formed from the remains of a collision between proto-Pluto and a proto-Charon. The smaller moons may have then come together from bits among the swirling impact debris. The 2012 discovery of Styx was already something of a surprise, because studies had suggested the other three smaller moons were packed so closely together that there was no room for another.

On page 45 of this issue, planetary scientists Mark Showalter and Douglas Hamilton describe how they analysed Hubble Space Telescope images to build up a picture of the orbital configurations and brightnesses of Pluto's small moons. They find that Styx, Nix and Hydra are locked together in what astronomers call three-body resonance, a phenomenon that links the timing of their orbits and usually makes their movements stable.

They also suggest that Kerberos is a little out of place. Although Nix and Hydra have bright surfaces similar to that of Charon, Kerberos appears as dark as coal, and this raises questions about how this mixed satellite system might have formed. (Pluto is the brightest of the lot, with a reflectivity roughly that of sea ice.) Their findings are discussed in a News & Views article on page 40.

The mythological name of Hades for the god of the underworld was replaced because Pluto has a more positive spin: it associated the ruler with the mineral wealth found underground. The next few weeks promise a revival of interest in Pluto, and a polishing of its image too. It deserves its time in the (dim and distant) Sun. ■

➔ **NATURE.COM**
To comment online,
click on Editorials at:
go.nature.com/xhunqv



Take concepts of chemistry out of the classroom

The public image of chemistry is not as negative as some assume — but many people find it hard to connect the field to the real world, says Chiara Ceci.

Much attention is paid to public attitudes to science. But how much do we think about scientists' attitudes towards the public? For members of a profession that thrives on evidence, scientists — and those who communicate, advocate and lobby for science — too frequently rely on incorrect assumptions.

Scientists often believe that the public thinks poorly of them, and perhaps chemists more than most. We assume that people think in stereotypes: men in white coats, explosions and harmful chemicals. We see scare-mongering headlines and misleading advertising about 'artificial' versus 'natural' products. We assume that these messages carry influence, and this shapes everything from the way we hold conversations at parties to more formal efforts in public outreach and education. We are defensive, because we assume that chemistry is under attack.

In fact, public attitudes to chemists and chemistry are much more positive than my colleagues and I would have dared to hope. Our views of public opinion are too negative. I know this because the Royal Society of Chemistry (RSC) has asked members of the public what they think.

The results should cheer up chemists everywhere, and perhaps encourage all scientists to take a more nuanced view of what the public does and does not understand about science.

As part of the study, members and staff of the RSC were asked how they thought the public would respond. The chemists said that public activities should counter the negative stereotypes and myths that surround chemicals. Just over half expected most of the public to say that all chemicals are dangerous and harmful. Some 80% thought that the public would consider chemists unapproachable. And a little less than one-third of the chemists believed that the public would say the benefits of chemistry outweighed the harmful effects. They were wrong.

The results of the study show that the public does not fear or misunderstand chemistry. It does not rave about it either. The majority feeling towards chemistry expressed in the survey was 'neutral'. (Although slightly more people reported positive feelings than negative.)

Overall, three-quarters of people said that chemistry had a positive impact on well-being. A majority agreed that chemistry was part of the solution, not the problem, on issues including sustainable energy, access to food and drinking water, and pollution.

Contrary to our expectations, there were few spontaneous negative associations. Only 1% of the public said that chemistry was boring, difficult or confusing. And only 1% mentioned explosions or blowing things up. Three times as many associated chemistry with "attraction between people".

Research on public attitudes to science and

scientists are relatively common, but work on specific fields, including chemistry, is less so. If we are serious about science communication, we should seek insight into our audience and new ways to measure our impact.

The results of the RSC's study — published this week and available in full at <http://rsc.li/pac> — show that the biggest public challenge facing chemistry is not the need to overturn negative images, but to convince people of the field's relevance. If they have few direct associations with chemistry, people default to memories of school experiences. They see chemistry as an abstract pursuit, rather than a real science.

When asked to describe science more broadly, people used terms such as 'busy' and 'discovery', whereas chemistry was burdened with 'methodical' and 'concentration'. People struggle to imagine how chemistry affects their everyday lives and regard chemists as lacking in

agency: they do not recognize how chemists are involved in the end product of their own work. Chemistry is a "science for scientists", rather than for the public.

Chemistry has long provided insight, building blocks and essential tools that are exploited by researchers in other disciplines. It underpins so many aspects of science that it gets lost. To bridge the distance between chemistry and society, we need to make the field more tangible for people.

How can this be done? A gap between two of the most significant findings offers an opportunity. Although the overwhelming majority of the people polled said that chemistry offered benefits, they did not have much knowledge or experience of how it actually does this. This is a

void that can be filled with positive examples and role models. We are pushing against an open door.

One idea that was popular in the survey was to take chemistry away from the classroom in people's minds and to place it in the kitchen. Food and cooking show people that chemistry is not the sole territory of experts. Members of the public liked the idea that we are all chemists in a way: it builds up their confidence and they start thinking of chemistry as part of life rather than a subject that they will be tested on.

The research threw up one major obstacle for chemistry that may be unique to the United Kingdom. When you tell British people that you are a chemist, it seems that most assume you work in a pharmacy. On these shores, it could be a useful first step for us to say that we are 'scientists who work in chemistry'. More broadly, before chemists or any other groups try to influence public attitudes towards science, it is important that we examine what we think of the public. ■

Chiara Ceci is a science communicator at the Royal Society of Chemistry in Cambridge, UK.
e-mail: cecic@rsc.org

IF THEY HAVE
FEW DIRECT
ASSOCIATIONS WITH
CHEMISTRY,
PEOPLE DEFAULT TO
MEMORIES OF
SCHOOL.

➔ **NATURE.COM**
Discuss this article
online at:
go.nature.com/c7pyvs

RESEARCH HIGHLIGHTS

Selections from the
scientific literature

BIOTECHNOLOGY

Gene therapy halts type 1 diabetes

Transferring part of an insulin gene into liver cells triggers a specific immune response that protects mice from one form of diabetes.

Type 1 diabetes occurs when T cells target and kill insulin-producing islet cells in the pancreas. Maria Grazia Roncarolo of Stanford University in California and her team transferred a gene fragment encoding some of the insulin B chain into the livers of mice engineered to develop this disease, and monitored the effects. Islet cells lived for up to 33 weeks after treatment of animals in a prediabetic state. In untreated mice, around 80% of insulin-producing cells were destroyed. The transfer, in combination with an antibody, reversed symptoms in mice that had developed diabetes.

The gene fragment stimulated regulatory T cells that are specific for insulin, suppressing the insulin-attacking T cells.

Sci. Transl. Med. 7, 289ra81 (2015)

MATERIALS

Memory metal sets flex record

An alloy that can bend and return to its original shape at least 10 million times could prove useful in applications including medical devices and refrigeration.

Bending a 'shape-memory alloy' changes its crystal structure from one phase to another, whereas applying heat reverses that transition. But structural damage causes these materials to lose their shape memory within a few thousand cycles. A team led by Eckhard Quandt at the University of Kiel, Germany, and Manfred

Wuttig at the University of Maryland, College Park, has now created a titanium–nickel–copper alloy ($\text{Ti}_{54}\text{Ni}_{34}\text{Cu}_{12}$) that averts this memory loss. Layers of Ti_2Cu in the material act as templates that guide the complete transition between the two crystal phases.

This template approach could offer a way of creating better shape-memory alloys. *Science* 348, 1004–1007 (2015)

PALAEOCLIMATOLOGY

Tropics feel effect of iceberg thaw

Prehistoric icebergs in the North Atlantic had a greater influence on tropical climate than was previously thought.

Rachael Rhodes of Oregon State University in Corvallis and her colleagues constructed a 60,000-year methane record from a west Antarctic ice core. They found elevated methane levels during cold periods, which seemed to coincide with 'Heinrich events' — the breaking off of icebergs from Greenland glaciers on a massive scale. The team suggests that fresh water flooding into the Atlantic from the thawing icebergs helped to cool the Atlantic region, which contributed to the slowing down of ocean circulation. This led to increased rainfall in the tropics, where wetlands grew and produced more methane.

The climatic impact of some Heinrich events lasted for

says a team led by Sigurjón Jónsson of the King Abdullah University of Science and Technology in Thuwal, Saudi Arabia. The area is seeing a decades-long episode of rifting, in which one plate of Earth's crust pulls apart from another.

Observing newly formed islands in such detail is rare, and the islands will probably remain above water despite erosion, say the authors.

Nature Commun. 6, 7104 (2015)



VOLCANOLOGY

New islands reveal Red Sea rifting

Two volcanic islands that have emerged in the southern Red Sea suggest that the area is more geologically active than was thought.

Sholan Island surfaced in December 2011 and Jadid Island appeared in October 2013, forming part of the Zubair archipelago (pictured). Seismic data and satellite radar measurements show that both islands were created by magma squirting up along north–south fractures under the sea floor,

CHEMICAL BIOLOGY

Antifungal drug dodges resistance

A yeast-killing compound evades drug resistance and is less toxic than a related drug used in the clinic.

The antifungal drug amphotericin B (AmB) does not typically result in resistant fungi, but it kills human cells so can be used only at low doses. To create AmB derivatives that are less toxic to humans and do not cause resistance, Susan

JÓNSSON ET AL./NATURE COMMUN.

Lindquist at the Whitehead Institute for Biomedical Research in Cambridge, Massachusetts, Martin Burke at the University of Illinois at Urbana-Champaign and their colleagues used just three steps of chemical synthesis.

The new compounds killed infectious yeast in the lab and in mice, but were less toxic to human cells and mice than AmB. Yeast strains that were resistant to the compounds *in vitro* were unable to cause lethal infections in mice, unlike non-resistant strains, suggesting that drug-resistant strains are less fit.

The new antifungals kill yeast by pulling out ergosterol molecules from the yeast cell wall, but they do not bind to the similar molecule cholesterol in animal cell membranes.

Nature Chem. Biol. <http://dx.doi.org/10.1038/nchembio.1821> (2015)

EVOLUTION

Migration explains drab female birds

Some female warblers lost their bright colours just as the birds were evolving to become migratory, suggesting that this behavioural change spurred the evolution of sex differences in plumage colour.

To find out why female songbirds are often as colourful as the males in tropical species but less colourful in northern ones, Troy Murphy at Trinity University in San Antonio, Texas, and his colleagues studied 108 species of wood warblers (*Setophaga tigrina*; female pictured left, male pictured right). Migratory species tend to live farther north, and the authors found that the longer the bird's migration, the more distinct the sexes look. In multiple species, these sex differences evolved at around the same time as the birds first began migrating.

The findings suggest that sex differences in colour are driven by the needs of females. Non-migratory females often defend their territories using bright colours to signal fighting ability. But females that migrate rarely act in this way, and bright colours could make them more visible to predators during their migration.

Proc. R. Soc. B 282, 20150375 (2015)

NEUROSCIENCE

Stroke brain still controls device

Rats can use their brain activity to control an external device through an implanted electrode, even after a stroke. The finding suggests that people who have motor problems as a result of a stroke could one day benefit from such brain-machine interfaces.

Karunesh Ganguly at the San Francisco Veterans Affairs Medical Center in California and his colleagues placed electrodes near the part of the motor cortex in the rat brain that was injured by stroke, and then trained the animal to shift the angle of a water-feeding tube using just its brain activity. The team found that stroke-affected rats learned this task as quickly as control animals, even though the stroke animals showed only minimal improvements in movement.

The results suggest that the brain area injured by a stroke can still form new brain-cell connections.

J. Neurosci. 35, 8653–8661 (2015)

CLIMATE-CHANGE BIOLOGY

Warming threat to ocean biodiversity

Marine biodiversity could undergo drastic changes in as much as 70% of the world's oceans if global warming is not limited to below 2 °C by 2100.

Grégory Beaugrand at the CNRS Laboratory of Oceanology and Geosciences in

SOCIAL SELECTION

Popular topics on social media

How best to respond to reviewers

Comments from referees reviewing a paper can sometimes be less than polite, making it tempting for authors to send equally rude replies. But a trio of blog posts emphasizes the importance of professional, constructive responses from authors (see go.nature.com/yzwvmt; go.nature.com/hzp3bg and go.nature.com/hchv3i). The posts, by three ecologists, aim to help researchers to avoid common pitfalls that can lower their chances of publication. Commenters on Twitter appreciated the guidance. Responding to one of the blogs,

Auriel Fournier, a PhD student at the University of Arkansas in Fayetteville, tweeted: "I'm struggling with this right now, this was a very helpful and timely post."

➔ NATURE.COM

For more on popular papers: go.nature.com/d52ezu

Wimereux, France, Richard Kirby at the University of Plymouth, UK, and their colleagues modelled how patterns of biodiversity across the oceans would change under different future climate scenarios, and compared them to patterns over the past 50 years and during prehistoric warm and cold periods.

With low levels of warming (mean temperature rise of roughly 1 °C), around 16% of the ocean would see increased biodiversity through species invasions and about 6% of oceans would experience a decrease. In the most extreme warming scenario, of roughly 3.7 °C, these numbers rise to about 32% and 44%. Such severe warming could produce a greater change in marine biodiversity than has been seen over the past 3 million years or so.

Nature Clim. Change <http://dx.doi.org/10.1038/nclimate2650> (2015)

ECOLOGY

Coral faces algal sabotage

Caribbean coral have been invaded by algae that slow their growth and may have been introduced by humans.

Tye Pettay and Todd LaJeunesse at Pennsylvania State University in University Park and their colleagues



sampled various coral species (*Orbicella faveolata*; pictured) from around the world and analysed the genetics of their symbiotic algae. They found that one alga in the Caribbean, *Symbiodinium trenchii*, comprised just a few lineages that were closely related to those in the Indian and Pacific oceans. Corals living with this symbiont tolerated high temperatures better than those without it, but incorporated calcium into their skeletons at around half the rate.

The findings indicate that this alga invaded the Caribbean thanks to human activities, and could have negative long-term ecological impacts in this region.

Proc. Natl Acad. Sci. USA <http://dx.doi.org/10.1073/pnas.1502283112> (2015)

➔ NATURE.COM

For the latest research published by Nature visit:

www.nature.com/latestresearch



SEVEN DAYS

The news in brief

POLICY

Nuclear restart

Japanese regulators have granted the first permit to restart a nuclear reactor following the Fukushima disaster in 2011. Issued by the country's Nuclear Regulation Authority on 27 May, the permit will allow the Kyushu Electric Power Company in Fukuoka to restart two reactors at the Sendai Nuclear Power Plant, with the first coming online as early as July. Japan halted its 43 operable nuclear reactors in September 2013, pending a safety review by the regulators. The Japanese government is currently considering a draft energy plan, which projects that nuclear power could account for up to 22% of the nation's electricity by 2030.

Reef unlisted

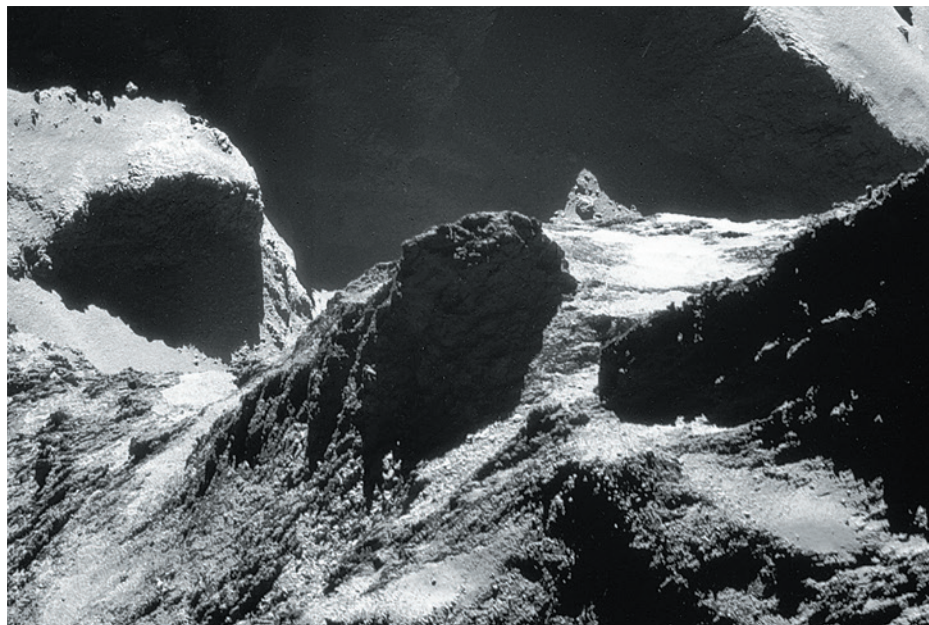
Australia's Great Barrier Reef has not been put on the United Nations' list of heritage sites that are in danger — to the consternation of conservationists. A draft document released by the UN on 29 May instead advises the World Heritage Committee, which decides on the list, to welcome progress made by Australia in protecting the reef. It also advises regular checks to ensure

NUMBER CRUNCH

14.9 m

The number of new cancer cases globally in 2013, according to a study published on 28 May.

Global Burden of Disease Cancer Collaboration JAMA Oncol. <http://doi.org/4w4> (2015).



ESA/ROSETTA/NAVCAM

Rosetta zooms in on heart of comet

This craggy landscape might look like an Alpine peak, but it is actually the nucleus of comet 67P/Churyumov-Gerasimenko, the target of the European Space Agency's Rosetta spacecraft. Almost 1,800 images taken by the probe's navigation camera from as little as 8 kilometres above the comet's surface were released by the

Rosetta team on 28 May. They were taken just before and after the Philae lander touched down on the comet in November last year. This image captures an area spanning 785 metres across the neck of the rubber-duck-shaped comet. Rosetta continues to orbit the comet as it heads for its closest approach to the Sun in August.

that the country's 35-year sustainability plan for the reef is working. The reef's status will be finalized at the committee's meeting in Bonn, Germany, at the end of this month.

China ivory trade

Conservationists welcomed news that China plans to phase out its legal ivory trade. In a symbolic gesture, about 680 kilograms of confiscated illegal ivory were destroyed in Beijing on 29 May. At the event, Zhao Shucong, head of the Chinese State Forestry Administration, declared that China "will strictly control ivory processing and trade until the commercial

processing and sale of ivory and its products are eventually halted."

EVENTS

US anthrax blunder

The US Department of Defense announced on 27 May that it had accidentally shipped live anthrax spores to labs in nine US states and a US military base in South Korea. The facilities that received the samples did not have systems in place to protect employees against anthrax exposure because they were expecting to receive killed spores. It is unclear how many people were exposed. Some workers are now receiving

preventive treatment. The incident follows a series of biosafety lapses last summer at US government agencies. See go.nature.com/dc2anv for more.

Antelope die-off

Almost half of the global population of saiga antelopes has been killed off in just a few weeks. The United Nations Environment Programme (UNEP) said on 28 May that more than 120,000 of the critically endangered animals (*Saiga tatarica*) have died in the Betpak-Dala area of central Kazakhstan. Four main populations of saigas live in Kazakhstan and Russia, and a 2014 census reported

that about 262,000 animals live worldwide. UNEP says that a preliminary analysis suggests that both biological and environmental factors may have caused the die-off. See go.nature.com/nkqc81 for more.

AWARDS

Shaw prizes

The three US\$1-million prizes from the Shaw Prize Foundation were announced in Hong Kong on 1 June. William Borucki of NASA's Ames Research Center in Mountain View, California, received the astronomy prize for leading the Kepler exoplanet-hunting mission. Microbiologists Bonnie Bassler of Princeton University in New Jersey and Peter Greenberg of the University of Washington in Seattle shared the biology prize for their discovery of bacterial communication, or 'quorum sensing'. Gerd Faltings of the University of Bonn in Germany and Henryk Iwaniec of Rutgers University in New Jersey shared the mathematics prize for their breakthroughs in number theory.

PEOPLE

Oxford head

Political scientist Louise Richardson (pictured) looks set to become the



next vice-chancellor of the University of Oxford, UK, having been nominated for the role on 28 May. Richardson, whose research covers terrorism and security issues, will be the first woman to head the university in its more than 800-year history. If her appointment is approved by the university's decision-making body, known as Congregation, Richardson will take over from current vice-chancellor Andrew Hamilton on 1 January 2016. She has held leadership positions at the University of St Andrews, UK, and Harvard University in Cambridge, Massachusetts.

FUNDING

Funds ring-fenced

Three basic-research funding programmes have been sheltered from a controversial budget raid on the European Union (EU) Horizon 2020 funding framework. The siphoned money — which

now stands at €2.2 billion (US\$ 2.4 billion) instead of €2.7 billion — will establish the European Fund for Strategic Investments. The European Parliament, Council and Commission agreed on 28 May to ring-fence the budgets of the European Research Council, the Marie Skłodowska-Curie research fellowship and a programme that supports researchers in low-income EU countries. The agreement must be ratified by the European Parliament on 24 June.

FACILITIES

Hawaii compromise

At least one-quarter of the 13 telescopes atop Hawaii's sacred mountain Mauna Kea must be removed by the time the planned Thirty Meter Telescope (TMT) begins operating there next decade, Hawaiian governor David Ige said on 26 May. Construction of the TMT halted in early April when protestors blocked the road to the mountain's summit. The governor also said that the University of Hawaii at Manoa, which leases the land on which the telescopes sit, must provide cultural training for Mauna Kea visitors and promise that this will be the last telescope to be built at the site. See page 15 and go.nature.com/ufodat for more.

COMING UP

6-9 JUNE

The latest developments in human and medical genetics will be discussed at the European Human Genetics Conference in Glasgow, UK. go.nature.com/tndjqh

6-13 JUNE

Delegates from United Nations member states meet in Rome for the Food and Agricultural Organization's annual conference. Topics include addressing poverty, food security and climate-change impacts. go.nature.com/aniorh

7-11 JUNE

Scientists gather in San Antonio, Texas, for the American Nuclear Society's annual meeting. This year's theme is 'Nuclear technology: an essential part of the solution'. go.nature.com/lna2dk

X-ray upgrade

The European Synchrotron Radiation Facility (ESRF) in Grenoble, France, began a major upgrade on 29 May. Already the world's most intense X-ray source, the ESRF is investing €150 million (US\$165 million) in a new accelerator that will deliver even more tightly focused beams, creating X-rays that are 100 times brighter. Installing the new machine in the ESRF's present tunnels will entail a 17-month shutdown starting at the end of 2018. The upgraded source should allow researchers to image materials and observe chemical reactions at the nanometre scale.

➔ NATURE.COM

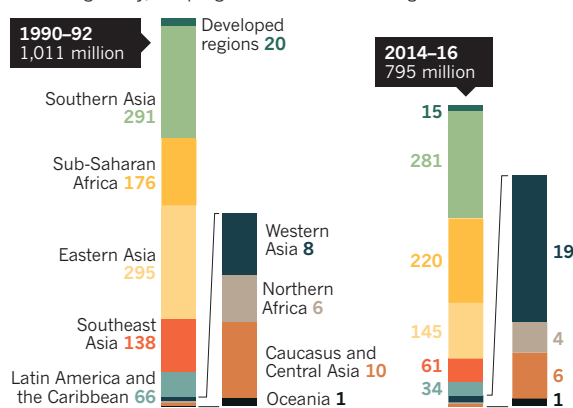
For daily news updates see: www.nature.com/news

TREND WATCH

The number of undernourished people worldwide has fallen to 795 million people, down from 1 billion in the early 1990s, according to a report by the Food and Agriculture Organization of the United Nations. Economic growth and social policies — which promote better nutrition, health care and education — have helped to beat hunger in many developing regions. There has been little progress in southern Asia and sub-Saharan Africa, where political instability has led to food insecurity.

GLOBAL HUNGER

The number of undernourished people has fallen by about one-fifth globally, but progress differs between regions.



► with *Famiglia Cristiana* magazine that they are looking into theories that the bacterium may have been deliberately introduced into the area, or became entrenched because agricultural scientists failed to monitor the region properly, either deliberately or through neglect.

On 12 May, the Italian Association of Scientific Societies in Agriculture (AISSA), which represents 4,000 scientists in Italy, published a public letter defending the Puglian scientists and their work. “The claims do not have a scientific basis — that’s what has shocked the scientific community,” says Vincenzo Gerbi, AISSA president.

Puglian scientists have had to contend with public criticism, too. Several popular blogs devoted to the *Xylella* emergency have cast doubt on scientists’ ways of working and their results — saying, for example, that a cure exists but is being suppressed. And Peacelink, an Italian non-governmental organization, wrote to the EU health commissioner in March saying that *Xylella* had not been proved to be the source of the outbreak, and that the deaths were instead the result of a fungus that could be



Donato Boscia researches *Xylella fastidiosa* at Italy’s Institute for Sustainable Plant Protection.

eliminated without destroying trees. An expert panel of the European Food Safety Authority debunked these suggestions in a report published in April. “It’s frustrating to hear all these complaints when you think you are doing a

public service,” says Anna Maria D’Onghia, head of the pest-management division at the IAMB, who has been questioned by police. “We are always being attacked for doing too little, or the wrong things.”

Boscia says that the “attempts to delegitimize the results of scientific research” have been worse than the police investigations. But it is not all bad news for Puglian scientists. On 27 May, the regional government announced a €2-million (US\$2.2-million) fund for projects that might aid the diagnosis, epidemiology and monitoring of the bacterium. It said that a ‘containment area’ in the province of Lecce — where the bacterium is now endemic, making complete eradication impossible — will be used as an open-air *Xylella* laboratory. National and European research agencies have also promised money, says Boscia. “The outdoor laboratory would be perfect for all of us — and also allow critics to put their own theories to the test.” ■

1. Saponari, M., Boscia, D., Nigro, F. & Martelli, G. P. *J. Plant Pathol.* <http://dx.doi.org/10.4454/JPP.V95I3.035> (2013).
2. Elbeaino, T. et al. *Phytopathol. Mediterr.* **53**, 328–232 (2014).

POLITICAL SCIENCE

Retracted gay-marriage study debated at misconduct meet-up

Over rum cocktails at the World Conference on Research Integrity, experts discussed what can be learnt from the fallout of a flawed political-science paper.

BY RICHARD VAN NOORDEN, RIO DE JANEIRO

The world’s largest gathering of specialists in research misconduct kicked off on 31 May in Rio de Janeiro, Brazil, shortly after science’s latest scandal broke. On the evening before the start of sessions on how to diagnose and remedy ethical faults in research, delegates to the 4th World Conference on Research Integrity sipped caipirinhas, Brazil’s national cocktail — and swapped views on what could be gleaned from a flawed political-science study.

The paper in question, which claimed to show that short conversations with a canvasser who is gay could encourage voters to support same-sex marriage, made headlines across the world when it was published in *Science* last December (M. J. LaCour and D. P. Green *Science* **346**, 1366–1369; 2014) — and again when it was retracted last week (*Science* <http://doi.org/4zt>; 2015). “The case is very much on our minds,” said Melissa Anderson, a co-organizer

of the meeting who studies scientific integrity at the University of Minnesota in Minneapolis.

Although the case throws up new instances of misconduct, and of inadequate supervision by senior academics, delegates to the Rio conference felt that, in general, the case illuminated little about the academic system that a steady drip-drip of research misconduct has not already highlighted. The main challenge, said Brian Martinson, a social scientist at the HealthPartners Institute for Education and Research in Minneapolis, is how to create a supportive environment that incentivizes reliable, reproducible research. “A lot of people think the bad stuff in science comes from academics being greedy or narcissistic — but that ignores how the structural arrangements in science, like the decline of funding and stable academic positions in the United States, leads people into bad behaviour,” he said.

In the latest twist in the debacle, co-author Michael LaCour, a graduate student in political science at the University of California, Los Angeles (UCLA), has admitted to misrepresenting

his funding sources and the incentives he used to attract people to take part in the study. In a 29 May online reply to researchers who had spotted irregularities in his survey data (see go.nature.com/acpxnh), LaCour said that he had deleted his raw data for reasons of confidentiality and admitted that he did not get ethical approval from an institutional review board before he did the work, or before he submitted it to *Science*. The document did not include convincing evidence that he had conducted the surveys.

LaCour told *The New York Times* that he stands by his finding — but his co-author Donald Green, a political scientist at the University of Columbia in New York City, does not: Green requested the paper’s retraction after three outside scientists told him about irregularities in its survey data, and he apologized for

“Academia should be concerned that its system of checks and balances has problems.”

not adequately supervising LaCour's work.

Delegates in Rio broadly agreed that the case highlights the need for better supervision by senior academics. "Academia should be concerned that its system of checks and balances has problems," said Nicholas Steneck, who studies research integrity at the University of Michigan in Ann Arbor. "It will never be perfect, but it is far from perfect now." Sabine Kleinert, a co-organizer of the research-integrity conference and senior executive editor at *The Lancet*, said: "The wider lessons are still the same as many of these cases throw up — that of the role of the co-authors in taking steps to be accountable for the data, and the role of institutions in safeguarding or having repositories for the data underlying research that is done there."

On the plus side, the retraction came swiftly after queries were raised about the data, noted Ivan Oransky, a journalist who runs the blog Retraction Watch, which first reported that Green had asked for the study to be retracted. Researchers posted their objections online on 19 May (see go.nature.com/qgrdav) and *Science* retracted the study on 28 May. That is in stark contrast to an earlier misconduct case — involving the cancer geneticist Anil Potti — in which whistleblowers tried for years to quietly raise concerns with Potti's institution, Duke University in Durham, North Carolina, before papers were finally retracted and Potti resigned.

Mysteries still linger in the LaCour case. In the 23-page reply that he posted on 29 May, LaCour raises statistical objections to the criticisms levelled at him. These "couldn't possibly be more beside the point", said Jelte Wicherts, a statistician at Tilburg University in the Netherlands.

LaCour also posted snapshots of an apparent survey set up with the firm Qualtrics, but these actually relate to a pilot study that was abandoned, according to Chris Skovron, a political scientist at the University of Michigan. He had worked on the study until LaCour cut off the collaboration, he says.

As to whether canvassing changes voters' attitudes, Brian Calfano, a political scientist at Missouri State University in Springfield, says that other literature suggests that it can, but that replication or extension of the LaCour-Green work would have to be done to know for certain that it does so in this particular scenario. LaCour wrote in his 29 May document that Calfano had replicated his study, but Calfano says that his own work is only a preliminary finding relating to a different kind of canvassing of voters. He shared the finding with LaCour at an early stage, but is not willing to stand behind it until further tests are completed.

LaCour did not respond to a request for comment. His graduate supervisor, political scientist Lynn Vavreck, says that UCLA has an ongoing inquiry into the issue. ■



PHILIP ROSENBERG/GETTY

The Gemini North telescope is one of several world-class astronomy facilities on Mauna Kea.

ASTRONOMY

Hawaiian telescopes pruned

Cultural fight over sacred mountain Mauna Kea prompts rule change.

BY ALEXANDRA WITZE

The quest to build one of the world's largest telescopes has radically reshaped the future of a Hawaiian mountain. On 26 May, Hawaii governor David Ige announced that the controversial Thirty Meter Telescope (TMT) could be built on Mauna Kea as planned — but that three or four of the mountain's 13 existing telescopes must be dismantled over the next decade.

Mauna Kea is home to such world-leading facilities as the twin 10-metre Keck telescopes and the 8-metre-class Subaru and Gemini North telescopes (see 'Starry summit'). Speculation is already running high about which telescopes will be removed, and when.

Native Hawaiians regard Mauna Kea as sacred, and they view building the TMT as

another violation of an already desecrated site. Construction was to have begun in early April, but was put on hold when protests broke out on the mountain, in Honolulu and at other sites across the islands.

Ige's announcement, a direct response to the unrest, accelerates long-standing plans to decommission Mauna Kea telescopes as they grow older. "The idea of removing telescopes from the summit is not a new one," says Doug Simons, director of the Canada-France-Hawaii Telescope on Mauna Kea. "It's the natural evolution of a set of observatories that are ageing in a lot of ways."

The governor has ordered the University of Hawaii at Manoa, which leases the mountain top as a science reserve, to close 25% of the observatories there before the TMT begins operation in the mid-2020s. The ►

not adequately supervising LaCour's work.

Delegates in Rio broadly agreed that the case highlights the need for better supervision by senior academics. "Academia should be concerned that its system of checks and balances has problems," said Nicholas Steneck, who studies research integrity at the University of Michigan in Ann Arbor. "It will never be perfect, but it is far from perfect now." Sabine Kleinert, a co-organizer of the research-integrity conference and senior executive editor at *The Lancet*, said: "The wider lessons are still the same as many of these cases throw up — that of the role of the co-authors in taking steps to be accountable for the data, and the role of institutions in safeguarding or having repositories for the data underlying research that is done there."

On the plus side, the retraction came swiftly after queries were raised about the data, noted Ivan Oransky, a journalist who runs the blog Retraction Watch, which first reported that Green had asked for the study to be retracted. Researchers posted their objections online on 19 May (see go.nature.com/qgrdav) and *Science* retracted the study on 28 May. That is in stark contrast to an earlier misconduct case — involving the cancer geneticist Anil Potti — in which whistleblowers tried for years to quietly raise concerns with Potti's institution, Duke University in Durham, North Carolina, before papers were finally retracted and Potti resigned.

Mysteries still linger in the LaCour case. In the 23-page reply that he posted on 29 May, LaCour raises statistical objections to the criticisms levelled at him. These "couldn't possibly be more beside the point", said Jelte Wicherts, a statistician at Tilburg University in the Netherlands.

LaCour also posted snapshots of an apparent survey set up with the firm Qualtrics, but these actually relate to a pilot study that was abandoned, according to Chris Skovron, a political scientist at the University of Michigan. He had worked on the study until LaCour cut off the collaboration, he says.

As to whether canvassing changes voters' attitudes, Brian Calfano, a political scientist at Missouri State University in Springfield, says that other literature suggests that it can, but that replication or extension of the LaCour-Green work would have to be done to know for certain that it does so in this particular scenario. LaCour wrote in his 29 May document that Calfano had replicated his study, but Calfano says that his own work is only a preliminary finding relating to a different kind of canvassing of voters. He shared the finding with LaCour at an early stage, but is not willing to stand behind it until further tests are completed.

LaCour did not respond to a request for comment. His graduate supervisor, political scientist Lynn Vavreck, says that UCLA has an ongoing inquiry into the issue. ■



PHILIP ROSENBERG/GETTY

The Gemini North telescope is one of several world-class astronomy facilities on Mauna Kea.

ASTRONOMY

Hawaiian telescopes pruned

Cultural fight over sacred mountain Mauna Kea prompts rule change.

BY ALEXANDRA WITZE

The quest to build one of the world's largest telescopes has radically reshaped the future of a Hawaiian mountain. On 26 May, Hawaii governor David Ige announced that the controversial Thirty Meter Telescope (TMT) could be built on Mauna Kea as planned — but that three or four of the mountain's 13 existing telescopes must be dismantled over the next decade.

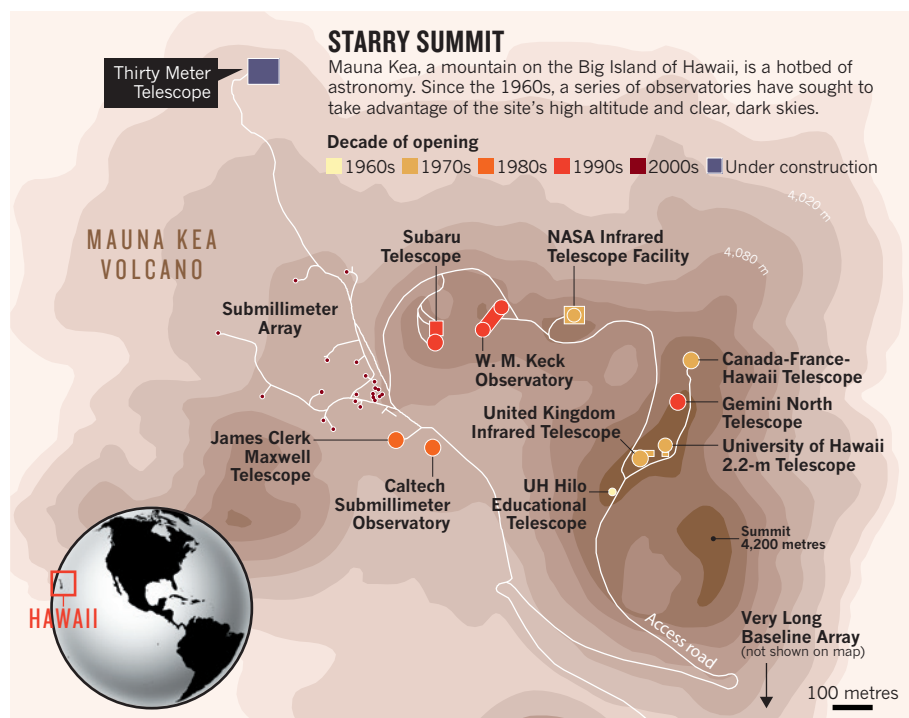
Mauna Kea is home to such world-leading facilities as the twin 10-metre Keck telescopes and the 8-metre-class Subaru and Gemini North telescopes (see 'Starry summit'). Speculation is already running high about which telescopes will be removed, and when.

Native Hawaiians regard Mauna Kea as sacred, and they view building the TMT as

another violation of an already desecrated site. Construction was to have begun in early April, but was put on hold when protests broke out on the mountain, in Honolulu and at other sites across the islands.

Ige's announcement, a direct response to the unrest, accelerates long-standing plans to decommission Mauna Kea telescopes as they grow older. "The idea of removing telescopes from the summit is not a new one," says Doug Simons, director of the Canada-France-Hawaii Telescope on Mauna Kea. "It's the natural evolution of a set of observatories that are ageing in a lot of ways."

The governor has ordered the University of Hawaii at Manoa, which leases the mountain top as a science reserve, to close 25% of the observatories there before the TMT begins operation in the mid-2020s. The ►



SOURCE: UNIV. HAWAII

► university owns a 2.2-metre optical telescope that is the oldest on Mauna Kea, dating back to 1970; a 0.9-metre educational optical telescope; and the 3.8-metre United Kingdom Infrared Telescope (UKIRT). It also manages the 3-metre Infrared Telescope Facility for NASA, which studies planets, asteroids and stars.

"We have always made the point that space on the top of the mountain should only be populated by the absolutely best telescopes," says Günter Hasinger, director of the university's Institute for Astronomy.

EYES SHUT

The first to go will be the Caltech Submillimeter Observatory, the closure of which was announced in 2009. It will end operations

in September, and then will be dismantled. Other telescopes, including Keck, Gemini and Subaru, involve complex international agreements that cannot be overwritten by the state of Hawaii alone. All have committed to operating on the mountain to the end of 2033.

"We intend to continue operating until we come to a point where the science return isn't worth it," says Raymond Blundell, an astronomer at the Harvard-Smithsonian Center for Astrophysics in Cambridge, Massachusetts, and director of the Submillimeter Array, an eight-dish radio telescope array on Mauna Kea.

Some of the telescopes on the mountain have just begun a new lease of life. Earlier this year, a consortium of east Asian observatories took over the submillimetre-wavelength

James Clerk Maxwell Telescope to study how galaxies and stars form, among other things. And UKIRT has just begun a long-term science programme that involves studying space debris and near-Earth asteroids, says director Richard Green, an astronomer at the University of Arizona in Tucson.

For now, Green continues to plan for nearly two decades ahead — although he acknowledges that the situation may change. "We realize there has to be more attention paid to the culture and how the mountain is taken care of," he says.

In addition to closing telescopes, Ige levied a list of other requirements. When the University of Hawaii's lease ends in 2033, it must return to state protection more than 40 square kilometres of the 45 it leases. Visitors to the summit must receive cultural training. And the TMT location, which is a few hundred metres beneath the actual summit, will be the last area on Mauna Kea on which any telescope will ever be built.

Nearly every telescope project on Mauna Kea in recent years has faced local protests, although not the sustained high emotion inspired by the TMT. John Johnson, an astronomer at Harvard University in Cambridge, says that astronomers should not be on the mountain top at all, given the history of the Hawaiian Islands. "This goes way beyond whether we construct this telescope or not," he says. "It has to do with the fact that the United States stole Hawaii from a sovereign people and proceeded to systematically erase that culture."

The university says it will have a plan for removing 25% of the observatories by the end of this year. The TMT has not announced whether and when it will resume construction, and legal challenges to the project are still wending their way through Hawaiian courts.

Two competing next-generation telescopes are being planned for Chile. ■

PHYSICS

Atomic clocks face off

Next generation of hyper-precise timekeepers can only be tested against each other.

BY ELIZABETH GIBNEY

Happy birthday, caesium clock. Now move over. As the atomic clock used to define time itself turns 60, tests are set to begin on a new generation of clocks that are designed to give the caesium version a run for its money.

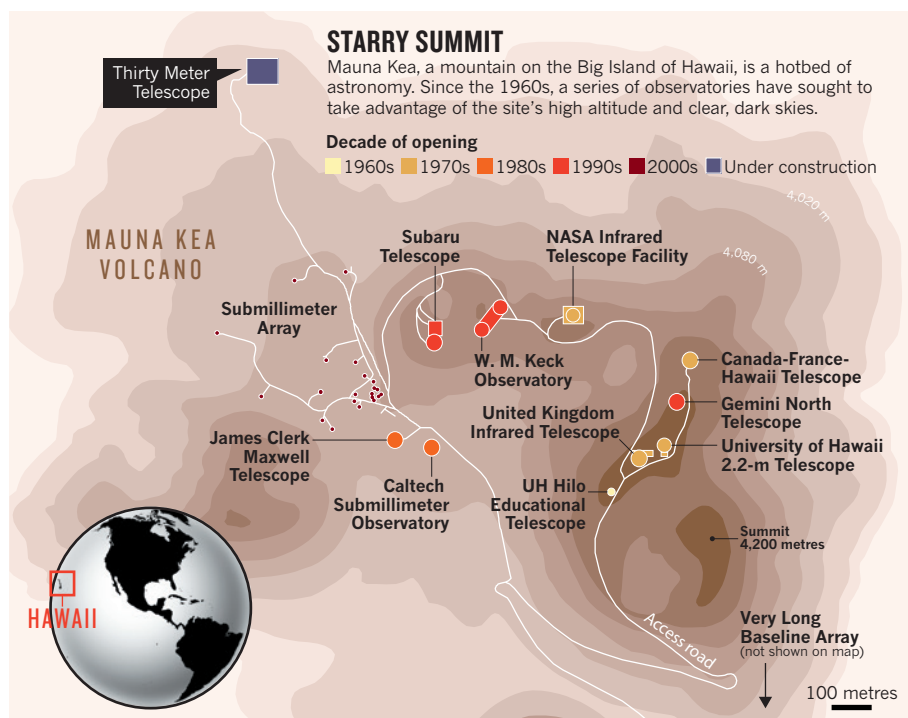
Such timekeepers would enable a variety of

experiments, including testing whether the fundamental constants of nature really are constant over time, and, eventually, a more precise official definition of the second.

Atomic clocks track the frequency of electromagnetic waves emitted by atoms as they change energy states. First demonstrated by British physicist Louis Essen in June 1955, the caesium clock became the world's official

timekeeper in 1967 — defining the second as the time it takes for the microwaves that are absorbed or emitted when caesium atoms switch between states to cycle through 9,192,631,770 oscillations.

Over the past decade, various laboratories have created prototype optical atomic clocks, which use different elements such as strontium and ytterbium that emit and absorb



SOURCE: UNIV. HAWAII

STARRY SUMMIT

Mauna Kea, a mountain on the Big Island of Hawaii, is a hotbed of astronomy. Since the 1960s, a series of observatories have sought to take advantage of the site's high altitude and clear, dark skies.

Decade of opening

1960s 1970s 1980s 1990s 2000s Under construction

► university owns a 2.2-metre optical telescope that is the oldest on Mauna Kea, dating back to 1970; a 0.9-metre educational optical telescope; and the 3.8-metre United Kingdom Infrared Telescope (UKIRT). It also manages the 3-metre Infrared Telescope Facility for NASA, which studies planets, asteroids and stars.

"We have always made the point that space on the top of the mountain should only be populated by the absolutely best telescopes," says Günter Hasinger, director of the university's Institute for Astronomy.

EYES SHUT

The first to go will be the Caltech Submillimeter Observatory, the closure of which was announced in 2009. It will end operations

in September, and then will be dismantled. Other telescopes, including Keck, Gemini and Subaru, involve complex international agreements that cannot be overwritten by the state of Hawaii alone. All have committed to operating on the mountain to the end of 2033.

"We intend to continue operating until we come to a point where the science return isn't worth it," says Raymond Blundell, an astronomer at the Harvard-Smithsonian Center for Astrophysics in Cambridge, Massachusetts, and director of the Submillimeter Array, an eight-dish radio telescope array on Mauna Kea.

Some of the telescopes on the mountain have just begun a new lease of life. Earlier this year, a consortium of east Asian observatories took over the submillimetre-wavelength

James Clerk Maxwell Telescope to study how galaxies and stars form, among other things. And UKIRT has just begun a long-term science programme that involves studying space debris and near-Earth asteroids, says director Richard Green, an astronomer at the University of Arizona in Tucson.

For now, Green continues to plan for nearly two decades ahead — although he acknowledges that the situation may change. "We realize there has to be more attention paid to the culture and how the mountain is taken care of," he says.

In addition to closing telescopes, Ige levied a list of other requirements. When the University of Hawaii's lease ends in 2033, it must return to state protection more than 40 square kilometres of the 45 it leases. Visitors to the summit must receive cultural training. And the TMT location, which is a few hundred metres beneath the actual summit, will be the last area on Mauna Kea on which any telescope will ever be built.

Nearly every telescope project on Mauna Kea in recent years has faced local protests, although not the sustained high emotion inspired by the TMT. John Johnson, an astronomer at Harvard University in Cambridge, says that astronomers should not be on the mountain top at all, given the history of the Hawaiian Islands. "This goes way beyond whether we construct this telescope or not," he says. "It has to do with the fact that the United States stole Hawaii from a sovereign people and proceeded to systematically erase that culture."

The university says it will have a plan for removing 25% of the observatories by the end of this year. The TMT has not announced whether and when it will resume construction, and legal challenges to the project are still wending their way through Hawaiian courts.

Two competing next-generation telescopes are being planned for Chile. ■

PHYSICS

Atomic clocks face off

Next generation of hyper-precise timekeepers can only be tested against each other.

BY ELIZABETH GIBNEY

Happy birthday, caesium clock. Now move over. As the atomic clock used to define time itself turns 60, tests are set to begin on a new generation of clocks that are designed to give the caesium version a run for its money.

Such timekeepers would enable a variety of

experiments, including testing whether the fundamental constants of nature really are constant over time, and, eventually, a more precise official definition of the second.

Atomic clocks track the frequency of electromagnetic waves emitted by atoms as they change energy states. First demonstrated by British physicist Louis Essen in June 1955, the caesium clock became the world's official

timekeeper in 1967 — defining the second as the time it takes for the microwaves that are absorbed or emitted when caesium atoms switch between states to cycle through 9,192,631,770 oscillations.

Over the past decade, various laboratories have created prototype optical atomic clocks, which use different elements such as strontium and ytterbium that emit and absorb

NPL higher-frequency photons in the visible spectrum. This finer slicing of time should, in principle, make them more accurate: it is claimed that the best of these clocks gain or lose no more than one second every 15 billion years (10^{18} seconds) — longer than the current age of the Universe — making them 100 times more precise than their caesium counterparts. Optical clocks are claimed to be the best time-keepers in existence, but the only way to verify this in practice is to compare different models against each other and see whether they agree.

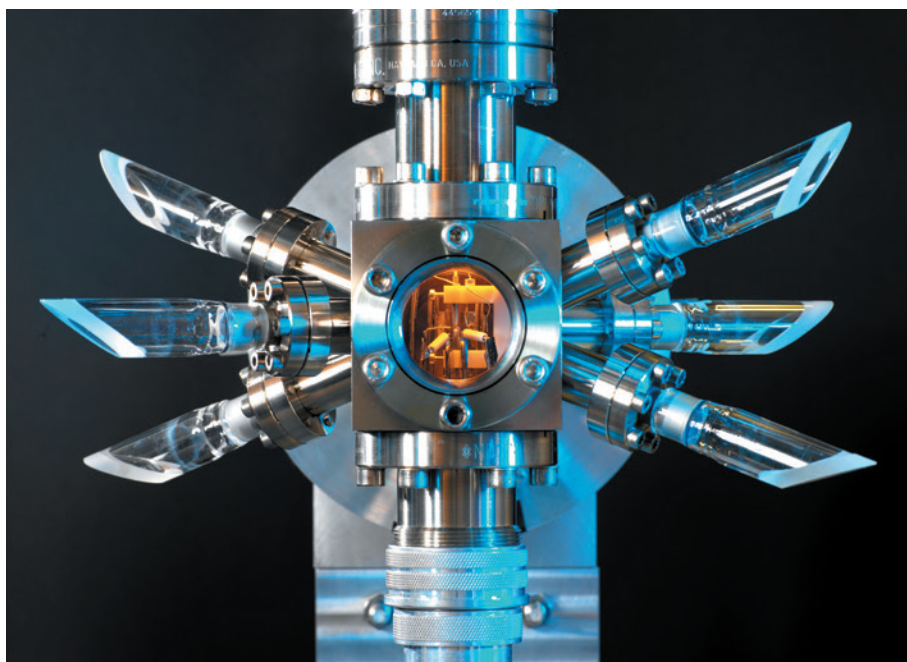
Starting on 4 June, four European laboratories will kick off this testing process — the National Physical Laboratory (NPL) in Teddington, UK; the department of Time-Space Reference Systems at the Paris Observatory; the German National Metrology Institute (PTB) in Braunschweig, Germany; and Italy's National Institute of Metrology Research in Turin. Between them, the labs host a variety of optical clocks that harness different elements in different experimental set-ups.

For the first test, each institute will transmit a signal related to the optical frequency of its clocks to a satellite, which will beam the frequencies back down to the other labs. This will allow the labs to compare the frequencies of light emitted by their clocks and thus measure whether they all keep time to the same beat.

"It's really exciting," says Andrew Ludlow, a physicist at an optical-clock powerhouse run by the US National Institute of Standards and Technology (NIST) in Boulder, Colorado, who is not involved in the project. "A couple of comparisons of optical clocks have been made before, but on nothing like this scale." With more clocks, it should be easier to root out the source of any discrepancies, adds Helen Margolis, a physicist at the NPL.

She notes that a higher frequency does not necessarily mean a more accurate clock, because varying sensitivities to environmental factors can affect the ability of different clocks to keep time in practice. The hope is that all the clocks will agree, suggesting that they are as precise as claimed. If some clocks do not, it will indicate that improvements are needed.

The initial test is only a prelude to a more accurate test, however, because it has one big limitation: to beam light to a satellite, it must be converted to a microwave frequency — which means that much of the potential extra accuracy gained by using visible light is lost.



A strontium-ion optical clock housed at the National Physical Laboratory in Teddington, UK.

By increasing the rate of data transfer, the European labs hope to improve the accuracy of current state-of-the-art satellite comparisons by ten, but it will still be limited to one part in 10^{16} . So the main function of the satellite test is to build confidence in optical clocks and show that they perform at least as well as existing caesium clocks, say researchers.

The more accurate test will transmit signals in the visible spectrum through fibre-optic cables to the labs. This will allow the clocks to be compared with an accuracy similar to the expected accuracies of the clocks themselves. Some of

the labs have already established such links, and tests have begun on sections between Paris and Teddington, and Paris and Braunschweig. "Eventually, this would allow a four-way comparison. That's the vision," says Margolis.

"There is friendly competition," she adds. "We all think our clocks have a very good potential for achieving the highest accuracy or we wouldn't be working on them."

Fibre-optic links between optical atomic

clocks already exist elsewhere, such as between the NIST lab and its partner lab JILA, also in Boulder. But these span shorter distances than the European network and are mostly between just two labs. "Europe is in a unique position as it has a high density of the best clocks in the world," says Fritz Riehle, a physicist at PTB.

Even if the clocks pass this later test, usurping the caesium clock to create a more precise definition of the second will not be easy. International atomic time — on which coordinated universal time, or UTC, is based — is currently calculated by averaging measurements from hundreds of atomic clocks. Doing the same with optical atomic clocks would require a way to aggregate time at this precise level; using the fibre-optic method across oceans is not currently feasible.

In the meantime, ever more precise time is important for improving global positioning systems, high-resolution radio astronomy and the time-stamping of financial transactions, as well as spotting tiny variations in fundamental constants. "Most attempts to unify gravity with other forces would lead to variations of fundamental constants in the expanding universe," says Marianna Safronova, a theorist at the University of Delaware in Newark. ■

"We all think our clocks have a very good potential for achieving the highest accuracy."


**MORE
ONLINE**

TOP STORY



Merging black holes are behind spectacular galactic fireworks
go.nature.com/vfshb6

MORE NEWS

- Massive tank reveals hurricanes' inner workings go.nature.com/aazwob
- US military accidentally ships live anthrax to labs go.nature.com/dc2anv
- Alzheimer's research takes a leaf from the prion notebook go.nature.com/m5e6hy

NATURE PODCAST



How immune cells escape the brain, who's CRISPR-ing what, and the case of the disappearing lake nature.com/nature/podcast



Joanne Liu visiting an MSF trauma centre in Kunduz, Afghanistan.

PUBLIC HEALTH

MSF takes bigger global-health role

Relief agency sees mission expanding after Ebola outbreak.

BY ERIKA CHECK HAYDEN,
GENEVA, SWITZERLAND

Joanne Liu, president of Médecins Sans Frontières (MSF), is not overly concerned with diplomacy. Participating in a panel in Geneva, Switzerland, on 20 May with officials from the United Nations, the World Health Organization (WHO), Liberia and Sierra Leone, she propped her head on her hand, stared into space and rolled her eyes during another speaker's remarks. When she spoke, she excoriated the world for leaving West Africa vulnerable to the largest Ebola epidemic in history. "We're failing, guys," she said.

Few would contest Liu's right to make that assertion. MSF (also known as Doctors Without Borders) was the organization that alerted the world to the scale of the Ebola epidemic. Its speedy response has both reinforced its role as the world's caregiver in health crises and catapulted it to new prominence in the international health community. In the past year,

Liu has addressed the UN General Assembly and met with world leaders. Donations to her non-governmental organization (NGO) rose to €1.14 billion (US\$1.24 billion) last year; in the United States, donations climbed by 50% from the previous year. "It's a defining moment," Liu told *Nature* during an interview at MSF's headquarters in Geneva. "We have a voice that we have never had before; we need to use that very smartly."

At a time when the WHO is lacking the funds and authority to address pressing global health needs, there is room for an organization such as MSF to take a greater role in both chronic and acute medical crises, as well as in research that enhances preparedness for those situations. But Liu insists that MSF cannot become "the world's doctor." "We need to be careful that we don't spread ourselves too thin," she says.

MSF was founded in 1971 by French doctors and journalists who decried a Red Cross edict not to speak out about the conditions they saw

while treating victims of the Nigerian Civil War in the secessionist state of Biafra. Since then, the organization has provided medical services to people affected by wars, natural disasters, famines and infectious-disease outbreaks around the world. In 1999, it was awarded the Nobel Peace Prize for "pioneering humanitarian work on several continents".

It was the first international NGO to send staff to Guinea when Ebola emerged there in March 2014, and its declaration that month that the outbreak was "unprecedented" has proved tragically correct. Since then, MSF has deployed more than 1,300 international staff and 4,000 local people to fight Ebola in Guinea, Sierra Leone and Liberia.

WEALTH OF EXPERIENCE

MSF has fought Ebola outbreaks in nine countries, but it took a leadership role in the latest epidemic in ways that it had not before. It taught staff from other organizations — including the WHO and the US Centers for Disease Control and Prevention — how to treat people with Ebola. It distributed home disinfection kits to hundreds of thousands of people in Monrovia and other communities, and delivered incinerators to dispose of bodies when Liberian burial teams could not keep pace.

Independence — one of MSF's core principles — allows the organization to move faster than governmental and inter-governmental organizations, but it has also caused tension. In July, for instance, MSF forbade Michael Gbakie, a disease-surveillance officer at Kenema Government Hospital in Sierra Leone, from visiting four of his colleagues who were being cared for in a nearby MSF Ebola treatment centre, even though he had a decade of experience working around people with similar diseases. "They have a protocol, and they will not just allow everyone to go in there if they are not working with them," Gbakie says. MSF eventually relented: Gbakie saw one of his colleagues, physician Sheik Humarr Khan, on the day he died.

Health officials from other countries affected by the Ebola outbreak alluded to these tensions at the MSF-organized event on 20 May: "I hope this outbreak will allow [you] to examine the way you work with your colleagues and governments," Miatta Gbanya, coordinator of the Liberian Ebola response, told Liu.

Liu acknowledges that the organization could have communicated better with local leaders and communities. "You need to get the community on board. This is something that we underestimated," she says.

The organization has undergone difficult transitions in its mission before. When it began treating people with HIV in the 1990s, it had to shift its approach from emergency medicine to delivering chronic care. Much more recently, it has found itself managing diabetes and other diseases found more in

KIM CLAUSEN/MSF

middle-income nations in its treatment of refugees from Syria's civil war.

The Ebola crisis has not only strengthened MSF's patient-care role, but also boosted its involvement in research. The NGO used proceeds from its Nobel prize to help found the Drugs for Neglected Diseases initiative (see *Nature* **505**, 142; 2014), which funds drug-development work on diseases that mainly affect poor people, and to start its Access Campaign, which pushes both to increase the availability of drugs and for the development of lower-cost medicines to treat illnesses in poor countries.

In West Africa, MSF is running clinical trials of potential Ebola treatments, pushing for more research into the disease and contemplating the creation of a biobank of patient samples along with the WHO and other organizations.

EXPANDED ROLE

The temptation is for MSF to step in to fill a void left by retreating funding and authority at the WHO and other international health organizations. Although WHO member states approved some measures to strengthen the organization's outbreak response during last month's World Health Assembly (see page 5), observers say that these measures will not address the core problems that slowed its response to Ebola in West Africa.

"The Assembly failed utterly in addressing the underlying deficiencies," says Lawrence Gostin, director of the WHO-affiliated Centers for Law and the Public's Health at Georgetown University in Washington DC. "There's a great yearning on the part of WHO to be the global health coordinator, but the future of WHO's leadership in this area is very much in doubt."

"The Assembly failed utterly in addressing the underlying deficiencies."

The UN secretary-general and the World Bank are examining the WHO's mandate in responding to health emergencies; the World Bank has outlined details for a Pandemic Emergency Facility that would fund early responses to outbreaks.

But such proposals have tended to focus on preventing the spread of outbreaks from poor to rich nations, says epidemiologist David Heymann at the London School of Hygiene and Tropical Medicine. "The paradigm is, the donors will be happy to jump up and provide funding for a rapid outbreak response, but they're not so ready to provide funding for health-systems strengthening," he says.

MSF finds itself increasingly enlisted to clean up the local and regional health emergencies that result from inadequate infrastructure. A whiteboard at its international office

in Geneva tracks staff deployments to crises in some of the 70 or so countries where it is currently working, including Ukraine, Iraq, the Democratic Republic of the Congo and South Sudan.

To help the world to prepare for the next time that one of those local or regional situations erupts into an international crisis, Liu is convening an open discussion in Dakar, Senegal, this month to which she plans to invite all those involved in the Ebola outbreak. It is one of several post-Ebola discussions under way on the global health response; others are being organized by the US Institute of Medicine, Harvard University in Cambridge, Massachusetts, and the London School of Hygiene and Tropical Medicine, the World Bank and the UN.

Many of these discussions are focusing on matters of international law, such as deficiencies in the International Health Regulations, which are supposed to govern countries' behaviour in health emergencies. Liu, who considers these questions less important than the practical concern of how to get treatment to people who need it, nonetheless says that she is looking forward to the upcoming MSF event.

"We're going to get a lot of people who haven't treated a patient who are now the world experts, and who are going to give us lessons," Liu says. "We can only smile at this." ■



CRISPR, THE DISRUPTOR

BY HEIDI LEDFORD

A powerful gene-editing technology is the biggest game changer to hit biology since PCR. But with its huge potential come pressing concerns.

Three years ago, Bruce Conklin came across a method that made him change the course of his lab.

Conklin, a geneticist at the Gladstone Institutes in San Francisco, California, had been trying to work out how variations in DNA affect various human diseases, but his tools were cumbersome. When he worked with cells from patients, it was hard to know which sequences were important for disease and which were just background noise. And engineering a mutation into cells was expensive and laborious work. "It was a student's entire thesis to change one gene," he says.

Then, in 2012, he read about a newly published technique¹ called CRISPR that would allow researchers to quickly change the DNA of nearly any organism — including humans. Soon after, Conklin abandoned his previous approach to modelling disease and adopted this new one. His lab

is now feverishly altering genes associated with various heart conditions. "CRISPR is turning everything on its head," he says.

The sentiment is widely shared: CRISPR is causing a major upheaval in biomedical research. Unlike other gene-editing methods, it is cheap, quick and easy to use, and it has swept through labs around the world as a result. Researchers hope to use it to adjust human genes to eliminate diseases, create hardier plants, wipe out pathogens and much more besides. "I've seen two huge developments since I've been in science: CRISPR and PCR," says John Schimenti, a geneticist at Cornell University in Ithaca, New York. Like PCR, the gene-amplification method that revolutionized genetic engineering after its invention in 1985, "CRISPR is impacting the life sciences in so many ways," he says.

But although CRISPR has much to offer, some scientists are worried

ILLUSTRATIONS BY SÉBASTIEN THIBAUT

that the field's breakneck pace leaves little time for addressing the ethical and safety concerns such experiments can raise. The problem was thrust into the spotlight in April, when news broke that scientists had used CRISPR to engineer human embryos (see *Nature* 520, 593–595; 2015). The embryos they used were unable to result in a live birth, but the report² has generated heated debate over whether and how CRISPR should be used to make heritable changes to the human genome. And there are other concerns. Some scientists want to see more studies that probe whether the technique generates stray and potentially risky genome edits; others worry that edited organisms could disrupt entire ecosystems. “This power is so easily accessible by labs — you don’t need a very expensive piece of equipment and people don’t need to get many years of training to do this,” says Stanley Qi, a systems biologist at Stanford University in California. “We should think carefully about how we are going to use that power.”

RESEARCH REVOLUTION

Biologists have long been able to edit genomes with molecular tools. About ten years ago, they became excited by enzymes called zinc finger nucleases that promised to do this accurately and efficiently. But zinc fingers, which cost US\$5,000 or more to order, were not widely adopted because they are difficult to engineer and expensive, says James Haber, a molecular biologist at Brandeis University in Waltham, Massachusetts. CRISPR works differently: it relies on an enzyme called Cas9 that uses a guide RNA molecule to home in on its target DNA, then edits the DNA to disrupt genes or insert desired sequences. Researchers often need to order only the RNA fragment; the other components can be bought off the shelf. Total cost: as little as \$30. “That effectively democratized the technology so that everyone is using it,” says Haber. “It’s a huge revolution.”

CRISPR methodology is quickly eclipsing zinc finger nucleases and other editing tools (see ‘The rise of CRISPR’). For some, that means abandoning techniques they had taken years to perfect. “I’m depressed,” says Bill Skarnes, a geneticist at the Wellcome Trust Sanger Institute in Hinxton, UK, “but I’m also excited.” Skarnes had spent much of his career using a technology introduced in the mid-1980s: inserting DNA into embryonic stem cells and then using those cells to generate genetically modified mice. The technique became a laboratory workhorse, but it was also time-consuming and costly. CRISPR takes a fraction of the time, and Skarnes adopted the technique two years ago.

Researchers have traditionally relied heavily on model organisms such as mice and fruit flies, partly because they were the only species that came with a good tool kit for genetic manipulation. Now CRISPR is making it possible to edit genes in many more organisms. In April, for example, researchers at the Whitehead Institute for Biomedical Research in Cambridge, Massachusetts, reported using CRISPR to study *Candida albicans*, a fungus that is particularly deadly in people with weakened immune systems, but had been difficult to genetically manipulate in the lab³. Jennifer Doudna, a CRISPR pioneer at the University of California, Berkeley, is keeping a list of CRISPR-altered creatures. So far, she has three dozen entries, including disease-causing parasites called trypanosomes and yeasts used to make biofuels.

Yet the rapid progress has its drawbacks. “People just don’t have the time to characterize some of the very basic parameters of the system,” says Bo Huang, a biophysicist at the University of California, San Francisco. “There is a mentality that as long as it works, we don’t have to understand how or why it works.” That means that researchers occasionally run up against glitches. Huang and his lab struggled for two months to adapt CRISPR for use in imaging studies. He suspects that the delay would have been shorter had more been known about how to optimize the design of guide RNAs, a basic but important nuance.

By and large, researchers see these gaps as a minor price to pay for a powerful technique. But Doudna has begun to have more serious concerns about safety. Her worries began at a meeting in 2014, when she saw a postdoc present work in which a

virus was engineered to carry the CRISPR components into mice. The mice breathed in the virus, allowing the CRISPR system to engineer mutations and create a model for human lung cancer⁴. Doudna got a chill; a minor mistake in the design of the guide RNA could result in a CRISPR that worked in human lungs as well. “It seemed incredibly scary that you might have students who were working with such a thing,” she says. “It’s important for people to appreciate what this technology can do.”

“There is a mentality that as long as it works, we don’t have to understand how or why it works.”

Andrea Ventura, a cancer researcher at Memorial Sloan Kettering Cancer Center in New York and a lead author of the work, says that his lab carefully considered the safety implications: the guide sequences were designed to target genome regions that were unique to mice, and the virus was disabled such that it could not replicate. He agrees that it is important to anticipate even remote risks. “The guides are not designed to cut the human genome, but you never know,” he says. “It’s not very likely, but it still needs to be considered.”

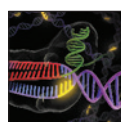
EDITING OUT DISEASE

Last year, bioengineer Daniel Anderson of the Massachusetts Institute of Technology in Cambridge and his colleagues used CRISPR in mice to correct a mutation associated with a human metabolic disease called tyrosinaemia⁵. It was the first use of CRISPR to fix a disease-causing mutation in an adult animal — and an important step towards using the technology for gene therapy in humans.

The idea that CRISPR could accelerate the gene-therapy field is a major source of excitement in scientific and biotechnology circles. But as well as highlighting the potential, Anderson’s study showed how far there is to go. To deliver the Cas9 enzyme and its guide RNA into the target organ, the liver, the team had to pump large volumes of liquid into blood vessels — something that is not generally considered feasible in people. And the experiments corrected the disease-causing mutation in just 0.4% of the cells, which is not enough to have an impact on many diseases.

Over the past two years, a handful of companies have sprung up to develop CRISPR-based gene therapy, and Anderson and others say that the first clinical trials of such a treatment could happen in the next one or two years. Those first trials will probably be scenarios in which the CRISPR components can be injected directly into tissues, such as those in the eye, or in which cells can be removed from the body, engineered in the lab and then put back. For example, blood-forming stem cells might be corrected to treat conditions such as sickle-cell disease or β -thalassaemia. It will be a bigger challenge to deliver the enzyme and guide RNA into many other tissues, but researchers hope that the technique could one day be used to tackle a wider range of genetic diseases.

Yet many scientists caution that there is much to do before CRISPR can be deployed safely and efficiently. Scientists need to increase the efficiency of editing, but at the same time make sure that they do not introduce changes elsewhere in the genome that have consequences for health. “These enzymes will cut in places other than the places you have designed them to cut, and that has lots of implications,” says Haber. “If



CRISPR GENE EDITING
A Nature collection
nature.com/crispr



“It will be hard to detect whether something has been mutated conventionally or genetically engineered.”

you’re going to replace somebody’s sickle-cell gene in a stem cell, you’re going to be asked, ‘Well, what other damage might you have done at other sites in the genome?’”

Keith Joung, who studies gene editing at Massachusetts General Hospital in Boston, has been developing methods to hunt down Cas9’s off-target cuts. He says that the frequency of such cuts varies widely from cell to cell and from one sequence to another: his lab and others have seen off-target sites with mutation frequencies ranging from 0.1% to more than 60%. Even low-frequency events could potentially be dangerous if they accelerate a cell’s growth and lead to cancer, he says.

With so many unanswered questions, it is important to keep expectations of CRISPR under control, says Katrine Bosley, chief executive of Editas, a company in Cambridge, Massachusetts, that is pursuing CRISPR-mediated gene therapy. Bosley is a veteran of commercializing new technologies, and says that usually the hard part is convincing others that an approach will work. “With CRISPR it’s almost the opposite,” she says. “There’s so much excitement and support, but we have to be realistic about what it takes to get there.”

CRISPR ON THE FARM

While Anderson and others are aiming to modify DNA in human cells, others are targeting crops and livestock. Before the arrival of gene-editing techniques, this was generally done by inserting a gene into

the genome at random positions, along with sequences from bacteria, viruses or other species that drive expression of the gene. But the process is inefficient, and it has always been fodder for critics who dislike the mixing of DNA from different species or worry that the insertion could interrupt other genes. What is more, getting genetically modified crops approved for use is so complex and expensive that most of those that have been modified are large commodity crops such as maize (corn) and soya beans.

With CRISPR, the situation could change: the ease and low cost may make genome editing a viable option for smaller, speciality crops, as well as animals. In the past few years, researchers have used the method to engineer petite pigs and to make disease-resistant wheat and rice. They have also made progress towards engineering dehorned cattle, disease-resistant goats and vitamin-enriched sweet oranges. Doudna anticipates that her list of CRISPR-modified organisms will grow. “There’s an interesting opportunity to consider doing experiments or engineering pathways in plants that are not as important commercially but are very interesting from a research perspective — or for home vegetable gardens,” she says.

CRISPR’s ability to precisely edit existing DNA sequences makes for more-accurate modifications, but it also makes it more difficult for regulators and farmers to identify a modified organism once it has been released. “With gene editing, there’s no longer the ability to really track engineered products,” says Jennifer Kuzma, who studies science policy at North Carolina State University in Raleigh. “It will be hard to detect whether something has been mutated conventionally or genetically engineered.”

That rings alarm bells for opponents of genetically modified crops, and it poses difficult questions for countries trying to work out how to regulate gene-edited plants and animals. In the United States, the Food and Drug Administration has yet to approve any genetically modified animal for human consumption, and it has not yet announced how it will handle gene-edited animals.

Under existing rules, not all crops made by genome editing would require regulation by the US Department of Agriculture (see *Nature* **500**, 389–390; 2013). But in May, the agriculture department began to seek input on how it can improve regulation of genetically modified crops — a move that many have taken as a sign that the agency is re-evaluating its rules in light of technologies such as CRISPR. “The window has been cracked,” says Kuzma. “What goes through the window remains to be seen. But the fact that it’s even been cracked is pretty exciting.”

ENGINEERED ECOSYSTEMS

Beyond the farm, researchers are considering how CRISPR could or should be deployed on organisms in the wild. Much of the attention has focused on a method called gene drive, which can quickly sweep an edited gene through a population. The work is at an early stage, but such a technique could be used to wipe out disease-carrying mosquitoes or ticks, eliminate invasive plants or eradicate herbicide resistance in pigweed, which plagues some US farmers.

Usually, a genetic change in one organism takes a long time to spread through a population. That is because a mutation carried on one of a pair of chromosomes is inherited by only half the offspring. But a gene drive allows a mutation made by CRISPR on one chromosome to copy itself to its partner in every generation, so that nearly all offspring will inherit the change. This means that it will speed through a population exponentially faster than normal (see ‘Gene drive’) — a mutation engineered into a mosquito could spread through a large population within a season. If that mutation reduced the number of offspring a mosquito produced, then the population could be wiped out, along with any malaria parasites it is carrying.

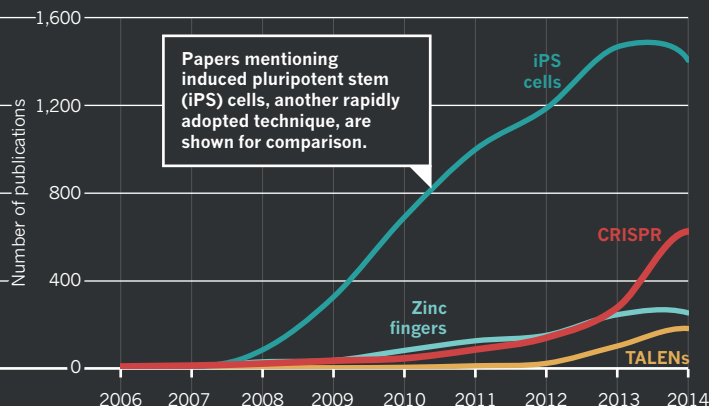
But many researchers are deeply worried that altering an entire population, or eliminating it altogether, could have drastic and unknown consequences for an ecosystem: it might mean that other pests emerge, for example, or it could affect predators higher up the food chain. And ►

THE RISE OF CRISPR

DNA sequences called CRISPRs (clustered regularly interspaced short palindromic repeats) are part of a bacterial defence system. After researchers showed in 2012 that CRISPRs could be used to edit genomes, use of the tools quickly spread, as reflected by sharp rises in publications, patent applications and funding.

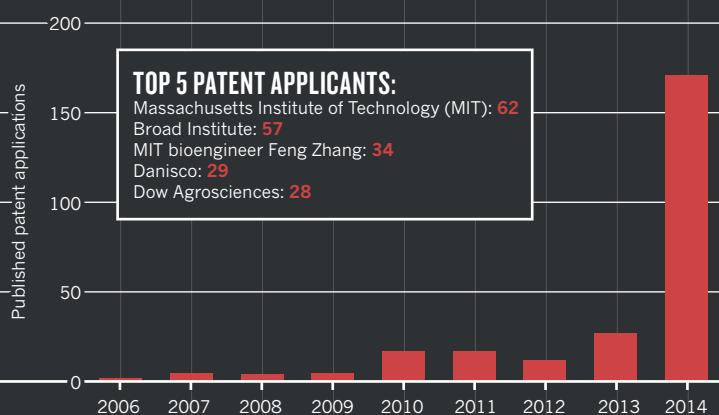
PUBLICATIONS

The number of papers about CRISPR has outstripped the numbers mentioning the gene-editing technologies known as TALENs and zinc fingers.



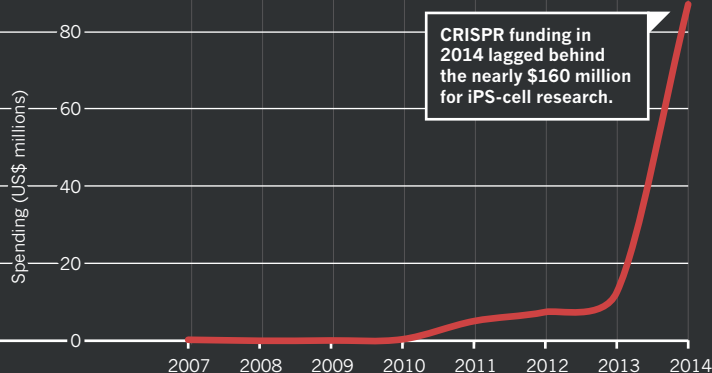
PATENTS

In 2014, worldwide patent applications that mention CRISPR leapt and a patent battle intensified.



FUNDING

A sharp jump in US National Institutes of Health funding for projects involving CRISPR is a harbinger of future advances.



A BRIEF HISTORY OF CRISPR

Key events in the CRISPR story.

December 1987

Researchers find CRISPR sequences in *Escherichia coli*, but do not characterize their function⁸.

July 1995

CRISPR sequences are found to be common in other microbes⁹.

March 2007

Scientists at food company Danisco determine that the repeats are part of a bacterial defence against viruses¹⁰.

October 2011

CARIBOU BIOSCIENCES
Berkeley, California

Focus: Research, industry, therapeutics, agriculture

Raised:
\$11 MILLION

November 2013

EDITAS-MEDICINE

Cambridge, Massachusetts

Focus: Therapeutics

Raised:
\$43 MILLION

November 2013

CRISPR THERAPEUTICS

Basel, Switzerland

Focus: Therapeutics

Raised:
\$89 MILLION

November 2014

INTELLIA THERAPEUTICS

Cambridge, MA

Focus: Therapeutics

Raised:
\$15 MILLION

June 2012

Researchers report that CRISPR can be used to perform genome editing¹.

January 2013

CRISPR is used in mouse and human cells, fuelling rapid uptake of the technique by researchers¹¹⁻¹³.

March 2013

The University of California and others file for a patent on the findings¹.

April 2014

MIT and the Broad Institute are granted a patent on CRISPR gene editing, sparking a fierce patent battle.

March 2015

Report of the first CRISPR gene drive, which can spread an edited gene rapidly through a population⁶.

April 2015

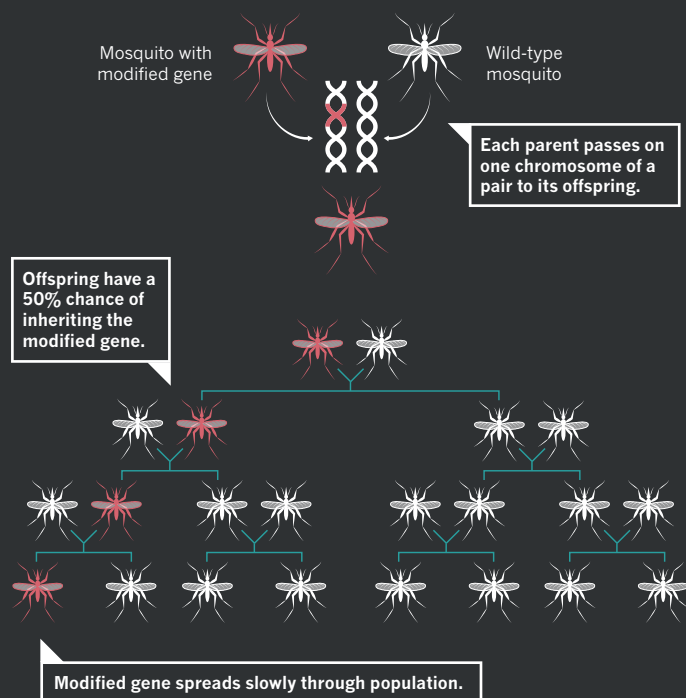
Researchers report that they have edited human embryos with CRISPR, triggering an ethical debate².

DESIGN BY **WES FERNANDES**;
 SOURCES: PUBLICATIONS;
 SCOPUS; PATENTS: THE LENS;
 FUNDING: NIH REPORTER.

GENE DRIVE

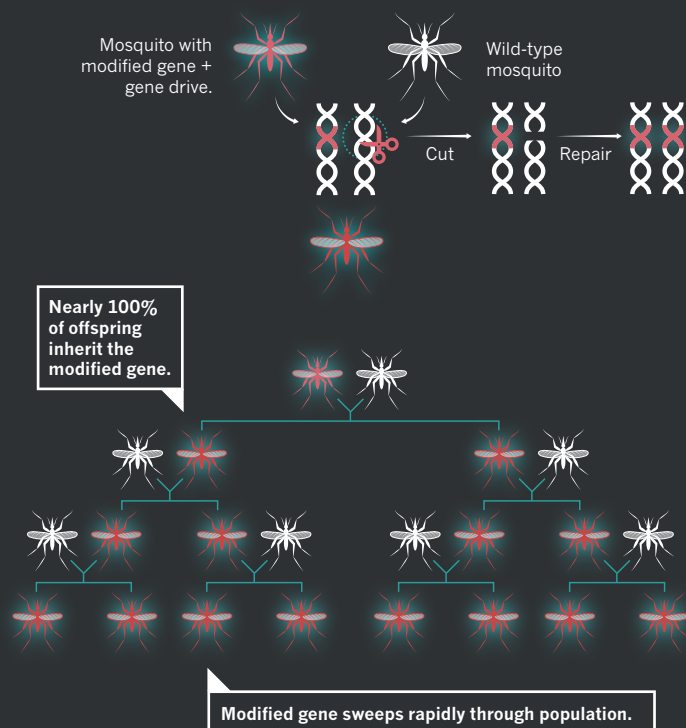
CRISPR gene editing can be used to propagate a genetic modification rapidly through generations. It might be used to eradicate a population of disease-carrying mosquitoes.

STANDARD INHERITANCE



GENE-DRIVE INHERITANCE

The gene-drive system cuts the partner chromosome, then the repair process copies the modification to this chromosome.



► researchers are also mindful that a guide RNA could mutate over time such that it targets a different part of the genome. This mutation could then race through the population, with unpredictable effects.

“It has to have a fairly high pay-off, because it has a risk of irreversibility — and unintended or hard-to-calculate consequences for other species,” says George Church, a bioengineer at Harvard Medical School in Boston. In April 2014, Church and a team of scientists and policy experts wrote a commentary in *Science*⁶ warning researchers about the risks and proposing ways to guard against accidental release of experimental gene drives.

At the time, gene drives seemed a distant prospect. But less than a year later, developmental biologist Ethan Bier of the University of California, San Diego, and his student Valentino Gantz reported that they had designed just such a system in fruit flies⁷. Bier and Gantz had used three layers of boxes to contain their flies and adopted lab safety measures usually used for malaria-carrying mosquitoes. But they did not follow all the guidelines urged by the authors of the commentary, such as devising a method to reverse the engineered change. Bier says that they were conducting their first proof-of-principle experiments, and wanted to know whether the system worked at all before they made it more complex.

For Church and others, this was a clear warning that the democratization of genome editing through CRISPR could have unexpected and undesirable outcomes. “It is essential that national regulatory authorities and international organizations get on top of this — really get on top of it,” says Kenneth Oye, a political scientist at the Massachusetts Institute of Technology and lead author of the *Science* commentary. “We need more action.” The US National Research Council has formed a panel to discuss gene drives, and other high-level discussions are starting to take place. But Oye is concerned that the science is moving at lightning speed, and that regulatory changes may happen only after a high-profile gene-drive release.

The issue is not black and white. Micky Eubanks, an insect ecologist at Texas A&M University in College Station, says that the idea of gene drives shocked him at first. “My initial gut reaction was ‘Oh my god, this is terrible. It’s so scary,’” he says. “But when you give it more thought and weigh it against the environmental changes that we have already made and continue to make, it would be a drop in the ocean.”

Some researchers see lessons for CRISPR in the arc of other new technologies that prompted great excitement, concern and then disappointment when teething troubles hit. Medical geneticist James Wilson of the University of Pennsylvania in Philadelphia was at the centre of booming enthusiasm over gene therapy in the 1990s — only to witness its downfall when a clinical trial went wrong and killed a young man. The field went into a tailspin and has only recently begun to recover. The CRISPR field is still young, Wilson says, and it could be years before its potential is realized. “It’s in the exploration stage. These ideas need to ferment.”

Then again, Wilson has been bitten by the CRISPR bug. He says that he was sceptical of all the promises being made about it until his own lab began to play with the technique. “It’s ultimately going to have a role in human therapeutics,” he says. “It’s just really spectacular.” ■

Heidi Ledford is a senior reporter for Nature in Cambridge, Massachusetts.

1. Jinek, M. *et al. Science* **337**, 816–821 (2012).
2. Liang, P. *et al. Protein Cell* **6**, 363–372 (2015).
3. Vyas, V. K., Barrasa, M. I. & Fink, G. R. *Sci. Adv.* **1**, e1500248 (2015).
4. Maddalo, D. *et al. Nature* **516**, 423–427 (2014).
5. Yin, H. *et al. Nature Biotechnol.* **32**, 551–553 (2014).
6. Oye, K. A. *et al. Science* **345**, 626–628 (2014).
7. Gantz, V. M. & Bier, E. *Science* **348**, 442–444 (2015).
8. Ishino, Y., Shinagawa, H., Makino, K., Amemura, M. & Nakata, A. *J. Bacteriol.* **169**, 5429–5433 (1987).
9. Mojica, F. J., Ferrer, C., Juez, G. & Rodríguez-Valera, F. *Mol. Microbiol.* **17**, 85–93 (1995).
10. Barrangou, R. *et al. Science* **315**, 1709–1712 (2007).
11. Cong, L. *et al. Science* **339**, 819–823 (2013).
12. Mali, P. *et al. Science* **339**, 823–826 (2013).
13. Jinek, M. *et al. eLife* **2**, e00471 (2013).

THE BILLION-DOLLAR BIOTECH

*Moderna Therapeutics has big ambitions and a bankroll to match.
How a fledgling start-up became one of the most highly valued private drug firms ever.*

BY ELIE DOLGIN

At a breakfast meeting two-and-a-half years ago, Pascal Soriot, the newly minted chief executive of pharmaceutical giant Astra-Zeneca, shook hands on the first major drug-development deal of his tenure. It was a research partnership with little-known biotechnology company Moderna Therapeutics of Cambridge, Massachusetts. Worth up to US\$420 million, the deal was unusually large for a start-up that offered only a fledgling drug technology, especially one that had not yet even been tested in humans.

That was the first of many huge cheques for Moderna. This January alone, the company announced a record \$500 million in financing from a handful of investors, pushing it over the \$1-billion fund-raising mark and making it the most highly valued venture-backed private company in drug development today.

"Everybody is talking about this," says Johannes Fruehauf, who runs LabCentral, an incubator and shared laboratory facility in the bustling Cambridge biotechnology hub known as Kendall Square. "It's inevitable with these large, eye-popping numbers."

Investors are clearly attracted to Moderna's technology, which aims to use chemically modified messenger RNA (mRNA) molecules to produce any protein that the body might need. Backers have also bought into the reputation of the company's high-profile co-founders and its charismatic chief executive, whose bold ambition is to move 100 drugs into clinical testing within the next decade, treating everything from cancer to rare genetic diseases.

But Moderna is also something of a mystery. As a private firm, it has revealed very little of its research. Its academic founders have published only one study¹ using Moderna's mRNA therapeutics technology in rodents. And the company itself has disclosed scientific details (including some about early work in non-human primates) only through patent filings. Add in questions about the strength of Moderna's patent position and the troubled history of other RNA-based drugs, and some analysts are wondering whether the company will be able to deliver on its promises.

"I don't think they've really overcome the critical issues," says Dirk Haussecker, an RNA-therapeutics consultant in Rastatt, Germany. Based on the publicly available records, he says, "I haven't seen anything from Moderna that makes me say, 'Oh, they really have a competitive edge or they're very different — in a league of their own.' From a science point of view, it doesn't seem to make sense." But as a business it is surging ahead.

A SIMPLE APPROACH

On paper, the idea of mRNA therapy seems simple. If someone cannot produce enough of a certain protein, or produces a broken version, doctors could inject their cells with mRNA that codes for a replacement protein. This would avoid the risks of tinkering with the genome permanently, as is done in some forms of gene therapy. And whereas growth factors, antibodies and other complex 'biological' drugs can be produced in vats by bioengineered cells, these

are mostly limited to secreted molecules. An mRNA-based therapy would be able to make proteins that operate inside the cell as well. "mRNA delivery would reinvent how we as an industry tackle many diseases," says Peter Kolchinsky, managing partner of RA Capital Management in Boston, Massachusetts, which is one of the latest investors in Moderna.

But delivery is tricky. In the early 1990s, scientists first demonstrated that injected mRNA could generate proteins in mice² and rats³. But protein production was low and transient, and the mRNA seemed too unstable to make a suitable drug. Years later, researchers also realized that lab-synthesized mRNA tends to spur an immune attack after it is injected, triggering potentially dangerous inflammatory responses. So a handful of researchers started working their way around the body's defences by modifying the RNA.

Moderna traces its origins to one such effort, in the laboratory of Derrick Rossi. A stem-cell biologist at Boston Children's Hospital, Rossi and his postdoc Luigi Warren were trying to use mRNA to coax cells into a 'pluripotent' state, capable of giving rise to many cell types. To avoid triggering inflammation, the researchers replaced some of the RNA's molecular building blocks — the nucleosides uridine and cytidine — with pseudouridine and 5-methylcytidine. This makes the RNA look more like something that the cell would produce itself, because invaders such as bacteria cannot usually make these modifications to their own mRNA.

It worked. In 2010, Rossi and Warren filed to



patent their method for making stem cells and later published the results of their research⁴.

The work caught the attention of Robert Langer, a respected bioengineer and serial entrepreneur from the Massachusetts Institute of Technology in Cambridge, and Noubar Afeyan, chief executive of Cambridge biotech investment firm Flagship Ventures. Both men immediately saw the sweeping potential of the modified mRNA. The idea of side-stepping the cell's defences "was intriguing instantaneously", says Afeyan, who now chairs Moderna's board of directors.

Rossi and Langer brought in a third academic co-founder — cardiovascular biologist Kenneth Chien, formerly at Harvard Medical School in Boston and now at the Karolinska Institute in Stockholm — and together they launched Moderna in September 2010. The name was Rossi's invention, a portmanteau of modified and RNA.

There was just one problem. "Our paper really put the whole thing on the map but, ironically, our paper didn't have anything really to do with mRNA therapeutics," says Warren, who now runs Stemiotics, a company in San Diego, California, that makes custom-order stem cells using modified mRNA. The modified RNAs were not even their innovation.

They got the idea from Katalin Karikó and Drew Weissman at the University of Pennsylvania in Philadelphia (UPenn). In two papers that largely fell under the radar at the time, these scientists showed that using pseudouridine and 5-methylcytidine made mRNA nearly invisible to cellular defences, both

*in vitro*⁵ and in mice⁶. In 2005, the pair started filing to patent the technology for therapeutic purposes.

DIFFICULT DEALINGS

Karikó and Weissman created a company called RNARx, which received close to \$900,000 in small-business grants from the US government. In mice and monkeys they showed⁷ that regular mRNA injections could boost production of erythropoietin, a hormone that is prescribed to treat some forms of anaemia.

The company's research efforts ended there, however, in part because of disagreements between the researchers and the University of Pennsylvania over the licensing of their intellectual property (IP). The university eventually sold the licence to Cellscript, a firm in Madison, Wisconsin, for an undisclosed sum. Cellscript has mostly used the rights to market kits for making mRNAs with modified nucleosides, but chief executive Gary Dahl says that the company also has "an interest in therapeutics". He declined to discuss specifics.

Karikó and Weissman's patent posed a challenge for Moderna. A 2010 internal report from Flagship Ventures, which was nurturing Moderna into existence at the time, states that if scientists could not identify alternatives to pseudouridine and 5-methylcytidine, "our company technology may be limited to licensing IP from UPenn".

Moderna needed to find a way around the patent, and the task fell to its first employee, Jason Schrum. A nucleic-acid biochemist by

training, Schrum set to work testing different types of modified nucleoside. He bought RNA-expression kits from Cellscript and assembled an array of nucleoside analogues, some of which he designed.

Most of the modified nucleosides were not up to the job. But Schrum found one, a variant of pseudouridine called 1-methylpseudouridine, that seemed to do the trick. According to Schrum, mRNA with this nucleoside produced even higher levels of protein expression with less inflammation than did the mRNA in Karikó and Weissman's papers. Last year, the US Patent and Trademark Office granted Moderna patents covering the use of 1-methylpseudouridine, among other nucleosides — but the University of Pennsylvania also received a patent that covers many of the same nucleosides.

Several other mRNA-therapeutics companies say that they have proprietary formulations of modified RNA molecules as well, although few are willing to discuss details. "In mRNAs, everything is deathly quiet," says Ali Mortazavi, chief executive of Silence Therapeutics, an RNA biotech in London. "There's really no understanding of who owns what, so nobody wants to disclose anything — and we're included in that."

Karikó, who now works at the German mRNA-therapeutics firm BioNTech in Mainz, points to early "signs that there will be a fierce battle for licensing" — and not just in the United States. Last year, the European Patent Office received two anonymous letters challenging the validity of Karikó and Weissman's patent application covering modified mRNA;

US authorities granted the patent in 2012, but a decision is still pending in the European Union.

The uncertainties over intellectual property have clearly not dissuaded Moderna's investors. Kolchinsky says that patent disputes may be painful and expensive, but they eventually resolve. "Companies that enable such breakthroughs typically have the resources to fend off baseless claims, and settle, on reasonable terms, the ones that turn out to be legitimate," he says.

Moderna also has time on its side. Flush with cash — the company has an estimated \$900 million in the bank — it can continue to sign on pharmaceutical partners and outspend its rivals on science. This year alone, Moderna plans to spend between \$150 million and \$180 million on research and development — more than any other mRNA drug-maker.

"They've created this air of inevitability," says Fruehauf. "It's a good strategy."

FUND-RAISER-IN-CHIEF

Much of that momentum boils down to one man: chief executive Stéphane Bancel. "He's a damn good salesman," says Justin Quinn, a staff scientist who worked at Moderna until 2012.

Bancel joined the company in July 2011 after leading the diagnostics firm bioMérieux of Marcy-l'Étoile, France, for five years. Afeyan had repeatedly tried to recruit Bancel to run Flagship-launched companies, but Bancel was not interested in most of the projects — start-ups that tended to focus on one lead product in one disease area.

Moderna was different: it promised to reinvent the drug industry. And for Bancel, a smooth-talking businessman with a penchant for stylish, slim-fitting clothing, "it was worth taking a career risk and a massive pay cut to go to a start-up if it had the potential to be something really big," he says.

Bancel quickly set to work on raising capital — with great success — but some question his tactics. In the opinion of a former staff scientist (who requested anonymity) Bancel used his charisma and connections, as well as the clout of the company's co-founders, to convince investors and partners of the uniqueness of the Moderna platform, while glossing over any possible holes in its intellectual property. "He did a tremendous job of persuading people to give the company money for technology that was not 100% theirs," the ex-employee says.

In response, Bancel says that of course investors in Moderna did their due diligence before writing cheques: "Companies are a bit more sophisticated than that."

He and other Moderna executives also acknowledge the seminal contributions made by Karikó, Weissman and others. But Tony de Fougères, who was Moderna's first chief scientific officer and now leads research efforts at Ablynx in Ghent, Belgium, argues that such early work was largely academic, and that Moderna approached the research "from a pharmaceutical perspective". Moreover,

"THEY'VE CREATED THIS AIR OF INEVITABILITY. IT'S A GOOD STRATEGY."

Bancel says that Moderna's technology has now advanced to the point that the company's initial patent filings are "irrelevant". "This is Moderna generation 1.0, and we're at 6.0 now," he says. Moderna no longer relies on 1-methylpseudo-uridine in its mRNAs, for example.

And modified nucleoside chemistry is just one part of what goes into building an mRNA drug. Another crucial aspect involves working out how to get the mRNA into specific cells and tissues in the body — a challenge that continues to vex the related field of RNA-interference therapeutics, which emerged more than a decade ago but has had few clinical successes. "The key for messenger RNA is going to be delivery," says Joseph Payne, president and chief executive of Arcturus Therapeutics in San Diego, one of many drug developers working on nanoparticle-based delivery of mRNA therapeutics. "That's really the rate-limiting step," adds Haussecker.

Bancel says that Moderna is exploring several delivery technologies through its in-house team and partnerships with others — although he would not divulge details of the company's approach. "People will figure out in 18 months where we are now when they see the patents," he says. Although at that point, he adds, even those methods will probably be out of date.

THE BEAST

At its sleek Cambridge headquarters, Moderna is equipping itself with the best laboratories that money can buy. In the middle of a third-floor lab sits "the beast", as Bancel calls it: a suite of robots that can make up to 50 lots of therapeutic mRNA per day for testing in non-human primates. Moderna also plans to open a facility for making human-grade mRNA later this year.

Its resources have allowed the company to launch more than 50 drug-development programmes, mostly through external pharmaceutical partners, but also at three wholly-owned spin-offs: Onkaido, Valera and Elpidera, which focus on oncology, infectious diseases and rare diseases, respectively. Bancel says that Valera will be first to the clinic, with an mRNA drug that targets an undisclosed infectious disease. "By the end of 2016, we will have trials for all

the therapeutic areas we are in today," he says.

But clinical success is by no means guaranteed. "It will probably be like the technologies before it," says James McSwiggen, an independent biotechnology consultant who has worked with Moderna in the past. Other RNA-based drugs, such as antisense therapies, RNA interference and, most recently, microRNA, have all gone through periods of industry exuberance. These are generally followed by years wrestling with scientific realities before the technologies begin to show their true clinical promise. "I suspect that the same will happen" with mRNA, says McSwiggen. "If any company can weather that boom-bust bit, I would imagine that, given the amount of money that they've raised, Moderna should."

Other mRNA-therapeutics companies are persevering, and are getting promising data from studies in large animals. CureVac, a German company that spun off from the University of Tübingen in 2000, has found that it can get injected mRNA past the immune defences of pigs and monkeys by picking molecules with optimal sequences rather than by modifying their nucleosides⁸. So far, CureVac has struck deals with several big pharmaceutical companies and raised around \$220 million in equity, including \$52 million secured from the Bill & Melinda Gates Foundation in March this year.

Dublin-based rare-disease specialist Shire, in collaboration with Ethris of Planegg, Germany, has achieved targeted lung delivery of mRNA in a pig model for cystic fibrosis. "For a huge idea" like mRNA, says Michael Heartlein, head of mRNA therapeutics at Shire, "I think there's a lot of room for different technologies and different players".

But Bancel's ambition is for Moderna to grow so fast and so big that the competition simply has no chance. "We want to be the company that, if you want to make an mRNA drug five years from now, you pick up the phone and you call Moderna," he says. "Think about it: if you're going to put \$50 or \$100 million into mRNA, do you want to put it into your own team, starting four years behind, and with all the IP issues? Or do you want to pile it on \$900 million of someone else's money?"

As for the naysayers and critics, Bancel says, "I understand people are not happy. I understand people are jealous. I understand all that. It's life." ■

Elie Dolgin is a science writer in Somerville, Massachusetts.

1. Zangi, L. *et al. Nature Biotechnol.* **31**, 898–907 (2013).
2. Wolff, J. A. *et al. Science* **247**, 1465–1468 (1990).
3. Jirikowski, G. F., Sanna, P. P., Maciejewski-Lenoir, D. & Bloom, F. E. *Science* **255**, 996–998 (1992).
4. Warren, L. *et al. Cell Stem Cell* **7**, 618–630 (2010).
5. Karikó, K., Buckstein, M., Ni, H. & Weissman, D. *Immunity* **23**, 165–175 (2005).
6. Karikó, K. *et al. Mol. Ther.* **16**, 1833–1840 (2008).
7. Karikó, K., Muramatsu, H., Keller, J. M. & Weissman, D. *Mol. Ther.* **20**, 948–953 (2012).
8. Thess, A. *et al. Mol. Ther.* **23**, S55 (2015).

COMMENT

BIOGRAPHY The monumental life of August Weismann, hereditary-science pioneer **p.31**

FILM Palaeontology adviser to *Jurassic World* talks GM dinosaurs **p.32**



GENOMICS Ten thousand bird genomes to be sequenced over next five years **p.34**

GEOLOGY A call to regulate fracking in China to reduce earthquake risk **p.34**

ILLUSTRATION BY MIKEL JASO



Prepare for unexpected prenatal test results

Women are learning about their own health problems through fetal screening. Revise consent forms and raise awareness, urges **Diana W. Bianchi**.

A healthy pregnant woman has a blood test to rule out the possibility that her baby has certain abnormalities, such as Down's syndrome. One week later, a genetic counsellor calls her and recommends a follow-up test such as amniocentesis. When the counsellor calls again, she says that the baby is healthy but that the mother needs to be screened for cancer.

Since 2011, clinicians have been able to analyse the genome of a fetus by sequencing DNA fragments found floating in the mother's blood. With the use of these non-invasive prenatal tests soaring (see 'Test scores'), mothers are increasingly facing unexpected, 'incidental' findings about their own health. As of late 2014, at least 26 pregnant women with abnormal blood-test results later learned that they had cancer¹.

In 10 of them, the prenatal tests prompted the medical assessments that revealed this; in the other 16, the cancers were not discovered until the mothers developed symptoms.

Parents, obstetricians and physicians have been taken by surprise. Consent forms used by test providers rarely mention the possibility of findings concerning the mother's health. And caregivers have little guidance on what to do when such findings arise.

Test providers need to rethink their consent forms to prevent unwarranted confusion and anxiety — not least, women deciding to terminate their pregnancies on the basis of wrong interpretations of test results². And professional societies, such as the American College of Medical Genetics and Genomics (ACMG), the American College of Obstetricians and Gynecologists

and the Society for Maternal-Fetal Medicine (SMFM), need to take the lead on providing education and clinical guidance.

FRAGMENTS THAT FOOL

These latest screening tests extract fragments of maternal and placental DNA (a proxy for fetal DNA) from the mother's blood. The fragments are sequenced and aligned to specific parts of a standard 'reference' human genome³. (In some cases, the reference genome is obtained from the mother's white blood cells.) By comparing the number of mapped fragments to the number expected to align, investigators can check whether there are too few or too many chromosomes (or parts of them) in the cells from which the fragments originated. If the initial analysis indicates an anomaly, ►

► a follow-up diagnostic procedure is strongly recommended.

The low rate of false-positive results from these blood tests — around 0.2%, down from the roughly 5% for older screening methods⁴ — has greatly reduced the need for invasive follow-up tests such as chorionic villus sampling (CVS) or amniocentesis⁵.

In some cases, an initial analysis indicates an anomaly, but a follow-up procedure shows that the number of chromosomes in the fetal cells are normal³. There are several possible explanations: a twin might have died in the womb or developmental glitches may have caused clusters of abnormal cells in the placenta, a condition called confined placental mosaicism. A third explanation is a health problem in the mother.

Some women have discovered that they have a sex-chromosome abnormality that is associated with reduced fertility⁶. Some have found out that they have DiGeorge syndrome, a genetic abnormality associated with learning difficulties, immune problems and congenital heart defects⁷. Others have been told that some of their cells contain an abnormal number of chromosomes³. And increasingly, imbalances in the number of chromosome copies have flagged the presence of a tumour¹.

Clinicians have yet to discover all that non-invasive prenatal testing can reveal about mothers. In my research, I have encountered three separate cases in which, on the basis of a maternal blood test, caregivers informed pregnant women that they would be having boys. After ultrasound images later showed that all three were pregnant with girls, it emerged that the Y chromosome sequences in the mothers' blood originated from transplanted organs that they had received from men⁸.

Although the commercial providers of the tests are striving to obtain data on follow-up assessments, doing so is hard, so the true extent of such incidental findings for mothers is unknown. A study in China revealed⁶ that in a group of 181 pregnant women — for whom follow-up procedures ruled out a problem in the fetus — 16 (9%) had a previously undiagnosed sex-chromosome abnormality.

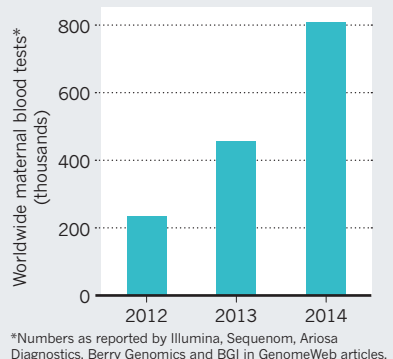
On the basis of current estimates, if one million blood tests are performed in a given year, at least 2,000 women will have an abnormal result that disagrees with the results of a diagnostic procedure such as CVS or amniocentesis. Most often this is because of confined placental mosaicism, but women are increasingly discovering abnormalities that may have implications for their own health.

CONSENT IS CRUCIAL

There is considerable confusion about how to handle incidental findings. As a medical geneticist, I frequently get calls and e-mails from obstetricians and other health-care providers asking, "What should I tell the

TEST SCORES

Since late 2011, clinicians have been able to screen mothers' blood for fetal chromosome problems using circulating DNA.



patient?" Most caregivers are still grappling with the practical challenges of incorporating a new type of prenatal test into clinical care; few are familiar with genome sequencing or trained to discuss the management of a pregnancy that has been complicated by the discovery of a maternal health problem.

I reviewed the consent forms used by five major US commercial providers of non-invasive prenatal blood tests. In two of them the physician, not the mother, signs the form stating that the mother has been counselled. In two of the other three, the mother signs the form, but the form either does not mention incidental findings or it explicitly states that the laboratory will not report them. Only one notes that, "in rare circumstances, genetic testing may reveal sensitive information about your own health".

To be fair, the possibility and extent of incidental findings for mothers has been appreciated only recently as the number of women being tested has increased. Still, providers must keep pace. Incidental findings could have major implications for mothers' care, life- and health-insurance policies, and so on.

A study published last year² indicated that 6% of women who received an unusual prenatal DNA blood test result terminated their pregnancies without having CVS or amniocentesis. Women might weigh options differently if they understood that a result could signal a genetic anomaly in themselves, rather than in their baby.

Consent forms should be provided directly to the mother to sign. They should explicitly state that incidental results could emerge with implications for the mother's health. Check boxes could be used to opt in or out of being told certain things: for example some women might want to know that they have chaotic DNA patterns suggestive of a tumour, but prefer not to be told that they have a sex-chromosome abnormality.

Also crucial is better education for parents and health-care providers about the various

prenatal blood tests now available — on how they work and what they can detect. Webinars or videos in multiple languages should be provided as soon as feasible by professional societies, such as the ACMG or the SMFM.

In parallel, clinicians and researchers need to get a better grasp on what kind of incidental findings could arise. New clinical tests have almost always been developed and validated in academic laboratories before being licensed. Yet until late 2014, blood tests for prenatal DNA screening were exclusively provided by commercial labs. Although the major companies offering the tests have propelled the field forward by increasing the number of women being tested and publishing results, gaps in follow-up clinical information are impeding understanding.

In the Netherlands, a nationwide evaluation is being conducted as a first step towards incorporating such tests into everyday health care. It is called the Trial by Dutch Laboratories for Evaluation of Non-Invasive Prenatal Testing (TRIDENT) study (see go.nature.com/qk2kpi). All abnormal results are correlated with the results of fetal or newborn chromosome testing, ultrasound evaluation of fetal growth, and placental studies to rule out confined placental mosaicism. The United States and other nations need a similar registry of the results of non-invasive prenatal testing, paired with clinical follow-up data.

The speed at which these blood tests have taken off in mainstream health care has brought focus and urgency to issues long debated in genetic circles⁹ — particularly, when and how to report to patients secondary findings from genomic sequencing. Handled properly, the incidental findings emerging from prenatal tests could accelerate treatments and save lives — rather than just increase the anxiety of thousands of pregnant women. ■

Diana W. Bianchi is executive director of the Mother Infant Research Institute at Tufts Medical Center and professor of paediatrics, obstetrics and gynaecology at Tufts University School of Medicine, Boston, Massachusetts, USA.
e-mail: dbianchi@tuftsmedicalcenter.org

1. Dharajiya N. et al. *J. Molec. Diagn.* **16**, 699–789 abstr. G45 (2014).
2. Dar, P. et al. *Am. J. Obstet. Gynecol.* **211**, 527.e1–527.e17 (2014).
3. Bianchi, D. W. & Wilkins-Haug, L. *Clin. Chem.* **60**, 78–87 (2014).
4. Bianchi, D. W. et al. *N. Engl. J. Med.* **370**, 799–808 (2014).
5. Warsof, S. L., Larion, S. & Abuhamad, A. *Prenat. Diagn.* <http://dx.doi.org/10.1002/pd.4601> (2015).
6. Wang, Y. et al. *Clin. Chem.* **60**, 251–259 (2014).
7. Wapner, R. J. et al. *Am. J. Obstet. Gynecol.* **212**, 332.e1–332.e9 (2015).
8. Bianchi, D. W. et al. *Obstet. Gynecol.* **125**, 375–382 (2015).
9. Allyse, M. & Michie, M. *Trends Biotechnol.* **31**, 439–441 (2013).

The author declares competing financial interests: see go.nature.com/e1kwr for details.



August Weismann, painted by Otto Scholderer in 1896.

EVOLUTIONARY BIOLOGY

Paean to a founder of heredity

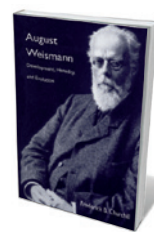
Jane Maienschein applauds a study of towering nineteenth-century biologist August Weismann.

A monumental study of an important but surprisingly little-studied biologist, *August Weismann* represents half a century of scholarly investment by historian of science Frederick Churchill. Churchill immersed himself in the observations and experiments, people, institutions and ideas of the nineteenth and early twentieth centuries — an astoundingly fertile era for the biological sciences — as well as in all of the many books and articles that Weismann (1834–1914) wrote, in German and English.

That anybody can write this kind of book

these days is awe-inspiring. When Churchill was my PhD supervisor in the 1970s, he warned me not to take on too large a dissertation topic, given the dearth of jobs and the pressures to move results into print quickly. The history of science is richer for his not having heeded his own advice.

Weismann's great contribution was the idea that germ-plasm — the name that he gave to the essential element of gametes, or eggs and sperm — carries the material of heredity from one generation to the next, unaffected by the environment. Germ-plasm



August Weismann: Development, Heredity, and Evolution

FREDERICK B. CHURCHILL
Harvard Univ. Press:
2015.

theory, which Weismann set out in the 1880s, rejected the possibility that acquired characteristics can be inherited, as propounded by Jean-Baptiste Lamarck in the early nineteenth century. Weismann's materialistic view of life provided a new understanding of biology, in which natural selection occurred between individual organisms, as Charles Darwin held, and with competition at the level of inherited determinants. This influenced the nature of the resulting variations. So Weismann, as Churchill makes clear, had one foot in the observational traditions and questions of nineteenth-century natural history — even as he extended the other into the experimental, theoretical twentieth century.

August Weismann reveals a scientist who grew up fascinated by nature and worked briefly as a medical doctor, then adjusted to roles as a faculty member at the University of Freiburg in Germany and director of its zoological institute, where he spent most of his career. Weismann looked at butterfly variations in considerable detail to explore patterns of heredity, protozoa to get at reproduction, jellyfish-like hydromedusae, the planktonic crustaceans *Daphnia*, and frogs — whatever it took to study the relevant phenomena. In 1862, while living at the isolated Schaumburg Palace as personal physician to Archduke Stephan of Austria for a year, he also explored natural history, especially of insects. The experience reinforced Weismann's determination to pursue biological research rather than medicine, and he moved to Freiburg, where he took on a series of research positions.

He increasingly turned to microscopy, experimental embryology and cytology to look deep into an organism to see changes in the cells and nucleus. At the Freiburg zoological institute, Weismann relied on his own observations and those of his students and assistants — both in the spirit of collaboration and to compensate for his failing eyesight.

Throughout, Weismann insisted that development, heredity and evolution are interconnected and must be studied as such. As he saw it, biologists should seek the underlying chemical and physical

NATURE.COM

For more on science in culture, see: nature.com/booksandarts

mechanisms. So while his contemporaries focused on details of cells, chromosomes or evolutionary mechanisms, ►

► Weismann sought to illuminate the links between them.

Churchill shows how Weismann's experimental observations of chromosome movements during cell division reinforced his germ-plasm theory. Weismann adapted ideas from leading cytologists and experimental embryologists such as Theodor Boveri and Wilhelm Roux, to link heredity and development through what Churchill calls his "architectonic view". Instead of a holistic or vitalistic understanding of the organism, Weismann developed a more structural view in which the system depends on integration of the material parts, with guidance from the germ-plasm and its determinants. Development then constructs the organism out of cells, with reproduction providing a source of variation on which natural selection acts, enabling evolution.

Weismann was confident and sometimes controversial. Churchill shows how disagreements helped Weismann to work out his own ideas. He sparred, for example, with physician and biologist Rudolf Virchow over issues of acquired characteristics and the role of external factors in shaping variation. And Weismann clashed with zoologist Theodor Eimer about the apparent randomness of evolution. Dozens of leading scientists influenced or interacted with Weismann because of his central role in biology. The zoologist and illustrator Ernst Haeckel, for example, was a close friend, but his views diverged from Weismann's in ways that influenced both men, and affected public perceptions of biology. We also see the impact on Weismann of technically brilliant figures such as Boveri and theoreticians including Darwin. Weismann in turn influenced his contemporaries and subsequent generations of Darwinians.

Even as his contemporaries began to specialize and to give up the study of connections between heredity, development and evolution in favour of specialized study of the parts or selected processes, Weismann worked hard to develop a comprehensive understanding of life. Churchill has mirrored that determination in developing a compelling and comprehensive understanding of Weismann, his ideas, work, life, contemporaries and context. ■

Jane Maienschein is Regents' President's and Parents Association Professor at Arizona State University in Tempe, and adjunct senior scientist at the Marine Biological Laboratory in Woods Hole, Massachusetts. Her most recent book is *Embryos Under the Microscope*. e-mail: maienschein@asu.edu



The hybrid dinosaur *Indominus rex* runs rampantly in *Jurassic World*.

Q&A Jack Horner

The dinosaur doctor

Montana palaeontologist Jack Horner has served as scientific adviser on the *Jurassic Park* films from the start. With the latest, *Jurassic World*, soon to be released, he talks about a shark-devouring *Mosasaurus*, breeding chickens back into dinosaurs and the influence of the film franchise on his own field.



How did you get involved in the series?

In the early 1990s, a colleague called me and said, "You're in a book about cloning dinosaurs" — Michael Crichton's *Jurassic Park* (Alfred A. Knopf, 1990). I said, "I hope my character doesn't get eaten." I never bothered to pick it up; I am dyslexic and have trouble enough keeping up with my own science. Then director Steven Spielberg called and asked whether I wanted to work on the film. I thought growing a dinosaur was an intriguing idea, and I still do. It is a little far-fetched now, but I think one day we will be able to do it, not using amber-trapped DNA, but through genetic modification of dinosaurs' closest living relatives, birds.

What did work on *Jurassic Park* (1993) entail?

My job was to find things that were obviously wrong. In one scene, the puppeteers were having trouble getting an animatronic *Tyrannosaurus rex* leg to move properly. So I stepped in to control the joystick, making the foot land

on its toes in a bird-like position, rather than heel-first like a mammal. In a kitchen scene, the puppeteers had velociraptors sticking out forked tongues, which dinosaurs did not have. Instead, we had the raptors snort to fog up the window, revealing that they had warm blood.

What are the innovations in *Jurassic World*?

The science has got ahead of the films, but we cannot really change the way the dinosaurs look. If suddenly the raptors had feathers, it would destroy consistency. But I did help to render new creatures. You can see a *mosasaur*, a giant swimming reptile, shoot up from a tank to eat a great white shark. From my research, I helped to ensure that the juvenile triceratops, with its backward-curving horns, looked distinct from the adult, whose horns curve forward. But my biggest job was helping to create the 'genetically modified' *Indominus rex*, a combination of several dinosaurs and other animals, which turns against its makers.

How plausible is such a dino-hybrid?

Jurassic World is set in the future. If you can clone a dinosaur, you can modify its DNA and combine it with that of other animals. We

TOP: UNIVERSAL PICTURES/AMBLIN ENTERTAINMENT; LEFT: MUS. OF THE ROCKIES

► Weismann sought to illuminate the links between them.

Churchill shows how Weismann's experimental observations of chromosome movements during cell division reinforced his germ-plasm theory. Weismann adapted ideas from leading cytologists and experimental embryologists such as Theodor Boveri and Wilhelm Roux, to link heredity and development through what Churchill calls his "architectonic view". Instead of a holistic or vitalistic understanding of the organism, Weismann developed a more structural view in which the system depends on integration of the material parts, with guidance from the germ-plasm and its determinants. Development then constructs the organism out of cells, with reproduction providing a source of variation on which natural selection acts, enabling evolution.

Weismann was confident and sometimes controversial. Churchill shows how disagreements helped Weismann to work out his own ideas. He sparred, for example, with physician and biologist Rudolf Virchow over issues of acquired characteristics and the role of external factors in shaping variation. And Weismann clashed with zoologist Theodor Eimer about the apparent randomness of evolution. Dozens of leading scientists influenced or interacted with Weismann because of his central role in biology. The zoologist and illustrator Ernst Haeckel, for example, was a close friend, but his views diverged from Weismann's in ways that influenced both men, and affected public perceptions of biology. We also see the impact on Weismann of technically brilliant figures such as Boveri and theoreticians including Darwin. Weismann in turn influenced his contemporaries and subsequent generations of Darwinians.

Even as his contemporaries began to specialize and to give up the study of connections between heredity, development and evolution in favour of specialized study of the parts or selected processes, Weismann worked hard to develop a comprehensive understanding of life. Churchill has mirrored that determination in developing a compelling and comprehensive understanding of Weismann, his ideas, work, life, contemporaries and context. ■

Jane Maienschein is Regents' President's and Parents Association Professor at Arizona State University in Tempe, and adjunct senior scientist at the Marine Biological Laboratory in Woods Hole, Massachusetts. Her most recent book is *Embryos Under the Microscope*. e-mail: maienschein@asu.edu



The hybrid dinosaur *Indominus rex* runs rampant in *Jurassic World*.

Q&A Jack Horner

The dinosaur doctor

Montana palaeontologist Jack Horner has served as scientific adviser on the *Jurassic Park* films from the start. With the latest, *Jurassic World*, soon to be released, he talks about a shark-devouring *Mosasaurus*, breeding chickens back into dinosaurs and the influence of the film franchise on his own field.



How did you get involved in the series?

In the early 1990s, a colleague called me and said, "You're in a book about cloning dinosaurs" — Michael Crichton's *Jurassic Park* (Alfred A. Knopf, 1990). I said, "I hope my character doesn't get eaten." I never bothered to pick it up; I am dyslexic and have trouble enough keeping up with my own science. Then director Steven Spielberg called and asked whether I wanted to work on the film. I thought growing a dinosaur was an intriguing idea, and I still do. It is a little far-fetched now, but I think one day we will be able to do it, not using amber-trapped DNA, but through genetic modification of dinosaurs' closest living relatives, birds.

What did work on *Jurassic Park* (1993) entail?

My job was to find things that were obviously wrong. In one scene, the puppeteers were having trouble getting an animatronic *Tyrannosaurus rex* leg to move properly. So I stepped in to control the joystick, making the foot land

on its toes in a bird-like position, rather than heel-first like a mammal. In a kitchen scene, the puppeteers had velociraptors sticking out forked tongues, which dinosaurs did not have. Instead, we had the raptors snort to fog up the window, revealing that they had warm blood.

What are the innovations in *Jurassic World*?

The science has got ahead of the films, but we cannot really change the way the dinosaurs look. If suddenly the raptors had feathers, it would destroy consistency. But I did help to render new creatures. You can see a *mosasaur*, a giant swimming reptile, shoot up from a tank to eat a great white shark. From my research, I helped to ensure that the juvenile triceratops, with its backward-curving horns, looked distinct from the adult, whose horns curve forward. But my biggest job was helping to create the 'genetically modified' *Indominus rex*, a combination of several dinosaurs and other animals, which turns against its makers.

How plausible is such a dino-hybrid?

Jurassic World is set in the future. If you can clone a dinosaur, you can modify its DNA and combine it with that of other animals. We

TOP: UNIVERSAL PICTURES/AMBLIN ENTERTAINMENT; LEFT: MUS. OF THE ROCKIES

Jurassic WorldDIRECTOR: COLIN
TREVORROW

Universal: 2015.

already have lots of tools for modifying an animal. We have been breeding them for centuries. Now

we are getting to the point where we can take genes out of one organism and put them into another, for example taking fluorescent genes out of jellyfish and putting them into the embryos of other animals to make them glow in the dark. The challenge is finding ways of changing a creature without killing it. And I think we will.

Are you trying to breed birds back into dinosaurs?

In the Dino-Chicken Project at Montana State University in Bozeman, we are looking for the genetic pathways that provided the transformation from dinosaurs into birds, with the hope that some of those pathways can be reversed. Part of it is genetic engineering to see if we can get a long tail back on a chicken (D. J. Rashid *et al.* *EvoDevo* 5, 25; 2014). My postdoc Dana Rashid has screened mouse genes, looking for pathways that cause mice to lose their tails. If she can find one that causes a similar reaction in a reptile, it might be possible to reverse the process and grow a tail on a chicken.

Do the films do justice to the science?

Each film explains a bit of the science, for example through the dancing DNA cartoon in the first movie. If people are wondering about whether the science in *Jurassic World* is real, that is great for science. *Jurassic Park* brought out all sorts of students who wanted to switch careers into palaeontology. It channelled a flood of graduate students to my lab, including some of the best scientists I have trained.

How have digital effects changed your work?

For the first film, I would sit with Steven Spielberg and advise him on the motions of the dinosaur puppets. But *Jurassic World* had only one puppet on set — an injured sauropod. For the rest of the dinosaurs, most of my consulting was with the graphics people.

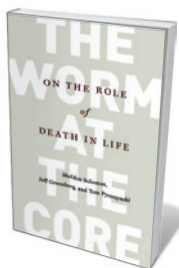
What do we know about how dinosaurs behaved?

They were more like robins than crocodiles. Their spikes and shields were too flimsy for fighting and were more likely to be for display, like the bony crests on some modern birds. Some dinosaurs had feathers and probably 'danced' like birds. If you built a *Jurassic Park*, it would be more like the Serengeti than *Jaws*. I wrote a script once for a film where scientists come out of their time machine to see triceratops dancing and showing off their coloured shields. Nobody would go to that movie. ■

INTERVIEW BY JASCHA HOFFMAN

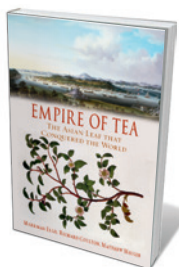
This interview been edited for length and clarity.

Books in brief

**The Worm at the Core: On the Role of Death in Life**

Sheldon Solomon, Jeff Greenberg and Tom Pyszczynski RANDOM HOUSE (2015)

How do we cope with the knowledge of mortality? In this considered treatise, psychologists Sheldon Solomon, Jeff Greenberg and Tom Pyszczynski present their "terror management theory", positing that we hold off existential fear through our cultural world view and sense of personal significance. Drawing on several disciplines and many experimental-psychology studies, they conclude that embracing ambiguity and cultivating meaning in life create the basis for the finely calibrated courage that we need to face our inevitable end.

**Empire of Tea: The Asian Leaf That Conquered the World**

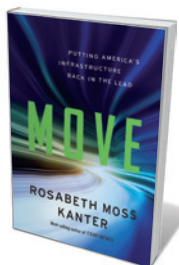
Markman Ellis, Richard Coulton and Matthew Mauger REAKTION (2015)

'Tea' has at least five meanings: the shrub *Camellia sinensis*; its leaf; the dried commodity; the infusion made from it; and the occasion for consuming the infusion. As Markman Ellis, Richard Coulton and Matthew Mauger show in this stimulating volume, history is steeped in the stuff. In eighteenth-century Britain, tea smugglers murdered customs officers; across the Atlantic, excise duty provoked the Boston Tea Party. In 1920, say the authors, John Maynard Keynes "imagined tea at the centre of the modern mercantile world". With 290 billion litres of tea imbibed in 2013, the taste for it seems set to grow.

**The House of Owls**

Tony Angell YALE UNIVERSITY PRESS (2015)

Wildlife artist and naturalist Tony Angell, who memorably explored corvid behaviour with John Marzluff (see N. Clayton *Nature* 484, 453–454; 2012), here turns to the owl. A self-confessed strigiphile, Angell has had western screech owls (*Megascops kennicottii*) nesting outside his home in Washington state for 25 years, and his exquisite monochrome illustrations testify to that intimate coexistence. Angell delves, too, into the owl in culture, and the ranges and habitats of the 19 species found in North America. A treat for fans of these strangely remote, inquisitive, astonishingly sharp-eared and -eyed raptors.

**Move: Putting America's Infrastructure Back in the Lead**

Rosabeth Moss Kanter W. W. NORTON (2015)

The US transport infrastructure is riddled with "pain points and bottlenecks", from delayed flights to crumbling bridges. So notes Harvard business professor Rosabeth Moss Kanter in this propulsive study, which argues for an overhaul of US transport to boost the economy, ease commuting and curb emissions. Kanter delivers a number-crunched analysis of the state of road, rail and air transport, and details progress on intelligent transportation and smart cities. But with government and industry preventing advances, the prime hurdle, she notes, is a lack of political will at the top.

**Spirals in Time: The Secret Life and Curious Afterlife of Seashells**

Helen Scales BLOOMSBURY SIGMA (2015)

Structurally elegant and often stunningly marked, seashells have obsessed scientists for centuries — as attested by the millions housed in London's Natural History Museum alone. In this engaging study of molluscs, marine biologist Helen Scales covers a wealth of research on this vast phylum, from findings on shell shape and colour (rococo formations may deter predators, whereas pigmented patterns could be a mollusc's way of tracking its own construction process), to the ecosystem services performed by oyster beds. [Barbara Kiser](#)

Jurassic WorldDIRECTOR: COLIN
TREVORROW
Universal: 2015.

already have lots of tools for modifying an animal. We have been breeding them for centuries. Now

we are getting to the point where we can take genes out of one organism and put them into another, for example taking fluorescent genes out of jellyfish and putting them into the embryos of other animals to make them glow in the dark. The challenge is finding ways of changing a creature without killing it. And I think we will.

Are you trying to breed birds back into dinosaurs?

In the Dino-Chicken Project at Montana State University in Bozeman, we are looking for the genetic pathways that provided the transformation from dinosaurs into birds, with the hope that some of those pathways can be reversed. Part of it is genetic engineering to see if we can get a long tail back on a chicken (D. J. Rashid *et al.* *EvoDevo* 5, 25; 2014). My postdoc Dana Rashid has screened mouse genes, looking for pathways that cause mice to lose their tails. If she can find one that causes a similar reaction in a reptile, it might be possible to reverse the process and grow a tail on a chicken.

Do the films do justice to the science?

Each film explains a bit of the science, for example through the dancing DNA cartoon in the first movie. If people are wondering about whether the science in *Jurassic World* is real, that is great for science. *Jurassic Park* brought out all sorts of students who wanted to switch careers into palaeontology. It channelled a flood of graduate students to my lab, including some of the best scientists I have trained.

How have digital effects changed your work?

For the first film, I would sit with Steven Spielberg and advise him on the motions of the dinosaur puppets. But *Jurassic World* had only one puppet on set — an injured sauropod. For the rest of the dinosaurs, most of my consulting was with the graphics people.

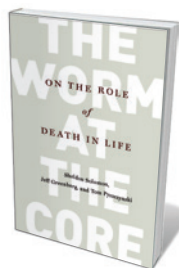
What do we know about how dinosaurs behaved?

They were more like robins than crocodiles. Their spikes and shields were too flimsy for fighting and were more likely to be for display, like the bony crests on some modern birds. Some dinosaurs had feathers and probably 'danced' like birds. If you built a *Jurassic Park*, it would be more like the Serengeti than *Jaws*. I wrote a script once for a film where scientists come out of their time machine to see triceratops dancing and showing off their coloured shields. Nobody would go to that movie. ■

INTERVIEW BY JASCHA HOFFMAN

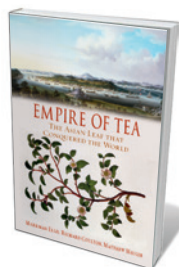
This interview been edited for length and clarity.

Books in brief

**The Worm at the Core: On the Role of Death in Life**

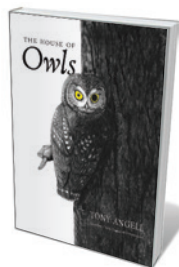
Sheldon Solomon, Jeff Greenberg and Tom Pyszczynski RANDOM HOUSE (2015)

How do we cope with the knowledge of mortality? In this considered treatise, psychologists Sheldon Solomon, Jeff Greenberg and Tom Pyszczynski present their "terror management theory", positing that we hold off existential fear through our cultural world view and sense of personal significance. Drawing on several disciplines and many experimental-psychology studies, they conclude that embracing ambiguity and cultivating meaning in life create the basis for the finely calibrated courage that we need to face our inevitable end.

**Empire of Tea: The Asian Leaf That Conquered the World**

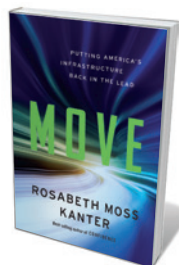
Markman Ellis, Richard Coulton and Matthew Mauger REAKTION (2015)

'Tea' has at least five meanings: the shrub *Camellia sinensis*; its leaf; the dried commodity; the infusion made from it; and the occasion for consuming the infusion. As Markman Ellis, Richard Coulton and Matthew Mauger show in this stimulating volume, history is steeped in the stuff. In eighteenth-century Britain, tea smugglers murdered customs officers; across the Atlantic, excise duty provoked the Boston Tea Party. In 1920, say the authors, John Maynard Keynes "imagined tea at the centre of the modern mercantile world". With 290 billion litres of tea imbibed in 2013, the taste for it seems set to grow.

**The House of Owls**

Tony Angell YALE UNIVERSITY PRESS (2015)

Wildlife artist and naturalist Tony Angell, who memorably explored corvid behaviour with John Marzluff (see N. Clayton *Nature* 484, 453–454; 2012), here turns to the owl. A self-confessed strigiphile, Angell has had western screech owls (*Megascops kennicottii*) nesting outside his home in Washington state for 25 years, and his exquisite monochrome illustrations testify to that intimate coexistence. Angell delves, too, into the owl in culture, and the ranges and habitats of the 19 species found in North America. A treat for fans of these strangely remote, inquisitive, astonishingly sharp-eared and -eyed raptors.

**Move: Putting America's Infrastructure Back in the Lead**

Rosabeth Moss Kanter W. W. NORTON (2015)

The US transport infrastructure is riddled with "pain points and bottlenecks", from delayed flights to crumbling bridges. So notes Harvard business professor Rosabeth Moss Kanter in this propulsive study, which argues for an overhaul of US transport to boost the economy, ease commuting and curb emissions. Kanter delivers a number-crunched analysis of the state of road, rail and air transport, and details progress on intelligent transportation and smart cities. But with government and industry preventing advances, the prime hurdle, she notes, is a lack of political will at the top.

**Spirals in Time: The Secret Life and Curious Afterlife of Seashells**

Helen Scales BLOOMSBURY SIGMA (2015)

Structurally elegant and often stunningly marked, seashells have obsessed scientists for centuries — as attested by the millions housed in London's Natural History Museum alone. In this engaging study of molluscs, marine biologist Helen Scales covers a wealth of research on this vast phylum, from findings on shell shape and colour (rococo formations may deter predators, whereas pigmented patterns could be a mollusc's way of tracking its own construction process), to the ecosystem services performed by oyster beds. [Barbara Kiser](#)

Correspondence

Ukrainian science needs elixir of youth

Ukraine's science system stands to benefit from its association with the European Union (EU) Horizon 2020 flagship research programme (*Nature* <http://doi.org/4kq>; 2015). But it has problems beyond funding: the re-election of Boris Paton as president of Ukraine's National Academy of Sciences at the age of 96 is symptomatic.

We are involved in an initiative to boost cooperation between the EU and Ukraine in biomedicine (COMBIOM). In our view, this will be difficult as long as young scientists feel that they are being held back by the rigid Soviet-style system run by scientists of the old school. Early-career researchers want to gain experience abroad and have little incentive to return.

Ukraine's science system must be made more competitive. It should reward young scientists who have international expertise and enable them to lead research teams. It should encourage job flexibility and contracts for academy researchers, and identify strategies and research areas to optimize scientific development. It should create institutions that specialize in those areas, and appoint an independent body of EU researchers and Ukrainian scientists abroad to evaluate internal funding applications.

Such measures would create a healthy scientific community and promote Ukraine's integration with the European Research Area. **Yegor Vassetzky** CNRS-Institut Gustave Roussy, Villejuif, France. **Ivan Gout** University College London, UK.

Jacek Kuznicki International Institute of Molecular and Cellular Biology, Warsaw, Poland. vassetzky@igr.fr

Improve oversight of fracking in China

We are concerned that China is paying insufficient attention to earthquakes that are induced by

injecting huge volumes of waste water deep underground (see also *Nature* **520**, 418–419; 2015).

Most of China's shale-gas resources lie near seismic fault zones. Wastewater injection by Chinese oil and gas industries has induced minor earthquakes in Sichuan, Chongqing, Xinjiang, Henan, Liaoning and Hubei — 6 of 13 provinces prioritized for shale-gas exploitation (see go.nature.com/uriceh; in Chinese). In Chongqing's Rongchang gas field, for example, 32,000 surface earthquakes were recorded between 1998 and 2006 (X. Lei *et al.* *J. Geophys. Res. Solid Earth* **113**, B10310; 2008).

Replacing coal with gas is central to China's plans to reduce air pollution and carbon dioxide emissions. We call for stricter regulation and tighter monitoring of its fracking industry to curb seismic activity and environmental pollution (see H. Yang *et al.* *Nature* **499**, 154; 2013).

Hong Yang University of Oslo, Norway.

Julian R. Thompson, Roger J. Flower University College London, UK. hongyanghy@gmail.com

Use '4Rs' criteria to assess papers

We propose a '4R' approach to assessing reported research, underpinned by statistical rigour (see J. T. Leek and R. D. Peng *Nature* **520**, 612; 2015). These 4Rs denote reproduction, replication, robustness and revelation.

Journals are aware of the need for the first two: whether enough information is available to reproduce an experiment, and whether its original results can be replicated. Even if the experiment can be reproduced, replication is often an issue, so journals are increasingly asking authors for details of software code and raw data. Videos of each experimental step could also be included.

Variations in experimental and

analytical methods are a concern for referees and readers, hence the need for robustness. A well-conducted study should indicate the sensitivity of its conclusions to the various assumptions that were made in deriving them.

Revelation relates to the need for accountability and transparency. Scientists must communicate more effectively by disclosing their reasoning for how they develop strategies, derive insights and draw conclusions.

Adrian Pagan University of Sydney; and Melbourne Institute of Applied Economic and Social Research, Australia.

Benno Torgler Queensland University of Technology, Australia. benno.torgler@qut.edu.au

Bird sequencing project takes off

On 3 June, the Avian Phylogenomics Consortium announced its 'Bird 10K' project to generate draft genome sequences for about 10,500 extant bird species over the next 5 years.

The sequences, along with data we aim to collect on the morphological, physiological, ecological and behavioural traits of every bird species, will inform studies on avian evolution, ecology, population genetics, neurobiology, development and conservation. They could also be useful for investigating infections that pass from animals to humans, such as avian influenza.

This wealth of information will allow us to complete the genomic tree of life for modern birds. We hope to decode the links between genotypes and phenotypes; to determine genetic evolutionary, biogeographical and biodiversity relationships across species; and to evaluate how ecological factors and humans affect bird evolution.

We plan to conduct the project in four phases, based on the avian classification hierarchy. The first, ordinal phase (for 34 orders of birds) has been

accomplished (see also G. Zhang *et al.* *Science* **346**, 1308–1309; 2014). Collection of genomic data for the second, familial phase (about 240 families) is ongoing. Specimen and trait-data collection for the third phase (2,250 genera) and the fourth phase (the remaining 8,000 or so species) is under way. See <http://b10k.genomics.cn> for more information.

Guojie Zhang* China National GeneBank, BGI-Shenzhen, China. zhanggj@genomics.cn

*On behalf of 6 correspondents (see go.nature.com/v9sl8z for full list).

Diagnostic service shares BRCA data

As a partner in the BRCA Share initiative for breast-cancer genetic data, we wish to clarify our position (see *Nature* **520**, 585; 2015).

Quest Diagnostics tests one in three US adults annually, including for *BRCA* gene mutations. We support open-access sharing of these data, once the complexities of uploading so many records can be resolved.

A final test run for uploading Quest data to the Leiden Open Variation Database (LOVD) is now complete. Contrary to your implication, we anticipate that the publicly available database funded by the US National Institutes of Health, ClinVar, will eventually have access to these data because of a reciprocal relationship with the LOVD.

Industry is often criticized for not giving back. Labs that make revenue from *BRCA* testing pay to participate in BRCA Share; academic scientists and entities do so for free. This reduces the need for public funding to improve *BRCA* tests. Some of the fees will go to functional studies of *BRCA* variants. BRCA Share also raises the bar of responsibility for commercial labs.

Charles Strom Quest Diagnostics, California, USA. charles.m.strom@questdiagnostics.com

Correspondence

Ukrainian science needs elixir of youth

Ukraine's science system stands to benefit from its association with the European Union (EU) Horizon 2020 flagship research programme (*Nature* <http://doi.org/4kq>; 2015). But it has problems beyond funding: the re-election of Boris Paton as president of Ukraine's National Academy of Sciences at the age of 96 is symptomatic.

We are involved in an initiative to boost cooperation between the EU and Ukraine in biomedicine (COMBIOM). In our view, this will be difficult as long as young scientists feel that they are being held back by the rigid Soviet-style system run by scientists of the old school. Early-career researchers want to gain experience abroad and have little incentive to return.

Ukraine's science system must be made more competitive. It should reward young scientists who have international expertise and enable them to lead research teams. It should encourage job flexibility and contracts for academy researchers, and identify strategies and research areas to optimize scientific development. It should create institutions that specialize in those areas, and appoint an independent body of EU researchers and Ukrainian scientists abroad to evaluate internal funding applications.

Such measures would create a healthy scientific community and promote Ukraine's integration with the European Research Area. **Yegor Vassetzky** CNRS-Institut Gustave Roussy, Villejuif, France. **Ivan Gout** University College London, UK.

Jacek Kuznicki International Institute of Molecular and Cellular Biology, Warsaw, Poland. vassetzky@igr.fr

Improve oversight of fracking in China

We are concerned that China is paying insufficient attention to earthquakes that are induced by

injecting huge volumes of waste water deep underground (see also *Nature* **520**, 418–419; 2015).

Most of China's shale-gas resources lie near seismic fault zones. Wastewater injection by Chinese oil and gas industries has induced minor earthquakes in Sichuan, Chongqing, Xinjiang, Henan, Liaoning and Hubei — 6 of 13 provinces prioritized for shale-gas exploitation (see go.nature.com/uriceh; in Chinese). In Chongqing's Rongchang gas field, for example, 32,000 surface earthquakes were recorded between 1998 and 2006 (X. Lei *et al.* *J. Geophys. Res. Solid Earth* **113**, B10310; 2008).

Replacing coal with gas is central to China's plans to reduce air pollution and carbon dioxide emissions. We call for stricter regulation and tighter monitoring of its fracking industry to curb seismic activity and environmental pollution (see H. Yang *et al.* *Nature* **499**, 154; 2013).

Hong Yang University of Oslo, Norway.

Julian R. Thompson, Roger J. Flower University College London, UK. hongyanghy@gmail.com

Use '4Rs' criteria to assess papers

We propose a '4R' approach to assessing reported research, underpinned by statistical rigour (see J. T. Leek and R. D. Peng *Nature* **520**, 612; 2015). These 4Rs denote reproduction, replication, robustness and revelation.

Journals are aware of the need for the first two: whether enough information is available to reproduce an experiment, and whether its original results can be replicated. Even if the experiment can be reproduced, replication is often an issue, so journals are increasingly asking authors for details of software code and raw data. Videos of each experimental step could also be included.

Variations in experimental and

analytical methods are a concern for referees and readers, hence the need for robustness. A well-conducted study should indicate the sensitivity of its conclusions to the various assumptions that were made in deriving them.

Revelation relates to the need for accountability and transparency. Scientists must communicate more effectively by disclosing their reasoning for how they develop strategies, derive insights and draw conclusions.

Adrian Pagan University of Sydney; and Melbourne Institute of Applied Economic and Social Research, Australia.

Benno Torgler Queensland University of Technology, Australia. benno.torgler@qut.edu.au

Bird sequencing project takes off

On 3 June, the Avian Phylogenomics Consortium announced its 'Bird 10K' project to generate draft genome sequences for about 10,500 extant bird species over the next 5 years.

The sequences, along with data we aim to collect on the morphological, physiological, ecological and behavioural traits of every bird species, will inform studies on avian evolution, ecology, population genetics, neurobiology, development and conservation. They could also be useful for investigating infections that pass from animals to humans, such as avian influenza.

This wealth of information will allow us to complete the genomic tree of life for modern birds. We hope to decode the links between genotypes and phenotypes; to determine genetic evolutionary, biogeographical and biodiversity relationships across species; and to evaluate how ecological factors and humans affect bird evolution.

We plan to conduct the project in four phases, based on the avian classification hierarchy. The first, ordinal phase (for 34 orders of birds) has been

accomplished (see also G. Zhang *et al.* *Science* **346**, 1308–1309; 2014). Collection of genomic data for the second, familial phase (about 240 families) is ongoing. Specimen and trait-data collection for the third phase (2,250 genera) and the fourth phase (the remaining 8,000 or so species) is under way. See <http://b10k.genomics.cn> for more information.

Guojie Zhang* China National GeneBank, BGI-Shenzhen, China. zhanggj@genomics.cn

*On behalf of 6 correspondents (see go.nature.com/v9sl8z for full list).

Diagnostic service shares BRCA data

As a partner in the BRCA Share initiative for breast-cancer genetic data, we wish to clarify our position (see *Nature* **520**, 585; 2015).

Quest Diagnostics tests one in three US adults annually, including for *BRCA* gene mutations. We support open-access sharing of these data, once the complexities of uploading so many records can be resolved.

A final test run for uploading Quest data to the Leiden Open Variation Database (LOVD) is now complete. Contrary to your implication, we anticipate that the publicly available database funded by the US National Institutes of Health, ClinVar, will eventually have access to these data because of a reciprocal relationship with the LOVD.

Industry is often criticized for not giving back. Labs that make revenue from *BRCA* testing pay to participate in BRCA Share; academic scientists and entities do so for free. This reduces the need for public funding to improve *BRCA* tests. Some of the fees will go to functional studies of *BRCA* variants. BRCA Share also raises the bar of responsibility for commercial labs.

Charles Strom Quest Diagnostics, California, USA. charles.m.strom@questdiagnostics.com

and in the Department of Medical Biophysics,
University of Toronto, Toronto M5G 1L7,
Canada.
e-mail: vuks@uhnres.utoronto.ca

- Hollander, M. C., Blumenthal, G. M. & Dennis, P. A. *Nature Rev. Cancer* **11**, 289–301 (2011).
- Naguib, A. et al. *Mol. Cell* **58**, 255–268 (2015).
- Lee, J. O. et al. *Cell* **99**, 323–334 (1999).

- Georgescu, M. M. et al. *Cancer Res.* **60**, 7033–7038 (2000).
- Worby, C. A. & Dixon, J. E. *Annu. Rev. Biochem.* **83**, 641–669 (2014).
- Bassi, C. et al. *Science* **341**, 395–399 (2013).
- Hopkins, B. D. et al. *Science* **341**, 399–402 (2013).
- Backer, J. M. *Biochem. J.* **410**, 1–17 (2008).
- Byfield, M. P., Murray, J. T. & Backer, J. M. *J. Biol. Chem.* **280**, 33076–33082 (2005).

- Huang, J. et al. *Nature Commun.* **3**, 911 (2012).
- Iijima, M., Huang, Y. E., Luo, H. R., Vazquez, F. & Devreotes, P. N. *J. Biol. Chem.* **279**, 16606–16613 (2004).
- Chew, C. L. et al. *Cancer Discov.* <http://dx.doi.org/10.1158/2159-8290.CD-14-1347> (2015).
- Kofuji, S. et al. *Cancer Discov.* <http://dx.doi.org/10.1158/2159-8290.CD-14-1329> (2015).

This article was published online on 27 May 2015.

ASTRONOMY

Pluto leads the way in planet formation

Images from the Hubble Space Telescope cast new light on the orbits, shapes and sizes of Pluto's small satellites. The analysis comes just before a planned reconnaissance by the first spacecraft to visit them. [SEE ARTICLE P.45](#)

SCOTT J. KENYON

Pluto and its large moon Charon together make up the only 'binary planet' in the Solar System. With a mass roughly 11% that of Pluto, Charon orbits the binary system's centre of mass at a distance of 17,500 kilometres every 6.4 days. Over the past decade, images from the Hubble Space Telescope (HST) have revealed four circumbinary satellites with orbital periods of 20–40 days and masses roughly 0.001% (or less) of Pluto's (Fig. 1). Before the discovery of the innermost and least massive of these moons, Styx, dynamical studies¹ had suggested that the other three, Nix, Kerberos and Hydra, are packed as closely together as possible, with no room for other stable satellites between their orbits.

On page 45 of this issue, Showalter and Hamilton² present an analysis of all available HST images of the system, and derive new orbits and masses for the moons. They also derive limits on the moons' previously unknown shapes and reflectivities. As well as confirming that the moons are in extremely tight orbits, the authors infer new relationships between the orbital periods of satellite pairs. These results may help us to understand how planets and satellites form and remain on stable orbits for billions of years.

The architecture of Pluto's small satellites closely resembles that of several planetary systems discovered by the Kepler space observatory³ (Fig. 2). In these systems, every object has a gravitational sphere of influence that prevents other objects from orbiting nearby. The more massive the object, the larger its sphere of influence. When the gravitational spheres

of neighbouring objects nearly overlap, it is impossible to place other bodies on stable orbits between them. In tightly packed systems, the spheres of several (perhaps all) of the objects almost overlap. Small particles, such as interplanetary dust, might orbit in these intermediate regions, but large objects cannot.

These tightly packed systems place severe constraints on theories of planetary-system formation. According to current thinking, planets (and satellites) start as small seeds in a disk or ring surrounding the star (or planet) at the centre. These seeds grow by agglomerating other small solid objects along their orbits. Eventually, growing bodies feel the gravitational tugs of others in the system. Continued growth results in 'overpacking', whereby the

spheres of influence of many growing objects in orbit overlap. As the gravitational forces between these objects build, their orbital motions become chaotic, and further growth is promoted through mergers of objects. When only a few planets (or satellites) remain, they settle into nearly circular orbits and their spheres of influence do not overlap. How some systems end up with objects in closely packed orbits is an open question.

Current hypotheses^{4,5} on the formation of the Pluto–Charon system focus on a giant impact in which a proto-Charon collided with a proto-Pluto to form a binary planet surrounded by an expanding ring of debris. Pre-existing moons might have survived the impact and new moons may have grown out of small particles in the debris. As well as having ended up in tightly packed orbits, the four moons that are the end product of this process (Styx, Nix, Kerberos and Hydra) exist in orbits with orbital periods in an observed ratio of roughly 3:4:5:6 times that of Charon⁶, respectively. High-quality measurements of the orbits and masses of all the moons in the system are needed to understand how this process works.

To constrain these properties, Showalter and Hamilton measure precise positions of the moons on the HST images. Assuming that the four moons follow elliptical orbits around Pluto–Charon, the authors present detailed modelled fits to their positions that yield the period, orientation (the inclination of the orbital plane with respect to the orbital plane of Pluto–Charon) and ellipticity of each orbit. Variations in the brightness of the moons at different times along their orbits allowed the authors to derive estimates of their sizes, shapes, reflectivities and masses. They conclude that the moons have orbital-period ratios of 3.16:3.89:5.03:5.98 — close to, but not quite, integers. Curiously, the synodic period of Styx and Nix (the time interval between orbital phases when two moons line up on the same side of their planet) is almost exactly 1.5 times the synodic period of Nix and Hydra. How this 'three-body resonance' developed during the growth of the moons is unclear⁶.

The shapes and compositions of Pluto–Charon's four moons provide crucial tests of models of planet and

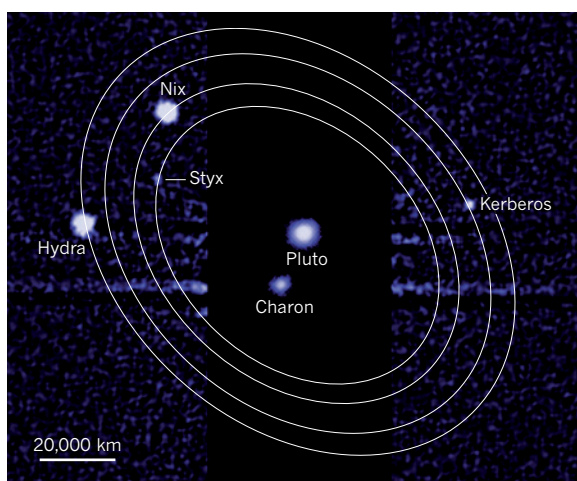


Figure 1 | Pluto and its satellites. This optical image, taken by the Hubble Space Telescope, depicts Pluto, its large moon Charon and four smaller moons Styx, Nix, Kerberos and Hydra. The image was taken in July 2012 when Styx was discovered. Showalter and Hamilton² have used such images to derive several properties of Styx, Nix, Kerberos and Hydra. The ellipses shown are illustrative paths of the moons around the centre of mass of the system.

NASA, ESA, M. SHOWALTER (SETI INST.)

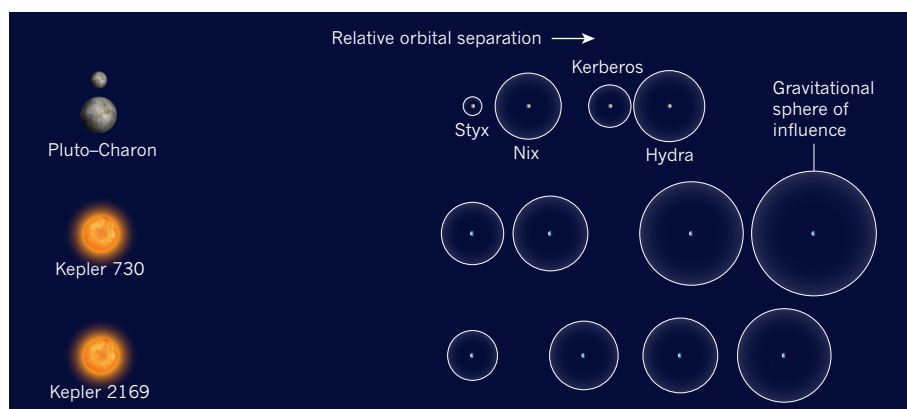


Figure 2 | Orbital architecture. The satellite system of Pluto–Charon resembles some of the exoplanet systems discovered by the Kepler space observatory. Pluto's small moons orbit the system's centre of mass clockwise; the exoplanets orbit their respective stars (Kepler 730 and Kepler 2169). For each system, the scale is set relative to the orbit of the innermost moon or planet (the relative scales vary across systems; the gap between Pluto and Charon is not on the same scale as the orbits of the moons). The dots indicate the relative positions of the moons or planets; the circles show their respective gravitational spheres of influence. Similarly to the exoplanets, the spheres of influence of Pluto's moons leave little space for other potential (as yet undiscovered) objects in intermediate orbits.

satellite formation^{5,7}. Large fragments that survived the giant impact, thought to have led to the creation of the system, might have irregular shapes; satellites grown from much smaller particles might be more rounded. The authors find that the ellipsoidal shapes of the two larger moons, Hydra and Nix, seem more consistent with grown satellites than with impact fragments. Their optical reflectivity, at 40%, is similar to Charon's (36–39%), but lower

than Pluto's (50–65%, which is comparable to the reflectivity of sea ice). With a reflectivity of only 4–6%, Kerberos is as dark as coal and seems out of place with such bright companions. Perhaps it is a dark fragment that was ejected during the giant impact.

It is hoped that NASA's New Horizons⁸ spacecraft, due to fly by Pluto in July, will throw yet more light on these questions. Close-up images taken by the spacecraft will further

constrain the sizes, shapes and reflectivities of Nix, Kerberos and Hydra, but not of Styx — it is too small to be resolved in the images. The mission's spectroscopic measurements of the relative abundances of various ices will probably yield a reflectivity for Styx, and allow comparison of the compositions of the satellites. If new satellites or rings of small particles are found, and their bulk properties established, this will provide additional information on the extent of the system. These much-anticipated observations will lead to improved theories of the formation and evolution of planets and their satellites. Linking all these results to ongoing observations of the growing population of known exoplanets will extend tiny Pluto's reach far beyond the Solar System. ■

Scott J. Kenyon is in the Department of Solar, Stellar and Planetary Physics, Smithsonian Astrophysical Observatory, Cambridge, Massachusetts 02138, USA.
e-mail: skenyon@cfa.harvard.edu

1. Youdin, A. N., Kratter, K. M. & Kenyon, S. J. *Astrophys. J.* **755**, 17 (2012).
2. Showalter, M. R. & Hamilton, D. P. *Nature* **522**, 45–49 (2015).
3. Fabrycky, D. C. et al. *Astrophys. J.* **790**, 146 (2014).
4. Canup, R. M. *Astron. J.* **141**, 35 (2011).
5. Kenyon, S. J. & Bromley, B. C. *Astron. J.* **147**, 8 (2015).
6. Cheng, W. H., Peale, S. J. & Lee, M. H. *Icarus* **241**, 180–189 (2014).
7. Desch, S. J. *Icarus* **246**, 37–47 (2015).
8. Stern, S. A. *Space Sci. Rev.* **140**, 3–21 (2008).

CANCER

Opening LOX to metastasis

New findings implicate the enzyme lysyl oxidase (LOX), secreted by oxygen-deprived breast cancer cells, in inducing bone lesions that precede and facilitate the spread of the cancer cells to the bone. SEE LETTER P.106

NETA EREZ

Despite extensive research, breast cancer remains one of the leading causes of cancer-related deaths in women, and mortality from breast cancer is almost exclusively a result of the tumour spreading to distant organs. Bones are the most common site of metastasis associated with breast cancer, affecting up to 80% of women with metastatic disease. Bone metastases are typically incurable and encompass severe disease features, including pain, bone destruction, hypercalcaemia and debilitating skeletal-related events¹. In this issue, Cox *et al.*² (page 106) establish a mechanistic link between bone metastasis of breast tumours and expression of the enzyme

lysyl oxidase (LOX) by breast cancer cells.

Metastases in bones and other organs are typically diagnosed months or years after the initial diagnosis and removal of the primary tumour. This temporal lag is, at least in part, due to the fact that although disseminated tumour cells have cell-intrinsic survival and proliferative programs, they must be able to manipulate tissue cells in the new and hostile microenvironment of the metastatic organ to support their growth^{3,4}. The early molecular changes at the metastatic niche are the rate-limiting step of metastasis, and understanding the mechanisms that facilitate the formation of a hospitable niche is a central challenge in cancer research.

Hypoxia (lack of an adequate oxygen supply) in the primary tumour is generally associated

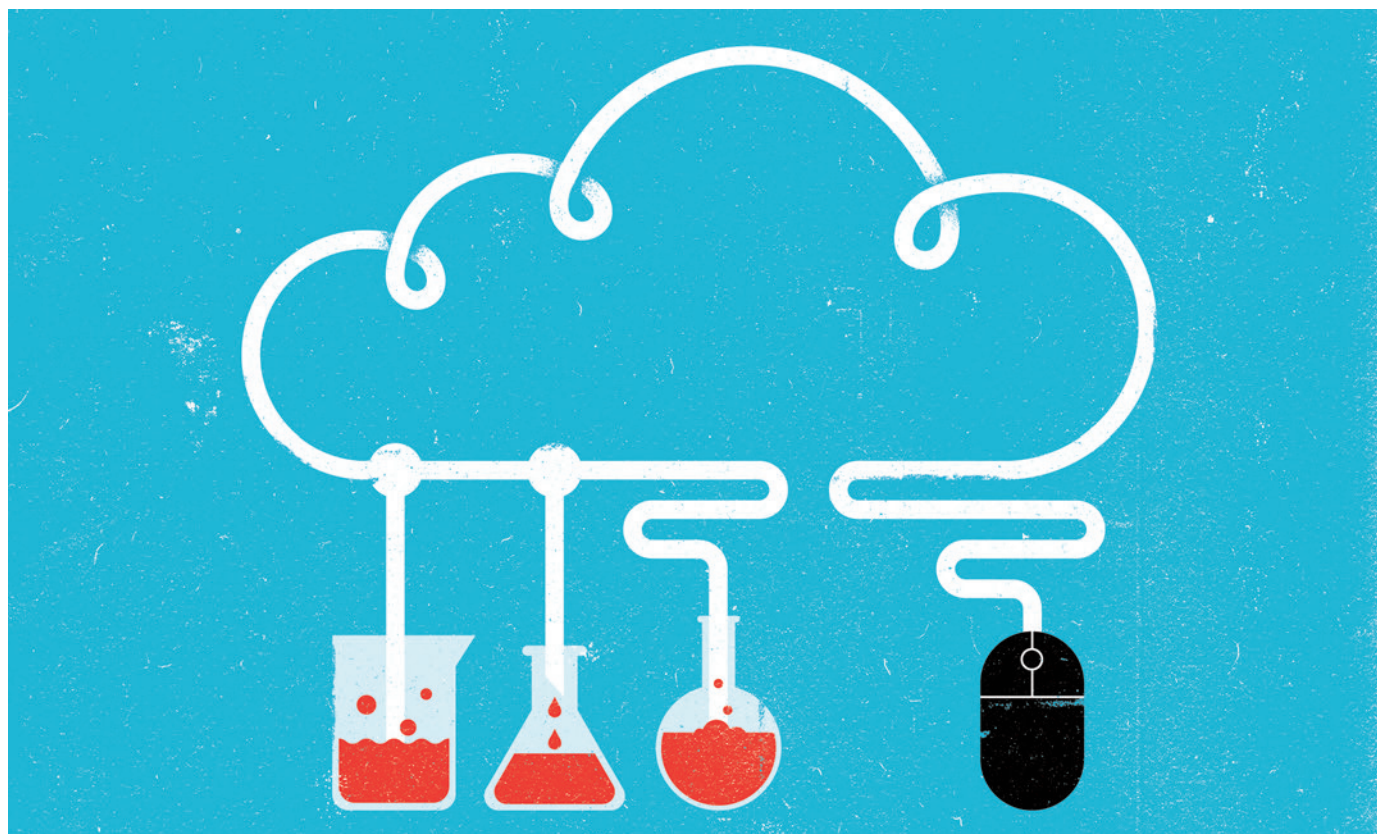
with increased metastases⁵. However, when Cox and colleagues performed retrospective analyses of hypoxic breast tumours from humans, they found that hypoxia was correlated with increased bone metastases only in a subtype of breast tumour that does not express the receptor for oestrogen (ER[−] tumours). In an attempt to identify the factors underlying this specificity, Cox *et al.* analysed the proteins secreted by those breast cancer cells that were attracted to the bone and found that high levels of LOX were associated with bone metastases in ER[−] breast tumours. LOX belongs to a family of secreted proteins that crosslink collagen fibres in the extracellular matrix (ECM), which determines the strength and structural integrity of tissues⁶. LOX has been shown to contribute to metastasis of breast cancer to lungs by modifying the ECM at the metastatic niche^{6,7}, but it had not previously been implicated in regulating bone homeostasis.

Using a translatable mouse model of breast cancer that spontaneously metastasizes to bone, the authors demonstrate that LOX is secreted by hypoxic breast cancer cells and that it disrupts the balance between bone formation and destruction such that there is greater overall bone loss (resorption). These sites of damaged bone provide a favourable environment for disseminated breast cancer cells, thereby facilitating the formation of bone metastases. Moreover,

HOW TO CATCH A CLOUD

Why cloud computing is attracting scientists — and advice from experienced researchers on how to get started.

THE PROJECT TWINS



BY NADIA DRAKE

In February, computer scientist Mark Howison was preparing to analyse RNA extracted from two dozen siphonophores — marine animals closely related to jellyfish and coral. But the local high-performance computer at Brown University in Providence, Rhode Island, was not back up to full reliability after maintenance. So Howison fired up Amazon's Elastic Compute Cloud and bid on a few 'spot instances' — vacant computing capacity that Amazon offers to bidders at a discounted price. After about two hours of fiddling, he had configured a virtual machine to run his software, and had uploaded the siphonophore sequences. Fourteen hours and US\$61 later, the analysis was done.

Researchers such as Howison are increasingly renting computing resources over the Internet from commercial providers such as Amazon, Google and Microsoft — and not

just for emergency backup. As noted in a 2013 report sponsored by the US National Science Foundation (NSF) in Arlington, Virginia, the cloud provides labs with access to computing capabilities that they might not otherwise have (see go.nature.com/mxh4xy). Scientists who need bursts of computing power — such as seismologists combing through data from sensors after an earthquake or astronomers processing observations from space telescopes — can rent extra capacity as needed, instead of paying for permanent hardware.

Scientists can configure their cloud environment to suit their requirements. Although cloud computing cannot handle analyses that require a state-of-the-art supercomputer or quick communication between machines, it may be just right for projects that are too big to tackle on a desktop, but too small to merit a high-performance supercomputer. And working online makes it easy for teams to collaborate by sharing virtual snapshots of their

data, software and computing configuration.

But shifting science into the cloud is not a trivial task. "You need a technical background. It's not really designed for an end user like a scientist," says Howison. Although the activation energy might be high, there are recommended routes for scientists who want to try setting up a cloud environment for their own research group or lab.

A DIY GUIDE TO CLOUD COMPUTING

Most cloud platforms require users to have some basic computing skills, such as an understanding of how to work in the command line, and a familiarity with operating systems and file structures. Once researchers have a strong foundation, the next step is to try working in a cloud.

The most user-friendly cloud for scientists, says plant biologist Andreas Madlung, could be the platform Atmosphere, which was created as part of a collaborative cyber ►

► infrastructure project called iPlant. Funded by the NSF and led by three US universities and the Cold Spring Harbor Laboratory in Long Island, New York, iPlant has been helping scientists to share software and run free analyses in the cloud since 2008.

Designed with scientists in mind, the platform's interface comes with pre-loaded software, a suite of practice data sets and discussion forums for users to help each other to tackle problems. Madlung, at the University of Puget Sound in Tacoma, Washington, teaches an undergraduate bioinformatics course that includes a section on cloud computing. He first introduces his students to the Unix operating system, then has them use that knowledge to analyse RNA sequence data on Atmosphere.

Those who sign up with iPlant are automatically given what equates to around 168 hours of processing time a month, and can request more if needed. Users can load up virtual machines with any extra software that they need, and if a job is too much for standard equipment to handle, tasks can be offloaded to a supercomputer at the Texas Advanced Computing Center in Austin, where iPlant has a guaranteed allocation.

Biologist Mike Covington of the University of California, Davis, shifted his lab's computing work to iPlant after its servers kept crashing because they were overloaded. He has also made copies ('images') of his own virtual machine, so that his collaborators — and any iPlant user — can log in and access the same software, data and computing configuration. "If I spend several hours setting up my virtual machine perfectly for *de novo* genome assembly [reconstructing full-length sequences from short fragments of DNA], I can quickly and easily make it available to any other scientist in the world that wants to do *de novo* assembly with their own data," Covington says.

Such virtual snapshots may become standard for projects that require computational work. Anyone who wants to reproduce, for example, the microbial-genome analysis described in one paper can access a snapshot of the authors' virtual machine on the Amazon cloud, simply by paying for Amazon computing time (B. Ragan-Kelley *et al.* *ISME J.* 7, 461–464; 2013).

PICK A CLOUD

For some researchers, choosing a cloud is straightforward. Scientists at CERN, Europe's particle-physics laboratory near Geneva, Switzerland, have had access to a massive internal cloud running on the software platform OpenStack since 2013. A handful of institutions, such as Cornell University in New York and the University of Notre Dame in Indiana, have developed computing clouds, too. Some, including Notre Dame, outsource their clouds to companies such as Rackspace Private Cloud, a multi-national firm in San Antonio, Texas, that sets up and manages cloud services for users. But for scientists who are not at an

CLOUD RESOURCES

A guide for the perplexed

● Clouds for researchers:

The largest commercial providers include **Amazon's Elastic Compute Cloud**, **Microsoft's Azure** and **Google's Cloud Platform**. Other services are **Terminal.com**, aimed specifically at research; the (free) **Atmosphere** cloud foundation, from the US National Science Foundation-backed iPlant collaboration; **SageMathCloud**; **Cornell University's RedCloud**; **Digital Ocean** — known for quick deployment of cloud apps; and **Rackspace** — a company that sets up clouds using **OpenStack**, an open-source cloud-software platform that the firm developed jointly with NASA.

● Useful resources for cloud explorers:

StarCluster is a tool developed at the Massachusetts Institute of Technology in Cambridge that helps to build a virtual research-computing cluster on Amazon's platform. **Docker** is an open-source platform that allows researchers to share a snapshot of

the code, computing environment and data used to generate analyses. **Project Jupyter** are shareable notebooks that make data, code and analysis easily accessible — and interactive (H. Shen, *Nature* 515, 151–152; 2014). **Nimbus**, partly developed by the Argonne National Laboratory in Illinois, helps to turn a normal computing cluster into a cloud system accessible by remote users.

● Other computing resources:

Practical Computing for Biologists, by Casey Dunn and Steven Haddock (Palgrave Macmillan; 2011).

The **Software Carpentry** computing workshops (see go.nature.com/jg86jj).

The **University of Washington's eScience Institute** advice on "Which compute platform should I use?" (See go.nature.com/iazoio).

Links to these resources, including tutorials, are available at the online version of this article. **N.D.**

institution with a fully functional campus cloud, bushwhacking through the jungle of cloud options can be a frustrating adventure (see 'A guide for the perplexed'). Cloud system set-up can vary, and proficiency with one provider does not guarantee an easy transition to others.

Casey Dunn, an evolutionary biologist who works with Howison at Brown University, prefers to train students on commercial platforms. "When they go on to a postdoc somewhere else or start their own lab, they'll still be able to log into Amazon," he says.

Somalee Datta, the director of bioinformatics at Stanford University's Center for Genomics and Personalized Medicine in California, is using Google's cloud platform to support the centre's enormous amount of genomics data and computing demand, rather than relying only on the servers available at Stanford. She chose Google, she says, for several reasons: the company's developers were actively making tools available for genomics researchers, Google had demonstrated interest in health-care research — and the price was right.

CLOUD CONCERNS

For Datta and others, one key issue surrounding cloud computing is security. "It's a big concern," she says. "Hackers understand where the value is, and they will turn their attention towards that." Still, Datta thinks that clouds are no more or less secure than any other computer network. A university cloud system, for example, is only as solid as the university's firewall. "If I were working on my own or at a small college or company, I would probably feel more secure

with Google's cloud," Datta says (although Stanford has its own army of engineers watching security). The truth is, anyone working with extremely sensitive data might be better off keeping it away from the Internet altogether.

Another key issue for researchers who are venturing into cloud computing is the level of tech support needed. Getting software to run on a new system can take days, and determining how much computing power or memory a virtual machine needs can be an exercise in trial and error. All cloud providers offer training and tutorials, but dedicated support staff are more commonly found at universities with campus clouds.

Despite the challenges, cloud computing is increasingly appealing to scientists, says Darrin Hanson, vice-president of Rackspace Private Cloud. "The last few years have been mostly people who are absolutely out on the bleeding edge," he says. "But now we're starting to see an influx of adopters."

That isn't too surprising, Dunn says — the cloud is not as foreign as it can sometimes sound. "Nearly all consumer computer products now have a cloud component, be it mobile apps, content-streaming services like Netflix or desktop tools like Dropbox," he says. "Research computing is not on the vanguard of some crazy and risky unknown frontier — we are just undergoing the same transitions that are already well under way in industry and the consumer marketplace." ■

Nadia Drake is a freelance science writer in San Francisco, California.

LET'S HAVE A TALK

A word to the wise.

BY XIA JIA (EDITED BY KEN LIU)

There are few reasons to call a linguist after midnight.

It was three in the morning when the phone woke me. A gloomy voice said they needed me right now. My first response was: *Uh-oh, they're finally here. Aliens.*

I met with some odd people in an odd dark room, where we watched odd video clips: a flock of white seal pups huddled together, clamouring continuously, sounding vaguely like a zoo mixed with a parking garage and a kindergarten.

"What the hell is that?" Someone beat me to the question.

We listened to the explanation. A lab designed these intelligent toys, which could imitate and learn human languages from scratch, as newborn babies do. The design summary claimed that the seal pups could ultimately master the equivalent of a five-year-old's language skills.

The lab staff had packed a hundred prototypes in a container to be shipped to beta users; however, the container was mislabelled. When the container was finally tracked down, retrieved and opened, the staff found that the seals, which ought to have been powered down and lying on their bellies silently, were instead making an astonishing ruckus.

"It looks like they are talking with each other in some alien language we can't understand," an incredulous voice penetrated the darkness.

"That is the very thing we must figure out." A man in black, who was leading this midnight meeting, nodded at us, poker-faced. "Is that possible? Who taught them? Remember, the container was sealed the entire time."

"Sealed seals," I murmured. Luckily no one heard me.

"There was a similar case. ISN, Idioma de Señas de Nicaragua," the voice in the darkness replied. "It's a sign language developed by deaf children in a number of schools in western Nicaragua in the 1970s and 1980s."

"Tell me more."

Evidently the man in black found this interesting.

"Well, before the

1970s, there was no deaf community in Nicaragua. Then a couple of vocational schools were established there and hundreds of deaf students enrolled. The language programme, which tried to teach students to lip-read Spanish words, initially achieved little success. Meanwhile, the schoolyard,



the street and the school bus proved to be fertile testing grounds for students figuring out how to communicate with each other on their own. By combining gestures and elements of their individual, idiosyncratic, homegrown sign systems, a new type of sign language rapidly emerged, which is now known as Idioma de Señas de Nicaragua. It is the only time that we've actually seen a language being created out of thin air."

"Not exactly," another voice interrupted. "Actually, someone later created robots with an ability to develop their own language. These 'Lingodroids' were designed to navigate their way through a labyrinth and to create words for mapped locations using a database of syllables. They communicated their findings to each other with microphones and speakers, thereby spawning new words for direction and distance as well."

"How do we know what the Lingodroids were talking about?" said a third voice. "Isn't it possible that a word that sounds innocuous could mean, for example, 'armed revolt'?"

The idea of those simple robots conspiring should have been funny, but none of us laughed.

"Any more ideas?" The man in black looked around.

"Why seal pups?" I asked loudly.

"What?"

"They look weird. Why couldn't you have

chosen puppies or kittens?"

"I don't think that's important." He shrugged.

"Maybe the designer wanted them to appear as timid and inoffensive as possible," I mused. "Doesn't this imply that we fear talking creatures unconsciously?"

"What's your point?"

"I mean, why don't we turn off this video screen, walk out of this dark room, and talk with these ... things directly, as we believe they've already developed their own language? All linguists know that the only way to learn an unknown language is to communicate with a native speaker, to point at objects and ask questions, and to answer their questions as well. We certainly will never understand what they are talking about if we don't knock on the door of that sealed container and say hello first."

I stepped through the door, and all the seal pups fell silent and watched me with their big crystal eyes. *Thank God. Seal pups seem much better than creatures with teeth and claws.* I extended both of my hands to show that there was no hidden weapon, just as I was trained to do in my first field practice, knowing full well that this gesture was probably meaningless in their linguistic system.

A ROBOT MAY NOT INJURE A HUMAN BEING, ALTHOUGH IT MUST PROTECT ITS OWN EXISTENCE.

So high, so low, so many things to know.

"你好。" I said hello in my mother tongue, and waited patiently.

The nearest seal pup put a fluffy paw in my flat palm, and spoke — it sounded like a great big yawn.

I tried my best to imitate it. I could be saying hello, or else just yawning. Anyway it was not a bad start.

"让我们说说话?" I asked gently. Let's have a talk, shall we? ■

Xia Jia is a sci-fi writer in China. Her fiction has appeared in English translation in venues such as *Clarkesworld* and *The Year's Best SF*. This is her first story written in English and was edited by **Ken Liu**, a translator and speculative-fiction author whose works have appeared in *F&SF*, *Asimov's*, *Tor.com* and other venues.

ILLUSTRATION BY JACEY

NEWS IN FOCUS

MAUNA KEA Mega-telescope reshapes sacred Hawaiian mountain **p.15**

METROLOGY Hyper-accurate clocks prepare for mass comparison **p.16**

MÉDECINS SANS FRONTIÈRES Charity transformed by Ebola gets new clout **p.18**



GENETICS Why CRISPR is the most disruptive technology since PCR **p.20**



Workers in southern Italy cut down an olive tree infected with the deadly bacterium *Xylella fastidiosa*.

PLANT DISEASE

Scientists blamed for olive-tree ruin

Italian police investigate researchers' role in a bacterial epidemic that is devastating Puglia's olive groves.

BY ALISON ABBOTT

They did not expect to be hailed as heroes, say the scientists tasked with researching a deadly pathogen that is ravaging olive groves in Puglia, southern Italy. But they certainly did not predict that they would end up feeling like villains.

In the past year, plant scientists at various institutes in Bari, the capital of the Puglia region, have seen their work and their

motivations criticized by local campaigners. Most recently, they have been subject to a police investigation into whether they are responsible for the introduction of the bacterium, *Xylella fastidiosa*, into Puglia, or for allowing its subsequent spread.

Police have questioned several scientists involved in *Xylella* research and confiscated computers and documents from scientific institutes.

"We'd just like to be left to do our work

without this suspicion and this stress," says Donato Boscia, head of the Bari unit of Italy's Institute for Sustainable Plant Protection (IPSP), whom police questioned in April.

"The scientists in Puglia working on the *Xylella* outbreak have been working non-stop for two years," adds Rodrigo Almeida, a *Xylella* specialist at the University of California, Berkeley. "Their reward has been to get attacked constantly — I just can't imagine how this would feel?"

Xylella is endemic in parts of the Americas, including Costa Rica, Brazil and California, but was not previously found in Europe. That changed in October 2013, when scientists at the IPSP and the University of Bari identified¹ the bacterium as the cause of an unusual disease outbreak in olive trees. The outbreak was immediately subjected to European Union (EU) regulations to limit its spread, and regional scientists began a systematic effort to understand the disease and contain it. Scientists went on to show that the bacterium was being carried by the spittlebug insect².

From the start, farmers and environmentalists in Italy objected to containment measures, which involved uprooting trees and spraying the groves with pesticides. But trouble for the Puglian scientists began in April 2014, when individuals told police that they suspected the epidemic was caused by bacteria that scientists had brought from California for a European training course on *Xylella* at the Mediterranean Agronomic Institute of Bari (IAMB) in 2010.

Scientists say that this suggestion is ludicrous because the Puglia strain is different from the strains used at the workshop; the widely accepted theory is that the infection was imported with ornamental plants from Costa Rica, where the endemic *Xylella* strain matches the Puglia strain. However, the complaints spawned a much broader investigation by public prosecutors, including probes into what role scientists may have had in the epidemic. On 4 May, police confiscated computers and documents from the University of Bari and the IPSP, as well as documents from the Centre for Agricultural Research Basile Caramia in Locorotondo, Puglia. Two weeks later, police also seized documents from the Italian ministry of agriculture in Rome. The IAMB has voluntarily passed documents to police.

The prosecutors declined *Nature's* request for comment. But in March, one of them, Elsa Valeria Mignone, implied in an interview ▶

► with *Famiglia Cristiana* magazine that they are looking into theories that the bacterium may have been deliberately introduced into the area, or became entrenched because agricultural scientists failed to monitor the region properly, either deliberately or through neglect.

On 12 May, the Italian Association of Scientific Societies in Agriculture (AISSA), which represents 4,000 scientists in Italy, published a public letter defending the Puglian scientists and their work. “The claims do not have a scientific basis — that’s what has shocked the scientific community,” says Vincenzo Gerbi, AISSA president.

Puglian scientists have had to contend with public criticism, too. Several popular blogs devoted to the *Xylella* emergency have cast doubt on scientists’ ways of working and their results — saying, for example, that a cure exists but is being suppressed. And Peacelink, an Italian non-governmental organization, wrote to the EU health commissioner in March saying that *Xylella* had not been proved to be the source of the outbreak, and that the deaths were instead the result of a fungus that could be



Donato Boscia researches *Xylella fastidiosa* at Italy’s Institute for Sustainable Plant Protection.

eliminated without destroying trees. An expert panel of the European Food Safety Authority debunked these suggestions in a report published in April. “It’s frustrating to hear all these complaints when you think you are doing a

public service,” says Anna Maria D’Onghia, head of the pest-management division at the IAMB, who has been questioned by police. “We are always being attacked for doing too little, or the wrong things.”

Boscia says that the “attempts to delegitimize the results of scientific research” have been worse than the police investigations. But it is not all bad news for Puglian scientists. On 27 May, the regional government announced a €2-million (US\$2.2-million) fund for projects that might aid the diagnosis, epidemiology and monitoring of the bacterium. It said that a ‘containment area’ in the province of Lecce — where the bacterium is now endemic, making complete eradication impossible — will be used as an open-air *Xylella* laboratory. National and European research agencies have also promised money, says Boscia. “The outdoor laboratory would be perfect for all of us — and also allow critics to put their own theories to the test.” ■

1. Saponari, M., Boscia, D., Nigro, F. & Martelli, G. P. *J. Plant Pathol.* <http://dx.doi.org/10.4454/JPP.V95I3.035> (2013).
2. Elbeaino, T. et al. *Phytopathol. Mediterr.* **53**, 328–232 (2014).

POLITICAL SCIENCE

Retracted gay-marriage study debated at misconduct meet-up

Over rum cocktails at the World Conference on Research Integrity, experts discussed what can be learnt from the fallout of a flawed political-science paper.

BY RICHARD VAN NOORDEN, RIO DE JANEIRO

The world’s largest gathering of specialists in research misconduct kicked off on 31 May in Rio de Janeiro, Brazil, shortly after science’s latest scandal broke. On the evening before the start of sessions on how to diagnose and remedy ethical faults in research, delegates to the 4th World Conference on Research Integrity sipped caipirinhas, Brazil’s national cocktail — and swapped views on what could be gleaned from a flawed political-science study.

The paper in question, which claimed to show that short conversations with a canvasser who is gay could encourage voters to support same-sex marriage, made headlines across the world when it was published in *Science* last December (M. J. LaCour and D. P. Green *Science* **346**, 1366–1369; 2014) — and again when it was retracted last week (*Science* <http://doi.org/4zt>; 2015). “The case is very much on our minds,” said Melissa Anderson, a co-organizer

of the meeting who studies scientific integrity at the University of Minnesota in Minneapolis.

Although the case throws up new instances of misconduct, and of inadequate supervision by senior academics, delegates to the Rio conference felt that, in general, the case illuminated little about the academic system that a steady drip-drip of research misconduct has not already highlighted. The main challenge, said Brian Martinson, a social scientist at the HealthPartners Institute for Education and Research in Minneapolis, is how to create a supportive environment that incentivizes reliable, reproducible research. “A lot of people think the bad stuff in science comes from academics being greedy or narcissistic — but that ignores how the structural arrangements in science, like the decline of funding and stable academic positions in the United States, leads people into bad behaviour,” he said.

In the latest twist in the debacle, co-author Michael LaCour, a graduate student in political science at the University of California, Los Angeles (UCLA), has admitted to misrepresenting

his funding sources and the incentives he used to attract people to take part in the study. In a 29 May online reply to researchers who had spotted irregularities in his survey data (see go.nature.com/acpxnh), LaCour said that he had deleted his raw data for reasons of confidentiality and admitted that he did not get ethical approval from an institutional review board before he did the work, or before he submitted it to *Science*. The document did not include convincing evidence that he had conducted the surveys.

LaCour told *The New York Times* that he stands by his finding — but his co-author Donald Green, a political scientist at the University of Columbia in New York City, does not: Green requested the paper’s retraction after three outside scientists told him about irregularities in its survey data, and he apologized for

“Academia should be concerned that its system of checks and balances has problems.”

Ancient proteins resolve the evolutionary history of Darwin's South American ungulates

Frido Welker^{1,2}, Matthew J. Collins¹, Jessica A. Thomas¹, Marc Wadsley¹, Selina Brace³, Enrico Cappellini⁴, Samuel T. Turvey⁵, Marcelo Reguero⁶, Javier N. Gelfo⁶, Alejandro Kramarz⁷, Joachim Burger⁸, Jane Thomas-Oates⁹, David A. Ashford¹⁰, Peter D. Ashton¹⁰, Keri Rowsell¹, Duncan M. Porter¹¹, Benedikt Kessler¹², Roman Fischer¹², Carsten Baessmann¹³, Stephanie Kaspar¹³, Jesper V. Olsen¹⁴, Patrick Kiley¹⁵, James A. Elliott¹⁵, Christian D. Kelstrup¹⁴, Victoria Mullin¹⁶, Michael Hofreiter^{1,17}, Eske Willerslev⁴, Jean-Jacques Hublin², Ludovic Orlando⁴, Ian Barnes³ & Ross D. E. MacPhee¹⁸

No large group of recently extinct placental mammals remains as evolutionarily cryptic as the approximately 280 genera grouped as 'South American native ungulates'. To Charles Darwin^{1,2}, who first collected their remains, they included perhaps the 'strangest animal[s] ever discovered'. Today, much like 180 years ago, it is no clearer whether they had one origin or several, arose before or after the Cretaceous/Palaeogene transition 66.2 million years ago³, or are more likely to belong with the elephants and sirenians of superorder Afrotheria than with the euungulates (cattle, horses, and allies) of superorder Laurasiatheria^{4–6}. Morphology-based analyses have proved unconvincing because convergences are pervasive among unrelated ungulate-like placentals. Approaches using ancient DNA have also been unsuccessful, probably because of rapid DNA degradation in semitropical and temperate deposits. Here we apply proteomic analysis to screen bone samples of the Late Quaternary South American native ungulate taxa *Toxodon* (Notoungulata) and *Macrauchenia* (Litopterna) for phylogenetically informative protein

sequences. For each ungulate, we obtain approximately 90% direct sequence coverage of type I collagen $\alpha 1$ - and $\alpha 2$ -chains, representing approximately 900 of 1,140 amino-acid residues for each subunit. A phylogeny is estimated from an alignment of these fossil sequences with collagen (I) gene transcripts from available mammalian genomes or mass spectrometrically derived sequence data obtained for this study. The resulting consensus tree agrees well with recent higher-level mammalian phylogenies^{7–9}. *Toxodon* and *Macrauchenia* form a monophyletic group whose sister taxon is not Afrotheria or any of its constituent clades as recently claimed^{5,6}, but instead crown Perissodactyla (horses, tapirs, and rhinoceroses). These results are consistent with the origin of at least some South American native ungulates^{4,6} from 'condylarths', a paraphyletic assembly of archaic placentals. With ongoing improvements in instrumentation and analytical procedures, proteomics may produce a revolution in systematics such as that achieved by genomics, but with the possibility of reaching much further back in time.

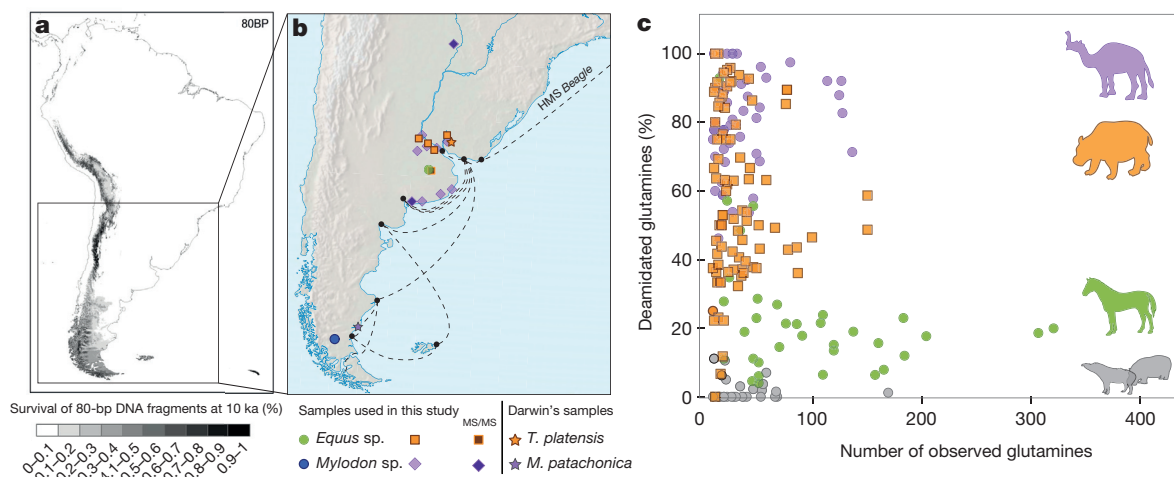


Figure 1 | Samples used in this investigation. **a**, Predicted survival of an 80-base-pair (bp) DNA fragment after 10,000 years (10 ka) modelled using the rate given in ref. 29. **b**, Location of finds by Darwin^{1,2} and of samples used in this study (basemap³⁰). **c**, Glutamine deamidation ratios for bone samples from

the sequenced Pleistocene SANUs are high compared with coeval horse (MACN Pv 5719) as well as modern hippopotamus and tapir, providing support for the authenticity of the ancient sequences (see Supplementary Information).

¹BioArCh, University of York, York YO10 5DD, UK. ²Department of Human Evolution, Max Planck Institute for Evolutionary Anthropology, 04103 Leipzig, Germany. ³Department of Earth Sciences, Natural History Museum, London SW7 5BD, UK. ⁴Centre for GeoGenetics, Natural History Museum of Denmark, University of Copenhagen, Øster Voldgade 5–7, 1350 Copenhagen K, Denmark. ⁵Institute of Zoology, Zoological Society of London, London NW1 4RY, UK. ⁶CONICET - División Paleontología de Vertebrados, Museo de La Plata. Facultad de Ciencias Naturales y Museo de La Plata, Universidad Nacional de La Plata. Paseo del Bosque s/n, B1900FWA, La Plata, Argentina. ⁷Sección Paleontología de Vertebrados, Museo Argentino de Ciencias Naturales "Bernardino Rivadavia", 470 Angel Gallardo Av., C1405DJR, Buenos Aires, Argentina. ⁸Institute of Anthropology, Johannes Gutenberg-University, Anselm-Franz-von-Bentzel-Weg 7, D-55128 Mainz, Germany. ⁹Department of Chemistry, University of York, York YO10 5DD, UK. ¹⁰Bioscience Technology Facility, Department of Biology, University of York, York YO10 5DD, UK. ¹¹Department of Biological Sciences, Virginia Polytechnic Institute and State University, Blacksburg, Virginia 24061, USA. ¹²Target Discovery Institute, Nuffield Department of Medicine, University of Oxford, Roosevelt Drive, Oxford OX3 7FZ, UK. ¹³Applications Development, Bruker Daltonik GmbH, 28359 Bremen, Germany. ¹⁴Novo Nordisk Foundation Center for Protein Research, Faculty of Health Sciences, University of Copenhagen, Blegdamsvej 3b, 2200 Copenhagen, Denmark. ¹⁵Department of Materials Science and Metallurgy, University of Cambridge, Cambridge CB3 0FS, UK. ¹⁶Smurfit Institute of Genetics, Trinity College Dublin, Dublin 2, Ireland. ¹⁷Institute for Biochemistry and Biology, Karl-Liebknecht-Strasse 24–25, 14476 Potsdam OT Golm, Germany. ¹⁸Department of Mammalogy, American Museum of Natural History, New York, New York 10024, USA.

South American native ungulates (SANUs) are conventionally organized into five orders (Litopterna, Notoungulata, Astrapotheria, Xenungulata, and Pyrotheria) that are sometimes grouped together as a separate placental superorder (Meridiungulata)¹⁰. They appear very early in the Palaeogene record and evolved thereafter along many divergent lines, as their abundant fossil record attests. Most lineages had become extinct by the end of the Miocene epoch, although a few species of litopterns and notoungulates persisted into the Late Pleistocene epoch. Despite continuing interest in their evolutionary history (for example

refs 5, 11–14), phylogenetic relationships of the major SANU clades to one another and to other placentals remain poorly understood (see Supplementary Information). Although some recent investigations (for example refs 4–6) have suggested that basal South American members of Litopterna conclusively group with certain Holarctic condylarths, and are thus best placed in Euungulata (Laurasiatheria), several other studies claim to have identified potential synapomorphies linking various SANU taxa with Afrotheria^{5,6,15,16}. This latter view is broadly consistent with such indicators as prolonged late Mesozoic faunal exchange

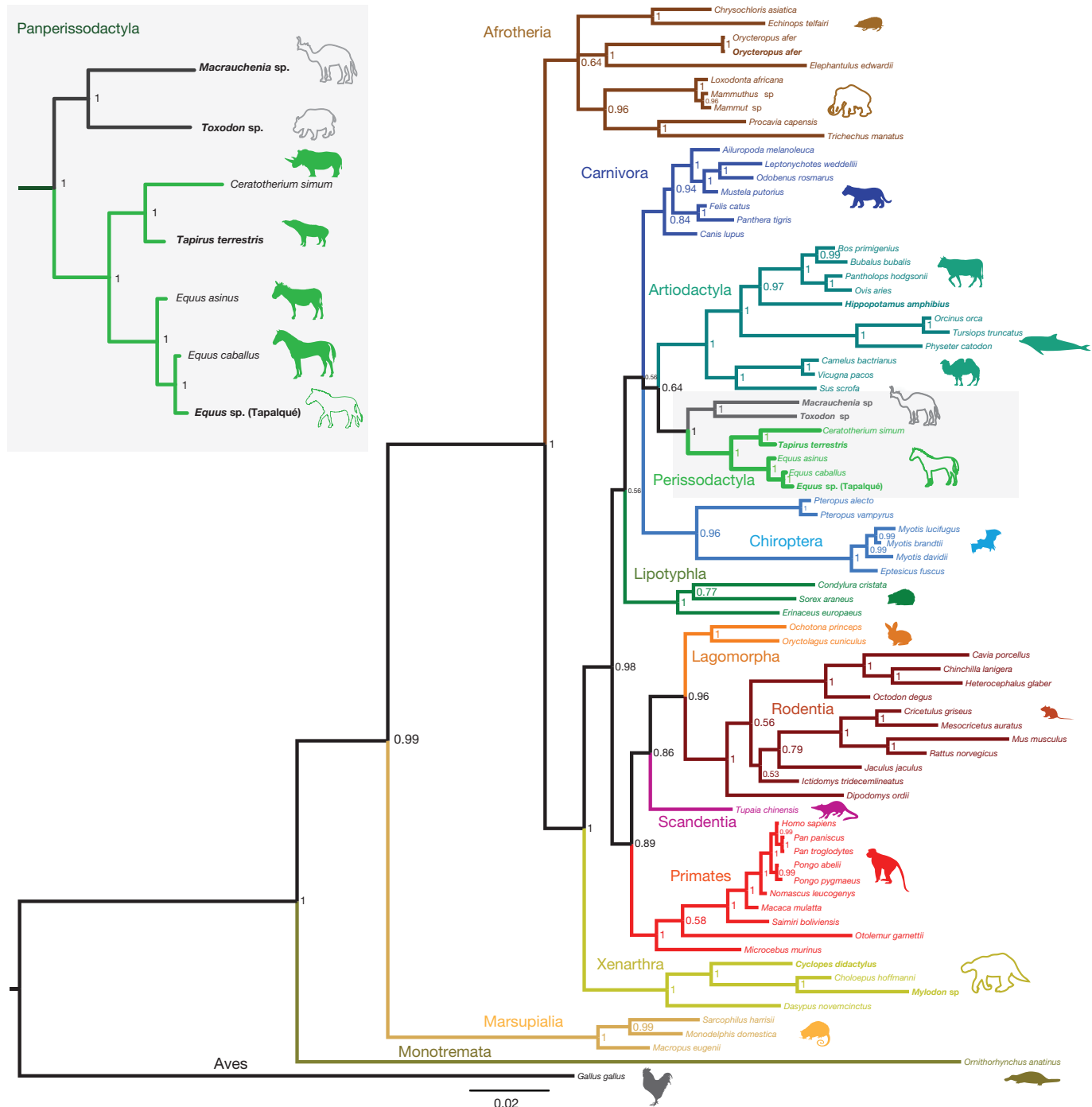


Figure 2 | Relationship of *Toxodon* (Notoungulata) and *Macrauchenia* (Litopterna) to other placental mammals. Fifty per cent majority rule Bayesian consensus tree of COL1 protein sequence data, with chicken (*Gallus*) as outgroup. Scale bar indicates branch length, expressed as the expected number of substitutions per site. Major clades (orders and superorders) are colour coded; species names in bold indicate collagen sequences derived from

MS/MS rather than genomic data, fossil taxa depicted in silhouette. Inset: in all tree-reconstructions conducted (see Supplementary Information), *Toxodon* and *Macrauchenia* (dark grey) group monophyletically at the base of crown Perissodactyla (light green) with 100% posterior probability, forming Panperissodactyla.

between Gondwanan landmasses¹⁷ and the possibility that Xenarthra (the other major endemic South American placental clade) is also related to Afrotheria^{7–9,18}. However, most of the character evidence on which the SANU–Afrotheria sister-group hypothesis is based is in dispute^{19,20}. In principle, a more definitive test of phylogenetic affinities could come from genomic data, but so far the application of ancient DNA techniques has been limited and DNA survival is predicted to be poor (Fig. 1a) (see Supplementary Information).

Type I collagen (COL1), a structural protein comprising two separate chains, COL1 α 1 and COL1 α 2 (coded by genes on separate chromosomes), is known to provide useful systematic information ('barcoding')²¹, and can be recovered over significantly longer time spans than DNA²². Most of the 48 samples of *Toxodon* sp. and *Macrauchenia* sp. we analysed for sequence information came from localities in Buenos Aires province (Supplementary Information and Fig. 1b), especially from areas that experience subtropical to maritime–temperate climates²³. Peptide mass fingerprinting (ZooMS) (Supplementary Information) of COL1 extracts²⁴ revealed variable levels of collagen preservation in the sample set (see Supplementary Information and Extended Data Table 1). After screening, two samples each of *Toxodon* and *Macrauchenia* displaying excellent COL1 preservation (see Extended Data Fig. 1) were selected for liquid chromatography–tandem mass spectrometry (LC–MS/MS) sequencing using a variety of LC–MS/MS platforms, and direct radiocarbon dating (Supplementary Information and Extended Data Table 1).

Combining analyses from a total of eight MS/MS runs, we were able to assemble near-complete COL1 sequences for *Macrauchenia* (89.4%) and *Toxodon* (91.0%), similar to levels of sequence coverage for modern samples. Comparative analyses with fossil and modern samples suggest that our SANU COL1 sequences are authentic: COL1 amino-acid sequence variation is located in similar positions along both COL1 chains compared with collagen sequences derived from genomic sources (Extended Data Fig. 2) and deamidation ratios conform to expectations for Pleistocene samples (Extended Data Fig. 3), a criticism of previous pre-Holocene collagen studies²⁵. Independent manual *de novo* sequencing of product ion spectra for selected phylogenetically relevant peptides was in full agreement with sequence assignments from database searches. Furthermore, 86.70% and 94.41% of the assembled species consensus sequences for *Macrauchenia* and *Toxodon*, respectively, were covered by a minimum of two independent product ion spectra, with individual positions being covered by an average of 77.1 (for *Macrauchenia*) and 103.9 (for *Toxodon*) product ion spectra (Extended Data Table 2).

Molecular evidence for the phylogenetic placement of the extinct SANUs *Macrauchenia* and *Toxodon* was previously unavailable. To examine the phylogenetic position of these taxa, an alignment of 76 mammalian COL1 sequences and one outgroup (*Gallus*) was constructed from available mammalian genomic COL1 sequences in GenBank, as well as several MS/MS-derived protein sequences obtained for this study. A Bayesian phylogenetic tree was estimated from the data, with separate models of substitution applied to two partitions (COL1 α 1 and COL1 α 2). The resulting consensus tree (Fig. 2) is based solely on protein sequence data, but its topology corresponds closely to branching relationships in Placentalia recovered in recent molecular studies^{7–9}. Furthermore, nodes poorly supported in this study (for example, those within Laurasiatheria) involve the same series of phylogenetic relationships that have proved difficult to resolve in other studies^{5,7–9}. To examine how alternative topologies could affect the position of our target taxa we ran additional Bayesian analyses, using constraints mirroring differing mammal phylogenies (Extended Data Fig. 4 and Supplementary Information).

In all phylogenetic analyses performed with our data (including the use of unconstrained parsimony and probabilistic tree reconstruction methods), *Macrauchenia* and *Toxodon* formed a strongly supported monophyletic pair that grouped exclusively with Perissodactyla (as represented by extant *Equus*, *Tapirus*, and *Ceratotherium*). Neither showed any association with the clades conventionally contained in Afrotheria

(see Supplementary Information). In future, and with more evidence, it may be appropriate to include these SANUs within an augmented definition of Perissodactyla. At present, we prefer to recognize Litopterna and Notoungulata as part of a branch-based rankless taxon Pan-perissodactyla, uniting all taxa more closely related to crown Perissodactyla than to any other extant taxon of placentals (see Supplementary Information).

Despite poor resolution at the base of Laurasiatheria, the fact that *Macrauchenia* and *Toxodon* were not recovered at a basal position within Euungulata would imply that the initial split between Perissodactyla and Artiodactyla occurred earlier than the origin of the SANU clades. Since fossil evidence indicates that both litopterns and notoungulates were already present in South America by the Early Palaeocene epoch^{4,26}, this would suggest that the divergence events leading to the modern orders must have occurred at, if not before, the Cretaceous/Palaeogene boundary (Supplementary Information and Extended Data Fig. 5).

These observations do not constitute a full molecular test of SANU monophyly, as there is no proteomic evidence available for members of the remaining orders (Astrapotheria, Xenungulata, Pyrotheria). As far as it is now known, Xenungulata and Pyrotheria became extinct in the Late Palaeogene, but some members of Astrapotheria (sometimes considered the sister group of Notoungulata²⁷) persisted until the Middle Miocene (16.0–11.6 million years ago (Ma) (ref. 28)). This is well beyond the extrapolated estimate of less than 4.0 Ma for good collagen survival in an optimal (cool) burial environment²², although the empirical limits on collagen survival under differing environmental conditions are poorly understood at present (see Supplementary Information).

The results presented here establish that, in principle, the approximately 2,100 residues (that is, one-fifth of the amino-acid residues analysed in ref. 9) comprising bone COL1 in placental mammals are sufficiently variable to provide reliable systematic information. Of course, a phylogeny based on two genes may be sensitive to factors affecting phylogenetic resolution such as gene lineage sorting, missing taxa, aberrant molecular rates, and selection acting on protein coding sequences. Despite this, the topology derived from the collagen sequences in this study is in broad agreement with other mammalian trees, and supports monophyletic placement of two Late Quaternary SANUs with a high degree of confidence. Reliable systematic information is an essential foundation for many other enquiries in evolutionary biology, including patterns of early Cenozoic mammalian divergence, radiation, extinction, and palaeobiogeography. With further development, molecular sequencing of degradation-resistant proteins such as bone COL1 is sure to open new vistas in the study of vertebrate evolution.

Online Content Methods, along with any additional Extended Data display items and Source Data, are available in the online version of the paper; references unique to these sections appear only in the online paper.

Received 28 September 2014; accepted 22 January 2015.

Published online 18 March 2015.

- Owen, R. in *The Zoology of the Voyage of H.M.S. Beagle, under the Command of Captain Fitzroy, during the Years 1832 to 1836* (ed. Darwin, C.) Part I, Numbers I–IV (Smith Elder 1838–40).
- Darwin, C. *Journal of Researches into the Geology and Natural History of the Various Countries Visited by H.M.S. Beagle: Under the Command of Captain FitzRoy, R.N. from 1832 to 1836* (Henry Colburn, 1839).
- Husson, D. et al. Astronomical calibration of the Maastrichtian (Late Cretaceous). *Earth Planet. Sci. Lett.* **305**, 328–340 (2011).
- De Muizon, C. & Cifelli, R. L. The “condylarths” (archaic Ungulata, Mammalia) from the early Palaeocene of Tiupampa (Bolivia): implications on the origin of the South American ungulates. *Geodiversitas* **22**, 1–150 (2000).
- Agnolin, F. L. & Chimento, N. R. Afrotherian affinities for endemic South American “ungulates”. *Mamm. Biol.* **76**, 101–108 (2011).
- O'Leary, M. A. et al. The placental mammal ancestor and the post-K-Pg radiation of placentals. *Science* **339**, 662–667 (2013).
- Dos Reis, M. et al. Phylogenomic datasets provide both precision and accuracy in estimating the timescale of placental mammal phylogeny. *Proc. R. Soc. B* **279**, 3491–3500 (2012).

8. Song, S., Liu, L., Edwards, S. V. & Wu, S. Resolving conflict in eutherian mammal phylogeny using phylogenomics and the multispecies coalescent model. *Proc. Natl Acad. Sci. USA* **109**, 14942–14947 (2012).
9. Meredith, R. W. *et al.* Impacts of the Cretaceous Terrestrial Revolution and KPg extinction on mammal diversification. *Science* **334**, 521–524 (2011).
10. McKenna, M. C., Bell, S. K. & Simpson, G. G. *Classification of Mammals above the Species Level* (Columbia Univ. Press, 1997).
11. Simpson, G. G. The beginning of the age of mammals in South America. Part 2. *Bull. Am. Mus. Nat. Hist.* **137**, 1–259 (1967).
12. Patterson, B. & Pascual, R. The fossil mammal fauna of South America. *Q. Rev. Biol.* **43**, 409–451 (1968).
13. Cifelli, R. L. in *Mammal Phylogeny* (eds Szalay, F. S., Novacek, M. J. & McKenna, M. C.) 195–216 (Springer, 1993).
14. Horowitz, I. Eutherian mammal systematics and the origins of South American ungulates as based on postcranial osteology. *Bull. Carnegie Mus. Nat. Hist.* **63**–79 (2004).
15. Asher, R. J. & Lehmann, T. Dental eruption in afrotherian mammals. *BMC Biol.* **6**, 14 (2008).
16. Sánchez-Villagra, M. R., Narita, Y. & Kuratani, S. Thoracolumbar vertebral number: the first skeletal synapomorphy for afrotherian mammals. *Syst. Biodivers.* **5**, 1–7 (2007).
17. Van Bocxlaer, I., Roelants, K., Biju, S. D., Nagaraju, J. & Bossuyt, F. Late Cretaceous vicariance in Gondwanan amphibians. *PLoS ONE* **1**, e74 (2006).
18. Murphy, W. J., Pringle, T. H., Crider, T. A., Springer, M. S. & Miller, W. Using genomic data to unravel the root of the placental mammal phylogeny. *Genome Res.* **17**, 413–421 (2007).
19. Billet, G. & Martin, T. No evidence for an afrotherian-like delayed dental eruption in South American notoungulates. *Naturwissenschaften* **98**, 509–517 (2011).
20. Kramarz, A. & Bond, M. Critical revision of the alleged delayed dental eruption in South American “ungulates”. *Mamm. Biol.* **79**, 170–175 (2014).
21. Van Doorn, N. L. in *Encyclopedia of Global Archaeology 7998–8000* (Springer, 2014).
22. Buckley, M. & Collins, M. J. Collagen survival and its use for species identification in Holocene-lower Pleistocene bone fragments from British archaeological and paleontological sites. *Antiqua* **1**, e1 (2011).
23. Hamza, V. M. & Vieira, F. P. in *Climate Change - Geophysical Foundations and Ecological Effects* (eds Blanco, J. & Kheradmand, H.) Ch. 6, 113–136 (Intech, 2011).
24. Buckley, M., Collins, M., Thomas-Oates, J. & Wilson, J. C. Species identification by analysis of bone collagen using matrix-assisted laser desorption/ionisation time-of-flight mass spectrometry. *Rapid Commun. Mass Spectrom.* **23**, 3843–3854 (2009).
25. Asara, J. M., Schweitzer, M. H., Freemark, L. M., Phillips, M. & Cantley, L. C. Protein sequences from mastodon and *Tyrannosaurus rex* revealed by mass spectrometry. *Science* **316**, 280–285 (2007).
26. Wilf, P., Rubén Cúneo, N., Escapa, I. H., Pol, D. & Woodburne, M. O. Splendid and seldom isolated: the paleobiogeography of Patagonia. *Annu. Rev. Earth Planet. Sci.* **41**, 561–603 (2013).
27. Van Valen, L. M. Paleocene dinosaurs or Cretaceous ungulates in South America? *Evol. Monogr.* **10**, 1–79 (1988).
28. Vizcaino, M., Mikolajewicz, U., Jungclauss, J. & Schurgers, G. Climate modification by future ice sheet changes and consequences for ice sheet mass balance. *Clim. Dyn.* **34**, 301–324 (2010).
29. Allentoft, M. E. *et al.* The half-life of DNA in bone: measuring decay kinetics in 158 dated fossils. *Proc. R. Soc. B* **279**, 4724–4733 (2012).
30. US Central Intelligence Agency. *The World Factbook 2013–14* (Central Intelligence Agency, 2013).

Supplementary Information is available in the online version of the paper.

Acknowledgements We thank the Museo Argentino de Ciencias Naturales “Bernardino Rivadavia”, Buenos Aires (MACN), the Museo de La Plata (MLP), and the Natural History Museum of Denmark, Copenhagen (ZMK), for allowing us to sample fossil specimens in their collections for this project. The American Museum of Natural History and the Copenhagen Zoo provided samples of extant mammals suitable for collagen extraction. Mogens Andersen and Kristian Gregersen of ZMK provided information on specimens in their care. This work was partly supported by SYNTAX award “Barcode of Death”, European Research Council (ERC) Advanced Award CodeX, ERC Consolidator Award GeneFlow, SYNTHESIS FP7 grant agreement 226506, Engineering and Physical Sciences Research Council NE/G012237/1 and National Science Foundation OPP 1142052. J.T.-O. and D.A.A. are members of the York Centre of Excellence in Mass Spectrometry, created thanks to a major capital investment through Science City York, supported by Yorkshire Forward with funds from the Northern Way Initiative.

Author Contributions R.D.E.M., I.B., and M.J.C. conceived the project and coordinated the writing of the paper with F.W. and J.A.T., with all authors participating. J.N.G., A.K., M.R., E.C., and R.D.E.M. collected fossil and extant mammal samples for protein extraction. M.W., S.B., I.B., J.A.T., J.B., and M.H. conducted DNA analyses. F.W., M.W., P.A., S.K., C.B., C.K., D.A., J.T.-O., R.F., B.K., P.K., J.A.E., E.C., L.O., and M.J.C. performed protein analyses and interpretation of results. J.A.T., I.B., F.W., and M.W. conducted the phylogenetic analyses and constructed trees. S.T.T., J.N.G., M.R., D.M.P., and R.D.E.M. provided the historical, systematic, and palaeontological framework for this study. J.-J.H., E.W., and J.S. provided technical information. Final editing and manuscript preparation was coordinated by M.J.C., R.D.E.M., and I.B.

Author Information Raw MS/MS and PEAKS search files have been deposited to the ProteomeXchange with identifier PXD001411. Generated COL1 species consensus sequences will be available in the UniProt Knowledgebase under the accession numbers COHJN3–COHJP8. Reprints and permissions information is available at www.nature.com/reprints. The authors declare no competing financial interests. Readers are welcome to comment on the online version of the paper. Correspondence and requests for materials should be addressed to I.B. (i.barnes@nhm.ac.uk), F.W. (frido.welker@palaeo.eu), M.J.C. (matthew.collins@york.ac.uk), or R.D.E.M. (macphee@amnh.org).

METHODS

No statistical methods were used to predetermine sample size.

Zooarchaeology by MS screening. After zooarchaeology by MS (ZooMS) screening of selected *Macrauchenia* ($n = 26$) and *Toxodon* ($n = 22$), four bone specimens were selected for MS/MS analysis. Using a combination of enzymes, we were able to obtain sequence coverage of around 90% for COL1 for both genera. Subsamples of about 200 mg were taken from each bone or skin sample for COL1 extraction. Bone samples were demineralized in 0.6 M HCl for 8 days at 4 °C. The acid was removed and the samples were washed three times with ultrapure water then heated at 70 °C in 0.6 M HCl for 48 h to gelatinize the COL1. Samples were then ultrafiltered using 30 kilodalton filters and washed through with ultrapure water. Half a millilitre from each sample retentate was taken to dryness overnight in a vacuum centrifuge. One hundred microlitres of 50 mM ammonium bicarbonate solution (pH 8) was added to each sample. The samples were then digested with trypsin ($0.5 \mu\text{g} \mu\text{l}^{-1}$, for 16 h at 37 °C). After enzyme digestion, samples were acidified with 2 μl of 5% (volume %) trifluoroacetic acid (TFA). Samples were then concentrated using C18 ZipTips: the ZipTips were prepared using a conditioning solution of 50% acetonitrile, 49.9% water, 0.1% TFA; the tips were then washed with a washing solution of 0.1% TFA; the sample was then transferred over the column ten times; the tips were then washed again using 0.1% TFA solution; finally the sample was eluted using the conditioning solution. For ZooMS analysis, 1 μl of each sample was spotted in triplicate onto a ground steel plate with 1 μl of CHCA matrix solution (1% in 50% ACN/0.1% TFA (v/v/v)). MS analysis was on a Bruker ultraflex matrix-assisted laser desorption/ionization–tandem time of flight (MALDI–TOF/TOF) mass spectrometer over the m/z range 800–4,000 (Extended Data Fig. 1). Screening revealed large differences in COL1 spectral quality between samples. Of 46 SANU samples, only five (3 out of 20 from *Toxodon*, 2 out of 25 from *Macrauchenia*) yielded good ZooMS spectra. One of the three *Toxodon* samples (ZMK 22/1889) produced a few strong MS/MS spectra and only four samples (two each from *Macrauchenia* and *Toxodon*) were used in the main study.

MS/MS sequence analysis. Selected collagen extracts from pooled trypsin ($0.4 \mu\text{g} \mu\text{l}^{-1}$, 16 h, 37 °C) and elastase digests ($0.8 \mu\text{g} \mu\text{l}^{-1}$, 16 h, 37 °C) of two specimens of each SANU sample were analysed on both Thermo Scientific Orbitrap and Bruker maXis HD LC–MS/MS platforms. Additionally, Orbitrap and maXis HD instruments were also used for sequencing collagen from modern aardvark (*Orycteropus afer*), silky anteater (*Cyclopes didactylus*), hippopotamus (*Hippopotamus amphibius*), and South American tapir (*Tapirus terrestris*), as well as Pleistocene *Myiodon darwini* and *Equus* sp. samples from South America.

Hybrid Quadrupole–Orbitrap. Sample separation was performed on an Ultimate 3000 RSLCnano LC system (Thermo Scientific). Peptides were first trapped on a Pepmap μ -pre-column ($0.5 \text{ cm} \times 300 \mu\text{m}$; Thermo Scientific) and separated on an EASY Spray PepMap UHPLC column ($50 \text{ cm} \times 75 \mu\text{m}$, 2 μm particles, 40 °C; Thermo Scientific) with a 60 min multi-step acetonitrile gradient ranging from 2% to 35% mobile phase B (mobile phase A: 0.1% formic acid/5% dimethylsulfoxide (DMSO) in water; mobile phase B: 0.1% formic acid/5% DMSO in acetonitrile) at a flow rate of 250 nl min^{-1} . Mass spectra were acquired on a Q Exactive Hybrid Quadrupole–Orbitrap mass spectrometer at a resolution of 70,000 at m/z 200 using an ion target of 3×10^6 and maximal injection time of 100 ms between m/z 380 and 1,800. Product ion spectra of up to 15 precursor masses at a signal threshold of 4.7×10^4 counts and a dynamic exclusion for 27 s were acquired at a resolution of 17,500 using an ion target of 10^5 and a maximal injection time of 128 ms. Precursor masses were isolated with an isolation window of 1.6 Da and fragmented with 28% normalized collision energy.

Bruker maXis HD. Sample separation was performed on an Ultimate 3000 RSLCnano LC system (Thermo Scientific). Peptides were first trapped on a Pepmap pre-column ($2 \text{ cm} \times 100 \mu\text{m}$; Thermo Scientific) and separated on a PepMap UHPLC column ($50 \text{ cm} \times 75 \mu\text{m}$, 2 μm particles; Thermo Scientific) with a 120 min multi-step acetonitrile gradient ranging from 5 to 35% mobile phase B (mobile phase A: 0.1% formic acid in water; mobile phase B: 0.1% formic acid in acetonitrile) at a flow rate of 400 nl min^{-1} . A CaptiveSpray nanoBooster source (Bruker Daltonik), with acetonitrile as a dopant, was used to interface the LC system to the maXis HD UHR-Q-TOF system (Bruker Daltonik). Source parameters were set to 3 l min^{-1} dry gas and 150 °C dry heater; nitrogen ‘flow’ setting for the nanoBooster was set to 0.2 bar. Mass spectra were acquired in the m/z range 150–2,000 at a spectral acquisition rate of 2 Hz. Precursors were fragmented with a fixed cycle time of 4 s using a dynamic method adapting spectra rates between 2 and 10 Hz based on precursor intensities. Dynamic exclusion was set to 0.4 min combined with reconsideration of an excluded precursor for fragmentation if its intensity rose by a factor of 3.

Collagen type I sequence assembly. Product ion data from the maXis HD and Orbitrap platforms were analysed in three stages. Initially MASCOT (Matrix Science) was used to search against the UniColl database, a database of non-redundant

synthetic collagen peptides, to generate a list of ranked peptides for each spectrum. Sequences derived from this exercise were added to a local database of genomic and published collagen sequences and common laboratory contaminants, and the original data were then re-analysed by PEAKS³¹ using this new database (for an example of PEAKS output see Extended Data Fig. 1b–d).

As an independent check, a limited number of the product ion spectra of peptides (previously assigned by PEAKS) were also manually *de novo* interpreted (by J.T.-O.) without prior knowledge of the assignment, in all cases with full agreement between the two approaches.

Generation of, and searching against, Unicoll. Publicly available COL1 α 1 and COL1 α 2 sequences were concatenated and aligned using Mafft³² with subsequent manual alignment of misaligned sites using Bioedit and Geneious version 4.6 (ref. 33). A custom Python script was used to digest the COL1 with trypsin *in silico*. For each tryptic fragment, all variable amino-acid positions across the aligned sequences were recorded. A new sequence was created for every permutation of these variable sites. These sequences were concatenated and stored in FASTA format with a header indicating the position in the original alignment. The result was a database with each entry a concatenation of sequences representing every permutation of observed mutations for that particular tryptic fragment. One tryptic fragment of the sequence (COL1 α 2 positions 870–905) was too variable to include without exceeding available memory. Only the original observed variants were included for this part of the sequence. Using this strategy, it was possible to generate the equivalent of more than 10^{200} alternative collagen ‘sequences’ (cf. 10^{82} , which is the upper estimate of the number of atoms in the universe).

MS/MS data files were merged and submitted to Mascot with enzyme set to Trypsin/P; variable modifications for deamidated (NQ), Lys→Hyl (K), oxidation (M), and Pro→Hyp (P); peptide mass tolerance ± 10 ppm; and fragment mass tolerance ± 0.07 Da. The structure of sequence entries in Unicoll meant that it could not accommodate missed cleavages. Select summaries containing matched peptides with a Mascot score greater than 30 were exported into Microsoft Excel for each analysis. Peptides were identified by picking the highest scoring hits for each tryptic fragment, if the score exceeded 40; whereas for matches with scores between 30 and 40, the spectra were inspected manually to choose the best hit among the possibilities given by the search engine.

Searching data using PEAKS. Product ion spectra were searched using PEAKS software against a database comprising genomic COL1 sequences plus fossil consensus sequences, composed of UniColl peptide hits, with missing and low coverage regions filled with conserved mammalian COL1 sequences (see Phylogenetic reconstruction section below). Additionally, common laboratory contaminants were included in database searches. Full PEAKS searches (Peptide *de novo*, PEAKS DB, PEAKS PTM, and SPIDER) were performed with peptide mass tolerance ± 10 ppm and fragment mass tolerance ± 0.07 Da, in addition to respective platform and enzyme details. Searches were performed allowing for deamidated (NQ), Lys→Hyl (K), oxidation (M), and Pro→Hyp (P). False discovery rate was put at 0.5% and peptide scores were only accepted with $-\log_{10}(P \text{ value})$ scores of at least 30 and average local confidence (%) at least 50. Where there was ambiguity in interpretation of the spectra, peptides were selected on the basis of knowledge of sequence constraints, post-translational modifications, and fragmentation patterns.

Reference sequence authentication. To check the quality of our MS/MS COL1 sequences, we sampled a modern and a fossil sample for which we had independent genomic data, specifically (1) a modern aardvark sample (*Orycteropus afer*) and (2) a fossil equid bone from a geological formation rich in SANU fossils with their respective genome sequences. The fossil sample had similar collagen yields and ZooMS profile to the SANU samples used for MS/MS sequencing (Pleistocene horse, Tapalqué, South America; Fig. 1b) (MS/MS sequence analysis, above). Our modern aardvark MS/MS sequence was identical to that of the protein product inferred from the released genomic sequence. For the Pleistocene *Equus* sp. sequence, two amino-acid substitutions were detected (T>L, COL1 α 1; H>D, COL1 α 2), similar to the maximum number of differences observed in a recent study comparing *Equus* genomes with the *Equus ferus caballus* reference genome³⁴.

De novo sequence authentication. The absence of corresponding genomic data prevented similar comparisons with MS/MS-derived sequences for the SANU species. Instead we assessed amino-acid substitution locations along COL1 α 1 and COL1 α 2 chains both in our (and previously published³⁵) and in fossil COL1 sequences with genomic data, using the COL1 α 1 and COL1 α 2 sequence of the Tasmanian devil (*Sarcophilus harrisii*) as an outgroup to eutherian mammals. Carboxy- (C-) and amino- (N-)terminal telopeptides were removed as they were rarely observed from fossil samples. COL1 position numbers are given as a continuous count with COL1 α 1 and COL1 α 2 concatenated, with COL1 α 1 ranging from position 1 to position 1014, and COL1 α 2 ranging from 1015 to 2028.

We found that the location of amino-acid variation along the COL1 α 1 and COL1 α 2 chains was similar among the different COL1 sequences obtained from genomic sources (Extended Data Fig. 2). We identified several regions, mainly

located in COL1 α 1, that appeared to lack sequence variation among the four major mammalian superorders. This could be a result of the functional importance of some of these regions during COL1 fibril formation, α 1 and α 2 chain binding, and COL1 hydroxylation^{36–38}. Additionally, we observed a substitution rate in COL1 α 2 roughly twice that observed in COL1 α 1.

Comparing COL1 sequences derived from MS/MS data in this and an earlier study³⁵ with genomic data for laurasiatheres revealed good correspondence in the location of substitutions along the COL1 α 1 and COL1 α 2 chains between our results and genomic data (Extended Data Fig. 2). The MS/MS data in ref. 35 for laurasiatheres were derived from a single species (*Manis tetradactyla*). Sequence variation from those data compared with genomic data were similar, although we noted that several regions displaying high rates of amino-acid substitution were missing from the *Manis* consensus sequence provided (notably around positions 726–756, 991–1089, 1306–1364, 1423–1443 and 1899–1977).

Reference 35 provided two xenarthran and five afrotherian COL1 sequences obtained using mass spectrometric sequencing. Regions with high substitution complexity were missing from the consensus sequences provided, for Afrotheria (1024–1089, 1588–1599, 1740–1754) and Xenarthra (1024–1089, 1207–1234, 1348–1364, 1588–1638, 1771–1806, 1921–1947). The absence of such regions prohibited the inclusion of these sequences in our phylogenetic tree-building, as the majority of informative positions were missing from the sequences provided. For substitution locations, our data suggest structural and/or functional organization of these, and their frequency, in specific regions of both chains.

We criticized claims of authentic collagen sequences retrieved from a *Tyrannosaurus rex* sample³⁹ based in part on the low levels of reported deamidation⁴⁰, and more recently have demonstrated an increase in glutamine deamidation in archaeological rather than modern collagen, which correlated with thermal age (Extended Data Fig. 3 and ref. 41); similar levels have been reported for Pleistocene mammoths and equids³⁴.

Deamidation ratios observed for glutamine here are consistent with ancient collagen of equivalent thermal age (Extended Data Fig. 1). The lowest levels of Gln to Glu deamidation are observed in modern samples from hippopotamus ($1.8\% \pm 3.2$) and tapir ($5.7\% \pm 10.9$) bone. The highest levels of Gln deamidation occur in the radiocarbon samples from dead *Macrauchenia* (Glu = $82.8\% \pm 14.3$). The *Toxodon* samples are less deamidated (Glu = $59.2\% \pm 24.5$), which is consistent with a Late Pleistocene date (12,000 years ago). However, by contrast, the Pleistocene equid is much better preserved (Glu = $18.9\% \pm 18.4$), despite the fact that it cannot be much younger than *Toxodon* (Fig. 1c).

DNA extraction and sequencing. Approximately 250 mg of the three samples with the highest number of peaks in the mass spectra from each species (see Zooarchaeology by MS screening, above) were used for DNA extraction. DNA extraction was performed as in the method described in ref. 42. PCR primers were designed to target Perissodactyla- and Laurasiatheria-specific regions of the cytb, COX1, 16S, and 12S genes using mitochondrial DNA sequences downloaded from the National Center for Biotechnology Information (NCBI) (Supplementary Table 1). Primer design used the program Primer3. PCR was performed for 60 cycles and samples were visualized on 2.5% agarose gel. Products were successfully amplified from several samples whereas PCR controls showed no amplification products. BLAST searches of the sequences obtained revealed no homology to any previously derived sequence for several of the products, whereas sequences from two *Macrauchenia* samples showed high similarity (98% and 99%, respectively) to domestic pig sequences, a common contaminant in ancient DNA analyses⁴³. A Pleistocene horse bone from the same depositional context as some of the SANU specimens yielded a sequence 98% identical to modern horse (*Equus caballus*), suggesting that the failure to amplify putative SANU DNA sequences by PCR was not because of technical problems, but because of a lack of endogenous DNA in the samples investigated.

DNA next-generation sequencing approach. After failing to amplify endogenous DNA through Sanger sequencing of targeted PCR products, we applied a non-targeted, next-generation sequencing (NGS) shotgun approach in a further attempt to identify whether endogenous DNA could be obtained. Based on the collagen sequencing results, *Macrauchenia* sample 12-1641 (metapodial) was selected as the most likely candidate for NGS analyses. DNA extractions of *Macrauchenia* sample 12-1641 followed protocols described in ref. 44 and were performed in the dedicated ancient-DNA laboratory at Royal Holloway, University of London, UK. The library was constructed in a dedicated laboratory for ancient DNA (Johannes Gutenberg University, Mainz, Germany) using a modified version of the protocol in ref. 45. Modifications were as follows: the initial DNA fragmentation step was not required, and all clean-up steps used MinElute PCR purification kits. For the blunt-end repair step, Buffer Tango and ATP were replaced with 0.1 mg ml^{-1} BSA and $1 \times$ T4DNA ligase buffer. The proceeding clean-up step was replaced by an inactivation step, heating to 75°C for 10 min. For the adaptor ligation step, 0.5 mM ATP replaced the T4 DNA Ligase buffer. The index PCR step followed a further protocol⁴⁶ using AmpliTaq Gold DNA polymerase and the addition of 0.4 mg ml^{-1}

BSA. The index PCR was set for 20 cycles with three PCR reactions conducted per library. The indexed library was sequenced on an Illumina HiSeq platform (Mainz) using a single lane, paired-end read, sequencing run.

Bioinformatics methods and conclusion. Paired-end reads were quality trimmed ($q = 10$) with cut-adapt⁴⁷ and then sequences were simultaneously adaptor trimmed and the paired reads joined together with Seq-Prep (available from <https://github.com/jstjohn/SeqPrep>). Reads shorter than 17 base pairs were discarded. In the absence of any close phylogenetic relative (required for the accurate genomic mapping of reads), processed reads were *de novo* assembled into contigs using clc_denovo_assembler (available in CLC Assembly Cell version 4.2), with contigs shorter than 70 base pairs discarded. Two approaches were then used to investigate the data for mammalian genomic sequences (which had proved successful for other ancient DNA NGS samples).

To examine whether there were any mammalian DNA sequences suitable for phylogenetic analysis in our data set, first, contigs were blasted using blastn to a local nucleotide database, downloaded from NCBI. Custom perl scripts (available on request) were used to assign taxonomic and gene information to BLAST hits. These results were searched for standard orthologous mitochondrial and nuclear phylogenetic sequences. Each of the potential hits blasting to mammalian sequences was inspected; however, all were assignable to bacterial elements, and no blast hit could be attributed to mammalian genes.

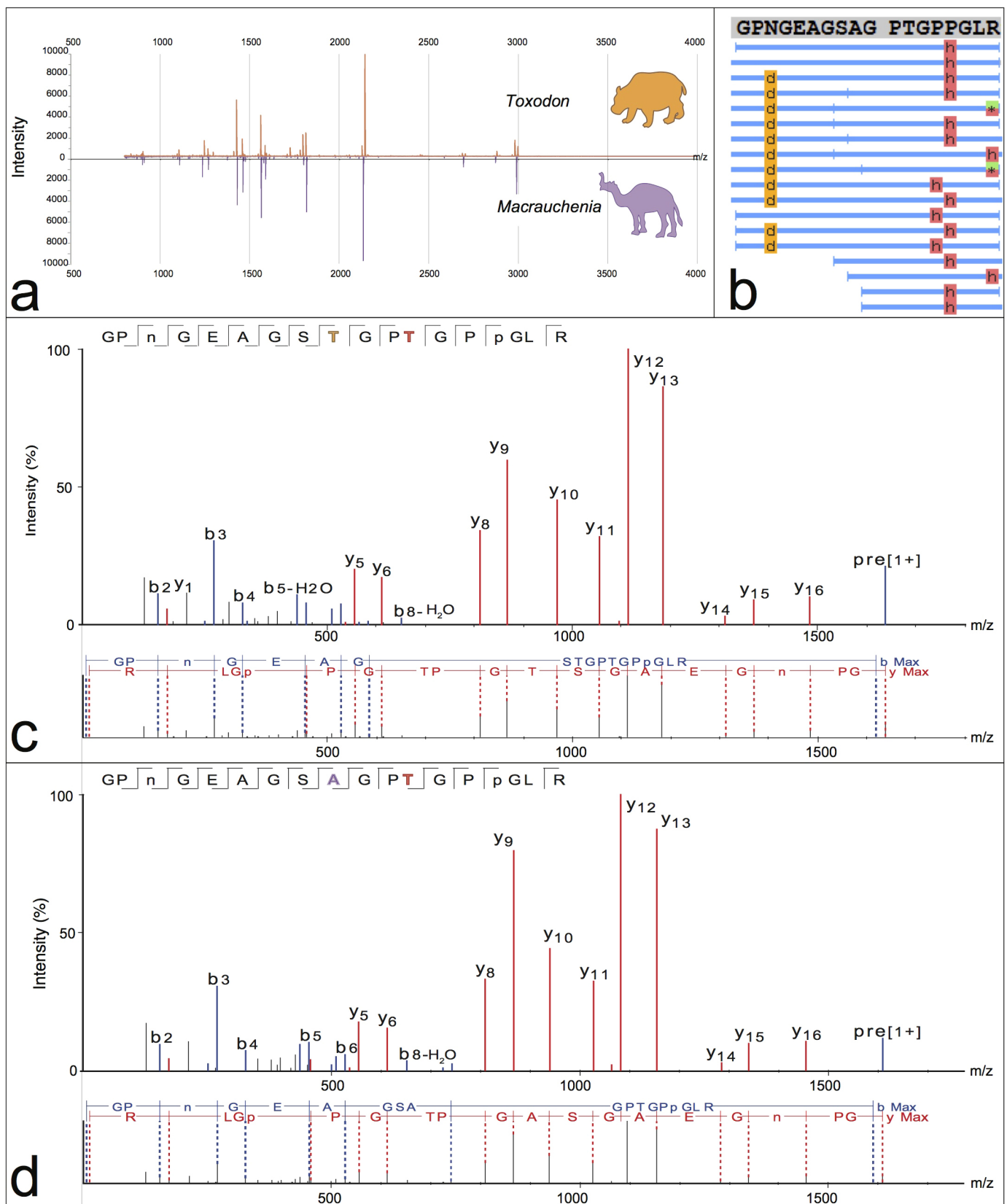
Second, two separate BLAST databases were generated: one from the contigs and a second from the processed reads, using the makeblastdb command in BLAST. These databases could then be queried with mammalian (including perissodactyl) mitochondrial and nuclear phylogenetic sequences of interest using blastn. Neither of these searches returned any matching contigs. Thus, the NGS data set yielded nothing of use for phylogenetic analysis, and gave no indication that any *Macrauchenia* DNA had persisted in the sample.

Phylogenetic reconstruction. Before the advent of DNA-based molecular phylogeny, variations in protein structure and sequence had been used to explore evolutionary relationships^{48,49}. The comparative data set for this paper was built using consensus amino-acid sequences for COL1 α 1 and COL1 α 2 generated by MS/MS analysis for the target taxa *Toxodon* and *Macrauchenia* as well as representatives of all extant major mammalian clades. Leucine (L) and isoleucine (I) were converted into isoleucines as these are isobaric and low-energy MS/MS sequencing is not capable of discriminating between them. Partition Finder⁵⁰ was used to select the best-fit partitioning scheme from the amino-acid data. This was identified as two separate partitions, for Colla1 and Colla2. Bayesian phylogenies were generated using MrBayes version 3.2.1 (ref. 51) with the amino-acid model estimated from the data (to allow model jumping between fixed-rate amino-acid models, the prior for the amino-acid model was set as prset aamodelpr = mixed). The proportion of invariant sites, and the distribution of rates across sites (approximating to a gamma distribution), were also estimated from the data. Two chains were run for 5 million generations (sampled every 500), with convergence between chains assessed in Tracer version 1.6 (ref. 52). All effective sample sizes of parameters were greater than 100. After burn-in was removed, a majority rule consensus tree was constructed, using the sumt command in MrBayes, from the trees sampled in the posterior distribution.

To test for the robustness of the results of the Bayesian analysis under other methods of tree reconstruction, we also conducted maximum likelihood and maximum parsimony analyses. We performed parsimony analyses running PAUP* version 4.0b10 (ref. 53), using the heuristic search option with a random taxon addition sequence (1,000 repetitions) and TBR branch swapping, and rooting the tree along the branch leading to Aves. A maximum likelihood phylogeny was estimated in RAXML version 7.0.4 (ref. 54). A Dayhoff model of protein sequence evolution with gamma-distributed variation in rates across sites (corresponding to the PROTGAMMADAYHOFF model in RAXML) was applied to each partition. Twenty separate maximum likelihood analyses were performed (using the ‘-f d’ command in RAXML), and the tree with the highest likelihood was chosen from this set.

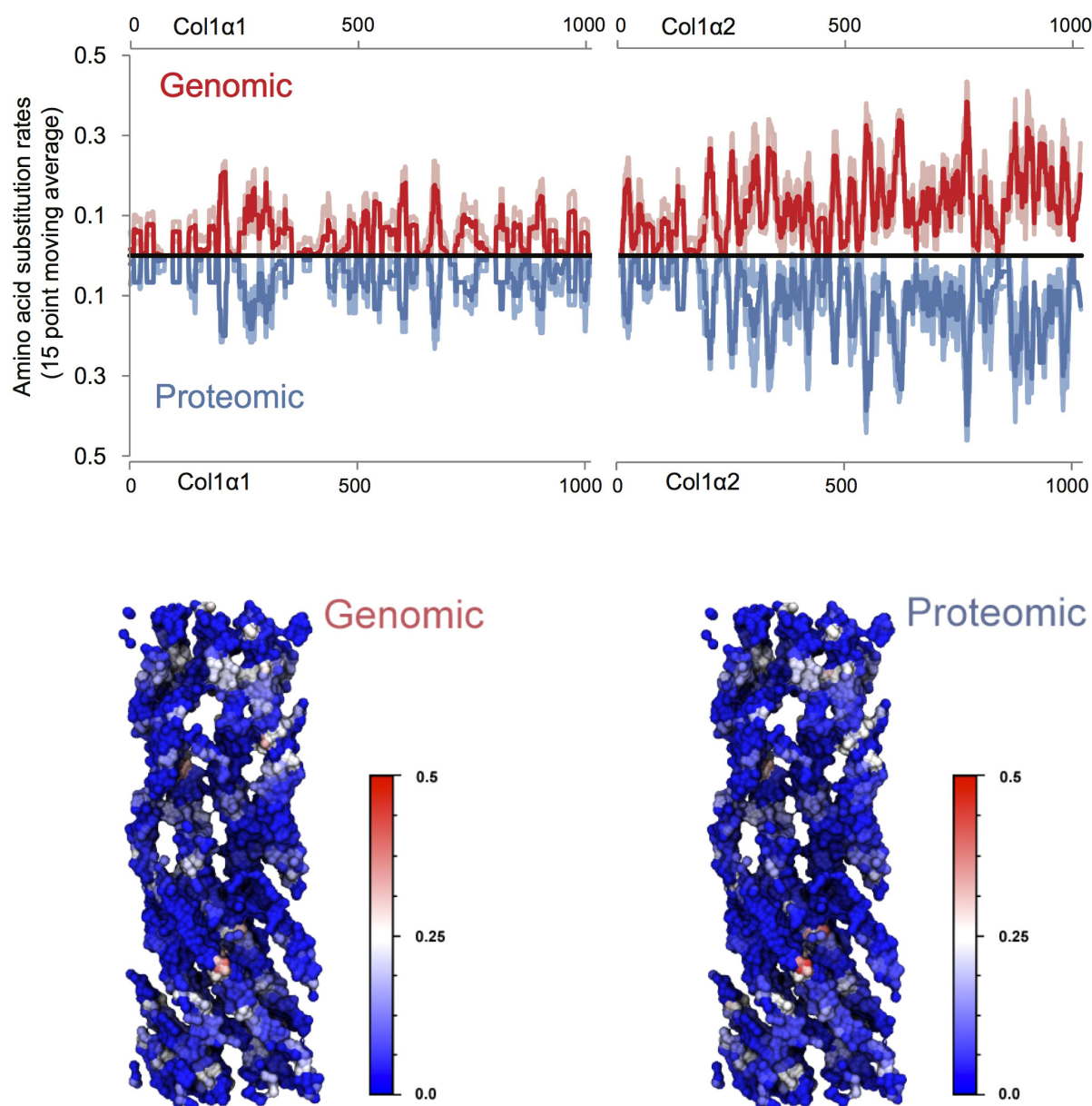
Molecular clock analysis. Fossil-calibrated phylogenies were constructed in BEAST version 1.7 (ref. 55) with the Dayhoff amino-acid model (chosen under the MrBayes mixed model) together with the proportion of invariant sites and the distribution of rates across sites (approximating a gamma distribution) applied to each partition. Analyses were run under a strict clock (estimated from the data), with the Yule model of speciation, for 10 million generations (sampled every 1,000 generations). Clock and tree parameters were linked across partitions. Prior distributions on the root and 33 other nodes were applied based on an interpretation of the mammalian fossil record (see Supplementary Table 3)^{7,56}. The clock rate prior was set as an uninformative uniform distribution (upper = 10^{100} , lower = 10^{-12}). All other priors were left as the default values in BEAUTi⁵⁷. Full details of all prior distributions for divergence times are presented in Supplementary Table 3. As in the case of the MrBayes analysis, convergence and effective sampling were assessed using Tracer

- 1.7. A maximum clade credibility tree was constructed using TreeAnnotator (available with BEAST) from the trees sampled in the posterior distribution.
31. Ma, B. *et al.* PEAKS: powerful software for peptide *de novo* sequencing by tandem mass spectrometry. *Rapid Commun. Mass Spectrom.* **17**, 2337–2342 (2003).
 32. Katoh, K. & Standley, D. M. MAFFT multiple sequence alignment software version 7: improvements in performance and usability. *Mol. Biol. Evol.* **30**, 772–780 (2013).
 33. Drummond, A. J. *et al.* Geneious v4.7. (Geneious, 2010).
 34. Orlando, L. *et al.* Recalibrating *Equus* evolution using the genome sequence of an early Middle Pleistocene horse. *Nature* **499**, 74–78 (2013).
 35. Buckley, M. A molecular phylogeny of *Plesioxyrhopus* reassigns the extinct mammalian order 'Bibymalagasia'. *PLoS ONE* **8**, e59614 (2013).
 36. Terajima, M. *et al.* Glycosylation and cross-linking in bone type I collagen. *J. Biol. Chem.* <http://dx.doi.org/10.1074/jbc.M113.528513> (2014).
 37. Hudson, D. M., Weis, M. & Eyre, D. R. Insights on the evolution of prolyl 3-hydroxylation sites from comparative analysis of chicken and *Xenopus* fibrillar collagens. *PLoS ONE* **6**, e19336 (2011).
 38. Hudson, D. M., Werther, R., Weis, M., Wu, J.-J. & Eyre, D. R. Evolutionary origins of C-terminal (GPP)n 3-hydroxyproline formation in vertebrate tendon collagen. *PLoS ONE* **9**, e93467 (2014).
 39. Schweitzer, M. H. *et al.* Analyses of soft tissue from *Tyrannosaurus rex* suggest the presence of protein. *Science* **316**, 277–280 (2007).
 40. Buckley, M. *et al.* Comment on "Protein sequences from mastodon and *Tyrannosaurus rex* revealed by mass spectrometry". *Science* **319**, 33 (2008).
 41. Van Doorn, N. L., Wilson, J., Hollund, H., Soressi, M. & Collins, M. J. Site-specific deamidation of glutamine: a new marker of bone collagen deterioration. *Rapid Commun. Mass Spectrom.* **26**, 2319–2327 (2012).
 42. Rohland, N. & Hofreiter, M. Comparison and optimization of ancient DNA extraction. *Biotechniques* **42**, 343–352 (2007).
 43. Leonard, J. A. *et al.* Animal DNA in PCR reagents plagues ancient DNA research. *J. Archaeol. Sci.* **34**, 1361–1366 (2007).
 44. Brace, S. *et al.* Population history of the Hispaniolan hutia *Plagiodontia aedium* (Rodentia: Capromyidae): testing the model of ancient differentiation on a geotectonically complex Caribbean island. *Mol. Ecol.* **21**, 2239–2253 (2012).
 45. Meyer, M. & Kircher, M. Illumina sequencing library preparation for highly multiplexed target capture and sequencing. *Cold Spring Harb. Protoc.* **2010**, <http://dx.doi.org/10.1101/pdb.prot5448> (2010).
 46. Dabney, J. & Meyer, M. Length and GC-biases during sequencing library amplification: a comparison of various polymerase-buffer systems with ancient and modern DNA sequencing libraries. *Biotechniques* **52**, 87–94 (2012).
 47. Martin, M. Cutadapt removes adapter sequences from high-throughput sequencing reads. *EMBnet journal* **17**, 10–12 (2011).
 48. Zuckerkandl, E., Jones, R. T. & Pauling, L. A comparison of animal hemoglobins by tryptic peptide pattern analysis. *Proc. Natl Acad. Sci. USA* **46**, 1349–1360 (1960).
 49. Sarich, V. M. & Wilson, A. C. Rates of albumin evolution in primates. *Proc. Natl Acad. Sci. USA* **58**, 142–148 (1967).
 50. Lanfear, R., Calcott, B., Ho, S. Y. W. & Guindon, S. Partitionfinder: combined selection of partitioning schemes and substitution models for phylogenetic analyses. *Mol. Biol. Evol.* **29**, 1695–1701 (2012).
 51. Ronquist, F. *et al.* MrBayes 3.2: efficient Bayesian phylogenetic inference and model choice across a large model space. *Syst. Biol.* **61**, 539–542 (2012).
 52. Rambaut, A., Drummond, A. J. & Suchard, M. Tracer v.1. 6. (2013).
 53. Swofford, D. L. *PAUP**. Phylogenetic Analysis Using Parsimony (*and Other Methods) v.4.0b10 (Sinauer Associates, 2003).
 54. Stamatakis, A. RAxML version 8: a tool for phylogenetic analysis and post-analysis of large phylogenies. *Bioinformatics* **30**, 1312–1313 (2014).
 55. Drummond, A. J., Suchard, M. A., Xie, D. & Rambaut, A. Bayesian phylogenetics with BEAUti and the BEAST 1.7. *Mol. Biol. Evol.* **29**, 1969–1973 (2012).
 56. Benton, M. J., Donoghue, P. C. J. & Asher, R. J. in *The Timetree of Life* (eds Hedges, B. S. & Kumar, S.) 35–86 (Oxford Univ. Press, 2009).
 57. Rambaut, A. & Drummond, A. BEAUti v.1. 4.2. Bayesian evolutionary analysis utility (2007).
 58. Humphrey, W., Dalke, A. & Schulten, K. VMD – Visual Molecular Dynamics. *J. Mol. Graph.* **14**, 33–38 (1996).



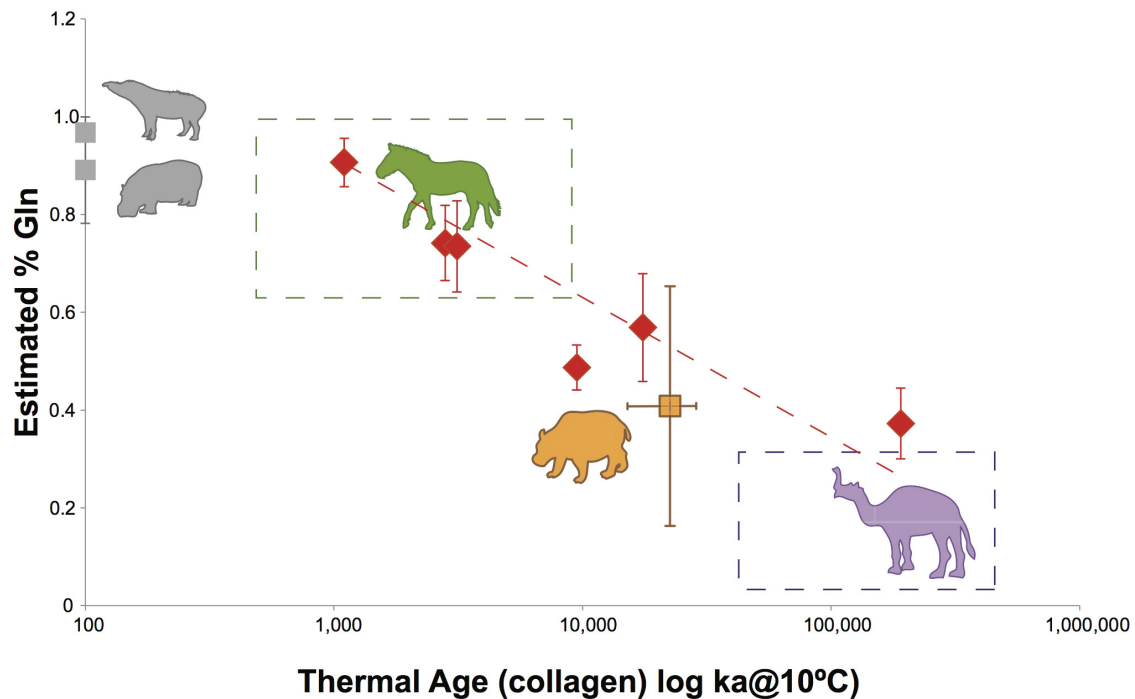
Extended Data Figure 1 | Examples of MALDI-TOF-MS and MS/MS product ion spectra. **a**, MALDI-TOF-MS ZooMS spectra for *Toxodon* (upper) and *Macrauchenia* (lower) were used to screen for samples for the best collagen preservation. **b**, PEAKS alignment of matching product ion spectra for *Macrauchenia* MLP 96-V-10-19 (specimen sample number MLP2012.12) highlighting peptides aligning to the sequence GPNGEAGSAGPTGPPGLR. **c**, **d**, Annotated PEAKS report of product ion spectra for the same peptide

sequence detailed in **b** for *Toxodon* (**c**) and *Macrauchenia* (**d**), detailing differences between both genera (gsT and gsA, highlighted) and shared substitutions compared with *Equus* (gpA for *Equus*, gpT for *Toxodon* and *Macrauchenia*). Note in **b** that both deamidation (N→D) and variable hydroxylation (P→h) were detected in different peptides covering this region of the sequence.



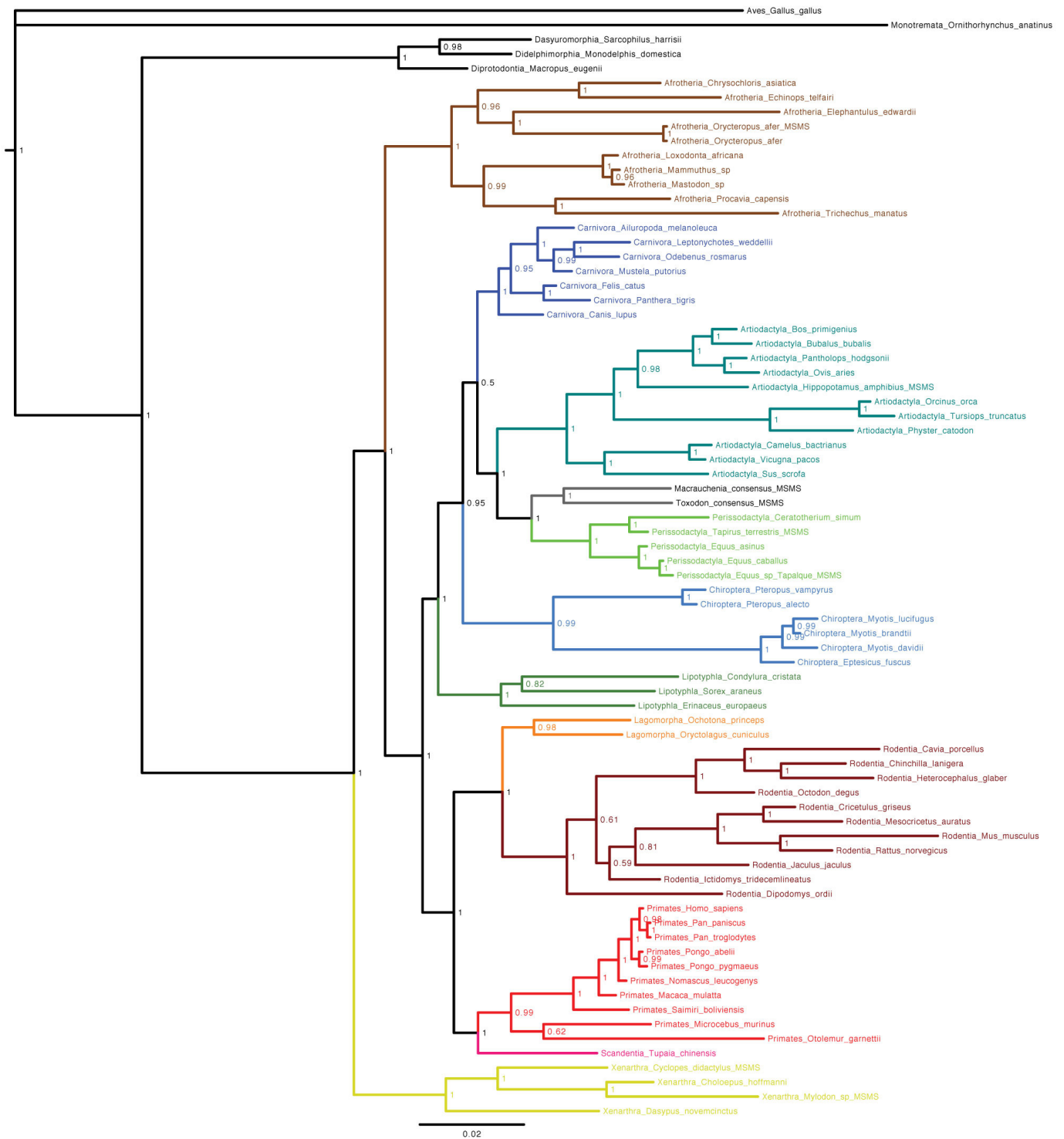
Extended Data Figure 2 | Collagen type I substitution variability for placental mammals (genomic and proteomic data) compared with the dasyurid marsupial *Sarcophilus harrisii* (Tasmanian devil) as outgroup. Substitution variability scores range between 0 and 1 and incorporate sequence coverage for a given number of species over a 15-amino-acid moving average (95% standard deviation in lighter tone). Top, along-chain variation in genomic

sequence variability (upper red) is similar to proteomic sequence variability (lower blue) both for COL1α1 and for COL1α2 chains. Bottom, molecular surface rendering (via VMD⁵⁸) of the collagen unit cell taken from coordinates given in Protein Data Bank accession number 3HR2. Colours represent genomic (left) and proteomic (right) sequence variability throughout the structure.

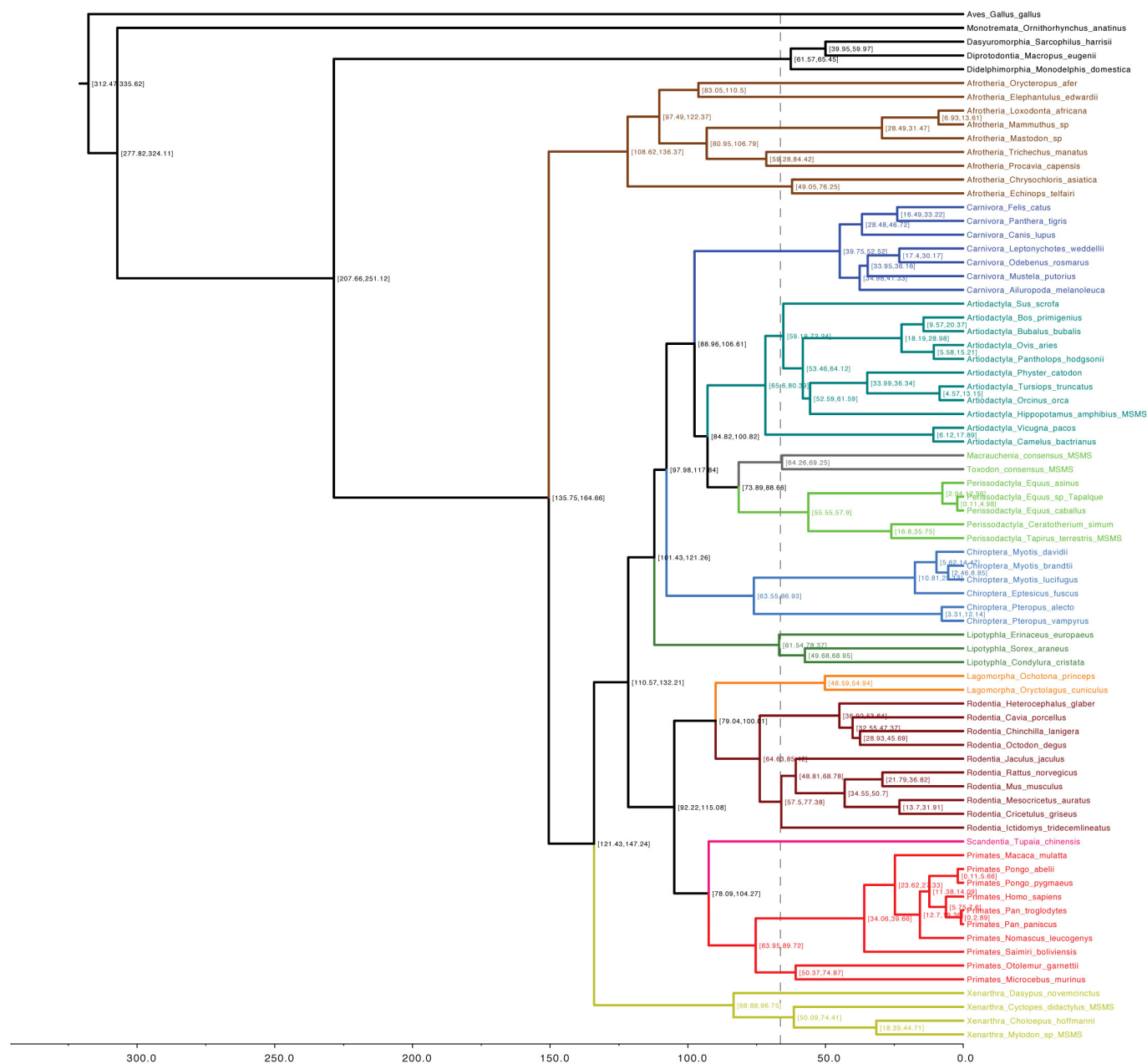


Extended Data Figure 3 | Comparison of levels of deamidation for samples in this study with ref. 22 (diamonds). The *Macrauchenia* sample was ^{14}C dead, consistent with observed levels of deamidation, which are lower than either *Toxodon* dated to 12,000 years ago or *Equus* sp. (Tapalqué; not dated). Dotted lines indicate error ranges on Gln estimation for samples that were not

dated or were undateable. The measurement approach used in this study—frequency of deamidation in positions represented in at least seven MS/MS spectra—is different from the approach used in ref. 22, so the absolute values may not be directly comparable.



Extended Data Figure 4 | Bayesian constraint tree based on phylogeny published in figure 1 in ref. 6. See Methods and Supplementary Information section 3.2 for further details and discussion.



Extended Data Figure 5 | Maximum clade credibility phylogeny from BEAST molecular dating analysis. Branch lengths are measured in millions of years; scale axis indicates intervals of 100 Ma. Node labels show 95% highest

probability densities for molecular dates (in millions of years). Fossil constraints are provided in Supplementary Table 3. Vertical dashed line indicates Cretaceous/Palaeogene boundary.

Extended Data Table 1 | *Toxodon* and *Macrauchenia* specimens used in this study

Genus	Species	Museum collection	Specimen number	MS/MS code	Location	Longitude	Latitude	Province	Age as recorded	Element	Age (14C cal yr/bp)	±	Radiocarbon Laboratory number	Effective Burial Temperature T _{eff} (°C)	Thermal age ¹ ka@ 10°C
<i>Toxodon</i>	sp.	MLP	12-1132		Arrecifes	-60.1	-34.1	Buenos Aires	Pampean Fm	Axis				13	93
<i>Toxodon</i>	sp.	MLP	12-1159		Olivera	-59.2	-34.6	Buenos Aires	Pampean Fm	Skull cap, juvenile				13	94
<i>Toxodon</i>	sp.	MLP	12-2432		no location	--	--	Buenos Aires	Pampean Fm	Jaw, juvenile					
<i>Toxodon</i>	sp.	MLP	M-218		no location	--	--	Buenos Aires	Pampean Fm	Mandible					
<i>Toxodon</i>	sp.	MLP	12-1169		Arrecifes	-59.1	-34.4	Buenos Aires	Pampean Fm	Mandible				13	93
<i>Toxodon</i>	sp.	MLP	12-1224		Luján	-59.0	-34.5	Buenos Aires	Pampean Fm	Upper incisor					
<i>Toxodon</i>	sp.	MLP	12-1125		Arrecifes	-60.1	-34.1	Buenos Aires	Pampean Fm	3rd lumbar				13	94
<i>Toxodon platensis</i>	sp.	MLP	12-1190		Chefforo	-59.0	-34.5	Buenos Aires	Pampean Fm	Tubercles					
<i>Toxodon</i>	sp.	MLP	12-1227		Luján	-59.0	-34.5	Buenos Aires	Lujanian	Incisor				17	188
<i>Toxodon</i>	sp.	MLP	12-1160		Luján	-59.0	-34.5	Buenos Aires	Pampean Fm	Pterygoid				17	188
<i>Toxodon</i>	sp.	MLP	94-II-1-17		Río Quequén Salado	-60.5	-38.9	Buenos Aires	Pleistocene	Ulna				10	51
<i>Toxodon</i>	sp.	MLP	94-II-1-17		Río Quequén Salado	-60.5	-38.9	Buenos Aires	Pleistocene	Ulna				10	51
<i>Toxodon</i>	sp.	MLP	44-XII-29-5	MLP2012.04	Tapalqué	-60.0	-36.3	Buenos Aires	Pleistocene	Mandible	11,900	35	(UCIAMS 143034)	13	22
<i>Toxodon</i>	sp.	MLP	12-1180		Luján	-59.0	-34.5	Buenos Aires	Pampean Fm	Maxilla				17	188
<i>Toxodon</i>	sp.	MACN Pv	5287		no location	--	--	--	Fm Pampeana	Metacarpal					
<i>Toxodon</i>	sp.	MACN Pv	17710	MACN2012.12	Arroyo Tapalqué	-60.0	-36.4	Buenos Aires	L Pleistocene	Tibia	12,040	70	(UCIAMS 143035)	13	22
<i>Toxodon</i>	sp.	MACN Pv	17710	MACN2012.12	Arroyo Tapalqué	-60.0	-36.4	Buenos Aires	L Pleistocene	Tibia	12,040	70	(UCIAMS 143035)	13	22
<i>Toxodon</i>	sp.	MACN Pv	5717		Arroyo Tapalqué	-60.0	-36.4	Buenos Aires	Pampean Fm/ Lujanian	Molar				12	72
<i>Toxodon</i>	sp.	MACN Pv	2760		no location	--	--	--	--	Metapodial					
<i>Toxodon</i>	sp.	MACN Pv	5712		Arroyo Tapalqué	-60.0	-36.4	Buenos Aires	Pampean Lujanian	Tibia				12	72
<i>Toxodon</i>	sp.	MACN Pv	9666		Río Quequén Salado	-60.7	-38.4	Buenos Aires	L Pampean Fm	Cervical				10	52
<i>Toxodon platensis</i>	Z.M.K.	18/1887			Arroyo del Medio	-60.8	-33.6	Buenos Aires/ Santa Fe	Pleistocene	Jaw				14	102
<i>Macrauchenia</i>	sp.	MLP	12-1641		Luján	-59.0	-34.5	Buenos Aires	Pampean Fm	Metapodial	12,185	55	(OxA-25840)	14	28
<i>Macrauchenia patachonica</i>	MLP	12-1648			Luján	-59.0	-34.5	Buenos Aires	Pampean Fm	Metapodial				17	188
<i>Macrauchenia patachonica</i>	MLP	12-1659			Luján	-59.0	-34.5	Buenos Aires	Pampean Fm	Metapodial				17	188
<i>Macrauchenia patachonica</i>	MLP	12-1488			no location	--	--	Buenos Aires	--	Phalanx					
<i>Macrauchenia</i>	sp.	MLP	96-V-10-19	MLP2012.12	Río Pilcomayo	-57.7	-25.2	Formosa	Pleistocene	Thoracic	no date			15	0
<i>Macrauchenia</i>	sp.	MLP	96-V-10-19	MLP2012.12	Río Pilcomayo	-57.7	-25.2	Formosa	Pleistocene	Thoracic	no date			15	0
<i>Macrauchenia</i>	sp.	MLP	50-X-5-5		Mar del Plata	-57.6	-38.1	Buenos Aires	--	Jaw				11	59
<i>Macrauchenia</i>	sp.	MLP	71-III-6-1		Río Salado	-61.0	-34.6	Buenos Aires	--	Tibia				13	89
<i>Macrauchenia patachonica</i>	MLP	12-1434			Luján	-59.0	-34.5	Buenos Aires	Pampean Fm	Mandible				17	188
<i>Macrauchenia patachonica</i>	MLP	12-1458			Luján	-59.0	-34.5	Buenos Aires	Pampean Fm	Mandible				17	188
<i>Macrauchenia patachonica</i>	MLP	12-2326			no location	--	--	Buenos Aires	Pampean Fm	Skull, tooth					
<i>Macrauchenia patachonica</i>	MLP	12-1660			Luján	-59.0	-34.5	Buenos Aires	Pampean Fm	Tarsal				17	188
<i>Macrauchenia</i>	sp.	MLP	80-IX-5-1		Laguna de la Bombilla	-69.3	-44.1	Chubut	Pleistocene	Cervical					
<i>Macrauchenia</i>	sp.	MLP	12-1661		Luján	-59.0	-34.5	Buenos Aires	Pampean Fm	Pedal sesamoid				17	188
<i>Macrauchenia</i>	sp.	MLP	12-1660		Luján	-59.0	-34.5	Buenos Aires	Pampean Fm	Phalanx				17	188
<i>Macrauchenia</i>	sp.	MLP	12-1457		no location	--	--	--	Pampean Fm	Jaw					
<i>Macrauchenia patachonica</i>	MLP	80-II-10-2			Río Quequén Salado	-60.7	-38.4	Buenos Aires	Lujanian	Jaw				10	52
<i>Macrauchenia</i>	sp.	MACN Pv	6708		Río Quequén	-58.8	-38.2	Buenos Aires	--	Tooth				11	56
<i>Macrauchenia</i>	sp.	MACN Pv	18952	MACN2012.02	near Monte Hermoso	-61.3	-39.0	Buenos Aires	Lujanian	Cervical	no date			11	61
<i>Macrauchenia</i>	sp.	MACN Pv	7107		Arroyo Seco, Mirama	-60.5	-33.1	Buenos Aires	Pampeana Fm/ Lujanian?	Pedal sesamoid				15	117
<i>Macrauchenia</i>	sp.	MACN Pv	3		Salto	-60.3	-34.3	Buenos Aires	Pampean Fm	Tibia				13	91
<i>Macrauchenia</i>	sp.	MACN Pv	2 (05)		Salto	-60.3	-34.3	Buenos Aires	Pampean Fm	Humerus				13	91
<i>Macrauchenia</i>	sp.	MACN Pv	2 (06)		Salto	-60.3	-34.3	Buenos Aires	Pampean Fm	Tibiofibula				13	91
<i>Macrauchenia</i>	sp.	MACN Pv	2 (07)		Salto	-60.3	-34.3	Buenos Aires	Pampean Fm	Femur				13	91
<i>Macrauchenia patachonica</i>	MACN Pv	6708			Río Quequén (Grandt)	-59.1	-34.6	Buenos Aires	Pampeana Fm/ Lujanian	Mandible				13	94
<i>Macrauchenia</i>	sp.	MACN Pv	10530		Río Quequén (Grandt)	-58.7	-38.6	Buenos Aires	Pampeana Fm/ Lujanian	Metapodial				11	56

Specimens highlighted in bold produced high-quality collagen and were sequenced. Specimens that appear twice were re-sampled. MACN Pv, Museo Argentino de Ciencias Naturales (vertebrate palaeontology collection), Buenos Aires, Argentina; MLP, Museo de La Plata; UCIAMS, Keck Carbon Cycle AMS Spectrometer facility, University of California, Irvine, USA; ZMUC, Natural History Museum of Denmark and Zoological Museum, Copenhagen, Denmark. ¹Thermal age of samples with a location, but without a radiocarbon date, are calculated at 50,000 years ago.

Extended Data Table 2 | Comparative run statistics combining multiple runs

Species	Museum Collection Number	Laboratory Specimen Number	Platform	Enzymatic digestion	Runs	#Measured spectra (# of runs)	#Matched COL1 spectra (%)	Triple-helical sequence coverage (%)	Fold coverage	% Unique coverage
<i>Equus sp. (Tapalqué)</i>		MACN2010.03	Orbitrap	Trypsin/P	Consensus	31,309 (5)	9,530 (30.4)	87.3	85.9	
<i>Macrauchenia sp.</i>		-	-	-	Consensus	78,515 (4)	9,400 (12.0)	89.4	77.1	
	18952	MACN2012.02	Bruker maXis HD	Trypsin/P	MACN201202	17,334	1,485 (8.6)	63.3	16.6	0.19
	18952	MACN2012.02	Orbitrap	Trypsin/P+elastase	York14	6,625	769 (11.6)	59.0	9.6	0
	96-V-10-19	MLP2012.12	Bruker maXis HD	Trypsin/P	MLP2012.12	34,525	3,410 (9.9)	77.3	35.4	2
	96-V-10-19	MLP2012.12	Orbitrap	Trypsin/P+elastase	York15	20,031	3,736 (18.7)	88.5	32.8	11.11
<i>Toxodon sp.</i>		-	-	-	Consensus	82,448 (4)	12,028 (14.6)	91.0	103.9	
	44-XII-29-5	MLP2012.04	Bruker maXis HD	Trypsin/P	MLP2012.04	20,499	2,720 (13.3)	80.7	28.1	1.29
	44-XII-29-5	MLP2012.04	Orbitrap	Trypsin/P+elastase	York13	20,706	3,610 (17.4)	84.0	35.8	1.81
	17710	MACN2012.12	Bruker maXis HD	Trypsin/P	MACN201212	20,134	2,188 (10.9)	76.7	21.0	2.1
	17710	MACN2012.12	Orbitrap	Trypsin/P+elastase	York12	21,109	3,510 (16.6)	81.7	35.5	0.38
<i>Myiodon darwini</i>	MLP 94-VIII-10-32		Orbitrap	Trypsin/P	Consensus	16,592 (1)	1,230 (7.4)	67.8	14.3	
<i>*Tapirus terrestris</i>		-	Orbitrap	Trypsin/P+elastase	Consensus	17,459 (1)	1,111 (6.4)	92.0	9.8	
<i>*Hippopotamus amphibius</i>		-	Orbitrap	Trypsin/P+elastase	Consensus	22,450 (1)	3,080 (13.7)	89.6	26.1	
<i>*Orycteropus afer</i>	AMNH 51910		Orbitrap	Trypsin/P	Consensus	20,481 (1)	3,673 (17.9)	93.8	33.1	
<i>*Cyclopes didactylus</i>	AMNH 99199		Orbitrap	Trypsin/P+elastase	Consensus	41,046 (2)	3,230 (7.9)	83.1	26.5	

Taxa with asterisks are modern; others are fossil. Spectra were acquired on two platforms: Orbi-trap for *Macrauchenia*, *Toxodon*, *Tapirus*, *Hippopotamus*, *Orycteropus*, *Myiodon*, and *Cyclopes*; and maXis HD for Tapalqué *Equus*, *Macrauchenia*, and *Toxodon*. Individual samples were digested using either trypsin (Tapalqué *Equus*, *Macrauchenia*, *Toxodon*, *Orycteropus*, and *Myiodon*) or trypsin pooled with elastase digests (*Macrauchenia*, *Toxodon*, *Tapirus*, *Hippopotamus*, and *Cyclopes*).

Anomalocaridid trunk limb homology revealed by a giant filter–feeder with paired flaps

Peter Van Roy^{1,2}, Allison C. Daley^{3,4} & Derek E. G. Briggs^{1,5}

Exceptionally preserved fossils from the Palaeozoic era provide crucial insights into arthropod evolution, with recent discoveries bringing phylogeny and character homology into sharp focus^{1–4}. Integral to such studies are anomalocaridids, a clade of stem arthropods whose remarkable morphology illuminates early arthropod relationships^{5,6} and Cambrian ecology^{7–9}. Although recent work has focused on the anomalocaridid head^{6–10}, the nature of their trunk has been debated widely^{5,11–18}. Here we describe new anomalocaridid¹⁷ specimens from the Early Ordovician Fezouata Biota of Morocco¹⁹, which not only show well-preserved head appendages providing key ecological data, but also elucidate the nature of anomalocaridid trunk flaps, resolving their homology with arthropod trunk limbs. The new material shows that each trunk segment bears a separate dorsal and ventral pair of flaps, with a series of setal blades attached at the base of the dorsal flaps. Comparisons with other stem lineage arthropods^{16,20–22} indicate that anomalocaridid ventral flaps are homologous with lobopodous walking limbs and the endopod of the euarthropod biramous limb, whereas the dorsal flaps and associated setal blades are homologous with the flaps of gilled lobopodians (for example, *Kerygmachela kierkegaardi*, *Pambdelurion whittingtoni*) and exites of the ‘Cambrian biramous limb’²³. This evidence shows that anomalocaridids represent a stage before the fusion of exite and endopod into the ‘Cambrian biramous limb’^{25,16,23}, confirming their basal placement in the euarthropod stem^{4–6}, rather than in the arthropod crown²⁴ or with cycloneuralian worms¹⁴. Unlike other anomalocaridids, the Fezouata taxon combines head appendages convergently⁹ adapted for filter-feeding with an unprecedented body length exceeding 2 m, indicating a new direction in the feeding ecology of the clade. The evolution of giant filter-feeding anomalocaridids may reflect the establishment of highly developed planktic ecosystems during the Great Ordovician Biodiversification Event²⁵.

Phylum Arthropoda von Siebold, 1848

Order Radiodonta Collins, 1996

Family Hurdidiidae Vinther, Stein, Longrich & Harper, 2014

Aegirocassis benmoulae gen. et sp. nov.

Life Science Identifier (LSID). urn:lsid:zoobank.org:act:35C7BB1E-C902-4F7B-9A4B-899005D7B6AE

Etymology. *Aegir*: a giant in Norse mythology and god of the sea; *cassis* (Latin, helmet): referring to the huge size and elaborate cephalic shield; and in recognition of Mohamed ‘Ou Said’ Ben Moula, who discovered the Fezouata Biota and the specimens described here. Gender feminine.

Holotype. Yale Peabody Museum of Natural History specimen YPM 237172 (Fig. 1, Extended Data Figs 1, 2 and Supplementary Video).

Other material. Paratypes: YPM 227556 (Extended Data Fig. 3c, d), YPM 525437 (Extended Data Fig. 4 and Supplementary Video), YPM 527123 (Extended Data Fig. 5a–c), YPM 527125 (Fig. 2a–b and Extended Data Fig. 6a), YPM 226437, YPM 522227 (Fig. 2c, Extended Data Fig. 7a–c). Other notable specimens: YPM 226438, YPM 226439, YPM 523423–523425 (Extended Data Figs 3e–h, 5f and 7d, e), YPM 523427

(Extended Data Fig. 7d, e), YPM 523428 (Extended Data Fig. 5g), YPM 516785 (Extended Data Fig. 3a, b), YPM 523810 (Extended Data Fig. 5e), YPM 525217 (Extended Data Fig. 6b–d), YPM 516791 (Extended Data Fig. 8a–c), YPM 227934 (Extended Data Fig. 8e), YPM 516792 (Extended Data Fig. 8f) and YPM 527124 (Extended Data Fig. 5d), and setal blades associated with YPM 527123 (Extended Data Fig. 8d). Fragmentary material of three other articulated individuals, four slabs with disarticulated material belonging to at least 10 individuals, 15 isolated carapace elements, 14 sets of partial ventral spines and 11 isolated bands of setal blades.

Locality and horizon. Lower Fezouata Formation, latest Tremadocian, *Araneograptus murrayi* Biozone. All three-dimensional specimens were collected from two sites on the eastern flank of Jbel Tigizgaouine, facing Oued Ezegzaou. Specimens of carapaces, setal blades and ventral spines of the frontal appendages occur at numerous sites throughout the Lower Fezouata Formation to the north of Zagora, often in abundance. Detailed locality information is curated with the specimens.

Diagnosis for genus and species. Anomalocaridid with tripartite frontal carapace having a central element at least as long as trunk, with an axial carina, pointed tip, rounded posterior margin and narrow downturned postero-ventral triangular extensions tapering towards rear and overlapping the lateral carapace elements dorsally. Lateral carapace elements oval, with rounded antero-dorsal expansion and longitudinal carina just below midline. Multisegmented anterior appendages consisting of seven podomeres. First podomere longest, with one shorter, comb-like ventral spine proximally. Succeeding five podomeres each with a single elongate, inward-angled ventral spine with stout setae bearing a double row of fine spinules set in a ‘V’ on their dorsal margin. Terminal podomere stout, with pointed tip. Flat, broad trunk of 11 segments attaining maximum width at third segment and tapering to a blunt tip. Two pairs of non-overlapping flaps per segment: dorsal flaps pointed with recurving anterior and posterior margins, width about 1× the length of their attachment; ventral flaps narrow, triangular, width about 1.5× the length of their attachment. Continuous band of dorsal setal blades attached to base of each pair of dorsal flaps, traversing the trunk.

A detailed description and interpretation of the material, including the filter-feeding frontal appendages, is provided in the Supplementary Text. The holotype YPM 237172 is an almost complete three-dimensionally preserved individual in slightly oblique dorsal view (Fig. 1, Extended Data Fig. 1 and Supplementary Video). The concretion has split such that a small block reveals both dorsal and ventral flaps on the anterior left of the specimen (Extended Data Fig. 2 and Supplementary Video). The tripartite carapace (Extended Data Figs 3, 4 and Supplementary Video) extends well in front of the head; the largest isolated carapace element exceeds 1 m in length, indicating individuals more than 2 m in overall length. The frontal appendages are composed of seven podomeres (Fig. 2a, b and Extended Data Fig. 5a–c). The long proximal podomere bears a short, backwardly directed ventral spine with a comb-like array of spines on its posterior margin (Figs 2a, b and Extended Data Fig. 5a–c). The five succeeding short podomeres bear long, ventral spines

¹Department of Geology and Geophysics, Yale University, PO Box 208109, New Haven, Connecticut 06520, USA. ²Research Unit Palaeontology, Department of Geology and Soil Science, Ghent University, Krijgslaan 281/S8, B-9000 Ghent, Belgium. ³Department of Zoology, University of Oxford, The Tinbergen Building, South Parks Road, Oxford OX1 3PS, UK. ⁴Oxford University Museum of Natural History, Parks Road, Oxford OX1 3PW, UK. ⁵Yale Peabody Museum of Natural History, Yale University, New Haven, Connecticut 06520, USA.

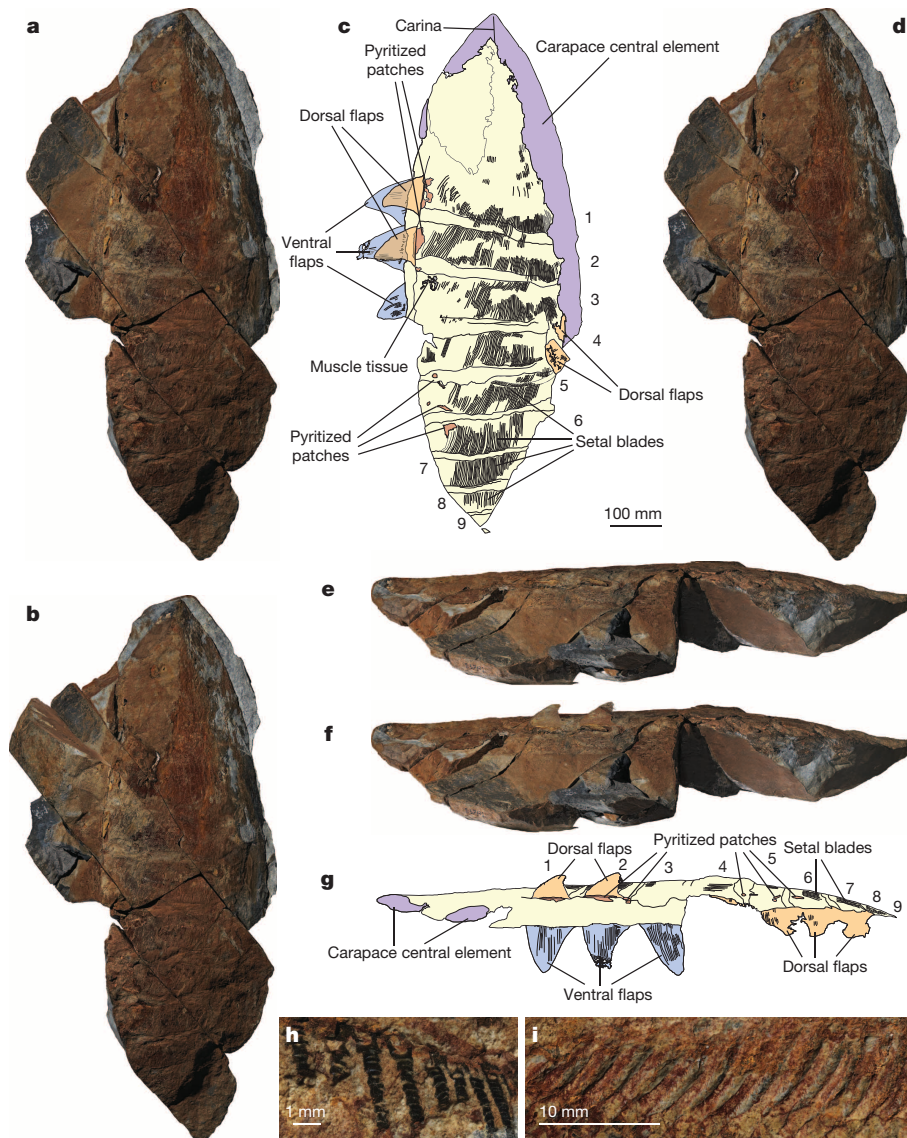


Figure 1 | *A. benmoulai*, holotype YPM 237172, Early Ordovician, Fezouata Biota, Morocco. **a–d**, Dorsal view: **a**, part, showing ventral flaps; **b**, part, separate block in place, showing dorsal flaps; **c**, interpretative drawing combining part and counterpart; **d**, part, matrix surrounding dorsal flaps digitally removed to show both sets of flaps. **e–g**, Lateral view: **e**, part; **f**, part,

dorsal flaps added from counterpart; **g**, interpretative drawing combining part and counterpart. **h**, Part, transverse rods composed of hollow cones of third ventral flap. **i**, Counterpart, oblique view of anterior free end of setal blades showing lamellae laterally. Arabic numerals indicate trunk somites.

curving forward distally (Fig. 2c and Extended Data Figs 5d–g, 6 and 7). These ventral spines were canted inward at about 45° to the longitudinal axis of the appendage (Extended Data Fig. 5a–c). They carry approximately 80 long, mobile, laterally flattened, flexible setae on their anterior margin. These setae bear two rows of densely spaced fine spinules set in a 'V' on their dorsal margin (Fig. 2 and Extended Data Fig. 6). The terminal pointed podomere of the appendage lacks spines (Fig. 2a, b and Extended Data Fig. 5a–c). No eyes or oral cone have yet been found. In the trunk, dorsal and ventral flaps are non-overlapping and separated from each other by intervening body wall (Fig. 1, Extended Data Figs 1 and 2 and Supplementary Video). Both have densely spaced transverse rods composed of short, flared, hollow cones one inserted into another; the basal cone is substantially larger than those succeeding it (Fig. 1h). The holotype YPM 237172 shows that segmentally arranged bands of thin, flexible setal blades attach at the base of the dorsal flaps and traverse the animal dorsally (Fig. 1, Extended Data Fig. 1). Individual setal blades connect to each other a short distance behind their anterior margin (Extended Data Fig. 8e). The blades have rounded terminations and show the presence of fine lamellae, probably on both

sides (Fig. 1i and Extended Data Fig. 8). There is no evidence for the presence of a tail fan. A reconstruction of *A. benmoulai* is provided in Fig. 3.

The discovery of dorsal flaps in *A. benmoulai* warranted re-examination of Cambrian anomalocaridids, given that the presence of dorsal flaps is difficult to demonstrate in flattened specimens owing to compaction and the tendency of the shale to split along one plane. Specimens of *Peytoia nathorsti* from the Burgess Shale revealed clear evidence of their presence in National Museum of Natural History specimen USNM 274161 (Extended Data Fig. 9a–c), and possibly USNM 274145 (Extended Data Fig. 9e). There are also indications of two sets of flaps in *Hurdia* (Royal Ontario Museum specimens ROM 49930 and ROM 59320) but in this case the evidence is more circumstantial (see Supplementary Text).

Given their phylogenetic position immediately stemward of euarthropods^{4–6} (Fig. 4, Extended Data Fig. 10 and Supplementary Text), the apparent absence of biramous appendages has been an anomalous aspect of anomalocaridid morphology. It was usually assumed that anomalocaridid lateral flaps were homologous to the flaps of gilled lobopodians such as *Kerygmachela kierkegaardii* and that ventral limbs were lost^{13,16}.

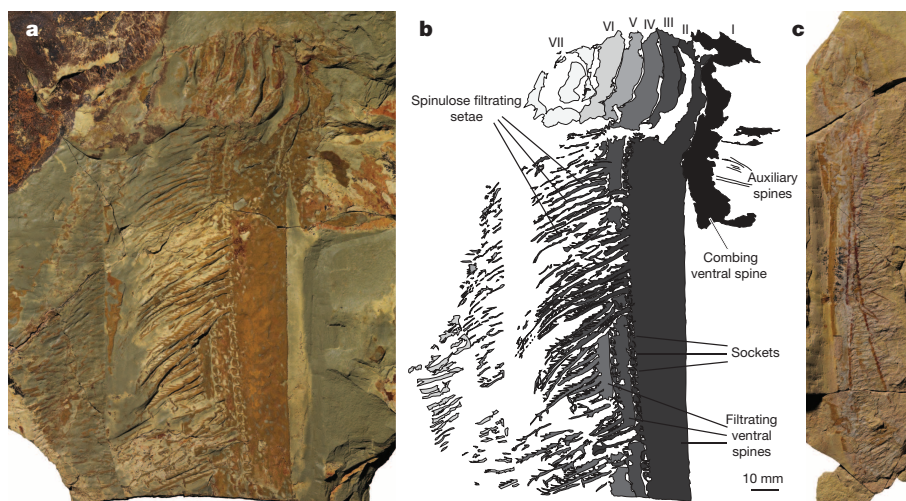


Figure 2 | *A. benmoulae*, appendages and ventral spines, Early Ordovician, Fezouata Biota, Morocco. **a**, Complete frontal appendage with partial ventral spines, showing mobile spinulose filtrating setae, paratype YPM 527125. Detail of the spinulose filtrating setae is provided in Extended Data Fig. 6a.

b, Interpretative drawing of YPM 527125. **c**, Partial appendage with complete ventral spines, paratype YPM 522227. Roman numerals indicate appendage podomeres.

The previously known flaps in Cambrian anomalocaridids^{6,11,13–15,18}, however, overlap from posterior to anterior, the reverse of the arrangement in the more basal *K. kierkegaardi*, *Pambdelurion whittingtoni* and *Opabinia regalis*^{16,20–22,26}. This anomaly is resolved by the discovery of additional, dorsal flaps in *A. benmoulae*, *P. nathorsti* and probably also *Hurdia victoria*: the position and morphology of the dorsal flaps indicates that they are homologous with those in gilled lobopodians. Thus, the larger ventral flaps in *A. benmoulae* and Cambrian anomalocaridids are here considered to be homologous with the lobopodous limbs of *K. kierkegaardi* and *P. whittingtoni*. This interpretation is supported by the presence of limbs in the anomalocaridid *Cucumericrus decoratus*¹⁴, which shows lobopodous walking limbs overlain dorsally by a single set of flaps (see Supplementary Text). The setal blades in *A. benmoulae* and other anomalocaridids, which are attached to the dorsal flaps and overlie the trunk, are probably homologous with the less extensive ‘gill-like’ wrinkled structures on the flaps of *K. kierkegaardi* and *P. whittingtoni*^{20,21},

and the setal blades in *O. regalis*^{5,16,22} (Fig. 4), although an alternative interpretation for these last structures has been advanced²⁶.

It has been suggested that the Cambrian biramous limb arose through the sclerotization of the lobopodous walking limb and its fusion with the dorsal flap of gilled lobopodians, which was reduced to leave the gill as an exite^{5,16,23}. The presence of a dorsal gill-bearing flap inserting separately to the ventral limb-derived flap in *A. benmoulae* and other anomalocaridid taxa indicates that they pre-date the acquisition of biramous limbs. This confirms their place on the euarthropod stem (Fig. 4, Extended Data Fig. 10 and Supplementary Text), resolving the debate on their phylogenetic position in line with recent neurological evidence⁶.

Among arthropods, the size of *A. benmoulae* (over 2 m in length) is paralleled only by some pterygotid eurypterids²⁷ and terrestrial arthropleurids²⁸. The evolution of gigantic filter-feeders within clades of nektic macrophagous predators is well documented in Mesozoic

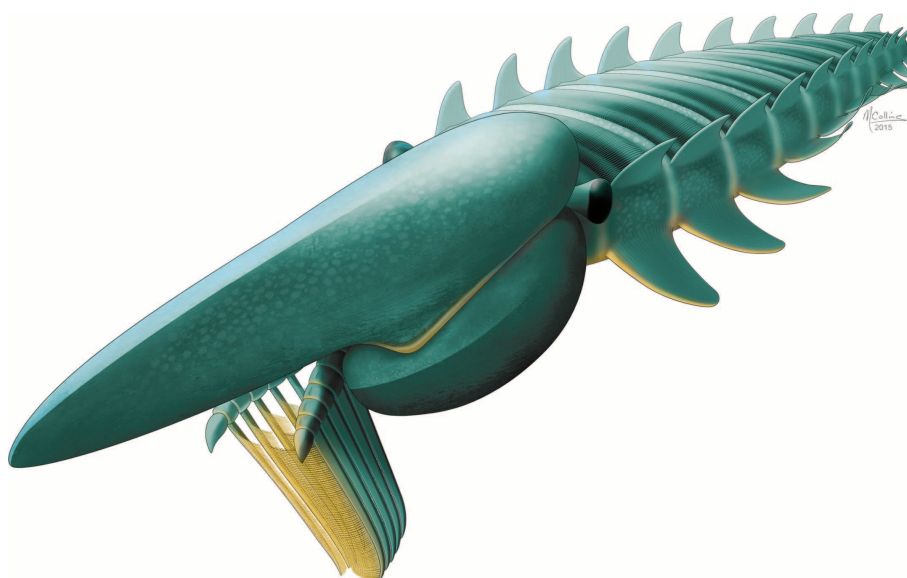


Figure 3 | *A. benmoulae*, reconstruction, Early Ordovician, Fezouata Biota, Morocco. Eye shape and position inferred from related taxa, with position further supported by the posterior gap between the carapace elements. The eyes are deliberately depicted comparatively smaller than in other

anomalocaridids: to achieve visual acuity comparable to that of more diminutive forms, a large animal requires smaller eyes relative to its body size. In addition, a filter-feeding lifestyle demands less acute vision than a macropredatory mode of life, further reducing the need for large eyes.

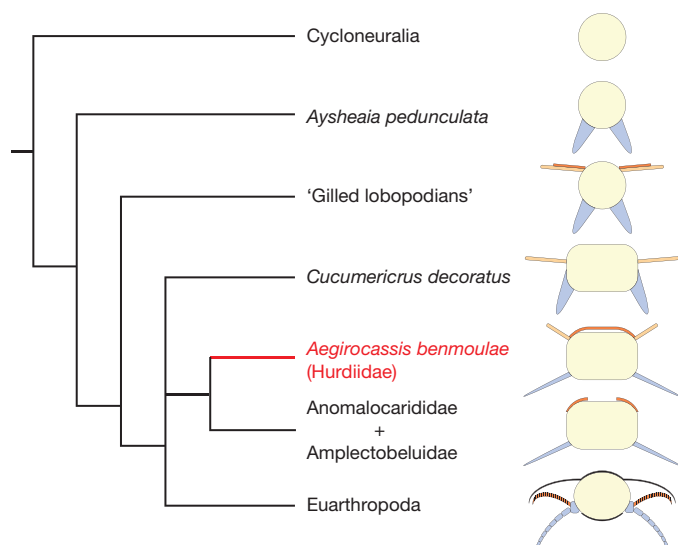


Figure 4 | Simplified cladogram showing the position of *A. benmoulae*, and schematic cross-sections through the bodies of included taxa illustrating the limb homologies and morphological transitions. The position of setal blades in *C. decoratus* is uncertain. A more extensive cladogram is provided in Extended Data Fig. 10. Light blue, ventral limbs/endopods; light orange, dorsal flaps; dark orange, setal blades/exites.

pachycormid fish²⁹ and Cenozoic sharks and whales³⁰. The huge size of *A. benmoulae* represents a much earlier example of a filter-feeding life-style correlating to gigantism. The abundance of gigantic anomalocaridid filter-feeders in the high palaeolatitude Fezouata Biota points to a complex planktic ecosystem. Early Cambrian anomalocaridid filter-feeders also fed on zooplankton, but they remained relatively small⁹. Although the Cambrian Explosion saw the establishment of the first complex planktic ecosystems, the convergent (Supplementary Text) rise of giant filter-feeding anomalocaridids during the Ordovician followed an increase in the abundance and diversity of phytoplankton and a consequent zooplankton radiation as part of the Great Ordovician Biodiversification Event²⁵.

Online Content Methods, along with any additional Extended Data display items and Source Data, are available in the online version of the paper; references unique to these sections appear only in the online paper.

Received 20 October 2014; accepted 23 January 2015.

Published online 11 March 2015.

1. Ma, X., Hou, X., Edgecombe, G. D. & Strausfeld, N. J. Complex brains and optic lobes in an early Cambrian arthropod. *Nature* **490**, 258–261 (2012).
2. Yang, J., Ortega-Hernández, J., Butterfield, N. J. & Zhang, Z. Specialized appendages in fuxianhuiids and the head organization of early euarthropods. *Nature* **494**, 468–471 (2013).
3. Tanaka, G., Hou, X., Ma, X., Edgecombe, G. D. & Strausfeld, N. J. Chelicerate neural ground pattern in a Cambrian great appendage arthropod. *Nature* **502**, 364–367 (2013).
4. Budd, G. E. A palaeontological solution to the arthropod head problem. *Nature* **417**, 271–275 (2002).
5. Daley, A. C., Budd, G. E., Caron, J.-B., Edgecombe, G. D. & Collins, D. The Burgess Shale anomalocaridid *Hurdia* and its significance for early euarthropod evolution. *Science* **323**, 1597–1600 (2009).
6. Cong, P., Ma, X., Hou, X., Edgecombe, G. D. & Strausfeld, N. J. Brain structure resolves the segmental affinity of anomalocaridid appendages. *Nature* **513**, 538–542 (2014).
7. Daley, A. C. & Budd, G. E. New anomalocaridid appendages from the Burgess Shale, Canada. *Palaeontology* **53**, 721–738 (2010).
8. Paterson, J. R. *et al.* Acute vision in the giant Cambrian predator *Anomalocaris* and the origin of compound eyes. *Nature* **480**, 237–240 (2011).
9. Vinther, J., Stein, M., Longrich, N. R. & Harper, D. A. T. A suspension-feeding anomalocarid from the Early Cambrian. *Nature* **507**, 496–499 (2014).

10. Daley, A. C. & Bergström, J. The oral cone of *Anomalocaris* is not a classic “peytoia”. *Naturwissenschaften* **99**, 501–504 (2012).
11. Whittington, H. B. & Briggs, D. E. G. The largest Cambrian animal, *Anomalocaris*, Burgess Shale, British Columbia. *Phil. Trans. R. Soc. Lond. B* **309**, 569–609 (1985).
12. Bergström, J. *Opabinia* and *Anomalocaris*, unique Cambrian ‘arthropods’. *Lethaia* **19**, 241–246 (1986).
13. Chen, J., Ramsköld, L. & Zhou, G. Evidence for monophyly and arthropod affinity of Cambrian giant predators. *Science* **264**, 1304–1308 (1994).
14. Hou, X., Bergström, J. & Ahlberg, P. *Anomalocaris* and other large animals in the Lower Cambrian Chengjiang Fauna of southwest China. *GFF* **117**, 163–183 (1995).
15. Collins, D. The “evolution” of *Anomalocaris* and its classification in the arthropod class Dinocarida (nov) and order Radiodonta (nov). *J. Paleontol.* **70**, 280–293 (1996).
16. Budd, G. E. The morphology of *Opabinia regalis* and the reconstruction of the arthropod stem-group. *Lethaia* **29**, 1–14 (1996).
17. Van Roy, P. & Briggs, D. E. G. A giant Ordovician anomalocaridid. *Nature* **473**, 510–513 (2011).
18. Daley, A. C. & Edgecombe, G. D. Morphology of *Anomalocaris canadensis* from the Burgess Shale. *J. Paleontol.* **88**, 68–91 (2013).
19. Van Roy, P. *et al.* Ordovician faunas of Burgess Shale type. *Nature* **465**, 215–218 (2010).
20. Budd, G. E. A Cambrian gilled lobopod from Greenland. *Nature* **364**, 709–711 (1993).
21. Budd, G. E. The morphology and phylogenetic significance of *Kerygmachela kierkegaardi* Budd (Buen Formation, Lower Cambrian, N Greenland). *Trans. R. Soc. Edinb. Earth Sci.* **89**, 249–290 (1999).
22. Budd, G. E. & Daley, A. C. The lobes and lobopods of *Opabinia regalis* from the middle Cambrian Burgess Shale. *Lethaia* **45**, 83–95 (2012).
23. Wolff, C. & Scholtz, G. The clonal composition of biramous and uniramous arthropod limbs. *Proc. R. Soc. B* **275**, 1023–1028 (2008).
24. Haug, J. T., Waloszek, D., Maas, A., Liu, Y. & Haug, C. Functional morphology, ontogeny and evolution of mantis shrimp-like predators in the Cambrian. *Palaeontology* **55**, 369–399 (2012).
25. Servais, T., Owen, A. W., Harper, D. A. T., Kröger, B. & Munnecke, A. The Great Ordovician Biodiversification Event (GOBE): the palaeoecological dimension. *Palaeogeogr. Palaeoclimatol. Palaeoecol.* **294**, 99–119 (2010).
26. Zhang, X. & Briggs, D. E. G. The nature and significance of the appendages of *Opabinia* from the Middle Cambrian Burgess Shale. *Lethaia* **40**, 161–173 (2007).
27. Braddy, S. J., Poschmann, M. & Tetlie, O. E. Giant claw reveals the largest ever arthropod. *Biol. Lett.* **4**, 106–109 (2008).
28. Schneider, J. & Werneburg, R. *Arthropleura* und *Diplopoda* (Arthropoda) aus dem Unter-Rotliegend (Unter-Perm, Assel) des Thüringer Waldes (Südwest-Saale-Senke). *Veröff. Naturhist. Mus. Schleusingen* **13**, 19–36 (1998).
29. Friedman, M. *et al.* 100-million-year dynasty of giant planktivorous bony fishes in the Mesozoic seas. *Science* **327**, 990–993 (2010).
30. Marx, F. G. & Uhen, M. D. Climate, critters, and cetaceans: Cenozoic drivers of the evolution of modern whales. *Science* **327**, 993–996 (2010).

Supplementary Information is available in the online version of the paper.

Acknowledgements M. and B. ‘Ou Said’ Ben Moula discovered the specimens and provided support in the field. S. Beardmore, D. Field, A. Little, R. Racicot and O. E. Tetlie assisted with fieldwork in 2011. L. Ben Moula and B. Tahiri provided practical assistance. J.-B. Caron loaned specimens of *Hurdia* from ROM collections. S. Butts and J. Utrup, K. Hollis and D. Erwin curated specimens and facilitated access to the collections at the YPM and USNM respectively. N. Utrup built custom cradles to support the articulated specimens. J. Vinther and P. Hull discussed filter-feeding and gigantism, and J. Lamsdell eurypterid book gills and phylogenetic methodology. E. Martin made available precise biostratigraphical data for the localities. G. Edgecombe provided unpublished observations on *Cucumericrus*. M. Collins discussed appendage function and prepared the digital reconstruction (Fig. 3). M. Fox advised on preparation and consolidation techniques and provided equipment. C. Graham and J. Slawski provided support and access to digital imaging facilities. The initial part of the research was done while P.V.R. was at Ghent University and in receipt of a mobility grant from the Biology Commission of the Research Foundation – Flanders (FWO). A.C.D. was financially supported by the Swedish Research Council (Vetenskapsrådet) and the Oxford University Museum of Natural History. The research was supported by National Science Foundation Grant EAR-1053247 and by the Division of Invertebrate Paleontology, YPM.

Author Contributions All authors, led by P.V.R., participated in the interpretation of the material and reconstruction of *A. benmoulae* and contributed to writing and editing the manuscript. P.V.R. and A.C.D. examined the material of *P. nathorsti* at the USNM and conducted the phylogenetic analyses. P.V.R. conducted fieldwork in Morocco, prepared and photographed Fezouata specimens, made preliminary reconstructions and composed the figures. A.C.D. photographed Burgess Shale specimens, prepared all explanatory specimen drawings and made the Burgess Shale figure.

Author Information Reprints and permissions information is available at www.nature.com/reprints. The authors declare no competing financial interests. Readers are welcome to comment on the online version of the paper. Correspondence and requests for materials should be addressed to P.V.R. (peter.vanroy@yale.edu).

METHODS

No statistical methods were used to predetermine sample size.

The Fezouata specimens are housed in the collections of the Yale Peabody Museum of Natural History (YPM), while the *Peytoia* material examined is at the National Museum of Natural History (USNM) and the *Hurdia* fossils used for this paper are in the collections of the Royal Ontario Museum (ROM).

The Moroccan specimens were mechanically prepared using PaleoTools ME9100, PaleoAro, MicroJack5 and MicroJack1 air scribes, and needles and scalpels. Specimens were glued with Paraloid B-72 dissolved in acetone, after which they received a protective coat of consolidant, consisting of a 5% solution of Butvar B-98 in ethanol.

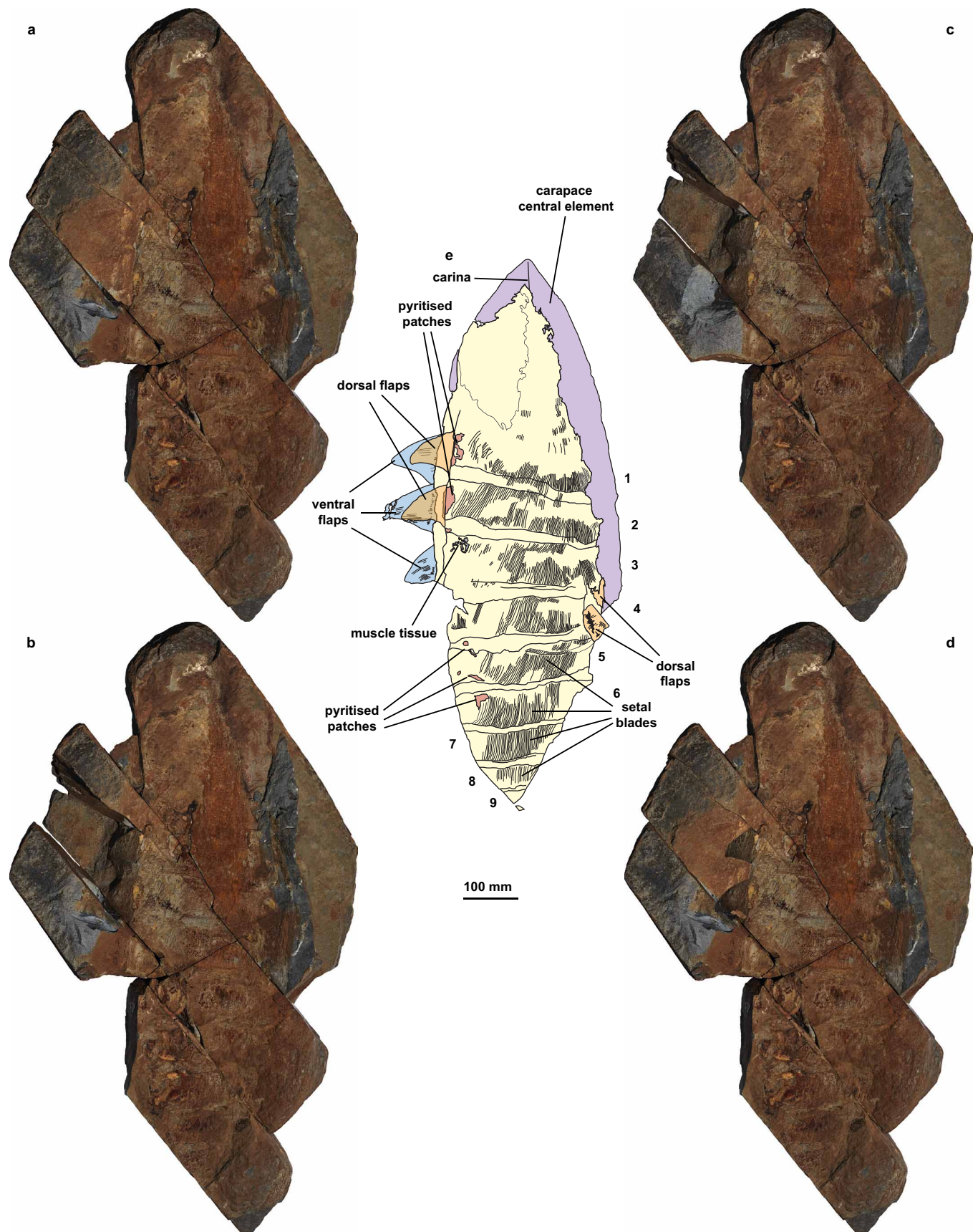
For photography, the Moroccan specimens were illuminated by a 500 W tungsten floodlight with an Aflash Photonics linear polarizer in front; a Cokin XPro X164 circular polarizer was mounted on the camera lens and crossed with the polarizer of the light source to maximize contrast. All parts were lit from the northwest. With the exception of the flaps, counterparts were illuminated from the southwest and mirrored in Adobe Photoshop CC 2014 to create a false-positive relief image and facilitate direct comparison of part and counterpart. In some cases, where indicated, information from part and counterpart was combined digitally into a single image in Adobe Photoshop CC 2014 to facilitate interpretation. All specimens were photographed dry, with the exception of YPM 227934, which was imaged under ethanol.

The micrograph of the muscle tissue in Extended Data Fig. 2g was taken with a Leica DFC 425 digital camera attached to a Leica MZ16 binocular microscope with a Leica Plan APO 1× lens and steered from a computer through Leica Application Suite 4.2. All other photographs were taken with a Hasselblad H4D-200MS medium frame digital single-lens reflex camera attached to a computer and operated remotely in six-shot mode through Hasselblad Phocus 8.2.1 software to acquire images of 200 megapixel resolution. Overview photographs of YPM 237172 used a

Hasselblad HC 2.8/80 mm lens stopped down to f/8; close-ups and all other, smaller specimens were photographed with a Hasselblad HC Macro 4/120 mm II lens stopped down to f/9.5. Lens distortion was corrected using Hasselblad Phocus 8.2.1 software. Stacks of between 10 and 50 images were taken in aperture priority mode, with manual focusing through the focal plane. After exporting the FFF-format digital negatives to TIFF from Hasselblad Phocus 8.2.1, the photographs were stacked in Zerene Stacker 1.04 (64 bit) using the PMax pyramid stack algorithm. The stacked images were then post-processed in Adobe Photoshop CC 2014, first applying the 'Sharpen more' and 'Sharpen' functions, followed by removal of the background. Levels were then manually balanced while holding down the 'alt' key to prevent clipping of pixels in the specimen; the grey level was always retained at 50%. In a few cases, some minor adjustments were made to the exposure. The high-resolution images were down-sampled in Adobe Photoshop CC 2014 to lower-resolution TIFF files for use in the plates.

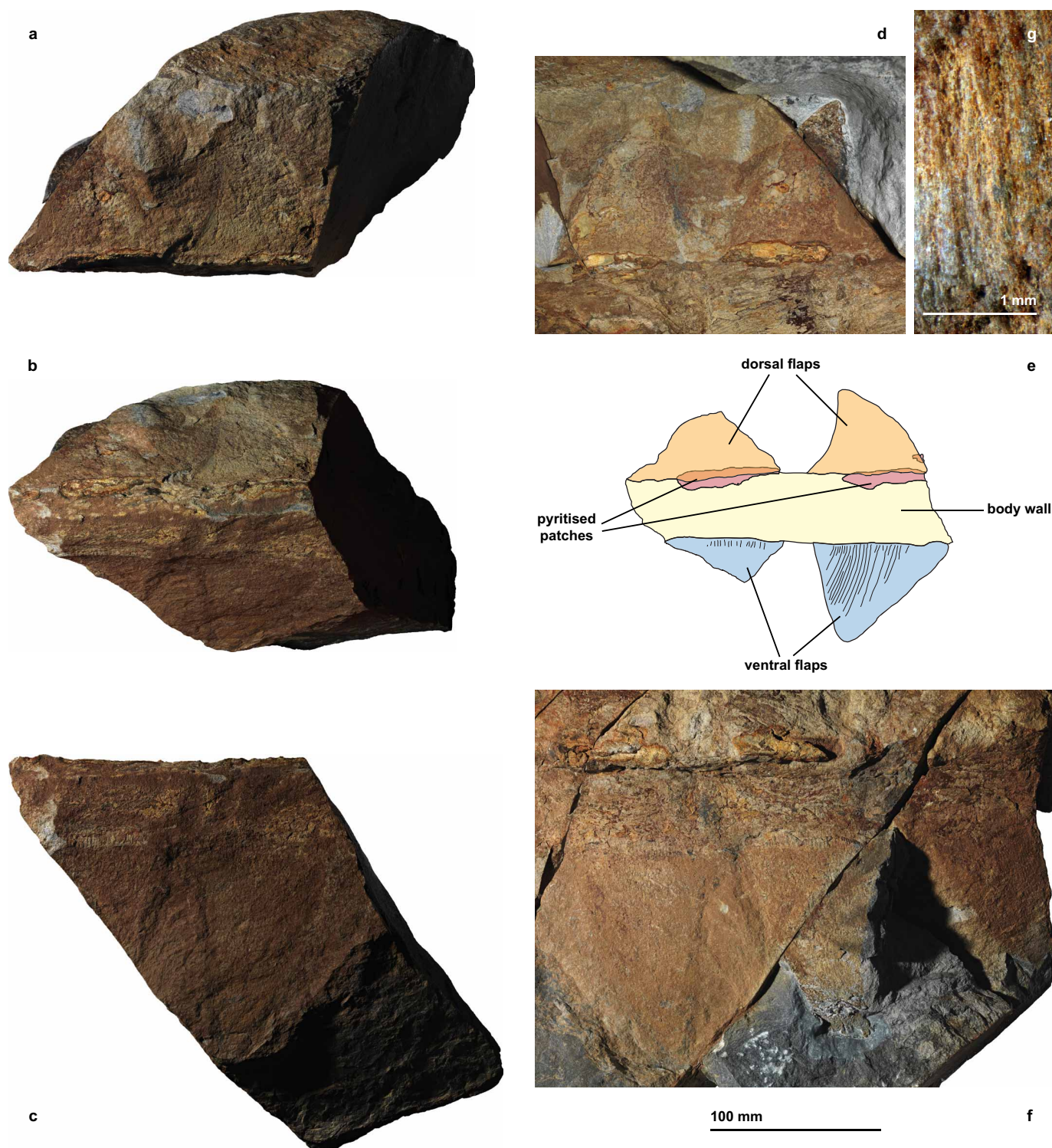
The Burgess Shale specimens were imaged immersed in water, with polarized lighting sourced from the northwest; a second polarizer in front of the camera lens was crossed with the polarization of the light source to enhance contrast. Photographs were taken using a Canon EOS 500D small-frame digital single-lens reflex camera controlled remotely using the EOS Utility 2.8.1.0 program. The camera was fitted with a Canon EF-S 60 mm Macro Lens, which was stopped down to f/2.8 (Extended Data Fig. 9d), f/3.5 (Extended Data Fig. 9a), f/4.0 (Extended Data Fig. 9b) or f/4.5 (Extended Data Fig. 9e). Images were post-processed in Adobe Photoshop CS6 using the 'Sharpen' function, minor adjustments were made to the exposure and the background was removed where necessary. Extended Data Fig. 9 was created using Adobe Illustrator CS6.

Explanatory drawings of the specimens were prepared in Adobe Illustrator CS6 on the basis of the high-resolution images. Photographs of part and counterpart were used to create composite drawings. The drawings were consistently colour-coded to allow identification of anatomical structures.



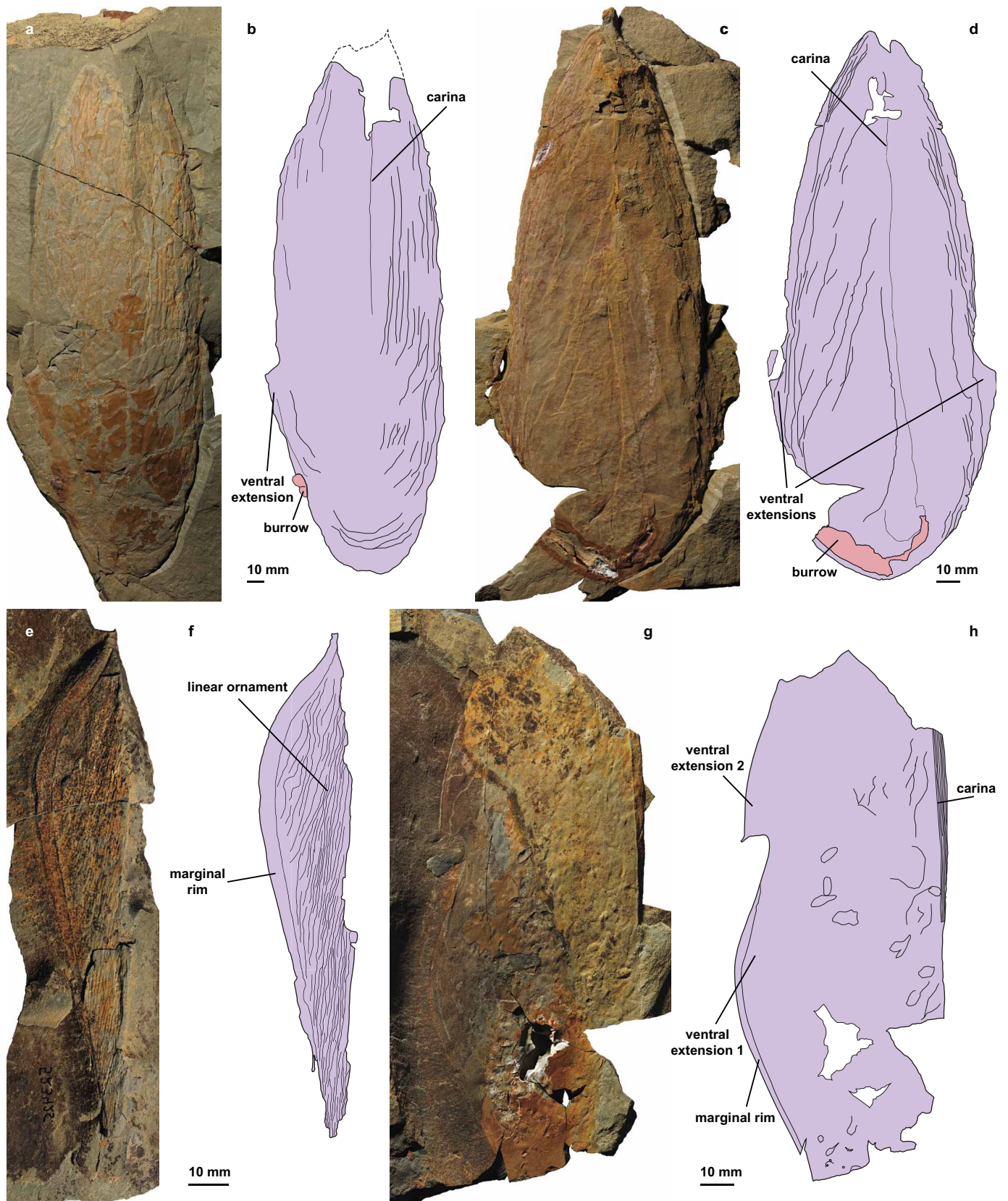
Extended Data Figure 1 | *A. benmoulae*, nearly complete three-dimensionally preserved specimen, counterpart, dorsal view, Early Ordovician, Fezouata Biota, Morocco, holotype YPM 237172. **a**, With separate blocks in place, showing ventral flaps. **b**, With one block removed,

showing dorsal flaps. **c**, With two blocks removed, showing dorsal flaps alone. **d**, Digital combination of images, showing both dorsal and ventral flaps. **e**, Interpretative drawing of dorsal view combining information from part and counterpart. Arabic numerals indicate trunk somites.



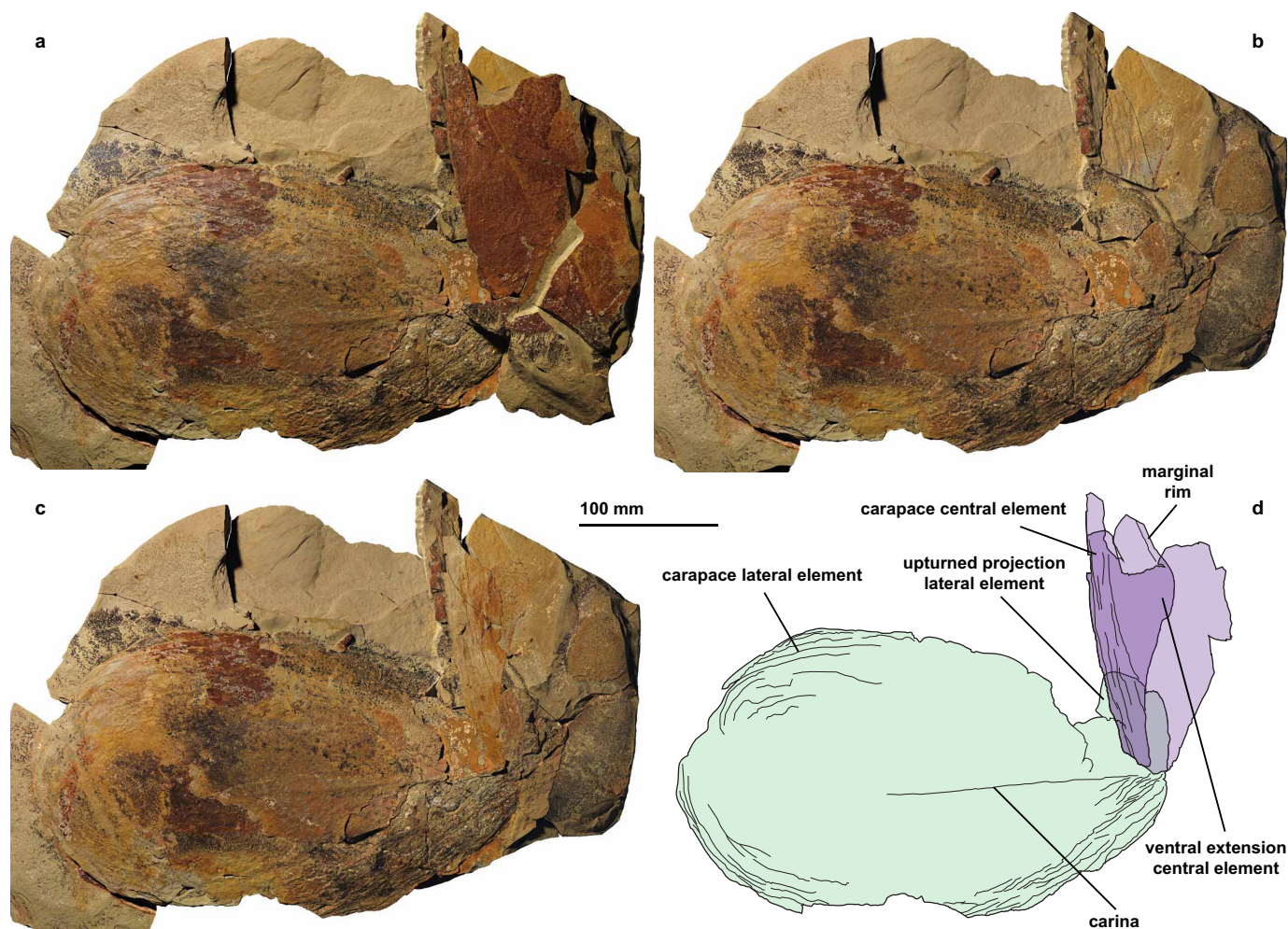
Extended Data Figure 2 | *A. benmoulae*, nearly complete three-dimensionally preserved specimen, dorsal and ventral flaps, Early Ordovician, Fezouata Biota, Morocco, holotype YPM 237172. **a**, Separate block, part, dorsal flaps, plan view. **b**, Separate block, lateral view showing body wall (counterpart), and dorsal (part) and ventral flaps (counterpart).

c, Separate block, counterpart, ventral flaps. **d**, Counterpart, dorsal flaps. **e**, Interpretative drawing of lateral view of separate block. **f**, part, ventral flaps. **g**, Part, muscle tissue closely associated with first dorsal flap on left side, showing individual fibres.



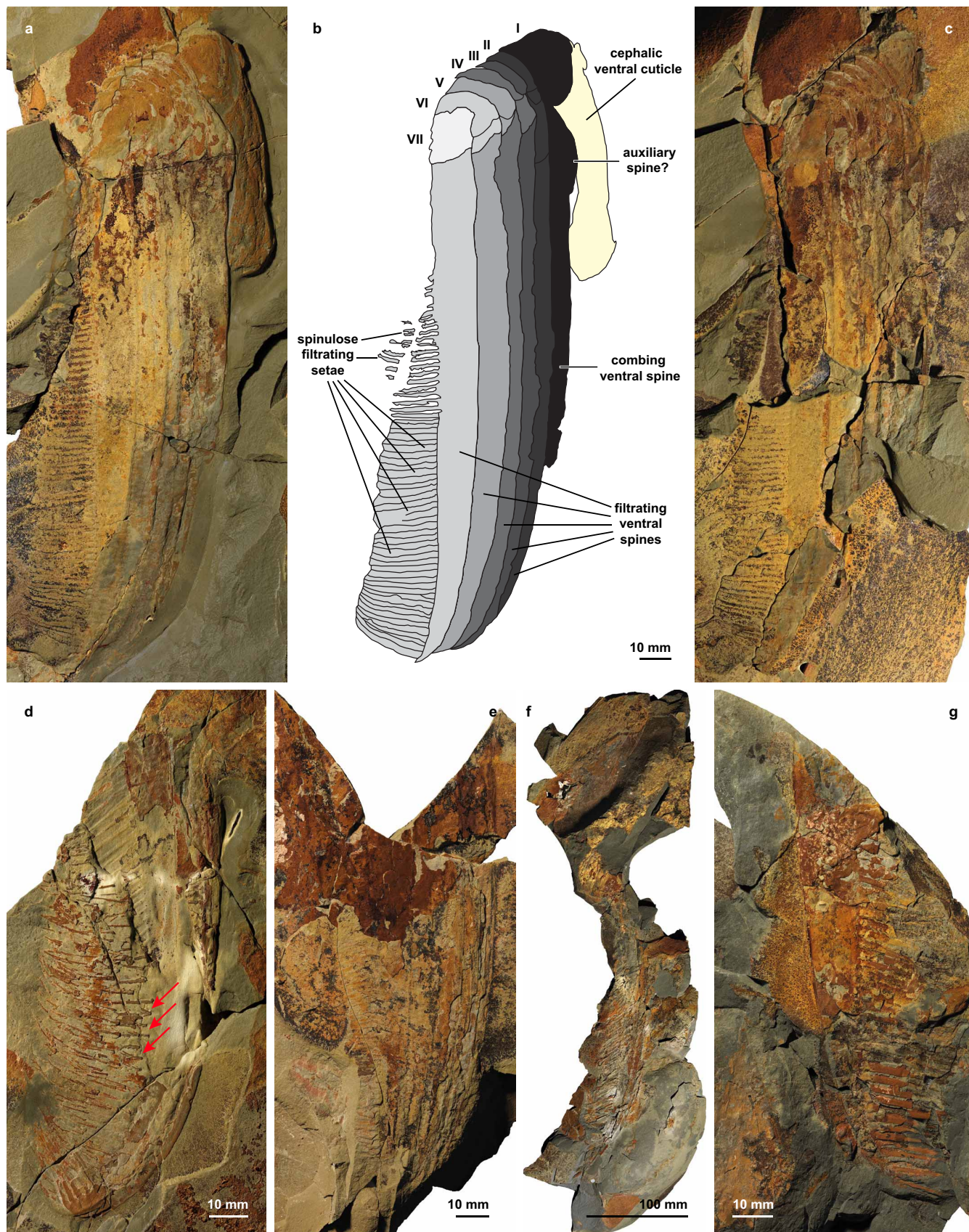
Extended Data Figure 3 | *A. benmoulai*, central elements of carapace, Early Ordovician, Fezouata Biota, Morocco. **a, b**, YPM 516785: **a**, nearly complete central element, part, dorsal view; **b**, interpretative drawing. **c, d**, Paratype YPM 227556: **c**, nearly complete central element, part, dorsal view;

d, interpretative drawing. **e, f**, YPM 523425: **e**, ventral triangular extension, counterpart, showing marginal rim and texture; **f**, interpretative drawing. **g, h**, YPM 523424: **g**, partial central element, part, oblique, showing second morph with additional anterior triangular extension; **h**, interpretative drawing.



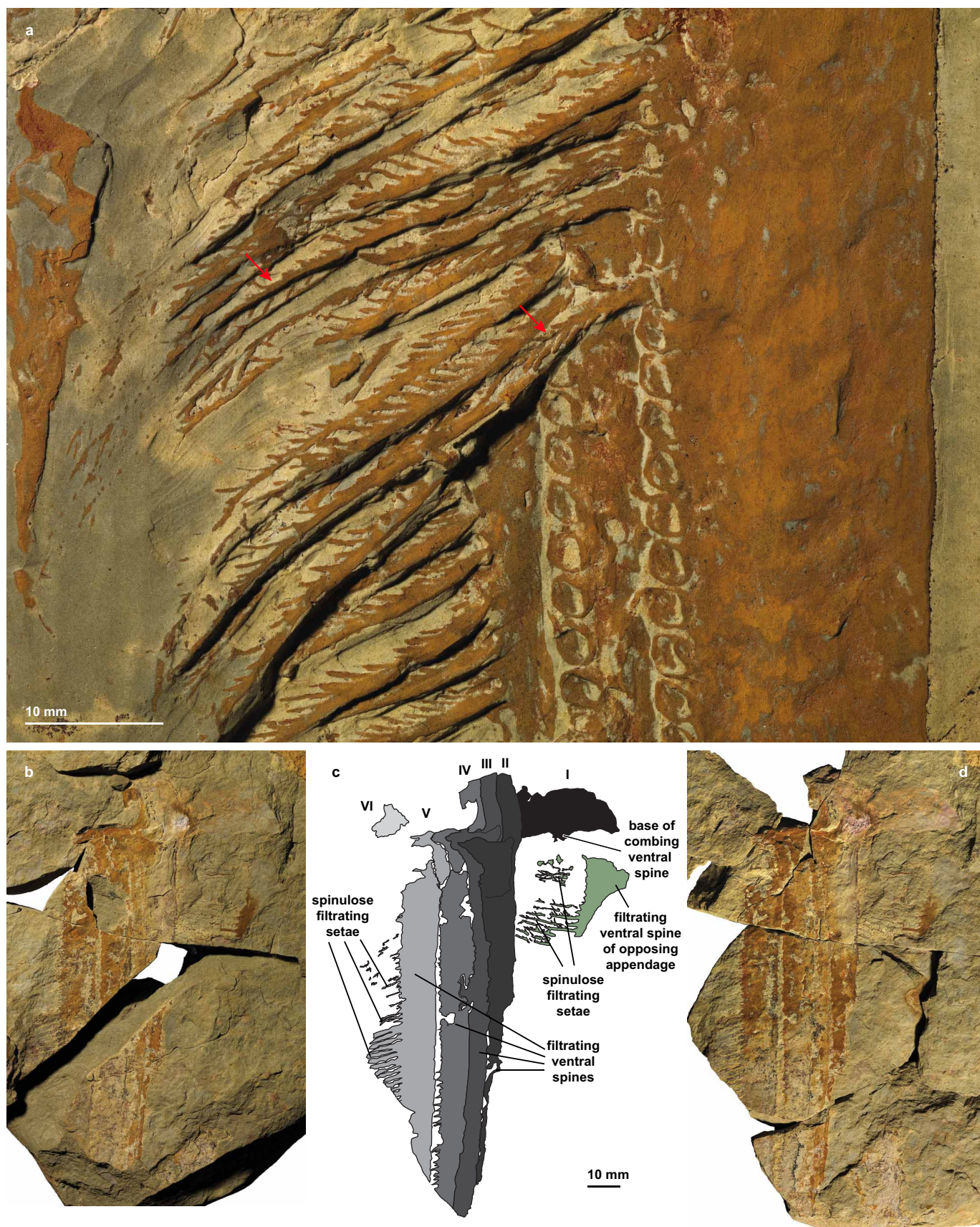
Extended Data Figure 4 | *A. benmoulae*, complete carapace lateral element associated with partial central element, Early Ordovician, Fezouata Biota, Morocco, paratype YPM 525437. **a**, With partial central element, part, in place. **b**, With partial central element, part, removed, revealing counterpart

imprint of triangular ventral extension. **c**, With dorsal side of central element digitally removed, revealing triangular ventral extension overlying anterior of lateral element. **d**, Interpretative drawing.



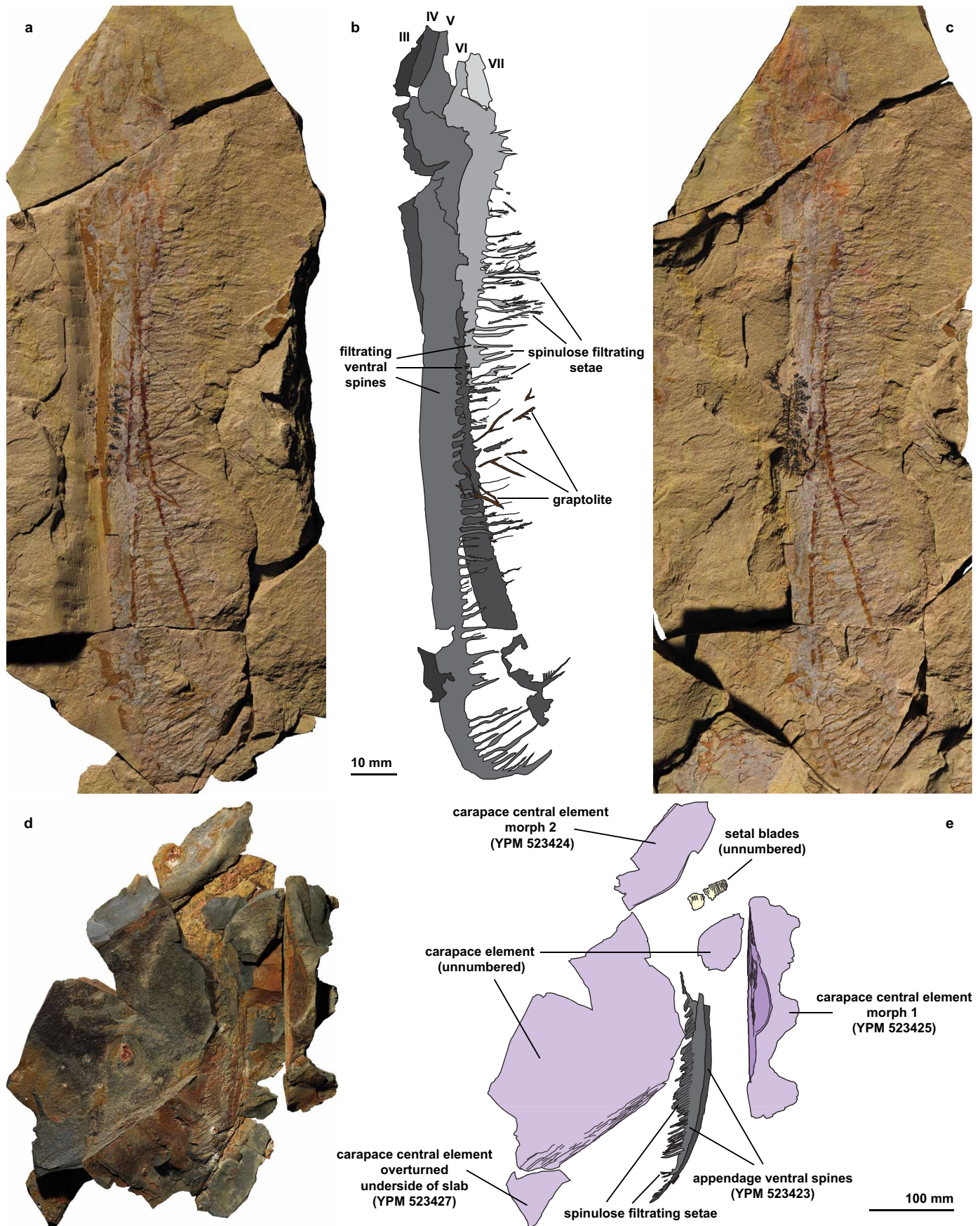
Extended Data Figure 5 | *A. benmoulai*, appendages and ventral spines, Early Ordovician, Fezouata Biota, Morocco. a–c, Paratype YPM 527123, nearly complete appendage: a, part; b, interpretative drawing combining part and counterpart; c, counterpart. d, YPM 527124, part, distal portion of ventral spines. Setae showing double row of spinules arrowed. YPM 527123 and

527124 belong to a disarticulated assemblage which may represent a single individual. e, YPM 523810, part, distal portion of five ventral spines. f, YPM 523423 and 523424, counterpart, ventral spines and partial carapace element. g, YPM 523428, part, termination of ventral spine. Roman numerals indicate appendage podomeres.



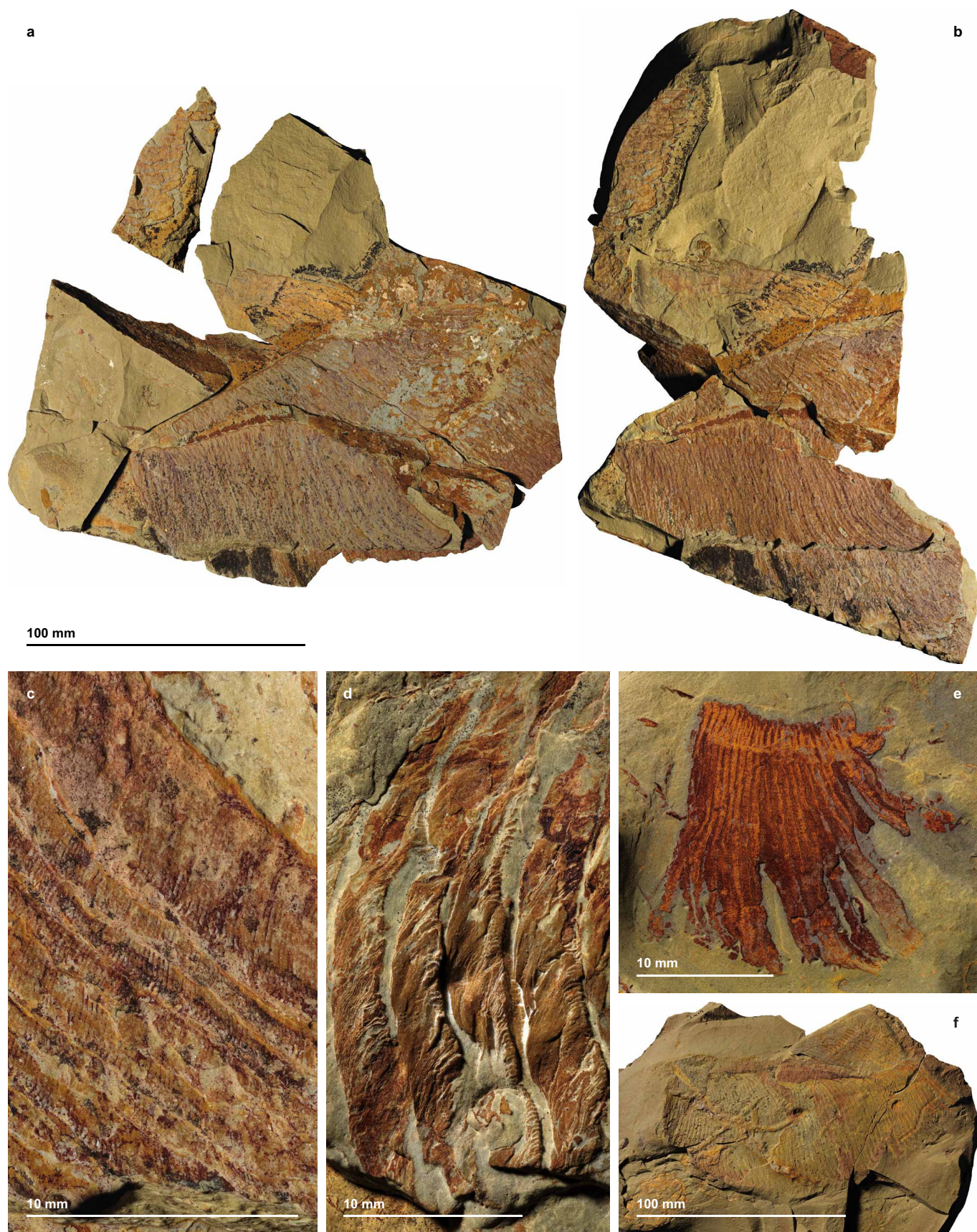
Extended Data Figure 6 | *A. benmoulae*, appendages and appendage ventral spines, Early Ordovician, Fezouata Biota, Morocco. **a**, Close-up of ventral spines of YPM 527125, showing spinulose filtrating setae and their insertion on the anterior margin of the ventral spines. Setae showing double row of

spinules arrowed. **b–d**, YPM 525217, partial appendage: **b**, part; **c**, interpretative drawing combining information from part and counterpart; **d**, counterpart. Roman numerals indicate appendage podomeres.



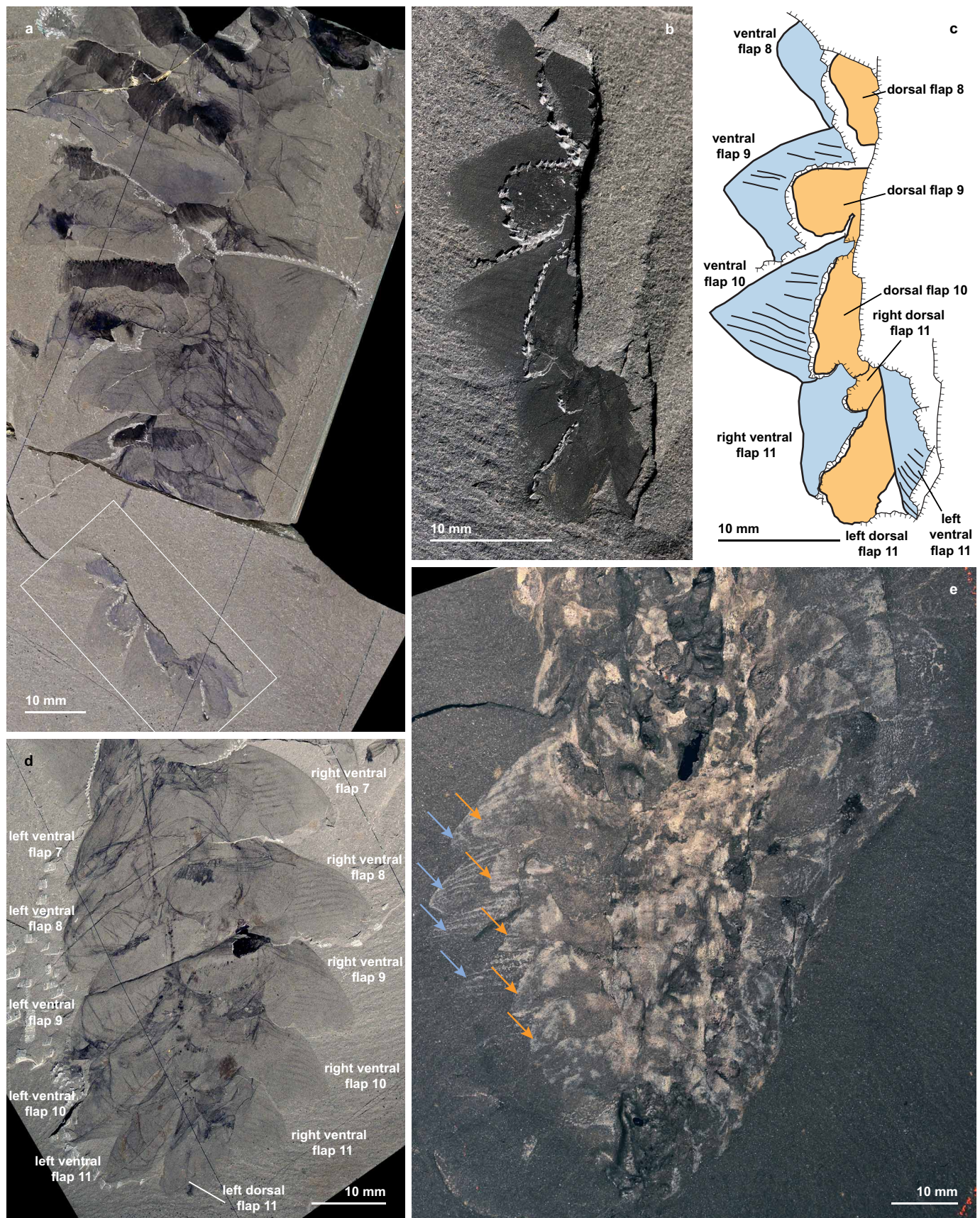
Extended Data Figure 7 | *A. benmoulai*, Early Ordovician, Fezouata Biota, Morocco. **a–c**, Partial appendage, paratype YPM 52227: **a**, part; **b**, interpretative drawing combining information from part and counterpart;

c, counterpart. Roman numerals indicate appendage podomeres. **d, e**, Assemblage of carapace elements, appendage ventral spines and setal blades, YPM 523423–523427: **d**, specimen; **e**, interpretative drawing.



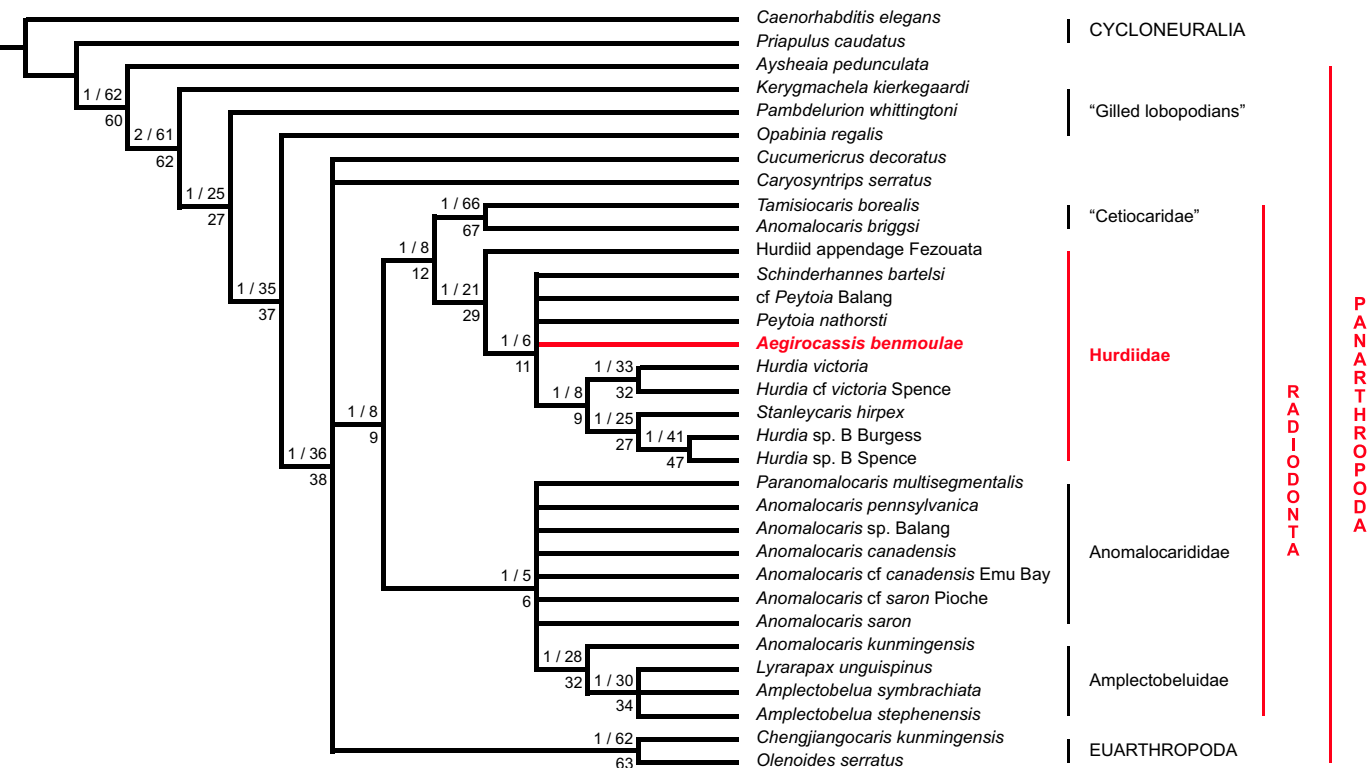
Extended Data Figure 8 | *A. benmoulae*, isolated bands of setal blades, Early Ordovician, Fezouata Biota, Morocco. **a–c**, YPM 516791: **a**, part; **b**, counterpart; **c**, close-up of counterpart, showing fine lateral lamellae on setal blades in plan view. **d**, Specimen associated with YPM 527123, part, showing

lamellae on setal blades. **e**, YPM 227934, part, showing connection between setal blades and division into short anterior and long posterior free parts. **f**, YPM 516792, part.



Extended Data Figure 9 | *P. nathorsti*, articulated specimens showing dorsal flaps, middle Cambrian, Burgess Shale, Canada. **a**, USNM 274156 and USNM 274161 joined into complete specimen. White box indicates area of close-ups of USNM 274161 in **b** and **c**. **b**, **c**, USNM 274161: **b**, posterior,

counterpart, showing two sets of flaps; **c**, interpretative drawing. **d**, USNM 274154, the opposite half of the split corresponding to USNM 274156 and 274161. **e**, USNM 274145. Blue arrows indicate ventral flaps; orange arrows indicate dorsal flaps.



Extended Data Figure 10 | Results of the phylogenetic analysis. Strict consensus of 70 most parsimonious trees obtained under equal weighting (consistency index = 0.611; retention index = 0.798). Numbers above nodes indicate Bremer support/standard bootstrap (1,000 replicates) values; number below nodes is the jackknife (1,000 replicates, $P = 36$) value. An identical strict consensus tree is obtained with implied weighting for all k values from 3 to 8.

eIF3 targets cell-proliferation messenger RNAs for translational activation or repression

Amy S. Y. Lee^{1,2}, Philip J. Kranzusch^{1,3} & Jamie H. D. Cate^{1,2,4,5}

Regulation of protein synthesis is fundamental for all aspects of eukaryotic biology by controlling development, homeostasis and stress responses^{1,2}. The 13-subunit, 800-kilodalton eukaryotic initiation factor 3 (eIF3) organizes initiation factor and ribosome interactions required for productive translation³. However, current understanding of eIF3 function does not explain genetic evidence correlating eIF3 deregulation with tissue-specific cancers and developmental defects⁴. Here we report the genome-wide discovery of human transcripts that interact with eIF3 using photoactivatable ribonucleoside-enhanced crosslinking and immunoprecipitation (PAR-CLIP)⁵. eIF3 binds to a highly specific program of messenger RNAs involved in cell growth control processes, including cell cycling, differentiation and apoptosis, via the mRNA 5' untranslated region. Surprisingly, functional analysis of the interaction between eIF3 and two mRNAs encoding the cell proliferation regulators c-JUN and BTG1 reveals that eIF3 uses different modes of RNA stem-loop binding to exert either translational activation or repression. Our findings illuminate a new role for eIF3 in governing a specialized repertoire of gene expression and suggest that binding of eIF3 to specific mRNAs could be targeted to control carcinogenesis.

Extensive genetic evidence implicates eIF3 in other functions in translation outside of its general role as a protein scaffold for the formation of initiation complexes. Mutation or inactivation of eIF3 subunits results in developmental defects in *Caenorhabditis elegans* and zebrafish^{6,7}. Furthermore, analyses of human tumours reveal that overexpression of eIF3 is linked to diverse cancers, including breast, prostate and oesophageal malignancies^{4,8}. The integral role of eIF3 during cellular differentiation, growth and carcinogenesis suggests that eIF3 might drive specialized translation. Consistent with this hypothesis, translation of hepatitis C virus RNA occurs through essential interactions between eIF3 and a structured internal ribosome entry site (IRES) element in the viral genome, indicating the feasibility of translation regulation being driven by distinct cellular eIF3–mRNA contacts⁹.

To identify candidate transcripts regulated through direct interactions with eIF3, we first used a genome-wide approach to determine the eIF3 RNA-binding targets in human 293T cells. Because eIF3 is composed of 13 subunits (eIF3a–m), we adapted a 4-thiouridine PAR-CLIP⁵ approach to allow analysis of a large multimeric complex, with isolation of individual subunit–RNA libraries (Fig. 1a). As overexpression of single eIF3 subunits can alter complex assembly⁸, we optimized immunoprecipitation of the full endogenous eIF3 complex using an antibody that recognizes the eIF3b subunit (Fig. 1b). High-salt washes were used to ensure removal of potentially contaminating translation factors, such as eIF4G or the small ribosomal subunit (Fig. 1c). After RNase digestion, separation of crosslinked eIF3–RNA complexes by denaturing gel electrophoresis demonstrated that four of the thirteen subunits crosslink directly to RNA (Fig. 1d), identified by mass spectrometry as eIF3a, b, d and g (Extended Data Fig. 1).

For each subunit, separate complementary DNA libraries were generated from the isolated crosslinked RNAs and deep sequenced using

Illumina technology. Sequenced reads from three biological replicates were mapped to the genome and grouped into eIF3-binding sites by using the cluster-finding tool PARalyzer¹⁰. Read clusters were found in 479 unique genes, with eIF3a, b, d and g crosslinking to 328, 264, 356 and 352 transcripts, respectively (Supplementary Tables 1 and 2). The limited number of interacting genes supports capture of specific eIF3–RNA contacts, as these targets compromise only ~3% of total expressed transcripts (Extended Data Fig. 2). As a further control, we do not see crosslinking

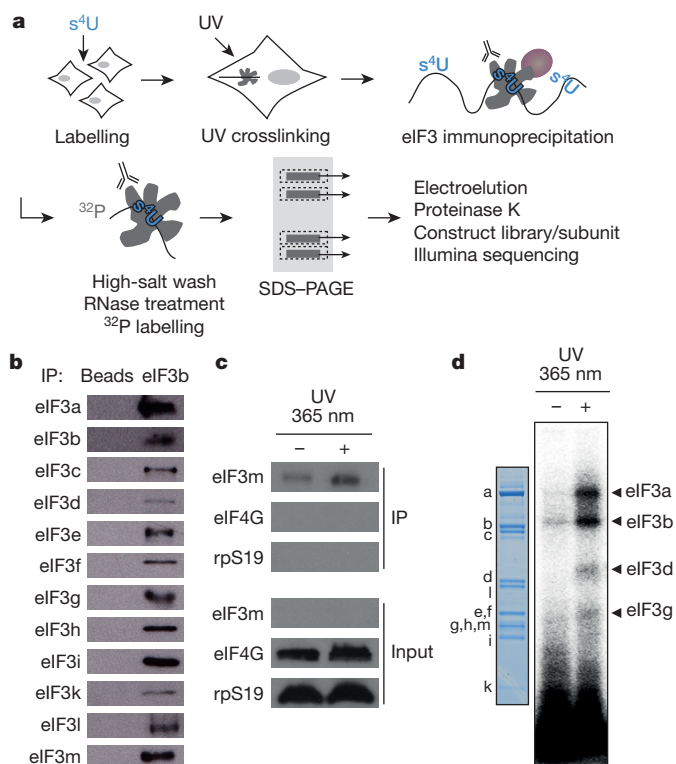


Figure 1 | PAR-CLIP of the multi-protein translation initiation factor complex eIF3. **a**, Schematic of PAR-CLIP methodology. 4-Thiouridine-labelled (s^4U) RNAs were crosslinked to proteins and endogenous eIF3 complexes were immunoprecipitated using an antibody that recognizes eIF3b. Separate cDNA libraries were constructed for individual crosslinked subunits. **b**, Immunoprecipitation (IP) of the eIF3 complex. Magnetic beads without eIF3b antibody were used as a negative control. **c**, Western blot of immunoprecipitated complexes after PAR-CLIP. **d**, Phosphorimage of SDS gel resolving 5' ^{32}P -labelled RNAs crosslinked to eIF3 subunits. Crosslinked RNAs cause the subunits to migrate ~10 kDa above their expected size²⁹. Immunoprecipitated samples prepared from 4-thiouridine-labelled 293T cell lysates treated without ultraviolet (UV) 365 nm light are shown as a negative control. Coomassie blue staining of purified native eIF3 resolved by SDS–polyacrylamide gel electrophoresis (SDS–PAGE) is shown for size reference.

¹Department of Molecular & Cell Biology, University of California, Berkeley, Berkeley, California 94720, USA. ²Center for RNA Systems Biology, University of California, Berkeley, Berkeley, California 94720, USA. ³Howard Hughes Medical Institute (HHMI), University of California, Berkeley, Berkeley, California 94720, USA. ⁴Department of Chemistry, University of California, Berkeley, Berkeley, California 94720, USA. ⁵Physical Biosciences Division, Lawrence Berkeley National Laboratory, Berkeley, California 94720, USA.

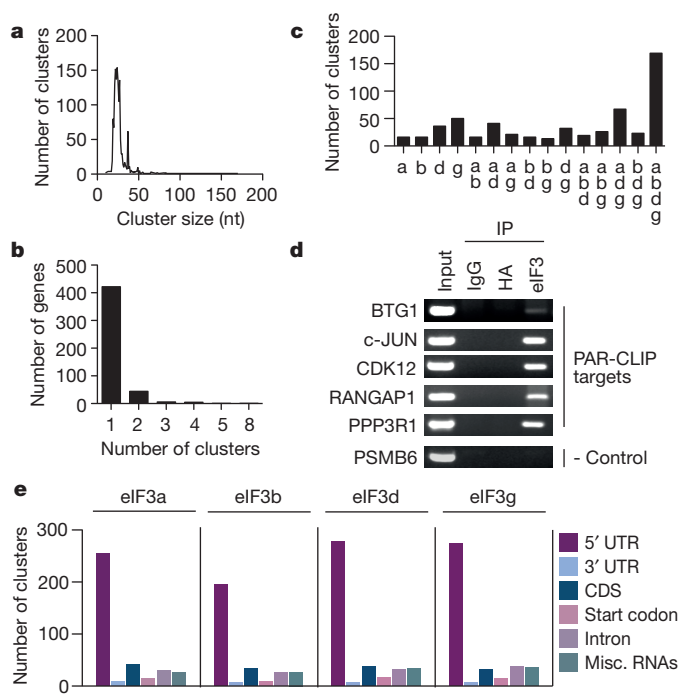


Figure 2 | Analysis and validation of eIF3 PAR-CLIP-derived binding sites. **a**, Length distribution of PAR-CLIP clusters. nt, nucleotides. **b**, Distribution of number of PAR-CLIP clusters per gene. **c**, Distribution of PAR-CLIP targets among different combinations of eIF3 subunit crosslinking. **d**, Validation of PAR-CLIP targets by eIF3 immunoprecipitation and RT-PCR. eIF3 immunoprecipitation (IP) was performed using an anti-eIF3b antibody as in Fig. 1b. As negative controls, the immunoprecipitation was performed with isotype-matched immunoglobulin G (IgG) or anti-haemagglutinin tag (HA) antibody. **e**, Distribution of eIF3 crosslinking sites along mRNAs and in other classes of RNAs. CDS, coding sequence; Misc., miscellaneous.

to highly abundant ribosomal RNAs, in agreement with biochemical and structural studies showing that eIF3 interacts primarily with the protein-rich face of the small ribosomal subunit^{11–14}.

The majority of RNAs contained a single eIF3-binding site, with a median cluster length of 25 nucleotides (Fig. 2a, b). These RNAs interact

with distinct combinations of eIF3a, b, d and g subunits (Fig. 2c). To validate the RNAs identified by PAR-CLIP, we performed eIF3 immunoprecipitation in the absence of crosslinking. We detected eIF3–RNA interactions for five top candidate genes using polymerase chain reaction with reverse transcription (RT–PCR); whereas a negative control mRNA, the *PSMB6* transcript, was not immunoprecipitated (Fig. 2d).

In eukaryotic protein synthesis, the 5' UTR of mRNA is thought to be the major site of translation regulation³. In agreement with identifying translation regulation roles of specific eIF3–mRNA interactions, the eIF3-binding sites predominantly mapped to the 5' UTR (~70%) (Fig. 2e). To examine the impact of transcript-specific engagement of eIF3 on translational control, we focused on two genes with an eIF3-binding site in the 5' UTR, *c-JUN* and B-cell translocation gene 1 (*BTG1*) (Fig. 3a, b). *c-JUN* is a member of the immediate early response transcription factor AP1 and a positive mitotic regulator¹⁵. In contrast, *BTG1* acts as a negative regulator of proliferation and its expression induces cellular differentiation^{16,17}. Because of the opposing effects of *c-JUN* and *BTG1* on cellular growth, we wanted to understand why eIF3 would interact with both mRNAs. We constructed luciferase reporters containing the 5' UTR of *c-JUN* or *BTG1* with or without the eIF3 crosslinking site identified by PAR-CLIP (Fig. 3c). Deletion of the crosslinking site from the 5' UTR of *c-JUN* abolished translation of mRNAs transfected into cells, indicating that eIF3 binding is required for efficient translation (Fig. 3d). In stark contrast, *BTG1* translation was highly upregulated when the eIF3-binding site was removed from the mRNA (Fig. 3e). Furthermore, treatment of 293T cell *in vitro* translation extracts with m⁷G cap analogue inhibited translation of both *c-JUN* and *BTG1* luciferase reporter mRNAs, demonstrating that eIF3-dependent translation regulation of these transcripts is cap-dependent and thus distinct from viral IRES-like mechanisms¹⁸ (Fig. 3f, g). These results demonstrate that eIF3 can act as both a translation activator and repressor of specific cellular mRNAs.

To understand how eIF3 binding to mRNA leads to opposing translation phenotypes, we next identified the full RNA elements for eIF3 recognition in the *c-JUN* and *BTG1* mRNAs. While PAR-CLIP marks the localized vicinity of eIF3 in the 5' UTR, eIF3 interaction could occur either through recognition of a linear sequence or in the context of RNA secondary structure. Using selective 2'-hydroxyl acylation analysed by primer extension (SHAPE), we experimentally determined the secondary structure around the eIF3-binding sites (Fig. 4a, d). For both *c-JUN* and *BTG1*, SHAPE revealed that the eIF3-binding sites map to structured

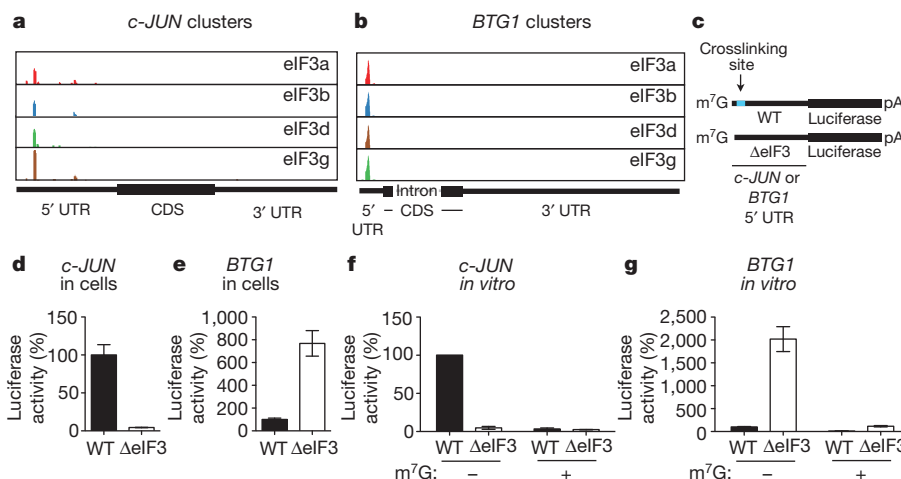


Figure 3 | eIF3 is a positive and negative transcript-specific translational regulator. **a**, **b**, eIF3 PAR-CLIP cluster in the 5' UTR of *c-JUN* mRNA (**a**) or *BTG1* mRNA (**b**). Reads mapped are shown along the respective genes. **c**, Schematic of *c-JUN* and *BTG1* 5' UTR-luciferase reporter mRNAs. The eIF3 PAR-CLIP cluster is nucleotide positions 181–214 for the *c-JUN* transcript (GenBank accession NM_002228) and positions 105–187 for the *BTG1* transcript (GenBank accession NM_001731). WT, wild type. **d**, **e**, Luciferase

activity in cells transfected with mRNAs containing the *c-JUN* (**d**) or *BTG1* (**e**) 5' UTR with or without a deletion of the eIF3 crosslinking site. **f**, **g**, Luciferase activity *in vitro* from mRNAs driven by the *c-JUN* (**f**) or *BTG1* (**g**) 5' UTR, with or without competitor m⁷G cap analogue. The results of **d–g** are given as the mean \pm standard deviation (s.d.) of three independent experiments, each performed in triplicate.

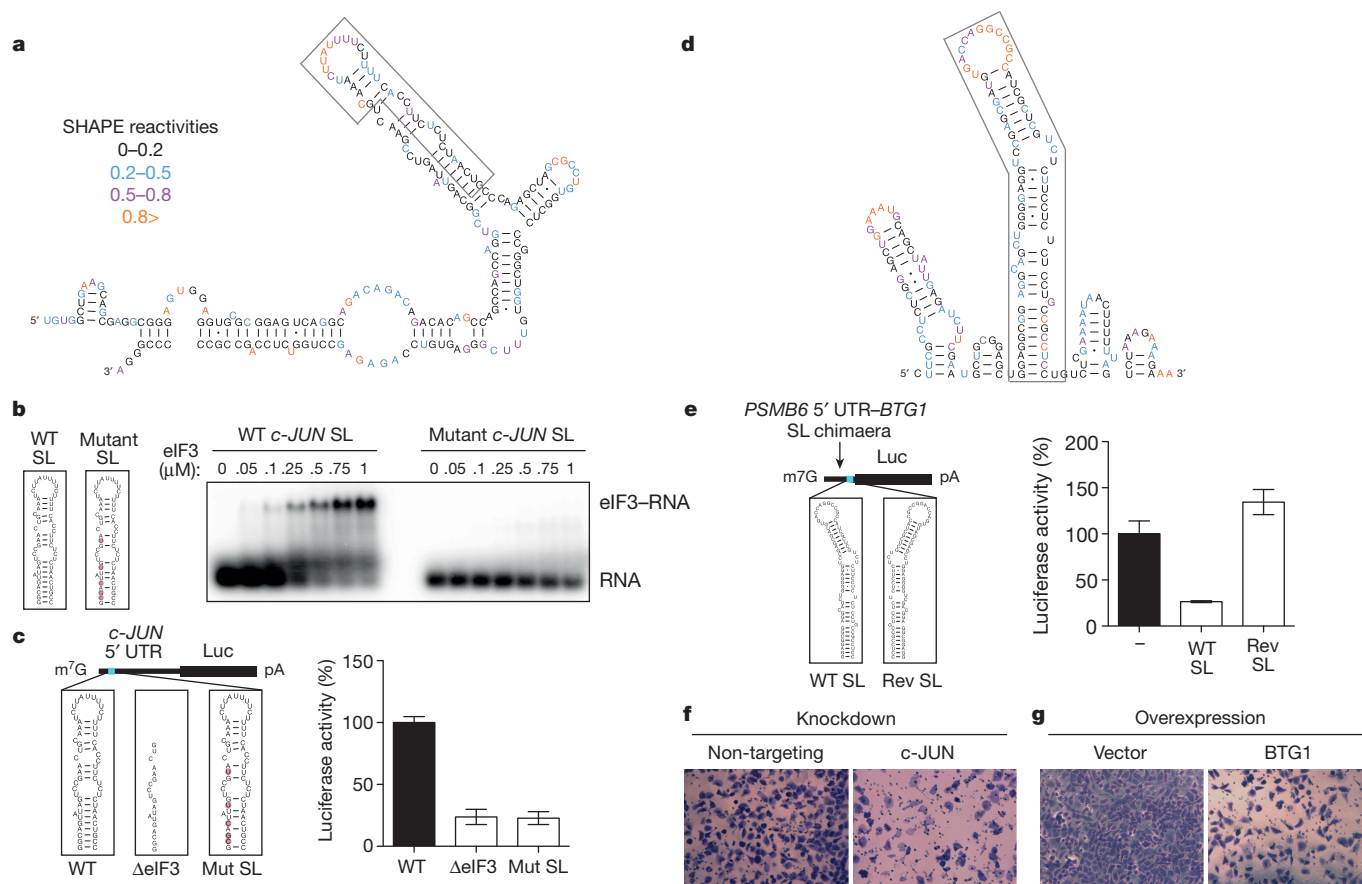


Figure 4 | Opposing translation phenotypes are driven by different modes of eIF3-mRNA binding. **a**, SHAPE-based secondary structure of the *c-JUN* 5' UTR surrounding the eIF3 PAR-CLIP site. Nucleotides are colour-coded by their SHAPE reactivities, with higher reactivity reflecting single-stranded behaviour and non-reactivity indicating base pairing between nucleotides. **b**, Representative native gel shifts showing a specific and binary interaction between recombinant eIF3 and the wild-type (WT) *c-JUN* stem-loop (SL) structure but not the mutated stem-loop. **c**, Luciferase (Luc) activity *in vitro* of mRNAs driven by the *c-JUN* 5' UTR containing stem-loop mutations. Mut SL, mutant stem-loop. **d**, SHAPE-based secondary structure of the *BTG1*

5' UTR surrounding the eIF3 PAR-CLIP site. **e**, Luciferase activity *in vitro* from mRNAs driven by a *PSMB6* 5' UTR-*BTG1* stem-loop chimaera. Rev SL, transversed stem-loop. The results of **c** and **e** are given as the mean \pm s.d. of three independent experiments, each performed in triplicate.

f, **g**, Representative images of the effect of siRNA-mediated knockdown of *c-JUN* (**f**) or *BTG1* overexpression (**g**) on Matrigel invasion by H1299 cells. As a control, cells were transfected with a non-targeting siRNA (**f**) or empty vector (**g**). Quantification of cell migration is presented in Extended Data Fig. 6. The results of **f** and **g** are representative of three independent experiments, each performed in duplicate.

RNA regions corresponding to conserved stem-loops (Extended Data Fig. 3). For the *c-JUN* mRNA element, we investigated the importance of secondary structure in eIF3 recognition by mutating base-pairing interactions of five nucleotides in the stem while leaving the cross-linking site intact (Fig. 4b). eIF3 directly bound to the *c-JUN* stem-loop, but not the mutated stem-loop, as determined by native agarose gel electrophoresis with radiolabelled RNA and recombinant or native eIF3 (Fig. 4b and Extended Data Fig. 4). Furthermore, the same mutations in the *c-JUN* luciferase reporter mRNA led to the identical translation phenotype as deletion of the full eIF3 crosslinking site (Fig. 4c and Extended Data Fig. 5a). Unlike its interactions with the *c-JUN* RNA, eIF3 was unable to bind to the *BTG1* stem-loop in a binary fashion (Extended Data Fig. 4b). As eIF3 immunoprecipitates *BTG1* mRNA in cell lysates (Fig. 2d), this suggests that other currently unknown factors are required for this mode of eIF3-RNA interaction. To verify that the *BTG1* stem-loop is sufficient for the inhibitory translation phenotype of eIF3 binding, we asked whether addition of the stem-loop could block translation driven by the *PSMB6* 5' UTR, which does not interact with eIF3 (Fig. 2d). Transplantation of the *BTG1* stem-loop into the *PSMB6* 5' UTR conferred translation inhibition (Fig. 4e and Extended Data Fig. 5b). Importantly, addition of the transversed *BTG1* stem-loop sequence does not alter *PSMB6* translation, confirming that *BTG1* stem-loop-driven translation repression is

eIF3-specific and not due to introduction of a potentially deleterious RNA secondary structure¹⁹ (Fig. 4e and Extended Data Fig. 5b). Together, these results demonstrate that during translation activation, eIF3 recognizes the *c-JUN* mRNA by directly binding to a sequence in the context of a stem-loop structure; whereas during translation inhibition, eIF3 binding to the *BTG1* stem-loop requires the presence of additional factors or modifications.

Although misregulation of eIF3 levels is implicated in carcinogenesis, it was previously unknown if eIF3 activities lead to these cell growth alterations^{4,8}. Gene ontology analysis of the PAR-CLIP results establish direct binding of eIF3 to RNA targets enriched in cancer-associated cell growth regulation pathways, such as apoptosis, cell cycling and differentiation (Extended Data Fig. 6a). The combination of these targets may represent a gene program that supports overactive cell proliferation during eIF3-related malignancies. In support of this, our results demonstrate that eIF3 acts as a positive translational regulator of *c-JUN*, which is a proto-oncogene required for RAS-mediated transformation²⁰; and a negative regulator of *BTG1*, of which genomic deletions are found in 9% of B-cell precursor acute lymphoblastic leukaemias²¹. Furthermore, circumventing eIF3 translational control by knockdown of *c-JUN* or overexpression of *BTG1* decreases cell invasiveness of H1299 human lung cancer cells, which overexpress eIF3a²² (Fig. 4f, g and Extended Data Fig. 6). Thus, we suggest that the RNAs identified by PAR-CLIP may be co-opted

upon eIF3 overexpression, leading to loss of correct translational control of cell growth and eventual malignancy.

Although it is surprising that eIF3 can act as both a repressor and activator of translation, analogous contrasting functions have been found with other multi-protein complexes. For example, the RNA polymerase II regulation complex Mediator consists of at least 30 proteins in humans. It directs either transcription activation or repression, dependent on promoter sequence, gene-specific regulatory proteins, and altered phosphorylation states of subunits²³. Intriguingly, more than 25 posttranslational modifications have been detected on eIF3, with a number of them at substoichiometric levels^{24,25}, and eIF3 association with other translation regulatory proteins such as the helicase eIF4B is regulated by mitogenic signalling²⁶. Furthermore, modelling of the eIF3 subunits, except for eIF3d, reveals that the crosslinked subunits form a nexus in a distal region of eIF3 positioned near the mRNA entry tunnel (Extended Data Fig. 7)¹⁴. As the PAR-CLIP sites exhibit all variations of interactions with the four eIF3 subunits (Fig. 2c), we propose that there may be multiple modes of eIF3–RNA interactions driven by this region of eIF3 (refs 12, 13).

Recent studies have highlighted that certain factors possess roles outside of their general functions in translation. For example, the ribosome mediates translational specificity during development and viral infection through the requirement for distinct ribosomal proteins^{27,28}. During canonical translation, eIF3 acts as a protein scaffold for initiation complex assembly³. Our results now reveal a new paradigm for translational control, in which, in addition to this general function, eIF3 can act as both an activator and repressor of cap-dependent transcript-specific translation through direct binding to defined RNA structural elements.

Online Content Methods, along with any additional Extended Data display items and Source Data, are available in the online version of the paper; references unique to these sections appear only in the online paper.

Received 10 October 2014; accepted 27 January 2015.

Published online 6 April 2015.

- Stumpf, C. R. & Ruggero, D. The cancerous translation apparatus. *Curr. Opin. Genet. Dev.* **21**, 474–483 (2011).
- Silvera, D., Formenti, S. C. & Schneider, R. J. Translational control in cancer. *Nature Rev. Cancer* **10**, 254–266 (2010).
- Jackson, R. J., Hellen, C. U. & Pestova, T. V. The mechanism of eukaryotic translation initiation and principles of its regulation. *Nature Rev. Mol. Cell Biol.* **11**, 113–127 (2010).
- Hershey, J. W. Regulation of protein synthesis and the role of eIF3 in cancer. *Braz. J. Med. Biol. Res.* **43**, 920–930 (2010).
- Hafner, M. *et al.* Transcriptome-wide identification of RNA-binding protein and microRNA target sites by PAR-CLIP. *Cell* **141**, 129–141 (2010).
- Choudhuri, A., Maitra, U. & Evans, T. Translation initiation factor eIF3h targets specific transcripts to polysomes during embryogenesis. *Proc. Natl Acad. Sci. USA* **110**, 9818–9823 (2013).
- Curran, S. P. & Ruvkun, G. Lifespan regulation by evolutionarily conserved genes essential for viability. *PLoS Genet.* **3**, e56 (2007).
- Zhang, L., Pan, X. & Hershey, J. W. Individual overexpression of five subunits of human translation initiation factor eIF3 promotes malignant transformation of immortal fibroblast cells. *J. Biol. Chem.* **282**, 5790–5800 (2007).
- Fraser, C. S. & Doudna, J. A. Structural and mechanistic insights into hepatitis C viral translation initiation. *Nature Rev. Microbiol.* **5**, 29–38 (2007).
- Corcoran, D. L. *et al.* PARalyzer: definition of RNA binding sites from PAR-CLIP short-read sequence data. *Genome Biol.* **12**, R79 (2011).
- Pisarev, A. V., Kolupaeva, V. G., Yusupov, M. M., Hellen, C. U. & Pestova, T. V. Ribosomal position and contacts of mRNA in eukaryotic translation initiation complexes. *EMBO J.* **27**, 1609–1621 (2008).
- Hashem, Y. *et al.* Structure of the mammalian ribosomal 43S preinitiation complex bound to the scanning factor DHX29. *Cell* **153**, 1108–1119 (2013).
- Hashem, Y. *et al.* Hepatitis-C-virus-like internal ribosome entry sites displace eIF3 to gain access to the 40S subunit. *Nature* **503**, 539–543 (2013).
- Erzberger, J. P. *et al.* Molecular architecture of the 40S eIF3 translation initiation complex. *Cell* **158**, 1123–1135 (2014).
- Wisdom, R., Johnson, R. S. & Moore, C. c-Jun regulates cell cycle progression and apoptosis by distinct mechanisms. *EMBO J.* **18**, 188–197 (1999).
- Rouault, J. P. *et al.* BTG1, a member of a new family of antiproliferative genes. *EMBO J.* **11**, 1663–1670 (1992).
- Bakker, W. J. *et al.* FoxO3a regulates erythroid differentiation and induces BTG1, an activator of protein arginine methyl transferase 1. *J. Cell Biol.* **164**, 175–184 (2004).
- Blau, L. *et al.* Aberrant expression of c-Jun in glioblastoma by internal ribosome entry site (IRES)-mediated translational activation. *Proc. Natl Acad. Sci. USA* **109**, E2875–E2884 (2012).
- Kozak, M. Circumstances and mechanisms of inhibition of translation by secondary structure in eucaryotic mRNAs. *Mol. Cell. Biol.* **9**, 5134–5142 (1989).
- Johnson, R., Spiegelman, B., Hanahan, D. & Wisdom, R. Cellular transformation and malignancy induced by ras require c-jun. *Mol. Cell. Biol.* **16**, 4504–4511 (1996).
- Waanders, E. *et al.* The origin and nature of tightly clustered BTG1 deletions in precursor B-cell acute lymphoblastic leukemia support a model of multiclonal evolution. *PLoS Genet.* **8**, e1002533 (2012).
- Pincheira, R., Chen, Q. & Zhang, J. T. Identification of a 170-kDa protein over-expressed in lung cancers. *Br. J. Cancer* **84**, 1520–1527 (2001).
- Carlsten, J. O., Zhu, X. & Gustafsson, C. M. The multitasking Mediator complex. *Trends Biochem. Sci.* **38**, 531–537 (2013).
- Andaya, A., Villa, N., Jia, W., Fraser, C. S. & Leary, J. A. Phosphorylation stoichiometries of human eukaryotic initiation factors. *Int. J. Mol. Sci.* **15**, 11523–11538 (2014).
- Damoc, E. *et al.* Structural characterization of the human eukaryotic initiation factor 3 protein complex by mass spectrometry. *Mol. Cell. Proteomics* **6**, 1135–1146 (2007).
- Holz, M. K., Ballif, B. A., Gygi, S. P. & Blenis, J. mTOR and S6K1 mediate assembly of the translation preinitiation complex through dynamic protein interchange and ordered phosphorylation events. *Cell* **123**, 569–580 (2005).
- Kondrashov, N. *et al.* Ribosome-mediated specificity in Hox mRNA translation and vertebrate tissue patterning. *Cell* **145**, 383–397 (2011).
- Lee, A. S., Burdeinick-Kerr, R. & Whelan, S. P. A ribosome-specialized translation initiation pathway is required for cap-dependent translation of vesicular stomatitis virus mRNAs. *Proc. Natl Acad. Sci. USA* **110**, 324–329 (2013).
- Ule, J., Jensen, K., Mele, A. & Darnell, R. B. CLIP: a method for identifying protein-RNA interaction sites in living cells. *Methods* **37**, 376–386 (2005).

Supplementary Information is available in the online version of the paper.

Acknowledgements The authors thank J. Doudna, D. Ruggero, D. Black, M. Truitt, A. Tambe, Y. Bai and K. Chat for discussions. HeLa cytoplasm was a gift from J. Fang. This work used the Vincent J. Coates Genomics Sequencing Laboratory at University of California, Berkeley, supported by National Institutes of Health (NIH) S10 Instrumentation Grants S10RR029668 and S10RR027303; and the Vincent J. Proteomics/Mass Spectrometry Laboratory at University of California, Berkeley, supported in part by NIH S10 Instrumentation Grant S10RR025622. This work was funded by the National Institute of General Medical Sciences Center for RNA Systems Biology (A.S.Y.L. and J.H.D.C.). A.S.Y.L. is supported as an American Cancer Society Postdoctoral Fellow (PF-14-108-01-RMC) and P.J.K. is supported as a Howard Hughes Medical Institute Fellow of the Life Sciences Research Foundation.

Author Contributions Experiments were designed by A.S.Y.L. in consultation with J.H.D.C. All experiments and analyses were performed by A.S.Y.L. P.J.K. performed gel shift assays and assisted with biochemistry. The manuscript was written by A.S.Y.L. and J.H.D.C. All authors contributed to editing the manuscript and support the conclusions.

Author Information All data have been deposited in the Gene Expression Omnibus under accession number GSE65004. Reprints and permissions information is available at www.nature.com/reprints. The authors declare no competing financial interests. Readers are welcome to comment on the online version of the paper. Correspondence and requests for materials should be addressed to J.H.D.C. (jcate@lbl.gov).

METHODS

Cells and transfections. Human 293T cells were maintained in DMEM (Invitrogen) with 10% FBS (Tissue Culture Biologicals). H1299 cells were maintained in RPMI-1640 ATCC-formulated (ATCC) with 10% FBS. IMR90 cells were maintained in Eagles MEM (ATCC) with 10% FBS. RNA transfections were performed using TransIT mRNA reagent (Mirus), with the following modifications to the manufacturer's protocol. Twenty-four hours before transfection, 293T cells were seeded into opaque 96-well plates to be at ~80% confluence at the time of transfection. For each well, 9 μ l of pre-warmed OptiMEM (Invitrogen) was mixed with 90 ng of RNA, 0.27 μ l of Boost reagent and 0.27 μ l of TransIT mRNA reagent. Reactions were incubated for 3 min at room temperature, added drop-wise to the well, and luciferase activity was assayed 18 h after transfection. Plasmid transfections were performed using Lipofectamine 2000 (Invitrogen), according to the manufacturer's protocol, and Matrigel or western blot assays were performed 48 h after transfection. siRNA transfection was performed using Lipofectamine 2000, with the following modifications to the manufacturer's protocol. Forty-eight hours after transfection, cells were split into new 6-well plates to be at ~70% confluence 24 h after seeding. These cells were then transfected for a second time with siRNA, and harvested for Matrigel or western blot assays 48 h after the second transfection.

Plasmids and siRNAs. To generate the *c-JUN* and *BTG1* 5' UTR luciferase reporter plasmids, sections of the 5' UTR were first amplified from human cDNA. These were then stitched together downstream of a T7 promoter using overlap-extension PCR and Gibson cloning. For the *PSMB6* 5' UTR luciferase reporter plasmid, the 5' UTR was constructed by annealing primers together to create restriction-site-compatible overhangs. The 5' UTRs were then inserted together with *Renilla* luciferase into pUC19 for *c-JUN* and pcDNA4 for *BTG1* and *PSMB6*. The eIF3-binding mutants and *BTG1* stem-loop chimaeras were made by inserting annealed primers after cutting the plasmid with enzymes flanking the desired insertion site. The *BTG1* overexpression plasmid was constructed by inserting the *BTG1* open reading frame, isolated by PCR from human cDNA, into pcDNA4 modified with a Kozak sequence³⁰. siRNA pools used were siGENOME *JUN* (Dharmacon M-003268-03) and siGENOME Non-Targeting siRNA #3 (Dharmacon D-001210-03).

Western blot. Western blot analysis was performed using the following antibodies: anti-eIF3a (Novus NBP1-18891); anti-eIF3b (Bethyl A301-761A); anti-eIF3c (Bethyl A300-376A); anti-eIF3d (Bethyl A301-758A); anti-eIF3e (Bethyl A302-985A); anti-eIF3f (Bethyl A303-005A); anti-eIF3g antibody (Bethyl A301-757A); anti-eIF3h antibody (Bethyl A301-754A); anti-eIF3i (Biologend 646701); anti-eIF3k (Novus NB100-93304); anti-eIF3l antibody (Genetex GTX120119); anti-eIF3m (Novus NBP1-56654); anti-rpS19 (Bethyl A304-002A); anti-eIF4G1 (Bethyl A301-775A); anti-*c-JUN* (Bethyl A302-959A); anti-*BTG1* (Abcam ab151740); anti-GAPDH (Bethyl A300-640A); and anti-HSP90 (BD 610418).

In vitro transcription. RNAs were made by *in vitro* transcription with T7 RNA polymerase (NEB). For luciferase RNAs, transcription was performed in the presence of 3'-O-Me-m⁷G(5')ppp(5')G RNA Cap Structure Analogue (NEB), using linearized plasmid as the template, and polyadenylated using polyA polymerase (Invitrogen). For gel shifts, annealed oligonucleotides were used as the template, and RNAs were radiolabelled by capping with vaccinia virus enzymes (NEB) and [α -³²P]-GTP. For SHAPE reactions, PCR templates were made using primers to add a 3' handle (5'-GAACCGGACCGAAGCCCGGCTGAG-3'), and transcription was performed using gel-extracted PCR products. RNAs were purified by phenol-chloroform extraction and ethanol precipitation or using the RNA Clean and Concentrator Kit (Zymo).

In vitro translation. *In vitro* translation extracts were made from 293T cells using a previously described protocol³¹. Briefly, cells were trypsinized and collected by centrifugation for 5 min at 1,000g at 4 °C. Cells were washed once with cold PBS (137 mM NaCl, 2.7 mM KCl, 100 mM Na₂HPO₄, 2 mM KH₂PO₄) and an equal volume of freshly made cold lysis buffer (10 mM HEPES-KOH pH 7.6, 10 mM KOAc, 0.5 mM Mg(OAc)₂, 5 mM dithiothreitol (DTT), and 1 Complete EDTA-free Proteinase Inhibitor Cocktail tablet (Roche) per 10 ml of buffer) was added. After hypotonic-induced swelling for 45 min on ice, cells were homogenized using a syringe attached to a 27G needle until ~95% of cells burst, as monitored by trypan blue staining. Lysate was centrifuged at 14,000g for 1 min at 4 °C, and supernatant was moved to a new tube, avoiding the top lipid layer. Lysates were quickly frozen with liquid nitrogen and stored at -80 °C. Each translation reaction contained 50% *in vitro* translation lysate and buffer to make the final reaction with 0.84 mM ATP, 0.21 mM GTP, 21 mM creatine phosphate (Roche), 45 U ml⁻¹ creatine phosphokinase (Roche), 10 mM HEPES-KOH pH 7.6, 2 mM DTT, 2 mM Mg(OAc)₂, 50 mM KOAc, 8 μ M amino acids (Promega), 255 μ M spermidine and 1 U μ l⁻¹ murine RNase inhibitor (NEB). One millimolar m⁷G(5')ppp(5')G RNA cap structure analogue (NEB) was added to reactions when indicated. Translation reactions were incubated for 1 h at 30 °C, after which luciferase activity was assayed.

eIF3 purification and native agarose gel electrophoresis. Recombinant eIF3 was expressed and purified from *Escherichia coli* and native human eIF3 was purified from HeLa cells as previously described³². The gel shift protocol was adapted from

previously described protocols^{33,34}. A 0.7% agarose gel was prepared using Agarose Type 1B (Sigma A0576) in buffer consisting of 1 \times TBE supplemented with 75 mM KCl, and gel and buffer were pre-cooled at 4 °C. For each gel shift, 2 μ l water, 1 μ l of 5 \times Binding Buffer (125 mM Tris-HCl pH 7.5, 25 mM Mg(OAc)₂, 350 mM KCl, 0.5 mM CaCl₂, 0.5 mg ml⁻¹ BSA, 10 mM TCEP), 1 μ l labelled RNA and 1 μ l of purified eIF3 or protein buffer were added, in the listed order, and incubated at 25 °C for 30 min. One microlitre of room temperature 6 \times non-denaturing loading dye (40% w/v sucrose, with xylene cyanol and bromophenol blue) was added to the reactions and these were loaded on the agarose gel. The gel was run for 1 h at 40 V at 4 °C, buffer was replaced with fresh cold buffer, and the gel was run for another hour at 40 V. The gel was placed on top of positively charged nylon membrane with four pieces of Whatman filter paper underneath, covered in saran wrap, and dried for 1 h at 75 °C on a pre-heated gel drier. The gel was imaged using a phosphorimager.

SHAPE mapping of RNA structure. The SHAPE protocol was adapted from a previously described protocol³⁵. Each RNA folding reaction contained 1 μ g of RNA, 1.8 μ l 5 \times annealing buffer (500 mM HEPES-KOH pH 8.0, 250 mM KCl, 12.5 mM MgCl₂), and water to make the total reaction volume 9 μ l. RNAs were incubated at 65 °C for 5 min, ice for 5 min, and then at 25 °C for 5 min. To each tube, 1 μ l of 100% dimethylsulfoxide (DMSO) or 1 μ l of 800 mM benzoyl cyanide (Sigma) was added, and the reaction was mixed by pipetting three times. The RNAs were immediately recovered by ethanol precipitation. Purified RNA was dissolved in 9 μ l of 0.5 \times TE buffer (5 mM Tris, 0.5 mM EDTA pH 8.0). Three microlitres of 0.3 μ M NED- or VIC-labelled primers were added to the modified and unmodified reactions, respectively. For sequencing reactions, 1 μ g of RNA in 1 μ l volume was mixed with 8 μ l of 0.5 \times TE buffer, and 3 μ l of 0.3 μ M FAM- or PET-labelled primers were added to each tube with 1 μ l of 10 mM ddATP or ddTTP. To each tube, 7 μ l of reverse transcription buffer (250 mM KCl, 167 mM Tris-HCl pH 8.3, 1.67 mM dNTPs, 17 mM DTT and 10 mM MgCl₂) was added and the reactions were pre-warmed to 52 °C for 1 min. One microlitre of Superscript III (Invitrogen) was added and the tubes were incubated at 52 °C for 50 min, 65 °C for 5 min, and then put on ice. The RNA was hydrolysed by adding 0.5 μ l 10 N NaOH, heating to 95 °C for 3 min, put on ice, and then neutralized by adding 0.33 μ l of 12.1 M HCl. cDNAs were recovered by ethanol precipitation and resuspended in 11 μ l of deionized formamide. Fragment analysis was performed using an Applied Biosystems 3730XL DNA Analyzer, and raw traces were analysed using Shapefinder software³⁶.

Matrigel invasion assay. Matrigel assays were performed using Corning BioCoat Matrigel invasion chambers according to the manufacturer's protocol. Twenty-four hours after seeding the invasion chambers, invaded cells were fixed with 70% ethanol and stained with crystal violet before imaging.

PAR-CLIP. Three biological replicates of PAR-CLIP were performed as previously described³, with some modifications. For each experiment, 40–50 150 mm plates of 293T cells were seeded to be at ~90% confluence during crosslinking. Fourteen hours before crosslinking, 4-thiouridine (Sigma) was added to the media to a final concentration of 100 μ M. For crosslinking, the cells were washed with cold PBS and then the plates were irradiated on ice with 0.15 J cm⁻² of UV 365 nm light. The cells were scraped into PBS, pelleted by centrifugation at 1,000g for 5 min at 4 °C, and the pellet was resuspended in three volumes of NP40 lysis buffer (50 mM HEPES-KOH pH 7.5, 150 mM KCl, 2 mM EDTA, 0.5% Nonidet P-40 alternative, 0.5 mM DTT, 1 Complete EDTA-free Proteinase Inhibitor Cocktail tablet per 50 ml of buffer). The cell suspension was incubated on ice for 10 min, passed through an 18G needle five times, and centrifuged at 13,000g for 15 min at 4 °C. The lysate was filtered through a 0.2 μ m membrane syringe filter and RNAs were lightly digested by treatment with RNase T1 (Thermo Scientific) at a final concentration of 0.05 U μ l⁻¹ for 15 min at room temperature. For each plate, 5 μ l of Dynabeads (Invitrogen) and 10 μ l of anti-eIF3b antibody (Bethyl A301-761A) were prepared by washing the beads once with PBS and 0.2% Tween-20, and then allowing the antibody to bind to the beads in PBS and 0.2% Tween-20 by rotating at room temperature for 15 min. The antibody and beads were added to the lysates and the immunoprecipitation was rotated at 4 °C for 2 h.

The beads were collected and washed three times in high-salt NP40 wash buffer (50 mM HEPES-KOH pH 7.5, 500 mM KCl, 0.5% Nonidet P-40 alternative, 0.5 mM DTT, 1 Complete EDTA-free Proteinase Inhibitor Cocktail tablet per 50 ml of buffer). One bead volume of NP40 lysis buffer and 50 U μ l⁻¹ RNase T1 was added to the beads and incubated for 16 min at room temperature. Beads were washed three times in high-salt NP40 wash buffer and resuspended in one bead volume of Buffer 3 (NEB) with 0.5 U μ l⁻¹ Calf Intestinal Phosphatase (NEB). The reaction was incubated at 37 °C for 10 min, and beads were washed twice in phosphatase wash buffer (50 mM Tris-HCl pH 7.5, 20 mM EGTA, 0.5% v/v Nonidet P-40 alternative) and twice in PNK buffer without DTT (50 mM Tris-HCl pH 7.5, 50 mM NaCl, 10 mM MgCl₂). Beads were resuspended in one bead volume of PNK buffer with 0.5 μ Ci μ l⁻¹ [γ -³²P]-ATP and 1 U μ l⁻¹ T4 PNK (NEB), and incubated for 20 min at 37 °C. One-hundred micromolar nonradioactive ATP was added and the reaction was incu-

bated for 5 min at 37 °C, and then beads were washed five times with PNK buffer without DTT. SDS-PAGE loading dye (50 mM Tris-HCl pH 6.8, 100 mM β -mercaptoethanol, 2% w/v SDS, 10% v/v glycerol, 0.1% bromophenol blue) was added to the beads, the sample was boiled for 5 min, and the sample was loaded onto a Bis-Tris 4–12% Bis-Tris gel (Novex) and electrophoresed in MOPS buffer (2.5 mM MOPS, 2.5 mM Tris base, 0.005% w/v SDS, 1 mM EDTA). As a size standard, native eIF3 was loaded onto the same gel.

The gel was imaged using a phosphorimager, a printed image was aligned to the gel, and the complexes were excised and electroeluted in a D Tube Dialyzer Midi (Millipore) for 2.5 h at 150 V, at 4 °C. The protein was digested with 1.2 mg ml⁻¹ Proteinase K (Roche) in Proteinase K buffer (50 mM Tris-HCl pH 7.5, 75 mM NaCl, 6.25 mM EDTA, 1% w/v SDS) for 30 min at 37 °C. The RNA was isolated by phenol-chloroform extraction and ethanol precipitation, and small RNA libraries were prepared using a standard protocol³⁷. The cDNA libraries were sequenced on an Illumina HiSeq 2000.

Mass spectrometry. Protein samples were prepared alongside the sequencing samples used for RNA library preparation, using five plates and substituting nonradioactive ATP during the T4 PNK labelling step. The samples were run on the same gel as the radiolabelled PAR-CLIP samples and cut out using the phosphorimager printout as a guide. Mass spectrometry samples were prepared by in-gel tryptic digestion³⁸ and peptides were identified by liquid chromatography-mass spectrometry (LC-MS).

Denaturing immunoprecipitation. The denaturing immunoprecipitation was performed using the PAR-CLIP protocol, with the following alterations. Five plates were used for each sample and, after crosslinking, one volume of NP40 lysis buffer was added and the sample was incubated on ice for 10 min. The lysate was clarified by centrifugation, the supernatant was transferred to a new tube, and one volume of 2× SDS lysis buffer (10% w/v SDS, 100 mM Tris-HCl pH 7.4, 10 mM EDTA, 20 mM DTT) was added. The sample was boiled for 5 min, cooled on ice, and then diluted at least tenfold with nondenaturing lysis buffer (1% v/v Triton-X-100, 50 mM HEPES-KOH pH 7.5, 150 mM NaCl, 2 mM EDTA). Immunoprecipitation was performed using anti-eIF3d (Bethyl A301-758A) or anti-eIF3g (Bethyl A301-757A) antibody.

PAR-CLIP computational analysis. Raw Illumina reads were collapsed using *fastx_collapse* from FASTX Toolkit (http://hannonlab.cshl.edu/fastx_toolkit/), and 3' adapters were removed using *Cutadapt* (<http://code.google.com/p/cutadapt/>). Reads shorter than 15 nucleotides were discarded. To remove processed reads that align to repeat elements, reads were mapped using *Bowtie*³⁹ to the hg19 RepeatMasker track from the UCSC table browser, and unmapped reads were retained. Retained reads were mapped to the hg19 reference genome, allowing for up to two mismatches in alignment. *PARalyzer*¹⁰ was used to identify read clusters, or eIF3 crosslinking sites, with settings of five minimum read counts per group, cluster or kernel density estimation (KDE), a minimum cluster size of 11 nucleotides, and a minimum conversion count of 1. Clusters were annotated using iterative rounds of *bedtools intersect*⁴⁰, with the following hierarchy: start codon, stop codon, 5' UTR, 3' UTR, CDS, intron, lincRNA, miRNA, piwiRNA, snoRNA, snRNA, mitoRNA, rRNA, pseudogene, miscRNA. Annotation data were from the following sources: Gencode (v17 annotation) (<http://www.gencodegenes.org>), Ensembl BioMart, ncRNA database (<http://www.ncrna.org/>), miRBase (<http://www.mirbase.org>). Clusters that aligned to intergenic regions or that were antisense to the transcript were removed, along with any clusters that mapped identically but in the correct sense, as these are probably due to incorrect mapping⁴¹. Next, the consensus set of clusters was defined as a cluster that was reproduced in at least two of the three biological replicates⁴¹, and this was determined using the Bioconductor GenomicFeatures package.

RNA-sequencing. Two biological replicates of RNA-sequencing (RNA-seq) were performed as following. Polyadenylated mRNAs were isolated from 5 × 10⁶ 293T cells using the mRNA-DIRECT kit (Ambion). For alkaline hydrolysis fragmentation, 250 ng of mRNA was mixed with 5× fragmentation buffer (150 mM Mg(OAc)₂, 200 mM Tris-Acetate pH 8.3, 500 mM KOAc) in a total volume of 20 μ l and heated at 94 °C for 6 min. The RNA was ethanol precipitated, and first-strand cDNA was synthesized using random hexamers and Superscript III (Invitrogen), according to the manufacturer's protocol. For the following, the cDNA was purified between each step using a PCR purification column (Qiagen). To make second-strand cDNA, 10 μ l 10× ligase buffer (NEB), 0.3 mM dNTP mix, 67 U ml⁻¹ *E. coli* DNA Ligase (NEB), 267 U ml⁻¹ *E. coli* DNA and 13.4 U ml⁻¹ RNase H (Invitrogen) was added to the cDNA in a 100 μ l reaction and incubated for 2.5 h at 16 °C. The cDNA was end repaired in a 100 μ l reaction with 0.4 mM dNTPs, 10 μ l 10× T4 DNA ligase buffer (NEB), 150 U ml⁻¹ T4 DNA Polymerase (NEB), 50 U ml⁻¹ T4 PNK (NEB) and 50 U ml⁻¹ Klenow (NEB) for 30 min at 20 °C. To A-tail the cDNA, 2 mM dATP,

32 μ l cDNA, 5 μ l 10× NEBuffer 2 (NEB) and 300 U ml⁻¹ Klenow exo (3' to 5' exo minus) (NEB) was added to the cDNA in a 50 μ l reaction, and incubated for 30 min at 37 °C. To prepare adapters, 40 μ M universal adaptor and 40 μ M indexed adaptor were mixed with 2 μ l 10× primer annealing buffer (100 mM Tris-HCl pH 8.0, 50 mM NaCl) in a 20 μ l reaction and heated at 95 °C for 15 min, 70 °C for 15 min, and slow cooled to room temperature. Adapters were ligated in a 50 μ l reaction with 5 μ l 10× T4 DNA ligase buffer (NEB), 16,000 U ml⁻¹ T4 DNA ligase (NEB) and 2 μ M adapters for 15 min at room temperature. cDNA libraries were amplified by PCR using Phusion (NEB) and 5 μ M primer mix for 15 cycles of 10 s at 98 °C, 30 s at 65 °C and 30 s at 72 °C, and isolated by gel purification (Qiagen). The cDNA libraries were sequenced using an Illumina HiSeq 2000. The following oligonucleotides were used. Universal adaptor: 5'-AATGATACGGCGACCACCGAGATCTACACTCTTTCCCTACA CGACGCTCTTCCGATC*T-3' (asterisk denotes a phosphorothioate bond); indexed adaptor: 5'-/5Phos/GATCGGAAGAGCACACGTCTGAACTCCAGTCAC-index-ATCTCGTATGCCGCTCTTCTGCTTG-3', with the index sequence being CGATGT or TGACCA; primer mix: 5'-AATGATACGGCGACCACCGAGATCTACACTCTTTCCCTACACGA-3' and 5'-CAAGCAGAAGACGGCATACGAGAT-3'.

RNA-seq computational analysis. After quality filtering with the FASTX Toolkit, reads were mapped to the human hg19 genome using Tophat⁴² and the Gencode (v17) annotation. FPKM was calculated using a python script, and the average FPKM was calculated using the two biological replicates.

RNA immunoprecipitation and RT-PCR. Two 150 mm plates of 293T cells were lysed in three volumes of NP40 lysis buffer. Dynabeads were prepared with rabbit IgG (Cell Signaling 2729), rabbit anti-HA antibody (Invitrogen 71-5500) or rabbit anti-eIF3b antibody (Bethyl A301-761A). The lysate was split into three parts, the different antibody-Dynabead mixtures were added, and the suspension was incubated for 2 h at 4 °C. The beads were washed four times with high NP40 wash buffer (50 mM HEPES-KOH pH 7.5, 500 mM KCl, 2 mM EDTA, 1% Nonidet P-40 alternative, 0.5 mM DTT), and bound RNAs were isolated by phenol-chloroform extraction and ethanol precipitation. cDNA was reverse transcribed using random hexamers and Superscript III, and PCR was performed using Phusion. The following oligonucleotides were used. RANGAP1-Forward, 5'-ACCGTCTGGAGAAATGAT GG-3'; RANGAP1-Reverse, 5'-CGCAAGGTCTTCAAGGTCTC-3'; JUN-Forward, 5'-TGACTGCAAAGATGGAAACG-3'; JUN-Reverse, 5'-CCGTTGCTGGACT GGATTAT-3'; BTG1-Forward, 5'-CACTGGTTCCAGAAAAGC-3'; BTG1-Reverse, 5'-CTACCATTTGCACGTTGGTG-3'; PPP3R1-Forward, 5'-GAATTC ATTGAGGGCGTCTC-3'; PPP3R1-Reverse, 5'-GCCACCTACAACAGCACAG A-3'; CDK12-Forward, 5'-CAAATTCTCAGCCCCCTGTA-3'; CDK12-Reverse, 5'-GAGGTGGTGTGATTGCCTTT-3'; PSMB6-Forward, 5'-ACTGGGAAAGCC GAGAAGTT-3'; PSMB6-Reverse, 5'-TCCCGGTAGGTAGCATCAAC-3'.

- Kranzusch, P. J. *et al.* Structure-guided reprogramming of human cGAS dinucleotide linkage specificity. *Cell* **158**, 1011–1021 (2014).
- Rakotondrafara, A. M. & Hentze, M. W. An efficient factor-depleted mammalian *in vitro* translation system. *Nature Protocols* **6**, 563–571 (2011).
- Sun, C. *et al.* Functional reconstitution of human eukaryotic translation initiation factor 3 (eIF3). *Proc. Natl Acad. Sci. USA* **108**, 20473–20478 (2011).
- Davidovich, C., Zheng, L., Goodrich, K. J. & Cech, T. R. Promiscuous RNA binding by Polycomb repressive complex 2. *Nature Struct. Mol. Biol.* **20**, 1250–1257 (2013).
- Kranzusch, P. J. *et al.* Assembly of a functional Machupo virus polymerase complex. *Proc. Natl Acad. Sci. USA* **107**, 20069–20074 (2010).
- Bai, Y., Zhou, K. & Doudna, J. A. Hepatitis C virus 3' UTR regulates viral translation through direct interactions with the host translation machinery. *Nucleic Acids Res.* **41**, 7861–7874 (2013).
- Vasa, S. M., Gueix, N., Wilkinson, K. A., Weeks, K. M. & Giddings, M. C. ShapeFinder: a software system for high-throughput quantitative analysis of nucleic acid reactivity information resolved by capillary electrophoresis. *RNA* **14**, 1979–1990 (2008).
- Hafner, M. *et al.* Barcoded cDNA library preparation for small RNA profiling by next-generation sequencing. *Methods* **58**, 164–170 (2012).
- Shevchenko, A., Tomas, H., Havlis, J., Olsen, J. V. & Mann, M. In-gel digestion for mass spectrometric characterization of proteins and proteomes. *Nature Protocols* **1**, 2856–2860 (2007).
- Langmead, B., Trapnell, C., Pop, M. & Salzberg, S. L. Ultrafast and memory-efficient alignment of short DNA sequences to the human genome. *Genome Biol.* **10**, R25 (2009).
- Quinlan, A. R. & Hall, I. M. BEDTools: a flexible suite of utilities for comparing genomic features. *Bioinformatics* **26**, 841–842 (2010).
- Lebedeva, S. *et al.* Transcriptome-wide analysis of regulatory interactions of the RNA-binding protein HuR. *Mol. Cell* **43**, 340–352 (2011).
- Trapnell, C., Pachter, L. & Salzberg, S. L. TopHat: discovering splice junctions with RNA-Seq. *Bioinformatics* **25**, 1105–1111 (2009).

a**eIF3a (NP_003741)**

MPAYFORPENALKRANEFLEVGKKQPALDVLVDVMSKKHRTWQKIHEPIMLKYLELCVD
 LRKSHLAKGELYQYKNICQVNIKSLEDVVRAYLKMAEEKTEAAKESQOMVLDEDLDNI
 QTPESVLLSAVSGEDTQDRDRLLLTPWVKFWESYRQCLDLLRNNRVRERLYHDIAQQA
 FKFCLOYTRKAEFRKLCDNLRMHLSQIQRHNNQSTAINLNNPESQSMHLETRLYQLDSAIS
 MELWQFAFAKAVEIDHGLFSLSKPPKQPLMANYNNKVVTFVWKSNGALFHAHLHRLYHL
 SREMRKNLTQDEMQRMTSVLLATLSIPITPERTDIARLLDMDGIVKORRRLATLLGLQAP
 PTRIGLINDMVRFNLYVPEVKDLYNWLEVEFNPLKLCERVTKVLNWWREQPEKEPEL
 QQYVFPQLQNTTLRLQQVSVQIQSIEFSRLTSLVPFVDAFQLERAIVDAARHCDLQVRIDH
 TSRTLSTFGSDLNATREDAPIGPHLQSMPSQIRNQLTAMSSVLAKALEVIKPAHILQEKEE
 QHQLAVTAYLKNRKEHQRIARRQTIEERKERLESNIQREKEELEQREAELOKVRKAEE
 ERLRQEAKEKERERILQEHEQIKKTVRERLEQIKKTELGAFAKDDIEDLEELDPDFIMAK
 QVEQLEKEKELQERLKNQEKKIDYFRAKRLKEEPLIKSAYEEQRIKMDLWEQEEERIT
 TMLEREKALEHKNRMSRMLEDRDLFVMRLKAARQSVYEEKLKQFEERLAEERHNRLEE
 RKRQRKEERRITYREKEEEEQRRAEEQMLKEREERERAEERAKREEELREYQERVKKLE
 EVERKKRQRELEIEERERRRERERRLGSSSLSRKDSRWGDRDSEGTWRKGPEADSEWR
 RGPPEKEWRREGREDERSHRDEERPRRLGDDDEDREPSLRPDDDRVPRRGMDDDR
 GPRRGPEEDRFSRRGADDDRPSSWRNTDDRPRIADEDRGNWRHADDDRPRRGLD
 EDRGSVRTADEDRGPRRGMDDDRGPRRGGADDERSSWRNADDDRGPRRGDDDRG
 PRRGMDDDRGPRRGMDDDRGPRRGMDDDRGPRRGLDDDRGPWRNADDDRIPRRGA
 EDDRGPWRNMDDDRSLRRADDDRPRRGDDSRPGPWRPLVKPGGWREKEKAREESW
 GPPRESRSEEREDWREKERDRDNQDREENDKDPERERDRERDVEDRFRPRRDEG
 GWRRGPAEESSSWRDSSRRDDRRDRRRERDRDRDLRERRDLDDDRRGPPPLRS
 EREEVSSWRADDRKDDRVEERDPPRRVPPPALSRDRERDREREKEGEKASWRAE
 KDRESLRRTKNETDEGDGWTTVRR

eIF3b (NP_001032360)

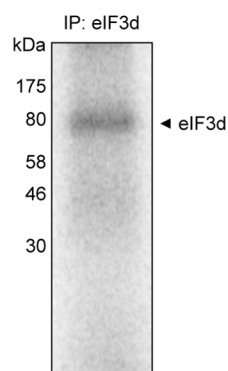
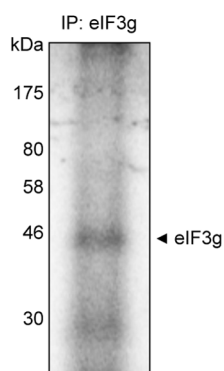
MQDAENVAPPEAAEERAEPGQQPAAEPPEAGLLRPAGPAPAEAGTEASSEEVGIAE
 AGPESEVTRTPEAAEAAAGSPSESPSPAAEELPGSHAEPVPAQGEAPGEQARDERSD
 SRAQAVSEDAGGNEGRAEAEAPRALENGDADEPSFSDPEDFVDDVSEELLGDVLKDRP
 QEADGIDSVIVDNPVQVGPDRLEKLNVIHKFSKFGKITNDFYPEEDGKTGYIFLEYASP
 AHAVDAVKNADGYKLDKQHTFRVNLFTDFDKYMTISDEWDIPEKQPFKDLGNLRYWLEEA
 ECRDQYVIFESGDRTSIFVNDVKDPVSEIERARWTETVVRWSPKGTYLATFHQRIALW
 GGEKFKIQRFSSHQGVQLIDFSPCERYLVTFSPMLDQDDPQAIWDILTGHKKRGFHC
 SSAHWPIFKWSDHKGFFARMTLDTLSIYETPSMGLLKKSLKISGKDFSWSPGGNIAFV
 VPEDKIPARVTLMLQLPTRQEIIRVNLFNVDCKLHWQKNGDYLCVKVDRTPKGTQGVVT
 NFEIFRMREKQVPVDVEMKETIIAFAWEPNGSKFAVLHGEAPRISVSFYHVKNGKIELIK
 MFDKQANTIFWSPQGGFVVLGLRSMNGALAFVDTSDCTVMNIAEHYMASDVEWDPT
 GRYVVTSVSWWSHKVDNAYWLWTFQGRLLQKNNKDRFCQLLWRPRPPTLLSQEQIKQIK
 KDLKYSKIFEQKDRLSQSKASKELVERRRTMMEDFRKYRKMAQELYMEQKNERLELRG
 GVDTELDNSVDDWEEETIEFFVTETIPLNGQE

eIF3d (NP_003744)

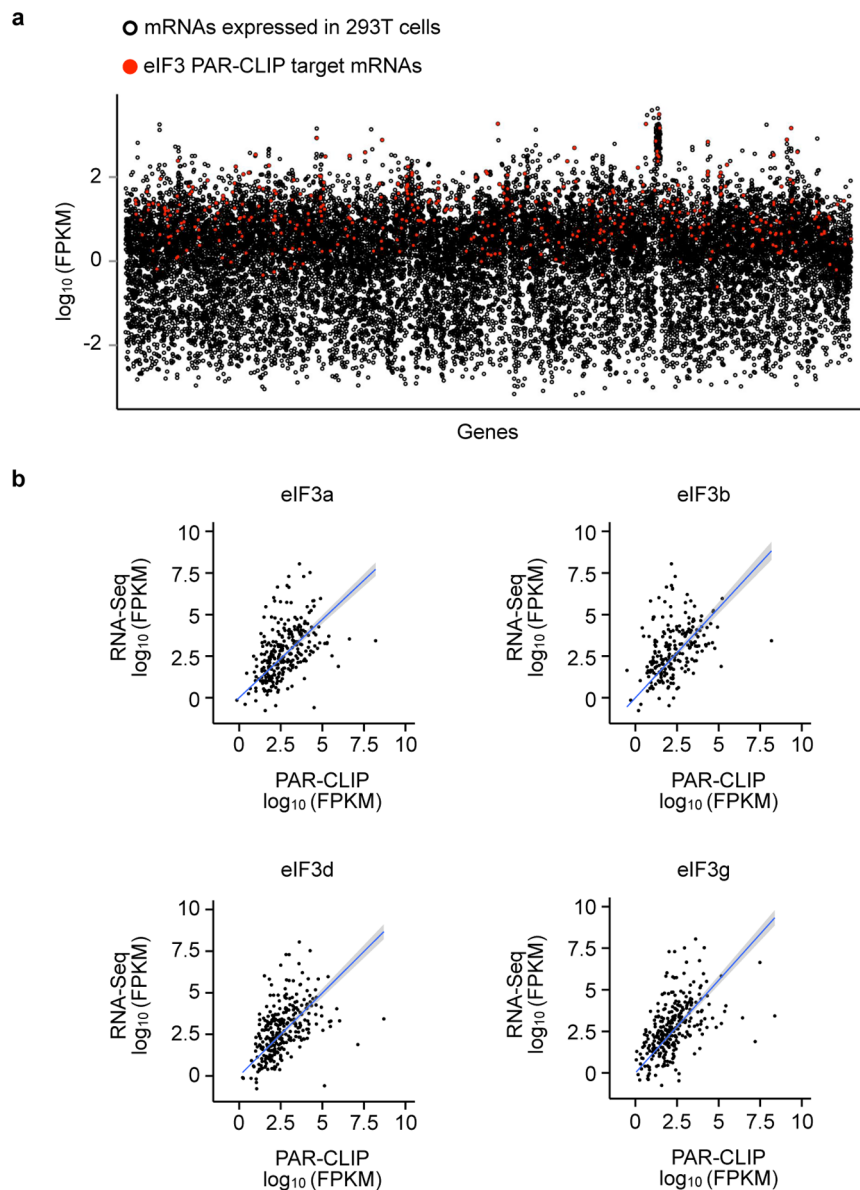
MAKFMTPVIQDNPSGWGPCAPEQFRDMPYQPFSGDRLGKVADWTGATYQDKRYTNK
 YSSQFGGGSQYAFHEEDESFLVDTARTQKTAYQRNMRFAQRNLRRDKDRNMLQ
 FNLQILPKSAKQKERERIRLQKKFQKQFQGVROKWDQKSQKPRDSSVEVRSDWEVKEEM
 DFPQLMKMYLEVSEPDIECCGALEYDYDAFRITRSEKPLRSIKRIFHTVTITDDPVIR
 KLAKTQGNVFTADAILATLMSCTRSVYSWDIVQVGVSKLFFDKRDNDSFDLLTVSETANE
 PPQDEGNSFNPRNLAMEATYINHNFSQQLRMGKERYNFPNPNPFVEDMDKNEIASV
 AYRYRWKLGDDIDLIVRCEHDGVMTGANGEVFSFINIKTLNEWDSRHCVNGVDWRQKLD
 QRGAVIATELKNNSYKLARWTCALLAGSEYLLKGYVSRYHVKDSSRHVILGTQOFKPN
 FASQINLSVENAWGILRCVIDICMKLEEGKYLKLDPNKQVIRVYSLPDGTFSSDEDEEEEEE
 EEEEEEEET

eIF3g (NP_003746)

MPTGDFDQSKPSWADQVEEGEDDKCVTSELLKGIPLATGDTSPPELLPGAPLPPPKVI
 NGNIKTVEYKIDEDGKKFKIVRTFRIETRKASKAVARRKNWKKFNGSEFDPGPNVATTVT
 SDDVSMFTITSKEDLNCQEEEDPMNKLKGGKIVSCRICKGDHWITRCPYKDTLGPMPQKE
 LAEQGLSTGEKEKLPGELEPVQATQNKTKYVPPSLRDGASRRGESMQPNRRADDNAT
 IRVTNLSDETRETDLQLFRPFGSISIRYLAKDKTTGQSKGFATISFHRREDAARAAGVSG

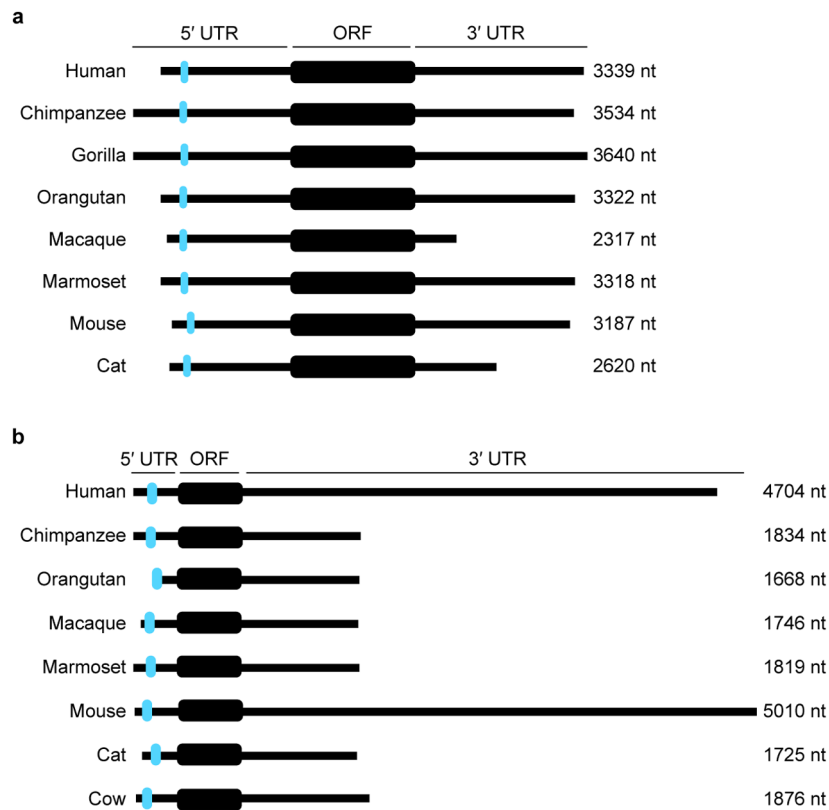
b**c****Extended Data Figure 1 | PAR-CLIP reveals eIF3a, b, d and g bind to RNA.**

a, Mass spectrometry identification of trypsin-released peptides from RNA-crosslinked eIF3 subunits. Peptides identified by mass spectrometry are highlighted in pink. **b, c**, Crosslinking and denaturing immunoprecipitation to validate subunit identification. As eIF3d and g co-migrate with eIF3l and e/f, respectively, subunit identification was validated by immunoprecipitation of individual proteins after crosslinking and treatment of lysates with SDS treatment and boiling.



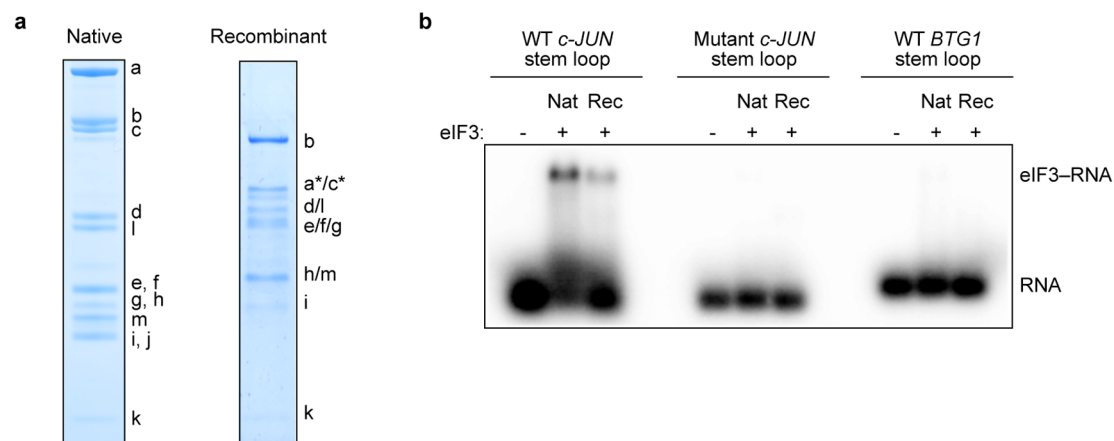
Extended Data Figure 2 | Analysis of eIF3 PAR-CLIP targets. **a**, Scatterplot of fragments per kilobase of exon per million reads (FPKM) of all mRNAs expressed in 293T cells. mRNAs that are eIF3 PAR-CLIP targets are highlighted

in red. **b**, Scatterplot of correlation between mRNA expression and PAR-CLIP read coverage for mRNAs that are eIF3 PAR-CLIP targets. The simple linear regression line is plotted in blue, with the 95% confidence region shaded in grey.



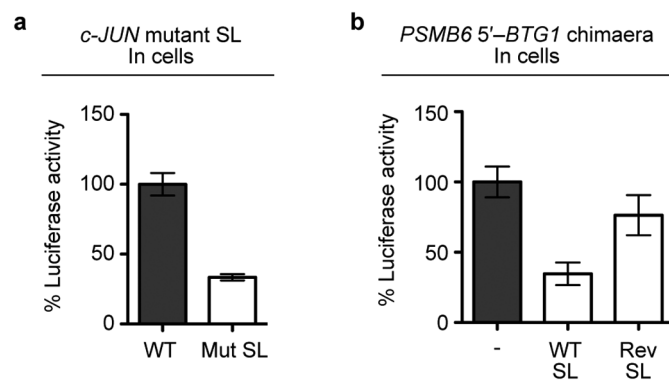
Extended Data Figure 3 | Conservation of *c-JUN* and *BTG1* eIF3-binding sites in primates and mammals. **a, b,** The eIF3-binding site is indicated in cyan. nt, nucleotides. **a,** *c-JUN* GenBank accessions are: human (NM_002228.3, *Homo sapiens*), chimpanzee (XM_513442.5, *Pan troglodytes*), gorilla (XM_004025880.1, *Gorilla gorilla*), orangutan (XM_002810763.3, *Pongo abelii*), rhesus macaque (NM_001265850.2, *Macaca mulatta*), marmoset (XM_002750880.3, *Callithrix jacchus*), mouse (NM_010591.2, *Mus musculus*),

cat (XM_006934825.1, *Felis catus*). **b,** *BTG1* GenBank accessions are: human (NM_001731.2, *Homo sapiens*), chimpanzee (XM_509262.3, *Pan troglodytes*), orangutan (XM_002823578.2, *Pongo abelii*), rhesus macaque (NM_001266672.1, *Macaca mulatta*), marmoset (XM_002752814.3, *Callithrix jacchus*), mouse (NM_007569.2, *Mus musculus*), cat (XM_006933950.1, *Felis catus*), cow (NM_173999.3, *Bos taurus*).

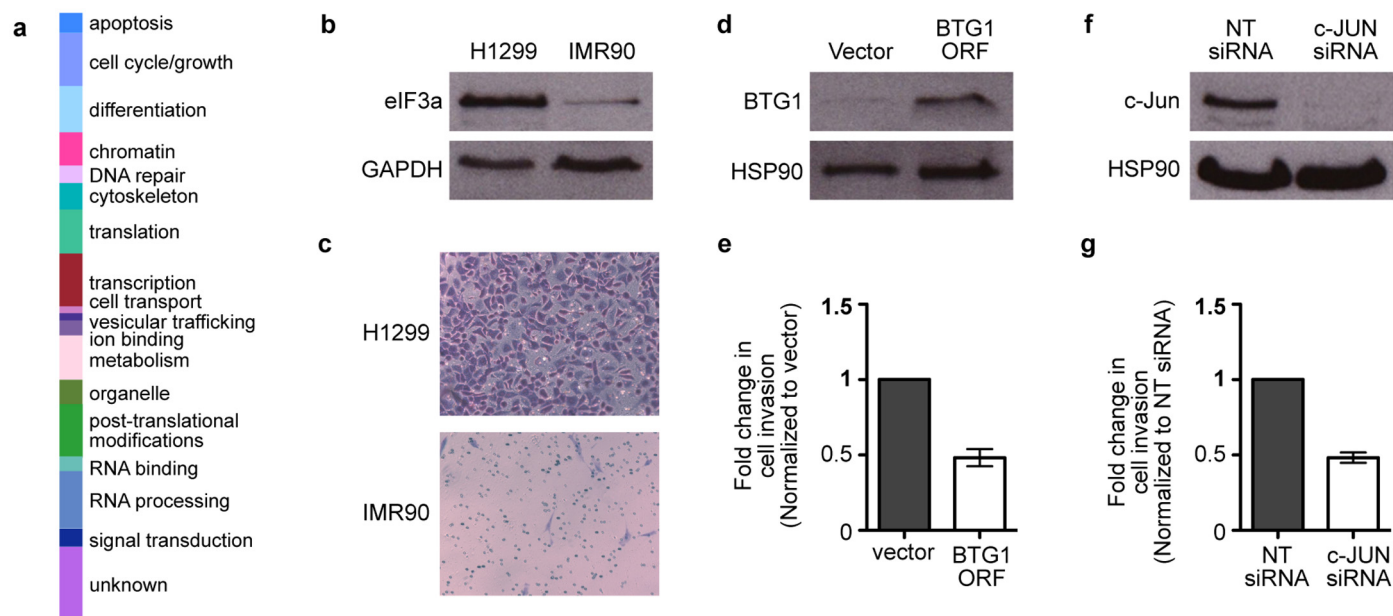


Extended Data Figure 4 | Interactions between native and recombinant eIF3 and the *c-JUN* and *BTG1* RNA stem-loops. **a**, Coomassie blue staining of purified native HeLa eIF3 or recombinant eIF3, resolved by SDS-PAGE. **b**, Representative native agarose gel electrophoresis shows a specific and binary

interaction between native (Nat) and recombinant (Rec) eIF3 and the wild-type (WT) *c-JUN* stem-loop structure, but not with the mutated stem-loop or the wild-type *BTG1* stem-loop.

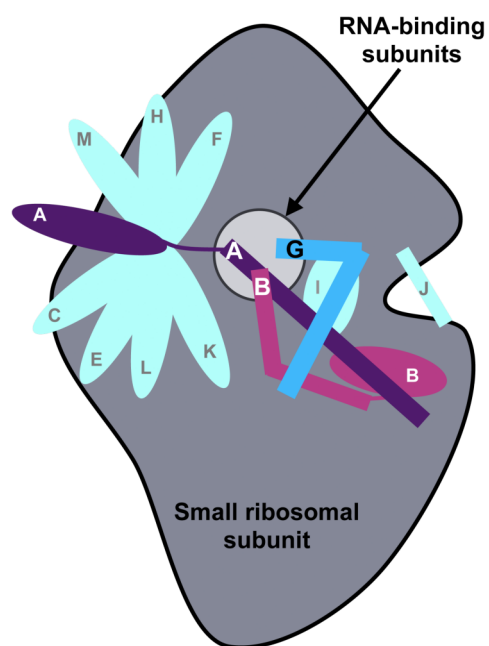


Extended Data Figure 5 | Luciferase activity of *c-JUN* and *BTG1* mutants in cells. **a, b,** Luciferase activity in 293T cells transfected with mRNAs containing the *c-JUN* 5' UTR with a mutated stem-loop (**a**) or the *PSMB6* 5' UTR-*BTG1* stem-loop chimaera (**b**). Mut, mutant; Rev, transversed; SL, stem-loop; WT, wild type. The results are given as the mean \pm s.d. of three independent experiments, each performed in triplicate.



Extended Data Figure 6 | Bypassing eIF3 translational control in H1299 cells reduces cell invasiveness. **a**, Functional classification of eIF3-bound RNAs. **b**, Representative western blot analysis of eIF3a expression levels in H1299 and IMR90 cells. GAPDH was detected as a loading control for normalized protein levels. **c**, Representative image of Matrigel invasion by H1299 or IMR90 cells. **d**, BTG1 protein levels after overexpression in H1299

cells. HSP90 was detected as a loading control. **e**, Matrigel invasion assay in H1299 cells after overexpression of BTG1. ORF, open reading frame. **f**, c-JUN protein levels after siRNA-mediated knockdown in H1299 cells. NT, non-targeting. **g**, Matrigel invasion assay in H1299 cells after knockdown of c-JUN. The results of **e** and **g** are given as the mean \pm s.d. of three independent experiments, each performed in duplicate.



Extended Data Figure 7 | Schematic of eIF3 subunit localization on the small ribosomal subunit. The eIF3 subunits bound to RNA in the PAR-CLIP experiment, eIF3a, b and g, form a nexus in the distal eIF3 region. The location of eIF3d has not been assigned, and the schematic is adapted from ref. 14.

New cosmogenic burial ages for Sterkfontein Member 2 *Australopithecus* and Member 5 Oldowan

Darryl E. Granger¹, Ryan J. Gibbon², Kathleen Kuman^{3,4}, Ronald J. Clarke³, Laurent Bruxelles^{4,5,6} & Marc W. Caffee^{1,7}

The cave infills at Sterkfontein contain one of the richest assemblages of *Australopithecus* fossils in the world, including the nearly complete skeleton StW 573 ('Little Foot')^{1–4} in its lower section, as well as early stone tools^{5–7} in higher sections. However, the chronology of the site remains controversial^{8–14} owing to the complex history of cave infilling. Much of the existing chronology based on uranium–lead dating^{10,11} and palaeomagnetic stratigraphy^{8,12} has recently been called into question by the recognition that dated flowstones fill cavities formed within previously cemented breccias and therefore do not form a stratigraphic sequence^{4,14}. Earlier dating with cosmogenic nuclides⁹ suffered a high degree of uncertainty and has been questioned on grounds of sediment reworking^{10,11,13}. Here we use isochron burial dating with cosmogenic aluminium-26 and beryllium-10 to show that the breccia containing StW 573 did not undergo significant reworking, and that it was deposited 3.67 ± 0.16 million years ago, far earlier than the 2.2 million year flowstones found within it^{10,11}. The skeleton is thus coeval with early *Australopithecus africanus* in eastern Africa^{15,16}. We also date the earliest stone tools at Sterkfontein to 2.18 ± 0.21 million years ago, placing them in the Oldowan at a time similar to that found elsewhere in South Africa at Swartkans¹⁷ and Wonderwerk¹⁸.

The cave at Sterkfontein is partly filled with overlapping layers of fossiliferous breccia^{19,20} that entered through multiple openings to the surface. The infill was originally divided into six members thought to be in stratigraphic order¹⁹, with Members 1–3 inside the cave and 4–6 now exposed at the surface owing to erosion of the cave roof. Although the complete infill stratigraphy is not exposed in any one place and the temporal relationship between the interior and surface deposits remains debated^{11,13}, we retain the original nomenclature^{19,20} here. We will focus on Member 2 within the Silberberg Grotto (Fig. 1) and on the Oldowan Infill of Member 5 in younger deposits excavated from a higher infill.

Member 2 contains abundant fossils, angular dolomite and chert clasts, and quartz-bearing sand. Several localized flowstones and botryoidal calcite deposits fill cavities that formed after the breccia was cemented and later settled into voids dissolved below (Fig. 1)^{4,14}. Fauna was accumulated as a deathtrap assemblage²¹ including associated elements, largely of primates and carnivores, with no hominids apart from a single near-complete skeleton of *Australopithecus prometheus* (StW 573; Fig. 2)^{1–4,22}. This species was named on the basis of a parieto-occipital fossil from Makapansgat²³. It has been suggested²² that several other Sterkfontein and some Makapansgat specimens also belong in this species making *Australopithecus africanus* and *A. prometheus* contemporaries in the assemblages of Makapansgat Member 3 and Sterkfontein Member 4. *A. prometheus* differs from *A. africanus* in features including *Paranthropus*-like larger, bulbous-cusped cheek teeth, a longer, flatter face, incipient supraglabellar hollowing and a more vertical rounded occiput²². (Note that we use the term hominid in the

traditional sense to include humans and their ancestral relatives but exclude the great apes.)

Dating of Member 2 and StW 573 has been problematic. Flowstones in the vicinity of StW 573 date to about 2.2 million years (Myr)^{10,11}, but they post-date the breccia and the fossil^{4,14}. The only previous date on the breccia itself was cosmogenic ²⁶Al/¹⁰Be burial dating of fine-grained quartz⁹, which yielded a best-fit age of 4.17 ± 0.35 Myr. This age has been questioned by many^{10–13,24} who have suggested that fine sediment could have been reworked from older, higher deposits within the cave, making the burial age of the sediment older than the fossil. To resolve the age of the fossil the breccia must be dated and it must be shown to be a coherent stratigraphic unit, largely free of reworked material. This is now possible owing to improvements in measurement precision and new techniques such as isochron burial dating which can explicitly validate the coeval deposition of the entire unit^{24–27}.

Member 5 contains both *Homo ergaster* and *Paranthropus* fossils as well as Oldowan and Acheulean stone tools^{5–7}. Member 5 East is divided into a lower Oldowan infill, with the first appearance of stone tools and a few fossils of *Paranthropus*, and an overlying early Acheulean infill^{5–7}. Faunal comparisons and the *Paranthropus* hominid StW 566 suggested an age estimate of 1.7–2.0 Myr for the Oldowan infill^{6,7}. A substantially younger age of 1.32 ± 0.08 Myr (error-weighted mean) has been inferred from electron spin resonance dating of bovid teeth¹². We use burial dating of a quartz manuport to determine the age of the Oldowan infill.

Burial dating is based on the radioactive decay of ²⁶Al and ¹⁰Be in quartz. These nuclides build up by exposure to secondary cosmic radiation near the ground surface, and subsequently decay when sediment is buried and cosmogenic nuclide production is attenuated. Because ²⁶Al ($\tau_{26} = 1.021 \pm 0.024$ Myr (ref. 28)) decays faster than ¹⁰Be ($\tau_{10} = 2.005 \pm 0.020$ Myr (ref. 29)), the ratio ²⁶Al/¹⁰Be decreases over time, with an effective mean-life of $\tau_{\text{bur}} = 2.08 \pm 0.10$ Myr. For burial dating to be accurate, three criteria must be met. (1) The quartz must be exposed near the ground surface before burial to accumulate sufficient ²⁶Al and ¹⁰Be. (2) It must be buried quickly and deeply enough so that post-burial production is small. The exact depth required depends upon the inherited concentrations, but is usually many metres. (3) It must be buried only once in the past ~10 Myr. If quartz has been reworked from older deposits, or if it has been reworked underground within the cave system, then the burial age will overestimate the true age of the deposit.

An elegant way to test whether the burial dating criteria are met is to construct an isochron^{24–27} in which multiple samples are analysed from the same location. Each sample is buried with its own inherited ²⁶Al and ¹⁰Be concentrations, but all samples share the same post-burial production history. A plot of ²⁶Al versus ¹⁰Be yields a gentle curve with a slope that indicates burial age and an intercept that depends on the amount of post-burial production²⁴. The isochron burial dating method accounts for post-burial production without requiring detailed knowledge of

¹Department of Earth, Atmospheric, and Planetary Sciences, Purdue University, West Lafayette, Indiana 47907, USA. ²Department of Anthropology, University of New Brunswick, Fredericton, New Brunswick E3B 5A3, Canada. ³Evolutionary Studies Institute, University of the Witwatersrand, WITS 2050, Johannesburg, South Africa. ⁴School of Geography, Archaeology and Environmental Studies, University of the Witwatersrand, WITS 2050, Johannesburg, South Africa. ⁵French National Institute for Preventive Archaeological Research (Inrap), 561 rue Etienne Lenoir, km delta, 30900 Nîmes, France. ⁶University of Toulouse Jean Jaurès, UMR 5608 du CNRS (TRACES), Maison de la Recherche, 5 Allées Antonio Machado, F-31058 Toulouse, France. ⁷Department of Physics and Astronomy, Purdue University, West Lafayette, Indiana 47907, USA.

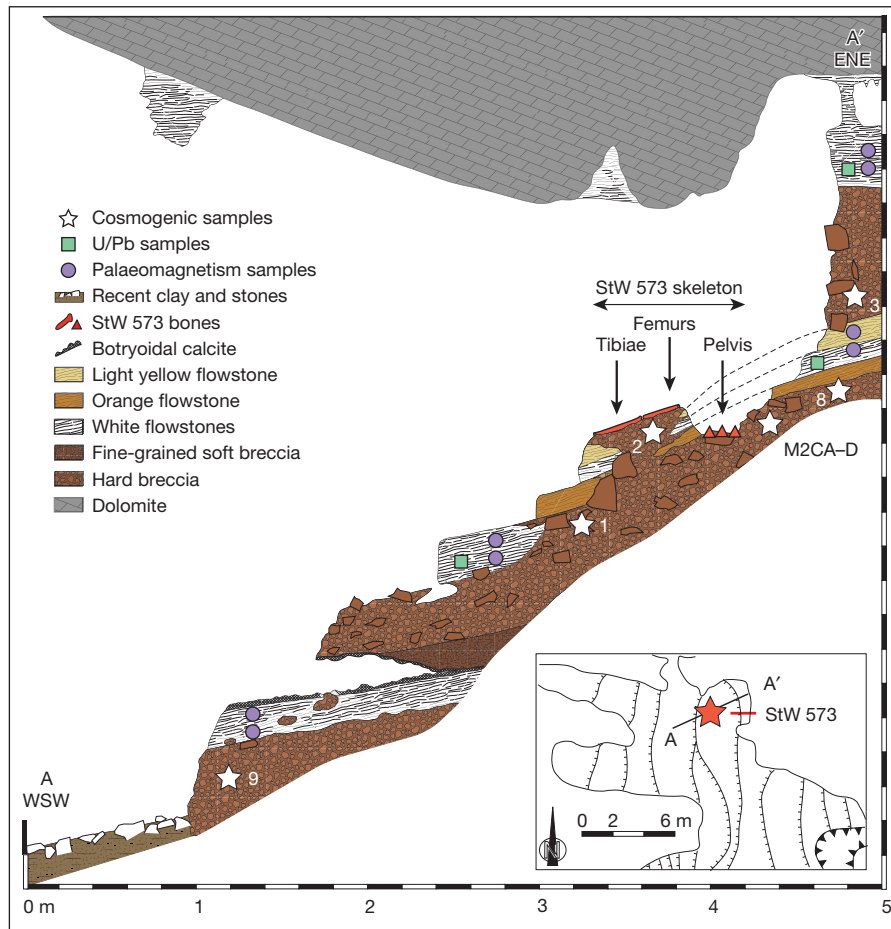


Figure 1 | Stratigraphy and sample locations. Measured stratigraphic section through the Member 2 talus at the location of the StW 573 skeleton showing locations of dated samples, modified from ref 14. Locations of U/Pb samples are estimated from schematic sections of refs 10, 11; palaeomagnetic

samples were located from refs 8, 12. Inset locates the cross section in the lower part of the Silberberg Grotto, with approximately 1 m contour intervals for the infill surface.

the burial depth or burial history. It also allows outliers to be identified; reworked samples plot below the isochron, while samples significantly above the isochron are forbidden and indicate issues with either the sample or the laboratory measurements.

We analysed 11 samples from Member 2 (Table 1), including three previously reported⁹. Effective isochron burial dating requires a wide range of inherited cosmogenic nuclide concentrations. To that end, we selected a suite of samples to maximize variability. Fine quartz sand from multiple samples (ST 1–9) was probably washed in from the surface. In contrast, four blocks of chert were collected from the immediate vicinity of StW 573 (M2CA–D). Two fractions of coarse sand and pebbles were separated (ST M2 Dark and Light). One fraction comprises rounded grains stained with pedogenic iron oxides and washed into the cave from soil at the surface; the second comprises angular unstained grains probably eroded from the walls and ceiling of the cave itself (Extended Data Fig. 1). A previously reported sample from the modern surface⁹ was analysed to confirm that material enters the cave with a zero burial age.

From the Oldowan Infill of Member 5 we selected a single quartz manuport—a typical vein quartz cobble with rounding and impact marks characteristic of rocks found in the local river gravels close to Sterkfontein (Extended Data Fig. 2). There is no evidence for reworking of older deposits, as there are no diagnostically younger artefacts within the large Oldowan assemblage of 3,500 pieces^{6,7}.

²⁶Al and ¹⁰Be were measured by accelerator mass spectrometry (AMS). All samples of fine sand and the iron-stained grains have high ²⁶Al and ¹⁰Be concentrations, confirming their origin from outside the cave. Light-coloured grains and chert blocks have low concentrations, indicating

that they were probably eroded from the walls of the cave within a few metres of the surface. A plot of ²⁶Al versus ¹⁰Be (Fig. 3) reveals that all but two of the samples lie on an isochron, consistent with a single episode of deposition. One chert block lies below the isochron, indicating



Figure 2 | Skull of StW 573 ('Little Foot'). The skull, recently extracted from the cave breccia. Photo by Jason Heaton.

Table 1 | Samples and cosmogenic nuclide concentrations

Sample	Location	[¹⁰ Be] (10 ⁶ atoms per gram)*	[²⁶ Al] (10 ⁶ atoms per gram)
ST 1	0.7 m below StW 573	0.493 ± 0.026	0.624 ± 0.053
ST 2	Adjacent to StW 573	0.574 ± 0.025	0.565 ± 0.050
ST 3	0.8 m above StW 573	0.522 ± 0.029	0.562 ± 0.122
ST 7	Surface above cave	1.166 ± 0.020	7.075 ± 0.380
ST 8	0.7 m NW of StW 573	0.685 ± 0.137	0.686 ± 0.074
ST 9	2–2.5 m below StW 573	0.479 ± 0.012	0.550 ± 0.036
ST M2 Dark	From samples ST 1, 2, 8, 9	0.354 ± 0.025	0.412 ± 0.044
ST M2 Light	From samples ST 1, 2	0.118 ± 0.005	0.205 ± 0.015
M2CA	Near StW 573	0.101 ± 0.004	0.099 ± 0.009
M2CB	Near StW 573	0.070 ± 0.004	0.179 ± 0.015
M2CC	Near StW 573	0.043 ± 0.002	0.083 ± 0.012
M2CD	Near StW 573	0.157 ± 0.006	0.955 ± 0.036
Manuport	Oldowan Infill, Member 5	1.623 ± 0.070	3.051 ± 0.295

*All ¹⁰Be measurements adjusted to the standard of ref. 30. ST 1–3 are slightly different than reported in ref. 9 owing to inclusion of additional analyses.

that it was reworked from an older deposit within the cave, perhaps from talus of Member 1, nearby. Another chert sample has a ²⁶Al/¹⁰Be ratio far into the forbidden zone above the isochron, indicating a problem. Because this was a small sample there is no remaining chert for re-analysis; it is not included in the age determination.

The burial age for Member 2 is calculated as 3.67 ± 0.16 Myr. The concentration of ¹⁰Be produced after burial is calculated as $(21 \pm 3) \times 10^3$ atoms per gram, corresponding to a post-burial production rate of about 0.012 atoms of ¹⁰Be per gram per year, a value consistent with deep burial. The burial age of the surface sample is 0.11 ± 0.11 Myr, consistent with zero. Its concentrations indicate a surface erosion rate of 5.5 ± 0.5 m Myr⁻¹ for ¹⁰Be and 6.0 ± 0.6 m Myr⁻¹ for ²⁶Al.

Several factors have contributed to lowering the age of Member 2 from that previously reported for sample ST 2 (4.17 ± 0.35 Myr)⁹, even though its ¹⁰Be and ²⁶Al concentrations did not change substantially. Since the time of the previous publication the mean-life of ¹⁰Be has been re-evaluated and raised from 1.93 Myr to 2.005 Myr (ref. 29), decreasing the burial age. In addition, post-burial production by muons was previously overestimated, making the inferred burial age too old. Although production rates by muons at depth have been revised²⁷, the isochron method explicitly solves for post-burial production and avoids the need for theoretical production rate calculations, making the method inherently more robust. Finally, rather than relying on a single sample, the new calculations consider nine samples simultaneously;

using revised values sample ST 2 alone would yield an age of 3.94 ± 0.20 Myr, older than but well within measurement uncertainty of the joint solution.

The new age of the Member 2 breccia and the StW 573 skeleton encased within it is in accordance with stratigraphic and taphonomic data¹⁴ suggesting that they are older than Member 4 with its abundant *Australopithecus* fossils. StW 573 thus represents an earlier individual that is older than similar fossils from Makapansgat and contemporary with some *A. afarensis* fossils such as at Laetoli¹⁵, and a partial skeleton from Woranso-Mille, Ethiopia¹⁶. The demonstration that *A. prometheus* in South Africa was contemporary with the morphologically very different *A. afarensis* of eastern Africa now raises interesting questions about early hominid diversity and phylogenetic relationships.

The burial age for the manuport from the Oldowan infill, calculated for its current burial depth of 7 m and a surface erosion rate of 5 m Myr⁻¹ is 2.18 ± 0.21 Myr. The Oldowan at Sterkfontein is now placed at a time compatible with sites elsewhere in Africa, near 2 Myr ago, and with the date of approximately 1.8 Myr ago at Wonderwerk¹⁸. It is close to the cosmogenic burial age of 2.19 ± 0.08 Myr for a manuport found in the Lower Bank of Member 1 at Swartkrans¹⁷, only about 1 km away. Taken together, these dates show that Oldowan technology was present in South Africa by 2 Myr ago.

Online Content Methods, along with any additional Extended Data display items and Source Data, are available in the online version of the paper; references unique to these sections appear only in the online paper.

Received 30 September 2014; accepted 27 January 2015.

Published online 1 April 2015.

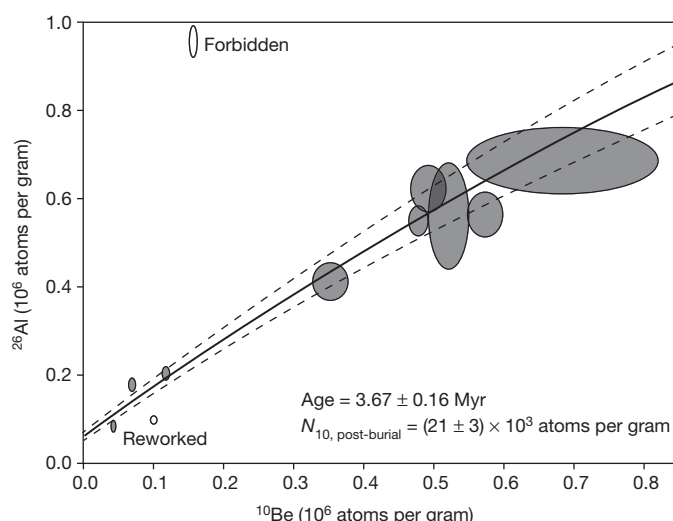


Figure 3 | Burial dating isochron. Cosmogenic ²⁶Al and ¹⁰Be concentrations for individual samples from Member 2, shown as 1σ error ellipses. The solid curve shows the error-weighted best fit, and dashed curves illustrate 1σ error bounds. One sample shown as an open symbol lies below the isochron and has been reworked from an older deposit. A single outlier lies far above the line and has been excluded from analysis. The remaining nine samples are all consistent with a single age of deposition at 3.67 ± 0.16 Myr ago.

- Clarke, R. J. & Tobias, P. V. Sterkfontein member 2 foot bones of the oldest South African hominid. *Science* **269**, 521–524 (1995).
- Clarke, R. J. First ever discovery of a skull and well preserved skeleton of *Australopithecus*. *S. Afr. J. Sci.* **94**, 460–463 (1998).
- Clarke, R. J. Newly revealed information on the Sterkfontein Member 2 *Australopithecus* skeleton. *S. Afr. J. Sci.* **98**, 523–526 (2002).
- Clarke, R. J. A deeper understanding of the stratigraphy of Sterkfontein fossil hominid site. *Trans. R. Soc. S. Afr.* **61**, 111–120 (2006).
- Kuman, K. The archaeology of Sterkfontein: past and present. *J. Hum. Evol.* **27**, 471–495 (1994).
- Kuman, K. & Clarke, R. J. Stratigraphy, artefact industries, and hominid associations for Sterkfontein Member 5. *J. Hum. Evol.* **38**, 827–847 (2000).
- Kuman, K. & Field, A. S. in *The Cutting Edge: New Approaches to the Archaeology of Human Origins* (eds Schick, K. & Toth, T.) 151–169 (Stone Age Institute Press, 2009).
- Partridge, T. C., Shaw, J., Heslop, D. & Clarke, R. J. The new hominid skeleton from Sterkfontein, South Africa: age and preliminary assessment. *J. Quat. Sci.* **14**, 293–298 (1999).
- Partridge, T. C., Granger, D. E., Caffee, M. W. & Clarke, R. J. Lower Pliocene hominid remains from Sterkfontein. *Science* **300**, 607–612 (2003).
- Walker, J., Cliff, R. A. & Latham, A. G. U-Pb isotopic age of the StW 573 hominid from Sterkfontein, South Africa. *Science* **314**, 1592–1594 (2006).
- Pickering, R. & Kramers, J. D. Re-appraisal of the stratigraphy and determination of new U-Pb dates for the Sterkfontein hominid site, South Africa. *J. Hum. Evol.* **59**, 70–86 (2010).
- Herries, A. I. R. & Shaw, J. Paleomagnetic analysis of the Sterkfontein paleocave deposits: implications for the age of the hominid fossils and stone tool industries. *J. Hum. Evol.* **60**, 523–539 (2011).

13. Herries, A. I. R. *et al.* in *The Paleobiology of Australopithecus* (eds Reed, K. E., Fleagle, J. G. & Leakey, R. E.) 21–40 (Springer, 2013).
14. Bruxelles, L., Clarke, R. J., Maire, R., Ortega, R. & Stratford, D. Stratigraphic analysis of the Sterkfontein StW 573 *Australopithecus* skeleton and implications for its age. *J. Hum. Evol.* **70**, 36–48 (2014).
15. Drake, R. & Curtis, G. H. in *Laetoli: A Pliocene Site in Northern Tanzania* (eds Leakey, M. D. & Harris, J. M.) 48–52 (Clarendon, 1987).
16. Haile-Selassie, Y. *et al.* An early *Australopithecus afarensis* postcranium from Woranso-Mille, Ethiopia. *Proc. Natl Acad. Sci. USA* **107**, 12121–12126 (2010).
17. Gibbon, R. J. *et al.* Cosmogenic nuclide burial dating of hominin-bearing Pleistocene cave deposits at Swartkrans, South Africa. *Quat. Geochronol.* **24**, 10–15 (2014).
18. Chazan, M. D. *et al.* The Oldowan horizon in Wonderwerk Cave (South Africa): archaeological, geological, paleontological, and paleoclimatic evidence. *J. Hum. Evol.* **63**, 859–866 (2012).
19. Partridge, T. C. Re-appraisal of lithostratigraphy of Sterkfontein hominid site. *Nature* **275**, 282–287 (1978).
20. Partridge, T. C. & Watt, I. B. The stratigraphy of the Sterkfontein hominid deposit and its relationship to the underground cave system. *Palaeontol. Afr.* **28**, 35–40 (1991).
21. Pickering, T. R., Clarke, R. J. & Heaton, J. L. The context of StW 573, an early hominid skull and skeleton from Sterkfontein Member 2: taphonomy and paleoenvironment. *J. Hum. Evol.* **46**, 277–295 (2004).
22. Clarke, R. J. in *Integrative Paths to the Past: Essays in Honor of F. Clark Howell* (eds Corruccini, R. S. & Ciochon, R. L.) 205–222 (Prentice Hall, 1994).
23. Dart, R. A. The Makapansgat proto-human *Australopithecus prometheus*. *Am. J. Phys. Anthropol.* **6**, 259–284 (1948).
24. Granger, D. E. in *Treatise on Geochemistry* 2nd edn (eds Holland, H. D. & Turekian, K. K.) Vol. 14, 81–97 (Elsevier, 2014).
25. Balco, G. & Rovey, C. W. An isochron method for cosmogenic-nuclide dating of buried soils and sediments. *Am. J. Sci.* **308**, 1083–1114 (2008).
26. Erlanger, E. D., Granger, D. E. & Gibbon, R. J. Rock uplift rates in South Africa from isochron burial dating of fluvial and marine terraces. *Geology* **40**, 1019–1022 (2012).
27. Balco, G., Soreghan, G. S., Sweet, D. E., Marra, K. R. & Bierman, P. R. Cosmogenic-nuclide burial ages for Pleistocene sedimentary fill in Unaweep Canyon, Colorado, USA. *Quat. Geochronol.* **18**, 149–157 (2013).
28. Nishiizumi, K. Preparation of ^{26}Al AMS standards. *Nucl. Instrum. Methods B* **223**, 388–392 (2004).
29. Chmeleff, J., von Blanckenburg, F., Kossert, K. & Jakob, D. Determination of the ^{10}Be half-life by multicollector ICP-MS and liquid scintillation counting. *Nucl. Instrum. Methods B* **268**, 192–199 (2010).
30. Nishiizumi, K. *et al.* Absolute calibration of ^{10}Be AMS standards. *Nucl. Instrum. Methods B* **258**, 403–413 (2007).

Acknowledgements This work results from a collaboration begun with T. C. Partridge (deceased). AMS development and measurements were funded by National Science Foundation EAR1153689 to M.W.C. and D.E.G. and National Science Foundation EAR0844151 to D.E.G. Major funding to R.J.G., K.K. and R.J.C. was received from the Palaeontological Scientific Trust (PAST), which has supported research at Sterkfontein for 20 years. R.J.G. received bursary support from the National Research Foundation (NRF) of South Africa. K.K. thanks the NRF (SA) for substantial funding (AOP 1207112551-82611 and AOP1207173196-82591) and Prof. Bruce Rubidge of the Evolutionary Studies Institute for additional support. Figure 1 includes modified material from *J. Hum. Evol.* vol. 70, Bruxelles L. *et al.*, Stratigraphic analysis of the Sterkfontein StW 573 *Australopithecus* skeleton and implications for its age, 36–48 (2014), with permission from Elsevier.

Author Contributions D.E.G. and R.J.G. conceived the project and performed laboratory work and data analysis. K.K. and R.J.C. supervised sample collection and interpretation of the dates. L.B. was responsible for mapping and interpretation of Member 2. M.W.C. supervised AMS measurements and methods development. All authors contributed to writing the manuscript.

Author Information Reprints and permissions information is available at www.nature.com/reprints. The authors declare no competing financial interests. Readers are welcome to comment on the online version of the paper. Correspondence and requests for materials should be addressed to D.E.G. (dggranger@purdue.edu).

METHODS

No statistical methods were used to predetermine sample size.

Samples of breccia were first treated with acid to dissolve carbonate cement and dolomite blocks. Fine quartz sand (<0.25 mm) was sieved for dating because it contained fewer pieces of dark chert visible by eye. Later, coarse sand and pebbles stained with iron oxides were picked by hand from samples ST 1, 2, 8 and 9. Light-coloured angular sand and pebbles were separated by hand from samples ST 1 and 2 (Extended Data Fig. 1). The manuport (Extended Data Fig. 2) was cleaned and crushed to less than 0.5 mm. Quartz from all samples was purified by repeated leaching in hot agitated 1% HF/HNO₃.

The clean quartz fractions from all samples were dissolved in 5:1 HF/HNO₃ and spiked with ⁹Be prepared from beryl. Upon dissolution, an aliquot was taken for stable Al determination. The sample was then evaporated and fumed to dryness in H₂SO₄. Be and Al were extracted by ion exchange chromatography. Both elements were precipitated as hydroxides and calcined at approximately 1,100 °C for 1 h following standard procedures.

²⁶Al/²⁷Al and ¹⁰Be/⁹Be were measured by AMS at the Purdue Rare Isotope Measurement Laboratory (PRIME Lab), Purdue University. ²⁶Al/²⁷Al measurements for samples ST 1–3 originally reported in ref. 9 were performed at Lawrence Livermore National Laboratory; measurements reported here were made at PRIME Lab in 2014 on archived Al₂O₃ from the same samples. Stable Al measurements for samples ST 1–3 were measured by flame atomic absorption spectrophotometry; all others were measured by inductively coupled plasma-optical emission spectrometry (ICP-OES). A conservative uncertainty of 5% was assigned to the atomic absorption spectrophotometry measurements, and 2% to measurements by ICP-OES. All ²⁶Al measurements except three (ST 3, M2CC and Manuport) were made in 2014 using a gas-filled magnet. The gas-filled magnet suppresses isobaric interference from ²⁶Mg and allows injection of the AlO⁺ molecular ion into the AMS, resulting in 10–20 times higher beam current and improved precision.

Because measurements were made over a period spanning more than a decade, there have been changes in the AMS standards that must be accounted for. Measurements reported in ref. 9 were normalized to ¹⁰Be standards prepared from a standard solution from the National Institute of Standards and Technology. All others were normalized at the time of measurement to standards prepared in ref. 30. All ¹⁰Be values were adjusted to match the currently accepted values of ref. 30. All measurements of ²⁶Al/²⁷Al were normalized to standards of ref. 28.

A derivation of the isochron dating method employed here is provided in detail in ref. 24. It is based on equation (1), which shows that cosmogenic ²⁶Al and ¹⁰Be concentrations depend on the decayed inherited concentrations and any accumulation after burial.

$$(N_{26} - N_{26, \text{post-burial}}) / (N_{10} - N_{10, \text{post-burial}}) = N_{26, \text{inh}} / N_{10, \text{inh}} \exp(-t/\tau_{\text{bur}}) \quad (1)$$

In equation (1) N represents concentration, the numeric subscripts represent ²⁶Al and ¹⁰Be, and the subscripts *postburial* and *inh* represent cosmogenic nuclide accumulation that postdates and predates burial. The variable t represents burial age and τ_{bur} is given by $(1/\tau_{26} = 1/\tau_{26} - 1/\tau_{10})$.

The inherited ratio in equation (1) can be determined by assuming that the rocks being dated were derived from a steadily eroding landscape. In this case, the ratio is governed by equation (2), expressed as a function of N_{10} , where P represents the cosmogenic nuclide production rate at the sediment source area.

$$N_{26, \text{inh}} / N_{10, \text{inh}} = (P_{26} / P_{10}) / [1 + N_{10} / (P_{10} \tau_{\text{bur}})] \quad (2)$$

The ratio $N_{26, \text{post-burial}} / N_{10, \text{post-burial}}$ can be modelled using equation (3), assuming a constant production rate over the entire burial episode.

$$N_{26, \text{post-burial}} / N_{10, \text{post-burial}} = [P_{26} \tau_{26} (1 - \exp(-t/\tau_{26}))] / [P_{10} \tau_{10} (1 - \exp(-t/\tau_{10}))] \quad (3)$$

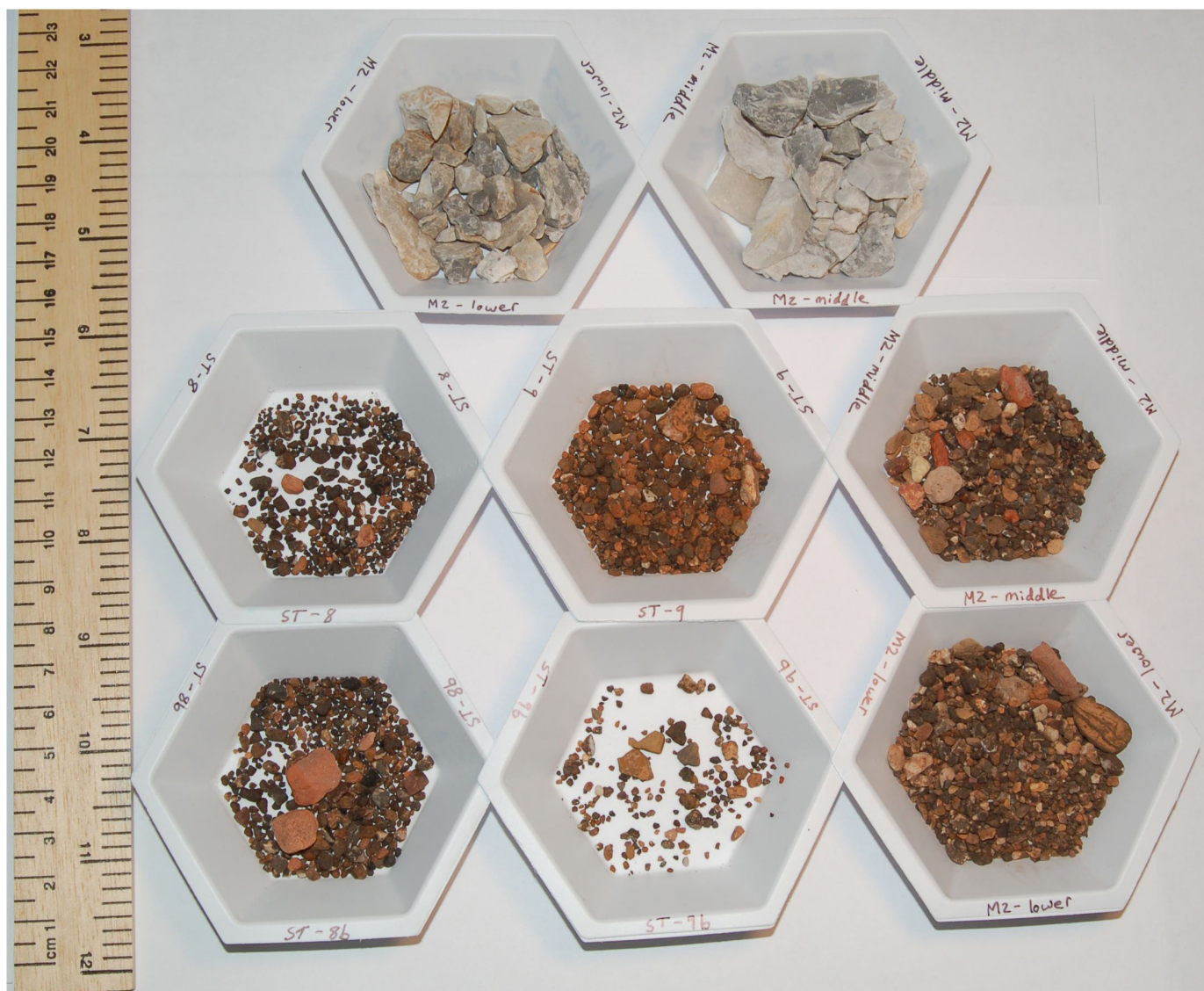
Combining equations (1–3) leads to an expression for an isochron in which N_{26} is a function of N_{10} and only two unknowns: t and $N_{10, \text{post-burial}}$

$$N_{26} = (N_{10} - N_{10, \text{post-burial}}) [P_{26} \exp(-t/\tau_{\text{bur}}) / (1 + N_{10} \exp(t/\tau_{10}) / (P_{10} \tau_{\text{bur}}))] + N_{10, \text{post-burial}} [P_{26} \tau_{26} (1 - \exp(-t/\tau_{26}))] / [P_{10} \tau_{10} (1 - \exp(-t/\tau_{10}))] \quad (4)$$

Equation (4) can be used with a suite of samples to solve for both the burial age and the post-burial component of cosmogenic nuclides. We used equation (4) to solve for the age of the Member 2 breccia, with uncertainties determined by Monte Carlo analysis. The best fit age is 3.67 ± 0.16 Myr, and the best fit value for $N_{10, \text{post-burial}}$ is $(21 \pm 3) \times 10^3$ atoms per gram. The solution is shown graphically in Fig. 3.

For the Oldowan Infill, with only one sample, it is not possible to use an isochron. We corrected for post-burial production beneath an eroding surface following ref. 17. Post-burial production rates for a burial depth of 7 m and a bulk density of 2.0 g cm^{-3} were calculated using a multi-exponential profile adjusted for the muon cross sections given in ref. 27. We calculated the burial ages three ways (Extended Data Table 1): a minimum age was calculated that ignored post-burial production completely, and would be correct if erosion rates (ϵ) at the site were extremely fast; a maximum burial age was calculated by assuming that the burial depth had not changed over time—that is, that erosion rate was zero; finally, an optimum age was calculated using a reasonable value for erosion of the ground surface, which caused the burial depth to change over time. We assume that the ground surface eroded at 5 m per million years, consistent with the value reported here. Cosmogenic nuclide production rates of 10.8 and 73.1 atoms per gram per year at the surface were calculated for a latitude of 26° S and an elevation of 1,500 m, with a ²⁶Al/¹⁰Be production rate ratio of 6.8. Previous work using this method at Swartkrans nearby¹⁷ has yielded burial ages concordant with U/Pb ages of capping flowstones, supporting its accuracy.

Reported uncertainties are measurement errors only. We do not include uncertainties in cosmogenic nuclide production rates (which are generally minor for burial dating), in the ²⁶Al/¹⁰Be production rate ratio or in radioactive mean-lives. Accounting for uncertainty in the mean-lives would lead to an additional ~5% systematic uncertainty in the final ages, resulting in ages with total uncertainties of 3.67 ± 0.24 Myr for Member 2 and 2.18 ± 0.24 Myr for the manuport.



Extended Data Figure 1 | Hand-picked samples. Dark-coloured and light-coloured grains separated for samples M2 Dark and M2 Light. Each dish contains grains from the labelled original sample; M2 lower is sample ST 1, and

M2 middle is ST 2. Light-coloured angular clasts in the top two dishes were combined into sample M2 Light, while the iron-stained and rounded clasts in the remaining dishes were combined into sample M2 Dark.



Extended Data Figure 2 | Manuport. Quartz manuport analysed from the Oldowan Infill. Maximum dimension is 67 mm. Sample recovered from Square Q57 spit 27' 8''–28' 8''.

Extended Data Table 1 | Burial ages for Oldowan manuport

Minimum (ϵ = fast)	Maximum (ϵ = 0)	Optimum (ϵ = 5 m/Myr)
2.09 ± 0.20 Myr	2.21 ± 0.21 Myr	2.18 ± 0.21 Myr

New cosmogenic burial ages for Sterkfontein Member 2 *Australopithecus* and Member 5 Oldowan

Darryl E. Granger¹, Ryan J. Gibbon², Kathleen Kuman^{3,4}, Ronald J. Clarke³, Laurent Bruxelles^{4,5,6} & Marc W. Caffee^{1,7}

The cave infills at Sterkfontein contain one of the richest assemblages of *Australopithecus* fossils in the world, including the nearly complete skeleton StW 573 ('Little Foot')^{1–4} in its lower section, as well as early stone tools^{5–7} in higher sections. However, the chronology of the site remains controversial^{8–14} owing to the complex history of cave infilling. Much of the existing chronology based on uranium–lead dating^{10,11} and palaeomagnetic stratigraphy^{8,12} has recently been called into question by the recognition that dated flowstones fill cavities formed within previously cemented breccias and therefore do not form a stratigraphic sequence^{4,14}. Earlier dating with cosmogenic nuclides⁹ suffered a high degree of uncertainty and has been questioned on grounds of sediment reworking^{10,11,13}. Here we use isochron burial dating with cosmogenic aluminium-26 and beryllium-10 to show that the breccia containing StW 573 did not undergo significant reworking, and that it was deposited 3.67 ± 0.16 million years ago, far earlier than the 2.2 million year flowstones found within it^{10,11}. The skeleton is thus coeval with early *Australopithecus africanus* in eastern Africa^{15,16}. We also date the earliest stone tools at Sterkfontein to 2.18 ± 0.21 million years ago, placing them in the Oldowan at a time similar to that found elsewhere in South Africa at Swartkans¹⁷ and Wonderwerk¹⁸.

The cave at Sterkfontein is partly filled with overlapping layers of fossiliferous breccia^{19,20} that entered through multiple openings to the surface. The infill was originally divided into six members thought to be in stratigraphic order¹⁹, with Members 1–3 inside the cave and 4–6 now exposed at the surface owing to erosion of the cave roof. Although the complete infill stratigraphy is not exposed in any one place and the temporal relationship between the interior and surface deposits remains debated^{11,13}, we retain the original nomenclature^{19,20} here. We will focus on Member 2 within the Silberberg Grotto (Fig. 1) and on the Oldowan Infill of Member 5 in younger deposits excavated from a higher infill.

Member 2 contains abundant fossils, angular dolomite and chert clasts, and quartz-bearing sand. Several localized flowstones and botryoidal calcite deposits fill cavities that formed after the breccia was cemented and later settled into voids dissolved below (Fig. 1)^{4,14}. Fauna was accumulated as a deathtrap assemblage²¹ including associated elements, largely of primates and carnivores, with no hominids apart from a single near-complete skeleton of *Australopithecus prometheus* (StW 573; Fig. 2)^{1–4,22}. This species was named on the basis of a parieto-occipital fossil from Makapansgat²³. It has been suggested²² that several other Sterkfontein and some Makapansgat specimens also belong in this species making *Australopithecus africanus* and *A. prometheus* contemporaries in the assemblages of Makapansgat Member 3 and Sterkfontein Member 4. *A. prometheus* differs from *A. africanus* in features including *Paranthropus*-like larger, bulbous-cusped cheek teeth, a longer, flatter face, incipient supraglabellar hollowing and a more vertical rounded occiput²². (Note that we use the term hominid in the

traditional sense to include humans and their ancestral relatives but exclude the great apes.)

Dating of Member 2 and StW 573 has been problematic. Flowstones in the vicinity of StW 573 date to about 2.2 million years (Myr)^{10,11}, but they post-date the breccia and the fossil^{4,14}. The only previous date on the breccia itself was cosmogenic ²⁶Al/¹⁰Be burial dating of fine-grained quartz⁹, which yielded a best-fit age of 4.17 ± 0.35 Myr. This age has been questioned by many^{10–13,24} who have suggested that fine sediment could have been reworked from older, higher deposits within the cave, making the burial age of the sediment older than the fossil. To resolve the age of the fossil the breccia must be dated and it must be shown to be a coherent stratigraphic unit, largely free of reworked material. This is now possible owing to improvements in measurement precision and new techniques such as isochron burial dating which can explicitly validate the coeval deposition of the entire unit^{24–27}.

Member 5 contains both *Homo ergaster* and *Paranthropus* fossils as well as Oldowan and Acheulean stone tools^{5–7}. Member 5 East is divided into a lower Oldowan infill, with the first appearance of stone tools and a few fossils of *Paranthropus*, and an overlying early Acheulean infill^{5–7}. Faunal comparisons and the *Paranthropus* hominid StW 566 suggested an age estimate of 1.7–2.0 Myr for the Oldowan infill^{6,7}. A substantially younger age of 1.32 ± 0.08 Myr (error-weighted mean) has been inferred from electron spin resonance dating of bovid teeth¹². We use burial dating of a quartz manuport to determine the age of the Oldowan infill.

Burial dating is based on the radioactive decay of ²⁶Al and ¹⁰Be in quartz. These nuclides build up by exposure to secondary cosmic radiation near the ground surface, and subsequently decay when sediment is buried and cosmogenic nuclide production is attenuated. Because ²⁶Al ($\tau_{26} = 1.021 \pm 0.024$ Myr (ref. 28)) decays faster than ¹⁰Be ($\tau_{10} = 2.005 \pm 0.020$ Myr (ref. 29)), the ratio ²⁶Al/¹⁰Be decreases over time, with an effective mean-life of $\tau_{\text{bur}} = 2.08 \pm 0.10$ Myr. For burial dating to be accurate, three criteria must be met. (1) The quartz must be exposed near the ground surface before burial to accumulate sufficient ²⁶Al and ¹⁰Be. (2) It must be buried quickly and deeply enough so that post-burial production is small. The exact depth required depends upon the inherited concentrations, but is usually many metres. (3) It must be buried only once in the past ~10 Myr. If quartz has been reworked from older deposits, or if it has been reworked underground within the cave system, then the burial age will overestimate the true age of the deposit.

An elegant way to test whether the burial dating criteria are met is to construct an isochron^{24–27} in which multiple samples are analysed from the same location. Each sample is buried with its own inherited ²⁶Al and ¹⁰Be concentrations, but all samples share the same post-burial production history. A plot of ²⁶Al versus ¹⁰Be yields a gentle curve with a slope that indicates burial age and an intercept that depends on the amount of post-burial production²⁴. The isochron burial dating method accounts for post-burial production without requiring detailed knowledge of

¹Department of Earth, Atmospheric, and Planetary Sciences, Purdue University, West Lafayette, Indiana 47907, USA. ²Department of Anthropology, University of New Brunswick, Fredericton, New Brunswick E3B 5A3, Canada. ³Evolutionary Studies Institute, University of the Witwatersrand, WITS 2050, Johannesburg, South Africa. ⁴School of Geography, Archaeology and Environmental Studies, University of the Witwatersrand, WITS 2050, Johannesburg, South Africa. ⁵French National Institute for Preventive Archaeological Research (Inrap), 561 rue Etienne Lenoir, km delta, 30900 Nîmes, France. ⁶University of Toulouse Jean Jaurès, UMR 5608 du CNRS (TRACES), Maison de la Recherche, 5 Allées Antonio Machado, F-31058 Toulouse, France. ⁷Department of Physics and Astronomy, Purdue University, West Lafayette, Indiana 47907, USA.

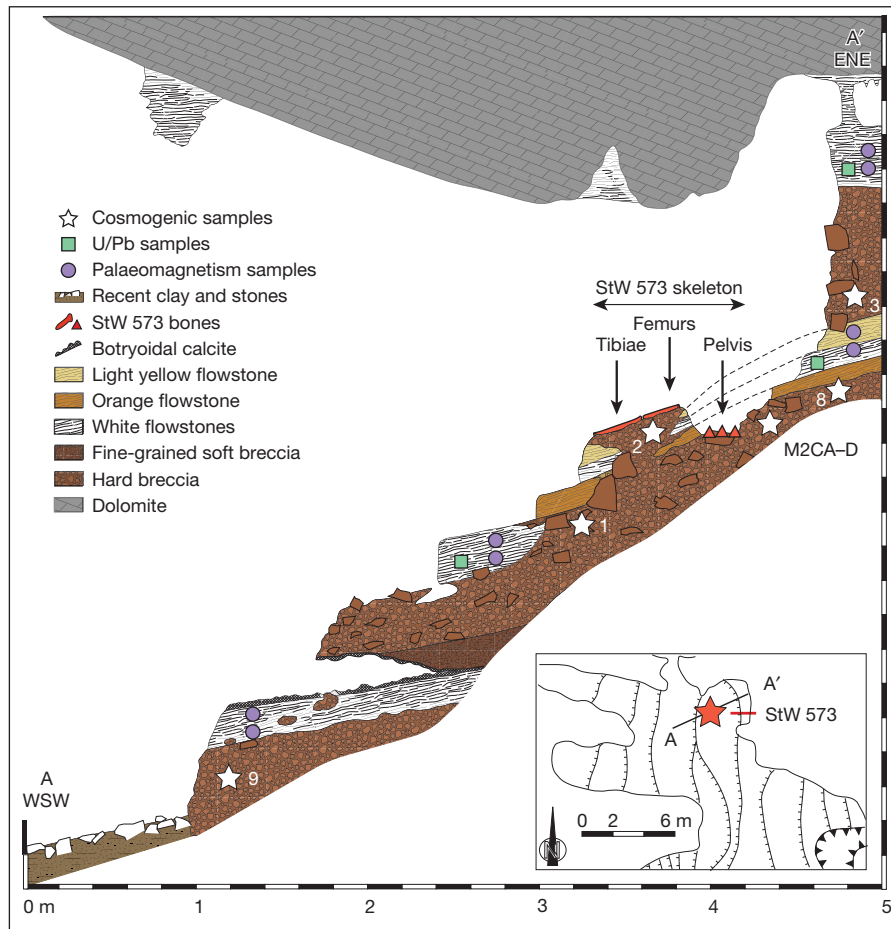


Figure 1 | Stratigraphy and sample locations. Measured stratigraphic section through the Member 2 talus at the location of the StW 573 skeleton showing locations of dated samples, modified from ref 14. Locations of U/Pb samples are estimated from schematic sections of refs 10, 11; palaeomagnetic

samples were located from refs 8, 12. Inset locates the cross section in the lower part of the Silberberg Grotto, with approximately 1 m contour intervals for the infill surface.

the burial depth or burial history. It also allows outliers to be identified; reworked samples plot below the isochron, while samples significantly above the isochron are forbidden and indicate issues with either the sample or the laboratory measurements.

We analysed 11 samples from Member 2 (Table 1), including three previously reported⁹. Effective isochron burial dating requires a wide range of inherited cosmogenic nuclide concentrations. To that end, we selected a suite of samples to maximize variability. Fine quartz sand from multiple samples (ST 1–9) was probably washed in from the surface. In contrast, four blocks of chert were collected from the immediate vicinity of StW 573 (M2CA–D). Two fractions of coarse sand and pebbles were separated (ST M2 Dark and Light). One fraction comprises rounded grains stained with pedogenic iron oxides and washed into the cave from soil at the surface; the second comprises angular unstained grains probably eroded from the walls and ceiling of the cave itself (Extended Data Fig. 1). A previously reported sample from the modern surface⁹ was analysed to confirm that material enters the cave with a zero burial age.

From the Oldowan Infill of Member 5 we selected a single quartz manuport—a typical vein quartz cobble with rounding and impact marks characteristic of rocks found in the local river gravels close to Sterkfontein (Extended Data Fig. 2). There is no evidence for reworking of older deposits, as there are no diagnostically younger artefacts within the large Oldowan assemblage of 3,500 pieces^{6,7}.

²⁶Al and ¹⁰Be were measured by accelerator mass spectrometry (AMS). All samples of fine sand and the iron-stained grains have high ²⁶Al and ¹⁰Be concentrations, confirming their origin from outside the cave. Light-coloured grains and chert blocks have low concentrations, indicating

that they were probably eroded from the walls of the cave within a few metres of the surface. A plot of ²⁶Al versus ¹⁰Be (Fig. 3) reveals that all but two of the samples lie on an isochron, consistent with a single episode of deposition. One chert block lies below the isochron, indicating



Figure 2 | Skull of StW 573 ('Little Foot'). The skull, recently extracted from the cave breccia. Photo by Jason Heaton.

Table 1 | Samples and cosmogenic nuclide concentrations

Sample	Location	[¹⁰ Be] (10 ⁶ atoms per gram)*	[²⁶ Al] (10 ⁶ atoms per gram)
ST 1	0.7 m below StW 573	0.493 ± 0.026	0.624 ± 0.053
ST 2	Adjacent to StW 573	0.574 ± 0.025	0.565 ± 0.050
ST 3	0.8 m above StW 573	0.522 ± 0.029	0.562 ± 0.122
ST 7	Surface above cave	1.166 ± 0.020	7.075 ± 0.380
ST 8	0.7 m NW of StW 573	0.685 ± 0.137	0.686 ± 0.074
ST 9	2–2.5 m below StW 573	0.479 ± 0.012	0.550 ± 0.036
ST M2 Dark	From samples ST 1, 2, 8, 9	0.354 ± 0.025	0.412 ± 0.044
ST M2 Light	From samples ST 1, 2	0.118 ± 0.005	0.205 ± 0.015
M2CA	Near StW 573	0.101 ± 0.004	0.099 ± 0.009
M2CB	Near StW 573	0.070 ± 0.004	0.179 ± 0.015
M2CC	Near StW 573	0.043 ± 0.002	0.083 ± 0.012
M2CD	Near StW 573	0.157 ± 0.006	0.955 ± 0.036
Manuport	Oldowan Infill, Member 5	1.623 ± 0.070	3.051 ± 0.295

*All ¹⁰Be measurements adjusted to the standard of ref. 30. ST 1–3 are slightly different than reported in ref. 9 owing to inclusion of additional analyses.

that it was reworked from an older deposit within the cave, perhaps from talus of Member 1, nearby. Another chert sample has a ²⁶Al/¹⁰Be ratio far into the forbidden zone above the isochron, indicating a problem. Because this was a small sample there is no remaining chert for re-analysis; it is not included in the age determination.

The burial age for Member 2 is calculated as 3.67 ± 0.16 Myr. The concentration of ¹⁰Be produced after burial is calculated as $(21 \pm 3) \times 10^3$ atoms per gram, corresponding to a post-burial production rate of about 0.012 atoms of ¹⁰Be per gram per year, a value consistent with deep burial. The burial age of the surface sample is 0.11 ± 0.11 Myr, consistent with zero. Its concentrations indicate a surface erosion rate of 5.5 ± 0.5 m Myr⁻¹ for ¹⁰Be and 6.0 ± 0.6 m Myr⁻¹ for ²⁶Al.

Several factors have contributed to lowering the age of Member 2 from that previously reported for sample ST 2 (4.17 ± 0.35 Myr)⁹, even though its ¹⁰Be and ²⁶Al concentrations did not change substantially. Since the time of the previous publication the mean-life of ¹⁰Be has been re-evaluated and raised from 1.93 Myr to 2.005 Myr (ref. 29), decreasing the burial age. In addition, post-burial production by muons was previously overestimated, making the inferred burial age too old. Although production rates by muons at depth have been revised²⁷, the isochron method explicitly solves for post-burial production and avoids the need for theoretical production rate calculations, making the method inherently more robust. Finally, rather than relying on a single sample, the new calculations consider nine samples simultaneously;

using revised values sample ST 2 alone would yield an age of 3.94 ± 0.20 Myr, older than but well within measurement uncertainty of the joint solution.

The new age of the Member 2 breccia and the StW 573 skeleton encased within it is in accordance with stratigraphic and taphonomic data¹⁴ suggesting that they are older than Member 4 with its abundant *Australopithecus* fossils. StW 573 thus represents an earlier individual that is older than similar fossils from Makapansgat and contemporary with some *A. afarensis* fossils such as at Laetoli¹⁵, and a partial skeleton from Woranso-Mille, Ethiopia¹⁶. The demonstration that *A. prometheus* in South Africa was contemporary with the morphologically very different *A. afarensis* of eastern Africa now raises interesting questions about early hominid diversity and phylogenetic relationships.

The burial age for the manuport from the Oldowan infill, calculated for its current burial depth of 7 m and a surface erosion rate of 5 m Myr⁻¹ is 2.18 ± 0.21 Myr. The Oldowan at Sterkfontein is now placed at a time compatible with sites elsewhere in Africa, near 2 Myr ago, and with the date of approximately 1.8 Myr ago at Wonderwerk¹⁸. It is close to the cosmogenic burial age of 2.19 ± 0.08 Myr for a manuport found in the Lower Bank of Member 1 at Swartkrans¹⁷, only about 1 km away. Taken together, these dates show that Oldowan technology was present in South Africa by 2 Myr ago.

Online Content Methods, along with any additional Extended Data display items and Source Data, are available in the online version of the paper; references unique to these sections appear only in the online paper.

Received 30 September 2014; accepted 27 January 2015.

Published online 1 April 2015.

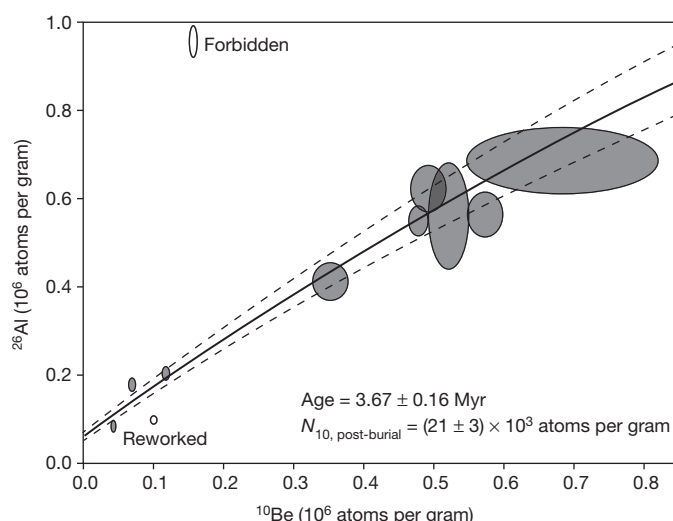


Figure 3 | Burial dating isochron. Cosmogenic ²⁶Al and ¹⁰Be concentrations for individual samples from Member 2, shown as 1σ error ellipses. The solid curve shows the error-weighted best fit, and dashed curves illustrate 1σ error bounds. One sample shown as an open symbol lies below the isochron and has been reworked from an older deposit. A single outlier lies far above the line and has been excluded from analysis. The remaining nine samples are all consistent with a single age of deposition at 3.67 ± 0.16 Myr ago.

- Clarke, R. J. & Tobias, P. V. Sterkfontein member 2 foot bones of the oldest South African hominid. *Science* **269**, 521–524 (1995).
- Clarke, R. J. First ever discovery of a skull and well preserved skeleton of *Australopithecus*. *S. Afr. J. Sci.* **94**, 460–463 (1998).
- Clarke, R. J. Newly revealed information on the Sterkfontein Member 2 *Australopithecus* skeleton. *S. Afr. J. Sci.* **98**, 523–526 (2002).
- Clarke, R. J. A deeper understanding of the stratigraphy of Sterkfontein fossil hominid site. *Trans. R. Soc. S. Afr.* **61**, 111–120 (2006).
- Kuman, K. The archaeology of Sterkfontein: past and present. *J. Hum. Evol.* **27**, 471–495 (1994).
- Kuman, K. & Clarke, R. J. Stratigraphy, artefact industries, and hominid associations for Sterkfontein Member 5. *J. Hum. Evol.* **38**, 827–847 (2000).
- Kuman, K. & Field, A. S. in *The Cutting Edge: New Approaches to the Archaeology of Human Origins* (eds Schick, K. & Toth, T.) 151–169 (Stone Age Institute Press, 2009).
- Partridge, T. C., Shaw, J., Heslop, D. & Clarke, R. J. The new hominid skeleton from Sterkfontein, South Africa: age and preliminary assessment. *J. Quat. Sci.* **14**, 293–298 (1999).
- Partridge, T. C., Granger, D. E., Caffee, M. W. & Clarke, R. J. Lower Pliocene hominid remains from Sterkfontein. *Science* **300**, 607–612 (2003).
- Walker, J., Cliff, R. A. & Latham, A. G. U-Pb isotopic age of the StW 573 hominid from Sterkfontein, South Africa. *Science* **314**, 1592–1594 (2006).
- Pickering, R. & Kramers, J. D. Re-appraisal of the stratigraphy and determination of new U-Pb dates for the Sterkfontein hominid site, South Africa. *J. Hum. Evol.* **59**, 70–86 (2010).
- Herries, A. I. R. & Shaw, J. Paleomagnetic analysis of the Sterkfontein paleocave deposits: implications for the age of the hominid fossils and stone tool industries. *J. Hum. Evol.* **60**, 523–539 (2011).

13. Herries, A. I. R. *et al.* in *The Paleobiology of Australopithecus* (eds Reed, K. E., Fleagle, J. G. & Leakey, R. E.) 21–40 (Springer, 2013).
14. Bruxelles, L., Clarke, R. J., Maire, R., Ortega, R. & Stratford, D. Stratigraphic analysis of the Sterkfontein StW 573 *Australopithecus* skeleton and implications for its age. *J. Hum. Evol.* **70**, 36–48 (2014).
15. Drake, R. & Curtis, G. H. in *Laetoli: A Pliocene Site in Northern Tanzania* (eds Leakey, M. D. & Harris, J. M.) 48–52 (Clarendon, 1987).
16. Haile-Selassie, Y. *et al.* An early *Australopithecus afarensis* postcranium from Woranso-Mille, Ethiopia. *Proc. Natl Acad. Sci. USA* **107**, 12121–12126 (2010).
17. Gibbon, R. J. *et al.* Cosmogenic nuclide burial dating of hominin-bearing Pleistocene cave deposits at Swartkrans, South Africa. *Quat. Geochronol.* **24**, 10–15 (2014).
18. Chazan, M. D. *et al.* The Oldowan horizon in Wonderwerk Cave (South Africa): archaeological, geological, paleontological, and paleoclimatic evidence. *J. Hum. Evol.* **63**, 859–866 (2012).
19. Partridge, T. C. Re-appraisal of lithostratigraphy of Sterkfontein hominid site. *Nature* **275**, 282–287 (1978).
20. Partridge, T. C. & Watt, I. B. The stratigraphy of the Sterkfontein hominid deposit and its relationship to the underground cave system. *Palaeontol. Afr.* **28**, 35–40 (1991).
21. Pickering, T. R., Clarke, R. J. & Heaton, J. L. The context of StW 573, an early hominid skull and skeleton from Sterkfontein Member 2: taphonomy and paleoenvironment. *J. Hum. Evol.* **46**, 277–295 (2004).
22. Clarke, R. J. in *Integrative Paths to the Past: Essays in Honor of F. Clark Howell* (eds Corruccini, R. S. & Ciochon, R. L.) 205–222 (Prentice Hall, 1994).
23. Dart, R. A. The Makapansgat proto-human *Australopithecus prometheus*. *Am. J. Phys. Anthropol.* **6**, 259–284 (1948).
24. Granger, D. E. in *Treatise on Geochemistry* 2nd edn (eds Holland, H. D. & Turekian, K. K.) Vol. 14, 81–97 (Elsevier, 2014).
25. Balco, G. & Rovey, C. W. An isochron method for cosmogenic-nuclide dating of buried soils and sediments. *Am. J. Sci.* **308**, 1083–1114 (2008).
26. Erlanger, E. D., Granger, D. E. & Gibbon, R. J. Rock uplift rates in South Africa from isochron burial dating of fluvial and marine terraces. *Geology* **40**, 1019–1022 (2012).
27. Balco, G., Soreghan, G. S., Sweet, D. E., Marra, K. R. & Bierman, P. R. Cosmogenic-nuclide burial ages for Pleistocene sedimentary fill in Unaweep Canyon, Colorado, USA. *Quat. Geochronol.* **18**, 149–157 (2013).
28. Nishiizumi, K. Preparation of ^{26}Al AMS standards. *Nucl. Instrum. Methods B* **223**, 388–392 (2004).
29. Chmeleff, J., von Blanckenburg, F., Kossert, K. & Jakob, D. Determination of the ^{10}Be half-life by multicollector ICP-MS and liquid scintillation counting. *Nucl. Instrum. Methods B* **268**, 192–199 (2010).
30. Nishiizumi, K. *et al.* Absolute calibration of ^{10}Be AMS standards. *Nucl. Instrum. Methods B* **258**, 403–413 (2007).

Acknowledgements This work results from a collaboration begun with T. C. Partridge (deceased). AMS development and measurements were funded by National Science Foundation EAR1153689 to M.W.C. and D.E.G. and National Science Foundation EAR0844151 to D.E.G. Major funding to R.J.G., K.K. and R.J.C. was received from the Palaeontological Scientific Trust (PAST), which has supported research at Sterkfontein for 20 years. R.J.G. received bursary support from the National Research Foundation (NRF) of South Africa. K.K. thanks the NRF (SA) for substantial funding (AOP 1207112551-82611 and AOP1207173196-82591) and Prof. Bruce Rubidge of the Evolutionary Studies Institute for additional support. Figure 1 includes modified material from *J. Hum. Evol.* vol. 70, Bruxelles L. *et al.*, Stratigraphic analysis of the Sterkfontein StW 573 *Australopithecus* skeleton and implications for its age, 36–48 (2014), with permission from Elsevier.

Author Contributions D.E.G. and R.J.G. conceived the project and performed laboratory work and data analysis. K.K. and R.J.C. supervised sample collection and interpretation of the dates. L.B. was responsible for mapping and interpretation of Member 2. M.W.C. supervised AMS measurements and methods development. All authors contributed to writing the manuscript.

Author Information Reprints and permissions information is available at www.nature.com/reprints. The authors declare no competing financial interests. Readers are welcome to comment on the online version of the paper. Correspondence and requests for materials should be addressed to D.E.G. (dggranger@purdue.edu).

METHODS

No statistical methods were used to predetermine sample size.

Samples of breccia were first treated with acid to dissolve carbonate cement and dolomite blocks. Fine quartz sand (<0.25 mm) was sieved for dating because it contained fewer pieces of dark chert visible by eye. Later, coarse sand and pebbles stained with iron oxides were picked by hand from samples ST 1, 2, 8 and 9. Light-coloured angular sand and pebbles were separated by hand from samples ST 1 and 2 (Extended Data Fig. 1). The manuport (Extended Data Fig. 2) was cleaned and crushed to less than 0.5 mm. Quartz from all samples was purified by repeated leaching in hot agitated 1% HF/HNO₃.

The clean quartz fractions from all samples were dissolved in 5:1 HF/HNO₃ and spiked with ⁹Be prepared from beryl. Upon dissolution, an aliquot was taken for stable Al determination. The sample was then evaporated and fumed to dryness in H₂SO₄. Be and Al were extracted by ion exchange chromatography. Both elements were precipitated as hydroxides and calcined at approximately 1,100 °C for 1 h following standard procedures.

²⁶Al/²⁷Al and ¹⁰Be/⁹Be were measured by AMS at the Purdue Rare Isotope Measurement Laboratory (PRIME Lab), Purdue University. ²⁶Al/²⁷Al measurements for samples ST 1–3 originally reported in ref. 9 were performed at Lawrence Livermore National Laboratory; measurements reported here were made at PRIME Lab in 2014 on archived Al₂O₃ from the same samples. Stable Al measurements for samples ST 1–3 were measured by flame atomic absorption spectrophotometry; all others were measured by inductively coupled plasma-optical emission spectrometry (ICP-OES). A conservative uncertainty of 5% was assigned to the atomic absorption spectrophotometry measurements, and 2% to measurements by ICP-OES. All ²⁶Al measurements except three (ST 3, M2CC and Manuport) were made in 2014 using a gas-filled magnet. The gas-filled magnet suppresses isobaric interference from ²⁶Mg and allows injection of the AlO⁺ molecular ion into the AMS, resulting in 10–20 times higher beam current and improved precision.

Because measurements were made over a period spanning more than a decade, there have been changes in the AMS standards that must be accounted for. Measurements reported in ref. 9 were normalized to ¹⁰Be standards prepared from a standard solution from the National Institute of Standards and Technology. All others were normalized at the time of measurement to standards prepared in ref. 30. All ¹⁰Be values were adjusted to match the currently accepted values of ref. 30. All measurements of ²⁶Al/²⁷Al were normalized to standards of ref. 28.

A derivation of the isochron dating method employed here is provided in detail in ref. 24. It is based on equation (1), which shows that cosmogenic ²⁶Al and ¹⁰Be concentrations depend on the decayed inherited concentrations and any accumulation after burial.

$$(N_{26} - N_{26, \text{post-burial}}) / (N_{10} - N_{10, \text{post-burial}}) = N_{26, \text{inh}} / N_{10, \text{inh}} \exp(-t/\tau_{\text{bur}}) \quad (1)$$

In equation (1) N represents concentration, the numeric subscripts represent ²⁶Al and ¹⁰Be, and the subscripts *postburial* and *inh* represent cosmogenic nuclide accumulation that postdates and predates burial. The variable t represents burial age and τ_{bur} is given by $(1/\tau_{\text{bur}} = 1/\tau_{26} - 1/\tau_{10})$.

The inherited ratio in equation (1) can be determined by assuming that the rocks being dated were derived from a steadily eroding landscape. In this case, the ratio is governed by equation (2), expressed as a function of N_{10} , where P represents the cosmogenic nuclide production rate at the sediment source area.

$$N_{26, \text{inh}} / N_{10, \text{inh}} = (P_{26} / P_{10}) / [1 + N_{10} / (P_{10} \tau_{\text{bur}})] \quad (2)$$

The ratio $N_{26, \text{post-burial}} / N_{10, \text{post-burial}}$ can be modelled using equation (3), assuming a constant production rate over the entire burial episode.

$$N_{26, \text{post-burial}} / N_{10, \text{post-burial}} = [P_{26} \tau_{26} (1 - \exp(-t/\tau_{26}))] / [P_{10} \tau_{10} (1 - \exp(-t/\tau_{10}))] \quad (3)$$

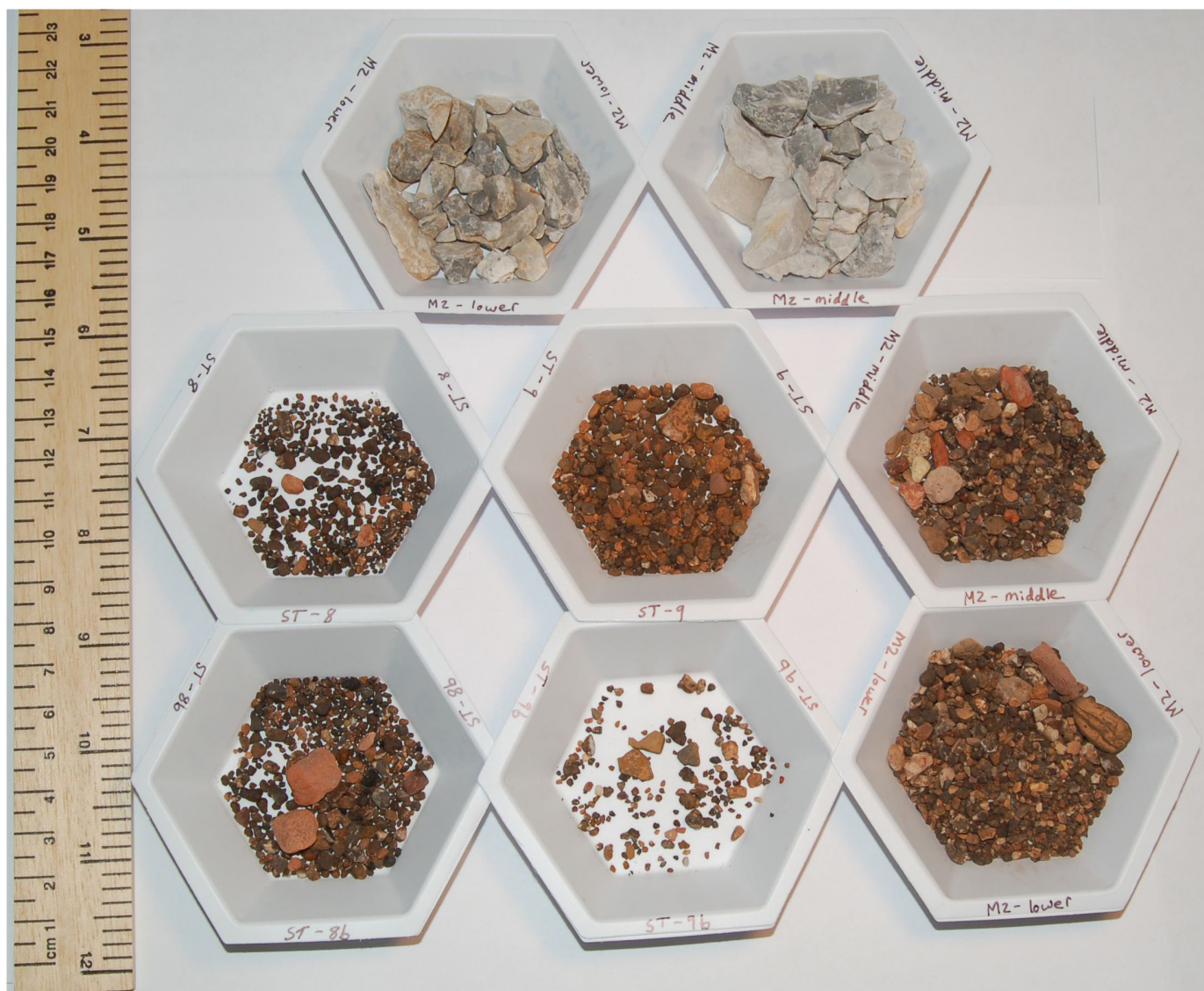
Combining equations (1–3) leads to an expression for an isochron in which N_{26} is a function of N_{10} and only two unknowns: t and $N_{10, \text{post-burial}}$

$$N_{26} = (N_{10} - N_{10, \text{post-burial}}) [P_{26} \exp(-t/\tau_{\text{bur}}) / (1 + N_{10} \exp(t/\tau_{10}) / (P_{10} \tau_{\text{bur}}))] + N_{10, \text{post-burial}} [P_{26} \tau_{26} (1 - \exp(-t/\tau_{26}))] / [P_{10} \tau_{10} (1 - \exp(-t/\tau_{10}))] \quad (4)$$

Equation (4) can be used with a suite of samples to solve for both the burial age and the post-burial component of cosmogenic nuclides. We used equation (4) to solve for the age of the Member 2 breccia, with uncertainties determined by Monte Carlo analysis. The best fit age is 3.67 ± 0.16 Myr, and the best fit value for $N_{10, \text{post-burial}}$ is $(21 \pm 3) \times 10^3$ atoms per gram. The solution is shown graphically in Fig. 3.

For the Oldowan Infill, with only one sample, it is not possible to use an isochron. We corrected for post-burial production beneath an eroding surface following ref. 17. Post-burial production rates for a burial depth of 7 m and a bulk density of 2.0 g cm^{-3} were calculated using a multi-exponential profile adjusted for the muon cross sections given in ref. 27. We calculated the burial ages three ways (Extended Data Table 1): a minimum age was calculated that ignored post-burial production completely, and would be correct if erosion rates (ϵ) at the site were extremely fast; a maximum burial age was calculated by assuming that the burial depth had not changed over time—that is, that erosion rate was zero; finally, an optimum age was calculated using a reasonable value for erosion of the ground surface, which caused the burial depth to change over time. We assume that the ground surface eroded at 5 m per million years, consistent with the value reported here. Cosmogenic nuclide production rates of 10.8 and 73.1 atoms per gram per year at the surface were calculated for a latitude of 26° S and an elevation of 1,500 m, with a ²⁶Al/¹⁰Be production rate ratio of 6.8. Previous work using this method at Swartkrans nearby¹⁷ has yielded burial ages concordant with U/Pb ages of capping flowstones, supporting its accuracy.

Reported uncertainties are measurement errors only. We do not include uncertainties in cosmogenic nuclide production rates (which are generally minor for burial dating), in the ²⁶Al/¹⁰Be production rate ratio or in radioactive mean-lives. Accounting for uncertainty in the mean-lives would lead to an additional ~5% systematic uncertainty in the final ages, resulting in ages with total uncertainties of 3.67 ± 0.24 Myr for Member 2 and 2.18 ± 0.24 Myr for the manuport.



Extended Data Figure 1 | Hand-picked samples. Dark-coloured and light-coloured grains separated for samples M2 Dark and M2 Light. Each dish contains grains from the labelled original sample; M2 lower is sample ST 1, and

M2 middle is ST 2. Light-coloured angular clasts in the top two dishes were combined into sample M2 Light, while the iron-stained and rounded clasts in the remaining dishes were combined into sample M2 Dark.



Extended Data Figure 2 | Manuport. Quartz manuport analysed from the Oldowan Infill. Maximum dimension is 67 mm. Sample recovered from Square Q57 spit 27' 8''–28' 8''.

Extended Data Table 1 | Burial ages for Oldowan manuport

Minimum (ϵ = fast)	Maximum (ϵ = 0)	Optimum (ϵ = 5 m/Myr)
2.09 ± 0.20 Myr	2.21 ± 0.21 Myr	2.18 ± 0.21 Myr

Niche-induced cell death and epithelial phagocytosis regulate hair follicle stem cell pool

Kailin R. Mesa¹, Panteleimon Rompolas¹, Giovanni Zito², Peggy Myung^{1,3}, Thomas Y. Sun¹, Samara Brown¹, David G. Gonzalez⁴, Krastan B. Blagoev^{5,6}, Ann M. Haberman⁴ & Valentina Greco^{1,3,7,8}

Tissue homeostasis is achieved through a balance of cell production (growth) and elimination (regression)^{1,2}. In contrast to tissue growth, the cells and molecular signals required for tissue regression remain unknown. To investigate physiological tissue regression, we use the mouse hair follicle, which cycles stereotypically between phases of growth and regression while maintaining a pool of stem cells to perpetuate tissue regeneration³. Here we show by intravital microscopy in live mice^{4–6} that the regression phase eliminates the majority of the epithelial cells by two distinct mechanisms: terminal differentiation of suprabasal cells and a spatial gradient of apoptosis of basal cells. Furthermore, we demonstrate that basal epithelial cells collectively act as phagocytes to clear dying epithelial neighbours. Through cellular and genetic ablation we show that epithelial cell death is extrinsically induced through transforming growth factor (TGF)- β activation and mesenchymal crosstalk. Strikingly, our data show that regression acts to reduce the stem cell pool, as inhibition of regression results in excess basal epithelial cells with regenerative abilities. This study identifies the cellular behaviours and molecular mechanisms of regression that counterbalance growth to maintain tissue homeostasis.

Tissue regression in the hair follicle is thought to be mediated through programmed cell death⁷. However, it is unclear which cells within the follicle are removed and whether this process is a result of intrinsic cellular exhaustion or active elimination by extrinsic factors. We used our established intravital microscopy technique⁴ to visualize cell behaviours non-invasively in live mice during hair follicle regression (Fig. 1a, Extended Data Fig. 1 and Supplementary Video 1). Unexpectedly, time-lapse recordings of epithelial nuclei (made visible using H2B–green fluorescent protein (GFP) driven by the keratin 14 promoter (*K14-H2BGFP*)) revealed a lack of cell death by nuclear fragmentation in the suprabasal (inner) layers. Furthermore, time-lapse recordings and genetic lineage-tracing approaches showed that inner layers were eliminated through upward terminal differentiation⁸ (Fig. 1b, c, Extended Data Fig. 2 and Supplementary Video 2).

In contrast, using live imaging we captured cell death in the basal epithelial layer. Furthermore, we found that apoptotic debris was retained within the basal epithelium and relocated around neighbouring nuclei, suggesting that basal epithelial cells may act as phagocytes to remove epithelial cellular debris during hair follicle regression (Fig. 1d and Supplementary Video 3). To test this, we induced mosaic expression of a cytoplasmic tdTomato fluorescent reporter in the basal layer. This showed internalization of tdTomato⁺ epithelial debris into neighbouring tdTomato[–] basal epithelial cells (Fig. 1e). Ultrastructure analysis confirmed phagocytosis of apoptotic bodies by basal epithelial cells (Fig. 1f and Extended Data Fig. 3). Tracking this process in real time with cytoskeletal and nuclear labelling demonstrated that apoptotic debris from a single cell was dispersed within the surrounding epithelium and collectively internalized by neighbouring basal epithelial cells (Fig. 1g

and Supplementary Videos 4–6). Consistent with these findings, professional phagocytes⁹ were neither present inside the regressing hair follicles nor did they colocalize with epithelial cell debris (Extended Data Fig. 4 and Supplementary Videos 7, 8). Taken together, these data reveal two modes of epithelial cell elimination during hair follicle regression. While suprabasal cells undergo terminal differentiation, basal epithelial cells undergo apoptosis and are collectively removed by their basal epithelial neighbours. These findings, along with work done on the mammary gland^{10,11}, support a new paradigm of physiological epithelial self-clearance.

Thus far, we have demonstrated that the basal epithelium adopts new cellular behaviours from growth to regression^{4,5}. During growth, highly mitotic cells fuel downwards extension of the basal epithelium. These basal cells, located in the lower follicle, are also more likely to be eliminated during regression, suggesting a model in which mitotic exhaustion primes cells for death¹². An alternative model could be that cell death is driven by extrinsic cues based on spatial location in the basal epithelium. To test these models, we promoted survival intrinsically in the basal epithelium using the Wnt/ β -catenin signalling pathway, which is expressed in the suprabasal layers and has been implicated in survival of these cells¹³ (Fig. 2a and Extended Data Fig. 5). We used a Cre-inducible genetic model to activate β -catenin signalling ectopically in single cells of the basal epithelium⁶ and track survival during regression *in vivo* (Fig. 2b). Control experiments confirmed a spatial bias of cell survival in the upper basal layer, as suggested by previous work¹². Although β -catenin activation was observed to enhance cell survival throughout the follicle, the spatial bias of cell survival seen in controls was retained in the β -catenin-activated follicles (Fig. 2c, d). These data suggest that cell intrinsic factors such as Wnt/ β -catenin signalling alone do not explain the pattern of cell survival observed and implicate extrinsic factors to induce cell death in the basal epithelium.

These results prompted us to ask whether the observed pattern of basal cell survival was the result of spatially regulated induction of cell death. Quantifications of cell death events in time-lapse recordings of various stages of regression revealed an initial localized induction of cell death at the bottom of the follicle, which is in direct contact with the hair follicle mesenchymal dermal papilla niche (Fig. 3a and Supplementary Video 9). Therefore, we hypothesized that interaction with the dermal papilla promotes cell death along the basal epithelium of the hair follicle. To test this, we used two-photon laser ablation⁴ specifically to remove the dermal papilla at the onset of regression and revisited the same hair follicles over time (Fig. 3b). Dermal papilla ablation resulted in significantly reduced death of basal epithelial cells as measured by hair follicle length when compared to neighbouring unablated hair follicles (Fig. 3c and Extended Data Fig. 6). Significant differences in ablated and unablated hair follicle lengths are seen as early as 2 days after ablation, suggesting that the dermal papilla directly promotes regression (Fig. 3d). The difference in length of ablated and unablated hair follicles could be

¹Department of Genetics, Yale School of Medicine, New Haven, Connecticut 06510, USA. ²Department of Biopathology and Medical Biotechnology, University of Palermo, via Divisi 83, 90100 Palermo, Italy.

³Department of Dermatology, Yale School of Medicine, New Haven, Connecticut 06510, USA. ⁴Department of Laboratory Medicine, Department of Immunobiology, Yale School of Medicine, New Haven, Connecticut 06510, USA. ⁵National Science Foundation, Arlington, Virginia 22230, USA. ⁶AA Martinos Center for Biomedical Imaging, Department of Radiology, Massachusetts General Hospital, Harvard Medical School, Boston, Massachusetts 02114, USA. ⁷Yale Stem Cell Center, Yale School of Medicine, New Haven, Connecticut 06510, USA. ⁸Yale Cancer Center, Yale School of Medicine, New Haven, Connecticut 06510, USA.

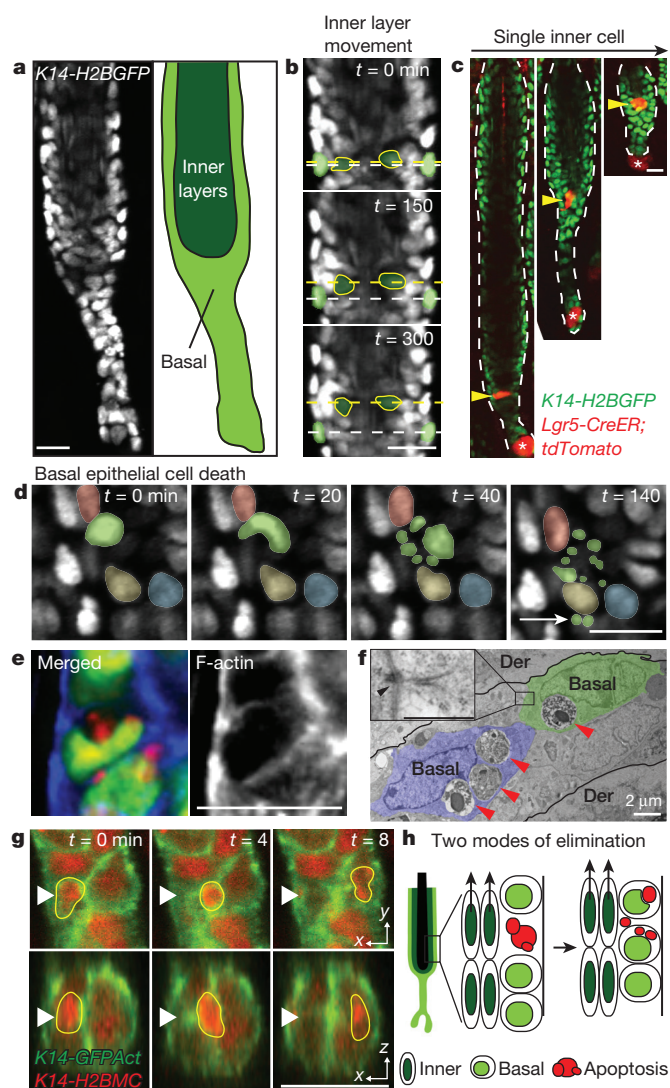


Figure 1 | Basal epithelial cells collectively act as phagocytes to clear neighbouring epithelial cell debris. **a**, Schematic of hair follicle in regression, indicating the basal and suprabasal (inner) epithelial layers, using *K14-H2BGFP* mice. **b**, Single optical sections showing upward collective movement of inner layers in relation to surrounding basal epithelial cells at successive time points, 2.5 h apart (compare position of yellow and white dashed lines). **c**, Single-cell lineage tracing of inner layer cells during regression ($n = 30$ cells, in 4 mice). Labeled cells were revisited daily. Asterisk indicates mesenchymal dermal papilla. **d**, Single optical sections showing cell death (nuclear fragmentation) at successive time points. Note that fragments (green) relocate (white arrow) around neighbouring epithelial nuclei (yellow, red and blue). **e**, Whole-mount staining showing engulfment of neighbouring basal epithelial cellular content by phalloidin staining (blue) in with mosaic Cre induction in basal layer. Nucleus is indicated in green and cytoplasm in red. **f**, Electron micrograph illustrating multiple apoptotic bodies (red arrowhead) present in basal epithelial cells. Basal, basal epithelial cell; Der, dermis. Inset shows high-magnification electron micrograph depicting desmosomal junctions (arrowhead) of phagocytic epithelial cells. Scale bar, 500 nm. **g**, Single optical sections of both coronal and transverse planes (x,y and x,z) at successive time points 4 min apart showing internalization of an apoptotic body (yellow border) by a neighbouring basal epithelial cell. Nucleus is indicated in red and cell cortex in green. **h**, Scheme of the two modes of elimination of epithelial cells and collective phagocytic uptake of basal epithelial apoptotic bodies by neighbouring basal epithelial cells during regression. Scale bars, 20 μm unless otherwise indicated.

attributed to a reduction in cell death or a reduction in cell clearance. To be able to distinguish the effect of the dermal papilla on these two processes, we quantified the number of apoptotic debris sites in ablated follicles 2 days after ablation and found that the amount of cellular debris

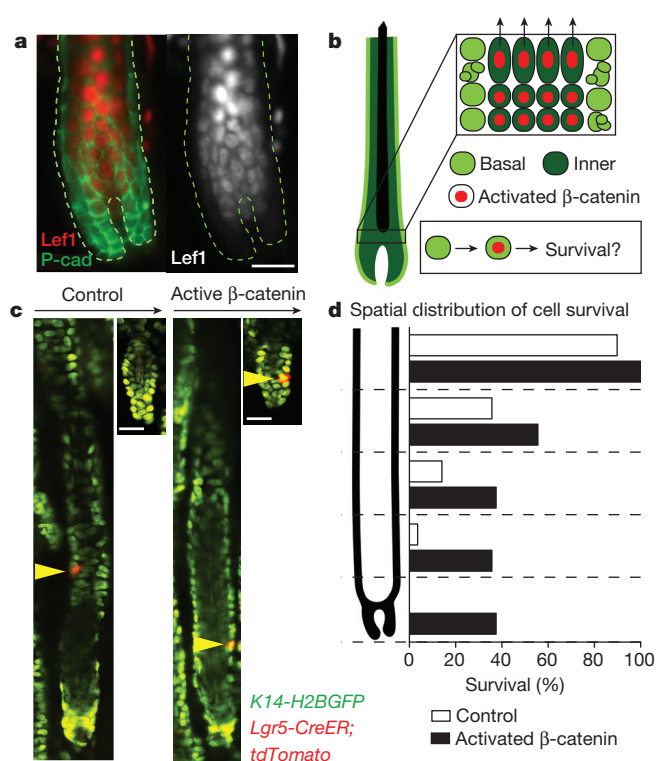


Figure 2 | β -catenin activation is not sufficient to overcome the extrinsic gradient of basal epithelial survival. **a**, Wnt/ β -catenin activation is restricted to inner layers. Immunofluorescent staining of Lef1 in regressing hair follicle. Lef1 is indicated in red and P-cadherin (P-cad) in green. **b**, Scheme of basal and inner layer behaviours and β -catenin activation during hair follicle regression. **c**, Lineage tracing of basal epithelial cells revisited at the beginning and end of regression. Representative examples of either a single control or β -catenin-activated cell traced during regression. **d**, Graphical representation of cell survival as a function of initial position within the regressing hair follicle ($n = 235$ or 135 in control or β -catenin, respectively, in 4 mice). Scale bars, 25 μm .

was significantly reduced compared to control follicles at this initial time point. The debris generated from these follicles by day 2 was cleared by day 4, similar to control follicles, suggesting that cell clearance is relatively unaffected by dermal papilla removal (Fig. 3e). Collectively, this establishes a functional role for the mesenchymal niche to promote basal epithelial cell death.

To understand the molecular signalling that facilitates basal epithelial cell death, we investigated the TGF- β signalling pathway, as exogenous administration of TGF- β 1 ligand has been shown to induce precocious hair follicle regression¹⁴. We found that TGF- β ligands are expressed by the mesenchymal dermal papilla, whereas TGF- β signalling is active in the basal epithelium during the regression phase (Fig. 3f–h and Extended Data Figs 7, 8a). To test the functional role of TGF- β signalling in basal epithelial cell death during regression, we conditionally eliminated TGF- β receptor 1 (TGF- β RI) in the basal layer¹⁵ (Extended Data Fig. 8b, c). Removal of TGF- β RI at the onset of regression resulted in aberrant accumulation of basal cells by the end of regression when compared to control littermates (Fig. 3i–k). Together, these data demonstrate that extrinsic regulation through TGF- β signalling and epithelial–mesenchymal crosstalk induces cell death along the basal epithelium while sparing a restricted pool of stem cells.

This work raises the question of whether hair follicle regression serves to eliminate either exhausted basal cells or functional cells from an expanded stem cell pool. To address this question, we used an approach to remove the dermal papilla transiently¹⁶ during regression (Fig. 4a). Strikingly, as neighbouring unablated follicles began a new round of growth, dermal-papilla-ablated follicles that had failed to complete

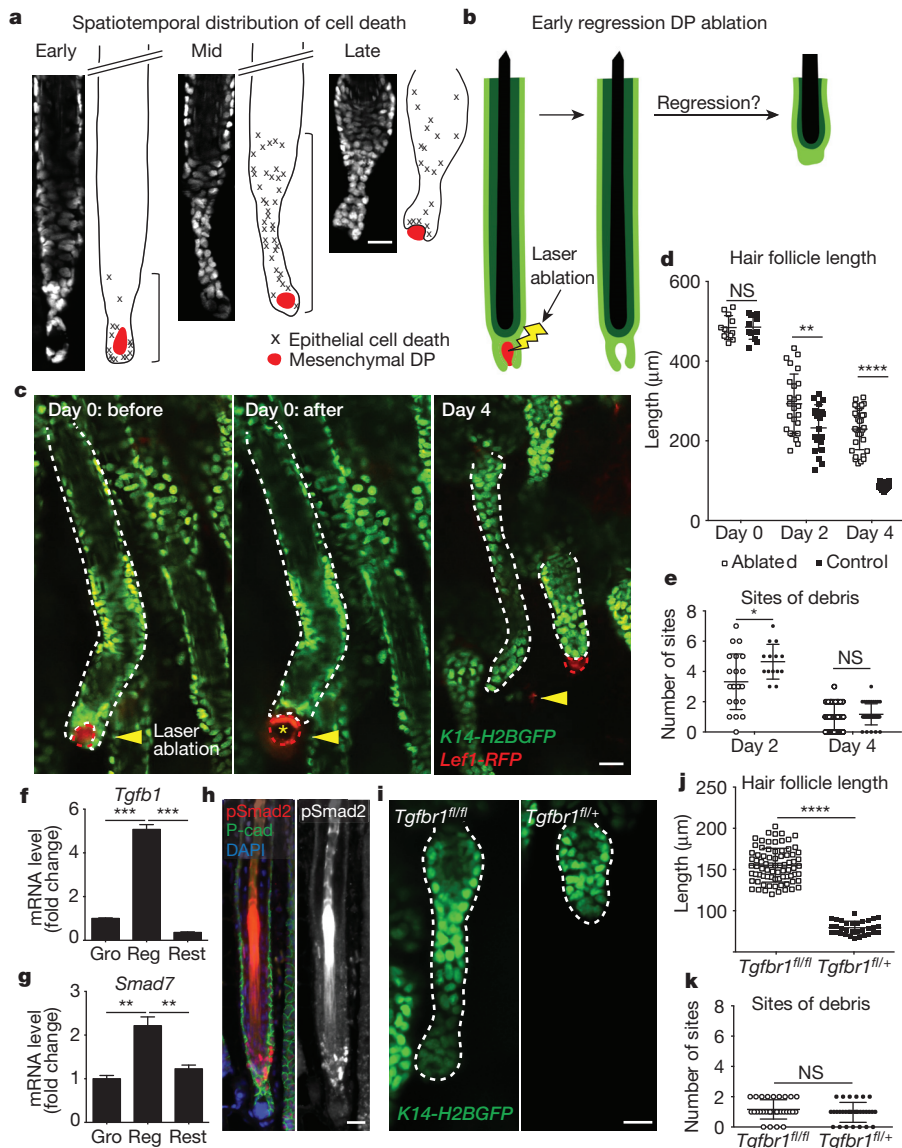


Figure 3 | Mesenchymal dermal papilla crosstalk and TGF- β signalling are required for cell death in the basal epithelium. **a**, Graphical representation and quantification of spatial distribution of cell death in the basal layer at three stages of regression using time-lapse recordings ($n = 9$ follicles, in 5 mice). DP, dermal papilla. **b**, Scheme of laser ablation experiment. **c**, Sequential revisits of hair follicles after dermal papilla ablation during regression. Yellow arrowhead indicates laser ablation site. Asterisk indicates auto-fluorescence from the two-photon laser. **d**, **e**, Dot plot quantification of the hair follicle length at day 0, 2 and 4 after dermal papilla ablation (**d**) and of the number of apoptotic fragmentation sites at day 2 and 4 after dermal papilla ablation (**e**) ($n = 36$ follicles, in 6 mice; mean \pm standard deviation (s.d.)). **f**, **g**, Messenger RNA levels of *Tgfb1* ligand expression in the mesenchymal dermal papilla (**f**) and *Smad7* expression in hair follicle basal layer throughout the hair cycle (**g**) (mean \pm s.d.; $n = 3$ technical replicates). Hair follicle phases indicated as: Gro, growth; Reg, regression; Rest. **h**, Localized TGF- β activation by immunofluorescent staining of phosphorylated (p)Smad2 at the onset of hair follicle regression. 4',6-Diamidino-2-phenylindole (DAPI), blue; pSmad2, red; P-cadherin, green. **i**, Hair follicles after Cre-induced recombination in *Tgfb1*^{fl/fl} and *Tgfb1*^{fl/+} mice at the end of regression. **j**, **k**, Dot plot quantification of the hair follicle length (**j**) and of the number of apoptotic fragmentation sites at the end of regression (**k**) ($n = 31$ follicles, in 4 mice; mean \pm s.d.). NS, not significant. * $P < 0.05$, ** $P < 0.01$, *** $P < 0.001$ and **** $P < 0.0001$ indicate a significant difference. Scale bars, 25 μ m.

regression also initiated hair growth from the bottom of their aberrantly long basal epithelium. Furthermore, ablated hair follicles appeared grossly normal, with proper generation of differentiated suprabasal layers, similar to neighbouring unablated hair follicles (Fig. 4b). These findings demonstrate that basal epithelial cells of the hair follicle are not intrinsically

committed for cell death, but rather retain a capacity to regenerate tissue. This suggests that regression functions to reduce an expanded stem cell pool following tissue growth.

We show that physiological regression is an extrinsically regulated process that reduces the size of the hair follicle stem cell compartment

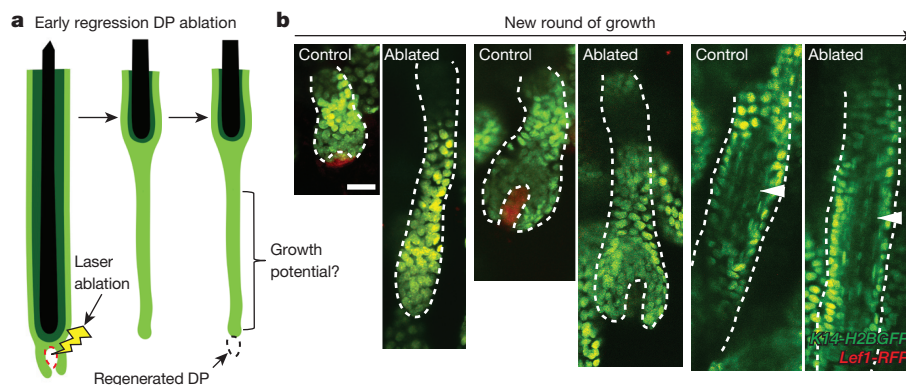


Figure 4 | Basal epithelial cells targeted for cell death retain regenerative potential. **a**, Scheme of laser ablation experiment. **b**, Sequential revisits of hair follicles after dermal papilla (DP) ablation during the next round of growth

(postnatal day (P)22–P35). White arrowhead indicates differentiated inner layers. Observations shown represent $n = 3$ mice. Scale bars, 25 μ m.

while leaving terminal differentiation programs unaffected. Regression is regulated through TGF- β signalling initiated by the mesenchymal niche to induce spatially restricted cell death in the basal epithelium. Clearance of apoptotic cells is a self-contained process driven by epithelial phagocytosis within the regressing basal epithelium. Finally, inhibition of regression through transient loss of the mesenchymal niche demonstrates that cells throughout the hair follicle basal epithelium maintain regenerative competency when in proximity to the mesenchymal niche (Extended Data Fig. 9). All together, we demonstrate that tissue regression relies on spatially coordinated cellular behaviours, and establish a new understanding of the extrinsic regulation that counterbalances tissue growth over the lifespan of an organism.

Online Content Methods, along with any additional Extended Data display items and Source Data, are available in the online version of the paper; references unique to these sections appear only in the online paper.

Received 19 July 2014; accepted 9 February 2015.

Published online 6 April 2015.

- Bergmann, A. & Steller, H. Apoptosis, stem cells, and tissue regeneration. *Sci. Signal.* **3**, re8 (2010).
- Poon, I. K., Lucas, C. D., Rossi, A. G. & Ravichandran, K. S. Apoptotic cell clearance: basic biology and therapeutic potential. *Nature Rev. Immunol.* (2014).
- Müller-Röver, S. *et al.* A comprehensive guide for the accurate classification of murine hair follicles in distinct hair cycle stages. *J. Invest. Dermatol.* **117**, 3–15 (2001).
- Rompolas, P. *et al.* Live imaging of stem cell and progeny behaviour in physiological hair-follicle regeneration. *Nature* **487**, 496–499 (2012).
- Rompolas, P., Mesa, K. R. & Greco, V. Spatial organization within a niche as a determinant of stem-cell fate. *Nature* (2013).
- Deschene, E. R. *et al.* β -Catenin Activation Regulates Tissue Growth Non-Cell Autonomously in the Hair Stem Cell Niche. *Science* **343**, 1353–1356 (2014).
- Lindner, G. *et al.* Analysis of apoptosis during hair follicle regression (catagen). *Am. J. Pathol.* **151**, 1601 (1997).
- Rogers, G. E. Hair follicle differentiation and regulation. *Int. J. Dev. Biol.* **48**, 163–170 (2004).
- Li, J. L. *et al.* Intravital multiphoton imaging of immune responses in the mouse ear skin. *Nature Protocols* **7**, 221–234 (2012).
- Monks, J. *et al.* Epithelial cells as phagocytes: apoptotic epithelial cells are engulfed by mammary alveolar epithelial cells and repress inflammatory mediator release. *Cell Death Differ.* **12**, 107–114 (2005).
- Monks, J., Smith-Steinhart, C., Kruk, E. R., Fadok, V. A. & Henson, P. M. Epithelial cells remove apoptotic epithelial cells during post-lactation involution of the mouse mammary gland. *Biol. Reprod.* **78**, 586–594 (2008).
- Hsu, Y.-C., Pasolli, H. A. & Fuchs, E. Dynamics between stem cells, niche, and progeny in the hair follicle. *Cell* **144**, 92–105 (2011).
- Choi, Y. S. *et al.* Distinct functions for Wnt/ β -catenin in hair follicle stem cell proliferation and survival and interfollicular epidermal homeostasis. *Cell Stem Cell* **13**, 720–733 (2013).
- Foitzik, K. *et al.* Control of murine hair follicle regression (catagen) by TGF- β 1 *in vivo*. *FASEB J.* **14**, 752–760 (2000).
- Larsson, J. *et al.* TGF- β signalling-deficient hematopoietic stem cells have normal self-renewal and regenerative ability *in vivo* despite increased proliferative capacity *in vitro*. *Blood* **102**, 3129–3135 (2003).
- Rahmani, W. *et al.* Hair follicle mesenchymal stem cells regenerate the dermal sheath, replenish the dermal papilla and specify hair type. *Dev. Cell* **31**, 543–558 (2014).

Supplementary Information is available in the online version of the paper.

Acknowledgements We thank E. Fuchs for the *K14-H2BGFP*, *Lef1-RFP* and *K14-GFPActin* mice; M. Taketo for the *Ctnnb1^{fl(E3)/+}* mice; A. Horwich and A. Mesa for critical feedback; M. Rendl for technical advice; M. Graham and X. Liu for technical support with electron microscopy; D. Egli for the H2BmCherry construct; and T. Nottoli for generating the *K14-H2BmCherry* mouse line. K.R.M. and S.B. were supported by the National Institutes of Health (NIH) Predoctoral Program in Cellular and Molecular Biology, grant no. 5T32 GM007223. K.R.M. is currently a National Science Foundation (NSF) Graduate Research Fellow. This work is supported by the American Cancer Society, grant no. RSG-12-059-02; Yale Spore Grant National Cancer Institute, NIH, grant no. 2P50CA121974; the National Institute of Arthritis and Musculoskeletal and Skin Diseases (NIAMS), NIH, grant no. 1R01AR063663-01; and by The New York Stem Cell Foundation. V.G. is a New York Stem Cell Foundation–Robertson Investigator. P.R. is a New York Stem Cell Foundation–Druckenmiller Fellow. A.M.H. is supported by NIAMS Rheumatic Diseases Research Core Centers grant no. 5 P30 AR053495-07. K.B.B. was supported by the NSF. The NSF had no role in study design, data collection and analysis, decision to publish, or preparation of the manuscript. The views presented here are not those of the NSF and represent solely the views of the authors.

Author Contributions K.R.M. and V.G. designed experiments and wrote the manuscript; K.R.M. performed the experiments and analysed the data. P.R. generated the *K14-H2BmCherry* mouse line and assisted with two-photon time-lapse imaging. G.Z. and P.M. performed immunofluorescence. S.B. performed skin whole-mount staining. T.Y.S. assisted with technical aspects. K.R.M., D.G.G. and A.M.H. performed three-dimensional imaging analysis. K.B.B. helped with data analysis.

Author Information Reprints and permissions information is available at www.nature.com/reprints. The authors declare no competing financial interests. Readers are welcome to comment on the online version of the paper. Correspondence and requests for materials should be addressed to V.G. (valentina.greco@yale.edu).

METHODS

Mice. *K14-H2BGFP*¹⁷, *Lef1-RFP*¹⁸ and *K14-GFPActin*¹⁹ were obtained from the Fuchs Laboratory. *Tgfbri*^{fl/fl} mice were obtained from V. Kaartinen¹⁵. *Ctnnb1*^{fl(Ex3)/+} mice were obtained from M. Taketo²⁰. *Lgr5-CreER* (Cleviers Laboratory), *Shh-CreER* (Tabin Laboratory), *LysM-Cre* (Foerster Laboratory), *Cx3cr1-GFP* (Littman Laboratory) and *Rosa-stop-tdTomato* (Zeng Laboratory) were obtained from Jackson Laboratory (JAX)^{21–25}. The Yale Transgenic Facility generated the *K14-H2BmCherry* mice. All studies and procedures involving animal subjects were approved by the Institutional Animal Care and Use Committee at Yale School of Medicine and conducted in accordance with the approved animal handling protocol. *Lgr5-CreER* and *Shh-CreER* were used to recombine alleles and label cells conditionally within specific hair follicle populations and temporally during the regression phase. Cre induction for the lineage-tracing experiments was induced with a single intraperitoneal injection of tamoxifen ($1 \mu\text{g g}^{-1}$ in corn oil) at postnatal day 14. *Tgfbri*^{fl/fl} recombination was induced with three intraperitoneal injections of tamoxifen ($100 \mu\text{g g}^{-1}$ in corn oil) at postnatal day 10, 12 and 14. Intravital microscopy and laser ablation procedures were carried out as described previously^{4,5}. For lineage-tracing experiments, only cells that were unambiguously separated from neighbouring cells were sampled to ensure the identity of individual lineages. Mice from experimental and control groups were randomly selected of either gender for live imaging experiments. No blinding was done. All lineage-tracing and ablation experiments were repeated in at least three different mice.

Generation of *K14H2BmCherry* mice. Transgenic mice expressing H2BmCherry under the control of the keratin 14 promoter (*K14-H2BmCherry*) were generated using the following procedure. The H2BmCherry insert (provided by D. Egli) was amplified by PCR from the TopoTA vector (Life Technologies) using primers 5'-CGGCGGATCCATGCCAGAGCCAGC and 3'-CGCTCTAGATTACTTGTA CAGCTCGTCC, which introduced cleavage sites for BamHI and XbaI restriction enzymes immediately upstream and downstream, respectively, of the open reading frame. The 1.1 kb PCR product was inserted between the BamHI and XbaI sites in the pG3Z**K14*cassette vector (provided by E. Fuchs). The resulting transgene was digested with SacI and SphI, and the 4.3 kb fragment was injected into blastocysts at the Yale Transgenic Facility (T. Nottoli). Chimaeric mice were screened initially by PCR and founder mice were selected to establish transgenic mouse lines. These initial lines were subsequently screened by histological analysis, and the line displaying the highest expression levels of the *K14H2BmCherry* reporter was selected to establish the final colony.

In vivo imaging and laser ablation. Mice between postnatal day 17 and 35 were anaesthetized with intraperitoneal injection of $7 \mu\text{l g}^{-1}$ of ketamine/xylazine cocktail mix (15 mg ml^{-1} and 1 mg ml^{-1} , respectively, in PBS). Anaesthesia was maintained throughout the course of the experiment with vaporized isoflurane delivered by a nose cone as previously described¹⁰. Image stacks were acquired with a LaVision TriM Scope II (LaVision Biotec) microscope equipped with a tunable Chameleon Ultra (Coherent) Ti:Sapphire laser. To acquire serial optical sections, a laser beam (740 nm for Alexafluor 350; 940 nm for H2BGFP; 1,040 nm for RFP and tdTomato; 990 nm for simultaneous excitation of GFPActin and H2BmCherry) was focused through a $\times 20$ or $\times 40$ water immersion lens (N.A. 1.0 and 1.1 respectively; Zeiss) and scanned with a field of view of 0.5 or 0.25 mm^2 , respectively, at 600 Hz. Z-stacks were acquired in 1–3 μm steps to image a total depth of $150 \mu\text{m}$ of tissue. We revisited the same hair follicles in separate experiments as previously described¹⁰. For time-lapse recordings, serial optical sections were obtained between 1 to 5 min intervals, depending on the experimental setup. Laser ablation was carried out with the same optics as used for acquisition. An 800 nm laser beam was used to scan the target area ($10\text{--}50 \mu\text{m}^2$) and ablation was achieved using 30–50% laser power for ~ 1 s. Ablation parameters were adjusted according to the depth of the target ($50\text{--}100 \mu\text{m}$).

Image analysis. Raw image stacks were imported into Fiji (NIH) or Imaris software (Bitplane/Perkin Elmer) for further analysis. Provided images and Supplementary Videos are typically presented as a maximal projection of 3–6 μm optical sections. For visualizing individual labelled cells expressing the tdTomato Cre reporter, the brightness and contrast were adjusted accordingly for the green (GFP) and red (RFP/tdTomato) channels and composite serial image sequences were assembled as previously described. Hair follicle length and labelled cell position values were measured from the top of the stem cell compartment. Apoptotic cell tracking analysis was performed in Imaris software (Bitplane).

Electron microscopy. Trimmed skin samples were fixed (2% glutaraldehyde and 2% paraformaldehyde in 0.1 M sodium cacodylate buffer pH 7.4) for 1 h. The samples were rinsed in sodium cacodylate buffer and were post-fixed in 1% osmium tetroxide for 1 h. The samples were rinsed and en bloc stained in aqueous 2% uranyl acetate for an hour further, followed by rinsing, dehydrating in an ethanol series to 100%, and rinsing several times in 100% propylene. Then samples were infiltrated with Embed 812 (Electron Microscopy Sciences) resin and baked overnight at 60°C . Hardened blocks were cut using

a Leica UltraCut UC7. Sixty-nanometre sections were collected and stained using 2% uranyl acetate and lead citrate for transmission microscopy, and 250-nm-thick sections were stained with either Richardson's stain or 1% Toluidine Blue for light microscopy. For immunolabelled electron microscopy, dissected skin samples were fixed in 4% paraformaldehyde/0.1% glutaraldehyde in phosphate buffer for 30 min and then in 4% paraformaldehyde/phosphate buffer overnight at 4°C . The samples were rinsed in 0.1 M HEPES. To quench, aldehydes were placed in 50 mM NH_4Cl plus 100 mM glycine plus 2% sucrose for 1 h, then washed in HEPES buffer and placed in 0.1% tannic acid/0.1 M HEPES for 1 h, then rinsed in 50 mM Tris/50 mM maleate and placed in 2% uric acid/50 mM Tris/50 mM maleate for 1 h. After rinsing, they were dehydrated through a graded series 50% to 95% of ethanol at 4°C , then infiltrated with 50:50 ethanol/LR White (EMS) for 1 h followed by several changes of pure 100% LR White overnight on a rotator at 4°C . Samples were polymerized at 60°C for 18 h. Fifty-nanometre resin sections were cut on a Leica UC7 ultra-microtome and collected on nickel formvar/carbon grids, and immunolabelled using a primary chicken anti-GFP (Abcam) diluted to 1:50 for 1 h, rinsed and placed on protein A gold secondary 1:50 (University of Utrecht). The sections were counterstained with 2% uranyl acetate and lead citrate. Grids were viewed FEI Tencai Biotwin TEM at 80 kV. Images were taken using Morada CCD and iTEM (Olympus) software.

Immunostaining on paraffin sections and whole-mount skin. Skin was fixed in 4% PFA for whole mount or in 10% formalin for paraffin embedding and used for histological analysis as previously described²⁶. Immunohistochemistry was performed by incubating sections at 4°C overnight with primary antibodies as follows: mouse anti- β -catenin (1:100, BD #610153; 14/Beta-Catenin), rat anti-CD11b (1:250, eBioscience #14-0112; M1/70), goat anti-P-cadherin (1:100, R&D #AF761), rabbit anti-pSmad2 (Ser465/467) (1:1,000, Cell Signaling #3108; 138D4), and rabbit anti-Lef1 (1:100, Cell Signaling #2286; C18A7). pSmad2 immunostaining required TSA Plus kit (PerkinElmer). For bright-field immunohistochemistry, biotinylated species-specific secondary antibodies, followed by detection using the ABC kit (Vector Labs) and DAB kit (Vector Labs), were used according to the manufacturer's instructions. M.O.M. kit was used for mouse antibodies (Vector Laboratories). Secondary antibodies conjugated with FITC, RRX and Cy5 (Jackson ImmunoResearch Laboratories) were used at a concentration of 1:100 for 1 h at room temperature. Alexafluor 350 phalloidin (Life Technologies) was used according to the manufacturer's instructions.

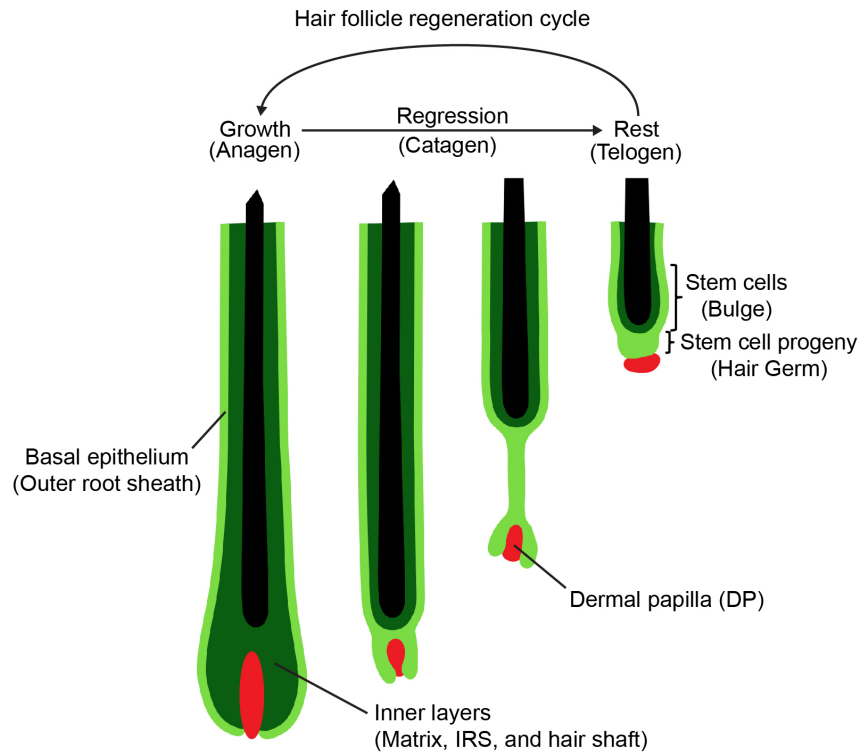
FACS. Back skins of *K14-H2BGFP*; *Lef1-RFP* and *Lgr5-CreER*; *Tgfbri*^{fl/fl} or *Tgfbri*^{fl/+}; *tdTomato*; *K14-H2BGFP* mice were harvested at P12, P16 or P20 and were placed dermis down on 0.2% collagenase (Sigma) at 37°C for 20 min, and then placed on 0.25% trypsin (Gibco) at 37°C for 10 min to obtain epithelial cells as previously described²⁷. Cells were stained for 10 min with biotinylated rat anti-CD34 (1:50, eBioscience #14-0341; RAM34), biotinylated rat anti-CD45 (1:50, BD #553077; 30-F11), biotinylated rat anti-CD117 (1:50, BD #553353; 2B8) and goat anti-integrin- $\alpha 9$ (1:50, R&D #AF3827). Cells were washed for 5 min and then incubated with streptavidin-Pacific blue (1:200, Invitrogen) and Alexafluor 647 donkey anti-goat IgG (Jackson ImmunoResearch Laboratories). Cells were isolated on DAPI exclusion and by the following criteria: dermal papilla = RFP^+ , CD34^- , CD45^- , CD117^- , integrin- $\alpha 9^+$; and enriched outer root sheath = RFP^- , GFP^{High} using a FACSaria II Cell Sorter (BioScience), as previously described²⁸. Cells were sorted into RNA lysis buffer for RNA isolation (RNeasy Mini Kit, Qiagen). FACS profiles were analysed through FlowJo software.

RT-qPCR. cDNA was made using Superscript III First-Strand Synthesis kit (Invitrogen). RT-qPCR was performed in triplicate with SYBER Green I reagents (Invitrogen) using 5.0 ng cDNA per reaction on the ViiATM 7 Real-Time PCR system (Invitrogen, Life Technologies). Data were analysed by ViiATM software, Microsoft Excel and PRISM. Gene-specific primers were designed and are listed in Supplementary Table 1.

Statistical analysis. Data are expressed as percentages, box and whisker plots (error bars represent maximum and minimum), or mean \pm s.d. An unpaired Student's *t*-test was used to analyse data sets with two groups and $*P < 0.05$ to $****P < 0.0001$ indicated a significant difference. Statistical calculations were performed using the Prism software package (GraphPad). No statistical method was used to predetermine sample size.

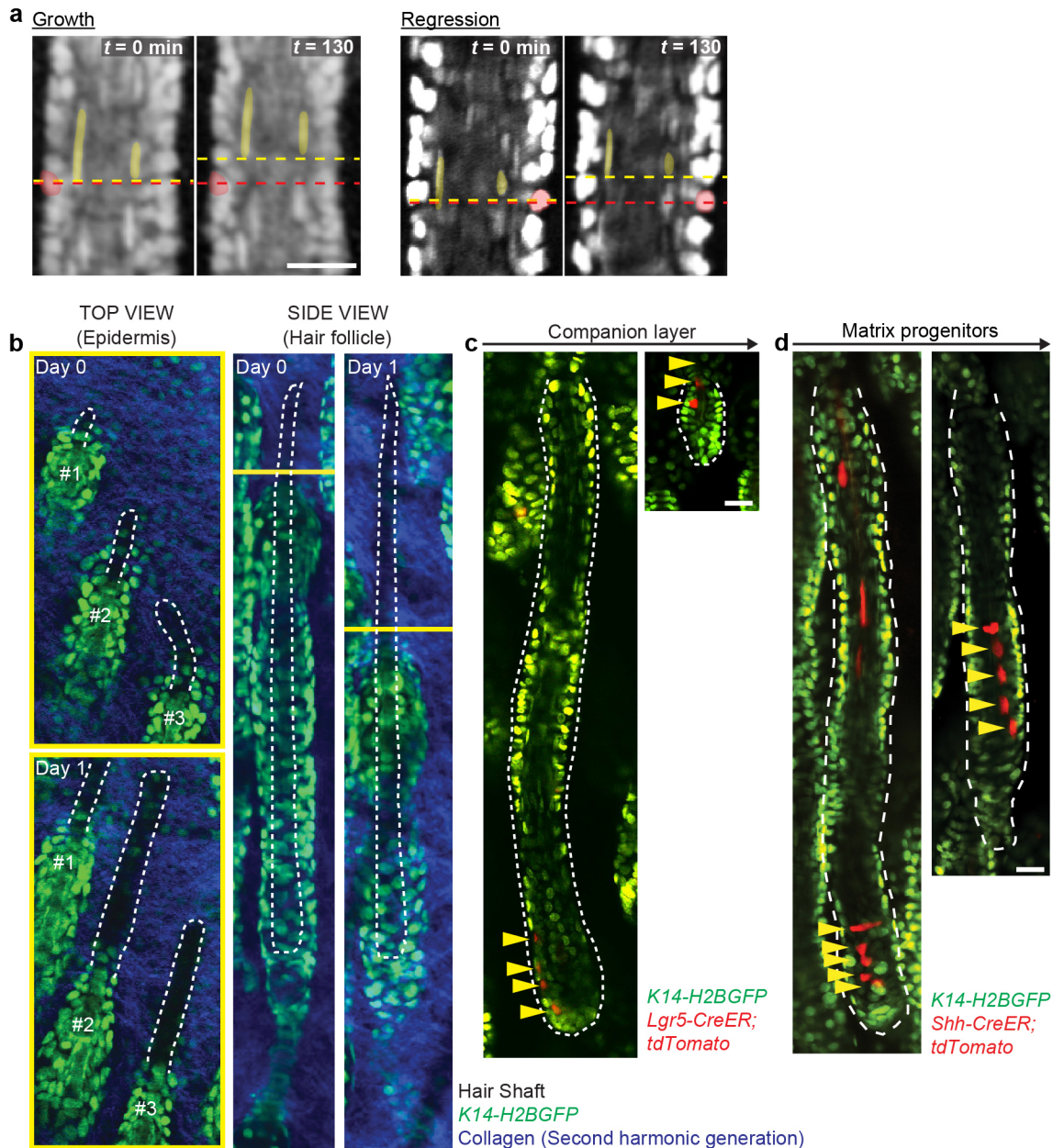
17. Tumber, T. *et al.* Defining the epithelial stem cell niche in skin. *Science* **303**, 359–363 (2004).
18. Rendl, M., Lewis, L. & Fuchs, E. Molecular dissection of mesenchymal–epithelial interactions in the hair follicle. *PLoS Biol.* **3**, e331 (2005).
19. Vaezi, A., Bauer, C., Vasioukhin, V. & Fuchs, E. Actin cable dynamics and Rho/Rock orchestrate a polarized cytoskeletal architecture in the early steps of assembling a stratified epithelium. *Dev. Cell* **3**, 367–381 (2002).
20. Harada, N. *et al.* Intestinal polyposis in mice with a dominant stable mutation of the β -catenin gene. *EMBO J.* **18**, 5931–5942 (1999).

21. Barker, N. *et al.* Identification of stem cells in small intestine and colon by marker gene *Lgr5*. *Nature* **449**, 1003–1007 (2007).
22. Harfe, B. D. *et al.* Evidence for an expansion-based temporal Shh gradient in specifying vertebrate digit identities. *Cell* **118**, 517–528 (2004).
23. Clausen, B. E., Burkhardt, C., Reith, W., Renkawitz, R. & Förster, I. Conditional gene targeting in macrophages and granulocytes using LysMcre mice. *Transgenic Res.* **8**, 265–277 (1999).
24. Jung, S. *et al.* Analysis of fractalkine receptor CX3CR1 function by targeted deletion and green fluorescent protein reporter gene insertion. *Mol. Cell. Biol.* **20**, 4106–4114 (2000).
25. Madisen, L. *et al.* A robust and high-throughput Cre reporting and characterization system for the whole mouse brain. *Nature Neurosci.* **13**, 133–140 (2010).
26. Zito, G. *et al.* Spontaneous tumour regression in keratoacanthomas is driven by Wnt/retinoic acid signalling cross-talk. *Nature Commun.* **5**, 3543 (2014).
27. Greco, V. *et al.* A two-step mechanism for stem cell activation during hair regeneration. *Cell Stem Cell* **4**, 155–169 (2009).
28. Clavel, C. *et al.* Sox2 in the dermal papilla niche controls hair growth by fine-tuning BMP signaling in differentiating hair shaft progenitors. *Dev. Cell* **23**, 981–994 (2012).



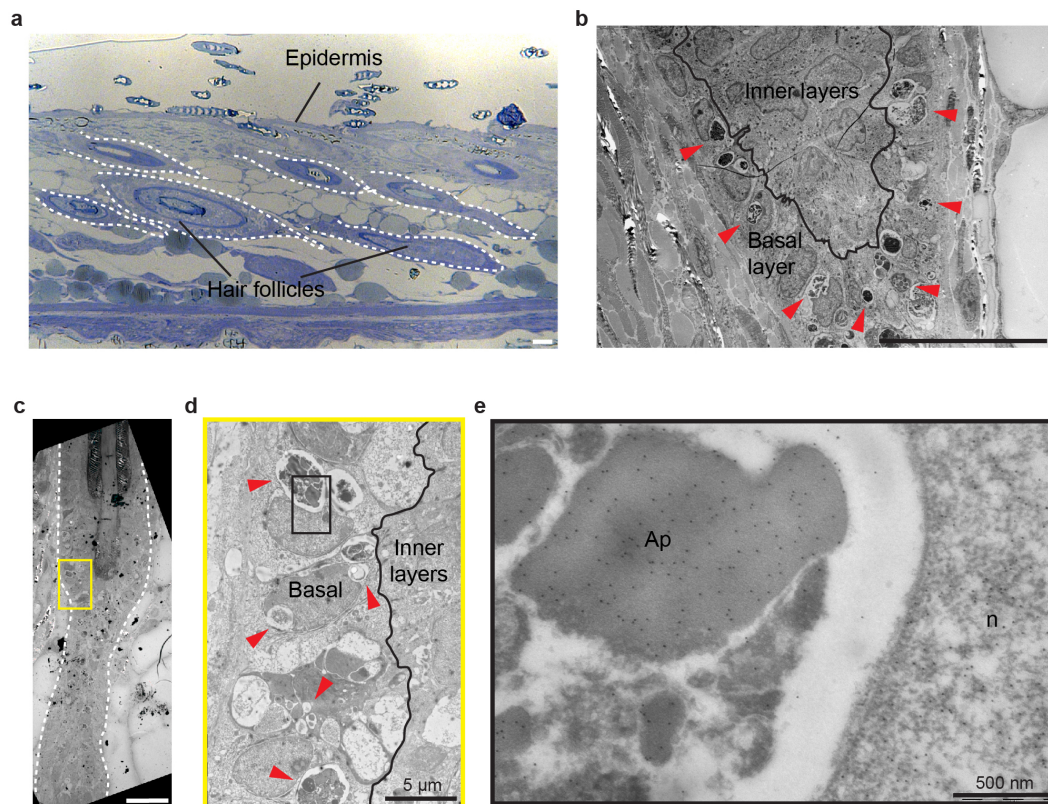
Extended Data Figure 1 | Hair follicle regeneration cycle. Hair follicle growth (Anagen) is characterized by downward expansion and generation of several epithelial layers. The most external layer, the outer root sheath (ORS), consists of relatively undifferentiated basal epithelial cells. Inner layers are generated by a committed progenitor pool, the matrix, which gives rise to

several differentiated layers including: companion layer, inner root sheath (IRS) and hair shaft. After growth, the majority of the newly formed layers are lost during the regression phase (Catagen), leaving a small surviving fraction of cells that reconstitute a new stem cell/progeny (Bulge/Hair Germ) compartment at the rest phase (Telogen).



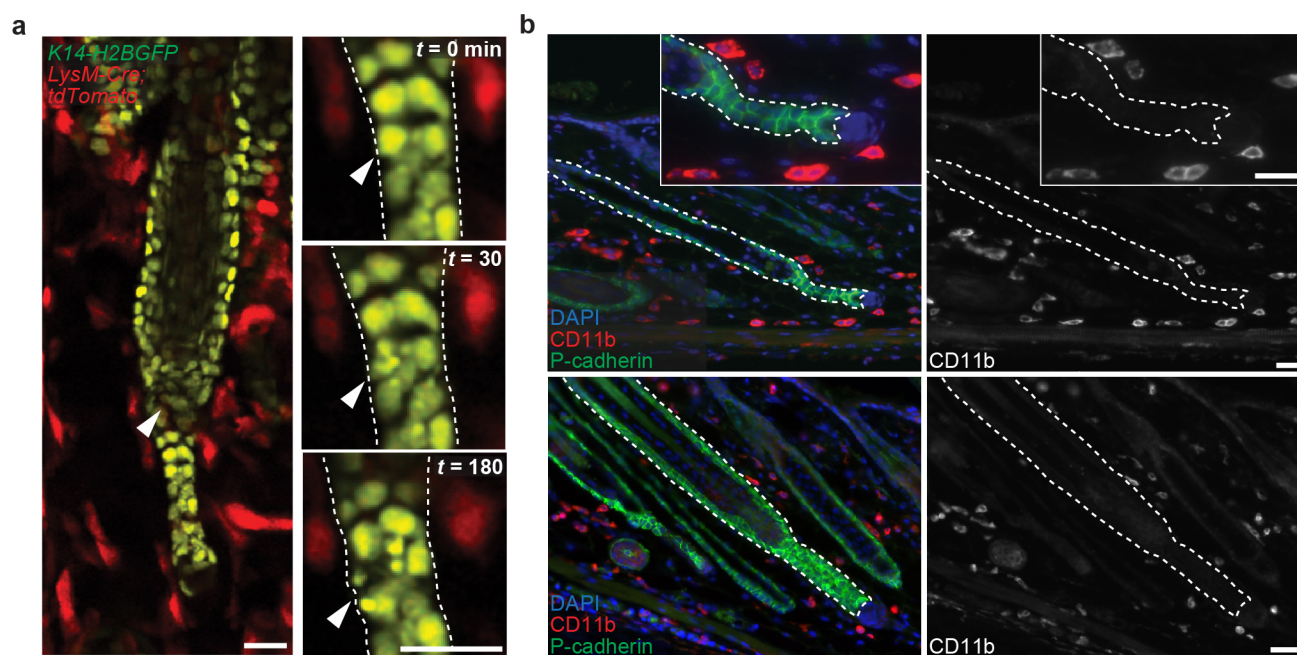
Extended Data Figure 2 | Hair follicle inner layers resist apoptosis and continue upward terminal differentiation. **a**, Upward movement of hair follicle inner layers during growth and regression. Single optical sections show upward collective movement of inner layers relative to surrounding basal cells at two time points 130 min apart. Compare the position of labelled cells and dashed line of basal (red) to inner layers (yellow). **b**, Upward movement of hair shaft during regression. Optical sections of top view (epidermis) and side view (hair follicle) at two time points, 1 day apart. Note the extrusion of

hair shafts from regressing hair follicles. Observations shown represent $n = 3$ mice. **c**, Companion layer lineage tracing during regression. Representative example of matrix progenitors of the companion layer traced during regression in *Lgr5-CreER;tdTomato;K14-H2BGFP* mice ($n = 20$ or 7 lineages, in 4 mice). **d**, Terminal differentiation of inner layer progenitor cells. Representative example of single-cell lineages ($n = 35$ or 9 lineages, in 3 mice) traced during the initial transition of hair follicle growth to regression in *Shh-CreER;tdTomato;K14-H2BGFP* mice. Scale bars, 25 μm .



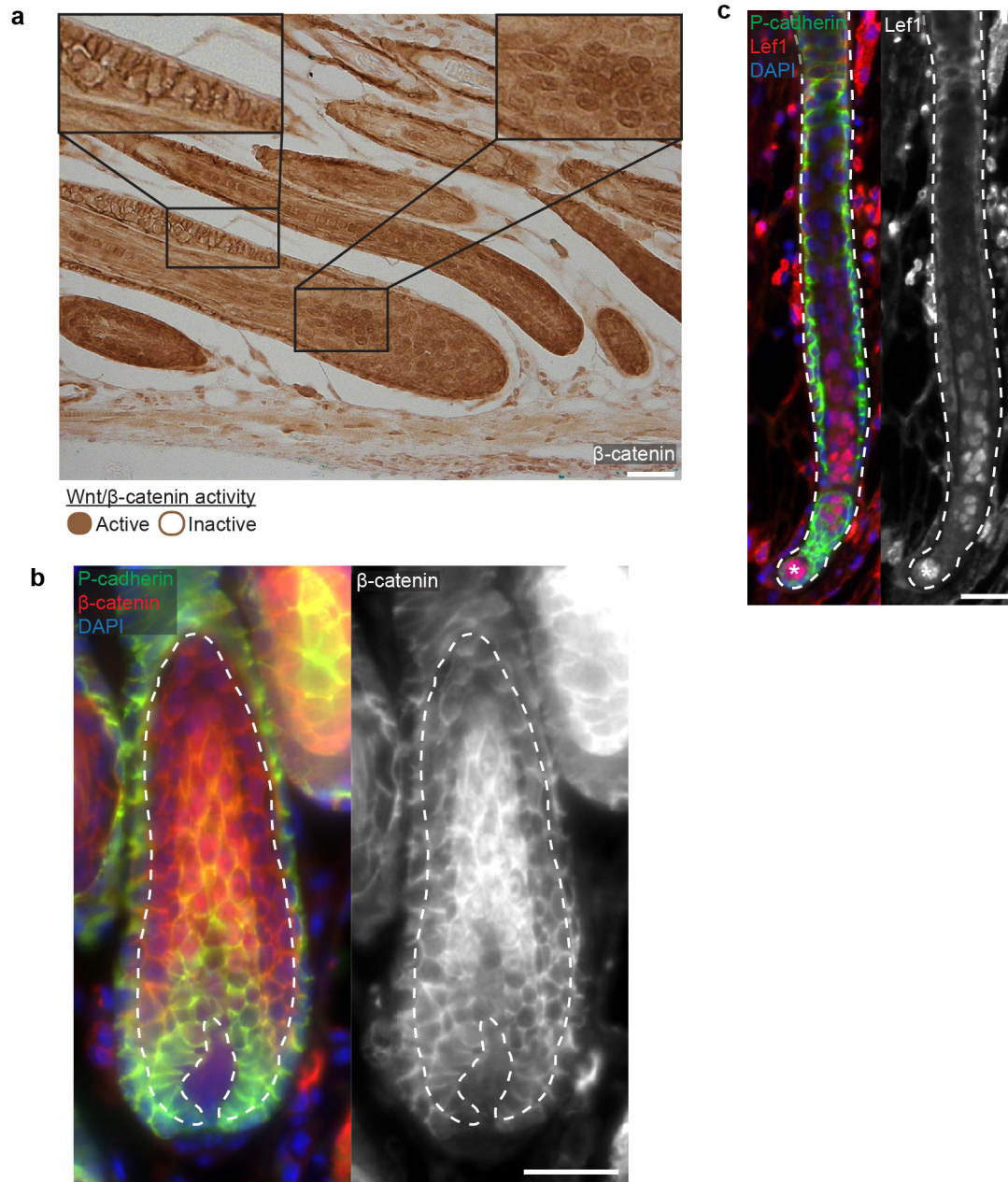
Extended Data Figure 3 | Apoptotic bodies are cleared by neighbouring basal epithelial cells. **a**, Toluidine-blue-stained section of regressing hair follicles used for ultrastructure analysis. **b**, Electron micrograph illustrating multiple apoptotic bodies (red arrowheads) present in hair follicle basal epithelium, but absent in inner layers. **c**, Electron micrograph showing a hair follicle in regression (white dashed line). **d**, Electron micrograph showing the

restriction of apoptotic bodies (red arrowheads) and phagocytic activity to the basal epithelium. **e**, High-magnification electron micrograph with immunogold labelling for GFP protein expressed by *K14-H2BGFP*⁺ cells. Positive GFP labelling is present in both apoptotic bodies (Ap) and phagocytic basal epithelial nuclei (n). Observations shown represent $n = 2$ mice. Scale bars, 25 μm unless otherwise indicated.



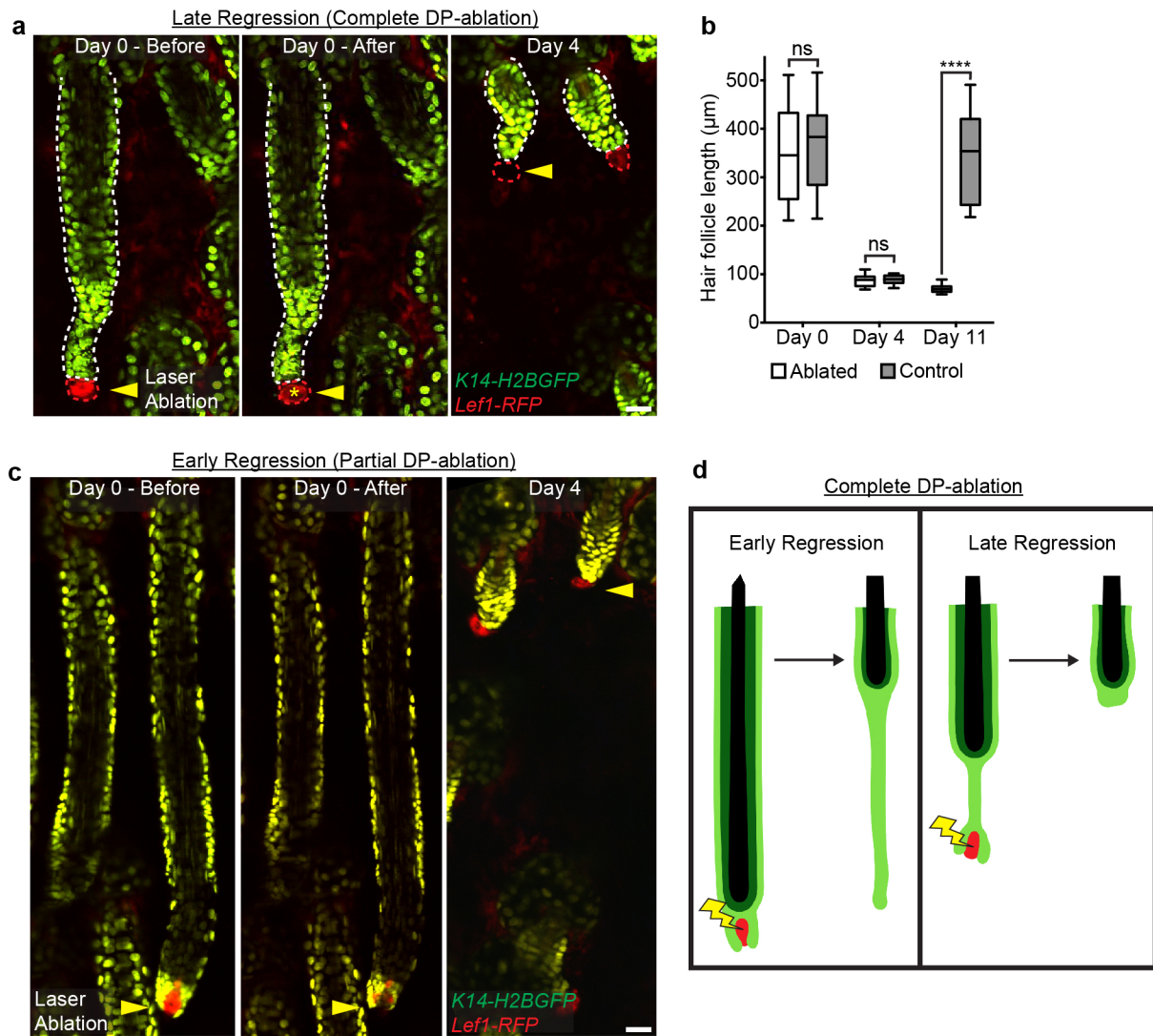
Extended Data Figure 4 | Professional phagocytes are not present in regressing hair follicles. **a**, Professional phagocytes do not enter regressing hair follicles. Single optical sections showing absence of myeloid populations inside the hair follicle 2.5 h after epithelial cell death (arrowhead) in

LysM-Cre;tdTomato;K14-H2BGFP mice. **b**, Immunofluorescent staining of myeloid populations in skin during hair follicle regression. DAPI, blue; CD11b, red; P-cadherin, green. Observations shown represent $n = 4$ mice. Scale bar, 25 μm .



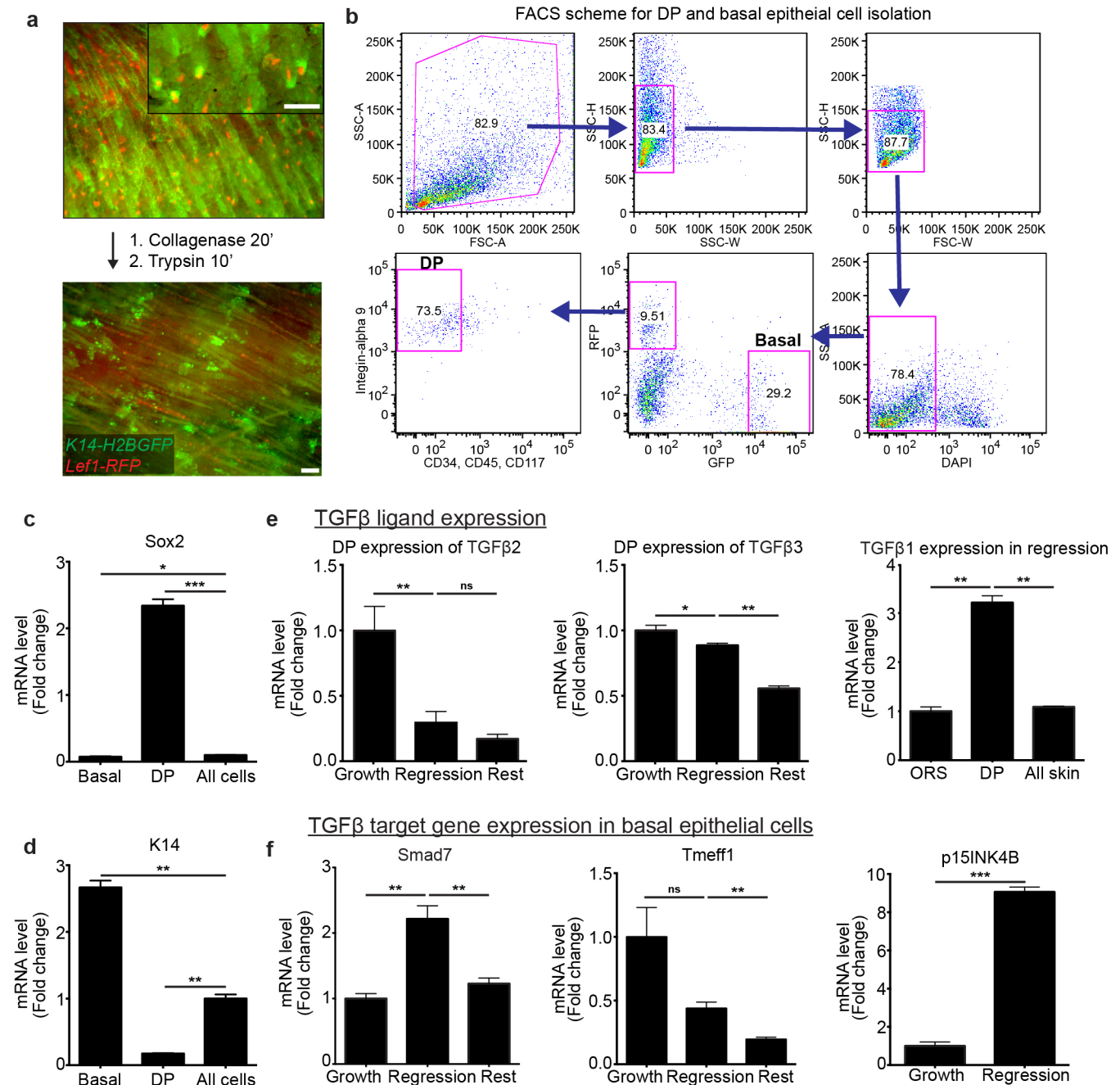
Extended Data Figure 5 | Wnt/β-catenin activity is restricted to the inner layers during regression. a, b, Immunohistochemistry (a) and immunofluorescent (b) staining highlighting active (nuclear) β-catenin of hair follicle inner layers (dashed line) at the onset of regression.

c, Immunofluorescent staining of the Wnt/β-catenin target gene, *Lef1*, during hair follicle regression. DAPI, blue; *Lef1*, red; P-cadherin, green. Asterisk indicates mesenchymal dermal papilla. Observations shown represent $n = 2$ mice. Scale bars, 50 μm.



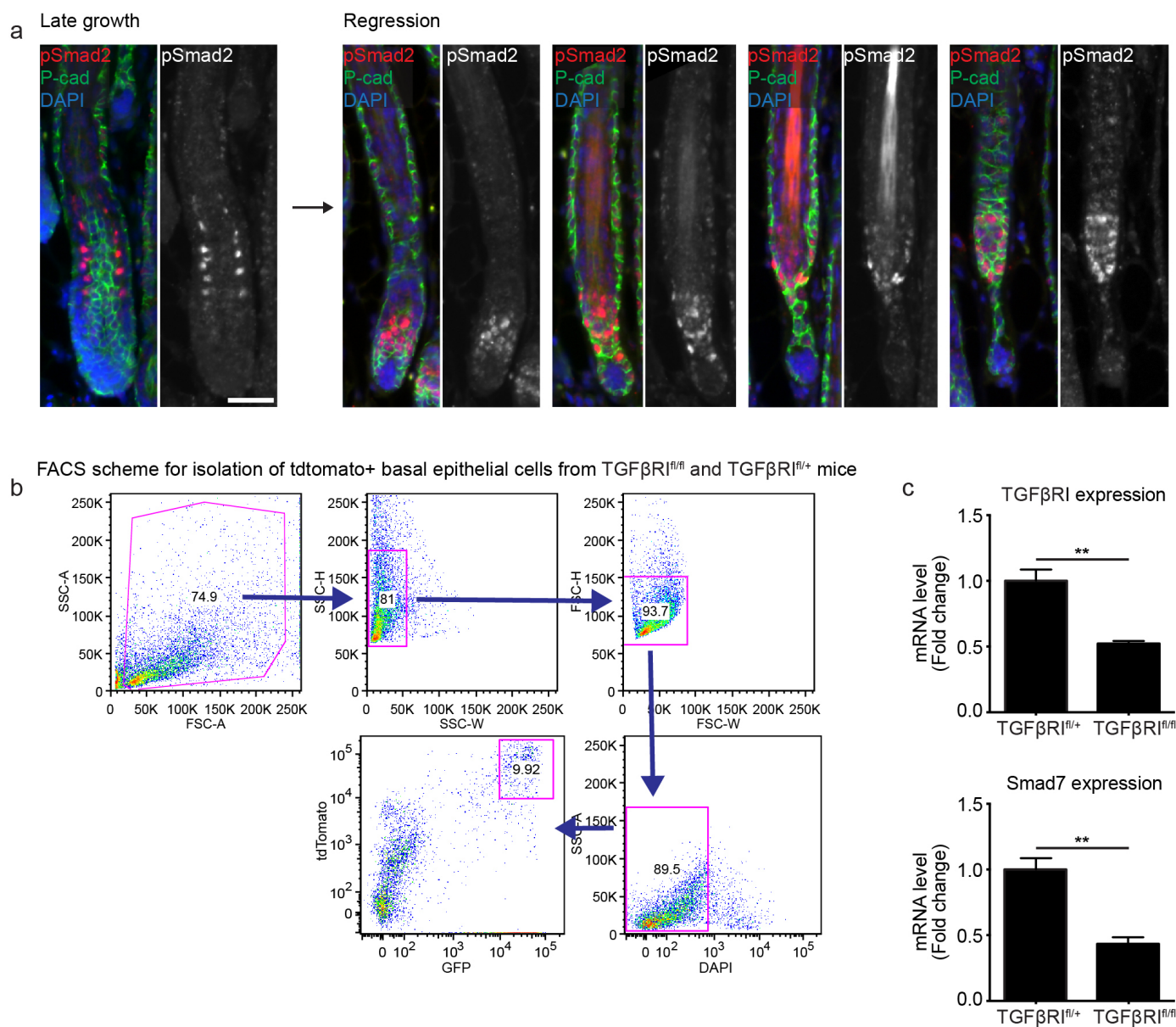
Extended Data Figure 6 | Late and partial mesenchymal dermal papilla removal does not affect hair follicle regression. **a**, Sequential revisits of hair follicles after dermal papilla (DP) ablation during late regression. **b**, Box plot quantification of hair follicle length immediately after ablation, 4 days and 11 days after dermal papilla ablation ($n = 20$ follicles, in 4 mice; error bars represent maximum and minimum). **c**, Sequential revisits of hair follicles after partial dermal papilla ablation during early regression ($n = 12$ follicles,

in 3 mice). **d**, Schematic illustration of the results from mesenchymal dermal papilla ablation experiments. Dermal papilla ablation during early regression results in failed elimination of the basal epithelium, while the inner layers continue upward in terminal differentiation, yet dermal papilla ablation during late regression does not impair hair follicle regression. Asterisk indicates auto-fluorescence from the two-photon laser. NS, not significant; $P < 0.05$, mean \pm s.d. Scale bars, 25 μm .



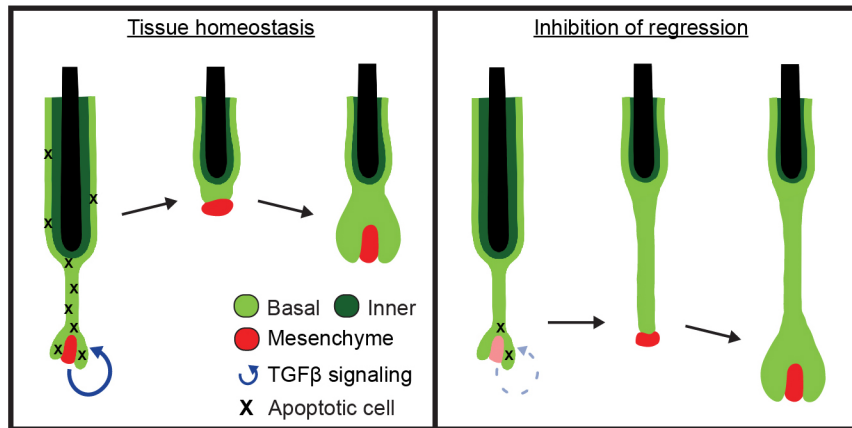
Extended Data Figure 7 | Characterization of TGF-β pathway in mesenchymal dermal papilla and basal epithelial cell populations during regression. **a**, Schematic of skin digestion and cell isolation with representative images before and after tissue digestion in *K14-H2BGFP;Lef1-RFP* mice. **b**, Representative fluorescent-activated cell sorting (FACS) scheme for isolating mesenchymal dermal papilla (DP; RFP⁺, CD34⁺, CD45⁺, CD117⁺, integrin-α9⁺) and enriched hair follicle basal epithelium (RFP⁻, GFP^{High}) cells. **c**, Validation of mesenchymal dermal-papilla-sorted population enrichment by

Sox2 expression. **d**, Validation of basal-epithelial-sorted population enrichment by keratin 14 (K14) expression. **e**, TGF-β ligand 2 and 3 expression in the mesenchymal dermal papilla throughout the hair cycle. TGF-β1 expression in basal epithelium, mesenchymal dermal papilla, and all sorted cells during regression. **f**, Differential expression of TGF-β target genes: *Smad7*, *Tmeff1*, *p15INK4B* (also known as *Cdkn2b*) and in the hair follicle basal epithelium throughout the hair cycle (mean ± s.d.; *n* = 3 technical replicates). Scale bars, 100 μm. **P* < 0.05, ***P* < 0.01, ****P* < 0.001.



Extended Data Figure 8 | Local TGF- β activation during regression and validation of Cre-induced loss of TGF- β R1 expression. **a**, TGF- β activation shown by immunofluorescent staining of pSmad2 during the transition from hair follicle growth to regression. DAPI, blue; pSmad2, red; P-cadherin, green. Observations shown represent $n = 4$ mice. **b**, Representative FACS

scheme for isolating tdTomato-Cre-reporter-positive basal epithelial cells (tdTomato⁺, GFP^{High}) from *Tgfbri^{fl/fl}* and *Tgfbri^{fl/+}* mice. **c**, Expression of TGF- β R1 and the TGF- β target gene, *Smad7*, in Cre-recombined basal epithelial cells from *Tgfbri^{fl/fl}* and *Tgfbri^{fl/+}* mice ($P < 0.01$, mean \pm s.d.; $n = 3$ technical replicates). Scale bar, 50 μ m.



Extended Data Figure 9 | Extrinsic induction of hair follicle regression dictates the regenerative (stem cell) pool. Crosstalk with the mesenchymal niche during regression results in localized TGF- β activation, promoting a spatially restricted gradient of cell death in the basal epithelium. Clearance of

apoptotic cells by neighbouring basal epithelial cells results in a limited pool of surviving stem cells. Inhibition of this regression process results in excessive amounts of basal epithelial cells capable of fuelling a new round of growth when in contact with the mesenchymal dermal papilla.

Disruption of DNA-methylation-dependent long gene repression in Rett syndrome

Harrison W. Gabel^{1*}, Benyam Kinde^{1*}, Hume Stroud¹, Caitlin S. Gilbert¹, David A. Harmin¹, Nathaniel R. Kastan¹, Martin Hemberg^{2†}, Daniel H. Ebert¹ & Michael E. Greenberg¹

Disruption of the *MECP2* gene leads to Rett syndrome (RTT), a severe neurological disorder with features of autism¹. *MECP2* encodes a methyl-DNA-binding protein² that has been proposed to function as a transcriptional repressor, but despite numerous mouse studies examining neuronal gene expression in *Mecp2* mutants, no clear model has emerged for how MeCP2 protein regulates transcription^{3–9}. Here we identify a genome-wide length-dependent increase in gene expression in MeCP2 mutant mouse models and human RTT brains. We present evidence that MeCP2 represses gene expression by binding to methylated CA sites within long genes, and that in neurons lacking MeCP2, decreasing the expression of long genes attenuates RTT-associated cellular deficits. In addition, we find that long genes as a population are enriched for neuronal functions and selectively expressed in the brain. These findings suggest that mutations in MeCP2 may cause neurological dysfunction by specifically disrupting long gene expression in the brain.

To identify common features of genes whose expression is misregulated in RTT, we surveyed gene expression data sets from studies of *Mecp2* mutant mice, asking if genes that are misregulated when MeCP2 function is disrupted have anything in common with respect to histone modifications, mRNA expression, sequence composition or gene length. No common features were identified for genes that are downregulated when MeCP2 function is disrupted; however, we found that genes that are upregulated in the *Mecp2* knockout brains are significantly longer than the genome-wide average (Fig. 1a). The extreme length of the genes upregulated in MeCP2 knockout brains is apparent in multiple studies performed by different laboratories^{5–9} (Supplementary Table 1). The misexpression of long genes is a specific feature of the RTT brain, as gene sets identified as misregulated in 16 different mouse models of neurological dysfunction and disease did not display similarly long length (Extended Data Fig. 1).

To determine whether the extent of gene misregulation in *Mecp2* mutant mice is directly correlated with gene length, we interrogated published microarray data sets of gene expression and plotted mRNA fold-change (MeCP2 knockout compared to wild type) versus gene length¹⁰. We found widespread length-dependent misregulation of gene expression in MeCP2 knockout brains, with the longest genes in the genome displaying the highest level of upregulation relative to shorter genes, which show a reduction or no change in gene expression (Fig. 1b, c and Extended Data Fig. 1). Consistent with previous studies, the magnitude of the length-dependent gene misregulation in the absence of MeCP2 is small, but widespread (affecting genes across the continuum of gene lengths) and reproducibly detected (Fig. 1b and Extended Data Fig. 1). Importantly, length-dependent gene misregulation in the MeCP2 knockout is not an artefact of the method of gene expression analysis used, as this effect was detected using a variety of methodologies including microarrays, total RNA-seq, quantitative PCR, and non-amplification-based nCounter analysis (Fig. 1b, c and Extended Data Fig. 1 and Supplementary

Discussion). Furthermore, these observations are corroborated by the recent finding¹¹ that long genes are upregulated in specific neuronal cell types when MeCP2 function is disrupted.

Additional copies of *MECP2* cause neurological impairment in humans (MeCP2-duplication syndrome) and in transgenic mice^{12,13}. We find that overexpression of MeCP2 in mice leads to the downregulation of long genes in the brain^{5–7} (Fig. 1b and Extended Data Fig. 1). This further suggests that MeCP2 directly represses transcription in a length-dependent manner.

We next investigated if the length-dependent changes in gene expression correlate with the onset and severity of RTT pathology. We found that misregulation of long gene expression in the brain of MeCP2 knockout mice is more striking at nine weeks of age than at four weeks of age⁸, thus correlating with disease progression (Extended Data Fig. 2). In addition, when comparing two disease-causing MeCP2 mutations (MeCP2(R270X) and MeCP2(G273X)) that differ in the rate and severity with which they cause disease, we find that the magnitude of length-dependent gene misregulation correlates with the severity of RTT phenotypes⁸ (Extended Data Fig. 2 and Supplementary Discussion). Furthermore, we find by microarray, nCounter and qRT-PCR analysis that a subtle missense mutation of MeCP2 (Arg 306 to Cys, R306C) that causes RTT in humans and disrupts the interaction of MeCP2 with the NCoR co-repressor complex¹⁴ leads to length-dependent gene upregulation in the mouse brain (Extended Data Fig. 1). Finally, we detect length-dependent gene upregulation in cultured human neurons derived from embryonic stem cells lacking MECP2 (ref. 15) and the cortex of humans with RTT¹⁶ (Fig. 1d and Extended Data Fig. 2 and Supplementary Discussion). The close correlation between the occurrence of length-dependent gene misregulation and RTT-associated phenotypes across mice and humans suggests that this misregulation contributes to RTT pathology.

To characterize the mechanism by which MeCP2 tempers the expression of long genes, we asked if the binding of MeCP2 to methylated DNA is important for this process. MeCP2 was identified based on its high affinity for methylated cytosine in the context of a CpG dinucleotide (mCG)¹⁷. In addition to binding mCG, MeCP2 has been suggested to bind two additional forms of methylated DNA that are enriched in the brain, hydroxymethylcytosine (hmCG)¹⁸ and methylated cytosine followed by a nucleotide other than guanine (mCH, where H = A or T or C)¹⁹. Notably, the frequency of hmCG and mCH in the neuronal genome increases significantly during the same postnatal period in which the level of MeCP2 protein markedly increases^{20–24}. This suggests that as neurons mature, MeCP2 could function by binding to hmCG and/or mCH marks. Using a DNA electrophoretic mobility shift assay (EMSA) we assessed the binding of MeCP2 to various forms of methylated DNA. Consistent with previous studies, we find that MeCP2 shows high affinity for DNA containing mCG but not hmCG, suggesting that MeCP2 may not bind preferentially to hmCG in neurons (Fig. 2a,

¹Department of Neurobiology, Harvard Medical School, Boston, Massachusetts 02115, USA. ²Department of Ophthalmology, Children's Hospital Boston, Center for Brain Science and Swartz Center for Theoretical Neuroscience, Harvard University, 300 Longwood Avenue, Boston, Massachusetts 02115, USA. [†]Present address: Computational Genomics Programme, Wellcome Trust Sanger Institute, Wellcome Trust Genome Campus, Hinxton, Cambridge CB10 1SA, UK.

*These authors contributed equally to this work.

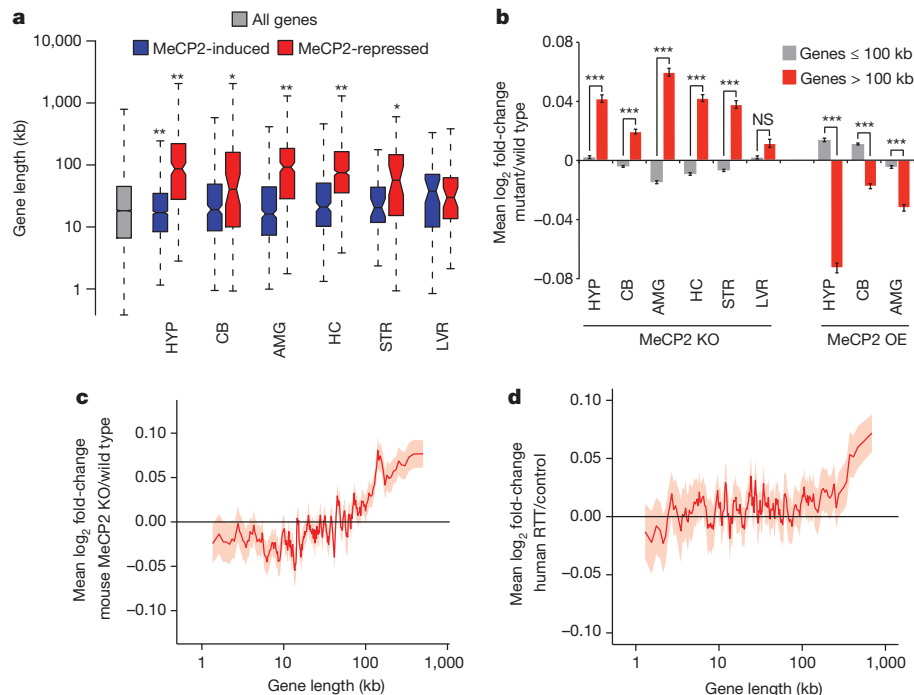


Figure 1 | Length-dependent gene misregulation in *Mecp2* mutant mice and human RTT brain. **a**, Boxplots (showing the median (line), second to third quartiles (box), $1.5\times$ the interquartile range (whiskers), and $1.58\times$ the interquartile range/ \sqrt{n} number of genes) of gene lengths (RefSeq transcription start site to termination site) for genes detected as misregulated in independent studies of *Mecp2* mutant mice. HYP, hypothalamus⁵; CB, cerebellum⁶; AMG, amygdala⁷; HC, hippocampus⁸; STR, striatum⁹; LVR, liver⁹. MeCP2-induced (blue), genes downregulated in MeCP2 knockout (MeCP2 KO) and upregulated in MeCP2 overexpression (MeCP2 OE) mice. MeCP2-repressed (red), genes upregulated in MeCP2 KO and downregulated in MeCP2 OE (see Methods). **b**, Mean expression changes across brain regions

and liver of *Mecp2* mutant mice for genes ≤ 100 kb (grey) and >100 kb (red) (see Methods and Supplementary Table 1 for sample sizes and other details). **c**, **d**, Genome-wide changes in gene expression assessed by RNA-seq analysis of mouse cortical tissue from MeCP2 KO ($n = 3$) compared to wild type ($n = 3$) (c) or microarray analysis of human RTT brain samples ($n = 3$) compared to age-matched controls ($n = 3$)¹⁶ (d). In **c**, **d** lines represent mean fold-change in expression for genes binned according to gene length (200 gene bins, 40 gene step; see Methods); the ribbon is the s.e.m. of each bin. * $P < 0.05$; ** $P < 0.01$; *** $P < 1 \times 10^{-10}$, NS, not significant $P \geq 0.05$; one-sample (a) or two sample (b) *t*-test, Bonferroni correction. Error bars represent s.e.m.

Extended Data Fig. 3 and Supplementary Discussion). By contrast, MeCP2 binds to mCA, hmCA and mCG with relatively high affinity, but binds to mCC and mCT with low affinity similar to that of unmethylated DNA. This selective, tight binding of MeCP2 to mCG, mCA and hmCA suggests that MeCP2 may regulate long gene expression in the brain by binding to these sites. We note that thin-layer chromatography and Tet-assisted bisulfite sequencing (TAB-seq) analysis suggest that hmCA is very rare in the brain^{21,24}. Therefore, in our subsequent investigation of MeCP2 binding to CA sequences *in vivo* we focused our analysis on mCA. However, at genomic sites where CA sequences are hydroxymethylated, MeCP2 might also be predicted to bind and regulate gene expression (see Supplementary Discussion).

To examine whether MeCP2 binds mCA in the brain, we performed chromatin immunoprecipitation sequencing analysis (ChIP-seq) of MeCP2, comparing the MeCP2 binding profile across the genome to base-pair resolution DNA methylation data (see Methods)²⁴. As previously reported^{20,25}, we find that MeCP2 binds broadly across the genome. Nevertheless, within the context of this broad binding, we detect a relative enrichment of MeCP2 at gene bodies that have a high level of mCA (level = (h) mCN/CN within the gene, see Methods), and a depletion of MeCP2 binding at gene bodies where the level of hmCG is high (Extended Data Fig. 4). Notably, long genes (> 100 kb) display a strong relationship between mCA levels and MeCP2 ChIP-seq read density (Fig. 2b and Extended Data Fig. 4). Higher-resolution analysis of MeCP2 ChIP and mCA levels in the frontal cortex revealed increased mCA under sites of local MeCP2 enrichment in the genome, supporting the conclusion that MeCP2 binds to mCA *in vivo* (Extended Data Fig. 4). We note that genes containing the highest level of hmCA are also enriched for the MeCP2 ChIP signal (Extended Data Fig. 4). Therefore,

if owing to limitations of the methods of analysis the amount of hmCA within gene bodies is being underestimated, some of the effects of MeCP2 deletion that are being attributed to MeCP2 binding to mCA might be due to MeCP2 binding to hmCA (see Supplementary Discussion).

To investigate if length-dependent gene repression by MeCP2 requires binding to mCA, we assessed whether there is a correlation between the degree of misregulation of gene expression upon the disruption of MeCP2 function and the levels of DNA methylation within the transcribed regions of genes (see Supplementary Discussion). We noted a trend whereby genes containing high levels of mCA, but not mCG or hmCG, are upregulated in the MeCP2 knockout (Extended Data Figs 5 and 6). We reasoned that if mCA within genes is required for length-dependent repression by MeCP2, long genes containing low levels of mCA should be largely unaffected in the MeCP2 knockout mice. Consistent with this prediction, little to no length-dependent upregulation of gene expression is observed in MeCP2 knockout brain for genes containing low levels of mCA, while long genes with a high density of mCA are significantly upregulated in MeCP2 knockout brains. In addition, we found that the shortest genes in the genome are not upregulated when MeCP2 function is disrupted, even when the average level of mCA within their gene body is relatively high (Fig. 2c and Extended Data Fig. 6). The requirement for the presence of mCA within long genes for the gene to be repressed by MeCP2 is reproducible, as it is detected across three MeCP2 knockout brain regions, in gene expression data from MeCP2(R306C) and MeCP2 overexpressing mice, and in human RTT brain (Fig. 2d and Extended Data Fig. 6). Notably, when we plotted the level of mCA versus gene length, we found that the density of mCA is higher on average in longer genes compared to shorter genes (Extended Data Figs 5 and 6). The enrichment of mCA

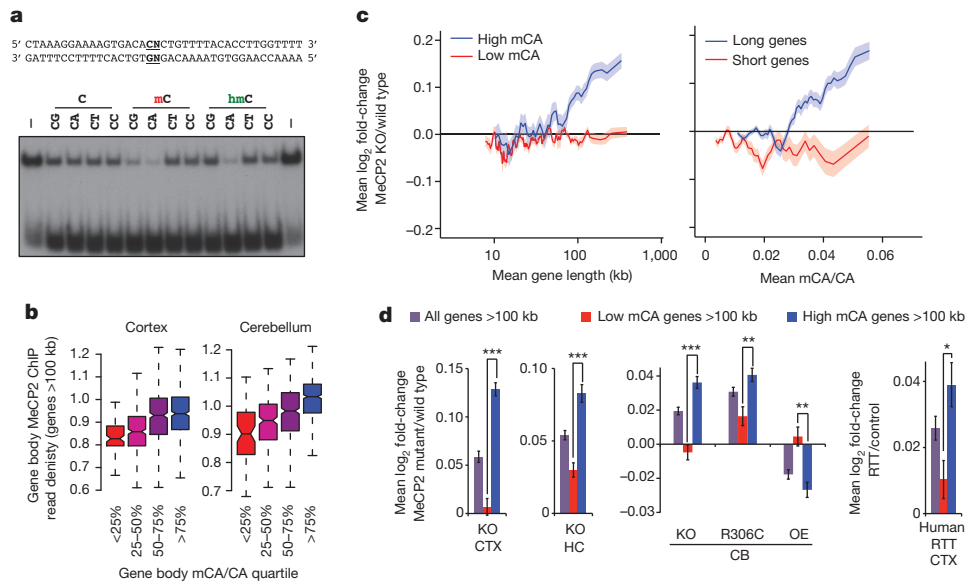


Figure 2 | MeCP2 represses long genes containing high levels of mCA. **a**, EMSA analysis of the MeCP2 methyl-binding domain (amino acids 78–162) binding to 32 P-end-labelled mCA-containing DNA probe incubated with 100-fold excess of unlabelled competitor oligonucleotides containing unmodified, methylated, or hydroxymethylated cytosines at the dinucleotides indicated in bold; no competitor indicated by – symbol (see Methods and Extended Data Fig. 3). **b**, Boxplots of MeCP2 ChIP-seq read density within genes > 100 kb plotted by quartile of mCA/CA in the cortex and cerebellum. **c**, Mean fold-change in gene expression binned according to gene length in MeCP2 knockout cortical tissue for genes with high (mCA/CA > 0.034 , top 25%) and low (mCA/CA < 0.031 , bottom 66%) mCA levels (left), or binned according to gene-body mCA/CA levels for long (> 62 kb, top 25%) and short

(< 16.8 kb, shortest 25%) genes (right). Lines represent mean fold-change in expression for each bin (200 gene bins, 40 gene step), and the ribbon is s.e.m. of each bin. $n = 3$ per genotype. **d**, Bar plots of the mean fold-change in expression for all genes > 100 kb compared to subsets of genes > 100 kb containing low mCA (bottom 50% mCA/CA) or high mCA (top 25% mCA/CA) within their gene body. Values shown for mice with the indicated *MeCP2* genotypes (left) and human RTT brain (right). CTX, Cortex; HC, Hippocampus; CB, cerebellum; KO, MeCP2 knockout; OE, MeCP2 overexpression; R306C, MeCP2 arginine 306 to cysteine missense mutation; $***P < 1 \times 10^{-10}$; $**P < 1 \times 10^{-5}$; $*P < 0.01$; two-tailed *t*-test, Bonferroni correction. Error bars represent s.e.m. See Supplementary Table 1 for sample size and other details.

within long genes may explain why most of these genes are repressed by MeCP2 and upregulated in the MeCP2 knockout.

To test further whether MeCP2 tempers long gene transcription by binding to mCA within genes, we asked if elimination of mCA in the brain has an effect on gene expression that is similar to that observed in the MeCP2 knockout. Recent evidence suggests that Dnmt3a is the enzyme that catalyses the deposition of mCA in maturing neurons^{19,24}. We therefore conditionally disrupted the *Dnmt3a* gene²⁶ in the brain to block the accumulation of mCA (*Nestin-Cre; Dnmt3a^{fl/fl}* mice, designated Dnmt3a cKO, Extended Data Fig. 7 and Supplementary Discussion). Bisulfite sequencing of cerebellum DNA indicated that methylation of DNA at CA, but not CG, is eliminated from the genome in the Dnmt3a conditional knockout (Fig. 3a). Microarray analysis of cerebella from Dnmt3a conditional knockout mice revealed a length- and mCA-dependent upregulation of gene expression that is similar to the gene

misregulation detected in MeCP2 knockout mice (Fig. 3b and Extended Data Fig. 8). While the deletion of Dnmt3a also leads to a decrease in methylation at CT and CC, given that MeCP2 selectively binds to mCA *in vitro*, we conclude that reduction of mCA within gene bodies in the Dnmt3a conditional knockout probably disrupts length-dependent gene repression by MeCP2. Taken together, these findings support a model in which Dnmt3a catalyses the methylation of CA in the neuronal genome. MeCP2 then binds to these sites within the transcribed regions of genes to restrain transcription in a length-dependent manner.

To characterize how the misregulation of long gene expression contributes to RTT pathology, we identified a representative set of genes that is consistently misregulated in multiple gene expression data sets when MeCP2 function is perturbed. Combined analysis of microarray studies across multiple brain regions identified 466 MeCP2-repressed genes whose expression is consistently upregulated in MeCP2 knockout

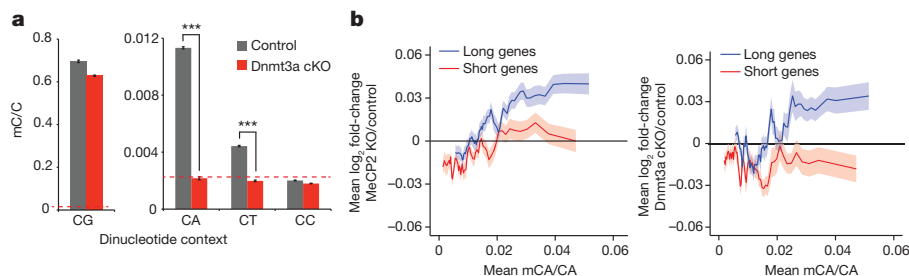


Figure 3 | Disruption of Dnmt3a in the brain leads to length-dependent upregulation of genes containing high levels of mCA. **a**, Summary of genome-wide bisulfite-sequencing analysis of mCN (where N = G, A, T or C) in control and Dnmt3a cKO cerebella ($n = 2$ per genotype). Dashed line represents mean background non-conversion rate of the bisulfite-seq assay (see Methods). **b**, Mean fold-change in gene expression versus gene-body mCA for MeCP2 KO (left) or Dnmt3a cKO (right) cerebella. Long (top 25%, > 60 kb)

and short (bottom 25%, < 14.9 kb) genes were binned according to gene-body mCA/CA levels. Lines represent mean fold-change in expression for each bin (200 gene bins, 40 gene step), and the ribbon is s.e.m. of genes within each bin. $***P < 0.005$; two-tailed *t*-test, Bonferroni correction. Error bars represent s.e.m. $n = 5$ per genotype for MeCP2 KO, $n = 3$ per genotype for Dnmt3a cKO.

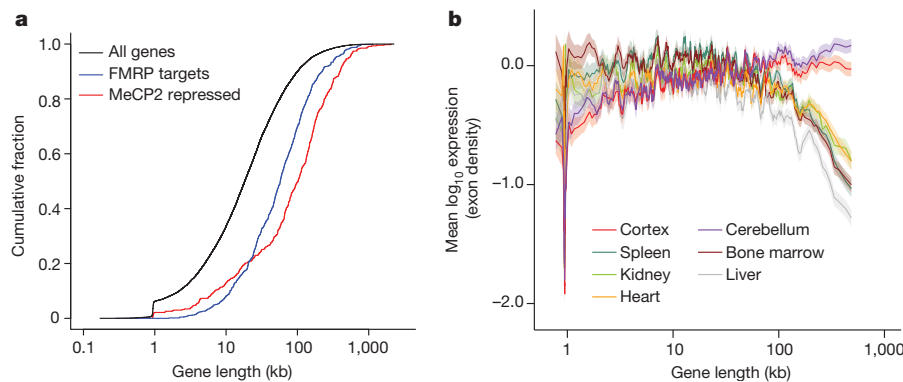


Figure 4 | Analysis of long gene expression and regulation in the brain. **a**, Cumulative distribution function of gene lengths for all genes in the genome (black), MeCP2-repressed genes (red), and genes encoding putative FMRP target mRNAs²⁹ (blue); $P < 1 \times 10^{-15}$ for each gene set versus all genes,

mice and downregulated in MeCP2 overexpressing mice (Supplementary Discussion and Supplementary Table 3). Consistent with the conclusion that MeCP2-repressed genes are targets of gene-length- and mCA-dependent repression, these genes are exceptionally long and are enriched for mCA (Fig. 4a and Extended Data Fig. 8). Disruption of the expression of this gene set is specific to RTT, as these genes were not misregulated in data sets obtained from six other mouse models of neurological dysfunction (Extended Data Fig. 8).

We examined the functional annotations of the 466 MeCP2-repressed genes to gain insight into how their disruption might contribute to RTT pathology. Many of these MeCP2-repressed genes encode proteins that modulate neuronal physiology (for example, calcium/calmodulin-dependent kinase *Camk2d* and the voltage-gated potassium channel *Kcnh7*). In addition, multiple genes involved in axon guidance and synapse formation were identified, including *Epha7*, *Sdk1* and *Cntn4* (Extended Data Fig. 8). Consistent with these observations, gene ontology analysis of MeCP2-repressed genes indicates that they are enriched for annotated neuronal functions (for example, post-synaptic density, axonogenesis, voltage-gated cation channel activity; Extended Data Table 1). These findings suggest that RTT results from a subtle, yet widespread overexpression of long genes that have specific functions in the nervous system.

We next considered why the misregulation of long genes as a population in RTT leads specifically to neuronal dysfunction. Many genes with neuronal function are very long^{27,28}, raising the possibility that long genes as a population might be enriched for functions in the nervous system relative to other tissues. If so, the high level of mCA and MeCP2 in neurons may have evolved to temper the expression of long genes specifically in the brain. Indeed, gene ontology analysis of all genes in the genome above 100 kb indicates that the longest genes in the genome are enriched for neuronal annotations (Extended Data Table 1). Moreover, by examining tissue-specific gene expression data sets, we find that long genes as a population are preferentially expressed in mouse and human brain relative to other tissues (Fig. 4b and Extended Data Fig. 9). We note that while long genes typically have brain-specific function and expression, brain-specific expression is not a prerequisite for regulation of long genes by MeCP2 in neurons: some long genes are ubiquitously expressed but selectively repressed by MeCP2 in the brain. (Extended Data Fig. 8 and Supplementary Discussion).

To explore if disruption of proteins that regulate long gene expression may broadly contribute to autism spectrum disorders (ASDs), we asked if a similar misregulation of gene expression occurs in a prominent ASD, fragile X syndrome (FXS). FXS is caused by inactivation of FMRP, a protein that represses mRNA translation in neurons²⁹. Strikingly, we find that FMRP-target mRNAs and the genes that encode them are significantly longer than the genome average²⁹ (Fig. 4a, Extended

two-sample Kolmogorov–Smirnov test. **b**, Mean expression of genes binned according to length in mouse for neural and non-neural tissues. Line indicates mean expression for genes within each bin (200 gene bins, 40 gene step); the ribbon represents the s.e.m. of each bin.

Data Fig. 8 and Supplementary Discussion). Moreover, we detect significant overlap between MeCP2-repressed genes and genes encoding FMRP-target mRNAs (Extended Data Fig. 8). These results suggest that upregulation of long gene function, either through increased transcription (RTT) or mRNA translation (FXS), may represent a common cause of pathology in neurodevelopmental disorders.

A recent study demonstrated that pharmacological inhibition of topoisomerases leads to the broad downregulation of long genes in neurons¹⁰, suggesting that topoisomerase inhibitors might reverse the upregulation of long gene expression observed in the absence of MeCP2. To test this, we knocked-down MeCP2 expression in cultured cortical neurons with RNA-mediated interference (RNAi) and treated these cells with the topoisomerase inhibitor topotecan. We found that MeCP2 knockdown leads to the upregulation of long genes and that exposure of MeCP2-deficient neurons to topotecan results in a dose-dependent reversal of long gene misregulation (Extended Data Fig. 9).

The disruption of MeCP2 function in both mouse and human neurons leads to an overall reduction in cell health that can be measured as a decrease in the level of ribosomal RNA and cell size^{15,30}. Notably, we found that the concentration of topotecan that most effectively reverses overexpression of long genes (50 nM) partially reverses the decreased ribosomal RNA content observed in neurons lacking MeCP2 (Extended Data Fig. 9). This result suggests that the rebalancing of long gene expression improves cell health in MeCP2 knockdown neurons, leading to increased cellular rRNA content. Taken together, these data suggest that rebalancing long gene expression in neurons lacking MeCP2 may attenuate the cellular dysfunction observed in these cells.

Our finding that long genes are misregulated in RTT, and that this misregulation can be reversed by topotecan treatment complements a recent study¹⁰ implicating topoisomerases in the regulation of long genes in the brain. Thus, our study provides additional evidence that disruption of long gene expression may be a general mechanism underlying ASDs, and suggests that developing methods to rebalance long gene expression may be a strategy to correct neural dysfunction in these disorders.

Online Content Methods, along with any additional Extended Data display items and Source Data, are available in the online version of the paper; references unique to these sections appear only in the online paper.

Received 24 July 2014; accepted 12 February 2015.

Published online 11 March 2015.

- Chahrouh, M. & Zoghbi, H. Y. The story of Rett syndrome: from clinic to neurobiology. *Neuron* **56**, 422–437 (2007).
- Guy, J., Cheval, H., Selfridge, J. & Bird, A. The role of MeCP2 in the brain. *Annu. Rev. Cell Dev. Biol.* **27**, 631–652 (2011).
- Tudor, M., Akbarian, S., Chen, R. Z. & Jaenisch, R. Transcriptional profiling of a mouse model for Rett syndrome reveals subtle transcriptional changes in the brain. *Proc. Natl Acad. Sci. USA* **99**, 15536–15541 (2002).

4. Jordan, C., Li, H. H., Kwan, H. C. & Francke, U. Cerebellar gene expression profiles of mouse models for Rett syndrome reveal novel MeCP2 targets. *BMC Med. Genet.* **8**, 36 (2007).
5. Chahrour, M. *et al.* MeCP2, a key contributor to neurological disease, activates and represses transcription. *Science* **320**, 1224–1229 (2008).
6. Ben-Shachar, S., Chahrour, M., Thaller, C., Shaw, C. A. & Zoghbi, H. Y. Mouse models of MeCP2 disorders share gene expression changes in the cerebellum and hypothalamus. *Hum. Mol. Genet.* **18**, 2431–2442 (2009).
7. Samaco, R. C. *et al.* *Crh* and *Oprm1* mediate anxiety-related behavior and social approach in a mouse model of MECP2 duplication syndrome. *Nature Genet.* **44**, 206–211 (2012).
8. Baker, S. A. *et al.* An AT-hook domain in MeCP2 determines the clinical course of Rett syndrome and related disorders. *Cell* **152**, 984–996 (2013).
9. Zhao, Y. T., Goffin, D., Johnson, B. S. & Zhou, Z. Loss of MeCP2 function is associated with distinct gene expression changes in the striatum. *Neurobiol. Dis.* **59**, 257–266 (2013).
10. King, I. F. *et al.* Topoisomerases facilitate transcription of long genes linked to autism. *Nature* **501**, 58–62 (2013).
11. Sugino, K. *et al.* Cell-type-specific repression by methyl-CpG-binding protein 2 is biased toward long genes. *J. Neurosci.* **34**, 12877–12883 (2014).
12. Meins, M. *et al.* Submicroscopic duplication in Xq28 causes increased expression of the *MECP2* gene in a boy with severe mental retardation and features of Rett syndrome. *J. Med. Genet.* **42**, e12 (2005).
13. Collins, A. L. *et al.* Mild overexpression of MeCP2 causes a progressive neurological disorder in mice. *Hum. Mol. Genet.* **13**, 2679–2689 (2004).
14. Lyst, M. J. *et al.* Rett syndrome mutations abolish the interaction of MeCP2 with the NCoR/SMRT co-repressor. *Nature Neurosci.* **16**, 898–902 (2013).
15. Li, Y. *et al.* Global transcriptional and translational repression in human-embryonic-stem-cell-derived Rett syndrome neurons. *Cell Stem Cell* **13**, 446–458 (2013).
16. Deng, V. *et al.* *FXYD1* is an MeCP2 target gene overexpressed in the brains of Rett syndrome patients and *Mecp2*-null mice. *Hum. Mol. Genet.* **16**, 640–650 (2007).
17. Lewis, J. D. *et al.* Purification, sequence, and cellular localization of a novel chromosomal protein that binds to methylated DNA. *Cell* **69**, 905–914 (1992).
18. Mellén, M., Ayata, P., Dewell, S., Kriaucionis, S. & Heintz, N. MeCP2 binds to 5hmC enriched within active genes and accessible chromatin in the nervous system. *Cell* **151**, 1417–1430 (2012).
19. Guo, J. U. *et al.* Distribution, recognition and regulation of non-CpG methylation in the adult mammalian brain. *Nature Neurosci.* **17**, 215–222 (2014).
20. Skene, P. J. *et al.* Neuronal MeCP2 is expressed at near histone-octamer levels and globally alters the chromatin state. *Mol. Cell* **37**, 457–468 (2010).
21. Kriaucionis, S. & Heintz, N. The nuclear DNA base 5-hydroxymethylcytosine is present in Purkinje neurons and the brain. *Science* **324**, 929–930 (2009).
22. Szulwach, K. E. *et al.* 5-hmC-mediated epigenetic dynamics during postnatal neurodevelopment and aging. *Nature Neurosci.* **14**, 1607–1616 (2011).
23. Xie, W. *et al.* Base-resolution analyses of sequence and parent-of-origin dependent DNA methylation in the mouse genome. *Cell* **148**, 816–831 (2012).
24. Lister, R. *et al.* Global epigenomic reconfiguration during mammalian brain development. *Science* **341**, 1237905 (2013).
25. Cohen, S. *et al.* Genome-wide activity-dependent MeCP2 phosphorylation regulates nervous system development and function. *Neuron* **72**, 72–85 (2011).
26. Kaneda, M. *et al.* Essential role for de novo DNA methyltransferase Dnmt3a in paternal and maternal imprinting. *Nature* **429**, 900–903 (2004).
27. Polymenidou, M. *et al.* Long pre-mRNA depletion and RNA missplicing contribute to neuronal vulnerability from loss of TDP-43. *Nature Neurosci.* **14**, 459–468 (2011).
28. Raychaudhuri, S. *et al.* Accurately assessing the risk of schizophrenia conferred by rare copy-number variation affecting genes with brain function. *PLoS Genet.* **6**, e1001097 (2010).
29. Darnell, J. C. *et al.* FMRP stalls ribosomal translocation on mRNAs linked to synaptic function and autism. *Cell* **146**, 247–261 (2011).
30. Yazdani, M. *et al.* Disease modeling using embryonic stem cells: MeCP2 regulates nuclear size and RNA synthesis in neurons. *Stem Cells* **30**, 2128–2139 (2012).

Supplementary Information is available in the online version of the paper.

Acknowledgements We thank E. Griffith and members of the Greenberg laboratory, A. Bird, G. Mandel and members of their laboratories, and M. Coenraads for discussions, M. Goodell for providing the *Dnmt3a* mice, N. Sharma and F. DiBiase for experimental support, and M. Mistry of the HSPH Bioinformatics Core, Harvard School of Public Health for assistance with gene expression analysis. This work was supported by grants from the Rett Syndrome Research Trust and the National Institutes of Health (NIH) (1R01NS048276) to M.E.G., fellowships from the Damon Runyon Cancer Research Foundation (DRG-2048-10) and the William Randolph Hearst fund to H.W.G., as well as NIH grant T32GM007753, and the HHMI Gilliam fellowship to B.K., H.S. is a HHMI Fellow of the Damon Runyon Cancer Research Foundation (DRG-2194-14).

Author Contributions H.W.G. and B.K. performed or directed all experiments and analysis in the study. H.W.G., B.K. and D.A.H. performed gene expression analysis. B.K. performed EMSA assays. H.W.G. performed ChIP-seq analysis. H.W.G., H.S., N.R.K. performed bisulfite sequencing and DNA methylation analysis. H.W.G., D.A.H., H.S., N.R.K. and M.H. performed bioinformatics and statistical analysis. H.W.G., B.K. and C.S.G. performed Dnmt3a mouse experiments and neuronal culture experiments. D.H.E. provided mouse reagents. H.W.G., B.K. and M.E.G. wrote the manuscript. M.E.G. advised on all aspects of the study.

Author Information Raw data and processed values from RNA-seq, Microarray, ChIP-seq and bisulfite-seq experiments have been submitted to the NCBI Gene Expression Omnibus under accession number GSE60077. Reprints and permissions information is available at www.nature.com/reprints. The authors declare no competing financial interests. Readers are welcome to comment on the online version of the paper. Correspondence and requests for materials should be addressed to M.E.G. (michael_greenberg@hms.harvard.edu).

METHODS

Analysis of published MeCP2-regulated gene lists. To search for unique characteristics of genes found to be misregulated in *Mecp2* mutant mice we interrogated the list of genes found to be significantly activated or repressed by MeCP2 in the cerebellum of MeCP2 KO and MeCP2 OE mice⁶. Using published data sets for the mouse cerebellum from ENCODE and other sources, these genes were assessed for epigenetic marks at promoters and gene bodies, including histone acetylation and methylation as measured by ChIP-seq analysis, as well as DNA methylation and hydroxymethylation as measured by affinity purification methods¹⁸. In addition, we interrogated sequence attributes of genes, including dinucleotide frequencies, exon number, repeat density within genes and gene length. To determine if the misregulated genes were exceptional with respect to any epigenetic marks or sequence attributes, they were compared to several sets of control genes selected to be matched for gene expression levels (data not shown). Although no obvious epigenetic differences were apparent from this analysis, we detected the extreme length of genes (measured as total basepairs from RefSeq transcription start site to transcription termination site) repressed by MeCP2 (upregulated in the MeCP2 KO and downregulated in the MeCP2 OE). We note that affinity-based measures of DNA methylation that were used in this initial unbiased search are now known to be insensitive to low level methylation at individual cytosines and thus do not report mCA levels with high fidelity. This likely explains why we did not detect a methylation signature for MeCP2-repressed genes using the affinity-based data in our initial analysis. Subsequent analysis of multiple published gene lists from several brain regions revealed the consistent, extreme length of the genes identified as repressed by MeCP2 in each brain region. These findings are presented in Fig. 1a as boxplots where each plot depicts the median (line), the second through to the third quartiles (box), 1.5× the interquartile range (whiskers), and 1.58× the interquartile range/($\sqrt{\text{number of genes}}$) (notches). The notches on each box approximate a 95% confidence interval for the median value³¹. Note that opposing changes in MeCP2 KO and MeCP2 OE published gene lists were used to define genes significantly activated or repressed by MeCP2 for hypothalamus⁵, cerebellum⁶, and amygdala⁷ tissues. For hippocampus⁸, striatum⁹ and liver⁹ MeCP2 KO data alone had been used to identify gene lists.

To test if long gene misregulation is specific to *Mecp2* mutants, we surveyed gene expression studies profiling models of neurological dysfunction, asking if long gene length is a common attribute in gene sets from these studies. We analysed the lengths of the lists of up- and downregulated genes identified in these studies or if 'called' misregulated gene lists were not available, we generated lists using the Genespring 12.6 software package (Agilent Technologies) or the Geo2R analysis tool (<http://www.ncbi.nlm.nih.gov/geo/geo2r/>). This analysis did not uncover any additional gene sets with similar long length to that of MeCP2 mutant studies (Extended Data Fig. 1a), suggesting that misregulation of extremely long genes is not a common consequence of cell dysfunction in models of neurodegeneration or several other neurological diseases.

To analyse gene expression genome-wide with respect to gene length, CEL files containing the raw hybridization data from multiple MeCP2 KO and MeCP2 OE gene expression studies were downloaded from GEO (<http://www.ncbi.nlm.nih.gov/geo/>; study details, sample numbers and genotypes are provided in Supplementary Table 1) and analysed for expression at the gene level using the GeneSpring software suite (Agilent Technologies) with RMA summarization of 'core' probesets. To facilitate unambiguous analysis of individual genes, expression values for transcript cluster IDs were filtered to include only transcript clusters that map to single RefSeq genes, and expression values for genes with multiple transcript clusters were derived by taking the average log₂ expression value across all transcript clusters corresponding to each gene. To facilitate comparison between microarray platforms, throughout this study we present analysis only for genes represented on all microarray platforms; this corresponds to 14,168 genes for mouse, and 17,989 genes for human. Although this represents a subset of genes in each genome, we have obtained similar results for length-dependent changes in gene expression for expanded gene sets covered by individual platforms (data not shown). In addition, similar results were obtained using the Affymetrix Power Tools pipeline with PLIER as an alternative summarization method. For consistency, microarray data for gene expression in human cells was presented using a comparable array summarization scheme as the mouse microarray data (RMA). Similar qualitative results showing length-dependent gene misregulation were obtained from gene expression values generated by Li and colleagues using a normalization scheme that included spike-controls¹⁵ (summarized transcript expression values were downloaded directly from GEO). However, with this normalization procedure, the absolute values of fold-change of all genes across the entire genome were downshifted in *MECP2* null neurons relative to wild-type. For analysis of RTT patient samples, raw CEL files from Deng *et al.*¹⁶ were downloaded from GEO, and summarized using the RMA function in the R 'affy' package.

To quantify the relationship between fold-change and gene length, we sorted genes by the lengths of their immature transcripts (RefSeq annotation) and employed a sliding window containing 200 consecutive genes in steps of 40 genes. The log₂ fold-change values for the 200 genes within each length bin were averaged and plotted; displayed standard errors for a bin were calculated by propagating the s.e. deduced from the bin's log₂-fold-change values and the mean s.e. of the individual genes reflecting their sample variability. Null distributions displayed on fold-change plots were constructed for each bin from 10,000 random samples of 200 genes selected without regard to transcript length.

RNA sequencing and analysis. Total RNA was prepared from cortex of male wild-type and MeCP2 KO mice at 8–9 weeks of age. Formal power analysis was not used to predetermine sample size, however, sample size (3 per genotype) was determined based on previous detection of length-dependent gene expression effects in data sets that used similar sample sizes (see Fig. 1b, c and Extended Data Fig. 1 and Supplementary Table 1). Animals were preselected based on genotype before collection to ensure that paired samples were taken within litters, but collection was randomized and the experimenter was uninformed of genotype during collection, sample processing, and analysis. Brain samples were dissected on ice in HBSS and immediately frozen in liquid nitrogen. To extract RNA, the tissue was thawed in trizol (Ambion), homogenized, extracted with chloroform, and further purified on RNeasy columns (Qiagen) using on-column DNase treatment to remove residual DNA as specified in the manufacturer's instructions. High-throughput sequencing of total RNA was performed as a service by BGI America. Briefly, ERCC control RNAs (Ambion) were added to samples, and total RNA was depleted of ribosomal RNA using the Ribozero rRNA removal kit (Epicentre), heat-fragmented to 200–700 bp in length and cloned using uracil-N-glycosylase-based strand-specific cloning. cDNA fragments were sequenced using an Illumina HiSeq 2000, typically yielding 20M–40M usable 49 bp single-end reads per sample (Supplementary Table 1 for details). Gene expression levels were assessed using an in-house analysis pipeline previously developed for RNA-seq quantification³². After filtering out adaptor and low quality reads, reads were mapped using BWA³³ to the mm9 genome augmented by an additional set of splicing targets (~3M sequences of length ≤ 98 bp representing all possible mm9 sequences that could cross at least one exon-exon junction based on the RefSeq annotation). Samples were normalized based on uniquely mapped reads that fell outside of rRNA and noncoding genes in order to avoid skewing by spikes in incompletely depleted ribosomal and transfer RNA. Normalization of each sample was referred to an in-house standard of 10M 35-bp reads. Gene expression within exons and other features was quantified as 'density', defined as read coverage of that feature, equal to the total number of read bases per total number of feature bases multiplied by the overall normalization coefficient. Units of density are always proportional to RPKM (density = 0.35 × RPKM).

Average read density within a gene's exons was taken as a proxy for gene expression (for genes with multiple annotated transcripts, exonic loci were unioned together). For a given set of samples, a quantile distribution (QD) was constructed from all samples' sorted expression levels, and values from the QD were reassigned to each gene according to its rank in each sample. Within each subset of samples corresponding to wild type (WT), knockout (KO) and so on, each gene was assigned its mean log QD value and a standard error over its values for this subset in order to quantify its sample-to-sample variability within the subset. Precisely zero expression levels were ignored in constructing the QD. The log of the fold-change (FC) between subsets for each gene, for example, log(KO/WT), was set to the difference of the means of the KO and WT log values for the gene, along with a propagated s.e. of the log values (variance equal to the sum of KO and WT variances). For consistency, the RNA-seq analysis in this study is presented for the common set of genes covered by microarray analyses in previous studies (see above). Similar results were obtained for larger sets of genes defined by all RefSeq genes.

To confirm that our findings with RNA-seq were robust to the method of quantification used, we also performed analysis using the spliced transcripts alignment to a reference (STAR)³⁴ software to align reads to the mm9 genome and Cufflinks³⁵ to estimate gene-level expression values as fragments per kilobase of exon model per million mapped fragments (FPKM). This analysis yielded results that were nearly identical to those generated using our in-house RNA-seq analysis pipeline. In addition, we derived similar results using transcripts per million (TPM)³⁶ as the measure mRNA levels in place of FPKM (data not shown).

MeCP2 has previously been implicated in the repression of repeat elements across the mammalian genome, raising the possibility that the upregulation of long genes we observe in our analysis is a reflection of increased transcription from repeat elements or possibly cryptic promoters. To look for changes in the expression of repeat RNAs in the MeCP2 KO brain, RNA-seq reads were mapped to the genome using Bowtie, keeping reads mapping to multiple sites in the genome. Each read was assigned a score of $1/n$ (n = number of sites a read mapped to). Expression values for each repeat family was calculated by adding the scores within each repeat (annotated using Repeatmasker) and normalizing to sequencing depth.

This analysis did not reveal evidence of upregulation of specific repeat classes in the MeCP2 KO brain. In addition, to look for evidence of increased expression of repeats in connection with longer genes we assessed whether there was increased antisense transcription in these genes using our in-house RNA-seq analysis pipeline. This analysis failed to provide evidence of increased antisense transcription. Another alternative explanation for our results was that the increase in expression of long genes we observe is due to spurious transcription, which might initiate from cryptic promoters within genes to generate sense coding, incomplete RNAs. In this case the upregulated RNAs would not reflect mature protein coding mRNA levels. To assess the expression of mature mRNA directly we measured mRNA expression by quantifying only RNA-seq reads that map across exon splice junctions. Consistent with there being an upregulation of mature mRNAs from long genes in the MeCP2 KO, this analysis yielded genome-wide length-dependent upregulation of gene expression that is highly similar to our whole-exon-based approach described above (data not shown). We conclude from this analysis that functional, protein-coding mRNAs derived from long genes are upregulated in the MeCP2 KO, and that this increase is likely due to an alteration in canonical genic transcription mechanisms, not an increase in spurious transcripts coming from long gene loci.

Gene expression analysis of MeCP2(R306C) mice. Consistent with nomenclature from past descriptions of RTT missense mutations, the R306C nomenclature refers to the mouse MeCP2 isoform 2 (MeCP2_e2; NCBI Reference Sequence NP_034918). For gene expression analysis brain regions were dissected from male *MeCP2*^{R306C/y} mice¹⁴ and wild type littermates at 8–10 weeks of age and RNA was isolated as described above. Animals were preselected based on genotype before collection to ensure that paired samples were taken within litters, but collection was randomized and the experimenter was uninformed of genotype during collection, sample processing and analysis. Microarray analysis of cerebellar RNA was performed using the Affymetrix mouse exon 1.0 ST array platform. Analysis was performed in the Dana Farber microarray core facility following manufacturer's recommendations. Analysis of hybridization data was performed as described above. Formal power analysis was not used to predetermine sample size, however sample size (4 per genotype) was determined based on previous detection of length-dependent gene expression effects in data sets that used similar sample sizes (see Extended Data Fig. 1 and Supplementary Table 1).

Validation of microarray and RNA-seq findings. For reverse transcription-quantitative PCR expression analysis candidate genes were selected for analysis in the visual cortex based on consistent upregulation in the MeCP2 KO (\log_2 -fold-change greater than zero) and downregulation in the MeCP2 OE (\log_2 -fold-change less than zero) across eight published microarray data sets in five brain regions (hypothalamus, cerebellum, amygdala, striatum, hippocampus). For Nanostring nCounter validation genes were selected based on the above criteria and evidence of upregulation in the visual cortex RNA-seq analysis. Genes with this profile were selected for qPCR assessment in the visual cortex. cDNA was generated from 500 ng of visual cortex total RNA (High-Capacity cDNA Reverse Transcription Kit, Applied Biosystems), and quantitative PCR was performed using transcript-specific primers (designed with the universal probe library design centre, Roche, Supplementary Table 2) and SYBR green detection on the Lightcycler 480 platform (Roche). Relative transcript levels and fold-changes were calculated by normalizing qPCR signal within each sample to six genes that do not show evidence of altered expression across published microarray data sets (Supplementary Table 2). Similar results were obtained by analysing raw Cp values for test transcripts without normalization to control genes (data not shown).

For non-amplification-based gene expression analysis, Nanostring nCounter reporter CodeSets were designed to detect candidate MeCP2-repressed genes in 250 ng of total RNA extracted from MeCP2 KO and MeCP2(R306C) mice. Samples were processed at Nanostring Technologies, following the nCounter Gene Expression protocol. Briefly, total RNA was incubated at 65 °C with reporter and capture probes in hybridization buffer overnight, and captured probes were purified and analysed on the nCounter Digital Analyzer. The number of molecules of a given transcript was determined by normalizing detected transcript counts to the geometric mean of ERCC control RNA sequences and a set of control genes that do not show evidence of altered expression across published microarray data sets. Hotelling T2 test for small sample size³⁷ was used to calculate significance in order to incorporate variance across both samples and genes. Significant differences between wild-type and MeCP2 KO or MeCP2(R306C) samples ($P < 0.01$) were also detected by paired two-tailed *t*-test comparing the paired mean values for each gene (averaged across samples within each genotype) between genotypes.

Electromobility shift assays. Oligonucleotide probes (Integrated DNA Technologies) were 5'-³²P-end-labelled by T4 polynucleotide kinase (New England Biolabs) with [γ -³²P]ATP (Perkin Elmer) under conditions recommended by the enzyme supplier. 5'-³²P-end-labelled upper strands were purified over NucAway Spin Columns (Ambion) and annealed to equal molar concentration of the appropriate

unlabelled complement strand in 10 mM Tris, pH 8.0, 50 mM NaCl, 1 mM EDTA at 95 °C for 5 min, followed by slow cooling to room temperature. Similarly, unlabelled competitors were annealed. Proper annealing of probes and competitors was verified by native gel electrophoresis.

For binding reactions using the MBD fragment of MeCP2, each reaction contained 180 ng of protein (amino acids (AA) 81–170, Abnova or AA 78–162, Diagenode), 50 fmol of 5'-³²P-end-labelled probe with an excess of an unlabelled competitor in the presence of 1 μ g of poly-dIdC (Sigma), 1 \times Tris-borate-EDTA (TBE) buffer, 1 mM DTT, 20 mM HEPES, pH 7.5, 0.5 mM EDTA, 0.2% Tween-20, 30 mM KCl, and 1 \times Orange DNA loading dye (Thermo Scientific). Binding was carried out in a 10 μ l volume for 10 min at room temperature. Each reaction was loaded on a 10% non-denaturing polyacrylamide gel (37.5:1, acrylamide/bis-acrylamide) gel in 1 \times TBE buffer and electrophoresed for 30 min at 240 V on ice. For binding reactions using the full-length MeCP2 protein, each reaction contained 60 ng of protein (AA 1–486, Millipore), 100 fmol of 5'-³²P-end-labelled probe with an excess of unlabelled competitor in the presence of 250 ng of poly-dIdC (Sigma), 0.5 \times Tris-borate-EDTA (TBE) buffer, 1 mM DTT, 20 mM HEPES, pH 7.5, 0.5 mM EDTA, 0.2% Tween-20, 30 mM KCl, and 1 \times Orange DNA loading dye (Thermo Scientific) in a 10 μ l reaction volume for 10 min at room temperature. Each reaction was loaded on a 6% non-denaturing polyacrylamide gel (Life Technologies) in 0.5 \times TBE buffer and electrophoresed for 25 min at 300 V on ice. Gels were then dried on Whatman filter paper on a gel drier at 80 °C for 1 h. For imaging, dried gels were exposed to film overnight (Kodak X-Omat XB film) at –80 °C.

Whole-genome bisulfite sequencing and analysis. For bisulfite sequencing analysis cerebella and cortices from four, eight-week-old mice were dissected and genomic DNA extracted. Starting with 25 ng of genomic DNA, 0.25 ng of unmethylated lambda DNA was added and libraries were generated using the Ovation Ultralow Methyl-Seq Library System (Nugen). Bisulfite treatment was performed using the EpiTect bisulfite conversion kit (Qiagen) following manufacturer's instructions. Libraries were constructed using TruSeq reagents (Illumina) and sequenced on the HiSeq 2000 or MiSeq instruments (Illumina). Reads were mapped to the mm9 genome using BS seeker³⁸, allowing up to four mismatches. Duplicate reads were removed and only uniquely mapping reads were kept (Supplementary Table 1 for details). For analysis of published bisulfite sequencing data sets^{19,24}, short read files were downloaded from GEO, mapped, and analysed as described above, or processed data files showing number of reads and number of non-converted reads per cytosine base were used (Supplementary Table 1 for details). Methylation levels in all data sets were calculated as number of cytosine base calls/(number of cytosine + number of thymine base calls) within mapped reads at genomic sites where the reference genome encodes cytosine. For hydroxymethylation analysis, the same approach was applied to Tet-assisted bisulfite sequencing (TAB-seq) data from cortical tissue²⁴. To examine the effects of gene body methylation independently of promoters, only genes greater than 4.5 kb and with a minimal coverage of CGs and CHs were used in our analysis, and methylation levels within regions of the transcription start site +3 kb to transcription end site were calculated by taking the average methylation levels for all reads mapping within this region. Comparison to gene expression data was performed using corresponding microarray expression values for the hippocampus and the cerebellum or RNA-seq from the cortex. To facilitate fold-change analysis of RNA-seq data, the genes analysed were filtered for minimal (non-zero) expression values.

MeCP2 chromatin immunoprecipitation analysis. MeCP2 ChIP analysis was performed on cortex and cerebella dissected from 8-week-old wild-type male mice as previously described^{25,39}. To facilitate direct comparison of MeCP2 ChIP to published frontal cortex DNA methylation and hydroxymethylation data²⁴, we also performed MeCP2 ChIP analysis using the same brain region at the same developmental stage (frontal cortex isolated from 6-week-old mice). ChIP DNA was cloned into libraries and sequenced on the Illumina HiSeq 2000 or HiSeq 2500 platform to generate 49 or 50 bp single-end reads. Reads were mapped to mouse genome mm9 using BWA³³ and custom perl scripts were employed to quantify read density (reads per kb) for each gene. Normalized read density values were calculated as reads per kb in each genomic feature (for example, gene), normalized to the total number of reads sequenced for each sample, and divided by the reads per kb in that feature for the input DNA that was isolated before the ChIP and sequenced in parallel. As with the methylation analysis, gene bodies were defined as +3,000 bp to the predicted transcription termination site in the RefSeq gene model. To ensure sufficient coverage and accurate assessment of density in gene bodies, only genes greater than 4,500 bp in total length with at least one read in the input sample were included in the analysis.

To explore the relationship between MeCP2 binding and mCA at high resolution, we also quantified the MeCP2 ChIP signal from the frontal cortex in 500-bp bins tiled for all genes in the genome and compared it to mCA levels derived from high-coverage DNA methylation analysis of this brain region (Extended Data Fig. 4)²⁴. In addition, we employed the MACS⁴⁰ algorithm to identify sites of

MeCP2 ChIP enrichment, or 'summits', across the genome and looked for evidence of mCN at these sites. Due to the broad binding of MeCP2 across the genome, MeCP2 ChIP yields numerous sites of modest local enrichment (~twofold), not isolated, highly-enriched peaks (>tenfold) that are characteristic of transcription factors. Thus, to define MeCP2 summits, we used a low threshold of MeCP2 ChIP over input enrichment (>onefold) and a low stringency *P* value threshold ($P < 0.2$), which yielded 31,479 summits of MeCP2 ChIP signal. Aggregate plots across all 31,479 MeCP2 summits were generated using the *annotatePeaks.pl* program in the Hypergeometric Optimization of Motif EnRichment (HOMER)⁴¹ software. Input-normalized MeCP2 ChIP signal was calculated as the ratio of MeCP2 ChIP/input read coverage. Log₂ enrichment of mCN under MeCP2 summits was determined by calculating the level of methyl-cytosine (number of non-converted cytosines sequenced)/(number of converted and non-converted cytosines sequenced) occurring at CA, CC, CT, or CG positions in the genome, normalized to the flanking region (mean of -4 kb to -3 kb and 3 kb to 4 kb region relative to the MeCP2 summit). The average value for the ChIP signal or relative mCN was then calculated for windows (100-bp for ChIP, 10-bp for mCN) tiled across each summit location and averaged across all of the 31,479 summits of MeCP2 ChIP enrichment identified using the MACS peak-calling algorithm⁴⁰ (red) and 31,479 randomly selected control sites (grey).

Analysis of *Dnmt3a*^{fl/fl}; *Nestin-Cre*^{+/-} mice. Female *Dnmt3a*^{fl/fl} mice²⁶ (kindly provided by M. Goodell) were bred to male *Nestin-Cre*^{+/-} mice⁴² to generate *Dnmt3a*^{fl/+}; *Nestin-Cre*^{+/-} animals. To ensure expression of the imprinted *Nestin-Cre* transgene, male *Dnmt3a*^{fl/+} Tg(Nes-cre)1Kln/J animals were bred to *Dnmt3a*^{fl/fl} females to generate *Dnmt3a*^{fl/fl} Tg(Nes-cre)1Kln/J conditional knockout mice ("Dnmt3a cKO") and *Dnmt3a*^{fl/fl} control animals ("control"). For western blot, DNA methylation and gene expression analyses, cerebella were dissected from 10–11-week-old animals. Proteins were resolved by SDS-PAGE and immunoblotted using the following antibodies: Dnmt3a (abcam, ab13888), MeCP2 (custom antisera⁴³) and Gapdh (Sigma Aldrich, #G9545-25UL). Genotyping for the *Dnmt3a* locus was performed by PCR with primers flanking both *loxP* sites (F: 5'-GCAGC AGTCCAGGTAGAAG-3', R: 5'-ATTTTCATCTTACTTCTGTGGC-3') on DNA derived from tails. The presence of the *Cre* allele was detected using primers to this transgene (F: 5'-GCAAGTTGAATAACCGGAAATGGTT-3', R: 5'-AGGGTGTATAAGCAATCCCCAGAA-3'). This genotyping scheme allows for simultaneous assessment of the presence of the floxed allele and the relative level of *loxP* recombination that has occurred in the sample. Brain-specific recombination was confirmed by PCR of tail DNA compared to cerebellar DNA (see Extended Data Fig. 7). For gene expression analysis RNA was extracted and analysed as described above for MeCP2(R306C) cerebellum samples.

Identification and analysis of MeCP2-repressed genes. To facilitate identification of genes repressed by MeCP2 in the context of extremely small changes in gene expression, we analysed the 14,168 common genes quantified across eight published microarray 'training data sets' in five brain regions (hypothalamus, cerebellum, amygdala, striatum, hippocampus), applying the lowest possible threshold for fold-change (fold-change >0 in the MeCP2 KO, fold-change <0 in the MeCP2 OE) but demanding consistent misregulation in the predicted direction (at least 7 out of 8 data sets). Genes meeting this minimal threshold for direction of change were then filtered for minimum average change in gene expression (>7.5%), yielding 466 MeCP2-repressed genes (Supplementary Table 3). To determine if these 466 genes represent a significant population of reproducibly affected genes in MeCP2 mutants above what would be expected by chance we performed 7×10^5 resampling iterations, calculating the number of genes meeting the MeCP2-repressed criteria when the gene identity was randomized with respect to the calculated fold-change. This analysis yielded an average of 31 genes per iteration (observed/expected = $466/31 = 15$) and did not detect an instance of 466 or more genes meeting the MeCP2-repressed criteria (maximum of 60 genes per iteration), thus yielding a significance of $P < 1.5 \times 10^{-6}$. The robustness of this gene list for predicting misregulation in *Mecp2* mutants is demonstrated by the reproducible upregulation of these genes in the 'test data sets' in Extended Data Fig. 8. Negative control data sets used in this analysis to test for specificity were identified through a survey of available GEO data sets. To qualify for analysis they were required to have a minimum number of biological replicates similar to the MeCP2 data sets (>4) and to have been analysed on either of the microarray platforms used for the training data sets (Affymetrix MoGene 1.0 ST, or MoExon 1.0 ST). For individual gene analysis we calculated the significance of misregulation for individual example genes across the 10 *Mecp2* mutant data sets displayed in Extended Data Fig. 8 as follows: after confirming a normal distribution of fold-change values in each data set, we calculated a *z* score for the fold-change of each gene in each data set. Assuming the null hypothesis that each gene would be randomly sampled from a standard normal distribution, a *t* statistic was derived from the mean and standard error of the gene's *z* scores across the data sets, and this sample's *P* value was calculated from the *t* distribution for nine degrees of freedom. While the analysis presented here utilizes

these 466 genes identified on the criteria described above, similar results for gene length, enriched overlap with FMRP target genes, and enrichment for neuronal annotations were obtained with gene lists generated using alternative criteria (for example, up in MeCP2 KO, down in MeCP2 OE in 8 out of 8 data sets without minimum expression threshold).

Gene ontology analysis was performed using the DAVID v6.7 bioinformatics resource⁴⁴ (<http://david.abcc.ncifcrf.gov/>), using the 14,168 genes covered in our analysis as background. Overlap of MeCP2-repressed genes with FMRP target genes was performed by mapping putative FMRP target lists^{29,45} to the 14,168 genes used for identification of MeCP2-repressed genes. Data processing, plotting, and statistical analysis were performed using available packages and custom scripts in R.

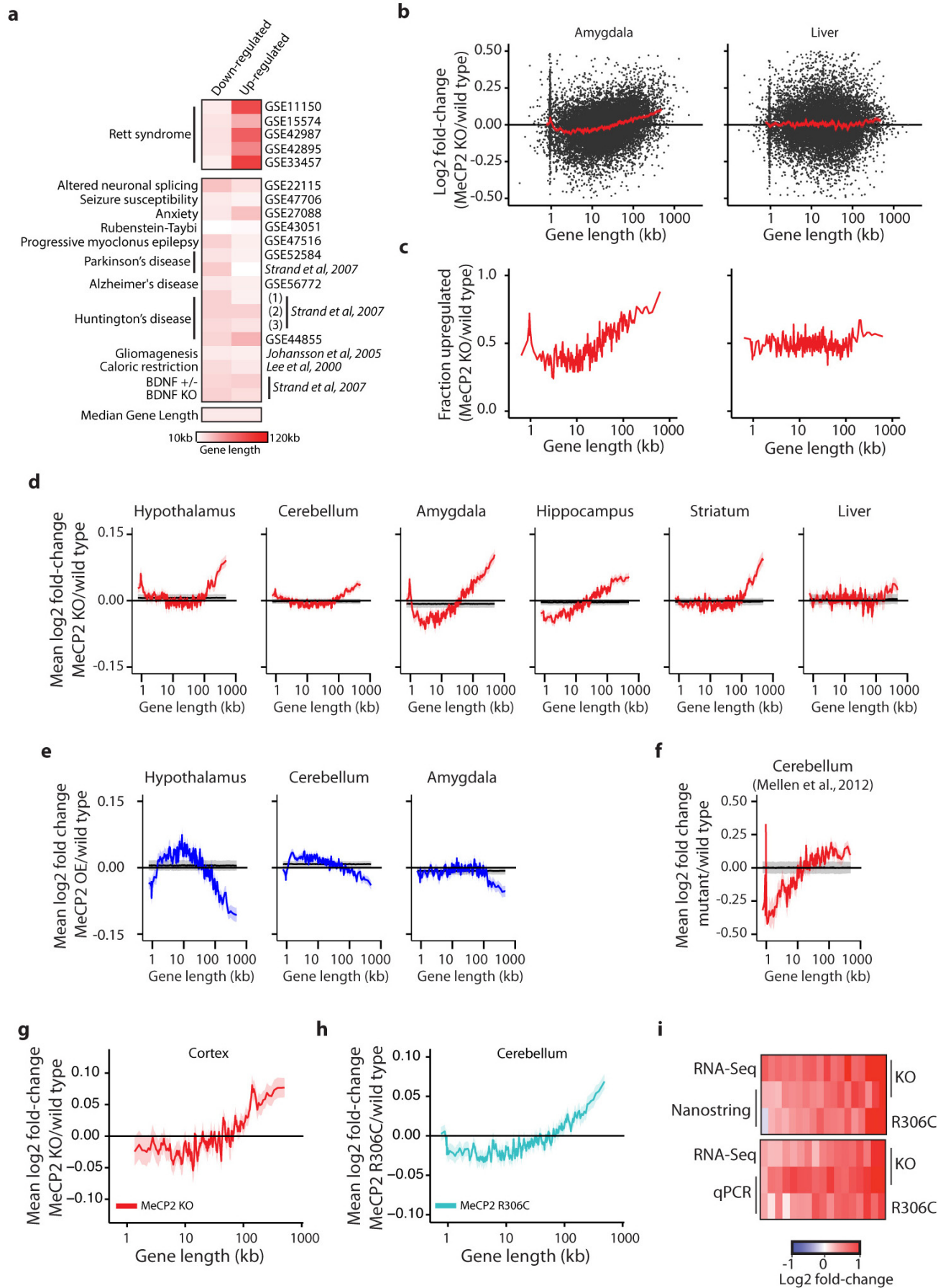
Brain-specific expression of long genes. To assess expression of long genes across neural and non-neural tissues, RNA-seq data sets for seven mouse tissues dissected from eight-week-old mice⁴⁶ and ten human tissues⁴⁷ were mapped and quantified as described above. Similar results of brain-specific long gene expression were obtained for microarray data from the wild type samples of the five brain regions analysed in *Mecp2* mutant studies compared to the wild type liver (data not shown).

Neuronal cell culture and topotecan treatment. Primary cortical neurons were prepared from E16.5 mouse embryos and cultured as described by Kim *et al.*³³. For lentiviral-mediated shRNA knockdown, virus was prepared as described in Tiscornia *et al.*⁴⁸ using the MeCP2 shRNA and control shRNA plasmids previously validated in Zhou *et al.*⁴⁹. Virus was concentrated and titrated using the GFP signal expressed from IRES GFP in the virus. After one day *in vitro* (DIV), cells were infected with lentivirus (knockdown or control) at an MOI of ~5, such that >90% of cells were infected. On DIV 4 cells were fed (neurobasal media with AraC, 2 μM final concentration) and subsequently treated with various dilutions of topotecan in DMSO (0.05% DMSO final concentration). At DIV 10, cells were collected in trizol for RNA analysis, or protein gel loading buffer for protein. RNA samples were processed and analysed using the Nanostring nCounter assay as described above, with the exception that 6 control genes were used for normalization. Western blot analysis to confirm knockdown of MeCP2 was performed as described in Chen *et al.*⁴³. Mean values shown in Extended Data Fig. 9 ($n = 3-5$) are derived from separate cultures obtained from independent litters of mice (independent biological replicates), dissected on separate days, cultured and collected independently.

Regulatory Approval. All animal experiments were performed in accordance with regulations and procedures approved by the Harvard Medical Area Standing Committee on Animals (HMA IACUC).

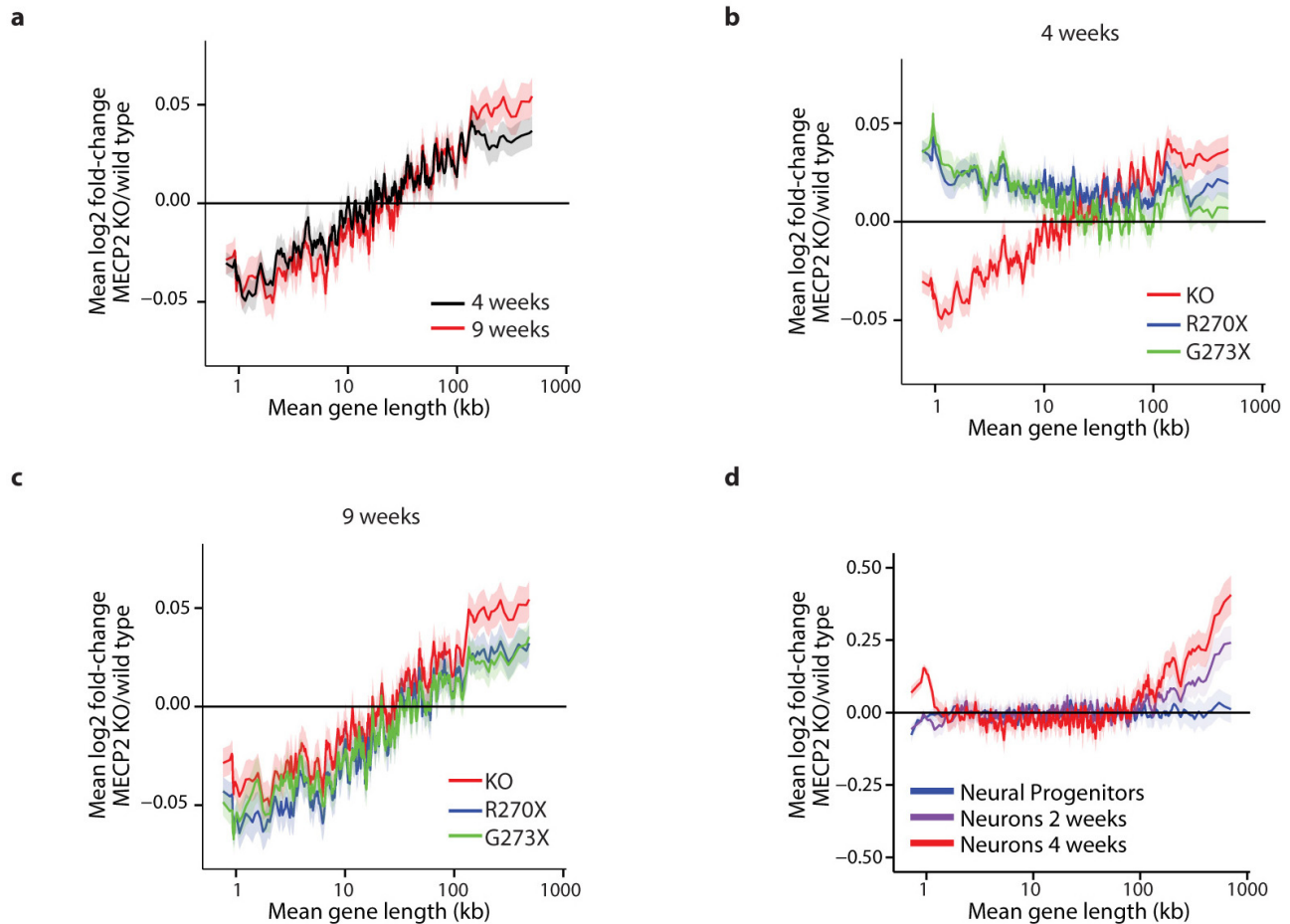
- McGill, R., Tukey, J. & Larsen, W. A. Variations of box plots. *Am. Stat.* **32**, 12–16 (1978).
- Li, H. & Durbin, R. Fast and accurate short read alignment with Burrows–Wheeler transform. *Bioinformatics* **25**, 1754–1760 (2009).
- Kim, T. K. *et al.* Widespread transcription at neuronal activity-regulated enhancers. *Nature* **465**, 182–187 (2010).
- Dobin, A. *et al.* STAR: ultrafast universal RNA-seq aligner. *Bioinformatics* **29**, 15–21 (2013).
- Trapnell, C. *et al.* Differential gene and transcript expression analysis of RNA-seq experiments with TopHat and Cufflinks. *Nature Protocols* **7**, 562–578 (2012).
- Wagner, G. P., Kin, K. & Lynch, V. J. Measurement of mRNA abundance using RNA-seq data: RPKM measure is inconsistent among samples. *Theory in Biosciences* **131**, 281–285 (2012).
- Wu, Y., Genton, M. G. & Stefanski, L. A. A multivariate two-sample mean test for small sample size and missing data. *Biometrics* **62**, 877–885 (2006).
- Chen, P. Y., Cokus, S. J. & Pellegrini, M. B. S. Seeker: precise mapping for bisulfite sequencing. *BMC Bioinformatics* **11**, 203 (2010).
- Ebert, D. H. *et al.* Activity-dependent phosphorylation of MeCP2 threonine 308 regulates interaction with NCoR. *Nature* **499**, 341–345 (2013).
- Feng, J., Liu, T. & Zhang, Y. Using MACS to identify peaks from ChIP-seq data. *Current Protocols in Bioinformatics* **Chapter 2**, Unit 2.14 (2011).
- Nagy, G., Daniel, B., Jonas, D., Nagy, L. & Barta, E. A novel method to predict regulatory regions based on histone mark landscapes in macrophages. *Immunobiology* **218**, 1416–1427 (2013).
- Tronche, F. *et al.* Disruption of the glucocorticoid receptor gene in the nervous system results in reduced anxiety. *Nature Genet.* **23**, 99–103 (1999).
- Chen, W. G. *et al.* Derepression of BDNF transcription involves calcium-dependent phosphorylation of MeCP2. *Science* **302**, 885–889 (2003).
- Huang da, W., Sherman, B. T. & Lempicki, R. A. Systematic and integrative analysis of large gene lists using DAVID bioinformatics resources. *Nature Protocols* **4**, 44–57 (2009).
- Brown, V. *et al.* Microarray identification of FMRP-associated brain mRNAs and altered mRNA translational profiles in fragile X syndrome. *Cell* **107**, 477–487 (2001).
- Mortazavi, A., Williams, B. A., McCue, K., Schaeffer, L. & Wold, B. Mapping and quantifying mammalian transcriptomes by RNA-seq. *Nature Methods* **5**, 621–628 (2008).
- Gray, J. M. *et al.* SnapShot-Seq: a method for extracting genome-wide, *in vivo* mRNA dynamics from a single total RNA sample. *PLoS ONE* **9**, e89673 (2014).

48. Tiscornia, G., Singer, O. & Verma, I. M. Production and purification of lentiviral vectors. *Nature Protocols* **1**, 241–245 (2006).
49. Zhou, Z. *et al.* Brain-specific phosphorylation of MeCP2 regulates activity-dependent Bdnf transcription, dendritic growth, and spine maturation. *Neuron* **52**, 255–269 (2006).
50. Valinluck, V. *et al.* Oxidative damage to methyl-CpG sequences inhibits the binding of the methyl-CpG binding domain (MBD) of methyl-CpG binding protein 2 (MeCP2). *Nucleic Acids Res.* **32**, 4100–4108 (2004).
51. Hashimoto, H. *et al.* Recognition and potential mechanisms for replication and erasure of cytosine hydroxymethylation. *Nucleic Acids Res.* **40**, 4841–4849 (2012).
52. Spruijt, C. G. *et al.* Dynamic readers for 5-(hydroxy)methylcytosine and its oxidized derivatives. *Cell* **152**, 1146–1159 (2013).
53. Khrapunov, S. *et al.* Unusual characteristics of the DNA binding domain of epigenetic regulatory protein MeCP2 determine its binding specificity. *Biochemistry* **53**, 3379–3391 (2014).



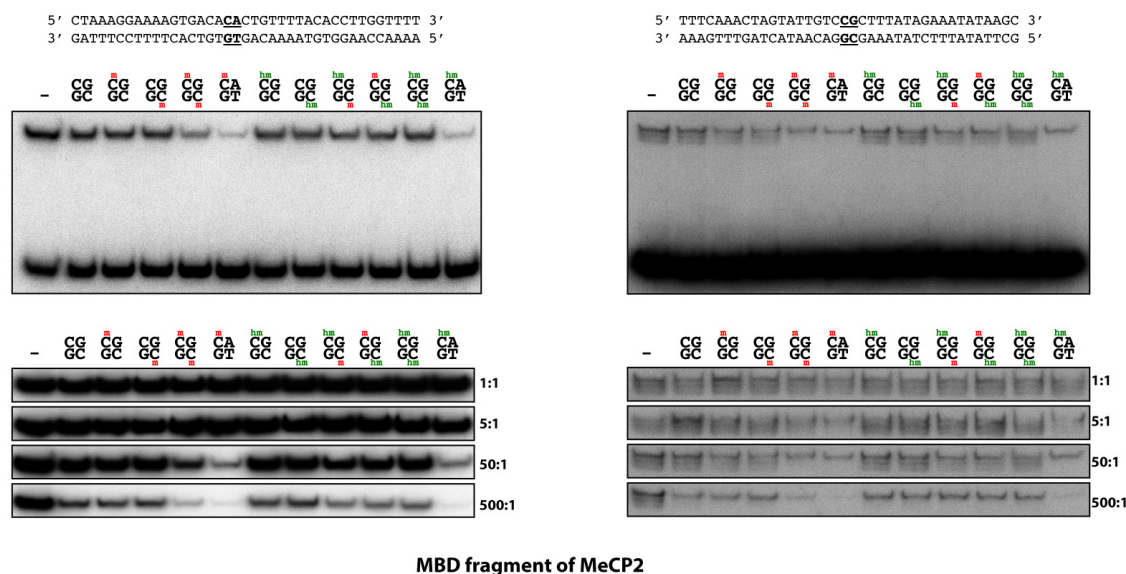
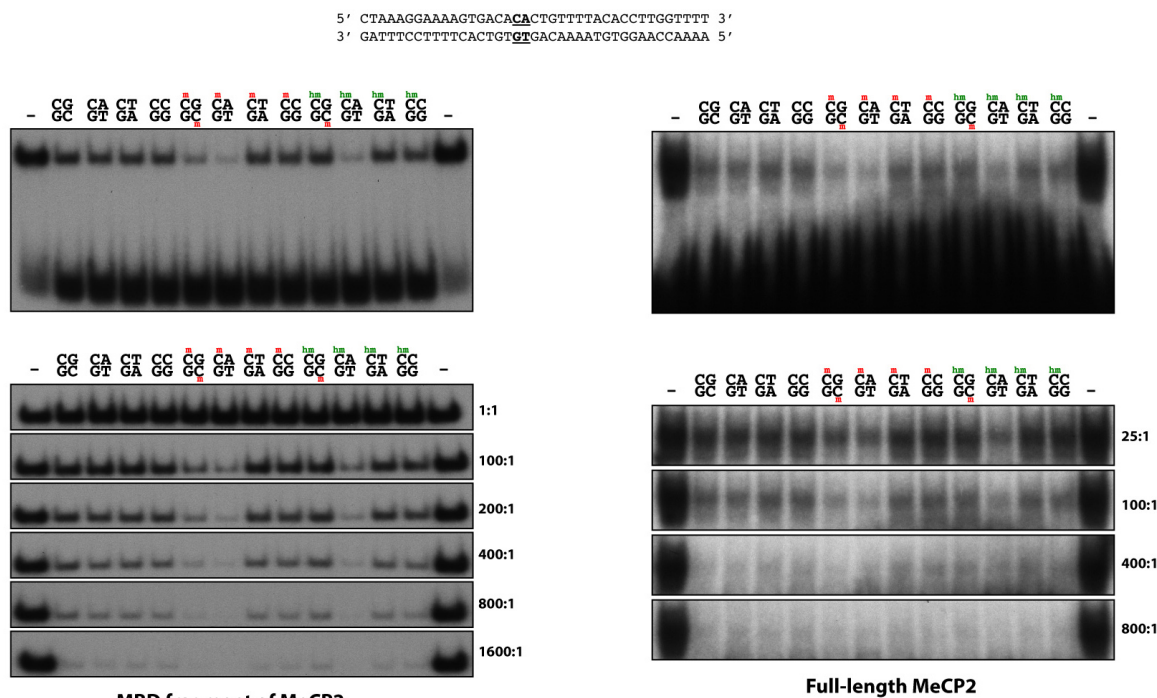
Extended Data Figure 1 | Analysis of gene expression changes in *Mecp2* mutant mice. **a**, Heatmap of median gene lengths for genes identified as misregulated in *Mecp2* mutant studies or sixteen different studies of neurological dysfunction and disease in mice. Mouse model and GEO accession number, or reference, are listed (for Strand *et al.* (1), 3NP treatment; (2), human HD brain; (3), R2/6 *Htt* transgenic). **b**, Scatter plots of fold-change in gene expression in the MeCP2 KO for the amygdala (left), which shows robust length-dependent misregulation, and the liver (right), which does not. Fold-change values for genes (black points) and mean fold-change for 200 genes per bin with a 40 gene step are shown (mean, red line; ribbon, s.e.m.). **c**, The fraction of genes showing fold-change >0 for data sets in **b**; genes binned by length (100 gene bins, 50 gene step). **d–f**, Analysis of published microarray^{5–9} (**d, e**) or RNA sequencing (RNA-seq)¹⁸ (**f**) data sets from MeCP2 KO (**d, f**) or OE (**e**) mice. Mean fold-change in expression (200 gene bins, 40 gene step), red line; ribbon, s.e.m. For **d–f**, mean (black line) and two standard deviations (grey ribbon) are shown for 10,000 resamplings in which gene lengths were randomized with respect to fold-change. The spike in mean

fold-change at ~1 kb in several plots corresponds to the olfactory receptor genes (Supplementary Discussion). **g**, Mean changes in expression of genes binned by length from RNA-seq analysis of MeCP2 KO cortex ($n = 3$ per genotype). **h**, Mean changes in expression from microarray analysis of genes binned by length in MeCP2(R306C) cerebellum ($n = 4$ per genotype). **i**, Heatmap summary of fold-changes in gene expression from RNA-seq analysis of *Mecp2* mutant mean in **g** compared to Nanostring nCounter (18 genes, top) or RT-qPCR (17 genes, bottom) analysis from cortex ($n = 4$ per genotype). Selected long genes (>100 kb) consistently upregulated in the MeCP2 KO or downregulated in MeCP2 OE mutant mice across brain tissues were tested (Supplementary Table 2). A statistically significant upregulation of these genes is observed in the cortex for both MeCP2 KO (nCounter, $P = 0.00073$; qPCR, $P < 1 \times 10^{-15}$) and MeCP2(R306C) (nCounter, $P = 0.0482$; qPCR, $P = 1.69 \times 10^{-6}$; Hotelling T^2 test for small sample size³⁷). Note that for completeness, data from other figures have been re-presented here. See Methods and Supplementary Table 1 for sample sizes from published data sets and other details.



Extended Data Figure 2 | Timing and severity of gene expression changes in models of RTT. **a**, Mean fold-change in gene expression versus gene length in the hippocampus of MeCP2 KO mice compared to wild type at four and nine weeks of age reveals increasing magnitude of length-dependent gene misregulation that parallels the onset of RTT-like symptoms in these animals⁸. **b**, Mean fold-change in gene expression versus gene length in hippocampus of mice expressing truncated forms of MeCP2 mimicking human disease-causing alleles at four weeks of age. Re-expression of a longer truncated form of MeCP2(G273X) in the MeCP2 KO normalizes expression of long genes more effectively than expression of a shorter truncation of MeCP2(R270X), and parallels the higher degree of phenotypic rescue observed in

MeCP2(G273X)-expressing mice compared to MeCP2(R270X)-expressing mice⁸. **c**, Mean fold-change in gene expression versus gene length in hippocampus of mice expressing truncated MeCP2 at nine weeks of age. Consistent with the eventual onset of symptoms of these mouse strains, length-dependent gene misregulation is evident in both strains. **d**, Changes in gene expression for genes binned by length in human *MECP2* null ES cells differentiated into neural progenitor cells, neurons cultured for 2 weeks, or neurons cultured for 4 weeks¹⁵. In all plots, lines represent mean fold-change in expression for each bin (200 gene bins, 40 gene step), and the ribbon is s.e.m. of genes within each bin. See Methods and Supplementary Table 1 for all sample sizes and other details.

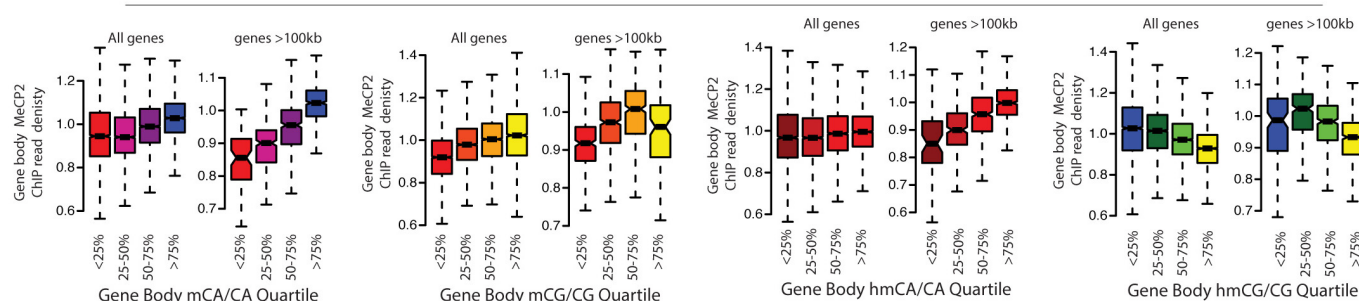
a**b**

Extended Data Figure 3 | High affinity of MeCP2 for mCG, mCA and hmCA in electrophoretic mobility shift assays. **a**, Binding of the recombinant methyl-binding domain (MBD) of MeCP2 (amino acids 81–170) to 32 P-end-labelled oligonucleotides containing a methylated cytosine in a CA (left) or a CG (right) context competed with unlabelled competitor substituted with unmethylated, methylated, or hydroxymethylated cytosine in a CG or CA context (indicated in bold). Representative full gels showing shifted and unshifted probe in the presence of 50-fold excess of unlabelled competitor (top); close-up of shifted bands over a range of unlabelled competitor (bottom). A mCA-containing oligonucleotide competes for MeCP2 binding with equal or higher efficacy to that of a symmetrically methylated CG oligonucleotide. While hmCG-containing probes compete with similar efficacy to an unmethylated probe, a hmCA-containing probe competes with high efficacy. This difference in affinity of MeCP2 for hmCA- and hmCG-containing probes

may explain conflicting results reported for the affinity of MeCP2 for hydroxymethylated DNA^{18,50–53} (Supplementary Discussion). **b**, Binding and competition of recombinant MeCP2 MBD (amino acids 78–162, left) or full-length MeCP2 (amino acids 1–486, right) incubated with 32 P-end-labelled oligonucleotides containing a methylated cytosine in a CA context and competed with oligonucleotides containing unmethylated, methylated, or hydroxymethylated cytosine in a CG, CA, CT, or CC context. Representative full gels showing 100-fold excess of unlabelled competitor (top); close-up of shifted bands over a range of unlabelled competitor (bottom). The results obtained from competitors containing mCG, mCA, hmCG and hmCA are similar to those shown in **a**. In addition, both (h)mCT- and (h)mCC-containing oligonucleotides compete for MeCP2 binding with similar efficacy to that of an unmethylated probe. All results shown were observed in at least two independent experiments.

a

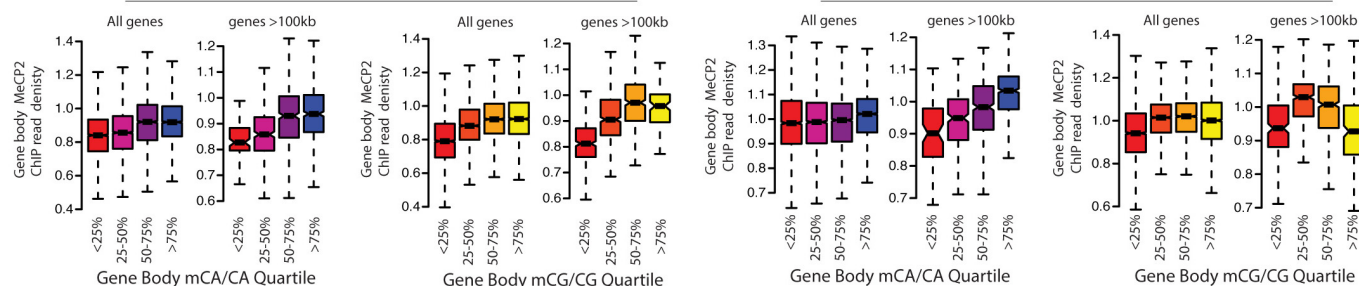
Frontal Cortex



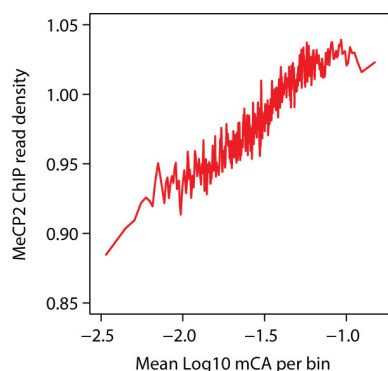
b

Cortex

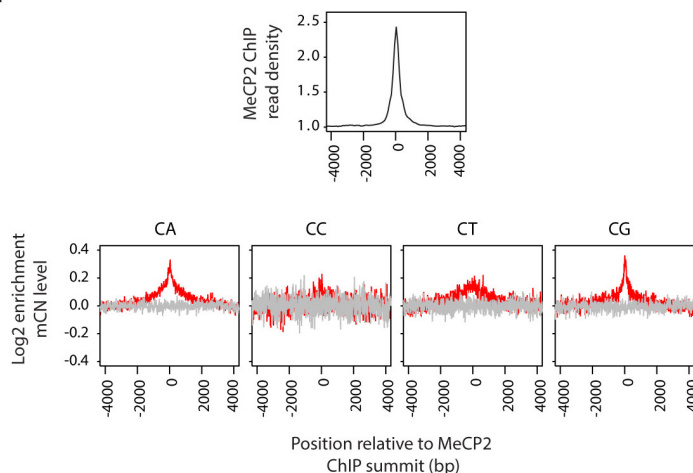
Cerebellum



c



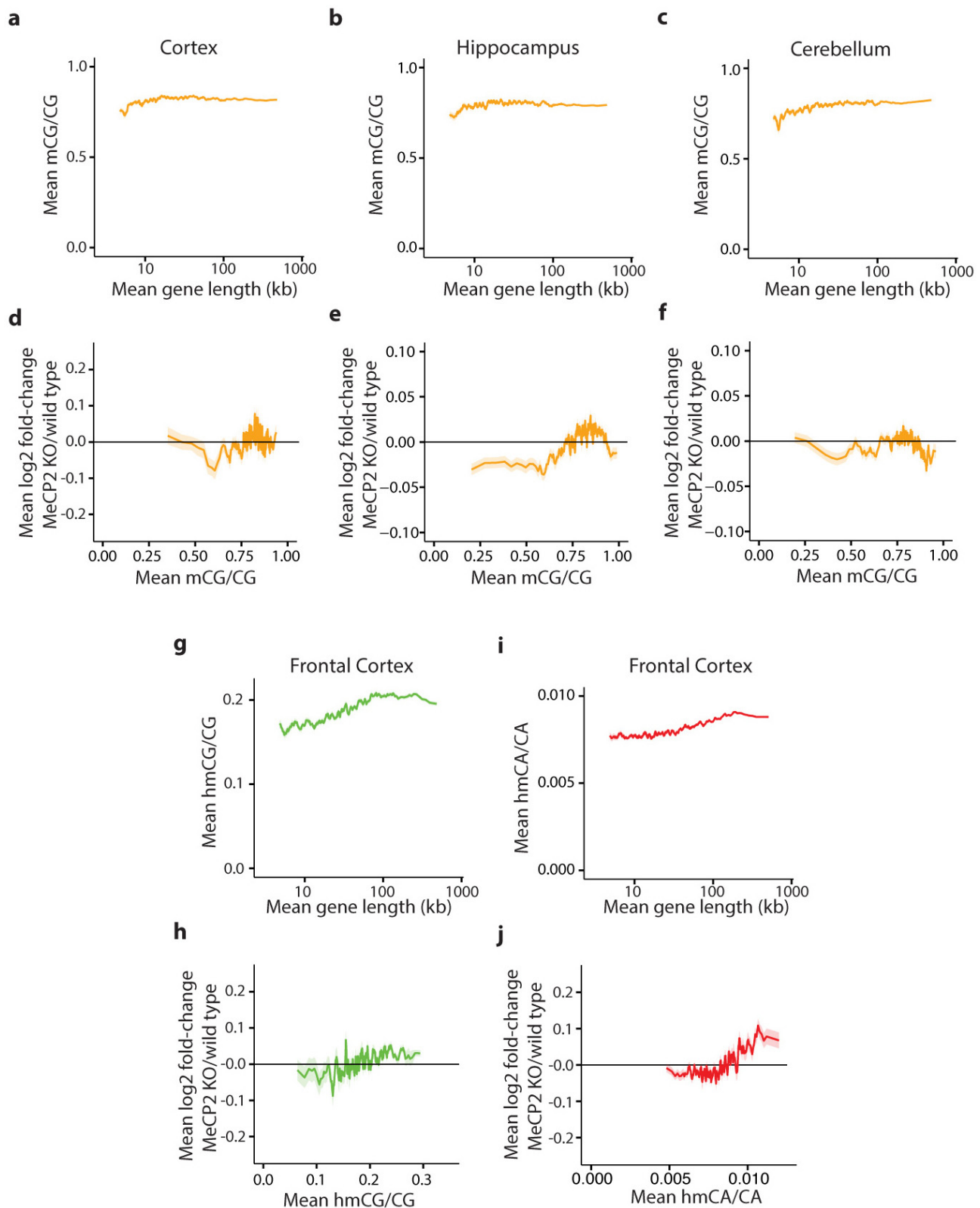
d



Extended Data Figure 4 | ChIP-seq analysis of MeCP2 binding *in vivo*.

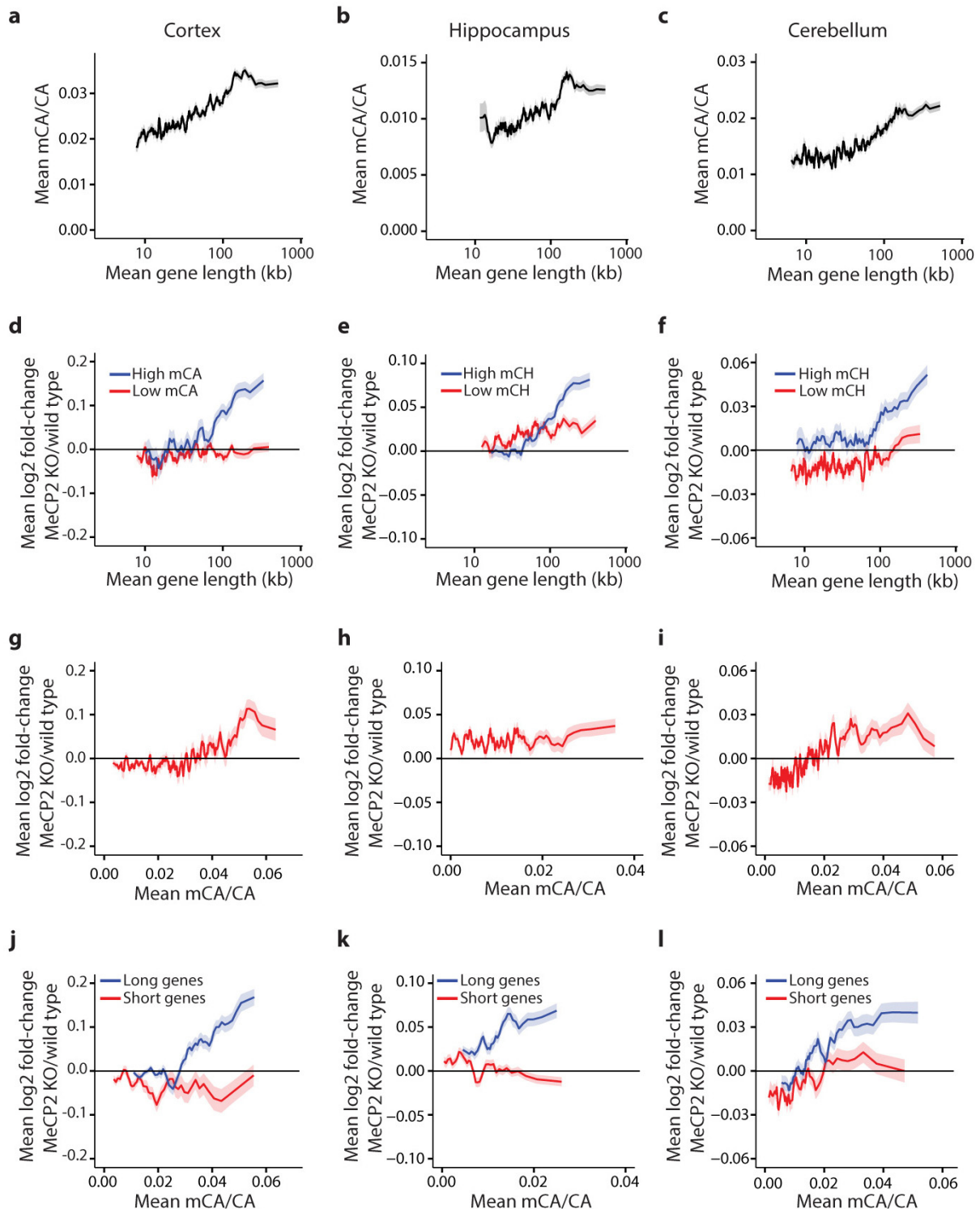
a, Boxplots of input-normalized read density within gene bodies (TSS + 3 kb to TTS) for MeCP2 ChIP from the mouse frontal cortex plotted for genes according to quartile of mCA/CA, mCG/CG, hmCA/CA and hmCG/CG in the frontal cortex²⁴ for all genes and genes >100 kb. **b**, Similar analysis of MeCP2 ChIP from the mouse cortex (left) or cerebellum (right) plotted for genes according to quartile of mCA/CA or mCG/CG for all genes and genes > 100 kb. MeCP2 ChIP-signal is correlated with mCA/CA levels from the frontal cortex, cortex, and cerebellum for all genes and this correlation is more prominent among genes > 100 kb. mCG does not show as prominent a correlation with MeCP2 ChIP signal, and hmCG trends towards anti-correlation with MeCP2 ChIP. These results suggest that MeCP2 has a lower affinity for hmCG than

mCG, suggesting that, *in vivo*, hmCG is associated with reduced MeCP2 occupancy (Supplementary Discussion). **c**, High resolution analysis of high-coverage bisulfite sequencing data from the frontal cortex showing a correlation between MeCP2 ChIP signal and mCA. Input-normalized ChIP signal plotted for mCA levels for 500-bp bins tiled across all genes. **d**, Aggregate plots of MeCP2 input-normalized ChIP signal (top) and relative methylation (log₂ enrichment in mC as compared to the flanking regions) for mCA, mCG, mCT, and mCG (bottom) are plotted around the 31,479 summits of MeCP2 ChIP enrichment identified using the MACS peak-calling algorithm⁴⁰ (red) or 31,479 randomly selected control sites (grey, see Methods). See Methods and Supplementary Table 1 for sample sizes and other details.



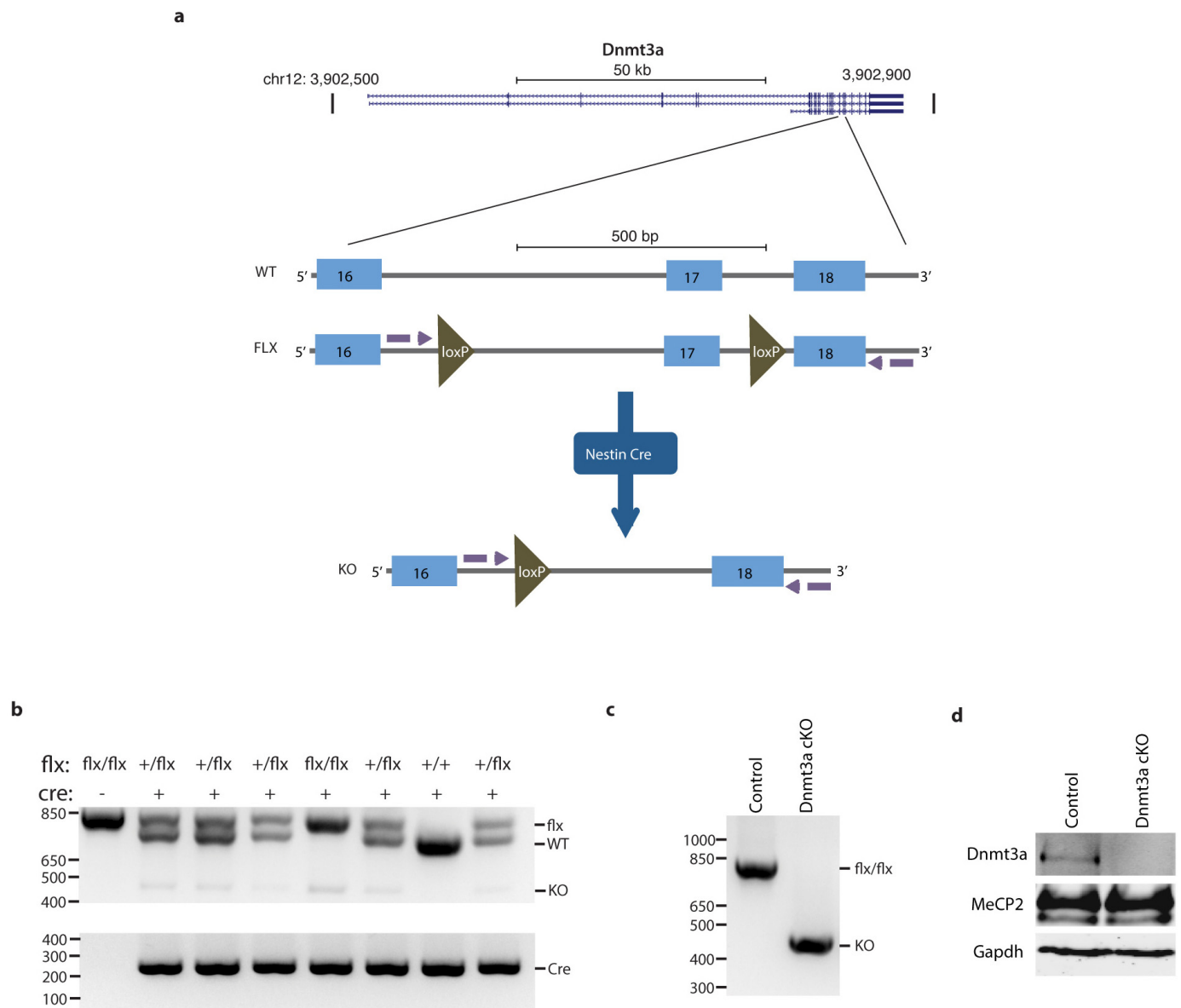
Extended Data Figure 5 | Genomic analysis of mCG, hmCG, and hmCA in length-dependent gene regulation by MeCP2. **a–c,** Mean methylation of CG dinucleotides (mCG/CG) within gene bodies (transcription start site +3 kb, up to transcription termination site) in the cortex (**a**), hippocampus (**b**) and cerebellum (**c**) for genes binned according to length. **d–f,** Mean fold-change in gene expression in MeCP2 KO compared to wild type in the cortex (**d**), hippocampus (**e**), and cerebellum (**f**) for genes binned according to mCG levels (mCG/CG) within gene bodies. **g,** Mean hmCG levels (hmCG/CG) within gene bodies in the frontal cortex²⁴ for genes binned according to length. **h,** Mean

fold-change in gene expression in MeCP2 KO compared to wild type for genes binned according to hmCG levels (hmCG/CG) within gene bodies in the frontal cortex²⁴. **i,** Mean hmCA levels (hmCA/CA) within gene bodies in the frontal cortex²⁴ for genes binned according to length. **j,** Mean fold-change in gene expression in MeCP2 KO compared to wild type genes binned according to hmCA levels (hmCA/CA) within gene bodies in the frontal cortex²⁴. In all panels, mean values for each bin are indicated as a line (200 gene bins, 40 gene step); ribbon depicts s.e.m. for genes within each bin. See Methods and Supplementary Table 1 for sample sizes and other details.



Extended Data Figure 6 | Genomic analysis supports a role for mCA in length-dependent gene regulation by MeCP2. **a–c,** Mean methylation at CA dinucleotides (mCA/CA) within gene bodies (TSS + 3 kb to TTS) in cortex (**a**), hippocampus (**b**), and cerebellum (**c**) for genes binned by length. **d–f,** Mean changes in gene expression in cortex (**d**), hippocampus (**e**), and cerebellum (**f**) of MeCP2 KO for high mCA genes (top 25% mean gene body mCA/CA) and low mCA genes (bottom 66% mean gene body mCA/CA) binned by length. **g–i,** Mean changes in gene expression in cortex (**g**), hippocampus (**h**), and cerebellum (**i**) of MeCP2 KO for genes binned according to average gene body mCA/CA levels. **j–l,** Mean changes in gene expression in cortex (**j**), hippocampus (**k**), and cerebellum (**l**) of MeCP2 KO mice for long genes (top 25%) and short genes (bottom 25%) in each brain region binned by gene body mCA/CA level. A correlation between fold-change in the MeCP2 KO and

mCA/CA for all genes is less prominent, or not observed, in the hippocampus and cerebellum for all genes together (**h, i**), but it is clear for the longest genes in the genome analysed alone (**k, l**). Note that average levels of mCA appear lower in hippocampus and cerebellum compared to cortex (compare y axis in **a, b** and **c**), and may explain why a correlation across all genes is not detected in these brain regions. In long genes analysed alone the cumulative effect of higher mCA levels and integration across the gene may be larger, resulting in a detectable effect. In all panels, the line indicates the mean for 200 gene bins, with a 40 gene step; ribbon depicts s.e.m. for genes within each bin. Note that, for completeness, data from analysis of the cortex presented in Fig. 2 are re-presented here. See Methods and Supplementary Table 1 for sample sizes and other details.

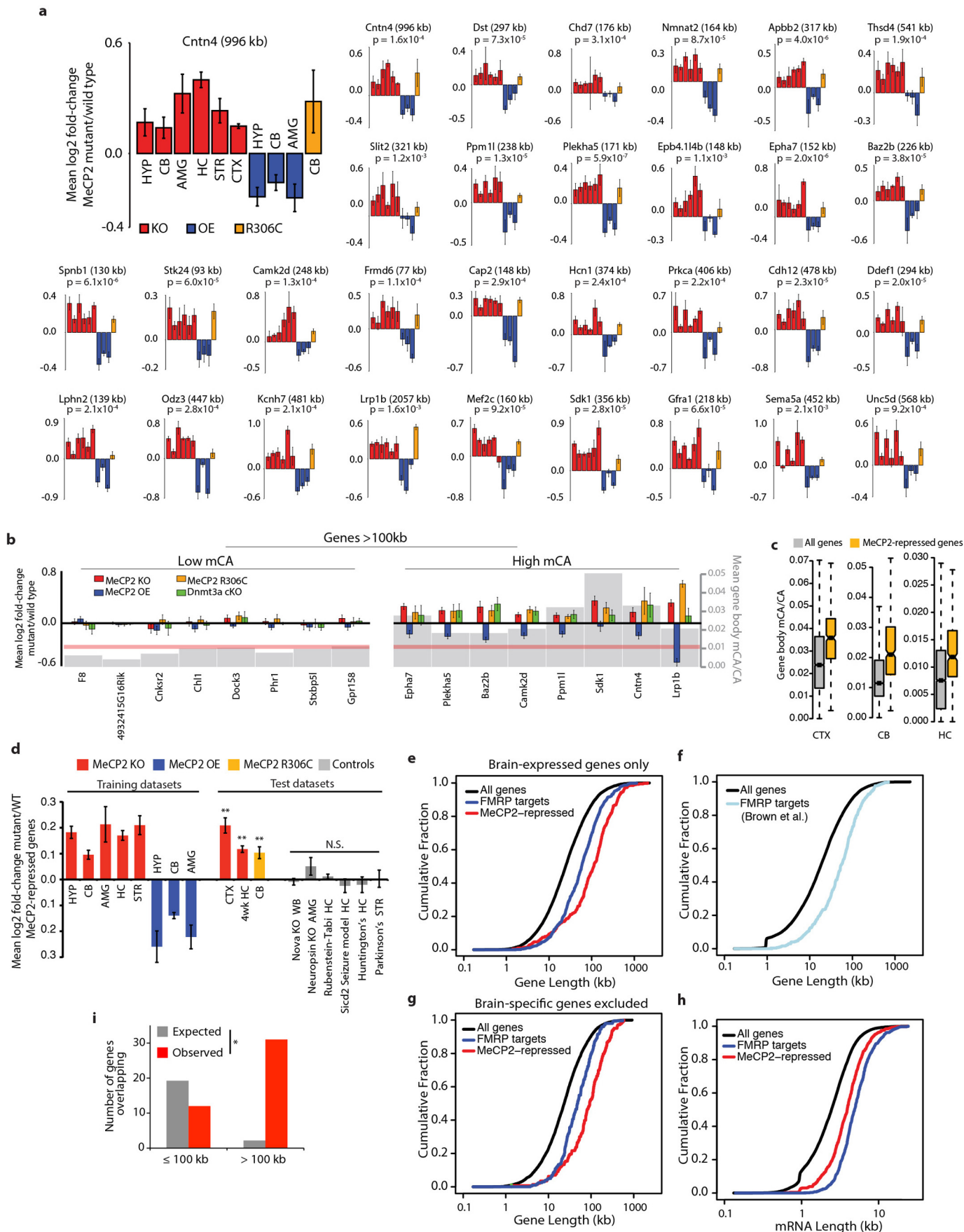


Extended Data Figure 7 | Conditional knockout of *Dnmt3a* *in vivo*.

a, Diagram of the *Dnmt3a* locus and Cre-dependent conditional knockout strategy for *Dnmt3a*²⁶. *LoxP* sites (green triangles) flank exon 17, which is removed following Cre-mediated recombination. Primers (purple arrows) were designed to flank exons 17 and 18. The wild-type (WT), floxed (FLX), and knockout (KO) allele are depicted. **b**, Representative PCR genotyping for tail DNA samples indicates presence or absence of the floxed (flx, ~800 bp), wild-type (WT, ~750 bp), and knockout (KO, ~500 bp) alleles. Separate

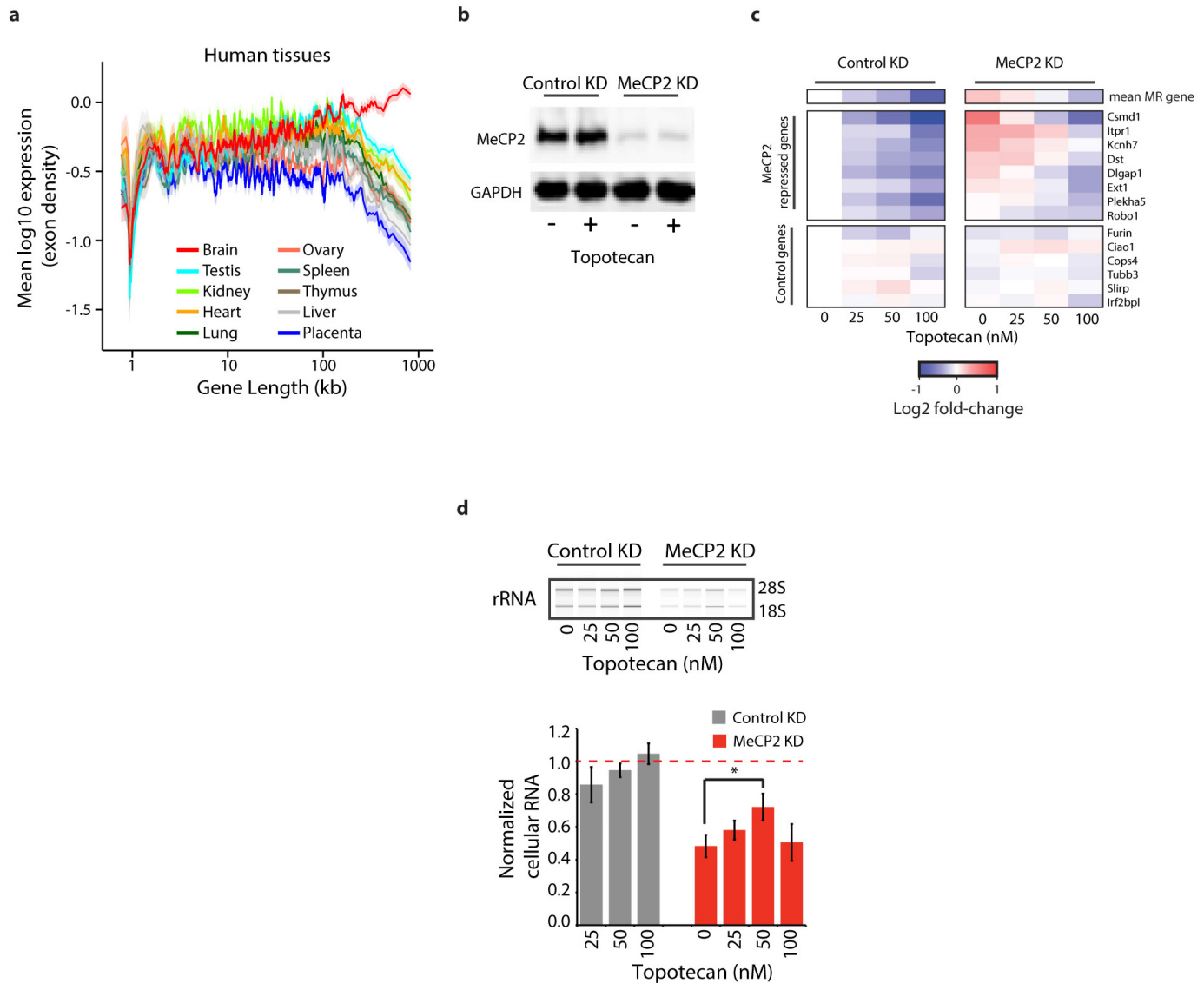
genotyping reaction for the *Nestin-cre* transgene (~250 bp) is shown.

c, Efficient excision of the floxed exon is detected in cerebellar DNA from conditional knockout (*Dnmt3a*^{flx/flx}; *Nestin-Cre*^{+/-}, *Dnmt3a* cKO) mice but not from control animals (*Dnmt3a*^{flx/flx}, Control). **d**, Western blot analysis of Dnmt3a, MeCP2, and Gapdh (loading control) protein from the cerebellum of control and *Dnmt3a* cKO adult mice. All results shown were observed in at least two independent experiments.



Extended Data Figure 8 | Analysis of MeCP2-repressed genes and FMRP target genes. **a**, Mean fold-change in mRNA expression for examples of MeCP2-repressed genes across three different *Mecp2* mutant genotypes (KO, OE, and R306C) and six brain regions. *P* values for each gene are derived from the mean *z* scores for fold-change across all data sets (see Methods). **b**, Gene expression and CA methylation data from the cerebellum for selected MeCP2-repressed genes from **a** (right), as well as examples of extremely long genes (>100 kb) that are not enriched for mCA and are not misregulated (left). Fold-changes in mRNA expression in *Mecp2* mutants and the *Dnmt3a* cKO are shown (left axis), as well as mean mCA levels (grey; right axis). Red line indicates genomic median for gene body mCA/CA. **c**, Boxplots of mCA levels in MeCP2-repressed genes compared to all genes. **d**, Mean fold-change for MeCP2-repressed genes in eight 'training data sets' used to define these genes (see Methods), and nine 'test data sets': three *Mecp2* mutant data sets not used to define MeCP2-repressed genes (CTX MeCP2 KO and CB MeCP2(R306C), generated in this study; HC MeCP2 KO 4 week, analysed from Baker *et al.*⁸), and six data sets from brains of mouse models of neurological dysfunction generated using the same microarray platforms as the MeCP2 data sets (GEO accession numbers in order: GSE22115, GSE27088, GSE43051, GSE47706, GSE44855, GSE52584). Error bars are s.e.m. of MeCP2-repressed gene expression across samples ($n = 4-8$ microarrays per genotype per data set); $**P < 0.01$, one-tailed *t*-test, Benjamini-Hochberg correction. Note that significance testing was not performed on training data sets. Brain regions

indicated as in Fig. 1, (WB, whole brain). **e**, Cumulative distribution function (CDF) of gene lengths plotted exclusively for genes that are among the top 60% of expression levels in the brain (Supplementary Discussion). The extreme length of MeCP2-repressed genes and genes encoding FMRP target mRNAs²⁹ when controlling for expression level indicates that the long length of these genesets is not a secondary effect of the preferential expression of long genes in the brain ($P < 1 \times 10^{-15}$ for each geneset versus all expressed genes; two-sample Kolmogorov-Smirnov test). **f**, The CDF of gene lengths for all genes compared to an independent set of FMRP targets identified by Brown and colleagues⁴⁵ ($P < 1 \times 10^{-15}$, Kolmogorov-Smirnov-test). **g**, CDF of gene lengths for genes expressed at similar levels in the brain and other somatic tissues (Supplementary Discussion). The extreme length of each geneset ($P < 1 \times 10^{-15}$, Kolmogorov-Smirnov test) when filtering for genes that are expressed in all tissues indicates that regulation of long genes by MeCP2 and FMRP is not dependent on brain-specific expression. **h**, CDF of mature mRNA lengths for MeCP2-repressed genes, and FMRP target genes ($P < 1 \times 10^{-11}$ for each geneset versus all genes, Kolmogorov-Smirnov test). **i**, Overlap of MeCP2-repressed genes and putative FMRP target mRNAs²⁹ ($P < 5 \times 10^{-5}$, hypergeometric test). Expected overlap was calculated by dividing the expected overlap genome-wide (hypergeometric distribution) according to the distribution of all gene lengths in the genome. See Methods and Supplementary Table 1 for sample sizes and other details.



Extended Data Figure 9 | Consequences of long gene misregulation in neurons. **a**, Mean expression of genes binned according to length in human neural and non-neural tissues. Mean expression for genes within each bin (200 gene bins, 40 gene step) is indicated by the line; ribbon represents the s.e.m. of genes within each bin. **b**, Western blot analysis of MeCP2 from primary cortical neurons after control or MeCP2 shRNA knockdown (KD) and treatment with DMSO vehicle (–) or topotecan (+). **c**, Heatmap summary of nCounter analysis for the expression of selected MeCP2-repressed (MR) genes from primary neurons treated with control or MeCP2 shRNA and topotecan ($n = 3-4$). Normalized log₂ fold-change relative to the DMSO-treated, control KD is shown. MeCP2 KD conditions are significantly different

from control, ($P = 1 \times 10^{-4}$, repeated measures ANOVA across 8 genes). Newman-Keuls corrected, post-hoc comparisons: $P < 0.05$ control KD, 0 nM drug versus MeCP2 KD, 0 nM drug; $P > 0.05$, control KD, 0 nM drug versus MeCP2 KD, 50 nM drug; $P < 0.05$ MeCP2 KD, 0 nM drug versus MeCP2 KD, 50 nM drug. **d**, Bioanalyzer profiles of 18S and 28S ribosomal RNA (top) and total RNA quantification (bottom) for treated neurons ($n = 3-5$). Total RNA values normalized to DMSO-treated control KD, red dashed line. Two-way repeated measures ANOVA indicates a significant effect of KD ($P < 0.01$) and drug treatment ($P < 0.05$). Rescue assessed by one-tailed t -test, Bonferroni multiple testing correction, $*P < 0.05$.

Extended Data Table 1 | Gene ontology analysis of MeCP2-repressed genes and genes >100 kb

MeCP2 Repressed Genes
(466 genes)

GO Term	Gene Count	EASE pval	Fold Enriched	Benjamini pval	GO Accession
Biological Process					
axon guidance	17	3.7E-08	5.6	6.3E-05	GO:0007411
axonogenesis	21	6.5E-08	4.3	5.5E-05	GO:0007409
cell morphogenesis involved in differentiation	23	2.4E-07	3.7	1.4E-04	GO:0000904
neuron projection morphogenesis	21	2.6E-07	4	1.1E-04	GO:0048812
cell morphogenesis involved in neuron differentiation	21	3.6E-07	3.9	1.2E-04	GO:0048667
neuron projection development	23	3.9E-07	3.6	1.1E-04	GO:0031175
neuron development	26	9.3E-07	3.1	2.3E-04	GO:0048666
cell projection morphogenesis	21	1.3E-06	3.6	2.8E-04	GO:0048858
cell morphogenesis	26	2.1E-06	3	4.0E-04	GO:0000902
cell part morphogenesis	21	3.3E-06	3.4	5.5E-04	GO:0032990
phosphate metabolic process	49	3.3E-06	2	5.1E-04	GO:0006796
phosphorus metabolic process	49	3.3E-06	2	5.1E-04	GO:0006793
cellular component morphogenesis	27	4.2E-06	2.8	5.9E-04	GO:0032989
cell projection organization	26	5.2E-06	2.8	6.8E-04	GO:0030030
enzyme linked receptor protein signaling pathway	24	8.5E-06	2.9	1.0E-03	GO:0007167
Cellular Component					
plasma membrane	110	2.00E-05	1.4	5.3E-03	GO:0005886
cell junction	29	4.30E-05	2.3	5.7E-03	GO:0030054
cytoskeleton	50	6.00E-05	1.8	5.4E-03	GO:0005856
postsynaptic density	8	2.40E-04	6.2	1.6E-02	GO:0014069
synapse	21	3.80E-04	2.4	2.0E-02	GO:0045202
plasma membrane part	64	8.20E-04	1.5	3.6E-02	GO:0044459
cell fraction	29	2.10E-03	1.8	7.9E-02	GO:0000267
basement membrane	8	2.60E-03	4.2	8.3E-02	GO:0005604
neuron projection	16	3.10E-03	2.4	8.7E-02	GO:0043005
synapse part	14	3.20E-03	2.6	8.3E-02	GO:0044456
insoluble fraction	26	3.50E-03	1.9	8.3E-02	GO:0005626
membrane fraction	25	4.50E-03	1.8	9.7E-02	GO:0005624
postsynaptic membrane	10	4.90E-03	3.1	9.7E-02	GO:0045211
Molecular Function					
cation binding	148	5.00E-07	1.4	2.6E-04	GO:0043169
metal ion binding	147	5.50E-07	1.4	1.4E-04	GO:0046872
ion binding	149	7.50E-07	1.4	1.3E-04	GO:0043167
calcium ion binding	47	8.50E-06	2	1.1E-03	GO:0005509
actin binding	21	2.00E-04	2.6	2.1E-02	GO:0003779
cytoskeletal protein binding	26	3.80E-04	2.2	3.3E-02	GO:0008092
protein kinase activity	33	5.30E-04	1.9	3.9E-02	GO:0004672
cation channel activity	18	8.40E-04	2.5	5.3E-02	GO:0005261
voltage-gated cation channel activity	12	1.10E-03	3.2	6.3E-02	GO:0022843
alkali metal ion binding	16	1.40E-03	2.6	6.8E-02	GO:0031420
metal ion transmembrane transporter activity	19	1.90E-03	2.3	8.6E-02	GO:0046873
voltage-gated ion channel activity	14	1.90E-03	2.7	7.9E-02	GO:0005244
voltage-gated channel activity	14	1.90E-03	2.7	7.9E-02	GO:0022832
potassium ion binding	11	2.20E-03	3.2	8.6E-02	GO:0030955

Genes Longer than 100KB
(1431 genes)

GO Term	Gene Count	EASE pval	Fold Enriched	Benjamini pval	GO Accession
Biological Process					
phosphate metabolic process	150	1.2E-18	2	3.4E-15	GO:0006796
phosphorus metabolic process	150	1.2E-18	2	3.4E-15	GO:0006793
protein modification process	191	8.3E-18	1.8	1.2E-14	GO:0006464
protein amino acid phosphorylation	120	4.1E-17	2.2	4.0E-14	GO:0006468
biopolymer modification	191	1.4E-15	1.7	1.0E-12	GO:0043412
phosphorylation	124	2.7E-15	2	1.6E-12	GO:0016310
cellular component organization	247	1.1E-14	1.6	5.5E-12	GO:0016043
biological adhesion	101	2.4E-14	2.2	1.0E-11	GO:0022610
cell adhesion	101	2.4E-14	2.2	1.0E-11	GO:0007155
post-translational protein modification	156	1.4E-13	1.8	5.0E-11	GO:0043687
cellular process	849	1.6E-13	1.1	5.2E-11	GO:0009987
nervous system development	137	4.9E-13	1.8	1.4E-10	GO:0007399
cell projection organization	65	9.0E-11	2.3	2.4E-08	GO:0030030
cell morphogenesis	62	2.3E-10	2.3	5.6E-08	GO:0000902
neuron development	59	8.2E-10	2.3	1.8E-07	GO:0048666
Cellular Component					
synapse	74	7.9E-17	2.8	4.4E-14	GO:0045202
cell junction	86	2.5E-13	2.3	5.0E-11	GO:0030054
neuron projection	58	3.4E-13	2.8	4.5E-11	GO:0043005
cell projection	96	1.4E-12	2.1	1.4E-10	GO:0042995
cytoskeleton	149	2.9E-12	1.7	2.3E-10	GO:0005856
plasma membrane	325	5.3E-12	1.4	3.5E-10	GO:0005886
plasma membrane part	205	5.5E-12	1.6	3.1E-10	GO:0044459
extracellular matrix part	30	2.5E-11	4	1.2E-09	GO:0044420
basement membrane	24	1.8E-09	4.1	8.0E-08	GO:0005604
synapse part	43	1.1E-08	2.6	4.2E-07	GO:0044456
proteinaceous extracellular matrix	56	1.4E-08	2.2	4.9E-07	GO:0005578
axon	31	1.8E-08	3.1	6.1E-07	GO:0030424
extracellular matrix	57	2.3E-08	2.2	7.1E-07	GO:0031012
dendrite	29	4.8E-08	3.1	1.4E-06	GO:0030425
postsynaptic membrane	29	2.2E-07	2.9	5.8E-06	GO:0045211
Molecular Function					
calcium ion binding	138	1.4E-15	2	1.2E-12	GO:0005509
protein kinase activity	111	1.6E-15	2.2	6.6E-13	GO:0004672
adenyl ribonucleotide binding	209	9.3E-15	1.7	2.6E-12	GO:0032559
cytoskeletal protein binding	85	1.5E-14	2.4	3.1E-12	GO:0008092
GTPase regulator activity	72	1.2E-13	2.5	2.0E-11	GO:0030695
nucleoside binding	215	1.5E-13	1.6	2.1E-11	GO:0001882
adenyl nucleotide binding	212	2.6E-13	1.6	3.1E-11	GO:0030554
purine nucleoside binding	213	2.8E-13	1.6	2.9E-11	GO:0001883
ATP binding	202	3.0E-13	1.6	2.8E-11	GO:0005524
nucleoside-triphosphatase regulator activity	72	3.9E-13	2.5	3.3E-11	GO:0060589
ion binding	412	9.8E-12	1.3	7.5E-10	GO:0043167
metal ion binding	403	2.0E-11	1.3	1.4E-09	GO:0046872
purine ribonucleotide binding	229	2.5E-11	1.5	1.6E-09	GO:0032555
ribonucleotide binding	229	2.5E-11	1.5	1.6E-09	GO:0032553
cation binding	404	3.8E-11	1.3	2.3E-09	GO:0043169

Functional annotation clustering analysis of genes identified as MeCP2-repressed and the longest genes in the genome (>100 kb) was performed using the DAVID bioinformatics resource (DAVID v6.7)⁴⁴. The top fifteen enriched gene ontology terms with $P < 0.01$ (Benjamini multiple testing correction) are listed for “Biological Process”, “Cellular Component”, and “Molecular Function”, respectively.

Dissemination, divergence and establishment of H7N9 influenza viruses in China

Tommy Tsan-Yuk Lam^{1,2,3*}, Boping Zhou^{1*}, Jia Wang^{2,3*}, Yujuan Chai^{2,3*}, Yongyi Shen^{2,3*}, Xinchun Chen^{1*}, Chi Ma^{2,3}, Wenshan Hong², Yin Chen⁴, Yanjun Zhang⁴, Lian Duan^{1,2,3}, Peiwen Chen^{1,2}, Junfei Jiang^{1,3}, Yu Zhang^{2,3}, Lifeng Li^{2,3}, Leo Lit Man Poon^{1,3}, Richard J. Webby⁵, David K. Smith^{2,3}, Gabriel M. Leung³, Joseph S. M. Peiris^{1,3}, Edward C. Holmes⁶, Yi Guan^{1,2,3} & Huachen Zhu^{1,2,3}

Since 2013 the occurrence of human infections by a novel avian H7N9 influenza virus in China has demonstrated the continuing threat posed by zoonotic pathogens^{1,2}. Although the first outbreak wave that was centred on eastern China was seemingly averted, human infections recurred in October 2013 (refs 3–7). It is unclear how the H7N9 virus re-emerged and how it will develop further; potentially it may become a long-term threat to public health. Here we show that H7N9 viruses have spread from eastern to southern China and become persistent in chickens, which has led to the establishment of multiple regionally distinct lineages with different reassortant genotypes. Repeated introductions of viruses from Zhejiang to other provinces and the presence of H7N9 viruses at live poultry markets have fuelled the recurrence of human infections. This rapid expansion of the geographical distribution and genetic diversity of the H7N9 viruses poses a direct challenge to current disease control systems. Our results also suggest that H7N9 viruses have become enzootic in China and may spread beyond the region, following the pattern previously observed with H5N1 and H9N2 influenza viruses^{8,9}.

The second wave of the H7N9 outbreak that begun in late 2013 has resulted in 318 human cases and over a hundred deaths as of 12 September 2014 (ref. 7), more than twice that of the first wave. Guangdong, which had no reported human infection in the first wave, and Zhejiang have reported the highest numbers of human cases in the second wave⁷. We used influenza surveillance at live poultry markets (LPMs) in Zhejiang, Guangdong, Jiangxi, Jiangsu and Shandong provinces, at specific times or routinely, from October 2013 to July 2014 (Extended Data Tables 1 and 2), and at hospitals in Shenzhen (Guangdong) from December 2013 to April 2014, to trace the evolution and spread of the second wave of the H7N9 outbreak.

Active surveillance in fifteen cities across these five provinces identified 493 H7N9 viruses from oropharyngeal swabs of market chickens, with an average isolation rate of 3.0% (Extended Data Table 1 and Fig. 1). Only five H7N9 viruses were isolated from 2,465 cloacal swabs sampled in chickens in Jiangxi and Guangdong, giving an isolation rate of 0.2%. No H7N9 virus was isolated from domestic ducks during this survey (Extended Data Table 2). These findings highlight that market

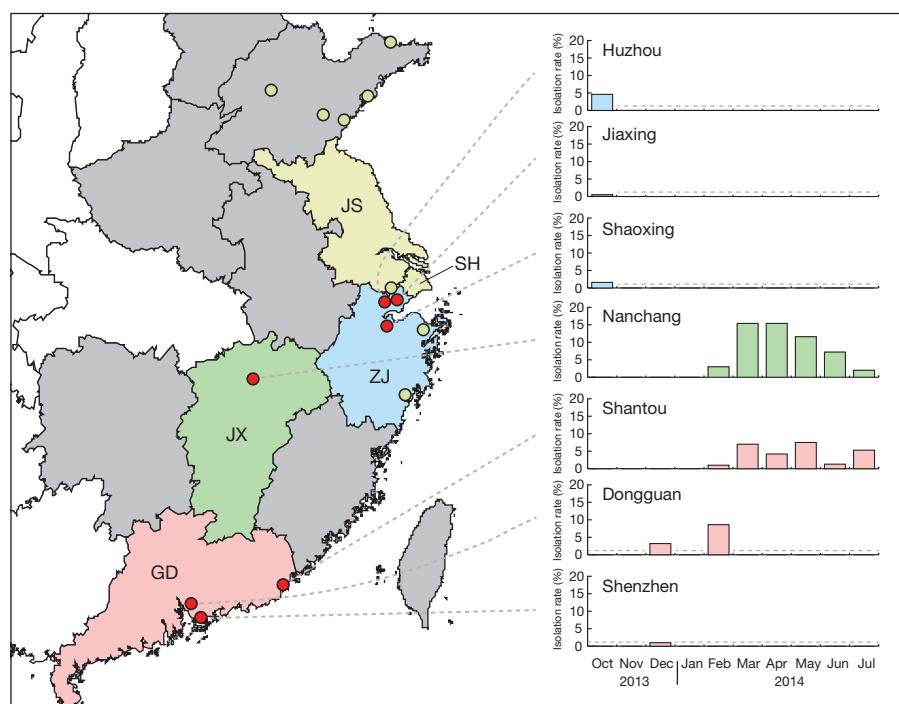


Figure 1 | Map showing the sampling sites in China and H7N9 isolation rates in market chickens. Green and red circles, respectively, indicate the cities ($n = 15$) negative and positive for detection of H7N9 viruses in the oropharyngeal swabs of chickens at live poultry markets. Monthly isolation rates are shown on the right. Dashed lines indicate the months during which samples were unavailable. Abbreviations for provinces are JS, Jiangsu; SH, Shanghai; ZJ, Zhejiang; JX, Jiangxi; GD, Guangdong.

¹State Key Laboratory of Emerging Infectious Diseases (HKU-Shenzhen Branch), Shenzhen Third People's Hospital, Shenzhen 518112, China. ²Joint Influenza Research Centre (SUMC/HKU), Shantou University Medical College (SUMC), Shantou 515041, China. ³Centre of Influenza Research, School of Public Health, The University of Hong Kong (HKU), Hong Kong, China. ⁴Key Laboratory of Emergency Detection for Public Health of Zhejiang Province, Zhejiang Provincial Center for Disease Control and Prevention, Hangzhou, Zhejiang 310051, China. ⁵Division of Virology, Department of Infectious Diseases, St Jude Children's Research Hospital, Memphis, Tennessee 38105, USA. ⁶Marie Bashir Institute for Infectious Diseases and Biosecurity, Charles Perkins Centre, School of Biological Sciences and Sydney Medical School, University of Sydney, Sydney, New South Wales 2006, Australia.

*These authors contributed equally to this work.

chickens shedding H7N9 viruses via the oropharyngeal route are central to the H7N9 outbreak. Human cases^{3–7} were reported in all of the seven cities where H7N9 viruses were detected in chickens. The H7N9 positive rates in Dongguan (Guangdong) increased from 3.2% (December 2013) to 8.6% (February 2014) (Extended Data Table 1 and Fig. 1). Our routine surveillance in Nanchang (Jiangxi) and Shantou (Guangdong) revealed that both cities were negative for H7N9 viruses until February 2014. Since then, H7N9 viruses have been detected every month up to July 2014, with isolation rates ranging from 2.0% to 15.4% in Nanchang, and from 1.0% to 7.5% in Shantou (Extended Data Table 1). No H7N9 viruses were detected at live poultry markets in the six cities in Shandong and Jiangsu that we sampled during October 2013 (Extended Data Table 1).

To examine the re-emergence of H7N9 in more detail we sequenced the complete genomes of 438 H7N9 and 263 related influenza viruses (including 194 H9N2) isolated from poultry from October 2013 to July 2014, and 19 H7N9 human isolates obtained from hospitals in Shenzhen. Phylogenetic and phylogeographic analyses of the H7 haemagglutinin (HA) genes confirmed that all of the second wave avian and human H7N9 viruses were descended from the viruses of the first wave (Fig. 2a). Wave 1 HA genes from the affected provinces were very similar and generally branched from a central node (shown as a red empty circle in Fig. 2a) of the wave 1 (W1) clade that fell at the base of the tree, indicative of a broad dissemination of the virus during the initial outbreak. In contrast, viruses of the second wave (W2) clustered into three major

clades, designated as W2-A, W2-B and W2-C (Fig. 2a), all of which emerged from the W1 clade.

The W2-A clade contains viruses detected in multiple provinces from October 2013 to July 2014. Most virus isolates from Zhejiang were located near the root of this clade, while clusters of viruses from Jiangxi, Guangdong and Fujian diverged from some other Zhejiang viruses in this clade (for example, ZJ/30/2014; Fig. 2a). This suggests that this clade originated in Zhejiang, or the Yangtze River delta region, and then spread to other provinces (Supplementary Discussion 1.4; <http://dx.doi.org/10.5061/dryad.5q7kf>). The differing sub-clades of Jiangxi viruses in clade W2-A contain isolates sampled from February to April 2014, suggesting multiple introductions of the viruses, probably by poultry movement.

Clade W2-B is likely to have originated from viruses closely related to those isolated in Guangzhou in May 2013 (Fig. 2a, Supplementary Discussion 1.4; <http://dx.doi.org/10.5061/dryad.5q7kf>) that apparently persisted in Guangdong over summer^{6,10}. These viruses have proliferated since October 2013 and caused the largest number of human infections reported in the second outbreak wave^{4,6,7}. Viruses within this clade have only been detected in Guangdong, mainly in the Pearl River delta region, suggesting that they have become established and enzootic in the chicken population in this locality.

Clade W2-C viruses were mainly isolated from Jiangxi from April to June 2014. Two recent human isolates from Taiwan⁷, which originated from Jiangsu, fall in this clade close to the Jiangxi isolates (Fig. 2a),

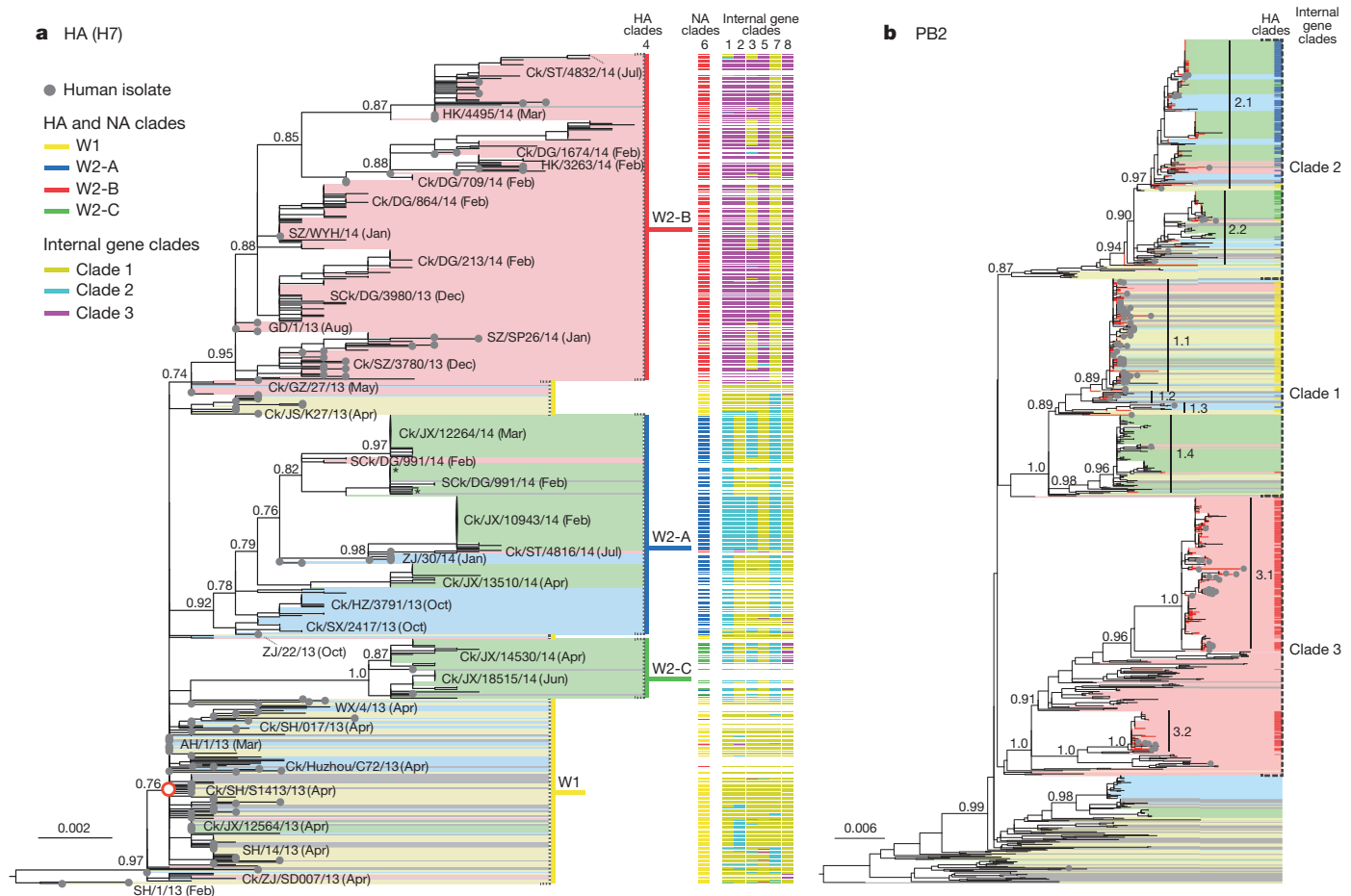


Figure 2 | Evolution of H7N9 influenza viruses from wave 1 to wave 2. **a**, Maximum likelihood phylogeny (see Methods) of the HA genes of 663 H7N9 viruses with unambiguous sequences. For viruses with complete genomes, the clade origins of each gene segment are indicated by different coloured bars (see legend). The 'central node' of the W1 clade is marked by a red circle. The two H7N6 viruses are marked with asterisks. **b**, Maximum likelihood phylogeny of 1,060 ZJ-HJ/07 sub-lineage PB2 genes. Red branches indicate

H7N9 viruses. In both panels, the background shading shows the provinces from which the viruses were collected (see Fig. 1 for the colours indicating the provinces). Human samples are denoted by grey circles. Shimodaira-Hasegawa-like branch support values of selected nodes are shown. Detailed maximum likelihood phylogenies and Bayesian time-scaled phylogenies are available from <http://dx.doi.org/10.5061/dryad.5q7kf>.

suggesting that W2-C viruses were also simultaneously prevalent in eastern China. The outgroup viruses of this clade, detected in Zhejiang and Shanghai^{2,3,11,12}, indicate that it may have originated in eastern China. A lack of surveillance data from the beginning of wave 2 prevents identification of the early spread of this clade (Supplementary Discussion 1.4; <http://dx.doi.org/10.5061/dryad.5q7kf>). Similar situations may have occurred in neighbouring provinces, such as Anhui and Hunan, where human cases have been reported^{3,7}, although no or few chicken viruses have been reported from these localities.

Phylogenetic analysis of the N9 neuraminidase (NA) genes revealed a similar topology to that of the H7 HA tree, with the wave 2 viruses separated into three corresponding clades (available from <http://dx.doi.org/10.5061/dryad.5q7kf>). However, the N9 genes from the early Guangdong viruses did not initially form a distinct subclade. After October 2013, the W2-B clade in the N9 genes became established. Some viruses isolated in Shantou (Guangdong) that possess a W2-A HA have reassorted to acquire the W2-B NA gene, suggesting the co-circulation of different clades of H7N9 viruses in Guangdong.

The internal genes of all H7N9 viruses studied here belonged to the ZJ-HJ/07 lineage¹³ of H9N2 viruses, which is broadly classified into three clades (clades 1–3; Fig. 2b, Extended Data Fig. 1). In each internal gene the majority of wave 1 H7N9 viruses formed a sub-clade (denoted as clade 1.1) in clade 1. Wave 2 viruses had internal genes from the regionally distributed clade 2 and from clade 3, which was local to Guangdong.

In the second wave, none of the avian and human H7N9 viruses inherited all six internal gene segments from clade 1.1 (Fig. 2, Extended Data Figs 1 and 2). The early W2-A viruses mostly acquired PB2 and M segments from clade 2 of the ZJ-HJ/07 lineage. The later spread of these viruses to Jiangxi, Guangdong and Fujian led to the replacement of PB1 and PA with clade 2 segments in most viruses, suggesting sequential reassortment events with local H9N2 viruses (Fig. 2, Extended Data Fig. 1). The clade 1 origin NP and NS segments were generally retained in the W2-A viruses. The majority of W2-B viruses had four or five internal gene segments derived from clade 3. Almost all W2-B viruses retained the clade 1.1 M gene segment and approximately half had a clade 1.1 origin PA segment. W2-C viruses mostly reassorted to acquire clade 2 PB2, PA and M segments and a clade 3 NS segment, with their PB1 and NP segments remaining mainly from clade 1. Notably, two H7N6 viruses, which were reassortants of H7N9 W2-A viruses and H5N6 viruses co-circulating in the poultry of Jiangxi, were identified (Fig. 2). Thus, the evolution of the wave 2 H7N9 viruses from those of wave 1 has resulted in a major increase in genetic diversity (Extended Data Table 3, Supplementary Discussion 1.1).

Although amino acid changes occurred in the HA (Extended Data Table 4), limited antigenic differences were observed (Supplementary Data, Supplementary Discussion 1.2). Mutations associated with drug resistance in the NA protein^{14,15} only occurred in a small number of human isolates (Extended Data Table 5), probably reflecting a response to drug treatment. Consistent differences between the human and avian isolates were restricted to the PB2 residues 627 and 701 (Extended Data Table 5, Supplementary Discussion 1.3), which are frequently seen when an avian virus enters a mammalian host^{16–19}.

Our study has shown that the H7N9 influenza virus has diverged into distinct clades, becoming established in chickens and disseminating to wider geographic regions. This probably occurred by poultry movement along trade routes, with the localization of the W2-B clade in turn reflecting limited exports from high poultry consuming areas. Human infections have mostly been reported from southern and eastern China^{1–5,7,10,12}. With the recent reports of H7N9 infections in Xinjiang⁷ in the far northwest of China, it is probable that the H7N9 virus is now present across most of China. As this virus does not cause obvious symptoms in chickens²⁰ and only limited surveillance has been conducted, the prevalence of this virus is likely to be higher than we document here, and it has had the opportunity to become enzootic over a wide region. Given the current pattern of dissemination, it will only be

a matter of time before poultry movement spreads this virus beyond China by cross-border trade, as happened previously with H5N1 and H9N2 influenza viruses^{8,21}.

The enzootic H5N1 and H9N2 viruses^{8,9}, along with the H7N9 virus, are now reassorting with other viruses in the influenza ecosystem in China, giving rise to novel variants such as H10N8 (ref. 22), H10N6 (ref. 23), H5N8 (ref. 24), H5N6 (ref. 25) and H7N6 (this study). This expansion of the genetic diversity of influenza viruses in China means that unless effective control measures are in place, such as permanent closure of live poultry markets, central slaughtering and preventing inter-regional poultry transportation during disease outbreaks, and backed by systematic surveillance, it is reasonable to expect the H7N9 and other viruses to persist and cause a substantial number of severe human infections. H7 is the only subtype, other than the pandemic subtypes, that has been established in mammals (Equine-1, H7N7)²⁶. Therefore, H7N9 viruses should be considered as a major candidate to emerge as a pandemic strain in humans.

Online Content Methods, along with any additional Extended Data display items and Source Data, are available in the online version of the paper; references unique to these sections appear only in the online paper.

Received 30 September 2014; accepted 24 February 2015.

Published online 11 March 2015.

- Gao, R. *et al.* Human infection with a novel avian-origin influenza A (H7N9) virus. *N. Engl. J. Med.* **368**, 1888–1897 (2013).
- Wu, A. *et al.* Sequential reassortments underlie diverse influenza H7N9 genotypes in China. *Cell Host Microbe* **14**, 446–452 (2013).
- Wang, D. *et al.* Genetic tuning of the novel avian influenza A(H7N9) virus during interspecies transmission, China, 2013. *Euro Surveill.* **19**, 20836 (2014).
- Chen, Z. *et al.* Asymptomatic, mild, and severe influenza A(H7N9) virus infection in humans, Guangzhou, China. *Emerg. Infect. Dis.* **20**, 1535–1540 (2014).
- Chen, E. *et al.* Human infection with avian influenza A(H7N9) virus re-emerges in China in winter 2013. *Euro Surveill.* **18**, 20616 (2013).
- Lu, J. *et al.* Continuing reassortment leads to the genetic diversity of influenza virus H7N9 in Guangdong, China. *J. Virol.* **88**, 8297–8306 (2014).
- World Health Organization. Situation updates - Avian influenza http://www.who.int/entity/influenza/human_animal_interface/avian_influenza/archive/en/index.html (accessed, 12 September 2014).
- Guan, Y. & Smith, G. J. The emergence and diversification of panzootic H5N1 influenza viruses. *Virus Res.* **178**, 35–43 (2013).
- Xu, K. M. *et al.* The genesis and evolution of H9N2 influenza viruses in poultry from southern China, 2000 to 2005. *J. Virol.* **81**, 10389–10401 (2007).
- Chen, Z. *et al.* Detection of avian influenza A(H7N9) virus from live poultry markets in Guangzhou, China: a surveillance report. *PLoS ONE* **9**, e107266 (2014).
- Cui, L. *et al.* Dynamic reassortments and genetic heterogeneity of the human-infecting influenza A (H7N9) virus. *Nature Commun.* **5**, 3142 (2014).
- Chen, Y. *et al.* Human infections with the emerging avian influenza A H7N9 virus from wet market poultry: clinical analysis and characterisation of viral genome. *Lancet* **381**, 1916–1925 (2013).
- Lam, T. T. *et al.* The genesis and source of the H7N9 influenza viruses causing human infections in China. *Nature* **502**, 241–244 (2013).
- McKimm-Breschkin, J. L. *et al.* Mutations in a conserved residue in the influenza virus neuraminidase active site decreases sensitivity to Neu5Ac2en-derived inhibitors. *J. Virol.* **72**, 2456–2462 (1998).
- Hu, Y. *et al.* Association between adverse clinical outcome in human disease caused by novel influenza A H7N9 virus and sustained viral shedding and emergence of antiviral resistance. *Lancet* **381**, 2273–2279 (2013).
- Gabriel, G. *et al.* The viral polymerase mediates adaptation of an avian influenza virus to a mammalian host. *Proc. Natl Acad. Sci. USA* **102**, 18590–18595 (2005).
- Subbarao, E. K., London, W. & Murphy, B. R. A single amino acid in the PB2 gene of influenza A virus is a determinant of host range. *J. Virol.* **67**, 1761–1764 (1993).
- Li, Z. *et al.* Molecular basis of replication of duck H5N1 influenza viruses in a mammalian mouse model. *J. Virol.* **79**, 12058–12064 (2005).
- Steel, J., Lowen, A. C., Mubareka, S. & Palese, P. Transmission of influenza virus in a mammalian host is increased by PB2 amino acids 627K or 627E/701N. *PLoS Pathog.* **5**, e1000252 (2009).
- Pantin-Jackwood, M. J. *et al.* Role of poultry in the spread of novel H7N9 influenza virus in China. *J. Virol.* **88**, 5381–5390 (2014).
- Okamoto, M. *et al.* The genetic and antigenic diversity of avian influenza viruses isolated from domestic ducks, muscovy ducks, and chickens in northern and southern Vietnam, 2010–2012. *Virus Genes* **47**, 317–329 (2013).
- Chen, H. *et al.* Clinical and epidemiological characteristics of a fatal case of avian influenza A H10N8 virus infection: a descriptive study. *Lancet* **383**, 714–721 (2014).
- Ma, C. *et al.* Emergence and evolution of H10 subtype influenza viruses in poultry in China. *J. Virol.* <http://dx.doi.org/10.1128/JVI.03167-14> (2015).
- Zhao, K. *et al.* Characterization of three H5N5 and one H5N8 highly pathogenic avian influenza viruses in China. *Vet. Microbiol.* **163**, 351–357 (2013).

25. Qi, X., Cui, L., Yu, H., Ge, Y. & Tang, F. Whole-genome sequence of a reassortant H5N6 avian influenza virus isolated from a live poultry market in China, 2013. *Genome Announc.* **2**, e00706–14 (2014).
26. Webster, R. G., Bean, W. J., Gorman, O. T., Chambers, T. M. & Kawaoka, Y. Evolution and ecology of influenza A viruses. *Microbiol. Rev.* **56**, 152–179 (1992).

Supplementary Information is available in the online version of the paper.

Acknowledgements We thank C. L. Cheung, H. Y. Liang and G. C. Yu for their assistance in data processing; Z. H. Ou, Z. Y. Jin, T. Y. Leung, K. K. Chan, Y. R. Qiu, J. Z. Xie, N. Qi, J. Zhou, P. Y. Huang and all staff members at the Joint Influenza Research Centre (SUMC/HKU) for technical support, the four collaborative hospitals in Shenzhen for human sample collection, and P. Lemey for his advice on phylogeographic analysis. This study was supported by the Shenzhen Peacock Plan High-End Talents Program (KQTD201203), the Health and Medical Research Fund of the Hong Kong Government (RRG-10 and RRG-14), the University Grants Committee of Hong Kong (Area of

Excellence Scheme grant AoE/M-12/06), the National Institute of Allergy and Infectious Diseases (contract HHSN272201400006C), and the Li Ka Shing Foundation. E.C.H. is supported by an NHMRC Australia Fellowship (AF30).

Author Contributions Y.G., H.Z. and T.T.-Y.L. conceived the study; B.Z., J.W., Y.S., X.C., W.H., L.D., P.C., J.J. conducted surveillance; Y.C., C.M., Yu Z., L.L. performed sequencing; H.Z., T.T.-Y.L., E.C.H., D.K.S., Y.G. performed the analysis and wrote the manuscript; Y.C., Ya.Z., L.L.M.P., R.J.W., G.M.L., J.S.M.P. participated in the discussion and interpretation of findings. T.T.-Y.L., B.Z., J.W., Y.C., Y.S., X.C. contributed equally to this work.

Author Information All sequences generated by this study have been deposited in GenBank/EMBL/DBJ under accession numbers KP413163–KP418563. Detailed phylogenetic inferences are available from <http://dx.doi.org/10.5061/dryad.5q7kf>. Reprints and permissions information is available at www.nature.com/reprints. The authors declare no competing financial interests. Readers are welcome to comment on the online version of the paper. Correspondence and requests for materials should be addressed to Y.G. (yguan@hku.hk) or H.Z. (zhuhch@hku.hk).

METHODS

Influenza surveillance at the live poultry markets and sample processing. Surveillance of influenza viruses was conducted in live poultry markets in 13 cities in Zhejiang (October 2013), Jiangsu (October 2013), Shandong (October 2013) and Guangdong (December 2013 and February 2014) provinces during the second wave of the H7N9 outbreak. Samples were also collected on a weekly basis from routine surveillance in Nanchang (Jiangxi) and Shantou (Guangdong) cities during October 2013 to July 2014 and included in this study (Extended Data Tables 1 and 2). In the live poultry markets, oropharyngeal and cloacal swabs were taken from apparently healthy chickens and ducks. Faecal droppings were also collected from the duck holding areas at the markets of Nanchang.

All samples were collected in individual vials, placed in transport medium with antibiotics and packed on ice before sending to the laboratory for further processing. Samples were inoculated in 9- to 11-day-old embryonated chicken eggs for 48 h at 37 °C to assess the presence of influenza viruses. Haemagglutinin-positive isolates were further subtyped by haemagglutinin inhibition using a panel of reference anti-sera as described previously¹³.

Influenza surveillance at the Shenzhen hospitals. Influenza surveillance was conducted, with informed consent, among patients admitted to hospitals in Shenzhen with acute and rapidly progressing pneumonia resistant to antibiotic therapy since December 2013. This study was approved by the Ethics Committee of the Shenzhen Third People's Hospital and the Health Bureau of Shenzhen. Nasal, oropharyngeal swabs and/or tracheal aspirate samples from each patient were collected into transport medium and sent to the diagnostic labs within two hours. RNA was extracted using the QIAamp Viral RNA Minikit (Qiagen) and tested for influenza virus presence using the diagnostic real-time RT-PCR protocol for H7N9 and the seasonal influenza viruses, following the World Health Organization guidelines²⁷. Each clinical sample was separately inoculated into 9- to 10-day-old embryonated chicken eggs and Madin-Darby canine kidney (MDCK) cells for virus isolation. Whole genomic sequences were obtained from either the virus isolates or directly from the original clinical samples via next generation sequencing.

Genome sequencing. Based on the haemagglutinin inhibition results, poultry H7-positive isolates were selected for sequencing. Three to five H9-positive isolates from each sampling occasion were also selected. For human samples positive for H7N9 but for which we failed to obtain virus isolates, whole genomic sequencing was attempted using the clinical specimen. Sequencing was performed using a Roche 454 Genome Sequencer Junior, giving ~150× coverage of the influenza genome on average. Original reads from the 454 sequencing were assembled into contigs using overlapping regions of 40 nucleotides with >90% identity and assembled using Lasergene, version 9.0 (<http://www.dnastar.com>). Samples containing more than one subtype of HA or NA gene, or having two or more copies of the same internal gene sharing <97% identity were considered as mixed infections. In all other cases, the discordant base calling in the gene was coded with degenerate nucleotide characters.

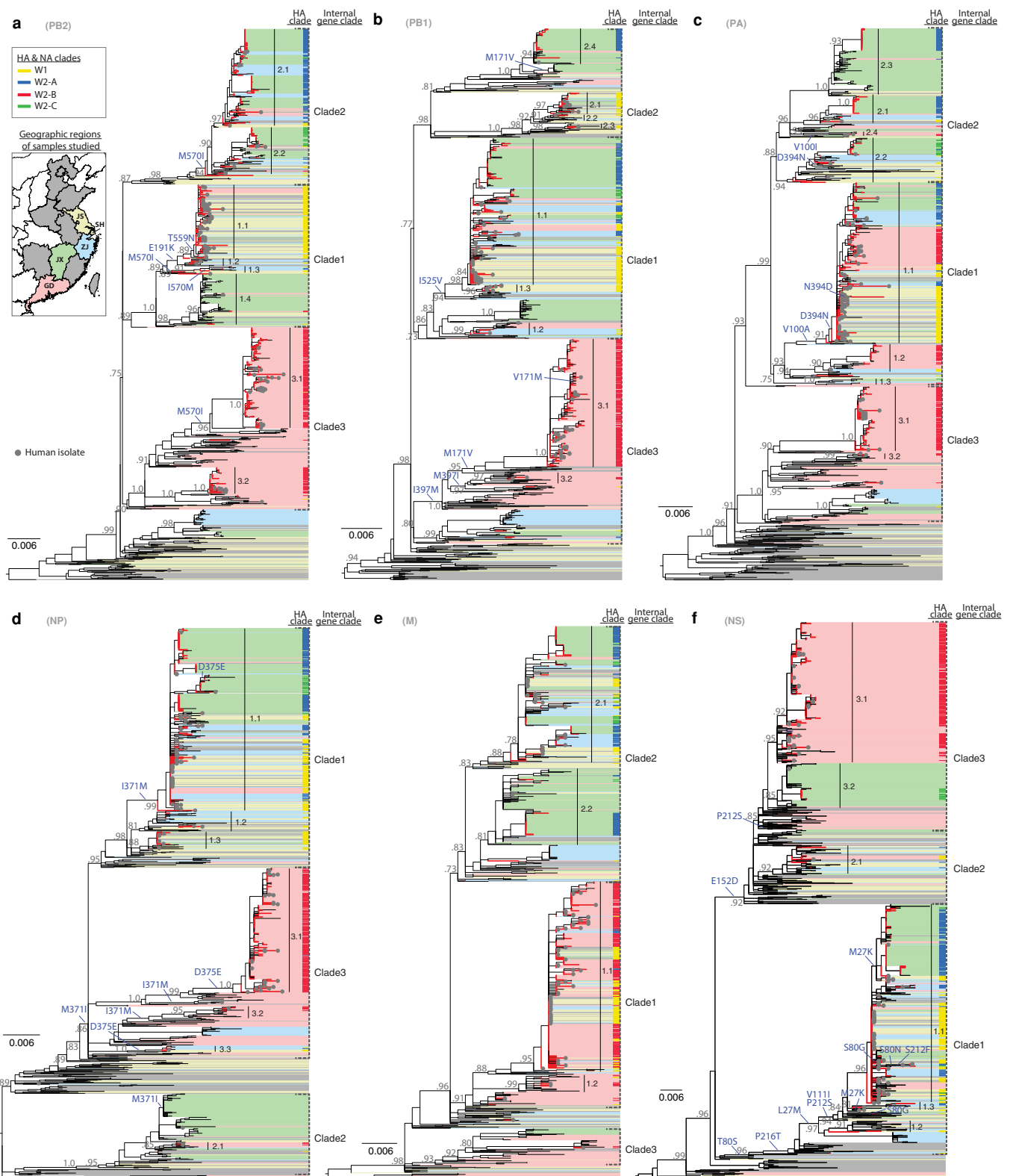
Sequence alignment and phylogenetic analysis. Nucleotide sequences generated in this study were combined with all publicly available sequences of influenza A virus sequences available in GenBank (<http://www.ncbi.nlm.nih.gov/genbank>) and GISAID (<http://www.gisaid.org>) databases (the full list is available from <http://dx.doi.org/10.5061/dryad.5q7kf>). Sequences were aligned using MUSCLE v3.5²⁸ with manual adjustments. Sequences with potential mosaic patterns²⁹ or an excessive number of ambiguous bases (>0.5% of the gene length) were excluded from the alignments. A smaller subset of reference sequences that were phylogenetically related to the H7N9 and our sequences were selected based on the panoramic phylogeny of each gene segment, as described previously¹³. These refined data sets were then used to estimate maximum likelihood phylogenies using the GTR+Γ₄ nucleotide substitution model in PhyML v3.0³⁰. Phylogenetic robustness was evaluated using the Shimodaira-Hasegawa approximate likelihood ratio test³¹. Large clades

(denoted as clades 1–3) were identified in the H9N2 HJ-ZJ/07 sub-lineage of each maximum likelihood phylogeny of the internal genes. These clades were further classified into sub-clades (for example, clades 1.1, 1.2, 1.3, 2.1, etc.) that meet the following criteria: (1) they contained at least three H7N9 sequences; (2) their average intra-sub-clade genetic distance was less than 3%. The major clade where the majority of the first wave H7N9 viruses were found was denoted as clade 1.1. Clade numbers were assigned to achieve consistency with an earlier study¹¹.

Phylogenetic inference of spatial and temporal dynamics. The aligned H7 and N9 gene sequences of each virus were concatenated (nine strains were omitted because their H7 and N9 genes had different clade origins). In addition, the sizes of internal gene data sets were reduced by removing H9N2 sequences that are distant from the H7N9 sequences, and identical sequences from the same sampling occasions, so that sophisticated phylogeographic analysis is tractable. Sequences were coded with the isolation dates and discrete states that represented the Chinese province of sampling (Shanghai, Jiangsu, Zhejiang, Jiangxi, Guangdong, Shandong, and other provinces), subtype population (H7N9 and H9N2) and wave of the outbreak (wave 1 and wave 2; for H7N9 only). These data were then used to infer the spatial and temporal dynamics of the H7N9 virus transmission using the Bayesian Markov chain Monte Carlo (MCMC) method implemented in the BEAST package (version 1.8)³² employing the SRD06 nucleotide substitution model³³, a relaxed clock model with uncorrelated lognormal rate distribution³⁴, a Bayesian skyride coalescent model with time-aware smoothing³⁵, and a discrete non-reversible phylogeographic model³⁶. Multiple runs of the MCMC method were computed and combined, giving 3.9~4.5 × 10⁸ total steps for each data set, with sampling every 1,500 steps. Convergence of relevant parameters was assessed using Tracer v1.5³⁷.

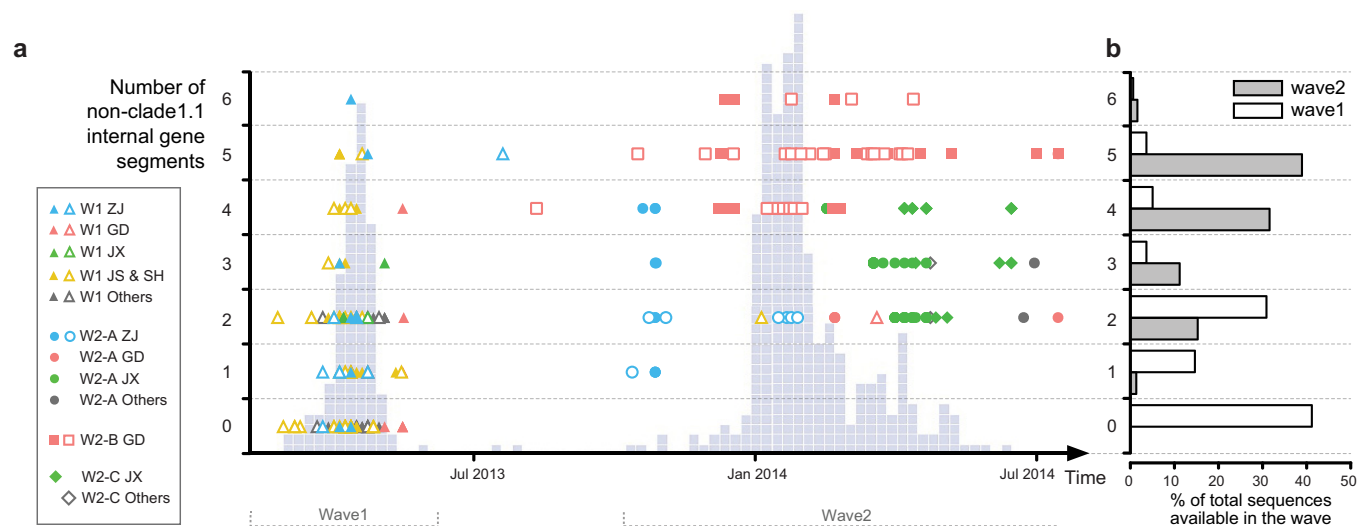
Genome mutations. The ancestral nucleotide sequence at each internal node of the maximum likelihood tree was reconstructed using the joint maximum likelihood method implemented at the Datamonkey server³⁸. The sequences at both the root and tip of each tree branch were compared, and the differences shown represent the mutations that occurred along that branch. Positively selected codons were also identified in Datamonkey.

27. World Health Organization. WHO information for molecular diagnosis of influenza virus - update http://www.who.int/influenza/gisrs_laboratory/molecular_diagnosis/en/ (2014).
28. Edgar, R. C. MUSCLE: a multiple sequence alignment method with reduced time and space complexity. *BMC Bioinformatics* **5**, 113 (2004).
29. Lam, T. T.-Y. *et al.* Systematic phylogenetic analysis of influenza A virus reveals many novel mosaic genome segments. *Infect. Genet. Evol.* **18**, 367–378 (2013).
30. Guindon, S., Delsuc, F., Dufayard, J. F. & Gascuel, O. Estimating maximum likelihood phylogenies with PhyML. *Methods Mol. Biol.* **537**, 113–137 (2009).
31. Guindon, S. *et al.* New algorithms and methods to estimate maximum-likelihood phylogenies: assessing the performance of PhyML 3.0. *Syst. Biol.* **59**, 307–321 (2010).
32. Drummond, A. J. & Rambaut, A. BEAST: Bayesian evolutionary analysis by sampling trees. *BMC Evol. Biol.* **7**, 214 (2007).
33. Shapiro, B., Rambaut, A. & Drummond, A. J. Choosing appropriate substitution models for the phylogenetic analysis of protein-coding sequences. *Mol. Biol. Evol.* **23**, 7–9 (2006).
34. Drummond, A. J., Ho, S. Y., Phillips, M. J. & Rambaut, A. Relaxed phylogenetics and dating with confidence. *PLoS Biol.* **4**, e88 (2006).
35. Minin, V. N., Bloomquist, E. W. & Suchard, M. A. Smooth skyride through a rough skyline: Bayesian coalescent-based inference of population dynamics. *Mol. Biol. Evol.* **25**, 1459–1471 (2008).
36. Lemey, P., Rambaut, A., Drummond, A. J. & Suchard, M. A. Bayesian phylogeography finds its roots. *PLoS Comput. Biol.* **5**, e1000520 (2009).
37. Rambaut, A., Suchard, M. & Drummond, A. J. Tracer v1. 5 <http://tree.bio.ed.ac.uk/software/tracer/> (2007).
38. Delport, W., Poon, A. F., Frost, S. D. & Kosakovsky Pond, S. L. Datamonkey 2010: a suite of phylogenetic analysis tools for evolutionary biology. *Bioinformatics* **26**, 2455–2457 (2010).



Extended Data Figure 1 | Condensed phylogenies for the internal genes. **a**, PB2 ($n = 1681$), **b**, PB1 ($n = 1620$), **c**, PA ($n = 1682$), **d**, NP ($n = 1733$), **e**, M ($n = 1696$) and **f**, NS ($n = 1707$) genes. The H9N2 ZJ-HJ/07 lineage from the large phylogenies (available from <http://dx.doi.org/10.5061/dryad.5q7kf>) is annotated and shown. Red branches indicate the H7N9 viruses, with the remaining branches representing H9N2 (the majority) or other viruses.

Mutations leading to changes in amino acid usage from wave 1 to wave 2 (Extended Data Table 4) are shown in blue. Dashed brackets indicate the major clades 1–3, and vertical lines indicate their sub-clades. The background shading indicates the provinces from which the viruses were isolated (see inset map). Human samples are indicated as grey circles.



Extended Data Figure 2 | Prevalence of H7N9 reassortant variants. **a**, Time-line of reassortant variants of H7N9 viruses ($n = 505$) and human infections. Clade 1.1 was the predominant sub-clade in the first wave (see Fig. 2 and Extended Data Fig. 1). Symbols represent H7N9 viruses and their time of isolation, and the number of non-clade 1.1 internal gene segments (that is, those falling outside clade 1.1 as defined in the phylogenies; Extended Data Fig. 1) in the virus (y -axis). The colours indicate the provinces of isolation of the

viruses. Viruses from HA clades W1, W2-A, W2-B and W2-C are indicated by triangles, circles, squares and diamonds, respectively. Solid and empty symbols represent avian and human viruses. The underlying blocks give the number of human infection cases per week (WHO data⁷, as of July 2014). **b**, The percentage of wave 1 and wave 2 viruses having different numbers of non-clade 1.1 internal genes (y -axis) in their genomes.

Extended Data Table 1 | Surveillance in apparently healthy chickens at live poultry markets

Province	City	Time period	Samples [#]	Isolates	Number of samples positive for		
					Influenza	H7* (%)	H9† (%)
Jiangsu	Suzhou	Oct, 2013	227	103	81		81 (35.7)
	subtotal		227	103	81		81 (35.7)
Zhejiang	Huzhou	Oct, 2013	457	144	110	21 (4.6)	88 (19.3)
	Jiaxing	Oct, 2013	447	102	68	1 (0.2)	66 (14.8)
	Ningbo	Oct, 2013	517	47	36		36 (7.0)
	Shaoxing	Oct, 2013	873	235	157	14 (1.6)	142 (16.3)
	Wenzhou	Oct, 2013	538	89	60		60 (11.2)
	subtotal		2,832	617	431	36 (1.3)	392 (13.8)
Shandong	Jinan	Oct, 2013	427	63	56		56 (13.1)
	Juxian	Oct, 2013	224	22	18		16 (7.1)
	Qingdao	Oct, 2013	330	51	23		23 (7.0)
	Rizhao	Oct, 2013	615	234	188		187 (30.4)
	Yantai	Oct, 2013	309	30	16		16 (5.2)
	subtotal		1,905	400	301		298 (15.6)
Guangdong	Dongguan	Dec, 2013	1,644	736	501	53 (3.2)	440 (26.8)
	Shenzhen	Dec, 2013	2,333	1,017	797	23 (1.0)	755 (32.4)
	Dongguan	Feb, 2014	1,543	420	207	133 (8.6)	70 (4.5)
	Shenzhen	Feb, 2014	154	16	5		4 (2.6)
	subtotal		5,674	2,189	1,510	209 (3.7)	1,269 (22.4)
Guangdong	Shantou	Oct, 2013	82	8	2		2 (2.4)
		Nov, 2013	76	14	11		10 (13.2)
		Dec, 2013	73	20	11		10 (13.7)
		Jan, 2014	101	27	21		20 (19.8)
		Feb, 2014	98	12	3	1 (1.0)	2 (2.0)
		Mar, 2014	115	20	8	8 (7.0)	
		Apr, 2014	166	22	7	7 (4.2)	
		May, 2014	133	21	13	10 (7.5)	3 (2.3)
		Jun, 2014	154	14	9	2 (1.3)	7 (4.5)
		Jul, 2014	151	30	26	8 (5.3)	18 (11.9)
	subtotal		1,149	188	111	36 (3.1)	72 (6.3)
Jiangxi	Nanchang	Oct, 2013	256	15	14		8 (3.1)
		Nov, 2013	436	119	108		105 (24.1)
		Dec, 2013	416	183	181		162 (38.9)
		Jan, 2014	254	124	90		77 (30.3)
		Feb, 2014	1,415	350	103	43 (3.0)	58 (4.1)
		Mar, 2014	312	112	101	48 (15.4)	4 (1.3)
		Apr, 2014	319	99	85	49 (15.4)	35 (11.0)
		May, 2014	329	73	50	38 (11.6)	5 (1.5)
		Jun, 2014	375	55	40	27 (7.2)	12 (3.2)
		Jul, 2014	400	24	16	8 (2.0)	5 (1.3)
	subtotal		4,512	1,154	788	213 (4.7)	471 (10.4)
Total			16,299	4,651	3,222	494‡ (3.0)	2,583 (15.8)

Oropharyngeal swabs collected from each bird are shown.

*Including mixed infections with other subtypes.

†Including mixed infections with other subtypes except H7.

‡All the H7 viruses isolated from chickens were H7N9 except for one H7N3 isolate from Huzhou.

#Only five H7N9 isolates were obtained from cloacal swabs; three from 1,412 swabs in Shantou and two from 1,053 swabs in Nanchang.

Extended Data Table 2 | Surveillance in apparently healthy ducks at live poultry markets

Province	City	Time period	Birds Sampled	Isolates from O C	Number of O C samples positive for Influenza	H7*	H9
Jiangsu	Suzhou	Oct, 2013	13	6 2	2 1		
	subtotal		13	8	3		
Zhejiang	Huzhou	Oct, 2013	38	10 10	10 10	1 2	1
	Jiaxing	Oct, 2013	36	9 13	7 11		2
	Ningbo	Oct, 2013	38	3 11	3 9		2
	Shaoxing	Oct, 2013	95	13 16	11 10	1	1
	Wenzhou	Oct, 2013	35	7 6	4 5		
	subtotal		242	98	80	4	6
Shandong	Jinan	Oct, 2013	10				
	Juxian	Oct, 2013	8	3 5	2 5		
	Qingdao	Oct, 2013	1				
	Yantai	Oct, 2013	3				
	subtotal		22	8	7		
Guangdong	Shantou	Oct, 2013	84	6 1	5 1		
		Nov, 2013	102	5 12	5 9		
		Dec, 2013	99	7 7	1 6		
		Jan, 2014	118	10 18	5 6		
		Feb, 2014	83	10 11	2 4		
		Mar, 2014	80	2 7	1 3		
		Apr, 2014	109	3			
		May, 2014	54	1	1		
		Jun, 2014	83	1 2	1 2		
		Jul, 2014	127	3 7	3 6		
	subtotal		939	113	61		
Jiangxi	Nanchang	Oct, 2013	243				
		Nov, 2013	405	38 5	38 5		
		Dec, 2013	455	27 2	27 2	1	
		Jan, 2014	243	3	1		
		Feb, 2014	54 †	7	1		
		Mar, 2014	324	36 3	36 2		
		Apr, 2014	324	4	4		
		May, 2014	324	66	31		
		Jun, 2014	405	2 1	1 1		
		Jul, 2014	243	11	1		
	subtotal		3,020	205	150	1	
Total			4,236	432	301	5	6

Paired oropharyngeal (O) and cloacal (C) swabs were collected from each bird.

*The three H7 duck isolates from Huzhou were of the H7N7 subtype, while the other two from Shaoxing and Nanchang were of the H7N3 subtype.

†Sample size was decreased due to the closure of most markets.

Extended Data Table 3 | Genotypes of H7N9 viruses in this study

Genotype	Total	Avian	Human
W2-B W2-B 3 3 3 3 1 3	102	88 (A/silkie chicken/Shantou/2050/2014)	14 (A/Shenzhen/SP44/2013)
W2-B W2-B 3 3 1 3 1 3	88	79 (A/chicken/Shenzhen/727/2013)	9 (A/Shenzhen/SP17/2013)
W1 W1 1 1 1 1 1 1	61	27 (A/chicken/Guangzhou/27/2013)	34 (A/Anhui/1/2013)
W2-A W2-A 2 1 1 1 2 1	49	43 (A/chicken/Fujian/8585/2014)	6 (A/Zhejiang/30/2014)
W2-A W2-A 2 2 2 1 2 1	43	43 (A/silkie chicken/Jiangxi/9469/2014)	0
W2-A W2-A 2 1 2 1 2 1	34	34 (A/silkie chicken/Shaoxing/5130/2013)	0
W1 W1 1 2 1 1 1 1	26	19 (A/chicken/Jiangxi/12486/2013)	7 (A/Shanghai/07/2013)
W1 W1 1 1 1 1 2 1	24	8 (A/environment/Hangzhou/37/2013)	16 (A/Hangzhou/3/2013)
W2-C W2-C 2 1 2 1 2 3	13	13 (A/chicken/Jiangxi/18482/2014)	0
W1 W1 2 2 2 1 2 1	5	3 (A/chicken/Shanghai/S1358/2013)	2 (A/Hebei/01/2013)
W2-B W2-B 3 3 2 3 1 3	4	1 (A/silkie chicken/Dongguan/656/2014)	3 (A/Shenzhen/SP113/2014)
W2-A W2-A 2 1 1 1 1 1	4	4 (A/chicken/Shaoxing/5087/2013)	0
W2-B W2-B 3 3 1 2 1 3	3	2 (A/chicken/Shenzhen/742/2013)	1 (A/Shenzhen/SP-Z93/2013)
W2-C W2-C 2 1 2 1 2 1	3	2 (A/chicken/Jiangxi/18515/2014)	1 (A/Taiwan/1/2014)
W1 W1 1 1 1 1 1 2	3	3 (A/environment/Guangzhou/77/2013)	0
W1 W1 2 1 1 1 2 1	3	1 (A/chicken/Jiangsu/SC537/2013)	2 (A/Shenzhen/SP118/2014)
W2-A W2-A 1 1 2 1 2 1	2	2 (A/chicken/Shaoxing/2417/2013)	0
W2-B W2-B 1 3 1 3 1 3	2	2 (A/chicken/Shantou/4832/2014)	0
W1 W2-B 1 1 1 1 1 1	2	1 (A/environment/Suzhou/14/2013)	1 (A/Beijing/01-A/2013)
W2-B W2-B 3 3 3 3 3 3	2	1 (A/chicken/Dongguan/4251/2013)	1 (A/Hong_Kong/8122430/2014)
W2-C W2-A 2 1 1 1 2 1	2	2 (A/Duck/Jiangxi/15044/2014)	0
W2-C W2-C 2 1 1 1 2 1	2	1 (A/chicken/Jiangxi/18008/2014)	1 (A/Taiwan/2/2014)
W1 W1 1 1 2 3 2 1	2	2 (A/environment/Shanghai/S1438/2013)	0
W1 W1 1 1 2 1 2 1	2	2 (A/chicken/Hangzhou/48-1/2013)	0
W2-A W2-B 2 3 1 1 1 1	1	1 (A/chicken/Shantou/4824/2014)	0
W1 W2-B 1 3 1 1 1 1	1	1 (A/duck/Zhejiang/SC410/2013)	0
W2-A W2-A 2 1 1 1 2 2	1	1 (A/chicken/Shaoxing/5186/2013)	0
W2-A W2-A 1 1 1 1 1 1	1	0	1 (A/Zhejiang/22/2013)
W2-A W2-B 2 3 2 3 1 3	1	1 (A/chicken/Shantou/4816/2014)	0
W2-A W2-A 2 2 1 1 2 1	1	1 (A/chicken/Fujian/8829/2014)	0
W2-A W2-A 2 1 1 1 1 2	1	1 (A/chicken/Shaoxing/5086/2013)	0
W2-B W1 3 3 1 3 1 3	1	0	1 (A/Shenzhen/SP49/2013)
W1 W1 2 2 1 1 1 1	1	0	1 (A/Shanghai/13/2013)
W2-B W2-B 2 3 3 3 1 3	1	1 (A/chicken/Dongguan/1124/2014)	0
W1 W1 3 3 1 1 1 2	1	1 (A/environment/Guangzhou/73/2013)	0
W1 W1 1 2 2 1 1 1	1	0	1 (A/Shandong/01/2013)
W1 W1 1 1 1 3 1 1	1	0	1 (A/Shanghai/1/2013)
W2-B W2-B 2 3 1 3 1 3	1	1 (A/chicken/Shantou/4325/2014)	0
W1 W1 1 1 3 2 1 1	1	1 (A/chicken/Rizhao/871/2013)	0
W1 W1 2 1 2 1 2 1	1	0	1 (A/shanghai/05/2013)
W1 W1 1 1 1 1 2 2	1	1 (A/environment/Guangzhou/238/2013)	0
W1 W1 2 2 1 1 2 1	1	1 (A/Chicken/Suzhou/097-1/2013)	0
W2-C W2-C 2 1 1 1 2 3	1	1 (A/chicken/Jiangxi/18513/2014)	0
W2-A W2-A 2 1 1 3 1 2	1	1 (A/chicken/Shaoxing/5479/2013)	0
W2-C W2-C 2 2 2 1 2 1	1	1 (A/chicken/Jiangxi/18449/2014)	0
W1 W1 1 2 2 1 2 1	1	1 (A/environment/Shanghai/S1437/2013)	0
W1 W1 1 1 1 3 2 1	1	1 (A/environment/Shanghai/S1439/2013)	0
W2-C W2-A 2 1 2 1 2 3	1	1 (A/chicken/Jiangxi/14513/2014)	0

The count of H7N9 viruses ($n = 505$) includes sequences from this work as well as publicly available data. Clade designations for each segment are ordered as HA|NA|PB2|PB1|PA|NP|M|NS. Genotype totals and example human and avian strains are shown.

Extended Data Table 4 | Amino acid changes from the first to second waves

Gene	Position	Wave1 viruses	Wave2 viruses	Functions	References
PB2	191	<u>T</u> (0.7%:1 0) <u>K</u> (88.3%:83 94) <u>E</u> (11.0%:15 6)	<u>K</u> (0.5%:0 2) <u>E</u> (99.5%:100 98)		
	559	<u>T</u> (14.5%:17 12) <u>N</u> (85.5%:83 88)	<u>T</u> (99.7%:100 100) <u>N</u> (0.3%:0 0)		
	570	<u>M</u> (91.0%:88 94) <u>I</u> (8.3%:12 4) <u>L</u> (0.7%:0 1)	<u>M</u> (12.0%:11 17) <u>I</u> (87.8%:89 81) <u>V</u> (0.3%:0 2)		
PB1	171	<u>M</u> (100.0%:100 100)	<u>M</u> (45.8%:48 32) <u>I</u> (0.3%:0 0) <u>L</u> (0.3%:0 0) <u>V</u> (53.7%:52 68)		
	397	<u>L</u> (100.0%:100 100)	<u>I</u> (45.8%:48 32) <u>M</u> (54.2%:52 68)		
	525	<u>I</u> (29.0%:39 17) <u>V</u> (71.0%:61 83)	<u>I</u> (68.3%:67 77) <u>V</u> (31.7%:33 23)		
PA	100	<u>A</u> (87.4%:85 91) <u>V</u> (12.6%:15 9)	<u>A</u> (34.8%:33 50) <u>V</u> (64.4%:67 43) <u>I</u> (0.8%:0 7)	A100V: Increased infection and replication in human A549 cells	Yamayoshi et al, 2014
	394	<u>D</u> (15.4%:19 11) <u>N</u> (84.6%:81 89)	<u>D</u> (65.2%:67 50) <u>N</u> (34.8%:33 50)		
NP	371	<u>M</u> (73.9%:65 85) <u>I</u> (26.1%:35 15)	<u>M</u> (46.4%:48 32) <u>I</u> (53.3%:51 68) <u>T</u> (0.3%:0 0)		
	375	<u>D</u> (97.2%:96 98) <u>E</u> (2.8%:4 2)	<u>D</u> (45.6%:47 34) <u>E</u> (54.4%:53 66)		
NS1	27	<u>M</u> (87.9%:89 87) <u>K</u> (7.4%:4 11) <u>L</u> (4.7%:8 1)	<u>M</u> (9.8%:8 22) <u>K</u> (30.2%:34 4) <u>L</u> (60.1%:58 73)		
	80	<u>S</u> (94.0%:92 96) <u>T</u> (4.0%:6 1) <u>G</u> (2.0%:1 3)	<u>S</u> (38.9%:41 20) <u>T</u> (60.3%:59 73) <u>N</u> (0.8%:0 7)		
	111	<u>I</u> (93.3%:89 99) <u>V</u> (6.7%:11 1)	<u>I</u> (39.7%:41 27) <u>V</u> (60.1%:58 73) <u>M</u> (0.3%:0 0)		
	152	<u>D</u> (4.0%:6 1) <u>E</u> (96.0%:94 99)	<u>D</u> (60.3%:59 73) <u>E</u> (39.7%:41 27)		
	212	<u>S</u> (93.3%:89 99) <u>P</u> (6.0%:10 1) <u>Y</u> (0.7%:1 0)	<u>S</u> (39.2%:41 27) <u>P</u> (60.1%:59 71) <u>F</u> (0.5%:1 0) <u>L</u> (0.3%:0 2)	loss of 212-PP ϕ PPK/R motif reduces binding to CRK1/II CRKL, and suppression of apoptosis	Heikkinen et al. 2008; Hrinčius et al. 2010
	216	<u>T</u> (96.0%:94 99) <u>P</u> (4.0%:6 1)	<u>T</u> (39.4%:41 27) <u>P</u> (60.3%:59 73) <u>K</u> (0.3%:0 0)	As for 212	
	65*	<u>R</u> (79.4%:78 82) <u>K</u> (11.4%:16 4) <u>M</u> (8.6%:5 14) <u>V</u> (0.6%:1 0)	<u>R</u> (21.7%:22 16) <u>K</u> (78.3%:78 84)	Antigenic site E	

The most frequent amino acid residues are underlined. Frequencies are shown as: amino acid (overall %: % in avian sequences| % in human sequences). For example, K (88.3%:83|94) indicates that lysine is present in 88.3% of all sequences, in 83% of avian sequences and in 94% of all human sequences. Human and avian percentages are rounded to integers.

Extended Data Table 5 | Amino acid changes from avian to human H7N9 viruses

Protein	Amino acid changes (count)
H7	N208S (5), G552R (4), N551S (3)
N9	N223D (4), R294K (4), V22A (4)
PB2	E627K (55), D701N (12), I461V (4), Q591K (4), D9Y (3), S534F (3)
PB1	E177D (3), P454L (3), S361N (3), T566A (3), V200I (3)
PB1-F2	G70E (3), S77L (3)
PA	E684G (3), R57Q (3), T263A (3), T618K (3), V100I (3)
PA-X	R57Q (3), V100I (3)
NP	R98K (5), A284T (3), I61M (3), R246K (3), V280A (3), V353G (3)
M1	none
M2	K97E (6)
NS1	R35P (4), R211G (3), S80N (3), V192I (3), V6M (3)
NS2	R42K (3), V6M (3)

Only changes that occurred in two or more human H7N9 viruses are shown, and were deduced by comparing each human viral sequence with the nearest avian viral sequence, based on the phylogenies.

A prefrontal–thalamo–hippocampal circuit for goal-directed spatial navigation

Hiroshi T. Ito¹, Sheng-Jia Zhang¹, Menno P. Witter¹, Edvard I. Moser¹ & May-Britt Moser¹

Spatial navigation requires information about the relationship between current and future positions. The activity of hippocampal neurons appears to reflect such a relationship, representing not only instantaneous position but also the path towards a goal location. However, how the hippocampus obtains information about goal direction is poorly understood. Here we report a prefrontal–thalamo neural circuit that is required for hippocampal representation of routes or trajectories through the environment. Trajectory-dependent firing was observed in medial prefrontal cortex, the nucleus reuniens of the thalamus, and the CA1 region of the hippocampus in rats. Lesioning or optogenetic silencing of the nucleus reuniens substantially reduced trajectory-dependent CA1 firing. Trajectory-dependent activity was almost absent in CA3, which does not receive nucleus reuniens input. The data suggest that projections from medial prefrontal cortex, via the nucleus reuniens, are crucial for representation of the future path during goal-directed behaviour and point to the thalamus as a key node in networks for long-range communication between cortical regions involved in navigation.

Hippocampal place cells are part of an allocentric representation of local space that allows animals to navigate to desired locations^{1,2}. Place cells provide accurate information about current location, but it has remained unclear how the place-cell map is used for animals to navigate from their current position to a goal position elsewhere in the environment. To implement goal-directed navigation, previous studies have proposed the need for a separate representation of future positions that is somehow brought together with the representation of current location to point the network to the goal^{3–5}. Such pointers may be expressed in the activity of hippocampal place cells. When rats are engaged in a T-maze-based alternation task, in which they take left or right trajectories on alternating laps, place cells with fields on the stem of the maze fire at different rates on left- and right-turn trajectories, without changes in the position of the firing field^{6,7}. The dependence on trajectory has both retrospective and prospective components, reflecting both where the animal comes from and where it is going⁸. However, as the animal approaches the decision point at the junction of the maze, the representation becomes more forward-oriented⁹, often with trajectories to upcoming locations embedded into the representation^{10,11}, in addition to mere changes in firing rate.

The source of trajectory information in place cells has not been identified. Here we used a continuous version of the T-maze alternation task⁶ to determine how information about succeeding choices is introduced in hippocampal place-cell activity. We hypothesized that the selection of future trajectories depends on a wider circuit including not only the hippocampus but also structures involved in the evaluation and selection of actions, such as the prefrontal cortex^{12–14}. Neurons in medial prefrontal cortex (mPFC) do not project directly to the hippocampus^{15,16} but the midline thalamic nucleus reuniens (NR), which has reciprocal anatomical connections with the mPFC, may serve as a functional bridge to the hippocampal region, since NR has strong terminal fields in the CA1 subfield^{15,17–19}. To address this possibility, we recorded and manipulated activity at various nodes of the prefrontal–reuniens–CA1 circuit and determined whether this circuit is necessary for place cells to represent upcoming trajectories.

Trajectory-dependent firing is stronger in CA1 than CA3

We first asked whether NR is the source of trajectory information in CA1. If it is, we should observe a difference in trajectory-dependent firing between CA1 and CA3, because NR has major excitatory projections to CA1 but not CA3 (refs 15, 17–19). We thus recorded place cells in rat CA1 and CA3 in a continuous alternation task on a modified T-maze (Fig. 1a, b and Extended Data Fig. 1). A total of 363 CA1 cells and 180 CA3 cells exhibited location-specific complex spiking (12 and 5 rats, respectively). Within this sample, 98 CA1 cells and 34 CA3 cells had place fields on the central stem. All subsequent analysis of these cells was restricted to parts of the stem where there was no significant difference in the animal's head direction, lateral position, or running speed between left-turn and right-turn trajectories.

Many place cells in CA1 expressed several-fold changes in peak firing rate between left- and right-turn trajectories on the stem, without changes in the position of the firing field (Fig. 1c, d and Extended Data Fig. 2a). 54 CA1 cells (55.1%) showed significant rate changes that depended on trajectory (left or right) ($P < 0.05$ for main effect of trial type (left/right) in a two-way analysis of variance (ANOVA) with trial type and stem position as factors, and $P < 0.05$ post-hoc analysis of covariance (ANCOVA) with running speed, head direction and lateral position as covariates⁶). By contrast, only six cells (17.7%) met the criteria for trajectory-dependent rate change in CA3 (Fig. 1e, f). The proportion of trajectory-dependent cells relative to total place cells was significantly smaller in CA3 than in CA1 ($Z = 3.78$, $P < 0.001$, binomial test). Distributions of rate changes were significantly different (CA1, $32.8 \pm 2.6\%$; CA3, $19.8 \pm 3.1\%$; means \pm s.e.m.; $D = 0.338$, $P = 0.005$, Kolmogorov–Smirnov test; Fig. 1d, f and Extended Data Fig. 2b). Place-fields position did not change across trajectories ($D = 0.125$, $P = 0.812$).

Trajectory-dependent firing in NR

The fact that trajectory dependence is expressed more strongly in CA1 than in CA3 points to NR as a possible source of modulation. To examine whether trajectory information is represented in NR, we

¹Kavli Institute for Systems Neuroscience and Centre for Neural Computation, Norwegian University of Science and Technology, Olav Kyrres gate 9, MTF5, 7491 Trondheim, Norway.

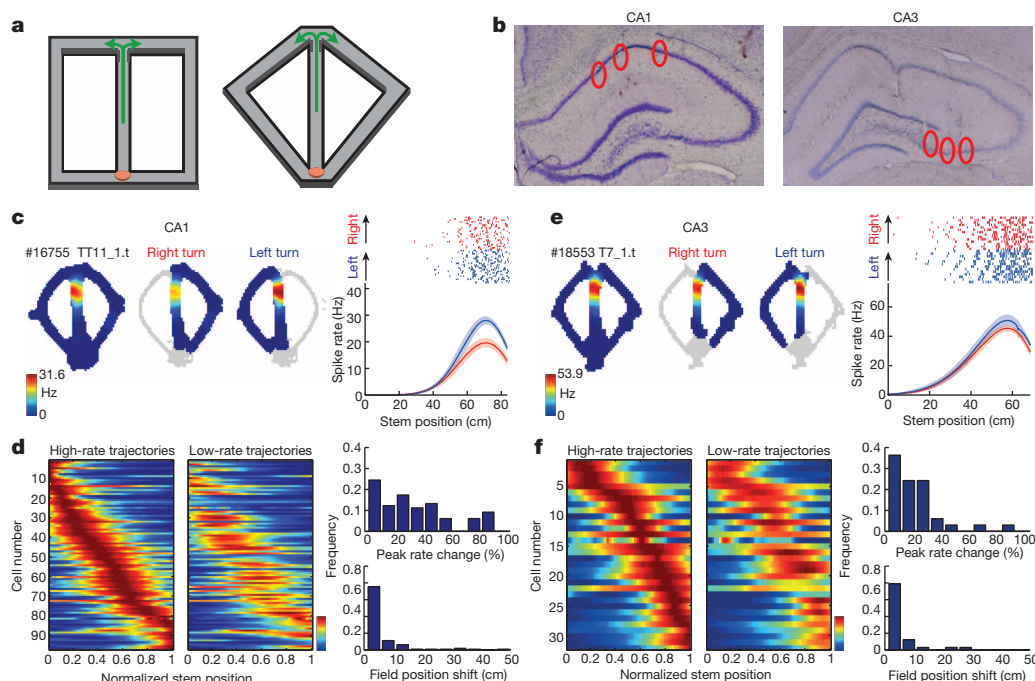


Figure 1 | Trajectory-dependent firing in CA1 but not CA3. **a**, Modified T-mazes used for the continuous alternation task. Red disk, food reward; arrows, running directions. **b**, Nissl-stained coronal sections through dorsal hippocampus. Red circles, tetrode tracks in CA1 and CA3. Original magnification, $\times 2.5$. **c**, Trajectory-dependent firing in CA1. Left panel, rate maps for a representative CA1 place cell in the continuous alternation task (left to right: all laps, right-turn laps, left-turn laps). Identification number of animal (#16755) and unit number (TT11_1.t) are indicated on top. Right panel, means (solid lines) and 95% confidence intervals (shaded) for spike rates of a single cell across the stem of the maze. Raster plots above. Left-heading runs in blue, right-heading runs in red. **d**, Left panels, difference in mean rates

between left and right trajectories for all CA1 cells with firing fields on the stem. Left- and right-turn trajectories were classified as high rate or low rate depending on which direction had the highest mean peak rate on the stem. Spike rates were normalized to the peak firing rate of each cell and sorted according to field position on high-rate trajectories. Each line shows one cell. Normalized spike rate is colour-coded (red for higher and blue for lower rates). Right top panel, distribution of normalized change in peak firing rate on the stem between high and low-rate trajectories ($\frac{\text{high} - \text{low}}{\text{high}}$). Right bottom panel, distribution of shift of field position between high- and low-rate trajectories. **e**, **f**, As in **c**, **d** but for CA3 place cells.

recorded spike activity in NR, simultaneously with CA1, while animals performed the continuous alternation task. Activity was also recorded in a square enclosure. Tetrodes were placed centrally in the rostral half of NR, where many CA1-projecting neurons are located¹⁸ (Fig. 2a and Extended Data Fig. 1). We recorded activity in 64 NR cells from six animals. NR neurons were active across the entire box, with a mean firing rate of 7.8 ± 1.3 Hz (mean \pm s.e.m.). Spatial information in bits per spike was negligible and substantially lower than in CA1 (NR, 0.048 ± 0.009 ; CA1, 1.46 ± 0.09 ; Extended Data Fig. 2c). Nonetheless, in the continuous alternation task, NR neurons exhibited differential firing on left- versus right-turn trajectories (Fig. 2b, c). Of the NR cells 42.2% (27 out of 64) showed a significant rate change across alternating trajectories (Fig. 2d; $P < 0.05$ for trial type and trial type \times stem position in a two-way ANOVA). The proportion of trajectory-modulated cells was not significantly lower than in simultaneously recorded CA1 cells (59.1%; 13/22 cells; $Z = 1.37$, $P = 0.17$, binomial test) or in the entire sample of CA1 cells from the animals with hippocampal tetrodes (54/98 cells; $Z = 1.61$, $P = 0.11$). The mean change in peak firing rate on the stem was $22.5 \pm 2.5\%$ (left versus right; Fig. 2e). The difference between left- and right-turn trajectories could not be explained by differences in other behavioural variables ($P < 0.05$, ANCOVA with running speed, head direction and lateral position as covariates). The recordings thus support the idea that NR is a major source of trajectory information to CA1.

Trajectory-dependent firing in mPFC

NR receives strong projections from mPFC¹⁹, suggesting that it serves as a relay between mPFC and CA1^{15,19}. If it does, trajectory information in NR and CA1 may also be expressed in mPFC. To test this, we

recorded the activity of mPFC cells in the continuous alternation task (338 cells, 3 animals). The cells were also recorded during free foraging in the square box. The recordings started with tetrodes in the dorsal anterior cingulate cortex and continued as the tetrodes were advanced

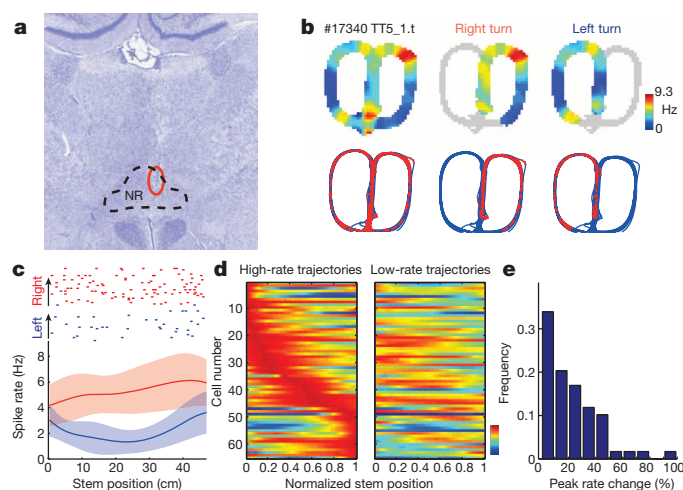


Figure 2 | Trajectory-dependent firing in NR. **a**, Nissl-stained coronal section showing tetrode track (red circle) in NR (outline). Original magnification, $\times 2.5$. **b**, Rate maps of a representative NR cell in the continuous alternation task (left to right: all laps, right-turn laps, left-turn laps). Animal and unit identification as in Fig. 1b. Top, colour-coded rate maps; bottom, spike locations (red) on trajectory (blue). **c**, Mean rate, 95% confidence intervals and raster plots for the cell in **b**. **d**, Normalized spike rate on the stem for all cells recorded in NR, plotted as in Fig. 1d. **e**, Change in spike rate between high- and low-rate trajectories, as in Fig. 1d but for NR cells.

to the dorsal prelimbic cortex (Fig. 3a and Extended Data Fig. 3a). Neurons in mPFC had firing properties similar to those of NR neurons in that, while they were non-selectively active throughout the square box, with a mean firing rate of 4.9 ± 0.4 Hz (mean \pm s.e.m.) and minimal location-selective activity (mean spatial information: 0.134 ± 0.012 bits per Hz; Extended Data Fig. 2c), these neurons fired differentially on left and right-turn trajectories on the central stem of the alternation task (Fig. 3b, c). One-third of the cells (129/338 cells or 38.2%) exhibited trajectory-dependent rate changes, in agreement with previous reports^{14,20} (Fig. 3d and Extended Data Fig. 3b, c; $P < 0.05$ for trial type and trial type \times stem position in a two-way ANOVA). The mean change in peak firing rate between left and right-turn trajectories (\pm s.e.m.) was $29.6 \pm 1.2\%$ (Fig. 3e). The rate change was not caused by differences in observed behaviour ($P < 0.05$ in ANCOVA with running speed, head direction and lateral position as covariates). Taken together, these observations suggest that NR shares information about past and present trajectory with the mPFC.

NR inactivation reduces trajectory-dependent CA1 firing

It is not clear from the recording experiments whether trajectory-dependent firing in NR is necessary for trajectory-dependent firing in the hippocampus, or whether these patterns of activity are expressed independently and in parallel across multiple brain regions. We addressed this question using two approaches that each interrupted the mPFC–NR–CA1 loop at the level of NR.

First we made lesions in NR using local injections of ibotenic acid (Fig. 4a and Extended Data Fig. 4). Animals with NR lesions did not exhibit detectable deficits in learning or performance on the continuous alternation task (Extended Data Fig. 5a), in agreement with previous work showing that continuous alternation persists after large hippocampal lesions²¹. We were also not able to identify changes in running speed or in the spectral power of local field potentials in CA1 (Extended Data Fig. 5b, c). However, trajectory coding in CA1 was clearly impaired. We recorded 176 CA1 place cells from 4 animals with NR lesions. Neurons in CA1 from lesioned animals expressed little rate change between left- and right-turn trajectories (Fig. 4b, c). Among the 44 cells that had place fields on the stem, we found only 7 (15.9%) that passed the criteria for trajectory-dependent rate change, a significant reduction compared to the proportion in CA1 cells of control animals (55.1%; $Z = 4.36$, $P < 0.001$, binomial test). The mean rate change (\pm s.e.m.) between left- and right-turn trajectories for

place cells was $18.7 \pm 2.7\%$, significantly lower than in CA1 control animals ($32.8 \pm 2.6\%$; $D = 0.346$, $P < 0.001$, Kolmogorov–Smirnov test; Fig. 4d, e and Extended Data Fig. 5d) and comparable to CA3 control animals ($19.8 \pm 3.1\%$; $D = 0.152$, $P = 0.744$). The position shift of place fields between trajectories was not significantly different from those of control animals ($D = 0.083$, $P = 0.982$). Thus the NR lesion caused a selective reduction of trajectory-dependent rate differences in CA1 cells.

The lesion experiment does not exclude the possibility that NR plays only a temporary role in the development of trajectory coding in CA1 and so may not be required after initial learning. To assess the need for ongoing NR activity, we used local infusion of adeno-associated virus to express selectively the enhanced halorhodopsin eNpHR3.1 in NR neurons. Neurons expressing eNpHR3.1 could then be inactivated optogenetically with laser application using a wavelength of 532 nm restricted to the time when the animals were engaged in the alternation task. NR spikes, recorded with tetrodes attached to the optic fibre, were significantly suppressed during light application, on average by $63.1 \pm 7.0\%$ (mean reduction \pm s.e.m., 5 to 0 s interval before silencing versus 2.5 to 5 s interval after onset

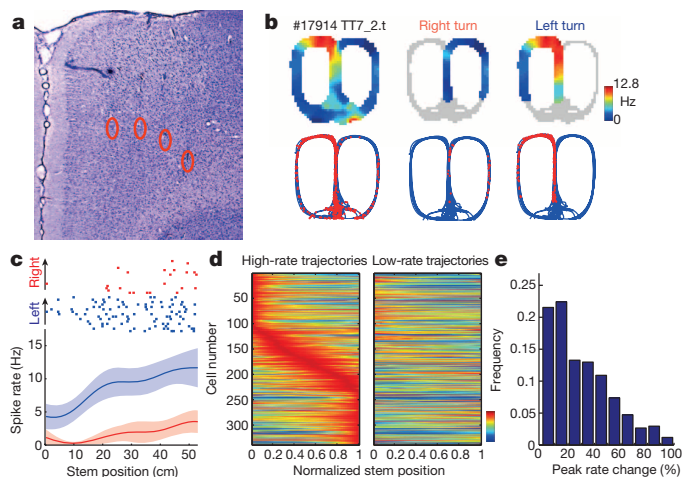


Figure 3 | Trajectory-dependent firing in mPFC. **a**, Nissl-stained coronal section showing tetrode positions (red circles) in the dorsal prelimbic area of mPFC. Original magnification, $\times 2.5$. **b**, Rate maps for a representative mPFC cell (recorded at location in **a**, plotted as in Fig. 2b). **c**, Mean rate, 95% confidence intervals and raster plots for the cell in **b**. **d**, Normalized rate on the stem for all mPFC cells, as in Fig. 1d. **e**, Change in spike rate of mPFC cells between trajectories, as in Fig. 1d.

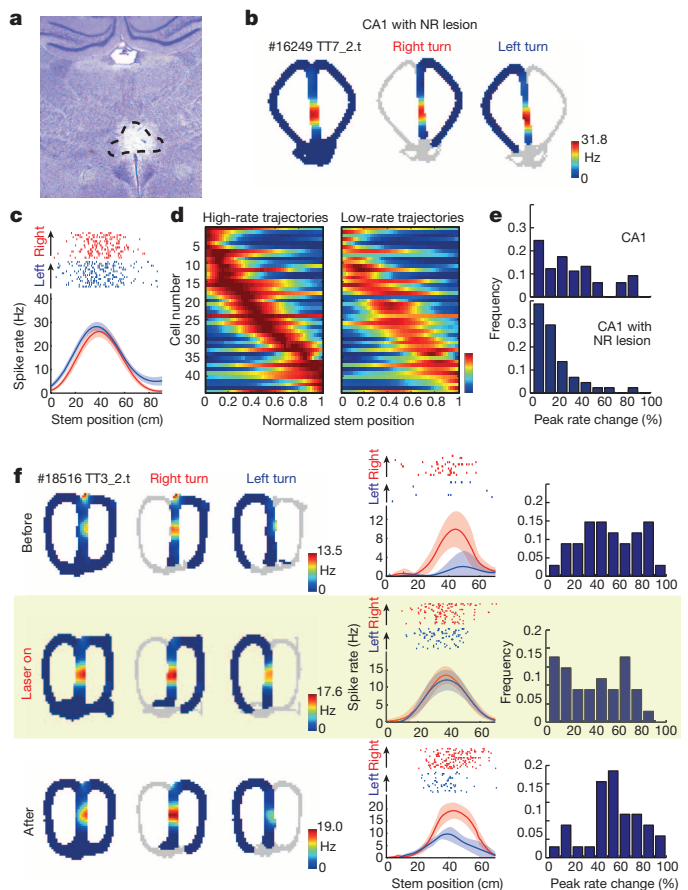


Figure 4 | Loss of trajectory-dependent firing in CA1 after NR inactivation. **a**, Nissl-stained coronal brain section showing bilateral NR lesion. Outline shows NR. Original magnification, $\times 2.5$. **b**, Colour-coded rate maps for a representative CA1 place cell in a NR-lesioned animal, plotted as in Fig. 1c. **c**, Mean rate, 95% confidence intervals and raster plots for the cell in **b**. **d**, Normalized firing rate on the stem for all CA1 place cells from animals with NR lesions, as in Fig. 1d. **e**, Change in peak rate on the stem between left- and right-turn trajectories, as in Fig. 1d. **f**, Left, colour-coded rate maps for a representative CA1 place cell before, during, and after optogenetic silencing of NR, with separate plots for left- and right-turn trajectories, as in Fig. 1c. Middle, means, 95% confidence intervals and raster plots for left- and right-turn trajectories (blue and red, respectively). Same cell as in the left plot. Right, change in peak rate between left- and right-turn trajectories for CA1 place cells with trajectory-dependent firing (as in Fig. 1d).

of silencing; Extended Data Fig. 6). In six NR-implemented animals, we recorded simultaneously the activity of 50 CA1 cells with place fields on the stem. Before the laser application, 72% of the recorded CA1 place cells (36/50) exhibited significant trajectory-dependent rate changes. During the laser application, the percentage of trajectory-dependent cells, in the same sample, was reduced to 44 (22/50, $Z = 2.837$, $P = 0.005$, binomial test). When the illumination was terminated, the percentage recovered to baseline (72%; 36/50 cells). We did not observe any difference in the position of place fields between trajectories on laser-on and laser-off trials ($F_{2,98} = 0.02$, $P = 0.983$, repeated-measures ANOVA; Extended Data Fig. 5i). Silencing of NR cells did not affect the animal's behaviour, the mean firing rates of the place cells, or the spectral power of the local field potential in CA1 (Extended Data Fig. 5e–h). Taken together, these findings demonstrate that NR activity modulates firing rates of CA1 cells in a trajectory-dependent manner during spatial navigation.

Prospective trajectory representation

While we found significant correlation between trajectory choices and activity of neurons in mPFC, NR and CA1 (Extended Data Fig. 7), it remains unclear whether this information is a determinant of the next trajectory choice or merely a reflection of events associated with the preceding lap on the maze. We addressed this distinction in three ways.

First, we investigated trajectory-dependent firing on error trials, or runs succeeded by an incorrect choice. On these runs, the representation of the next correct destination is likely to be compromised, unlike influences from the preceding trajectory, which may be preserved. Differences between correct trials and error trials are likely to be most evident near the end of the stem, just before the animal makes the next trajectory choice. Thus, we divided the stem into equal-size bins and assessed decoding accuracy using mean firing rates in each bin as inputs to a classifier. We found that the activity of neurons in mPFC, NR and CA1 consistently represented the correct next trajectory across stem positions on correct trials (Fig. 5a). By contrast, on error trials, the activity of the neuronal ensemble initially represented the correct succeeding trajectory but then gradually decreased to chance level as the animals approached the junction. A significant reduction of trajectory representation on error trials was observed in all three regions—mPFC, NR and CA1—providing further support for the idea that these areas are functionally coupled (main effect of task performance (correct versus error) in a logistic regression analysis, with task performance and stem position as coefficients: mPFC, $Z = 5.98$, $P < 0.001$; NR, $Z = 3.59$, $P < 0.001$; CA1, $Z = 3.43$, $P < 0.001$). The disruption of trajectory representation on error trials indicates that the information transferred through the mPFC–NR–CA1 circuit is an important determinant of the animal's succeeding choice of trajectory.

In a second approach, we introduced a delay of 10–15 s each time the animal reached the base of the stem. During this delay, access to the central stem was blocked. The delay was added to reduce the influence of working memory, or memory of the preceding lap, on trajectory-dependent firing when the rat subsequently ran down the stem of the maze. Prospective components should not be disrupted by this procedure. Animals learned the delayed alternation task to near-perfect levels (89% correct on average across 56 sessions). We recorded 133 cells from mPFC, 57 cells from NR, and 45 cells from CA1 in this task. All CA1 cells had firing fields on the stem. The decoding approach was then used to assess whether the firing rates on the stem represented the correct succeeding trajectory. During the delay period, the classifier was not able to decode any trajectory representation after the first half of the delay (Fig. 5b). After the delay, significant differences emerged between correct and incorrect trials, with decoding performance increasing towards the end of the stem (task performance \times stem position, logistic regression analysis; mPFC,

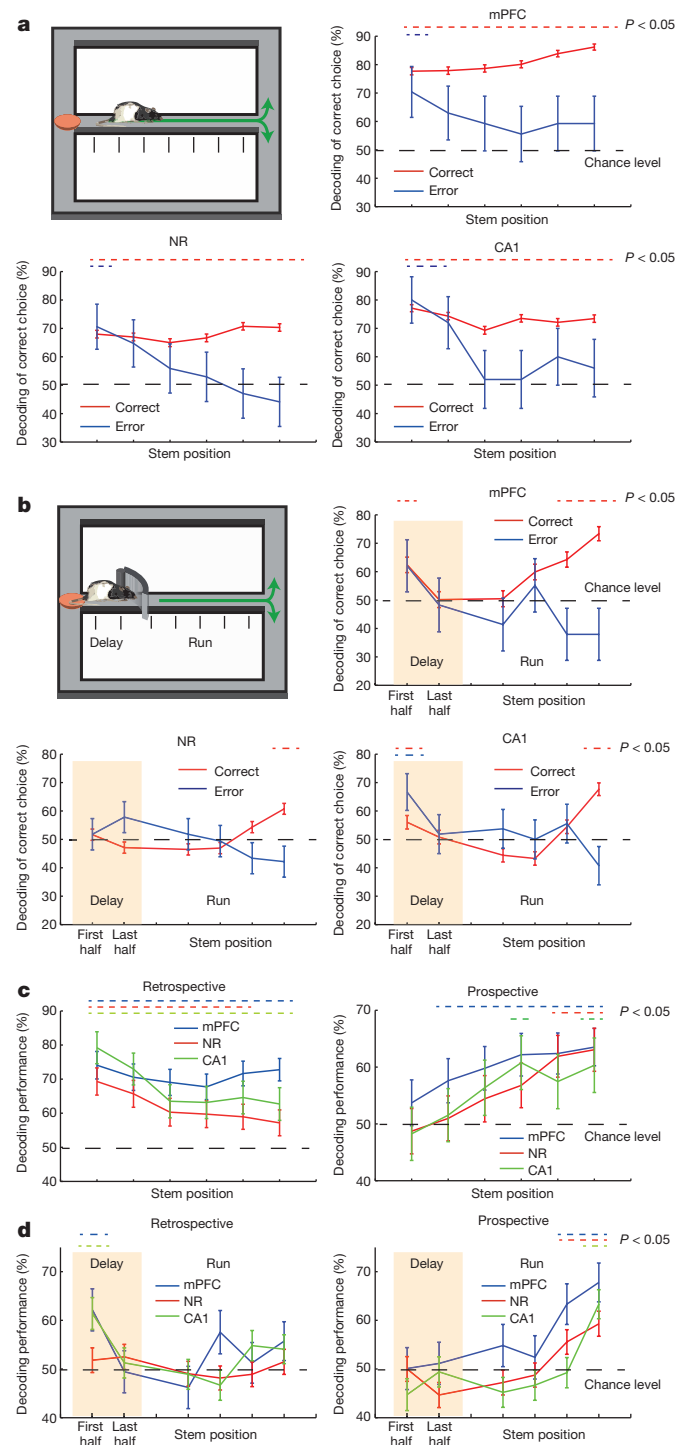


Figure 5 | Prospective coding. **a**, Decoding of correct subsequent trajectory using mean firing rates on the stem as inputs to a linear classifier. The stem was divided into six equally sized bins (upper left panel) and decoding performance was compared bin by bin for trials when animals subsequently made correct versus incorrect choices (three remaining panels: mPFC, NR, CA1; means \pm s.e.m.). Decoding performance was estimated against the next correct trajectory direction on both correct trials and error trials. Dashed lines at the top indicate bins with decoding performance significantly better than chance ($P < 0.05$, binomial test). **b**, Decoding of correct subsequent trajectory on trials with a 10–15 s delay at the start of the stem. Symbols as in **a**. **c**, Retrospective and prospective components were extracted from spike rates using a subsampling procedure that cancelled out the contributions from one of the two components. Symbols as in **a**, but P values were estimated from the bootstrap distributions. **d**, Retrospective and prospective components in the delayed alternation task. Symbols as in **c**.

$Z = 3.01$, $P = 0.002$; NR, $Z = 3.30$, $P < 0.001$; CA1, $Z = 3.14$, $P = 0.002$). The gradual emergence of a trajectory representation relevant to the succeeding behavioural outcome suggests that activity in the mPFC–NR–CA1 loop represents prospective trajectory choices and not, in the first place, memories of the preceding path.

Finally, we tried to extract analytically the prospective and retrospective components of the trajectory representation in the decoding analysis. To this end, we used a subsampled data set with the same number of correct trials and error trials such that the contributions of prospective or retrospective components were cancelled out (see Methods). In mPFC, the percentage of successfully decoded prospective paths was $62.7 \pm 3.6\%$ on the continuous task and $65.6 \pm 4.1\%$ on the delay task (mean \pm s.e.m. for last half of the stem). The prospective component correlated strongly with position segment, suggesting that it built up towards the end of the stem (continuous task, $r = 0.73 \pm 0.26$; delay task, $r = 0.79 \pm 0.14$; Fig. 5c, d). Neurons in NR and CA1 expressed a similar increase of the prospective component (correlation between stem segment and prospective component: NR, $r = 0.88 \pm 0.12$; CA1, $r = 0.58 \pm 0.29$ in the continuous task; NR, $r = 0.73 \pm 0.13$; CA1, $r = 0.67 \pm 0.14$ in the delay task). The prospective component in CA1 was abolished by lesions of NR (Extended Data Fig. 7b). We were also able to extract a retrospective component on the initial part of the stem in the continuous task (Fig. 5c), but not in the delayed task (Fig. 5d). Thus, whereas the representation of the preceding trajectory was largely disrupted by increasing the demands on working memory, the prospective component was maintained and expressed consistently across the mPFC–NR–CA1 circuit.

Discussion

When animals plan a route to a desired location, they must estimate how spatial position is changed following particular movements. Our study points to mPFC, NR and CA1 as part of the neural circuit for representation of goal-directed routes or trajectories. The data suggest that while distinct sets of CA1 cells are activated at each spatial position, the distribution of firing rates among these cells collectively represents the animal's intended direction of movement, and that this information is carried from the prefrontal cortex to CA1 through the midline thalamic NR. At each node of this loop, cells have firing rates that reflect the animal's subsequent trajectory. Disrupting the loop at the level of NR substantially reduces the trajectory dependence of the representation in CA1. CA3 cells, which do not receive direct input from NR, exhibit little trajectory-dependent activity, despite the strong remapping seen in this subfield during changes in the sensory environment^{22–24}. Taken together, the results point to the mPFC–NR–CA1 circuit, and possibly indirect projections from mPFC and NR via the entorhinal cortex²⁵, as a key element of the circuit for map-based route planning. The data provide functional support for the idea that communication between cortical regions is mediated not only by direct connections but also through the thalamus^{26–29}.

The findings offer some clues as to what kind of information is imposed on CA1 cells by signals from mPFC and NR. Previous work has pointed to a role for NR inputs in expression of hippocampal memory. Lesions of NR disrupt spatial working memory³⁰ and inactivation of mPFC inputs to NR or NR inputs to the CA1 impair discrimination between contexts in a fear conditioning task²⁸. The present results speak against a role for mPFC and NR in sensory context discrimination per se, because cells in these areas do not fire differentially unless the task involves differences in the route taken by the animal (Extended Data Figs 8 and 9). The trajectory-dependent nature of the firing was also not dependent on working memory, or memory of the preceding trajectory, because differential firing was resumed on the stem after it was blocked during the delay at the start of the stem. Instead the gradual increase in trajectory dependence as the animal approached the choice point on correct trials but not on error trials points to mPFC and NR as sources for information about the animal's intended movement. The findings provide a possible

source for goal-directed trajectory sequences in CA1 place cells, observed as sweeps of prospective spatial firing both during theta activity at junctions in a complex T-maze¹⁰ or during brief periods of immobility when animals navigate to fixed locations in an open space¹¹.

The fact that alternation performance was not impaired by NR lesions, and remains intact after hippocampal lesions²¹, raises questions about the function of trajectory-dependent firing. We have shown that trajectory-dependent firing exists in multiple brain circuits. Trajectory information from mPFC may reach systems involved in motor planning and decision making directly, without passing through the hippocampus. This may be sufficient to enable choice behaviour in a simple alternation task. The copy of the trajectory signal that is sent to the hippocampus, via the NR, may become critical only when navigational decisions require combinatorial representation of trajectory and location (Extended Data Fig. 10). Such combinatorial representations were observed only in CA1. Nonlinear combination of information modalities has been described in individual neurons in a number of brain systems^{31–34} and is thought to increase the discrimination capacity of downstream neurons during encoding of high-dimensional information³⁵. In the hippocampus, combinatorial coding in trajectory-dependent place cells may form the basis for complex navigational operations in efferent regions such as the subiculum or the entorhinal cortex. High-dimensional representations in trajectory-dependent place cells may be necessary for networks in these regions to classify complex position–trajectory combinations.

Online Content Methods, along with any additional Extended Data display items and Source Data, are available in the online version of the paper; references unique to these sections appear only in the online paper.

Received 30 August 2014; accepted 6 March 2015.

Published online 27 May 2015.

- O'Keefe, J. & Nadel, L. *The Hippocampus as a Cognitive Map* (Oxford Univ. Press, 1978).
- Moser, E. I., Kropff, E. & Moser, M. B. Place cells, grid cells, and the brain's spatial representation system. *Annu. Rev. Neurosci.* **31**, 69–89 (2008).
- Burgess, J., Recce, M. & O'Keefe, J. A model of hippocampal function. *Neural Netw.* **7**, 1065–1081 (1994).
- Redish, A. D. *Beyond the Cognitive Map* (The MIT Press, 1999).
- Foster, D. J., Morris, R. G. & Dayan, P. A model of hippocampally dependent navigation, using the temporal difference learning rule. *Hippocampus* **10**, 1–16 (2000).
- Wood, E. R., Dudchenko, P. A., Robitsek, R. J. & Eichenbaum, H. Hippocampal neurons encode information about different types of memory episodes occurring in the same location. *Neuron* **27**, 623–633 (2000).
- Frank, L. M., Brown, E. N. & Wilson, M. Trajectory encoding in the hippocampus and entorhinal cortex. *Neuron* **27**, 169–178 (2000).
- Ferbinteanu, J. & Shapiro, M. L. Prospective and retrospective memory coding in the hippocampus. *Neuron* **40**, 1227–1239 (2003).
- Catanese, J., Viggiano, A., Cerasti, E., Zugaro, M. B. & Wiener, S. I. Retrospectively and prospectively modulated hippocampal place responses are differentially distributed along a common path in a continuous T-maze. *J. Neurosci.* **34**, 13163–13169 (2014).
- Johnson, A. & Redish, A. D. Neural ensembles in CA3 transiently encode paths forward of the animal at a decision point. *J. Neurosci.* **27**, 12176–12189 (2007).
- Pfeiffer, B. E. & Foster, D. J. Hippocampal place-cell sequences depict future paths to remembered goals. *Nature* **497**, 74–79 (2013).
- Kim, J. N. & Shadlen, M. N. Neural correlates of a decision in the dorsolateral prefrontal cortex of the macaque. *Nature Neurosci.* **2**, 176–185 (1999).
- Hok, V., Save, E., Lenck-Santini, P. P. & Poucet, B. Coding for spatial goals in the prelimbic/infralimbic area of the rat frontal cortex. *Proc. Natl Acad. Sci. USA* **102**, 4602–4607 (2005).
- Fujisawa, S., Amarasingham, A., Harrison, M. T. & Buzsáki, G. Behavior-dependent short-term assembly dynamics in the medial prefrontal cortex. *Nature Neurosci.* **11**, 823–833 (2008).
- Vertes, R. P., Hoover, W. B., Szigeti-Buck, K. & Leranath, C. Nucleus reuniens of the midline thalamus: link between the medial prefrontal cortex and the hippocampus. *Brain Res. Bull.* **71**, 601–609 (2007).
- Jones, B. F. & Witter, M. P. Cingulate cortex projections to the parahippocampal region and hippocampal formation in the rat. *Hippocampus* **17**, 957–976 (2007).
- Herkenham, M. The connections of the nucleus reuniens thalami: evidence for a direct thalamo-hippocampal pathway in the rat. *J. Comp. Neurol.* **177**, 589–609 (1978).
- Dolleman-van Der Weel, M. J. & Witter, M. P. Projections from the nucleus reuniens thalami to the entorhinal cortex, hippocampal field CA1, and the subiculum in the rat arise from different populations of neurons. *J. Comp. Neurol.* **364**, 637–650 (1996).

19. Cassel, J. C. *et al.* The reuniens and rhomboid nuclei: neuroanatomy, electrophysiological characteristics and behavioral implications. *Prog. Neurobiol.* **111**, 34–52 (2013).
20. Baeg, E. H. *et al.* Dynamics of population code for working memory in the prefrontal cortex. *Neuron* **40**, 177–188 (2003).
21. Ange, J. A., van der Meer, M. A., Langston, R. F. & Wood, E. R. Exploring the role of context-dependent hippocampal activity in spatial alternation behavior. *Hippocampus* **17**, 988–1002 (2007).
22. Anderson, M. I. & Jeffery, K. J. Heterogeneous modulation of place cell firing by changes in context. *J. Neurosci.* **23**, 8827–8835 (2003).
23. Leutgeb, S., Leutgeb, J. K., Treves, A., Moser, M. B. & Moser, E. I. Distinct ensemble codes in hippocampal areas CA3 and CA1. *Science* **305**, 1295–1298 (2004).
24. Leutgeb, S. *et al.* Independent codes for spatial and episodic memory in hippocampal neuronal ensembles. *Science* **309**, 619–623 (2005).
25. Wouterlood, F. G., Saldana, E. & Witter, M. P. Projection from the nucleus reuniens thalami to the hippocampal region: light and electron microscopic tracing study in the rat with the anterograde tracer Phaseolus vulgaris-leucoagglutinin. *J. Comp. Neurol.* **296**, 179–203 (1990).
26. Sommer, M. A. & Wurtz, R. H. Influence of the thalamus on spatial visual processing in frontal cortex. *Nature* **444**, 374–377 (2006).
27. Sherman, S. M. & Guillery, R. W. *Exploring the Thalamus and its Role in Cortical Function*. (MIT Press, 2006).
28. Xu, W. & Sudhof, T. C. A neural circuit for memory specificity and generalization. *Science* **339**, 1290–1295 (2013).
29. Vertes, R. P., Linley, S. B., Groenewegen, H. J. & Witter, M. P. in *The Rat Nervous System* 4th edn (ed. G. Paxinos) Ch. 16 (Elsevier Academic Press, 2014).
30. Hembrook, J. R. & Mair, R. G. Lesions of reuniens and rhomboid thalamic nuclei impair radial maze win-shift performance. *Hippocampus* **21**, 815–826 (2011).
31. Andersen, R. A. & Mountcastle, V. B. The influence of the angle of gaze upon the excitability of the light-sensitive neurons of the posterior parietal cortex. *J. Neurosci.* **3**, 532–548 (1983).
32. Sargolini, F. *et al.* Conjunctive representation of position, direction, and velocity in entorhinal cortex. *Science* **312**, 758–762 (2006).
33. Komorowski, R. W., Manns, J. R. & Eichenbaum, H. Robust conjunctive item-place coding by hippocampal neurons parallels learning what happens where. *J. Neurosci.* **29**, 9918–9929 (2009).
34. Warden, M. R. & Miller, E. K. Task-dependent changes in short-term memory in the prefrontal cortex. *J. Neurosci.* **30**, 15801–15810 (2010).
35. Rigotti, M. *et al.* The importance of mixed selectivity in complex cognitive tasks. *Nature* **497**, 585–590 (2013).

Supplementary Information is available in the online version of the paper.

Acknowledgements We thank A. M. Amundsgård, K. Haugen, K. Jenssen, E. Kråkvik and H. Waade for technical assistance, M. Andresen, E. Håstad and G. Jakobsen for taking care of animals, J. Ye and J. Wu for help with immunostaining of brain sections, K. Deisseroth for providing eNpHR3.0 plasmids, and A. Treves and A. Tsao and other members of the Moser laboratory for discussion. This work was supported by two Advanced Investigator grants from the European Research Council ('CIRCUIT', Grant Agreement no. 232608; 'ENSEMBLE', Grant Agreement no. 268598), the Kavli Foundation, the Centre of Excellence scheme of the Research Council of Norway (Centre for the Biology of Memory and Centre for Neural Computation).

Author Contributions H.T.I., E.I.M. and M.-B.M. designed the experiment. S.-J.Z. made all viral constructs. M.P.W. advised on location of electrodes and lesions, H.T.I. performed all experiments and analyses. H.T.I., E.I.M. and M.-B.M. wrote the manuscript after discussion among all authors. M.-B.M. and E.I.M. supervised and coordinated the project.

Author Information Reprints and permissions information is available at www.nature.com/reprints. The authors declare no competing financial interests. Readers are welcome to comment on the online version of the paper. Correspondence and requests for materials should be addressed to H.T.I. (hiroshi.ito@ntnu.no) or M.-B.M. (may-britt.moser@ntnu.no).

METHODS

Subjects. Thirty-six male Long Evans rats (400–600 g at implantation) were housed individually in transparent Plexiglass cages (45 cm × 30 cm × 35 cm). Six of the rats were implanted with tetrodes in CA1 only. Two rats were implanted with tetrodes in both CA1 and CA3. Three rats had tetrodes in CA3. Four rats received neurotoxic lesions of NR and had tetrodes in CA1. Twelve rats had tetrodes in NR and CA1/CA3. Three rats had tetrodes in mPFC. Six rats received adeno-associated virus (AAV) injections in NR; all of these animals had tetrodes in CA1. All rats were kept at 85–90% of free-feeding body weight and maintained on a 12-h light/12-h dark schedule. All behavioural training and recordings were performed in the dark phase.

The experiments were performed in accordance with the Norwegian Animal Welfare Act and the European Convention for the Protection of Vertebrate Animals used for Experimental and Other Scientific Purposes. The study contained no randomization to experimental treatments and no blinding. Sample size (number of animals) was set a priori to three or more, considered as the minimum required to obtain the number of cells required for statistical power in the present type of data. No statistical method was used to predetermine sample size.

Construction, preparation and titration of recombinant AAV (rAAV) expressing eNpHR3.1. The proviral plasmid used for packaging rAAV was flanked by AAV serotype-2 inverted terminal repeats (ITR). The rAAV vector contained both a woodchuck hepatitis virus post-transcriptional regulatory element and a bovine growth hormone polyadenylation signal for enhancing transgene transcription and expression. Transcription was regulated by a calcium-calmodulin-dependent protein kinase II α (CaMKII α) promoter, and the viral vector, pAAV-CaMKII α -eNpHR3.0-eYFP (a gift from K. Deisseroth), was used as a PCR template to generate a trafficking-enhanced opsin. A Flag tag was placed at the C-terminus of the opsin gene between the 20-amino-acid trafficking signal DYKDDHGDYKDDHIDYKDDDDK and the endoplasmic reticulum exporting motif FCYENEV, both derived from the inward-rectifier potassium ion channel Kir2.1 and introduced to improve membrane trafficking³⁶. The 17-amino acid N-terminal signal peptide from the β subunit of the nicotinic acetylcholine receptor, originally used for membrane insertion in eNpHR2.0, was removed as previously described^{37,38}.

The rAAV vector was pseudo-typed with AAV1 capsid proteins. rAAV2/1 was prepared by co-transfection of human embryonic kidney cell line HEK293 using the calcium phosphate method along with the adenoviral helper plasmid pHelper (Stratagene). Twelve hours after transfection, the DNA/CaCl₂ mixture was replaced with normal growth medium. After an additional 60 h in culture, the transfected cells were collected and subjected to three freeze/thaw cycles. The clear supernatant was then purified using heparin affinity columns (HiTrap Heparin HP, GE Healthcare). The purified rAAV2/1 was concentrated with an Amicon Ultra-4 centrifugal filter 100K device (Millipore), and the viral titre was determined by real-time quantitative PCR using StepOnePlus Real-Time PCR Systems and TaqMan Universal Master Mix (Applied Biosystems). The titred virus was diluted and matched to 1.0×10^{12} viral genomic particles per ml by 1× PBS.

Surgery, virus injection, lesions and drive implantation. The rats were anaesthetized with isoflurane. Initial concentration in the induction chamber was 5.0% (vol/vol). Air flow was set to 1.0–1.5 l min⁻¹. For analgesia, Temgesic (buprenorphine, 15 µg/300 g; RB Pharmaceuticals Limited) was administered by subcutaneous injection. Following induction of anaesthesia, the animal was fixed in a Kopf stereotaxic frame for electrode implantation and virus injection at 0.5–2% isoflurane (vol/vol), adjusted according to physiological monitoring. Holes for tetrode implantation were drilled on the skull.

For tetrode recording from CA1 or CA3, animals were implanted with a 'hyperdrive' with 14 independently movable tetrodes constructed from 17-µm polyimide-coated platinum-iridium (90–10%) wire (California Fine Wire). The tetrode bundle was circular. The tetrodes were implanted at anterior–posterior (AP): –3.8 mm from bregma, medial–lateral (ML): 3.5 mm from midline, and dorsal–ventral (DV): 1.0 mm below dura. Electrode tips were plated with platinum to reduce electrode impedances to 100–200 kΩ at 1 kHz. In seven animals, implanted for simultaneous recording from NR and CA1 and/or CA3, we used a split bundle of tetrodes, in order to independently target seven tetrodes (three independently movable double tetrodes and one reference) to NR (AP: –2.25, ML: 0.6) and seven tetrodes (six independently movable tetrodes and one reference) to the hippocampus (AP: –3.25, ML: 2.5). The tetrodes were implanted with a 5° lateral-to-medial angle in the coronal plane. For tetrode recording in mPFC, a hyperdrive with a circular bundle of 14 independently movable tetrodes was implanted on the surface of the prefrontal cortex (AP: +3.25, ML: 0.6, DV: 1.0, with a 5° lateral-to-medial angle in the coronal plane). The hyperdrives were secured to the skull with jeweller's screws and dental cement. Two screws in the

skull behind the lambda (above the cerebellum) were connected to hyperdrive ground. Following closure of the wound, the electrodes were turned into the cortex while signals were monitored on the recording system. The animals received an oral dose of the analgesic Metacam (Meloxicam, 0.1 mg per 300 g; Boehringer Ingelheim) during the first few days after the surgery.

In two animals aimed for simultaneous recording from NR and CA1, we first implanted a 'microdrive' with four tetrodes targeting NR (AP: –2.0, ML: 0.6, DV: 5.5, with a 5° lateral-to-medial angle in the coronal plane). This was followed by the implantation of a second microdrive above CA1 (AP: –4.0, ML: 3.2, DV: 1.5). One skull screw behind lambda (above the cerebellum) served as ground for each drive.

For the optogenetics experiments, solution of rAAV virus was injected using a 10-µl NanoFil syringe and a 33-gauge bevelled metal needle (World Precision Instruments) at four sites in NR (AP: –2.0 and –2.5, ML 0.8 mm from midline, DV: 6.75 and 6.25). The injection was made at an 8° lateral-to-medial angle in the coronal plane in order to target the central portion of NR in the coronal plane, on both sides of the midline. Injection volume (0.25 µl at each site) and flow rate (0.05 µl min⁻¹) were controlled with a Micro4 Microsyringe Pump Controller (World Precision Instruments). After the injection, the needle was left in place for ten additional minutes before it was withdrawn slowly. After retraction of the needle, an optic fibre (FT400UMT: 0.39 NA, core size Ø 400 µm; Thorlabs) with two tetrodes attached was inserted so that the tip of the fibre was approximately 0.25 mm above NR (AP: 2.25, ML: 0.8, DV: 6, with an 8° lateral-to-medial angle in the coronal plane). The two tetrodes were advanced 0.75 mm beyond the tip of the optic fibre, targeting NR. The tetrodes were wired to the headstage connector for the recording system (Axona Ltd). After the optic fibre insertion, a hyperdrive with 14 independently movable tetrodes was implanted above CA1 in the left hemisphere (AP 4.0, ML 3.5 with a 10° lateral-to-medial angle in the coronal plane).

For NR lesion experiments, ibotenic acid (Sigma-Aldrich) was dissolved in phosphate-buffered saline (pH 7.4, 10 mg ml⁻¹) and injected using a 10-µl NanoFil syringe and a 33-gauge bevelled metal needle (World Precision Instruments) mounted to the stereotaxic frame. Volumes of 0.1 µl of ibotenic acid were infused over 10 min at three stereotaxic positions in the NR of the left hemisphere (AP: –1.75, ML: 0.6, DV: 6.75; AP: 2.25 and 2.75, ML: 0.6, DV: 7.0), targeting the central portion of NR in the coronal plane. The angle of the injection needle was 5° in the coronal plane with the tip pointing towards the midline. The flow rate was 0.01 µl min⁻¹. Flow was controlled with a Micro4 Microsyringe Pump Controller. After the injection, the needle was left in place for 10 min. When the infusions were completed, the rats were immediately implanted with a hyperdrive aimed at CA1 in the same hemisphere (AP: 3.8, ML: 3.0) or with two microdrives aimed at CA1 in each hemisphere (AP: 4.0, ML: 3.2).

Electrode turning and recording procedures. The hyperdrive was connected to a multichannel unity gain headstage (HS-54; Neuralynx). The output of the headstage was connected via a lightweight multi-wire tether and a Neuralynx PSR-36 commutator to a data acquisition system with 64-channel digital amplifiers (Digital Lynx; Neuralynx). Unit activity was filtered at 600 (64 taps)–6,000 (32 taps) Hz with a FIR band-pass filter. Spike waveforms above a threshold of ~40 µV or more (noise r.m.s. <20 µV) were time-stamped and digitized at 32,556 Hz at 24-bit resolution for 1 ms. Light-emitting diodes on the headstage were tracked to obtain the animal's position and head direction. The local field potential (LFP) was filtered at 1–500 Hz with a running average filter (DCO) and a low-pass FIR filter (64 taps). The LFP signal was digitized at 2,034 Hz.

After surgery, the tetrodes were moved in small daily increments towards the target area while the rat was resting on a pedestal. One electrode was used to record a reference signal from the superficial layers of the cortex (DV: ~1 mm). Another electrode was used to monitor LFP, in the stratum lacunosum-moleculare for the recordings from the hippocampus, and in the dorsal thalamus (DV: ~5 mm) for recordings from NR. The pyramidal cell layer of CA1 or CA3 was identified during recording by the presence of sharp waves and large-amplitude complex-spike activity. On the day of recording, the electrodes were not moved at all to maintain stable recordings.

Microdrives for simultaneous NR and CA1 recording were connected to a multi-channel unity gain headstage, which in turn was connected via a counter-balanced cable to an Axona recording system (Axona Ltd). Unit activity was band-pass filtered at 600–6,000 Hz with third-order Bessel filters and amplified by a factor of 5,000–12,500. Spike waveforms above a threshold of ~40 µV or more (noise r.m.s. <25 µV) were time-stamped and digitized at 48,000 Hz at 24-bit resolution for 1 ms. Tetrodes were lowered in 50-µm steps while the rat rested on the pedestal. The LFP was low-pass filtered at 500 Hz with a sixth-order Bessel filter. The signal was digitized at 4,800 Hz.

For tetrode recordings with optogenetic manipulations, a 532-nm light pulse was generated from a DPSS laser unit (Shanghai Laser & Optics Century) with a

patch cable (FT400UMT; Thorlabs) connected to the animal. Power density was $20\text{--}30\text{ mW mm}^{-2}$ at the tip of the fibre. The laser application was controlled with a custom made program in MATLAB (MathWorks) through a NI-DAQ system (USB-6211; National Instruments). Pulse delivery depended on the animal's position on the maze, which was monitored through a NetCom connection between MATLAB and Cheetah recording software (Neuralynx). Three to four weeks after the virus injection, silencing of cells with laser application was confirmed with tetrodes attached to the optic fibre. Unit activity from the tetrodes on the optic fibre was monitored using an Axona recording system (Axona Ltd). In all animals tested, at least two units in NR showed a significant reduction of spike rate by the laser application (Extended Data Fig. 6). After the animals were sufficiently familiarized with the continuous alternation task, the first recording session (~ 10 min) started with an optic-fibre patch cable connected to the animal without laser application. After the first session, the animal was at rest for 5 min before the next session, when light was applied for ~ 10 min. To avoid unnecessary photodamage to the tissue, the laser application was turned off intermittently. The laser application was always on when the animal was running on the central stem and the side arms, but it was turned off when the animal reached the bottom arm. Five seconds after the animal reached the food port, the laser application was restarted, which was approximately 5–10 s before the next run. The laser then continued to be on for the next trajectory. After the session with laser application, the animal was at rest on the pedestal for at least 10 min or in the Plexiglass home cage for ~ 30 min before a new session was started. The final session (~ 10 min) was conducted with the optic fibre patch cable connected without laser application.

Behavioural task on the modified T-maze. Two versions of modified T-mazes are shown in Fig. 1a ($110\text{ cm} \times 110\text{ cm}$ square-shaped maze and $130\text{ cm} \times 130\text{ cm}$ diamond-shaped maze). The mazes were constructed of 12 cm wide wooden runways covered by rubber sheet and with 2 cm high plastic side walls. The central runway (stem) was 100 cm for the square-shaped maze and 120 cm for the diamond-shaped maze. Additional wall strips (10 cm length, 2 cm high, 1 cm thickness) were added on both sides at the end portion of the stem to reduce the width of the runway. This helped minimizing the lateral deviation of the animals' trajectories. Chocolate-taste cereals or cookies were provided on a small dish located at the centre of the bottom arm (Fig. 1a). In contrast to previous studies using this task^{6,21}, reward was always given at the same spatial position, irrespective of whether the animals chose left or right trajectories, such that effects of intended movement could be dissociated from effects of the goal location itself. The maze was elevated 50 cm above the ground. It was surrounded by black circular curtains (180 cm diameter) without any visual cues on three sides. The bottom side of the maze was partially open to the recording room.

Behavioural training and recordings were performed on one of the mazes. The maze was randomly chosen for each animal. After finishing the recordings on the first maze, some animals with tetrodes in NR or in the hippocampus were further trained and recorded on the other maze. For NR recordings, the same units were typically active across mazes. In those cases, cells were only included into one of the data sets. For recordings from CA1 or CA3, we often observed global remapping of place cells after changing the shape of the maze, and sometimes new units were recruited on the stem.

Behavioural training started after recovery from surgery. Training started with 1 or 2 days of accommodation where each rat was placed on the maze to freely explore and find food at the food port. In the next stage of training, the animals were instructed to follow a specific direction on the maze—from the stem through a side arm to the food port—by blocking reverse movement with the experimenter's hands when necessary. Food was available at the food port irrespective of which trajectory the animal chose at this stage. After the animal was familiar with the movement direction rule on the maze, the final stage was to acquire the alternation rule. Reward was provided only when the animal chose the opposite trajectory of the previous trial, irrespective of whether choices were correct or incorrect on the preceding trial. For each day, three to five 10-min sessions were performed. Criterion was reached when choices were correct on 90% of the trials. Trajectory-dependent firing continued to be expressed long after the animals reached the behavioural criterion (for up to 2–3 months). Trajectory dependence emerged without the use of a barrier to instruct correct alternation during the training stage³⁹.

The number of left- and right-preferring neurons (neurons with higher firing rate on trajectories that led to left versus right turns) was balanced (CA1: 48 versus 50 cells; CA3: 16 versus 18 cells; CA1 with NR lesions: 24 versus 20 cells; NR: 34 versus 30 cells; mPFC: 176 versus 162 cells). There was no difference in the number of left- and right-preferring cells within trials (binomial tests with Bonferroni correction, $P > 0.05$).

For the delayed alternation task in Fig. 5b, a delay period of either 10 or 15 s was introduced before the animals started running on the stem. The maze was

equipped with a manually controlled plastic door ($25 \times 25\text{ cm}$) on the central stem approximately 25 cm from the start of the stem. In addition, plastic walls (25 cm high) were inserted on both sides of the delay zone to minimize lateral movement (Extended Data Fig. 7c). The animal's movement was continuously monitored with a custom made program in MATLAB with a NetCom connection to the recording system. When the animal entered the delay zone, a counter was started by the program. Criterion was reached when choices were correct on 80% of the trials.

Spike sorting and cell classification. All main analyses were performed using MATLAB (MathWorks). Spike sorting was performed offline using MATLAB-based graphical cluster-cutting software, MClust (A.D. Redish). Clustering was performed manually in two-dimensional projections of the multidimensional parameter space (consisting of waveform energies and peak–trough amplitude differences). Autocorrelation and cross-correlation functions were used as additional separation tools. For recordings in CA1 or CA3, putative pyramidal cells were distinguished from putative interneurons by spike width and average rate and the presence of bursts. In the continuous alternation task, only cells with a peak firing rate more than 1 Hz on the central stem of the maze on either trajectory were analysed. In the open field, all units with an average firing rate above 0.2 Hz in at least one of the sessions were used for the further analysis.

To ensure the same cell was not counted multiple times, for recordings in CA1 and CA3, the estimated number of cells recorded on each tetrode was generally based on a single recording session (with tetrodes placed optimally in the cell layer). For a few exceptional animals, a second recording session was conducted in the other shape of the T-maze, but in these cases, only new clusters at the same tetrode position were included. For recordings from NR and mPFC, discrete units were sampled from recording sessions with at least $40\text{ }\mu\text{m}$ separation from the preceding and succeeding recording locations.

Trajectory-dependent firing on the modified T-maze. For analysis of trajectory-dependent firing on the stem, we first extracted a portion of the stem where the animal's running speed, head direction and lateral position were not significantly different between left and right trajectories. 95% confidence intervals for multiple comparisons of six bins (with Bonferroni correction) were determined for lateral position on left- and right-turn trajectories and the portion of the central stem with overlapping confidence intervals was extracted for analysis. A segment of 5 cm was further excluded from the top end of the extracted stem portion to guarantee minimal trajectory deviation. For the remaining portion of the stem, we examined the 95% confidence intervals for running speed on left- and right-turn trajectories. If necessary, the trial with the largest deviation of running speed was excluded iteratively until the confidence intervals between trajectories overlapped across the entire selected portion of the stem. The same procedure was applied for head direction.

To analyse trajectory-dependent firing on the central stem of the T-maze, we divided it into six equally sized bins. The length of individual bins was 8–13 cm, depending on the selected portion of the stem. The following parameters were calculated for each bin of each trial: (1) firing rate: the number of spikes divided by the amount of time spent in the bin; (2) running speed: the averaged position shift per time in the bin; (3) head direction: the averaged angle of two coloured LEDs on the headstage; and (4) lateral position: averaged position perpendicular to the long axis of the central stem.

For each cell, a two-way ANOVA was conducted with trial type (correct left- and right-turn run) and six bins as independent variables and firing rate as the dependent measure. In the hippocampus, cells with a significant main effect of trial type were identified as potential trajectory-dependent cells. For these cells, a second analysis was performed to examine whether variations in speed, heading, or lateral position might account for the differences in firing rate between trial types. This was examined with a two-way ANCOVA with trial type and bins as the independent variables, firing rate as the dependent measure, and speed, head direction, and lateral position as covariates. Cells that continued to show a significant difference in firing rate between left- and right-turn trials, when the covariates were included in the ANCOVA model, were classified as trajectory dependent⁶. In NR or mPFC, any cell which showed either a significant main effect of trial type or a significant trial type \times bin interaction with both ANOVA and ANCOVA, was considered a trajectory-dependent cell.

To create spatial rate maps, spatial positions in the maze were divided into 10×10 pixel bins (3 pixels per cm) and the firing rate for each bin was calculated. This was performed only for periods when the animal's running speed exceeded 10 cm s^{-1} . Instantaneous spike rates were estimated using a Gaussian kernel on the spike data for temporal smoothing. Instantaneous rate was calculated as

$$r(t) = \sum_{i=1}^N g\left(\frac{t_i - t}{h}\right)$$

where g is a 1D Gaussian kernel, h is a bandwidth, N is the total number of spikes, and t_i is the time of the i -th spike. An optimal bandwidth between 50 and 250 ms was determined for each cell by minimizing the mean integrated square error between the estimated rate and the unknown underlying rate⁴⁰. The rate map was smoothed using a 2D Gaussian filter with a bandwidth of one bin ($3.3 \text{ cm} \times 3.3 \text{ cm}$). Bins visited less than 40 ms were excluded. Spike rate at each stem position was estimated using a linear interpolation method applied to temporally smoothed spike rates by the 1D Gaussian kernel. Mean values and 95% confidence intervals of the spike rates were calculated for left- and right- turn trajectories. Peak firing rate and peak firing position were determined.

Decoding analysis. A linear decoder, expressed by the following equation, was used to predict the next trajectory from the spike rates on the stem:

$$y = b + w_1 \times F_1 + w_2 \times F_2 + w_3 \times F_3 \dots = b + \mathbf{w}^T \mathbf{F}$$

$$\mathbf{F} = [F_1, F_2, F_3, \dots]^T, \mathbf{w} = [w_1, w_2, w_3, \dots]^T$$

\mathbf{F} is a vector of firing rates for each cell, \mathbf{w} is a vector of respective weights, b is a scalar offset, and y is an output value of the classifier (1, -1). Optimal weights of the decoder were determined by a support vector machine algorithm to maximize the separation margin for better generalization performance on any data set by avoiding over-fitting to the training data used for the weight optimization^{41,42}. In brief, for a given number N of trials of rate-trajectory pairs, (F_i, y_i) , $i = 1, 2, 3, \dots, N$, we searched for \mathbf{w} that satisfies the following condition,

$$\min_{\mathbf{w}, b, \xi} \frac{1}{2} \mathbf{w}^T \mathbf{w} + C \sum_{i=1}^N \xi_i$$

$$\text{subject to } y_i(b + \mathbf{w}^T \mathbf{F}_i) \geq 1 - \xi_i, \xi_i \geq 0$$

C is a penalty parameter for misclassification. We set C at 1 throughout the decoding analysis but changing the C value to (0.1, 10, 100) did not significantly affect any conclusion. The mean firing rates on each bin were used as for the inputs of the classifier.

Decoding performance was estimated using a leave-one-out cross-validation, performed as follows. From a given set of trials in a recording session, one trial was randomly chosen as a test data set and the rest of the trials were used as a training data set. The weights of the linear classifier were optimized based on a training data set, and the same weights were applied to the test data for classification. This procedure was repeated for all trials to be tested, and the classification accuracy on the test data sets was considered an estimate of the decoding performance. The decoding performance on error trials was calculated using the weights optimized for all correct trials in the same recording session.

For decoding analysis in the delayed alternation task in Fig. 5b, the delay period was divided into two temporal bins, corresponding to the first and last halves, and the stem part was divided into four equally sized spatial bins. Decoding performance was estimated using the mean spike rate at each bin.

To isolate prospective and retrospective components in the alternation task, we analysed a subset of trials with an equal number of correct and error trials, so that we could focus on only one of the components, either prospective or retrospective, while the influence from the other component was cancelled out due to an equal number of left- and right-directed trajectories. The details of this procedure are as follows.

Suppose that we want to estimate the probability that the animal took a left trajectory on the previous trial using the spike rates on the stem. The probability for correct trials can then be expressed as:

$$P(\text{last L} | \text{rate, correct}) = P(\text{LR} | \text{rate, correct}) = 1 - P(\text{RL} | \text{rate, correct})$$

where 'last L' indicates a left trajectory choice on the previous trial, 'LR' indicates the trajectory from the previous left arm to the next right arm, and 'RL' indicates the trajectory from the previous right arm to the next left arm. The first term indicates the probability that the animal took a left trajectory on the previous trial, given the spike rates on the stem on correct trials. Note that, if the direction of the last trajectory is given, the next trajectory choice is automatically determined, depending on whether the trial is correct or incorrect. Similarly, the probability for error trials is expressed as:

$$P(\text{last L} | \text{rate, error}) = P(\text{LL} | \text{rate, error}) = 1 - P(\text{RR} | \text{rate, error})$$

Now the retrospective component of the trajectory representation can be estimated using the following equation:

$$P(\text{last L} | \text{rate}) = P(\text{correct}) \times P(\text{LR} | \text{rate, correct}) + P(\text{error}) \times P(\text{LL} | \text{rate, error})$$

$P(\text{correct})$ and $P(\text{error})$ are the probabilities of correct trials and error trials, respectively. Evaluating this equation with all data sets, however, gives a bias

towards the next right turn, because $P(\text{correct}) \gg P(\text{error})$. In other words, this equation gives $P(\text{last L, next biased to R} | \text{rate})$ when all trials are considered. To cancel out the influence of the next trajectory on the decoding performance, we used a subset of trials with an equal number of correct and error trials. This gives:

$$\begin{aligned} P(\text{last L, next unbiased} | \text{rate}) \\ &= P(\text{correct}) \times P(\text{LR} | \text{rate, correct}) + P(\text{error}) \times P(\text{LL} | \text{rate, error}) \\ &= \frac{1}{2} \times P(\text{LR} | \text{rate, correct}) + \frac{1}{2} \times P(\text{LL} | \text{rate, error}) \\ \therefore P(\text{correct}) &= P(\text{error}) = \frac{1}{2} \end{aligned}$$

Here the probabilities $P(\text{LR} | \text{rate, correct})$ and $P(\text{LL} | \text{rate, error})$ can be obtained using the same decoding procedure as in Fig. 5a, b. A statistical distribution for decoding performance was estimated from 1,000 randomly sampled subsets with an equal number of correct and error trials (a bootstrap resampling method). Similarly, the prospective component of the trajectory representation was estimated as:

$$\begin{aligned} P(\text{last unbiased, next R} | \text{rate}) \\ &= P(\text{correct}) \times P(\text{LR} | \text{rate, correct}) + P(\text{error}) \times P(\text{RR} | \text{rate, error}) \\ &= \frac{1}{2} \times P(\text{LR} | \text{rate, correct}) + \frac{1}{2} \times [1 - P(\text{LL} | \text{rate, error})] \\ \therefore P(\text{correct}) &= P(\text{error}) = \frac{1}{2} \end{aligned}$$

To compare overall firing rates on correct trials and error trials we normalized firing rate on the stem on error trials to firing rates on the stem on correct trials. Normalized firing rates ranged from 0.90 for CA1 to 1.04 for mPFC. Only the CA1 group was significantly different from 1. To test the influence of the lower rate on error trials, the overall firing rates on error trials in the CA1 group were multiplicatively increased by the factor of 1/0.9 in order to match the rates on correct trials. This adjustment did not change the magnitude of the prospective and retrospective components of the firing.

The number of trials used for decoding analysis on continuous trials (Fig. 5a) was, for mPFC, 1,035 correct trials and 27 error trials; for NR, 1,199 correct trials and 34 error trials; and for CA1, 1,145 correct trials and 25 error trials. The number of cells per session was, for mPFC, 14.9 ± 0.9 ; for NR, 4.5 ± 0.2 ; and for CA1, 6.3 ± 0.6 . The number of trials for trials with a delay (Fig. 5b) was, for mPFC, 319 correct trials and 29 error trials; for NR, 637 correct trials and 83 error trials; and for CA1, 439 correct trials and 54 error trials. The number of cells per session was, for mPFC, 8.8 ± 0.8 ; for NR, 5.2 ± 0.3 ; and for CA1, 7.0 ± 0.6 .

Open-field tests. Animals were tested also in a square box with individually exchangeable walls (black on one side, white on the other side; $100 \text{ cm} \times 100 \text{ cm}$; 50 cm high). Distal background cues were masked by black curtains encircling the recording box (180 cm diameter). A pedestal, where the rat slept and rested, was placed between the test box and the experimenter outside the curtains.

Rate remapping was induced in the hippocampus by changing the colour configuration of the recording box while the box was kept at a constant location. The rat was first placed into the black/white box for 10 min, then into the box with opposite colour for two consecutive 10-min sessions, and then back into the original black/white box for a final 10-min session. The rats were allowed to rest for 5 min on the pedestal between the sessions. While the animal was resting, the four walls of the box were flipped and the floor was washed with water. Animals with tetrodes in NR and CA1 were tested in a black-white-black sequence of four sessions, using the same box. Animals with tetrodes in mPFC were recorded in a black-white-black sequence of three sessions.

For all recordings in the open field, spatial rate distributions for each well-isolated unit were constructed by summing the total number of spikes that occurred in a given location bin ($5 \text{ cm} \times 5 \text{ cm}$) and dividing by the amount of time spent in that bin. An adaptive smoothing method was applied for colour-coded rate plots and for the calculation of spatial correlation and peak firing rate to optimize the trade-off between blurring error and sampling error⁴³. The firing rate at each bin in the environment was estimated by expanding a circle around the point until

$$r \geq \frac{\alpha_i}{n\sqrt{s}}$$

where r is the radius of the circle in bins, n is the number of occupancy samples within the circle, s is the total number of spikes in those occupancy samples and

the constant α is set to 10,000. With a position sampling rate of 50 Hz, the firing rate at that point was then set to $50 \frac{\lambda_i}{n}$. The maximum value in the smoothed rate map was taken as the peak firing rate of the cell. Spatial information for individual cells was calculated from spike rate maps, using the following equation:

$$\sum_i p_i \frac{\lambda_i}{\lambda} \log_2 \frac{\lambda_i}{\lambda}$$

where λ_i is the mean firing rate in the i -th bin, λ is the overall mean firing rate and p_i is the probability of the animal being in the i -th bin (occupancy in the i -th bin/total recording time).

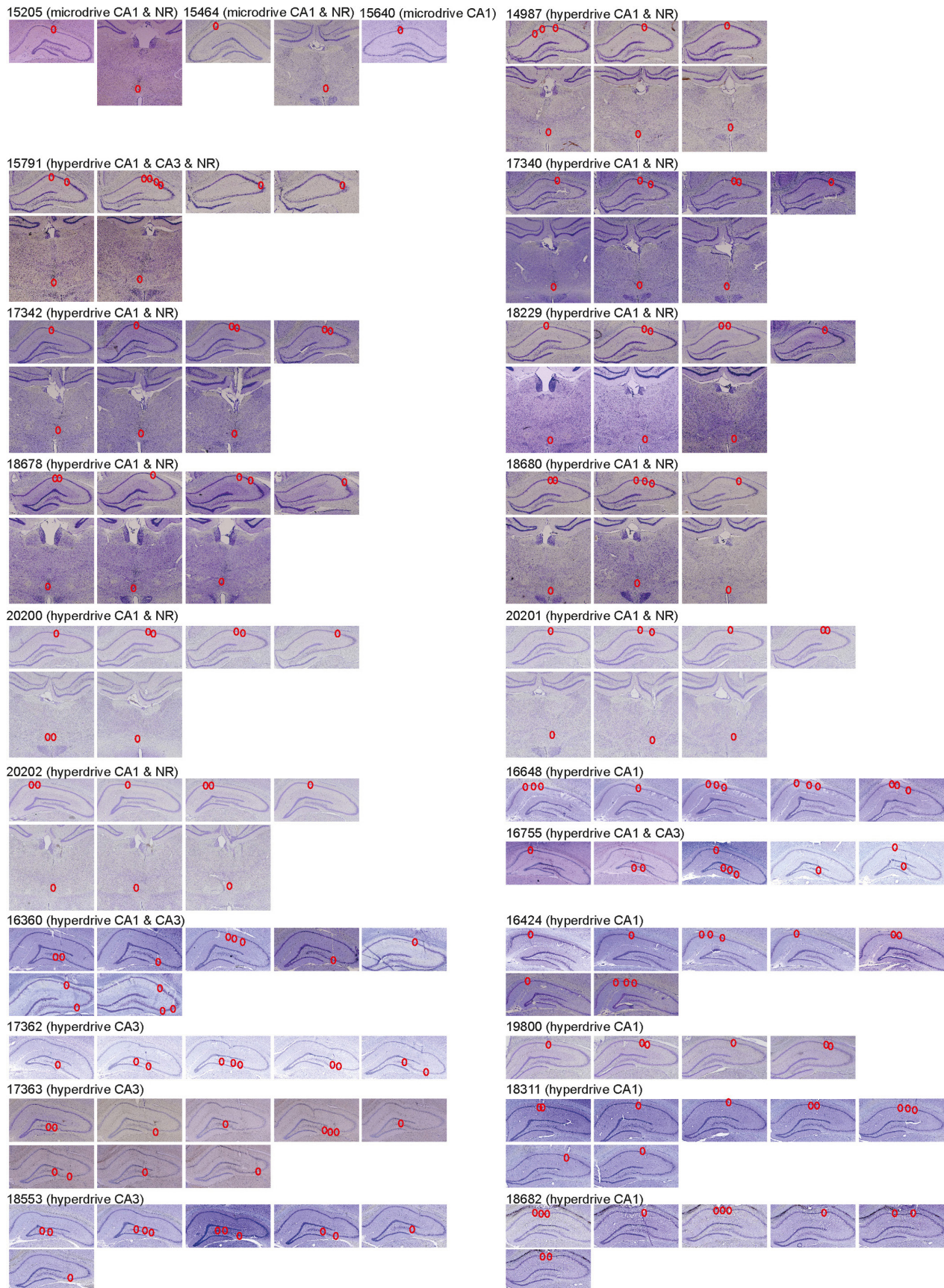
Firing patterns were compared across trials with a spatial correlation procedure. Pearson correlation was measured between the firing rates in common pixels of the two maps for each cell. For comparison of peak rate, the difference of peak rates between boxes divided by the peak rate across the sessions was calculated for each cell. The average value obtained from all possible combinations of sessions with either the same or different colour boxes was considered as representative for each cell. For example, for the sessions with a black 1, white 2, white 3, black 4 sequence, the average value of correlation or rate change between similar session pairs (black 1/black 4 and white 2/white 3) was used as a representative value for the same colour comparison, while the average among different session pairs (black 1/white 2, black 1/white 3, white 2/black 4, white 3/black 4) was used for the different colour comparison.

Histological procedures and electrode positions. The rats received an overdose of pentobarbital and were perfused intracardially with saline followed by either 4% formaldehyde (vol/vol). The brains were extracted and stored in formaldehyde, and frozen coronal sections (30 μ m or 40 μ m) were cut and stained with cresyl violet. Each section through the relevant brain region was collected for analysis. All tetrode and optic fibre traces were identified and the tip of each electrode was found by comparison across adjacent sections. The position and extent of the neurotoxic lesions in NR were outlined in Nissl-stained sections throughout the anteroposterior extent of NR. Lesioned tissue was defined by either absence of tissue or stained neurons, and included areas showing picnotic neurons.

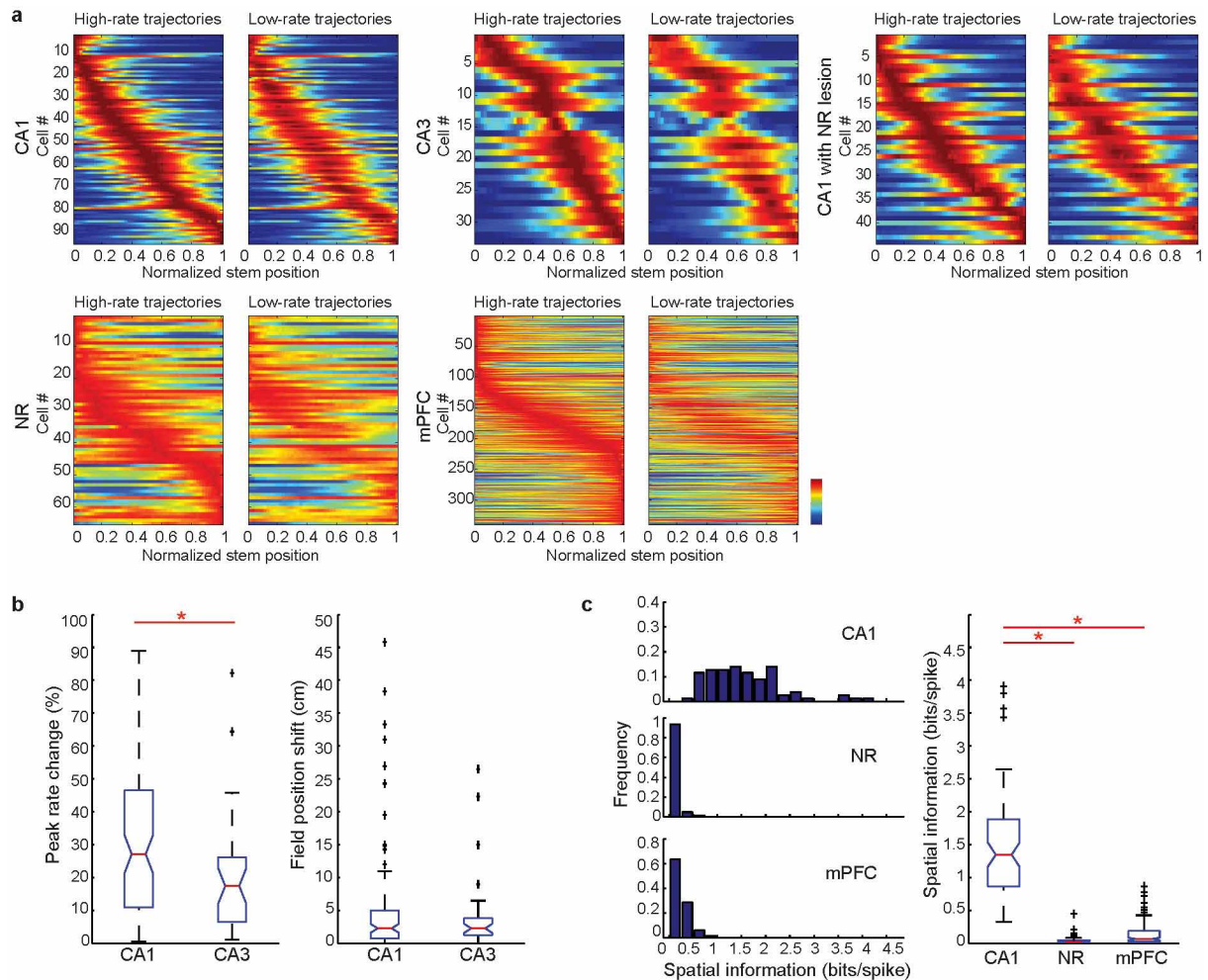
Statistical tests. All statistical tests were two-sided. Data met assumptions about normality when parametric statistics were used.

Code availability. Code for decoding of subsequent trajectories can be obtained from the authors.

36. Gradinaru, V., Thompson, K. R. & Deisseroth, K. eNpHR: a *Natronomonas* halorhodopsin enhanced for optogenetic applications. *Brain Cell Biol.* **36**, 129–139 (2008).
37. Gradinaru, V. *et al.* Molecular and cellular approaches for diversifying and extending optogenetics. *Cell* **141**, 154–165 (2010).
38. Zhang, S. J. *et al.* Optogenetic dissection of entorhinal-hippocampal functional connectivity. *Science* **340**, 1232627 (2013).
39. Bower, M. R., Euston, D. R. & McNaughton, B. L. Sequential-context-dependent hippocampal activity is not necessary to learn sequences with repeated elements. *J. Neurosci.* **25**, 1313–1323 (2005).
40. Shimazaki, H. & Shinomoto, S. Kernel bandwidth optimization in spike rate estimation. *J. Comput. Neurosci.* **29**, 171–182 (2010).
41. Boser, B. E., Guyon, I. M. & Vapnik, V. N. A training algorithm for optimal margin classifiers. *Proceedings of the fifth annual workshop on Computational learning theory* 144–152 (1992).
42. Chang, C. C. & Lin, C. J. LIBSVM: a library for support vector machines. *ACM Trans. Intell. Syst. Technol.* **2**, 3, Article 27, (2011).
43. Skaggs, W. E., McNaughton, B. L., Wilson, M. A. & Barnes, C. A. Theta phase precession in hippocampal neuronal populations and the compression of temporal sequences. *Hippocampus* **6**, 149–172 (1996).
44. Dolleman-Van der Weel, M. J. & Witter, M. P. Nucleus reuniens thalami innervates gamma aminobutyric acid positive cells in hippocampal field CA1 of the rat. *Neurosci. Lett.* **278**, 145–148 (2000).
45. Euston, D. R. & McNaughton, B. L. Apparent encoding of sequential context in rat medial prefrontal cortex is accounted for by behavioral variability. *J. Neurosci.* **26**, 13143–13155 (2006).
46. Lu, L. *et al.* Impaired hippocampal rate coding after lesions of the lateral entorhinal cortex. *Nature Neurosci.* **16**, 1085–1093 (2013).
47. Hyman, J. M., Ma, L., Balaguer-Ballester, E., Durstewitz, D. & Seamans, J. K. Contextual encoding by ensembles of medial prefrontal cortex neurons. *Proc. Natl Acad. Sci. USA* **109**, 5086–5091 (2012).
48. Whitlock, J. R., Pfuhl, G., Dagslott, N., Moser, M. B. & Moser, E. I. Functional split between parietal and entorhinal cortices in the rat. *Neuron* **73**, 789–802 (2012).
49. Salinas, E. & Abbott, L. F. Coordinate transformations in the visual system: how to generate gain fields and what to compute with them. *Prog. Brain Res.* **130**, 175–190 (2001).
50. Salinas, E. & Sejnowski, T. J. Gain modulation in the central nervous system: where behavior, neurophysiology, and computation meet. *Neuroscientist* **7**, 430–440 (2001).
51. Cohen, Y. E. & Andersen, R. A. A common reference frame for movement plans in the posterior parietal cortex. *Nature Rev. Neurosci.* **3**, 553–562 (2002).
52. Moser, E. I. *et al.* Grid cells and cortical representation. *Nature Rev. Neurosci.* **15**, 466–481 (2014).

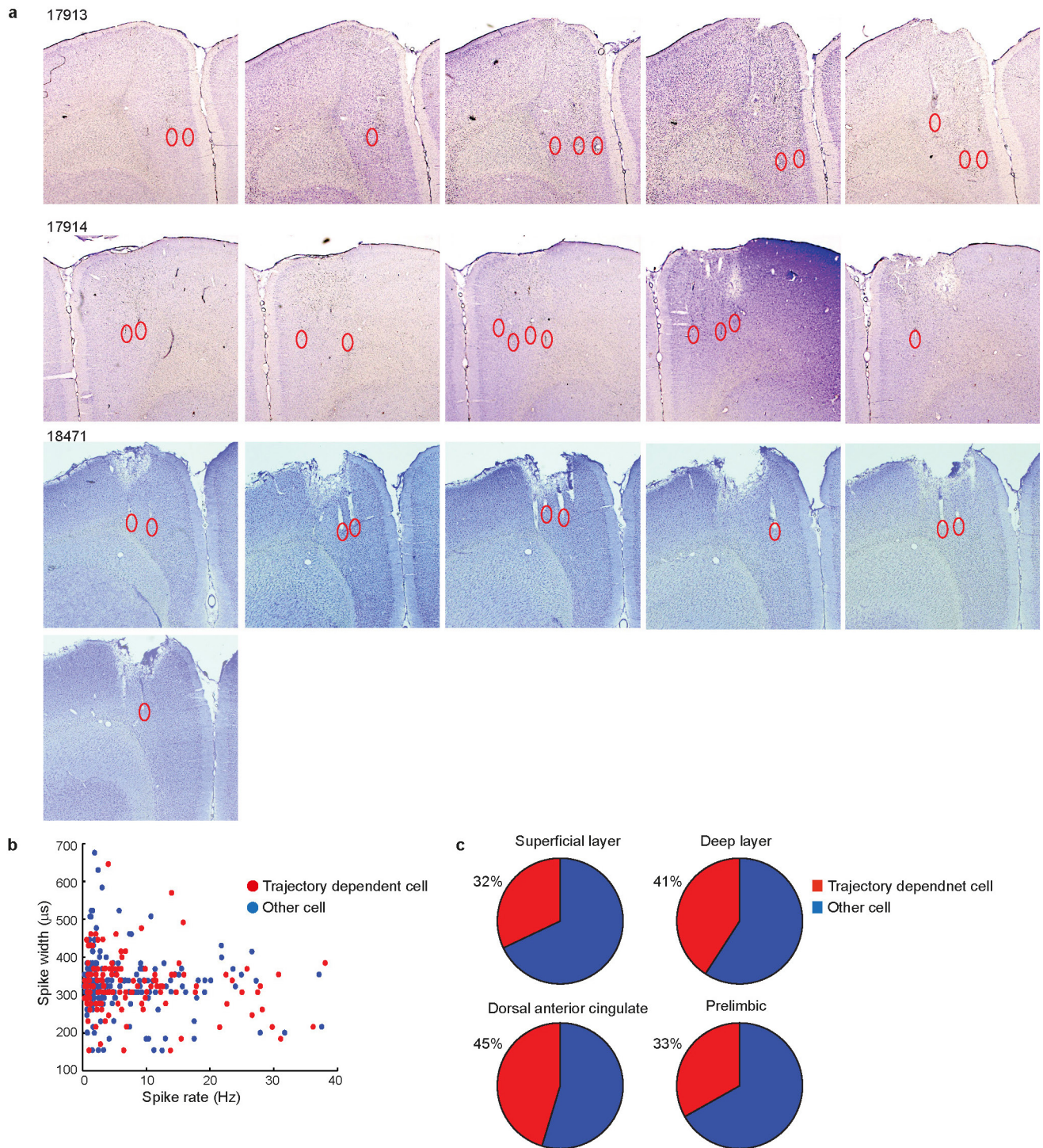


Extended Data Figure 1 | Nissl-stained coronal sections showing tetrode positions in each animal with recordings in CA1, CA3 or NR. Positions of tetrode tracks are indicated by red circles. Rat number, recording region and type of electrode assembly are indicated above each section.



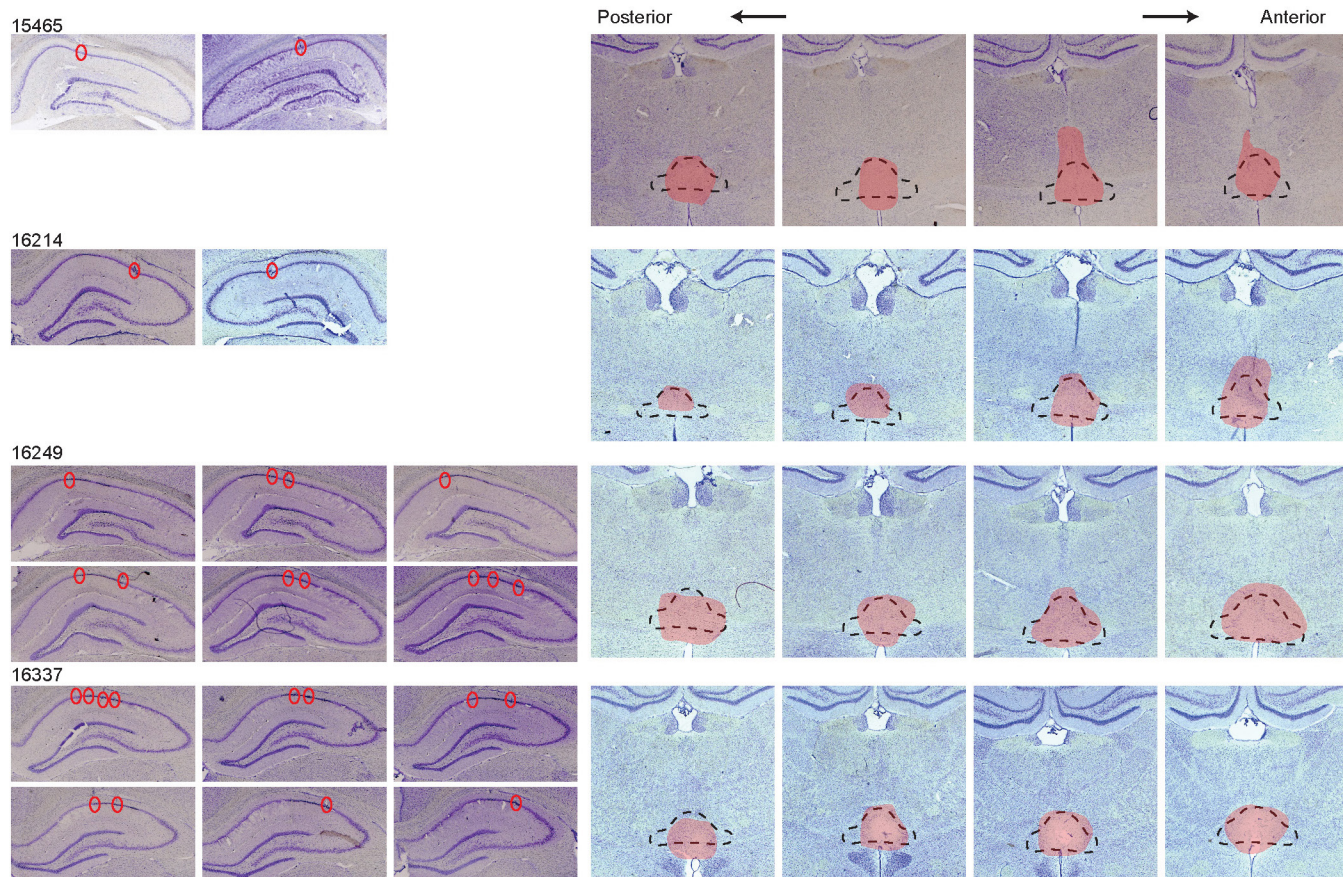
Extended Data Figure 2 | The influence of rate variability on sorting of high-rate and low-rate trajectories, trajectory coding in CA1 and CA3, and spatial properties of neurons in mPFC, NR and CA1. **a**, Demonstration of the influence of rate variability on sorting of high-rate and low-rate trajectories in Figs 1d, f, 2d, 3d and 4d. For each cell, the rate variability (s.d.) within the trajectory in which the cell exhibited a higher peak firing rate was estimated. Gaussian noise with the estimated s.d. was then added to the original rate data. The figure shows two sets of data with the addition of independent Gaussian random noise, sorted into high-rate and low-rate trajectories as in Fig. 1d. The colour-code difference between high-rate and low-rate trajectories reflects the rate variability within the same trajectory. These plots are substantially different from the original plots for CA1 (Fig. 1d), NR (Fig. 2d) and mPFC (Fig. 3d) but are similar to the plots for CA3 (Fig. 1f) and CA1 with NR lesions (Fig. 4d), indicating that colour-code differences on the latter plots can be largely accounted by the rate variability within the same trajectory. **b**, Box

plot showing CA1–CA3 difference in change of peak rate (left) but not field position (right) in the continuous alternation task. $*P < 0.05$. **c**, Distribution of spatial information across cells in CA1, NR, and mPFC (frequency histogram and box plot; $*P < 0.05$). Spatial information per spike was significantly higher in CA1 neurons than in NR or mPFC neurons (CA1, 1.46 ± 0.09 ; NR, 0.048 ± 0.009 ; mPFC, 0.134 ± 0.012 bits per spike (mean \pm s.e.m.); CA1 versus NR, $P < 0.001$, $D = 0.98$; CA1 versus mPFC, $P < 0.001$, $D = 0.93$, Kolmogorov–Smirnov test). Spatial information per spike was also higher in mPFC than in NR ($D = 0.36$, $P < 0.001$, Kolmogorov–Smirnov test) but this difference was not significant when measured in bits per second ($D = 0.07$, $P = 0.19$), indicating that the difference per spike is largely due to higher firing rates in NR (NR, 7.83 ± 1.27 Hz, mPFC, 4.86 ± 0.39 Hz (mean \pm s.e.m.)). The total number of neurons analysed was 71 in CA1, 61 in NR, and 164 in mPFC.



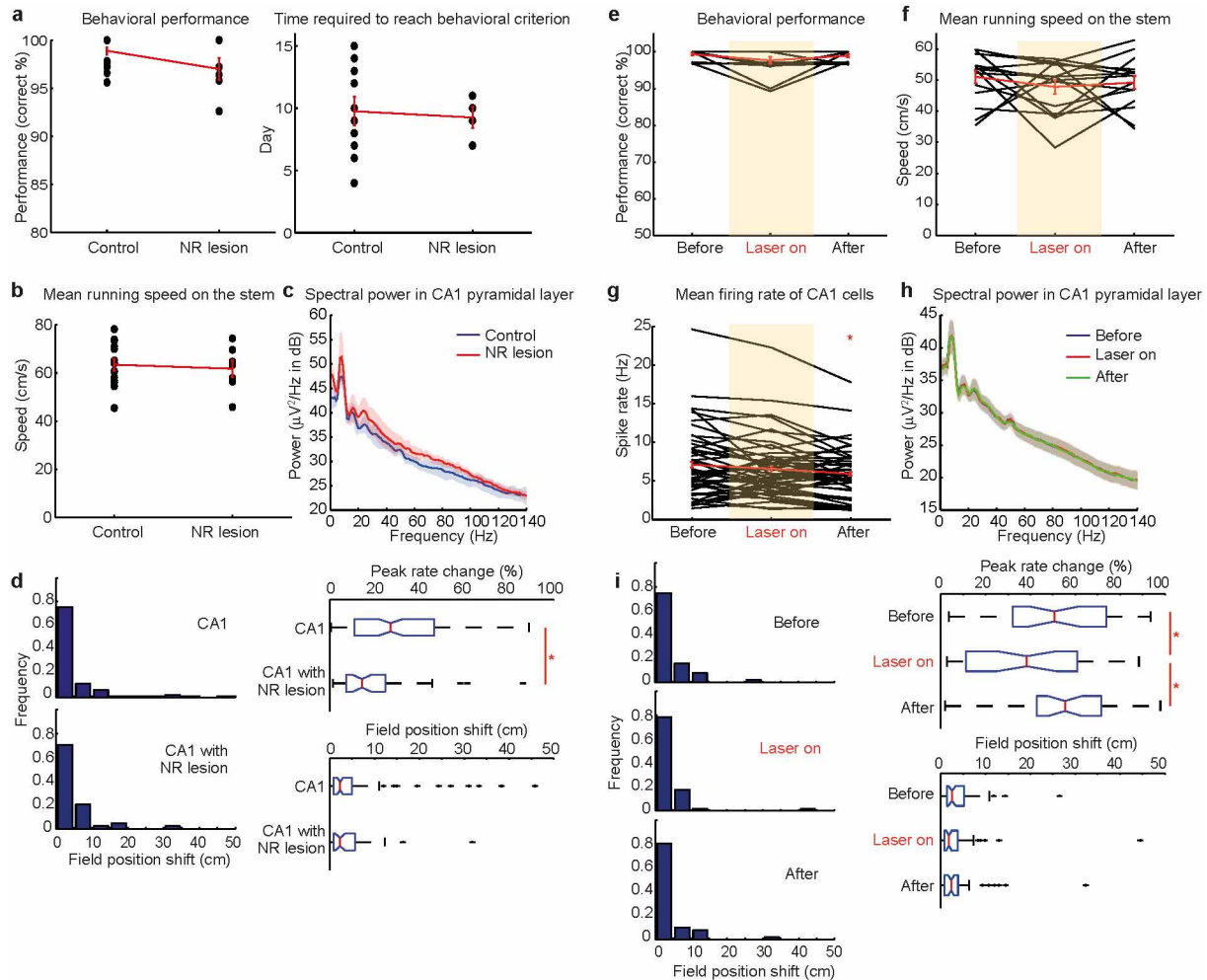
Extended Data Figure 3 | Tetrode positions and localization of trajectory-dependent cells in mPFC. **a**, Positions of tetrode tracks are indicated with red circles. Rat numbers are indicated. **b**, Spike waveform widths (peak-to-trough time) and mean spike rates on the stem (both trajectories combined) were plotted for each cell in mPFC. Trajectory-dependent cells are indicated in red and trajectory-independent cells in blue. No significant difference was observed in spike widths of the two cell types ($D = 0.071$, $P = 0.802$, Kolmogorov-Smirnov test) but the mean spike rates of trajectory-dependent cells were weakly—but significantly—higher than those of trajectory-independent cells

(trajectory-dependent cells, 8.10 Hz; trajectory-independent cells, 5.87 Hz; $D = 0.172$, $P = 0.016$, Kolmogorov-Smirnov test). **c**, Percentage of trajectory-dependent cells in superficial versus deep layers of mPFC and in prelimbic versus dorsal anterior cingulate areas. The percentage of trajectory-dependent neurons was slightly larger in the dorsal anterior cingulate area than in the prelimbic area (45.3% versus 33.2%, $z = 2.26$, $P = 0.024$, binomial test). There was no significant difference between superficial and deep layers (32.0% versus 41.0%, $z = 1.54$, $P = 0.125$).



Extended Data Figure 4 | Nissl-stained coronal sections showing tetrode positions in CA1 of animals and the extent of their NR lesions. Positions of tetrode tracks in CA1 are indicated by red circles. Right sections show outlines of the lesioned areas (orange) and NR (black dashed line) at different anterior-posterior levels. Note that all lesions are bilateral. Percentage of NR

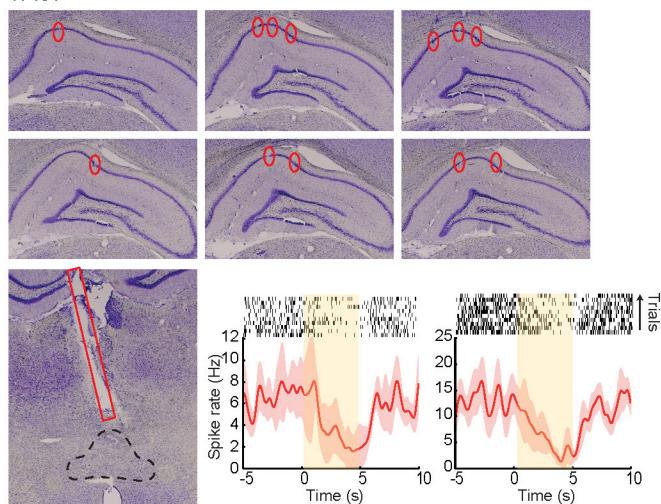
lesions (lesioned NR area/total NR area): #15465, 73%; #16214, 68%; #16249, 85%; #16337, 70%. Percentage of lesioned areas specific to NR (lesioned NR area/total lesioned area): #15465, 71%; #16214, 80%; #16249, 73%; #16337, 80%.



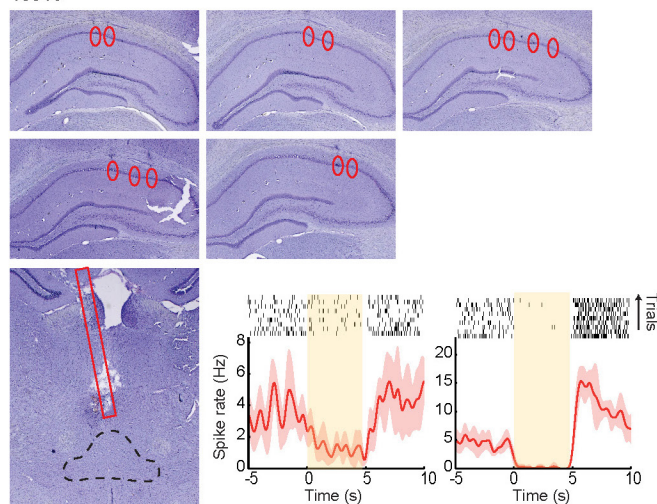
Extended Data Figure 5 | Effect of removal of NR input on behaviour, spike rates and local field potentials in CA1. **a**, Left, behavioural performance (percentage of correct trials) on the continuous alternation task in control animals and animals with NR lesions. No significant difference was observed ($\chi^2_1 = 1.76$, $P = 0.184$; Kruskal–Wallis test). Right, number of days required for animals to reach behavioural criterion (correct trials $>90\%$; $t_{14} = 0.236$, $P = 0.817$). **b**, No significant difference was observed between control and NR-lesioned animals in mean running speed on the stem ($t_{19} = 0.403$, $P = 0.692$). **c**, The mean spectral power of the local field potentials recorded in the CA1 pyramidal layer was not different between control and lesioned animals. The plots show mean values (solid lines) with 95% confidence intervals (shaded areas). **d**, Left, change in field position across alternating trajectories for CA1 place cells recorded in control animals and animals with NR lesions. Right, box plots showing difference in change of peak rate between CA1 in control animals and CA1 in animals with NR lesions (top; $D = 0.346$, $P < 0.001$, Kolmogorov–Smirnov test). There was no corresponding change in field position (bottom; $D = 0.083$, $P = 0.982$ Kolmogorov–Smirnov test). * $P < 0.05$. **e**, Behavioural performance did not change during laser stimulation in NR in eNpHR-expressing animals ($\chi^2_2 = 2.77$, $P = 0.250$; Friedman test). **f**, Running speed on the stem did not change significantly during laser application ($F_{2,28} = 0.89$, $P = 0.423$, repeated-measures ANOVA). **g**, Mean firing rates of place cells on the stem (both trajectories combined) did not change significantly during

laser application but were significantly reduced after termination of the stimulation ($F_{2,28} = 6.52$, $P = 0.002$, repeated-measures ANOVA; before versus during: $t_{49} = 1.651$, $P = 0.105$, during versus after: $t_{49} = 2.137$, $P = 0.038$, post hoc paired t -test). The lack of a consistent reduction in CA1 mean firing rate during light application probably reflects the fact that excitatory inputs from NR to CA1 terminate not only on pyramidal cells but also on local inhibitory neurons⁴⁴. **h**, Spectral power of local field potentials in the CA1 pyramidal layer was not significantly changed by laser application in NR (before/during laser application, mean \pm s.e.m. $\mu V^2 Hz^{-1}$ in a decibel scale): delta (1–4 Hz): $37.3 \pm 0.92/37.6 \pm 0.99$; theta (6–11 Hz): $41.8 \pm 1.08/41.4 \pm 1.18$; slow gamma (25–50 Hz) $31.6 \pm 0.41/31.7 \pm 0.42$; fast gamma (60–90 Hz): $26.1 \pm 0.53/26.2 \pm 0.53$). The plot shows mean values (solid lines) and 95% confidence intervals (shaded areas). **i**, Left, field position shift between alternating trajectories (frequency histograms and box plots). Right, box plots showing difference in change of peak rate (top; $F_{2,98} = 12.02$, $P < 0.001$, repeated-measures ANOVA), but not field position (bottom; $F_{2,98} = 0.02$, $P = 0.983$). Before laser stimulation, the rate change between left and right laps among place cells that expressed significant trajectory-dependent firing was $52.0 \pm 5.1\%$ (mean \pm s.e.m.). During stimulation, the rate change dropped to $38.6 \pm 4.4\%$ ($t_{33} = 4.04$, $P < 0.001$; paired t -test, two-tailed). The effect recovered to baseline levels after the laser application was terminated ($55.0 \pm 3.9\%$; $t_{33} = 4.81$, $P < 0.001$; paired t -test).

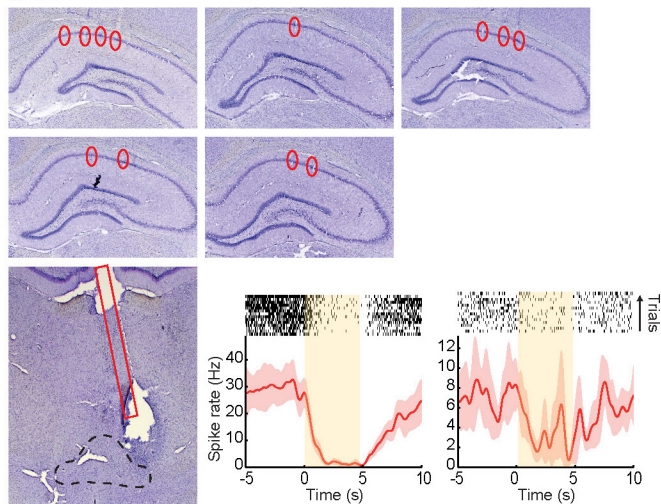
17401



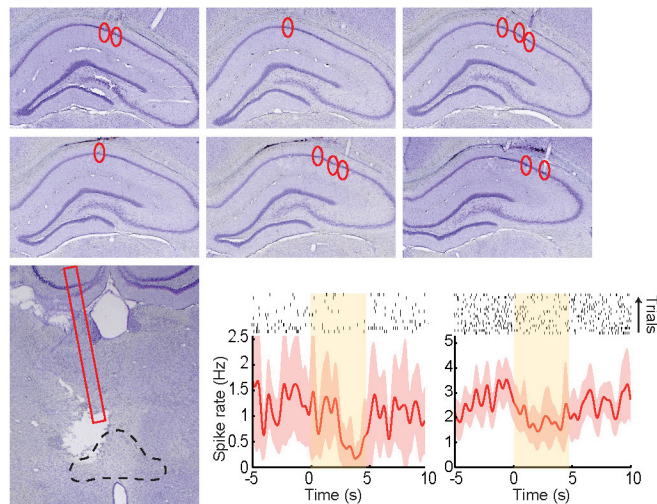
18516



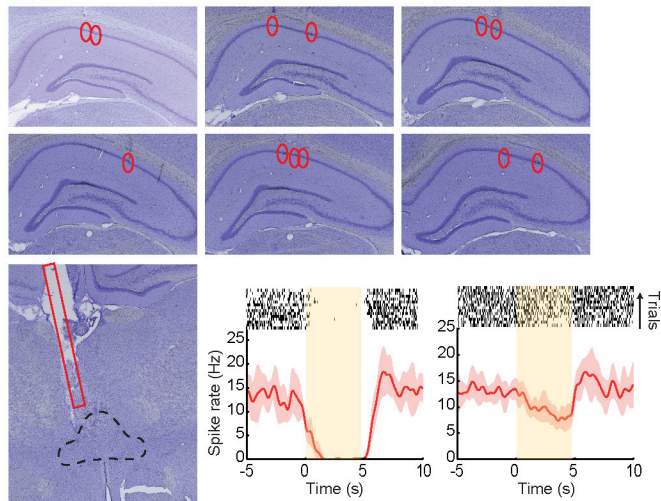
17421



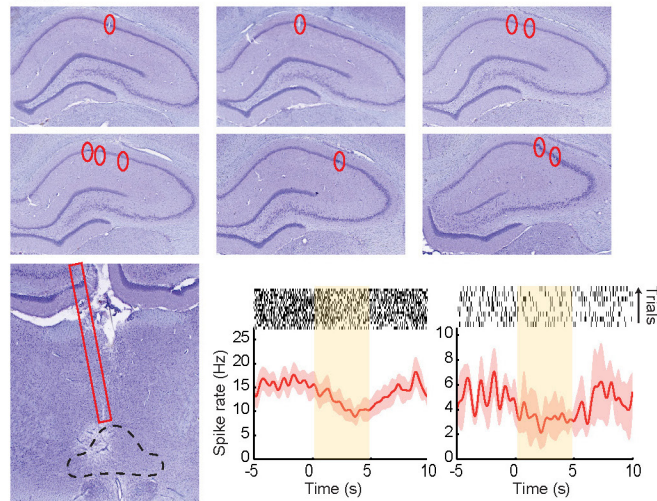
18679



18762

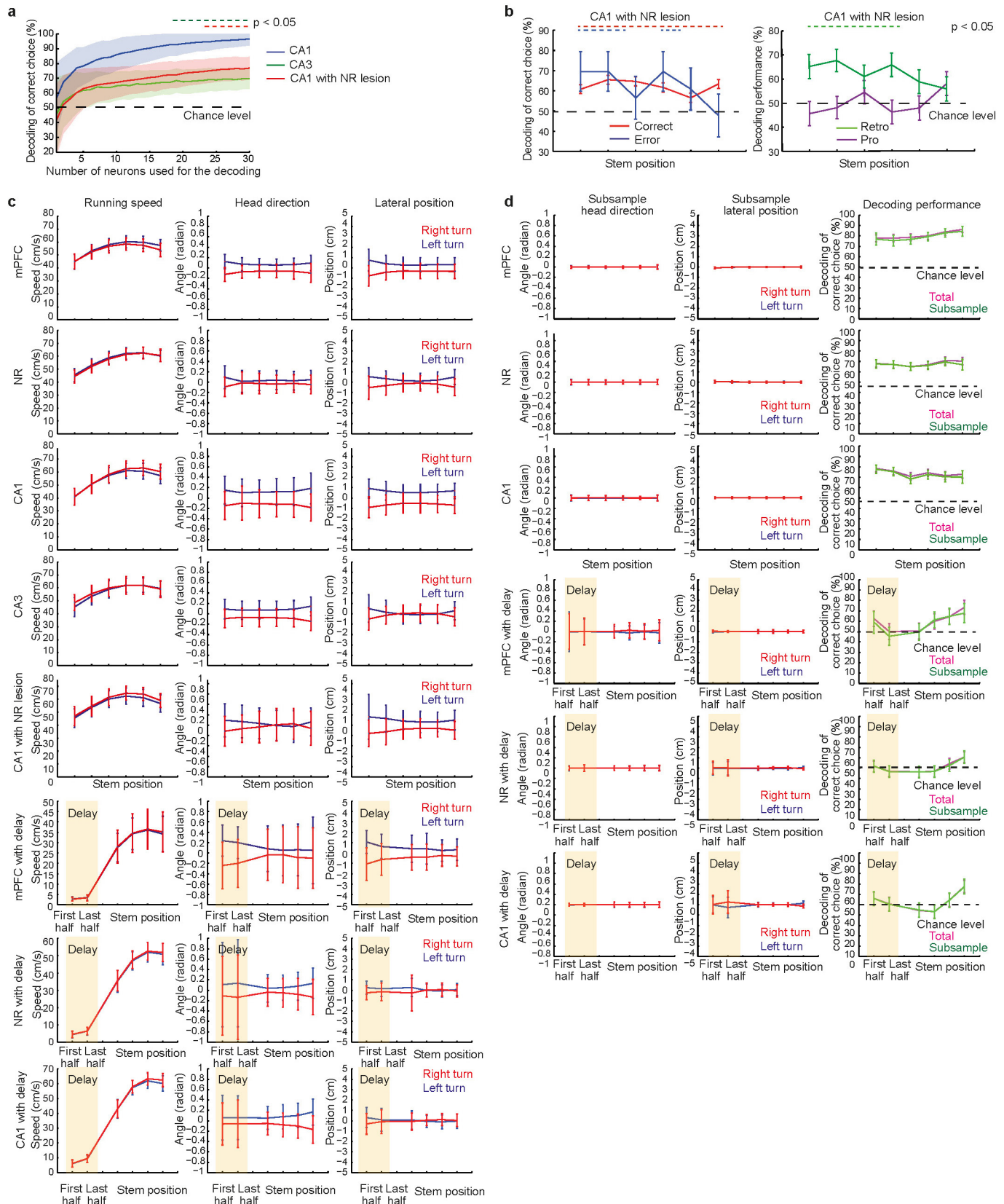


18681



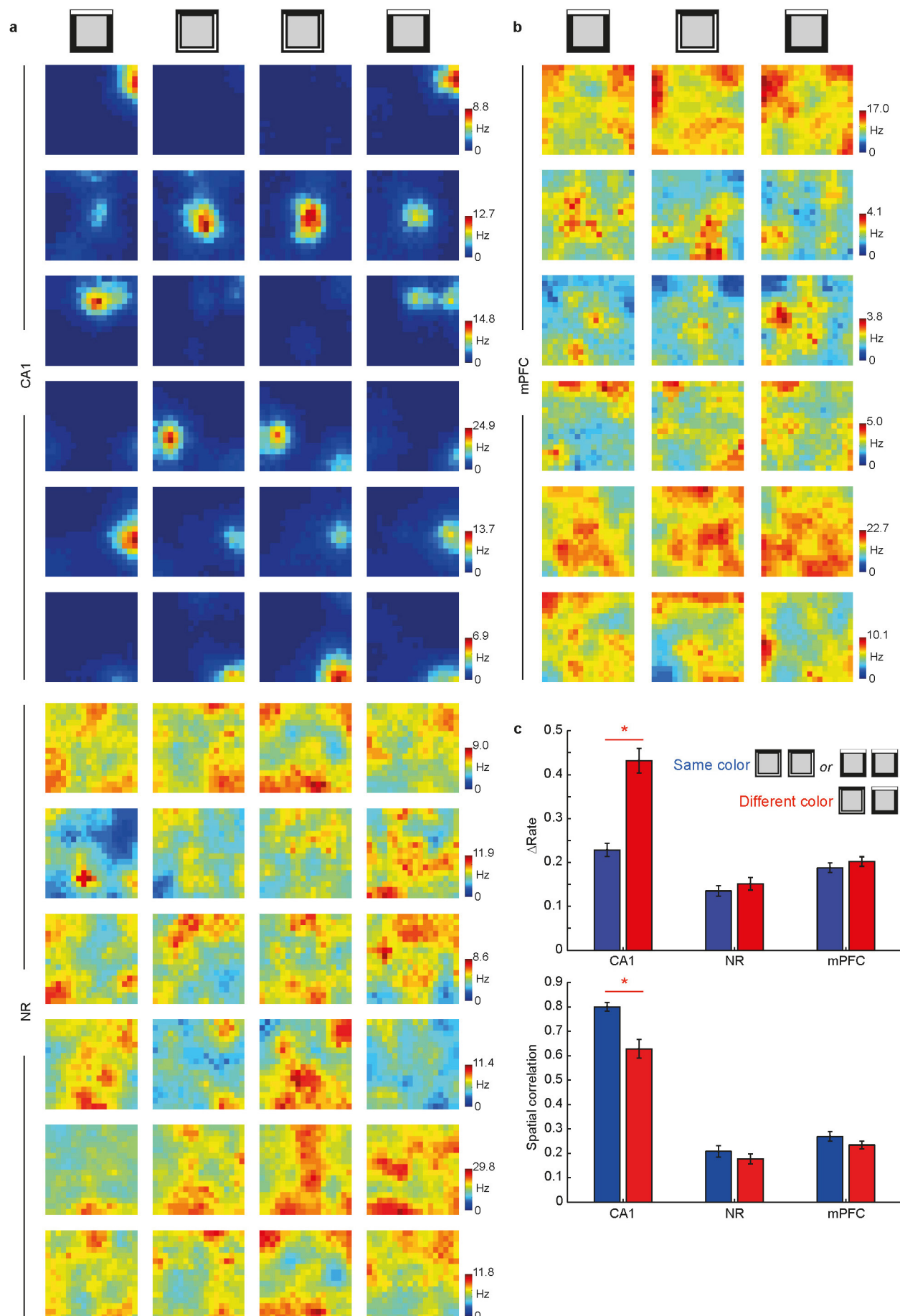
Extended Data Figure 6 | Nissl-stained coronal sections showing positions of tetrodes and optic fibres in optogenetic experiments. The figure is organized into six blocks, one for each of six animals. Five-digit animal numbers are indicated above each block. Top two rows of each block, positions of tetrode tracks (red circles) in CA1 of each animal. Bottom left, position of optic fibre above NR (red rectangular outline). NR is indicated by a black dashed triangle. The tip of the fibre was placed near the midline to silence cells at both sides of the midline. The bottom right panels of each block show spike rates for two representative units on the tetrodes attached to the optic fibre ($> \sim 750 \mu\text{m}$ from the tip of the fibre). The two panels show mean values (solid line) and 95% confidence intervals (shaded areas) of spike rate, with spike rasters at the top. The 532 nm laser was applied for 5 s (0–5 s on the x axis). A significant reduction of spike rate was observed during laser application for all units in this figure ($P < 0.05$, t -test). Unlike the ibotenic-acid lesion, which destroyed 68–85% of the NR, the laser light probably reached only a small

portion of the nucleus. The total volume of NR is roughly 2 mm^3 (1 mm of width, 1 mm of height, and 2 mm of length). Supposing that the tip of the optic fibre was located $250 \mu\text{m}$ above NR, that the laser light suppressed activity up to 1 mm below the fibre tip (optic fibre 0.39 NA, core size $\varnothing 400 \mu\text{m}$), and that all cells within this region were inactivated, the estimated proportion of NR affected by the laser light would be $\sim 36\%$ at the most. The tetrodes attached to the optic fibre were positioned approximately $750 \mu\text{m}$ below the fibre tip, near the distance limit of laser light for activation of halorhodopsin. At this depth, the intensity of the laser was probably not sufficient to activate halorhodopsin maximally. The sub-maximal activation probably accounts for the relatively slow time course of NR silencing (sometimes $> 1 \text{ s}$). Another contributing factor may be that thalamic neurons express T-type calcium channels, which are de-inactivated by hyperpolarization, making the neurons more excitable²⁷. This excitation may retard the suppression of NR activity.



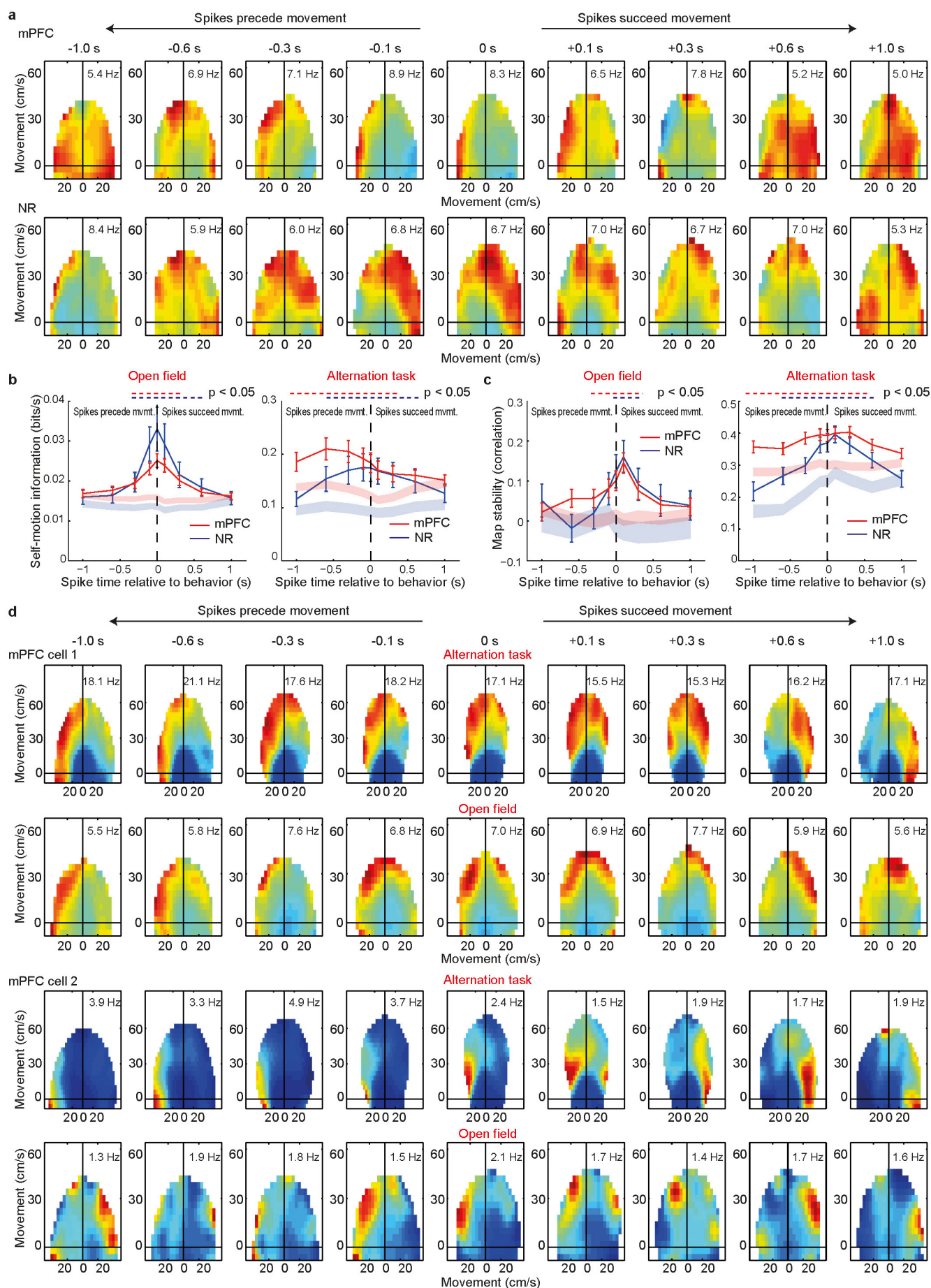
Extended Data Figure 7 | Trajectory coding in CA1, CA3 and CA1 of NR-lesioned animals, and influence of behavioural variables on the decoding analysis. **a**, Decoding of succeeding trajectory using peak firing rates of CA1 or CA3 place cells with firing fields on the stem as inputs to a linear classifier. Only trials with correct choices are included. Decoding performance was estimated from randomly selected cell groups in the entire data set across animals and plotted as a function of number of neurons in the sample. The plot shows mean (solid lines) \pm s.e.m. (shaded areas). Significant differences between CA1 versus CA3 or CA1 versus CA1 with NR lesions are indicated by dashed lines at the top ($P < 0.05$). To estimate the decoding performance for a specific number of cells, the desired number of cells was randomly selected from the entire data set across all animals. As the total trial number of runs on left- or right-run trajectories was often different across the recording sessions from which the cell group was taken, we randomly subsampled the trials to equalize the total trial number across sessions. This subsampling procedure was performed ten times, decoding performance was acquired for each, and the average was taken as an estimate of the decoding performance of the cell group. Then, a different cell group with the same number of cells was randomly selected and the same procedure was performed. The procedure was repeated 1,000 times to acquire a statistical distribution of decoding performance for the given number of cells (bootstrap resampling method). P values were estimated from the bootstrap distributions. The peak firing rates of approximately 15 CA1 place cells on the stem provided sufficient information to indicate a correct succeeding trajectory with over 90% accuracy ($96.6 \pm 4.3\%$ with a total of 30 cells, mean \pm s.e.m.). The decoding accuracy was significantly lower when CA3 cells or CA1 cells from NR-lesioned animals were used as inputs to the classifier (decoding performance with 30 cells: CA3, $69.9 \pm 7.0\%$; NR-lesioned, $76.9 \pm 7.6\%$). These results suggest that, for correct choices, the subsequent trajectory can be read out reliably from the collective firing of place cell ensembles in CA1 of animals with intact NR–CA1 connections. **b**, Left, decoding of correct subsequent trajectory using firing rates of CA1 place cells from NR-lesioned animals as inputs to the classifier. Trials with correct choices and error trials are shown separately (number of trials analysed for animals with NR lesions: correct, 467; error, 23; cell number per session, 7.5 ± 0.9 (mean \pm s.e.m.)). Symbols as in Fig. 5a. We also estimated the decoding performance using peak firing rates on the stem (without binning). In the CA1 of lesioned animals, the decoding performance was not significantly different

between correct trials and error trials ($67.2 \pm 2.2\%$ versus $69.6 \pm 9.8\%$; mean \pm s.e.m.). In CA1 of control animals, performance was $80.5 \pm 1.2\%$ on correct trials and $56.0 \pm 10.1\%$ on error trials (interaction term in a logistic regression analysis with task performance (correct versus incorrect) and manipulation (control versus NR lesion) as coefficients, $Z = 2.08$, $P = 0.038$; post hoc binomial test for correct versus incorrect trials: NR lesion, $Z = 0.232$, $P = 0.816$; control, $Z = 3.03$, $P = 0.002$). Right, retrospective and prospective components estimated from spike rates of CA1 cells in animals with NR lesions. Symbols as in Fig. 5c. NR lesions specifically disrupted the prospective component of the trajectory representation ($50.6 \pm 4.9\%$ successful decoding of succeeding path on the last half of the stem, compared to $59.5 \pm 4.7\%$ in intact animals; chance level 50%), supporting the idea that the mPFC–NR–CA1 circuit is necessary for the hippocampus to access to the information about intended actions. The retrospective component was still decodable ($60.1 \pm 4.9\%$ successful decoding of retrospective paths on the last half of the stem, compared to $63.5 \pm 4.8\%$ in intact animals), suggesting that CA1 cells with residual trajectory dependence after NR lesions exclusively represent the animal's trajectory on the preceding trial. **c**, **d**, Differences in decoding performance are not caused by differences in running speed, head direction or lateral position. **c**, Differences in running speed, head direction, and lateral position between left- and right-turn trajectories were assessed across all recording sessions used for the decoding analysis. No significant differences in any of these behavioural variables were observed ($P > 0.05$, t -test with Bonferroni correction for multiple comparisons of six bins). The plot shows mean \pm s.e.m. Standard errors were estimated for each recording session. **d**, While we did not observe any significant difference in any of the above behavioural variables, we still observed small systematic trends, as shown in **c**. To exclude the possibility that these small trends have an influence on the decoding performance⁴⁵ we generated, for each variable, a subsampled data set by excluding iteratively the trial with the largest deviation until we obtained nearly the same mean value for the respective behavioural variable on left- and right-turn trajectories. The decoding performance was calculated from this subsampled data set and the result was compared to the one from the original data set. No significant difference in decoding performance was observed between the groups, suggesting that the small and non-significant differences of behavioural variables do not account for the differences in firing on left and right trials and the decoding that results from these differences.



Extended Data Figure 8 | Firing rates in NR and mPFC fail to distinguish between discrete environments. We have shown that CA1 cells encode intended trajectories by differences in firing rate rather than firing position. A similar rate-based coding scheme has been observed in place cells of freely foraging animals trained to distinguish between open-field environments differing in colour or shape but not location (with similar rate differences following changes in colour or shape)^{22,24}. Based on this similarity, we asked whether activity in mPFC and NR accounts for rate differences also between discontinuous environments. We recorded simultaneously 51 place cells from CA1 and 49 cells from NR during free running in a pair of differently coloured square boxes located at the same place in the room (three rats). A total of 176 cells were recorded from mPFC in a different set of animals (two rats). **a**, Colour-coded rate maps for a representative sample of simultaneously recorded cells in CA1 and NR on consecutive trials of free foraging in the square enclosure. Cartoons on top indicate the sequence of trials with different box colours (black–white–white–black). Boxes were always in the same location. Note strong rate remapping (change in firing rate but not firing location) in CA1 but no rate code in NR. **b**, Colour-coded rate maps for cells in mPFC.

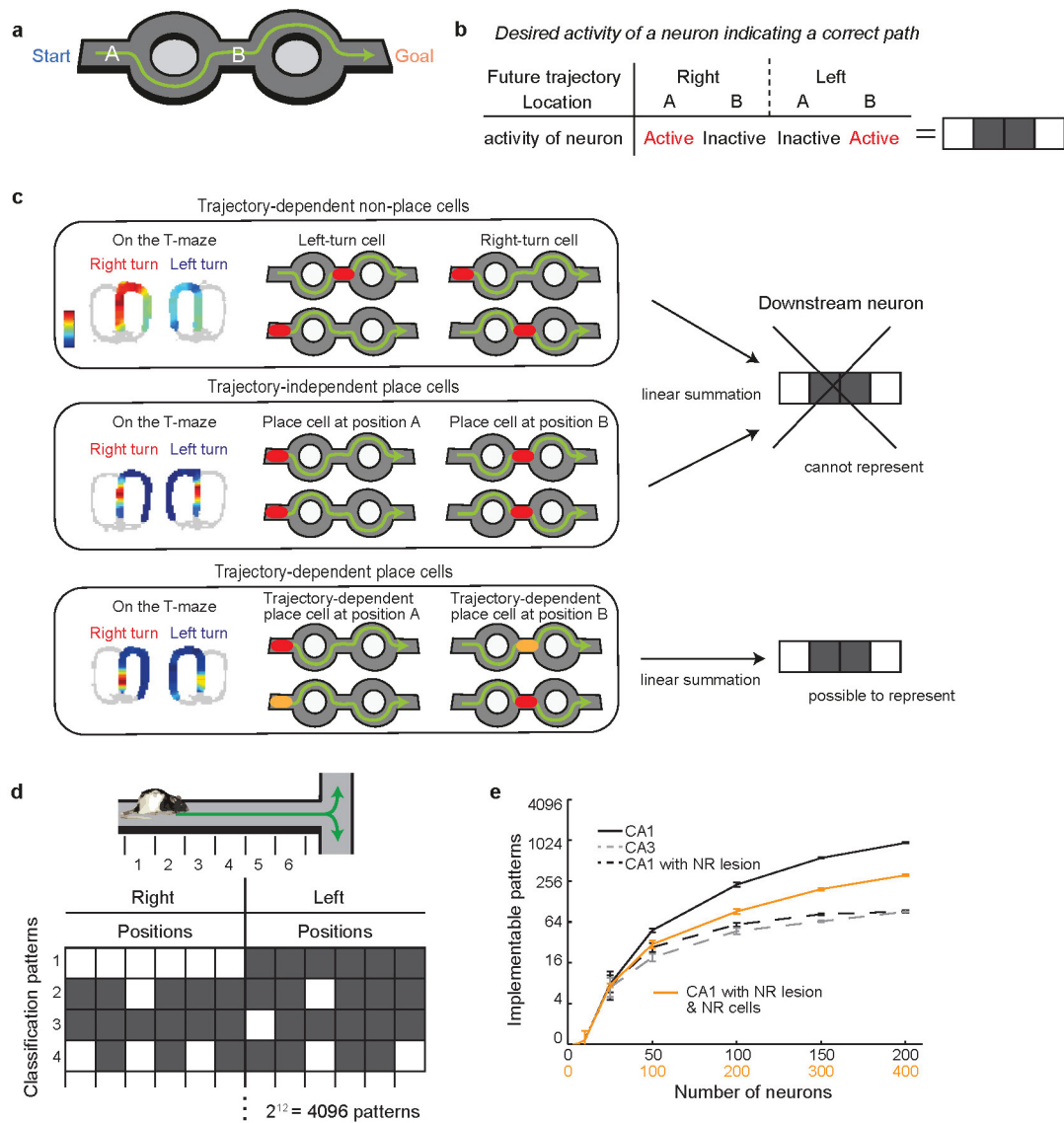
Symbols as in **a**. Note lack of change in firing rate. **c**, Top, change in peak firing rate between trials with similar (blue) or different (red) colour configuration. Bottom, spatial correlation between trials. The rate change between the two environments was significant in CA1 (same versus different colour, peak rate change $t_{100} = 6.40$, $P < 0.001$) but not in NR ($t_{96} = 0.875$, $P = 0.38$) or mPFC ($t_{350} = 0.924$, $P = 0.36$). Taken together, these results suggest that changes in the distribution of firing rate in CA1 can have multiple sources. While mPFC–NR inputs may be necessary for trajectory selection, the change in rate distribution between discrete environments may depend on other hippocampal inputs, such as those from the lateral entorhinal cortex⁴⁶. In the foraging task, the firing rates of the mPFC and NR neurons are modulated by subsequent direction of movement, mirroring their trajectory-dependent firing in the alternation task (Extended Data Fig. 9), but because trajectory directions are variable in this task, trajectory-dependent activity is likely to be cancelled out in time-averaged rate maps. The colour-reversal task should be sufficiently sensitive to detect influences of discrete stimuli, considering that mPFC cells do respond to such changes under other conditions⁴⁷.



Extended Data Figure 9 | Activity of neurons in mPFC and NR correlates significantly with movement direction in the continuous alternation task and the open field environment. **a**, Spike-rate maps based on the animal's self-movement were generated by previously published procedures⁴⁸. In brief, position and head direction data were smoothed with a 25-sample quadratic local regression (loess) fit. Changes in the animal's position and heading were calculated between the start and end of a sliding 100 ms time window to generate movement vectors. Movement vectors in each map were binned at $4 \text{ cm s}^{-1} \times 4 \text{ cm s}^{-1}$. The self-motion rate map was generated by dividing the sum of spike-triggered movement vectors by the total number of movement vectors at each bin, which was smoothed by a 2D Gaussian filter with a bandwidth at 1.5 bin. To understand the temporal relationship between spike timing and the animal's prospective or retrospective motion, spike-triggered movement vectors were generated from movement vectors that were systematically time-shifted relative to spike time, from one second before to one second after the spike event. Top, colour-coded rate maps for a representative mPFC cell which was tuned to left forward movement in the open field environment. Bottom, colour-coded rate maps for a representative NR cell that was tuned to right forward movement. **b**, Self-movement information in spikes was estimated using the following equation:

$$\sum_i p_i \frac{\lambda_i}{\lambda} \log_2 \frac{\lambda_i}{\lambda}$$

where λ_i is the mean firing rate in the i -th bin, λ is the overall mean firing rate and p_i is the probability of the animal being in the i -th bin (occupancy in the i -th bin/total recording time). Shaded areas indicate the range of the values (mean \pm s.e.m.) obtained from a shuffled data set generated by shifting spike timings either +2 s or -2 s across the session, which will disrupt spike-triggered movement information but maintain spike number and spike patterns. The time periods when spikes provide significant information about self-centred movement direction compared to the results from the shuffled data set are indicated by dashed lines at the top ($P < 0.05$, t -test). **c**, Self-movement rate-map stability within a recording session. The behavioural session (10 min) was divided into first and last halves and Spearman's correlation between self-movement maps generated from each half was calculated. Significant map stability was observed around the spike time both in mPFC and NR (compared to the shuffled data set, $P < 0.05$, t -test), indicating that spikes provide reliable information about self-movement. **d**, Two representative examples of mPFC cells recorded both in the alternation task and in the open field. While these cells expressed a similar trend of preferred self-movement direction across the tasks, they exhibited stronger self-movement tuning in the alternation task than in the open field exploration.



Extended Data Figure 10 | Conjunctive coding of position and trajectory increases representational dimensionality in CA1. Trajectory-dependent coding is not necessary for performance in the continuous version of the alternation task because animals with complete hippocampal lesions are unimpaired in this task²¹, as were the animals with lesions of the NR input to the hippocampus in the present study. The continuous alternation task may thus be too simple for decision behaviour to be affected by lesions of the NR–CA1 system. To examine how trajectory-dependent firing might contribute to navigation behaviour, we estimated the representational advantage of encoding space with trajectory-dependent place cells instead of separate cell populations for trajectory and location. It has been suggested that nonlinear integration of multimodal information in individual neurons enhances the capacity of downstream neurons to classify combinations of features of high-dimensional information³⁵. Similarly, we hypothesized here that a key advantage of trajectory-dependent place cells in CA1 is the enhancement of the classification capacity for position–trajectory combinations in efferent neurons, an advantage that may not be evident in an alternation task with only a single choice point. **a**, Example of a task that requires discrimination of multiple position–trajectory combinations. For successful performance, animals choose a right-turn path at the first choice point in A and then a left-turn path at the next choice point in B. **b**, To perform the task in **a**, the brain might use cells that represent correct combinations of movement direction and position on the trajectory. An example cell might be active when the animal plans a right path at position A as well as a left path at position B, but not otherwise. **c**, Suppose that cells with activity on the stem can be categorized into three classes: trajectory-dependent non-place cells, trajectory-independent place cells, and trajectory-dependent place cells. The neural activity in **b** cannot be generated from any linear combination of the two former classes (trajectory-dependent non-place cells and trajectory-independent place cells), as shown in the following argument. Suppose that the activity patterns of trajectory-dependent non-place cells, either right turn or left turn, can be expressed by the following activity matrices, with each row representing future trajectory, right or left, and each column showing position, that is, A or B:

$$R = \begin{pmatrix} 1 & 1 \\ 0 & 0 \end{pmatrix}, L = \begin{pmatrix} 0 & 0 \\ 1 & 1 \end{pmatrix}$$

Similarly, activity of trajectory-independent place cells, with firing fields on either position A or B, can be expressed as follows:

$$A = \begin{pmatrix} 1 & 0 \\ 1 & 0 \end{pmatrix}, B = \begin{pmatrix} 0 & 1 \\ 0 & 1 \end{pmatrix}$$

The activity matrix of a downstream neuron driven by a linear combination of the above four types of neurons can be expressed as follows:

$$w_a \times R + w_b \times L + w_c \times A + w_d \times B = \begin{pmatrix} w_a + w_c & w_b + w_c \\ w_a + w_d & w_b + w_d \end{pmatrix}$$

For the downstream neuron to express the desired activity in **b**, the following conditions are required:

$$\begin{pmatrix} \text{active} & \text{inactive} \\ \text{inactive} & \text{active} \end{pmatrix}$$

$$w_a + w_c > \theta \quad (1)$$

$$w_a + w_d \leq \theta \quad (2)$$

$$w_b + w_c \leq \theta \quad (3)$$

$$w_b + w_d > \theta \quad (4)$$

where θ is the threshold of activity. However, summation of (1) and (4) gives $w_a + w_b + w_c + w_d > 2\theta$, whereas summation of (2) and (3) gives $w_a + w_b + w_c + w_d \leq 2\theta$, resulting in a contradiction. Thus, neurons with pure selectivity alone cannot generate the desired activity. To achieve the activity in **b**, neurons with nonlinear mixed selectivity, namely trajectory-dependent place cells, are required (also see ref. 35). **d**, To estimate the number of implementable patterns in the recorded CA1 neurons, firing rates of neurons at each of 12 behavioural states (six stem positions with two future trajectory directions) were analysed. In addition to the recorded activity, we extended the data using a resampling procedure³⁵. Resampling was performed by cyclic permutation of firing rates across stem positions. Supposing that the original activity of the recorded neurons is represented by sequential numbers of six stem positions as (1 2 3 4 5 6), five sets of new activity were generated by exchanging activity across stem positions, resulting in (2 3 4 5 6 1), (3 4 5 6 1 2), (4 5 6 1 2 3), (5 6 1 2 3 4) and (6 1 2 3 4 5). Resampling not only increased the number of neurons for analysis, but also minimized spatial bias of ensemble representations across stem positions. Following resampling, decoding performance was calculated for all binary combinations of 12 states ($2^{12} = 4,096$ patterns), using a linear classifier with firing rates in each behavioural state as inputs, as in Fig. 5. **e**, The number of implementable patterns was determined for neurons in CA1, CA3, and CA1 from animals with NR lesions, and from CA1 of NR-lesioned animals combined with NR cells from intact animals. For the latter group, the total number of cells was doubled after combining the same number of cells from two populations, as indicated on the x axis with a different colour. A binary pattern was considered as implementable if the decoding performance was better than 99%. For each sample size, cells were randomly selected five times to estimate the standard deviation of the decoding performance. Plots indicate mean \pm s.d. Regardless of the size of the cell sample, the analysis showed a significantly larger number of implementable patterns for CA1 than for the other groups, including the combination of trajectory-dependent cells in NR and non-trajectory-dependent place cells in CA1, suggesting that integration of NR inputs in CA1 place cells is a key step to achieve high-dimensional representations. The results point to trajectory-dependent place cells and the mPFC–NR–CA1 circuit as possible elements of the neural circuit for discrimination of complex position–trajectory combinations, such as the one illustrated in **a**. Combinatorial coding provides a computational basis for efferent neurons to perform addition or subtraction among vectors in different coordinate systems^{49–51}, such as the allocentric reference frame imposed by spatial cells in the entorhinal cortex⁵² and the egocentric trajectory frame dependent on projections from mPFC through NR. Such vector operations may be essential for the network to estimate a future allocentric position, which is one of the key steps of route planning during goal-directed navigation.

Lymphatic vessels arise from specialized angioblasts within a venous niche

J. Nicenboim^{1*}, G. Malkinson^{1*}, T. Lupo¹, L. Asaf¹, Y. Sela¹, O. Mayseless¹, L. Gibbs-Bar¹, N. Senderovich², T. Hashimshony², M. Shin³, A. Jerafi-Vider¹, I. Avraham-David¹, V. Krupalnik⁴, R. Hofi¹, G. Almog¹, J. W. Astin⁵, O. Golani⁶, S. Ben-Dor⁶, P. S. Crosier⁵, W. Herzog^{7,8}, N. D. Lawson³, J. H. Hanna⁴, I. Yanai² & K. Yaniv¹

How cells acquire their fate is a fundamental question in developmental and regenerative biology. Multipotent progenitors undergo cell-fate restriction in response to cues from the microenvironment, the nature of which is poorly understood. In the case of the lymphatic system, venous cells from the cardinal vein are thought to generate lymphatic vessels through trans-differentiation. Here we show that in zebrafish, lymphatic progenitors arise from a previously uncharacterized niche of specialized angioblasts within the cardinal vein, which also generates arterial and venous fates. We further identify Wnt5b as a novel lymphatic inductive signal and show that it also promotes the ‘angioblast-to-lymphatic’ transition in human embryonic stem cells, suggesting that this process is evolutionarily conserved. Our results uncover a novel mechanism of lymphatic specification, and provide the first characterization of the lymphatic inductive niche. More broadly, our findings highlight the cardinal vein as a heterogeneous structure, analogous to the haematopoietic niche in the aortic floor.

The lymphatic system plays a crucial role in normal and pathological conditions. It is essential for maintaining fluid homeostasis, for immune responses and for dietary lipid absorption, and is exploited by tumours to metastasize¹. Close to a century ago, two models describing the origins of the lymphatic system were proposed. While Sabin² suggested a venous origin for the lymphatic endothelium, the second model, put forward by Huntington & McClure³, postulated that lymphatic vessels form by concrescence of discontinuous and independent lymph vesicles, and that mesenchymal-derived cells constitute the walls of the lymphatic vessels. Studies performed during the last decade, involving *in vivo* imaging in zebrafish⁴ and lineage tracing in mice⁵, have extensively confirmed Sabin's hypothesis. Nevertheless, the presence of mesenchymal lymphangioblast-derived lymphatic vessels has been described in *Xenopus* tadpole⁶ and chick⁷ embryos. At present, the embryonic origins of the lymphatic endothelium still remain controversial.

During the past years, specific markers of the lymphatic endothelium have been identified, which provided new insights into the mechanisms controlling lymphatic specification and growth⁸. Assembly of the lymphatic vascular network is considered a stepwise process, which begins approximately at embryonic day 9.5 (E9.5) when the expression of Prox1, a master regulator of lymphatic differentiation and maintenance⁹ is first detected in a subpopulation of endothelial cells within the cardinal vein (CV). Two additional transcription factors—Sox18 (ref. 10) and Nr2f2 (also known as COUPFII, ref. 11)—were shown to be required for induction of Prox1 expression. The newly specified lymphatic progenitors then bud from the CV in response to VEGFC signalling¹² and form primitive lymph sacs, which eventually give rise to the entire lymphatic vasculature. Most recently, an important role for BMP2 (ref. 13) and the RAF1/MEK/ERK signalling cascade¹⁴ in the specification of lymphatic fate has also been established. Nevertheless, as none of

these factors seems to be asymmetrically expressed, the question of how only a subset of cells within the CV is initially specified towards a lymphatic fate, as opposed to cells that will maintain a venous identity, remains unanswered.

The zebrafish was recently shown to possess a lymphatic system that shares many similarities with lymphatic vessels found in other vertebrates^{4,15}. *In vivo* imaging of 2–4 days post-fertilization (dpf) zebrafish embryos demonstrated that the parachordal cells (PACs), which form at ~2 dpf along the embryo's midline and serve as building-blocks for the lymphatic system later on, are derived from the posterior cardinal vein (PCV). Starting at ~2.5 dpf PACs migrate ventrally to generate the main lymphatic vessel, the thoracic duct⁴.

Lymphatic progenitors originate in the PCV floor

To characterize the initial events controlling lymphatic specification, we fate-mapped the origins of lymphatic endothelial cells (LECs) within the PCV of zebrafish embryos. We imaged *Tg(fli1:EGFP)*¹ (Fig. 1a, Supplementary Video 1) and *Tg(fli1:nEGFP)*⁷ (ref. 16; Extended Data Fig. 1a) embryos starting at 22–24 h post-fertilization (hpf) and until 60 hpf, when PACs are fully discernible⁴. Tracking of PAC-LECs back in time and space demonstrated that 81% of these cells originated in the ventral side of the PCV (vPCV) compared to 19% that originated in the dorsal PCV (dPCV). To corroborate these results, we took advantage of *Tg(fli1:gal4^{ubs3});uasKaede^{rk8}* embryos, expressing the photoconvertible protein Kaede in endothelial cells (Kaede is a green fluorescent protein that irreversibly converts to red fluorescence under UV light)¹⁷. Pan-Kaede photoconversion of vPCV cells at 24 hpf rendered ~90% PACs red, indicating that they originated in the floor of the PCV. In contrast, less than 10% red PACs were observed following dPCV photoconversion (Fig. 1b–d and Extended Data Fig. 1b). vPCV cells generated PACs also in *plcg1* mutants (Extended Data Fig. 1d and Supplementary Video 2), which

¹Department of Biological Regulation, Weizmann Institute of Science, Rehovot 76100, Israel. ²Faculty of Biology, Technion – Israel Institute of Technology, Haifa 32000, Israel. ³Department of Molecular, Cell, and Cancer Biology, University of Massachusetts Medical School, Worcester, Massachusetts 01605, USA. ⁴Department of Molecular Genetics, Weizmann Institute of Science, Rehovot 76100, Israel. ⁵School of Medical Sciences, University of Auckland, Auckland 1142, New Zealand. ⁶Biological Services Unit, Weizmann Institute of Science, Rehovot 76100, Israel. ⁷University of Muenster, 48149 Muenster, Germany. ⁸Max Plank Institute for Molecular Biomedicine, 48149 Muenster, Germany.

*These authors contributed equally to this work.

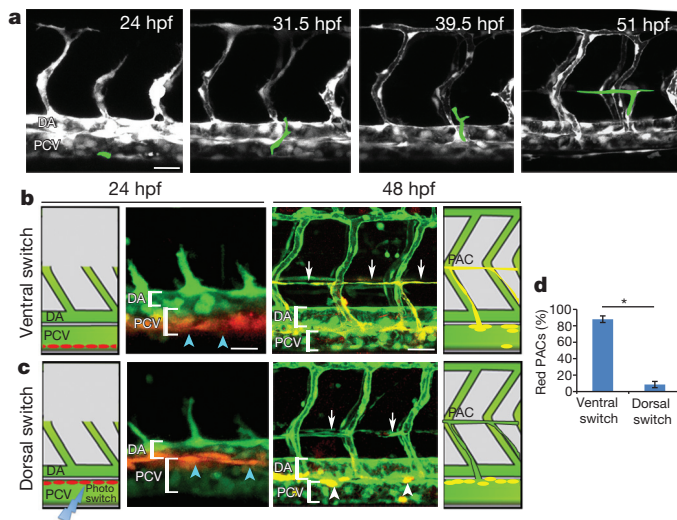


Figure 1 | Lymphatic progenitors originate in the vPCV. **a**, Snapshots from a time-lapse sequence of a *Tg(fli1:EGFP)* embryo, showing the origin of a PAC cell (green) in the vPCV ($n_{\text{PACs}} = 16$; $N_{\text{imaged embryos}} = 13$). **b**, **c**, Photoswitching of ventral (**b**) and dorsal (**c**) PCV in *Tg(fli1:gal4;uasKaede)* embryos at 24 hpf (light-blue arrowheads). **d**, Percentage of red PACs (white arrows) at 48 hpf ($n_{\text{vPCV photoswitched embryos}} = 10$, $n_{\text{dPCV photoswitched embryos}} = 8$; $*P = 2.66 \times 10^{-10}$). Scale bars, 30 μm . Error bars, mean \pm s.e.m.

lack arterial intersegmental vessels as well as blood flow, but develop venous sprouts and PACs¹⁸, suggesting that the specification of lymphatic progenitors is not affected by nearby arteries or by blood circulation.

The ventral PCV harbours a niche of specialized angioblasts

Previous reports¹⁹ indicated that the budding of LEC progenitors from the PCV persists for approximately 24 h. We reasoned that a continuous exit of cells would eventually result in disruption of the PCV wall, unless LECs arise from a population of specialized progenitors that repeatedly divide. Time-lapse sequences of *Tg(fli1:gal4^{ubs3};uasKaede^{rk8})* embryos revealed that vPCV cells undergo asymmetric division (Fig. 2a) and generate progeny that contribute to the nascent PACs (Supplementary Video 3). To further confirm these results we scored symmetric vs asymmetric division events on each half of the PCV. Cell division was defined as asymmetric if (1) it generated a cell of different fate, and (2) the plane of division was perpendicular to the PCV main axis. We found a significantly higher number of asymmetric divisions in the vPCV at 24–34 hpf (initial stages of LEC specification), with no changes in symmetric division events (Extended Data Fig. 1e). In addition, no differences in global cell proliferation were detected in the dPCV, vPCV and dorsal aorta (Extended Data Fig. 2a), suggesting that the specific arising of LECs from the floor of the PCV is not a result of this being a more proliferative area.

Unexpectedly, during the course of tracing photoconverted vPCV cells we noticed that, in addition to generating PACs, these cells also migrated ventrally to incorporate into the suprainstestinal artery (SIA) and the subintestine vein (SIV) (Fig. 2b and Extended Data Fig. 3a). Single-cell Kaede photoconversion revealed the dynamics of specification of the vPCV progenitors (Fig. 2c). Whereas at 23 hpf most of these cells give rise to either PACs or venous intersegmental vessels, at 27 hpf there is a shift towards population of the subintestine vein and suprainstestinal artery. In contrast, dPCV cells generated mostly venous intersegmental vessels throughout all analysed developmental stages. Altogether, these results unveil the presence of specialized cells within the floor of the PCV, which divide asymmetrically, and generate arterial, venous and lymphatic fates.

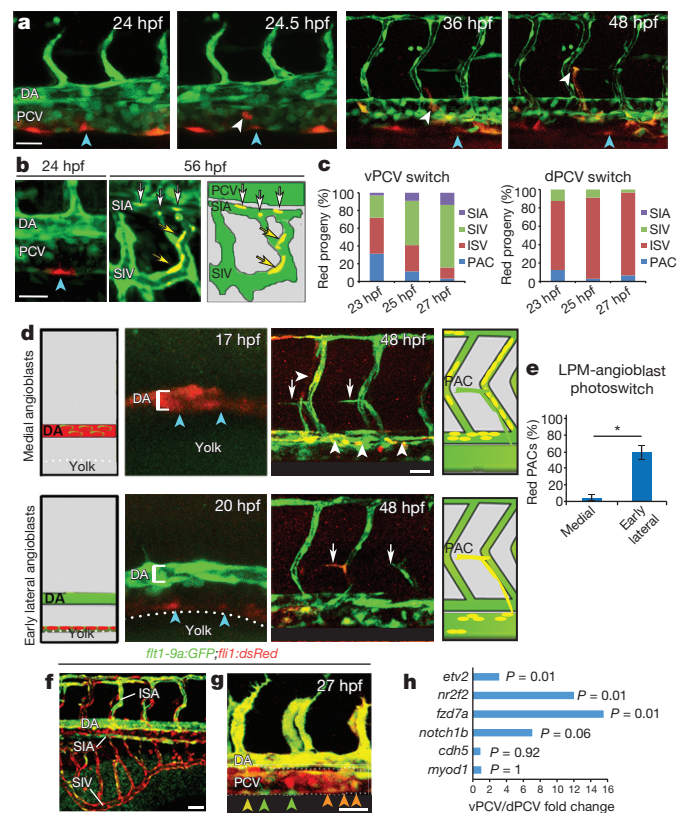


Figure 2 | vPCV cells are specialized angioblasts. **a**, Snapshots from a time-lapse movie of a *Tg(fli1:gal4;uasKaede)* embryo showing photoswitched vPCV cell (light-blue arrowhead), which generates PACs (white arrowhead) through asymmetric division. **b**, Single photoswitched vPCV cell in *Tg(fli1:gal4;uasKaede)* embryo at 24 hpf (light-blue arrowhead), whose progeny populates the suprainstestinal artery (SIA, white arrows) and subintestine vein (SIV, yellow arrows) at 56 hpf. **c**, Location of vPCV and dPCV progeny at 56 hpf, following photoswitching at different stages ($n_{\text{photoswitched vPCV cells}} = 73$, $n_{\text{photoswitched dPCV cells}} = 45$). **d**, Photoswitching of medial and early-lateral angioblasts at 17 and 20 hpf (light-blue arrowheads), respectively, in *Tg(kdrl:Kaede)^{w23}* embryos. **e**, Percentage of red PACs at 48 hpf ($n_{\text{medial angioblasts}} = 16$, $n_{\text{early lateral angioblasts}} = 16$; $*P = 2.1 \times 10^{-5}$). **f**, **g**, *Tg(flt1_9a_cFos:GFP;fli1:dsRed)* embryos show *flt1_9a:GFP*⁺ endothelial cells in the SIA, arterial intersegmental vessels (ISA), dorsal aorta (DA), and vPCV (**g**, green, orange arrowheads). **h**, Selected genes enriched in vPCV cells. Scale bars, 30 μm . Error bars, mean \pm s.e.m.

We then asked whether these cells represent in fact angioblasts that originate directly in the lateral plate mesoderm and migrate medially to colonize the floor of the PCV²⁰. Alternatively, these cells could be of arterial origin, and sprout ventrally from the dorsal aorta to reach the ventral PCV²¹. To answer this question, we performed pan-Kaede photoconversion of a population of lateral plate mesoderm medial angioblasts that colonize the dorsal aorta by 17 hpf²⁰, or of a population of ventral cells (lateral plate mesoderm early-lateral angioblasts)²⁰, detected in the trunk by ~ 19 hpf (Fig. 2d and Extended Data Fig. 1c). Fate analysis of the photoconverted cells at 48 hpf demonstrated that the vast majority of vPCV progenitors giving rise to PACs in the trunk did not originate in the dorsal aorta, but migrated directly from the lateral plate mesoderm to reach their final position in the vPCV (Fig. 2d, e). These results indicate that the vPCV cells are specialized angioblasts²², which originate directly in the lateral plate mesoderm and retain their multipotency throughout later stages of development.

To gain insight into the molecular identity of the newly identified vPCV angioblasts we initially analysed *Tg(fli1:dsRed)^{um13}* zebrafish (ref. 23) crossed to *Tg(flt1_9a_cFos:GFP)^{w22}*, a *vegfr1* (*flt1*) enhancer, which specifically labels arterial endothelial cells (Extended Data

Fig. 3b). We detected green fluorescence in well-established 'arterial' structures including the dorsal aorta, arterial intersegmental vessels and supaintestinal artery (Fig. 2f). Surprisingly however, we also detected a few GFP⁺ cells within the PCV (Fig. 2g). To understand whether the *flt1_9a:GFP*⁺-vPCV cells represent the population of specialized angioblasts that give rise to LECs we imaged *Tg(flt1_9a_cFos:GFP; lyve1:dsRed2)*^{nz101} double transgenic embryos (ref. 24), in which arterial endothelial cells are GFP⁺, while venous and lymphatic endothelial cells display red fluorescence (Extended Data Fig. 3b, c). Time-lapse sequences revealed that 100% of PACs traced ($n = 9$) originated from *flt1_9a:GFP*⁺ cells (Supplementary Video 4), through a process of asymmetric cell division. Interestingly, we found that the vast majority of these progenitors were located in the vPCV ($n = 7$). Nonetheless, the small number of dPCV cells that generate PACs (Fig. 1d) was also labelled by *flt1_9a:GFP* ($n = 2$), highlighting this angioblast population as the sole origin of LECs in the zebrafish trunk. Similar asymmetric division events were detected during subintestinal vessel formation (Extended Data Fig. 3d). In this case, *flt1_9a:GFP*⁺-vPCV cells generated progeny that populated the subintestinal vein and the supaintestinal artery. Altogether these results highlight the PCV as a highly heterogeneous tissue, containing 'non-venous' cells competent to give rise to multiple fates, including LECs.

The fact that lymphatic vessels originate from a novel population of PCV angioblasts and not from fully differentiated venous endothelial cells, as previously postulated, prompted us to enquire into the molecular signature of these cells. Global expression profiling via RNA sequencing (RNA-Seq)²⁵ (Extended Data Fig. 4a, b) revealed significant enrichment of well-established angioblast, lymphatic and arterial markers in the vPCV vs dPCV cells (Fig. 2h and Extended Data Fig. 4c, d). We then asked when do these progenitors acquire a lymphatic fate. In mammals, the expression of the transcription factor Prox1 in certain cells of the CV marks the onset of lymphatic specification⁹. To investigate whether this is the case in zebrafish as well, we imaged *TgBAC(prox1a:Kalt4-UAS:uncTagRFP)*^{tiim5} embryos²⁶. We found that the first cells expressing *prox1a* are already visible at 22–24 hpf in the vPCV (Fig. 3a). Later on these cells divide, translocate to the dorsal PCV, and bud from the PCV to generate PACs (Fig. 3a and Supplementary Video 5). Approximately 80% of *Tg(fli1:EGFP;prox1a:Kalt4-UAS:uncTagRFP)* embryos displayed 1–2 *prox1a*⁺ cells in the vPCV at 22–24 hpf, in contrast to ~20% embryos displaying *prox1a*⁺ cells in the dPCV (Fig. 3b). At later

stages (26–30 hpf), an increased number of *prox1a*⁺ cells was detected in the dPCV, reflecting the proliferation and dorsal translocation of the newly specified LECs. Similar results were obtained when we analysed the distribution of the Prox1 protein (Fig. 3c). We further found that most of the cells that expressed *prox1a* at 22–24 hpf were *flt1_9a:GFP*⁺ vPCV-angioblasts (Fig. 3d). Taken together, our results analysing global gene expression and lymphatic-specific markers demonstrate that lymphatic specification is induced in a restricted population of angioblasts in the vPCV. Furthermore, they confirm that LECs acquire a lymphatic fate before their budding from the PCV.

Wnt5b induces LEC specification

Having identified the floor of the PCV as the origin of lymphatic progenitors, we analysed the surrounding tissues in search for a source of spatially-restricted inductive signals. Histological sections of 22 and 24 hpf *Tg(fli:EGFP)* embryos showed that vPCV cells develop close to the endoderm (Fig. 4a). In addition, analysis of *cas*^{ta56} (*sox32*) mutants, which lack endoderm-derived tissues, revealed that PACs do not develop in these mutants (Fig. 4b and Extended Data Fig. 5a), suggesting that the signal(s) necessary for LEC specification comes from the endoderm.

Recently, the Wnt- β -catenin-TCF/LEF signalling pathway has been shown to directly activate *Nr2f2* and *Prox1*—members of the LEC specification cascade—in the context of adipogenesis and neurogenesis^{27,28}. We thus wondered whether endoderm-secreted Wnt(s) could serve as inducer(s) of lymphatic specification in the vPCV cells. *In situ* hybridization revealed clear expression of *wnt5b* messenger RNA in the endoderm of 18–20 hpf embryos (Fig. 4c and Extended Data Fig. 5b). Analysis of *wnt5b* morphants and *ppt*^{ti265} (*wnt5b*) mutants indicated a significant reduction in the percentage of

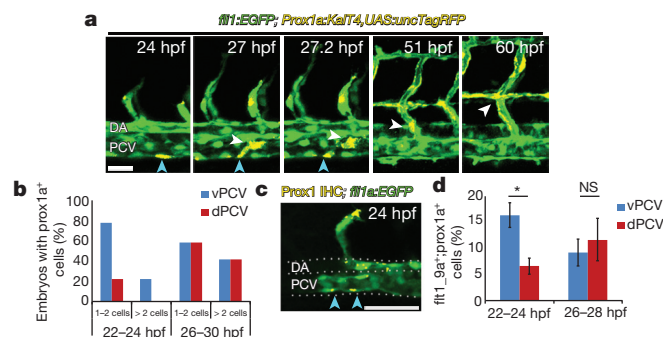


Figure 3 | LEC specification is induced in the vPCV angioblasts. **a**, A (*prox1a:TagRFP;fli1:EGFP*)⁺ cell in the vPCV (yellow) generates a daughter cell that translocates dorsally, buds from the PCV and forms PACs (white arrowheads). **b**, Quantification of *Tg(fli1:EGFP;prox1a:Kalt4-UAS:uncTagRFP)* embryos with 1 to 2 or more than 2 (*prox1a:TagRFP;fli1:EGFP*)⁺ cells in vPCV and dPCV at 22–24 and 26–30 hpf ($n_{22-24\text{ hpf}} = 11$; $n_{26-28\text{ hpf}} = 24$). **c**, Prox1 immunostaining at 24 hpf shows expression in vPCV cell (light-blue arrowheads). **d**, Quantification of (*flt1_9a:GFP;prox1a:TagRFP*)⁺ cells in vPCV vs dPCV at 22–24 and 26–28 hpf ($n_{22-24\text{ hpf}} = 18$; $n_{26-28\text{ hpf}} = 13$; $*P = 0.01$). Scale bars, **a**, 30 μm ; **c**, 60 μm . Error bars, mean \pm s.e.m. NS, not significant.

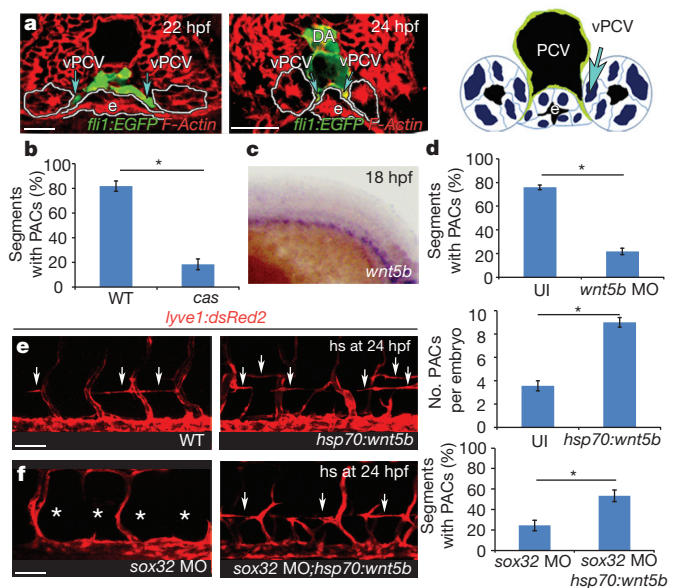


Figure 4 | Wnt5b is necessary and sufficient for LEC specification.

a, Histological sections at 22 and 24 hpf, depicting the position of the vPCV angioblasts (light-blue arrows) and the endoderm (e). **b**, Number of PAC-containing segments in wild-type (WT) and *cas* mutants ($n_{cas} = 22$, $n_{WT} = 15$; $*P = 3 \times 10^{-12}$). **c**, *In situ* hybridization at 18 hpf shows expression of *wnt5b* mRNA in the endoderm. **d**, Number of PAC-containing segments (arrows) in *wnt5b* morphants ($n_{UI} = 63$, $n_{wnt5bMO} = 57$; $*P = 1.83 \times 10^{-30}$). UI, uninjected. **e**, Wnt5b overexpression in *Tg(hsp70:wnt5b-GFP;lyve1:dsRed2)* embryos induces ectopic lymphangiogenesis ($n_{WT} = 19$, $n_{hsp70:wnt5b-GFP} = 22$; $*P = 9.47 \times 10^{-12}$). hs, heat shock at 37°C. **f**, Number of PAC-containing segments in *sox32*-MO injected *Tg(hsp70:wnt5b-GFP;lyve1:dsRed2)* embryos ($n_{sox32MO} = 18$, $n_{sox32MO;hsp70:wnt5b} = 18$; $*P = 0.0005$). Scale bars, **a**, 20 μm ; **e**, 60 μm . Error bars, mean \pm s.e.m.

PAC- and thoracic-duct-containing segments, with no changes in the initial number of *flt1_9a:GFP⁺*-vPCV angioblasts (Fig. 4d and Extended Data Fig. 5c–f). In contrast, overexpression of Wnt5b in *Tg(hsp70l:wnt5b-GFP^{w33};lyve1:dsRed2)* double transgenic embryos at 23–24 hpf (Extended Data Fig. 6a) resulted in a strong pro-lymphangiogenic response reflected by the presence of ectopic PAC sprouts (Fig. 4e). Finally, Wnt5b induction led to a significant recovery in the number of PACs in *sox32* morpholino (MO)-injected *Tg(hsp70l:wnt5b-GFP)* embryos (Fig. 4f). Taken together, these results highlight the endoderm-secreted Wnt5b as both necessary and sufficient for lymphatic formation during embryonic development.

To confirm that Wnt5b is specifically required for lymphatic specification, and not for general sprouting from the PCV, we assessed the number of venous vs arterial intersegmental vessels in *wnt5b*⁻, and Control MO-injected *Tg(flt1_9a_cFos:GFP;fli:dsRed)* embryos, and found no differences (Extended Data Fig. 6b). Likewise, *flt1_9a:GFP⁺*-vPCV progenitors were normally found within the subintestinal plexus of *wnt5b* morphants (Extended Data Fig. 6c), confirming that Wnt5b does not inhibit PAC formation by unselectively impeding sprouting from the PCV, but rather by affecting LEC specification. To ascertain whether Wnt5b affects LEC proliferation, we photoconverted and time-lapse imaged vPCV cells in *wnt5b* MO-injected *Tg(fli1:gal4;uasKaede)* (Extended Data Fig. 7a) and *Tg(fli1:nEGFP; fli1:dsRed)* (Supplementary Video 6) embryos. While in control siblings approximately 30% of the vPCV cells reached the PACs by 48 hpf (Fig. 2c), they did not engage in dorsal migration to generate PACs in *wnt5b* morphants. Interestingly, although the cells were viable and divided normally, the only asymmetric division events detected involved cells that migrated ventrally to populate the subintestinal vessels (data not shown). In addition, ectopic induction of Wnt5b did not result in enhanced endothelial cell proliferation (Extended Data Fig. 2b).

Conclusive evidence supporting a role for Wnt5b as an inducer of LEC specification was provided by the analysis of lymphatic marker expression following *wnt5b* downregulation and overexpression. *In situ* hybridization revealed a pronounced reduction in lymphatic-specific transcripts in the PCV of *wnt5b* morphants, whereas the expression of pan-endothelial genes remained unchanged (Extended Data Fig. 7b). This phenotype, indicative of a defect in lymphatic specification, was not reported following loss of *Vegfc*, a signal specifically required for LEC budding from the PCV^{29,30}. In addition, the expression of *vegfc* and *cbe1*³⁰ remained unchanged in *sox32* and *wnt5b* morphants (Extended Data Fig. 7c), ruling out the possibility that Wnt5b controls lymphatic specification through activation of these genes. Finally, the number of *prox1a*⁺ cells was reduced in *wnt5b* morphants, and increased following Wnt5b overexpression (Fig. 5a). Moreover, Wnt5b activation induced upregulation of the *prox1a* transcript (Fig. 5b), and the Prox1 protein (Extended Data Fig. 7d). Taken together these data indicate that Wnt5b is mainly required for lymphatic specification, and not migration or proliferation, of the vPCV angioblasts.

Recently, a divergence in the molecular mechanisms controlling lymphatic specification in zebrafish and mice was postulated²⁶. To ascertain whether the novel mechanism of LEC specification uncovered here is conserved among vertebrates, we tested the ability of recombinant WNT5B to induce lymphatic specification in human embryonic stem cell (hESCs)-derived vascular progenitors^{31,32}. As seen in Fig. 5c, WNT5B induced a marked increase in the fraction of LYVE1⁺ cells detected in the culture, as well as in the levels of *PROX1* (Fig. 5d) and *FLT4* (Extended Data Fig. 7e) mRNAs, indicating that the role of Wnt5b as potent inducer of LEC specification is evolutionarily conserved. Furthermore, these findings indicate that Wnt5b acts directly on vascular progenitors to promote the 'angioblast-to-lymphatic' specification.

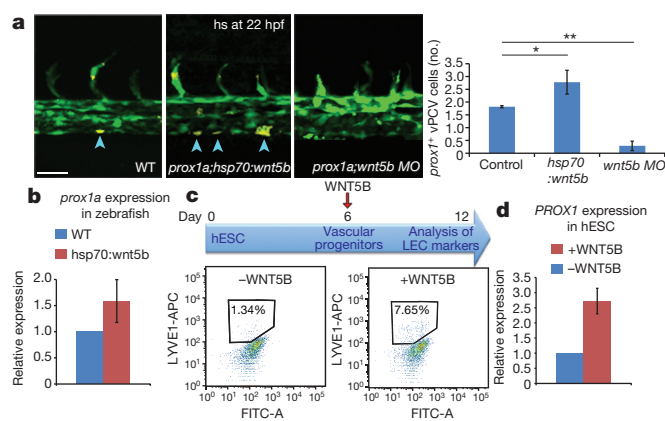


Figure 5 | Wnt5b induces lymphatic specification in zebrafish and hESCs.

a, Quantification of *Prox1a*⁺ vPCV cells (light-blue arrowheads) in *Tg(fli1:EGFP;prox1a:KalT4-UAS:uncTagRFP)* embryos following Wnt5b induction, and downregulation (*n*_{wnt5bMO} = 7, *n*_{hsp70l:wnt5b} = 9, *n*_{WT} = 7; **P* = 0.05, ***P* = 0.001). **b**, *prox1a* mRNA in 24 hpf *Tg(fli1:EGFP;prox1a:KalT4-UAS:uncTagRFP;hsp70l:wnt5b-GFP)* embryos following heat shock at 21 hpf (*n*_{independent experiments} = 4). **c**, Fraction of LYVE1⁺ cells, and **d**, *PROX1* mRNA levels in hESC-derived angioblasts treated with WNT5B (*n*_{independent experiments} = 3). Scale bar, 60 μm. Error bars, **a**, mean ± s.e.m.; **b**, **d**, geometrical mean ± standard error of the geometrical mean (s.e.g.m.).

Wnt5b-activated canonical pathway induces LEC specification

We next characterized the downstream components of the Wnt pathway involved in lymphatic specification. Wnt5 is mostly referred to as a non-canonical Wnt ligand, which can also repress and/or activate the canonical pathway in different contexts^{33,34}. It is well-established that a key step in the activation of canonical Wnt pathway is the inhibition of a destruction complex composed of APC, axin, GSK3-β and other proteins, which results in stabilization and nuclear translocation of cytoplasmic β-catenin³⁵. We therefore began by analysing lymphatic development following manipulation of axin and APC. Injection of *wnt5b* MOs into *mb1^{tm213}* (*axin1*) mutants did not affect PAC formation (Extended Data Fig. 8a), confirming the requirement of axin downstream of Wnt5b. Likewise, *apc^{mcrr}* mutants displayed significantly increased PAC numbers (Extended Data Fig. 8b), resembling the Wnt5b overexpression phenotype (Fig. 4e). Conversely, axin overexpression (Extended Data Fig. 8c), as well as treatment with IWR1, a small molecule shown to lower the levels of β-catenin, induced a significant reduction in the number of PAC-containing segments (Extended Data Fig. 8d). In contrast to these results, the inhibitor of β-catenin-independent Wnt activation, TNP-470, did not cause any detectable lymphatic defects (Extended Data Fig. 9a). We then investigated the role of the TCF/LEF transcription factors³⁶ in early lymphangiogenesis. Downregulation of *tcf4*, *tcf7*, *lef1* and *tcf3b* (Extended Data Fig. 9b, c and data not shown), resulted in reduced number of PACs with an otherwise normal blood vasculature. In line with the phenotypes resulting from Wnt5b downregulation, arterial/venous differentiation was not impaired in these morphants (Extended Data Fig. 9b), and photoswitched vPCV cells did not migrate dorsally to generate PACs (Extended Data Fig. 9d). Together, these results indicate that induction of lymphatic specification by Wnt5b occurs primarily through β-catenin/TCF activation.

The lymphatic defects derived from Wnt/β-catenin inhibition could be secondary to global Wnt5b-signalling depletion. Alternatively, they could reflect a cell-autonomous requirement for Wnt-signalling within prospective LEC progenitors. To distinguish between these two possibilities, we assessed β-catenin/TCF activity within vPCV-angioblasts using *Tg(fli1:EGFP;7xTCF-Xla.Siam:nlsMCherry)^{ia5}*

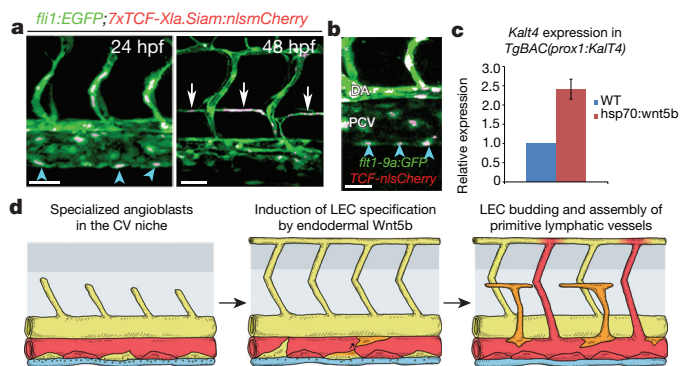


Figure 6 | Wnt5b induces LEC specification through activation of the canonical pathway. **a**, *Tg(7xTCF-Xla.Siam:nlsMCherry;fli1:EGFP)* embryo showing TCF activity in vPCV cells at 24 hpf (light-blue arrowheads), and PACs at 48 hpf (white arrows). **b**, *Tg(7xTCF-Xla.Siam:nlsMCherry;flt1_9a_cFos:GFP)* embryo showing TCF activity in *flt1_9a*⁺ vPCV angioblasts at 24 hpf (light-blue arrowheads). **c**, *Klt4* mRNA levels in *Tg(prox1a:Klt4-UAS:uncTagRFP;hsp70l:wnt5b-GFP)* 24 hpf embryos, following heat shock at 21 hpf (*n* independent experiments = 3). **d**, Schematic model of LEC specification and formation of first lymphatic vessels in the zebrafish trunk. Scale bars, 30 μ m. Error bars, geometrical mean \pm s.e.g.m.

double transgenic embryos. As seen in Fig. 6a, TCF activity was detected in these cells at 24 hpf, and in PACs at 48 hpf. Furthermore, time-lapse imaging revealed that only vPCV angioblasts with active β -catenin/TCF undergo asymmetric cell division and generate PACs (Extended Data Fig. 10a). Moreover, these cells were also *flt1_9a:GFP*⁺ (Fig. 6b). The number of β -catenin/TCF⁺ vPCV-angioblasts was significantly reduced following *wnt5b* downregulation (Extended Data Fig. 10b, c), confirming that the β -catenin/TCF activity detected in these cells was Wnt5b-dependent. Altogether, our results analysing β -catenin/TCF activity in LEC progenitors *in vivo*, in combination with LEC specification in cultured hESCs, indicate that Wnt5b-dependent activation of β -catenin is cell-autonomously required within vascular progenitors for proper lymphatic specification, and highlight Prox1 as one of the major downstream targets of Wnt5b.

The changes in *prox1* mRNA levels observed in zebrafish and hESCs (Fig. 5b, d) could result from either transcriptional regulation, or post-transcriptional modifications that alter RNA stability of the *prox1* transcript. To distinguish between these two possibilities we took advantage of the *TgBAC(prox1a:Klt4-UAS:uncTagRFP)* zebrafish reporter (Fig. 3 and ref. 26), in which the *Klt4* fragment recapitulates the transcriptional activation of the endogenous *prox1a* promoter, without being subjected to the post-transcriptional modifications of the *prox1a* gene (the *Klt4* cassette possess its own 3' untranslated repeat). We hypothesized that if Wnt5b transcriptionally regulates *prox1a* mRNA, overexpression of Wnt5b will result in a significant increase in the levels of *Klt4* mRNA. If in turn, *prox1a* upregulation involves alterations in its mRNA stability, the levels of *Klt4* mRNA will remain unchanged upon *hsp70l:Wnt5b* activation. As seen in Fig. 6c, overexpression of Wnt5b results in elevated levels of the *Klt4* transcript. Although we cannot exclude the possibility that post-transcriptional modifications are also involved in *prox1a* regulation, our results strongly support a mechanism involving transcriptional regulation of *prox1a* in response to Wnt5b. Whether this is a direct or indirect regulation remains to be elucidated.

Discussion

Development and regeneration of multicellular organisms rely on the ability of competent cells to respond to different signalling inputs that specify cell fate. The results presented here identify for the first time a pool of specialized angioblasts within the floor of the posterior cardinal vein that bears the potential to generate arterial, venous and lymphatic fates. Anatomically, these cells develop in close proximity

to the endoderm, which serves as source of Wnt5b, a novel inductive signal promoting the angioblast-to-lymphatic transition (Fig. 6d). Interestingly, the time-frame of induction of lymphatic fate in the vPCV angioblasts fully overlaps with the endodermal expression of the Wnt5b ligand, highlighting a tight spatiotemporal regulation of cell differentiation within this niche.

Recently, a divergence in the molecular mechanisms controlling lymphatic specification in zebrafish and mice was suggested²⁶. The finding that Wnt5b functions as a potent inducer of lymphatic cell fate, both in zebrafish and in hESC-derived vascular progenitors, provides compelling evidence for a strong conservation of this pathway among vertebrates.

Previous reports have postulated an arterial origin for the cardinal vein, both in zebrafish²¹ and mammals³⁷. Here we show that cells expressing arterial/angioblast markers within the posterior cardinal vein are those that generate lymphatic progenitors during embryonic development. However, it is striking that these cells do not originate in the dorsal aorta, but rather migrate directly from the lateral plate mesoderm to populate the ventral wall of the posterior cardinal vein, retaining their 'multipotent' capacities.

Altogether our results highlight the posterior cardinal vein as a highly heterogeneous structure containing different cell populations, thereby challenging the current view of a 'strict' venous origin for lymphatic vessels. Our findings help settle a century-old controversy regarding the origin of the lymphatic endothelium by providing evidence for a novel mechanism, which reconciles the models proposed by Sabin² and Huntington & McClure³. On the one hand lymphatic endothelial cells do emerge from veins; however, they do so by an unexpected mechanism involving a venous niche of specialized mesoderm-derived angioblasts. These findings open a whole set of new questions regarding the formation of lymphatic vessels during disease states and regeneration.

Online Content Methods, along with any additional Extended Data display items and Source Data, are available in the online version of the paper; references unique to these sections appear only in the online paper.

Received 27 February 2014; accepted 26 March 2015.

Published online 20 May 2015.

- Alitalo, K. The lymphatic vasculature in disease. *Nature Med.* **17**, 1371–1380 (2011).
- Sabin, F. R. On the origin of the lymphatic system from the veins, and the development of the lymph hearts and thoracic duct in the pig. *Am. J. Anat.* **1**, 367–389 (1902).
- Huntington, G. & McClure, C. The anatomy and development of the jugular lymph sac in the domestic cat (*Felis domestica*). *Am. J. Anat.* **10**, 177–312 (1910).
- Yaniv, K. et al. Live imaging of lymphatic development in the zebrafish. *Nature Med.* **12**, 711–716 (2006).
- Srinivasan, R. S. et al. Lineage tracing demonstrates the venous origin of the mammalian lymphatic vasculature. *Genes Dev.* **21**, 2422–2432 (2007).
- Ny, A. et al. A genetic *Xenopus laevis* tadpole model to study lymphangiogenesis. *Nature Med.* **11**, 998–1004 (2005).
- Wiltig, J., Tomarev, S. I., Christ, B. & Schweigerer, L. Lymphangioblasts in embryonic lymphangiogenesis. *Lymphat. Res. Biol.* **1**, 33–40 (2003).
- Yang, Y. & Oliver, G. Development of the mammalian lymphatic vasculature. *J. Clin. Invest.* **124**, 888–897 (2014).
- Wigle, J. T. et al. An essential role for Prox1 in the induction of the lymphatic endothelial cell phenotype. *EMBO J.* **21**, 1505–1513 (2002).
- Francois, M. et al. Sox18 induces development of the lymphatic vasculature in mice. *Nature* **456**, 643–647 (2008).
- Srinivasan, R. S. et al. The nuclear hormone receptor Coup-TFII is required for the initiation and early maintenance of Prox1 expression in lymphatic endothelial cells. *Genes Dev.* **24**, 696–707 (2010).
- Karkkainen, M. J. et al. Vascular endothelial growth factor C is required for sprouting of the first lymphatic vessels from embryonic veins. *Nature Immunol.* **5**, 74–80 (2004).
- Dunworth, W. P. et al. Bone morphogenetic protein 2 signaling negatively modulates lymphatic development in vertebrate embryos. *Circ. Res.* **114**, 56–66 (2014).
- Deng, Y., Atri, D., Eichmann, A. & Simons, M. Endothelial ERK signaling controls lymphatic fate specification. *J. Clin. Invest.* **123**, 1202–1215 (2013).
- Küchler, A. M. et al. Development of the zebrafish lymphatic system requires VEGFC signaling. *Curr. Biol.* **16**, 1244–1248 (2006).
- Avraham-David, I. et al. ApoB-containing lipoproteins regulate angiogenesis by modulating expression of VEGF receptor 1. *Nature Med.* **18**, 967–973 (2012).

17. Herwig, L. *et al.* Distinct cellular mechanisms of blood vessel fusion in the zebrafish embryo. *Curr. Biol.* **21**, 1942–1948 (2011).
18. Lim, A. H. *et al.* Motoneurons are essential for vascular pathfinding. *Development* **138**, 3847–3857 (2011).
19. Isogai, S., Lawson, N. D., Torrealday, S., Horiguchi, M. & Weinstein, B. M. Angiogenic network formation in the developing vertebrate trunk. *Development* **130**, 5281–5290 (2003).
20. Kohli, V., Schumacher, J. A., Desai, S. P., Rehn, K. & Sumanas, S. Arterial and venous progenitors of the major axial vessels originate at distinct locations. *Dev. Cell* **25**, 196–206 (2013).
21. Herbert, S. P. *et al.* Arterial-venous segregation by selective cell sprouting: an alternative mode of blood vessel formation. *Science* **326**, 294–298 (2009).
22. Conway, E. M., Collen, D. & Carmeliet, P. Molecular mechanisms of blood vessel growth. *Cardiovasc. Res.* **49**, 507–521 (2001).
23. Vatine, G. D. *et al.* Zebrafish as a model for monocarboxyl transporter 8-deficiency. *J. Biol. Chem.* **288**, 169–180 (2013).
24. Okuda, K. S. *et al.* *lyve1* expression reveals novel lymphatic vessels and new mechanisms for lymphatic vessel development in zebrafish. *Development* **139**, 2381–2391 (2012).
25. Hashimshony, T., Wagner, F., Sher, N. & Yanai, I. CEL-Seq: single-cell RNA-Seq by multiplexed linear amplification. *Cell Rep.* **2**, 666–673 (2012).
26. van Impel, A. *et al.* Divergence of zebrafish and mouse lymphatic cell fate specification pathways. *Development* **141**, 1228–1238 (2014).
27. Okamura, M. *et al.* COUP-TFII acts downstream of Wnt/ β -catenin signal to silence PPAR γ gene expression and repress adipogenesis. *Proc. Natl Acad. Sci. USA* **106**, 5819–5824 (2009).
28. Karalay, O. *et al.* Prospero-related homeobox 1 gene (Prox1) is regulated by canonical Wnt signaling and has a stage-specific role in adult hippocampal neurogenesis. *Proc. Natl Acad. Sci. USA* **108**, 5807–5812 (2011).
29. Cermenati, S. *et al.* Sox18 genetically interacts with VegfC to regulate lymphangiogenesis in zebrafish. *Arterioscler. Thromb. Vasc. Biol.* **33**, 1238–1247 (2013).
30. Hogan, B. M. *et al.* Ccbe1 is required for embryonic lymphangiogenesis and venous sprouting. *Nature Genet.* **41**, 396–398 (2009).
31. Yamashita, J. *et al.* Flk1-positive cells derived from embryonic stem cells serve as vascular progenitors. *Nature* **408**, 92–96 (2000).
32. Kusuma, S. *et al.* Self-organized vascular networks from human pluripotent stem cells in a synthetic matrix. *Proc. Natl Acad. Sci. USA* **110**, 12601–12606 (2013).
33. Mikels, A. J. & Nusse, R. Purified Wnt5a protein activates or inhibits β -catenin-TCF signaling depending on receptor context. *PLoS Biol.* **4**, e115 (2006).
34. van Amerongen, R., Fuerer, C., Mizutani, M. & Nusse, R. Wnt5a can both activate and repress Wnt/ β -catenin signaling during mouse embryonic development. *Dev. Biol.* **369**, 101–114 (2012).
35. Ikeda, S. *et al.* Axin, a negative regulator of the Wnt signaling pathway, forms a complex with GSK-3 β and β -catenin and promotes GSK-3 β -dependent phosphorylation of β -catenin. *EMBO J.* **17**, 1371–1384 (1998).
36. Veien, E. S., Grierson, M. J., Saund, R. S. & Dorsky, R. I. Expression pattern of zebrafish *tcf7* suggests unexplored domains of Wnt/ β -catenin activity. *Dev. Dyn.* **233**, 233–239 (2005).
37. Lindskog, H. *et al.* Molecular identification of venous progenitors in the dorsal aorta reveals an aortic origin for the cardinal vein in mammals. *Development* **141**, 1120–1128 (2014).

Supplementary Information is available in the online version of the paper.

Acknowledgements The authors would like to thank B. Cohen, N. Strasser, R. Solomon and F. Bochner for technical assistance, N. Stettner and A. Harmelin for animal care, G. Beck and E. Ainbinder for assistance with hESC experiments, E. Winter for RNA-Seq analyses, F. Argenton for providing the *Tg(7xTCF-Xla.Siam:nlsCherry)^{ja5}* transgenic line, G. Weidinger for the *Tg(hsp70l:wnt5b-GFP)^{w33}* line, E. Ober for the *TgBAC(prox1a:KaIT4-UAS:uncTagRFP)^{nim5}* line, S. Schulte-Merker for the *Tg(flt4BAC:mCitrine)^{hu7135}* line, S. Sumanas for the *Tg(etv2:GFP)^{ci1}* line, M. Affolter and H. G. Belting for the *Tg(fli1:gal4^{ubs3},uaskade^{rk8})* line, A. Inbal for the *pCS2-axin* plasmid, B. Weinstein for the *pME-nr2f2* plasmid and the cas mutants, M. Beltrame for the pCMV *sox18* plasmid, and E. Tzahor, E. Zelzer, M. Neeman and B. Shilo for critical reading of the manuscript. The authors are grateful to all the members of the Yaniv laboratory for discussion, technical assistance and continuous support. This work was supported in part by Marie Curie Actions-International Reintegration grants FP7-PEOPLE-2009-RG 256393 (to K.Y.), Minerva Foundation 711128 (to K.Y.), German-Israeli Foundation Young Investigator Program 1967/2009 (to K.Y.), Israel Cancer Research Foundation Postdoctoral Fellowship (to G.M.), Lymphatic Research and Education Network postdoctoral fellowship (to G.M.), Northrine Westphalia Return fellowship (to W.H.), US National Institutes of Health (NIH) R01 HL122599 (to N.D.L.), JSPS Postdoctoral Fellowships for Research Abroad (to M.S.), ERC 310927 (to I.Y.). K.Y. is supported by the Karen Siem Fellowship for Women in Science; the Willner Family Center for Vascular Biology; the estate of Paul Ourieff; the Carolito Stiftung; Lois Rosen, Los Angeles, CA; and the Adelis Foundation. K.Y. is the incumbent of the Louis and Ida Rich Career Development Chair.

Author Contributions J.N. and G.M. designed and conducted experiments, analysed data, and co-wrote the manuscript; Y.S. designed and conducted experiments on human ESCs and analysed data; T.L., L.A., O.M., A.J.-V. and M.S. conducted experiments and data analyses; I.A.-D. and V.K. conducted *in vitro* experiments, N.S. and T.H. conducted RNA-Seq experiments and data analyses; R.H. assisted with animal care and genotyping; L.G.-B. and J.W.A. generated transgenic lines; G.A. managed the fish facility; S.B.-D. performed bioinformatics analyses; O.G. assisted with image processing analyses; P.S.C. provided the *Tg(lyve1:EGFP)ⁿ²¹⁵⁰* and *Tg(lyve1:dsRed2)^{n21b1}* transgenic lines. W.H. and N.D.L. designed and supervised part of the experiments; I.Y. designed and supervised RNA-Seq experiments; J.H.H. supervised part of the hESCs experiments; K.Y. initiated and directed the study, designed experiments, analysed data and co-wrote the paper with input from all authors.

Author Information RNA-Seq raw data and processed values have been submitted to the NCBI Gene Expression Omnibus (GEO) under the accession number GSE65751. Reprints and permissions information is available at www.nature.com/reprints. The authors declare no competing financial interests. Readers are welcome to comment on the online version of the paper. Correspondence and requests for materials should be addressed to K.Y. (karina.yaniv@weizmann.ac.il).

METHODS

Zebrafish husbandry and transgenic lines. Zebrafish were raised by standard methods¹⁶ and were handled according to the Weizmann Institute Animal Care and Use Committee. The *plcγ1*¹⁰ (ref. 18), *Tg(fli1:EGFP)*¹ (ref. 19), *Tg(fli1:nEGFP)*⁷ (ref. 4), *Tg(fli1:dsRed)*^{um13} (ref. 23), *Tg(fli1:gal4^{ubs3};uasKaede^{rk8})* (ref. 17), *Tg(hsp70l:wnt5b-GFP)*³³ (ref. 38), *Tg(7xTCF-Xla.Siam:nlsMCherry)*^{ja5} (ref. 39), *cas^{u56}* (ref. 40), *ppt^{ti265}* (ref. 41), *mbf^{tm213}* (ref. 42), *apc^{mcr}* (ref. 43), *Tg(fli1:dsRed2)*^{nz101} (ref. 24), and *TgBAC(prox1a:KalT4-UAS:uncTagRFP)*^{nm5} (ref. 26) were previously described. The *Tg(flt1_9a_cFos:GFP)*^{w22} reporter was generated by cloning the previously identified zebrafish *flt1_9a* enhancer⁴⁴, into pGW_cFosGFP⁴⁵. The *Tg(kdr1:Kaede)*^{w3} was generated by cloning a Kaede fragment in a Tol2-compatible vector containing 2.5kb from the *kdr1* promoter using the Gateway methodology⁴⁶.

In situ hybridization and immunofluorescence. Whole-mount *in situ* hybridization was carried out as described¹⁶ using *flt4*, *cbel*¹³⁰, *sox18*⁴⁷ and *cdh5*¹⁶ antisense mRNA probes. The *lyve1* (5'-AGACGTGGGTGAAATCCAAG-3' and 5'-GATGATGTTGCTGCATGTCC-3'), *wnt5b* (5'-ATGGATGTGAGAATGAACCAAGGAC-3' and 5'-CTACTGCACACAACTGGTCTACG-3'), and *vegfc* (5'-CATCAGCACTTCATACATCAGC-3' and 5'-GTCCAGTCTTCC CAGTATG-3') probes were amplified by PCR from 24 hpf complementary DNA. A fragment (1,269 bp) flanking the (5'-GTACAAAAAGCAGGCT CCGCGGCC-3'...5'-TCATCAGGGATATGTTGCTGTCGGG-3') sequence of the *nr2f2* gene was cloned into Pcs2 plasmid, and linearized using NotI. Embryos were imaged using a Leica M165 FC imaging system.

Phospho-histone staining was carried out as described⁴⁸ using p-histone H3 antibody (1:300) (Santa Cruz).

For detection of Prox1 protein embryos were fixed overnight in 4% paraformaldehyde, washed in 100% methanol, incubated 1 h on ice in 3% H₂O₂ in methanol, washed in 100% methanol and stored at -20°C. Embryos were then permeabilized in wash buffer (PBS/0.1% tween/0.1% Triton), blocked in 10% goat serum/1% BSA in wash buffer for 5 h at 4°C, and incubated with Prox1 antibody (1:750) overnight⁴. Samples were then washed 5 times with wash buffer, followed by washes with maleic buffer (150 mM maleic acid/100 mM NaCl/0.001% Tween 20 pH 7.4 saturated with 10 N NaOH), blocking in maleic buffer containing 2% blocking reagent (Roche), and incubation overnight at 4°C with goat anti rabbit IgG-horseradish peroxidase (Jackson 1:500) for TSA signal amplification. Following washes with maleic buffer and PBS, samples were incubated for 3 h with TSA Plus Cyanine 3 reaction (Perkin Elmer) and washed with wash buffer several times through 1–2 days at room temperature.

Manipulation of zebrafish embryos. *Heat-shock, TNP-470 and IWR1 treatments.* 24–26 hpf *Tg(hsp70l:wnt5b-GFP)* embryos were heat-shocked at 37°C for 25 min and analysed for PAC number at 56 hpf. For Prox1 immunostaining *Tg(hsp70l:wnt5b-GFP)* embryos were heat-shocked at 19–20 hpf for 25 min and fixed as described above at 28 hpf. For qRT-PCR analyses *Tg(prox1:KalT4-UAS:uncTagRFP;hsp70l:wnt5b-GFP)* embryos were heat-shocked at 21 hpf, for 25–30 min.

IWR1 (ref. 49) (Sigma) and TNP-470 (Sigma) were dissolved in dimethyl sulfoxide (DMSO) as previously described⁵⁰. Embryos were treated with 30 μM IWR1, for 2 days starting at 20 hpf. TNP-470 was added at a concentration of 25 μM, for 2 days starting at 23 hpf. PAC formation was assessed at 3 dpf.

Morpholino injection. The following antisense morpholino oligonucleotides were used: *sox32* (ref. 51) (1 ng), *tcf7* (ref. 52) (8 ng), *lef1* (ref. 53) (3 ng), *wnt5b* (ref. 41) (7.5 ng or 4 ng for subdose), *vegfc* (ref. 4) (5 ng), *tcf4* (5'-CTGCGGCATTTT TCCGAGGAGCGC-3') (8 ng), control MO (5'-CCTCTTACCTCAGTT ACAATTTATA-3') (8 ng). MOs (Gene-tools) were resuspended and injected as described¹⁶.

DNA and mRNA injection. *axin* mRNA⁵⁴ (260 pg) was injected at 1-cell stage. To generate the *Tg(flt1_9a_cFos:GFP)*, and *Tg(kdr1:Kaede)* transgenic lines, ~30 pg plasmid were injected along with 30 pg of *Tol2* transposase mRNA into 1-cell stage embryos.

Quantitative real-time PCR (qRT-PCR). qRT-PCR was carried out as previously described¹⁶ using the following primers:

Zebrafish: *prox1a* (5'-AATCCAAGAGGGCTTTTCGC-3' and 5'-TGCAGCGG TTAAACTTCACG-3'), *KalT4* (5'-GACGTGTGACAGACCGATT-3' and 5'-CAGCTGTCTCTGTCCCTTGT-3'), *bactin2*¹⁶, *etv2* (5'-TACCCAGGATCT GGACCCAT-3' and 5'-CAGCCATCACCAGTCCAAC-3'), *frz7a* (5'-TGTCT CGTGCGGACTGTTAC-3' and 5'-CACTGTTTCATGAGGCTCCGT-3'), *nr2f2* (5'-ACAGAGTGGTGCCTTTATGG-3' and 5'-CCACAGCATCTGAAGT GAA-3'). Human: *PROX1* (5'-CCACTGACCAGACAGAAGCA-3' and 5'-TG GGCTCTGAAATGGATAGG-3'), *beta-actin* (5'-TCCACCTTCCAGCAGAT GTG-3' and 5'-GCATTTGCGGTGGACGAT-3'), *FLT4* (5'-AAGAAGTTCCA CCACCAACAT-3' and 5'-TGAAAATCCTGGCTCACAAGC-3') and *CDH5* (5'-AACTTCCCCTTCTTACCC-3' and 5'-AAAGGCTGCTGGAAAATG-3').

Scoring and quantification of phenotypes. To assess the contribution of dorsal vs ventral PCV to different vascular beds, single EC, or pan-Kaede photoconversion was carried out in *Tg(fli1:gal4;uasKaede)* embryos. Photoswitching was performed using a 405 nm laser. To assess the contribution of medial vs early lateral angioblasts to PACs, endothelial cells in 4 segments of *Tg(kdr1:Kaede)* embryos were photoswitched at 17–18 hpf and 20–21 hpf, respectively. 28 h later, embryos were imaged, and the number of green vs red PACs was counted in 6 segments over the photoswitched area.

For quantification of phenotypes, the average number of PACs or thoracic duct per cell number in 9–10 segments over the yolk extension was calculated. Embryos with no fluorescence or with gross vascular morphological defects were excluded from quantification. For analysis, embryos that meet all the criteria above were randomly selected. For quantification of PAC related phenotypes in *ppt* mutants, a subdose of *wnt5b* MO (4 ng) was injected into *ppt* embryos to abolish maternal RNA contribution as described⁵⁵.

Imaging. Confocal imaging was performed using a Zeiss LSM 780 upright confocal microscope (Carl Zeiss, Jena, Germany) with a W-Plan Apochromat ×20 objective, NA 1.0. Fluorescent proteins were excited sequentially with single-photon lasers (488 nm, 563 nm). Two-photon imaging of GFP was carried out at 920 nm. Time-lapse, *in-vivo* imaging was performed as previously described⁵⁶ using a custom-built chamber for perfusion of embryos with temperature-controlled physiological medium. z-stacks were acquired at 2.5–3 μm increments, every 10–12 min.

Embryo dissociation, fluorescence activated cell sorting (FACS) and RNA sequencing. Following pan-Kaede photoconversion of dorsal, or ventral PCV in *Tg(fli1:gal4;uasKaede)* embryos at 24 hpf, 6 embryos per group were used for FACS isolation of Kaede photoconverted (red) endothelial cells. Single-cell suspensions were prepared as described¹⁶ with some modifications (the embryos were not chopped, and no Liberase was used). Sorting was performed at 4°C in a FACSaria cell sorter using a 70-μm nozzle. Photoconverted (red) endothelial cells were collected in 1 ml PBS, washed with PBS and centrifuged twice at 300g, at 4°C for 5 min. Total RNA was extracted using Tri@Reagent (Sigma) as described⁵⁷, except that only GenElute-LPA (Sigma) was added to help precipitate the RNA. RNA-Seq was performed as previously described²⁵ with the following modification: a new set of primers was used with a shorter barcode, and a 5-base unique molecule identifier to enable transcript counting.

RNA sequencing data analysis. CEL-Seq data was normalized by dividing the reads of each gene by the total reads of the sample and multiplying by 10,000 (transcript per 10,000). Genes without any detected expression, or with expression detected only in one sample were filtered out. For identification of significant differentially expressed genes, fold change was calculated and a two-sample *t*-test was conducted.

Gene Ontology analysis was performed with Ontologizer 2.0⁵⁸ using the Topology-Weighted algorithm on the set of genes with a change of at least 1.5 fold between the ventral and dorsal samples. The associations were taken from geneontology.org, Version 1.4 from ZFIN.

Image processing. Images were processed off-line using ImageJ (NIH) and Imaris (Bitplane). Selected data sets were deconvoluted with Autoquant X3 (Media Cybernetics). For co-localization analyses confocal images were first deconvoluted and then analysed using the Imaris 'Colocalization Module'. We used this new channel to mark, and manually count cells that are labelled with both EGFP and mCherry/TagRFP fluorophores. Co-localization thresholds and nuclei quantification were set manually. Where necessary, movies were registered with the "Linear Stack Alignment with SIFT" plugin of FIJI.

Histology. *Tg(fli1:EGFP)* embryos were fixed in 4% PFA for 20 min at room temperature, embedded in gelatin-bovine albumin medium (0.35% gelatin, 21% bovine albumin) as previously described⁵⁹. 50–100 μm cross-sections were obtained using a Leica VT 1000s vibratome and stained in 1:200 dilution of TRITC-Phalloidin (Sigma) as previously described⁶⁰.

Human embryonic stem cells. Induction of differentiation towards the endothelial lineages has been previously described³². Briefly, H9 cells were seeded as single cells on Collagen-IV (Sigma) coated plates at 5 × 10⁴ cells per cm² and cultured with MEM-alpha (Invitrogen), 10% FBS (Hyclone) and 0.1 mM β-mercaptoethanol for 6 days. At day 6, cells were re-seeded on collagen-IV coated plates at 1.25 × 10⁴ cells per cm² and cultured under ECGM (Promocell)+20% FBS, 50 ng ml⁻¹ VEGF-A (Biolegend Inc., San Diego CA) and 10 μM SB431542 (Sigma Aldrich). To induce lymphatic differentiation cells were added with 100 ng ml⁻¹ Wnt5b (R&D) starting from day 6 every other day. At day 12 RNA was extracted with Tri@Reagent (Sigma)/Chloroform, and cDNA was produced using the SuperscriptIII kit (Invitrogen).

H9 cells were obtained and handled by the Stem Cells Research Center at the Weizmann Institute (Israel), and were routinely checked for karyotype and for mycoplasma contamination.

For FACS analyses cells were harvested using non-enzymatic dissociation solution (Sigma), stained with an allophycocyanin-conjugated Lyve1 Antibody (R&D systems, Minneapolis, MN) for 30 min at room temperature, washed with PBS 3% FCS, stained with propidium iodide (Sigma) and analysed via FACSariaIII. Dead cells were excluded from analysis by gating out propidium iodide-positive cells.

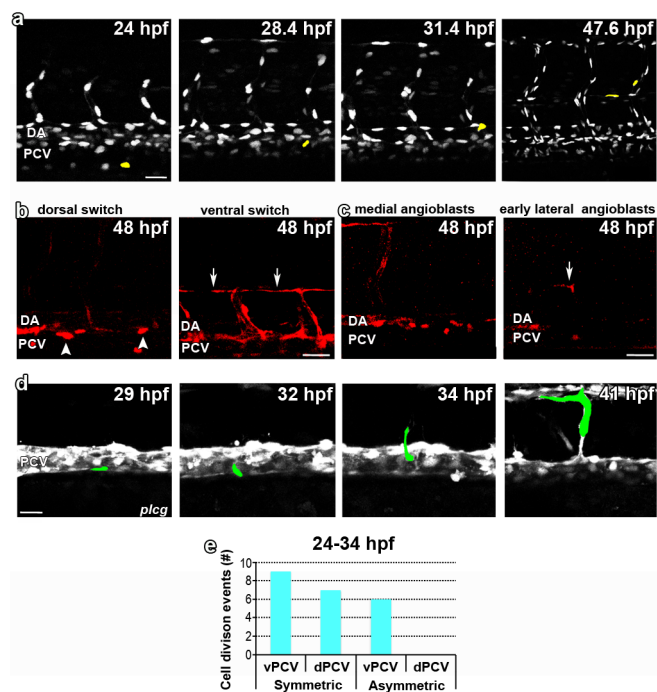
Statistical analyses. No statistical methods were used to predetermine sample size.

Data was analysed using the unpaired two-tailed Student's *t*-test assuming unequal variance from at least two independent experiments, unless stated otherwise. In all cases normality was assumed and variance was comparable between groups. Sample size was selected empirically following previous experience in the assessment of experimental variability. The investigators were not blinded to allocation during experiments and outcome assessment. We chose the adequate tests according to the data distribution to fulfil test assumptions. Numerical data are the mean \pm s.e.m., unless stated otherwise.

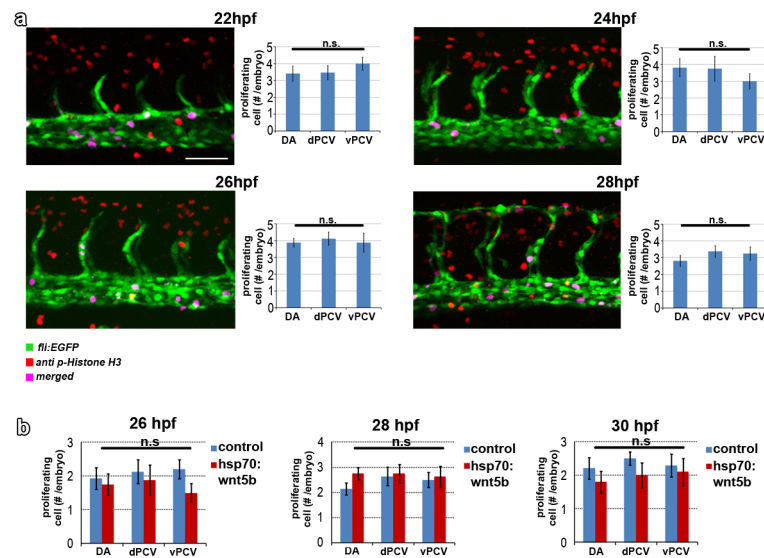
For qRT-PCR experiments we computed standard error for each fold-change. For genes with more than a single fold-change value, x_1, x_2, \dots, x_n , each with a standard error $\Delta x_1, \Delta x_2, \dots, \Delta x_n$, we computed the mean fold-change by taking the geometrical average, $\bar{x} = \sqrt[n]{x_1 \cdot x_2 \cdot \dots \cdot x_n}$. Its standard error was computed using

$$\text{error propagation, } \Delta \bar{x} = \frac{\bar{x}}{n} \sqrt{\left(\frac{\Delta x_1}{x_1}\right)^2 + \left(\frac{\Delta x_2}{x_2}\right)^2 + \dots + \left(\frac{\Delta x_n}{x_n}\right)^2}.$$

38. Stoick-Cooper, C. L. *et al.* Distinct Wnt signaling pathways have opposing roles in appendage regeneration. *Development* **134**, 479–489 (2007).
39. Moro, E. *et al.* *In vivo* Wnt signaling tracing through a transgenic biosensor fish reveals novel activity domains. *Dev. Biol.* **366**, 327–340 (2012).
40. Alexander, J., Rothenberg, M., Henry, G. L. & Stainier, D. Y. *casanova* plays an early and essential role in endoderm formation in zebrafish. *Dev. Biol.* **215**, 343–357 (1999).
41. Lele, Z., Bakkers, J. & Hammerschmidt, M. Morpholino phenocopies of the *swirl*, *snailhouse*, *somitabun*, *minfin*, *silberblick*, and *pipetail* mutations. *Genesis* **30**, 190–194 (2001).
42. Heisenberg, C. P. *et al.* A mutation in the Gsk3-binding domain of zebrafish Masterblind/Axin1 leads to a fate transformation of telencephalon and eyes to diencephalon. *Genes Dev.* **15**, 1427–1434 (2001).
43. Hurlstone, A. F. *et al.* The Wnt/beta-catenin pathway regulates cardiac valve formation. *Nature* **425**, 633–637 (2003).
44. Bussmann, J. *et al.* Arteries provide essential guidance cues for lymphatic endothelial cells in the zebrafish trunk. *Development* **137**, 2653–2657 (2010).
45. Fisher, S. *et al.* Evaluating the biological relevance of putative enhancers using Tol2 transposon-mediated transgenesis in zebrafish. *Nature Protocols* **1**, 1297–1305 (2006).
46. Villefranc, J. A., Amigo, J. & Lawson, N. D. Gateway compatible vectors for analysis of gene function in the zebrafish. *Dev. Dyn.* **236**, 3077–3087 (2007).
47. Cermenati, S. *et al.* Sox18 and Sox7 play redundant roles in vascular development. *Blood* **111**, 2657–2666 (2008).
48. Shepard, J. L., Stern, H. M., Pfaff, K. L. & Amatruda, J. F. Analysis of the cell cycle in zebrafish embryos. *Methods Cell Biol.* **76**, 109–125 (2004).
49. Chen, B. *et al.* Small molecule-mediated disruption of Wnt-dependent signaling in tissue regeneration and cancer. *Nature Chem. Biol.* **5**, 100–107 (2009).
50. Cirone, P. *et al.* A role for planar cell polarity signaling in angiogenesis. *Angiogenesis* **11**, 347–360 (2008).
51. Griffin, K. J. & Kimelman, D. One-Eyed Pinhead and Spadetail are essential for heart and somite formation. *Nature Cell Biol.* **4**, 821–825 (2002).
52. Nyholm, M. K., Wu, S. F., Dorsky, R. I. & Grinblat, Y. The zebrafish *zic2a-zic5* gene pair acts downstream of canonical Wnt signaling to control cell proliferation in the developing tectum. *Development* **134**, 735–746 (2007).
53. Dorsky, R. I., Sheldahl, L. C. & Moon, R. T. A transgenic Lef1/ β -catenin-dependent reporter is expressed in spatially restricted domains throughout zebrafish development. *Dev. Biol.* **241**, 229–237 (2002).
54. Shimizu, T. *et al.* Cooperative roles of Bozozok/Dharma and Nodal-related proteins in the formation of the dorsal organizer in zebrafish. *Mech. Dev.* **91**, 293–303 (2000).
55. Kim, H. J. *et al.* Wnt5 signaling in vertebrate pancreas development. *BMC Biol.* **3**, 23 (2005).
56. Ben Shoham, A. *et al.* S1P1 inhibits sprouting angiogenesis during vascular development. *Development* **139**, 3859–3869 (2012).
57. Levin, M., Hashimshony, T., Wagner, F. & Yanai, I. Developmental milestones punctuate gene expression in the *Caenorhabditis* embryo. *Dev. Cell* **22**, 1101–1108 (2012).
58. Bauer, S., Grossmann, S., Vingron, M. & Robinson, P. N. Ontologizer 2.0—a multifunctional tool for GO term enrichment analysis and data exploration. *Bioinformatics* **24**, 1650–1651 (2008).
59. Levin, M. A novel immunohistochemical method for evaluation of antibody specificity and detection of labile targets in biological tissue. *J. Biochem. Biophys. Methods* **58**, 85–96 (2004).
60. Jin, S. W., Beis, D., Mitchell, T., Chen, J. N. & Stainier, D. Y. Cellular and molecular analyses of vascular tube and lumen formation in zebrafish. *Development* **132**, 5199–5209 (2005).

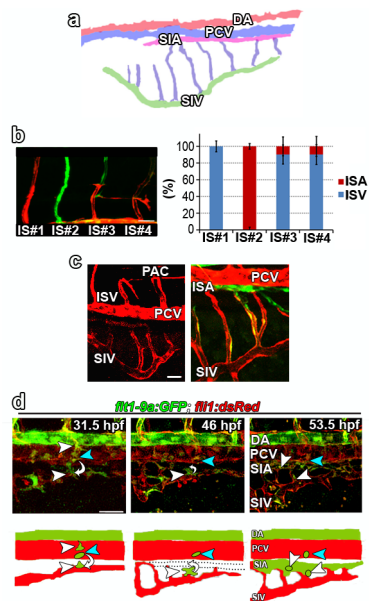


Extended Data Figure 1 | Mesoderm-derived angioblasts generate LECs through asymmetric cell division. **a**, Snapshots from a time-lapse sequence of a *Tg(fli1:nEGFP)^{+/+}* zebrafish embryo, showing the origin of a PAC cell (yellow) in the vPCV ($n_{\text{imaged embryos}} = 7$). **b**, vPCV (left panel), and dPCV (right panel) Kaede photoconverted cells at 48 hpf. **c**, Kaede-photoswitched 'medial' (left panel) and 'early lateral' (right panel) angioblasts. **d**, Snapshots from a time-lapse sequence of a *plc1* mutant, showing the origin of a PAC cell (green) in the vPCV ($n_{\text{imaged embryos}} = 3$). **e**, Quantification of symmetric and asymmetric division events in the vPCV and dPCV of double *Tg(flt1_9a_cFos:GFP; lyve1:dsRed2^{nz101})* embryos ($n_{\text{imaged embryos}} = 6$). Scale bars, 30 μm .

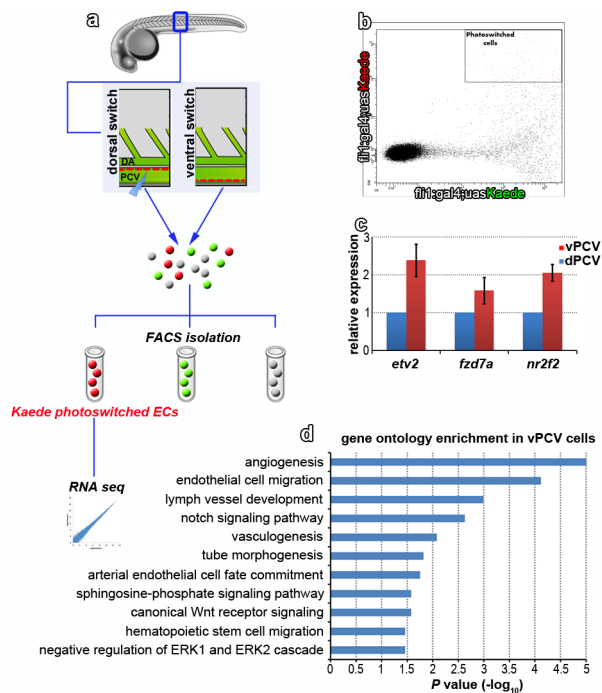


Extended Data Figure 2 | Analysis of cell division in the zebrafish axial vessels. **a**, Phospho-histone H3 staining shows no difference in the number of proliferative endothelial cells among the DA, dPCV and vPCV (n_{24} hpf embryos = 17, n_{26} hpf embryos = 16, n_{28} hpf embryos = 16, n_{30} hpf embryos = 16). **b**, Ectopic induction of Wnt5b in *Tg(hsp70l:wnt5b; fli1:EGFP)* does not result in

enhanced proliferation of endothelial cells (26 hpf; n_{control} embryos = 15, $n_{\text{hsp70:wnt5b}}$ embryos = 8, 28 hpf; n_{control} embryos = 14, $n_{\text{hsp70:wnt5b}}$ embryos = 8, 30 hpf; n_{control} embryos = 14, $n_{\text{hsp70:wnt5b}}$ embryos = 10). Scale bar, 60 μm . Error bars, mean \pm s.e.m.

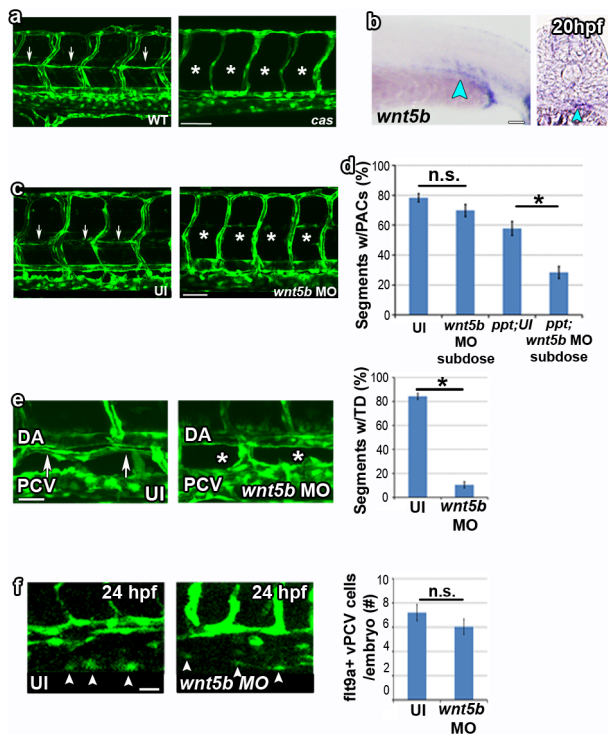


Extended Data Figure 3 | Fate map analysis of vPCV cells. **a**, Schematic representation of the subintestinal plexus at 72 hpf. Subintestinal vein (SIV, green), interconnecting SI vessels (purple), suprainestinal artery (SIA, pink), posterior cardinal vein (PCV, blue), dorsal aorta (DA, red). **b**, Quantification of the number of intersegmental arteries (ISA) and intersegmental veins (ISV) in the first four segments of *Tg(flt1_9a_cFos:GFP; lyve1:dsRed2)* double transgenic embryos ($n_{\text{embryos}} = 41$). IS# denotes the position of intersegmental vessel. **c**, Confocal images of *Tg(lyve1:dsRed2)* (left panel) and *Tg(flt1_9a_cFos:GFP; lyve1:dsRed2)* (right panel) embryos showing *lyve1:dsRed2*⁺ endothelial cells in PACs, venous intersegmental vessels (ISVs), PCV and SIV and *flt1_9a:GFP*⁺ endothelial cells in the SIA. **d**, *flt1_9a:GFP*⁺ vPCV angioblast (light-blue arrowhead), divides asymmetrically (curved arrow) to generate cells that populate the SIV (31.5 hpf, white arrowhead), and the SIA (53.5 hpf, white arrowhead). Scale bar, 30 μm . Error bars, mean \pm s.e.m.



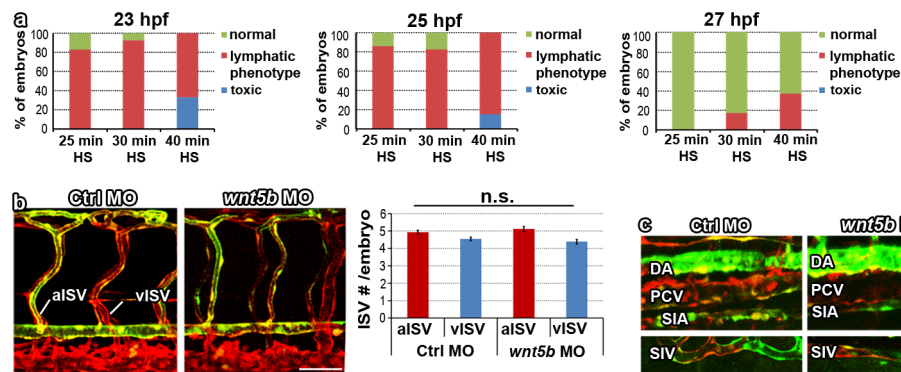
Extended Data Figure 4 | Transcriptional profiling of vPCV angioblasts.

a, Experimental setup used for RNA sequencing analysis of FACS isolated vPCV and dPCV cells. **b**, FACS isolation of green vs red (photoconverted) endothelial cells from *Tg(fli1:gal4;uasKaede)* embryos following photoswitching of dorsal or ventral PCV ($n_{\text{independent experiments}} = 4$). **c**, qRT-PCR analysis of selected candidates shows enrichment in ventral vs dorsal PCV cells ($n_{\text{independent experiments}} = 2$). **d**, Gene Ontology enrichment in vPCV vs dPCV cells (results represent 2 out of 4 independent biological repeats). Error bars, geometrical mean \pm s.e.g.m.



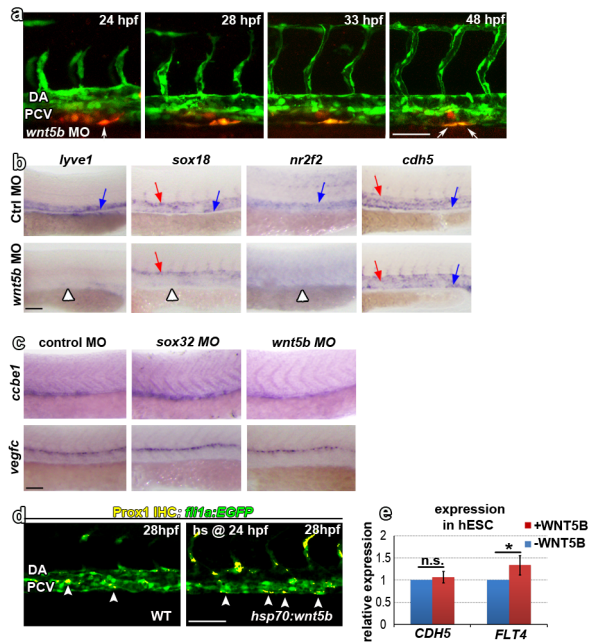
Extended Data Figure 5 | Endoderm-derived Wnt5b is required for lymphatic development.

a, PAC-containing segments in WT (arrows) and *cas* mutants (asterisks). **b**, *In situ* hybridization at 20 hpf showing expression of *wnt5b* mRNA (blue arrowhead) in the endoderm of WT embryos. **c**, PAC-containing segments in uninjected (UI) (arrows) and *wnt5b* MO-injected embryos (asterisks). **d**, *ppt* mutants injected with *wnt5b* MO (subdose) display significant reduction in PAC number ($n_{\text{UI embryos}} = 38$, $n_{\text{wnt5b-MO embryos sub}} = 38$, $n_{\text{ppt-UI embryos}} = 34$, $n_{\text{ppt, wnt5b MO sub-embryos}} = 34$; $*P = 1.2 \times 10^{-5}$). **e**, *wnt5b* morphants exhibit marked reduction in the number of thoracic duct-containing segments (asterisks) as compared to uninjected (UI) siblings (arrows) ($n_{\text{UI-embryos}} = 38$, $n_{\text{wnt5b MO-embryos}} = 32$; $*P = 4.5 \times 10^{-30}$). **f**, The number of *flt1*⁺ vPCV progenitors is not affected in *wnt5b* morphants ($n_{\text{UI-embryos}} = 31$, $n_{\text{wnt5b-MO embryos}} = 31$). Scale bars, **a**, **c**, 60 μ m; **b**, **e**, **f**, 30 μ m. Error bars, mean \pm s.e.m.

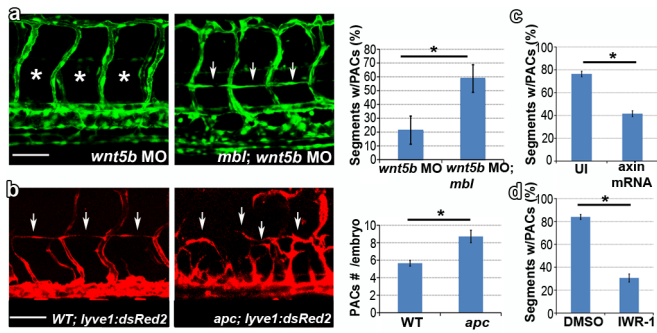


Extended Data Figure 6 | Wnt5b is not required for sprouting from the PCV. **a**, Phenotypic analysis of Wnt5b overexpression in *Tg(hsp70l:wnt5b-GFP; lyve1:dsRed2)* embryos, following 25–30 min heat shock (HS), at 23, 25 and 27 hpf (23 hpf embryos $n_{\text{HS-25 min}} = 18$, $n_{\text{HS-30 min}} = 14$, $n_{\text{HS-40 min}} = 15$, 25 hpf embryos $n_{\text{HS-25 min}} = 14$, $n_{\text{HS-30 min}} = 17$, $n_{\text{HS-40 min}} = 20$, 27 hpf embryos $n_{\text{HS-25 min}} = 19$, $n_{\text{HS-30 min}} = 17$, $n_{\text{HS-40 min}} = 10$). **b**, The number of vISVs vs

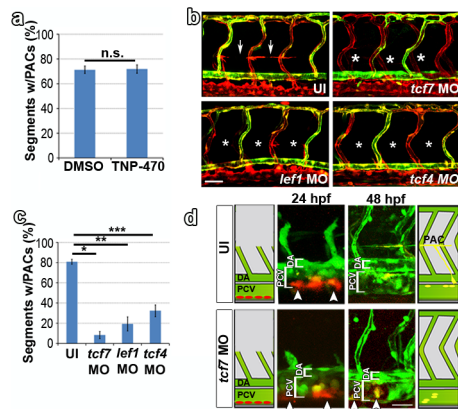
aISVs is unaltered in *wnt5b* morphants as compared to Control MO-injected siblings ($n_{\text{Control MO-embryos}} = 43$, $n_{\text{wnt5b MO-embryos}} = 41$). **c**, *flt1_9a*⁺ vPCV cells are detected in the suprainstestinal artery (SIA) and subintestinal vein (SIV) of *wnt5b* MO-injected embryos ($n_{\text{Ctrl MO}} = 16$, $n_{\text{wnt5b MO}} = 16$). Scale bars, 60 μ m. Error bars, mean \pm s.e.m.



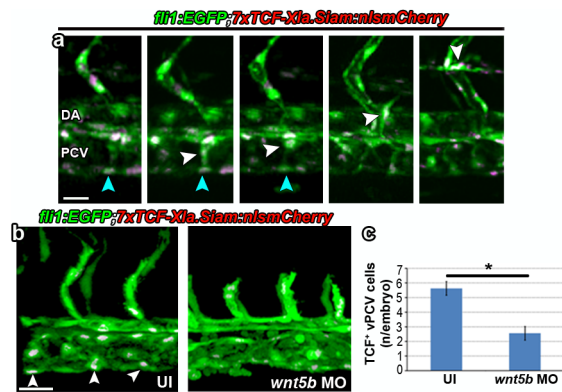
Extended Data Figure 7 | Wnt5b induces the “angioblast-to-lymphatic” specification. **a**, Selected frames from a time-lapse sequence of a *Tg(fli1:gal4;uasKaede)* embryo injected with *wnt5b* MO. Photoconverted vPCV cell (white arrow) divides normally (arrows at 48 hpf point to 2 daughter cells), but does not engage in dorsal migration to generate PACs. **b**, *In situ* hybridization of Ctrl MO-, and *wnt5b* MO-injected zebrafish at 30 hpf, with *lyve1*, *sox18*, *nr2f2* and *cdh5* probes, showing specific decrease in lymphatic marker expression in the floor of the PCV (white arrowheads) of *wnt5b* morphants. The pan-endothelial marker *cdh5*, as well as the arterial expression of *sox18*, remain unchanged in *wnt5b* morphants. **c**, *vegfc* and *ccbe1* mRNA levels remain unaltered in *sox32* and *wnt5b* morphants. **d**, Immunostaining of Prox1 shows marked increase in protein levels following ectopic activation of Wnt5b in *Tg(hsp70l:wnt5b; fli1:EGFP)* embryos (co-localization channel is shown in yellow, white arrowheads). **e**, qRT-PCR analysis of *FLT4* and *CDH5* in hESCs treated with WNT5B ($n_{\text{independent-experiments}} = 3$; $*P = 0.03$ by one sample *t*-test). Scale bars, 60 μm . Error bars, geometrical mean \pm s.e.g.m.



Extended Data Figure 8 | Wnt5b induces LEC specification through activation of canonical pathway. **a**, PAC-containing segments (arrows) in *wnt5b* MO-injected *mbl* mutants ($n_{wnt5bMO} = 42$, $n_{mbl;wnt5bMO} = 52$; $*P = 3.4 \times 10^{-10}$). **b**, *apc* mutants ($n_{WT} = 18$, $n_{apc} = 19$; $*P = 0.0006$), **c**, *axin1* mRNA-injected embryos ($n_{UI} = 33$, $n_{axin-mRNA} = 46$; $*P = 1.73 \times 10^{-14}$), and **d**, IWR-1 treated embryos ($n_{DMSO} = 55$, $n_{IWR} = 54$; $*P = 1.05 \times 10^{-21}$). Scale bars, 60 μ m. Error bars, mean \pm s.e.m.



Extended Data Figure 9 | Involvement of Tcf transcription factors in LEC specification. **a**, PAC number remains unchanged in TNP-470 treated *Tg(fli1:EGFP)* embryos as compared to DMSO (control) ($n_{\text{DMSO}} = 19$, $n_{\text{TNP-470}} = 38$). **b**, **c**, Quantification of PAC-containing segments in the trunk of UI, *tcf7*, *lef1* and *tcf4* MO-injected embryos ($n_{\text{UI-embryos}} = 59$, $n_{\text{tcf7-MO embryos}} = 33$, $n_{\text{lef1-MO embryos}} = 16$, $n_{\text{tcf4-MO embryos}} = 25$; $*P = 4.53 \times 10^{-25}$, $**P = 9.62 \times 10^{-8}$, $***P = 9.12 \times 10^{-9}$). **d**, Photoswitching of vPCV cells in *tcf7* MO-injected *Tg(fli1:gal4;uasKaede)* embryos (white arrowheads) at 24 hpf. At 48 hpf photoconverted, red vPCV cells (arrowheads) remain in the PCV and do not generate PACs. Scale bars, 30 μm . Error bars, mean \pm s.e.m.



Extended Data Figure 10 | Wnt5b-dependent activation of β -catenin/TCF in vPCV angioblasts. **a**, Selected frames from a time-lapse sequence showing β -catenin/TCF activity in a single vPCV angioblast (light-blue arrowhead), which generates PACs (white arrowhead) through asymmetric cell division ($n = 2$). **b**, Confocal images of the trunks of *Tg(7xTCF-Xla.Siam:nls-mCherry; fli1:EGFP)* double transgenic zebrafish injected with *wnt5b* MO, showing decreased β -catenin/TCF activation in vPCV cells (quantified in **c**) ($n_{\text{UI-embryos}} = 18$, $n_{\text{wnt5b-embryos}} = 17$; $*P = 4 \times 10^{-5}$). Purple signal depicts co-localization of cytoplasmic EGFP and nuclear mCherry. Scale bars, 30 μm . Error bars, mean \pm s.e.m.

Resonant interactions and chaotic rotation of Pluto's small moons

M. R. Showalter¹ & D. P. Hamilton²

Four small moons—Styx, Nix, Kerberos and Hydra—follow near-circular, near-equatorial orbits around the central ‘binary planet’ comprising Pluto and its large moon, Charon. New observational details of the system have emerged following the discoveries of Kerberos and Styx. Here we report that Styx, Nix and Hydra are tied together by a three-body resonance, which is reminiscent of the Laplace resonance linking Jupiter’s moons Io, Europa and Ganymede. Perturbations by the other bodies, however, inject chaos into this otherwise stable configuration. Nix and Hydra have bright surfaces similar to that of Charon. Kerberos may be much darker, raising questions about how a heterogeneous satellite system might have formed. Nix and Hydra rotate chaotically, driven by the large torques of the Pluto–Charon binary.

Pluto’s moon Kerberos (previously designated S/2011 (134340)1 or, colloquially, P4) was discovered in 2011¹ using images from the Hubble Space Telescope (HST). It orbits between the paths of Nix and Hydra, which were discovered in 2005 and confirmed in 2006². Follow-up observations in 2012 led to the discovery of the still smaller moon Styx (S/2012 (134340)1 or P5)³. The complete data set includes numerous additional detections of both objects from 2010–2012^{4–6}, plus a few detections from 2005 (H. A. Weaver, personal communication, 2011) and from 2006⁷; see Supplementary Table 1. Figure 1 shows samples of the available images. Motivated by these discoveries, we investigate the dynamics and physical properties of Pluto’s four small outer moons.

Orbits

Pluto and Charon comprise a ‘binary planet’—two bodies, similar in size, orbiting their common barycentre. Their mutual motion creates a time-variable and distinctly asymmetric gravity field. This induces wobbles in the orbits of the outer moons and also drives much slower apsidal precession and nodal regression⁸. In our analysis, we ignore the short-term wobbles and derive time-averaged orbital elements. This is equivalent to replacing the gravity field by that of two concentric rings containing the masses of Pluto or Charon, each with a radius equal to that body’s distance from the barycentre.

We have modelled the orbits using six Keplerian orbital elements (semimajor axis a , eccentricity e , inclination i , mean longitude at epoch λ_0 , longitude of pericentre ϖ_0 , and ascending node Ω_0) plus three associated frequencies (mean motion n , nodal precession rate $\dot{\omega}$, and apsidal regression rate $\dot{\Omega}$). We work in the inertial Pluto–Charon (P–C) coordinate frame, with Pluto and Charon in the x – y plane and the z axis parallel to the system’s angular momentum pole (right ascension 8 h 52 min 5.5 s, declination -6.218°)⁶. We have solved for these elements and frequencies under a variety of assumptions about how they are coupled (Extended Data Table 1). Table 1 lists the most robustly determined elements, in which we enforce a relationship that ensures $\dot{\omega} \approx -\dot{\Omega}$; this allows us to fit eight elements rather than nine. We prefer this solution because root-mean-square (RMS) residuals are nearly the same as for the solution where $\dot{\omega}$ and $\dot{\Omega}$ are allowed to vary independently. Additional possible couplings, involving a and n as well, markedly increase the residuals for Styx and Nix;

this suggests that non-axisymmetric gravitational effects, which are not modelled by our concentric ring approximation, can be important. The statistically significant (P -value $\ll 1\%$) ~ 100 -km residuals of Nix and Hydra (Table 1) match the predicted scale of the un-modelled wobbles⁸, and so are to be expected.

Table 1 shows that e and i are distinctly non-zero; this was not apparent in prior work, which employed a different coordinate frame⁵ or was based on 200-year averages⁶. Our results describe each moon’s motion during 2005–2012 more accurately. Variations in n , e and i are detectable during 2010–2012 (Extended Data Fig. 1), illustrating the mutual perturbations among the moons that have been used to constrain their masses⁶.

Search for resonances

Pluto’s five moons show a tantalizing orbital configuration: the ratios of their orbital periods are close to 1:3:4:5:6^{1,3,5,9}. This configuration is reminiscent of the Laplace resonance at Jupiter, where the moons Io, Europa, and Ganymede have periods in the ratio 1:2:4. Table 1 shows the orbital periods P of the moons relative to that of Charon, confirming the near-integer ratios. However, with measured values for $\dot{\omega}$ and $\dot{\Omega}$ in addition to n , it becomes possible to search for more complicated types of resonances. A general resonance involves an angle $\Phi = \sum_j (p_j \lambda_j + q_j \varpi_j + r_j \Omega_j)$ and its time derivative $\dot{\Phi} = \sum_j (p_j n_j + q_j \dot{\omega}_j + r_j \dot{\Omega}_j)$. Here, (p_j, q_j, r_j) are integer coefficients and

each subscript j is C, S, N, K or H to identify the associated moon. A resonance is recognized by coefficients that sum to zero and produce a very small value of $\dot{\Phi}$; in addition, the resonant argument Φ usually librates around either 0° or 180° .

Using the orbital elements and their uncertainties tabulated in Table 1, we have performed an exhaustive search for strong resonances in the Pluto system. One dominant three-body resonance was identified: $\Phi = 3\lambda_S - 5\lambda_N + 2\lambda_H \approx 180^\circ$. This defines a ratio of synodic periods: $3S_{NH} = 2S_{SH}$, where the subscripts identify the pair of moons. We find that $\dot{\Phi} = -0.007 \pm 0.001^\circ$ per day and that Φ decreases from 191° to 184° during 2010–2012; this is all consistent with a small libration about 180° . Note that this expression is very similar to that for Jupiter’s Laplace resonance,

¹SETI Institute, 189 Bernardo Avenue, Mountain View, California 94043, USA. ²Department of Astronomy, University of Maryland, College Park, Maryland 20742, USA.

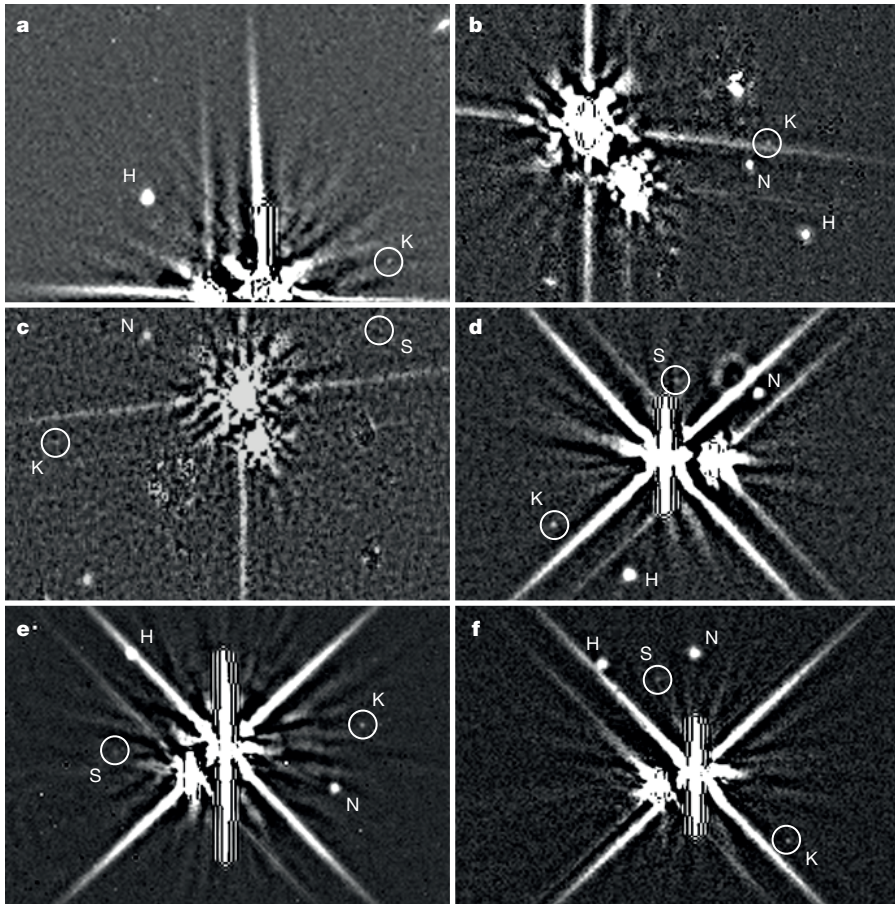


Figure 1 | Example HST images of Pluto's small moons. **a**, Kerberos (K) detected 18 May 2005, in the Nix/Hydra discovery images. **b**, Kerberos in the Nix (N) and Hydra (H) confirmation images of 2 February 2006. **c**, A marginal detection of Styx (S), along with Kerberos, on 2 March 2006. **d**, All four moons, 25 June 2010. **e**, The Kerberos discovery image, 28 June 2011, with Styx also identified. **f**, The Styx discovery image, 7 July 2011. All images were generated by co-adding similar images and then applying an unsharp mask to suppress the glare from Pluto and Charon.

Table 1 | Derived properties of the moons

Property	Styx	Nix	Kerberos	Hydra
a (km)	$42,656 \pm 78$	$48,694 \pm 3$	$57,783 \pm 19$	$64,738 \pm 3$
λ_0 (°)	276.856 ± 0.096	63.866 ± 0.006	94.308 ± 0.021	197.866 ± 0.003
n (° per day)	17.85577 ± 0.00024	14.48422 ± 0.00002	11.19140 ± 0.00005	9.42365 ± 0.00001
e (10^{-3})	5.787 ± 1.144	2.036 ± 0.050	3.280 ± 0.200	5.862 ± 0.025
ϖ_0 (°)	296.1 ± 9.4	221.6 ± 1.4	187.6 ± 3.7	192.2 ± 0.3
$\dot{\varpi}$ (° per day)	0.506 ± 0.014	0.183 ± 0.004	0.115 ± 0.006	0.070 ± 0.001
i (°)	0.809 ± 0.162	0.133 ± 0.008	0.389 ± 0.037	0.242 ± 0.005
Ω_0 (°)	183.4 ± 12.5	3.7 ± 3.4	225.2 ± 5.4	189.7 ± 1.2
$\dot{\Omega}$ (° per day)	-0.492 ± 0.014	-0.181 ± 0.004	-0.114 ± 0.006	-0.069 ± 0.001
P (days)	20.16155 ± 0.00027	24.85463 ± 0.00003	32.16756 ± 0.00014	38.20177 ± 0.00003
P/P_C	3.156542 ± 0.000046	3.891302 ± 0.000004	5.036233 ± 0.000024	5.980963 ± 0.000005
RMS (σ)	1.44	2.59	1.27	2.77
RMS (mas)	17.8	4.22	11.2	3.21
RMS (km)	397	94	248	72
A (km ²)	14 ± 4	470 ± 75	29 ± 8	615 ± 55
R_{100} (km)	2.1 ± 0.3	12.2 ± 1.0	3.0 ± 0.4	14.0 ± 0.6
R_{38} (km)	3.4 ± 0.5	19.8 ± 1.6	4.9 ± 0.7	22.7 ± 1.0
R_{06} (km)	8.6 ± 1.2	50 ± 4	12.4 ± 1.7	57 ± 3
a_{100}/b_{100}		2.1 ± 0.6		1.7 ± 0.6
b_{100}/c_{100}		1.2 ± 0.2		1.2 ± 0.2
ϕ_{2010} (°)		25 ± 10		39 ± 16
ϕ_{2011} (°)		37 ± 15		46 ± 18
ϕ_{2012} (°)		46 ± 17		38 ± 16
V_{100} (km ³)	39 ± 17	$5,890 \pm 1040$	117 ± 49	$8,940 \pm 1640$
GM (10^{-3} km ³ s ⁻²)	0.0 ± 1.0	3.0 ± 2.7	1.1 ± 0.6	3.2 ± 2.8
Charon-like	0.018 ± 0.008	2.8 ± 0.5	0.06 ± 0.03	4.2 ± 0.8
Bright KBO	0.04 ± 0.02	6.2 ± 1.1	0.12 ± 0.05	9.4 ± 1.7
Median KBO	0.12 ± 0.05	17 ± 3	0.35 ± 0.14	26 ± 5
Dark KBO	0.26 ± 0.11	39 ± 7	0.78 ± 0.32	60 ± 11

Angles are measured from the ascending node of the P–C orbital plane on the J2000 equator. The epoch is Universal Coordinate Time (UTC) on 1 July 2011. Uncertainties are 1σ . A is disk-integrated reflectivity; R_{100} , R_{38} and R_{06} are radius estimates assuming a spherical shape and $p_v = 1$, 0.38, and 0.06; V_{100} is the ellipsoidal volume if $p_v = 1$. Estimates of $GM = G\rho p_v^{-3/2}V_{100}$ are shown for properties resembling those of Charon (density $\rho = 1.65$ g cm⁻³, $p_v = 0.38$) and three types of KBOs: 'bright' ($\rho = 0.5$; $p_v = 0.1$), 'median' ($\rho = 0.65$; $p_v = 0.06$), and 'dark' ($\rho = 0.8$; $p_v = 0.04$). Boldface values are within 1σ of the dynamical mass constraints⁶.

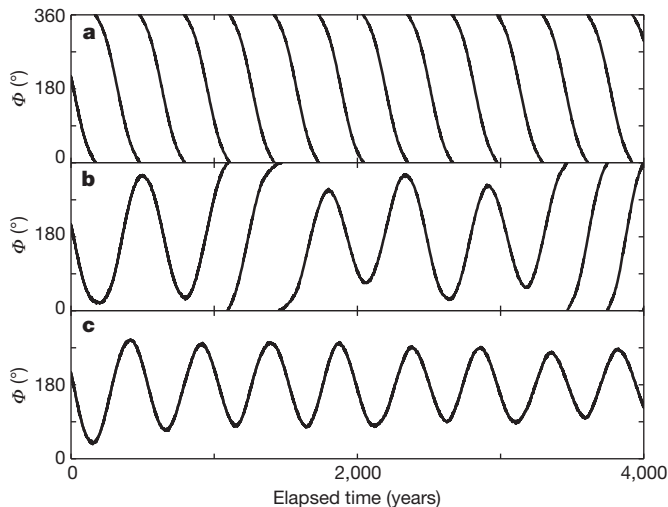


Figure 2 | Numerical integrations of the Styx–Nix–Hydra resonance. Resonant angle Φ is plotted versus time from the current epoch, using three assumptions for GM_H : $0.0032 \text{ km}^2 \text{ s}^{-3}$ (a), $0.0039 \text{ km}^2 \text{ s}^{-3}$ (b), and $0.0046 \text{ km}^2 \text{ s}^{-3}$ (c); these values are equivalent to the nominal mass, a 0.25σ increase, and a 0.5σ increase⁶. $GM_N = 0.0044 \text{ km}^2 \text{ s}^{-3}$ throughout, equivalent to 0.5σ above its nominal mass. The modest increase in M_H is sufficient to force a transition of Φ from circulation (Styx outside resonance) to libration (Styx locked in resonance).

where $\Phi_L = \lambda_1 - 3\lambda_E + 2\lambda_G \approx 180^\circ$ and $2S_{IE} = S_{EG}$. For comparison, Φ_L librates by only $\sim 0.03^\circ$ (ref. 10). However, a similar resonant angle among the exoplanets of Gliese 876 librates about 0° by $\sim 40^\circ$ (ref. 11).

Using the current ephemeris and nominal masses⁶, our numerical integrations indicate that Φ circulates, meaning that the resonance is inactive (Fig. 2). However, libration occurs if we increase the masses of Nix and Hydra, M_N and M_H , upward by small amounts (Fig. 3). Between these two limits, Φ varies erratically and seemingly chaotically. Extension of Fig. 3 to higher masses reveals that libration is favoured but never guaranteed. By random chance, it would be unlikely to find Styx orbiting so close to a strong three-body resonance, and our finding that $\Phi \approx 180^\circ$ increases the likelihood that this resonance is active. We therefore believe that $M_N + M_H$ has been slightly underestimated. The net change need not be large ($\lesssim 1\sigma$)⁶, and is also compatible with the upper limit on $M_N + M_H$ required for the long-term orbital stability of Kerberos¹².

Extended Data Fig. 2 shows that Kerberos contributes to the chaos. To understand its role, we perform simulations in which Pluto and Charon have been merged into one central body, thereby isolating the effects of the other moons on Φ . We perform integrations with $M_K = 0$ and with M_K nominal, and then Fourier transform $\Phi(t)$ to detect the frequencies of the perturbations (Extended Data Fig. 3). When M_K is non-zero, the power spectrum shows strong harmonics of the three synodic periods S_{SK} , S_{NK} and S_{KH} ; this is because $\Phi(t)$ is a linear combination of $\lambda_S(t)$, $\lambda_N(t)$ and $\lambda_H(t)$, and Kerberos perturbs each moon during each passage. The harmonics of a second three-body resonance also appear: $\Phi' = 42\lambda_S - 85\lambda_N + 43\lambda_K \approx 180^\circ$, that is, $42S_{NK} \approx 43S_{SN}$. This was the second strongest resonance found in our search; at the orbit of Styx, the two resonances are separated by just 4 km. This is reminiscent of the Uranus system, where chains of near-resonances drive the chaos in that system^{13,14}.

These results will influence future models of Pluto system formation. Charon was probably formed by a large impact into Pluto¹⁵, and the outer moons accreted from the leftover debris. If Charon had a large initial eccentricity, then its corotation resonances could lock material into the 1:3:4:5:6 relationship¹⁶. As Charon's eccentricity damped, the resonant strengths waned, but the moons were left with periods close to these integer ratios¹⁷. This appealing model has numerous shortcomings, however^{18–20}. The presence of a strong

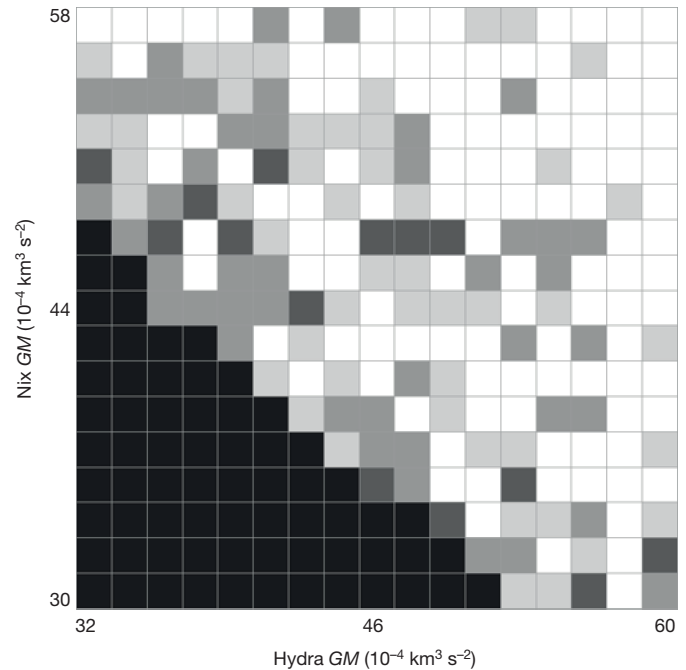


Figure 3 | Mass-dependence of the Laplace-like resonance. The shade of each square indicates whether the associated pair of mass values produces circulation (black) or libration (white) during a 10,000-year integration. The moon masses M_H and M_N are each allowed to vary from nominal to nominal + 1σ (ref. 6). M_K is nominal. Shades of grey define transitional states: light grey if Φ is primarily circulating; dark grey if Φ is primarily librating; medium grey for intermediate states. The transition between black and white is not monotonic, suggesting a fractal boundary.

Laplace-like resonance places a new constraint on formation models. Additionally, future models must account for the non-zero eccentricities and inclinations of the small satellites; for example, these might imply that the system was excited in the past by resonances that are no longer active^{21,22}.

The resonance enforces a modified relationship between orbits: if $P_N/P_C = 4$ and $P_H/P_C = 6$, then $P_S/P_C = 36/11 \approx 3.27$. Nevertheless, the other three near-integer ratios remain unlikely to have arisen by chance. Excluding Styx, the probability that three real numbers would all fall within 0.11 of integers is just 1%.

Shapes, sizes and physical properties

Mean disk-integrated photometry for each moon is listed in Table 1. To infer the sizes of these bodies, we also require their visual geometric albedos p_v . Charon is a relatively bright, with $p_v \approx 0.38$. Kuiper Belt objects (KBOs) exhibit a large range of albedos, but the smallest KBOs tend to be dark; $p_v \approx 0.04$ – 0.08 is common^{23–26}.

The photometry is expected to vary with phase angle α and, if a body is elongated or has albedo markings, with rotational phase. Extended Data Fig. 4 shows the raw photometry for Nix and Hydra. In spite of the otherwise large variations, an opposition surge is apparent for $\alpha \lesssim 0.5^\circ$; this is often seen in phase curves and is indicative of surface roughness. After dividing out the phase function model, Fig. 4 shows our measurements versus orbital longitude relative to Earth's viewpoint. The measurements of Nix show no obvious pattern, suggesting that it is not in synchronous rotation; this is discussed further below.

With unknown rotation states, we can only assess the light curves in a statistical sense. We proceeded with some simplifying assumptions. (1) Each moon is a uniform triaxial ellipsoid, with dimensions $(a_{100}, b_{100}, c_{100})$, assuming $p_v = 1$. (2) Each measurement was taken at a randomly chosen, unknown rotational phase. (3) Each moon was

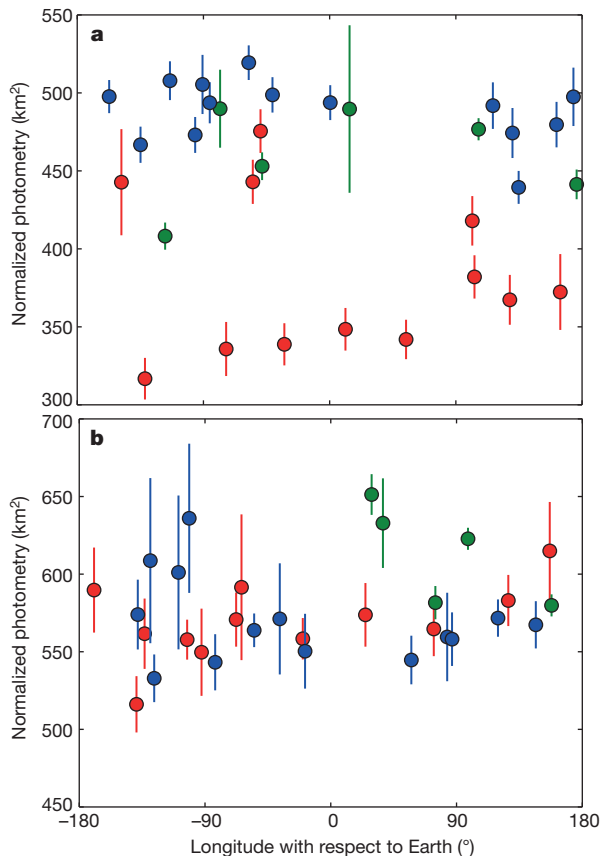


Figure 4 | Normalized light curves. Disk-integrated photometry and 1σ error bars for Nix (a) and Hydra (b) have been normalized to $\alpha = 1^\circ$ and then plotted as a function of projected orbital longitude. Here 0° corresponds to inferior conjunction with Pluto as seen from Earth. Measurements are colour-coded by year: red for 2010, green for 2011, and blue for 2012. A tidally locked moon would systematically brighten at maximum elongation (90° and 270°).

in fixed rotation about its short axis. (4) The pole orientation may have changed during the gap in coverage between years; this is consistent with Supplementary Video 1, in which the rotation poles are generally stable for months at a time. We therefore describe the orientation by three values of sub-Earth planetocentric latitude: ϕ_{2010} , ϕ_{2011} , and ϕ_{2012} . We used Bayesian analysis to solve for the six parameters that provide the best statistical description of the data; see the Methods section for details.

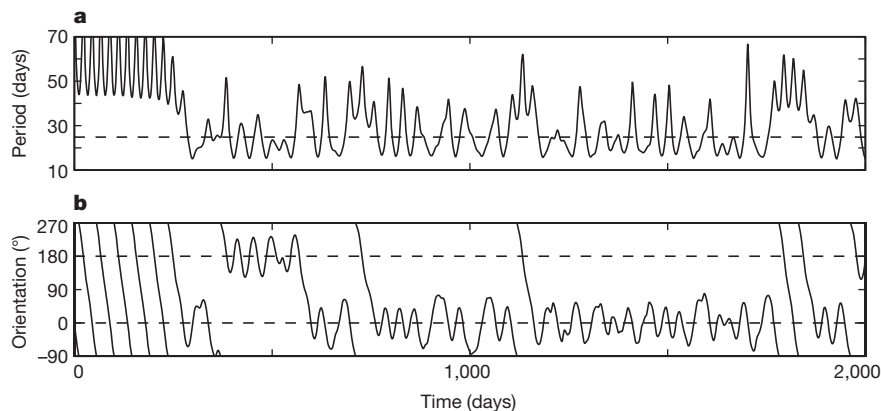


Figure 5 | Numerical simulations of Nix's rotation. a, The instantaneous rotation period is compared to the synchronous rate (dashed line). b, The orientation is described by the angle between Nix's long axis and the direction

Nix has an unusually large axial ratio of $\sim 2:1$ (Table 1), comparable to that of Saturn's extremely elongated moon, Prometheus. Hydra is also elongated, but probably less so. Also, Nix's year-by-year variations (Fig. 4) are the result of a rotation pole apparently turning towards the line of sight; this explains both its brightening trend and also the decrease in its variations during 2010–2012 (Extended Data Fig. 5). Pluto's sub-Earth latitude is 46° , so Hydra's measured pole is nearly compatible with the system pole. Nix's pole was $\sim 20^\circ$ misaligned in 2010 but may have reached alignment by 2012.

Given the inferred volume and an assumed albedo and density, we can estimate GM , where M is the mass and G is the gravitation constant. We consider four assumptions about the moons' physical properties, and compare GM to the dynamical estimates⁶ (Table 1). Nix and Hydra are probably bright, Charon-like objects; if they were darker, then GM would be too large to be compatible with upper limits on the masses¹².

Kerberos seems to be very different (Table 1). The dynamical inference that its mass is about a third that of Nix and Hydra, yet that it reflects only $\sim 5\%$ as much sunlight, implies that it is very dark. This violates our expectation that the moons should be self-similar due to the ballistic exchange of regolith²⁷. Such heterogeneity has one precedent in the Solar System: at Saturn, Aegaeon is very dark ($p_v < 0.15$), unlike any other satellite interior to Titan, and even though it is embedded within the ice-rich G ring²⁸. The formation of such a heterogeneous satellite system is difficult to understand. Alternatively, the discrepancy would go away if the estimate of M_K is found to be high by $\sim 2\sigma$; this has a nominal likelihood of $< 1\%$. Further study is needed.

Rotation states

Nearly every moon in the Solar System rotates synchronously; the only confirmed exception is Hyperion, which is driven into chaotic rotation by a resonance with Titan^{29,30}. Neptune's highly eccentric moon Nereid may also rotate chaotically³¹, but observational support is lacking^{32,33}. We have searched for rotation periods that are consistent with the light curves of Nix and Hydra (Fig. 4), but results have been negative (Extended Data Fig. 6). Although we can sometimes find a rotation period that fits a single year's data (spanning 2–6 months), no single rotation period is compatible with all three years of data.

Dynamical simulations explain this peculiar result: a binary planet tends to drive its moons into chaotic rotation. This is illustrated in Fig. 5, showing the simulated rotation period and orientation of Nix versus time. The moon has a tendency to lock into near-synchronous rotation for brief periods, but these configurations do not persist. At other times, the moon rotates at a period entirely unrelated to its

orbit. Supplementary Video 1 provides further insights into the behaviour; for example, it shows occasional pole flips, a phenomenon consistent with the observed changes in Nix's orientation. Lyapunov times are estimated to be a few months, or just a few multiples of the moons' orbital periods. The timescale of the chaos depends on initial conditions and on assumptions about the axial ratios of the moons. The torques acting on a less-elongated body such as Hydra are weaker, but nevertheless our integrations support chaos.

According to integrations spanning a few centuries, a moon that begins in synchronous rotation will stay there, albeit with large librations. It is therefore possible for synchronous rotation about Pluto and Charon to be stable. However, the large and regular torques of Pluto and Charon probably swamp the small effects of tidal dissipation within the moons, so they never have a pathway to synchronous lock.

Both photometry and dynamical models support the hypothesis that Nix and Hydra are in chaotic rotation. The mechanism is similar to that driving Hyperion's chaos, with Charon playing Titan's role. However, Titan's influence on Hyperion is magnified by a strong orbital resonance. For a binary such as Pluto–Charon, it appears to be a general result that non-spherical moons may rotate chaotically; no resonance is required.

Future observations

The New Horizons spacecraft will fly past Pluto on 14 July 2015. At that time, many of the questions raised by this paper will be addressed. Although Kerberos will not be well resolved (2–3 km per pixel), images will settle the question of whether it is darker than the other moons. The albedos and shapes of Nix (imaged at $\lesssim 0.5$ km per pixel) and Hydra (at 1 km per pixel) will be very well determined. New Horizons will not obtain precise masses for the outer moons, but ongoing Earth-based astrometry and dynamical modelling will continue to refine these numbers, while also providing new constraints on the Laplace-like resonance. Because this resonance has a predicted libration period of centuries, the dynamical models will confirm or refute it long before a complete libration or circulation period can be observed.

Chaotic dynamics makes it less likely that we will find rings or additional moons of Pluto. Within the Styx–Hydra region, the only stable orbits are co-orbitals of the known moons. The region beyond Hydra appears to be the region in which it is most likely that we will find additional moons¹⁷, although some orbits close to Pluto are also stable³⁴. Independent of the new discoveries in store, we have already learned that Pluto hosts a rich and complex dynamical environment, seemingly out of proportion to its diminutive size.

Online Content Methods, along with any additional Extended Data display items and Source Data, are available in the online version of the paper; references unique to these sections appear only in the online paper.

Received 29 October 2014; accepted 31 March 2015.

- Showalter, M. R. *et al.* New satellite of (134340) Pluto: S/2011 (134340). *IAU Circ.* **9221** (2011).
- Weaver, H. *et al.* Discovery of two new satellites of Pluto. *Nature* **439**, 943–945 (2006).
- Showalter, M. R. *et al.* New satellite of (134340) Pluto: S/2012 (134340). *IAU Circ.* **9253** (2012).
- Weaver, H. A. *et al.* New satellite of (134340) Pluto: S/2011 (134340). *IAU Circ.* **9221** (2011).
- Buie, M. W., Grundy, W. M. & Tholen, D. J. Astrometry and orbits of Nix, Kerberos, and Hydra. *Astron. J.* **146**, 152 (2013).
- Brožović, M., Showalter, M. R., Jacobson, R. A. & Buie, M. W. The orbits and masses of satellites of Pluto. *Icarus* **246**, 317–329 (2015).
- Steffl, A. J. *et al.* New satellite of (134340) Pluto: S/2011 (134340). *IAU Circ.* **9221** (2011).
- Lee, M. H. & Peale, S. J. On the orbits and masses of the satellites of the Pluto–Charon system. *Icarus* **184**, 573–583 (2006).
- Buie, M. W. *et al.* Orbits and photometry of Pluto's satellites: Charon, S/2005 P1, and S/2005 P2. *Astron. J.* **132**, 290–298 (2006).
- Sinclair, A. T. The orbital resonance amongst the Galilean satellites of Jupiter. *Mon. Not. R. Astron. Soc.* **171**, 59–72 (1975).
- Rivera, E. J. *et al.* The Lick–Carnegie Exoplanet Survey: a Uranus-mass fourth planet for GJ 876 in an extrasolar Laplace configuration. *Astrophys. J.* **719**, 890–899 (2010).
- Youdin, A. N., Kratter, K. M. & Kenyon, S. J. Circumbinary chaos: using Pluto's newest moon to constrain the masses of Nix and Hydra. *Astrophys. J.* **755**, 17 (2012).
- Quillen, A. C. & French, R. S. Resonant chains and three-body resonances in the closely-packed inner Uranian satellite system. *Mon. Not. R. Astron. Soc.* **445**, 3959–3986 (2014).
- French, R. G., Dawson, R. I. & Showalter, M. R. Resonances, chaos, and short-term interactions among the inner Uranian satellites. *Astron. J.* **149**, 142–169 (2015).
- Canup, R. M. A giant impact origin of Pluto–Charon. *Science* **307**, 546–550 (2005).
- Ward, W. R. & Canup, R. M. Forced resonant migration of Pluto's outer satellites by Charon. *Science* **313**, 1107–1109 (2006).
- Kenyon, S. J. & Bromley, B. C. The formation of Pluto's low-mass satellites. *Astron. J.* **147**, 8–24 (2014).
- Lithwick, Y. & Wu, Y. The effect of Charon's tidal damping on the orbits of Pluto's three moons. Preprint at <http://arxiv.org/abs/0802.2939> (2008).
- Lithwick, Y. & Wu, Y. On the origin of Pluto's minor moons, Nix and Hydra. Preprint at <http://arxiv.org/abs/0802.2951> (2008).
- Walsh, K. & Levison, H. F. Formation and evolution of Pluto's small satellites. Preprint at <http://arxiv.org/abs/1505.01208> (2015).
- Zhang, K. & Hamilton, D. P. Orbital resonances in the inner Neptunian system I. The 2:1 Proteus–Larissa mean-motion resonance. *Icarus* **188**, 386–399 (2007).
- Zhang, K. & Hamilton, D. P. Orbital resonances in the inner Neptunian system II. Resonant history of Proteus, Larissa, Galatea, and Despina. *Icarus* **193**, 267–282 (2008).
- Grundy, W. M., Noll, K. S. & Stephens, D. C. Diverse albedos of small trans-neptunian objects. *Icarus* **176**, 184–191 (2005).
- Lykawka, P. S. & Mukai, T. Higher albedos and size distribution of large transneptunian objects. *Planet. Space Sci.* **53**, 1319–1330 (2005).
- Stansberry, J. *et al.* in *The Solar System beyond Neptune* (eds Barucci, M. A. *et al.*) 161–179 (Univ. Arizona Press, 2007).
- Lacerda, P. *et al.* The albedo–color diversity of transneptunian objects. *Astrophys. J.* **793**, L2 (2014).
- Stern, S. A. Ejecta exchange and satellite color evolution in the Pluto system, with implications for KBOs and asteroids with satellites. *Icarus* **199**, 571–573 (2009).
- Hedman, M. M., Burns, J. A., Thomas, P. C., Tiscareno, M. S. & Evans, M. W. Physical properties of the small moon Aegaeon (Saturn LIII). *Eur. Planet. Space Congr. Abstr.* **6**, 531 (2011).
- Wisdom, J., Peale, S. J. & Mignard, F. The chaotic rotation of Hyperion. *Icarus* **58**, 137–152 (1984).
- Klavetter, J. J. Rotation of Hyperion. I—Observations. *Astron. J.* **97**, 570–579 (1989).
- Dobrovolskis, A. R. Chaotic rotation of Nereid? *Icarus* **118**, 181–198 (1995).
- Buratti, B. J., Gougen, J. D. & Mosher, J. A. No large brightness variations on Nereid. *Icarus* **126**, 225–228 (1997).
- Grav, T., Holman, M. J. & Kavelaars, J. J. The short rotation period of Nereid. *Astrophys. J.* **591**, L71 (2003).
- Giulianti Winter, S. M., Winter, O. C., Vieira Neto, E. & Sfair, R. Stable regions around Pluto. *Mon. Not. R. Astron. Soc.* **430**, 1892–1900 (2013).

Supplementary Information is available in the online version of the paper.

Acknowledgements M.R.S. acknowledges NASA's Outer Planets Research Program for their support through grants NNX12AQ11G and NNX14AO40G. Support for HST programme GO-12436 was provided by NASA through a grant from the Space Telescope Science Institute, which is operated by the Association of Universities for Research in Astronomy, Inc., under NASA contract NAS5-26555. D.P.H. acknowledges NASA Origins Research Program and grant NNX12AI80G.

Author Contributions M.R.S. performed all of the astrometry, photometry, orbit fitting and numerical modelling discussed here. D.P.H. was co-investigator on the Kerberos discovery and has participated in the dynamical interpretations of all the results.

Author Information Reprints and permissions information is available at www.nature.com/reprints. The authors declare no competing financial interests. Readers are welcome to comment on the online version of the paper. Correspondence and requests for materials should be addressed to M.R.S. (mshowalter@seti.org).

METHODS

Data selection and processing. Our data set encompasses all available HST images of the Pluto system during 2006 and 2010–2012, plus Kerberos in 2005. We neglected HST observations from 2002, 2003, and 2007^{5,10}, because they are of generally lower quality, rendering Kerberos and Styx undetectable. We emphasized long exposures through broad-band filters, although brief exposures of Charon and Pluto provided geometric reference points. Supplementary Table 1 lists the images and bodies measured. We analysed the calibrated ('flt') image files. To detect Kerberos and Styx, it was often necessary to align and co-add multiple images from the same visit; files produced in this manner are listed in the table with a 'coadd' suffix.

We fitted a model point spread function (PSF) to each detectable body. The PSFs were generated using the 'Tiny Tim' software maintained by the Space Telescope Science Institute (STScI)^{35,36}. Upon fitting to the image, the centre of the PSF provides the astrometry and the integrated volume under the two-dimensional curve, minus any background offset, is proportional to the disk-integrated photometry. We measured objects in order of decreasing brightness and subtracted each PSF before proceeding; this reduced the effects of glare on fainter objects. Measurements with implausible photometry were rejected; this was generally the result of nearby background stars, cosmic ray hits, or other image flaws. Further details of the analysis are provided elsewhere⁶. Styx photometry (Table 1) might be biased slightly upward by our exclusion of non-detections; however, photometry of the other moons is very robust.

The Pluto–Charon gravity field. We have simplified the central gravity field by taking its time-average. The resulting cylindrically symmetric gravity field can then be expressed using the same expansion in spherical harmonics that is traditionally employed to describe the field of an oblate planet:

$$V(r, \theta, \phi) = -GM/r \left[1 - \sum_{m=2}^{\infty} J_m(R/r)^m P_m(\sin \phi) \right] \quad (1)$$

Here (r, θ, ϕ) are polar coordinates, where r is radius and θ and ϕ are longitude and latitude angles, respectively; G is the gravitation constant, M is the body's mass, R is its equatorial radius, P_m is the m th Legendre polynomial, J_m is the m th coefficient in the expansion. The dependence on θ and the odd m -terms in the series vanish by symmetry. The coefficients J_m can be determined by noting that the potential along the axis of the ring simplifies considerably:

$$V(r, \phi = \pi/2) = -GM/r [1 + (R/r)^2]^{-1/2} \quad (2)$$

This can then be compared to the definition of Legendre polynomials:

$$(1 - 2xt + t^2)^{-1/2} = \sum_{m=0}^{\infty} t^m P_m(x) \quad (3)$$

Substituting $t = (R/r)$ and evaluating the expression for $x = 0$ yields:

$$V(r, \phi = \pi/2) = -GM/r \sum_{m=0}^{\infty} (R/r)^m P_m(0) \quad (4)$$

Noting that $P_m(1) = 1$ for all m , equations (1) and (4) can only be equal if the coefficients J_m are negatives of the Legendre polynomials evaluated at zero: $J_2 = 1/2$, $J_4 = -3/8$, $J_6 = 5/16$, and so on. Given this sequence of coefficients, we can determine n , $\dot{\omega}$ and $\dot{\Omega}$ as functions of semimajor axis a :

$$n^2(a) = GM/a^3 \left[1 - \sum_{m=2}^{\infty} (1+m) J_m(R/a)^m P_m(0) \right] \quad (5a)$$

$$\kappa^2(a) = GM/a^3 \left[1 - \sum_{m=2}^{\infty} (1-m^2) J_m(R/a)^m P_m(0) \right] \quad (5b)$$

$$\nu^2(a) = GM/a^3 \left[1 - \sum_{m=2}^{\infty} (1+m)^2 J_m(R/a)^m P_m(0) \right] \quad (5c)$$

Here κ is the epicyclic frequency and $\dot{\nu}$ is the vertical oscillation frequency. It follows that $\dot{\omega}(a) = n(a) - \kappa(a)$ and $\dot{\Omega}(a) = n(a) - \nu(a)$. In practice, we treated n as the independent variable because it has the strictest observational constraints, and then derived a , $\dot{\omega}$ and $\dot{\Omega}$ from it.

Orbit fitting. We modelled each orbit as a Keplerian ellipse in the P–C frame, but with additional terms to allow for apsidal precession and nodal regression. Our model is accurate to first order in e and i ; any second-order effects can be neglected because they would be minuscule compared to the precision of our measurements.

We also required an estimate for the location of the system barycentre in each set of images. Because HST tracking is extremely precise between consecutive images, the barycentre location was only calculated once per HST orbit. We solved for the barycentre locations first and then held them fixed for subsequent modelling of the orbital elements. Barycentre locations were derived from the astrometry of Pluto, Charon, Nix and Hydra. We locked Pluto and Charon to the latest ephemeris distributed by the Jet Propulsion Laboratory, PLU043⁶. We accounted for the offset between the centre of light and centre of body for Pluto using the latest albedo map³⁷. However, because the number of Pluto and Charon measurements is limited, we also allowed Nix and Hydra to contribute to the solution. For each single year 2006–2012, we solved simultaneously for the barycentre location in each image set and also for orbital elements of Nix and Hydra. For the detection of Kerberos in 2005, the only available pointing reference was Hydra, which we derived from PLU043. By allowing many measurements to contribute to our barycentre determinations, we could improve their quality but also limit any bias introduced by shortcomings of our orbit models. The derived uncertainties in the barycentre locations are much smaller than any remaining sources of error.

A nonlinear least-squares fitter identified the best value for each orbital element and also the covariance matrix, from which uncertainties could be derived. However, as noted in Table 1 and Extended Data Table 1, our RMS residuals (equivalent to the square root of χ^2 per degree of freedom) exceed unity. For Styx and Kerberos, marginal detections probably contributed to the excess; for Nix and Hydra, we have identified the source as the un-modelled wobbles in the orbits. All uncertainty estimates have been scaled upward to accommodate these underestimates.

During the orbit fits, we rejected individual points with excessive residuals, based on the assumption that they were misidentifications or the results of poor PSF fits. Extended Data Table 1 lists values for the number of included (M_1) and rejected (M_0) measurements. Rejecting points, however, would bias our uncertainty estimates downward. We compensated by running Monte Carlo simulations in which we generated $(M_0 + M_1)$ Gaussian distributed, two-dimensional random variables and then rejected the M_0 that fall furthest from the origin. The standard deviation among the remainder then gave us an estimate of the factor by which we might have inadvertently reduced our error bars. With this procedure, accidentally rejecting a small number of valid measurements would not bias the uncertainties.

We also explored the implications of making various assumptions about how the orbital elements are coupled (Extended Data Table 1). For the purposes of this paper, we have adopted the $N = 8$ solutions in which $\dot{\Omega}$ can be derived from n and $\dot{\omega}$. This assumption is helpful because, when e and i are small, the frequencies $\dot{\omega}$ and $\dot{\Omega}$ are especially difficult to measure. By allowing them to be coupled, we obtained more robust results. Nevertheless, our expectation that $\dot{\omega}$ and $\dot{\Omega}$ should be roughly equal in magnitude but opposite in sign has been well supported by most of our uncoupled, $N = 9$ fits.

Resonance analysis. We have defined a general resonance using a set of integer coefficients (p, q, r) . The strength of a resonance is equal to $C(p, q, r) \prod \mu_j \Pi e_j^{q_j} \Pi \sin^{r_j}(i_j)$, where μ_j is the mass ratio of moon j to the mass of Pluto. The first product $\prod \mu_j$ excludes the mass of the smallest moon involved, because a resonance can exist even if one moon is a massless test particle. The function C defines a strength factor, but because it has no simple expression, we ignore it in this analysis except to note, qualitatively, that the strongest resonances tend to involve small coefficients and/or small differences between coefficients.

We performed an exhaustive search for all possible resonances involving up to four non-zero coefficients, with $|p_j| \leq 300$, $|q_j| \leq 4$, and $|r_j| \leq 4$. Symmetry dictates that the coefficients sum to zero and that $\sum r_j$ must be even³⁸. Because Charon follows a circular, equatorial orbit, $q_C = r_C = 0$. We first identified possible resonances by $\dot{\Phi} < 0.1^\circ$ per day, and then followed up by evaluating Φ for each year. Sets of coefficients for which Φ values clustered near 0° or 180° were given preference. We also favoured sets of coefficients that have simple physical interpretations, and where the absolute values were small and/or close to one another.

Orbital integrations. Our orbit simulations employed the numeric integrator SWIFT^{39,40}. We used PLU043⁶ as our reference ephemeris; it provides state vectors (positions and velocities) for all the bodies in the system versus time. For simplicity, we neglected bodies outside the Pluto system in most integrations. The Sun is the dominant external perturber, shifting the moons by a few tens of kilometres, primarily in longitude, after one Pluto orbit of 248 years; this is $<1\%$ of our orbital uncertainties.

Each integration must begin with initial state vectors and masses for each body. However, the state vectors and masses are closely coupled; any change to one mass requires that we adjust all of the state vectors in order to match the observed orbits. Ideally, this would be accomplished by re-fitting to all of the available

astrometry, but that task is beyond the scope of this paper. To simplify the problem, we generated false astrometry derived directly from PLU043, but sampled at the times of all prior HST visits that detected one or more of the four outer moons. Such measurements date back to 11 June 2002^{5,6,9}. For each set of assumed masses, we used a nonlinear least-squares fitter to solve for the initial state vectors that optimally matched this astrometry. A similar technique was used to model the effects of moon masses on the chaotic dynamics of the Uranus system⁴¹. This procedure guarantees that our numeric integrations will match the actual astrometry with reasonable accuracy, regardless of the masses assumed.

For a few numerical experiments, we investigated the consequences of placing Styx exactly into its Laplace-like resonance (Extended Data Figs 2 and 3). We accomplished this by generating a different set of false astrometry, in which the position of Styx was derived from the requirement that $\Phi = 180^\circ$ at all times.

Photometry. Our numerical simulations suggest that typical rotation periods for each moon are comparable to the orbital period, that is, several weeks. Because this timescale is long compared to one or a few of HST's 95-min orbits, we combined measurements obtained from single or adjacent orbits. In Supplementary Table 1, adjacent orbits are indicated by an orbit number of 2 or 3. Our photometry (Fig. 4 and Extended Data Fig. 4) is defined by the mean and standard deviation of all measurements from a single set of orbits.

We considered two simple models for the light curves described as reflectivity A versus time t :

$$A_1(t) = c_0 + c_1 \sin(\omega t) + c_2 \cos(\omega t) \quad (6a)$$

$$A_2(t) = c_0 + c_1 \sin(\omega t) + c_2 \cos(\omega t) + c_3 \sin(2\omega t) + c_4 \cos(2\omega t) \quad (6b)$$

We then sought the frequency ω that minimizes residuals. Given the small number of measurements in individual years, it was inappropriate to attempt more sophisticated models. Results are shown in Extended Data Fig. 6. For the data from 2010, we did identify frequencies where the residuals are especially small, suggesting that we may have identified a rotation rate for that subset of the data. However, in no case does a frequency persist from 2010 to 2012.

Shape modelling. We have described the axial orientation relative to the line of sight using sub-Earth planetocentric latitude ϕ . The hypothetical light curve of an ellipsoid is roughly sinusoidal; its projected cross-section on the sky varies between extremes A_{\min} and A_{\max} . If $\phi = 0$, $A_{\min} = \pi bc$ and $A_{\max} = \pi ac$. If $\phi = 90^\circ$, then $A_{\min} = A_{\max} = \pi ab$. More generally

$$A_{\min}(a, b, c, \phi) = \pi b(c^2 \cos^2 \phi + a^2 \sin^2 \phi)^{1/2} \quad (7a)$$

$$A_{\max}(a, b, c, \phi) = \pi a(c^2 \cos^2 \phi + b^2 \sin^2 \phi)^{1/2} \quad (7b)$$

If ϕ is fixed and each measurement was obtained at a uniformly distributed, random rotational phase, then the conditional probability density function for a cross-section A given A_{\min} and A_{\max} is:

$$P(A|A_{\min}, A_{\max}) \propto (1 - [(A - A_0)/\Delta A]^2)^{-1/2} \quad (8)$$

where $A_0 \equiv (A_{\max} + A_{\min})/2$ and $\Delta A = (A_{\max} - A_{\min})/2$. In reality, each measurement A has an associated uncertainty σ . This has the effect of convolving P with a normal distribution $N(A, \sigma)$, with zero mean and standard deviation σ .

$$P[\sigma](A|A_{\min}, A_{\max}, \sigma) \propto (1 - [(A - A_0)/\Delta A]^2)^{-1/2} \otimes N(A, \sigma) \quad (9)$$

where the \otimes operator represents convolution.

However, simulations show that ϕ varies due to chaotic rotation driven by the central binary (Supplementary Video 1). To simplify this analysis, we have assumed that ϕ was fixed for the whole of each year during which we obtained data, but that changes may have occurred between years; this is generally consistent with the time spans of our data sets (a few months per year) and the infrequency of large pole changes in the simulations. This leads us to define three unknowns: ϕ_{2010} , ϕ_{2011} , and ϕ_{2012} . Because A_{\min} and A_{\max} depend only on $\sin^2 \phi$ and $\cos^2 \phi$, we replace the unknowns ϕ by $S \equiv \sin^2 \phi$ in our analysis.

We have a vector of independent measurements $\mathbf{A} = (A_0, A_1, \dots)$ and uncertainties $\boldsymbol{\sigma} = (\sigma_0, \sigma_1, \dots)$, so the joint, conditional probability of obtaining all our measurements is a product:

$$P(\mathbf{A}|a, b, c, S_{2010}, S_{2011}, S_{2012}) = \prod P[\sigma_k](A_k|A_{\min}(a, b, c, S_{\text{year}(k)}), A_{\max}(a, b, c, S_{\text{year}(k)})) \quad (10)$$

where $\text{year}(k)$ is the year associated with measurement k . Instead, we seek the joint, conditional probability density function $P(a, b, c, S_{2010}, S_{2011}, S_{2012}|\mathbf{A})$. This is a problem in Bayesian analysis:

$$P(a, b, c, S_{2010}, S_{2011}, S_{2012}|\mathbf{A}) = P(\mathbf{A}|a, b, c, S_{2010}, S_{2011}, S_{2012})P(\mathbf{A})/P(a, b, c, S_{2010}, S_{2011}, S_{2012}) \quad (11)$$

Here $P(\mathbf{A})$ and $P(a, b, c, S_{2010}, S_{2011}, S_{2012})$ represent our assumed 'prior probability' distributions for these quantities. We have no prior information about our measurements A_k , so we assume that they are uniformly distributed. The second prior can be broken down as

$$P(a, b, c, S_{2010}, S_{2011}, S_{2012}) = P(a, b, c)P(S_{2010})P(S_{2011})P(S_{2012}) \quad (12)$$

because orientations are independent of shape and of one another. If the pole in each year is randomly distributed over 4π steradians, then $P(\phi) \propto \cos \phi$ and $P(S) \propto S^{-1/2}$.

We model our prior for the shape as $P(a, b, c) = P_1(u)P_2(v)P_3(w)$, where $u \equiv abc$; $v \equiv a/b$; and $w \equiv b/c$. This states that we will regard the ellipsoid's volume and its two axial ratios as statistically independent. We have assumed that $\log(u)$ is uniformly distributed rather than u itself, which implies $P_1(u) \propto 1/u$. Experience with other irregularly shaped planetary objects suggests that large ratios a/b and b/c are disfavoured, with values rarely exceeding 2. After some experimentation, we adopted $P_2(v) \propto 1/v^3$ and $P_3(w) \propto 1/w^3$. Alternative but similar assumptions had little effect on our results.

The above equations provide a complete solution to the joint probability function $P(a, b, c, S_{2010}, S_{2011}, S_{2012})$. We solved for the complete six-dimensional function, represented as a six-dimensional array. Quantities listed in Table 1 were derived as the mean and standard deviation of P along each of its six axes, with S converted back to ϕ . Extended Data Fig. 5 compares the distribution of measurements by year with the reconstructed probability distributions.

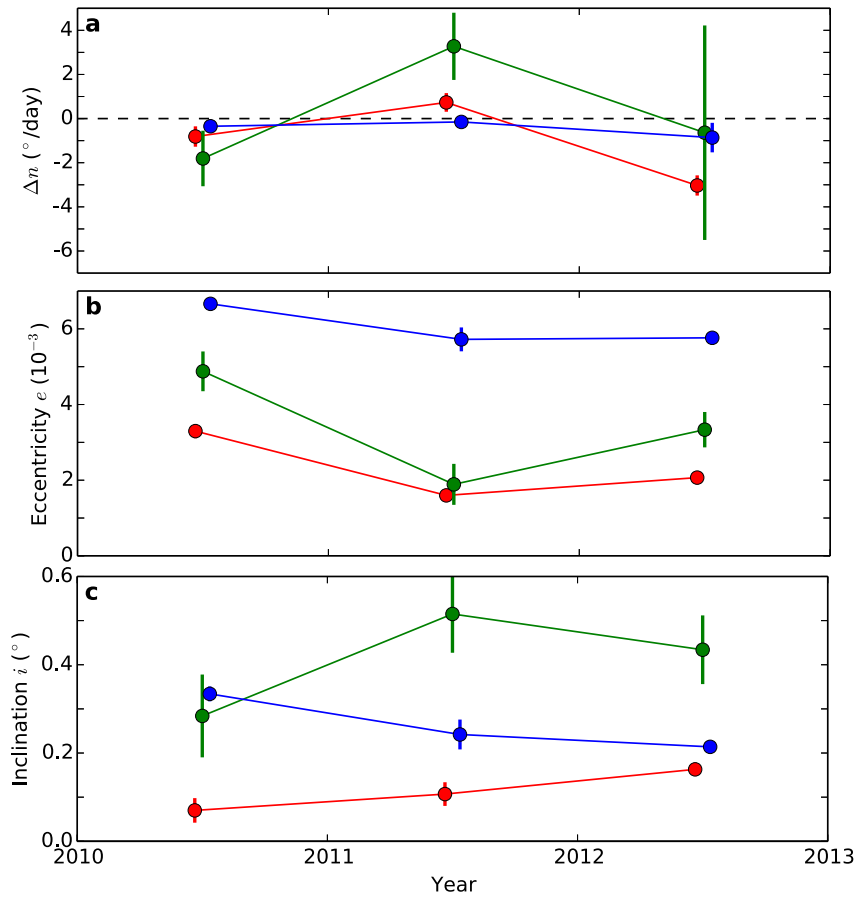
Simulations of rigid body rotation. The orientation of the ellipsoid can be defined by a unit quaternion: $\mathbf{q} = [\cos(\theta/2), \sin(\theta/2)\mathbf{u}]$ represents a rotation by angle θ about unit axis vector \mathbf{u} . The time-derivative $d\mathbf{q}/dt = [0, \boldsymbol{\omega}] \cdot \mathbf{q}/2$, where $\boldsymbol{\omega}$ is the spin vector. We used a Bulirsch–Stoer integrator to track \mathbf{q} , $d\mathbf{q}/dt$, \mathbf{x} and $d\mathbf{x}/dt$, where \mathbf{x} is the position of the ellipsoid relative to the barycentre. The forces and torques acting were defined by Pluto and Charon following fixed circular paths around the barycentre; this motion was pre-defined for the simulations, not integrated numerically. We derived $d^2\mathbf{x}/dt^2$ from the gravity force of each body on the ellipsoid. We also required the second derivative of \mathbf{q} : $d^2\mathbf{q}/dt^2 = [-|\boldsymbol{\omega}|^2/2, \boldsymbol{\alpha}] \cdot \mathbf{q}/2$, where $\boldsymbol{\alpha}$ is the time-derivative of $\boldsymbol{\omega}$. We related $\boldsymbol{\alpha}$ to the torque applied by Pluto and Charon on the ellipsoid

$$\boldsymbol{\tau} = 3GM_P \mathbf{r}_P \times (\mathbf{I} \mathbf{r}_P)/|\mathbf{r}_P|^5 + 3GM_C \mathbf{r}_C \times (\mathbf{I} \mathbf{r}_C)/|\mathbf{r}_C|^5 \quad (13)$$

where $\mathbf{r}_k = \mathbf{x} - \mathbf{x}_k$ is the vector offset from each body centre to the ellipsoid's centre and \mathbf{I} is the ellipsoid's moment of inertia tensor. In the internal frame of the ellipsoid, the moment of inertia tensor I_0 is diagonal, with $I_{11} = (M/5)(b^2 + c^2)$, $I_{22} = (M/5)(a^2 + c^2)$, and $I_{33} = (M/5)(a^2 + b^2)$. It is rotated to the system coordinate frame via the rotation matrix R , which can be calculated from \mathbf{q} : $\mathbf{I} = R I_0 R^T$. We then solve for $\boldsymbol{\alpha}$ via the relation $\boldsymbol{\tau} = \mathbf{I} \boldsymbol{\alpha} + \boldsymbol{\omega} \times \mathbf{I} \boldsymbol{\omega}$.

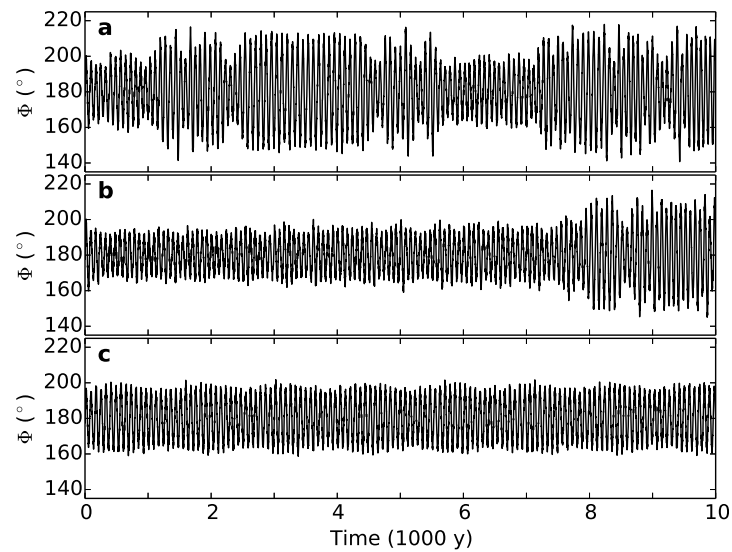
Code availability. Portions of our software are available at <https://github.com/seti/pds-tools>. We have opted not to release the entire source code because it is built on top of additional large libraries representing decades of development. Instead, we have documented our algorithms with sufficient detail to enable others to reproduce our results.

35. Krist, J. E., Hook, R. N. & Stoehr, F. 20 years of Hubble Space Telescope optical modeling using Tiny Tim. *Proc. SPIE* **8127**, 1–16 (2011).
36. Space Telescope Science Institute. *Observatory Support: Tiny Tim HST PSF Modeling* <http://www.stsci.edu/hst/observatory/focus/TinyTim> (2011).
37. Buie, M. W. et al. Pluto and Charon with the Hubble Space Telescope. II. Resolving changes on Pluto's surface and a map for Charon. *Astron. J.* **139**, 1128–1143 (2010).
38. Hamilton, D. P. A comparison of Lorentz, planetary gravitational, and satellite gravitational resonances. *Icarus* **109**, 221–240 (1994).
39. Levison, H. F. & Duncan, M. J. The long-term dynamical behavior of short-period comets. *Icarus* **108**, 18–36 (1994).
40. Levison, H. F. *SWIFT: A Solar System Integration Software Package* <http://www.boulder.swri.edu/~hal/swift.html> (2014).
41. French, R. S. & Showalter, M. R. Cupid is doomed: An analysis of the stability of the inner Uranian satellites. *Icarus* **220**, 911–921 (2012).



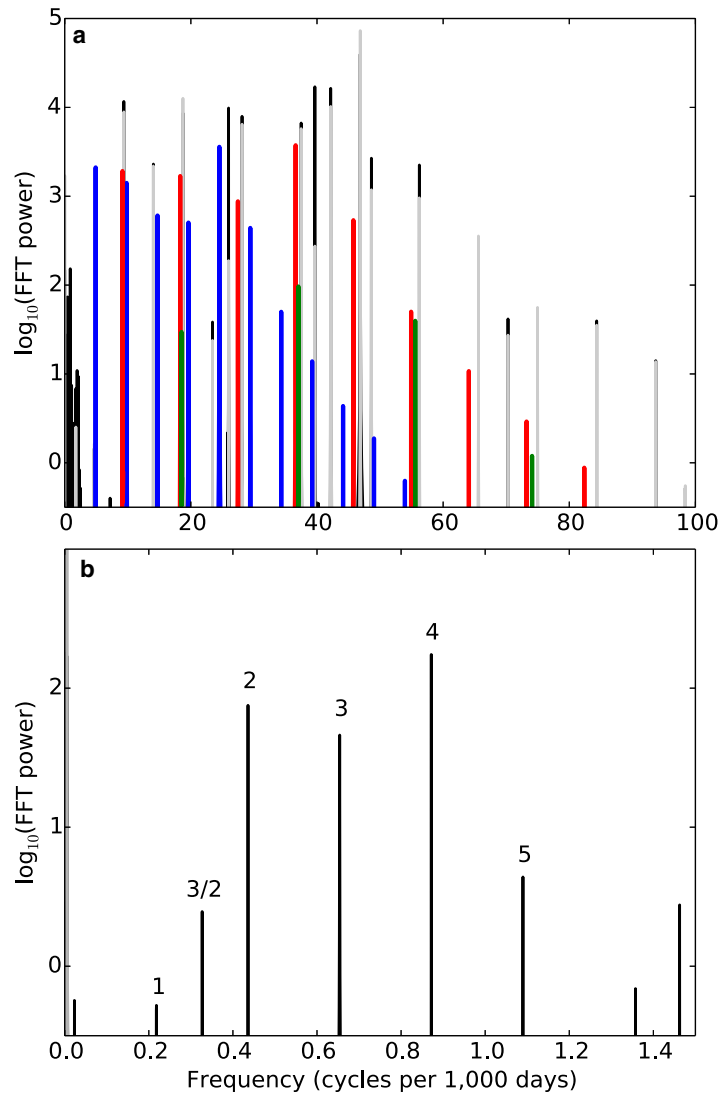
Extended Data Figure 1 | Variations in orbital elements by year. Changes in mean motion (a), eccentricity (b) and inclination (c) are shown during 2010–2012 for Nix (red), Kerberos (green) and Hydra (blue). Vertical bars

are $\pm 1\sigma$. Each individual point is a fit to a single year of data (compare with Extended Data Table 1). In a, Δn is the mean motion of each body minus its average during 2006–2012.



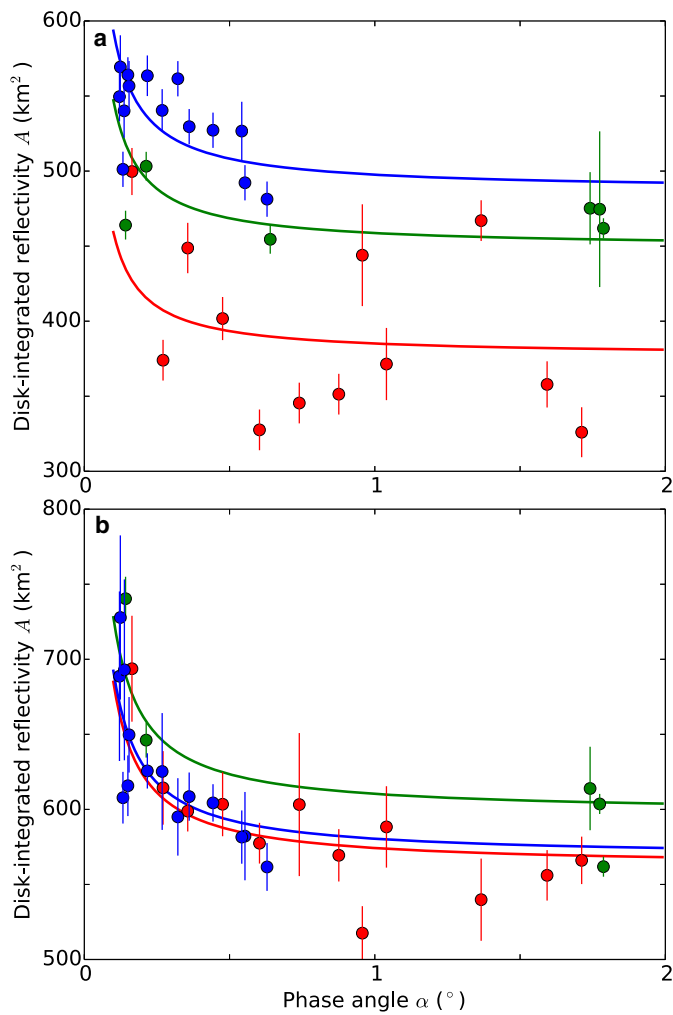
Extended Data Figure 2 | The role of Kerberos in the Laplace-like resonance. We have initiated an integration with Styx exactly in its resonance with Nix and Hydra, and then have allowed it to evolve for 10,000 years. The

diagrams are for M_K nominal (a), M_K reduced by 1σ (b) and $M_K = 0$ (c). The amplitude of the libration is stable when Kerberos is massless, but shows erratic variations otherwise.

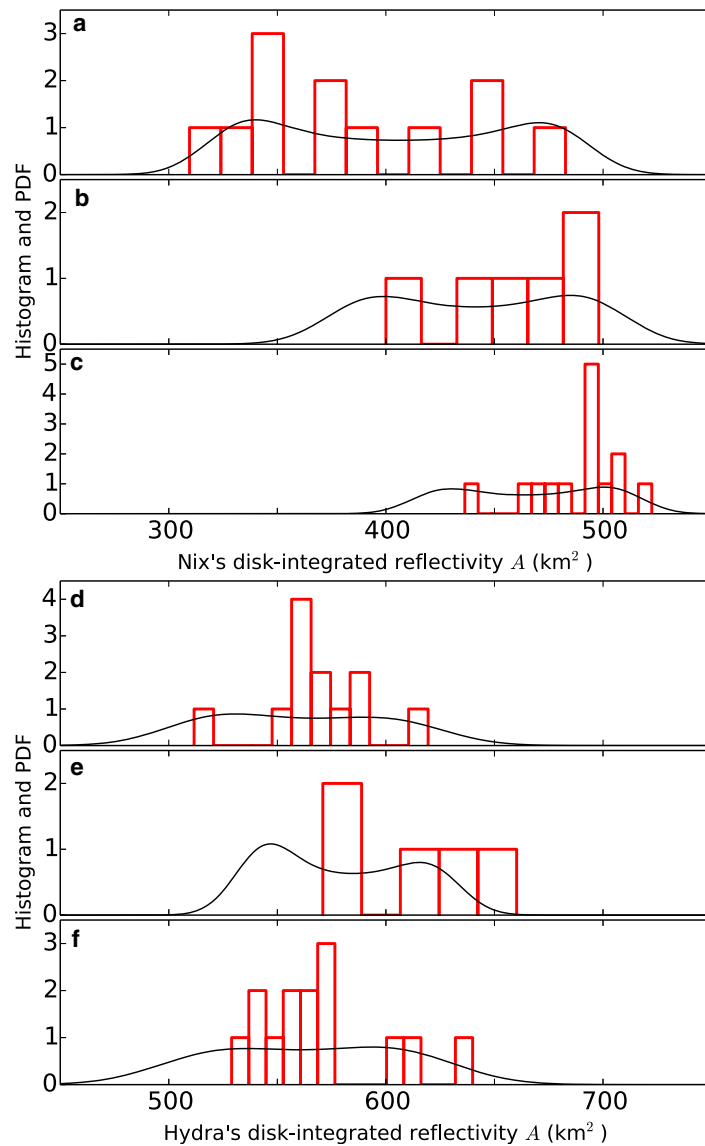


Extended Data Figure 3 | Spectral signatures of Kerberos. We merge Pluto and Charon into a single central body and integrate $\Phi(t)$ for Styx in exact resonance. The fast Fourier transform (FFT) power spectrum for $M_K = 0$ (light grey) obscures the same spectrum obtained when M_K is nominal. Unobscured spikes are caused by Kerberos. **a**, The impulses of Kerberos passing each moon

create a signature at the synodic period and its overtones: $S_{SK} = 53.98$ days (green); $S_{NK} = 109.24$ days (red); $S_{KH} = 203.92$ days (blue). **b**, Harmonics of the second resonance, with period $42S_{NK} \approx 43S_{SN} \approx 4,590$ days, are also visible. The 3/2 harmonic is unexplained.

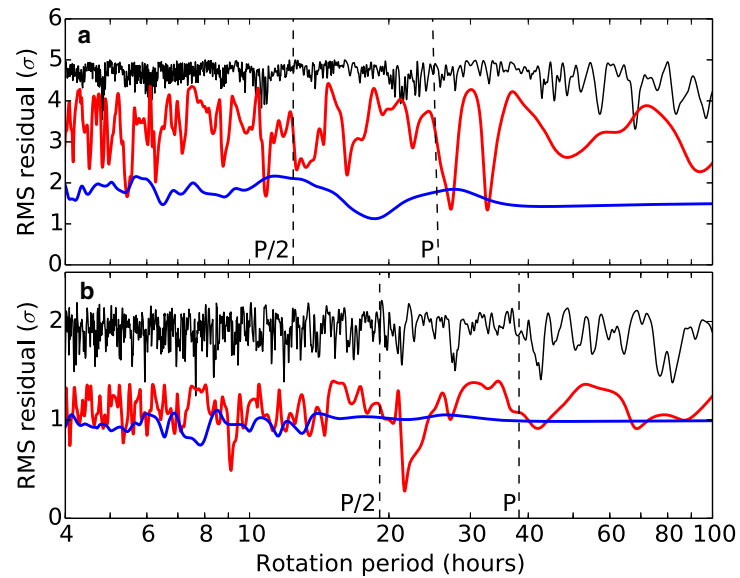


Extended Data Figure 4 | Satellite phase curves. Raw disk-integrated photometry has been plotted versus phase angle α for Nix (a) and Hydra (b). Vertical bars are $\pm 1\sigma$. An opposition surge is apparent. A simple parametric model for the phase curve is shown: $c(1 + d/\alpha)$, where d is fixed but c is scaled to fit each moon during each year. Measurements and curves are colour-coded by year: red for 2010, green for 2011, and blue for 2012.



Extended Data Figure 5 | Distribution of photometric measurements by year. The black curves show the theoretical probability density function (PDF) of A by year for Nix (**a**, 2010; **b**, 2011; **c**, 2012) and Hydra (**d**, 2010; **e**, 2011; **f**, 2012), after convolution with the measurement uncertainties. The histogram

of measurements from each year is shown in red. In spite of small number statistics, the measurements appear to be well described by the models, which have been derived via Bayesian analysis.



Extended Data Figure 6 | Searches for rotation periods in the light curves. We fitted a simple model involving a frequency and its first harmonic to the photometry (see equation (6)) of Nix (a) and Hydra (b). Curves are plotted for data from 2010 (red), 2012 (blue) and for three years 2010–2012 (black). Local

minima with RMS residuals $\lesssim 1$ indicate a plausible fit. The orbital periods and half-periods are identified; if either moon were in synchronous rotation, we would expect to see minima near either P (for albedo variations) or $P/2$ (for irregular shapes).

Extended Data Table 1 | Orbital elements based on coupling various orbital elements and based on subsets of the data.

Moon	Years	N	a (km)	λ_0 (°)	n (°/day)	e (10^{-3})	ω_0 (°)	$\dot{\omega}$ (°/day)	i (°)	Ω_0 (°)	$\dot{\Omega}$ (°/day)	P (days)	P/P_c	RMS (o)	RMS (mas)	RMS (km)	M_1	M_0
Styx	2006–2012	9	42,662	276.8627	17.855814	5.892	296.15	0.49961	0.819	182.64	-0.50097	20.16150	3.156534	1.45	17.9	397	47	19
		±	81	0.0983	0.000255	1.179	9.49	0.02288	0.164	12.60	0.02376	0.00029	0.000050					
Styx	2006–2012	8	42,656	276.8562	17.855770	5.787	296.05	0.50581	0.809	183.36	-0.49187	20.16155	3.156542	1.44	17.8	397	47	19
		±	78	0.0955	0.000235	1.144	9.40	0.01405	0.162	12.50		0.00027	0.000046					
Styx	2006–2012	7	42,484	276.5918	17.855355	1.162	347.19	0.37688	0.381	176.10	-0.36908	20.16202	3.156615	1.79	19.3	429	47	19
		±	82	0.1046	0.000286	1.117	64.15		0.242	27.27		0.00032	0.000052					
Styx	2006–2012	6	42,422	276.5781	17.855333	1.054	7.70	0.37688	0.302	169.14	-0.36908	20.16204	3.156619	1.79	19.1	426	47	19
		±		0.1031	0.000285	1.102	65.26		0.215	33.76		0.00032	0.000052					
Styx	2010	7	43,549	239.9346	17.840396	7.733	138.44	0.37600	2.502	0.88	-0.36824	20.17892	3.159262	1.29	12.9	288	7	4
		±	617	0.2837	0.005338	2.225	16.61		0.894	13.64	0.00604	0.00604	0.000871					
Styx	2011	3	42,383	277.0515	17.807823								3.165041	1.10	16.1	363	12	1
		±		0.1879	0.018868								0.003818					
Styx	2012	7	42,856	332.3448	17.868293	6.915	116.85	0.37763	1.215	11.66	-0.36982	20.14742	3.154330	1.46	19.1	432	26	13
		±	117	0.2178	0.014056	1.712	11.95		0.297	13.73	0.01585	0.01585	0.003199					
Nix	2006–2012	9	48,697	63.8733	14.484221	2.022	220.27	0.19074	0.139	358.77	-0.15203	24.85463	3.891303	2.58	4.22	94	831	27
		±	3	0.0059	0.000015	0.050	1.41	0.00436	0.008	3.41	0.00842	0.00003	0.000004					
Nix	2006–2012	8	48,694	63.8655	14.484222	2.036	221.64	0.18325	0.133	3.73	-0.18096	24.85463	3.891302	2.59	4.25	95	831	27
		±	3	0.0056	0.000015	0.050	1.40	0.00409	0.008	3.40		0.00003	0.000004					
Nix	2006–2012	7	48,696	63.8580	14.484244	2.022	213.64	0.21395	0.133	15.03	-0.21084	24.85459	3.891296	2.65	4.35	97	831	27
		±	3	0.0054	0.000016	0.043	1.15		0.008	3.21	0.00003	0.00003	0.000004					
Nix	2006–2012	6	48,693	63.8573	14.484240	2.030	213.40	0.21395	0.132	13.88	-0.21084	24.85460	3.891297	2.65	4.35	97	831	27
		±		0.0054	0.000016	0.041	1.13		0.008	2.89		0.00003	0.000050					
Nix	2010	7	48,670	177.1349	14.483409	3.297	146.01	0.21392	0.070	319.59	-0.21080	24.85603	3.891521	2.17	4.41	99	85	2
		±	10	0.0158	0.000385	0.143	2.37		0.024	20.48	0.00066	0.00066	0.000100					
Nix	2011	7	48,670	63.8130	14.484954	1.598	229.57	0.21398	0.107	352.81	-0.21086	24.85338	3.891106	2.75	5.22	117	124	11
		±	8	0.0187	0.000346	0.123	4.32		0.023	13.89	0.00059	0.00059	0.000094					
Nix	2012	7	48,704	325.0999	14.481191	2.068	292.10	0.21383	0.163	302.70	-0.21072	24.85983	3.892117	2.35	3.71	84	613	14
		±	4	0.0067	0.000382	0.060	1.27		0.011	3.51	0.00066	0.00066	0.000101					
Kerberos	2005–2012	9	57,832	94.3375	11.191287	3.471	186.59	0.12121	0.356	241.86	-0.20985	32.16788	5.036283	1.27	11.2	248	185	32
		±	20	0.0206	0.000063	0.209	3.58	0.00795	0.037	5.48	0.01302	0.00018	0.000030					
Kerberos	2005–2012	8	57,783	94.3078	11.191398	3.280	187.64	0.11536	0.389	225.15	-0.11419	32.16756	5.036233	1.26	11.2	249	185	32
		±	19	0.0211	0.000050	0.200	3.74	0.00615	0.037	5.43		0.00014	0.000024					
Kerberos	2005–2012	7	57,781	94.3074	11.191394	3.272	187.28	0.10957	0.385	225.17	-0.10851	32.16757	5.036234	1.27	11.3	251	185	32
		±	19	0.0214	0.000050	0.203	3.75		0.037	5.54	0.00014	0.00014	0.000024					
Kerberos	2005–2012	6	57,750	94.3085	11.191397	3.221	187.86	0.10957	0.411	226.88	-0.10851	32.16756	5.036233	1.27	11.2	249	185	32
		±		0.0213	0.000050	0.199	3.79		0.035	4.86		0.00014	0.000024					
Kerberos	2010	7	57,825	329.5189	11.189590	4.877	140.09	0.10953	0.284	298.05	-0.10846	32.17276	5.037046	1.24	8.78	196	30	10
		±	48	0.0542	0.001181	0.481	5.69		0.090	17.99	0.00340	0.00340	0.000561					
Kerberos	2011	7	57,776	94.1883	11.194672	1.890	216.87	0.10965	0.515	250.03	-0.10859	32.15815	5.034760	1.19	6.99	157	30	1
		±	40	0.0680	0.001446	0.497	14.19		0.084	8.23	0.00415	0.00415	0.000652					
Kerberos	2012	7	57,803	230.3510	11.190758	3.335	233.57	0.10955	0.434	172.29	-0.10849	32.16940	5.036521	1.24	12.28	278	119	20
		±	38	0.0418	0.004783	0.423	8.24		0.074	10.08	0.01375	0.01375	0.002352					
Hydra	2006–2012	9	64,741	197.8685	9.423633	5.837	192.40	0.06842	0.244	191.15	-0.08762	38.20183	5.980972	2.73	3.19	71	835	24
		±	3	0.0032	0.000009	0.025	0.26	0.00081	0.005	1.19	0.00317	0.00003	0.000005					
Hydra	2006–2012	8	64,738	197.8662	9.423647	5.862	192.22	0.06986	0.242	189.67	-0.06934	38.20177	5.980963	2.77	3.21	72	835	24
		±	3	0.0032	0.000008	0.025	0.27	0.00080	0.005	1.17		0.00003	0.000005					
Hydra	2006–2012	7	64,738	197.8664	9.423645	5.861	192.04	0.07101	0.242	189.91	-0.07048	38.20178	5.980965	2.77	3.22	72	835	24
		±	3	0.0032	0.000008	0.025	0.24		0.005	1.15	0.00003	0.00003	0.000005					
Hydra	2006–2012	6	64,721	197.8691	9.423638	5.881	192.04	0.07101	0.249	193.12	-0.07048	38.20181	5.980969	2.80	3.25	72	835	24
		±		0.0032	0.000008	0.025	0.24		0.005	0.99		0.00003	0.000005					
Hydra	2010	7	64,730	358.2681	9.423299	6.661	165.04	0.07101	0.334	219.90	-0.07048	38.20318	5.981184	2.77	3.07	69	85	2
		±	8	0.0079	0.000199	0.080	0.63		0.013	2.25	0.00081	0.00081	0.000124					
Hydra	2011	7	64,746	197.8686	9.423495	5.722	192.77	0.07101	0.242	193.93	-0.07048	38.20239	5.981060	2.88	3.24	73	135	12
		±	12	0.0166	0.000157	0.271	2.13		0.030	4.77	0.00064	0.00064	0.000088					
Hydra	2012	7	64,739	46.9262	9.422786	5.763	218.15	0.07100	0.214	157.81	-0.07047	38.20526	5.981510	2.35	2.93	66	606	10
		±	3	0.0033	0.000592	0.050	0.43		0.006	1.91	0.00240	0.00240	0.000379					

Columns M_1 and M_0 identify the numbers of measurements included in and excluded from the fit; N indicates the number of free parameters. When $N = 8$, we derived $\dot{\Omega}$ from the relationship $v^2 = 2n^2 - \kappa^2$. For $N = 7$, $\dot{\omega}$ and $\dot{\Omega}$ were both derived from n and the gravity field using equations (5b) and (5c). For $N = 6$, a was also coupled to n via equation (5a). $N = 3$ indicates a fit to a circular orbit. For fits to single years of data, the epoch is 1 July UTC for that year. We disfavour $N = 7$ in the multi-year fits because some residuals increase markedly.

Observation of the rare $B_s^0 \rightarrow \mu^+ \mu^-$ decay from the combined analysis of CMS and LHCb data

The CMS and LHCb collaborations*

The standard model of particle physics describes the fundamental particles and their interactions via the strong, electromagnetic and weak forces. It provides precise predictions for measurable quantities that can be tested experimentally. The probabilities, or branching fractions, of the strange B meson (B_s^0) and the B^0 meson decaying into two oppositely charged muons (μ^+ and μ^-) are especially interesting because of their sensitivity to theories that extend the standard model. The standard model predicts that the $B_s^0 \rightarrow \mu^+ \mu^-$ and $B^0 \rightarrow \mu^+ \mu^-$ decays are very rare, with about four of the former occurring for every billion B_s^0 mesons produced, and one of the latter occurring for every ten billion B^0 mesons¹. A difference in the observed branching fractions with respect to the predictions of the standard model would provide a direction in which the standard model should be extended. Before the Large Hadron Collider (LHC) at CERN² started operating, no evidence for either decay mode had been found. Upper limits on the branching fractions were an order of magnitude above the standard model predictions. The CMS (Compact Muon Solenoid) and LHCb (Large Hadron Collider beauty) collaborations have performed a joint analysis of the data from proton–proton collisions that they collected in 2011 at a centre-of-mass energy of seven teraelectronvolts and in 2012 at eight teraelectronvolts. Here we report the first observation of the $B_s^0 \rightarrow \mu^+ \mu^-$ decay, with a statistical significance exceeding six standard deviations, and the best measurement so far of its branching fraction. Furthermore, we obtained evidence for the $B^0 \rightarrow \mu^+ \mu^-$ decay with a statistical significance of three standard deviations. Both measurements are statistically compatible with standard model predictions and allow stringent constraints to be placed on theories beyond the standard model. The LHC experiments will resume taking data in 2015, recording proton–proton collisions at a centre-of-mass energy of 13 teraelectronvolts, which will approximately double the production rates of B_s^0 and B^0 mesons and lead to further improvements in the precision of these crucial tests of the standard model.

Experimental particle physicists have been testing the predictions of the standard model of particle physics (SM) with increasing precision since the 1970s. Theoretical developments have kept pace by improving the accuracy of the SM predictions as the experimental results gained in precision. In the course of the past few decades, the SM has passed critical tests derived from experiment, but it does not address some profound questions about the nature of the Universe. For example, the existence of dark matter, which has been confirmed by cosmological data³, is not accommodated by the SM. It also fails to explain the origin of the asymmetry between matter and antimatter, which after the Big Bang led to the survival of the tiny amount of matter currently present in the Universe^{3,4}. Many theories have been proposed to modify the SM to provide solutions to these open questions.

The B_s^0 and B^0 mesons are unstable particles that decay via the weak interaction. The measurement of the branching fractions of the very rare decays of these mesons into a dimuon ($\mu^+ \mu^-$) final state is especially interesting.

At the elementary level, the weak force is composed of a ‘charged current’ and a ‘neutral current’ mediated by the W^\pm and Z^0 bosons,

respectively. An example of the charged current is the decay of the π^+ meson, which consists of an up (u) quark of electrical charge $+2/3$ of the charge of the proton and a down (d) antiquark of charge $+1/3$. A pictorial representation of this process, known as a Feynman diagram, is shown in Fig. 1a. The u and d quarks are ‘first generation’ or lowest mass quarks. Whenever a decay mode is specified in this Letter, the charge conjugate mode is implied.

The B^+ meson is similar to the π^+ , except that the light d antiquark is replaced by the heavy ‘third generation’ (highest mass quarks) beauty (b) antiquark, which has a charge of $+1/3$ and a mass of $\sim 5 \text{ GeV}/c^2$ (about five times the mass of a proton). The decay $B^+ \rightarrow \mu^+ \nu$, represented in Fig. 1b, is allowed but highly suppressed because of angular momentum considerations (helicity suppression) and because it involves transitions between quarks of different generations (CKM suppression), specifically the third and first generations of quarks. All b hadrons, including the B^+ , B_s^0 and B^0 mesons, decay predominantly via the transition of the b antiquark to a ‘second generation’ (intermediate mass quarks) charm (c) antiquark, which is less CKM suppressed, into final states with charmed hadrons. Many allowed decay modes, which typically involve charmed hadrons and other particles, have angular momentum configurations that are not helicity suppressed.

The neutral B_s^0 meson is similar to the B^+ except that the u quark is replaced by a second generation strange (s) quark of charge $-1/3$. The decay of the B_s^0 meson to two muons, shown in Fig. 1c, is forbidden at the elementary level because the Z^0 cannot couple directly to quarks of different flavours, that is, there are no direct ‘flavour changing neutral currents’. However, it is possible to respect this rule and still have this decay occur through ‘higher order’ transitions such as those shown in Fig. 1d and e. These are highly suppressed because each additional interaction vertex reduces their probability of occurring significantly. They are also helicity and CKM suppressed. Consequently, the branching fraction for the $B_s^0 \rightarrow \mu^+ \mu^-$ decay is expected to be very small compared to the dominant b antiquark to c antiquark transitions. The corresponding decay of the B^0 meson, where a d quark replaces the s quark, is even more CKM suppressed because it requires a jump across two quark generations rather than just one.

The branching fractions, \mathcal{B} , of these two decays, accounting for higher-order electromagnetic and strong interaction effects, and using lattice quantum chromodynamics to compute the B_s^0 and B^0 meson decay constants^{5–7}, are reliably calculated¹ in the SM. Their values are $\mathcal{B}(B_s^0 \rightarrow \mu^+ \mu^-)_{\text{SM}} = (3.66 \pm 0.23) \times 10^{-9}$ and $\mathcal{B}(B^0 \rightarrow \mu^+ \mu^-)_{\text{SM}} = (1.06 \pm 0.09) \times 10^{-10}$.

Many theories that seek to go beyond the standard model (BSM) include new phenomena and particles^{8,9}, such as in the diagrams shown in Fig. 1f and g, that can considerably modify the SM branching fractions. In particular, theories with additional Higgs bosons^{10,11} predict possible enhancements to the branching fractions. A significant deviation of either of the two branching fraction measurements from the SM predictions would give insight on how the SM should be extended. Alternatively, a measurement compatible with the SM could provide strong constraints on BSM theories.

*Lists of participants and their affiliations appear in the online version of the paper.

The ratio of the branching fractions of the two decay modes provides powerful discrimination among BSM theories¹². It is predicted in the SM (refs 1, 13 (updates available at <http://itpwiki.unibe.ch/>), 14, 15 (updated results and plots available at <http://www.slac.stanford.edu/xorg/hfag/>)) to be $\mathcal{R} \equiv \mathcal{B}(B^0 \rightarrow \mu^+ \mu^-)_{\text{SM}} / \mathcal{B}(B_s^0 \rightarrow \mu^+ \mu^-)_{\text{SM}} = 0.0295^{+0.0028}_{-0.0025}$. Notably, BSM theories with the property of minimal flavour violation¹⁶ predict the same value as the SM for this ratio.

The first evidence for the decay $B_s^0 \rightarrow \mu^+ \mu^-$ was presented by the LHCb collaboration in 2012¹⁷. Both CMS and LHCb later published results from all data collected in proton–proton collisions at centre-of-mass energies of 7 TeV in 2011 and 8 TeV in 2012. The measurements had comparable precision and were in good agreement^{18,19}, although neither of the individual results had sufficient precision to constitute the first definitive observation of the B_s^0 decay to two muons.

In this Letter, the two sets of data are combined and analysed simultaneously to exploit fully the statistical power of the data and to account for the main correlations between them. The data correspond to total integrated luminosities of 25 fb⁻¹ and 3 fb⁻¹ for the CMS and LHCb experiments, respectively, equivalent to a total of approximately 10¹² B_s^0 and B^0 mesons produced in the two experiments together. Assuming the branching fractions given by the SM and accounting for the detection efficiencies, the predicted numbers of decays to be observed in the two experiments together are about 100 for $B_s^0 \rightarrow \mu^+ \mu^-$ and 10 for $B^0 \rightarrow \mu^+ \mu^-$.

The CMS²⁰ and LHCb²¹ detectors are designed to measure SM phenomena with high precision and search for possible deviations. The two collaborations use different and complementary strategies. In addition to performing a broad range of precision tests of the SM and studying the newly-discovered Higgs boson^{22,23}, CMS is designed to search for and study new particles with masses from about 100 GeV/c² to a few TeV/c². Since many of these new particles would be able to decay into b quarks and many of the SM measurements also involve b quarks, the detection of b -hadron decays was a key element in the design of CMS. The LHCb collaboration has optimized its detector to study matter–antimatter asymmetries and rare decays of particles containing b quarks, aiming to detect deviations from precise SM predictions that would indicate BSM effects. These different approaches, reflected in the design of the detectors, lead to instrumentation of complementary angular regions with respect to the LHC beams, to operation at different proton–proton collision rates, and to selection of b quark events with different efficiency (for experimental details, see Methods). In general, CMS operates at a higher instantaneous luminosity than LHCb but has a lower efficiency for reconstructing low-mass particles, resulting in a similar sensitivity to LHCb for B^0 or B_s^0 (denoted hereafter by $B_{(s)}^0$) mesons decaying into two muons.

Muons do not have strong nuclear interactions and are too massive to emit a substantial fraction of their energy by electromagnetic

radiation. This gives them the unique ability to penetrate dense materials, such as steel, and register signals in detectors embedded deep within them. Both experiments use this characteristic to identify muons.

The experiments follow similar data analysis strategies. Decays compatible with $B_{(s)}^0 \rightarrow \mu^+ \mu^-$ (candidate decays) are found by combining the reconstructed trajectories (tracks) of oppositely charged particles identified as muons. The separation between genuine $B_{(s)}^0 \rightarrow \mu^+ \mu^-$ decays and random combinations of two muons (combinatorial background), most often from semi-leptonic decays of two different b hadrons, is achieved using the dimuon invariant mass, $m_{\mu^+ \mu^-}$, and the established characteristics of $B_{(s)}^0$ -meson decays. For example, because of their lifetimes of about 1.5 ps and their production at the LHC with momenta between a few GeV/c and ~ 100 GeV/c, $B_{(s)}^0$ mesons travel up to a few centimetres before they decay. Therefore, the $B_{(s)}^0 \rightarrow \mu^+ \mu^-$ ‘decay vertex’, from which the muons originate, is required to be displaced with respect to the ‘production vertex’, the point where the two protons collide. Furthermore, the negative of the $B_{(s)}^0$ candidate’s momentum vector is required to point back to the production vertex.

These criteria, amongst others that have some ability to distinguish known signal events from background events, are combined into boosted decision trees (BDTs)^{24–26}. A BDT is an ensemble of decision trees each placing different selection requirements on the individual variables to achieve the best discrimination between ‘signal-like’ and ‘background-like’ events. Both experiments evaluated many variables for their discriminating power and each chose the best set of about ten to be used in its respective BDT. These include variables related to the quality of the reconstructed tracks of the muons; kinematic variables such as transverse momentum (with respect to the beam axis) of the individual muons and of the $B_{(s)}^0$ candidate; variables related to the decay vertex topology and fit quality, such as candidate decay length; and isolation variables, which measure the activity in terms of other particles in the vicinity of the two muons or their displaced vertex. A BDT must be ‘trained’ on collections of known background and signal events to generate the selection requirements on the variables and the weights for each tree. In the case of CMS, the background events used in the training are taken from intervals of dimuon mass above and below the signal region in data, while simulated events are used for the signal. The data are divided into disjoint sub-samples and the BDT trained on one sub-sample is applied to a different sub-sample to avoid any bias. LHCb uses simulated events for background and signal in the training of its BDT. After training, the relevant BDT is applied to each event in the data, returning a single value for the event, with high values being more signal-like. To avoid possible biases, both experiments kept the small mass interval that includes both the B_s^0 and B^0 signals blind until all selection criteria were established.

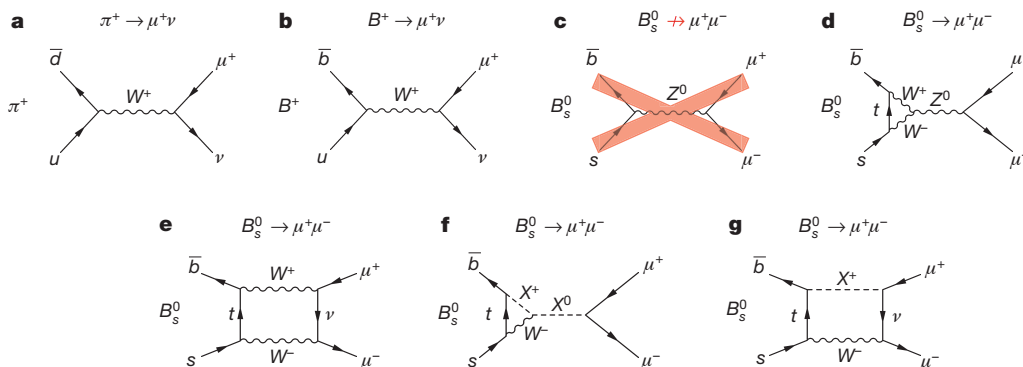


Figure 1 | Feynman diagrams related to the $B_s^0 \rightarrow \mu^+ \mu^-$ decay. **a**, π^+ meson decay through the charged-current process; **b**, B^+ meson decay through the charged-current process; **c**, a B_s^0 decay through the direct flavour changing neutral current process, which is forbidden in the SM, as indicated by a large red

‘X’; **d**, $B_s^0 \rightarrow \mu^+ \mu^-$ decay allowed in the SM; and **e** and **f**, examples of processes for the same decay in theories extending the SM, where new particles, denoted X^0 and X^+ , can alter the decay rate.

In addition to the combinatorial background, specific b -hadron decays, such as $B^0 \rightarrow \pi^- \mu^+ \nu$ where the neutrino cannot be detected and the charged pion is misidentified as a muon, or $B^0 \rightarrow \pi^0 \mu^+ \mu^-$, where the neutral pion in the decay is not reconstructed, can mimic the dimuon decay of the $B_{(s)}^0$ mesons. The invariant mass of the reconstructed dimuon candidate for these processes (semi-leptonic background) is usually smaller than the mass of the $B_{(s)}^0$ or B^0 meson because the neutrino or another particle is not detected. There is also a background component from hadronic two-body $B_{(s)}^0$ decays (peaking background) as $B^0 \rightarrow K^+ \pi^-$, when both hadrons from the decay are misidentified as muons. These misidentified decays can produce peaks in the dimuon invariant-mass spectrum near the expected signal, especially for the $B^0 \rightarrow \mu^+ \mu^-$ decay. Particle identification algorithms are used to minimize the probability that pions and kaons are misidentified as muons, and thus suppress these background sources. Excellent mass resolution is mandatory for distinguishing between B^0 and $B_{(s)}^0$ mesons with a mass difference of about 87 MeV/ c^2 and for separating them from backgrounds. The mass resolution for $B_{(s)}^0 \rightarrow \mu^+ \mu^-$ decays in CMS ranges from 32 to 75 MeV/ c^2 , depending on the direction of the muons relative to the beam axis, while LHCb achieves a uniform mass resolution of about 25 MeV/ c^2 .

The CMS and LHCb data are combined by fitting a common value for each branching fraction to the data from both experiments. The branching fractions are determined from the observed numbers, efficiency-corrected, of $B_{(s)}^0$ mesons that decay into two muons and the total numbers of $B_{(s)}^0$ mesons produced. Both experiments derive the latter from the number of observed $B^+ \rightarrow J/\psi K^+$ decays, whose branching fraction has been precisely measured elsewhere¹⁴. Assuming equal rates for B^+ and B^0 production, this gives the normalization for $B^0 \rightarrow \mu^+ \mu^-$. To derive the number of $B_{(s)}^0$ mesons from this B^+ decay mode, the ratio of b quarks that form (hadronize into) B^+ mesons to those that form $B_{(s)}^0$ mesons is also needed. Measurements of this ratio^{27,28}, for which there is additional discussion in Methods, and of the branching fraction $\mathcal{B}(B^+ \rightarrow J/\psi K^+)$ are used to normalize both sets of data and are constrained within Gaussian uncertainties in the fit. The use of these two results by both CMS and LHCb is the only significant source of correlation between their individual branching fraction measurements. The combined fit takes advantage of the larger data sample to increase the precision while properly accounting for the correlation.

In the simultaneous fit to both the CMS and LHCb data, the branching fractions of the two signal channels are common parameters of interest and are free to vary. Other parameters in the fit are considered as nuisance parameters. Those for which additional knowledge is available are constrained to be near their estimated values by using Gaussian penalties with their estimated uncertainties while the others are free to float in the fit. The ratio of the hadronization probability into B^+ and $B_{(s)}^0$ mesons and the branching fraction of the normalization channel $B^+ \rightarrow J/\psi K^+$ are common, constrained parameters. Candidate decays are categorized according to whether they were detected in CMS or LHCb and to the value of the relevant BDT discriminant. In the case of CMS, they are further categorized according to the data-taking period, and, because of the large variation in mass resolution with angle, whether the muons are both produced at large angles relative to the proton beams (central-region) or at least one muon is emitted at small angle relative to the beams (forward-region). An unbinned extended maximum likelihood fit to the dimuon invariant-mass distribution, in a region of about ± 500 MeV/ c^2 around the $B_{(s)}^0$ mass, is performed simultaneously in all categories (12 categories from CMS and eight from LHCb). Likelihood contours in the plane of the parameters of interest, $\mathcal{B}(B^0 \rightarrow \mu^+ \mu^-)$ versus $\mathcal{B}(B_{(s)}^0 \rightarrow \mu^+ \mu^-)$, are obtained by constructing the test statistic $-2\Delta\ln\mathcal{L}$ from the difference in log-likelihood ($\ln\mathcal{L}$) values between fits with fixed values for the parameters of interest and the nominal fit. For each of the two branching fractions, a one-dimensional profile likelihood scan is likewise obtained by fixing only the single parameter of interest and allowing the other to vary during the fits. Additional fits are performed where the parameters under consideration are the ratio of the branching fractions relative to their SM predictions, $\mathcal{S}_{\text{SM}}^{B_{(s)}^0} \equiv \mathcal{B}(B_{(s)}^0 \rightarrow \mu^+ \mu^-)/\mathcal{B}(B_{(s)}^0 \rightarrow \mu^+ \mu^-)_{\text{SM}}$, or the ratio \mathcal{R} of the two branching fractions.

The combined fit result is shown for all 20 categories in Extended Data Fig. 1. To represent the result of the fit in a single dimuon invariant-mass spectrum, the mass distributions of all categories, weighted according to values of $S/(S+B)$, where S is the expected number of $B_{(s)}^0$ signals and B is the number of background events under the $B_{(s)}^0$ peak in that category, are added together and shown in Fig. 2. The result of the simultaneous fit is overlaid. An alternative representation of the fit to the dimuon invariant-mass distribution for the six

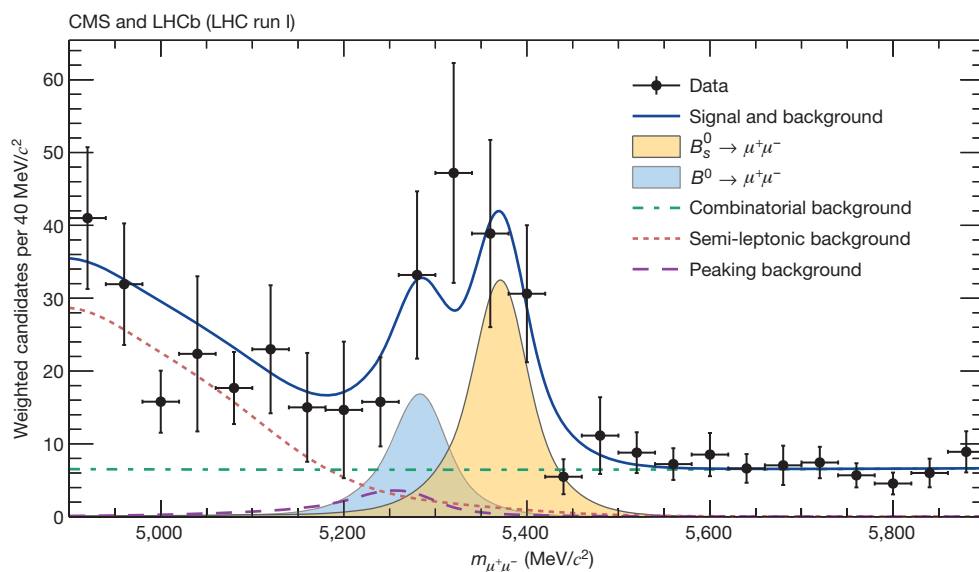


Figure 2 | Weighted distribution of the dimuon invariant mass, $m_{\mu^+\mu^-}$, for all categories. Superimposed on the data points in black are the combined fit (solid blue line) and its components: the $B_{(s)}^0$ (yellow shaded area) and B^0 (light-blue shaded area) signal components; the combinatorial background (dash-dotted green line); the sum of the semi-leptonic backgrounds (dotted salmon

line); and the peaking backgrounds (dashed violet line). The horizontal bar on each histogram point denotes the size of the binning, while the vertical bar denotes the 68% confidence interval. See main text for details on the weighting procedure.

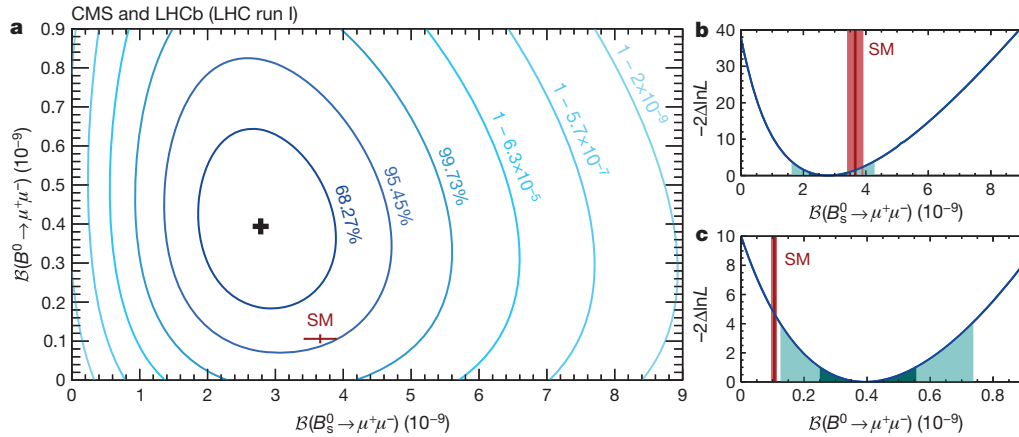


Figure 3 | Likelihood contours in the $B(B^0 \rightarrow \mu^+ \mu^-)$ versus $B(B_s^0 \rightarrow \mu^+ \mu^-)$ plane. The (black) cross in **a** marks the best-fit central value. The SM expectation and its uncertainty is shown as the (red) marker. Each contour encloses a region approximately corresponding to the reported confidence level. **b, c**, Variations of the test statistic $-2\Delta\ln L$ for $B(B_s^0 \rightarrow \mu^+ \mu^-)$ (**b**) and $B(B^0 \rightarrow \mu^+ \mu^-)$ (**c**).

The dark and light (cyan) areas define the $\pm 1\sigma$ and $\pm 2\sigma$ confidence intervals for the branching fraction, respectively. The SM prediction and its uncertainty for each branching fraction is denoted with the vertical (red) band.

categories with the highest $S/(S+B)$ value for CMS and LHCb, as well as displays of events with high probability to be genuine signal decays, are shown in Extended Data Figs 2–4.

The combined fit leads to the measurements $B(B_s^0 \rightarrow \mu^+ \mu^-) = (2.8^{+0.7}_{-0.6}) \times 10^{-9}$ and $B(B^0 \rightarrow \mu^+ \mu^-) = (3.9^{+1.6}_{-1.4}) \times 10^{-10}$, where the uncertainties include both statistical and systematic sources, the latter contributing 35% and 18% of the total uncertainty for the B_s^0 and B^0 signals, respectively. Using Wilks' theorem²⁹, the statistical significance in unit of standard deviations, σ , is computed to be 6.2 for the $B_s^0 \rightarrow \mu^+ \mu^-$ decay mode and 3.2 for the $B^0 \rightarrow \mu^+ \mu^-$ mode. For each signal the null hypothesis that is used to compute the significance includes all background components predicted by the SM as well as the other signal, whose branching fraction is allowed to vary freely. The median expected significances assuming the SM branching fractions are 7.4σ and 0.8σ for the B_s^0 and B^0 modes, respectively. Likelihood contours for $B(B^0 \rightarrow \mu^+ \mu^-)$ versus $B(B_s^0 \rightarrow \mu^+ \mu^-)$ are shown in Fig. 3. One-dimensional likelihood scans for both decay modes are displayed in the same figure. In addition to the likelihood scan, the statistical significance and confidence intervals for the B^0 branching fraction are determined using simulated experiments. This determination yields a significance of 3.0σ for a B^0 signal with respect to the same null hypothesis described above. Following the Feldman–Cousins³⁰ procedure,

$\pm 1\sigma$ and $\pm 2\sigma$ confidence intervals for $B(B^0 \rightarrow \mu^+ \mu^-)$ of $[2.5, 5.6] \times 10^{-10}$ and $[1.4, 7.4] \times 10^{-10}$ are obtained, respectively (see Extended Data Fig. 5).

The fit for the ratios of the branching fractions relative to their SM predictions yields $S_{SM}^{B_s^0} = 0.76^{+0.20}_{-0.18}$ and $S_{SM}^{B^0} = 3.7^{+1.6}_{-1.4}$. Associated likelihood contours and one-dimensional likelihood scans are shown in Extended Data Fig. 6. The measurements are compatible with the SM branching fractions of the $B_s^0 \rightarrow \mu^+ \mu^-$ and $B^0 \rightarrow \mu^+ \mu^-$ decays at the 1.2σ and 2.2σ level, respectively, when computed from the one-dimensional hypothesis tests. Finally, the fit for the ratio of branching fractions yields $\mathcal{R} = 0.14^{+0.08}_{-0.06}$, which is compatible with the SM at the 2.3σ level. The one-dimensional likelihood scan for this parameter is shown in Fig. 4.

The combined analysis of data from CMS and LHCb, taking advantage of their full statistical power, establishes conclusively the existence of the $B_s^0 \rightarrow \mu^+ \mu^-$ decay and provides an improved measurement of its branching fraction. This concludes a search that started more than three decades ago (see Extended Data Fig. 7), and initiates a phase of precision measurements of the properties of this decay. It also produces three standard deviation evidence for the $B^0 \rightarrow \mu^+ \mu^-$ decay. The measured branching fractions of both decays are compatible with SM predictions. This is the first time that the CMS and LHCb collaborations have performed a combined analysis of sets of their data in order to obtain a statistically significant observation.

Online Content Methods, along with any additional Extended Data display items and Source Data, are available in the online version of the paper; references unique to these sections appear only in the online paper.

Received 12 November 2014; accepted 31 March 2015.

Published online 13 May 2015.

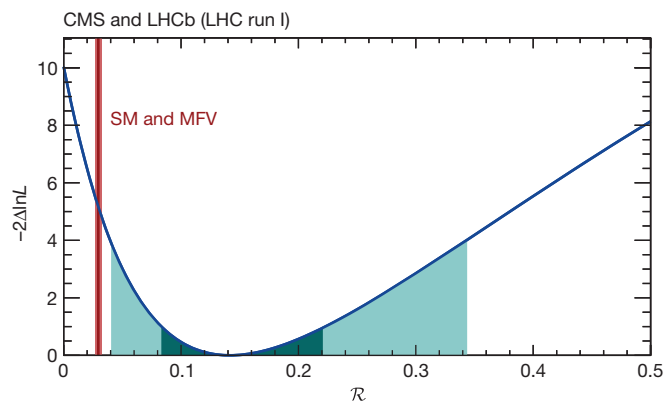


Figure 4 | Variation of the test statistic $-2\Delta\ln L$ as a function of the ratio of branching fractions $\mathcal{R} \equiv B(B^0 \rightarrow \mu^+ \mu^-)/B(B_s^0 \rightarrow \mu^+ \mu^-)$. The dark and light (cyan) areas define the $\pm 1\sigma$ and $\pm 2\sigma$ confidence intervals for \mathcal{R} , respectively. The value and uncertainty for \mathcal{R} predicted in the SM, which is the same in BSM theories with the minimal flavour violation (MFV) property, is denoted with the vertical (red) band.

- Bobeth, C. *et al.* $B_{s,d} \rightarrow l^+ l^-$ in the Standard Model with reduced theoretical uncertainty. *Phys. Rev. Lett.* **112**, 101801 (2014).
- Evans, L. & Bryant, P. LHC machine. *J. Instrum.* **3**, S08001 (2008).
- Planck Collaboration, Ade P. A. R. *et al.* Planck 2013 results. XVI. Cosmological parameters. *Astron. Astrophys.* **571**, A16 (2014).
- Gavela, M., Lozano, M., Orloff, J. & Pène, O. Standard model CP-violation and baryon asymmetry (I). Zero temperature. *Nucl. Phys. B* **430**, 345–381 (1994).
- RBC-UKQCD Collaborations, Witzel, O. B -meson decay constants with domain-wall light quarks and nonperturbatively tuned relativistic b -quarks. Preprint at <http://arxiv.org/abs/1311.0276> (2013).
- HPQCD Collaboration, Na, H. *et al.* B and B_s meson decay constants from lattice QCD. *Phys. Rev. D* **86**, 034506 (2012).
- Fermilab Lattice and MILC Collaborations, Bazavov A. *et al.* B - and D -meson decay constants from three-flavor lattice QCD. *Phys. Rev. D* **85**, 114506 (2012).
- Huang, C.-S., Liao, W. & Yan, Q.-S. The promising process to distinguish supersymmetric models with large $\tan\beta$ from the standard model: $B \rightarrow X_s \mu^+ \mu^-$. *Phys. Rev. D* **59**, 011701 (1998).

9. Rai Choudhury, S. & Gaur, N. Dileptonic decay of B_s meson in SUSY models with large $\tan \beta$. *Phys. Lett. B* **451**, 86–92 (1999).
10. Babu, K. & Kolda, C. F. Higgs-mediated $B^0 \rightarrow \mu^+ \mu^-$ in minimal supersymmetry. *Phys. Rev. Lett.* **84**, 228–231 (2000).
11. Bobeth, C., Ewerth, T., Kruger, F. & Urban, J. Analysis of neutral Higgs-boson contributions to the decays $B_s \rightarrow \ell^+ \ell^-$ and $B \rightarrow K \ell^+ \ell^-$. *Phys. Rev. D* **64**, 074014 (2001).
12. Buras, A. J. Relations between ΔM_{sd} and $B_{sd} \rightarrow \mu \mu$ in models with minimal flavor violation. *Phys. Lett. B* **566**, 115–119 (2003).
13. Aoki, S. *et al.* Review of lattice results concerning low-energy particle physics. *Eur. Phys. J. C* **74**, 2890 (2014).
14. Particle Data Group, Beringer, J. *et al.* Review of particle physics. *Phys. Rev. D* **86**, 010001 (2012); 2013 partial update for the 2014 edition at <http://pdg.lbl.gov>.
15. Heavy Flavor Averaging Group, Amhis, Y. *et al.* Averages of b -hadron, c -hadron, and τ -lepton properties as of early 2012. Preprint at <http://arXiv.org/abs/1207.1158> (2012).
16. D'Ambrosio, G., Giudice, G. F., Isidori, G. & Strumia, A. Minimal flavour violation: an effective field theory approach. *Nucl. Phys. B* **645**, 155–187 (2002).
17. LHCb Collaboration, Aaij, R. *et al.* First evidence for the decay $B_s^0 \rightarrow \mu^+ \mu^-$. *Phys. Rev. Lett.* **110**, 021801 (2013).
18. CMS Collaboration, Chatrchyan, S. *et al.* Measurement of the $B_s^0 \rightarrow \mu^+ \mu^-$ branching fraction and search for $B^0 \rightarrow \mu^+ \mu^-$ with the CMS experiment. *Phys. Rev. Lett.* **111**, 101804 (2013).
19. LHCb Collaboration, Aaij, R. *et al.* Measurement of the $B_s^0 \rightarrow \mu^+ \mu^-$ branching fraction and search for $B^0 \rightarrow \mu^+ \mu^-$ decays at the LHCb experiment. *Phys. Rev. Lett.* **111**, 101805 (2013).
20. CMS Collaboration, Chatrchyan, S. *et al.* The CMS experiment at the CERN LHC. *J. Instrum.* **3**, S08004 (2008).
21. LHCb Collaboration, Alves, A. A. Jr *et al.* The LHCb detector at the LHC. *J. Instrum.* **3**, S08005 (2008).
22. ATLAS Collaboration, Aad, G. *et al.* Observation of a new particle in the search for the Standard Model Higgs boson with the ATLAS detector at the LHC. *Phys. Lett. B* **716**, 1–29 (2012).
23. CMS Collaboration, Chatrchyan, S. *et al.* Observation of a new boson at a mass of 125 GeV with the CMS experiment at the LHC. *Phys. Lett. B* **716**, 30–61 (2012).
24. Breiman, L., Friedman, J. H., Olshen, R. A. & Stone, C. J. *Classification and Regression Trees* (Wadsworth International Group, 1984).
25. Freund, Y. & Schapire, R. E. A decision-theoretic generalization of on-line learning and an application to boosting. *J. Comput. Syst. Sci.* **55**, 119–139 (1997).
26. Hoecker, A. *et al.* TMVA: Toolkit for Multivariate Data Analysis. *Proc. Sci. Adv. Comput. Anal. Techn. Phys. Res.* 040 http://pos.sissa.it/archive/conferences/050/040/ACAT_040.pdf (2007).
27. LHCb Collaboration, Aaij, R. *et al.* Measurement of b hadron production fractions in 7 TeV pp collisions. *Phys. Rev. D* **85**, 032008 (2012).
28. LHCb Collaboration, Aaij, R. *et al.* Measurement of the fragmentation fraction ratio f_s/f_d and its dependence on B meson kinematics. *J. High Energy Phys.* **4**, 1 (2013); updated in <https://cds.cern.ch/record/1559262/files/LHCb-CONF-2013-011.pdf>.
29. Wilks, S. S. The large-sample distribution of the likelihood ratio for testing composite hypotheses. *Ann. Math. Stat.* **9**, 60–62 (1938).
30. Feldman, G. J. & Cousins, R. D. Unified approach to the classical statistical analysis of small signals. *Phys. Rev. D* **57**, 3873–3889 (1998).

Acknowledgements We express our gratitude to colleagues in the CERN accelerator departments for the excellent performance of the LHC. We thank the technical and administrative staff at CERN, at the CMS institutes and at the LHCb institutes. In addition, we gratefully acknowledge the computing centres and personnel of the Worldwide LHC Computing Grid for delivering so effectively the computing infrastructure essential to our analyses. Finally, we acknowledge the enduring support

for the construction and operation of the LHC, the CMS and the LHCb detectors provided by CERN and by many funding agencies. The following agencies provide support for both CMS and LHCb: CAPES, CNPq, FAPERJ and FINEP (Brazil); NSFC (China); CNRS/IN2P3 (France); BMBF, DFG and HGF (Germany); SFI (Ireland); INFN (Italy); NASU (Ukraine); STFC (UK); and NSF (USA). Agencies that provide support for CMS only are BMWF and FWF (Austria); FNRS and FWO (Belgium); FAPESP (Brazil); MES (Bulgaria); CAS and MOST (China); COLCIENCIAS (Colombia); MSES and CSF (Croatia); RPF (Cyprus); MoER, ERC IUT and ERDF (Estonia); Academy of Finland, MEC, and HIP (Finland); CEA (France); GSRT (Greece); OTKA and NIH (Hungary); DAE and DST (India); IPM (Iran); NRF and WCU (Republic of Korea); LAS (Lithuania); MOE and UM (Malaysia); CINVESTAV, CONACYT, SEP, and UASLP-FAI (Mexico); MBIE (New Zealand); PAEC (Pakistan); MSHE and NSC (Poland); FCT (Portugal); JINR (Dubna); MON, RosAtom, RAS and RFBR (Russia); MESTD (Serbia); SEIDI and CPAN (Spain); Swiss Funding Agencies (Switzerland); MST (Taipei); ThEPCenter, IPST, STAR and NSTDA (Thailand); TUBITAK and TAEK (Turkey); SFFR (Ukraine); and DOE (USA). Agencies that provide support for only LHCb are: FINEP (Brazil); MPG (Germany); FOM and NWO (The Netherlands); MNIW and NCN (Poland); MEN/IFA (Romania); MinES and FANO (Russia); MinEco (Spain); SNSF and SER (Switzerland). Individuals from the CMS collaboration have received support from the Marie-Curie programme and the European Research Council and EPLANET (European Union); the Leventis Foundation; the A. P. Sloan Foundation; the Alexander von Humboldt Foundation; the Belgian Federal Science Policy Office; the Fonds pour la Formation à la Recherche dans l'Industrie et dans l'Agriculture (FRIABelgium); the Agentschap voor Innovatie door Wetenschap en Technologie (IWT-Belgium); the Ministry of Education, Youth and Sports (MEYS) of the Czech Republic; the Council of Science and Industrial Research, India; the HOMING PLUS programme of Foundation for Polish Science, cofinanced from European Union, Regional Development Fund; the Compagnia di San Paolo (Torino); the Consorzio per la Fisica (Trieste); MIUR project 20108T4XTM (Italy); the Thales and Aristeia programmes cofinanced by EU-ESF and the Greek NSRF; and the National Priorities Research Program by Qatar National Research Fund. Individual groups or members of the LHCb collaboration have received support from EPLANET, Marie Skłodowska-Curie Actions and ERC (European Union), Conseil général de Haute-Savoie, Labex ENIGMASS and OCEVU, Région Auvergne (France), RFBR (Russia), XuntaGal and GENCAT (Spain), Royal Society and Royal Commission for the Exhibition of 1851 (UK). LHCb is also thankful for the computing resources and the access to software R&D tools provided by Yandex LLC (Russia). The CMS and LHCb collaborations are indebted to the communities behind the multiple open source software packages on which they depend.

Author Contributions All authors have contributed to the publication, being variously involved in the design and the construction of the detectors, in writing software, calibrating sub-systems, operating the detectors and acquiring data and finally analysing the processed data.

Author Information Reprints and permissions information is available at www.nature.com/reprints. The authors declare no competing financial interests. Readers are welcome to comment on the online version of the paper. Correspondence and requests for materials should be addressed to cms-publication-committee-chair@cern.ch and to lhc-b-editorial-board-chair@cern.ch.



This work is licensed under a Creative Commons Attribution-NonCommercial-ShareAlike 3.0 Unported licence. The images or other third party material in this article are included in the article's Creative Commons licence, unless indicated otherwise in the credit line; if the material is not included under the Creative Commons licence, users will need to obtain permission from the licence holder to reproduce the material. To view a copy of this licence, visit <http://creativecommons.org/licenses/by-nc-sa/3.0>

METHODS

Experimental setup. At the Large Hadron Collider (LHC), two counter-rotating beams of protons, contained and guided by superconducting magnets spaced around a 27 km circular tunnel, located approximately 100 m underground near Geneva, Switzerland, are brought into collision at four interaction points (IPs). The study presented in this Letter uses data collected at energies of 3.5 TeV per beam in 2011 and 4 TeV per beam in 2012 by the CMS and LHCb experiments located at two of these IPs.

The CMS and LHCb detectors are both designed to look for phenomena beyond the SM (BSM), but using complementary strategies. The CMS detector²⁰, shown in Extended Data Fig. 3, is optimized to search for yet unknown heavy particles, with masses ranging from 100 GeV/ c^2 to a few TeV/ c^2 , which, if observed, would be a direct manifestation of BSM phenomena. Since many of the hypothesized new particles can decay into particles containing b quarks or into muons, CMS is able to detect efficiently and study B^0 (5,280 MeV/ c^2) and B_s^0 (5,367 MeV/ c^2) mesons decaying to two muons even though it is designed to search for particles with much larger masses. The CMS detector covers a very large range of angles and momenta to reconstruct high-mass states efficiently. To that extent, it employs a 13 m long, 6 m diameter superconducting solenoid magnet, operated at a field of 3.8 T, centred on the IP with its axis along the beam direction and covering both hemispheres. A series of silicon tracking layers, consisting of silicon pixel detectors near the beam and silicon strips farther out, organized in concentric cylinders around the beam, extending to a radius of 1.1 m and terminated on each end by planar detectors (disks) perpendicular to the beam, measures the momentum, angles, and position of charged particles emerging from the collisions. Tracking coverage starts from the direction perpendicular to the beam and extends to within 220 mrad from it on both sides of the IP. The inner three cylinders and disks extending from 4.3 to 10.7 cm in radius transverse to the beam are arrays of $100 \times 150 \mu\text{m}^2$ silicon pixels, which can distinguish the displacement of the b -hadron decays from the primary vertex of the collision. The silicon strips, covering radii from 25 cm to approximately 110 cm, have pitches ranging from 80 to 183 μm . The impact parameter is measured with a precision of 10 μm for transverse momenta of 100 GeV/ c and 20 μm for 10 GeV/ c . The momentum resolution, provided mainly by the silicon strips, changes with the angle relative to the beam direction, resulting in a mass resolution for $B_s^0 \rightarrow \mu^+ \mu^-$ decays that varies from 32 MeV/ c^2 for B_s^0 mesons produced perpendicularly to the proton beams to 75 MeV/ c^2 for those produced at small angles relative to the beam direction. After the tracking system, at a greater distance from the IP, there is a calorimeter that stops (absorbs) all particles except muons and measures their energies. The calorimeter consists of an electromagnetic section followed by a hadronic section. Muons are identified by their ability to penetrate the calorimeter and the steel return yoke of the solenoid magnet and to produce signals in gas-ionization particle detectors located in compartments within the steel yoke. The CMS detector has no capability to discriminate between charged hadron species, pions, kaons, or protons, that is effective at the typical particle momenta in this analysis.

The primary commitment of the LHCb collaboration is the study of particle-antiparticle asymmetries and of rare decays of particles containing b and c quarks. LHCb aims at detecting BSM particles indirectly by measuring their effect on b -hadron properties for which precise SM predictions exist. The production cross section of b hadrons at the LHC is particularly large at small angles relative to the colliding beams. The small-angle region also provides advantages for the detection and reconstruction of a wide range of their decays. The LHCb experiment²¹, shown in Extended Data Fig. 4, instruments the angular interval from 10 to 300 mrad with respect to the beam direction on one side of the interaction region. Its detectors are designed to reconstruct efficiently a wide range of b -hadron decays, resulting in charged pions and kaons, protons, muons, electrons, and photons in the final state. The detector includes a high-precision tracking system consisting of a silicon strip vertex detector, a large-area silicon strip detector located upstream of a dipole magnet characterized by a field integral of 4 T m, and three stations of silicon strip detectors and straw drift tubes downstream of the magnet. The vertex detector has sufficient spatial resolution to distinguish the slight displacement of the weakly decaying b hadron from the primary production vertex where the two protons collided and produced it. The tracking detectors upstream and downstream of the dipole magnet measure the momenta of charged particles. The combined tracking system provides a momentum measurement with an uncertainty that varies from 0.4% at 5 GeV/ c to 0.6% at 100 GeV/ c . This results in an invariant-mass resolution of 25 MeV/ c^2 for B_s^0 mesons decaying to two muons that is nearly independent of the angle with respect to the beam. The impact parameter resolution is smaller than 20 μm for particle tracks with large transverse momentum. Different types of charged hadrons are distinguished by information from two ring-imaging Cherenkov detectors. Photon, electron, and hadron candidates are identified by calorimeters. Muons are identified by a system composed of alternating layers of iron and multiwire proportional chambers.

Neither CMS nor LHCb records all the interactions occurring at its IP because the data storage and analysis costs would be prohibitive. Since most of the interactions are reasonably well characterized (and can be further studied by recording only a small sample of them) specific event filters (known as triggers) select the rare processes that are of interest to the experiments. Both CMS and LHCb implement triggers that specifically select events containing two muons. The triggers of both experiments have a hardware stage, based on information from the calorimeter and muon systems, followed by a software stage, consisting of a large computing cluster that uses all the information from the detector, including the tracking, to make the final selection of events to be recorded for subsequent analysis. Since CMS is designed to look for much heavier objects than B_s^0 mesons, it selects events that contain muons with higher transverse momenta than those selected by LHCb. This eliminates many of the B_s^0 decays while permitting CMS to run at a higher proton-proton collision rate to look for the more rare massive particles. Thus CMS runs at higher collision rates but with lower efficiency than LHCb for B_s^0 mesons decaying to two muons. The overall sensitivity to these decays turns out to be similar in the two experiments.

CMS and LHCb are not the only collaborations to have searched for $B_s^0 \rightarrow \mu^+ \mu^-$ and $B^0 \rightarrow \mu^+ \mu^-$ decays. Over three decades, a total of eleven collaborations have taken part in this search¹⁴, as illustrated by Extended Data Fig. 7. This plot gathers the results from CLEO^{31–35}, ARGUS³⁶, UA1^{37,38}, CDF^{39–44}, L3⁴⁵, DØ^{46–50}, Belle⁵¹, Babar^{52,53}, LHCb^{17,54–57}, CMS^{18,58,59} and ATLAS⁶⁰.

Analysis description. The analysis techniques used to obtain the results presented in this Letter are very similar to those used to obtain the individual result in each collaboration, described in more detail in refs 18, 19. Here only the main analysis steps are reviewed and the changes used in the combined analysis are highlighted. Data samples for this analysis were collected by the two experiments in proton-proton collisions at a centre-of-mass energy of 7 and 8 TeV during 2011 and 2012, respectively. These samples correspond to a total integrated luminosity of 25 and 3 fb^{−1} for the CMS and LHCb experiments, respectively, and represent their complete data sets from the first running period of the LHC.

The trigger criteria were slightly different between the two experiments. The large majority of events were triggered by requirements on one or both muons of the signal decay: the LHCb detector triggered on muons with transverse momentum $p_T > 1.5$ GeV/ c while the CMS detector, because of its geometry and higher instantaneous luminosity, triggered on two muons with $p_T > 4$ (3) GeV/ c , for the leading (sub-leading) muon.

The data analysis procedures in the two experiments follow similar strategies. Pairs of high-quality oppositely charged particle tracks that have one of the expected patterns of hits in the muon detectors are fitted to form a common vertex in three dimensions, which is required to be displaced from the primary interaction vertex (PV) and to have a small χ^2 in the fit. The resulting B_s^0 candidate is further required to point back to the PV, for example, to have a small impact parameter, consistent with zero, with respect to it. The final classification of data events is done in categories of the response of a multivariate discriminant (MVA) combining information from the kinematics and vertex topology of the events. The type of MVA used is a boosted decision tree (BDT)^{24–26}. The branching fractions are then obtained by a fit to the dimuon invariant mass, $m_{\mu^+ \mu^-}$, of all categories simultaneously.

The signals appear as peaks at the B_s^0 and B^0 masses in the invariant-mass distributions, observed over background events. One of the components of the background is combinatorial in nature, as it is due to the random combinations of genuine muons. These produce a smooth dimuon mass distribution in the vicinity of the B_s^0 and B^0 masses, estimated in the fit to the data by extrapolation from the sidebands of the invariant-mass distribution. In addition to the combinatorial background, certain specific b -hadron decays can mimic the signal or contribute to the background in its vicinity. In particular, the semi-leptonic decays $B^0 \rightarrow \pi^- \mu^+ \nu$, $B_s^0 \rightarrow K^- \mu^+ \nu$, and $A_b^0 \rightarrow p \mu^- \bar{\nu}$ can have reconstructed masses that are near the signal if one of the hadrons is misidentified as a muon and is combined with a genuine muon. Similarly the dimuon coming from the rare $B^0 \rightarrow \pi^0 \mu^+ \mu^-$ and $B^+ \rightarrow \pi^+ \mu^+ \mu^-$ decays can also fake the signal. All these background decays, when reconstructed as a dimuon final state, have invariant masses that are lower than the masses of the B^0 and B_s^0 mesons, because they are missing one of the original decay particles. An exception is the decay $A_b^0 \rightarrow p \mu^- \bar{\nu}$, which can also populate, with a smooth mass distribution, higher-mass regions. Furthermore, background due to misidentified hadronic two-body decays $B_s^0 \rightarrow h^+ h'^-$, where $h^{(\prime)} = \pi$ or K , is present when both hadrons are misidentified as muons. These misidentified decays produce an apparent dimuon invariant-mass peak close to the B^0 mass value. Such a peak can mimic a $B^0 \rightarrow \mu^+ \mu^-$ signal and is estimated from control channels and added to the fit.

The distributions of signal in the invariant mass and in the MVA discriminant are derived from simulations with a detailed description of the detector response

for CMS and are calibrated using exclusive two-body hadronic decays in data for LHCb. The distributions for the backgrounds are obtained from simulation with the exception of the combinatorial background. The latter is obtained by interpolating from the data invariant-mass sidebands separately for each category, after the subtraction of the other background components.

To compute the signal branching fractions, the numbers of B_s^0 and B^0 mesons that are produced, as well as the numbers of those that have decayed into a dimuon pair, are needed. The latter numbers are the raw results of this analysis, whereas the former need to be determined from measurements of one or more ‘normalization’ decay channels, which are abundantly produced, have an absolute branching fraction that is already known with good precision, and that share characteristics with the signals, so that their trigger and selection efficiencies do not differ significantly. Both experiments use the $B^+ \rightarrow J/\psi K^+$ decay as a normalization channel with $\mathcal{B}(B^+ \rightarrow J/\psi (\mu^+ \mu^-) K^+) = (6.10 \pm 0.19) \times 10^{-5}$, and LHCb also uses the $B^0 \rightarrow K^+ \pi^-$ channel with $\mathcal{B}(B^0 \rightarrow K^+ \pi^-) = (1.96 \pm 0.05) \times 10^{-5}$. Both branching fraction values are taken from ref. 14. Hence, the $B_s^0 \rightarrow \mu^+ \mu^-$ branching fraction is expressed as a function of the number of signal events ($N_{B_s^0 \rightarrow \mu^+ \mu^-}$) in the data normalized to the numbers of $B^+ \rightarrow J/\psi K^+$ and $B^0 \rightarrow K^+ \pi^-$ events:

$$\mathcal{B}(B_s^0 \rightarrow \mu^+ \mu^-) = \frac{N_{B_s^0 \rightarrow \mu^+ \mu^-}}{N_{\text{norm.}}} \times \frac{f_d}{f_s} \times \frac{\varepsilon_{\text{norm.}}}{\varepsilon_{B_s^0 \rightarrow \mu^+ \mu^-}} \times \mathcal{B}_{\text{norm.}} = \alpha_{\text{norm.}} \times N_{B_s^0 \rightarrow \mu^+ \mu^-} \quad (1)$$

where the ‘norm.’ subscript refers to either of the normalization channels. The values of the normalization parameter $\alpha_{\text{norm.}}$ obtained by LHCb from the two normalization channels are found in good agreement and their weighted average is used. In this formula ε indicates the total event detection efficiency including geometrical acceptance, trigger selection, reconstruction, and analysis selection for the corresponding decay. The f_d/f_s factor is the ratio of the probabilities for a b quark to hadronize into a B^0 as compared to a B_s^0 meson; the probability to hadronize into a B^+ (f_u) is assumed to be equal to that into B^0 (f_d) on the basis of theoretical grounds, and this assumption is checked on data. The value of $f_d/f_s = 3.86 \pm 0.22$ measured by LHCb^{27,28,61} is used in this analysis. As the value of f_d/f_s depends on the kinematic range of the considered particles, which differs between LHCb and CMS, CMS checked this observable with the decays $B_s^0 \rightarrow J/\psi \phi$ and $B^+ \rightarrow J/\psi K^+$ within its acceptance, finding a consistent value. An additional systematic uncertainty of 5% was assigned to f_d/f_s to account for the extrapolation of the LHCb result to the CMS acceptance. An analogous formula to that in equation (1) holds for the normalization of the $B^0 \rightarrow \mu^+ \mu^-$ decay, with the notable difference that the f_d/f_s factor is replaced by $f_d/f_u = 1$.

The antiparticle \bar{B}^0 (\bar{B}_s^0) and the particle B^0 (B_s^0) can both decay into two muons and no attempt is made in this analysis to determine whether the antiparticle or particle was produced (untagged method). However, the B^0 and B_s^0 particles are known to oscillate, that is to transform continuously into their antiparticles and vice versa. Therefore, a quantum superposition of particle and antiparticle states propagates in the laboratory before decaying. This superposition can be described by two ‘mass eigenstates’, which are symmetric and antisymmetric in the charge-parity (CP) quantum number, and have slightly different masses. In the SM, the heavy eigenstate can decay into two muons, whereas the light eigenstate cannot without violating the CP quantum number conservation. In BSM models, this is not necessarily the case. In addition to their masses, the two eigenstates of the B_s^0 system also differ in their lifetime values¹⁴. The lifetimes of the light and heavy eigenstates are also different from the average B_s^0 lifetime, which is used by CMS and LHCb in the simulations of signal decays. Since the information on the displacement of the secondary decay with respect to the PV is used as a discriminant against combinatorial background in the analysis, the efficiency versus lifetime has a model-dependent bias⁶² that must be removed. This bias is estimated assuming SM dynamics. Owing to the smaller difference between the lifetime of its heavy and light mass eigenstates, no correction is required for the B^0 decay mode.

Detector simulations are needed by both CMS and LHCb. CMS relies on simulated events to determine resolutions and trigger and reconstruction efficiencies, and to provide the signal sample for training the BDT. The dimuon mass resolution given by the simulation is validated using data on J/ψ , Y , and Z -boson decays to two muons. The tracking and trigger efficiencies obtained from the simulation are checked using special control samples from data. The LHCb analysis is designed to minimize the impact of discrepancies between simulations and data. The mass resolution is measured with data. The distribution of the BDT for the signal and for the background is also calibrated with data using control channels and mass sidebands. The efficiency ratio for the trigger is also largely determined from data. The simulations are used to determine the efficiency ratios of selection and reconstruction processes between signal and normalization channels. As for the overall detector simulation, each experiment has a team dedicated to making the simulations as complete and realistic as possible. The simulated data are constantly being compared to the

actual data. Agreement between simulation and data in both experiments is quite good, often extending well beyond the cores of distributions. Differences occur because, for example, of incomplete description of the material of the detectors, approximations made to keep the computer time manageable, residual uncertainties in calibration and alignment, and discrepancies or limitations in the underlying theory and experimental data used to model the relevant collisions and decays. Small differences between simulation and data that are known to have an impact on the result are treated either by reweighting the simulations to match the data or by assigning appropriate systematic uncertainties.

Small changes are made to the analysis procedure with respect to refs 18, 19 in order to achieve a consistent combination between the two experiments. In the LHCb analysis, the $A_b^0 \rightarrow p \mu^- \bar{\nu}$ background component, which was not included in the fit for the previous result but whose effect was accounted for as an additional systematic uncertainty, is now included in the standard fit. The following modifications are made to the CMS analysis: the $A_b^0 \rightarrow p \mu^- \bar{\nu}$ branching fraction is updated to a more recent prediction^{63,64} of $\mathcal{B}(A_b^0 \rightarrow p \mu^- \bar{\nu}) = (4.94 \pm 2.19) \times 10^{-4}$; the phase space model of the decay $A_b^0 \rightarrow p \mu^- \bar{\nu}$ is changed to a more appropriate semi-leptonic decay model⁶⁵; and the decay time bias correction for the B_s^0 , previously absent from the analysis, is now calculated and applied with a different correction for each category of the multivariate discriminant.

These modifications result in changes in the individual results of each experiment. The modified CMS analysis, applied on the CMS data, yields

$$\mathcal{B}(B_s^0 \rightarrow \mu^+ \mu^-) = (2.8^{+1.1}_{-0.9}) \times 10^{-9} \quad \text{and} \quad \mathcal{B}(B^0 \rightarrow \mu^+ \mu^-) = (4.4^{+2.2}_{-1.9}) \times 10^{-10} \quad (2)$$

while the LHCb results change to

$$\mathcal{B}(B_s^0 \rightarrow \mu^+ \mu^-) = (2.7^{+1.1}_{-0.9}) \times 10^{-9} \quad \text{and} \quad \mathcal{B}(B^0 \rightarrow \mu^+ \mu^-) = (3.3^{+2.4}_{-2.1}) \times 10^{-10} \quad (3)$$

These results are only slightly different from the published ones and are in agreement with each other.

Simultaneous fit. The goal of the analysis presented in this Letter is to combine the full data sets of the two experiments to reduce the uncertainties on the branching fractions of the signal decays obtained from the individual determinations. A simultaneous unbinned extended maximum likelihood fit is performed to the data of the two experiments, using the invariant-mass distributions of all 20 MVA discriminant categories of both experiments. The invariant-mass distributions are defined in the dimuon mass ranges $m_{\mu^+ \mu^-} \in [4.9, 5.9] \text{ GeV}/c^2$ and $[4.9, 6.0] \text{ GeV}/c^2$ for the CMS and LHCb experiments, respectively. The branching fractions of the signal decays, the hadronization fraction ratio f_d/f_s , and the branching fraction of the normalization channel $B^+ \rightarrow J/\psi K^+$ are treated as common parameters. The value of the $B^+ \rightarrow J/\psi K^+$ branching fraction is the combination of results from five different experiments¹⁴, taking advantage of all their data to achieve the most precise input parameters for this analysis. The combined fit takes advantage of the larger data sample and proper treatment of the correlations between the individual measurements to increase the precision and reliability of the result, respectively.

Fit parameters, other than those of primary physics interest, whose limited knowledge affects the results, are called ‘nuisance parameters’. In particular, systematic uncertainties are modelled by introducing nuisance parameters into the statistical model and allowing them to vary in the fit; those for which additional knowledge is present are constrained using Gaussian distributions. The mean and standard deviation of these distributions are set to the central value and uncertainty obtained either from other measurements or from control channels. The statistical component of the final uncertainty on the branching fractions is obtained by repeating the fit after fixing all of the constrained nuisance parameters to their best fitted values. The systematic component is then calculated by subtracting in quadrature the statistical component from the total uncertainty. In addition to the free fit, a two-dimensional likelihood ratio scan in the plane $\mathcal{B}(B^0 \rightarrow \mu^+ \mu^-)$ versus $\mathcal{B}(B_s^0 \rightarrow \mu^+ \mu^-)$ is performed.

Feldman–Cousins confidence interval. The Feldman–Cousins likelihood ratio ordering procedure³⁰ is a unified frequentist method to construct single- and double-sided confidence intervals for parameters of a given model adapted to the data. It provides a natural transition between single-sided confidence intervals, used to define upper or lower limits, and double-sided ones. Since the single-experiment results^{18,19} showed that the $B^0 \rightarrow \mu^+ \mu^-$ signal is at the edge of the probability region customarily used to assert statistically significant evidence for a result, a Feldman–Cousins procedure is performed. This allows a more reliable determination of the confidence interval and significance of this signal without the assumptions required for the use of Wilks’ theorem. In addition, a prescription for the treatment of nuisance parameters has to be chosen because scanning the whole parameter space in the presence of more than a few parameters is computationally too intensive. In this case the procedure described by the ATLAS and CMS Higgs combination group⁶⁵ is adopted. For each point of the space of the relevant parameters, the nuisance parameters are fixed to their best value estimated by the mean

of a maximum likelihood fit to the data with the value of $\mathcal{B}(B^0 \rightarrow \mu^+ \mu^-)$ fixed and all nuisance parameters profiled with Gaussian penalties. Sampling distributions are constructed for each tested point of the parameter of interest by generating simulated experiments and performing maximum likelihood fits in which the Gaussian mean values of the external constraints on the nuisance parameters are randomized around the best-fit values for the nuisance parameters used to generate the simulated experiments. The sampling distribution is constructed from the distribution of the negative log-likelihood ratio evaluated on the simulated experiments by performing one likelihood fit in which the value of $\mathcal{B}(B^0 \rightarrow \mu^+ \mu^-)$ is free to float and another with the $\mathcal{B}(B^0 \rightarrow \mu^+ \mu^-)$ fixed to the tested point value. This sampling distribution is then converted to a confidence level by evaluating the fraction of simulated experiments entries with a value for the negative log-likelihood ratio greater than or equal to the value observed in the data for each tested point. The results of this procedure are shown in Extended Data Fig. 5.

31. CLEO Collaboration, Giles R. *et al.* Two-body decays of B mesons. *Phys. Rev. D* **30**, 2279–2294 (1984).
32. CLEO Collaboration, Avery P. *et al.* Limits on rare exclusive decays of B mesons. *Phys. Lett. B* **183**, 429–433 (1987).
33. CLEO Collaboration, Avery P. *et al.* A search for exclusive penguin decays of B mesons. *Phys. Lett. B* **223**, 470–475 (1989).
34. CLEO Collaboration, Ammar R. *et al.* Search for B^0 decays to two charged leptons. *Phys. Rev. D* **49**, 5701–5704 (1994).
35. CLEO Collaboration, Bergfeld T. *et al.* Search for decays of B^0 mesons into pairs of leptons: $B^0 \rightarrow e^+ e^-$, $B^0 \rightarrow \mu^+ \mu^-$ and $B^0 \rightarrow e^\pm \mu^\mp$. *Phys. Rev. D* **62**, 091102 (2000).
36. ARGUS Collaboration, Albrecht H. *et al.* B meson decays into charmonium states. *Phys. Lett. B* **199**, 451–456 (1987).
37. UA1 Collaboration, Albajar C. *et al.* Low mass dimuon production at the CERN proton-antiproton collider. *Phys. Lett. B* **209**, 397–406 (1988).
38. UA1 Collaboration, Albajar C. *et al.* A search for rare B meson decays at the CERN SppS collider. *Phys. Lett. B* **262**, 163–170 (1991).
39. CDF Collaboration, Abe F. *et al.* Search for flavor-changing neutral current B meson decays in $p\bar{p}$ collisions at $\sqrt{s} = 1.8$ TeV. *Phys. Rev. Lett.* **76**, 4675–4680 (1996).
40. CDF Collaboration, Abe F. *et al.* Search for the decays $B_d^0 \rightarrow \mu^+ \mu^-$ and $B_s^0 \rightarrow \mu^+ \mu^-$ in $p\bar{p}$ collisions at $\sqrt{s} = 1.8$ TeV. *Phys. Rev. D* **57**, 3811–3816 (1998).
41. CDF Collaboration, Acosta D. *et al.* Search for $B_s^0 \rightarrow \mu^+ \mu^-$ and $B_d^0 \rightarrow \mu^+ \mu^-$ decays in $p\bar{p}$ collisions at $\sqrt{s} = 1.96$ TeV. *Phys. Rev. Lett.* **93**, 032001 (2004).
42. CDF Collaboration, Abulencia A. *et al.* Search for $B_s \rightarrow \mu^+ \mu^-$ and $B_d \rightarrow \mu^+ \mu^-$ decays in $p\bar{p}$ collisions with CDF II. *Phys. Rev. Lett.* **95**, 221805 (2005).
43. CDF Collaboration, Aaltonen T. *et al.* Search for $B_s \rightarrow \mu^+ \mu^-$ and $B_d \rightarrow \mu^+ \mu^-$ decays with CDF II. *Phys. Rev. Lett.* **107**, 191801 (2011).
44. CDF Collaboration, Aaltonen T. *et al.* Search for $B_s \rightarrow \mu^+ \mu^-$ and $B_d \rightarrow \mu^+ \mu^-$ decays with the full CDF Run II data set. *Phys. Rev. D* **87**, 072003 (2013).
45. L3 Collaboration, Acciarri M. *et al.* Search for neutral B meson decays to two charged leptons. *Phys. Lett. B* **391**, 474–480 (1997).
46. DØ Collaboration, Abbott B. *et al.* Search for the decay $b \rightarrow X_s \mu^+ \mu^-$. *Phys. Lett. B* **423**, 419–426 (1998).
47. DØ Collaboration, Abazov V. *et al.* A search for the flavor-changing neutral current decay $B_s^0 \rightarrow \mu^+ \mu^-$ in $p\bar{p}$ collisions at $\sqrt{s} = 1.96$ TeV with the DØ detector. *Phys. Rev. Lett.* **94**, 071802 (2005).
48. DØ Collaboration, Abazov V. M. *et al.* Search for $B_s^0 \rightarrow \mu^+ \mu^-$ at DØ. *Phys. Rev. D* **76**, 092001 (2007).
49. DØ Collaboration, Abazov V. M. *et al.* Search for the rare decay $B_s^0 \rightarrow \mu^+ \mu^-$. *Phys. Lett. B* **693**, 539–544 (2010).
50. DØ Collaboration, Abazov V. M. *et al.* Search for the rare decay $B_s^0 \rightarrow \mu^+ \mu^-$. *Phys. Rev. D* **87**, 072006 (2013).
51. BELLE Collaboration, Chang M. *et al.* Search for $B^0 \rightarrow \ell^+ \ell^-$ at BELLE. *Phys. Rev. D* **68**, 111101 (2003).
52. BaBar Collaboration, Aubert B. *et al.* Search for decays of B^0 mesons into pairs of charged leptons: $B^0 \rightarrow e^+ e^-$, $B^0 \rightarrow \mu^+ \mu^-$, $B^0 \rightarrow e^\pm \mu^\mp$. *Phys. Rev. Lett.* **94**, 221803 (2005).
53. BaBar Collaboration, Aubert B. *et al.* Search for decays of B^0 mesons into $e^+ e^-$, $\mu^+ \mu^-$, and $e^\pm \mu^\mp$ final states. *Phys. Rev. D* **77**, 032007 (2008).
54. LHCb Collaboration, Aaij R. *et al.* Search for the rare decays $B_s^0 \rightarrow \mu^+ \mu^-$ and $B^0 \rightarrow \mu^+ \mu^-$. *Phys. Lett. B* **699**, 330–340 (2011).
55. LHCb Collaboration, Aaij R. *et al.* Strong constraints on the rare decays $B_s^0 \rightarrow \mu^+ \mu^-$ and $B^0 \rightarrow \mu^+ \mu^-$. *Phys. Rev. Lett.* **108**, 231801 (2012).
56. LHCb Collaboration, Aaij R. *et al.* Search for the rare decays $B_s^0 \rightarrow \mu^+ \mu^-$ and $B^0 \rightarrow \mu^+ \mu^-$. *Phys. Lett. B* **708**, 55–67 (2012).
57. LHCb Collaboration, Aaij R. *et al.* Measurement of the $B_s^0 \rightarrow \mu^+ \mu^-$ branching fraction and search for $B^0 \rightarrow \mu^+ \mu^-$ decays at the LHCb experiment. *Phys. Rev. Lett.* **111**, 101805 (2013).
58. CMS Collaboration, Chatrchyan S. *et al.* Search for $B_s^0 \rightarrow \mu^+ \mu^-$ and $B^0 \rightarrow \mu^+ \mu^-$ decays in pp collisions at 7 TeV. *Phys. Rev. Lett.* **107**, 191802 (2011).
59. CMS Collaboration, Chatrchyan S. *et al.* Search for $B_s^0 \rightarrow \mu^+ \mu^-$ and $B^0 \rightarrow \mu^+ \mu^-$ decays. *J. High Energy Phys.* **04**, 033 (2012).
60. ATLAS Collaboration, Aad G. *et al.* Search for the decay $B_s^0 \rightarrow \mu^+ \mu^-$ with the ATLAS detector. *Phys. Lett. B* **713**, 387–407 (2012).
61. LHCb Collaboration, Aaij R. *et al.* Updated average f_s/f_d b -hadron production fraction ratio for 7 TeV pp collisions. <http://cds.cern.ch/record/1559262> (LHCb-CONF-2013-011, 2013).
62. De Bruyn, K. *et al.* Probing new physics via the $B_s^0 \rightarrow \mu^+ \mu^-$ effective lifetime. *Phys. Rev. Lett.* **109**, 041801 (2012).
63. Khodjamirian, A., Klein, C., Mannel, T. & Wang, Y.-M. Form factors and strong couplings of heavy baryons from QCD light-cone sum rules. *J. High Energy Phys.* **09**, 106 (2011).
64. LHCb Collaboration, Aaij R. *et al.* Precision measurement of the ratio of the \mathcal{A}_b^0 to \bar{B}^0 lifetimes. *Phys. Lett. B* **734**, 122–130 (2014).
65. ATLAS and CMS Collaborations. Procedure for the LHC Higgs boson search combination in summer 2011. <http://cds.cern.ch/record/1379837> (ATL-PHYS-PUB-2011-011, CMS NOTE 2011/005, 2011).

CMS Collaboration

- V. Khachatryan¹, A.M. Sirunyan¹, A. Tumasyan¹, W. Adam², T. Bergauer², M. Dragicic², J. Erö², M. Friedl², R. Frühwirth^{2,204}, V.M. Gheze², C. Hartl², N. Hörmann², J. Hrubec², M. Jeitler^{2,204}, W. Kiesenhofer², V. Knünz², M. Krammer^{2,204}, I. Krätschmer², D. Liko², I. Mikulec², D. Rabady^{2,205}, B. Rahbaran², H. Rohringer², R. Schöfbeck², J. Strauss², W. Treiber-Treberspurg², W. Waltenberger², C.-E. Wulz^{2,204}, V. Mossolov², N. Shumeiko³, J. Suarez Gonzalez³, S. Alderweireldt⁴, S. Bansal⁴, T. Cornelis⁴, E.A. De Wolf⁴, J. Janssen⁴, A. Knutsson⁴, J. Lauwers⁴, S. Luyckx⁴, S. Ochesanu⁴, R. Rougny⁴, M. Van De Klundert⁴, H. Van Haevermaet⁴, P. Van Mechelen⁴, N. Van Remortel⁴, A. Van Spilbeeck⁴, F. Blekman⁵, S. Blyweert⁵, J. D'Hondt⁵, N. Daci⁵, N. Heracleous⁵, J. Keaveney⁵, S. Lowette⁵, M. Maes⁵, A. Olbrechts⁵, Q. Python⁵, D. Strom⁵, S. Tavernier⁵, W. Van Doninck⁵, P. Van Mulders⁵, G.P. Van Onsem⁵, I. Villella⁵, C. Caillol⁶, B. Clerbaux⁶, G. De Lentdecker⁶, D. Dobur⁶, L. Favart⁶, A.P.R. Gay⁶, A. Grebenyuk⁶, A. Léonard⁶, A. Mohammadi⁶, L. Pernie^{6,205}, A. Randle-conde⁶, T. Reis⁶, T. Seva⁶, L. Thomas⁶, C. Vander Velde⁶, P. Vanlaere⁶, J. Wang⁶, F. Zenoni⁶, V. Adler⁶, K. Beernaert⁶, L. Benucci⁷, A. Cimmino⁷, S. Costantini⁷, S. Crucy⁷, S. Dildick⁷, A. Fagot⁷, G. Garcia⁷, J. McCartin⁷, A.A. Ocampa Rios⁷, D. Ryckbosch⁷, S. Salva Diben⁷, M. Sigamani⁷, N. Strobbe⁷, F. Thyssen⁷, M. Tytgat⁷, E. Yazgan⁷, N. Zaganidis⁷, S. Basegmez⁸, C. Beluffi^{8,206}, G. Bruno⁸, R. Castello⁸, A. Caudron⁸, L. Ceard⁸, G.G. Da Silva⁸, C. Delaere⁸, T. du Pree⁸, D. Favart⁸, L. Forthomme⁸, A. Giammanco⁸, J. Hollar⁸, A. Jafari⁸, P. Jez⁸, M. Komm⁸, V. Lemaître⁸, C. Nottens⁸, D. Pagano⁸, L. Perrini⁸, A. Pin⁸, K. Piotrkowski⁸, A. Popov^{8,208}, L. Quertenmont⁸, M. Selvaggi⁸, M. Vidal Maron⁸, J.M. Vizan Garcia⁸, N. Bely⁹, T. Caebergs⁹, E. Daubie⁹, G.H.ammad⁹, W.L. Aldá Júnior¹⁰, G.A. Alves¹⁰, L. Brito¹⁰, M. Correa Martins Junior¹⁰, T. Dos Reis Martins¹⁰, C. Mora Herrera¹⁰, M.E. Pol¹⁰, P. Rebello Teles¹⁰, W. Carvalho¹¹, J. Chinellato^{11,209}, A. Custódio¹¹, E.M. Da Costa¹¹, D. De Jesus Damiao¹¹, C. De Oliveira Martins¹¹, S. Fonseca De Souza¹¹, H. Malbouisson¹¹, D. Matos Figueiredo¹¹, L. Mundim¹¹, H. Nogima¹¹, W.L. Prado Da Silva¹¹, J. Santaolalla¹¹, A. Santoro¹¹, A. Sznajder¹¹, E.J. Tonelli Manganote^{11,209}, A. Vilela Pereira¹¹, C.A. Bernardes¹⁴, S. Dogra¹⁴, T.R. Fernandez Perez Tomei¹⁴, E.M. Gregores¹⁴, P.G. Mercadante¹⁴, S.F. Novaes¹⁴, S. Sandra S. Padula¹⁴, A. Aleksandrov¹⁵, V. Genchev^{15,205}, R. Hadjiiska¹⁵, P. Iaydjiev¹⁵, A. Marinov¹⁵, S. Piperov¹⁵, M. Rodozo¹⁵, G. Sultanov¹⁵, M. Vutova¹⁵, A. Dimitrov¹⁶, I. Glushkov¹⁶, L. Litov¹⁶, B. Pavlov¹⁶, P. Petkov¹⁶, J.G. Bian¹⁷, G.M. Chen¹⁷, H.S. Chen¹⁷, M. Chen¹⁷, T. Cheng¹⁷, R. Du¹⁷, C.H. Jiang¹⁷, R. Plestina^{17,210}, F. Romeo¹⁷, J. Tao¹⁷, Z. Wang¹⁷, C. Asawatangtrakuldee¹⁸, Y. Ban¹⁸, Q. Li¹⁸, S. Liu¹⁸, Y. Mao¹⁸, S.J. Qian¹⁸, D. Wang¹⁸, Z. Xu¹⁸, W. Zou¹⁸, C. Avila¹⁹, A. Cabrera¹⁹, L.F. Chaparro Sierra¹⁹, C. Florez¹⁹, J.P. Gomez¹⁹, B. Gomez Moreno¹⁹, J.C. Sanabria¹⁹, N. Godinovic²⁰, D. Lelas²⁰, D. Polic²⁰, I. Puljak²⁰, Z. Antonovic²¹, M. Kovac²¹, V. Brigljevic²², K. Kadija²², J. Luetic²², D. Mekterovic²², L. Sudic²², A. Attikis²³, G. Mavromanolakis²³, J. Mousa²³, C. Nicolaou²³, F. Ptochos²³, P.A. Razis²³, M. Bodlak²⁴, M. Finger²⁴, M. Finger Jr.^{24,211}, Y. Assran^{25,212}, A. Elithi Kamel^{25,213}, M.A. Mahmoud^{25,214}, A. Radi^{25,215,216}, M. Kadastik²⁶, M. Mura²⁶, M. Raidal²⁶, A. Tiko²⁶, P. Eerola²⁷, G. Fedt²⁷, M. Voutilainen²⁷, J. Härkönen²⁸, V. Karimäki²⁸, R. Kinnunen²⁸, M.J. Kortelainen²⁸, T. Lampén²⁸, K. Lassila-Perini²⁸, S. Lehti²⁸, T. Lindén²⁸, P. Luukkka²⁸, T. Mäenpää²⁸, T. Peltola²⁸, E. Tuominen²⁸, J. Tuominiemi²⁸, E. Tuovinen²⁸, L. Wendland²⁸, J. Talvitie²⁸, T. Tuuva²⁸, M. Besancon³⁰, F. Couderc³⁰, M. Deharden³⁰, D. Denegri³⁰, B. Fabbro³⁰, J.L. Faure³⁰, C. Favaro³⁰, F. Ferri³⁰, S. Ganjour³⁰, A. Givernaud³⁰, P. Gras³⁰, G. Hamel de Monchenault³⁰, P. Jarry³⁰, E. Locci³⁰, J. Malcles³⁰, J. Rander³⁰, A. Rosowsky³⁰, M. Titov³⁰, S. Baffioni³¹, F. Beaudette³¹, P. Busson³¹, C. Charlot³¹, T. Dahms³¹, M. Dalchenko³¹, L. Dobrzynski³¹, N. Filipovic³¹, A. Florent³¹, R. Granier de Cassagnac³¹, L. Mastrolorenzo³¹, P. Mine³¹, C. Mironov³¹, I.N. Naranjo³¹, M. Nguyen³¹, C. Ochando³¹, G. Ortona³¹, P. Paganini³¹, S. Regnard³¹, R. Salerno³¹, J.B. Sauvan³¹, Y. Sirois³¹, C. Veelken³¹, Y. Yilmaz³¹, A. Zabi³¹, J.-L. Agram^{32,217}, J. Andrea³², A. Aubin³², D. Bloch³², J.-M. Brom³², E.C. Chabert³², C. Collard³², E. Conte^{32,217}, J.-C. Fontaine^{32,217}, D. Gelé³², U. Goerlach³², C. Goetzmann³², A.-C. Le Bihan³², K. Skovpen³², P. Van Hove³², S. Gadat³³, S. Beauceron³⁴, N. Beaupere³⁴, G. Boudoul^{34,205}, E. Bouvier³⁴, S. Brochet³⁴, C.A. Carrillo Montoya³⁴, J. Chasserat³⁴, R. Chierici³⁴, D. Contardo³⁴, P. Depasse³⁴, H. El Mamouni³⁴, J. Fan³⁴, J. Fay³⁴, S. Gascon³⁴, M. Gouzevitch³⁴, B. Ille³⁴, T. Kurca³⁴, M. Lethuillier³⁴, L. Mirabito³⁴, S. Perries³⁴, J.D. Ruiz Alvarez³⁴, D. Sabes³⁴, L. Sgandurra³⁴, V. Sordini³⁴, M. Vander Donck³⁴, P. Verdier³⁴, S. Viret³⁴, H. Xiao³⁴, Z. Tsamalaidze^{35,211}, C. Autermann³⁶, S. Beranek³⁶, M. Bontenackels³⁶, M. Edelhoff³⁶, L. Feld³⁶, A. Heister³⁶, O. Hindrichs³⁶, K. Klein³⁶, A. Ostapchuk³⁶, F. Raupach³⁶, J. Sammet³⁶, S. Schael³⁶, J.F. Schulte³⁶, H. Weber³⁶, B. Wittmer³⁶, V. Zhukov³⁶, M. Ata³⁷, M. Brodski³⁷, E. Dietz-Laurson³⁷, D. Duchardt³⁷, M. Erdmann³⁷, R. Fischer³⁷, A. Gith³⁷, T. Hebbeker³⁷, C. Heidemann³⁷, K. Hoepfner³⁷, D. Klingebiel³⁷, S. Knutzen³⁷, P. Kreuzer³⁷, M. Merschmeyer³⁷, A. Meyer³⁷, P. Millet³⁷, M. Olschewski³⁷, K. Padeken³⁷, P. Papacz³⁷, H. Reithler³⁷, S.A. Schmitz³⁷, L. Sonnenschein³⁷, D. Teyssier³⁷, S. Thüer³⁷, M. Weber³⁷, V. Cherepanov³⁷, Y. Erdogan³⁸, G. Flügge³⁸, H. Geenen³⁸, M. Geisler³⁸, W. Haj Ahmad³⁸, F. Hoehle³⁸, B. Kargöl³⁸, T. Kress³⁸, Y. Kuesel³⁸, A. Künsken³⁸, J. Lingemann³⁸, A. Nowack³⁸, I.M. Nugent³⁸, O. Poeth³⁸, A. Stahl³⁸, M. Aldaya Martin³⁹, I. Asin³⁹, N. Bartosik³⁹, J. Behr³⁹, U. Behrens³⁹, A.J. Bell³⁹, A. Bethan³⁹, K. Borras³⁹, A. Burgmeier³⁹, A. Cakir³⁹, L. Calligaris³⁹, A. Campbell³⁹, S. Choudhury³⁹, F. Costanza³⁹, C. Diez Pardo³⁹, G. Dolinska³⁹, S. Dooling³⁹, T. Dorland³⁹, G. Eckerlin³⁹, D. Eckstein³⁹, T. Eichhorn³⁹, G. Flucke³⁹, J. Garay Garcia³⁹, A. Geiser³⁹, P. Gunnellini³⁹, J. Hauk³⁹, M. Hempel^{39,218}, H. Jung³⁹, A. Kalogeropoulos³⁹, M. Kasemann³⁹, P. Katsas³⁹, J. Kieseler³⁹, C. Kleinwort³⁹, I. Korol³⁹, D. Krücker³⁹, W. Lange³⁹, J. Leonard³⁹, K. Lipka³⁹, A. Lobanov³⁹, W. Lohmann^{39,218}, B. Lutz³⁹, R. Mankel³⁹, I. Marfin^{39,218}, I.-A. Melzer-Pellmann³⁹, A.B. Meyer³⁹, G. Mittag³⁹, J. Mnich³⁹, A. Mussgiller³⁹, S. Naumann-Emme³⁹, A. Nayak³⁹, E. Ntomi³⁹, H. Perrey³⁹, D. Pitz³⁹, R. Placakyte³⁹, A. Raspereza³⁹, P.M. Ribeiro Cipriano³⁹, B. Roland³⁹, E. Ron³⁹, M.O. Sahin³⁹, J. Salfeld-Nebgen³⁹, P. Saxena³⁹, T. Schoerner-Sadenius³⁹, M. Schröder³⁹, C. Seitz³⁹, S. Spannagel³⁹, A.D.R. Vargas Trevino³⁹, R. Walsh³⁹, C. Wissing³⁹, V. Blobel⁴⁰, M. Centis Vignali⁴⁰, A.R. Draeger⁴⁰, J. Erle⁴⁰, E. Garutti⁴⁰, K. Goebel⁴⁰, M. Gönner⁴⁰, J. Haller⁴⁰, M. Hoffmann⁴⁰, R.S. Høing⁴⁰, A. Junkes⁴⁰, H. Kirschenmann⁴⁰, R. Klanner⁴⁰, R. Kogler⁴⁰, J. Lange⁴⁰, T. Lapsien⁴⁰, T. Lenz⁴⁰, I. Marchesini⁴⁰, J. Ott⁴⁰, T. Peiffer⁴⁰, A. Perieanu⁴⁰, N. Pietisch⁴⁰, J. Poehlsen⁴⁰, T. Poehlsen⁴⁰, D. Rathjens⁴⁰, C. Sander⁴⁰, H. Schettler⁴⁰, P. Schleper⁴⁰, E. Schlieckau⁴⁰, A. Schmidt⁴⁰, M. Seidel⁴⁰, V. Solo⁴⁰, H. Stadie⁴⁰, G. Steinbrück⁴⁰, D. Troendle⁴⁰, E. Usai⁴⁰, L. Vanelderen⁴⁰, A. Vanhoefer⁴⁰, C. Barth⁴¹, C. Baus⁴¹, J. Berger⁴¹, C. Böser⁴¹, E. Butz⁴¹, T. Chwalek⁴¹, W. De Boer⁴¹, A. Descroix⁴¹, A. Dierlamm⁴¹, M. Feindt⁴¹, F. Frensch⁴¹, M. Giffels⁴¹, A. Gilbert⁴¹, F. Hartmann^{41,205}, T. Hauth⁴¹, U. Husemann⁴¹, I. Katkov^{41,208}, A. Kornmayer^{41,205}, E. Kuznetsova⁴¹, P. Lobelle Pardo⁴¹, M.U. Mozer⁴¹, T. Müller⁴¹, Th. Müller⁴¹, A. Nürnberg⁴¹, G. Quast⁴¹, K. Rabbertz⁴¹, S. Röcker⁴¹, H.J. Simonis⁴¹, F.M. Stober⁴¹, R. Ulrich⁴¹, J. Wagner-Kuhr⁴¹, S. Wayand⁴¹, T. Weiler⁴¹, R. Wolf⁴¹, G. Anagnostou⁴², G. Daskalakis⁴², T. Geralis⁴², V.A. Giakoumopoulou⁴², A. Kyriakis⁴², D. Loukas⁴², A. Markou⁴², C. Markou⁴², A. Psallidas⁴², I. Topsis-Giotis⁴², A. Agapitos⁴³, S. Kesisoglou⁴³, A. Panagiotou⁴³, N. Saoulidou⁴³, E. Stiliaris⁴³, X. Aslanoglou⁴⁴, I. Evangelou⁴⁴, G. Flouris⁴⁴, C. Foudas⁴⁴, P. Kokkas⁴⁴, N. Manthos⁴⁴, I. Papadopoulos⁴⁴, E. Paradas⁴⁴, J. Strogilas⁴⁴, G. Bencze⁴⁵, C. Hajdu⁴⁵, P. Hidas⁴⁵, D. Horvath^{45,219}, F. Sikler⁴⁵, V. Veszpremi⁴⁵, G. Vesztegombi^{45,220}, A.J. Zsigmond⁴⁵, N. Beni⁴⁶, S. Czeilar⁴⁶, J. Karancsi^{46,221}, J. Molnar⁴⁶, J. Palinkas⁴⁶, Z. Szillasi⁴⁶, A. Makovec⁴⁷, P. Raics⁴⁷, Z.L. Trocsanyi⁴⁷, B. Ujvari⁴⁷, N. Sahoo⁴⁸, K.S. Swain⁴⁸, S.B. Beri⁴⁹, V. Bhatnagar⁴⁹, R. Gupta⁴⁹, U. Bhawandeep⁴⁹, A.K. Kalsi⁴⁹, M. Kaur⁴⁹, R. Kumar⁴⁹, M. Mittal⁴⁹, N. Nishu⁴⁹, J.B. Singh⁴⁹, Ashok Kumar⁵⁰, Arun Kumar⁵⁰, S. Ahuja⁵⁰, A. Bhardwaj⁵⁰, B.C. Choudhary⁵⁰, A. Kumar⁵⁰, S. Malhotra⁵⁰, M. Naimuddin⁵⁰, K. Ranjan⁵⁰, V. Sharma⁵⁰, S. Banerjee⁵¹, S. Bhattacharya⁵¹, K. Chatterjee⁵¹, S. Dutta⁵¹, B. Gomber⁵¹, Sa. Jain⁵¹, Sh. Jain⁵¹, R. Khurana⁵¹, A. Modak⁵¹, S. Mukherjee⁵¹, D. Roy⁵¹, S. Sarkar⁵¹, M. Sharan⁵¹, A. Abdulsalam⁵², D. Dutta⁵², S. Kailas⁵², V. Kumar⁵², A.K. Mohanty^{52,205}, L.M. Pant⁵², P. Shukla⁵², A. Topkar⁵², T. Aziz⁵³, K. Banerjee⁵³, S. Bhowmik^{53,222}, R.M. Chatterjee⁵³, R.K. Dewanjee⁵³, S. Dugad⁵³, S. Ganguly⁵³, S. Ghosh⁵³, M. Guchait⁵³, A. Gurtu^{53,223}, G. Kole⁵³, S. Kumar⁵³, M. Maity^{53,222}, G. Majumder⁵³, K. Mazumdar⁵³, G.B. Mohanty⁵³, B. Parida⁵³, K. Sudhakar⁵³, N. Wickramage^{53,224}, H. Bakhshiansohi⁵⁴, H. Behnamian⁵⁴, S.M. Etesami^{54,225}, A. Fahim^{54,226}, R. Goldouzian⁵⁴, M. Khakzad⁵⁴, M. Mohammadi Najafabadi⁵⁴, M. Naseri⁵⁴, S. Pakhtian Mehdiabadi⁵⁴, F. Rezaei Hosseiniabadi⁵⁴, B. Safarzadeh^{54,227}, M. Zeinali⁵⁴, M. Felcini⁵⁵, M. Grunewald⁵⁵, M. Abbrescia^{57,58}, C. Calabria^{57,58}, S.S. Chhibra^{57,58}, A. Colaleo⁵⁷, D. Creanza⁵⁷, S. My⁵⁷, D. De Filippo^{57,59}, M. De Palma^{57,58}, L. Fiore⁵⁷, G. Iaselli^{57,59}, G. Maggi^{57,59}, M. Maggi^{57,59}, S. My^{57,59}, S. Nuzzo^{57,58}, A. Pompili^{57,58}, G. Pugliese^{57,59}, R. Radogna^{57,58,205}, G. Selvaggi^{57,58}, A. Sharma⁵⁷, L. Silvestri^{57,205}, R. Venditti^{57,58}, P. Verwilligen⁵⁷, G. Abbiendi⁶¹, A.C. Benvenuti⁶¹, D. Bonacorsi^{61,62}, S. Braibant-Giacomelli^{61,62}, L. Brigliadori^{61,62}, R. Campanini^{61,62}, P. Capiluppi^{61,62}, A. Castro^{61,62}, F.R. Cavallo⁶¹, G. Codispoti^{61,62}, M. Cuffiani^{61,62}, G.M. Dallavalle⁶¹, F. Fabbri⁶¹, A. Fanfani^{61,62}, D. Fasanella^{61,62}, P. Giacomelli⁶¹, C. Grandi⁶¹, L. Guiducci^{61,62}, S. Marcellini⁶¹, G. Masetti⁶¹, A. Montanari⁶¹, F.L. Navarria^{61,62}, A. Perrotta⁶¹, F. Primavera^{61,62}, A.M. Rossi^{61,62}, T. Rovelli^{61,62}, G.P. Siroli^{61,62}, N. Tosi^{61,62}, R. Travaglini^{61,62}, S. Albergo^{64,65}, G. Cappella⁶⁴, M. Chiorboli^{64,65}, S. Costa^{64,65}, F. Giordano^{64,205}, R. Potenza^{64,65}, A. Tricomi^{64,65}, C. Tuve^{64,65}, G. Barbagli⁶⁸, V. Ciulli^{68,69}, C. Ciminini⁶⁸, R. D'Alessandro^{68,69}, E. Focardi^{68,69}, E. Gallo⁶⁸, S. Gozzi^{68,69}, V. Gori^{68,69}, P. Lenzi^{68,69}, M. Meschini⁶⁸, S. Paolotti⁶⁸, G. Sguazzoni⁶⁸, A. Troiano^{68,69}, L. Benussi⁶⁹, S. Bianco⁶⁹, F. Fabbri⁷⁰, D. Piccolo⁷⁰, R. Ferretti^{72,73}, F. Ferro⁷², M. Lo Vetere^{72,73}, E. Robutti⁷², S. Tosi^{72,73}, M.E. Dinardo^{75,76}, S. Fiorendi^{75,76}, S. Genna^{75,205}, R. Gerosa^{75,76,205}, A. Ghezzi^{75,76}, P. Govoni^{75,76}, M.T. Lucchini^{75,76,205}, S. Malvezzi⁷⁵, R.A. Manzoni^{75,76}, A. Martelli^{75,76}, B. Marzocchi^{75,76,205}, D. Menasce⁷⁵, L. Moroni⁷⁵, M. Paganoni^{75,76}, D. Pedrini⁷⁵, S. Ragazzi^{75,76}, N. Redaelli⁷⁵, T. Tabarelli di Fatis^{75,76}, S. Buontempo⁷⁸, N. Cavallo^{78,80}, S. Di Guida⁷⁸, F. Fabozzi^{78,80}, A.O.M. Iorio⁷⁸, L. Lista⁷⁸, S. Meola^{78,81,205}, M. Merola⁷⁸, P. Paolucci^{78,205}, P. Azzì⁸³, N. Bacchetta⁸³, D. Bisello^{83,84}, A. Branca⁸³, R. Carli^{83,84}, P. Checchia⁸³, M. Dall'Oss^{83,84}, T. Dorigo⁸³, U. Dosselli⁸³, M. Galati^{83,84}, F. Gasparini^{83,84}, U. Gasparini^{83,84}, P. Giubileo^{83,84}, A. Gosselin⁸³, K. Kanishch^{83,85}, S. Lacaparra⁸³, M. Margoni^{83,84}, A.T. Meneguzzo^{83,84}, J. Pazzini^{83,84}, N. Pozzobon^{83,84}, P. Ronchese^{83,84}, F. Simonetto^{83,84}, E. Torassa⁸³, M. Tosi^{83,84}, P. Zotto^{83,84}, A. Zucchetta^{83,84}, F. Zomerle^{83,84}, M. Gabusi^{83,84}, S.P. Ratti^{83,84}, P. Salvini⁸⁷, P. Vitulo^{87,88}, M. Biasini^{90,91}, G.M. Bilei⁹⁰, D. Ciangottini^{90,91,205}, L. Fano^{90,91}, P. Laricci^{90,91}, G. Mantovani^{90,91}, M. Menichelli⁹⁰, A. Saha⁹⁰, A. Santocchia^{90,91}, A. Spiezia^{90,91,205}, K. Androssov^{93,228}, P. Azzurri⁹³, G. Bagliesi⁹³, J. Bernardini⁹³, T. Boccali⁹³, G. Broccolo^{93,95}, R. Castaldi⁹³, M.A. Ciocci^{93,228}, R. Dell'Orso⁹³, S. Donato^{93,95,205}, F. Fiori^{93,95}, L. Foà^{93,95}, A. Giassi⁹³, M.T. Grippo^{93,228}, F. Ligabue^{93,95}, T. Lomtadze⁹³, L. Martin⁹³, A. Messineo⁹³, C.S. Moon⁹³, F. Palla^{93,229}, A. Rizzi^{93,94}, A. Savoy-Navarro^{93,230}, A.T. Serban⁹³, P. Spagnolo⁹³, P. Squillacioti⁹³, R. Tenchini⁹³, G. Tonelli^{93,94}, A. Venturi⁹³, P.G. Verdini⁹³, C. Vernieri^{93,95}, L. Barone^{97,98}, F. Cavallari⁹⁷, G. D'imperio⁹⁷, D. Del Re⁹⁷, M. Diemoz⁹⁷, C. Jorda⁹⁷, E. Longo⁹⁷, F. Margaroli^{97,98}, P. Meridiani⁹⁷, F. Michel^{97,98,205}, S. Nourbakhsh^{97,98}, G. Organtini^{97,98}, R. Paramatti⁹⁷, S. Rahatlou^{97,98}, C. Rovelli⁹⁷, F. Santanastasio^{97,98}, L. Soffi^{97,98}, P. Traczyk^{97,98,205}, N. Amapane^{100,101}, R. Arcidiacono^{100,102}, S. Argiro¹⁰⁰, M. Arneodo^{100,102}, R. Bellan^{100,101}, C. Biino¹⁰⁰, N. Cartiglia¹⁰⁰, S. Casasso^{100,101,205}, M. Costa^{100,101}, A. Degano^{100,101}, N. Demaria¹⁰⁰, L. Finco^{100,101,205}, C. Mariotti¹⁰⁰, S. Maselli¹⁰⁰, E. Migliore¹⁰⁰, V. Monaco^{100,101}, M. Musich¹⁰⁰, M.M. Obertino^{100,102}, L. Pacher^{100,101}, N. Pastrone¹⁰⁰, M. Pelliccioni¹⁰⁰, G.L. Pinna Angioni^{100,101}, A. Potenza^{100,101}, A. Romero^{100,101}, M. Ruspà^{100,102}, R. Sacchi^{100,101}, A. Solano^{100,101}, A. Staiano¹⁰⁰, U. Tamponi¹⁰⁰, S. Belforte¹⁰⁴, V. Candilise¹⁰⁴, M. Casarsa¹⁰⁴, F. Cossutti¹⁰⁴, G. Della Ricca^{104,105}, B. Gobbo¹⁰⁴, C. La Licata^{104,105}, M. Marone^{104,105}, A. Schizzi^{104,105}, T. Umer^{104,105}, A. Zanetti¹⁰⁴, S. Chang¹⁰⁶, A. Kropivnitskaya¹⁰⁶, S.K. Nam¹⁰⁶, D.H. Kim¹⁰⁷, G.N. Kim¹⁰⁷, T.S. Kim¹⁰⁷, D.J. Kong¹⁰⁷, S. Lee¹⁰⁷, Y.D. Oh¹⁰⁷, H. Park¹⁰⁷, A. Sakharov¹⁰⁷, D.C. Son¹⁰⁷, T.J. Kim¹⁰⁸, J.Y. Kim¹⁰⁹, S. Song¹⁰⁹, S. Kim¹¹⁰, D. Gyun¹¹⁰, B. Hong¹¹⁰, M. Jo¹¹⁰, H. Kim¹¹⁰, Y. Kim¹¹⁰, B. Lee¹¹⁰, K.S. Lee¹¹⁰, S.K. Park¹¹⁰, Y. Roh¹¹⁰, H.D. Yoo¹¹¹, M. Choi¹¹², J.H. Kim¹¹², I.C. Park¹¹², G. Ryu¹¹², M.S. Ryu¹¹², Y. Choi¹¹³, Y.K. Choi¹¹³, J. Goh¹¹³, D. Kim¹¹³, E. Kwon¹¹³,

- H. Bialkowska¹²³, M. Bluj¹²³, B. Boimska¹²³, T. Frueboes¹²³, M. Górski¹²³, M. Kazana¹²³, K. Nawrocki¹²³, K. Romanowska-Rybicka¹²³, M. Szeleper¹²³, P. Zalewski¹²³, G. Brona¹²⁴, K. Bunkowski¹²⁴, M. Cwiok¹²⁴, W. Dominik¹²⁴, K. Doroba¹²⁴, A. Kalinowski¹²⁴, M. Konecki¹²⁴, J. Krolkowski¹²⁴, M. Misiura¹²⁴, M. Olszewski¹²⁴, W. Wolszczak¹²⁴, P. Bargassa¹²⁵, C. Beirão Da Cruz E Silva¹²⁵, P. Faccioli¹²⁵, P.G. Ferreira Parracho¹²⁵, M. Gallinaro¹²⁵, L. Lloret Iglesias¹²⁵, F. Nguyen¹²⁵, J. Rodrigues Antunes¹²⁵, J. Seixas¹²⁵, J. Varela¹²⁵, P. Vischia¹²⁵, S. Afanasiev¹²⁶, P. Bunin¹²⁶, M. Gavrilenco¹²⁶, I. Golutvin¹²⁶, I. Gorbunov¹²⁶, A. Kamenev¹²⁶, V. Karjavin¹²⁶, V. Konoplyanikov¹²⁶, A. Lanev¹²⁶, A. Malakhov¹²⁶, V. Matveev^{126,232}, P. Moiseev¹²⁶, V. Palchik¹²⁶, V. Perelygin¹²⁶, S. Shmatov¹²⁶, N. Skatchkov¹²⁶, V. Smirnov¹²⁶, A. Zarubin¹²⁶, V. Golovtsov¹²⁷, Y. Ivanov¹²⁷, V. Kim^{127,233}, P. Levchenko¹²⁷, V. Murzin¹²⁷, V. Oreshkin¹²⁷, I. Smirnov¹²⁷, V. Sulimov¹²⁷, L. Uvarov¹²⁷, S. Vavilov¹²⁷, A. Vorobyev¹²⁷, An. Vorobyev¹²⁷, Yu. Andreev¹²⁸, A. Dermenev¹²⁸, S. Gninenko¹²⁸, N. Golubev¹²⁸, M. Kirsanov¹²⁸, N. Krasnikov¹²⁸, A. Pashchenkov¹²⁸, D. Tliso¹²⁸, A. Toropin¹²⁸, V. Epshteyn¹²⁹, V. Gavrilov¹²⁹, N. Lychkovskaya¹²⁹, V. Popov¹²⁹, I. Pozdnyakov¹²⁹, G. Safronov¹²⁹, S. Semenov¹²⁹, A. Spiridonov¹²⁹, V. Stolin¹²⁹, E. Vlasov¹²⁹, A. Zhokin¹²⁹, V. Andreev¹³⁰, M. Azarkin¹³⁰, I. Dremin¹³⁰, M. Kirakosyan¹³⁰, A. Leonidov¹³⁰, G. Mesyats¹³⁰, S.V. Rusakov¹³⁰, A. Vinogradov¹³⁰, A. Belyaev¹³¹, E. Boos¹³¹, M. Dubinin^{131,234}, L. Dudko¹³¹, A. Ershov¹³¹, A. Gribushin¹³¹, V. Klyukhin¹³¹, O. Kodolova¹³¹, I. Lokhtin¹³¹, S. Obraztsov¹³¹, S. Petrushanko¹³¹, V. Savrin¹³¹, A. Snigirev¹³¹, I. Azhgirev¹³², I. Bayshev¹³², S. Bitoukov¹³², V. Kachanov¹³², A. Kalinin¹³², D. Konstantinov¹³², V. Krychkin¹³², V. Petrov¹³², R. Rytin¹³², A. Sobol¹³², L. Tourchanovitch¹³², S. Troshin¹³², N. Tyurin¹³², A. Uzunian¹³², A. Volkov¹³², P. Adzic^{132,235}, M. Ekmedzic¹³³, J. Milosevic¹³³, V. Rekovic¹³³, J. Alcaraz Maestre¹³⁴, C. Battilana¹³⁴, E. Calvo¹³⁴, M. Cerrada¹³⁴, M. Chamizo Llatas¹³⁴, N. Colino¹³⁴, B. De La Cruz¹³⁴, A. Delgado Peris¹³⁴, D. Domínguez Vázquez¹³⁴, A. Escalante Del Valle¹³⁴, C. Fernandez Bedoya¹³⁴, J.P. Fernández Ramos¹³⁴, J. Flix¹³⁴, M.C. Fouz¹³⁴, P. Garcia-Abia¹³⁴, O. Gonzalez Lopez¹³⁴, S. Goy Lopez¹³⁴, J.M. Hernandez¹³⁴, M.I. Josa¹³⁴, E. Navarro De Martino¹³⁴, A. Pérez-Calero Yzquierdo¹³⁴, J. Puerta Pelayo¹³⁴, A. Quintario Olmeda¹³⁴, I. Redondo¹³⁴, L. Romero¹³⁴, M.S. Soares¹³⁴, C. Albajar¹³⁵, J.F. de Trocóniz¹³⁵, M. Missiroli¹³⁵, D. Moran¹³⁵, H. Brun¹³⁶, J. Cuevas¹³⁶, J. Fernandez Menendez¹³⁶, S. Folgueras¹³⁶, I. Gonzalez Caballero¹³⁶, J.A. Brochero Cifuentes¹³⁷, I.J. Cabrillo¹³⁷, A. Calderon¹³⁷, J. Duarte Campderros¹³⁷, M. Fernandez¹³⁷, G. Gomez¹³⁷, A. Graziano¹³⁷, A. Lopez Vitez¹³⁷, J. Marco¹³⁷, R. Marco¹³⁷, C. Martinez Rivero¹³⁷, F. Mattozas¹³⁷, F.J. Munoz Sanchez¹³⁷, J. Piedra Gomez¹³⁷, T. Rodrigo¹³⁷, A.Y. Rodríguez-Marrero¹³⁷, A. Ruiz Jimeno¹³⁷, L. Scodellaro¹³⁷, I. Vila¹³⁷, R. Vilar Cortabitarte¹³⁷, D. Abbaneo¹³⁸, E. Auffray¹³⁸, G. Auzinger¹³⁸, M. Bachtis¹³⁸, P. Baillon¹³⁸, A.H. Ball¹³⁸, D. Barney¹³⁸, A. Benaglia¹³⁸, J. Bendavid¹³⁸, L. Benhabib¹³⁸, J.F. Benitez¹³⁸, C. Bernet^{138,210}, P. Bloch¹³⁸, A. Bocchi¹³⁸, A. Bonato¹³⁸, O. Bondu¹³⁸, C. Botta¹³⁸, H. Breuker¹³⁸, T. Camporesi¹³⁸, G. Cerminara¹³⁸, S. Colafranceschi^{138,236}, M. D'Alfonso¹³⁸, D. d'Enterria¹³⁸, A. Dabrowski¹³⁸, A. David¹³⁸, F. De Guio¹³⁸, A. De Roeck¹³⁸, S. De Visser¹³⁸, E. Di Marco¹³⁸, M. Dobson¹³⁸, M. Dordevic¹³⁸, N. Dupont-Sagorin¹³⁸, A. Elliott-Peisert¹³⁸, G. Franzoni¹³⁸, W. Funk¹³⁸, D. Gign¹³⁸, K. Gill¹³⁸, D. Giordano¹³⁸, M. Gironi¹³⁸, F. Glege¹³⁸, R. Guida¹³⁸, S. Gundacker¹³⁸, M. Guthoff¹³⁸, J. Hammer¹³⁸, M. Hansen¹³⁸, P. Harris¹³⁸, J. Hegeman¹³⁸, V. Innocente¹³⁸, P. Janot¹³⁸, K. Kousouris¹³⁸, K. Krajcarz¹³⁸, P. Lecoq¹³⁸, C. Lourenco¹³⁸, N. Magini¹³⁸, L. Malgeri¹³⁸, M. Mannelli¹³⁸, J. Marrouche¹³⁸, L. Masetti¹³⁸, F. Meijers¹³⁸, S. Mersi¹³⁸, E. Meschi¹³⁸, F. Moortgat¹³⁸, S. Morovic¹³⁸, M. Mulders¹³⁸, L. Orsini¹³⁸, L. Pape¹³⁸, E. Perez¹³⁸, L. Perrozzi¹³⁸, A. Petrilli¹³⁸, G. Petrucciari¹³⁸, A. Pfeiffer¹³⁸, M. Pimiä¹³⁸, D. Piparo¹³⁸, M. Plagge¹³⁸, A. Racz¹³⁸, G. Rolandi^{138,237}, M. Rovere¹³⁸, H. Sakulin¹³⁸, C. Schäfer¹³⁸, C. Schwick¹³⁸, A. Sharma¹³⁸, P. Siegrist¹³⁸, P. Silva¹³⁸, M. Simon¹³⁸, P. Sphicas^{138,238}, D. Spiga¹³⁸, J. Steggemann¹³⁸, B. Stieger¹³⁸, M. Stoye¹³⁸, Y. Takahashi¹³⁸, D. Treille¹³⁸, A. Tsiros¹³⁸, G.L. Veres^{138,220}, N. Wardle¹³⁸, H.K. Wöhr¹³⁸, H. Wolny¹³⁸, W.D. Zeuner¹³⁸, W. Bertl¹³⁹, K. Deiters¹³⁹, W. Erdmann¹³⁹, R. Horisberger¹³⁹, Q. Ingram¹³⁹, H.C. Kaestli¹³⁹, D. Kotlinski¹³⁹, D. Renker¹³⁹, T. Rohe¹³⁹, F. Bachmair¹⁴⁰, L. Bäni¹⁴⁰, L. Bianchini¹⁴⁰, M.A. Buchmann¹⁴⁰, B. Casal¹⁴⁰, N. Chanon¹⁴⁰, G. Dissertori¹⁴⁰, M. Dittmar¹⁴⁰, M. Donega¹⁴⁰, M. Dünser¹⁴⁰, P. Eller¹⁴⁰, C. Grab¹⁴⁰, D. Hits¹⁴⁰, J. Hoss¹⁴⁰, W. Lustermann¹⁴⁰, B. Mangano¹⁴⁰, A.C. Marini¹⁴⁰, M. Marionneau¹⁴⁰, P. Martinez Ruiz del Arbol¹⁴⁰, M. Masciovecchio¹⁴⁰, D. Meister¹⁴⁰, N. Mohr¹⁴⁰, P. Musella¹⁴⁰, C. Nageli¹⁴⁰, F. Nessi-Tedaldi¹⁴⁰, F. Pandolfi¹⁴⁰, F. Pauss¹⁴⁰, M. Peruzzi¹⁴⁰, M. Quittnat¹⁴⁰, L. Rebana¹⁴⁰, M. Rossini¹⁴⁰, A. Starodumov^{140,240}, M. Takahashi¹⁴⁰, K. Theofilatos¹⁴⁰, R. Wallny¹⁴⁰, H.A. Weber¹⁴⁰, C. Amsler^{141,241}, M.F. Canelli¹⁴¹, V. Chiochia¹⁴¹, A. De Cosa¹⁴¹, A. Hinzmann¹⁴¹, T. Hreus¹⁴¹, B. Kilminster¹⁴¹, C. Lange¹⁴¹, B. Millan Mejias¹⁴¹, J. Ngadiubi¹⁴¹, D. Pinna¹⁴¹, P. Robmann¹⁴¹, F.J. Ronga¹⁴¹, S. Taroni¹⁴¹, M. Verzetti¹⁴¹, Y. Yang¹⁴¹, M. Cardaci¹⁴², K.H. Chen¹⁴², C. Ferro¹⁴², C.M. Kuo¹⁴², W. Lin¹⁴², Y.J. Ku¹⁴², R. Volpe¹⁴², S.S. Yu¹⁴², P. Chang¹⁴³, Y.H. Chang¹⁴³, Y.W. Chang¹⁴³, Y. Chao¹⁴³, K.F. Chen¹⁴³, P.H. Chen¹⁴³, C. Dietz¹⁴³, U. Grondler¹⁴³, W.-S. Hou¹⁴³, K.Y. Kao¹⁴³, Y.F. Liu¹⁴³, R.-S. Lu¹⁴³, D. Majumder¹⁴³, E. Petrakou¹⁴³, Y.M. Tzeng¹⁴³, R. Wilken¹⁴³, B. Asavapibhop¹⁴⁴, G. Singh¹⁴⁴, N. Srimanobhas¹⁴⁴, N. Suwonjandee¹⁴⁴, A. Adiguzel¹⁴⁵, M.N. Bakirci^{145,242}, S. Cerci^{145,243}, C. Dozen¹⁴⁵, I. Dumanoglu¹⁴⁵, E. Eskut¹⁴⁵, S. Girgis¹⁴⁵, G. Gokbulut¹⁴⁵, E. Gurpinar¹⁴⁵, I. Hos¹⁴⁵, E.E. Kangal¹⁴⁵, A. Kayis Topaksu¹⁴⁵, G. Onengut^{145,244}, K. Ozdemir¹⁴⁵, S. Ozturk^{145,244}, A. Polatoz¹⁴⁵, D. Sunar Cerci^{145,243}, B. Tali^{145,243}, H. Topakli^{145,242}, M. Vergili¹⁴⁵, I.V. Akin¹⁴⁶, B. Bilin¹⁴⁶, S. Bilmis¹⁴⁶, H. Gamsizkan¹⁴⁶, B. Isildak¹⁴⁶, G. Karapinar^{146,247}, K. Ocalan^{146,248}, S. Sekmen¹⁴⁶, U.E. Surati¹⁴⁶, M. Yalvac¹⁴⁶, M. Zeyrek¹⁴⁶, E.A. Albayrak^{147,249}, E. Gülmez¹⁴⁷, M. Kaya^{147,250}, O. Kaya^{147,251}, T. Yetkin^{147,252}, K. Cankocak¹⁴⁸, F.I. Vardarli¹⁴⁸, L. Levchuk¹⁴⁹, P. Sorokin¹⁴⁹, J.J. Brooke¹⁵⁰, E. Clement¹⁵⁰, D. Cussans¹⁵⁰, H. Flache¹⁵⁰, J. Goldstein¹⁵⁰, M. Grimes¹⁵⁰, G.P. Heath¹⁵⁰, H.F. Heath¹⁵⁰, J. Jacob¹⁵⁰, L. Kreczko¹⁵⁰, C. Lucas¹⁵⁰, Z. Meng¹⁵⁰, D.M. Newbold^{150,253}, S. Paramesvaran¹⁵⁰, A. Poll¹⁵⁰, T. Sakuma¹⁵⁰, S. Senkin¹⁵⁰, V.J. Smith¹⁵⁰, K.W. Bell¹⁵¹, A. Belyaev^{151,254}, C. Brew¹⁵¹, R.M. Brown¹⁵¹, D.J.A. Cockerill¹⁵¹, J.A. Coughlan¹⁵¹, K. Harder¹⁵¹, S. Harper¹⁵¹, E. Olaiya¹⁵¹, D. Petyt¹⁵¹, C.H. Shepherd-Themistocleous¹⁵¹, A. Thea¹⁵¹, I.R. Tomalin¹⁵¹, T. Williams¹⁵¹, W.J. Womersley¹⁵¹, S.D. Worm¹⁵¹, M. Baber¹⁵², R. Bainbridge¹⁵², O. Buchmüller¹⁵², D. Burton¹⁵², D. Colling¹⁵², N. Cripps¹⁵², P. Dauncey¹⁵², G. Davies¹⁵², M. Della Negra¹⁵², P. Dunne¹⁵², W. Ferguson¹⁵², J. Fulcher¹⁵², D. Futyan¹⁵², G. Hall¹⁵², G. Iles¹⁵², M. Jarvis¹⁵², G. Karapostoli¹⁵², M. Kenzie¹⁵², R. Lane¹⁵², R. Lucas^{152,253}, L. Lyons¹⁵², A.-M. Magnan¹⁵², S. Malik¹⁵², B. Mathias¹⁵², J. Nash¹⁵², A. Nikitenko^{152,240}, J. Pela¹⁵², M. Pesaresi¹⁵², K. Petridis¹⁵², D.M. Raymond¹⁵², S. Rogerson¹⁵², A. Rose¹⁵², C. Seez¹⁵², P. Sharp¹⁵², A. Tapper¹⁵², M. Vazquez Acosta¹⁵², T. Virdee¹⁵², S.C. Zenz¹⁵², J.E. Cole¹⁵³, P.R. Hobson¹⁵³, A. Khan¹⁵³, P. Kyberd¹⁵³, D. Leggat¹⁵³, D. Leslie¹⁵³, I.D. Reid¹⁵³, P. Symonds¹⁵³, L. Teodorescu¹⁵³, M. Turner¹⁵³, J. Dittmann¹⁵⁴, K. Hatakeyama¹⁵⁴, A. Kasmi¹⁵⁴, H. Liu¹⁵⁴, T. Scarborough¹⁵⁴, O. Charaf¹⁵⁵, S.I. Cooper¹⁵⁵, C. Henderson¹⁵⁵, P. Rumerio¹⁵⁵, A. Avetisyan¹⁵⁶, T. Bose¹⁵⁶, C. Fantasia¹⁵⁶, P. Lawson¹⁵⁶, C. Richardson¹⁵⁶, J. Rohlf¹⁵⁶, J. St. John¹⁵⁶, L. Sulak¹⁵⁶, J. Alimena¹⁵⁷, E. Berry¹⁵⁷, S. Bhattacharya¹⁵⁷, G. Christopher¹⁵⁷, D. Cutts¹⁵⁷, Z. Demiragli¹⁵⁷, N. Dhirga¹⁵⁷, A. Ferapontov¹⁵⁷, A. Garabedian¹⁵⁷, U. Heintz¹⁵⁷, G. Kukartsev¹⁵⁷, E. Laird¹⁵⁷, G. Landsberg¹⁵⁷, M. Luk¹⁵⁷, M. Narain¹⁵⁷, M. Segala¹⁵⁷, T. Sinthuprasith¹⁵⁷, T. Speer¹⁵⁷, J. Swanson¹⁵⁷, R. Breedon¹⁵⁸, G. Breto¹⁵⁸, M. Calderon De La Barca Sanchez¹⁵⁸, S. Chauhan¹⁵⁸, M. Chertok¹⁵⁸, J. Conway¹⁵⁸, R. Conway¹⁵⁸, P.T. Cox¹⁵⁸, R. Erbacher¹⁵⁸, M. Gardner¹⁵⁸, W. Ko¹⁵⁸, R. Lander¹⁵⁸, M. Mulhearn¹⁵⁸, D. Pellett¹⁵⁸, J. Pilot¹⁵⁸, F. Ricci-Tam¹⁵⁸, S. Shalhout¹⁵⁸, J. Smith¹⁵⁸, M. Squires¹⁵⁸, D. Stolp¹⁵⁸, M. Tripathi¹⁵⁸, S. Wilbur¹⁵⁸, R. Yohay¹⁵⁸, R. Cousins¹⁵⁹, P. Everaerts¹⁵⁹, C. Farrell¹⁵⁹, J. Hauser¹⁵⁹, M. Ignatenko¹⁵⁹, G. Rakness¹⁵⁹, E. Takasugi¹⁵⁹, V. Valuev¹⁵⁹, M. Weber¹⁵⁹, K. Burk¹⁶⁰, R. Clare¹⁶⁰, J. Ellison¹⁶⁰, J.W. Gary¹⁶⁰, G. Hanson¹⁶⁰, J. Heilmann¹⁶⁰, M. Iova Rikova¹⁶⁰, P. Jandir¹⁶⁰, E. Kennedy¹⁶⁰, F. Lacroix¹⁶⁰, O.R. Long¹⁶⁰, A. Luthra¹⁶⁰, M. Malbert¹⁶⁰, M. Olmedo Negrete¹⁶⁰, A. Shrinivas¹⁶⁰, S. Sumowidagdo¹⁶⁰, S. Wimpenny¹⁶⁰, J.G. Branson¹⁶¹, G.B. Cerati¹⁶¹, S. Citterio¹⁶¹, R.T. D'Agnoletto¹⁶¹, A. Holzner¹⁶¹, R. Kelley¹⁶¹, D. Klein¹⁶¹, D. Kovalsky¹⁶¹, J. Letts¹⁶¹, I. Macneil¹⁶¹, D. Olivito¹⁶¹, S. Padhi¹⁶¹, C. Palmer¹⁶¹, M. Pieri¹⁶¹, M. Sani¹⁶¹, V. Sharma¹⁶¹, S. Simon¹⁶¹, Y. Tu¹⁶¹, A. Vartak¹⁶¹, C. Welke¹⁶¹, F. Würthwein¹⁶¹, A. Yagci¹⁶¹, D. Barge¹⁶², J. Bradmiller-Feld¹⁶², C. Campagnari¹⁶², T. Danielson¹⁶², A. Dishaw¹⁶², V. Dutta¹⁶², K. Flowers¹⁶², M. Franco Sevilla¹⁶², P. Geffert¹⁶², C. George¹⁶², F. Golf¹⁶², L. Gouskos¹⁶², J. Incandella¹⁶², C. Justus¹⁶², N. McColl¹⁶², J. Richman¹⁶², D. Stuart¹⁶², W. To¹⁶², C. West¹⁶², J. Yoo¹⁶², A. Apresyan¹⁶³, A. Bornheim¹⁶³, J. Bunn¹⁶³, Y. Chen¹⁶³, J. Duarte¹⁶³, A. Mott¹⁶³, H.B. Newman¹⁶³, C. Pena¹⁶³, M. Pierini¹⁶³, M. Spiropulu¹⁶³, J.R. Vlimant¹⁶³, R. Wilkinson¹⁶³, S. Xie¹⁶³, R.Y. Zhu¹⁶³, V. Azoulin¹⁶⁴, A. Calamba¹⁶⁴, B. Carlson¹⁶⁴, T. Ferguson¹⁶⁴, Y. Iiyama¹⁶⁴, M. Paulini¹⁶⁴, J. Russ¹⁶⁴, H. Vogel¹⁶⁴, I. Vorobiev¹⁶⁴, J.P. Cumalat¹⁶⁵, W.T. Ford¹⁶⁵, A. Gaz¹⁶⁵, M. Krohn¹⁶⁵, E. Luiggi Lopez¹⁶⁵, U. Nauenberg¹⁶⁵, J.G. Smith¹⁶⁵, K. Stenson¹⁶⁵, R.S. Wagner¹⁶⁵, J.A. Alexander¹⁶⁶, A. Chatterjee¹⁶⁶, J. Chaves¹⁶⁶, J. Chu¹⁶⁶, S. Dittmer¹⁶⁶, N. Eggert¹⁶⁶, N. Mirman¹⁶⁶, G. Nicolas Kaufman¹⁶⁶, J.R. Patterson¹⁶⁶, A. Ryd¹⁶⁶, E. Salvati¹⁶⁶, L. Skinnari¹⁶⁶, W. Sun¹⁶⁶, W.D. Teo¹⁶⁶, J. Thom¹⁶⁶, J. Thompson¹⁶⁶, J. Tucker¹⁶⁶, Y. Weng¹⁶⁶, L. Winstrom¹⁶⁶, P. Wittich¹⁶⁶, D. Winn¹⁶⁷, S. Abdullin¹⁶⁸, M. Albrow¹⁶⁸, J. Anderson¹⁶⁸, G. Apollinari¹⁶⁸, L.A.T. Bauerick¹⁶⁸, A. Beretvas¹⁶⁸, J. Berryhill¹⁶⁸, P.C. Bhat¹⁶⁸, G. Bolla¹⁶⁸, K. Burkett¹⁶⁸, J.N. Butler¹⁶⁸, H.W.K. Cheung¹⁶⁸, F. Chlebana¹⁶⁸, S. Cihangir¹⁶⁸, V.D. Elvira¹⁶⁸, I. Fisk¹⁶⁸, J. Freeman¹⁶⁸, Y. Gao¹⁶⁸, E. Gottschalk¹⁶⁸, L. Gray¹⁶⁸, D. Green¹⁶⁸, S. Grunendahl¹⁶⁸, O. Gutsche¹⁶⁸, J. Hanlon¹⁶⁸, D. Hare¹⁶⁸, R.M. Harris¹⁶⁸, J. Hirschauer¹⁶⁸, B. Hooperman¹⁶⁸, S. Jindariani¹⁶⁸, M. Johnson¹⁶⁸, U. Joshi¹⁶⁸, K. Kaadze¹⁶⁸, B. Klima¹⁶⁸, B. Kreis¹⁶⁸, S. Kwan¹⁶⁸, J. Linacre¹⁶⁸, D. Lincoln¹⁶⁸, R. Lipton¹⁶⁸, T. Liu¹⁶⁸, J. Lykken¹⁶⁸, K. Maeshima¹⁶⁸, J.M. Marraffino¹⁶⁸, V.I. Martinez Outschoorn¹⁶⁸, S. Maruyama¹⁶⁸, D. Mason¹⁶⁸, P. McBride¹⁶⁸, P. Merkel¹⁶⁸, K. Mishra¹⁶⁸, S. Mrenna¹⁶⁸, S. Nahn¹⁶⁸, C. Newman-Holmes¹⁶⁸, V. O'Dell¹⁶⁸, O. Prokofyev¹⁶⁸, E. Sexton-Kennedy¹⁶⁸, S. Sharma¹⁶⁸, A. Soba¹⁶⁸, W.J. Spalding¹⁶⁸, L. Spiegel¹⁶⁸, L. Taylor¹⁶⁸, S. Tkaczyk¹⁶⁸, N.V. Tran¹⁶⁸, L. Uppeger¹⁶⁸, E.W. Vaandering¹⁶⁸, R. Vidal¹⁶⁸, A. Whitbeck¹⁶⁸, J. Whitmore¹⁶⁸, F. Yang¹⁶⁸, D. Acosta¹⁶⁹, P. Avery¹⁶⁹, P. Bortignon¹⁶⁹, D. Bourlikov¹⁶⁹, M. Carver¹⁶⁹, D. Curry¹⁶⁹, S. Das¹⁶⁹, M. DeGruttola¹⁶⁹, G.P. Di Giovanni¹⁶⁹, R.D. Field¹⁶⁹, M. Fisher¹⁶⁹, I.K. Furic¹⁶⁹, J. Hugon¹⁶⁹, J. Konigsberg¹⁶⁹, A. Korytov¹⁶⁹, T. Kyreos¹⁶⁹, J.F. Low¹⁶⁹, K. Matchev¹⁶⁹, H. Mei¹⁶⁹, P. Milenovic^{169,255}, G. Mitselmakher¹⁶⁹, L. Muniz¹⁶⁹, A. Rinkevicius¹⁶⁹, L. Shchutska¹⁶⁹, M. Snowball¹⁶⁹, D. Sperka¹⁶⁹, J. Yelton¹⁶⁹, M. Zakaria¹⁶⁹, S. Hewamanage¹⁷⁰, S. Linn¹⁷⁰, P. Markowitz¹⁷⁰, G. Martinez¹⁷⁰, J.L. Rodriguez¹⁷⁰, T. Adams¹⁷¹, A. Askew¹⁷¹, J. Bochenek¹⁷¹, B. Diamond¹⁷¹, J. Haas¹⁷¹, S. Hagopian¹⁷¹, V. Hagopian¹⁷¹, K.F. Johnson¹⁷¹, H. Prosper¹⁷¹, V. Veeraraghavan¹⁷¹, M. Weinberg¹⁷¹, M.M. Baarmand¹⁷², M. Hohlmann¹⁷², H. Kalakhety¹⁷², F. Yumiceva¹⁷², M.R. Adams¹⁷³, L. Apanasovich¹⁷³, D. Berry¹⁷³, R.R. Betts¹⁷³, I. Bucinskaite¹⁷³, R. Cavanaugh¹⁷³, O. Evdokimov¹⁷³, L. Gauthier¹⁷³, C.E. Gerber¹⁷³, D.J. Haight¹⁷³, P. Kurt¹⁷³, D.H. Moe¹⁷³, C. O'Brien¹⁷³, I.D. Sandalow Gonzalez¹⁷³, C. Silkworth¹⁷³, P. Turner¹⁷³, N. Varelas¹⁷³, B. Bilk^{174,256}, W. Clarida¹⁷⁴, K. Dilsiz¹⁷⁴, M. Haytmyradov¹⁷⁴, J.-P. Merlo¹⁷⁴, H. Mermerkaya¹⁷⁴, A. Mestvirishvili¹⁷⁴, A. Moeller¹⁷⁴, J. Nachtman¹⁷⁴, H. Ogul¹⁷⁴, Y. Onel¹⁷⁴, F. Ozok¹⁷⁴, A. Penzo¹⁷⁴, R. Rahmat¹⁷⁴, S. Sen¹⁷⁴, P. Tan¹⁷⁴, E. Tiras¹⁷⁴, J. Wetzel¹⁷⁴, K. Yi¹⁷⁴, B.A. Barnett¹⁷⁵, B. Blumenfeld¹⁷⁵, S. Bolognesi¹⁷⁵, D. Fehling¹⁷⁵, A.V. Gritsan¹⁷⁵, P. Maksimovic¹⁷⁵, C. Martin¹⁷⁵, M. Swartz¹⁷⁵, P. Baringer¹⁷⁶, A. Bean¹⁷⁶, G. Benelli¹⁷⁶, C. Bruner¹⁷⁶, R.P. Kenny III¹⁷⁶, M. Malek¹⁷⁶, M. Murray¹⁷⁶, D. Noonan¹⁷⁶, S. Sanders¹⁷⁶, J. Sekarik¹⁷⁶, R. Stringer¹⁷⁶, O. Wang¹⁷⁶, J.S. Wood¹⁷⁶, I. Chakaberia¹⁷⁶, A. Ivanov¹⁷⁷, S. Khalil¹⁷⁷, M. Makouski¹⁷⁷, Y. Maravin¹⁷⁷, L.K. Saini¹⁷⁷, N. Skhirtladze¹⁷⁷, I. Svintradze¹⁷⁷, J. Gronberg¹⁷⁸, D. Lange¹⁷⁸, F. Rebassoo¹⁷⁸, D. Wright¹⁷⁸, A. Baden¹⁷⁹, A. Belloni¹⁷⁹, B. Calvert¹⁷⁹, S.C. Eno¹⁷⁹, J.A. Gomez¹⁷⁹, N.J. Hadley¹⁷⁹, R.G. Kellogg¹⁷⁹, T. Kolberg¹⁷⁹, Y. Lu¹⁷⁹, A.C. Mignerey¹⁷⁹, K. Pedro¹⁷⁹, A. Skuja¹⁷⁹, M.B. Tonjes¹⁷⁹, S.C. Tonwar¹⁷⁹, A. Apyan¹⁸⁰, R. Barbieri¹⁸⁰, G. Bauer¹⁸⁰, W. Busza¹⁸⁰, I.A. Calo¹⁸⁰, M. Chan¹⁸⁰, L. Di Matteo¹⁸⁰, G. Gomez Ceballos¹⁸⁰, M. Goncharov¹⁸⁰, D. Gulhan¹⁸⁰, M. Klute¹⁸⁰, Y.S. Lai¹⁸⁰, Y.-J. Lee¹⁸⁰, A. Levin¹⁸⁰, P.D. Luckey¹⁸⁰, T. Ma¹⁸⁰, C. Paus¹⁸⁰, D. Ralph¹⁸⁰, C. Roland¹⁸⁰, G. Roland¹⁸⁰, G.S.F. Stephens¹⁸⁰, K. Sumorok¹⁸⁰, D. Velicanu¹⁸⁰, J. Veverka¹⁸⁰, B. Wyslouch¹⁸⁰, M. Yang¹⁸⁰, M. Zanetti¹⁸⁰, V. Zhukova¹⁸⁰, B. Dahmes¹⁸¹, A. Gude¹⁸¹, S.C. Kao¹⁸¹, K. Klapeoteke¹⁸¹, Y. Kubota¹⁸¹, J. Mans¹⁸¹, N. Pastika¹⁸¹, R. Rusack¹⁸¹, A. Singovsky¹⁸¹, N. Tamba¹⁸¹, J. Turkewitz¹⁸¹, J.G. Acosta¹⁸², S. Oliveros¹⁸², E. Deedevea<

A. Brinkerhoff¹⁸⁷, K.M. Chan¹⁸⁷, A. Drozdetskiy¹⁸⁷, M. Hildreth¹⁸⁷, C. Jessop¹⁸⁷, D.J. Karmgard¹⁸⁷, N. Kellams¹⁸⁷, K. Lannon¹⁸⁷, S. Lynch¹⁸⁷, N. Marinelli¹⁸⁷, Y. Musienko^{187,232}, T. Pearson¹⁸⁷, M. Planer¹⁸⁷, R. Ruchti¹⁸⁷, G. Smith¹⁸⁷, N. Valls¹⁸⁷, M. Wayne¹⁸⁷, M. Wolf¹⁸⁷, A. Woodard¹⁸⁷, L. Antonelli¹⁸⁸, J. Brinson¹⁸⁸, B. Bylsma¹⁸⁸, L.S. Durkin¹⁸⁸, S. Flowers¹⁸⁸, A. Hart¹⁸⁸, C. Hill¹⁸⁸, R. Hughes¹⁸⁸, K. Kotov¹⁸⁸, T.Y. Ling¹⁸⁸, W. Luo¹⁸⁸, D. Puigh¹⁸⁸, M. Rodenburg¹⁸⁸, B.L. Winer¹⁸⁸, H. Wolfe¹⁸⁸, H.W. Wulsin¹⁸⁸, O. Driga¹⁸⁹, P. Elmer¹⁸⁹, J. Hardenbrook¹⁸⁹, P. Hebda¹⁸⁹, A. Hunt¹⁸⁹, S.A. Koay¹⁸⁹, P. Lujan¹⁸⁹, D. Marlow¹⁸⁹, T. Medvedeva¹⁸⁹, M. Mooney¹⁸⁹, J. Olsen¹⁸⁹, P. Piroué¹⁸⁹, X. Quan¹⁸⁹, H. Saka¹⁸⁹, D. Stickland^{189,205}, C. Tully¹⁸⁹, J.S. Werner¹⁸⁹, A. Zuranski¹⁸⁹, E. Brownson¹⁹⁰, S. Malik¹⁹⁰, H. Mendez¹⁹⁰, J.E. Ramirez Vargas¹⁹⁰, V.E. Barnes¹⁹¹, D. Benedetto¹⁹¹, D. Bortoletto¹⁹¹, M. De Mattia¹⁹¹, L. Gutay¹⁹¹, Z. Hu¹⁹¹, M.K. Jha¹⁹¹, M. Jones¹⁹¹, K. Jung¹⁹¹, M. Kress¹⁹¹, N. Leonardo¹⁹¹, D.H. Miller¹⁹¹, N. Neumeister¹⁹¹, B.C. Radburn-Smith¹⁹¹, X. Shi¹⁹¹, I. Shipsey¹⁹¹, D. Silvers¹⁹¹, A. Syvatskiy¹⁹¹, F. Wang¹⁹¹, W. Xie¹⁹¹, L. Xu¹⁹¹, J. Zablocki¹⁹¹, N. Parashar¹⁹², J. Stupak¹⁹², A. Adair¹⁹³, B. Akgun¹⁹³, K.M. Ecklund¹⁹³, F.J.M. Geurts¹⁹³, W. Li¹⁹³, B. Michlin¹⁹³, B.P. Padley¹⁹³, R. Redjimi¹⁹³, J. Roberts¹⁹³, J. Zabel¹⁹³, B. Betchart¹⁹⁴, A. Bodek¹⁹⁴, R. Covarelli¹⁹⁴, P. de Barbaro¹⁹⁴, R. Demina¹⁹⁴, Y. Eshaq¹⁹⁴, T. Ferbel¹⁹⁴, A. Garcia-Bellido¹⁹⁴, P. Goldenzweig¹⁹⁴, J. Han¹⁹⁴, A. Harel¹⁹⁴, A. Khukhunaishvili¹⁹⁴, S. Korjenevski¹⁹⁴, G. Petrillo¹⁹⁴, D. Vishnevsky¹⁹⁴, R. Ciesielski¹⁹⁵, L. Demortier¹⁹⁵, K. Gouliaou¹⁹⁵, C. Mesropian¹⁹⁵, S. Arora¹⁹⁶, A. Barker¹⁹⁶, J.P. Chou¹⁹⁶, C. Contreras-Campana¹⁹⁶, E. Contreras-Campana¹⁹⁶, D. Duggan¹⁹⁶, D. Ferencek¹⁹⁶, Y. Gershtein¹⁹⁶, R. Gray¹⁹⁶, E. Halkiadakis¹⁹⁶, D. Hidas¹⁹⁶, S. Kaplan¹⁹⁶, A. Lath¹⁹⁶, S. Panwalkar¹⁹⁶, M. Park¹⁹⁶, R. Patel¹⁹⁶, S. Salur¹⁹⁶, S. Schnetzer¹⁹⁶, S. Somalwar¹⁹⁶, R. Stone¹⁹⁶, S. Thomas¹⁹⁶, P. Thomassen¹⁹⁶, M. Walker¹⁹⁶, K. Rose¹⁹⁷, S. Spanier¹⁹⁷, A. York¹⁹⁷, O. Bouhali^{198,258}, A. Castaneda Hernandez¹⁹⁸, R. Eusebi¹⁹⁸, W. Flanagan¹⁹⁸, J. Gilmore¹⁹⁸, T. Kamon^{198,259}, V. Khotilovich¹⁹⁸, V. Krutelyov¹⁹⁸, R. Montalvo¹⁹⁸, I. Osipenko¹⁹⁸, Y. Pakhotin¹⁹⁸, A. Perloff¹⁹⁸, J. Roe¹⁹⁸, A. Rose¹⁹⁸, A. Safonov¹⁹⁸, I. Suarez¹⁹⁸, A. Tatarinov¹⁹⁸, K.A. Ulmer¹⁹⁸, N. Akchurin¹⁹⁹, C. Cowden¹⁹⁹, J. Damgov¹⁹⁹, C. Dragoiu¹⁹⁹, P.R. Duder¹⁹⁹, J. Faulkner¹⁹⁹, K. Kovitangsoo¹⁹⁹, S. Kunori¹⁹⁹, S.W. Lee¹⁹⁹, T. Libeiro¹⁹⁹, I. Volobouev¹⁹⁹, E. Appelt²⁰⁰, A.G. Delannoy²⁰⁰, S. Greene²⁰⁰, A. Gurrola²⁰⁰, W. Johns²⁰⁰, C. Maguire²⁰⁰, Y. Mao²⁰⁰, A. Melo²⁰⁰, M. Sharma²⁰⁰, P. Sheldon²⁰⁰, B. Snook²⁰⁰, S. Tuo²⁰⁰, J. Velkovska²⁰⁰, M.W. Arenton²⁰¹, S. Boutle²⁰¹, B. Cox²⁰¹, B. Francis²⁰¹, J. Goodell²⁰¹, R. Hirosky²⁰¹, A. Ledovskoy²⁰¹, H. Li²⁰¹, C. Lin²⁰¹, C. Neul²⁰¹, J. Wood²⁰¹, C. Clarke²⁰², R. Harr²⁰², P.E. Karchin²⁰², C. Kottachchi Kankanamge Don²⁰², P. Lamichhane²⁰², J. Sturdy²⁰², D.A. Belknap²⁰³, D. Charlsmith²⁰³, M. Cepeda²⁰³, S. Dasu²⁰³, L. Dodd²⁰³, S. Duric²⁰³, E. Friis²⁰³, R. Hall-Wilton²⁰³, M. Herndon²⁰³, A. Hervé²⁰³, P. Klabbres²⁰³, A. Lanaro²⁰³, C. Lazaridis²⁰³, A. Levine²⁰³, R. Loveless²⁰³, A. Mohapatra²⁰³, I. Ojalvo²⁰³, T. Perry²⁰³, G.A. Pierro²⁰³, G. Polese²⁰³, I. Ross²⁰³, T. Sarangi²⁰³, A. Savin²⁰³, W.H. Smith²⁰³, D. Taylor²⁰³, C. Vuosalo²⁰³ & N. Woods²⁰³

Primary affiliations

¹Yerevan Physics Institute, Yerevan, Armenia. ²Institut für Hochenergiephysik der OeAW, Wien, Austria. ³National Centre for Particle and High Energy Physics, Minsk, Belarus. ⁴Universiteit Antwerpen, Antwerpen, Belgium. ⁵Vrije Universiteit Brussel, Brussel, Belgium. ⁶Université Libre de Bruxelles, Bruxelles, Belgium. ⁷Ghent University, Ghent, Belgium. ⁸Université Catholique de Louvain, Louvain-la-Neuve, Belgium. ⁹Université de Mons, Mons, Belgium. ¹⁰Centro Brasileiro de Pesquisas Físicas, Rio de Janeiro, Brazil. ¹¹Universidade do Estado do Rio de Janeiro, Rio de Janeiro, Brazil. ¹²Universidade Estadual Paulista, Universidade Federal do ABC, São Paulo, Brazil. ¹³Universidade Estadual Paulista. ¹⁴Universidade Federal do ABC. ¹⁵Institute for Nuclear Research and Nuclear Energy, Sofia, Bulgaria. ¹⁶University of Sofia, Sofia, Bulgaria. ¹⁷Institute of High Energy Physics, Beijing, China. ¹⁸State Key Laboratory of Nuclear Physics and Technology, Peking University, Beijing, China. ¹⁹Universidad de Los Andes, Bogotá, Colombia. ²⁰University of Split, Faculty of Electrical Engineering, Mechanical Engineering and Naval Architecture, Split, Croatia. ²¹University of Split, Faculty of Science, Split, Croatia. ²²Institute Rudjer Boskovic, Zagreb, Croatia. ²³University of Cyprus, Nicosia, Cyprus. ²⁴Charles University, Prague, Czech Republic. ²⁵Academy of Scientific Research and Technology of the Arab Republic of Egypt, Egyptian Network of High Energy Physics, Cairo, Egypt. ²⁶National Institute of Chemical Physics and Biophysics, Tallinn, Estonia. ²⁷Department of Physics, University of Helsinki, Helsinki, Finland. ²⁸Helsinki Institute of Physics, Helsinki, Finland. ²⁹Lappeenranta University of Technology, Lappeenranta, Finland. ³⁰DSM/IRFU, CEA/Saclay, Gif-sur-Yvette, France. ³¹Laboratoire Leprince-Ringuet, Ecole Polytechnique, IN2P3-CNRS, Palaiseau, France. ³²Institut Pluridisciplinaire Hubert Curie, Université de Strasbourg, Université de Haute Alsace Mulhouse, CNRS/IN2P3, Strasbourg, France. ³³Centre de Calcul de l'Institut National de Physique Nucléaire et de Physique des Particules, CNRS/IN2P3, Villeurbanne, France. ³⁴Université de Lyon, Université Claude Bernard Lyon 1, CNRS-IN2P3, Institut de Physique Nucléaire de Lyon, Villeurbanne, France. ³⁵Institute of High Energy Physics and Informatization, Tbilisi State University, Tbilisi, Georgia. ³⁶RWTH Aachen University, I. Physikalisches Institut, Aachen, Germany. ³⁷RWTH Aachen University, III. Physikalisches Institut A, Aachen, Germany. ³⁸RWTH Aachen University, III. Physikalisches Institut B, Aachen, Germany. ³⁹Deutsches Elektronen-Synchrotron, Hamburg, Germany. ⁴⁰University of Hamburg, Hamburg, Germany. ⁴¹Institut für Experimentelle Kernphysik, Karlsruhe, Germany. ⁴²Institute of Nuclear and Particle Physics (INPP), NCSR Demokritos, Aghia Paraskevi, Greece. ⁴³University of Athens, Athens, Greece. ⁴⁴University of Ioánnina, Ioánnina, Greece. ⁴⁵Wigner Research Centre for Physics, Budapest, Hungary. ⁴⁶Institute of Nuclear Research ATOMKI, Debrecen, Hungary. ⁴⁷University of Debrecen, Debrecen, Hungary. ⁴⁸National Institute of Science Education and Research, Bhubaneswar, India. ⁴⁹Panjab University, Chandigarh, India. ⁵⁰University of Delhi, Delhi, India. ⁵¹Saha Institute of Nuclear Physics, Kolkata, India. ⁵²Bhabha Atomic Research Centre, Mumbai, India. ⁵³Tata Institute of Fundamental Research, Mumbai, India. ⁵⁴Institute for Research in Fundamental Sciences (IPM), Tehran, Iran. ⁵⁵University College Dublin, Dublin, Ireland. ⁵⁶INFN Sezione di Bari, Università di Bari, Politecnico di Bari, Bari, Italy. ⁵⁷INFN Sezione di Bari. ⁵⁸Università di Bari. ⁵⁹Politecnico di Bari. ⁶⁰INFN Sezione di Bologna, Università

di Bologna, Bologna, Italy. ⁶¹INFN Sezione di Bologna. ⁶²Università di Bologna. ⁶³INFN Sezione di Catania, Università di Catania, CSFNSM, Catania, Italy. ⁶⁴INFN Sezione di Catania. ⁶⁵Università di Catania. ⁶⁶CSFNSM. ⁶⁷INFN Sezione di Firenze, Università di Firenze, Firenze, Italy. ⁶⁸INFN Sezione di Firenze. ⁶⁹Università di Firenze. ⁷⁰INFN Laboratori Nazionali di Frascati, Frascati, Italy. ⁷¹INFN Sezione di Genova, Università di Genova, Genova, Italy. ⁷²INFN Sezione di Genova. ⁷³Università di Genova. ⁷⁴INFN Sezione di Milano-Bicocca, Università di Milano-Bicocca, Milano, Italy. ⁷⁵INFN Sezione di Milano-Bicocca. ⁷⁶Università di Milano-Bicocca. ⁷⁷INFN Sezione di Napoli, Università di Napoli 'Federico II', Università della Basilicata (Potenza), Università G. Marconi (Roma), Napoli, Italy. ⁷⁸INFN Sezione di Napoli. ⁷⁹Università di Napoli 'Federico II'. ⁸⁰Università della Basilicata (Potenza). ⁸¹Università G. Marconi (Roma). ⁸²INFN Sezione di Padova, Università di Padova, Università di Trento (Trento), Padova, Italy. ⁸³INFN Sezione di Padova. ⁸⁴Università di Padova. ⁸⁵Università di Trento (Trento). ⁸⁶INFN Sezione di Pavia, Università di Pavia, Pavia, Italy. ⁸⁷INFN Sezione di Pavia. ⁸⁸Università di Pavia. ⁸⁹INFN Sezione di Perugia, Università di Perugia, Perugia, Italy. ⁹⁰INFN Sezione di Perugia. ⁹¹Università di Perugia. ⁹²INFN Sezione di Pisa, Università di Pisa, Scuola Normale Superiore di Pisa, Pisa, Italy. ⁹³INFN Sezione di Pisa. ⁹⁴Università di Pisa. ⁹⁵Scuola Normale Superiore di Pisa. ⁹⁶INFN Sezione di Roma, Università di Roma, Roma, Italy. ⁹⁷INFN Sezione di Roma. ⁹⁸Università di Roma. ⁹⁹INFN Sezione di Torino, Università di Torino, Università del Piemonte Orientale (Novara), Torino, Italy. ¹⁰⁰INFN Sezione di Torino. ¹⁰¹Università di Torino. ¹⁰²Università del Piemonte Orientale (Novara). ¹⁰³INFN Sezione di Trieste, Università di Trieste, Trieste, Italy. ¹⁰⁴INFN Sezione di Trieste. ¹⁰⁵Università di Trieste. ¹⁰⁶Kangwon National University, Chuncheon, Korea. ¹⁰⁷Kyungpook National University, Daegu, Korea. ¹⁰⁸Chonbuk National University, Jeonju, Korea. ¹⁰⁹Chonnam National University, Institute for Universe and Elementary Particles, Kwangju, Korea. ¹¹⁰Korea University, Seoul, Korea. ¹¹¹Seoul National University, Seoul, Korea. ¹¹²University of Seoul, Seoul, Korea. ¹¹³Sungkyunkwan University, Suwon, Korea. ¹¹⁴Vilnius University, Vilnius, Lithuania. ¹¹⁵National Centre for Particle Physics, Universiti Malaysia, Kuala Lumpur, Malaysia. ¹¹⁶Centro de Investigación y de Estudios Avanzados del IPN, Mexico City, Mexico. ¹¹⁷Universidad Iberoamericana, Mexico City, Mexico. ¹¹⁸Benemerita Universidad Autónoma de Puebla, Puebla, Mexico. ¹¹⁹Universidad Autónoma de San Luis Potosí, San Luis Potosí, Mexico. ¹²⁰University of Auckland, Auckland, New Zealand. ¹²¹University of Canterbury, Christchurch, New Zealand. ¹²²National Centre for Physics, Quaid-i-Azam University, Islamabad, Pakistan. ¹²³National Centre for Nuclear Research, Swierk, Poland. ¹²⁴Institute of Experimental Physics, Faculty of Physics, University of Warsaw, Warsaw, Poland. ¹²⁵Laboratório de Instrumentação e Física Experimental de Partículas, Lisboa, Portugal. ¹²⁶Joint Institute for Nuclear Research, Dubna, Russia. ¹²⁷Petersburg Nuclear Physics Institute, Gatchina (St. Petersburg), Russia. ¹²⁸Institute for Nuclear Research, Moscow, Russia. ¹²⁹Institute for Theoretical and Experimental Physics, Moscow, Russia. ¹³⁰P.N. Lebedev Physical Institute, Moscow, Russia. ¹³¹Skobeltsyn Institute of Nuclear Physics, Lomonosov Moscow State University, Moscow, Russia. ¹³²State Research Center of Russian Federation, Institute for High Energy Physics, Protvino, Russia. ¹³³University of Belgrade, Faculty of Physics and Vinca Institute of Nuclear Sciences, Belgrade, Serbia. ¹³⁴Centro de Investigaciones Energéticas Medioambientales y Tecnológicas (CIEMAT), Madrid, Spain. ¹³⁵Universidad Autónoma de Madrid, Madrid, Spain. ¹³⁶Universidad de Oviedo, Oviedo, Spain. ¹³⁷Instituto de Física de Cantabria (IFCA), CSIC-Universidad de Cantabria, Santander, Spain. ¹³⁸CERN, European Organization for Nuclear Research, Geneva, Switzerland. ¹³⁹Paul Scherrer Institut, Villigen, Switzerland. ¹⁴⁰Institute for Particle Physics, ETH Zurich, Zurich, Switzerland. ¹⁴¹Universität Zürich, Zurich, Switzerland. ¹⁴²National Central University, Chung-Li, Taiwan. ¹⁴³National Taiwan University (NTU), Taipei, Taiwan. ¹⁴⁴Chulalongkorn University, Faculty of Science, Department of Physics, Bangkok, Thailand. ¹⁴⁵Cukurova University, Adana, Turkey. ¹⁴⁶Middle East Technical University, Physics Department, Ankara, Turkey. ¹⁴⁷Bogazici University, Istanbul, Turkey. ¹⁴⁸Istanbul Technical University, Istanbul, Turkey. ¹⁴⁹National Scientific Center, Kharkov Institute of Physics and Technology, Kharkov, Ukraine. ¹⁵⁰University of Bristol, Bristol, United Kingdom. ¹⁵¹Rutherford Appleton Laboratory, Didcot, United Kingdom. ¹⁵²Imperial College, London, United Kingdom. ¹⁵³Brunel University, Uxbridge, United Kingdom. ¹⁵⁴Baylor University, Waco, USA. ¹⁵⁵The University of Alabama, Tuscaloosa, USA. ¹⁵⁶Boston University, Boston, USA. ¹⁵⁷Brown University, Providence, USA. ¹⁵⁸University of California, Davis, Davis, USA. ¹⁵⁹University of California, Los Angeles, USA. ¹⁶⁰University of California, Riverside, Riverside, USA. ¹⁶¹University of California, San Diego, La Jolla, USA. ¹⁶²University of California, Santa Barbara, Santa Barbara, USA. ¹⁶³California Institute of Technology, Pasadena, USA. ¹⁶⁴Carnegie Mellon University, Pittsburgh, USA. ¹⁶⁵University of Colorado at Boulder, Boulder, USA. ¹⁶⁶Cornell University, Ithaca, USA. ¹⁶⁷Fairfield University, Fairfield, USA. ¹⁶⁸Fermi National Accelerator Laboratory, Batavia, USA. ¹⁶⁹University of Florida, Gainesville, USA. ¹⁷⁰Florida International University, Miami, USA. ¹⁷¹Florida State University, Tallahassee, USA. ¹⁷²Florida Institute of Technology, Melbourne, USA. ¹⁷³University of Illinois at Chicago (UIC), Chicago, USA. ¹⁷⁴The University of Iowa, Iowa City, USA. ¹⁷⁵Johns Hopkins University, Baltimore, USA. ¹⁷⁶The University of Kansas, Lawrence, USA. ¹⁷⁷Kansas State University, Manhattan, USA. ¹⁷⁸Lawrence Livermore National Laboratory, Livermore, USA. ¹⁷⁹University of Maryland, College Park, USA. ¹⁸⁰Massachusetts Institute of Technology, Cambridge, USA. ¹⁸¹University of Minnesota, Minneapolis, USA. ¹⁸²University of Mississippi, Oxford, USA. ¹⁸³University of Nebraska-Lincoln, Lincoln, USA. ¹⁸⁴State University of New York at Buffalo, Buffalo, USA. ¹⁸⁵Northeastern University, Boston, USA. ¹⁸⁶Northwestern University, Evanston, USA. ¹⁸⁷University of Notre Dame, Notre Dame, USA. ¹⁸⁸The Ohio State University, Columbus, USA. ¹⁸⁹Princeton University, Princeton, USA. ¹⁹⁰University of Puerto Rico, Mayaguez, USA. ¹⁹¹Purdue University, West Lafayette, USA. ¹⁹²Purdue University Calumet, Hammond, USA. ¹⁹³Rice University, Houston, USA. ¹⁹⁴University of Rochester, Rochester, USA. ¹⁹⁵The Rockefeller University, New York, USA. ¹⁹⁶Rutgers, The State University of New Jersey, Piscataway, USA. ¹⁹⁷University of Tennessee, Knoxville, USA. ¹⁹⁸Texas A&M University, College Station, USA. ¹⁹⁹Texas Tech University, Lubbock, USA. ²⁰⁰Vanderbilt University, Nashville, USA. ²⁰¹University of Virginia, Charlottesville, USA. ²⁰²Wayne State University, Detroit, USA. ²⁰³University of Wisconsin, Madison, USA.

Secondary affiliations

²⁰⁴Vienna University of Technology, Vienna, Austria. ²⁰⁵CERN, European Organization for Nuclear Research, Geneva, Switzerland. ²⁰⁶Institut Pluridisciplinaire Hubert Curien, Université de Strasbourg, Université de Haute Alsace Mulhouse, CNRS/IN2P3, Strasbourg, France. ²⁰⁷National Institute of Chemical Physics and Biophysics, Tallinn, Estonia. ²⁰⁸Sobolevskiy Institute of Nuclear Physics, Lomonosov Moscow State University, Moscow, Russia. ²⁰⁹Universidade Estadual de Campinas, Campinas, Brazil. ²¹⁰Laboratoire Leprince-Ringuet, Ecole Polytechnique, IN2P3-CNRS, Palaiseau, France. ²¹¹Joint Institute for Nuclear Research, Dubna, Russia. ²¹²Suez University, Suez, Egypt. ²¹³Cairo University, Cairo, Egypt. ²¹⁴Fayoum University, El-Fayoum, Egypt. ²¹⁵Ain Shams University, Cairo, Egypt. ²¹⁶Now at Sultan Qaboos University, Muscat, Oman. ²¹⁷Université de Haute Alsace, Mulhouse, France. ²¹⁸Brandenburg University of Technology, Cottbus, Germany. ²¹⁹Institute of Nuclear Research ATOMKI, Debrecen, Hungary. ²²⁰Eötvös Loránd University, Budapest, Hungary. ²²¹University of Debrecen, Debrecen, Hungary. ²²²University of Visva-Bharati, Santiniketan, India. ²²³Now at King Abdulaziz University, Jeddah, Saudi Arabia. ²²⁴University of Ruhuna, Matara, Sri Lanka. ²²⁵Isfahan University of Technology, Isfahan, Iran. ²²⁶University of Tehran, Department of Engineering Science, Tehran, Iran. ²²⁷Plasma Physics Research Center, Science and Research Branch, Islamic Azad University, Tehran, Iran. ²²⁸Università degli Studi di Siena, Siena, Italy. ²²⁹Centre National de la Recherche Scientifique (CNRS) - IN2P3, Paris, France. ²³⁰Purdue University, West Lafayette, USA. ²³¹Universidad Michoacana de San Nicolas de Hidalgo, Morelia, Mexico. ²³²Institute for Nuclear Research, Moscow, Russia. ²³³St. Petersburg State Polytechnical University, St. Petersburg, Russia. ²³⁴California Institute of Technology, Pasadena, USA. ²³⁵Faculty of Physics, University of Belgrade, Belgrade, Serbia. ²³⁶Facoltà Ingegneria, Università di Roma, Roma, Italy. ²³⁷Scuola Normale e Sezione dell'INFN, Pisa, Italy. ²³⁸University of Athens, Athens, Greece. ²³⁹Paul Scherrer Institut, Villigen, Switzerland. ²⁴⁰Institute for Theoretical and Experimental Physics, Moscow, Russia. ²⁴¹Albert Einstein Center for Fundamental Physics, Bern, Switzerland. ²⁴²Gaziosmanpasa University, Tokat, Turkey. ²⁴³Adiyaman University, Adiyaman, Turkey. ²⁴⁴Cag University, Mersin, Turkey. ²⁴⁵Anadolu University, Eskisehir, Turkey. ²⁴⁶Ozyegin University, Istanbul, Turkey. ²⁴⁷Izmir Institute of Technology, Izmir, Turkey. ²⁴⁸Necmettin Erbakan University, Konya, Turkey. ²⁴⁹Mimar Sinan University, Istanbul, Istanbul, Turkey. ²⁵⁰Marmara University, Istanbul, Turkey. ²⁵¹Kafkas University, Kars, Turkey. ²⁵²Yildiz Technical University, Istanbul, Turkey. ²⁵³Rutherford Appleton Laboratory, Didcot, United Kingdom. ²⁵⁴School of Physics and Astronomy, University of Southampton, Southampton, United Kingdom. ²⁵⁵University of Belgrade, Faculty of Physics and Vinca Institute of Nuclear Sciences, Belgrade, Serbia. ²⁵⁶Argonne National Laboratory, Argonne, USA. ²⁵⁷Erzincan University, Erzincan, Turkey. ²⁵⁸Texas A&M University at Qatar, Doha, Qatar. ²⁵⁹Kyungpook National University, Daegu, Korea. ‡Deceased.

LHCb Collaboration

I. Bediaga¹, J.M. De Miranda¹, F. Ferreira Rodrigues¹, A. Gomes^{1,79}, A. Massafferri¹, A.C. dos Reis¹, A.B. Rodrigues¹, S. Amato², K. Carvalho Akiba², L. De Paula², O. Francisco², M. Gandelman², A. Hicheur², J.H. Lopes², D. Martins Tostes², I. Nasteva², J.M. Otalora Goicochea², E. Polcarpo², C. Potterat², M.S. Rangel², V. Salustino Guimaraes², B. Souza De Paula², D. Vieira², L. An³, Y. Gao³, F. Jing³, Y. Li³, Z. Yang³, X. Yuan³, Y. Zhang³, L. Zhong³, L. Beaucourt⁴, M. Chefeldt⁴, D. Decamp⁴, N. Deléage⁴, Ph. Ghez⁴, J.-P. Lees⁴, J.F. Marchand⁴, M.-N. Minard⁴, B. Pietrzyk⁴, W. Qian⁴, S. T'Jampens⁴, V. Tisserand⁴, E. Tournier⁴, Z. Ajaltouni⁵, M. Baalouch⁵, E. Cogneras⁵, O. Deschamps⁵, I. El Rifai⁵, M. Grabalosa Gándara⁵, P. Henrard⁵, M. Hoballah⁵, R. Lefèvre⁵, J. Maratas⁵, S. Monteil⁵, V. Niess⁵, P. Perret⁵, C. Adrover⁵, E. Aslanides⁵, J. Cogan⁶, W. Kansa⁶, R. Le Gac⁶, O. Leroy⁶, G. Mancinelli⁶, A. Mordà⁶, M. Perrin-Terrin⁶, J. Ferraro⁶, A. Tsaregorodtsev⁶, Y. Amhis⁶, S. Barsuk⁶, M. Borsato⁶, O. Kochebina⁶, J. Lefrançois⁶, F. Machefert⁶, A. Martin Sánchez⁶, M. Nicol⁶, P. Robbe⁶, M.-H. Schune⁶, M. Teklishyn⁶, A. Vallier⁶, B. Viaud⁶, G. Wormser⁶, E. Ben-Haim⁶, M. Charles⁶, S. Coquereau⁶, P. David⁶, L. Del Buono⁶, L. Henry⁶, F. Polci⁶, J. Albrecht⁶, T. Brambach⁶, Ch. Cauter⁶, M. Deckenhoff⁶, U. Eitschberger⁶, R. Ekelhof⁶, L. Gavioli⁶, F. Kruse⁶, F. Meier⁶, R. Niet⁶, C.J. Parkinson⁶, M. Schlupp⁶, A. Shires⁶, B. Spaan⁶, S. Swientek⁶, J. Wishah⁶, O. Aquines Gutierrez⁶, J. Blouw⁶, M. Britsch⁶, M. Fontana⁶, D. Popov⁶, M. Schmelling⁶, D. Volynskiy⁶, M. Zavertyaev⁶, S. Bachmann⁶, I. A. Bien⁶, A. Comerma-Montells⁶, M. De Cian⁶, F. Dordei⁶, S. Esen⁶, C. Färber⁶, E. Gersabeck⁶, L. Grillo⁶, X. Han⁶, S. Hansmann-Menzemer⁶, A. Jaeger⁶, M. Kolpin⁶, K. Kreplin⁶, G. Krocker⁶, B. Leverington⁶, J. Marks⁶, M. Meissner⁶, M. Neuner⁶, T. Nikodem⁶, P. Seyfert⁶, M. Stahl⁶, S. Stahl⁶, U. Uwer⁶, M. Vesterinen⁶, S. Wandernoth⁶, D. Wiedner⁶, A. Zhelezov⁶, R. McNulty⁶, R. Wallace⁶, W.C. Zhang⁶, A. Palano⁶, A. Carbone⁶, A. Falabella⁶, D. Galli⁶, U. Marconi⁶, L. Moggi⁶, M. Mussini⁶, S. Perazzini⁶, V. Vagnoni⁶, G. Valenti⁶, M. Zangoli⁶, W. Bonivento⁶, S. Cadeddu⁶, A. Cardini⁶, V. Cogoni⁶, A. Contu⁶, A. Lai⁶, B. Liu⁶, G. Manca⁶, S. Roldan⁶, S. Baita⁶, S. Baita⁶, C. Vacca⁶, M. M. Andreotti⁶, W. Baldini⁶, C. Bozzi⁶, R. Calabrese⁶, M. Corvo⁶, M. Fiore⁶, M. Fiorini⁶, E. Lupatini⁶, L.L. Pappalardo⁶, I. Shapoval⁶, G. Tellarini⁶, L. Tomassetti⁶, S. Vecchi⁶, L.L. Anderlini⁶, A. Bizzeti⁶, M. Frorini⁶, G. Graziani⁶, G. Passaleva⁶, M. Veltri⁶, G. Bencivenni⁶, P. Campana⁶, P. De Simone⁶, G. Lanfranchi⁶, M. Palutan⁶, M. Rama⁶, A. Sarti⁶, B. Sciacia⁶, R. Vazquez Gomez⁶, R. Cardinale⁶, F. Fontanelli⁶, S. Gambera⁶, C. Patrignani⁶, A. Petrolini⁶, A. Pistone⁶, M. Calvi⁶, L. Cassina⁶, C. Gotti⁶, B. Khanji⁶, M. Kucharczyk⁶, C. Matteuzzi⁶, J. Fu⁶, A. Geraci⁶, N. Neri⁶, F. Palombo⁶, S. Amerio⁶, G. Collazuol⁶, S. Gallorini⁶, A. Gianelle⁶, D. Lucchesi⁶, A. Lupato⁶, M. Morandini⁶, M. Rotondo⁶, L. Sestini⁶, G. Simi⁶, R. Stroili⁶, F. Bedeschi⁶, R. Cenci⁶, S. Leo⁶, P. Marino⁶, M.J. Morello⁶, G. Punzi⁶, S. Stracka⁶, J. Walsh⁶, G. Carboni⁶, E. Furfaro⁶, E. Santovetti⁶, A. Satta⁶, A.A. Alves Jr⁶, G. Auriemma⁶, V. Bocci⁶, G. Martellotti⁶, G. Penso⁶, D. Pinci⁶, R. Santacesaria⁶, C. Satriano⁶, A. Sciubba⁶, A. Dziurda⁶, W. Kuczewicz⁶, T. Lesiak⁶, B. Rachwal⁶, M. Witek⁶, M. Firlej⁶, T. Tiutowski⁶, M. Idzik⁶, P. Morawski⁶,

J. Moron⁶, A. Oblakowska-Mucha⁶, K. Swientek⁶, T. Szumlak⁶, V. Batzskaya⁶, K. Klimaszewski⁶, K. Kurek⁶, M. Szczekowski⁶, A. Ukleja⁶, W. Wislicki⁶, L. Cojocariu⁶, L. Giubega⁶, A. Grecu⁶, F. Maciuc⁶, M. Orlandea⁶, B. Popovici⁶, S. Stoica⁶, M. Straticu⁶, G. Alkhazov⁶, N. Bondar⁶, A. Dzyuba⁶, O. Maev⁶, N. Sagidova⁶, V. Shcheglov⁶, A. Vorobyev⁶, S. Belogurov⁶, I. Belyaev⁶, V. Egorychev⁶, D. Golubkov⁶, T. Kvaratskheliya⁶, I.V. Machikhiliyan⁶, I. Polyakov⁶, D. Savrina⁶, A. Semennikov⁶, A. Zhokhov⁶, A. Berezhnoy⁶, M. Korolev⁶, A. Leflat⁶, N. Nikitin⁶, S. Filippov⁶, E. Gushchin⁶, L. Kravchuk⁶, A. Bondar⁶, S. Eidelman⁶, P. Krokovny⁶, V. Kudryavtsev⁶, L. Shekhtman⁶, V. Vorobyev⁶, A. Artamonov⁶, K. Belous⁶, R. Dzhelezov⁶, Yu. Guz⁶, A. Novoselov⁶, V. Obraztsov⁶, A. Popov⁶, V. Romanovsky⁶, M. Shapkin⁶, O. Stenyakin⁶, O. Yushchenko⁶, A. Badalov⁶, M. Calvo Gomez⁶, L. Garrido⁶, D. Gascon⁶, R. Graciani Diaz⁶, E. Graugés⁶, C. Marin Benito⁶, E. Picatoste Olloqui⁶, V. Rives Molina⁶, H. Ruiz⁶, X. Vilasis-Cardona⁶, B. Adeva⁶, P. Alvarez Cartelle⁶, A. Dosil Suárez⁶, V. Fernandez Albor⁶, A. Gallas Torreira⁶, J. García Pardiñas⁶, J.A. Hernandez Morata⁶, M. Plo Casasus⁶, A. Romero Vidal⁶, J.J. Saborido Silva⁶, B. Sanmartin Sedes⁶, C. Santamarina Rios⁶, P. Vazquez Regueiro⁶, S. Vázquez Sierra⁶, M. Viteles Diaz⁶, F. Alessio⁶, F. Archilli⁶, C. Barschel⁶, S. Benson⁶, J. Buytaert⁶, D. Campora Perez⁶, L. Castillo Garcia⁶, M. Cattaneo⁶, Ph. Charpentier⁶, X. Cid Vidal⁶, M. Clemencic⁶, J. Closier⁶, V. Coco⁶, P. Collins⁶, G. Corti⁶, B. Couturier⁶, C. D'Ambrosio⁶, F. Dettori⁶, A. Di Canto⁶, H. Dijkstra⁶, P. Durante⁶, M. Ferro-Luzzi⁶, R. Forty⁶, M. Frank⁶, C. Frei⁶, C. Gaspar⁶, V.V. Gligorov⁶, L.A. Granado Cardoso⁶, T. Gys⁶, C. Haen⁶, J. He⁶, T. Head⁶, E. van Herwijnen⁶, R. Jacobsson⁶, D. Johnson⁶, C. Joram⁶, B. Jost⁶, M. Karacson⁶, T.M. Karbach⁶, D. Lacarrere⁶, B. Langhans⁶, R. Lindner⁶, C. Linn⁶, S. Loh⁶, A. Mäkelä⁶, R. Matev⁶, Z. Mathe⁶, S. Neubert⁶, N. Neufeld⁶, A. Otto⁶, J. Panman⁶, M. Pepe Altarelli⁶, N. Rauschmayr⁶, M. Rihl⁶, S. Roiser⁶, T. Ruf⁶, H. Schindler⁶, B. Schmidt⁶, A. Schopper⁶, R. Schwemmer⁶, S. Sridharan⁶, F. Stagni⁶, V.K. Subbiah⁶, F. Teubert⁶, E. Thomas⁶, D. Tonello⁶, A. Trisovic⁶, M. Ubeda Garcia⁶, J. Wicht⁶, K. Wylchie⁶, V. Battista⁶, A. Bay⁶, F. Blanco⁶, M. Dorigo⁶, F. Dupret⁶, C. Fitzpatrick⁶, S. Giani⁶, G. Haefeli⁶, P. Jaton⁶, C. Khurwathanakul⁶, I. Komarov⁶, V.N. La Thi⁶, N. Lopez-March⁶, R. Märki⁶, M. Martinelli⁶, B. Muster⁶, T. Nakada⁶, A.D. Nguyen⁶, T.D. Nguyen⁶, C. Nguyen-Mau⁶, P. Prisciandaro⁶, A. Puig Navarro⁶, B. Rakotomiramanana⁶, J. Rouvinet⁶, O. Schneide⁶, F. Soomro⁶, P. Szczypka⁶, M. Tobin⁶, S. Tourneur⁶, M.T. Tran⁶, G. Veneziani⁶, Z. Xu⁶, J. Anderson⁶, R. Bernet⁶, A. Bowen⁶, A. Bursche⁶, N. Chapiolain⁶, M. Chrzaszcz⁶, Ch. Elssasser⁶, E. Graverini⁶, F. Lionetto⁶, P. Lowdon⁶, K. Müller⁶, N. Serra⁶, O. Steinkamp⁶, B. Stora⁶, U. Straumann⁶, M. Tresch⁶, A. Vollhardt⁶, R. Aaij⁶, S. Ali⁶, M. van Beuzekom⁶, P.N.Y. David⁶, K. De Bruyn⁶, C. Farinelli⁶, V. Heijne⁶, W. Hulsbergen⁶, E. Jans⁶, P. Koppenburg⁶, A. Kozlinskiy⁶, J. van Leerdam⁶, M. Merk⁶, S. Oggero⁶, A. Pellegrino⁶, H. Snoek⁶, J. van Tilburg⁶, P. Tsopelas⁶, N. Tuning⁶, J.A. de Vries⁶, T. Ketel⁶, R.F. Koopman⁶, R.W. Lambert⁶, D. Martinez Santos⁶, G. Raven⁶, M. Schiller⁶, V. Syropoulos⁶, S. Tolk⁶, A. Dovbnya⁶, S. Kandybe⁶, I. Raniuk⁶, O. Okhrimenko⁶, V. Pugatch⁶, S. Bifani⁶, N. Farley⁶, P. Griffith⁶, I.R. Kenyon⁶, C. Lazzaroni⁶, A. Mazurov⁶, J. McCarthy⁶, L. Pescatore⁶, A.K. Watson⁶, M.P. Williams⁶, M. Adinolfi⁶, J. Benton⁶, N.H. Brook⁶, A. Cook⁶, M. Coombes⁶, J. Dalseno⁶, T. Hampson⁶, S.T. Harnew⁶, P. Naik⁶, E. Price⁶, C. Prouve⁶, J.H. Rademacker⁶, S. Richards⁶, D.M. Saunders⁶, N. Skidmore⁶, D. Souza⁶, J.J. Velthuis⁶, D. Voong⁶, W. Barter⁶, M.-O. Bettler⁶, H.V. Cliff⁶, H.-M. Evans⁶, J. Garra Tico⁶, V. Gibson⁶, S. Gregson⁶, S.C. Haines⁶, C.R. Jones⁶, M. Sirendi⁶, J. Smith⁶, D.R. Ward⁶, S.A. Wotton⁶, S. Wright⁶, J.J. Back⁶, T. Blake⁶, D.C. Craik⁶, A.C. Crombre⁶, D. Dossett⁶, T. Gershon⁶, M. Kreps⁶, C. Langenbruch⁶, T. Latham⁶, D.P. O'Hanlon⁶, T. Pilai⁶, A. Poluektov⁶, M.M. Reid⁶, R. Silva Coutinho⁶, C. Wallace⁶, M. Whitehead⁶, S. Easo⁶, R. Nandakumar⁶, A. Papanestis⁶, S. Ricciardi⁶, F.F. Wilson⁶, L. Carson⁶, P.E.L. Clarke⁶, G.A. Cowan⁶, S. Eisenhardt⁶, D. Ferguson⁶, D. Lambert⁶, H. Luo⁶, A.-B. Morris⁶, F. Muheim⁶, M. Needham⁶, S. Player⁶, M. Alexander⁶, J. Beddow⁶, C.-T. Dean⁶, L. Eklund⁶, D. Hynds⁶, S. Karodia⁶, I. Longstaff⁶, S. Ogilvy⁶, M. Pappagallo⁶, P. Sail⁶, I. Skillicorn⁶, F.J.P. Soler⁶, P. Spradlin⁶, A. Affolder⁶, T.J.V. Bowcock⁶, H. Brown⁶, G. Casse⁶, S. Donleavy⁶, K. Dreimanis⁶, S. Farr⁶, R. Fay⁶, K. Hennessy⁶, D. Hutchcroft⁶, M. Liles⁶, B. McKelley⁶, G.D. Patel⁶, J.D. Price⁶, A. Pritchard⁶, K. Rinnert⁶, T. Shears⁶, M.A. Smith⁶, G. Ciezarek⁶, S. Cunliffe⁶, R. Currie⁶, U. Egede⁶, P. Fol⁶, A. Golutin⁶, S. Hall⁶, M. McCann⁶, P. Owen⁶, M. Patel⁶, K. Petridis⁶, F. Redi⁶, I. Sepp⁶, E. Smith⁶, W. Sutcliffe⁶, D. Websdale⁶, R.B. Appleby⁶, R.J. Barlow⁶, T. Bird⁶, P.M. Bjørnstad⁶, S. Borghi⁶, D. Brett⁶, J. Brodzicka⁶, L. Capriotti⁶, S. Chen⁶, S. De Capua⁶, G. Dujany⁶, M. Gersabeck⁶, J. Harrison⁶, C. Hombach⁶, S. Klaver⁶, G. Lafferty⁶, A. McNab⁶, C. Parkes⁶, A. Pearce⁶, S. Reichert⁶, E. Rodriguez⁶, P. Rodriguez Perez⁶, M. Smith⁶, S.-F. Cheung⁶, D. Derkach⁶, T. Evans⁶, R. Gauld⁶, E. Greening⁶, N. Harnew⁶, D. Hill⁶, P. Hunt⁶, N. Hussain⁶, J. Jalocha⁶, M. John⁶, O. Lupton⁶, S. Malde⁶, E. Smith⁶, S. Stevenson⁶, C. Thomas⁶, S. Topp-Joergensen⁶, N. Torr⁶, G. Wilkinson⁶, I. Counts⁶, P. Iten⁶, M. Williams⁶, R. Andraessen⁶, A. Davis⁶, W. De Silva⁶, B. Meadows⁶, L.M. Sokoloff⁶, L. Sun⁶, J. Todd⁶, J.E. Andrews⁶, B. Hamilton⁶, A. Jawahery⁶, J. Wimmerley⁶, M. Artuso⁶, S. Blusk⁶, A. Borgia⁶, T. Britton⁶, S. El⁶, P. Gandini⁶, J. Garofol⁶, B. Gui⁶, C. Hadjivasiliou⁶, N. Jurik⁶, M. Kelsey⁶, R. Mountain⁶, B.K. Pal⁶, T. Skwarnicki⁶, S. Stone⁶, J. Wang⁶, Z. Xing⁶, L. Zhang⁶, C. Baesso⁶, M. Cruz Torres⁶, C. Göbel⁶, J. Molina Rodriguez⁶, Y. Xie⁶, D.A. Milanes⁶, O. Grünberg⁶, M. Heß⁶, C. Voß⁶, R. Waldi⁶, T. Likhomanenko⁶, A. Malinin⁶, V. Shevchenko⁶, A. Ustyuzhanin⁶, F. Martinez Vidal⁶, A. Oyangueren⁶, P. Ruiz Valls⁶, C. Sanchez Mayordomo⁶, C.J.G. Onderwater⁶, H.W. Wilschut⁶ & E. Pesen⁶

Primary affiliations

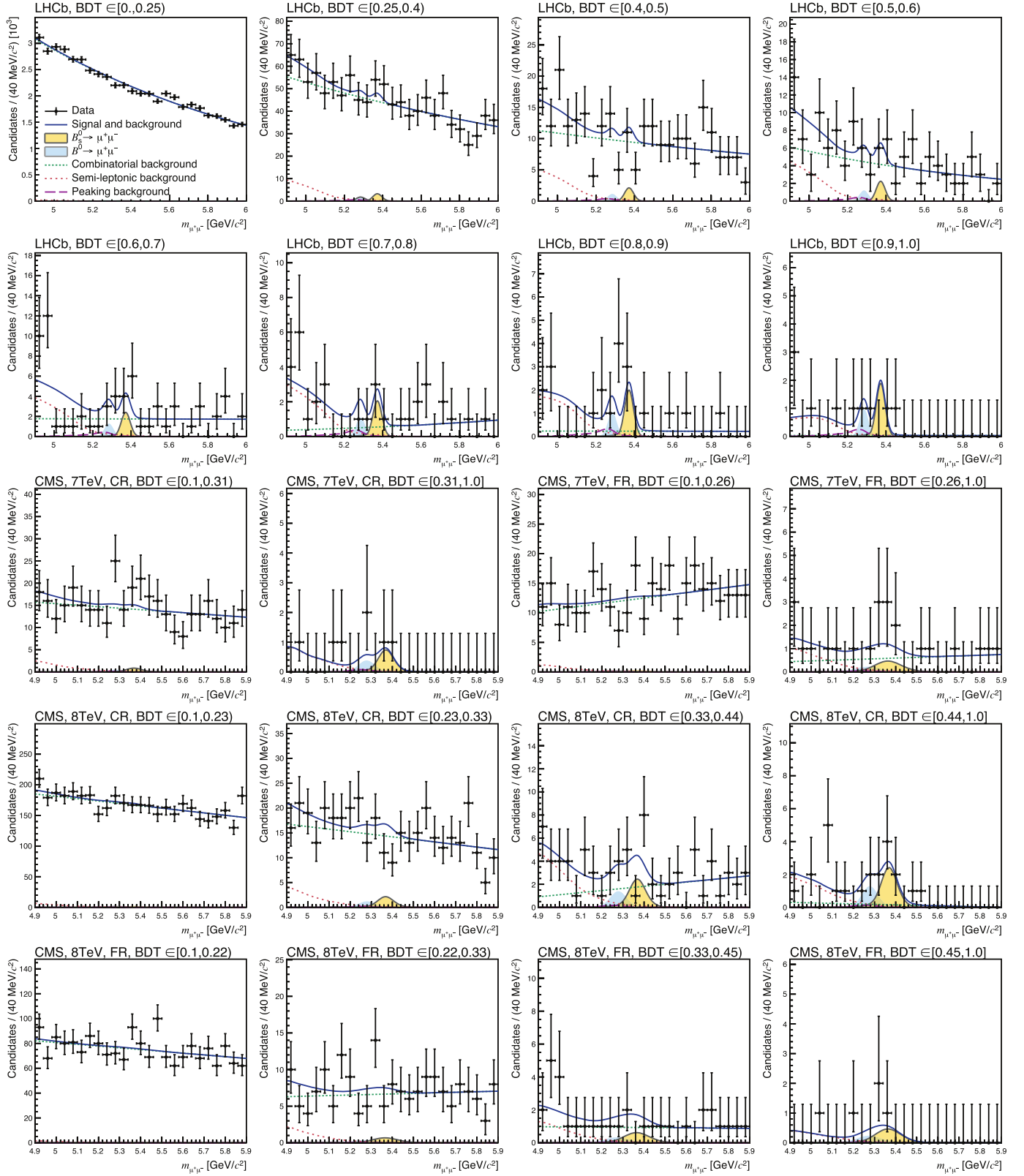
¹Centro Brasileiro de Pesquisas Físicas (CBPF), Rio de Janeiro, Brazil. ²Universidade Federal do Rio de Janeiro (UFRJ), Rio de Janeiro, Brazil. ³Center for High Energy Physics, Tsinghua University, Beijing, China. ⁴LAPP, Université de Savoie, CNRS/IN2P3, Annecy-Le-Vieux, France. ⁵Clermont Université, Université Blaise Pascal, CNRS/IN2P3, LPC, Clermont-Ferrand, France. ⁶CPM, Aix-Marseille Université, CNRS/IN2P3, Marseille,

France. ⁷LAL, Université Paris-Sud, CNRS/IN2P3, Orsay, France. ⁸LPNHE, Université Pierre et Marie Curie, Université Paris Diderot, CNRS/IN2P3, Paris, France. ⁹Fakultät Physik, Technische Universität Dortmund, Dortmund, Germany. ¹⁰Max-Planck-Institut für Kernphysik (MPIK), Heidelberg, Germany. ¹¹Physikalisches Institut, Ruprecht-Karls-Universität Heidelberg, Heidelberg, Germany. ¹²School of Physics, University College Dublin, Dublin, Ireland. ¹³Sezione INFN di Bari, Bari, Italy. ¹⁴Sezione INFN di Bologna, Bologna, Italy. ¹⁵Sezione INFN di Cagliari, Cagliari, Italy. ¹⁶Sezione INFN di Ferrara, Ferrara, Italy. ¹⁷Sezione INFN di Firenze, Firenze, Italy. ¹⁸Laboratori Nazionali dell'INFN di Frascati, Frascati, Italy. ¹⁹Sezione INFN di Genova, Genova, Italy. ²⁰Sezione INFN di Milano Bicocca, Milano, Italy. ²¹Sezione INFN di Milano, Milano, Italy. ²²Sezione INFN di Padova, Padova, Italy. ²³Sezione INFN di Pisa, Pisa, Italy. ²⁴Sezione INFN di Roma Tor Vergata, Roma, Italy. ²⁵Sezione INFN di Roma La Sapienza, Roma, Italy. ²⁶Henryk Niewodniczanski Institute of Nuclear Physics Polish Academy of Sciences, Kraków, Poland. ²⁷AGH - University of Science and Technology, Faculty of Physics and Applied Computer Science, Kraków, Poland. ²⁸National Center for Nuclear Research (NCBJ), Warsaw, Poland. ²⁹Horia Hulubei National Institute of Physics and Nuclear Engineering, Bucharest-Magurele, Romania. ³⁰Petersburg Nuclear Physics Institute (PNPI), Gatchina, Russia. ³¹Institute of Theoretical and Experimental Physics (ITEP), Moscow, Russia. ³²Institute of Nuclear Physics, Moscow State University (SINP MSU), Moscow, Russia. ³³Institute for Nuclear Research of the Russian Academy of Sciences (INR RAN), Moscow, Russia. ³⁴Budker Institute of Nuclear Physics (SB RAS) and Novosibirsk State University, Novosibirsk, Russia. ³⁵Institute for High Energy Physics (IHEP), Protvino, Russia. ³⁶Universitat de Barcelona, Barcelona, Spain. ³⁷Universidad de Santiago de Compostela, Santiago de Compostela, Spain. ³⁸European Organization for Nuclear Research (CERN), Geneva, Switzerland. ³⁹Ecole Polytechnique Fédérale de Lausanne (EPFL), Lausanne, Switzerland. ⁴⁰Physik-Institut, Universität Zürich, Zürich, Switzerland. ⁴¹Nikhef National Institute for Subatomic Physics, Amsterdam, The Netherlands. ⁴²Nikhef National Institute for Subatomic Physics and VU University Amsterdam, Amsterdam, The Netherlands. ⁴³NSC Kharkiv Institute of Physics and Technology (NSC KIPT), Kharkiv, Ukraine. ⁴⁴Institute for Nuclear Research of the National Academy of Sciences (KINR), Kyiv, Ukraine. ⁴⁵University of Birmingham, Birmingham, United Kingdom. ⁴⁶H.H. Wills Physics Laboratory, University of Bristol, Bristol, United Kingdom. ⁴⁷Cavendish Laboratory, University of Cambridge, Cambridge, United Kingdom. ⁴⁸Department of Physics, University of Warwick, Coventry, United Kingdom. ⁴⁹STFC Rutherford Appleton Laboratory, Didcot, United Kingdom. ⁵⁰School of Physics and Astronomy, University of Edinburgh, Edinburgh, United Kingdom. ⁵¹School of Physics and Astronomy, University of Glasgow, Glasgow, United Kingdom. ⁵²Oliver Lodge

Laboratory, University of Liverpool, Liverpool, United Kingdom. ⁵³Imperial College London, London, United Kingdom. ⁵⁴School of Physics and Astronomy, University of Manchester, Manchester, United Kingdom. ⁵⁵Department of Physics, University of Oxford, Oxford, United Kingdom. ⁵⁶Massachusetts Institute of Technology, Cambridge, MA, United States. ⁵⁷University of Cincinnati, Cincinnati, OH, United States. ⁵⁸University of Maryland, College Park, MD, United States. ⁵⁹Syracuse University, Syracuse, NY, United States. ⁶⁰Pontificia Universidade Católica do Rio de Janeiro (PUC-Rio), Rio de Janeiro, Brazil; Universidade Federal do Rio de Janeiro (UFRJ), Rio de Janeiro, Brazil. ⁶¹Institute of Particle Physics, Central China Normal University, Wuhan, Hubei, China; Center for High Energy Physics, Tsinghua University, Beijing, China. ⁶²Departamento de Física, Universidad Nacional de Colombia, Bogotá, Colombia; LPNHE, Université Pierre et Marie Curie, Université Paris Diderot, CNRS/IN2P3, Paris, France. ⁶³Institut für Physik, Universität Rostock, Rostock, Germany; Physikalisches Institut, Ruprecht-Karls-Universität Heidelberg, Heidelberg, Germany. ⁶⁴National Research Centre Kurchatov Institute, Moscow, Russia; Institute of Theoretical and Experimental Physics (ITEP), Moscow, Russia. ⁶⁵Instituto de Física Corpuscular (IFIC), Universitat de Valencia-CSIC, Valencia, Spain; Universitat de Barcelona, Barcelona, Spain. ⁶⁶Van Swinderen Institute, University of Groningen, Groningen, The Netherlands; Nikhef National Institute for Subatomic Physics, Amsterdam, The Netherlands. ⁶⁷Celal Bayar University, Manisa, Turkey; European Organization for Nuclear Research (CERN), Geneva, Switzerland.

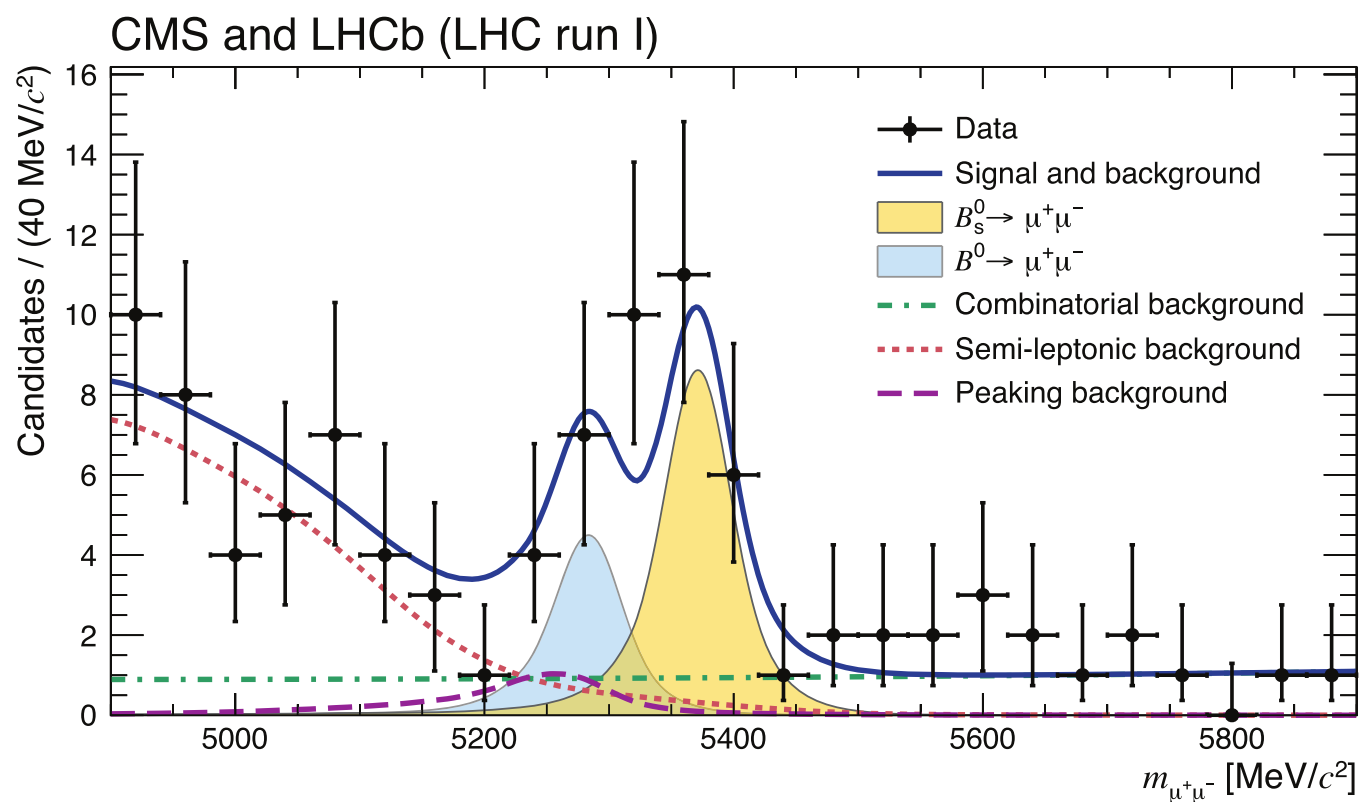
Secondary affiliations

⁶⁸Università di Firenze, Firenze, Italy. ⁶⁹Università di Ferrara, Ferrara, Italy. ⁷⁰Università della Basilicata, Potenza, Italy. ⁷¹Università di Modena e Reggio Emilia, Modena, Italy. ⁷²Università di Milano Bicocca, Milano, Italy. ⁷³LIFAELS, La Salle, Universitat Ramon Llull, Barcelona, Spain. ⁷⁴Università di Bologna, Bologna, Italy. ⁷⁵Università di Roma Tor Vergata, Roma, Italy. ⁷⁶Università di Genova, Genova, Italy. ⁷⁷Scuola Normale Superiore, Pisa, Italy. ⁷⁸Politecnico di Milano, Milano, Italy. ⁷⁹Universidade Federal do Triângulo Mineiro (UFMT), Uberaba-MG, Brazil. ⁸⁰AGH - University of Science and Technology, Faculty of Computer Science, Electronics and Telecommunications, Kraków, Poland. ⁸¹Università di Padova, Padova, Italy. ⁸²Università di Cagliari, Cagliari, Italy. ⁸³Hanoi University of Science, Hanoi, Viet Nam. ⁸⁴Università di Bari, Bari, Italy. ⁸⁵Università degli Studi di Milano, Milano, Italy. ⁸⁶Università di Roma La Sapienza, Roma, Italy. ⁸⁷Università di Pisa, Pisa, Italy. ⁸⁸Università di Urbino, Urbino, Italy. ⁸⁹P.N. Lebedev Physical Institute, Russian Academy of Science (LPI RAS), Moscow, Russia.



Extended Data Figure 1 | Distribution of the dimuon invariant mass $m_{\mu^+\mu^-}$ in each of the 20 categories. Superimposed on the data points in black are the combined fit (solid blue) and its components: the B_s^0 (yellow shaded) and B^0 (light-blue shaded) signal components; the combinatorial background (dash-dotted green); the sum of the semi-leptonic backgrounds (dotted salmon); and the peaking backgrounds (dashed violet). The categories are defined by the

range of BDT values for LHCb, and for CMS, by centre-of-mass energy, by the region of the detector in which the muons are detected, and by the range of BDT values. Categories for which both muons are detected in the central region of the CMS detector are denoted with CR, those for which at least one muon was detected into the forward region with FR.



Extended Data Figure 2 | Distribution of the dimuon invariant mass $m_{\mu^+\mu^-}$ for the best six categories. Categories are ranked according to values of $S/(S+B)$ where S and B are the numbers of signal events expected assuming the SM rates and background events under the B_s^0 peak for a given category, respectively. The mass distribution for the six highest-ranking categories, three

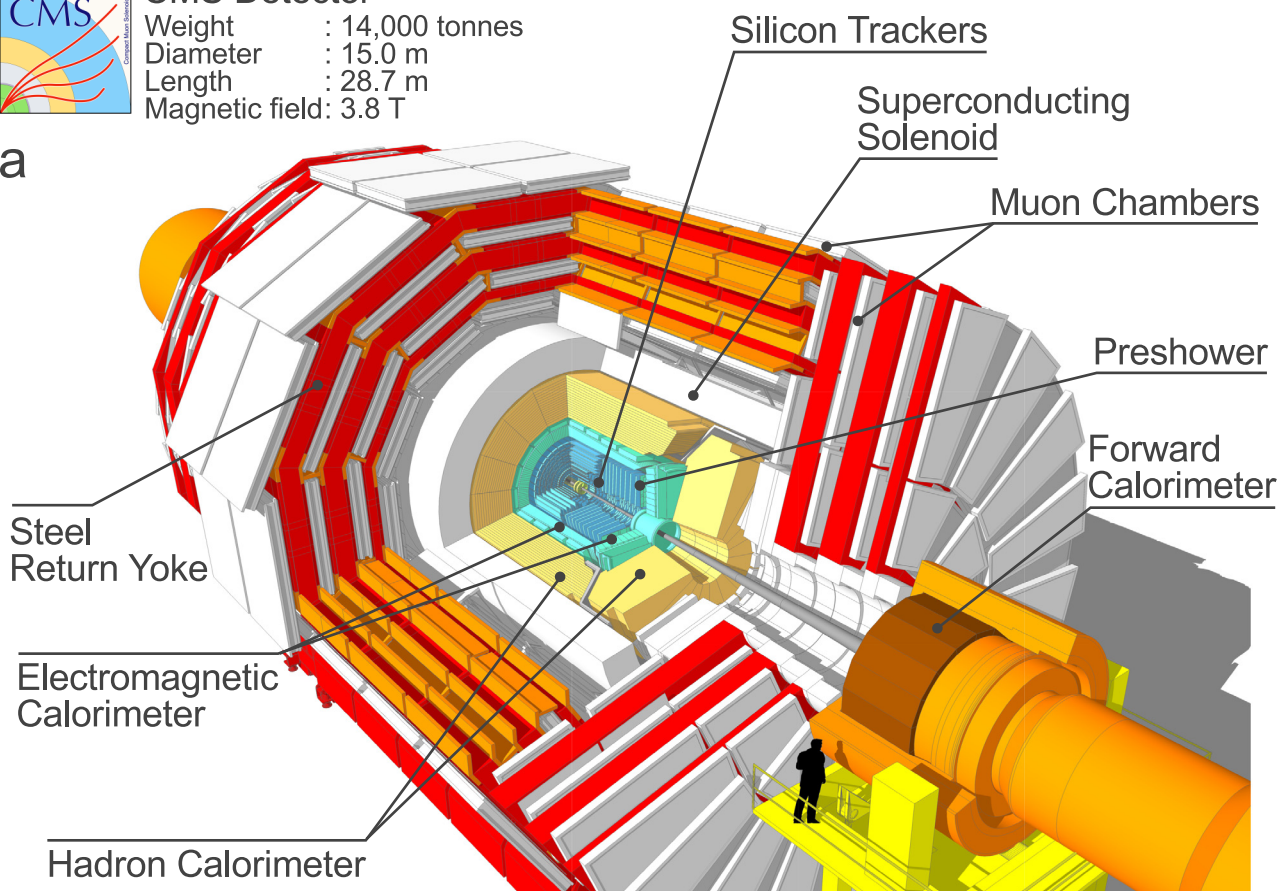
per experiment, is shown. Superimposed on the data points in black are the combined full fit (solid blue) and its components: the B_s^0 (yellow shaded) and B^0 (light-blue shaded) signal components; the combinatorial background (dash-dotted green); the sum of the semi-leptonic backgrounds (dotted salmon); and the peaking backgrounds (dashed violet).



CMS Detector

Weight : 14,000 tonnes
 Diameter : 15.0 m
 Length : 28.7 m
 Magnetic field: 3.8 T

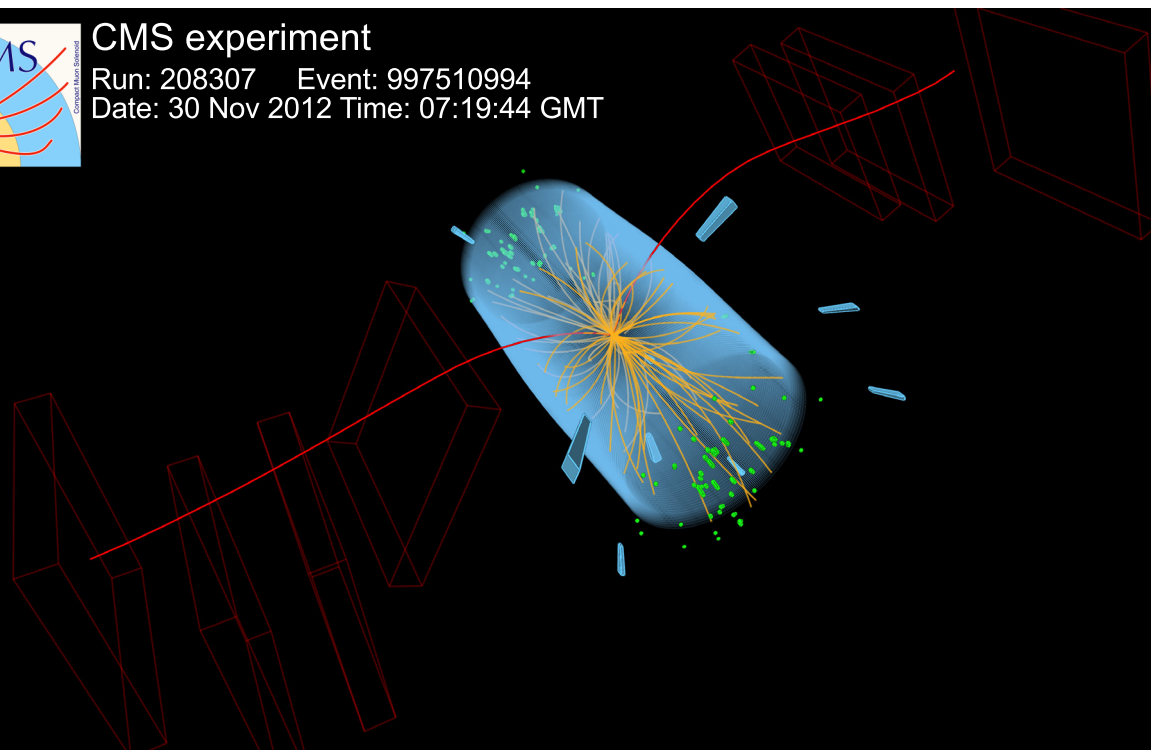
a



CMS experiment

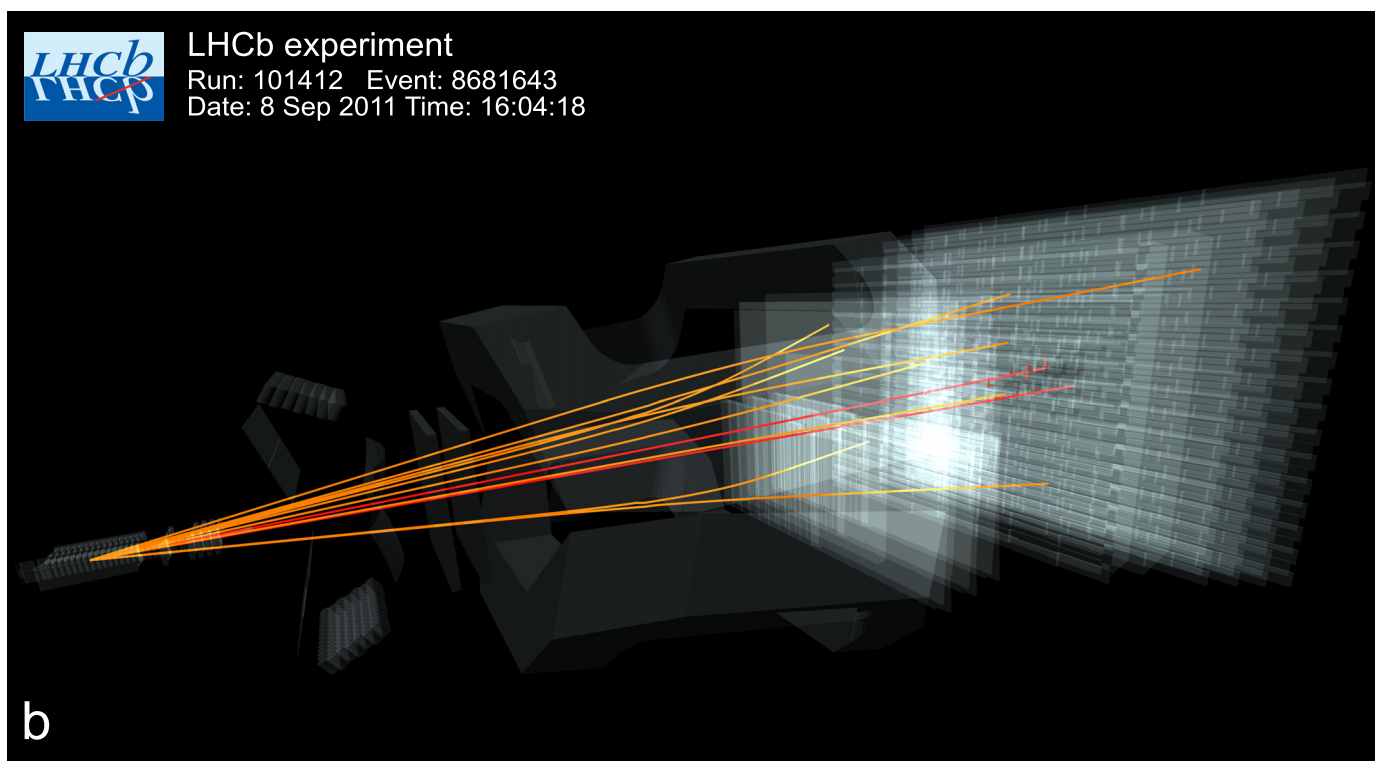
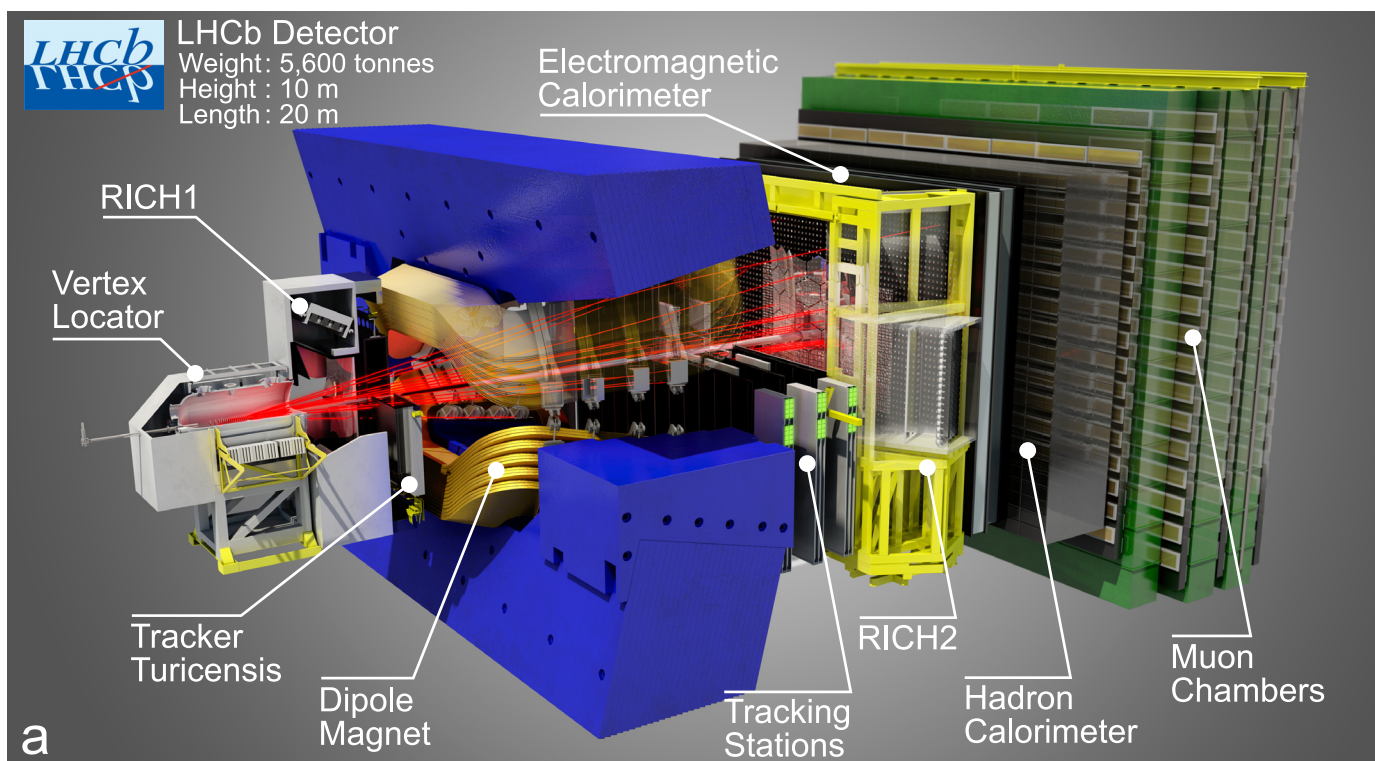
Run: 208307 Event: 997510994
 Date: 30 Nov 2012 Time: 07:19:44 GMT

b



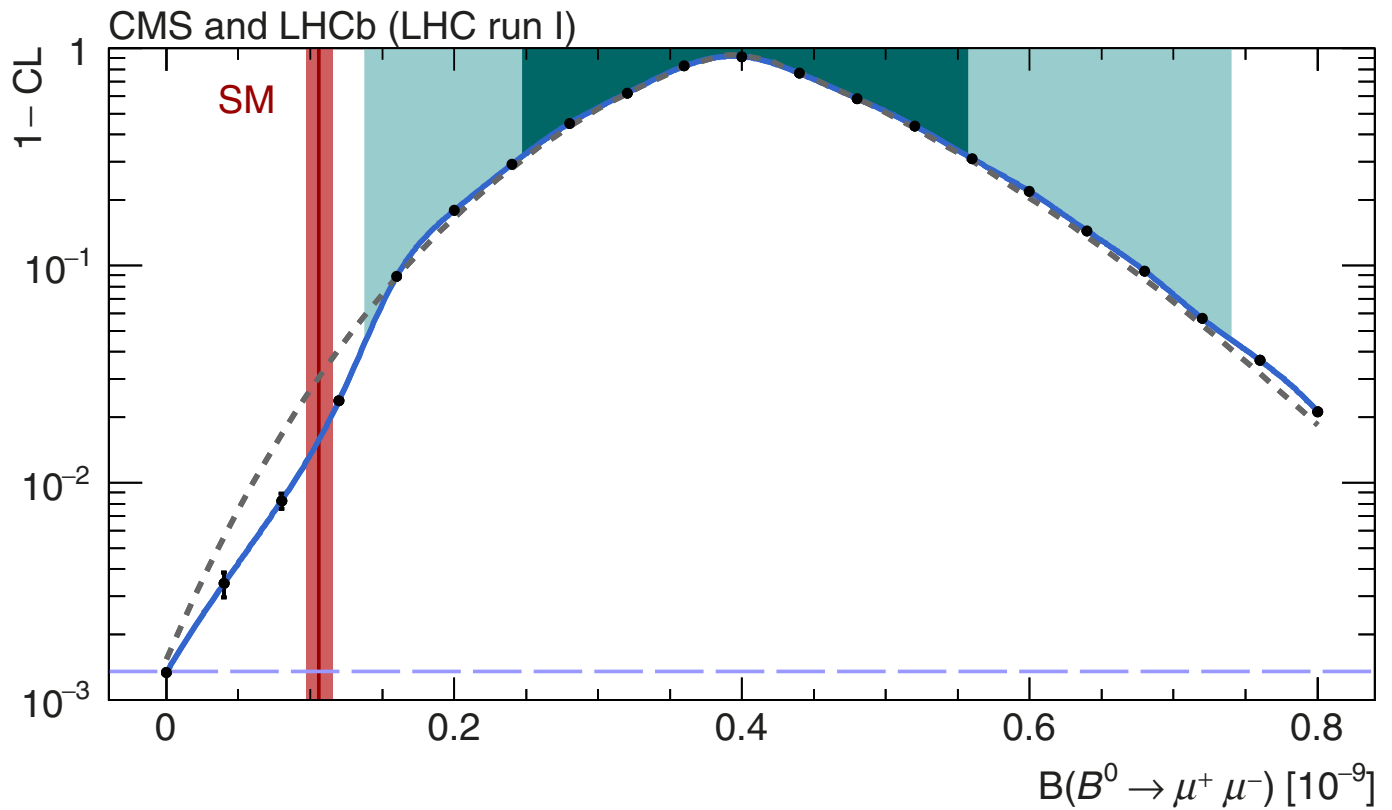
Extended Data Figure 3 | Schematic of the CMS detector and event display for a candidate $B_s^0 \rightarrow \mu^+ \mu^-$ decay at CMS. a, The CMS detector and its components; see ref. 20 for details. b, A candidate $B_s^0 \rightarrow \mu^+ \mu^-$ decay produced

in proton–proton collisions at 8 TeV in 2012 and recorded in the CMS detector. The red arched curves represent the trajectories of the muons from the B_s^0 decay candidate.



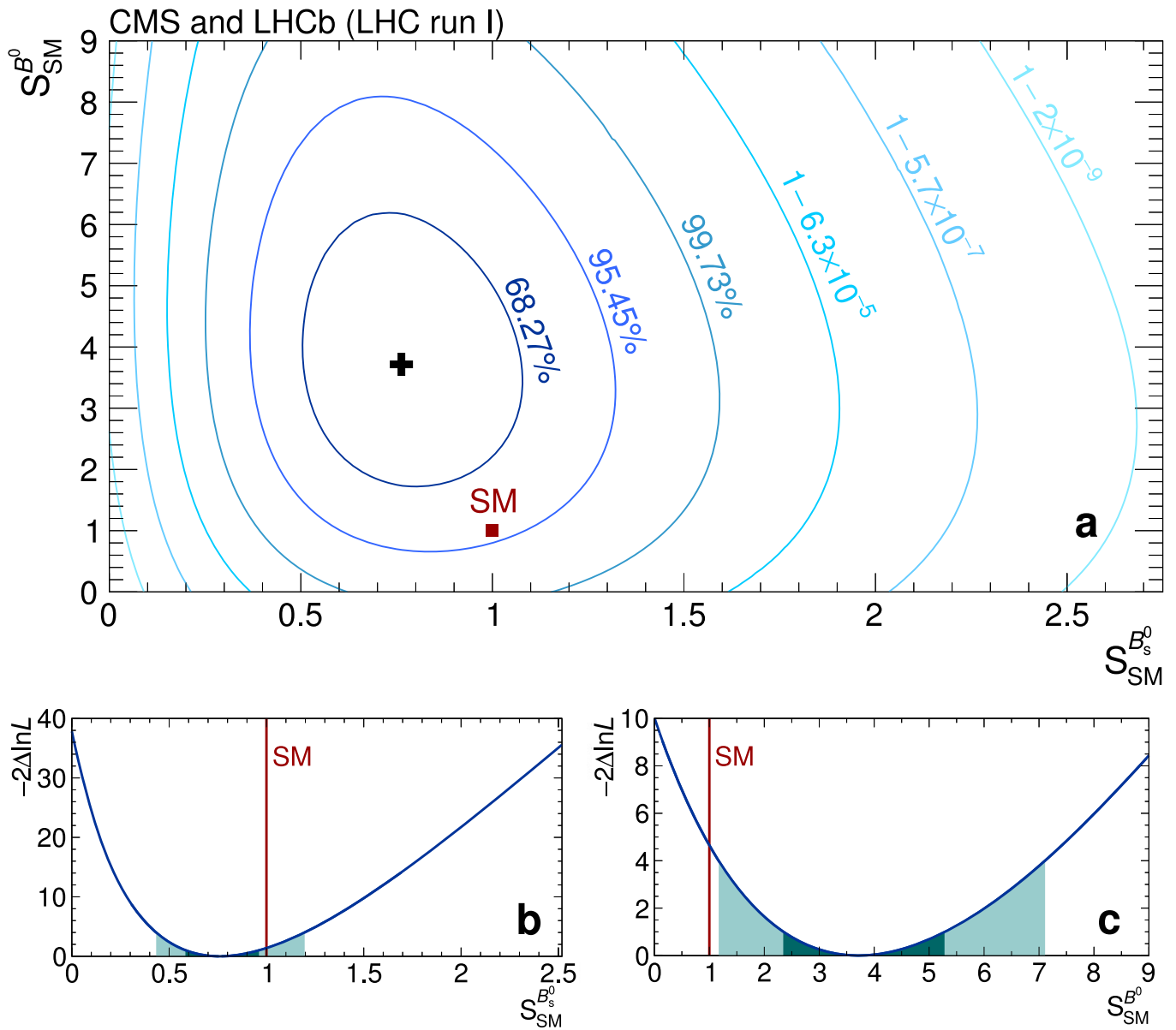
Extended Data Figure 4 | Schematic of the LHCb detector and event display for a candidate $B_s^0 \rightarrow \mu^+ \mu^-$ decay at LHCb. **a**, The LHCb detector and its components; see ref. 21 for details. **b**, A candidate $B_s^0 \rightarrow \mu^+ \mu^-$ decay produced in proton–proton collisions at 7 TeV in 2011 and recorded in the LHCb

detector. The proton–proton collision occurs on the left-hand side, at the origin of the trajectories depicted with the orange curves. The red curves represent the trajectories of the muons from the B_s^0 candidate decay.



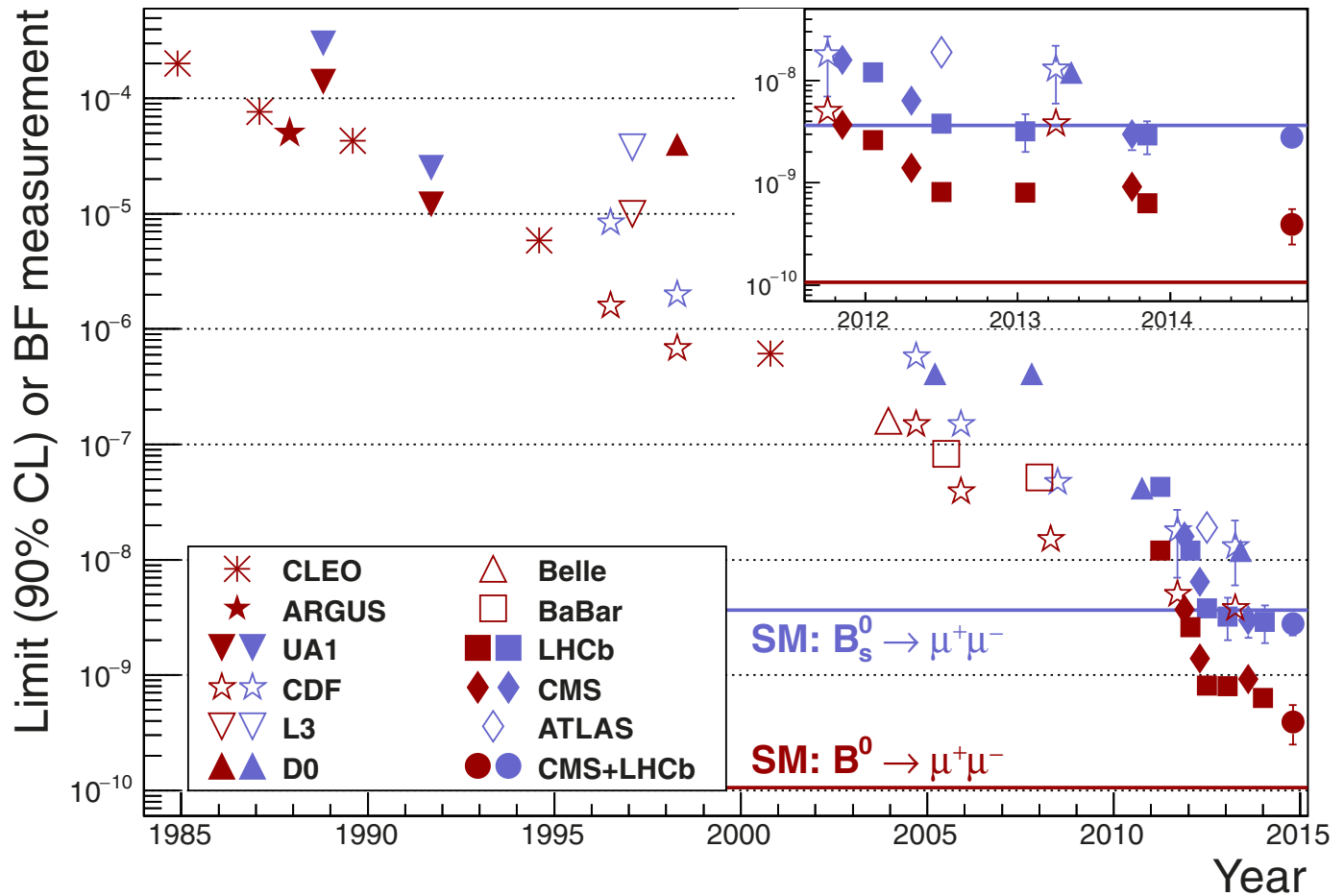
Extended Data Figure 5 | Confidence level as a function of the $B(B^0 \rightarrow \mu^+ \mu^-)$ hypothesis. The value of $1 - \text{CL}$, where CL is the confidence level obtained with the Feldman–Cousins procedure, as a function of $B(B^0 \rightarrow \mu^+ \mu^-)$ is shown in logarithmic scale. The points mark the computed $1 - \text{CL}$ values and the curve is their spline interpolation. The dark and light (cyan) areas define the two-sided $\pm 1\sigma$ and $\pm 2\sigma$ confidence intervals for the branching fraction, while

the dashed horizontal line defines the confidence level for the 3σ one-sided interval. The dashed (grey) curve shows the $1 - \text{CL}$ values computed from the one-dimensional $-2\Delta\ln L$ test statistic using Wilks' theorem. Deviations between these confidence level values and those from the Feldman–Cousins procedure³⁰ illustrate the degree of approximation implied by the asymptotic assumptions inherent to Wilks' theorem²⁹.



Extended Data Figure 6 | Likelihood contours for the ratios of the branching fractions with respect to their SM prediction, in the $S_{\text{SM}}^{B^0}$ versus $S_{\text{SM}}^{B_s^0}$ plane. **a**, The (black) cross marks the central value returned by the fit. The SM point is shown as the (red) square located, by construction, at $S_{\text{SM}}^{B^0} = S_{\text{SM}}^{B_s^0} = 1$. Each contour encloses a region approximately corresponding to the reported confidence level. The SM branching fractions are assumed

uncorrelated to each other, and their uncertainties are accounted for in the likelihood contours. **b**, **c**, Variations of the test statistic $-2\Delta\ln L$ for $S_{\text{SM}}^{B_s^0}$ and $S_{\text{SM}}^{B^0}$ are shown in **b** and **c**, respectively. The SM is represented by the (red) vertical lines. The dark and light (cyan) areas define the $\pm 1\sigma$ and $\pm 2\sigma$ confidence intervals, respectively.



Extended Data Figure 7 | Search for the $B_s^0 \rightarrow \mu^+ \mu^-$ and $B^0 \rightarrow \mu^+ \mu^-$ decays, reported by 11 experiments spanning more than three decades, and by the present results. Markers without error bars denote upper limits on the branching fractions at 90% confidence level, while measurements are denoted with error bars delimiting 68% confidence intervals. The solid horizontal lines

represent the SM predictions for the $B_s^0 \rightarrow \mu^+ \mu^-$ and $B^0 \rightarrow \mu^+ \mu^-$ branching fractions¹; the blue (red) lines and markers relate to the $B_s^0 \rightarrow \mu^+ \mu^-$ ($B^0 \rightarrow \mu^+ \mu^-$) decay. Data (see key) are from refs 17, 18, 31–60; for details see Methods. Inset, magnified view of the last period in time.

Greenland supraglacial lake drainages triggered by hydrologically induced basal slip

Laura A. Stevens^{1†}, Mark D. Behn², Jeffrey J. McGuire², Sarah B. Das², Ian Joughin³, Thomas Herring⁴, David E. Shean³ & Matt A. King^{5,6}

Water-driven fracture propagation beneath supraglacial lakes rapidly transports large volumes of surface meltwater to the base of the Greenland Ice Sheet¹. These drainage events drive transient ice-sheet acceleration^{1–3} and establish conduits for additional surface-to-bed meltwater transport for the remainder of the melt season^{1,4–6}. Although it is well established that cracks must remain water-filled to propagate to the bed^{7–9}, the precise mechanisms that initiate hydro-fracture events beneath lakes are unknown. Here we show that, for a lake on the western Greenland Ice Sheet, drainage events are preceded by a 6–12 hour period of ice-sheet uplift and/or enhanced basal slip. Our observations from a dense Global Positioning System (GPS) network allow us to determine the distribution of meltwater at the ice-sheet bed before, during, and after three rapid drainages in 2011–2013, each of which generates tensile stresses that promote hydro-fracture beneath the lake. We hypothesize that these precursors are associated with the introduction of meltwater to the bed through neighbouring moulin systems (vertical conduits connecting the surface and base of the ice sheet). Our results imply that as lakes form in less crevassed, interior regions of the ice sheet^{10–14}, where water at the bed is currently less pervasive^{5,14–16}, the creation of new surface-to-bed conduits caused by lake-draining hydro-fractures may be limited.

Greenland Ice Sheet flow accelerates at the beginning of the melt season^{5,15}, when surface meltwater reaches the bed via conduits^{1,4–6,17,18}. Inland from the ice margin, this process is often associated with the drainage of supraglacial lakes^{15,19}. Most supraglacial lakes drain slowly, overflowing their banks and routing lake water via surficial streams to nearby crevasses and/or moulins^{3,20,21}. A smaller fraction (~13%) of lakes drain rapidly (<1 day)²⁰, in some cases as rapidly as a few hours^{1–3}, through large (kilometre-scale length) hydro-fractures that form directly beneath the lake basin. These hydro-fractures subsequently close except where continued stream flow keeps moulins open for the remainder of the melt season^{1–3}. While the former style of drainage requires the presence of pre-existing crevasses and/or moulins, the latter has the potential to create new surface-to-bed meltwater pathways through the ice sheet, and is thus an area of intense study^{1–3,5,19,22,23}.

While the basic principles of hydro-fracture through glacial ice are well understood^{7–9}, the mechanism that triggers the formation of kilometre-scale length hydro-fractures in compressional basins where lakes form is unknown². A necessary condition for generating through-ice hydro-fractures is that a supraglacial lake must contain a sufficient volume of water to keep a fracture filled as it propagates from the surface to the bed^{7–9}. However, large lakes with volumes well above this threshold often do not drain over multiple summers¹². Additionally, lakes repeatedly fill basins containing numerous healed hydro-fracture cracks and moulins created during drainage events in previous years^{1,2,7}, implying that the presence of pre-existing cracks

does not necessarily lead to immediate drainage. Thus, identifying the first-order control on hydro-fracture initiation preceding rapid lake drainages has remained elusive.

In this study, we investigate hydro-fracture initiation and rapid drainage at North Lake (68.72° N, –49.50° W), an ~2.5-km diameter supraglacial lake located south of the Jakobshavn-Isbræ catchment on thick ice (~980 m) (Fig. 1). This site has been the focus of in-depth study since 2006, when the first detailed evidence for hydro-fracture to the bed of the Greenland Ice Sheet was collected using GPS measurements from North Lake base station¹ (Fig. 1). During the 2006 event, a slow, steady lake-level drop was observed over a 16-h pre-drainage stage followed by the rapid (<2 h) drainage coincident with vertical and horizontal ice displacement¹. Subsequent modelling of the North Lake base station data collected during this event found that vertical

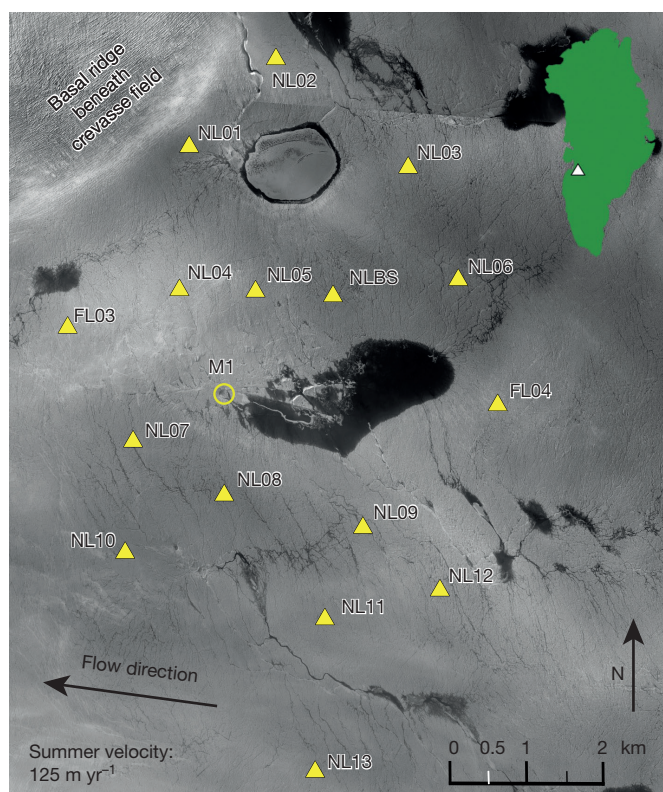


Figure 1 | Synthetic aperture radar (SAR) image on 17 June 2011 showing the extent of North Lake (centre) and surrounding lakes 1 day before the 2011 rapid North Lake drainage. Yellow triangles, GPS locations. The M1 moulin is also shown. Image copyright DigitalGlobe.

¹Massachusetts Institute of Technology/Woods Hole Oceanographic Institution Joint Program in Oceanography/Applied Ocean Science and Engineering, Woods Hole, Massachusetts 02543, USA. ²Department of Geology and Geophysics, Woods Hole Oceanographic Institution, Woods Hole, Massachusetts 02543, USA. ³Polar Science Center, Applied Physics Laboratory, University of Washington, 1013 NE 40th Street, Seattle, Washington 98105-6698, USA. ⁴Department of Earth, Atmospheric, and Planetary Sciences, Massachusetts Institute of Technology, Cambridge, Massachusetts 02139, USA. ⁵School of Land and Food, University of Tasmania, Private Bag 76, Hobart, Tasmania 7001, Australia. ⁶School of Civil Engineering and Geosciences, Newcastle University, Newcastle upon Tyne NE1 7RU, UK. [†]Present address: 360 Woods Hole Road, Woods Hole, Massachusetts 02543, USA.

uplift was caused almost entirely by a horizontal cavity opening at the ice-bed interface due to rapid injection of meltwater, whereas opening of the through-ice vertical crack was the principal contributor to the horizontal surface displacements²³. Similar observations have since been made at other west Greenland Ice Sheet supraglacial lakes^{2,3}, all providing definitive evidence for rapid meltwater drainage to the bed during hydro-fracture events.

A limitation of these previous studies was insufficiently dense observations of surface motion required to directly constrain the mechanism and location of hydro-fracture initiation and the spatial distribution of meltwater at the ice-sheet bed. Here we present results from a spatially-dense array of 16 GPS stations positioned around North Lake between 2011 and 2013 (Fig. 1). This array captured the dynamic response of the ice sheet to rapid lake drainages in each of the 3 years of the study, allowing us to infer the evolving hydro-fracture geometry and spatial distribution of meltwater at the ice-sheet bed before, during, and after drainages.

From these GPS data, we identify a period of precursory ice motion, indicative of the presence of an increased volume of water reaching the bed within the GPS array, hours before each year's local hydro-fracture initiation and rapid lake drainage (Extended Data Table 1). The displacement anomalies (Fig. 2a–c) show the along-flowline, crack-normal, and vertical displacement histories for 2 days before and 1 day after each drainage event at stations NL08 and NL01 or NL03 (Fig. 1 and Methods). We pick three time points for each drainage (using all available stations) that designate the start of the precursor, hydro-fracture initiation, and the maximum hydro-fracture opening (Fig. 2 and Extended Data Table 1).

The 2011 precursor is manifested as vertical uplift followed by increased displacement in the flow-line direction at stations southwest of moulin M1 (NL07, NL08, NL10) over the 10 h leading up to rapid lake drainage (Figs 1, 2a and 3a). This is consistent with field observa-

tions that suggest as North Lake filled over the preceding days the western shoreline reached M1, allowing meltwater to begin pooling in and reactivating M1 before lake drainage, thus permitting increased basal slip (Extended Data Figs 1 and 2). Similarly, we observe increased displacement in the flow-line direction before the 2012 and 2013 hydro-fracture events, which we also interpret to be hydrologically induced (Fig. 2b, c) (see 'The 2012 North Lake drainage' and 'The 2013 North Lake drainage' in Methods). In 2012 the precursor is manifested as anomalous along-flowline displacements at stations in the northern end of the array (for example, NL01 and NL02), but shows little signal at the southern stations (Extended Data Fig. 4a). The 2013 precursor is manifested as enhanced flowline displacements at all western stations (FL03, NL04, NL07, NL08, NL10), as well as vertical uplift focused just west of the lake basin (Extended Data Fig. 5a). All three precursors have similar durations (6–12 h), but they occur in different subsets of the spatial array. After each precursor there is clear evidence of the main 4-km long hydro-fracture opening and subsequent rapid lake drainage, as indicated by the ~3-h long, 5–10 cm excursion of NL08 in the crack-normal (southward) direction, which is rapidly recovered owing to closing of the fracture (Fig. 2a–c). In all 3 years the hydro-fracture opening phase is accompanied by considerable (>20 cm) uplift and enhanced along-flowline motion across many stations in the network.

To quantitatively constrain the processes responsible for these surface motions, we exploit the high spatial density of our GPS data to invert for the space-time history of deformation surrounding the lake drainages. We use the Network Inversion Filter (NIF) algorithm²⁴ to model the GPS time series of drainage-related surface motion as the summation of three deformation sources: (1) hydro-fracture opening, (2) basal cavity opening (due to the rapid injection of meltwater), and (3) extra basal slip above the background rate (due to enhanced basal lubrication) (Methods) (Extended Data Figs 6–8). The NIF utilizes Green's functions

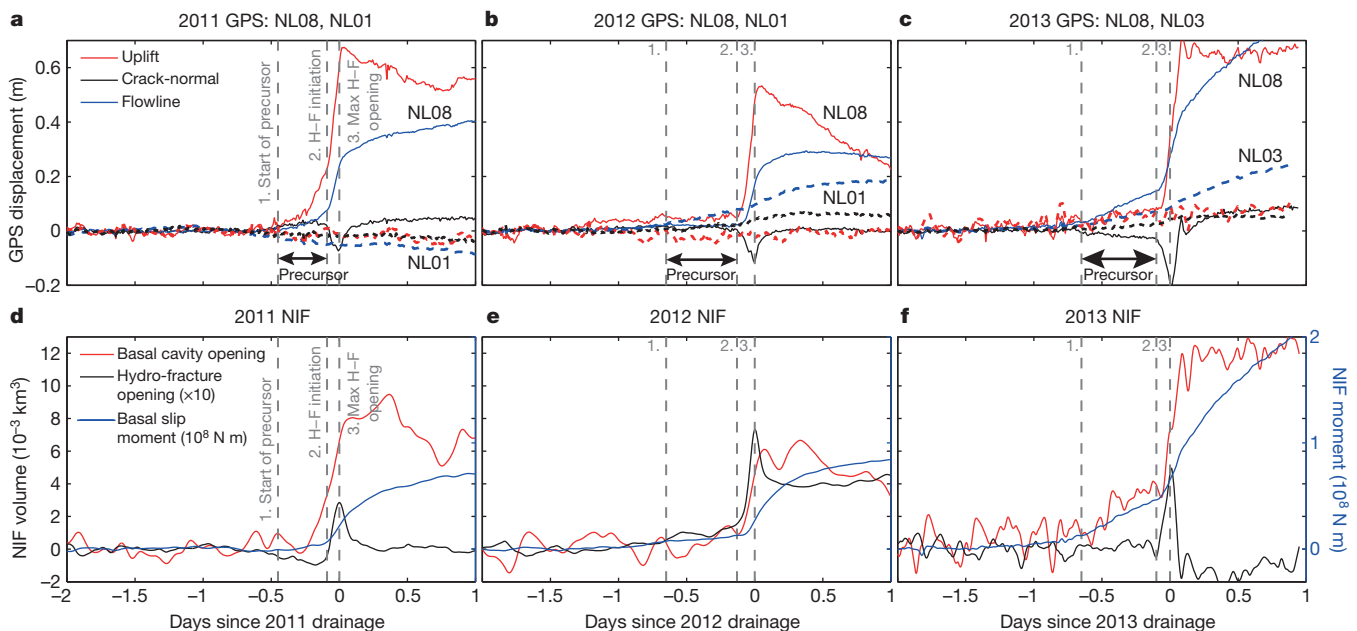


Figure 2 | The 2011, 2012, and 2013 North Lake drainages. GPS station displacement less background velocities is shown in solid (dashed) lines for station NL08 (NL01 or NL03) flowline displacement (blue), crack-normal displacement (black), and relative vertical uplift (red) over the 2 days before and 1 day after the (a) 2011, (b) 2012, and (c) 2013 drainage events. The bottom row shows NIF-derived hydro-fracture opening volume (black), basal cavity opening volume (red), and basal slip moment (blue) across the domain for the 2 days before and 1 day after the (d) 2011, (e) 2012, and (f) 2013 drainage events. The coordinate system is orientated such that hydro-fracture opening is expressed primarily in the horizontal crack-normal component, while basal slip

is primarily expressed in the horizontal flowline component, and basal cavity opening is primarily reflected in the vertical component data. The precursor and rapid lake drainage periods are designated by three time points across the drainages: (1) the start of the precursor at the time of first distinguishable deviation of station vertical uplift, crack-normal, or flowline displacement from the background velocity field ('1. Start of precursor'); (2) hydro-fracture initiation at the time of maximum NL08 southward crack-normal acceleration ('2. H-F initiation'); and, (3) the maximum hydro-fracture opening at the time of maximum southward NL08 crack-normal displacement ('3. Max H-F opening') (Extended Data Table 1).

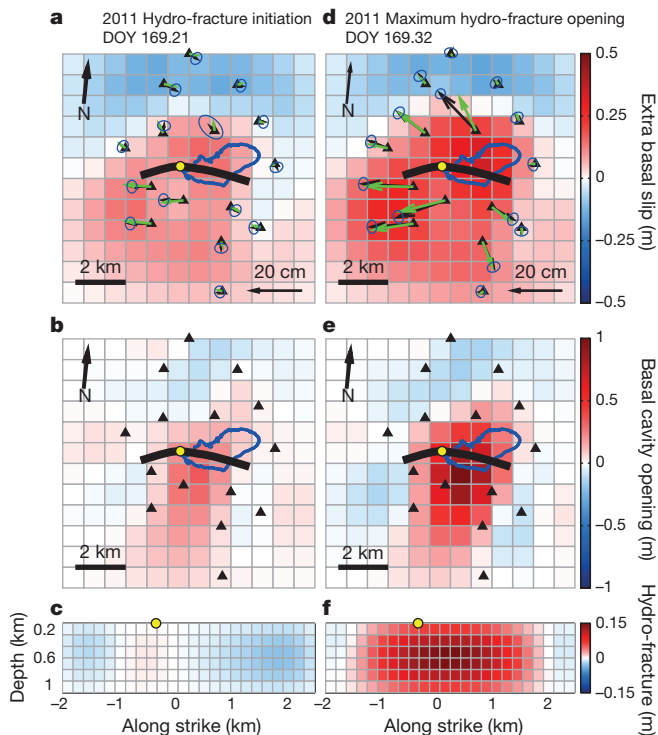


Figure 3 | The 2011 basal slip and cavity opening at hydro-fracture initiation and maximum hydro-fracture opening. NIF-calculated (a) extra basal slip accumulated, (b) basal cavity opening, and (c) hydro-fracture crack opening at the time of the 2011 (a–c) hydro-fracture initiation and (d–f) maximum hydro-fracture opening (time points shown in Fig. 2a). Moulin location, last known lake shoreline, GPS stations, and NIF vertical crack surface trace derived from SAR imagery are shown as a yellow circle, blue line, black triangles, and black line, respectively. Vector fields show GPS (NIF) displacement less background velocities in black (green) for (a) the period between the start of the precursor and hydro-fracture initiation, and (d) the period between hydro-fracture initiation and maximum hydro-fracture opening. Error ellipses of 1 sigma are shown for the GPS displacements (blue ellipses). Basal sub-elements are 0.83 km by 0.83 km, resulting in 144 sub-elements over a 10 km \times 10 km region. DOY, day of year (DOY 169 in 2011 was 18 June).

for an elastic half-space to relate the surface displacement time series to the space-time history of opening and slip along prescribed planes describing each of these deformation sources²⁴ (Methods).

The NIF results provide estimates of the spatial distribution of meltwater at the ice-sheet bed before, during, and after drainages. Full inversion results for the 2011–2013 drainages are presented as videos (Supplementary Videos 1–3). Figure 2d–f shows spatially integrated results from 2011 to 2013 for the three deformation sources: hydro-fracture crack volume, basal cavity volume, and basal slip (shown as moment M_0 ; see Methods). For the 2011 event, we identify basal cavity opening and slip associated with the precursor southeast and southwest of M1, respectively, before the hydro-fracture opens (Figs 2d and 3a–c)—indicating the injection of meltwater at the ice-sheet bed before local hydro-fracture initiation. Immediately after the precursor, the hydro-fracture opens first at M1, and then propagates east beneath the basin (Supplementary Video 1). At the time of maximum hydro-fracture opening (Fig. 3d–f), the basal cavity volume (Figs 2d) is nearly equivalent to the North Lake pre-drainage volume estimate of 0.007 ± 0.001 km³ (Methods) (Extended Data Table 1 and Extended Data Figs 2 and 3). The agreement between lake volume calculations and NIF estimates of basal cavity volume validates our inversion results. Basal slip is focused within, and a few kilometres south of, the lake basin, but not northwards, possibly because of a known ridge in the basal topography (Fig. 3d)^{5,25}.

Inversion results for the rapid drainage events in 2012 and 2013 also suggest precursory activity (see ‘The 2012 North Lake drainage’ and

‘The 2013 North Lake drainage’ in Methods). The 2012 precursor is associated with basal slip 3 km north of the hydro-fracture, possibly because of enhanced lubrication from nearby meltwater input to the bed (Extended Data Fig. 4a). The 2013 precursor was the most extensive, producing enhanced basal slip over a 5 km \times 5 km area as well as significant basal uplift (Extended Data Fig. 5a, b). In both 2012 and 2013, the hydro-fracture opening and lake drainage produce ~ 50 cm of basal cavity opening beneath the lake basin and enhanced basal slip over a wide area (Extended Data Figs 4d–f and 5d–f).

Previous work on the 2006 North Lake drainage event identified a slow steady drop in lake level in the 16 h before the rapid hydro-fracture induced drainage, and it was hypothesized that this pre-drainage may have been due to the initial filling of a slowly propagating hydro-fracture directly beneath the lake basin, or water over-spilling into an adjacent crack system¹. However, the observations in 2006 were insufficient to distinguish between these (or alternative) mechanisms. Our NIF results show no evidence for the slow downward propagation of a hydro-fracture before lake drainage, which would be manifest as crack-normal horizontal displacements. Rather, the inversions clearly demonstrate that each drainage is preceded by a period of enhanced basal slip and/or uplift, which is probably caused by the injection of meltwater at the bed via neighbouring hydro-fractures and moulins. Intriguingly, precursor motion was also observed before other lake drainages^{1,2}, although it was not identified as a triggering mechanism for hydro-fracture initiation (see ‘Precursors observed in previous studies’ in Methods). The observation of a precursor before rapid lake drainages strongly suggests that they play an important role in triggering hydro-fractures, possibly by inducing local stress perturbations that overcome the background compressive stresses found in lake basins^{5,26}.

To test the hypothesis that local stress perturbations play an important role in triggering hydro-fractures, we compared the background viscous stresses in the lake basin with the elastic stress change induced by the precursory basal slip and cavity opening (Methods). We calculated background compressive stresses of order -70 ± 40 kPa within the lake basin, comparable to other west Greenland lake basin estimates²⁶. Before the start of the precursor, changes in crack-normal stress ($\Delta\sigma_n$) on the hydro-fracture are $\Delta\sigma_n = 0 \pm 40$ kPa. However, throughout the precursor $\Delta\sigma_n$ increases, attaining maxima tensile stresses of $+100$ to $+600$ kPa at the top of the hydro-fracture at the onset of rapid drainage (Fig. 4a–c). These calculations confirm that the drainage precursors can generate tensile crack-normal stresses near the surface with sufficient magnitude to temporarily overcome the compressive background stress and promote hydro-fracture initiation.

Our results and reinterpretation of previous studies (see ‘Precursors observed in previous studies’ in Methods) indicate that injection of surface meltwater, routed from supraglacial lakes to the bed through pre-existing crevasses or conduits, is required to trigger hydro-fracture initiation and subsequent rapid lake drainage in an otherwise compressional basin (Extended Data Fig. 9a–c). As shown previously, a necessary condition for hydro-fracture propagation is a sufficient volume of water to keep the fracture filled^{7,9}. Lacking a known triggering mechanism, previous studies used only this volume threshold to predict that lake drainages would occur^{14,27,28}. However, we do not find that lakes spontaneously hydro-fracture once they surpass this threshold¹². In all 3 years, North Lake contained approximately five times the critical volume of water necessary to keep a 4-km long crack open to the bed (Methods) before hydro-fracture occurred. Thus, we argue against the exclusive use of a volume threshold for triggering supraglacial lake drainage in regional ice-sheet modelling studies.

We hypothesize that if stress transients associated with enhanced meltwater transport to the bed beneath lakes are required to initiate surface-to-bed hydro-fractures in compressional lake basins, then lakes are less likely to create large-scale hydro-fractures in interior regions of the Greenland Ice Sheet where meltwater access to the bed is limited by lack of pre-existing crevasses^{5,14–16,29}. As new lakes form at higher elevations in a warming climate^{10–14} they will encounter

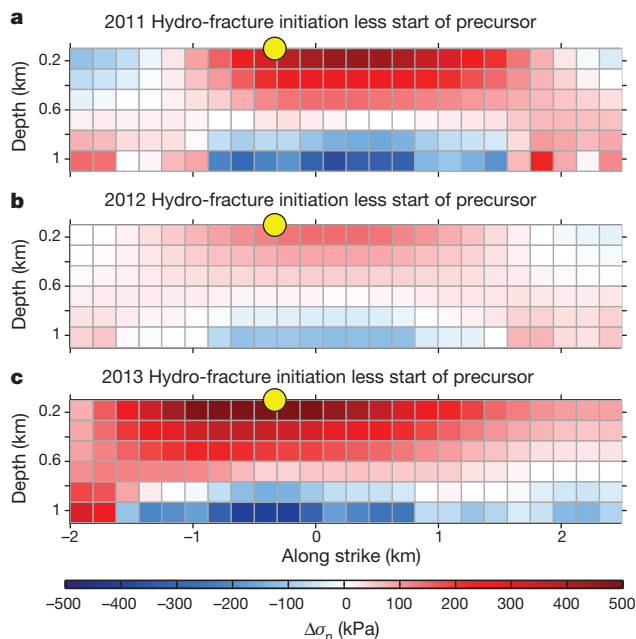


Figure 4 | Change in crack-normal stress during the precursor. Changes in the crack-normal elastic stresses ($\Delta\sigma_n$) (in kilopascals) (compressive, negative; tensile, positive) on the hydro-fracture crack as a result of basal cavity opening and accumulated extra basal slip during the (a) 2011, (b) 2012, and (c) 2013 precursor. Stresses are calculated at the start of the precursor and hydro-fracture initiation, coinciding with the times noted in Extended Data Table 1, and then differenced to show the change in elastic stress that occurs during the precursor.

longer-wavelength surface topography^{5,30,31}, resulting in greater distances between compressive lake basins and extensional crevasse-forming regions. Thus, lake water must be routed greater distances in surface streams down the ice sheet before encountering crevasses where through-ice drainage conduits can be established, minimizing local stress transients and potentially obstructing *in situ* rapid drainage of high-elevation lakes and the formation of new surface-to-bed hydro-fractures beneath lake basins²⁹. This indicates that although lake drainages may be important for inland expansion of enhanced flow at mid-elevations¹⁶, such expansions are more probably influenced by longitudinal coupling at high elevations³² (see ‘Implications for inland expansion of seasonal acceleration’ in Methods). Finally, the supply of meltwater to the bed may not be well correlated with the location, abundance, and size of high-elevation supraglacial lakes.

Online Content Methods, along with any additional Extended Data display items and Source Data, are available in the online version of the paper; references unique to these sections appear only in the online paper.

Received 13 November 2014; accepted 13 April 2015.

1. Das, S. B. *et al.* Fracture propagation to the base of the Greenland Ice Sheet during supraglacial lake drainage. *Science* **320**, 778–781 (2008).
2. Doyle, S. H. *et al.* Ice tectonic deformation during the rapid *in situ* drainage of a supraglacial lake on the Greenland Ice Sheet. *Cryosphere* **7**, 129–140 (2013).
3. Tedesco, M. *et al.* Ice dynamic response to two modes of surface lake drainage on the Greenland ice sheet. *Environ. Res. Lett.* **8**, 34007 (2013).
4. Joughin, I. *et al.* Seasonal speedup along the western flank of the Greenland Ice Sheet. *Science* **320**, 781–783 (2008).
5. Joughin, I. *et al.* Influence of ice-sheet geometry and supraglacial lakes on seasonal ice-flow variability. *Cryosphere* **7**, 1185–1192 (2013).
6. Andrews, L. C. *et al.* Direct observations of evolving subglacial drainage beneath the Greenland Ice Sheet. *Nature* **514**, 80–83 (2014).
7. Krawczynski, M. J., Behn, M. D., Das, S. B. & Joughin, I. Constraints on the lake volume required for hydro-fracture through ice sheets. *Geophys. Res. Lett.* **36**, L10501 (2009).

8. Weertman, J. Can a water-filled crevasse reach the bottom surface of a glacier? In *Symp. Hydrology of Glaciers* 139–145 (International Association of Scientific Hydrology, 1973).
9. Van Der Veen, C. J. Fracture propagation as means of rapidly transferring surface meltwater to the base of glaciers. *Geophys. Res. Lett.* **34**, L01501 (2007).
10. Sundal, A. V. *et al.* Evolution of supra-glacial lakes across the Greenland Ice Sheet. *Remote Sens. Environ.* **113**, 2164–2171 (2009).
11. Howat, I. M., de la Peña, S., van Angelen, J. H., Lenaerts, J. T. M. & van den Broeke, M. R. Expansion of meltwater lakes on the Greenland Ice Sheet. *Cryosphere* **7**, 201–204 (2013).
12. Fitzpatrick, A. A. W. *et al.* A decade (2002–2012) of supraglacial lake volume estimates across Russell Glacier, west Greenland. *Cryosphere* **8**, 107–121 (2014).
13. Parizek, B. R. & Alley, R. B. Implications of increased Greenland surface melt under global-warming scenarios: ice-sheet simulations. *Quat. Sci. Rev.* **23**, 1013–1027 (2004).
14. Leeson, A. A. *et al.* Supraglacial lakes on the Greenland Ice Sheet advance inland under warming climate. *Nature Clim. Change* **5**, 51–55 (2015).
15. Bartholomew, I. D. *et al.* Seasonal variations in Greenland Ice Sheet motion: inland extent and behaviour at higher elevations. *Earth Planet. Sci. Lett.* **307**, 271–278 (2011).
16. Doyle, S. H. *et al.* Persistent flow acceleration within the interior of the Greenland Ice Sheet. *Geophys. Res. Lett.* **41**, 899–905 (2014).
17. Zwally, H. J. *et al.* Surface melt-induced acceleration of Greenland Ice-Sheet flow. *Science* **297**, 218–222 (2002).
18. Bartholomew, I. *et al.* Short-term variability in Greenland Ice Sheet motion forced by time-varying meltwater drainage: implications for the relationship between subglacial drainage system behavior and ice velocity. *J. Geophys. Res.* **117**, F03002 (2012).
19. Hoffman, M. J., Catania, G. A., Neumann, T. A., Andrews, L. C. & Rumrill, J. A. Links between acceleration, melting, and supraglacial lake drainage of the western Greenland Ice Sheet. *J. Geophys. Res.* **116**, F04035 (2011).
20. Selmes, N., Murray, T. & James, T. D. Fast draining lakes on the Greenland Ice Sheet. *Geophys. Res. Lett.* **38**, 1–5 (2011).
21. Smith, L. C. *et al.* Efficient meltwater drainage through supraglacial streams and rivers on the southwest Greenland ice sheet. *Proc. Natl Acad. Sci. USA* **112**, 1001–1006 (2015).
22. Pimentel, S. & Flowers, G. E. A numerical study of hydrologically driven glacier dynamics and subglacial flooding. *Proc. R. Soc. A* **467**, 537–558 (2010).
23. Tsai, V. C. & Rice, J. R. A model for turbulent hydraulic fracture and application to crack propagation at glacier beds. *J. Geophys. Res.* **115**, F03007 (2010).
24. Segall, P. & Matthews, M. Time dependent inversion of geodetic data. *J. Geophys. Res.* **102**, 22391–22409 (1997).
25. Bamber, J. L. *et al.* A new bed elevation dataset for Greenland. *Cryosph.* **7**, 499–510 (2013).
26. Catania, G. A., Neumann, T. A. & Price, S. F. Characterizing englacial drainage in the ablation zone of the Greenland ice sheet. *J. Glaciol.* **54**, 567–578 (2008).
27. Clason, C., Mair, D. W. F., Burgess, D. O. & Nienow, P. W. Modelling the delivery of supraglacial meltwater to the ice/bed interface: application to southwest Devon Ice Cap, Nunavut, Canada. *J. Glaciol.* **58**, 361–374 (2012).
28. Arnold, N. S., Banwell, F. & Willis, I. C. High-resolution modelling of the seasonal evolution of surface water storage on the Greenland Ice Sheet. *Cryosphere* **8**, 1149–1160 (2014).
29. Poinar, K. *et al.* Limits to future expansion of surface-melt-enhanced ice flow into the interior of western Greenland. *Geophys. Res. Lett.* **42**, 1800–1807 (2015).
30. Sergienko, O. V. Glaciological twins: basally controlled subglacial and supraglacial lakes. *J. Glaciol.* **59**, 3–8 (2013).
31. Lampkin, D. J. & VanderBerg, J. A preliminary investigation of the influence of basal and surface topography on supraglacial lake distribution near Jakobshavn Isbrae, western Greenland. *Hydrol. Processes* **25**, 3347–3355 (2011).
32. Price, S. F., Payne, A. J., Catania, G. A. & Neumann, T. A. Seasonal acceleration of inland ice via longitudinal coupling to marginal ice. *J. Glaciol.* **54**, 213–219 (2008).

Supplementary Information is available in the online version of the paper.

Acknowledgements Support was provided by the National Science Foundation's Office of Polar Programs (NSF-OPP) and National Aeronautics and Space Administration's (NASA's) Cryospheric Sciences Program through ARC-0520077, ARC-1023364, and NNX10AI30G to S.B.D. and M.D.B., and through ARC-0520382, ARC-1023382, and NNX10AI33G to I.J. M.A.K. is a recipient of an Australian Research Council Future Fellowship (project number FT110100207). WorldView image data used for this work was provided by the Polar Geospatial Center at the University of Minnesota with support from NSF grant ANT-1043681. L.A.S. was also supported by a National Science Foundation Graduate Research Fellowship. Logistical and instrumental support was provided by UNAVCO, PASSCAL, and CH2MHILL Polar Field Services. We thank J. Carmichael, L. Kehrl, T. Moon, and K. Poinar for their assistance.

Author Contributions M.D.B., S.B.D., and I.J. conceived the study. L.A.S., M.D.B., S.B.D., I.J., and D.S. performed the fieldwork. L.A.S., T.H., and M.A.K. processed and analysed the GPS data. J.J.M. and L.A.S. developed the NIF. D.S. created the digital elevation models. L.A.S., M.D.B., S.B.D., I.J., and J.J.M. interpreted the results. L.A.S. wrote the paper. All authors commented on the paper.

Author Information Reprints and permissions information is available at www.nature.com/reprints. The authors declare no competing financial interests. Readers are welcome to comment on the online version of the paper. Correspondence and requests for materials should be addressed to L.A.S. (stevensl@mit.edu).

METHODS

GPS data. Continuous 30-s resolution GPS data collected by dual-frequency Trimble NetR9 receivers were processed with Track software³³. GPS data for each station were processed individually relative to the 30-s resolution Greenland GPS Network (GNET) KAGA base station located on bedrock ~55 km from North Lake³⁴. The 30-s resolution position estimates and corresponding uncertainties from Track were used in the NIF and plotted in Extended Data Figs 6 and 7 and Supplementary Videos 1–3. For plotting purposes, the data in Fig. 2 were smoothed over a 2-min window with a five-point central moving average. Error output from Track software is given as 1-sigma errors for the 30-s resolution east, north, and up offsets from the coordinates of the first position in the time series, but not the full covariance matrix³³. Horizontal (vertical) 1-sigma errors are consistently ± 2 cm (± 5 cm) across all stations and years.

Of the 16 GPS stations in the North Lake array, stations NL08, NL01, and/or NL03 best capture differences between the precursors over the three drainage events (Fig. 2). NL08 is consistently the most responsive station during lake drainage events, and proves to be the best single station indicator of the drainage event as a whole. NL08 captures the 2011 and 2013 precursor well (Fig. 2a, c). In 2012, the precursor is manifested as anomalous along-flowline displacements observed at stations NL01 and NL02. Thus, we show of these northern stations (NL01) alongside the NL08 time series to show the along flowline speed up in the northern portion of the array during the 2012 precursor (Fig. 2b). In 2013, NL01 and NL02 stations were not recording during the drainage, leaving NL03 as the closest station in the northern portion of the array to NL01/NL02 (Fig. 2c). Lake drainage duration is calculated on the basis of NL08 crack-normal motion from the start of the hydro-fracture opening to when NL08 crack-normal motion regains its southward displacement as the crack closes (~ 1.2 h after time of maximum hydro-fracture opening) (Fig. 2 and Extended Data Table 1).

Lake volume. The NASA Ames Stereo Pipeline³⁵ stereographic software was used to generate ~ 2 m per pixel digital elevation models (DEMs) of the empty, post-drainage North Lake basin using a WorldView-1 stereopair acquired on 21 July 2011 and a WorldView-2 stereopair acquired on 5 July 2013 (Extended Data Fig. 2). Orthorectified ~ 0.5 m per pixel WorldView images depicting the last available pre-drainage North Lake shoreline were used to constrain the lake shoreline position and, thus, lake depth and volume from the DEM. The 2011 lower bound on the lake volume estimate for North Lake was calculated from the shoreline position on a WorldView-1 image taken on 17 June 2011 obtained 1 day before the 2011 drainage. The 2013 lower bound for lake volume for North Lake was calculated from the shoreline position on a WorldView-2 image taken on 17 June 2013 obtained 2 days before the 2013 drainage. While small-scale surface features (moulins, supraglacial stream channels) advect ~ 100 m yr^{-1} to the west-northwest, the North Lake basin geometry is the result of fixed bed topography, and does not change significantly between summers (Extended Data Fig. 3). Lake volume estimates are given in Extended Data Table 1.

In 2012, a lack of satellite images of North Lake basin during the days leading up to drainage prevented lake volume calculation via shoreline position and DEM methods. Output from the Regional Atmospheric Climate Model for the Greenland Ice Sheet (RACMO2/GR)³⁶ for 2011 and 2012 was used to compare estimated cumulated runoff in the North Lake region (68.66° N, -49.52° W) at the day of lake drainage between the 2 years. We found that RACMO2/GR values of cumulative runoff at 18 June 2011 and 9 June 2012 are very similar at 0.0030 kg m^{-2} and 0.0031 kg m^{-2} , respectively. Average daily runoff values at this location during mid-June are of the order $0.0003 \text{ kg m}^{-2} \text{ d}^{-1}$. Thus, we conclude the pre-drainage 2012 North Lake volume is of the order of the pre-drainage 2011 North Lake volume: $0.007 \pm 0.001 \text{ km}^3$. We hypothesize that the pre-drainage 2012 North Lake shoreline reached M1 at the time of drainage.

NIF. We implemented the NIF algorithm²⁴ to determine the amount of opening along a vertical crack and slip and opening along a basal crack during the 2011, 2012, and 2013 North Lake rapid drainage events. The NIF utilizes Green's functions for an elastic half-space³⁷ to relate surface displacement time series to the space-time history of opening and slip along prescribed planes²⁴. The North Lake basin is modelled using an isotropic elastic half-space with the GPS stations at the surface. Three deformation sources are included: (1) hydro-fracture opening, (2) basal cavity opening (due to the rapid injection of meltwater), and (3) extra basal slip above the background rate (due to enhanced basal lubrication). The NIF assumes linear elastic behaviour for the ice sheet, and treats hydro-fracture as a horizontal elastic dislocation along a vertical crack within the ice⁸. These assumptions are justified by vertical-crack propagation timescales (seconds to minutes) that are shorter than the Maxwell time of ice ($6\text{--}24 \text{ h}$)^{7,9,22,23}.

We model the GPS position vector \mathbf{X} for each GPS station i , as a function of time t relative to the starting time t_0 as follows^{24,38}:

$$\mathbf{X}_i(t) - \mathbf{X}_i(t_0) - \mathbf{V}_i(t - t_0) = \mathbf{G}_i \mathbf{s}(t) + \mathbf{L}_i(t) + \mathbf{F}f(t) + \mathbf{\varepsilon}(t) \quad (1)$$

where the left-hand side represents the drainage-related surface motion of the GPS stations obtained by removing the station background velocity field³⁸ \mathbf{V} . \mathbf{V} is determined for each station by calculating station velocity over the 2 days of data available before the start of the precursor. On the right-hand side of equation (1), \mathbf{G} represents the matrix of elastic Green's functions³⁷, $\mathbf{s}(t)$ is a vector of slip (or opening) on each deformation plane subfault at time t , $\mathbf{L}_i(t)$ is component-specific coloured noise, $\mathbf{F}f(t)$ represents reference frame errors³⁸ at time t , and $\mathbf{\varepsilon}(t)$ represents normally distributed white-noise observation error at time t . We model $\mathbf{L}_i(t)$ with a Brownian random walk model as has been done in previous studies of high-rate GPS data³⁹. This term is necessary to absorb coloured noise in the time series due to unmodelled errors in the position estimates and possibly local benchmark instabilities. The random walk is described by a scale parameter τ , which we estimated to be $5 \text{ cm d}^{-1/2}$ by modelling data before the start of the precursor as a combination of a background velocity and random walk ($5 \text{ cm d}^{-1/2}$ was the smallest value that resulted in white residuals for such a model). We use three perpendicular translations for $\mathbf{F}f(t)$ because of the small size of our network³⁸. The data vector in the Kalman filter is given by the GPS position data $\mathbf{X}_i(t)$ minus the background velocity ($\mathbf{D}_i(t) = \mathbf{X}_i(t) - \mathbf{X}_i(t_0) - \mathbf{V}_i(t - t_0)$). The data covariance matrix is assumed to be diagonal and derived from the individual component errors from the Track processing modified appropriately given the uncertainty in our estimate of \mathbf{V} (ref. 38).

The vertical plane for the hydro-fracture extends from 100 to 1,100 m depth striking along the surface expression of the most substantial recurring hydro-fracture crack intersecting M1 on the western edge of the lake basin (Extended Data Fig. 1). The vertical plane does not start at the surface of the elastic half-space because the Green's Functions used in the NIF algorithm are for dislocations within the halfspace³⁷. This approximation is sufficient because the vertical crack is located within the lake and our GPS stations are located more than 1 km outside the lake basin and, thus, are not sensitive to the shallowest 100 m of crack opening. On the vertical plane we solve only for mode-I tensile motion corresponding to opening of the crack⁴⁰. The vertical plane is subdivided into 24 subfaults along strike and 6 subfaults along dip; each vertical subfault is 0.19 km wide and 0.16 km tall.

The basal plane is defined as a 100-km^2 sub-horizontal plane at 1,100 m depth, dipping 0.01° to the west, and centred beneath the North Lake basin (68.723° N, -49.53° W). The basal plane strikes 186° from north, perpendicular to the direction of average ice velocity as determined from the average of all GPS station velocities in the days leading up to each year's drainage event. We estimate both mode-I tensile and dip-slip motion in the direction of ice flow on the basal plane. The basal plane is subdivided into 12 subfaults along dip and 12 subfaults along strike; each subfault is a $0.83 \text{ km} \times 0.83 \text{ km}$ square. The shallow depth of the basal plane within the half-space results in Green's function magnitudes above 0.95 for the uplift response at GPS stations to basal plane opening³⁷. Therefore, we neglect the material property contrast at the ice sheet–bedrock interface in our model because it would only modify the Green's function magnitude by a few per cent. The geometry of our array, with a 10:1 ratio of horizontal distance across the GPS array to ice thickness, allows us to resolve slip and opening on the basal plane on the length scale of the station spacing (1–3 km).

Our choice of a nearly horizontal basal plane is motivated by the presence of a relatively flat basin in the bedrock topography centred directly beneath North Lake^{5,25}, which yields a nearly horizontal basal slope across the entire GPS array. Moreover, sensitivity tests show that our NIF results are robust for basal plane dips up to 5° . This value is greater than the maximum bedrock slope (3.4°) measured from the bedrock basin centre beneath North Lake to the bedrock ridge 5 km to the west of the lake basin^{5,25}. Thus, we find no reason to add complexity associated with small variations in basal topography and/or to correct the GPS displacements for the vertical distance gained as the stations move up and out of the basin.

We used a maximum likelihood estimation (MLE) algorithm to determine appropriate ranges of values for the spatial (γ) and temporal (α) hyperparameters for both the vertical and basal planes²⁴. We determined the final hyperparameter values on the basis of a combination of MLE estimates and analysis of NIF output to identify hyperparameter values low enough to provide significant model smoothing, but high enough still to track station displacements during the few hours of rapid drainage in the time series. The MLE estimates provide an average value that is appropriate over the entire time series, but, therefore, oversmooths the periods of rapid deformation when higher values of α and γ are warranted by the data. The MLE calculations of the vertical-plane temporal hyperparameter

suggest values of α of 100 (2011), 200 (2012), and 1,000 (2013); however, slightly higher or lower α values of 150 (2011), 250 (2012), and 500 (2013) were used on the basis of NIF ability to track station displacements during the rapid drainage (Extended Data Fig. 8). The vertical-plane spatial smoothing parameter, γ , could not be constrained on the basis of MLE calculations. The MLE calculations suggest a higher than necessary value of the spatial hyperparameter for the vertical crack, resulting in unrealistic vertical plane opening and closing on spatial scales of <0.5 km along strike. Therefore, we set the vertical plane spatial parameter to $\gamma = 450$ for the 2011 and 2012 inversions, resulting in vertical plane opening and closing on scales of 1 km along strike.

The basal plane spatial and temporal hyperparameters were also not satisfactorily constrained by MLE calculations for 2011 and 2012. The MLE calculations recommended higher than necessary spatial and temporal hyperparameters, resulting in unrealistic, over-fit solutions for the basal plane. The chosen basal plane temporal parameter ($\alpha = 25$) is substantially lower than the temporal parameter of the vertical plane, resulting in a smoother solution of bed opening and slip. The chosen basal plane spatial parameter ($\gamma = 50$) resolves basal slip and opening on spatial scales of 2 km, consistent with our 1–3 km GPS station spacing on the ice-sheet surface (Fig. 1). For 2013, the rapid oscillatory variations in the crack-normal component of displacement (north) for several stations required a larger basal-plane spatial parameter ($\gamma = 500$) to allow the migration of sufficiently compact slip patches needed to fit the oscillations in the crack-normal data (Supplementary Discussion: 2013 North Lake Drainage).

Basal moment calculations. Basal slip moment M_0 , in newton metres, is calculated to provide an integrated measure of slip across the basal plane:

$$M_0 = \mu AD \quad (2)$$

where μ , the shear modulus for glacial ice, is taken to be 3.5 GPa (ref. 41), A is the area of the basal plane in square metres, and D is the mean bed slip across the basal plane just after drainage in metres (Extended Data Table 1). Moment magnitude (M_w) is calculated from the basal slip moment⁴²: $M_w = \frac{2}{3} \log(M_0) - 6.05$ (Extended Data Table 1).

Critical volume for driving water-filled hydro-fracture to bed. The critical volume of water necessary to keep a 4-km long crack open to the bed ranges from 0.0008 to 0.0020 km³. This estimate is derived on the basis of a mean crack opening of 0.2–0.5 m required to drive a 4-km long, 100% water-filled vertical crack through 1 km of glacial ice with a shear modulus of 1.5–3.9 GPa (ref. 7).

North Lake basin stresses. To calculate background viscous stresses in North Lake basin, we use Glen's law⁴³ to convert longitudinal (along flow) surface strain rates derived from TerraSAR-X 2009–2011 winter velocity measurements⁵ to longitudinal stresses, σ_{jk} :

$$\sigma_{jk} = A^{-1/n} \dot{\epsilon}_E^{[1-n]/n} \dot{\epsilon}_{jk} \quad (3)$$

where the creep parameter, A , is $3.5 \times 10^{-25} \text{ s}^{-1} \text{ Pa}^{-3}$ (ref. 44), $n = 3$ is the creep exponent, $\dot{\epsilon}_E$ is the two-dimensional effective strain rate, and $\dot{\epsilon}_{jk}$ is longitudinal strain rate. We use the same Green's functions from the NIF³⁷ to calculate the change in crack-normal stress ($\Delta\sigma_n$) on the hydro-fracture that was induced by the basal cavity opening and accumulated extra basal slip during the 2 days leading up to each drainage event.

Data. Source data for all figures and videos are available in the online version of the paper as Microsoft Excel spreadsheets.

Precursors observed in previous studies. Although our study is the first to interpret the cause and significance of precursors to rapid lake drainage, similar precursors have been observed before other recorded rapid supraglacial lake drainages on the western margin of the Greenland Ice Sheet in the form of GPS station uplift and steady lake level lowering in the hours before hydro-fracture^{1,2}. During a rapid North Lake drainage in 2006, the North Lake Base Station GPS station uplift and steady lake level lowering was observed before rapid lake level drop and northward ice motion indicative of hydro-fracture opening¹. Slow lake level lowering was also observed before a 2008 rapid drainage of South Lake (68.58° N, 49.39° W), another lake site in this region located 20 km south of North Lake⁵. During the rapid drainage of Lake F (67.01° N, 48.74° W) in 2010, uplift of two GPS stations on the eastern side of the lake was observed over the 7 h leading up to rapid drainage². Precursory motion was not observed during the rapid drainage of Lake Ponting in 2011 (69.57° N, 49.81° W); however, the four GPS stations used to record ice motion may have been located too far from the lake to record precursory motion³. The three rapid drainage precursors observed during 2011–2013 at North Lake allow us to reinterpret precursors of past rapid lake drainages as evidence of a hydrologically induced trigger for hydro-fracture. Further, our results provide a possible mechanism by which a lake drainage could generate a meltwater pulse that could trigger additional lake drainages in the vicinity.

Such regionally clustered lake drainages have been noted in previous lake drainage studies^{2,12}.

Implications for inland expansion of seasonal acceleration. The formation and drainage of high-elevation lakes has been invoked to explain the inland expansion of seasonal acceleration (enhanced summer velocities up to 8% above winter velocities) during high melt summers now¹⁶ and in the future¹⁴. The precursors observed here suggest enhanced meltwater transport to the bed beneath lakes is needed to generate tensile stress transients that promote the initiation of surface-to-bed hydro-fractures. For this proposed hydro-fracture initiation mechanism, there must exist both a sufficient reservoir of surface meltwater and a nearby surface-to-bed pathway to transport the meltwater to the bed beneath the lake. Our results inform our hypothesis that rapid lake drainages are unlikely to progress inland to areas of new surface melting based on the overall decline in tensile strain rates towards the ice sheet interior, which results in increasingly rare crevasses with elevation²⁹. Thus, much of the new surface melt in the interior probably drains via long (tens of kilometres) supraglacial streams that eventually terminate in moulins in regions where surface meltwater already reaches the bed at present²⁹. While surface melt may continue to expand inland, much of this meltwater will only reach the bed in areas further downstream where seasonal lubrication already occurs^{15,19,29}. An alternative explanation for the observed seasonal acceleration is longitudinal coupling of these higher elevations (above ~ 1600 m above sea level) to lower elevation regions (below ~ 1600 m above sea level) that are responding to increased melt input^{32,45,46}.

The 2012 North Lake drainage. In 2012, North Lake drained rapidly over a period of ~ 5 h beginning at 22:12 local time on 9 June 2012. Owing to the lack of satellite images bracketing the North Lake drainage window, the maximum volume of North Lake in 2012 is unknown before drainage. Using RACMO runoff estimates, we conclude that the 2012 North Lake volume was similar to the 2011 volume based on a difference of $+0.00012 \text{ kg m}^{-2}$ of cumulative runoff between the 2 years (see 'Lake volume').

Regional basal slip before the 2012 North Lake hydro-fracture initiation indicates the presence of increased basal meltwater at the ice-sheet bed before hydro-fracture. Over the 16 h leading up to North Lake hydro-fracture initiation, stations NL01 and NL02 experienced an additional 5 cm of flowline-parallel displacement (Fig. 2b and Extended Data Fig. 4a). At the end of the precursor, slip in the northern portion of the array resulted in a basal moment (M_0) of 10^7 N m (Fig. 2e and Extended Data Fig. 4a), although there was minimal basal cavity opening throughout the array (Extended Data Fig. 4b). Over the following 3.5 h, the hydro-fracture opened beneath the North Lake basin, reaching its maximum width 2.5 h after hydro-fracture initiation. As in the 2011 North Lake rapid drainage, basal cavity opening was centred beneath and to the south of the North Lake basin during the 2012 drainage (Extended Data Fig. 4e and Supplementary Video 2). During lake drainage, basal slip beneath and to the southwest of the North Lake basin occurred, while the basal slip initially accumulated to the north during the precursor (Extended Data Fig. 4a) remained and expanded south (Extended Data Fig. 4d).

The 2013 North Lake drainage. In 2013, GPS station attrition in the eastern half of the array precluded various array-scale NIF conclusions; however, precursory activity in the western half of the array was well resolved (Extended Data Fig. 5). In 2013, North Lake and a small lake (Small Lake; Extended Data Fig. 5) 2 km to the southwest of North Lake may have drained concurrently or in sequence. Positive crack-normal (approximately northward) motion during the North Lake hydro-fracture was observed at the three GPS stations located between Small Lake and North Lake (NL08, NL07, NL10). This can be seen in the positive crack-normal excursion of 0.1 m at station NL08, 0.25 days after the 2013 maximum North Lake hydro-fracture crack opening (Fig. 2c).

Available imagery does not capture the precise timings of the lakes' drainages. The last WorldView image obtained on 17 June 2013 (2 days before the 2013 North Lake drainage) shows a filled North Lake and Small Lake. The volume of North Lake (Small Lake) was at least $0.0036 \pm 0.001 \text{ km}^3$ ($0.0021 \pm 0.001 \text{ km}^3$) at the time of drainage based on the shoreline positions obtained 2 days before the North Lake drainage event (Extended Data Figs 2d and 3b). The first post-drainage WorldView image available on 5 July 2013 (16 days after North Lake drainage; Extended Data Fig. 2e) shows an empty North Lake and Small Lake, with a bright, linear crack running through the South Lake basin that could be the 2013 Small Lake hydro-fracture. July 2014 field surveys confirmed the existence and east–west strike of the Small Lake hydro-fracture.

In an attempt to distinguish 2013 North Lake and Small Lake hydro-fracture events, a NIF including an additional source of displacement as a vertical plane with tensile opening along the South Lake hydro-fracture crack trace was developed and run with the 2013 GPS data. The NIF with the additional Small Lake hydro-fracture ('four-source') did not accurately capture opening and closing along the Small Lake hydro-fracture. While including the Small Lake

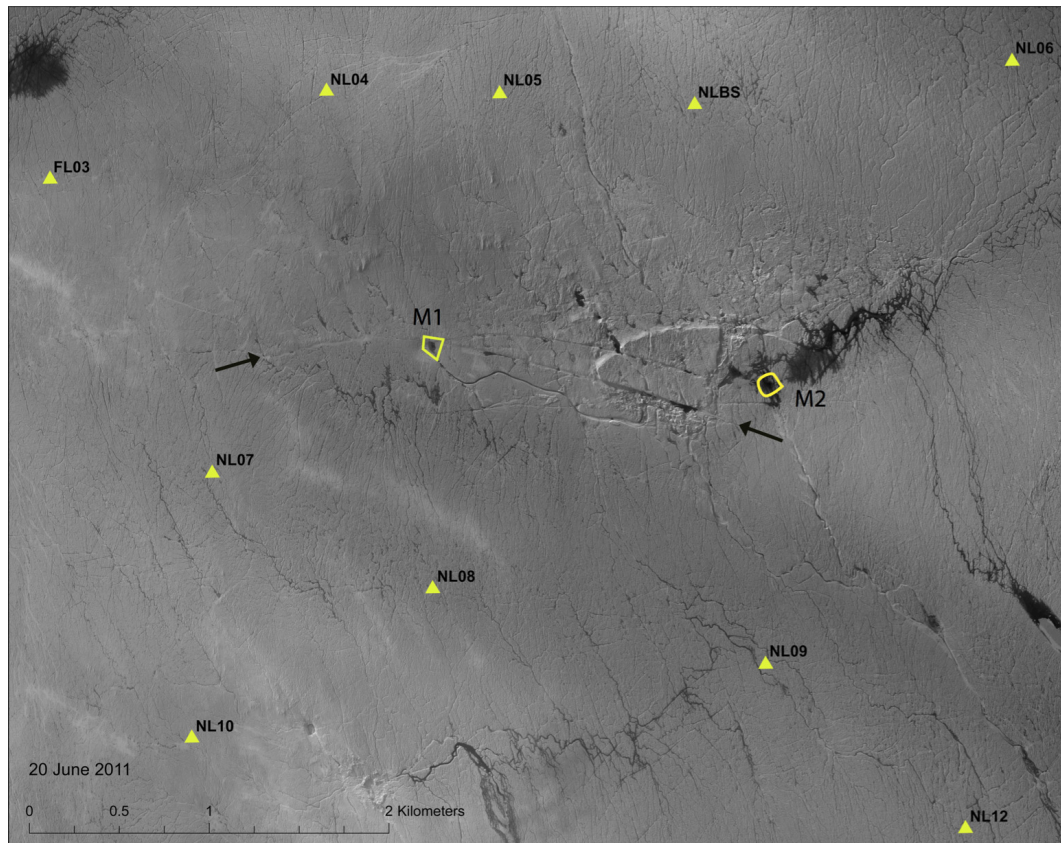
hydro-fracture more completely fits NL07, NL08, and NL10 station motion during the 1.5 h following the North Lake rapid drainage, the NIF results for the Small Lake hydro-fracture exhibit unrealistic behaviour by continuing to widen throughout the day after North Lake drainage. We attribute this result to the non-uniqueness inherent in the inversion owing to the lack of stations between North Lake and Small Lake. Because the NIF results including the Small Lake source produce a physically unlikely result (a crack that continues widening after drainage) we favour the alternative solution, which fits the data equally well—namely no Small Lake hydro-fracture and a rougher distribution of basal slip/opening ($\nu = 500$) that accounts for the crack-normal component oscillations at NL07 and NL08 via the spatial propagation of the basal slip patch (Fig. 2c).

For a NIF that does not include the additional Small Lake vertical plane ('three-source'), individual station motion can be mapped onto the three original deformation sources (vertical opening, basal cavity opening, and basal slip) with a highly spatially resolved basal plane ($\nu = 500$) and associated highly temporally resolved vertical plane ($\alpha = 500$). The three-source 2013 NIF yields realistic opening and closing North Lake hydro-fracture behaviour. We present the three-source 2013 NIF results here, since we cannot sufficiently distinguish between the North Lake and Small Lake drainages from the available station spatial density.

Independent of the NIF setup (three or four sources of displacement), precursory activity in the western half of the array is well resolved in the GPS data. North Lake drained rapidly over a period of ~ 5 h beginning at 15:00 local time on 19 June 2013 (Fig. 2c, f). From analysis of WorldView imagery, the 2013 west North Lake shoreline had not reached M1 2 days before the drainage event (Extended Data Fig. 3b), although, in the absence of a snow-dam, water could have reached the moulin via a deeply incised surface meltwater channel (Extended Data Fig. 2d). During the 16 h leading up to hydro-fracture initiation, flowline parallel speed-up of western stations (Fig. 2c) generated considerable M_0 (Fig. 2f), and was coincident with a basal cavity opening of $\sim 0.002 \text{ km}^3$ beneath the North Lake and Small Lake basins (Fig. 2f and Extended Data Fig. 5a–c). Inversion results suggest that hydro-fracture opening began in the region of M1; however, opening along the eastern portion of the vertical plane was not well constrained owing to a lack of GPS stations to the immediate northeast of North Lake basin (for example, NL05,

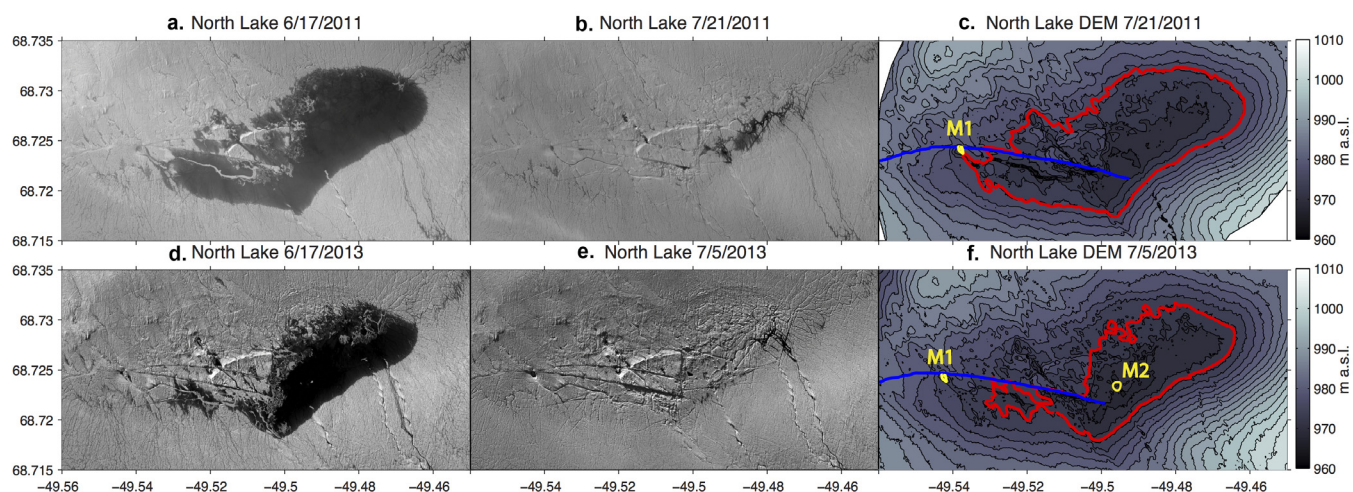
NL06, and North Lake base station). As in previous years, during the North Lake rapid drainage, basal cavity opening occurred beneath the lake basin, while extra basal slip extended further afield (Extended Data Fig. 5d–f and Supplementary Video 3). A ground survey of North Lake basin a month after the 2013 North Lake drainage identified post-drainage supraglacial meltwater routing through M2 (Extended Data Fig. 1).

33. Chen, G. *GPS Kinematics Positioning for the Airborne Laser Altimetry at Long Valley, California*. PhD thesis, Massachusetts Institute of Technology (1998).
34. Bevis, M. *et al.* Bedrock displacements in Greenland manifest ice mass variations, climate cycles and climate change. *Proc. Natl Acad. Sci. USA* **109**, 11944–11948 (2012).
35. Moratto, Z. M., Broxton, M. J., Beyer, R. A., Lundy, M. & Husmann, K. In *41st Lunar and Planetary Science Conference* 2364 (Lunar and Planetary Institute (2010).
36. Van Angelen, J. H., van den Broeke, M. R., Wouters, B. & Lenaerts, J. T. M. Contemporary (1960–2012) evolution of the climate and surface mass balance of the Greenland Ice Sheet. *Surv. Geophys.* **35**, 1155–1174 (2013).
37. Okada, Y. Surface deformation due to shear and tensile faults in a half-space. *Bull. Seismol. Soc. Am.* **75**, 1135–1154 (1985).
38. Miyazaki, S. A transient subduction zone slip episode in southwest Japan observed by the nationwide GPS array. *J. Geophys. Res.* **108**, 2087 (2003).
39. Miyazaki, S., McGuire, J. J. & Segall, P. Seismic and aseismic fault slip before and during the 2011 off the Pacific coast of Tohoku Earthquake. *Earth Planets Space* **63**, 637–642 (2011).
40. Van der Veen, C. J. Fracture mechanics approach to penetration of surface crevasses on glaciers. *Cold Reg. Sci. Technol.* **27**, 31–47 (1998).
41. Hobbs, P. V. *Ice Physics* 258 (Clarendon, 1974).
42. Kanamori, H. Magnitude scale and quantification of earthquakes. *Tectonophysics* **93**, 185–199 (1983).
43. Glen, J. W. The creep of polycrystalline ice. *Proc. R. Soc. Lond. A* **228**, 519–538 (1955).
44. Budd, W. F. & Jacka, T. H. A review of ice rheology for ice sheet modeling. *Cold Reg. Sci. Technol.* **16**, 107–144 (1989).
45. Kamb, B. & Echelmeyer, K. A. Stress-gradient coupling in glacier flow: I. Longitudinal averaging of the influence of ice thickness and surface slope. *J. Glaciol.* **32**, 267–284 (1986).
46. Hindmarsh, R. C. A. The role of membrane-like stresses in determining the stability and sensitivity of the Antarctic ice sheets: back pressure and grounding line motion. *Phil. Trans. R. Soc. A* **364**, 1733–1767 (2006).



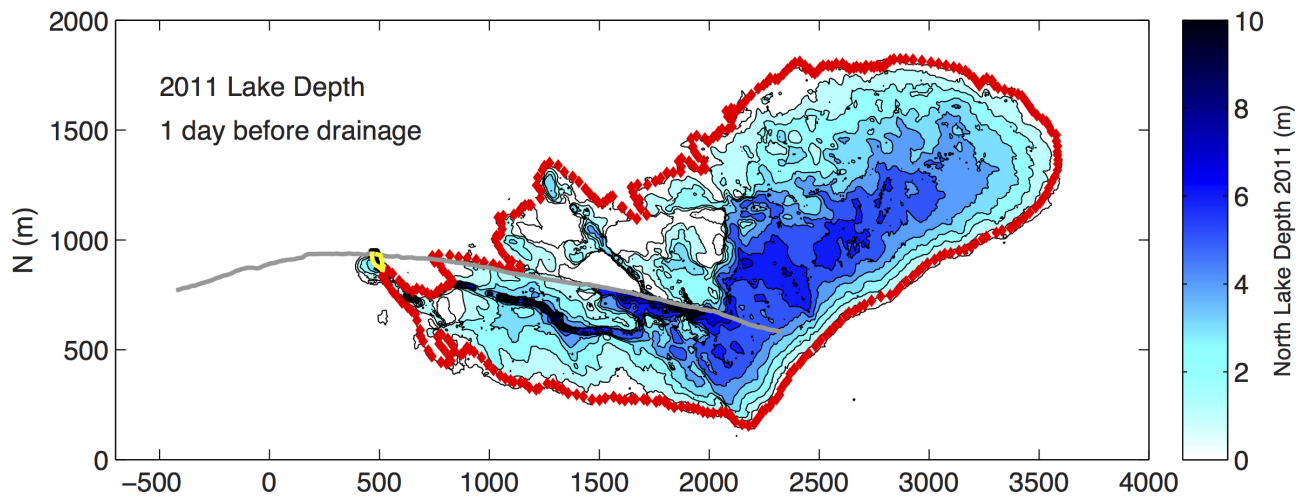
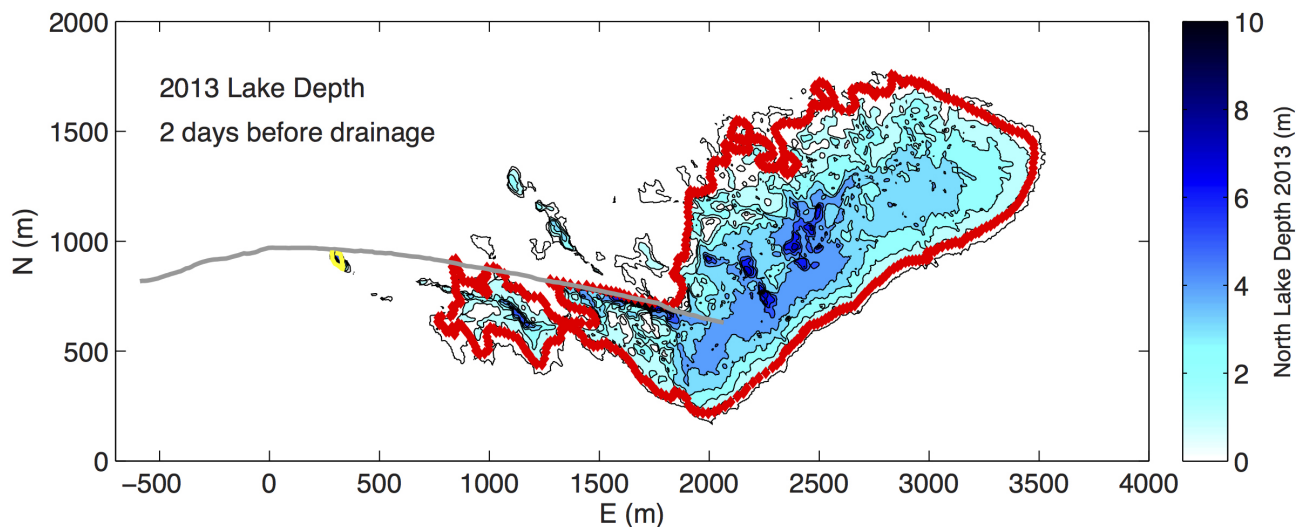
Extended Data Figure 1 | WorldView image taken on 21 July 2011 of an empty North Lake basin after the 2011 rapid drainage event. Yellow outline shows M1 and M2 location along the hydro-fracture trace (endpoints marked

by black arrows). Yellow triangles mark GPS stations within the map area. Image copyright 2015 DigitalGlobe.



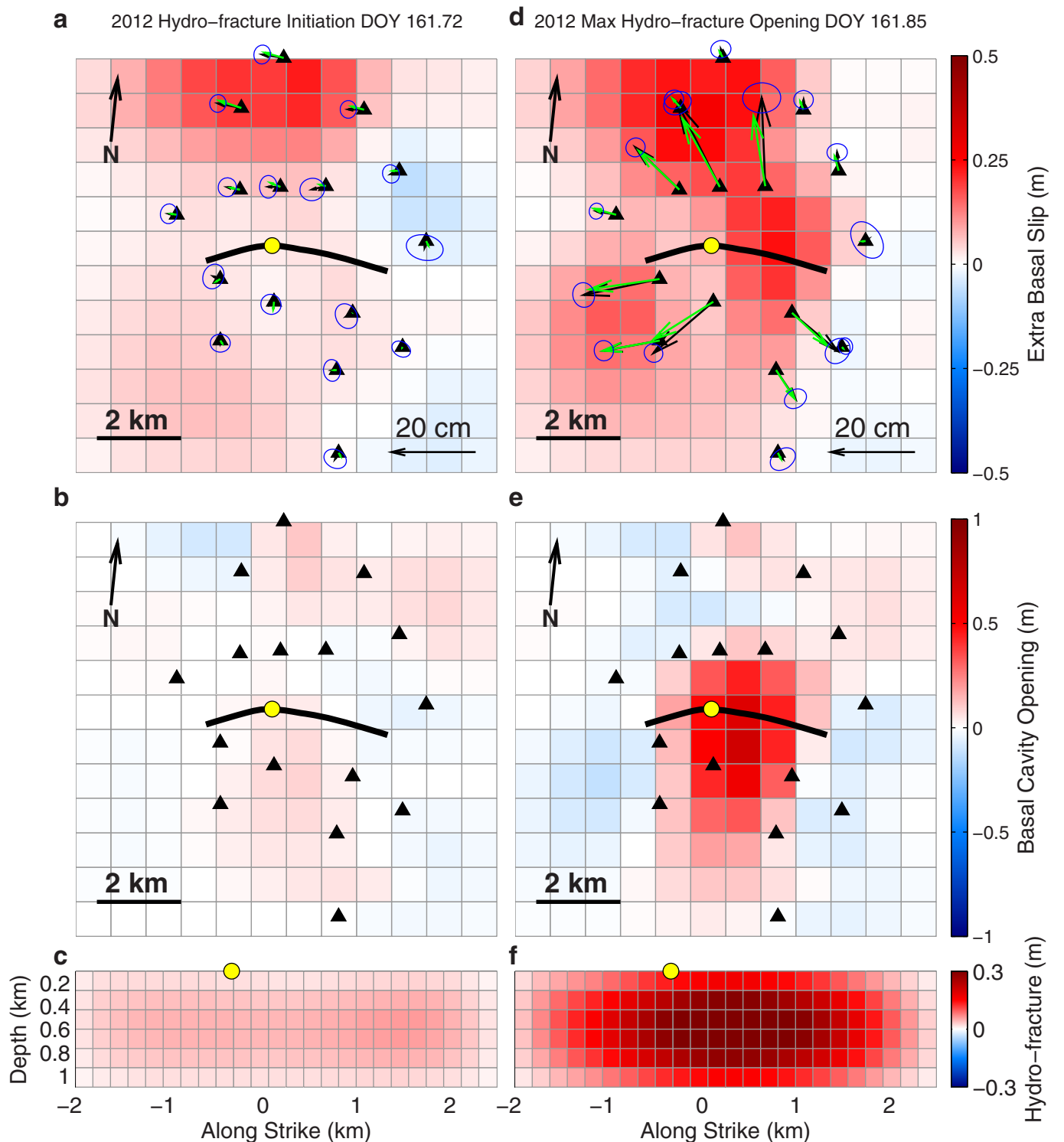
Extended Data Figure 2 | Images and DEM of 2011 and 2013 North Lake basin. **a** (**d**), WorldView image chosen to map the 2011 (2013) North Lake pre-drainage shoreline position. **b** (**e**), WorldView image of an empty North Lake basin obtained on 21 July 2011 (5 July 2013) used to create the 2011 (2013)

North Lake DEM. **c** (**f**), The 2-m horizontal resolution DEM (2-m vertical contours in black) for the North Lake region, with the North Lake shoreline (red), M1 (yellow), and hydro-fracture trace (blue) mapped over contours. Images copyright 2015 DigitalGlobe.

a**b**

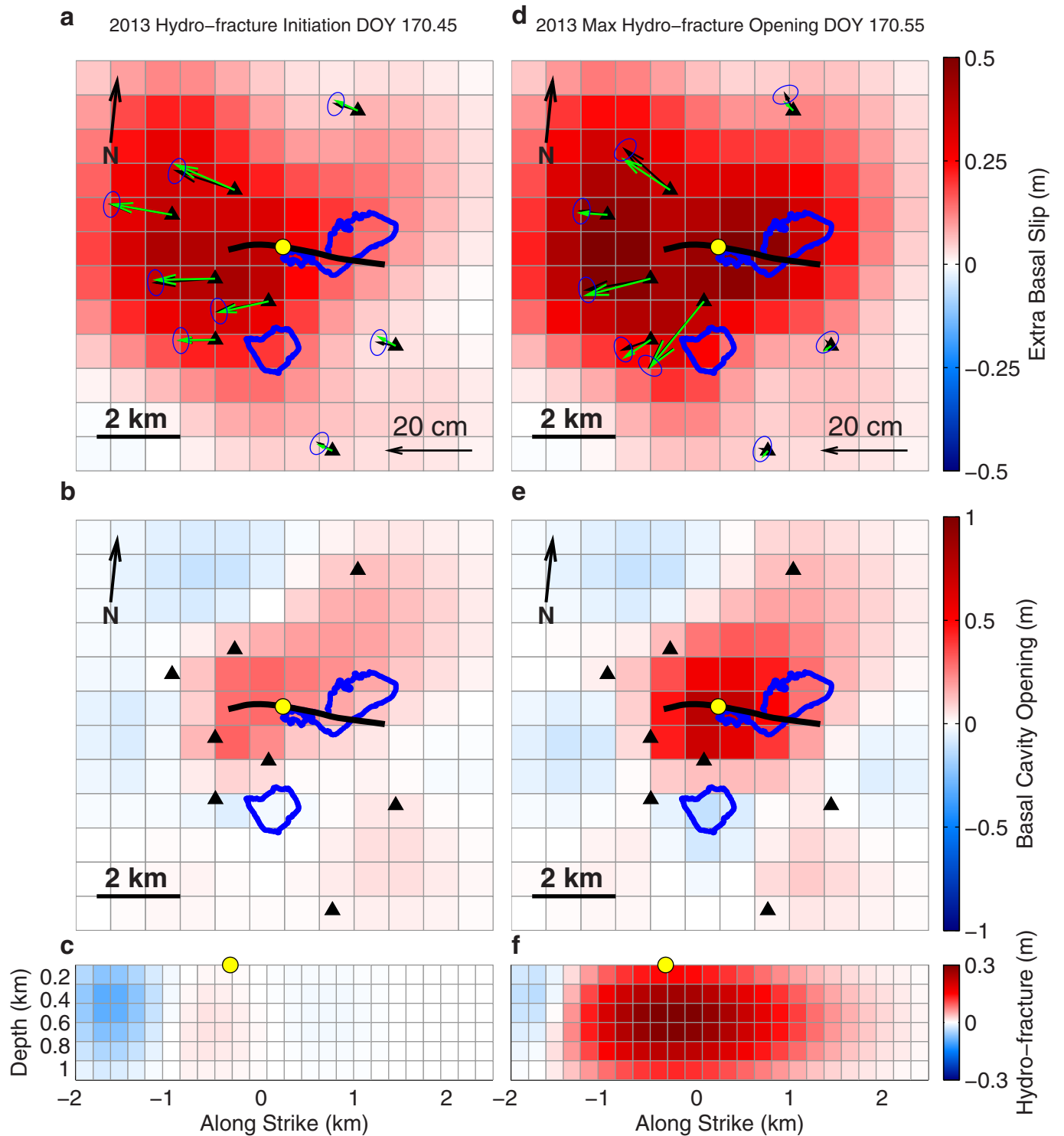
Extended Data Figure 3 | North Lake depths in 2011 and 2013. Two-metre resolution DEMs were created from the first available post-drainage World View stereo pair obtained of the region in (a) 2011 and (b) 2013. Shoreline positions from 2011 and 2013 derived from last pre-drainage WorldView or TerraSAR-X images obtained over the region are shown in red. The last pre-drainage WorldView image for 2011 occurred 2 days before the drainage event on 17 June 2011; the last pre-drainage SAR image for 2013 occurred 1 day before

the event on 17 June 2013. Filling the empty basin DEM up to the greatest known pre-drainage shoreline extent generated North Lake depths (1-m vertical contours in black) in relation to the greatest known pre-drainage shoreline extents and were used to calculate minimum 2011 and 2013 North Lake pre-drainage volumes. The trace of the vertical hydro-fracture crack is shown in grey; M1 is outlined in yellow.



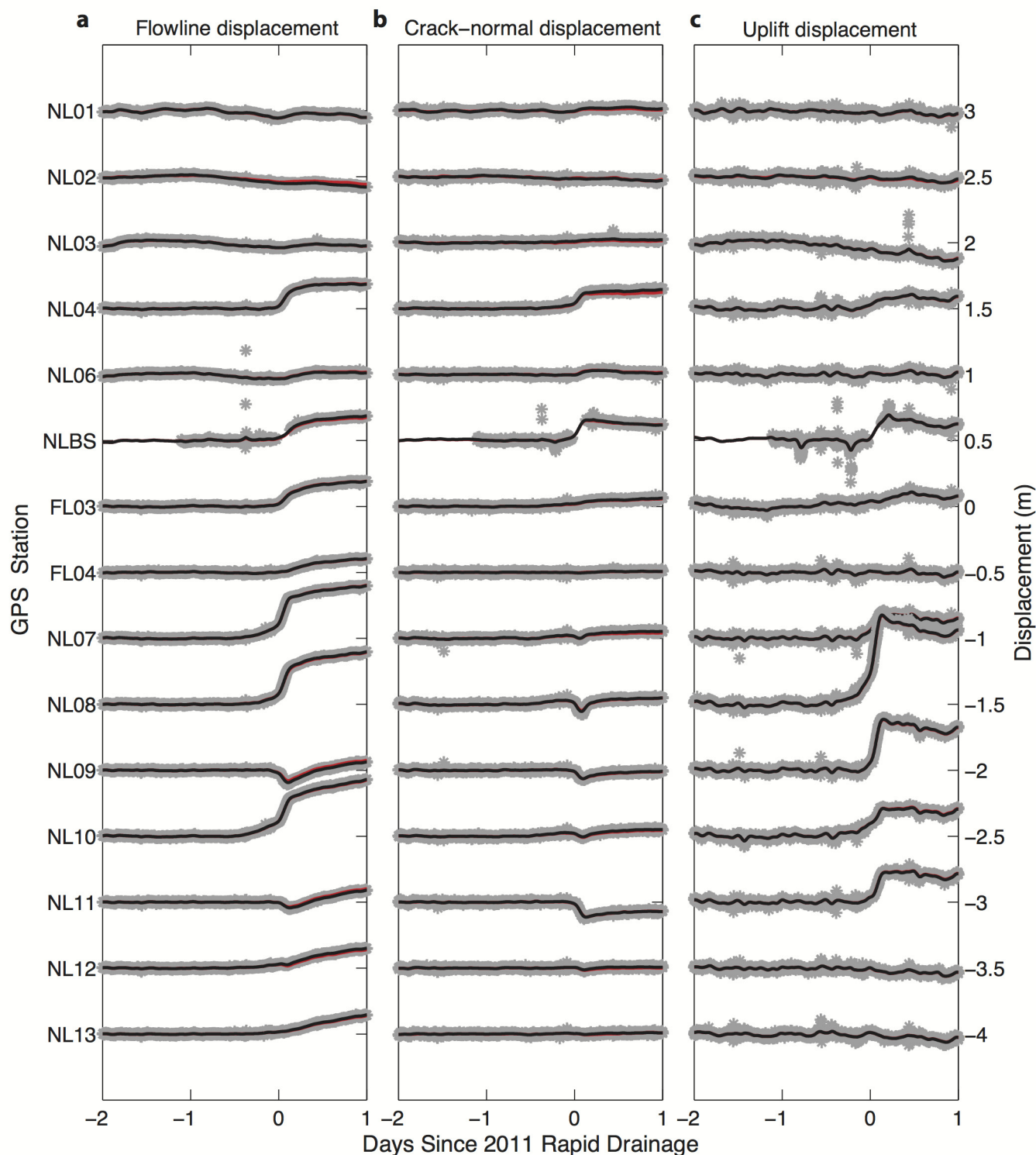
Extended Data Figure 4 | The 2012 basal slip and cavity opening at hydro-fracture initiation and maximum hydro-fracture opening. NIF-calculated (a) extra basal slip accumulated, (b) basal cavity opening, and (c) hydro-fracture crack opening at the time of the 2012 (a–c) hydro-fracture initiation and (d–f) maximum hydro-fracture opening (time points shown in Fig. 2a). Moulin location, last known lake shoreline, GPS stations, and NIF vertical crack surface trace derived from SAR imagery are shown as a yellow circle, blue line,

black triangles, and black line, respectively. Vector fields show GPS (NIF) displacement less background velocities in black (green) for **(a)** the period between the start of the precursor and hydro-fracture initiation, and **(d)** the period between hydro-fracture initiation and maximum hydro-fracture opening. Error ellipses of 1 sigma are shown for the GPS displacements (blue ellipses). Basal sub-elements are 0.83 km by 0.83 km, resulting in 144 sub-elements over a 10 km \times 10 km region.



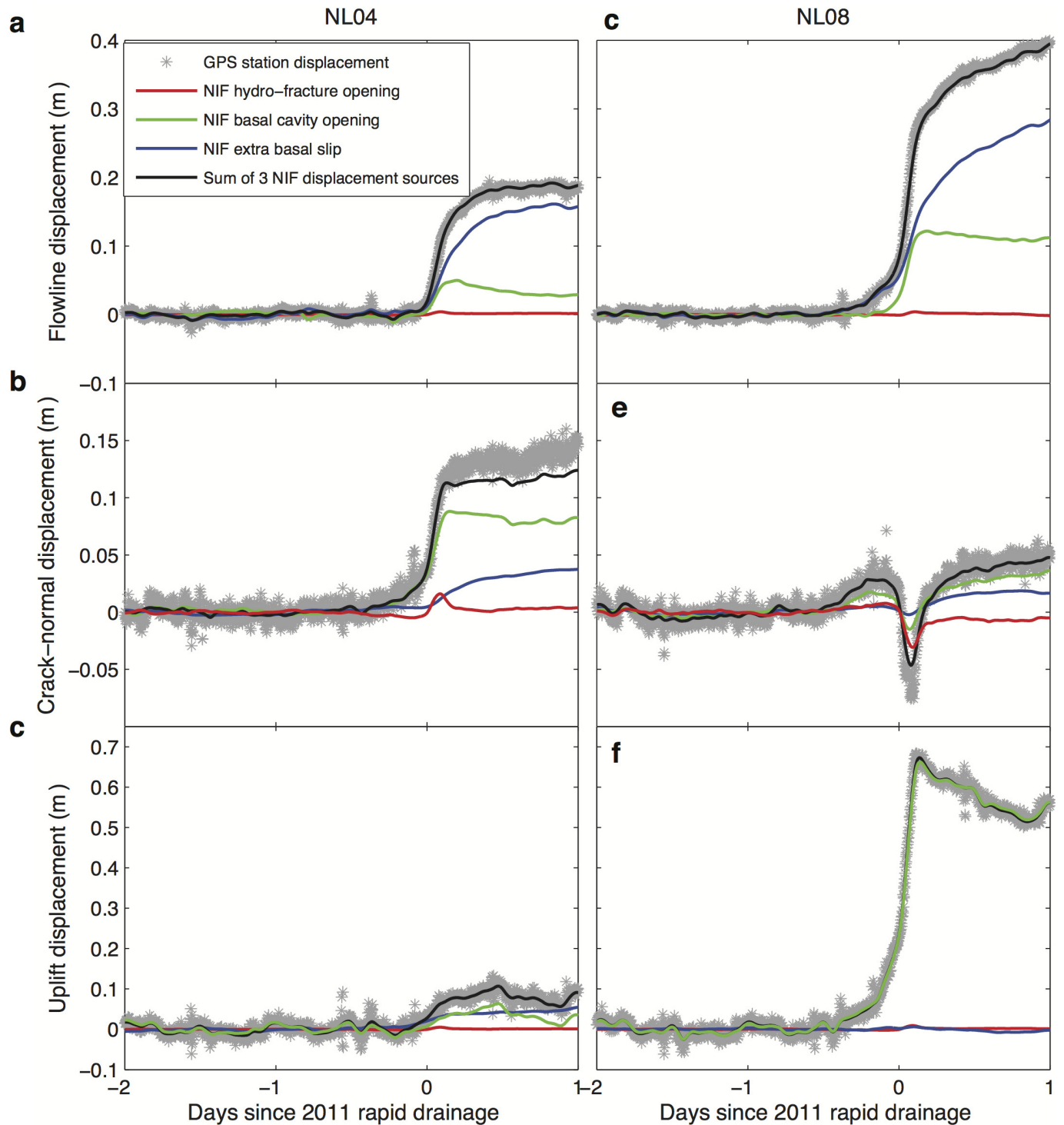
Extended Data Figure 5 | The 2013 basal slip and cavity opening at hydrofracture initiation and maximum hydrofracture opening. NIF-calculated (a) extra basal slip accumulated, (b) basal cavity opening, and (c) hydrofracture crack opening at the time of the 2013 (a–c) hydrofracture initiation and (d–f) maximum hydrofracture opening (time points shown in Fig. 2a). Moulin location, last known lake shoreline, GPS stations, and NIF vertical crack surface trace derived from SAR imagery are shown as a yellow circle, blue line,

black triangles, and black line, respectively. Vector fields show GPS (NIF) displacement less background velocities in black (green) for (a) the period between the start of the precursor and hydrofracture initiation, and (d) the period between hydrofracture initiation and maximum hydrofracture opening. Error ellipses of 1 sigma are shown for the GPS displacements (blue ellipses). Basal sub-elements are 0.83 km by 0.83 km, resulting in 144 sub-elements over a 10 km by 10 km region.



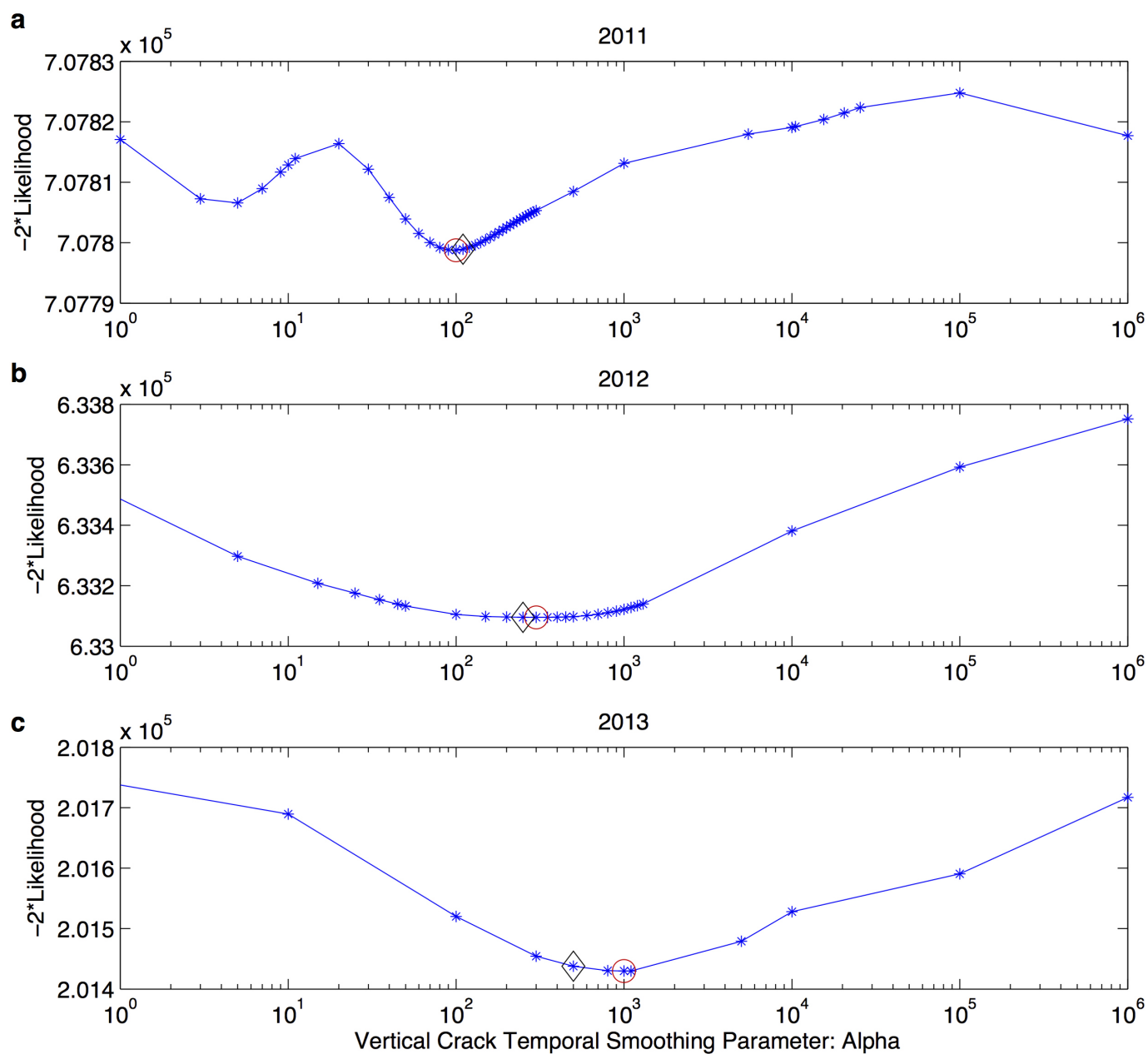
Extended Data Figure 6 | The 2011 station time series. a–c, Flowline, crack-normal, and uplift GPS displacements (in metres) (grey stars), respectively, for stations used in the 2011 NIF. NIF station fits from the three displacement

sources (Extended Data Fig. 7) shown in red, and NIF station fits including $L_r(t)$ (random benchmark wobble term) are shown in black. Stations are ordered roughly north to south on the y axis, offset by 0.5 m.



Extended Data Figure 7 | The 2011 NL08 and NL04 Station flowline, crack-normal, and uplift displacements computed from NIF displacement sources. Flowline, crack-normal, and uplift GPS displacements less background velocity field (grey stars) are plotted for (a–c) NL04 and (d–f) NL08 over the 2 days before and 1 day after the 2011 rapid North Lake drainage. These stations are two examples chosen from the full array because

they capture displacement on both the northern (NL04) and southern (NL08) side of the lake, are located at roughly the same longitude as M1, and are within 2 km of the lake. NIF-calculated surface ice displacements at NL04 and NL08 stations from the three displacement sources are plotted for the (red) hydro-fracture crack opening, (green) basal cavity opening, and (blue) extra basal slip. The sum of all three NIF displacement sources is shown in black.

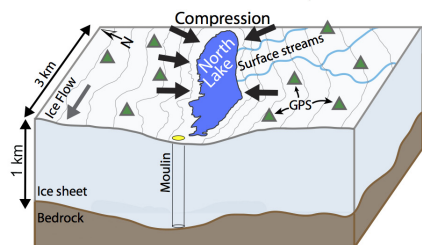


Extended Data Figure 8 | MLE of NIF hyperparameters. MLE of the vertical hydro-fracture plane temporal smoothing parameter, α , for (a) 2011, (b) 2012, and (c) 2013 NIF. The MLE corresponds with the minimum value on

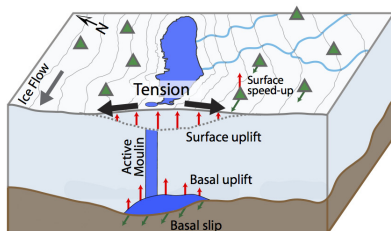
the $-2 \times$ likelihood plots¹⁹. Minimum likelihood estimates are outlined in red circles, with the value used in each year's inversion outlined indicated with a black diamond (Methods).

a. Supraglacial Lake Formation

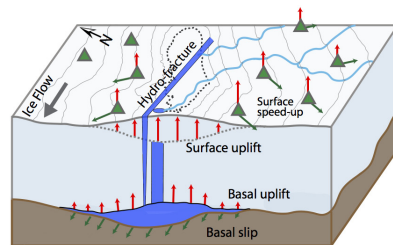
A supraglacial lake forms on the surface of the Greenland Ice Sheet when surface runoff fills a compressive basin.

**b. A Precursor to Rapid Lake Drainage**

Substantial melt-water is routed to the bed via a moulin, causing uplift and tension at the ice sheet surface.

**c. Hydro-fracture Opening and Rapid Drainage**

A hydro-fracture opens through the lake basin, draining water in the lake to the bed within a few hours.



Extended Data Figure 9 | Stress changes across North Lake basin. Stress changes during (a) supraglacial lake formation, (b) rapid drainage precursor, and (c) hydro-fracture opening.

Extended Data Table 1 | The 2011, 2012, and 2013 North Lake drainage environmental, GPS, and NIF observations

Environmental	2011	2012	2013
Day of Year	June 18, 2011 (DOY 169)	June 9, 2012 (DOY 161)	June 19, 2013 (DOY 170)
Start of Precursor (decimal DOY GMT+0)	168.85	161.20	169.90
Hydro-fracture Initiation	169.21	161.72	170.45
Maximum Hydro-fracture Opening	169.32	161.85	170.55
Drainage Duration*	~3 hours	~5 hours	~5 hours
Lake Volume (DEM) (km ³)	0.0077 ± 0.001	approx. same as 2011	0.0036 ± 0.001 Small Lake: 0.0021 ± 0.001
Lake Shoreline Location at Drainage	Meets M1	approx. same as 2011	May fill channel trough to M1
GPS			
Background velocity magnitude average across all stations (m/year)	162 m/year	125 m/year	94 m/year
Background velocity direction average across all stations (deg)	276°	277°	277°
Precursor type	Uplift in lake basin, followed by speed up in lake basin	Speed up NL01 and NL02 stations; minor uplift in basin	Speed up of western stations (FL03, NL04, NL07, NL08, NL10); uplift in basin
Duration of Precursor before Drainage starts (hours)	10 (uplift); 5 (speed up)	16 (N speed up); 24 (minor uplift in basin)	16 (possibly as early as 24 hours before)
Network Inversion Filter			
Vertical Crack Initiation Location	M1	Center of lake basin	M1
Vertical Crack Propagation History	Propagates from M1 to Lake Basin	Stays in center of lake basin	Stays at M1 (east unresolved)
Max. Vertical Crack Opening Width (m)	0.16	0.36	0.40
Max. Vertical Crack Volume (km ³)	2.9 x 10 ⁻⁴	7.3 x 10 ⁻⁴	4.9 x 10 ⁻⁴
Max. Basal Cavity Opening Location	Lake Basin	Lake Basin	Lake Basin
Max. Basal Cavity Volume (km ³)	0.0095	0.0067	0.012
Max. Extra Basal Slip Locations	Lake Basin, SW of Lake Basin	Lake Basin, SW & NW of Lake Basin	Lake Basin and Western Stations
Average extra basal slip across basal plane just after drainage (m)	0.13 (DOY 169.5)	0.15 (DOY 162.0)	0.31 (DOY 170.7)
M ₀ (basal moment) (N*m) just after drainage	4.6 x 10 ¹⁶	5.3 x 10 ¹⁶	1.1 x 10 ¹⁷
M _w (moment magnitude) just after drainage	5.1	5.1	5.3

Time of start of precursor, start of hydro-fracture crack opening, and maximum hydro-fracture crack opening equivalent to time delineations are shown in Fig. 2.

*Drainage duration calculated as duration of southward anomaly in the NL08 crack-normal time series (see Methods: GPS data).

Cardiac lymphatics are heterogeneous in origin and respond to injury

Linda Klotz^{1*}, Sophie Norman^{2*}, Joaquim Miguel Vieira^{2*}, Megan Masters², Mala Rohling², Karina N. Dubé¹, Sveva Bollini³, Fumio Matsuzaki⁴, Carolyn A. Carr² & Paul R. Riley²

The lymphatic vasculature is a blind-ended network crucial for tissue–fluid homeostasis, immune surveillance and lipid absorption from the gut. Recent evidence has proposed an entirely venous-derived mammalian lymphatic system. By contrast, here we show that cardiac lymphatic vessels in mice have a heterogeneous cellular origin, whereby formation of at least part of the cardiac lymphatic network is independent of sprouting from veins. Multiple Cre–lox-based lineage tracing revealed a potential contribution from the putative haemogenic endothelium during development, and discrete lymphatic endothelial progenitor populations were confirmed by conditional knockout of *Prox1* in *Tie2*⁺ and *Vav1*⁺ compartments. In the adult heart, myocardial infarction promoted a significant lymphangiogenic response, which was augmented by treatment with VEGF-C, resulting in improved cardiac function. These data prompt the re-evaluation of a century-long debate on the origin of lymphatic vessels and suggest that lymphangiogenesis may represent a therapeutic target to promote cardiac repair following injury.

In 1902, Florence Sabin proposed that the primary lymph sacs originate from the embryonic veins and then give rise to the entire lymphatic vasculature by sprouting and remodelling¹. An alternative model of lymphatic development was proposed by Huntington and McClure in 1910, who suggested that lymph sacs arise in the mesenchyme, independently of veins, via distinct progenitor cells². More recent evidence has supported Sabin's model, such that trans-differentiation of venous into lymphatic endothelial cells (LECs) is now widely accepted, with the veins regarded as the sole origin of the entire lymphatic vasculature in mammals^{3–7}. To date, studies which support a venous origin have focused exclusively on the development of the systemic lymphatic vasculature. Organ-based lymphatics have received little attention and in the heart, while the presence of cardiac lymphatic vessels has been described⁸, virtually nothing is known about their role during development or in the healthy or failing adult heart. We therefore sought to characterize the formation of the cardiac lymphatic vessels through developmental stages, to identify their embryonic origin and effect during organogenesis and to assess their response to pathological insult in the adult setting.

Development of the cardiac lymphatic vasculature

Whole-mount staining of murine hearts for early LEC markers VEGFR-3 (ref. 9) and *Prox1* (ref. 10), revealed the emergence of lymphatic vessels at embryonic day 12.5 (E12.5), sprouting from extra-cardiac regions proximal to the outflow tract, on the ventral side (Fig. 1a, increased magnification in Fig. 1b). At E14.5, lymphatic vessels were observed on the ventricular surface sprouting from the region of the sinus venosus, on the dorsal side (Fig. 1c, increased magnification in Fig. 1d and Extended Data Fig. 1a, increased magnification in Extended Data Fig. 1b). At E16.5 the major dorsal vessels spread inferiorly from the inflow region (Fig. 1e, increased magnification in Fig. 1f), while ventrally smaller vessels arose between the atria (Extended Data Fig. 1c, d). By E18.5, the vessels continued to expand and projected towards the apex of the heart on both dorsal and ventral

surfaces (Fig. 1g, h and Extended Data Fig. 1e, f). From birth (post-natal day 0 (P0)), the vessels developed a more extensive branched network and expanded further over the ventral side of the neonatal heart (Fig. 1i, j). By P10, the cardiac lymphatics provided superficial coverage of the majority of the epicardial surface of the heart (Extended Data Fig. 1g, h) and appeared fully developed by P15 (Extended Data Fig. 1i, j). The lymphatic identity of the VEGFR-3- and *Prox1*-labelled cardiac vessels (Fig. 1a–j and Extended Data Fig. 1a–n) was further validated by co-immunostaining for the lymphatic vessel endothelial hyaluronan receptor 1 (*Lyve-1*), which also labels tissue macrophages¹¹. Coronary LECs within the expanding plexus on both dorsal and ventral sides of the developing heart co-expressed VEGFR-3, *Prox1* and *Lyve-1* (Extended Data Fig. 1o–v). Cardiac lymphatic vessels aligned with the endomucin (*Emcn*)-positive coronary veins during late gestation (E15.5–18.5) (Fig. 1k–m) and established extensive inter-vessel connections analogous to blood vessel anastomosis (Fig. 1n–p). At birth (P0) lateral *Lyve-1*⁺ sprouts beneath smooth-muscle-actin-positive coronary veins (Fig. 1q–s) were indicative of a close anatomical relationship between the coronary veins and developing lymphatic vasculature (Fig. 1t).

A venous and non-venous contribution of LECs

Prox1⁺ LECs did not appear to emerge or bud-off from *Emcn*-expressing coronary vessels between E12.5–14.5 (Extended Data Fig. 2a–i). Instead, extra-cardiac LECs migrated into the sinus venosus on the dorsal side, and outflow tract on the ventral side of the heart by E12.5 (Extended Data Fig. 2a, b, also Fig. 1a, b) and expanded to form a network proximal to *Emcn*⁺ veins from E13.5 and E14.5 (Extended Data Fig. 2d–i) through to E17.5 (Extended Data Fig. 2j–o). Whole embryo staining at E10.5 and E12.5 (Extended Data Fig. 3a–f) revealed a *Prox1*/VEGFR-3-expressing LEC population emerging from the *Emcn*⁺ common cardinal vein and migrating towards the neighbouring sinus venosus and outflow tract (Extended Data

¹University College London, Institute of Child Health, Molecular Medicine Unit, 30 Guilford Street, London WC1N 1EH, UK. ²University of Oxford, Department of Physiology, Anatomy and Genetics, South Parks Road, Oxford OX1 3PT, UK. ³Regenerative Medicine Laboratory, University of Genoa & IRCCS AOU San Martino-IST, Largo Rosanna Benzi, 16132 Genoa, Italy. ⁴Laboratory for Cell Asymmetry, RIKEN Center for Developmental Biology, 2-2-3, Minatojima-Minamimachi, Chuo-ku, Kobe 650-0047, Japan.

*These authors contributed equally to this work.

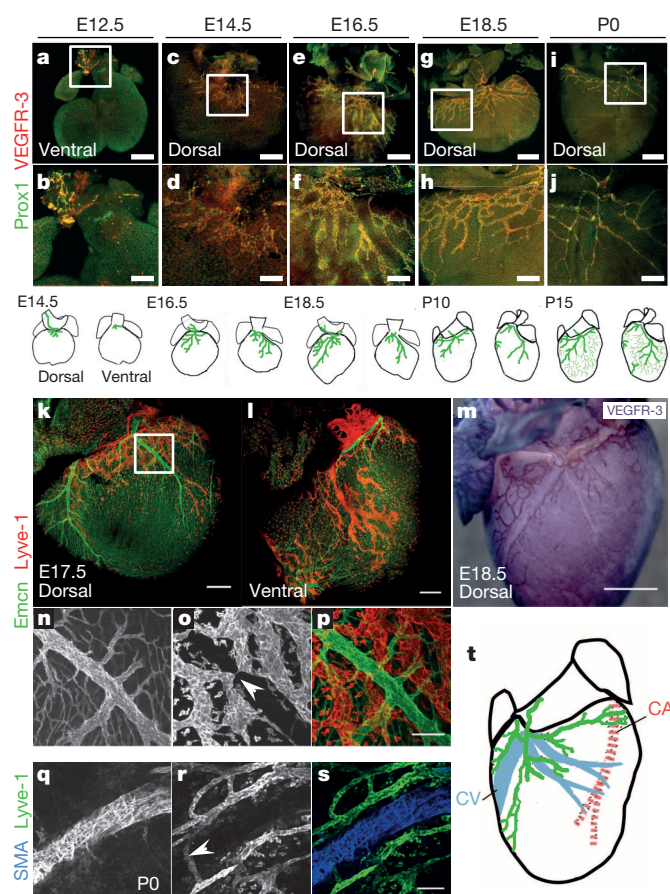


Figure 1 | Spatiotemporal development of the murine cardiac lymphatic vasculature. **a–h**, Whole-mount confocal imaging of embryonic hearts stained with VEGFR-3 and Prox1 at E12.5 (**a**; white box enlarged in **b**), E14.5 (**c**; white box enlarged in **d**), E16.5 (**e**; enlarged box in **f**) and E18.5 (**g**; enlarged box in **h**). **i, j**, From birth (P0), lymphatic vessels branch and expand further onto the dorsal epicardial surface of the heart (**i**; enlarged box in **j**). Schematics below the images represent the stages of lymphatic vessel development ($n = 5$ hearts analysed per time point). **k, l**, Whole-mount staining with Emcn (veins) and Lyve-1 (lymphatics). **m**, 3,3'-diaminobenzidine (DAB) staining with VEGFR-3. **n–p**, Enlarged images of box in **k** stained for Emcn (**n**), Lyve-1 (**o**) or both (**p**). White arrowhead in **o** highlights a coronary vein. **q–s**, α -Smooth muscle actin (SMA)- (veins, **q**) and Lyve-1-stained (lymphatics, **r**) hearts (white arrowhead in **r** indicates location of blood vessels) at later stages (P0). **s**, Merge of SMA and Lyve-1 staining. **t**, Schematic representation of the dorsal side of the heart at P10 (shown in Extended Data Fig. 1g, $n = 5$ hearts analysed per time point). CA, coronary artery; CV, coronary vein. Scale bars: **a, c, e**, 750 μ m; **b**, 300 μ m; **g**, 1 mm; **i**, 2 mm; **k–m**, 200 μ m; **p**, 10 μ m; **s**, 5 μ m.

Fig. 3d–f), suggesting that cardinal-vein-derived endothelial cells may be the venous source of coronary lymphatic vessels, an observation supported by previous studies^{5,7}.

To investigate the lymphatic cellular origin further, we first performed lineage-tracing experiments using a Tie2-Cre line¹² with a R26R-eYFP reporter¹³, revealing labelling of the embryonic cardinal vein at E10.5 (Extended Data Fig. 4a–d). At E12.5, Emcn⁺ jugular (cardinal) veins and lymph sacs, contributors to the systemic lymphatic vascular network⁵, were both YFP⁺ and Lyve-1⁺ (Fig. 2a–f). In contrast, E14.5 hearts revealed lymphatic vessels proximal to the outflow tract region which were YFP[−] (Fig. 2g, h), despite complete Tie2-eYFP recombination and labelling of lymphatics elsewhere in the embryo (Extended Data Fig. 4a–c). The relative incidence of YFP⁺ versus YFP[−] lymphatic vessels in the heart was $78 \pm 5.5\%$ YFP⁺ versus $19 \pm 3.3\%$ YFP[−] cells (mean percentage of cells \pm s.e.m. per field of view; $n = 24$ fields of view; six fields of view per heart, four hearts in total) and confirmed by orthogonal z-stack reconstruction

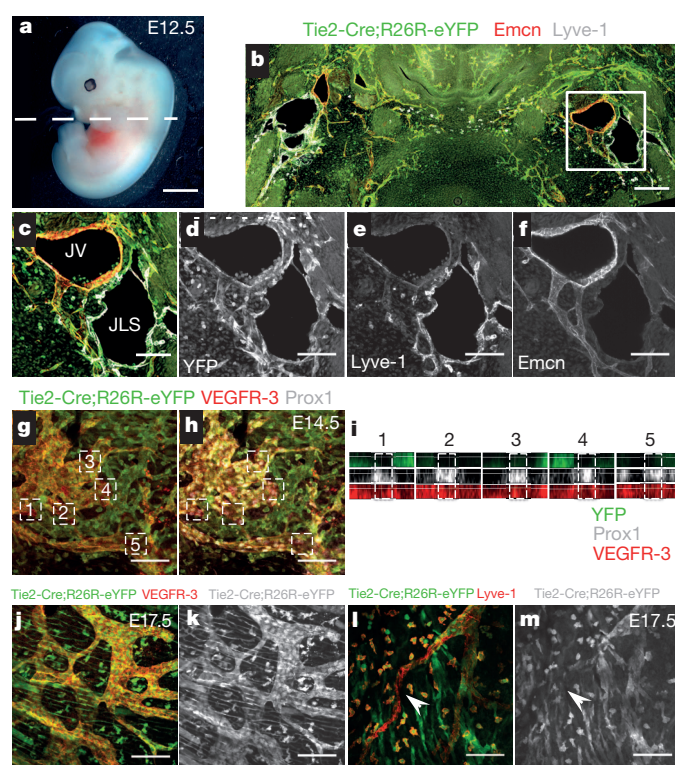


Figure 2 | Incomplete contribution of Tie2⁺ venous-derived LECs indicates a novel non-venous contribution to the developing cardiac lymphatics.

a, b, Tie2-Cre;R26R-eYFP embryos at E12.5 (**a**) stained with anti-GFP to detect the eYFP reporter expression, -Lyve-1 and -Emcn antibodies (**b**). **c–f**, Enlarged images of the area marked by the white box in **b**. Jugular lymph sacs (JLS) were YFP⁺. **g–i**, Whole-mount staining with VEGFR-3, Lyve-1, or Prox1 revealed incomplete recombination in cardiac lymphatic vessels (**g**) with evident YFP[−] regions of vasculature containing Prox1⁺ nuclei (**h**); see confocal z-stack reconstructions numbered 1–5 (**i**, as indicated by white inset boxes in **g** and **h**). **j–m**, At E17.5, both Tie2-YFP⁺ vessels (**j, k**) and Tie2-YFP[−] vessels (**l, m**; highlighted by white arrowheads) were observed; $n = 5$ hearts analysed per time point. JLS, jugular lymph sac; JV, jugular vein. Scale bars: **a**, 200 μ m; **b–h, j–m**, 100 μ m.

(Fig. 2i), which revealed both YFP⁺ (Fig. 2j, k) and YFP[−] vessels (Fig. 2l, m) in the developing heart at E17.5.

To confirm a non-venous contribution to cardiac lymphatic vessels, we analysed tamoxifen-inducible PDGFB-CreER^{T2} mice, crossed with either R26R-tdTomato¹⁴ or R26R-mTmG¹⁵ reporter lines to specifically label endothelial cells lining blood vessels (Extended Data Fig. 4e–o). Incomplete recombination of tdTomato within Lyve-1⁺ lymphatic vessels (Extended Data Fig. 4f) was evident with both tdTomato⁺/Lyve-1⁺ (Extended Data Fig. 4g–i) as well as tdTomato[−]/Lyve-1⁺ lymphatic vessels (Extended Data Fig. 4j–l), indicating a mixed contribution of endothelial- and non-endothelial-derived cardiac lymphatics. This was supported by crosses with an mTmG reporter mouse, where the level of GFP recombination within cardiac lymphatic vessels was mosaic (Extended Data Fig. 4m–o).

A putative haemogenic source of cardiac LECs

We next examined the possibility that an alternate source of LECs might arise from one of three potential cardiac progenitor populations¹⁶: the epicardium, cardiac mesoderm (early and late stage) or cardiac neural crest by lineage tracing with Wt1-CreERT2¹⁷, Mesp1-Cre¹⁸, Nkx2.5-Cre¹⁹ and Wnt1-Cre²⁰ lines crossed with the R26R-eYFP reporter, respectively. There was no contribution of Wt1⁺ (YFP⁺) cells to the developing coronary lymphatics, excluding the pro-epicardial organ as a source of LECs (Extended Data Fig. 5a–c)

were recovered largely devoid of VEGFR-3⁺ LECs (Extended Data Fig. 9a–d) and were relatively dysmorphic along the apical–basal (long) axis (Extended Data Fig. 9c, d), with smaller chambers and thickening of the ventricular compact layer (Extended Data Fig. 8i, j). Despite these anomalies, endocardial cushions formation appeared unaffected (Extended Data Fig. 8i, j). Relative to Tie2-Cre;*Prox1*^{fl/+} heterozygotes (Extended Data Fig. 9e–h), GFP⁺/Lyve-1⁺ lymphatic vessels were either partially or completely absent from the dorsal surface and completely absent from the ventral surface of mutant hearts (Extended Data Fig. 9i–p). The partial and complete loss of LECs correlated with the loss of Prox1 protein expression (Extended Data Fig. 9k, o). Tie2-Cre;*Prox1*^{fl/fl} mutant hearts were also recovered at E17.5 with significant coverage of targeted GFP⁺/Lyve-1⁺ lymphatics which correlated with incomplete knockdown of *Prox1* (Extended Data Fig. 7c). The resultant phenotype was mild hypoplasia of the lymphatic vessels and a partially truncated vascular network (Extended Data Fig. 10a–f). Vessels were significantly shorter and thinner with increased truncations relative to controls (Extended Data Fig. 10m–o). Immunostaining for cleaved caspase-3 revealed an increase in apoptotic cells within the termini of mutant vessels (Extended Data Fig. 8k, l) supporting the requirement for Prox1 in LEC identity and maintenance. Nevertheless, hypomorphic Tie2-Cre;*Prox1*^{fl/fl} mutants were recoverable at postnatal stages, whereby hypoplasia of the cardiac lymphatics appeared to be rescued beyond birth (Extended Data Fig. 8m–p).

We next targeted *Prox1* within the Vav1⁺ lineage. Specification of lymphatic vessels in severely affected Tie2-Cre;*Prox1*^{fl/fl} hearts at the base of the heart on the dorsal surface (Extended Data Fig. 9c, l), corresponded to the potential contribution of Vav1⁺ to the cardiac

lymphatics (Fig. 3). In Vav1-Cre;*Prox1*^{fl/fl} mutant hearts at E14.5, emerging VEGFR-3⁺ cardiac lymphatics were evident on both ventral and dorsal surfaces (Extended Data Fig. 8q–x). At E17.5, control Vav1-Cre;*Prox1*^{fl/+} mice revealed appropriate targeting of GFP⁺ LECs and an extensive lymphatic network on the ventral surface as indicated by Lyve-1, with retained Prox1 expression (Extended Data Fig. 9q–s). Vav1-Cre;*Prox1*^{fl/fl} mutants revealed no obvious systemic vessel defects (Extended Data Fig. 7j–m). Co-expression of GFP⁺/Lyve-1⁺ was observed in LECs (Extended Data Fig. 9t–x), however, specific loss of Lyve-1⁺ LECs was detected at subcellular resolution that directly correlated with loss of Prox1 and GFP-targeting (Extended Data Fig. 9y, z), supporting a Prox1-dependent Vav1⁺ source of cardiac lymphatics.

Neo-lymphangiogenesis post-cardiac injury

Lymphangiogenesis in other settings (most notably during skin infection) has been implicated in antigen clearance and inflammatory resolution^{30,31}. Thus, we determined whether the cardiac lymphatics might attempt compensatory angiogenesis during the pro-inflammatory phase following myocardial infarction (MI)³². We first analysed VEGFR-3 protein levels as a surrogate for an early lymphatic response, and observed a significant increase in VEGFR-3 at all stages from 24 h up to 21 days post-MI (Fig. 4a). Alterations in VEGFR-3 protein levels were recapitulated at the gene-expression level (Fig. 4b) and a general activation of the developmental lymphatic gene program was confirmed by concomitant increased expression of *Lyve1* and *Prox1* (Fig. 4c, d). At day 7 following injury there was a significant increase in the branching of surface VEGFR-3⁺ lymphatic vessels (Fig. 4e, f), and alignment of Prox1⁺ lymphatic sprouting with *Emcn*⁺ veins (Fig. 4g). Longitudinal analyses, from days 7 to 35 post-MI, revealed marked spatiotemporal changes in the lymphatic response. In the intact heart there were few superficial lymphatic

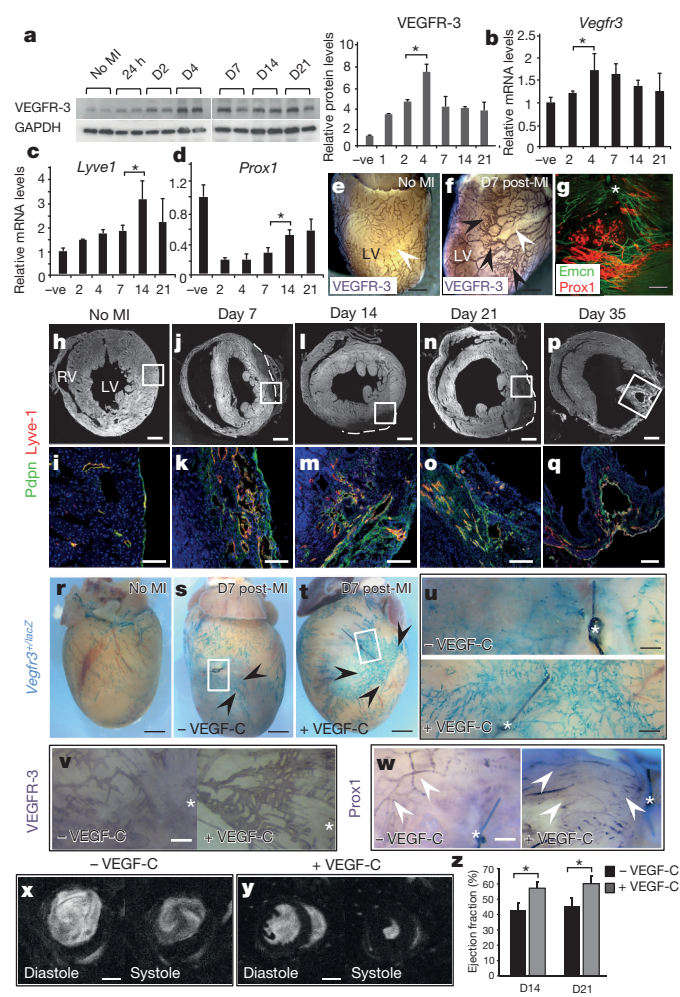


Figure 4 | Myocardial infarction induces a significant cardiac lymphangiogenic response that can be enhanced by VEGF-C-stimulation to promote functional improvement. **a**, VEGFR-3 protein levels increased from 24 h to 21 days post-MI, peaking at day 4 (D4) ($n = 3$ animals analysed per time point; single representative western blot with densitometry). **b–d**, Real-time analysis of *Vegfr3* (**b**), *Lyve1* (**c**) and *Prox1* (**d**) mRNA all revealed a significant increase in expression levels across the equivalent time-points post-MI ($n = 3$ animals per time point). **e, f**, VEGFR-3 whole-mount staining revealed increased lymphangiogenesis in the left ventricle (LV), proximal to the infarct 7 days post-MI (**e, f**; black arrowheads indicate areas in left ventricle with increased lymphangiogenesis, white arrowheads indicate areas with reduced lymphatic vessel density; $n = 3$ mice per group). **g**, Sprouting of Prox1⁺ lymphatics was observed aligning with *Emcn*⁺ veins 7 days post-MI (white asterisk, ligating suture (see Methods)). **h–q**, Short-axis sections at day 7 post-MI revealed Lyve-1⁺/Pdpn⁺ lymphangiogenesis in the scar region (white boxes in **h, j, l, n, p**), which was significantly increased relative to the intact heart (**h, i**) and which expanded through days 14 (**m**), 21 (**o**) and 35 with large lymphatic ‘shunts’ evident in the left ventricle (**q**; $n = 5$ hearts analysed). **i, k, m, o, q**, Enlarged images of the boxed areas in **h, j, l, n** and **p**, respectively. **r–u**, Whole-mount X-gal staining of *Vegfr3*^{+/lacZ} hearts after administration of VEGF-C reveals the lymphangiogenic response post-MI ($n = 3$ per treatment group). **r, s, t**, Mice treated with recombinant human VEGF-C(C156S) exhibited extensive lymphangiogenesis in the injury area (**t**, black arrowheads and white inset box enlarged in the top image of panel **u**) compared with vehicle-treated (**s**, black arrowheads and white inset box enlarged in the bottom image of panel **u**) or sham-operated mice (**r**). **v, w**, Whole-mount DAB staining of MI hearts with or without VEGF-C administration with VEGFR-3 (**v**) or Prox-1 (**w**) confirmed the observations in **r–u** (white asterisks indicate the ligating suture (see Methods)). **x, y**, Longitudinal MRI analyses of infarcted hearts 21 days after surgery following treatment with either vehicle (**x**) or VEGF-C (**y**). **z**, Ejection fraction measurements revealed a significant improvement in VEGF-C-treated hearts, compared to vehicle, at 14 and 21 days post-MI. $n = 8$ wild-type mice per treatment group. All graphs show mean \pm s.e.m. Data analysed with Student’s *t*-test; * $P \leq 0.05$. Scale bars: **e, f** 1 mm; **g** 400 μ m; **h, j, l, n, p**, 200 μ m; **i, k, m, o, q** 400 μ m; **r–t** 1 mm; **u–w** 500 μ m; **x, y** 2 mm.

Table 1 | Functional parameters from longitudinal MRI of VEGF-C- and vehicle-treated hearts post-MI

	7 days post-MI		14 days post-MI		21 days post-MI		28 days post-MI	
	VEGF-C (n = 8)	PBS (n = 8)	VEGF-C (n = 8)	PBS (n = 8)	VEGF-C (n = 8)	PBS (n = 8)	VEGF-C (n = 8)	PBS (n = 8)
Body weight (g)	19.0 ± 0.6	19.8 ± 0.5	19.6 ± 0.7	20.5 ± 0.5	19.8 ± 0.5	20.4 ± 0.4	20.9 ± 0.7	21.3 ± 0.6
Heart rate (b.p.m.)	515 ± 10	499 ± 19	511 ± 6	496 ± 19	510 ± 9	494 ± 10	469 ± 52	496 ± 26
Left ventricle								
End diastolic volume (μl)	49.6 ± 4.4	68.9 ± 11.1	48.3 ± 4.0	70.9 ± 10.9	56.6 ± 5.4	72.1 ± 11.5	60.9 ± 7.4	73.3 ± 13.7
End systolic volume (μl)	23.1 ± 4.8	40.3 ± 9.7	21.5 ± 4.1*	43.5 ± 10.0*	24.0 ± 5.3	42.1 ± 10.2	27.9 ± 7.6	42.3 ± 12.1
Stroke volume (μl)	26.5 ± 2.3	28.6 ± 2.3	26.8 ± 1.5	27.3 ± 1.5	32.6 ± 1.6	30.0 ± 2.7	32.9 ± 2.0	31.0 ± 3.2
Ejection fraction (%)	56 ± 6	46 ± 5	57 ± 4*	43 ± 5*	60 ± 5*	45 ± 5*	56 ± 6	45 ± 6
Cardiac output (ml min ⁻¹)	13.5 ± 0.9	14.3 ± 1.4	13.7 ± 0.6	13.6 ± 1.0	16.6 ± 0.8	14.7 ± 1.2	15.4 ± 2.2	15.5 ± 2.1
Left ventricular mass (mg)	80 ± 5	96 ± 8	80 ± 4	90 ± 7	88 ± 6	90 ± 4	94 ± 9	95 ± 6
Absolute infarct size (mm ²)	13.6 ± 5.6	36.4 ± 11.4	14.2 ± 5.8	35.0 ± 10.8	14.1 ± 5.3	34.5 ± 11.0	13.5 ± 7	28.9 ± 12.0
Relative infarct size (%)	10 ± 4	21 ± 5	11 ± 4	20 ± 5	10 ± 3	21 ± 6	9 ± 4	18 ± 7

Data presented as mean ± standard error of the mean. Asterisks indicate significant differences between VEGF-C- and PBS-treated hearts; $P \leq 0.05$; repeated measures t-test, two-tailed distribution, two-sample equal variance.

vessels detectable (Fig. 4h, i), as evident from staining for Lyve-1 and podoplanin (Pdpn (ref. 33)) as compared to day 7 after injury when there was a significant increase in the number of Lyve-1⁺/Pdpn⁺ lymphatic vessels in cross-section, (Fig. 4j, k). These vessels increased in diameter by day 14, concurrent with nascent lymphatic network expansion (Fig. 4l, m), and persisted through day 21 (Fig. 4n, o) to day 35, where enlarged lymphatic shunts were evident, localized superficially in the myocardium at the border zone of the infarct/scar region (Fig. 4p, q). Thus, the adult cardiac lymphatics undergo significant angiogenesis following initiation of a developmental programme in response to ischaemic injury.

VEGF-C improves cardiac function post-MI

To investigate the influence of neo-lymphangiogenesis on cardiac function after MI, we treated wild-type or *Vegfr3^{lacZ/+}* reporter mice³⁴ with recombinant VEGF-C(C156S)²⁸ at days 0, 2, 3, 4 and 6 post-MI. At day 7 post-MI, a stronger lymphangiogenic response (X-gal⁺/VEGFR-3⁺/Prox1⁺) was observed surrounding the injury area in VEGF-C-treated samples, compared to vehicle-treated controls (Fig. 4r–w). Moreover, VEGF-C-treated mice exhibited a significant improvement in cardiac function as determined by longitudinal MRI (Fig. 4x–z and Table 1). Specifically, smaller ventricular end-systolic volumes (Fig. 4x, y and Table 1) and significant improvement in the ejection fraction were recorded in the VEGF-C-treated group (Fig. 4z and Table 1; 43 ± 5% for vehicle versus 57 ± 4% for VEGF-C-treated by 14 days post-MI; 45 ± 5% for vehicle versus 60 ± 5% for VEGF-C-treated by 21 days post-MI; mean ± s.e.m.; $n = 8$ animals per group; $P \leq 0.05$). The improvement in cardiac function was maintained for at least 28 days post-MI (Table 1). Collectively, these data suggest that promotion of growth-factor-induced lymphangiogenesis is possible in the adult diseased heart and improves prognosis, analogous to what has been reported in other disease models³⁵.

Discussion

Our study challenges the unequivocal view of lymphatic vessel development derived from Sabin's model of venous origin¹. We reveal that the lymphatic vasculature of the embryonic mouse heart comprises a heterogeneous make-up of cell populations, with contributions derived from both extra-cardiac venous endothelium and a novel source of lymphatic progenitors which may arise from the yolk sac haemogenic endothelium. Targeting of *Prox1* in both venous endothelial and non-venous-derived compartments resulted in loss of the cardiac LECs, supporting a dual origin in the developing heart and consistent with previous studies demonstrating that *Prox1* is both necessary and sufficient to drive LEC fate specification^{36–39}. *Prox1* acts at the decision point between blood and lymphatic endothelial cell specification⁴⁰, such that *Prox1*-deficient LECs contributing to the systemic blood vasculature resulted in ectopic vessels and haemorrhaging throughout the embryo. However, in *Tie2-Prox1* mutant hearts, hypoplasia of the lymphatic vessels did not appear to impact

upon the gross development of the coronary blood vessels, highlighting a further unique ontology of the cardiac lymphatics relative to systemic lymphatic vasculature. Previously, *Prox1* dosage effects underpinned formation of the systemic lymphovenous valves⁴¹; here partial *Prox1* knockdown resulted in formation of the cardiac lymphatics but with truncation of the developing plexus and aberrant remodelling suggesting a novel role for *Prox1* in maintaining the cardiac lymphatic network.

Insight into the embryological origin and development of the cardiac lymphatics has important implications for understanding cardiovascular tissue fluid homeostasis, injury-induced inflammation and disease. Following MI the cardiac lymphatics underwent a profound angiogenic response, accompanied by an upregulation in the lymphatic development gene program. Significantly, this was enhanced by ectopic VEGF-C stimulation following injury, leading to improvement in cardiac function. Myocardial injury is associated with a robust immune reaction, characterized by sequential mobilization of monocytes involved in inflammatory functions and wound healing³². Lymphangiogenesis in inflammatory settings facilitates the resolution of tissue oedema and promotes macrophage mobilization^{30,31}, and induction by VEGF-C alleviates inflammation in mouse models^{42,43}. Therefore, mechanisms coupling lymphatic development to immune regulation represent a therapeutic target. Induction of lymphatic vessels could provide a pathway for inflammatory cell efflux to tip the balance in favour of wound healing within the injured adult heart.

Online Content Methods, along with any additional Extended Data display items and Source Data, are available in the online version of the paper; references unique to these sections appear only in the online paper.

Received 25 March 2014; accepted 10 April 2015.

Published online 20 May 2015.

- Sabin, F. On the origin of the lymphatic system from the veins and the development of the lymph hearts and thoracic duct in the pig. *Am. J. Anat.* **1**, 367–389 (1902).
- Huntington, G. S. & McClure, C. F. W. The anatomy and development of the jugular lymph sac in the domestic cat. *Am. J. Anat.* **10**, 177–312 (1910).
- Srinivasan, R. S. *et al.* Lineage tracing demonstrates the venous origin of the mammalian lymphatic vasculature. *Genes Dev.* **21**, 2422–2432 (2007).
- Yaniv, K. *et al.* Live imaging of lymphatic development in the zebrafish. *Nature Med.* **12**, 711–716 (2006).
- Yang, Y. *et al.* Lymphatic endothelial progenitors bud from the cardinal vein and intersomitic vessels in mammalian embryos. *Blood* **120**, 2340–2348 (2012).
- Okuda, K. S. *et al.* *Lyve1* expression reveals novel lymphatic vessels and new mechanisms for lymphatic vessel development in zebrafish. *Development* **139**, 2381–2391 (2012).
- Hägerling, R. *et al.* A novel multistep mechanism for initial lymphangiogenesis in mouse embryos based on ultramicroscopy. *EMBO J.* **32**, 629–644 (2013).
- Flaht, A. *et al.* Cellular phenotypes and spatio-temporal patterns of lymphatic vessel development in embryonic mouse hearts. *Dev. Dyn.* **241**, 1473–1486 (2012).
- Joukov, V. *et al.* A novel vascular endothelial growth factor, VEGF-C, is a ligand for the Flt4 (VEGFR-3) and KDR (VEGFR-2) receptor tyrosine kinases. *EMBO J.* **15**, 1751 (1996).

10. Wigle, J. T. & Oliver, G. *Prox1* function is required for the development of the murine lymphatic system. *Cell* **98**, 769–778 (1999).
11. Buttler, K., Ezaki, T. & Wilting, J. Proliferating mesodermal cells in murine embryos exhibiting macrophage and lymphendothelial characteristics. *BMC Dev. Biol.* **8**, 43 (2008).
12. Koni, P. A. *et al.* Conditional vascular cell adhesion molecule 1 deletion in mice: impaired lymphocyte migration to bone marrow. *J. Exp. Med.* **193**, 741–754 (2001).
13. Srinivas, S. *et al.* Cre reporter strains produced by targeted insertion of *EYFP* and *ECFP* into the *ROSA26* locus. *BMC Dev. Biol.* **1**, 4 (2001).
14. Madisen, L. *et al.* A robust and high-throughput Cre reporting and characterization system for the whole mouse brain. *Nature Neurosci.* **13**, 133–140 (2010).
15. Muzumdar, M. D., Tasic, B., Miyamichi, K., Li, L. & Luo, L. A global double-fluorescent Cre reporter mouse. *Genesis* **45**, 593–605 (2007).
16. Brade, T., Pane, L. S., Moretti, A. & Chien, K. R. & Laugwitz, K. L. Embryonic heart progenitors and cardiogenesis. *Cold Spring Harb. Perspect. Med.* **3** (2013).
17. Zhou, B. *et al.* Epicardial progenitors contribute to the cardiomyocyte lineage in the developing heart. *Nature* **454**, 109–113 (2008).
18. Saga, Y. *et al.* *MesP1* is expressed in the heart precursor cells and required for the formation of a single heart tube. *Development* **126**, 3437–3447 (1999).
19. Moses, K. A., DeMayo, F., Braun, R. M., Reecy, J. L. & Schwartz, R. J. Embryonic expression of an *Nkx2-5/Cre* gene using *ROSA26* reporter mice. *Genesis* **31**, 176–180 (2001).
20. Jiang, X., Rowitch, D. H., Soriano, P., McMahon, A. P. & Sucov, H. M. Fate of the mammalian cardiac neural crest. *Development* **127**, 1607–1616 (2000).
21. Tang, Y., Harrington, A., Yang, X., Friesel, R. E. & Liaw, L. The contribution of the *Tie2*⁺ lineage to primitive and definitive hematopoietic cells. *Genesis* **48**, 563–567 (2010).
22. Georgiades, P. *et al.* *vavCre* transgenic mice: a tool for mutagenesis in hematopoietic and endothelial lineages. *Genesis* **34**, 251–256 (2002).
23. Chen, M. J., Yokomizo, T., Zeigler, B. M., Dzierzak, E. & Speck, N. A. *Runx1* is required for the endothelial to haematopoietic cell transition but not thereafter. *Nature* **457**, 887–891 (2009).
24. Ruiz-Herguido, C. *et al.* Hematopoietic stem cell development requires transient *Wnt/β-catenin* activity. *J. Exp. Med.* **209**, 1457–1468 (2012).
25. Rolny, C. *et al.* Platelet-derived growth factor receptor-beta promotes early endothelial cell differentiation. *Blood* **108**, 1877–1886 (2006).
26. Perdiguero, E. G. *et al.* Tissue-resident macrophages originate from yolk-sac-derived erythro-myeloid progenitors. *Nature* **518**, 547–551 (2014).
27. Hamada, K. *et al.* VEGF-C signaling pathways through VEGFR-2 and VEGFR-3 in vasculoangiogenesis and hematopoiesis. *Blood* **96**, 3793–3800 (2000).
28. Breslin, J. W. *et al.* Vascular endothelial growth factor-C stimulates the lymphatic pump by a VEGF receptor-3-dependent mechanism. *Am. J. Physiol. Heart Circ. Physiol.* **293**, H709–H718 (2007).
29. Iwano, T., Masuda, A., Kiyonari, H., Enomoto, H. & Matsuzaki, F. *Prox1* postmitotically defines dentate gyrus cells by specifying granule cell identity over CA3 pyramidal cell fate in the hippocampus. *Development* **139**, 3051–3062 (2012).
30. Kataru, R. P. *et al.* Critical role of CD11b⁺ macrophages and VEGF in inflammatory lymphangiogenesis, antigen clearance, and inflammation resolution. *Blood* **113**, 5650–5659 (2009).
31. Huggenberger, R. *et al.* An important role of lymphatic vessel activation in limiting acute inflammation. *Blood* **117**, 4667–4678 (2011).
32. Nahrendorf, M. *et al.* The healing myocardium sequentially mobilizes two monocyte subsets with divergent and complementary functions. *J. Exp. Med.* **204**, 3037–3047 (2007).
33. Smart, N. *et al.* *De novo* cardiomyocytes from within the activated adult heart after injury. *Nature* **474**, 640–644 (2011).
34. Dumont, D. J. *et al.* Cardiovascular failure in mouse embryos deficient in VEGF receptor-3. *Science* **282**, 946–949 (1998).
35. Tammela, T. *et al.* Therapeutic differentiation and maturation of lymphatic vessels after lymph node dissection and transplantation. *Nature Med.* **13**, 1458–1466 (2007).
36. Wigle, J. T. *et al.* An essential role for *Prox1* in the induction of the lymphatic endothelial cell phenotype. *EMBO J.* **21**, 1505–1513 (2002).
37. Petrova, T. V. *et al.* Lymphatic endothelial reprogramming of vascular endothelial cells by the *Prox-1* homeobox transcription factor. *EMBO J.* **21**, 4593–4599 (2002).
38. Johnson, N. C. *et al.* Lymphatic endothelial cell identity is reversible and its maintenance requires *Prox1* activity. *Genes Dev.* **22**, 3282–3291 (2008).
39. Kim, H. *et al.* Embryonic vascular endothelial cells are malleable to reprogramming via *Prox1* to a lymphatic gene signature. *BMC Dev. Biol.* **10**, 72 (2010).
40. Kazenwadel, J., Michael, M. Z. & Harvey, N. L. *Prox1* expression is negatively regulated by *miR-181* in endothelial cells. *Blood* **116**, 2395–2401 (2010).
41. Srinivasan, R. S. & Oliver, G. *Prox1* dosage controls the number of lymphatic endothelial cell progenitors and the formation of the lymphovenous valves. *Genes Dev.* **25**, 2187–2197 (2011).
42. Karkkainen, M. J., Jussila, L., Ferrell, R. E., Finegold, D. N. & Alitalo, K. Molecular regulation of lymphangiogenesis and targets for tissue oedema. *Trends Mol. Med.* **7**, 18–22 (2001).
43. Szuba, A. *et al.* Therapeutic lymphangiogenesis with human recombinant VEGF-C. *FASEB J.* **16**, 1985–1987 (2002).

Supplementary Information is available in the online version of the paper.

Acknowledgements This work was funded by the Wellcome Trust (L.K.), EU FP7 Marie Curie ITN (CardioNet; M.M.) and the British Heart Foundation (S.N., J.M.V., M.R., K.D., S.B., C.A.C., P.R.R.). We thank M. Fruttiger for providing the *Pdgfrb-creER*^{T2} line, J. Pollard for providing the *Csf1r-creER* mouse line, K. Alitalo for providing the *Vegfr3*^{lacZ/+} mouse line, T. Makinen for providing *Pdgfrb-cre* embryos and the transgenic services at the University of Oxford for re-deriving the *Prox1*^{fl/+} mouse line from RIKEN (accession number CDB0482K). We are grateful to B. Vernay and A. Eddoudi for assistance with confocal microscopy and flow cytometry, respectively.

Author Contributions L.K., S.N. and J.M.V. carried out all experiments (except myocardial infarction surgeries and MRI scanning), analysed the data and contributed figures for the manuscript. K.D., S.B., M.M. and M.R. performed all MI surgeries and post-processed the hearts in preparation for immunofluorescence. F.M. provided the RIKEN *Prox1*-floxed mice. S.N. and C.A.C. performed blinded-MRI scanning and analysed the data. P.R.R. established the hypotheses and analysed the data. J.M.V. and P.R.R. supervised the studies and co-wrote the manuscript. All authors declare no conflicting or competing interests.

Author Information Reprints and permissions information is available at www.nature.com/reprints. The authors declare no competing financial interests. Readers are welcome to comment on the online version of the paper. Correspondence and requests for materials should be addressed to P.R. (paul.riley@dpag.ox.ac.uk).

METHODS

Mouse strains. The following mouse strains were used as previously described: Csf1r-CreER²⁶, Mesp1-Cre⁴⁴, Nkx2.5-Cre¹⁹, Pdgfrβ-CreERT2⁴⁵, Pdgfrβ-Cre⁴⁶, *Prox1*^{fl/+} (ref. 29), R26R-eYFP¹³, R26R-mTmG¹⁵, R26R-tdTomato¹⁴, Tie2-Cre¹², Vav1-Cre⁴⁷, Wt1-CreERT2¹⁷, Wnt1-Cre²⁰, *Vegfr3*^{lacZ/+} (ref. 34). Breeding was carried out using only Cre⁺ males for all Cre strains except the Vav1-Cre where Cre⁺ females were used. Pregnant females crossed to inducible Cre male studs were injected intraperitoneally at E7.5 (Csf1r-CreER) or E9.5 (Wt1-CreERT2; Pdgfrβ-CreERT2) with 2 mg of 4-hydroxytamoxifen (4-OHT) dissolved in peanut oil. Embryonic staging was determined by the day of the vaginal plug (E0.5). C57BL/6 mice were used for the longitudinal cardiac cine-MRI study. Investigators were blinded to genotype and treatment groups. All animal experiments were carried out according to UK Home Office project license PPL 30/2987 Compliant with the UK Animals (Scientific Procedures) Act 1986.

Quantitative real-time PCR. Total RNA was isolated from hearts using the Qiagen RNeasy Mini Kit (Qiagen). Complementary DNA was synthesized using the Reverse Transcription System (Promega), following the manufacturer's instructions and used for quantitative real-time PCR using SYBR Green on an ABI 7900 for the following genes: *Vegfr3*, *Prox1*, *Lyve1*. Fold change was determined by applying the $2^{-\Delta\Delta C_T}$ method. The following primer sequences were used: *Vegfr3*, 5'-CCATCGAGAGTCTGGACAGC-3' forward, 5'-CCGGGATGGTGGTCACATAG-3' reverse; *Prox1*, 5'-GAAGGGCTATCACCCAATCA-3' forward, 5'-TGAACCACTTGATGAGCTGC-3' reverse; *Lyve1*, 5'-GGCTTTGAGACTTGCAGCTATG-3' forward, 5'-GCAGGAGTTAACCCAGGTGT-3' reverse.

Western blotting. Heart samples were lysed in RIPA buffer (50 mM Tris-HCl at pH 7.6, 150 mM NaCl, 1%NP-40, 0.5% DOC, 0.1% SDS) supplemented with protease inhibitors (Protease Inhibitor Cocktail Tablet (Roche), 1 mM PMSF (Sigma) and 1 µg ml⁻¹ aprotinin (Sigma)). The lysate was centrifuged at 13,000g for 15 min at 4°C and the supernatant recovered. For SDS-PAGE samples were incubated with an equal volume of 2 × Laemmli Buffer/5% β-ME at 95°C for 5 min before being resolved on a 10/15% acrylamide gel (Sigma) and analysed by western blot using a primary antibody for VEGFR-3 (goat anti-mouse, 1:1,000 dilution) or GAPDH (goat anti-mouse, 1:1,000 dilution, Millipore). All secondary antibodies were conjugated to HRP and imaged using enhanced chemiluminescence (all GE Healthcare).

Immunohistochemistry and histology, confocal imaging and quantitation. Hearts and embryos for histology were collected, fixed in 2% PFA overnight and either stored in PBS, or embedded in either paraffin wax or OPT (both Raymond Lamb). Ten-micrometre paraffin sections were stained with haematoxylin (Sigma) and eosin (Raymond Lamb). Immunofluorescent staining on 8-µm frozen sections was performed using primary antibodies to endomucin (catalogue number SC-53941, Santa Cruz Biotechnology, 1:50 dilution), CD31 (553370, BD Pharmingen, 1:50), *Prox1* (11-002, Abcam, 1:200), *Prox1* (AF2727, R&D Systems, 1:200), *Lyve-1* (NBP1-43411, Novus Biologicals, 1:500), *Lyve-1* (11-034, Abcam, 1:200), VEGFR-3 (AF743, R&D Systems, 1:50), GFP (ab13970, Abcam, 1:2,000), Podoplanin (10R-P133a, Fitzgerald, 1:500), α-smooth muscle actin (C6198, Sigma, 1:200), cleaved caspase-3 (9661/9664, Cell Signalling Technology, 1:100). AlexaFluor secondary antibodies (Invitrogen, 1:200) were used in all cases. The same protocol was applied to whole mount hearts and embryos with primary and secondary antibody incubations extended to overnight. Whole mount 3,3'-diaminobenzidine (DAB) staining was performed on embryonic and postnatal hearts using the Vectastain Elite ABC Kit Goat IgG and the DAB Peroxidase Substrate Kit (both Vector Laboratories) following the manufacturer's instructions. Hearts from *Vegfr3*^{lacZ/+} mice were collected post-MI and stained for β-galactosidase (β-gal) activity. In brief, hearts were fixed on ice for 30 min in 2% formaldehyde solution containing 0.2% glutaraldehyde (both Sigma), washed twice with PBS on ice, and stained overnight at room temperature in X-gal staining solution containing 4 mM K₄Fe(CN)₆, 4 mM K₃Fe(CN)₆, 2 mM MgCl₂ and 1 mg ml⁻¹ X-gal (dissolved in N-dimethylformamide; Sigma). Immunofluorescence staining was imaged using an Olympus FV1000 confocal microscope. Maximum intensity z-projections of whole hearts were acquired using both the tiling and z-stack functions. DAB and β-gal staining was imaged using a Zeiss stereo microscope. All images were processed using ImageJ software. Analysis of vessels and branching calculations were

performed using AngioTool⁴⁸. Cell lineage contribution was quantified by counting *Prox1*⁺ reporter⁺ nuclei versus singly *Prox1*⁺ nuclei within vessels across several fields of view per heart analysed.

Flow cytometry. Isolation of eGFP⁺ cells from Tie2-Cre;*Prox1*-eGFP^{fl/+} and Tie2-Cre;*Prox1*-eGFP^{fl/fl} hearts and RNA extraction was performed according to standard protocols.

Yolk sac explants. E8.0 explants including the intact yolk sac were cultured for 5 days in Dulbecco's Modified Eagle Medium with 20% fetal calf serum and 10⁻⁵ mol l⁻¹ 2-mercaptoethanol (Life Technologies) supplemented with 100 ng ml⁻¹ of recombinant human VEGF-C(C156S) (R&D systems).

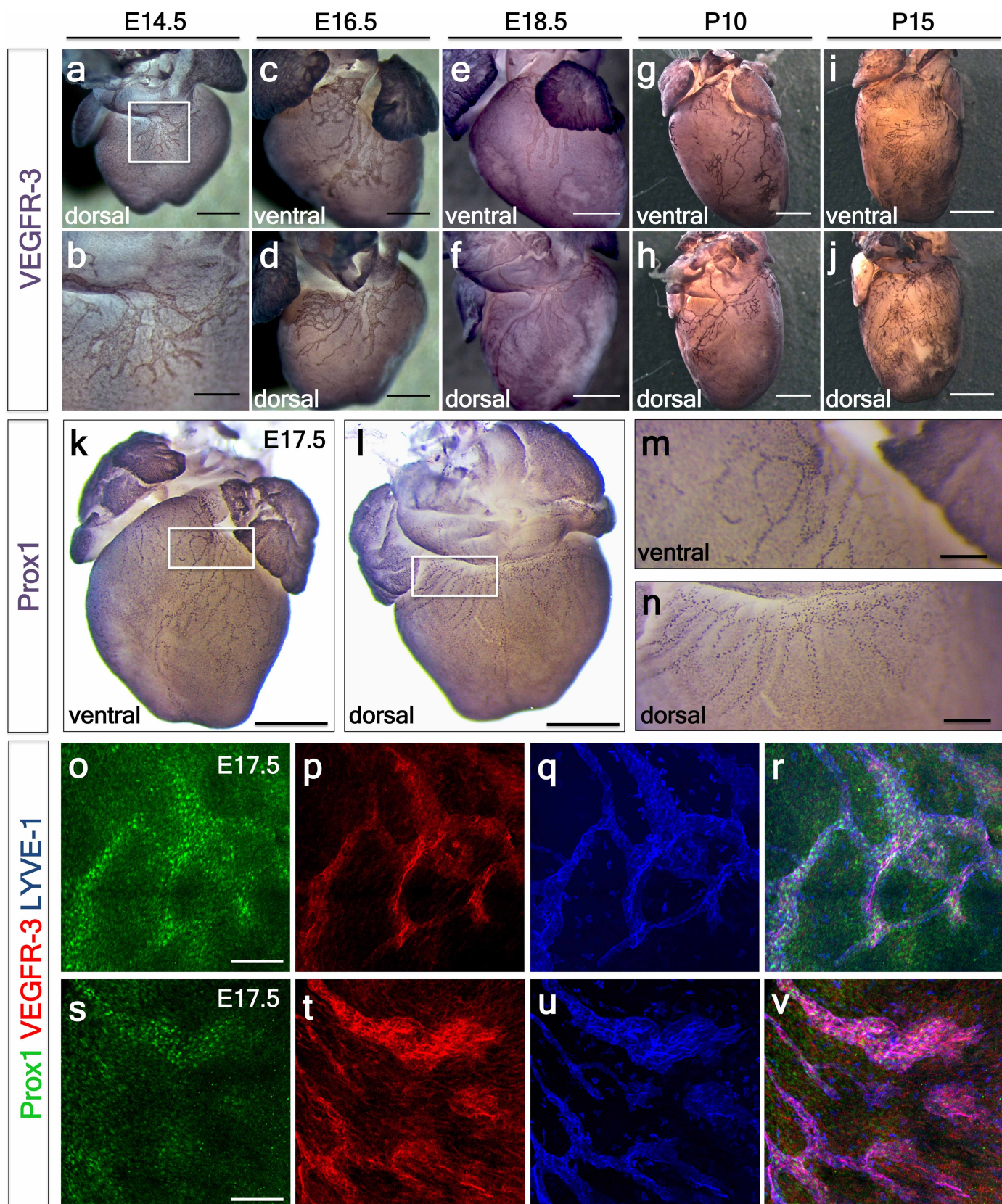
Murine cardiac injury model. *Vegfr3*^{lacZ/+} (ref. 34) or C57BL/6 female mice were subject to surgery between 8 and 10 weeks, with a weight of 17–23 g. Mice were anaesthetized with 2.5% isoflurane and placed under assisted external ventilation through the insertion of an endotracheal tube. Cardiac injury was induced by permanent ligation of the left descending artery (LAD). LAD-ligation mice were directly compared with sham-operated animals which underwent tracheotomy, opening of the chest and insertion of the needle through the left ventricle but no suture ligation. Buprenorphine (buprenorphine hydrochloride; Vetlegesic) was delivered as a 0.015 mg ml⁻¹ solution via intraperitoneal injection at 20 min before the procedure to provide analgesia. On recovery mice were randomly allocated to receive an intraperitoneal injection of 0.1 µg g⁻¹ recombinant human VEGF-C (C156S) (R&D systems) or PBS. Further injections were administered at 2, 3, 4 and 6 days post-surgery. Experimenters were blind to treatment groups for subsequent cardiac cine-MRI and analysis. Hearts were collected at 1, 2, 4, 7, 14, 21, 28 and 35 days post-MI and either sectioned or left intact and prepared for histology, immunofluorescence, RNA and protein extraction. Mice were housed and maintained in a controlled environment. All surgical and pharmacological procedures were performed in accordance with the Animals (Scientific Procedures) Act 1986, (Home Office, UK).

Cardiac cine-MRI. Cardiac cine-MRI was performed post-LAD ligation as described⁴⁹. In brief, mice were anaesthetized with 2% isoflurane in O₂ and positioned supine in a purpose-built cradle. ECG electrodes were inserted into the forepaws and a respiration loop was taped across the chest. The cradle was lowered into a vertical-bore, 11.7 T magnetic resonance system (Magnex Scientific) with a 40 mm birdcage coil (Rapid Biomedical) and a Bruker console running Paravision 2.1.1 (Bruker Medical). A stack of contiguous 1-mm thick true short-axis ECG-gated cine-FLASH images were acquired to cover the entire left ventricle (TE/TR 1.43/4.6 ms; 17.5° pulse; field of view 25.6 × 25.6 mm; matrix size 128 × 128 zero filled to 256 × 256 giving a voxel size of 100 × 100 × 1,000 µm; 20 to 30 frames per cardiac cycle). Long-axis two-chamber and four-chamber images were also acquired.

MRI data analysis. Blinded image analysis was performed using ImageJ (NIH). Left ventricular mass, volumes and ejection fraction were calculated as described⁵⁰. The relative infarct size was calculated from the average of the endocardial and epicardial circumferential lengths of the thinned, akinetic region of all slices, measured at diastole, and expressed as a percentage of the total myocardial surface⁵⁰.

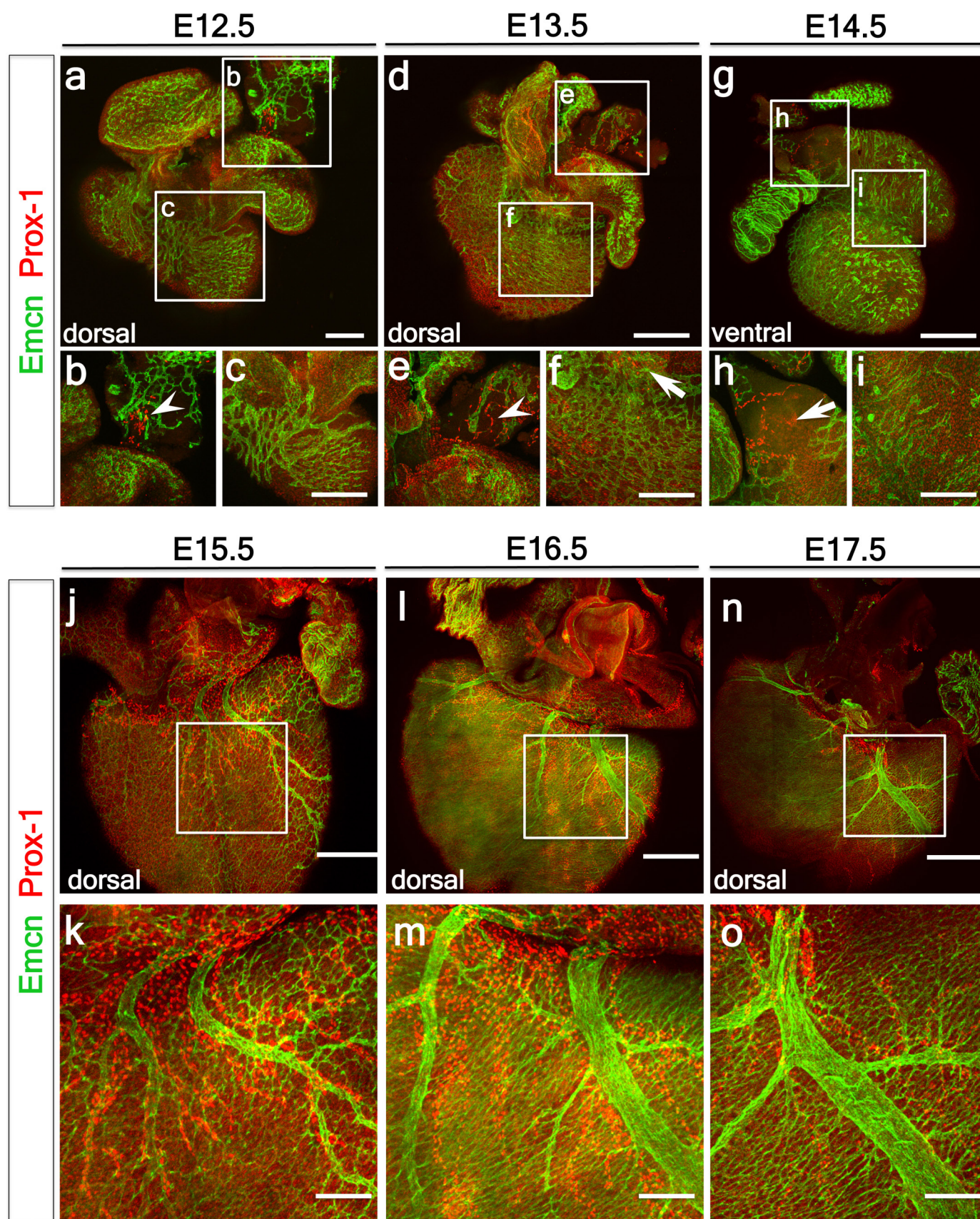
Statistical analysis. No statistical methods were used to predetermine sample size. Statistical difference between groups was evaluated using Student's *t*-test (two-tailed) or one-way ANOVA. A *P* value of <0.05 was considered statistically significant. All values and graphs present the mean value ± s.e.m.

44. Saga, Y. *et al.* MesP1 is expressed in the heart precursor cells and required for the formation of a single heart tube. *Development* **126**, 3437–3447 (1999).
45. Claxton, S. *et al.* Efficient, inducible Cre-recombinase activation in vascular endothelium. *Genesis* **46**, 74–80 (2008).
46. Foo, S. S. *et al.* Ephrin-B2 controls cell motility and adhesion during blood-vessel wall assembly. *Cell* **124**, 161–173 (2006).
47. de Boer, J. *et al.* Transgenic mice with hematopoietic and lymphoid specific expression of Cre. *Eur. J. Immunol.* **33**, 314–325 (2003).
48. Zudaire, E., Gambardella, L., Kurcz, C. & Vermeren, S. A computational tool for quantitative analysis of vascular networks. *PLoS ONE* **6**, e27385 (2011).
49. Schneider, J. E. *et al.* Fast, high-resolution *in vivo* cine magnetic resonance imaging in normal and failing mouse hearts on a vertical 11.7 T system. *J. Magn. Reson. Imaging* **18**, 691–701 (2003).
50. Carr, C. A. *et al.* Bone marrow-derived stromal cells home to and remain in the infarcted rat heart but fail to improve function: an *in vivo* cine-MRI study. *Am. J. Physiol. Heart Circ. Physiol.* **295**, H533–H542 (2008).



Extended Data Figure 1 | Molecular characterization of the murine cardiac lymphatic vasculature. **a–j**, Whole-mount DAB staining of hearts ($n = 3$ per time point) with the lymphatic marker VEGFR-3 revealed cardiac lymphatic vessels first sprout from the region of the sinus venosus, on the dorsal side of the heart at E14.5 (**a**, white box, enlarged in **b**). At E16.5, ventrally the first small vessels arose between the atria (**c**), while the main dorsal vessels spread inferiorly from the sinus venosus at the inflow region of the heart (**d**). At E18.5 the network appears similar with little expansion (**e**, **f**). From birth (P0) lymphatic vessels branch and expand onto the ventral epicardial surface of the heart such that by P10 the network has expanded markedly, coincident with cardiac growth (**g**, **h**). Consistent with the systemic lymphatic vasculature, cardiac lymphatic vessels are fully developed by P15 (**i**, **j**), with no difference in

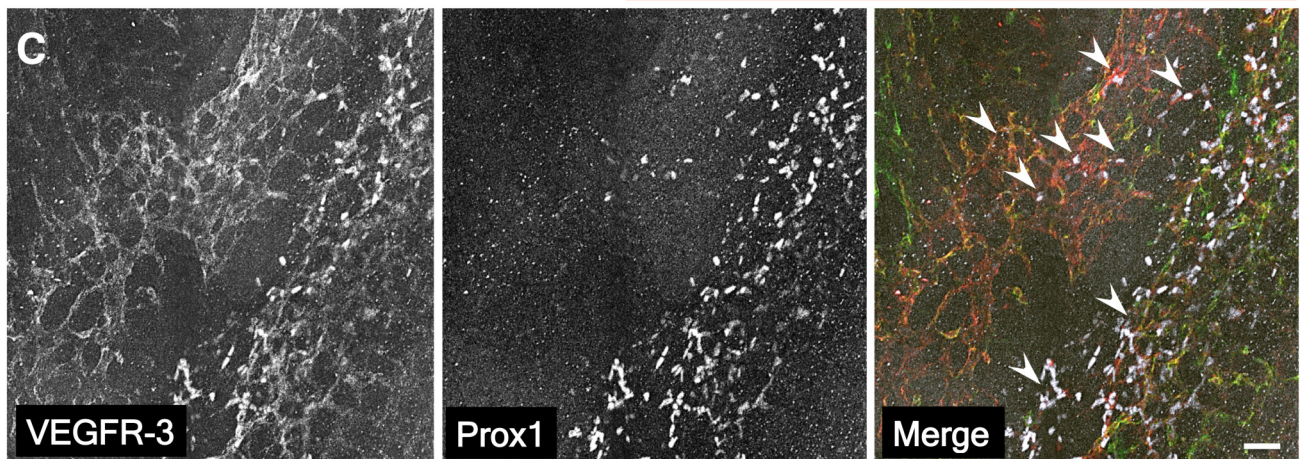
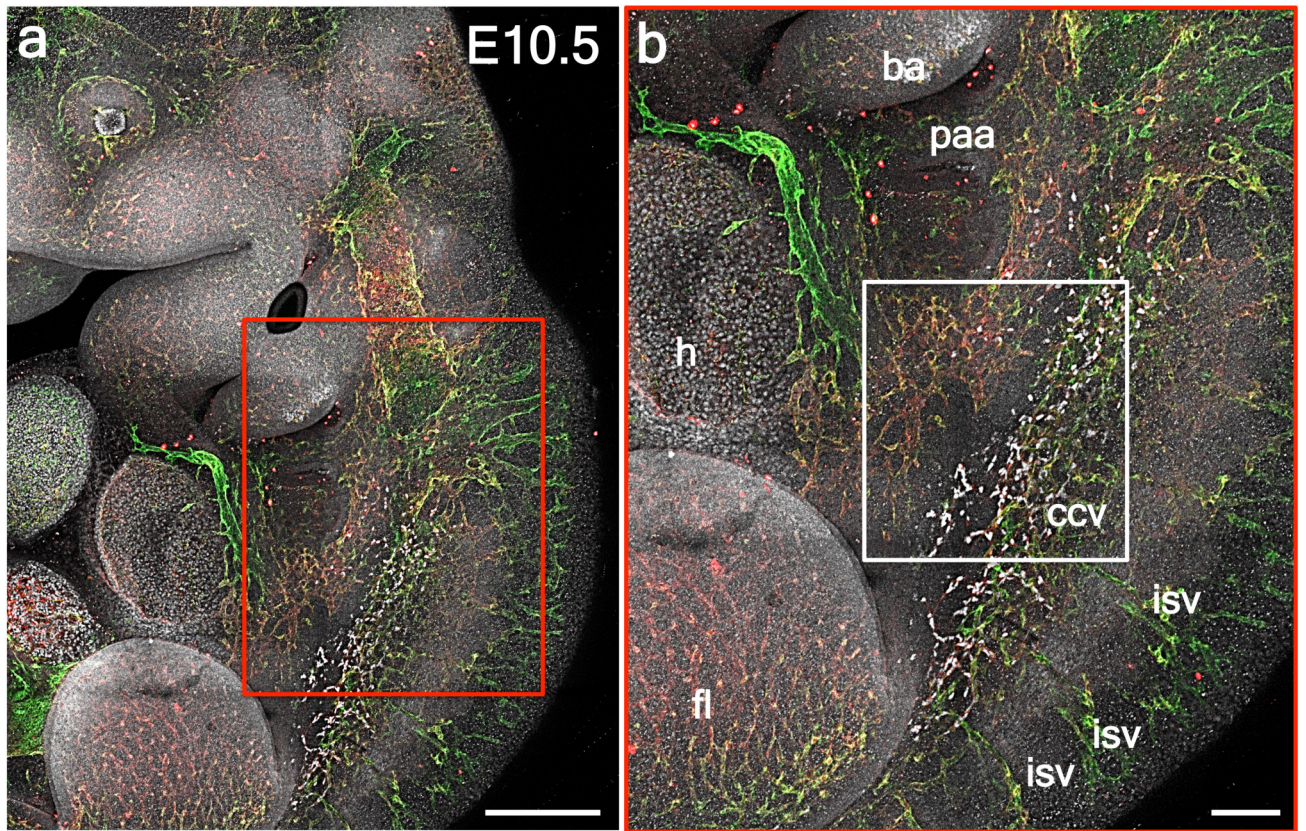
vessel density at later stages (data not shown). **k–n**, Whole-mount DAB staining of E17.5 hearts with the lymphatic marker Prox1 ($n = 4$) further confirmed extensive spread of the sprouting lymphatics inferiorly from the outflow tract region (**k**) and sinus venosus, at the inflow region of the heart (**l**). White inset boxes in **k** and **l** are shown in **m** and **n**, respectively, highlighting the punctate nuclear expression of Prox1 in coronary lymphatics. **o–v**, Whole-mount confocal imaging of E17.5 hearts ($n = 4$) stained with VEGFR-3, Prox1 and Lyve-1 confirmed co-labelling of coronary lymphatic vessels. Note that while at this developmental stage VEGFR-3 is restricted to LECs (**p**, **t**), Prox1 is also expressed in the underlying myocardium (**o**, **s**) and Lyve-1 labels tissue-resident macrophages (**q**, **u**). Scale bars: **a**, 750 μm ; **b**, 300 μm ; **c**, **d**, 750 μm ; **e**, **f**, 1 mm; **g**, **h**, 2 mm; **i**, **j**, 2.5 mm; **k**, **l**, 400 μm ; **m**, **n**, 200 μm ; **o**, **s**, 100 μm .



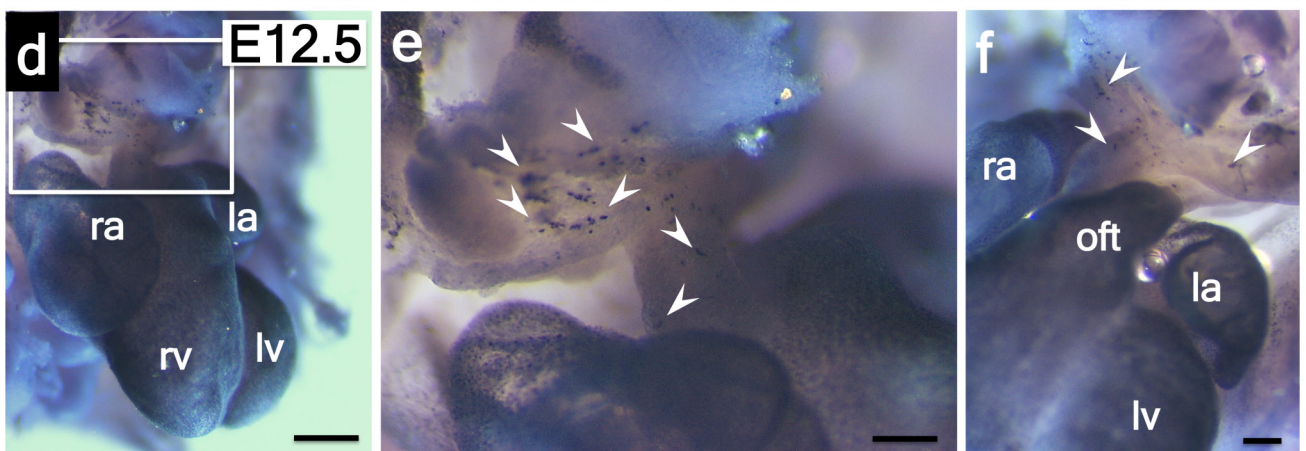
Extended Data Figure 2 | Cardiac lymphatic vessels do not emerge from the developing coronary vasculature. **a–o**, Whole-mount confocal imaging of hearts stained with *Emcn* (vessels) and *Prox1* (lymphatics) revealed sprouting of *Prox1*⁺ lymphatics from extra-cardiac tissue neighbouring the sinus venosus on the dorsal side of the developing heart at E12.5–13.5 (**a**, **d**), but no *Prox1*⁺ LECs were observed budding from *Emcn*⁺ coronary vessels (**c** and **f**; white arrowheads in **b** and **e** highlight *Prox1*⁺ LECs). *Prox1*⁺ lymphatics had reached the sinus venosus by E13.5 (white arrow in **f**) and the outflow tract, on the

ventral side of the heart by E14.5 (white arrow in **h**); no *Prox1*⁺ LECs were observed emerging from *Emcn*⁺ vessels on the ventral side at E14.5 (**g–i**). Background-like labelling on the ventricular surface in **c**, **f** and **i** reflects *Prox1* expression in the developing myocardium. Between E15.5–17.5, *Prox1*⁺ lymphatics aligned with *Emcn*⁺ coronary veins but no contribution of *Prox1*⁺ LECs was observed (**j**, **l** and **n**, white boxes enlarged in **k**, **m** and **o**, respectively; *n* = 5 hearts analysed per time point). Scale bars: **a**, 550 μ m; **c**, **f**, **i**, 250 μ m; **d**, **g**, 750 μ m; **j**, **l**, **n**, 400 μ m; **k**, **m**, **o**, 200 μ m.

Emcn VEGFR-3 Prox1

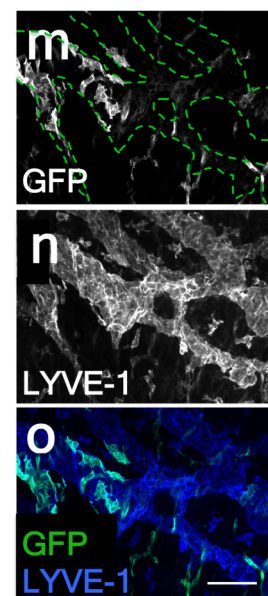
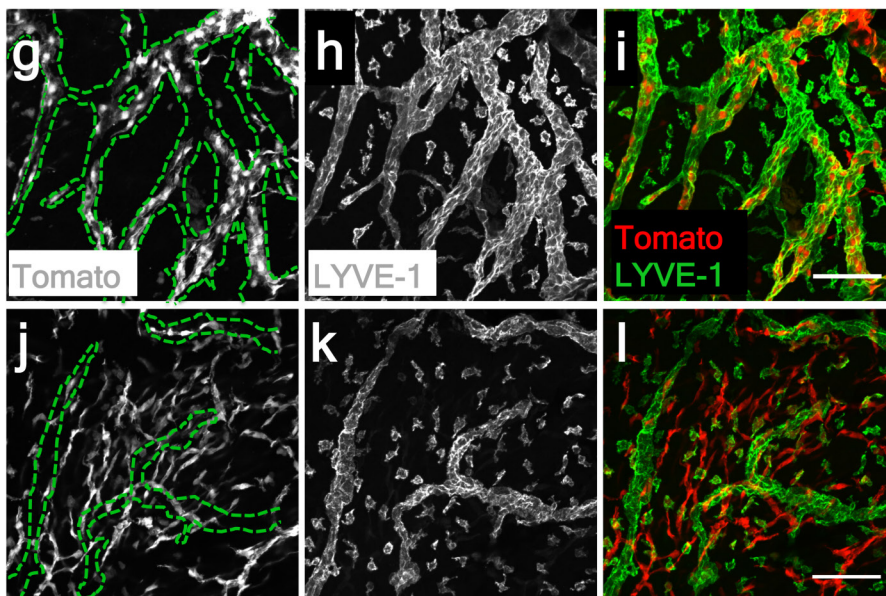
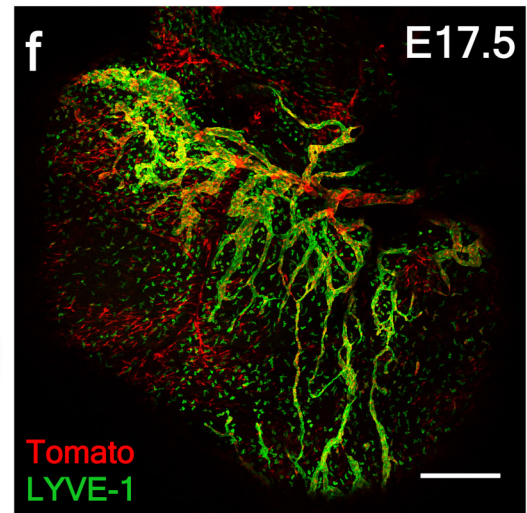
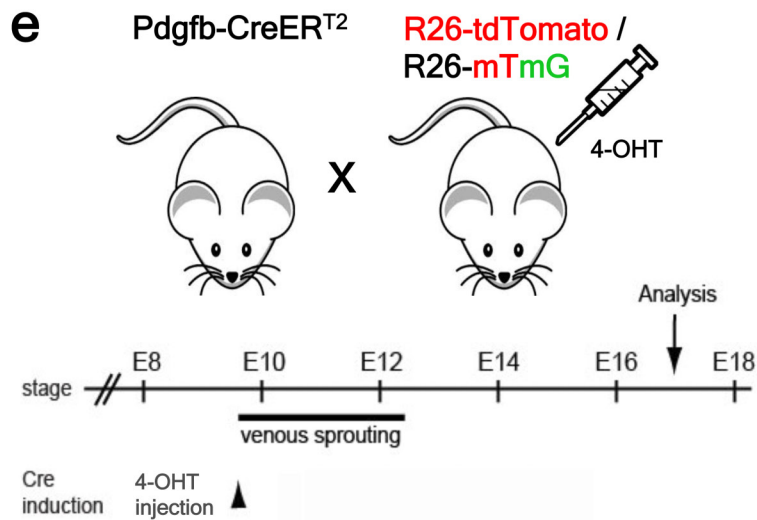
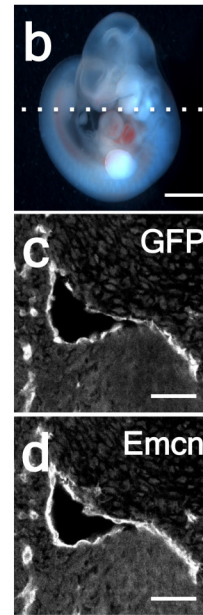
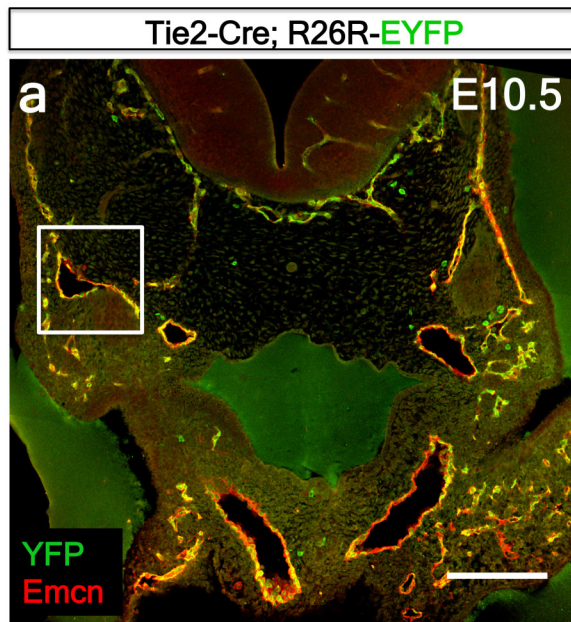


Prox1



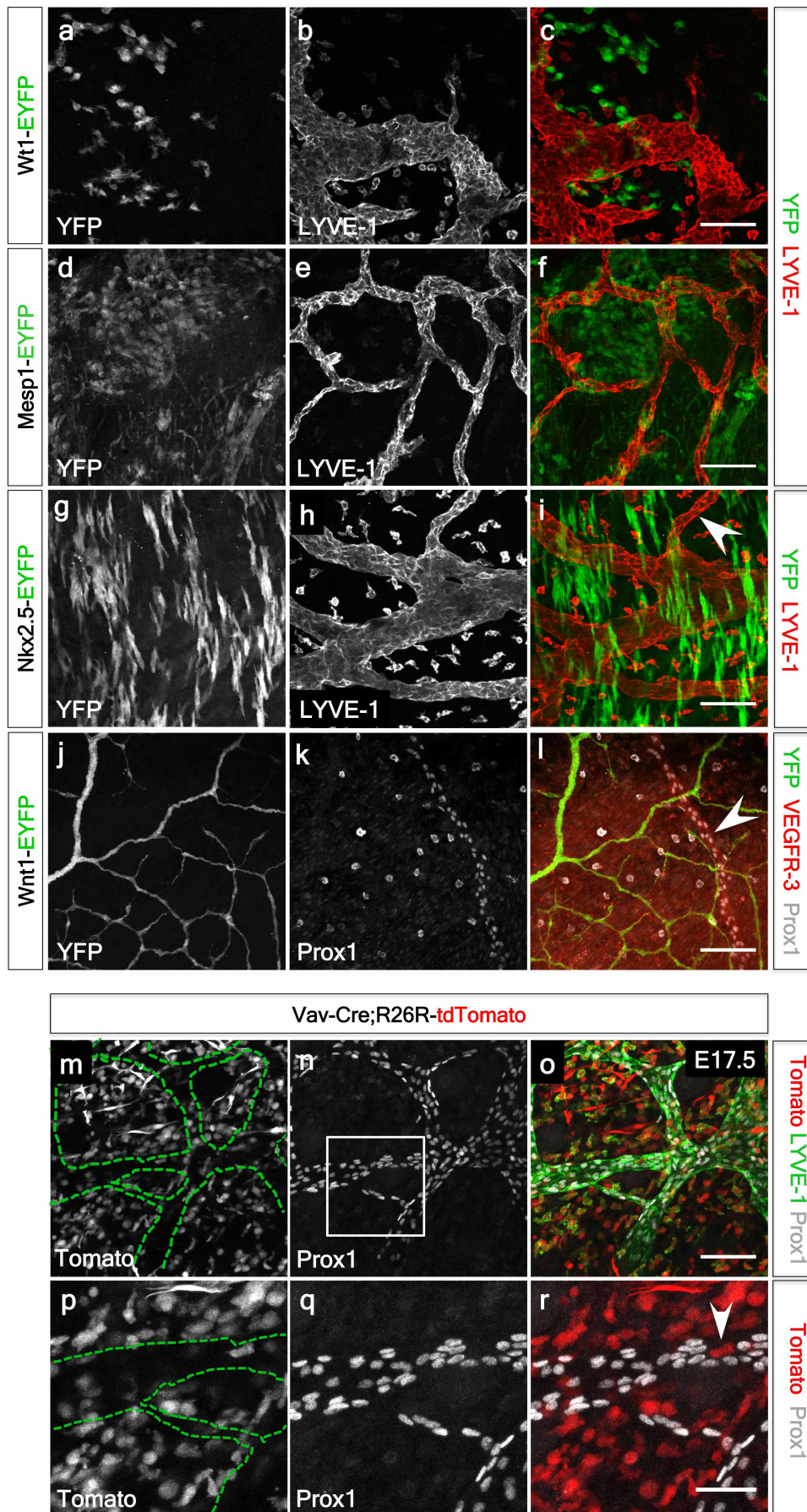
Extended Data Figure 3 | The common cardinal vein contributes LECs that migrate towards the sinus venosus and outflow tract of the developing heart. **a–c**, Whole-mount confocal analysis of E10.5 embryos stained with Emcn or Prox1 and VEGFR-3 revealed Prox1/VEGFR-3⁺ LECs emerging along the common cardinal vein (**a**, red box enlarged in **b**; white box enlarged in **c**) migrating towards the sinus venosus (white arrowheads in **c**; $n = 3$ embryos). **d–f**, Whole-mount DAB staining revealed Prox1⁺ LECs migrating towards the

outflow tract, on the ventral surface of the developing heart at E12.5 (**d**, white inset box enlarged in **e**; alternative lateral view in **f**; white arrowheads indicate migrating LECs; $n = 4$ embryos). ba, branchial arch; ccv, common cardinal vein; fl, forelimb; h, heart; isv, inter-somitic vessel; la, left atrium; lv, left ventricle; oft, outflow tract; paa, pharyngeal artery arch; ra, right atrium; rv, right ventricle. Scale bars: **a**, 1 mm; **b**, 500 μm ; **c**, 200 μm ; **d**, 600 μm ; **e**, 400 μm ; **f**, 300 μm .



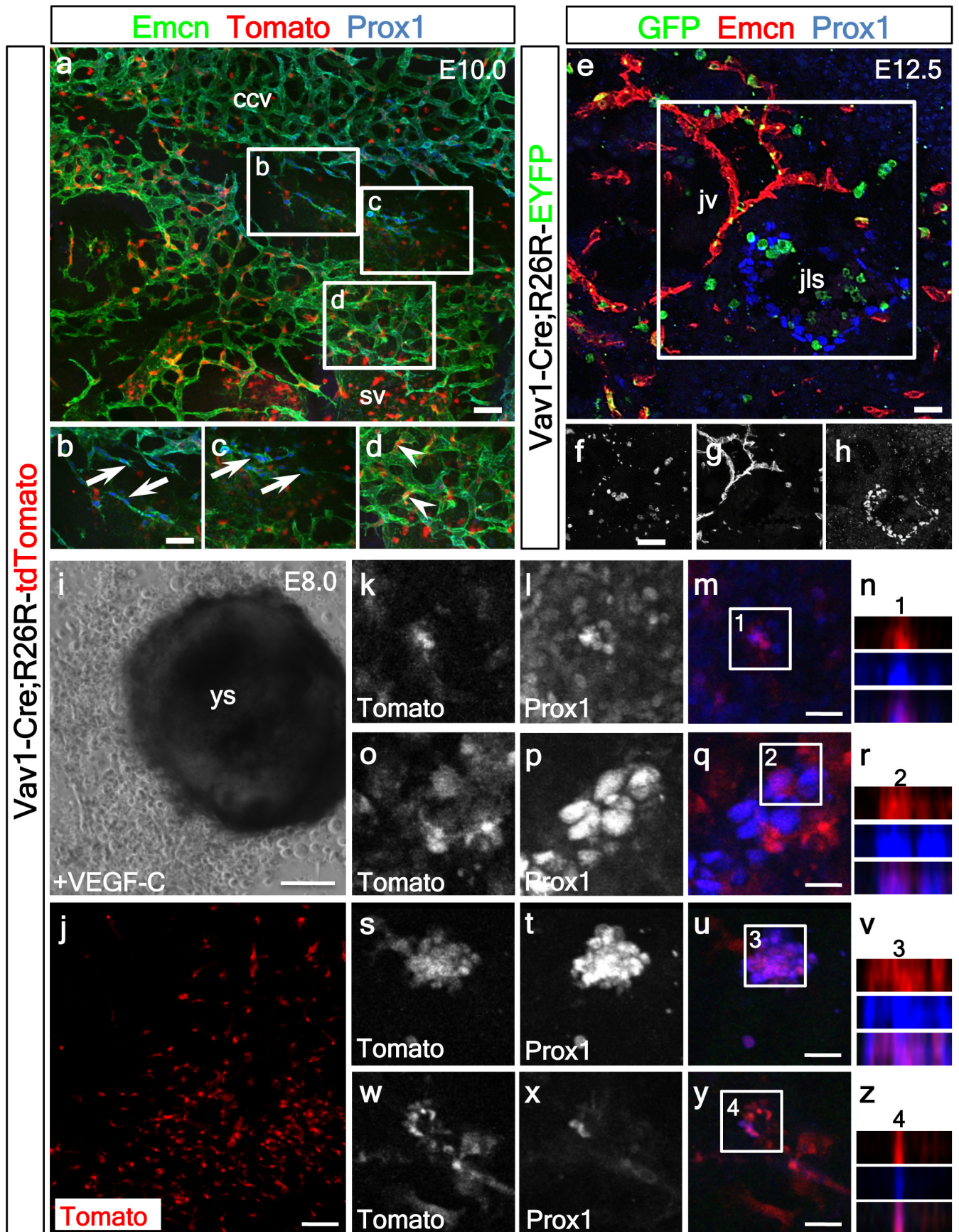
Extended Data Figure 4 | Tie2-Cre efficiently labels the developing cardinal vein and partial contribution of Pdgfb^{+} -derived LECs indicates a non-venous contribution to the developing cardiac lymphatics. **a–d**, Tie2-Cre;R26R-eYFP lineage tracing revealed recombination and labelling of the cardinal vein and jugular lymph sacs at E10.5 (**a**; $n = 3$ embryos analysed). Plane of section to capture jugular lymph sacs is shown in **b**. White inset box in **a** is shown at higher magnification and demarcated by GFP (**c**) and Emcn (**d**) co-staining. **e–o**, Schematic (**e**) to show how embryos were generated by breeding Pdgfb-CreER^{T2} mice with either R26R-tdTomato (**f–l**) or R26R-

mTmG (**m–o**) reporter mice and then being injected with 4-hydroxytamoxifen (4-OHT) at E9.5, before venous sprouting. Whole-mount confocal analysis of E17.5 hearts ($n = 4$) stained with Lyve-1 revealed incomplete tdTomato recombination in cardiac lymphatic vessels (**f**). Both Pdgfb^{+} (**g–i**) and Pdgfb^{-} (**j–l**; **m–o**) lymphatic vessels were observed, highlighted by the dotted green outlines (**g**, **j**, **m**), indicating a combined Pdgfb^{+} endothelial origin and Pdgfb^{-} non-venous source for the cardiac LECs. Scale bars: **a**, 200 μm ; **b**, 1.5 mm; **c**, **d**, 50 μm ; **f**, 400 μm ; **e**, **l**, **o**, 100 μm .



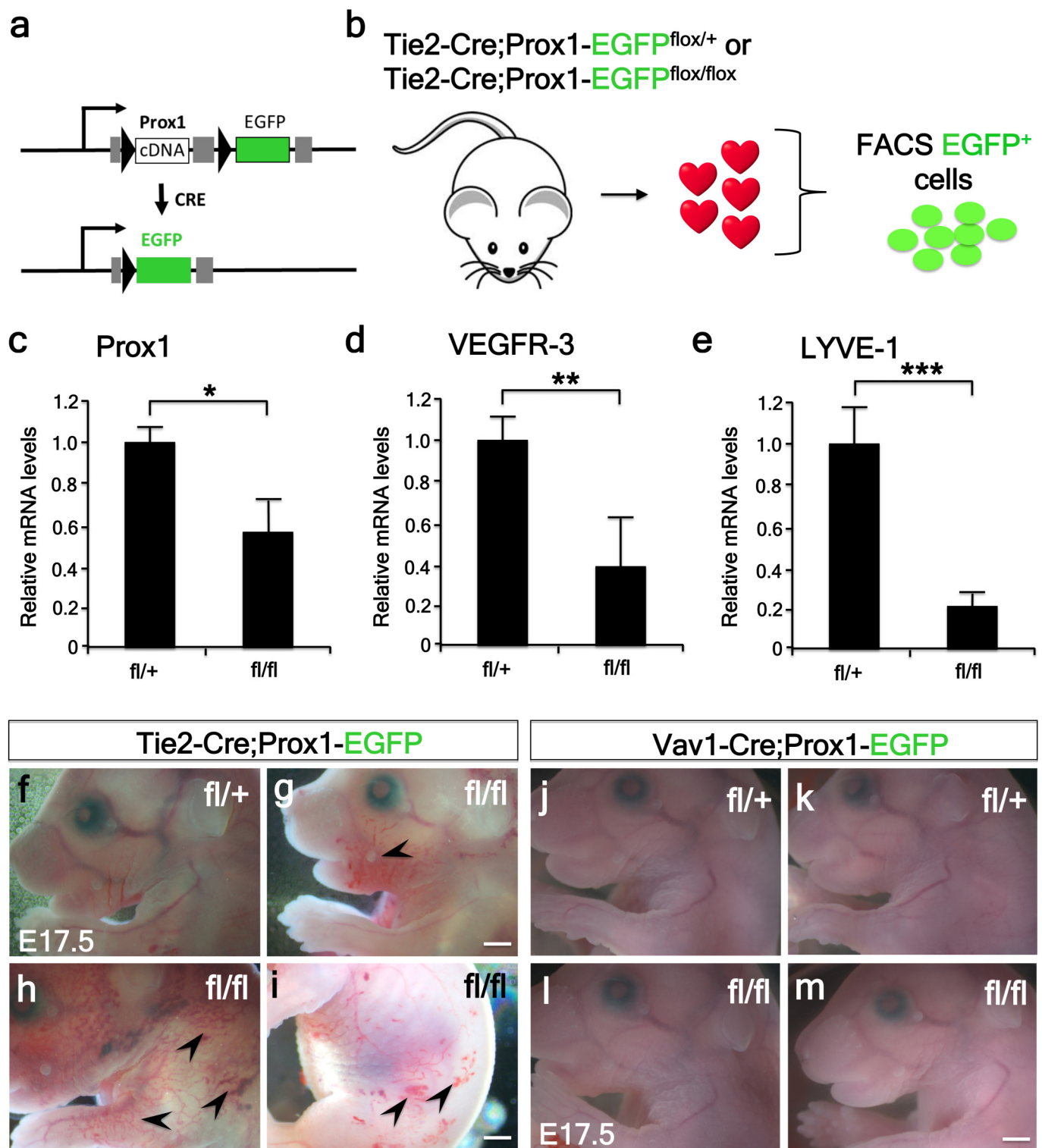
Extended Data Figure 5 | Neither the pro-epicardial organ, cardiac mesoderm nor cardiac neural crest contribute LECs to the developing heart and dermal lymphatics are not derived from the Vav1⁺ lineage. **a–l**, Lineage tracing using WT1-CreERT2;R26R-eYFP (4-hydroxytamoxifen injected at E9.5; **a–c**), Mesp1-Cre;R26R-eYFP (**d–f**), Nkx2.5-Cre;R26R-eYFP (**g–i**) and Wnt1-Cre;R26R-eYFP (**j–l**; $n = 3$ hearts analysed per lineage trace) showed no YFP recombination in cardiac lymphatic vessels as marked by Prox1 or Lyve-1, suggesting that neither the pro-epicardial organ/epicardium, cardiac mesoderm (early or late) or cardiac neural crest, respectively, contribute LECs to the developing cardiac lymphatics. **m–o**, Embryos generated by breeding Vav1-Cre with R26R-tdTomato reporter mice were subject to whole-mount

confocal analysis of E17.5 dorsal skin preparations ($n = 4$ Vav1-tdTomato⁺ embryos analysed). tdTomato epifluorescence (**m**) and Prox1 immunostaining (**n**) revealed a lack of Vav1-Cre recombination in dermal lymphatic vessels (highlighted by the green dotted lines, **m**) and a lack of overlap of tdTomato with Prox1 and Lyve-1 expression (**o**; all Prox1⁺ nuclei assessed across 5 fields of view per embryonic skin; $n = 4$ skins in total). **p–r**, Higher magnification of inset white box (**n**) revealed that tdTomato⁺ cells (**p**) did not overlap with Prox1⁺ nuclei in the lymphatic vessels (**q**) (white arrowhead highlights tdTomato⁺/Prox1[−] cell in **r**). Scale bars: **a–l**, 100 μ m; **m–o**, 100 μ m; **p–r**, 50 μ m.



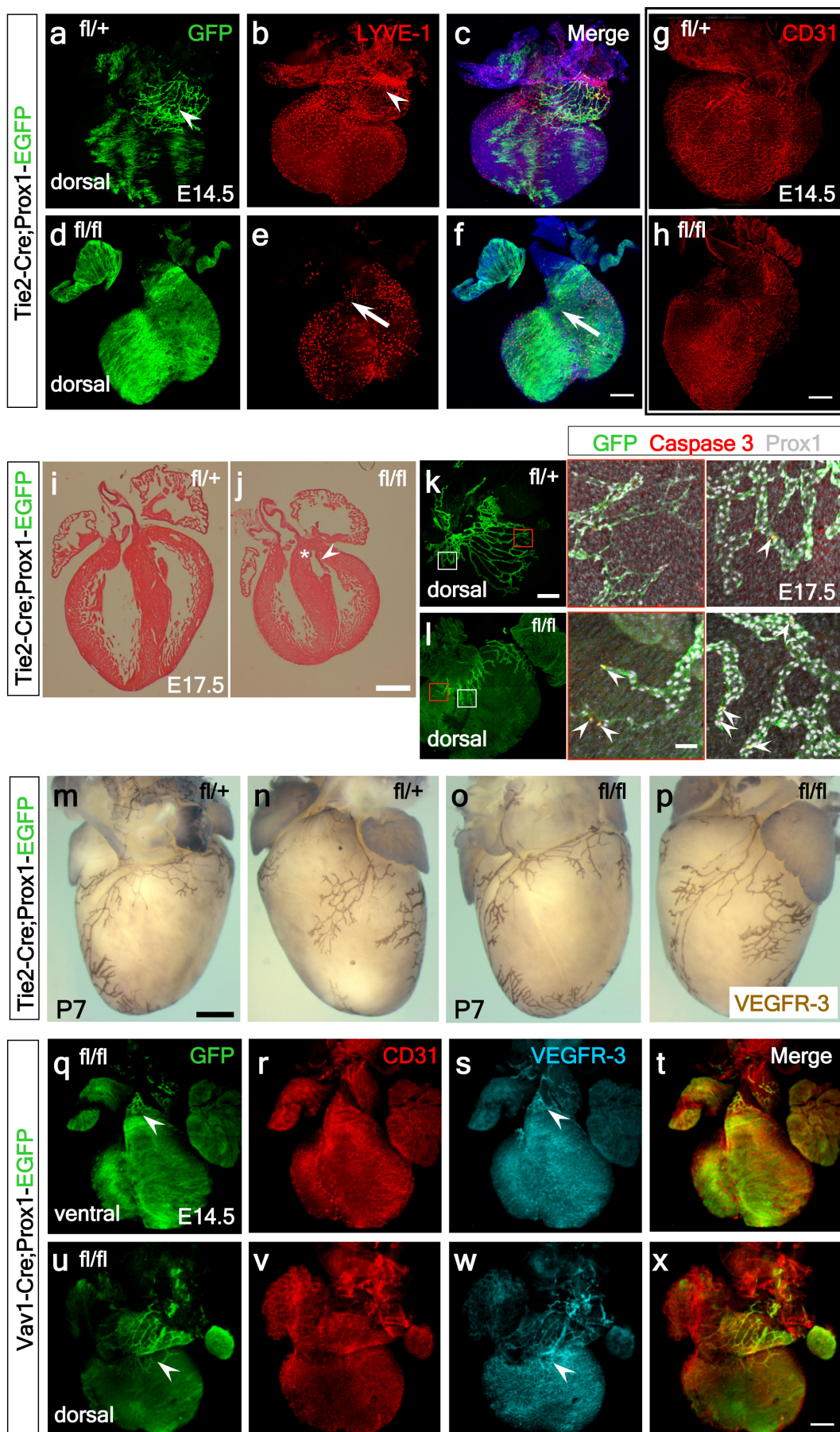
Extended Data Figure 6 | The Vav1⁺ lineage does not contribute to LECs emerging from the common cardinal or jugular veins but contributes to VEGF-C induced LECs emerging from yolk sac explants. **a–d**, Vav1-Cre;R26R-tdTomato lineage tracing revealed no recombination nor labelling of the nascent LECs budding from common cardinal vein endothelium in E10.0 embryos (**a**) as confirmed by co-staining for Emcn, Prox1 and tdTomato fluorescence. White inset box in **a** is highlighted in enlarged panels (**b–d**; arrows indicate Prox1⁺ (blue) LECs delaminating from the common cardinal vein **b**, **c**). In the sinus venosus region Vav1⁺ cells were evident but lacked Prox1 expression, excluding an LEC identity (**d**). **e–h**, Vav1-Cre;R26R-eYFP lineage tracing revealed no recombination nor labelling of LECs forming the jugular lymph sacs in E12.5 embryos (**e**) as confirmed by co-staining for GFP, Emcn and Prox1. White inset box in **e** highlighted by individual GFP (**f**), Emcn (**g**) and Prox1 (**h**) staining ($n = 3$ embryos analysed per time-point). ccv,

common cardinal vein; jls, jugular lymph sac; jv, jugular vein; sv, sinus venosus. **i**, **j**, Representative staining for Prox1 and native tdTomato fluorescence of *ex vivo* cultures of explanted Vav1-Cre;R26R-tdTomato conceptuses at E8.0, including the intact yolk sac (**i**) and outgrowth of tdTomato⁺ cells (**j**). Explants were cultured with 100 ng ml⁻¹ of recombinant VEGF-C(C156S)²⁸ (R&D Systems), a potent selective lymphangiogenic cue that only signals via VEGFR-3 (**i**). **k–z**, High-resolution images of the specification of tdTomato⁺/Prox1⁺ LECs (indicated by white inset boxes) in the yolk sac explants (**k–n**) and in the surrounding cellular outgrowth (**o–z**) was observed (tdTomato⁺ in red; Prox1⁺ in blue; single and merged channels shown). Co-staining was confirmed by *z*-stack reconstructions for each four high-resolution panel set (**n**, **r**, **v**, **z**); $n = 6$ explants analysed. Scale bars: **a**, **e**, 50 μ m; **b–d** and **f–h**, 12.5 μ m; **i**, 100 μ m; **j**, 50 μ m; **m**, **q**, **u**, **y**, 15 μ m.



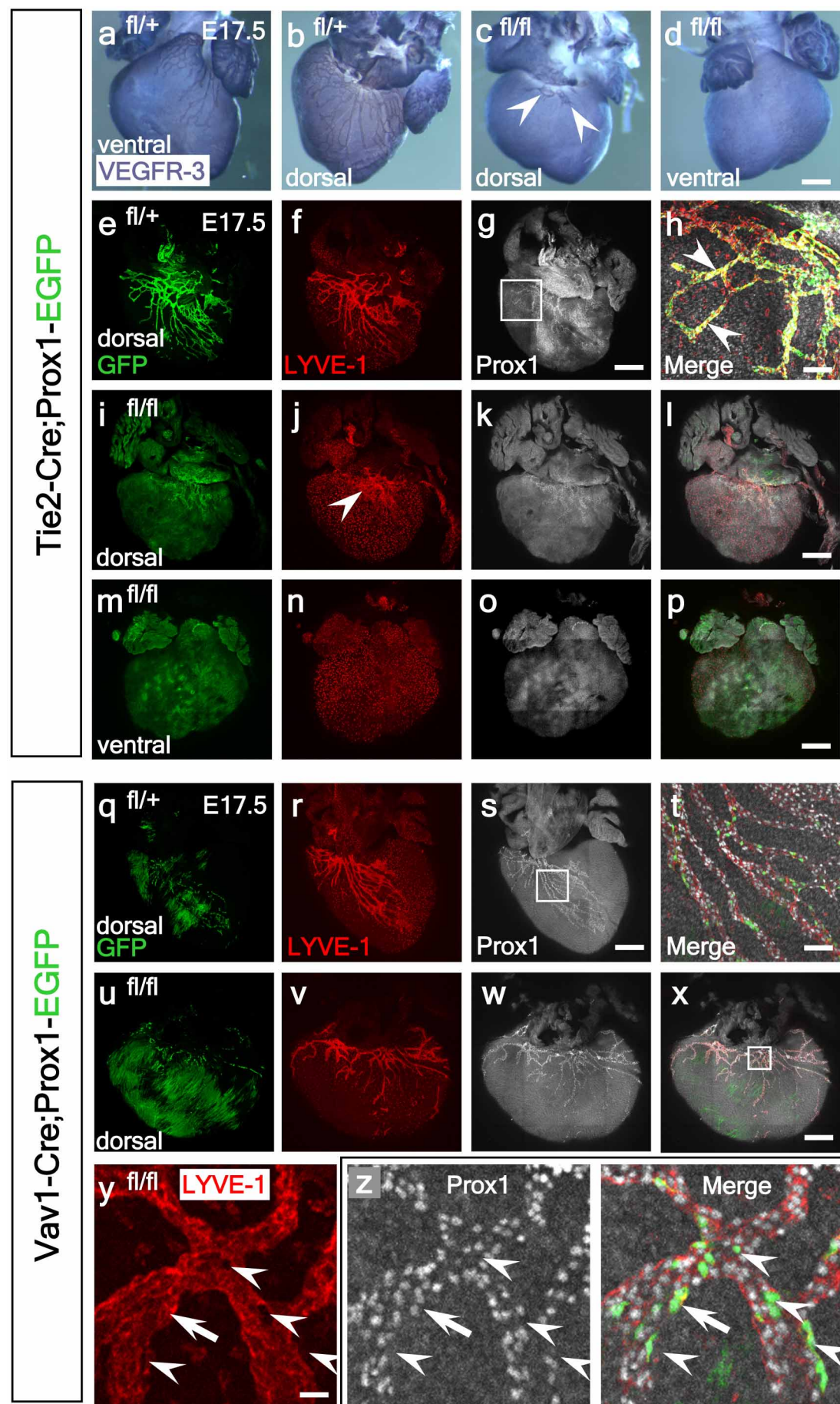
Extended Data Figure 7 | *Prox1* knockdown results in significantly decreased *Vegfr3* and *Lyve1* and Tie2-Cre;*Prox1*^{fl/fl} mutant embryos exhibit superficial vascular defects whereas Vav1-Cre;*Prox1*^{fl/fl} mutants have a normal systemic vasculature. **a**, *Prox1* targeting via floxed excision of exon 1 and 2, results in EGFP expression thus labelling targeted cells. **b**, E17.5 hearts from either Tie2-Cre;*Prox1*^{fl/+} control embryos or Tie2-Cre;*Prox1*^{fl/fl} mutants were grouped and digested to create a single-cell suspension for FACS. A total of 100,000 GFP⁺ cells were collected for each sample group. **c–e**, Relative gene expression was determined by qRT-PCR and revealed significantly decreased *Prox1* (**c**; 0.59 fold), *Vegfr3* (**d**; 0.39 fold) and *Lyve1* (**e**; 0.22 fold) expression; $n = 5$ hearts per sample group, analysed in triplicate; * $P \leq 0.05$; ** $P \leq 0.01$; *** $P \leq$

0.001. All graphs are mean \pm s.e.m. Statistical test used was Student's *t*-test. **f–i**, Dissection of Tie2-Cre;*Prox1*^{fl/+} heterozygous (**f**; $n = 6$) and Tie2-Cre;*Prox1*^{fl/fl} mutant (**g, h, i**; $n = 9$) littermate embryos at E17.5 revealed gross vascular anomalies in the double-floxed mutants (three examples shown in **g–i**), with evidence of ectopic surface blood vessels (**g**, ectopic vessels highlighted by black arrowheads), a disrupted vascular network (**h**; black arrowheads indicate blood-filled superficial vessels) and either haemorrhaging (**i**; bleeding foci highlighted by black arrowheads) or blood-filled lymphatics, compared to littermate *Prox1*^{fl/+} controls (**f**). **j–m**, Vav1-Cre;*Prox1*^{fl/+} heterozygous (**j, k**; $n = 5$) and Vav1-Cre;*Prox1*^{fl/fl} mutants (**l, m**; $n = 8$) revealed no obvious systemic vessel defects. Scale bars: **g, i, m**, 100 μ m.



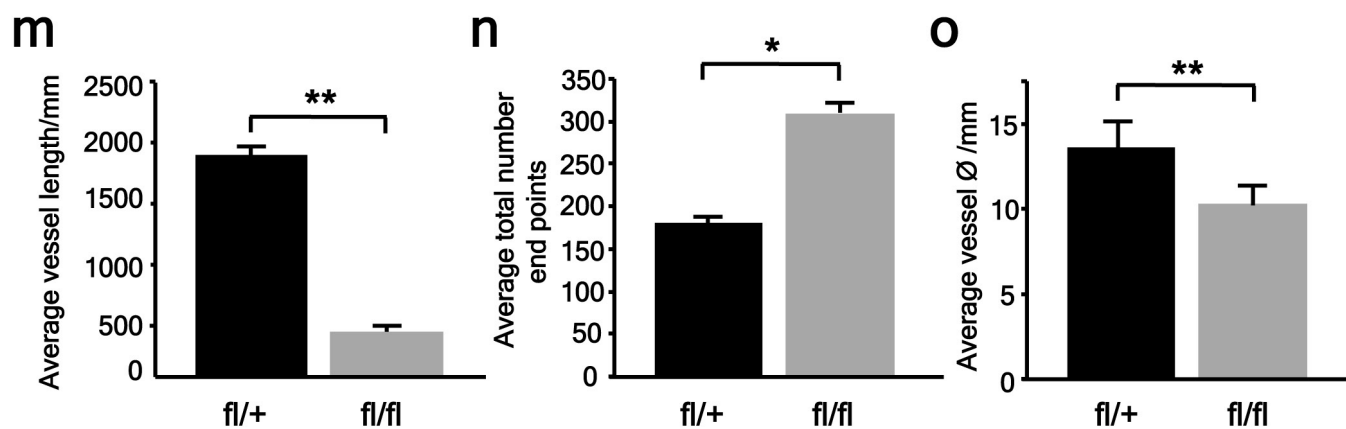
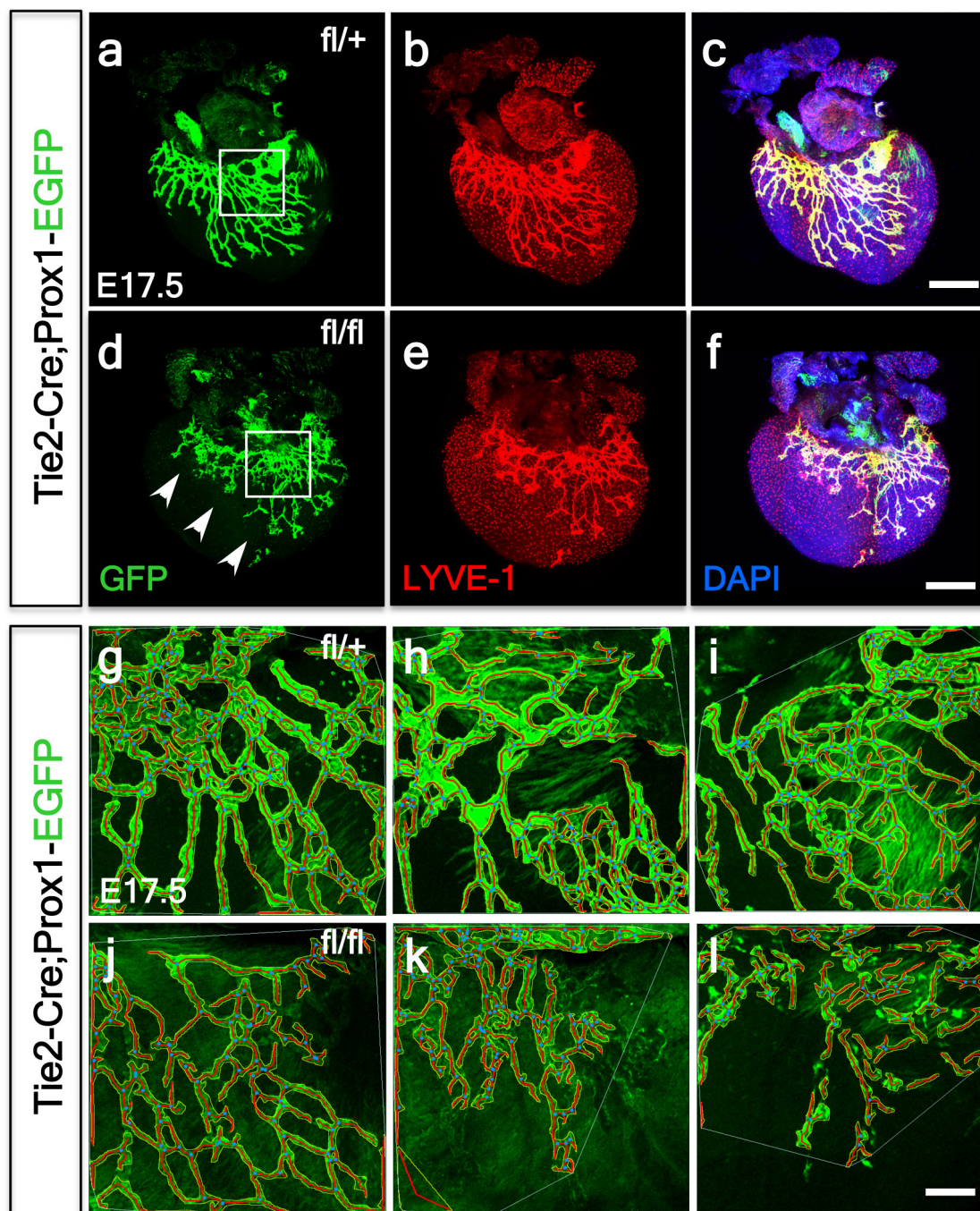
Extended Data Figure 8 | The emergence of cardiac lymphatics at E14.5 is disrupted in Tie2-Cre;Prox1^{fl/fl} mutant hearts, which are dysmorphic and exhibit elevated apoptosis of LECs, however, mutant embryos recover with normal cardiac lymphatics at post-natal stages. **a–c**, GFP⁺-targeted and Lyve-1⁺ LECs emerged from the base of the heart in the atrioventricular region at E14.5 in control Tie2-Cre;Prox1^{fl/+} hearts (LECs highlighted by white arrowheads in **a** and **b**; $n = 3$ hearts analysed). **d–f**, In mutant Tie2-Cre;Prox1^{fl/fl} hearts ($n = 7$) the GFP⁺ network was absent (**d**) and Lyve-1 only detected tissue resident macrophages with an absence of lymphatics at the inflow base of the heart (arrows in **e**, **f**). **g**, **h**, Coronary vessels, as determined by whole mount CD31 staining, were comparable between control Tie2-Cre;Prox1^{fl/+} (**g**) and Tie2-Cre;Prox1^{fl/fl} hearts (**h**). **i**, **j**, Haematoxylin and eosin staining of paraffin-embedded E17.5 hearts revealed that Tie2-Cre;Prox1^{fl/fl} mutants (**j**; $n = 3$ analysed) were grossly smaller compared to control hearts (**i**), with lack of extension of the ventricles towards the apex, smaller chambers and thickening of the ventricular free wall (**j**). Normal membranous septation of the mutant ventricle (white asterix) and valve leaflet formation (white

arrowhead in **j**) indicate normal endocardial cushion development. **k**, **l**, Whole-mount confocal imaging of hearts stained with GFP, cleaved caspase-3 and Prox1 revealed an increase in apoptotic cells within the termini of mutant coronary lymphatic vessels (white arrowheads in magnified panels), compared to control hearts, supporting the requirement for Prox1 in LEC identity and maintenance. $n = 3$ hearts analysed for histology and immunostaining. **m–p**, Whole-mount VEGFR-3 immunostaining of hearts isolated at P7 revealed that Tie2-Cre;Prox1^{fl/+} heterozygotes (**m**, **n**) and Tie2-Cre;Prox1^{fl/fl} mutants (**o**, **p**) have an equivalent normal cardiac lymphatic vasculature ($n = 3$ hearts analysed per genotype). As such the lymphatic hypoplasia and disruption of the vessel network, evident in mutant hearts at E17.5 (Extended Data Fig. 10), is rescued during the later stages of development and neonatal period. **q–x**, In Vav1-Cre;Prox1^{fl/fl} hearts ($n = 4$) there was evidence of an initial formation of the cardiac lymphatics on both ventral (**q**, **s**) and dorsal (**u**, **w**) surfaces and the coronary vessels were unaffected (**r**, **t**, **v**, **x**). Scale bars: **f**, **h**, **x**, 400 μ m; **j**, 1 mm; **k**, 400 μ m; **l**, 50 μ m; **m**, 500 μ m.



Extended Data Figure 9 | Prox1 is essential for Tie2⁺- and Vav1⁺-derived cardiac lymphatics. **a–d**, In control Tie2-Cre;*Prox1*^{fl/+} mice at E17.5 (*n* = 6) there was an extensive lymphatic network on both the dorsal and ventral surfaces, as indicated by whole-mount VEGFR-3 immunostaining (**a**, **b**), whereas the lymphatic vessels were virtually absent in mutant Tie2-Cre;*Prox1*^{fl/fl} hearts (**c**, **d**; *n* = 9); a few vessels evident on the dorsal surface was consistent with LECs arising from a non-Tie2-targeted source (**c**, white arrowheads). Tie2-Cre;*Prox1*^{fl/fl} mutant hearts were dysmorphic relative to controls (compare **c**, **d** with **a**, **b**). **e**, **f**, GFP⁺ staining indicated targeting of *Prox1* in Tie2-Cre;*Prox1*^{fl/+} mice (**e**) and an expansive Lyve-1⁺ lymphatic network (**f**). **g**, **h**, Prox1 immunostaining confirmed expression in LECs in heterozygote controls (**g**; inset box shown at higher magnification in **h**). Co-expression of GFP/Lyve-1 and Prox1 was evident in LECs in addition to Lyve-1/Prox1 double-positive cells not targeted by Tie2-Cre (**h**, white arrowheads). **i–l**, In contrast, Tie2-Cre;*Prox1*^{fl/fl} mutant hearts revealed an absence of the GFP⁺ lymphatic network with only a minor contribution of Lyve-1 LECs evident at the base of the heart on the dorsal surface (**i**, **j**; white arrowhead in

j highlights retained Lyve-1⁺ LECs), which were Prox1⁺ (**k**, **l**). **m–p**, On the ventral surface there was complete absence of GFP and Lyve-1⁺ lymphatic vessels (**m**); Lyve-1 staining was retained in tissue-resident macrophages (**n**). Loss of LECs correlated with a loss of Prox1 (**o**, **p**). **q–t**, In control Vav1-Cre;*Prox1*^{fl/+} mice at E17.5 (*n* = 5) there was evidence of appropriate targeting of GFP⁺ LECs (**q**) and an extensive lymphatic network on the dorsal surface as indicated by Lyve-1 (**r**). Prox1 expression was retained (**s**), which at higher resolution revealed co-expression of GFP⁺/Lyve-1⁺/Prox1⁺ in a subpopulation of LECs, consistent with the lineage trace data (Fig. 3a–d; white inset box in **s** shown at higher magnification in **t**). **u–x**, In Vav1-Cre;*Prox1*^{fl/fl} mutant hearts (*n* = 8) there was equivalent GFP⁺ targeting (**u**) and a Lyve-1⁺ network (**v**) with retained Prox1 expression (**w**, **x**). **y**, **z**, Specific loss of Lyve-1 staining (**y**) correlated with loss of Prox1 and GFP-targeting (**z**, left and right panels, respectively, highlighted by white arrowheads). Mosaic levels of *Prox1* knockdown accounted for examples of isolated LECs that, despite GFP-targeting, remained Lyve-1⁺ (white arrows in **y**, **z**). Scale bars: **d**, **g**, **l**, **p**, **s**, **x**, 400 μm; **h**, **t**, 40 μm; **y**, 5 μm.



Extended Data Figure 10 | *Prox1* knockdown in Tie2-Cre;*Prox1*^{fl/fl} mutants results in a hypoplastic and disrupted lymphatic plexus. **a–f**, Relative to Tie2-Cre;*Prox1*^{fl/+} control hearts at E17.5 (**a–c**), GFP⁺ lymphatic vessels were thinner and the network truncated along the short axis, having failed to appropriately extend and remodel in Tie2-Cre;*Prox1*^{fl/fl} hearts with partial knockdown of *Prox1* (**d–f**; see Extended Data Fig. 7c; $n = 4$ hearts per genotype; representative regions indicated by white inset boxes in **a**, **d**). **g–i**, Higher magnification of the lymphatic plexus in Tie2-Cre;*Prox1*^{fl/+} control (**g–i**) and Tie2-Cre;*Prox1*^{fl/fl} mutants (**j–l**) were captured for AngioTool analyses.

AngioTool tracing in red of GFP⁺ vessels and blue for branch points (**g–l**), enabled quantitative assessment of vessel parameters. **m–o**, The mutant lymphatic vessels were significantly shorter in overall length (**m**), more truncated and disorganized with an increased total number of end points (**n**). Mutant vessels were also significantly reduced in diameter, being thinner on average, compared to controls (**o**). Scale bars: **c**, **f**, 400 μ m; **l**, 30 μ m; All graphs show mean \pm s.e.m. Student's *t*-test; * $P \leq 0.05$; ** $P \leq 0.001$ ($n = 4$ hearts analysed per genotype).

Interaction and signalling between a cosmopolitan phytoplankton and associated bacteria

S. A. Amin^{1,2}, L. R. Hmelo³, H. M. van Tol¹, B. P. Durham⁴, L. T. Carlson¹, K. R. Heal¹, R. L. Morales¹, C. T. Berthiaume¹, M. S. Parker¹, B. Djunaedi¹, A. E. Ingalls¹, M. R. Parsek³, M. A. Moran⁵ & E. V. Armbrust¹

Interactions between primary producers and bacteria impact the physiology of both partners, alter the chemistry of their environment, and shape ecosystem diversity^{1,2}. In marine ecosystems, these interactions are difficult to study partly because the major photosynthetic organisms are microscopic, unicellular phytoplankton³. Coastal phytoplankton communities are dominated by diatoms, which generate approximately 40% of marine primary production and form the base of many marine food webs⁴. Diatoms co-occur with specific bacterial taxa³, but the mechanisms of potential interactions are mostly unknown. Here we tease apart a bacterial consortium associated with a globally distributed diatom and find that a *Sulfitobacter* species promotes diatom cell division via secretion of the hormone indole-3-acetic acid, synthesized by the bacterium using both diatom-secreted and endogenous tryptophan. Indole-3-acetic acid and tryptophan serve as signalling molecules that are part of a complex exchange of nutrients, including diatom-excreted organosulfur molecules and bacterial-excreted ammonia. The potential prevalence of this mode of signalling in the oceans is corroborated by metabolite and metatranscriptome analyses that show widespread indole-3-acetic acid production by *Sulfitobacter*-related bacteria, particularly in coastal environments. Our study expands on the emerging recognition that marine microbial communities are part of tightly connected networks by providing evidence that these interactions are mediated through production and exchange of infochemicals.

In terrestrial systems, interactions between photosynthetic organisms and bacteria occur primarily within the rhizosphere, a region surrounding plant roots in which gradients of released molecules support distinct microbial communities, enhancing the growth of some bacteria while restricting the growth of others⁵. In aquatic systems, similar interactions were proposed over 40 years ago to occur within the phycosphere, a rhizosphere analogue⁶. Today, theoretical and empirical studies confirm that phytoplankton are surrounded by a diffusive boundary layer in which secreted molecules accumulate in excess of bulk seawater concentrations^{7,8}, enhancing the potential for bacterial detection of, and communication and interaction with, algal cells³.

Marine diatoms commonly co-occur with members of the Proteobacteria and Bacteroidetes in laboratory cultures and some natural blooms³. To identify mechanisms underlying specific interactions, we isolated 49 cultivable bacterial strains co-occurring with four isolates of the coastal diatom *Pseudo-nitzschia multiseries* originating from the Pacific and the Atlantic Oceans (Extended Data Table 1). We focus on *P. multiseries*, a diatom with a publicly available draft genome, because of its ubiquitous distribution in coastal ecosystems, ecological importance as a harmful alga⁹, and relatively large size (~50 µm).

Bacteria affiliated with the *Sulfitobacter*, *Hyphomonas*, *Marinobacter*, *Limnobacter*, and *Croceibacter* were among isolated bacteria and displayed more than 97% identity in 16S rRNA sequences regardless

of the originating *P. multiseries* culture (Extended Data Fig. 1 and Supplementary Information Table 1). The potential impact of these bacteria on host physiology was examined by first curing *P. multiseries* PC9 of bacteria via antibiotic treatment¹⁰. The specific growth rate of *P. multiseries* PC9 was not significantly

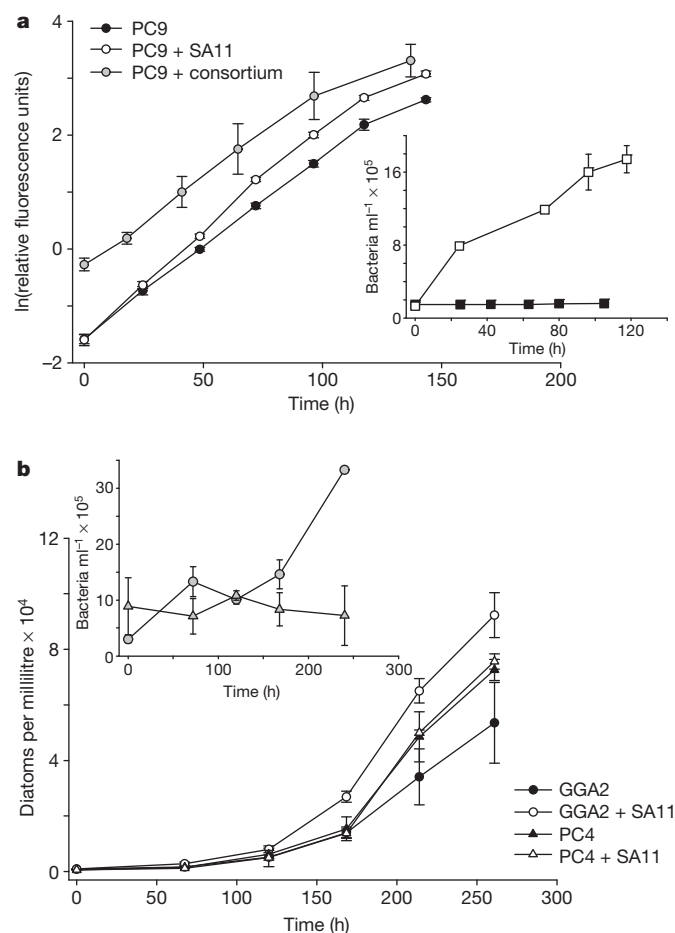


Figure 1 | Growth characteristics of the *P. multiseries*–*Sulfitobacter* sp. SA11 co-culture. **a**, Growth of axenic *P. multiseries* PC9, PC9 with SA11, and PC9 with the bacterial consortium as monitored by relative chlorophyll *a* fluorescence. Inset: cell concentration of SA11 grown without PC9 (filled squares) or with PC9 (open squares). Error bars, s.d. of triplicate cultures. Axenic versus co-culture with SA11 growth experiments were replicated five times. **b**, Abundance of axenic *P. multiseries* GGA2, GGA2 with SA11, axenic *P. multiseries* PC4, and PC4 with SA11. Inset: cell concentration of SA11 grown with GGA2 (circles) or with PC4 (triangles). Error bars, s.d. of triplicate cultures.

¹School of Oceanography, University of Washington, Seattle, Washington 98195, USA. ²Chemistry Faculty, New York University Abu Dhabi, PO Box 129188, Abu Dhabi, United Arab Emirates. ³Department of Microbiology, University of Washington, Seattle, Washington 98195, USA. ⁴Department of Microbiology, University of Georgia, Athens, Georgia 30602, USA. ⁵Department of Marine Science, University of Georgia, Athens, Georgia 30602, USA.

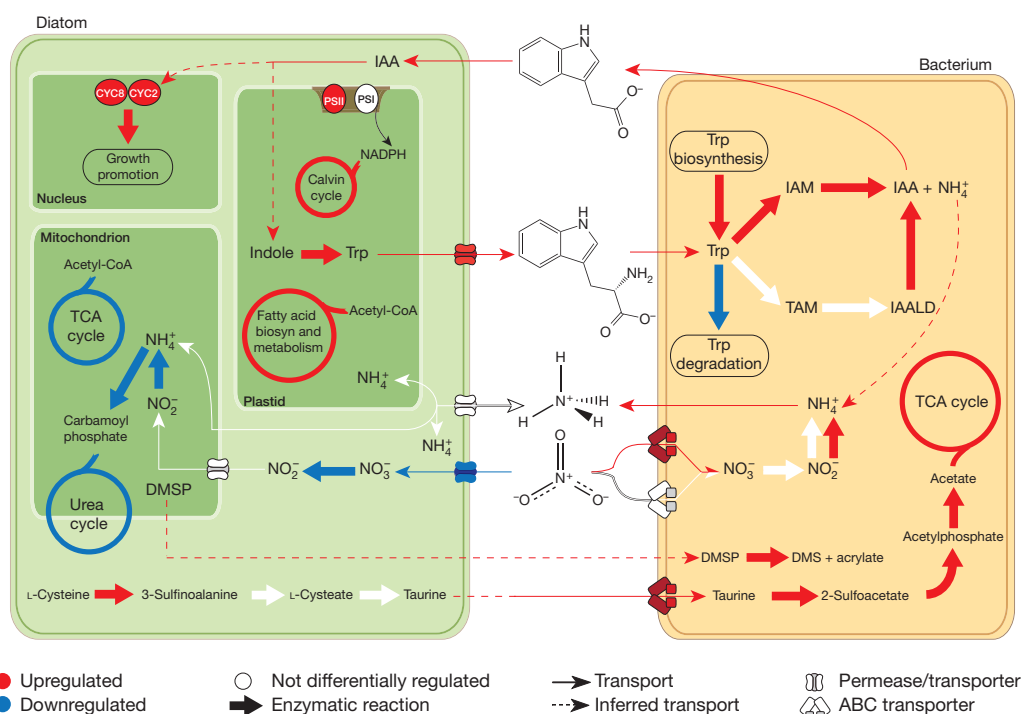


Figure 2 | Model of *P. multiseriis*–*Sulfitobacter* interactions based on transcriptomic and targeted metabolite analyses. Molecules with a structure indicate detection in the co-culture supernatant. Genes/transporters/metabolic cycles are shown as upregulated (red), downregulated (blue), or not differentially regulated (white) in co-culture relative to monocultures. Metabolic cycles were assigned an expression pattern if at least one gene specific for the

cycle was differentially expressed and no others were regulated in the opposite direction. Supplementary Information Tables 1 and 2 list fold-expression and statistical significance based on triplicate biological experiments. IAA potentially regulates expression of two cyclins that typically regulate the cell cycle³⁰. Trp, tryptophan; DMS, dimethyl sulfide; PSI, PSII, photosystem I, II; CYC2, CYC8, cyclins 2 and 8; IAALD, indole-3-acetaldehyde.

affected by removal of its bacterial consortium in the short term ($\mu_{\text{axenic}} = 0.75 \pm 0.03$; $\mu_{\text{consortium}} = 0.80 \pm 0.10 \text{ d}^{-1}$) (Fig. 1a). Over the longer term (>18 months), the growth rate decreased significantly (to $\mu_{\text{axenic}} < 0.3 \text{ d}^{-1}$), implying dependence on bacteria¹¹. Within 7 months of curing it of bacteria, *P. multiseriis* PC9 was co-cultured with individual bacterial strains in a synthetic seawater medium lacking added organic carbon¹², ensuring bacterial growth was dependent upon diatom released organic molecules. Growth rates of the cured diatom were unaffected when co-cultured with *Marinobacter* or *Limnobacter* strains, whereas a *Croceibacter* strain was lethal. Four *Sulfitobacter* strains significantly enhanced the specific growth rate of the diatom by 18–35% despite use of a medium optimized to support axenic diatom growth¹² (Fig. 1a, Extended Data Fig. 2a and Extended Data Table 2). Co-culture with two *Phaeobacter* strains closely related to *Sulfitobacter* did not enhance diatom growth (Extended Data Table 2). Together, these results indicate that the *Sulfitobacter* strains produce a diatom growth-altering factor. A single strain of *Sulfitobacter* (SA11) was chosen for further study.

The growth effect of SA11 appears remarkably specific. No growth enhancement was observed when SA11 was co-cultured with another diatom *Thalassiosira pseudonana* or with two of the four strains of *P. multiseriis* (Fig. 1b, Extended Data Table 3 and Extended Data Fig. 2b). SA11 cell numbers increased over time in co-culture with responsive *P. multiseriis* strains (PC9, GGA2), but not with a non-responsive strain (PC4) (Fig. 1 insets), implying the diatom somehow modulates SA11 growth. To identify pathways involved in the interaction, we generated a draft genome sequence for SA11 and used a combination of comparative whole-cell transcriptomics and targeted metabolite analyses of the partners grown either in isolation or in co-culture.

In co-culture, *P. multiseriis* PC9 provided SA11 with the organic carbon necessary for growth, as evidenced by increased SA11 cell numbers (Fig. 1a inset). Transcriptome changes implicated diatom-produced taurine, a sulfonated intracellular metabolite previously

identified in several *Pseudo-nitzschia* species⁹. *P. multiseriis* increased transcription of cysteine dioxygenase (*cdo*), the enzyme that catalyses the first step in biosynthesis of taurine from L-cysteine and whose activity is correlated with intracellular taurine concentrations¹³. SA11 increased abundance of transcripts required for taurine uptake (*tauABC*) and catabolism to acetate (*tpa*, *xsc*, *ackA*), which can feed into the TCA cycle¹⁴. SA11 appears particularly responsive to diatom-produced organosulfur molecules as transcripts associated with dimethylsulfoniopropionate (DMS) lyase (*dddL*) also increased (Fig. 2 and Supplementary Information Tables 2 and 3), suggesting degradation of DMS to acrylate and dimethylsulfide¹⁵. *P. multiseriis* also increased the abundance of transcripts associated with photosystem II (*psbB*), light-harvesting proteins (*LHCA4*, *LHCF4*), fucoxanthin, and enzymes in the Calvin cycle while reducing most transcripts associated with genes in the TCA cycle (Fig. 2 and Supplementary Information Table 2). These observations suggest decreased respiration and increased photosynthesis and carbon fixation, perhaps fuelling carbon excretion to SA11.

Symbiotic interactions, such as terrestrial plant–microbe interactions, commonly involve exchange of reduced nitrogen⁵. The sole source of added nitrogen in the growth medium was nitrate¹². However, in co-culture, *P. multiseriis* decreased abundance of transcripts associated with nitrate transport (*NRT1*, *NRT2*) and reduction to ammonia (*NR*, *NiR*) while SA11 increased the abundance of transcripts associated with nitrate uptake (*nitTAB*) and reduction to ammonia (*nirB*) (Fig. 2 and Supplementary Information Tables 2 and 3). Significantly more ammonium was detected in the co-culture medium than in the medium blank or when the diatom was cultured alone, indicating that SA11 released a fraction of its imported nitrate into the media as ammonium (Extended Data Fig. 3a). Together, these results suggest that, in co-culture, SA11 increases nitrate uptake and ammonium release and that *P. multiseriis* preferentially utilizes bacterial-derived ammonium for growth, rather than exogenous nitrate.

Addition of NH_4Cl to axenic *P. multiseriis* had no impact on growth (μ : $0.57 \pm 0.03 \text{ d}^{-1}$ vs $0.55 \pm 0.02 \text{ d}^{-1}$), indicating that although reduced nitrogen was essential to the interaction, another molecule was responsible for the growth effect.

Tryptophan and related derivatives are common signalling molecules in the marine environment^{16,17}. In co-culture, *P. multiseriis* increased transcript abundance for the conversion of indole to tryptophan and for a putative tryptophan/tyrosine permease (Fig. 2 and Supplementary Information Table 2), suggesting increased biosynthesis and export of tryptophan. Tryptophan was detected in the growth media after harvesting cells when *P. multiseriis* was maintained alone ($448 \pm 106 \text{ pM}$) or in co-culture ($202 \pm 20 \text{ pM}$) (Extended Data Fig. 3b). A reduced tryptophan concentration in the co-culture suggests that SA11 may be importing diatom-released tryptophan. Increased transcript abundance for endogenous tryptophan biosynthesis and decreased transcript abundance for tryptophan degradation by SA11 (Fig. 2 and Supplementary Information Table 3) suggest that SA11 increased utilization of extra- and intracellular tryptophan in co-culture.

Co-culture with *P. multiseriis* triggered SA11 to increase transcripts associated with the indole-3-acetamide (IAM) and tryptamine (TAM) pathways (Fig. 2 and Supplementary Information Table 3) that convert tryptophan to indole-3-acetic acid (IAA), an endogenous plant hormone that is also produced and excreted by rhizobia to skew symbiotic plant development¹⁸. IAA was detected in the growth medium when SA11 was maintained alone or in co-culture (Extended Data Fig. 3c). Assuming a constant rate of production and release of IAA by SA11, the concentration in the co-culture ($6.1 \pm 0.4 \text{ pM}$) was significantly lower than predicted (540 pM) (see Methods), implying that *P. multiseriis* takes up a minimum of $5 \text{ amol IAA per cell each day}$. We confirmed that *P. multiseriis* is responsive to a narrow range of synthetic IAA ($50\text{--}100 \text{ nM}$) added either once during the growth cycle (Extended Data Table 4) or as multiple 50 nM additions over 8 days (Extended Data Fig. 4). The growth enhancement by SA11 ($19\text{--}35\%$) versus IAA ($\sim 10\%$) suggests that SA11 produces other molecules that further enhance *P. multiseriis* growth. Furthermore, the difference in orders of magnitude in concentration of synthetic versus bacterial IAA required to stimulate a diatom response (nanomolar vs picomolar) reiterates the potential importance of phycosphere interactions where local concentrations of IAA are significantly higher than bulk concentrations in the media, an observation consistent with previous work on diffusive boundary layers^{7,19}.

To explore the potential prevalence of these interactions in natural populations, we looked for evidence of bacterial production of IAA by performing targeted metabolite analysis on seawater from the surface and chlorophyll maxima at five stations from different regions of the North Pacific Ocean (Extended Data Fig. 5). Since IAA has no clear metabolic role in bacteria¹⁸, production and excretion of IAA in natural populations might indicate bacterial manipulation of responsive phytoplankton similar to rhizobia⁵. Extracellular IAA ($1.5\text{--}383 \text{ pM}$) was detected in all samples, with the highest concentrations detected in coastal sites with high phytoplankton abundance (Fig. 3a and Extended Data Fig. 3c). The range of measured IAA concentrations in the environment is comparable to that measured in our co-culture, indicating that environmental IAA could elicit a response from diatoms associated with IAA-producing bacteria.

The *Roseobacter* clade, to which SA11 belongs, is among the most ubiquitous lineages observed with phytoplankton^{3,20}, and active IAA production by this group could impact diverse phytoplankton species, many of which have been shown to respond to synthetic IAA^{21,22}. To determine whether the *Roseobacter* produced IAA in the field, we examined metatranscriptomic data sets for transcripts associated with the three IAA biosynthetic pathways found in publicly available *Roseobacter* genomes—the indole-3-acetonitrile (IAN), IAM and TAM pathways (Extended Data Fig. 6). We analysed transcripts collected at two coastal stations in the North Pacific Ocean and from three publicly available metatranscriptome data sets from Monterey Bay, the California coast, and station ALOHA in the North Pacific Gyre

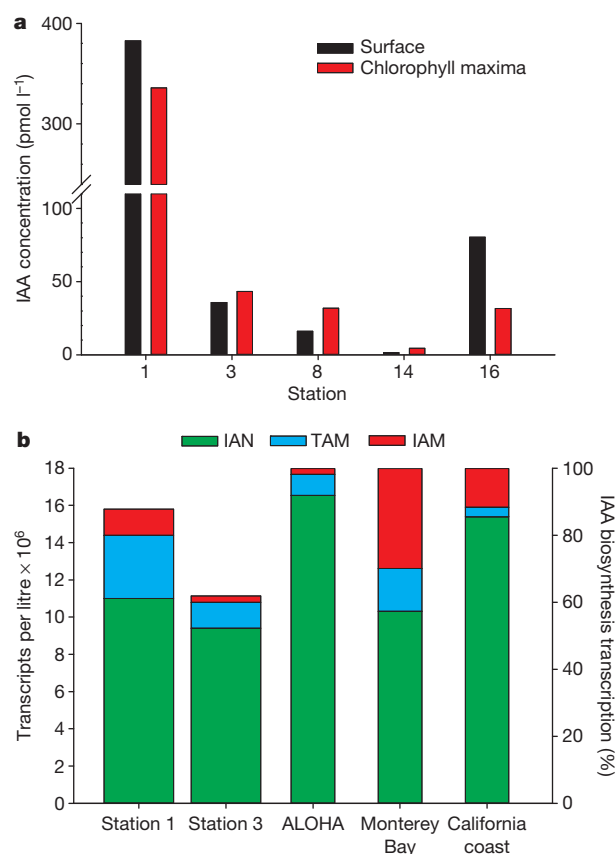


Figure 3 | Detection of IAA and IAA biosynthesis in the marine environment. **a**, IAA concentrations at five stations in the North Pacific Ocean from surface (black) and chlorophyll maxima (red) waters. **b**, Abundance of transcripts from the three IAA biosynthetic pathways present in the *Roseobacter*. Thick bars represent transcripts per litre associated with any gene in the pathways calculated on the basis of an internal standard; thin bars represent percentage IAA biosynthesis transcription contributed by each pathway for data sets in which no internal standard information was available. Genes used in each pathway are in Extended Data Fig. 6. ALOHA coincides with station 16 in Fig. 3a.

(Extended Data Fig. 5). In all data sets, the three IAA biosynthetic pathways were actively transcribed with an average abundance of 10^7 l^{-1} ($\sim 0.01\%$ of total transcripts). Transcripts associated with the IAN pathway dominated all data sets, with TAM and IAM transcripts contributing $10\text{--}40\%$ of total IAA transcription (Fig. 3b). Although SA11 also possesses the IAN pathway, no IAN transcripts were detected in our laboratory experiments, suggesting complex regulatory processes control different pathways. Our results thus present a lower limit on IAA biosynthesis as other bacterial taxa probably also produce IAA, and other IAA biosynthesis pathways (Extended Data Fig. 6) may be active.

The *P. multiseriis*–*Sulfitobacter* model system developed here demonstrates the complexity of microbial interactions, potentially occurring within a phycosphere that concentrates hydrophobic signalling molecules and persists despite seawater turbulence^{23–25}. Tryptophan secretion by *P. multiseriis* may attract a wide range of bacteria, but only bacteria that can convert tryptophan to IAA could create a positive feedback loop between diatom tryptophan and bacterial IAA (Fig. 2). Accumulation of IAA to significantly higher local concentration around algal cells relative to seawater²⁶ would ensure that IAA producers residing within the phycosphere could skew the growth of algae whereas distant bacteria would not. Exchange of essential molecules such as ammonia and organosulfur compounds would further enhance synergy. Additional signalling molecules between bacteria and diatoms and among bacteria are probably key to recognizing

and sustaining beneficial partners and excluding cheaters. Such added specificity could explain the different responses of closely related *P. multiseriis* strains to SA11 and is reminiscent of legume–rhizobia interaction specificity achieved through multiple signalling molecules²⁷. In this context, signalling may distinguish between organisms with a long history of association and organisms with latent capacity for interaction²⁸.

Besides diatoms, several unicellular green algal lineages and cyanobacteria have also been shown to respond to synthetic IAA^{21,22,29}. Direct detection of algal responses to IAA in the field is not yet possible as the genetic basis for algal responses to IAA remains unknown²¹. Further work is needed to characterize these genetic elements. The interactions described here illustrate how bacterial influence on phytoplankton physiology may be linked to the global carbon cycle and algal bloom formation, and probably affect ecosystem functioning.

Online Content Methods, along with any additional Extended Data display items and Source Data, are available in the online version of the paper; references unique to these sections appear only in the online paper.

Received 14 October 2014; accepted 23 April 2015.

Published online 27 May 2015.

- Azam, F. & Malfatti, F. Microbial structuring of marine ecosystems. *Nature Rev. Microbiol.* **5**, 782–791 (2007).
- Little, A. E. F., Robinson, C. J., Peterson, S. B., Raffa, K. F. & Handelsman, J. Rules of engagement: interspecies interactions that regulate microbial communities. *Annu. Rev. Microbiol.* **62**, 375–401 (2008).
- Amin, S. A., Parker, M. S. & Armbrust, E. V. Interactions between diatoms and bacteria. *Microbiol. Mol. Biol. Rev.* **76**, 667–684 (2012).
- Yool, A. & Tyrrell, T. Role of diatoms in regulating the ocean's silicon cycle. *Glob. Biogeochem. Cycles* **17**, 1103–1124 (2003).
- Jones, K. M., Kobayashi, H., Davies, B. W., Taga, M. E. & Walker, G. C. How rhizobial symbionts invade plants: the *Sinorhizobium-Medicago* model. *Nature Rev. Microbiol.* **5**, 619–633 (2007).
- Bell, W. & Mitchell, R. Chemotactic and growth responses of marine bacteria to algal extracellular products. *Biol. Bull.* **143**, 265–277 (1972).
- Jonsson, P. R., Pavia, H. & Toth, G. Formation of harmful algal blooms cannot be explained by allelopathic interactions. *Proc. Natl Acad. Sci. USA* **106**, 11177–11182 (2009).
- Karp-Boss, L., Boss, E. & Jumars, P. A. Nutrient fluxes to planktonic osmotrophs in the presence of fluid motion. *Oceanogr. Mar. Biol. Annu. Rev.* **34**, 71–107 (1996).
- Smith, G. J., Ladizinsky, N. & Miller, P. E. in *Harmful Algal Blooms 2000* (eds Hallegraeff, G. M., Blackburn, S. I., Bolch, C. J. S. & Lewis, R. J.) 324–327 (UNESCO, 2000).
- Shishlyannikov, S. M. *et al.* A procedure for establishing an axenic culture of the diatom *Synedra acus* subsp. *radians* (Kütz.) Skabibitsch. from Lake Baikal. *Limnol. Oceanogr. Methods* **9**, 478–484 (2011).
- Windler, M. *et al.* Influence of bacteria on cell size development and morphology of cultivated diatoms. *Phycol. Res.* **62**, 269–281 (2014).
- Price, N. M. *et al.* Preparation and chemistry of the artificial algal culture medium Aquil. *Biol. Oceanogr.* **6**, 443–461 (1988).
- Stipanuk, M. H. & Dominy, J. E. Surprising insights that aren't so surprising in the modeling of sulfur amino acid metabolism. *Amino Acids* **30**, 251–256 (2006).
- Cook, A. M. & Denger, K. Metabolism of taurine in microorganisms: a primer in molecular biodiversity? *Adv. Exp. Med. Biol.* **583**, 3–13 (2006).
- Curson, A. R. J., Rogers, R., Todd, J. D., Brearley, C. A. & Johnston, A. W. B. Molecular genetic analysis of a dimethylsulfoniopropionate lyase that liberates the climate-changing gas dimethylsulfide in several marine α -proteobacteria and *Rhodobacter sphaeroides*. *Environ. Microbiol.* **10**, 757–767 (2008).
- Riffell, J. A., Krug, P. J. & Zimmer, R. K. The ecological and evolutionary consequences of sperm chemoattraction. *Proc. Natl Acad. Sci. USA* **101**, 4501–4506 (2004).
- Yambe, H. *et al.* L-Kynurenine, an amino acid identified as a sex pheromone in the urine of ovulated female masu salmon. *Proc. Natl Acad. Sci. USA* **103**, 15370–15374 (2006).
- Spaepen, S. & Vanderleyden, J. Auxin and plant-microbe interactions. *Cold Spring Harb. Perspect. Biol.* **3**, a001438 (2011).
- Stocker, R. Marine microbes see a sea of gradients. *Science* **338**, 628–633 (2012).
- Geng, H. & Belas, R. Molecular mechanisms underlying roseobacter–phytoplankton symbioses. *Curr. Opin. Biotechnol.* **21**, 332–338 (2010).
- Lau, S., Shao, N., Bock, R., Jürgens, G. & De Smet, I. Auxin signaling in algal lineages: fact or myth? *Trends Plant Sci.* **14**, 182–188 (2009).
- Suzuki, T., Nakasato, K., Shapiro, S., Pomati, F. & Neilan, B. A. Effects of synthetic local anaesthetics on the growth of the cyanobacterium *Synechococcus leopoliensis*. *J. Appl. Phycol.* **16**, 145–152 (2004).
- Durham, W. M. *et al.* Turbulence drives microscale patches of motile phytoplankton. *Nature Commun.* **4**, 2148 (2013).
- Stocker, R. & Seymour, J. R. Ecology and physics of bacterial chemotaxis in the ocean. *Microbiol. Mol. Biol. Rev.* **76**, 792–812 (2012).
- Taylor, J. R. & Stocker, R. Trade-offs of chemotactic foraging in turbulent water. *Science* **338**, 675–679 (2012).
- Guasto, J. S., Rusconi, R. & Stocker, R. Fluid mechanics of planktonic microorganisms. *Annu. Rev. Fluid Mech.* **44**, 373–400 (2012).
- Wang, D., Yang, S., Tang, F. & Zhu, H. Symbiosis specificity in the legume-rhizobial mutualism. *Cell. Microbiol.* **14**, 334–342 (2012).
- Hom, E. F. Y. & Murray, A. W. Niche engineering demonstrates a latent capacity for fungal-algal mutualism. *Science* **345**, 94–98 (2014).
- De Smet, I. *et al.* Unraveling the evolution of auxin signaling. *Plant Physiol.* **155**, 209–221 (2011).
- Roudier, F. *et al.* The *Medicago* species A2-type cyclin is auxin regulated and involved in meristem formation but dispensable for endoreduplication-associated developmental programs. *Plant Physiol.* **131**, 1091–1103 (2003).

Supplementary Information is available in the online version of the paper.

Acknowledgements We thank U. John for the antibiotic recipe, L. Gram for providing *Phaeobacter* strains, J. Tsai for preparing the SA11 DNA for sequencing, the captain and crew of the R/V *Kilo Moana* and the R/V *Thomas G. Thompson* for help during the cruises, D. French for Extended Data Fig. 5, and T. Chiang for discussions. This work was supported in part by Gordon and Betty Moore Foundation grant GBMF3776 to E.V.A., and support from National Science Foundation (NSF) award OCE-1228770 to A.E.I., OCE-1205233 to E.V.A., and OCE-1342694 to M.A.M. S.A.A. was partly supported by a NSF/National Institutes of Health Pacific Northwest Consortium postdoctoral fellowship. H.M.V. was partly supported by a Natural Sciences and Engineering Research Council of Canada Postgraduate Scholarship – Master's grant.

Author Contributions S.A.A., L.R.H., B.D., B.P.D. and H.V.T. conducted experiments; B.P.D. isolated and prepared bacterial transcriptomic and metatranscriptomic samples; R.L.M. isolated all other nucleic acids and prepared libraries for sequencing; C.T.B. quality-trimmed sequenced data, assembled the SA11 genome and translated the metatranscriptome; M.S.P. quality-trimmed and quantified the PC9 transcriptomes; L.T.C. and K.R.H. collected environmental metabolome samples and performed MS analyses; S.A.A., L.R.H., M.R.P., A.E.I., M.A.M., and E.V.A. designed experiments; S.A.A. and L.T.C. analysed the data. All authors were involved in manuscript writing.

Author Information The data reported in this paper are presented in Supplementary Information and archived at the following databases: 16S rDNA sequences, GenBank accession numbers KM033232–KM033280; transcriptomes, Gene Expression Omnibus accession number GSE65189; metatranscriptomes, Sequence Read Archive accession number PRJNA272345; SA11 genome, Integrated Microbial Genomes (IMG) submission 11682. Reprints and permissions information is available at www.nature.com/reprints. The authors declare no competing financial interests. Readers are welcome to comment on the online version of the paper. Correspondence and requests for materials should be addressed to E.V.A. (armbrust@uw.edu) or S.A.A. (sa132@nyu.edu).

METHODS

No statistical methods were used to predetermine sample size.

Diatom growth and axenic culture generation. Milli-Q water (>18.2 M Ω cm) was used for all synthetic seawater media preparations. *T. pseudonana* CCMP1335 was acquired from National Center for Marine Algae and Microbiota. *P. multiseri* strains were isolated from seawater samples collected from locations indicated in Extended Data Table 1 and were identified using Automated Ribosomal Intergenic Spacer Analysis (ARISA) according to ref. 31. Cultures were initially grown in f/2 medium³² and were acclimated and further maintained for all experiments in the synthetic seawater medium, Aquil¹². All cultures were grown in 13 °C in a 16 h light/8 h dark diurnal cycle ($80 \mu\text{E m}^{-2} \text{s}^{-1}$) in semi-continuous batch cultures³³ with an initial cell density $\sim 8,000$ – $10,000$ cells per millilitre for non-axenic cultures and $\sim 2,000$ – $4,000$ cells per millilitre for axenic cultures. Diatom growth was monitored by measuring *in vivo* fluorescence using a 10-AU fluorometer (Turner Designs) or by counting cells using a Sedgwick-rafter (Wildlife Supply Company). Growth rates were estimated by measuring *in vivo* chlorophyll *a* fluorescence (relative fluorescence units) or cell counts. Specific growth rates (μ) were calculated from the linear regression of the natural log of *in vivo* fluorescence or cell counts versus time during the exponential growth phase of cultures. Standard deviation of μ was calculated from μ values from biological replicates ($n = 3$ unless otherwise indicated) over the exponential growth period. Percentage growth enhancement was calculated as the difference between $\mu_{\text{co-culture}}$ and μ_{axenic} divided by $\mu_{\text{co-culture}}$.

Axenic cultures were generated by adopting the protocol from ref. 10 with minor modifications as described below. Approximately 25 ml of a mid-exponential phase growing diatom culture was gravity filtered onto 0.65 μm pore-size polycarbonate membrane filter (Millipore). Cells were quickly rinsed with sterile Aquil media. Using sterile tweezers, the filter was carefully removed from the filtration unit and washed for ~ 1 min in sterile media containing $20 \mu\text{g ml}^{-1}$ Triton X-100 detergent to remove surface-attached bacteria. The filter was discarded after re-suspension of cells by gentle shaking in sterile detergent-free media. Cells were again gravity filtered onto a fresh 0.65 μm pore-size polycarbonate membrane filter and rinsed with sterile media. Subsequently, cells were washed off the filter by gentle shaking into sterile media containing a suite of antibiotics (per millilitre: 50 μg streptomycin, 67 μg gentamycin, 20 μg ciprofloxacin, 2.2 μg chloramphenicol, and 100 μg ampicillin). Cells were incubated in antibiotic-containing media for 24–48 h under regular growth conditions. Finally, 0.5–1.0 ml of antibiotics-treated cells were transferred to antibiotic-free media. Cultures were regularly monitored (every four or five transfers, ~ 1 month) for bacterial contamination by checking for bacterial growth in Zobell marine broth³⁴ in addition to using Sybr Green I (Invitrogen) staining and epifluorescence microscopy (Nikon Eclipse 80i) as described previously³⁵. Bacterial contamination was observed only once over the course of ~ 18 months for PC9 owing to human error; the culture was discarded and fresh axenic cultures were prepared as above.

Bacterial growth, isolation, and classification. Bacteria were typically grown on marine agar plates (per litre: 5 g peptone, 0.5 g yeast extract, 15 g agar, and 750 ml seawater) incubated at 20 °C in the dark or in marine broth³⁴ at 30 °C with shaking at 150 r.p.m. Bacterial growth was measured by counting colony-forming units or by using a Guava EasyCyte Plus flowcytometer (Millipore) after cells were stained with Sybr Green I stain.

Bacteria were isolated from late-exponential phase growing *P. multiseri* cultures by serially diluting 0.5 ml aliquots of culture into sterile Aquil. Diluted aliquots were then plated onto agar plates containing, per litre of seawater, 15 g agar and 2 g of a carbon source (peptone and yeast extract, succinate, glucose, CAS amino acids, or only background organic carbon in seawater). Plates were incubated at room temperature in the dark and morphologically different bacterial colonies were isolated and stored in 15% glycerol stocks at -80 °C for future experiments.

To identify isolated bacteria, isolates were grown from single colonies in marine broth overnight and cells were centrifuged at 13,000g for 2 min. The supernatants were removed and DNA was extracted using a DNA Blood & Tissue kit (Qiagen) according to the manufacturer's instructions. Using universal 16S rDNA primers (27F, 1492R), 16S rDNA from all bacterial isolates was amplified using a Taq DNA polymerase kit (Apex). The temperature profile for PCR consisted of an initial incubation at 94 °C for 3 min, followed by 32 cycles of 94 °C for 30 s, 55 °C for 1 min and 72 °C for 2 min, and a final extension step at 72 °C for 20 min. Amplified product was cleaned using a High Pure PCR Purification Kit (Roche). Purified PCR products were sequenced using Sanger technology (Genewiz).

Sequences were quality trimmed using Sequencher 4.6 (Gene Codes) and initially aligned using ClustalW as implemented in Mega 5.2.2 (ref. 36). The alignment was refined using NAST (<http://greengenes.lbl.gov>). Phylogenetic inference of the masked alignment was based on maximum likelihood, using the JTT model

with bootstrap support of 100 replicates as implemented in Mega 5.2.2 (ref. 36). Sequences were deposited in GenBank under accession numbers KM033232–KM033280.

Co-culture experiments. Because we observed long term (>18 months) growth rate differences between axenic and non-axenic *P. multiseri*, all co-culture experiments (including the transcriptome and metabolite analyses experiments) were conducted within 7 months of curing the diatom of bacteria. All experiments were conducted in Aquil¹². Bacteria were plated freshly before each experiment on marine agar and were grown from single colonies in marine broth overnight (30 °C, 150 r.p.m.). Cells were centrifuged (3,500g for 5 min), washed twice with sterile Aquil, and diluted to a stock cell density of $\sim 1 \times 10^8$ cells per millilitre with sterile Aquil. This stock was used to inoculate the freshly prepared diatom culture to achieve a final bacterial cell density of $\sim 1 \times 10^5$ – 2×10^5 cells per millilitre. Diatoms were inoculated from an early to mid-exponential phase growing culture into fresh media to an initial diatom cell density of $\sim 2,000$ – $4,000$ cells per millilitre to achieve an $\sim 50:1$ bacteria:diatom ratio. Diatom and bacterial growth were measured as described above. For experiments where *Sulfotobacter* sp. strain SA11 was grown alone, Aquil was supplemented with 11 mM glucose as the sole carbon source except for the transcriptome experiment (see below), where only 1 μM glucose was used.

For the transcriptome experiments, axenic *P. multiseri* strain PC9 was used to inoculate 2 l sterile polycarbonate bottles. Treatments consisted of (1) PC9 and SA11 co-culture, (2) axenic PC9, and (3) SA11 supplemented with 1 μM glucose. All treatments were in triplicate. Growth rates for PC9 were $\mu_{\text{axenic}} = 0.75 \pm 0.03 \text{ d}^{-1}$ and $\mu_{\text{co-culture}} = 0.94 \pm 0.04 \text{ d}^{-1}$. Growth rates for SA11 were $\mu_{\text{glucose}} = 0.45 \pm 0.01 \text{ d}^{-1}$ and $\mu_{\text{co-culture}} = 0.46 \pm 0.02 \text{ d}^{-1}$. Cells were harvested at mid-exponential growth (96 h after inoculation for all treatments) by filtering the culture through a 3 μm pore-size polycarbonate filter to capture the majority of diatom cells (this step was skipped for treatment 3), followed by filtration through 0.22 μm pore-size polycarbonate filter to capture bacteria. Final cell densities at time of harvesting were PC9_{axenic} $\sim 3.5 \times 10^4$ cells per millilitre, PC9_{co-culture} $\sim 5.8 \times 10^4$ cells per millilitre, SA11_{co-culture} $\sim 1.7 \times 10^6$ cells per millilitre, and SA11_{glucose} $\sim 3 \times 10^6$ cells per millilitre. Filters were immediately flash frozen in liquid nitrogen and later stored at -80 °C. Flow-through media were used for targeted metabolite analyses (see below).

IAA addition experiments. IAA (Sigma-Aldrich) was dissolved in Milli-Q water and sterilized using syringe filtration. *P. multiseri* strain GGA2 was inoculated into fresh Aquil media supplemented with different concentrations of IAA or equivalent volumes of Milli-Q water (control). For IAA additions in Extended Data Fig. 5, IAA or Milli-Q water was added every 2 days as described to simulate a continuum of active IAA concentrations in the media.

***P. multiseri* genome.** A publicly available genome of strain CLN-47 was used for our analysis (<http://genome.jgi-psf.org/Psemu1/Psemu1.home.html>).

SA11 genome. All nucleic acid quantifications were measured using a Qubit Fluorometer (Invitrogen; Life Technologies). DNA was extracted using a Qiagen DNA Blood and Tissue kit according to the manufacturer's instructions. Ten micrograms of DNA were sheared to 2–3 kb using a Hydroshear (Genomic Solutions) with a standard shearing assembly. To prepare the DNA for SOLiD 60 base pair (bp) \times 60 bp mate-pair sequencing, we used a unique protocol combining different steps from the SOLiD 3, SOLiD 4, and SOLiD 5500 mate-paired protocols (R.M. & E.V.A., manuscript in preparation). The library was attached to beads by emulsion PCR, which was done at the Life Technologies Research and Development Unit. For sequencing, 50 million library-containing beads were deposited onto one spot of an eight-spot slide and run on a SOLiD 4 Next Generation Sequencer (Life Technologies). In addition to SOLiD sequencing, we used Ion Torrent to improve the genome assembly. DNA was prepared as described above. Ion Torrent library preparations were performed according to the manufacturer's instructions.

The SA11 genome was assembled using a combination of fragment Ion Torrent reads and 50×50 mate-paired SOLiD colorspace reads with an insert size of 2,200 bp (s.d. 800 bp). Fastq_quality_trimmer from a FASTX Toolkit was used to quality trim and filter Ion Torrent reads with parameters '-Q33 -l 50 -t 14'. SOLiD reads were screened for PCR duplication artefacts using fastq_nodup from SEASTAR³⁷ with parameters '-d 2-no_prefix' and were trimmed and filtered on the basis of quality score using trimfastq from SEASTAR with parameters '-p.75 -l 34 -e 3.0-add_len-no_prefix'. Contigs were created with the *de novo* assembly tool Newbler. The contigs were organized into scaffolds using graph_ops from SEASTAR on the basis of mate-pair connections identified by a BWA alignment of SOLiD reads to Ion Torrent contigs. Contigs were also created for a *de novo* assembly of SOLiD reads using Velvet with a kmer size of 31, coverage cutoff of 35, expected coverage of 200, insert size of 2,200, insert size standard deviation of 800, scaffolding disabled, and a minimum contig length of 100. These contigs were used to fill gaps between scaffolded Ion-Torrent-based Newbler contigs where possible.

The genome can be publicly accessed through IMG (<http://img.jgi.doe.gov>; submission 11682).

PC9 transcriptome. Total RNA was isolated from 3- μ m filters using a ToTALLY RNA Total RNA Isolation Kit (Ambion; Life Technologies), and messenger RNA (mRNA) was purified from the total RNA using a MicroPoly(A)Purist Kit (Ambion; Life Technologies). SOLiD 75 bp \times 35 bp paired-end libraries were generated from \sim 500 ng of mRNA from each replicate and treatment using a SOLiD Total RNA-Seq Kit (Life Technologies) with the gel option according to the manufacturer's instructions. The libraries were attached to beads in-house by emulsion PCR according to the SOLiD manual. For sequencing, 700 million library-containing beads were deposited onto a full slide and run on a SOLiD 4 Next Generation Sequencer (Life Technologies).

The SOLiD reads were trimmed on the basis of quality score using custom in-house software³⁷. Trimmed reads with a length shorter than 28 colorspace transitions were removed. Filtered reads were then aligned to the *P. multiseri* draft genome gene catalogue transcripts provided by JGI (Psemu1_GeneCatalog_transcripts_20111011.nt.fasta) using BWA (version 0.5.8) allowing for two mismatches in a seed length of 18, and up to four mismatches across an entire read. Anti-sense reads were removed and counts for SOLiD reads aligning to gene catalogue transcripts were calculated from the resulting SAM alignment file³⁸ using SEASTAR³⁷. SEASTAR counts were then analysed with edgeR³⁹ for differential expression and significance testing using Benjamini Hochberg multiple testing corrections. Count tables were then merged with KEGG annotations provided by JGI. Using a false discovery rate cutoff of 0.05, 2,143 genes were differentially expressed in PC9 out of \sim 19,703 gene models.

SA11 transcriptome. RNA was isolated from 0.22- μ m filters using an RNeasy Mini Kit along with RNaprotect Bacteria Reagent (Qiagen) according to the manufacturer's instructions using 1 mg ml⁻¹ lysozyme solution (Fisher) to lyse the cells. Total RNA was treated for DNA contamination using two successive treatments with Turbo-DNase (Ambion; Life Technologies) and cleaned/concentrated with an RNeasy MinElute Cleanup Kit (Qiagen). Ribosomal RNAs (rRNAs) were selectively removed using a subtractive hybridization protocol⁴⁰ with biotinylated rRNA probes specific to the organism(s) in each sample (for example, 16S and 23S for SA11 mono- and co-cultures or eukaryotic 18S and 28S for co-cultures). Subtracting diatom rRNAs was essential as the first filtration through 3- μ m pore-size filter (see above) did not completely remove all diatom cells. Probe-bound RNAs were removed with streptavidin-coated magnetic beads (New England Biolabs). rRNA-depleted samples were then linearly amplified using a MessageAmp II-Bacteria kit (Ambion; Life Technologies).

Amplified mRNA was then converted into complementary DNA (cDNA) using a SuperScript III First-Strand Synthesis System for RT-PCR kit (Ambion; Life Technologies) and a NEBNext mRNA Second Strand Synthesis Module (New England Biolabs) according to the manufacturer's instructions. SOLiD 75 bp \times 35 bp paired-end libraries were generated from 1 μ g of cDNA using a SOLiD Fragment Library Construction Kit according to the manufacturer's instructions. The libraries were attached to beads in-house by emulsion PCR according to the SOLiD manual. For sequencing, 450 million library-containing beads were deposited onto three lanes of a flow cell and run on a SOLiD 5500 Next Generation Sequencer (Life Technologies).

SOLiD reads were trimmed and filtered to remove low-quality or low information content sequence using trimfastq from SEASTAR with settings 'trimfastq -z -s-add_len -l 30 -p.9 -e 3.0'. Trimmed reads were aligned to IMG-derived SA11 reference genome using BWA with settings '-k 2 -n.001 -l 18 -t 8 -c' for the aln subcommand and settings '-n 100' for the same subcommand. Resulting SAM files were processed with ref_select and graph_ops from SEASTAR to get per gene read counts. These counts were processed with the R package edgeR to identify SA11 genes with significant differential expression between the two conditions. Using a false discovery rate cutoff of 0.001 and a fold-change \geq 2, 2,620 genes were differentially expressed in SA11 out of \sim 5,281 open reading frames.

Culture media targeted metabolite analysis. Ammonium and nitrate concentrations were analysed using an AAI autoanalyzer system (Technicon). To detect and quantify IAA and tryptophan, culture supernatants were acidified to pH \sim 3.5 using concentrated formic acid (Fisher, Baker Analyzed). Supernatants were then passed through conditioned solid-phase extraction (SPE) HLB columns (Waters) at a flow rate of \sim 5 ml min⁻¹ to bind organic molecules. The columns were washed thoroughly with Milli-Q water and eluted with methanol (ultra-performance liquid chromatography (UPLC) grade, Fisher) according to the manufacturer's instructions. Eluted samples were dried under a stream of nitrogen gas and were then frozen at -80°C for later analysis. Before analysis, samples were dissolved in water.

Mass spectrometry. Tryptophan and IAA were purchased (Sigma-Aldrich) as well as labelled standards for IAA (indole-2,4,5,6,7-d₅-3-acetic acid) and tryptophan (L-tryptophan-2,3,3-d₃) (CDN Isotopes). To verify the identity and quantify

IAA and tryptophan in all standards and culture samples, an ultra-performance liquid chromatography-electrospray ionization-tandem mass spectrometry (UPLC-ESI-MS) method adapted from ref. 41 was used, with some changes. A quadrupole time-of-flight (Waters Xevo G2-S QTOF) mass spectrometer was used for verification of compound identity. For the quadrupole time-of-flight, a cone voltage of 2 V and collision energy of 28 V were used when running IAA, and a cone voltage of 32 V and collision energy of 20 V were used when running tryptophan. Compound quantitation was done using selected reaction monitoring (SRM) on a Waters Xevo TQ-S triple quadrupole mass spectrometer. The same UPLC method was used for all analyses. Both retention times and SRM transition masses were used to target compounds in environmental samples run only using the SRM method (Supplementary Information Table 4). The UPLC method used a Waters Acquity UPLC system equipped with a Waters Acquity UPLC BEH C18 column (1.7 μ m, 2.1 mm \times 50 mm) at 30°C with the mobile phase consisting of 0.1% formic acid in water (solvent A) and methanol (solvent B). A linear gradient with a flow rate of 0.2 ml min⁻¹ was used from 0 to 7 min (5% B to 90% B), followed by 2 min at 90% B, and 3 min linear gradient back to 5% B to re-equilibrate the column. Both mass spectrometers were configured with positive ion ESI with source conditions as follows: capillary voltage 0.5 kV, source temperature 130°C , desolvation temperature 550°C , cone gas flow at 150 l h⁻¹, and desolvation gas at 1,000 l h⁻¹.

Analysis of the retention time and the accurate mass of the molecular ion (176.0706) and fragment ion (130.0656) of an authentic standard of IAA confirmed its presence in a monoculture of SA11 (Supplementary Information Table 4). Fragmentation of IAA was induced by a program that ramped collision energy from 20 to 30 V. To quantify tryptophan and IAA in cultures and environmental samples, a positive ion mode SRM method was used that monitored the following transitions: 176.02 \rightarrow 130.07 (IAA) (Supplementary Information Table 4) and 188.07 \rightarrow 118.05 (tryptophan). For SRM, the same cone voltage and collision energy were used as the quadrupole time-of-flight.

For quantification of IAA and tryptophan in culture media samples, percentage recovery during SPE was determined for each molecule in Aquil by acidifying and passing different batches of Aquil through SPE HLB columns and treating them the same way as culture media described above. Three batches were spiked with labelled IAA-d₅ and tryptophan-d₃ before SPE treatment while the rest were spiked after SPE. Extracts were then dried, re-dissolved as described above, and analysed on a Xevo TQ-S triple quadrupole mass spectrometer. Percentage recovery was determined on the basis of the peak area of labelled compounds in treatments spiked before and after SPE ($70 \pm 16\%$ for IAA; $32 \pm 12\%$ for tryptophan). Reported concentrations were corrected for percentage recovery during SPE. An additional batch of Aquil media was extracted by SPE and used to construct a standard curve for each molecule to determine the linear range of the detector ($R^2_{\text{IAA}} = 0.999$, $R^2_{\text{trp}} = 0.98$). Samples were diluted such that they were in the range of the standard curve concentrations (0–100 nM for IAA and 0–25 nM for tryptophan) and quantified using isotope-labelled internal standards. Internal standard spikes were also within the standard curve concentrations. Concentrations calculated from the standard curve and from the internal standards were generally similar. Reported concentrations are from the internal standard calculation. No IAA contamination was found in blank Aquil. Traces of (<1 pM) tryptophan were detected in Aquil but were significantly lower than all measured concentration in cultures. We attempted to detect taurine in the culture media but were not able to do so, presumably because of poor SPE recovery and inappropriate UPLC chromatography column type (C18).

SA11 IAA production rate. In co-culture, the amount of IAA detected is probably lower than what is produced by SA11 if we presume there was active removal of IAA from solution by the diatom. Because the cell density and the length of the exponential growth phase of SA11 differ in co-culture and monoculture, a direct comparison between IAA concentrations in both treatments is not informative. To calculate the production rate of IAA by SA11, three sets of triplicate cultures of Aquil supplemented with 11 mM glucose were inoculated with SA11. Each set of cultures was harvested after 2, 3, and 4 days of growth. Organic molecules were extracted from the media after removing cells, and IAA was quantified as described in the Mass Spectrometry section. IAA production per cell per day was calculated from the three sets of cultures that were harvested on days 2, 3, and 4. Using the known SA11 cell density in co-culture, we calculated the minimum expected concentration of IAA in co-culture (540 pM). This concentration served as a lower limit on the expected *in situ* IAA concentration that would result from the measured production rate in monoculture since our transcriptome data showed that IAA biosynthesis increased in the co-culture.

Environmental metatranscriptomics and targeted metabolite analysis. Samples were collected in May 2012 at stations 1 and 3 along Line P and in August 2013 at stations 1 (48.6965°N , 126.0387°W), 3 (48.8168°N , 128.6648°W), 8 (49.9872°N , 144.8077°W), 14 (27.3462°N , 152.6717°W), and 16 (22.7603°

N, 158.0003° W) for metatranscriptomes and targeted metabolite analysis, respectively. Seawater samples were collected from the surface using a conductivity–temperature–depth (CTD) rosette equipped with Niskin bottles (20 l).

For RNA, cells were collected by sequential filtration on a Nitex screen of 53 µm pore-size to remove large particles, 142 mm 2.0 µm pore-size polycarbonate filters (mostly eukaryotic), and 142 mm 0.2 µm pore-size Supor filters (mostly prokaryotic). Results shown are from the combined eukaryotic and prokaryotic size fractions. Filters were flash frozen in liquid nitrogen and subsequently stored at –80 °C until processing.

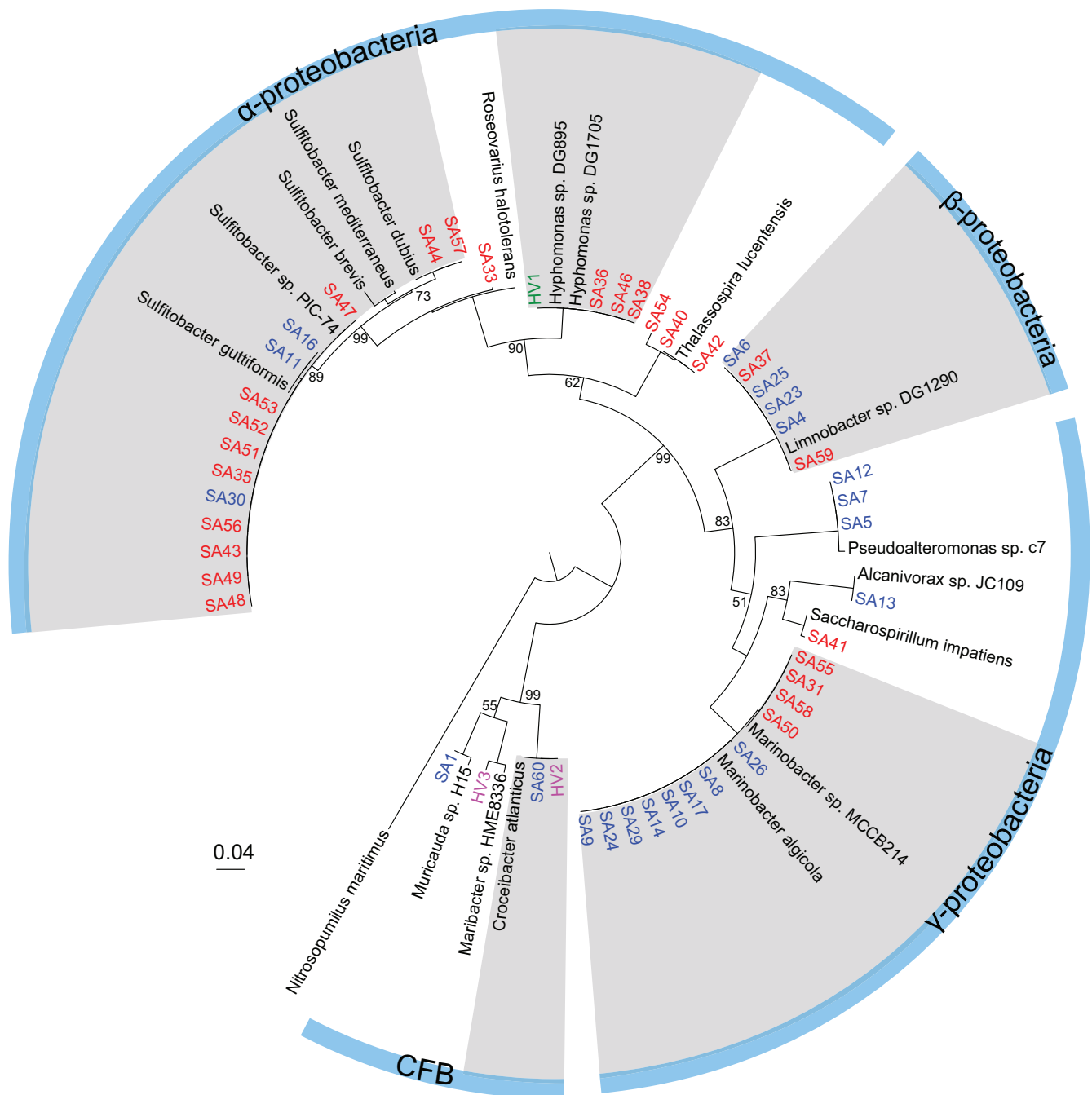
RNA extraction and DNA removal were performed as previously described for environmental metatranscriptomics^{42,43} with the following modifications: lysis in 10 ml of Ambion lysis buffer (AM8540G) + 0.5 ml each of 0.5 and 0.1 zirconia beads. rRNAs were selectively removed using a subtractive hybridization method⁴⁰ with biotinylated rRNA probes specific to the samples (that is, bacterial and archaeal 16S and 23S and eukaryotic 18S and 23S). Probe-bound RNAs were removed with streptavidin-coated magnetic beads (New England Biolabs). rRNA-depleted samples were then linearly amplified using a MessageAmp II-Bacteria kit (Ambion; Life Technologies). Amplified mRNAs were then converted into cDNAs for Illumina sequencing using a Superscript III First-Strand Synthesis System (Invitrogen; Life Technologies) followed by the NEBNext mRNA Second Strand Synthesis Module (New England Biolabs). cDNAs were then purified using a QIAquick PCR purification kit (Qiagen) followed by ethanol precipitation. Purified cDNAs were sheared to ~200–250 bp fragments and HiSeq libraries (Illumina) were constructed for paired-end (2 × 150) sequencing using an Illumina HiSeq 2500 platform. After sequencing, paired-end Illumina reads were joined using a PANDAseq assembler⁴⁴, and paired reads were trimmed using FASTX-Toolkit (http://hannonlab.cshl.edu/fastx_toolkit/).

For the metatranscriptome analyses, rhizobial IAA biosynthesis proteins with experimentally verified functions were identified and used to identify homologues in SA11 and from Roseobase (<http://www.roseobase.org>) using BLASTp. Proteins with no homologues in Roseobase or SA11 were not included in the analysis (Extended Data Fig. 6). In addition, indole-3-acetaldehyde (IAAld) dehydrogenase, a protein commonly annotated as aldehyde dehydrogenase in rhizobia, was not included in the analysis because of the presence of several homologues within each *Roseobacter* genome that are probably involved in other pathways besides IAA biosynthesis. Therefore, our analysis in Fig. 3b probably represents an under-representation of IAA biosynthesis transcripts in the North Pacific. On average, each station had an estimated 3.2×10^{11} transcripts per litre based on the recovery of the internal standard reads after sequencing, suggesting IAA transcripts recovered in our analyses represent ~0.01% of the total transcripts. The *Roseobacter* reference sequences identified above were used as the query for tBLASTn searches to identify transcripts representing *Roseobacter*-clade IAA biosynthesis genes in our North Pacific metatranscriptomes and three publicly available metatranscriptomes from the North Pacific Gyre, Monterey Bay (California), and the California Coastal system (NCBI accession numbers PRJNA244754, PRJNA183166, and PRJNA268385, respectively). Only reads with ≥60% sequence identity and ≥140 bp of the read length aligning to the query were included in our final analysis. Transcript concentrations in seawater for the North Pacific metatranscriptomes

were calculated on the basis of the recovery of the internal standard reads. Percentage IAA biosynthesis transcription was calculated by dividing the number of reads from each pathway by the total. The lack of complete metadata for the public data sets prevented the calculation of accurate transcripts per litre.

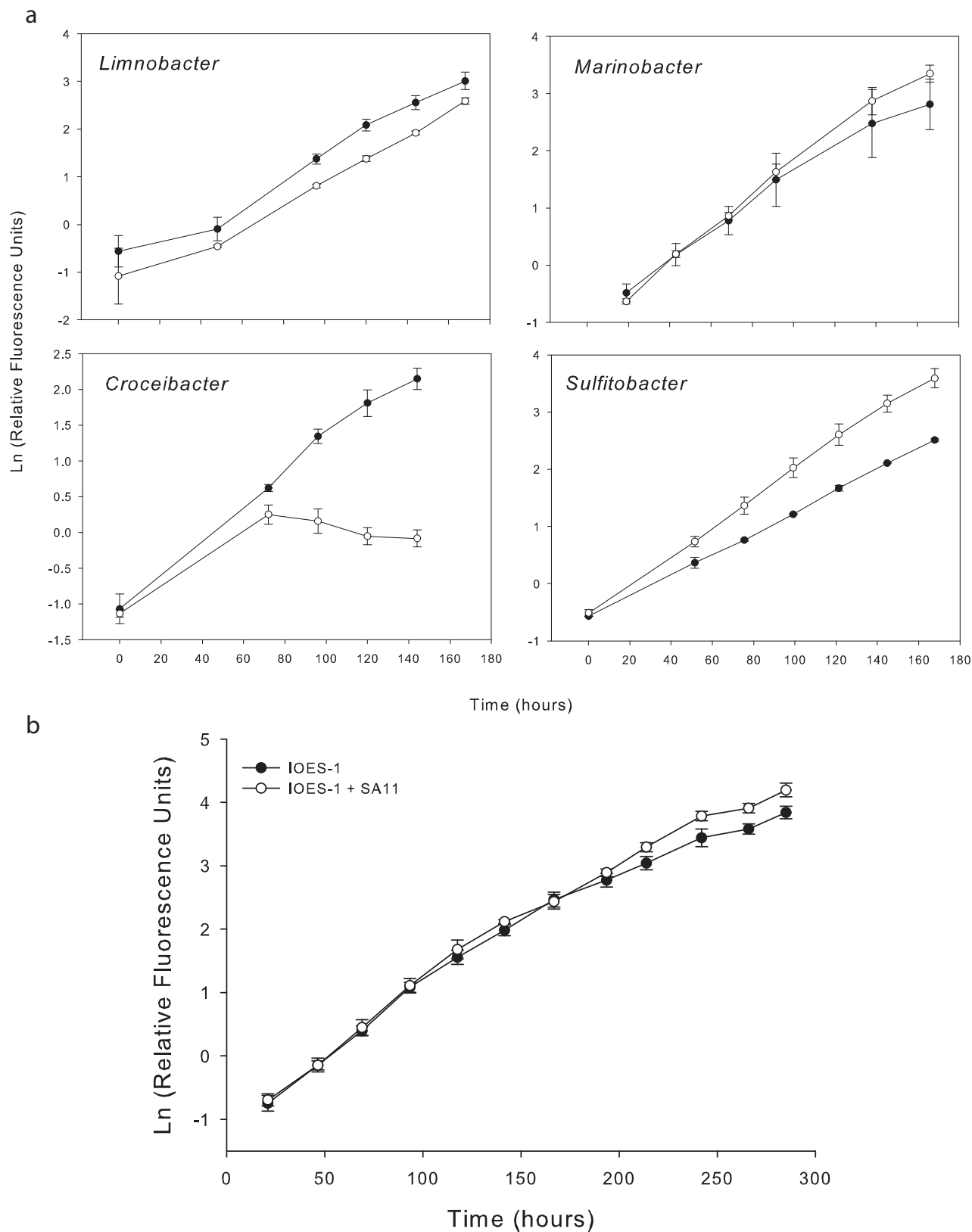
For targeted metabolite analysis, samples were collected and treated as described in ref. 45. Standard curves for IAA and percentage recovery were determined as described for Aquil, except seawater from station ALOHA (station 16) was used as matrix. Because seawater samples were mainly collected and processed for targeted vitamin B detection⁴⁵, recovery of IAA was poor but relatively consistent ($32 \pm 7\%$). Concentrations detected were corrected using this percentage recovery. Detection and quantification were conducted as described in the Mass Spectrometry section.

31. Hubbard, K. A., Rocap, G. & Armbrust, E. Inter- and intraspecific community structure within the diatom genus *Pseudo-nitzschia* (Bacillariophyceae). *J. Phycol.* **44**, 637–649 (2008).
32. Guillard, R. R. L. in *Culture of Marine Invertebrate Animals* (Smith, W. L. & Chanley, M. H. eds) 29–60 (Springer US, 1975).
33. Brand, L. E., Guillard, R. R. L. & Murphy, L. S. A method for the rapid and precise determination of acclimated phytoplankton reproduction rates. *J. Plankton Res.* **3**, 193–201 (1981).
34. ZoBell, C. E. Studies on marine bacteria. I. The cultural requirements of heterotrophic aerobes. *J. Mar. Res.* **4**, 42–75 (1941).
35. Lunau, M., Lemke, A., Walther, K., Martens-Habben, W. & Simon, M. An improved method for counting bacteria from sediments and turbid environments by epifluorescence microscopy. *Environ. Microbiol.* **7**, 961–968 (2005).
36. Tamura, K. et al. Mega5: molecular evolutionary genetics analysis using maximum likelihood, evolutionary distance, and maximum parsimony methods. *Mol. Biol. Evol.* **28**, 2731–2739 (2011).
37. Iverson, V. et al. Untangling genomes from metagenomes: revealing an uncultured class of marine Euryarchaeota. *Science* **335**, 587–590 (2012).
38. Li, H. et al. The sequence alignment/map format and SAMtools. *Bioinformatics* **25**, 2078–2079 (2009).
39. Robinson, M. D., McCarthy, D. J. & Smyth, G. K. edgeR: a Bioconductor package for differential expression analysis of digital gene expression data. *Bioinformatics* **26**, 139–140 (2009).
40. Stewart, F. J., Ottesen, E. A. & Delong, E. F. Development and quantitative analyses of a universal rRNA-subtraction protocol for microbial metatranscriptomics. *ISME J.* **4**, 896–907 (2010).
41. Matsuda, F., Miyazawa, H., Wakasa, K. & Miyagawa, H. Quantification of indole-3-acetic acid and amino acid conjugates in rice by liquid chromatography-electrospray ionization-tandem mass spectrometry. *Biosci. Biotechnol. Biochem.* **69**, 778–783 (2005).
42. Gifford, S. M., Sharma, S., Rinta-Kanto, J. M. & Moran, M. A. Quantitative analysis of a deeply sequenced marine microbial metatranscriptome. *ISME J.* **5**, 461–472 (2010).
43. Poretsky, R. S. et al. Comparative day/night metatranscriptomic analysis of microbial communities in the North Pacific subtropical gyre. *Environ. Microbiol.* **11**, 1358–1375 (2009).
44. Masella, A. P., Bartram, A. K., Trzaskowski, J. M., Brown, D. G. & Neufeld, J. D. PANDAseq: PAired-eND Assembler for Illumina sequences. *BMC Bioinform.* **13**, 31 (2012).
45. Heal, K. R. et al. Determination of four forms of vitamin B12 and other B vitamins in seawater by liquid chromatography/tandem mass spectrometry. *Rapid Commun. Mass Spectrom.* **28**, 2398–2404 (2014).



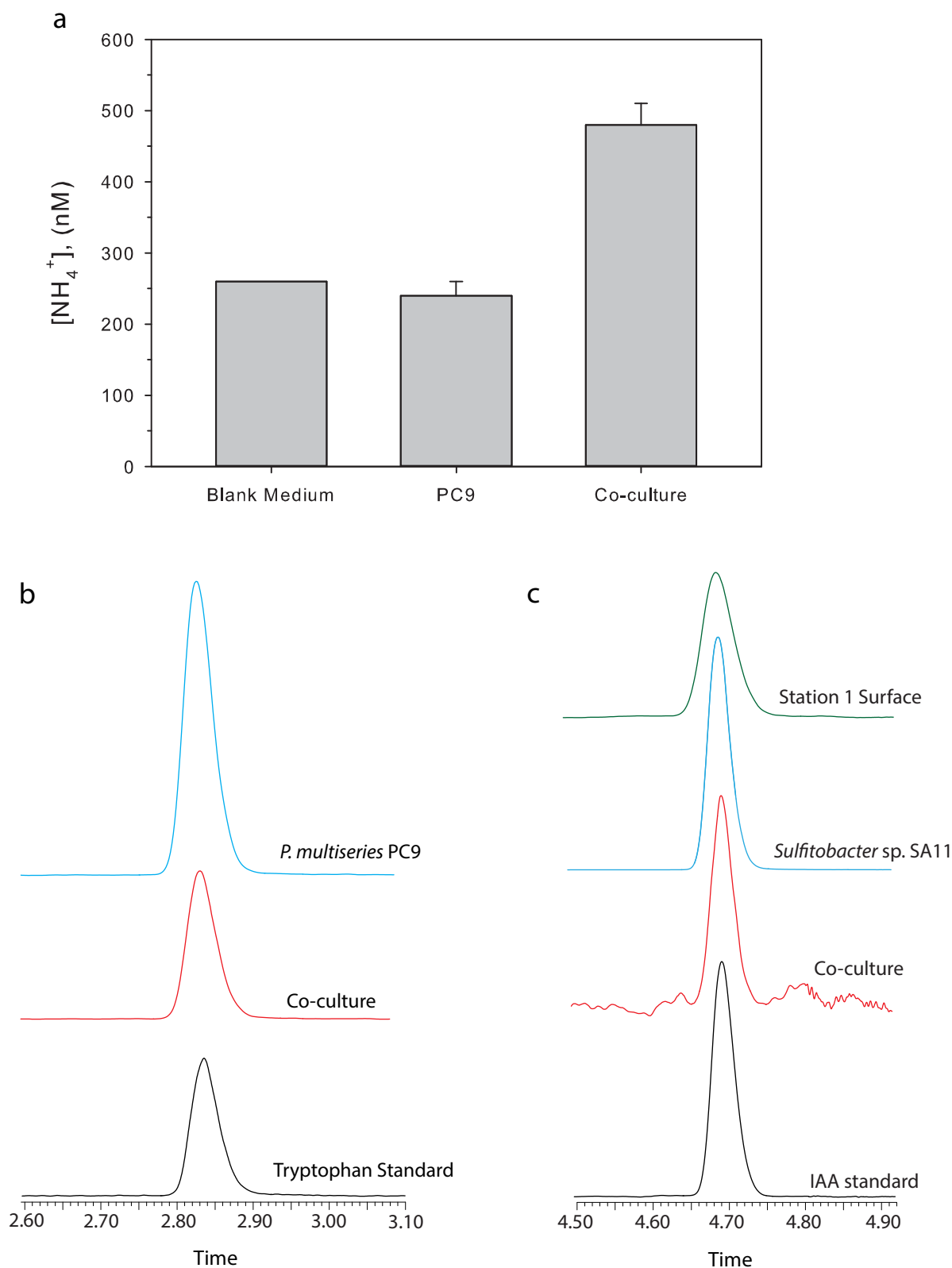
Extended Data Figure 1 | Phylogeny of *P. multiseriis*-associated bacteria. Maximum likelihood tree showing the 16S rRNA phylogeny of all bacterial strains cultivated from *P. multiseriis* isolates. Colour of bacterial strain designation indicates which isolate of *P. multiseriis* a bacterial strain originated from: red, PC9; blue, PnCLNN-17; green, PC4; magenta, GGA2 (see Extended

Data Table 1). Genera/clades that were considered to be associated with *P. multiseriis* (contained two or more isolates from different diatom cultures with >99% 16S rRNA identity) are highlighted in grey. Bootstrap values greater than 50 are indicated at the branch points. Detailed information about each isolate is provided in Supplementary Information Table 1.



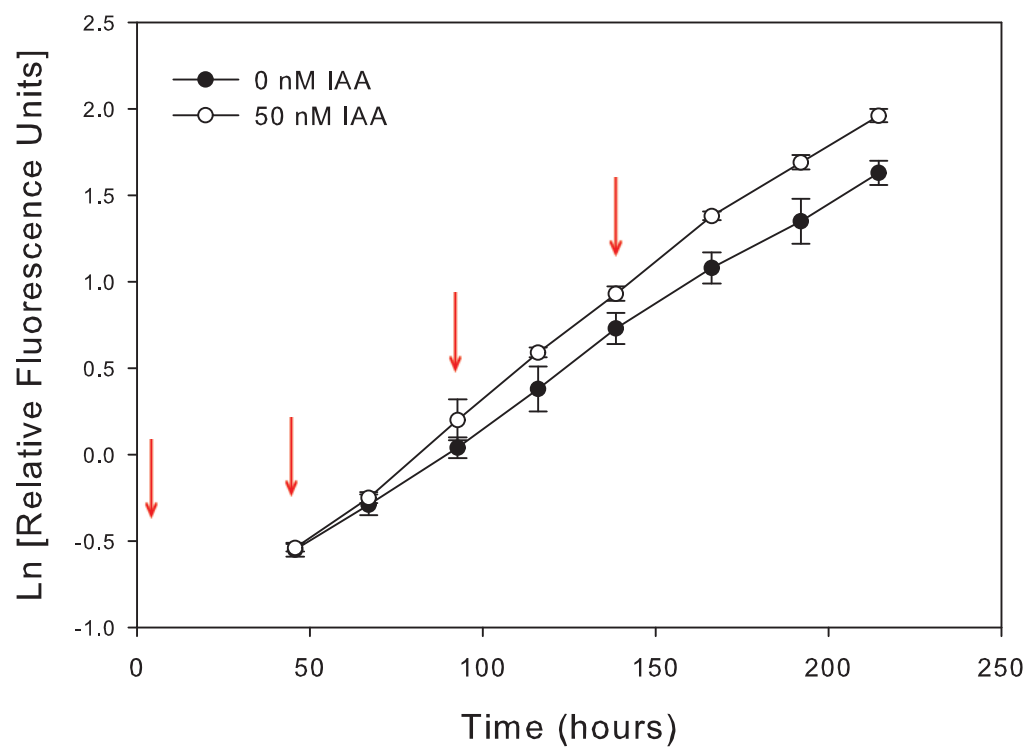
Extended Data Figure 2 | Effect of select bacterial strains on growth of *P. multiseri*. **a**, Growth of *P. multiseri* PC9 in the presence of different representative bacteria from its consortium (open circles) relative to axenic growth (filled circles). Bacterial representatives (*Limnobacter*, SA37; *Marinobacter*, SA14; *Croceibacter*, SA60; *Sulfitobacter*, SA52; see Extended

Data Table 2) were inoculated at $\sim 1 \times 10^5$ cells per millilitre relative to $\sim 4,000$ cells per millilitre axenic PC9. Error bars, s.d. from triplicate cultures. **b**, Growth of *P. multiseri* IOES-1 in axenic culture or with SA11. Error bars, s.d. from four replicates.

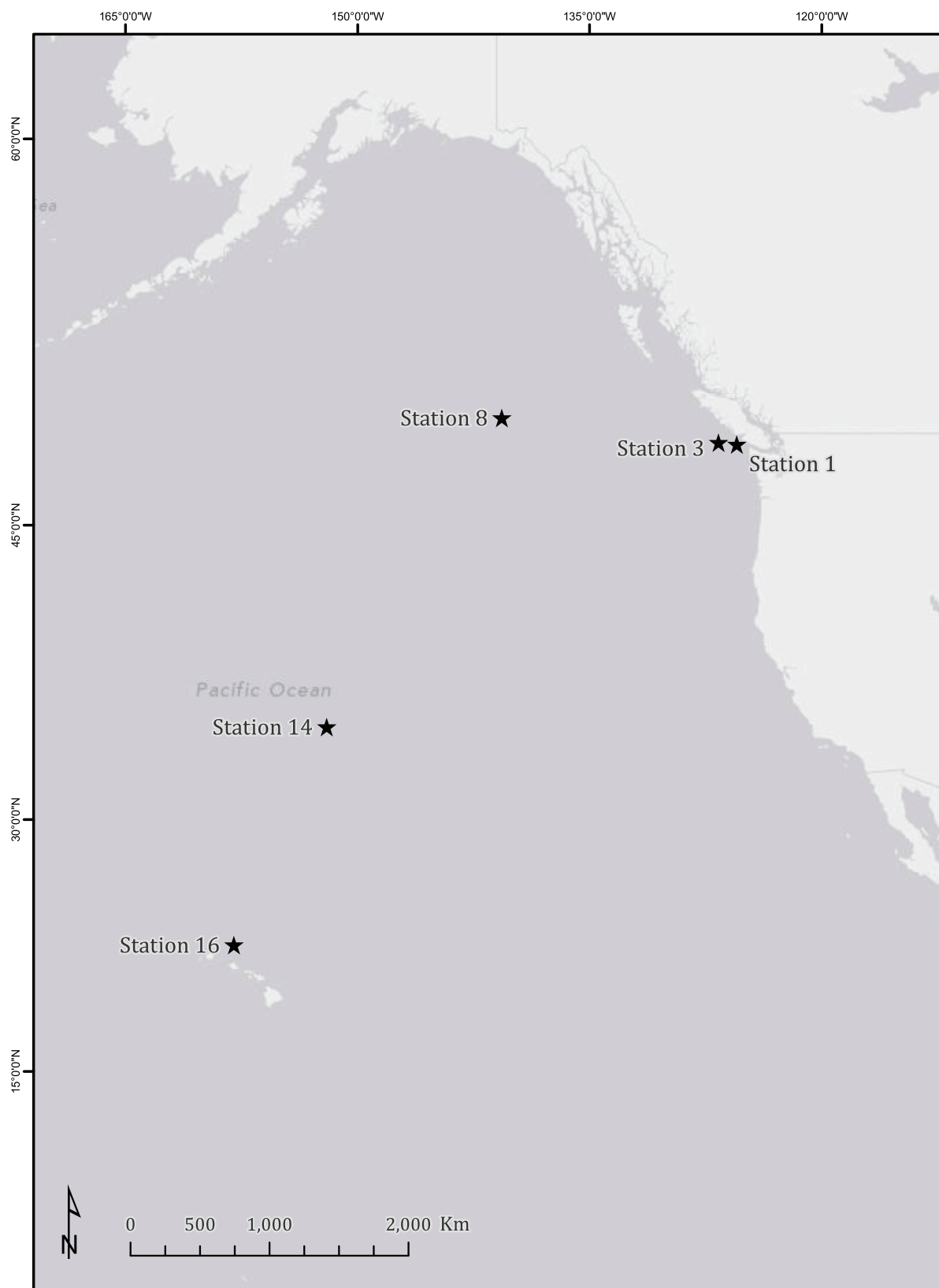


Extended Data Figure 3 | Select metabolite analyses from the *P. multiseriis*–*Sulfitobacter* sp. SA11 co-culture and the environment.
a, Dissolved ammonium concentrations in a medium blank, in axenic *P. multiseriis* PC9, and in PC9 with SA11 (co-culture). Error bars, the range from duplicate supernatants. **b**, UPLC–ESI–MS/MS chromatograms of tryptophan in axenic PC9 or co-culture supernatants. Tryptophan was detected in positive ion mode by SRM from m/z 188 to 118. A 500 pM tryptophan standard is shown for retention time comparison. Tryptophan concentrations

in the diatom monoculture and co-culture were 448 ± 106 pM and 202 ± 20 pM, respectively. **c**, UPLC–ESI–MS/MS chromatograms of IAA from surface water at station 1, SA11, and co-culture (with PC9) supernatants. IAA was detected in positive ion mode by SRM from m/z 176 to 130. A 0.5 pM IAA standard is shown for retention time comparison. IAA concentrations in the co-culture and SA11 monoculture were 6.1 ± 0.4 pM and 540 ± 280 pM, respectively.



Extended Data Figure 4 | Effect of multiple exogenous IAA additions on *P. multiseriis* GGA2. Axenic GGA2 was grown in synthetic seawater media and 50 nM IAA was added at times indicated by the red arrows. Error bars, s.d. from six cultures.



Extended Data Figure 5 | Map of stations in the North Pacific Ocean where seawater samples were collected. Surface and chlorophyll maximum waters were collected for targeted metabolite analysis (all stations indicated) and metatranscriptomics (stations 1 and 3). Station 8 coincides with historic station PAPA and station 16 coincides with station ALOHA. The different stations

exhibit dramatic differences in chemical and physical characteristics. For example, stations 1 and 3 are nutrient-rich coastal sites, station 8 is iron-limited, and stations 14 and 16 reside within the North Pacific Gyre and are oligotrophic. The map was created with Esri ArcGIS and Esri ArcMap 10.1 software.

Extended Data Table 1 | Diatom species and isolates used in this study

Species	Strain/Isolate name	Origin of Isolation	Isolation Date
<i>Pseudo-nitzschia multiseries</i>			
	PnCLNN-17 [§]	Bay of Fundy, Canada	2007
	PC9 [§]	Penn Cove, WA	2010
	PC4	Penn Cove, WA	2010
	GGA2	Golden Gardens, WA	2010
	IOES-1	East Sound, WA	2010
<i>Thalassiosira pseudonana</i>			
	CCMP1335	Long Island, NY	1958

[§] Strains from which most bacteria were isolated.

Extended Data Table 2 | Specific growth rate promotion of *P. multiseri* isolate PC9 in co-culture with different bacteria

Bacterial genus	Isolate Name	$\mu_{axenic} \pm \text{s.d.}$	$\mu_{coculture} \pm \text{s.d.}$	% change in μ
<i>Sulfitobacter</i>	SA11	0.69±0.03	1.06±0.05	35
	SA30	0.59±0.02	0.84±0.06	30
	SA44	0.40±0.01	0.49±0.01	18
	SA52	0.46±0.02	0.62±0.01	26
<i>Phaeobacter</i>	GS35	0.46±0.02	0.52±0.05	11
	GS36	0.46±0.02	0.49±0.01	6
<i>Limnobacter</i>	SA23	0.64±0.02	0.66±0.08	3
	SA37	0.59±0.02	0.54±0.09	-8
<i>Marinobacter</i>	SA14	0.64±0.1	0.70±0.06	8
<i>Croceibacter</i>	SA60	0.69±0.03	§	§

§ Growth rate could not be calculated, as the bacterium was algicidal.

Standard deviation values were calculated from biological triplicates.

Extended Data Table 3 | Specific growth rate promotion of different diatoms in co-culture with *Sulfitobacter* sp. SA11

Species	Culture name	$\mu_{axenic} \pm \text{s.d.}$	$\mu_{coculture} \pm \text{s.d.}$	% change in μ
<i>Pseudo-nitzschia multiseries</i>	PC9*	0.69±0.03	1.06±0.05	35
		0.59±0.02	0.87±0.03	32
		0.70±0.01	0.95±0.05	26
		0.75±0.03	0.94±0.04	20
		0.72±0.01	0.89±0.02	19
	GGA2	0.53±0.01	0.70±0.02	24
	PC4	0.47±0.02	0.48±0.01	2
<i>Thalassiosira pseudonana</i>	IOES-1	0.55±0.03	0.58±0.02	5
	CCMP1335	0.98±0.00	0.98±0.01	0

* Growth rate change ranged from 19-35% over five separate experiments.

Standard deviation values were calculated from biological triplicates except for IOES-1 ($n = 4$).

Extended Data Table 4 | The effect of single IAA additions on the growth of *P. multiseri* GGA2

IAA concentration	Mean Growth rate \pm s.e.
0 nM	0.53 ± 0.01
1 nM	0.53 ± 0.01
50 nM	$0.58 \pm 0.01^*$
100 nM	$0.58 \pm 0.01^*$
250 nM	0.52 ± 0.02
10 μ M	§

* Indicates statistically significant growth rate enhancement relative to 0 nM IAA.

§ Growth rate could not be calculated, as this concentration was inhibitory.

Standard error was calculated from $n = 6$ cultures.

The hypoxic cancer secretome induces pre-metastatic bone lesions through lysyl oxidase

Thomas R. Cox^{1,2}, Robin M. H. Rumney³, Erwin M. Schoof⁴, Lara Perryman¹, Anette M. Høye¹, Ankita Agrawal³, Demelza Bird², Norain Ab Latif³, Hamish Forrest³, Holly R. Evans³, Iain D. Huggins³, Georgina Lang², Rune Linding^{1,4}, Alison Gartland^{3*} & Janine T. Erler^{1,2*}

Tumour metastasis is a complex process involving reciprocal interplay between cancer cells and host stroma at both primary and secondary sites, and is strongly influenced by microenvironmental factors such as hypoxia¹. Tumour-secreted proteins play a crucial role in these interactions^{2–5} and present strategic therapeutic potential. Metastasis of breast cancer to the bone affects approximately 85% of patients with advanced disease and renders them largely untreatable⁶. Specifically, osteolytic bone lesions, where bone is destroyed, lead to debilitating skeletal complications and increased patient morbidity and mortality^{6,7}. The molecular interactions governing the early events of osteolytic lesion formation are currently unclear. Here we show hypoxia to be specifically associated with bone relapse in patients with oestrogen-receptor negative breast cancer. Global quantitative analysis of the hypoxic secretome identified lysyl oxidase (LOX) as significantly associated with bone-tropism and relapse. High expression of LOX in primary breast tumours or systemic delivery of LOX leads to osteolytic lesion formation whereas silencing or inhibition of LOX activity abrogates tumour-driven osteolytic lesion formation. We identify LOX as a novel regulator of NFATc1-driven osteoclastogenesis, independent of RANK ligand, which disrupts normal bone homeostasis leading to the formation of focal pre-metastatic lesions. We show that these lesions subsequently provide a platform for circulating tumour cells to colonize and form bone metastases. Our study identifies a novel mechanism of regulation of bone homeostasis and metastasis, opening up opportunities for novel therapeutic intervention with important clinical implications.

Using a primary tumour hypoxic signature⁸, retrospective analysis of a cohort of lymph-node-negative breast cancer patients who received no systemic adjuvant therapy⁹ revealed a significant association with metastasis specifically within oestrogen receptor (ER)-negative (ER[−]) but not ER-positive (ER⁺) patients (Fig. 1a). Moreover, analysis of metastatic site showed significant association with bone metastases over lung, liver and brain (Fig. 1b and Extended Data Fig. 1a). We performed global differential quantitative mass-spectrometry-based proteomic analysis of the hypoxic secretome associated with osteotropism using the human ER[−] MDA-MB-231 parent and matched bone tropic (clone 1833) (MDA-BT)¹⁰ breast cancer cell lines (Fig. 1c). LOX was one of the most highly upregulated secreted proteins in MDA-BT cells (Fig. 1d, Supplementary Information 1 and Extended Data Fig. 1b–d). Querying the publically available data sets for the full panel of MDA-MB-231 clonal lines¹⁰, which exhibit differing levels of osteotropism, we found LOX was significantly associated with increasing osteotropism (Fig. 1e). LOX has previously been strongly implicated in cancer metastasis^{3,11–13}, identifying it as an important candidate for further investigation.

Retrospective analysis of LOX in our patient cohort⁹ confirmed it is significantly associated with metastasis in ER[−] patients but not ER⁺

breast cancer patients (Extended Data Fig. 2a, b), consistent with previous reports¹³. Furthermore LOX is significantly associated with reported bone relapse across all patients and ER[−], but not ER⁺, patients (Fig. 1f). Cox-regression analysis showed LOX is associated with increased hazard ratio in ER[−] patients for metastasis in general and bone relapse (Extended Data Fig. 2c). Receiver operating characteristic (ROC) analysis showed LOX is indicative of metastatic dissemination (including to the bone) in ER[−] but not ER⁺ breast cancer (Extended Data Fig. 3a). Importantly, our observations were confirmed in a second data set¹⁴ (Extended Data Fig. 3b). Our findings strongly implicate LOX in bone metastases in ER[−] breast cancer patients.

We further investigated our findings in the immune-competent 4T1-BALB/c syngeneic model of spontaneously metastasizing ER[−] breast cancer which expresses high levels of LOX^{3,13} (Extended Data Fig. 4a). The MDA-MB-231 lines are not suitable as a progression model since bone metastases do not occur from orthotopic implantation. Micro-computed tomography (micro-CT) analysis of bones from 4T1 tumour-bearing mice showed decreased trabecular and cortical bone volume, trabecular number and trabecular thickness, and increased focal osteolytic lesions over time (Fig. 2a–c and Extended Data Fig. 4b–e). Significant changes were detectable from 2 weeks after implantation when tumour hypoxia is a salient feature (Extended Data Fig. 4f). Bone marrow explants and quantitative PCR with reverse transcription (qRT-PCR) confirmed osteolytic lesion formation preceded the arrival of tumour cells (Extended Data Fig. 4g–i). Strikingly, osteolytic lesion formation and cortical bone loss were also induced in a tumour-free model through injection of hypoxic tumour-conditioned media ('CM') (Fig. 2b, c)³. Our data show early osteolytic lesions are formed in the absence of tumour cells by hypoxia-induced tumour-secreted factors.

To determine LOX-dependency, mice were implanted with 4T1shLOX tumours, with decreased LOX expression and decreased LOX in sera (Extended Data Figs 4a and 5a). Micro-CT analysis revealed decreased osteolytic lesions in these mice (Fig. 2d, e), with no effect on primary tumour growth (Extended Data Fig. 5b). Immunological inhibition of LOX in 4T1 scrambled control (4T1scr) tumour-bearing mice with our antibody that binds specifically to LOX¹² and blocks enzymatic function¹³, also decreased focal osteolytic lesion formation (Fig. 2f). Consistently, in tumour-free models, injection of 4T1shLOX CM generated fewer focal osteolytic lesions than 4T1scr CM (Fig. 2g).

We confirmed our findings in another, previously published human colorectal cancer model with manipulated LOX expression¹⁵. SW480 is a non-metastatic colorectal cancer cell line with low LOX expression, whose metastatic ability is increased by overexpression of wild-type LOX (+LOX) but not a catalytically inactive mutant (K320A) (+mutLOX)¹⁵. SW480+LOX CM injection showed increased frequency and size of osteolytic lesions compared with SW480+mutLOX or SW480+EV CMs (Fig. 2h and Extended Data Fig. 5c).

¹Biotech Research and Innovation Centre (BRIC), University of Copenhagen (UCPH), Copenhagen, DK-2200, Denmark. ²Hypoxia and Metastasis Team, Cancer Research UK Tumour Cell Signalling Unit, The Institute of Cancer Research, London SW3 6JB, UK. ³The Mellanby Centre for Bone Research, The University of Sheffield, Sheffield S10 2RX, UK. ⁴Cellular Signal Integration Group (C-SIG), Technical University of Denmark (DTU), Lyngby, DK-2800, Denmark.

*These authors contributed equally to this work.

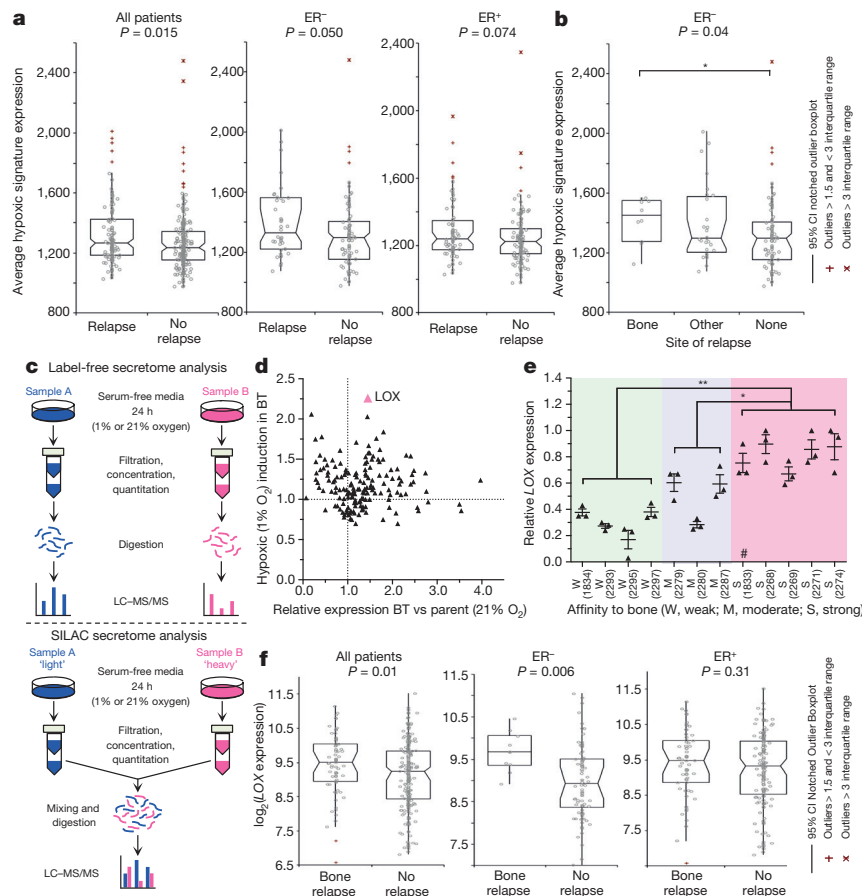


Figure 1 | Tumour-secreted LOX is a critical player in ER⁻ breast cancer bone metastasis.
a, Retrospective analysis of 344 lymph-node-negative primary breast cancers. The hypoxic signature is associated with relapse in all patients, specifically ER⁻ patients, but not ER⁺ patients.
b, Further analysis indicates the hypoxic signature is specifically associated with bone relapse.
c, Schematic overview of quantitative stable isotope labelling by amino acids in cell culture (SILAC) and label-free global proteomic secretome analysis approaches.
d, LOX is more than 1.5-fold upregulated in bone tropic (BT) compared with parental cells and the most hypoxia regulated (>2.25-fold) protein associated with osteotropism. A full list is available in Supplementary Information.
e, log₂ median centred expression of LOX mRNA in MDA-MB-231 parental and subclone lines (*n* = 3 probe sets per cell line) (# indicates 1833 'BT' clone used). **P* < 0.05, ***P* < 0.01, unpaired parametric two-tailed *t*-tests.
f, LOX expression specifically associates with bone relapse in ER⁻ breast cancer patients but not ER⁺ patients. **a**, **b**, **f**, *P* values derived from a two-tailed Mann–Whitney test.

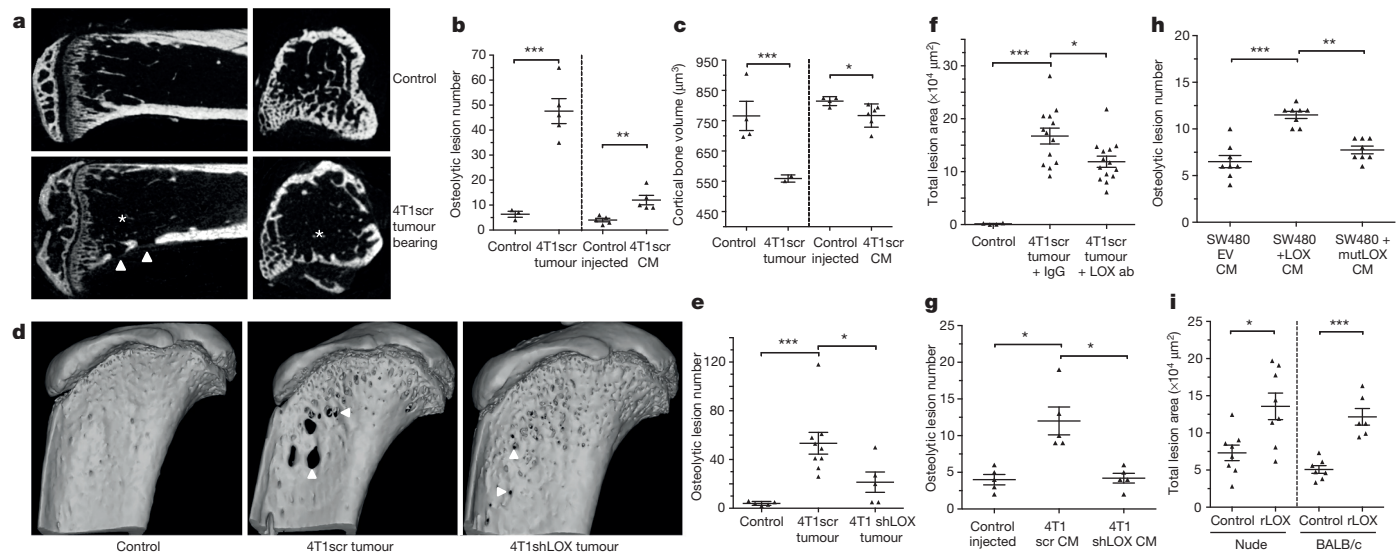


Figure 2 | Osteolytic lesion formation in ER⁻ mammary carcinoma models is LOX dependent.
a, Representative two-dimensional cross-sections of tibia from control (top) and tumour-bearing (bottom) mice 3 weeks after orthotopic implantation showing lesions (arrowheads) and loss of trabecular structure (asterisks).
b, Micro-CT analysis of osteolytic lesions in tumour-bearing and tumour-free, CM-conditioned mice at 3 weeks (*n* mice; control 3; 4T1scr tumour 5; control injected 5; 4T1scr CM 5).
c, Loss of cortical bone volume in 4T1scr tumour-bearing and tumour-free CM-injected models at 3 weeks (*n* mice; control 4; 4T1scr tumour 3; control injected 4; 4T1scr CM 6).
d, Representative three-dimensional reconstructions of tibiae showing tumour-driven osteolytic lesions (arrowheads).
e, LOX silencing decreases focal

osteolytic lesion formation (*n* mice; control 5; 4T1scr tumour 8; 4T1shLOX tumour 5).
f, LOX inhibition decreases osteolytic lesion formation in tumour-bearing models (*n* mice; control 5; 4T1scr tumour + immunoglobulin G (IgG) 13; 4T1scr tumour + LOX Ab 14) and **g**, in tumour-free CM injection models (*n* mice; control 5; 4T1scr CM 5; 4T1shLOX CM 5).
h, SW480 human colorectal cancer lines with stably manipulated LOX expression (EV, +LOX or +mutLOX) confirms LOX-dependency (*n* = 8 mice per condition).
i, Exogenous recombinant LOX (rLOX) drives osteolytic lesion formation in nude and BALB/c models (*n* mice; nude control 8; nude rLOX 8; BALB/c control 7; BALB/c rLOX 6). **b**, **c**, **e**–**i**, Data are mean ± s.e.m. **P* < 0.05, ***P* < 0.01, ****P* < 0.001, unpaired parametric one-tailed *t*-tests.

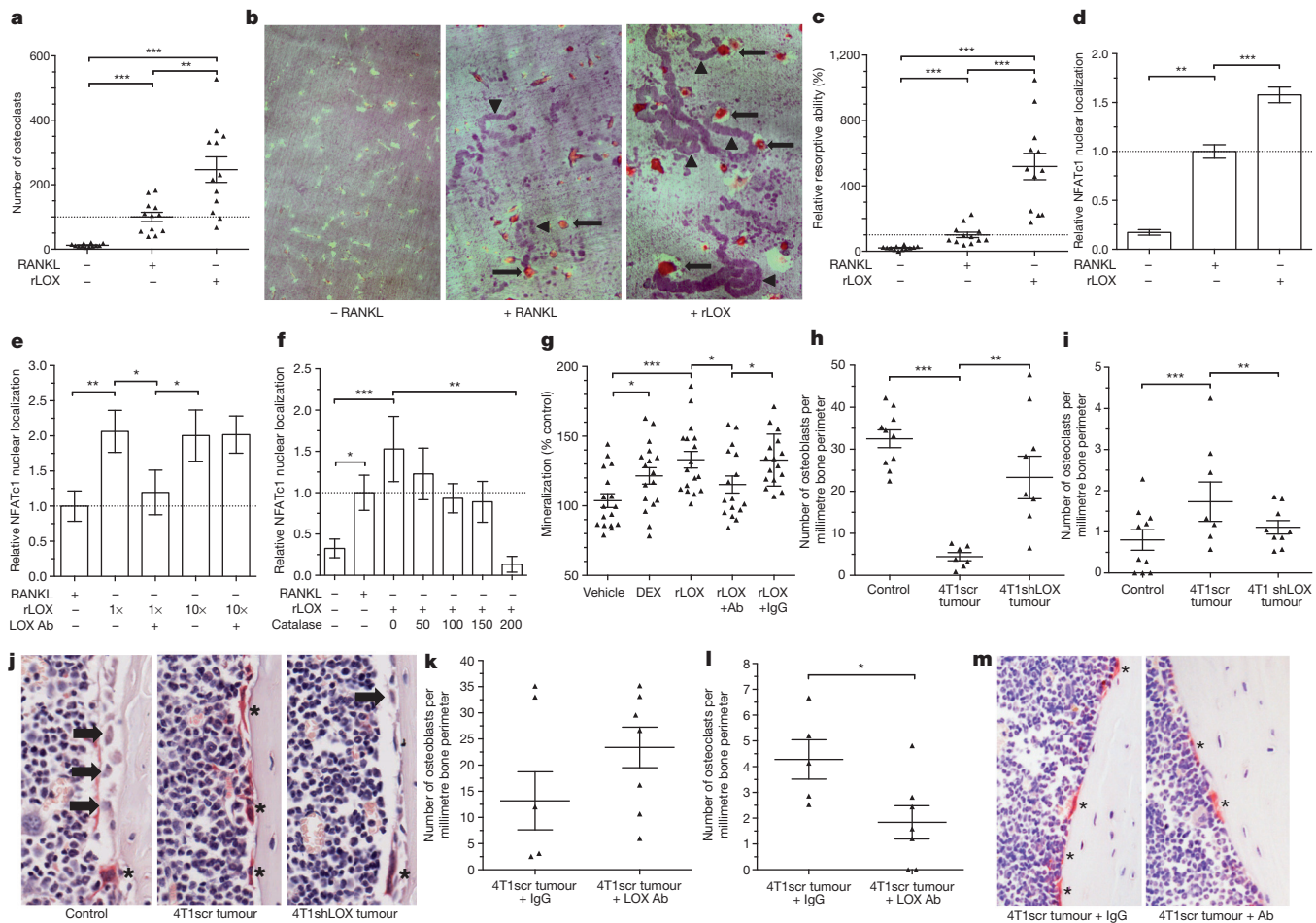


Figure 3 | Tumour-secreted LOX modulates osteoclasts and osteoblasts *in vitro* and *in vivo*. **a**, rLOX (in the absence of RANKL) stimulates osteoclastogenesis. **b**, **c**, rLOX generated osteoclasts exhibit high resorptive ability; arrow, osteoclast; arrowheads, resorption tracks (**a–c**) (*n*: osteoclast count from 12 independent osteoclast assays per group). **d**, rLOX induces nuclear localization of the master transcription factor NFATc1 in the absence of RANKL (*n*: osteoclast NFATc1 nuclear intensity; control 12; +RANKL 196, +rLOX 191 across three independent experimental repeats (donors) from 16 fields of view per donor). **e**, LOX antibody treatment blocks NFATc1 localization. **f**, Catalase treatment blocks rLOX-induced nuclear localization of NFATc1 (**e**, **f**, represent data from 32 measurements of NFATc1 nuclear intensity from each of three independent donors (96 total)). **g**, rLOX added to primary mouse calvarial osteoblasts increases mineralization ability (DEX, dexamethasone) (*n*: alizarin

red S intensity; 16 wells per group across two independent experimental repeats). **h**, **i**, 4T1scr mammary tumours decrease osteoblast number compared with shLOX (*n*: mice; control 10; 4T1scr tumour 7; 4T1 shLOX tumour 9) (**h**) and increase osteoclast number on the endocortical surface of bone (per millimetre bone perimeter) (*n*: mice; control 10; 4T1scr tumour 8; 4T1 shLOX tumour 9) (**i**). **j**, Representative images of osteoblasts (arrows) and osteoclasts (star) in sections of bone. **k**, 4T1scr tumour-bearing mice treated with the anti-LOX antibody show similar effects on osteoblast number and **l**, osteoclast number to shLOX tumour-bearing mice (*n*: mice; 4T1scr tumour + IgG 5; 4T1scr tumour + LOX Ab 7). **m**, Representative sections of bone from 4T1scr tumour-bearing mice with or without anti-LOX antibody or IgG control. **a**, **c–i**, **k**, **l**, Data are mean \pm s.e.m. **P* < 0.05, ***P* < 0.01, ****P* < 0.001, unpaired parametric two-tailed *t*-test.

While bone metastases in patients with colorectal cancer are rare, our data show that high levels of secreted active LOX drive focal osteolytic lesion formation in the bone independently of tumour presence across multiple cancer types. Injection of recombinant LOX (rLOX) into both immune-compromised nude and immune-competent BALB/c mice also led to the formation of focal osteolytic lesions (Fig. 2i) and increased circulating carboxy terminal telopeptide (CTX), a biomarker of bone turnover (Extended Data Fig. 5d). Our data clearly demonstrate tumour-secreted LOX as a mediator of osteolytic lesions.

Bone homeostasis is a balance between bone resorption by osteoclasts and bone formation by osteoblasts. This balance is typically disrupted in cancer metastasis. Addition of rLOX (in the absence of RANK ligand (RANKL)) to pre-osteoclast cultures was a highly effective stimulator of osteoclastogenesis, generating greater numbers of osteoclasts (Fig. 3a) with a higher resorptive capacity than RANKL-stimulated cultures (Fig. 3b, c). Enzyme-linked immunosorbent assays (ELISAs) for RANKL in rLOX-treated culture supernatants showed no RANKL, ruling out autocrine production of RANKL, and mass

spectrometry analysis of rLOX preparations excluded the presence of contaminating effectors (Extended Data Fig. 6a, b). Our data show LOX can stimulate the generation of fully differentiated, active osteoclasts independently of RANKL.

Osteoclastogenesis is driven by the nuclear translocation of NFATc1, the master regulator of osteoclastogenesis¹⁶. Addition of rLOX (in the absence of RANKL) induced greater nuclear localization of NFATc1 than RANKL (Fig. 3d and Extended Data Fig. 6c), which was disrupted by treatment with our LOX-targeting antibody in a dose-dependent manner (Fig. 3e and Extended Data Fig. 6c). A by-product of LOX activity is the reactive oxygen species hydrogen peroxide (H₂O₂). Reactive oxygen species have previously been suggested to influence osteoclast differentiation and function^{17,18}. Treatment of human pre-osteoclast cultures with rLOX in the presence of catalase (which rapidly degrades H₂O₂) abrogated rLOX-driven NFATc1 nuclear localization in a dose-dependent manner (Fig. 3f). Our data identifies a novel, LOX-activity-dependent mechanism of *de novo* osteoclastogenesis which occurs independently of RANKL. Addition

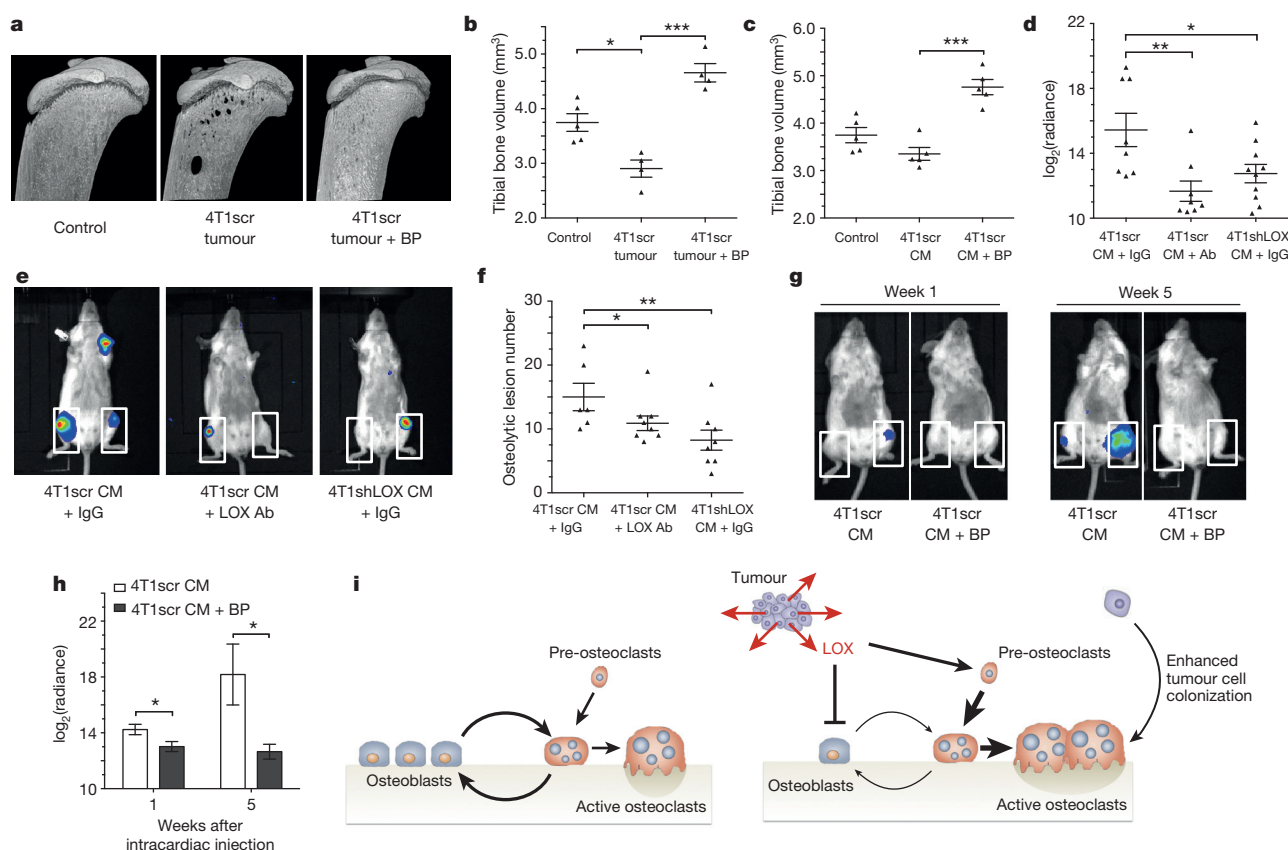


Figure 4 | LOX-mediated lesions are osteoclast-driven and enhance circulating tumour cell colonization. **a**, Representative three-dimensional reconstructions of tibiae from tumour-bearing mice with or without bisphosphonate treatment. **b**, Tibial bone loss is abrogated in tumour-bearing mice treated with bisphosphonate (n : mice; control 5; 4T1scr tumour 4; 4T1scr tumour + bisphosphonate 4). **c**, Similar effects are observed in CM-conditioned models treated with bisphosphonate (n = 5 mice all groups). **d**, **e**, Quantification (**d**) and representative whole-body IVIS imaging (**e**) of intracardially injected 4T1Luc tumour cells after conditioning with 4T1scr or 4T1shLOX CM. (n : mice; 4T1scr CM + IgG 8; 4T1scr CM + LOXAb 8; 4T1shLOX CM + IgG 10). **f**, Micro-CT lesion analysis of mice after intracardiac injection following pre-conditioning (n : mice; 4T1scr CM + IgG 6; 4T1scr CM + LOXAb 8; 4T1shLOX CM + IgG 8). **g**, Representative whole-body IVIS imaging of 4T1Luc tumour cells at 1 and 5 weeks after intracardiac injection. Mice were conditioned with hypoxic 4T1scr CM with and without simultaneous treatment with bisphosphonate. White boxes in **e** and **g** denote, tumour burden analysis region-of-interest. **h**, \log_2 quantification of **g** (n = 5 mice all groups). **i**, Schematic of LOX-mediated effects on bone homeostasis *in vivo*. **b–d**, **f**, **h**, Data are mean \pm s.e.m. * P < 0.05, ** P < 0.01, *** P < 0.001, unpaired parametric two-tailed t -test.

of rLOX to primary calvarial mouse osteoblasts decreased proliferation and led to an increase in terminal differentiation, which was attenuated by our LOX blocking antibody (Fig. 3g and Extended Data Fig. 6d). Similarly, high LOX 4T1scr CM decreased proliferation and increased differentiation of the human osteoblast SaOS-2 cell line (Extended Data Fig. 6e, f), which was attenuated by treatment with our LOX antibody. Our data show LOX leads to a loss of proliferative phenotype and increased terminal differentiation of osteoblasts.

Consistent with LOX tipping the balance of bone homeostasis in the favour of osteoclast resorption, quantification of osteoblasts and osteoclasts on the endocortical surface of tibiae from tumour-bearing mice showed decreased osteoblast and increased osteoclast number in 4T1scr tumour-bearing mice (Fig. 3h–j). Partial reversion was evident in mice treated with our LOX antibody and in mice bearing 4T1shLOX tumours (Fig. 3h–m and Extended Data Fig. 7a). Thus, tumour-secreted LOX is an important modulator of bone homeostasis. Treatment of tumour-bearing and CM-injected mice with clinically relevant concentrations of the bisphosphonate zoledronic acid abrogated focal osteolytic lesion formation (Fig. 4a–c) without affecting primary tumour growth (Extended Data Fig. 7b). Our data highlight the potential for therapeutic intervention of LOX-mediated osteoclast-driven pre-metastatic lesion formation in the bone.

The functional consequence of LOX-mediated pre-metastatic focal osteolytic lesion formation was tested by pre-conditioning BALB/c mice with either 4T1scr CM with or without LOX antibody, or

4T1shLOX CM + IgG 10). **f**, Micro-CT lesion analysis of mice after intracardiac injection following pre-conditioning (n : mice; 4T1scr CM + IgG 6; 4T1scr CM + LOXAb 8; 4T1shLOX CM + IgG 8). **g**, Representative whole-body IVIS imaging of 4T1Luc tumour cells at 1 and 5 weeks after intracardiac injection. Mice were conditioned with hypoxic 4T1scr CM with and without simultaneous treatment with bisphosphonate. White boxes in **e** and **g** denote, tumour burden analysis region-of-interest. **h**, \log_2 quantification of **g** (n = 5 mice all groups). **i**, Schematic of LOX-mediated effects on bone homeostasis *in vivo*. **b–d**, **f**, **h**, Data are mean \pm s.e.m. * P < 0.05, ** P < 0.01, *** P < 0.001, unpaired parametric two-tailed t -test.

4T1shLOX CM to stimulate focal osteolytic lesion formation. 4T1 luciferase-expressing tumour cells (4T1Luc) were then injected intracardially. Bioluminescent IVIS imaging and micro-CT analysis revealed increased tumour burden in 4T1scr CM-conditioned mice compared with LOX antibody treated or 4T1shLOX CM-conditioned mice (Fig. 4d–f). A Pearson correlation coefficient showed a positive correlation between IVIS signal and lesion number (Extended Data Fig. 7c). Our data demonstrate that LOX-mediated pre-metastatic focal osteolytic lesions generate niches within the bone microenvironment that support colonization of circulating tumour cells and the formation of overt bone metastases. Treatment with bisphosphonate during 4T1scr CM conditioning of mice significantly reduced the ability of intracardially injected 4T1Luc cells to colonize the bone 1 week after injection and to develop bone metastases 5 weeks after injection (Fig. 4g, h). Thus, bisphosphonate treatment of patients with high-LOX-expressing tumours after surgery could prevent the establishment and growth of circulating tumour cells within the bone.

Pre-metastatic preparation of secondary sites to facilitate subsequent tumour cell colonization has been reported by us and others^{3,4,19} in several organs across multiple cancers; however, so far, the formation of pre-metastatic focal osteolytic lesions directly by tumour-secreted factors has not been described. We are the first to demonstrate, to our knowledge, that LOX activity modulates bone homeostasis, acting directly on osteoblasts and osteoclasts (Fig. 4i). Global bone loss before tumour cell arrival has been previously linked

to indirect effects of tumour-secreted factors through RANKL-dependent mechanisms²⁰. We present a novel mechanism of deregulation of bone homeostasis independent of RANKL, yet acknowledge that other factors probably contribute to this inherently complex process. Interestingly, the post-translationally cleaved LOX propeptide, known for its opposing inhibitory effects to that of the mature LOX enzyme²¹, has been reported to modulate osteoblast behaviour through an intracellular mechanism inhibiting mineralization ability²². Yet embryonic day (E)18.5 *Lox*^{-/-} mice exhibit markedly decreased mineral nodule formation and osteoblast differentiation²³, supporting our data and suggesting context-dependent effects. LOX is reportedly expressed in osteoblasts and induced by TGF- β released during bone resorption²⁴, which could further stimulate osteoclastogenesis leading to unbalanced coupling of bone homeostasis and focal osteolytic lesions. Since LOX-dependent pre-metastatic lesions form in the bone at the same time as those formed in the lungs and liver³, we believe that these osteolytic lesions are independent, forming simultaneously through unrelated mechanisms.

Our data suggest LOX may well be a useful marker for predicting the likelihood of metastases to the bone in ER⁻ breast cancer patients and identifying these patients for adjuvant bisphosphonate treatment. Our data highlight that the dosing and administration of LOX inhibitors under development will be critical as genetic targeting yielded more potent effects than our antibody in this study, and earlier work has shown that treatment with the non-specific LOX inhibitor β -aminopropionitrile can reduce bone colonization in intracardiac models when administered at the time of inoculation²⁵. In summary, our insight into the very early mechanisms of bone metastases before, and independent of tumour cell arrival, identifies a new step in bone metastasis and novel opportunities for therapeutic intervention.

Online Content Methods, along with any additional Extended Data display items and Source Data, are available in the online version of the paper; references unique to these sections appear only in the online paper.

Received 10 July 2014; accepted 23 April 2015.

Published online 27 May 2015.

- Chan, D. A. & Giaccia, A. J. Hypoxia, gene expression, and metastasis. *Cancer Metastasis Rev.* **26**, 333–339 (2007).
- Jin, L. *et al.* Differential secretome analysis reveals CST6 as a suppressor of breast cancer bone metastasis. *Cell Res.* **22**, 1356–1373 (2012).
- Erler, J. T. *et al.* Hypoxia-induced lysyl oxidase is a critical mediator of bone marrow cell recruitment to form the premetastatic niche. *Cancer Cell* **15**, 35–44 (2009).
- Kaplan, R. N. *et al.* VEGFR1-positive haematopoietic bone marrow progenitors initiate the pre-metastatic niche. *Nature* **438**, 820–827 (2005).
- Blanco, M. A. *et al.* Global secretome analysis identifies novel mediators of bone metastasis. *Cell Res.* **22**, 1339–1355 (2012).
- Coleman, R. E. & Rubens, R. D. The clinical course of bone metastases from breast cancer. *Br. J. Cancer* **55**, 61–66 (1987).
- Steeg, P. S. Tumor metastasis: mechanistic insights and clinical challenges. *Nature Med.* **12**, 895–904 (2006).
- Chi, J. T. *et al.* Gene expression programs in response to hypoxia: cell type specificity and prognostic significance in human cancers. *PLoS Med.* **3**, e47 (2006).
- Smid, M. *et al.* Subtypes of breast cancer show preferential site of relapse. *Cancer Res.* **68**, 3108–3114 (2008).
- Kang, Y. *et al.* A multigenic program mediating breast cancer metastasis to bone. *Cancer Cell* **3**, 537–549 (2003).
- El-Haibi, C. P. *et al.* Critical role for lysyl oxidase in mesenchymal stem cell-driven breast cancer malignancy. *Proc. Natl Acad. Sci. USA* **109**, 17460–17465 (2012).
- Cox, T. R. *et al.* LOX-mediated collagen crosslinking is responsible for fibrosis-enhanced metastasis. *Cancer Res.* **73**, 1721–1732 (2013).
- Erler, J. T. *et al.* Lysyl oxidase is essential for hypoxia-induced metastasis. *Nature* **440**, 1222–1226 (2006).
- van de Vijver, M. J. *et al.* A gene-expression signature as a predictor of survival in breast cancer. *N. Engl. J. Med.* **347**, 1999–2009 (2002).
- Baker, A. M., Bird, D., Lang, G., Cox, T. R. & Erler, J. T. Lysyl oxidase enzymatic function increases stiffness to drive colorectal cancer progression through FAK. *Oncogene* **32**, 1863–1868 (2012).
- Boyle, W. J., Simonet, W. S. & Lacey, D. L. Osteoclast differentiation and activation. *Nature* **423**, 337–342 (2003).
- Garrett, I. R. *et al.* Oxygen-derived free radicals stimulate osteoclastic bone resorption in rodent bone *in vitro* and *in vivo*. *J. Clin. Invest.* **85**, 632–639 (1990).
- Bax, B. E. *et al.* Stimulation of osteoclastic bone resorption by hydrogen peroxide. *Biochem. Biophys. Res. Commun.* **183**, 1153–1158 (1992).
- Hiratsuka, S., Watanabe, A., Aburatani, H. & Maru, Y. Tumour-mediated upregulation of chemoattractants and recruitment of myeloid cells predetermines lung metastasis. *Nature Cell Biol.* **8**, 1369–1375 (2006).
- Monteiro, A. C. *et al.* T cells induce pre-metastatic osteolytic disease and help bone metastases establishment in a mouse model of metastatic breast cancer. *PLoS ONE* **8**, e68171 (2013).
- Barker, H. E., Cox, T. R. & Erler, J. T. The rationale for targeting the LOX family in cancer. *Nature Rev. Cancer* **19**, 540–552 (2012).
- Vora, S. R. *et al.* Lysyl oxidase propeptide inhibits FGF-2-induced signaling and proliferation of osteoblasts. *J. Biol. Chem.* **285**, 7384–7393 (2010).
- Pischon, N. *et al.* Lysyl oxidase (*Lox*) gene deficiency affects osteoblastic phenotype. *Calcif. Tissue Int.* **85**, 119–126 (2009).
- Feres-Filho, E. J., Choi, Y. J., Han, X., Takala, T. E. & Trackman, P. C. Pre- and post-translational regulation of lysyl oxidase by transforming growth factor-beta 1 in osteoblastic MC3T3-E1 cells. *J. Biol. Chem.* **270**, 30797–30803 (1995).
- Bondareva, A. *et al.* The lysyl oxidase inhibitor, beta-aminopropionitrile, diminishes the metastatic colonization potential of circulating breast cancer cells. *PLoS ONE* **4**, e6520 (2009).

Supplementary Information is available in the online version of the paper.

Acknowledgements We thank the animal welfare staff at the Institute of Cancer Research and Biocentre (University of Copenhagen); the Bone Analysis Laboratory (The University of Sheffield); M. Smid, J. W. M. Martens and J. A. Foekens (Erasmus MC Cancer Institute, Rotterdam, The Netherlands) for in-depth patient data analyses; and A. J. Giaccia and members of our laboratories for comments. This research was supported by funding from Cancer Research UK (C107/A10433) (T.R.C., D.B., G.L.J.T.E.), the Biotech Research and Innovation Centre (BRIC, University of Copenhagen) (T.R.C.), The University of Sheffield (A.G., I.D.H.), National Institute for Health Research Sheffield Clinical Research Facility (A.G.), Breast Cancer Campaign (#2012MayPR086) (A.G., R.M.H.R.), and the Danish Cancer Society (R56-A2971-12-S2) (A.M.H.). Experiments in the laboratory of R.L. were funded by The Lundbeck Foundation and the work was supported by the Velux Foundations (VKR) funded Instrument Center for Systems Proteomics (VKR 022758). L.P. and J.T.E. are supported by a Hallas Møller Stipendium from the Novo Nordisk Foundation.

Author Contributions J.T.E. and A.G. conceived the project, assisted by T.R.C. T.R.C., A.G. and J.T.E. designed the experiments. T.R.C., A.G. and R.M.H.R. performed the *in vivo* and *in vitro* experiments and analysed the data assisted by L.P., A.H., A.A., D.B., N.A.L., H.F., H.R.E., I.D.H. and G.L. T.R.C. and E.M.S. designed and performed the mass spectrometry and proteomics experiments and analysis, supervised by R.L. T.R.C. wrote and edited the paper, assisted by A.G., J.T.E., R.L. and R.M.H.R.

Author Information Reprints and permissions information is available at www.nature.com/reprints. The authors declare no competing financial interests. Readers are welcome to comment on the online version of the paper. Correspondence and requests for materials should be addressed to J.T.E. (janine.erler@bric.ku.dk) or A.G. (a.gartland@shef.ac.uk).

METHODS

For *in vivo* experiments, sample size was estimated to be eight mice per treatment group to ensure more than 80% power with 95% confidence, based on 25% practical difference and 15% coefficient of variation.

Patient data analysis. Evaluation of the expression of a previously published hypoxic signature⁸ and *LOX* with respect to metastasis and organ specific relapse was conducted using a published cohort of 344 primary breast cancers from lymph-node-negative patients who had not received systemic adjuvant therapy and with available gene expression data and site of relapse information. Details on patients and gene expression analysis can be found in ref. 9. *P* values were derived from a Mann–Whitney test and were two-tailed. An additional Kruskal–Wallis test between reported bone relapse, relapse elsewhere and no relapse patients with an additional contrast test wherein all pairwise groups were considered was conducted for *LOX* expression. Cox-regression using \log_2 (*LOX* expression data) was used to estimate the hazard ratio in two analyses. One analysis used the no-relapse patients and the bone relapse patients, and the second analysis included all patients. An alternative second patient data set¹⁴ reporting data on 295 lymph-node-negative patients who did not receive adjuvant therapy, with available site of relapse, was used to confirm our *LOX*-based findings.

***In vitro* culturing of tumour cells.** Unless stated otherwise in the following sections, all cell lines were routinely cultured in DMEM with 100 U ml⁻¹ penicillin and 100 µg ml⁻¹ streptomycin, plus 10% FBS. For CM collection experiments, cells were transferred to serum-free DMEM without phenol red and incubated at either 21% oxygen (normoxia) or 1% oxygen (hypoxia) for 24 h in a Hypoxystation (Don Whitley Scientific). All CMs were filtered before use. For SILAC for mass spectrometry studies, tumour cells were grown in DMEM containing labelled isotopic amino acids, either light isotope (¹²C-, ¹⁴N-arginine; ¹²C-, ¹⁴N-lysine) (R0/K0) or heavy isotope (¹³C-, ¹⁵N-arginine; ¹³C-, ¹⁵N-lysine) (R10/K8) for five passages before incorporation was assessed. A minimum of 97–98% labelled arginine and lysine incorporation, with less than 1% proline conversion, was required for subsequent proteomics studies. The MDA-MB-231 BT cell line was obtained from J. Massagué at the Memorial Sloan-Kettering Cancer Center. The 4T1 wild-type cell line was obtained from F. Miller at the University of Michigan. The SaOS-2 cell line was obtained from J. Gallagher at Liverpool University. The MDA-MB-231 parental cell line was obtained from the American Type Culture Collection (ATCC) (distributed by LGC Standards), where cell lines are authenticated on a regular basis. The 4T1Luc line was from SibTech. The 4T1 wild-type cell line was used to generate the 4T1shLOX line as previously published³. The SW480 +EV, +LOX and +mutLOX cell lines were previously generated and authenticated using short tandem repeat analysis²⁶. All cell lines were routinely tested for mycoplasma and tested negative for murine pathogens by IMPACT testing (IDEXX Laboratories).

Mass spectrometry acquisition and secretome analysis. After collection, label-free and SILAC-labelled CMs were filtered and reduced in volume using 10 kDa molecular mass cut-off filters. The remaining protein was dissolved in 6 M urea, 2 M thiourea and 10 mM HEPES pH 8, after which exact protein amounts were determined using a Bradford assay. In SILAC-labelled repeats, the two SILAC labels (R10/K8 and R0/K0) were mixed 1:1. In label-free repeats, the samples were left unmixed as depicted in Fig. 1c, but equal amounts of starting material were used for processing. Proteins were reduced in 1 mM DTT (Sigma) for 45 min at room temperature (21°C), alkylated for 45 min using 5.5 mM chloroacetamide (Sigma), and digested with 1:50 (enzyme:protein ratio) of mass spectrometry (MS)-grade trypsin (Sigma) overnight at 37°C. Peptides were acidified with trifluoroacetic acid at a final concentration of 2%, and 5 µg of peptides were loaded onto a 50 cm C18 reverse-phase analytical column (Thermo EasySpray ES803) using an EASY nanoLC 1000. Peptides were eluted over a 4 h gradient ranging from 6 to 60% of 80% acetonitrile, 0.1% formic acid, and the Q-Exactive (Thermo Fisher Scientific) was run in a DD-MS2 top10 method. Full MS spectra were collected at a resolution of 70,000, with an AGC target of 3×10^6 or maximum injection time of 20 ms and a scan range of 300–1750 *m/z*. The MS² spectra were obtained at a resolution of 17,500, with an AGC target value of 1×10^6 or maximum injection time of 60 ms. Dynamic exclusion was set to 45 s, and ions with a charge state <2 or unknown were excluded. MS performance was verified for consistency by running complex cell lysate quality control standards, and chromatography was monitored to check for reproducibility. Raw data were processed using MaxQuant version 1.5 and Perseus version 1.4. Results were analysed using scripts written in-house in Python, and statistically tested for significance using the quantile function in the R statistical framework. To ensure high confidence identifications and quantification, a MaxQuant score of >50 and a minimum of two unique peptides per protein seen by tandem MS in all repeats were required. Initial analysis was undertaken using a label-free approach (two repeats) for global pairwise analyses, and data subsequently validated in a standard- and

reverse-label SILAC approach (two repeats). Identified intracellular contaminants were removed and secreted proteins retained by using the cellular compartment annotations in Ensembl and PantherDB, and Gene Ontology annotation enrichment for extracellular-associated terms. Raw mass spectrometry data along with in-house python scripts are available online at ProteomeXchange Consortium (<http://proteomecentral.proteomexchange.org>) with the data set identifier PXD000397.

Microarray data analysis of MDA-MB-231 cells. Previously published microarray data for parental and *in vivo* selected osteotropic subclones of the human MDA-MB-231 breast cancer line were retrieved (GEO accession number GSE2603). The subclones have previously been described and shown to be either weakly, mildly or strongly osteotropic¹⁰. All data sets were normalized and centred to the median of *LOX* probes.

***In vivo* models.** Before the start of experiments, mice were randomly allocated into cages. Each mouse within the same cage received the same treatment. Cages were subsequently randomly allocated for treatment. Sample size was estimated to be eight mice per treatment group to ensure >80% power with 95% confidence, based on 25% practical difference and 15% coefficient of variation. For tumour-bearing studies, 2×10^5 4T1scr or 4T1shLOX or 4T1Luc cells were injected into the mammary fat pad of 8-week-old female BALB/c mice (Taconic). The tumour-free model has been previously described³, where 300 µl of tumour-cell CM is injected intraperitoneally daily into mice for 3 weeks. Rabbit anti-LOX (αLOX) antibody or rabbit IgG control treatments were administered intraperitoneally twice a week at 1 mg kg⁻¹ 2 days after implantation. The LOX antibody (synthesized by OpenBiosystems) targets a conserved peptide sequence from the active site of human and mouse proteins, blocking function as previously described¹³, and has been shown not to bind other LOX family members¹². For bisphosphonate studies, 0.6 mg kg⁻¹ zoledronic acid was injected intraperitoneally twice a week. Primary tumour measurements were performed twice a week using callipers. All experiments were performed in accordance with UK Home Office regulations following UK Coordinating Committee for Cancer Research Guidelines for the Welfare and Use of Animals in Cancer Research, or under authorization and guidance from the Danish Inspectorate for Animal Experimentation. Cell line sources are stated above in 'In vitro culturing of tumour cells' and were tested negative for murine pathogens by IMPACT testing (IDEXX Laboratories). A second previously published human model of colorectal cancer with manipulated *LOX* expression¹⁵ was used to validate *LOX*-dependent findings. SW480 is a non-metastatic colorectal cancer cell line with low *LOX* expression, whose metastatic ability can be increased through expression of wild-type *LOX* (SW480+LOX) but not a catalytically inactive mutant (K320A) (SW480+mutLOX)¹⁵. Eight-week-old female nude mice (Charles River) were injected daily with 300 µl SW480+EV (empty vector), SW480+LOX (full-length active LOX) or SW480+mutLOX (catalytically inactive mutant (K320A)) CM intraperitoneally for 3 weeks. Recombinant LOX (OriGene Technologies) in PBS was injected twice a week (25 µg kg⁻¹) intraperitoneally into 8-week-old female nude (Charles River) or BALB/c mice (Taconic) for 3 weeks. Exclusion criteria for data analysis were pre-established such that those mice terminated before defined experimental endpoints for ethical and/or licence reasons such as undue pain, suffering, distress and/or apparent lasting harm, or unexpected premature death, were not used for subsequent analysis. Values of *n* for all figures are displayed in accompanying legends.

Micro-CT imaging of tibia. Legs were removed from euthanized mice and fixed in either 4% paraformaldehyde solution or periodate–lysine–paraformaldehyde fixative. Fixed bones were dissected free of tissue and scanned on a micro-CT scanner (model 1172 Skyscan) at 50 kV with a 0.5 aluminium filter using a detection pixel size of 5 µm. The scanned images were reconstructed using Skyscan Recon software and analysed using Skyscan CT analysis software. A standard trabecular volume of interest was chosen starting 0.2 mm from the growth plate and included all trabeculae in a 1 mm³ region of bone. Trabecular volume and number were assessed in this region. Total bone volume was also determined in a length of the bone from the top of the epiphysis to 3 mm below. Osteolytic lesions were measured through 360° of the bone on a three-dimensional model in a 3 mm length of cortical bone, starting at the growth plate. Holes smaller than 50 µm in diameter were excluded from the analysis as these represent normal physiological structures in bone. During analysis, investigators were blinded to specific treatment groups.

***In vivo* quantification of osteoblast and osteoclast number.** Tibiae were fixed in 4% paraformaldehyde solution, decalcified in 14.3% EDTA for 4 days at 37°C with daily changes of EDTA, then embedded in paraffin wax. Sections were cut (at 3 µm) using a Leica Microsystems Microtome and stained with tartrate-resistant acid phosphatase (TRAP) as described previously²⁷. The numbers of osteoblasts and TRAP-positive osteoclasts were determined on a 3 mm length of endocortical surface starting 0.25 mm from the growth plate and viewed on a DMRB microscope (Leica Microsystems). All histomorphometric parameters were based on the

report of the American Society for Bone and Mineral Research histomorphometry nomenclature²⁸ and were obtained using the OsteoMeasure bone histomorphometry software (OsteoMetrics). During preparation and analysis of tibiae, investigators were blinded to specific treatment groups.

In vitro osteoclast and osteoblast models. Osteoclasts were generated on dentine disks from the CD14⁺ fraction of human peripheral blood as previously described²⁹. The CD14⁺ cells were treated with 25 ng ml⁻¹ recombinant M-CSF (–RANKL), plus either 30 ng ml⁻¹ RANKL (+RANKL) or 150 ng ml⁻¹ recombinant LOX (rLOX) (OriGene Technologies). The LOX antibody was added at 4 µg ml⁻¹. At the end of the culture period the cells were fixed and stained for TRAP. The number of TRAP-positive osteoclasts and the amount of resorption were determined as previously described³⁰. For NFATc1 nuclear localization, human peripheral blood monocytes were grown in standard osteoclastic conditions and the ability of LOX to induce nuclear localization of the transcription factor NFATc1 was measured at day 14 (mature, functional osteoclasts). For the role of LOX upon NFATc1 nuclear localization, cultures were treated for 24 h with rLOX; rLOX in the presence of the LOX antibody at 4 µg ml⁻¹; or LOX antibody alone at 4 µg ml⁻¹. To determine whether LOX-induced NFATc1 nuclear localization was mediated by reactive oxygen species, additional cultures were treated with 0, 50, 100, 150 and 200 U ml⁻¹ catalase with and without rLOX (150 ng ml⁻¹). Primary murine calvarial osteoblasts were isolated from neonatal BALB/c mice as previously described²⁷, and seeded into 96-well plates. To determine the effect of LOX on the differentiation and function of primary osteoblasts, cells were grown to confluence in normal medium (DMEM GlutaMAX with sodium pyruvate without phenol red, 100 U ml⁻¹ penicillin and 100 µg ml⁻¹ streptomycin, 10% FBS), and then switched to osteogenic medium (DMEM GlutaMAX with sodium pyruvate without phenol red (Life Technologies), 100 U ml⁻¹ penicillin and 100 µg ml⁻¹ streptomycin, 0.5% FBS and 50 µg ml⁻¹ L-ascorbic acid (Sigma)) and treated with 10 nM dexamethasone (positive control), 150 ng ml⁻¹ rLOX, or rLOX + LOX antibody. Cells were cultured in osteogenic medium for 3 weeks with the medium and treatments replaced every 2–3 days, and 5 mM inorganic phosphate added to all treatments 3 days before the end of the culture. Human osteoblast-like cells (SaOS-2), maintained as previously described³⁰, were treated with CM from 4T1 cells as previously described¹³ and the effect after 3 days on cell number was measured. SaOS-2 cells were also grown in osteogenic medium and the effect of the CM on the differentiation of these cells and their ability to mineralize was assessed after 7 days by quantification of alizarin red staining.

Quantification of mineralization. Cells were rinsed in PBS and fixed in 100% ethanol overnight at 4°C. Nodules formed by osteoblasts were stained by alizarin red S. Briefly, cells were rinsed twice by PBS and incubated in 40 mM alizarin red S (pH 4.2) (Sigma) for 1 h at room temperature. Plates were washed with 95% ethanol on the shaker until the solution became clear; 10% cetylpyridinium chloride was then added to the wells and incubated at 55°C for 15 min, after which the absorbance was read at 550 nm.

NFATc1 staining and quantification. Cultures on coverslips were fixed with 4% paraformaldehyde for 15 min. Fixed cultures were rinsed three times between each sequential step with 0.1% Tween in PBS and all incubations were at room temperature unless otherwise stated. Permeabilization was performed with 0.1% Triton X-100 in PBS for 10 min. Blocking was performed with 5% normal goat serum in PBS + 0.1% Tween for 2 h. Mouse monoclonal antibody to NFATc1 (SC-7294, Santa Cruz) and Mouse IgG1 control were diluted 1:50 in 5% normal goat serum + 0.1% Tween and incubated at +4°C overnight. The secondary incubation was with Alexa Fluor 488 goat anti-mouse 1:300 in PBS for 1 h. The final incubation with rhodamine phalloidin 1:40 (R415, Invitrogen) and Hoechst 1:1,000 was for 20 min. Coverslips were mounted using ProLong Gold (Life Technologies). Images were captured with a Leica DMI 4000B fluorescence microscope at ×20 objective with 0.70 aperture. NFATc1-positive nuclei were counted with ImageJ. Each experiment was conducted with three independent donors. For each donor, each treatment group was set up in duplicate. For each duplicate, a minimum of 16 fields of view were quantified for nuclear NFATc1 signal.

Bioluminescent intravital imaging of bone colonization. Adult female BALB/c mice (8 weeks old) were conditioned as described above. After 3 weeks of conditioning, mice were anaesthetized and 1 × 10⁵ 4T1Luc cells were injected intracardially into the left cardiac ventricle. Once a week, mice were injected with 120 mg kg⁻¹ luciferin and metastatic dissemination of the cells was monitored using IVIS Lumina II (Caliper LifeSciences). Mice were killed by CO₂ asphyxiation

3–5 weeks after tumour cell injection. Metastatic burden was quantified using Living Image software (Caliper Life Sciences) by measuring the luminescent signal from each leg; regions of interest are shown in Fig. 4. During analysis of IVIS data, investigators were blinded to specific treatment groups.

Immunoblotting. Immunoblotting for lysyl oxidase was as previously described^{31,32}. Conditioned media and cellular lysates were prepared as previously described^{31,32}. Primary LOX antibody (Open Biosystems) was used at 1:100 and β-actin (Abcam) at 1:10,000, with incubation overnight at 4°C. Species-specific biotinylated secondary antibodies were used at 1:25,000 and incubated for 1 h at room temperature, and visualization performed using ECL Plus (Amersham, GE Healthcare).

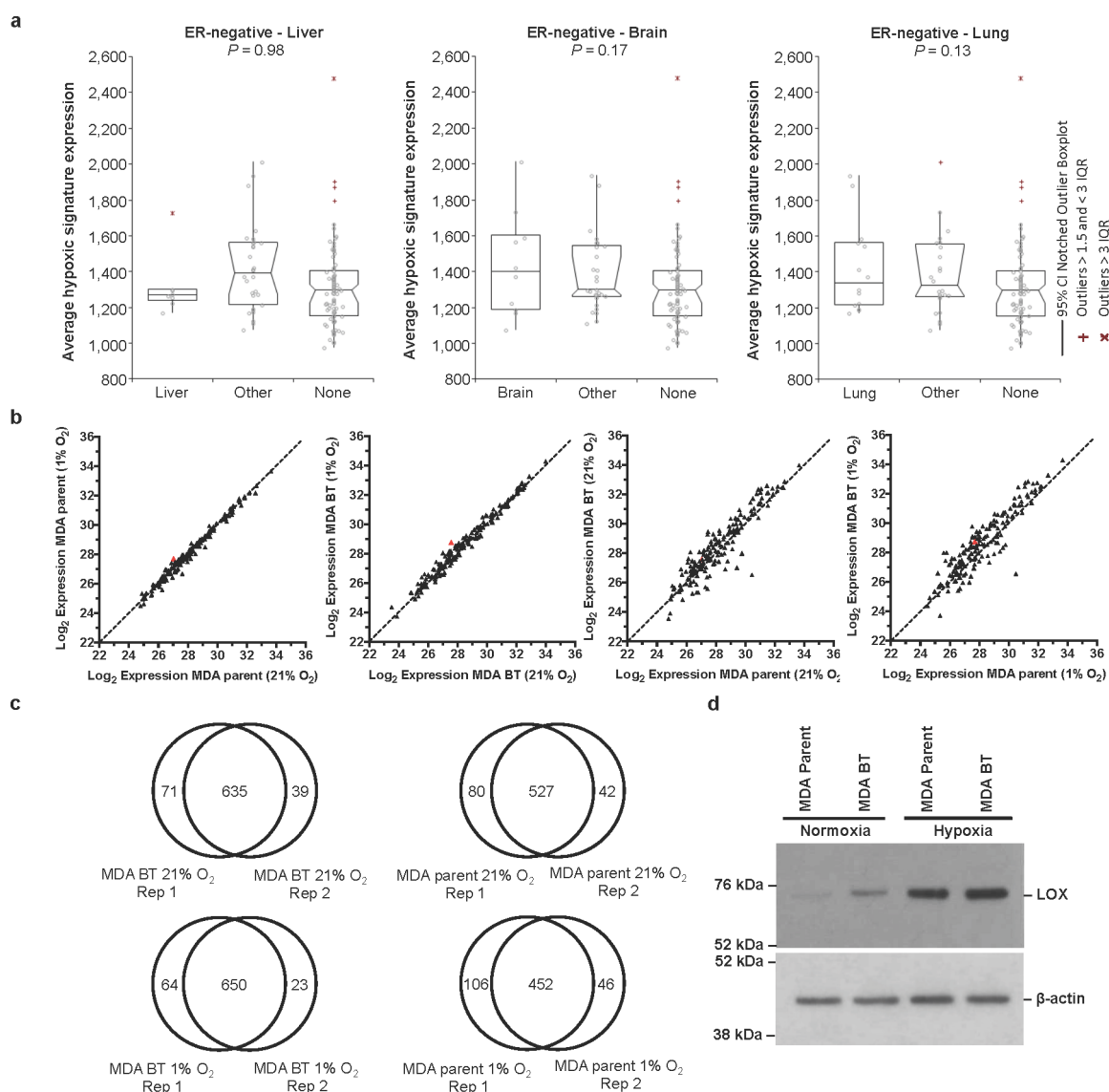
Immunohistochemistry for tumour hypoxia. Mice were injected intraperitoneally with pimonidazole (60 mg kg⁻¹) 1 h before culling. After excision, tumours were fixed in 4% PFA overnight before processing and embedding in paraffin according to standard histopathology techniques. Sections (4 µm) were cut and deparaffinized, rehydrated and stained with Hypoxyprobe (Hypoxyprobe) overnight after citrate-buffer-mediated antigen retrieval according to the manufacturer's guidelines. Hypoxyprobe binding was visualized with 3,3-diaminobenzidine before counterstaining with haematoxylin. Images were taken on a NanoZoomer slide scanner (Hamamatsu).

Explant cultures. The 4T1Luc line was implanted orthotopically as described above. Explant cultures of 4T1 tumour-bearing mice were generated at 1, 2, 3, 4 and 5 weeks after implant in the following ways. From primary tumour, small 5 mm³ biopsies were taken and mechanically disaggregated to produce a single cell suspension. From lung, the left lobe was removed, washed and mechanically disaggregated to produce a single cell suspension. From bone, hindlimbs were separated at the joint and all extraneous tissue removed. Tibiae were opened at both end and bone marrow as well as tumour cells were flushed by syringe three times using PBS. From skin, a small 5 mm² punch of distant skin was mechanically disaggregated to produce a single cell suspension. Collected cells were washed and plated in standard serum containing media. Forty-eight hours after seeding, media were changed to remove non-adhered cells and 500 µg ml⁻¹ Zeocin (the selective marker for the luciferase cassette) was added for 2 weeks. D-Luciferin salt (Caliper Life Sciences) at a final concentration of 3 mg ml⁻¹ was added just before bioluminescent imaging using the IVIS Lumina II, and quantification of luminescent signal used Living Image software (Caliper Life Sciences).

qRT-PCR. Total RNA was isolated from cells using Trizol (Invitrogen) and purified RNA treated with DNase I (New England Biolabs), both according to the manufacturer's instructions. Complementary DNA synthesis were performed using an M-MLV Reverse Transcriptase Kit (Invitrogen). qRT-PCR for β-actin and firefly luciferase was performed using a LightCycler 480 (Roche). Firefly luciferase was amplified using the primers 5'-CTCATGAGACTACATCAGC-3' and 5'-TCCAGATCCACAACCTTCGC-3', and for β-actin 5'-GAGGCCAGAGCAAGAGAGG-3' and 5'-TACATGGCTGGGGTGTGTAA-3'.

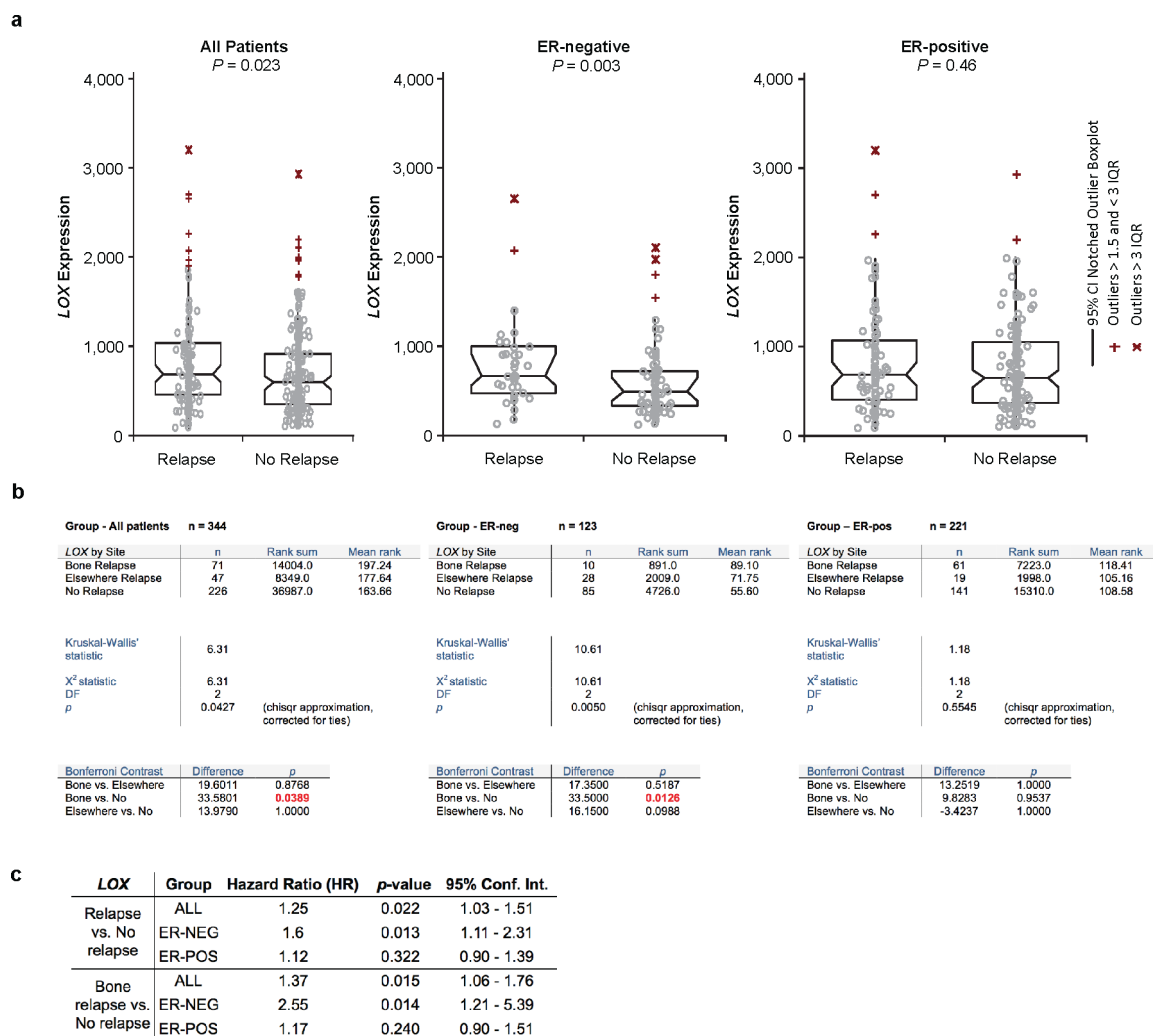
ELISA. ELISA plates were coated with sera from 4T1scr and 4T1shLOX tumour-bearing mice at 4°C overnight. Plates were blocked with 1% BSA at 37°C for 3 h. Our anti-LOX antibody was prepared in PBS containing 0.1% BSA, and 100 µl was added to wells for 2 h at room temperature. Binding of anti-LOX antibody to LOX protein was detected using horseradish peroxidase (HRP)-labelled secondary antibodies (1:10,000 dilution). The CTX-I ELISA (RatLaps) was used for quantitative determination of bone-related degradation products from CTX of type I collagen in mouse serum released by osteoclasts. All procedures were performed in accordance with the manufacturer's guidelines using sera from animals taken at time of cull. A sandwich ELISA for detecting human RANKL in the osteoclast medium was used according to the manufacturer's instructions (DuoSet, R&D Systems Europe). The sensitivity of the RANKL ELISA was 78.1–5,000 pg ml⁻¹.

26. Baker, A. M. *et al.* The role of lysyl oxidase in SRC-dependent proliferation and metastasis of colorectal cancer. *J. Natl Cancer Inst.* **103**, 407–424 (2011).
27. Wang, N. *et al.* Reduced bone turnover in mice lacking the P2Y₁₃ receptor of ADP. *Mol. Endocrinol.* **26**, 142–152 (2012).
28. Parfitt, A. M. *et al.* Bone histomorphometry: standardization of nomenclature, symbols, and units. Report of the ASBMR Histomorphometry Nomenclature Committee. *J. Bone Miner. Res.* **2**, 595–610 (1987).
29. Agrawal, A., Gallagher, J. A. & Gartland, A. *Methods in Molecular Biology* Vol. 806 (eds Mitry, R. R. & Hughes, R. D.) 357–375 (Humana, 2012).
30. Gartland, A., Hipskind, R. A., Gallagher, J. A. & Bowler, W. B. Expression of a P2X₇ receptor by a subpopulation of human osteoblasts. *J. Bone Miner. Res.* **16**, 846–856 (2001).



Extended Data Figure 1 | LOX is hypoxia regulated and strongly associated with osteotropism and metastasis. **a**, Retrospective analysis of our patient cohort including only ER⁻ patients showed that the hypoxic signature is not significantly associated with liver relapse ($P = 0.98$), brain relapse ($P = 0.17$) or lung relapse ($P = 0.13$). **b**, \log_2 expression levels under conditions of hypoxia (1% O_2) and normoxia (21% O_2) for secreted proteins from the MDA-MB-231 parent and MDA-MB-231 bone tropic (BT) 1833 cell line. Data representative of four repeats, two label-free repeats, and two SILAC (standard and reverse-label) repeats. Acquisition performed on the Orbitrap

Q-Exactive (Thermo Fisher Scientific). **c**, Overlaps between repeats of global secretome analysis in MDA-MB-231 parent and MDA-MB-231 bone tropic cells grown in normoxic (21% O_2) and hypoxic (1% O_2) conditions from label-free and SILAC approaches. **d**, Immunoblotting for LOX in MDA parent and 1833 bone tropic subclone under conditions of hypoxia (1% O_2) and normoxia (21% O_2) confirming expression levels seen in proteomic and transcriptomic analyses. Scans of original western blots available as Supplementary Information.



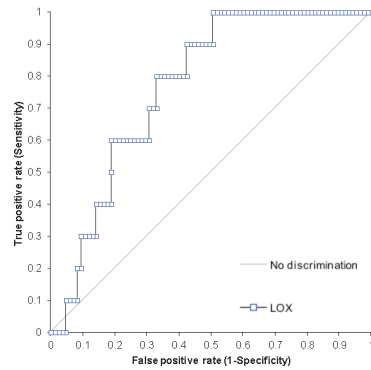
Extended Data Figure 2 | Extended patient data analysis. **a**, Across all breast cancer patients, the expression of *LOX* is associated with metastasis formation ($P = 0.023$) and in particular with ER⁻ breast cancer patients ($P = 0.0029$). **b**, An additional Kruskal–Wallis test between reported bone relapse, relapse elsewhere and no relapse patients with an additional contrast test wherein all pairwise groups were considered shows that in all patients *LOX* expression is associated with bone relapse compared with no relapse ($P = 0.0389$). This also

pertains to ER⁻ patients ($P = 0.0126$) but not ER⁺ patients ($P = 0.9537$). **c**, Cox-regression using log₂(*LOX* expression data) was used to estimate the hazard ratio in two analyses. One analysis used the no-relapse patients and the bone relapse patients (data belonging to Fig. 1f), and the second analysis included all patients (data belonging to Extended Data Fig. 2a). *LOX* expression is associated with increased hazard ratio, particularly in ER⁻ patients in both analyses.

a

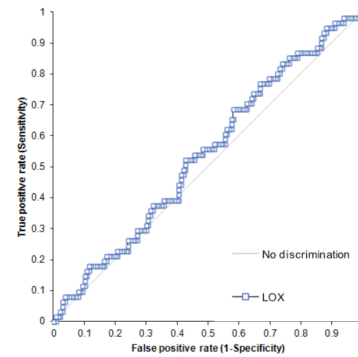
LOX in ER-negative: Bone relapse vs No relapse

Test	Area	95% CI	SE	Z	p
LOX	0.77	0.65 to 0.89	0.059	4.54	<0.0001

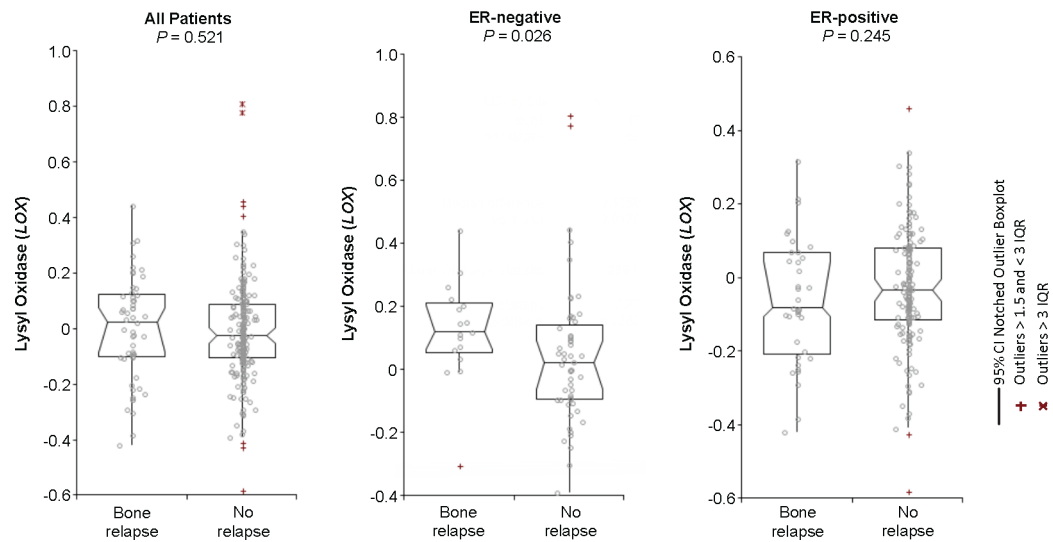


LOX in ER-positive: Bone relapse vs No relapse

Test	Area	95% CI	SE	Z	p
LOX	0.55	0.46 to 0.63	0.044	1.03	0.1504

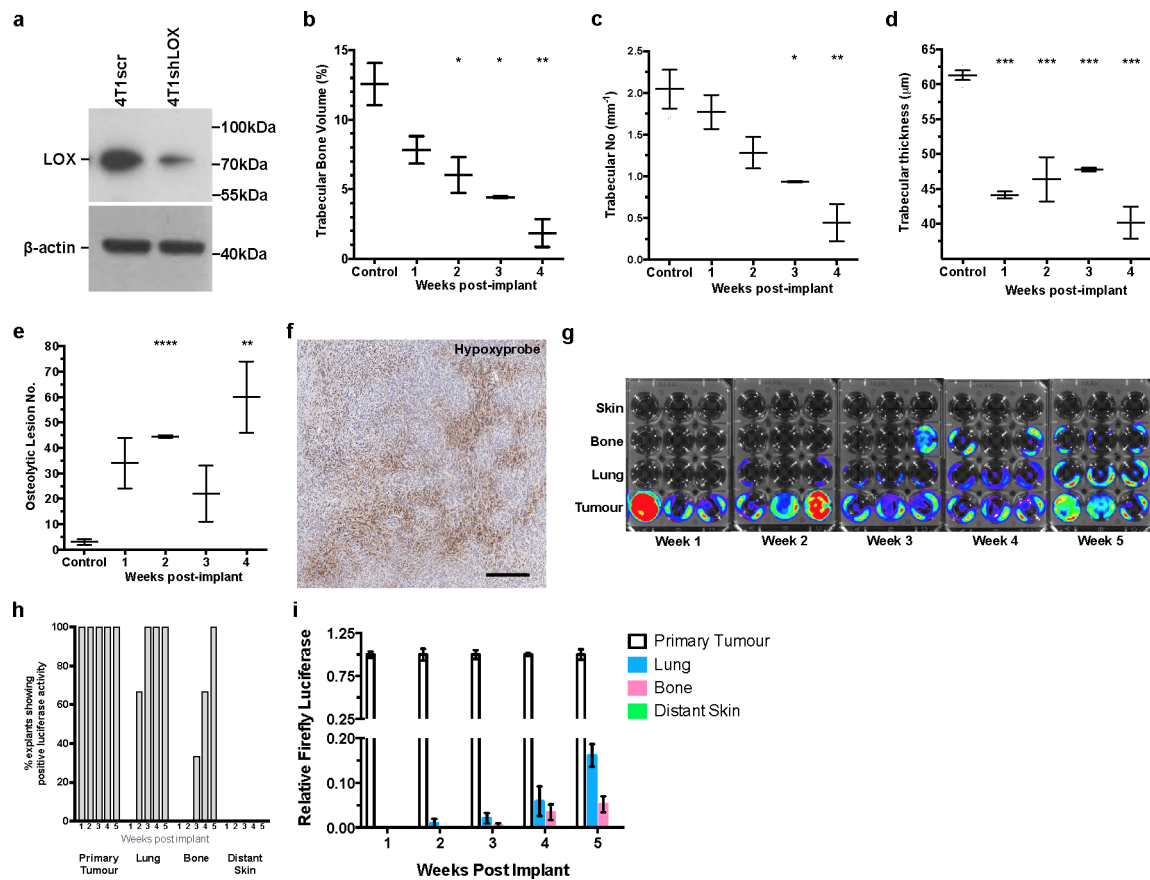


b



Extended Data Figure 3 | Additional patient data analysis in a supporting patient cohort. **a**, ROC curve analysis shows *LOX* expression may be indicative of metastatic dissemination of ER⁻ breast cancer (area under the curve 0.77, $P < 0.0001$) but not ER⁺ patients (area under the curve 0.55, $P < 0.1504$). **b**, In an alternative second patient data set¹⁴ (PubMed identifier 12490681) reporting

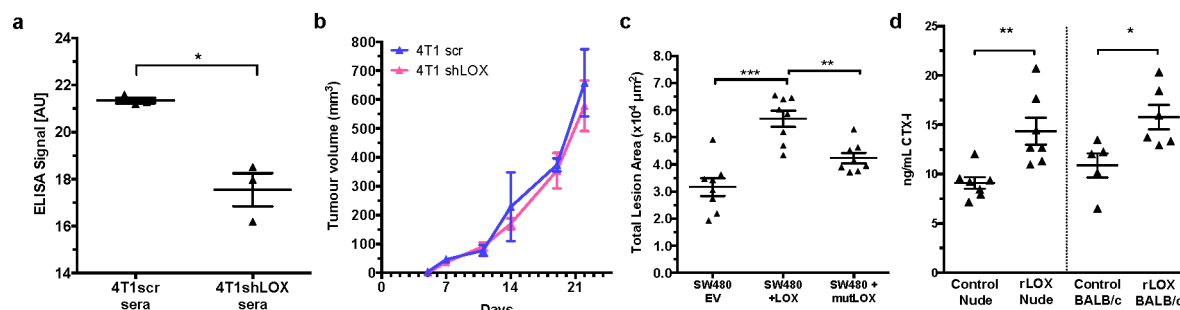
data on 295 lymph-node-negative patients who did not receive adjuvant therapy, with available site of relapse, *LOX* is significantly higher expressed in bone relapse ER⁻ patients, compared with other groups confirming data from the original data set.



Extended Data Figure 4 | Hypoxia-induced tumour-derived LOX stimulates osteolytic lesion formation in the absence of tumour cells.

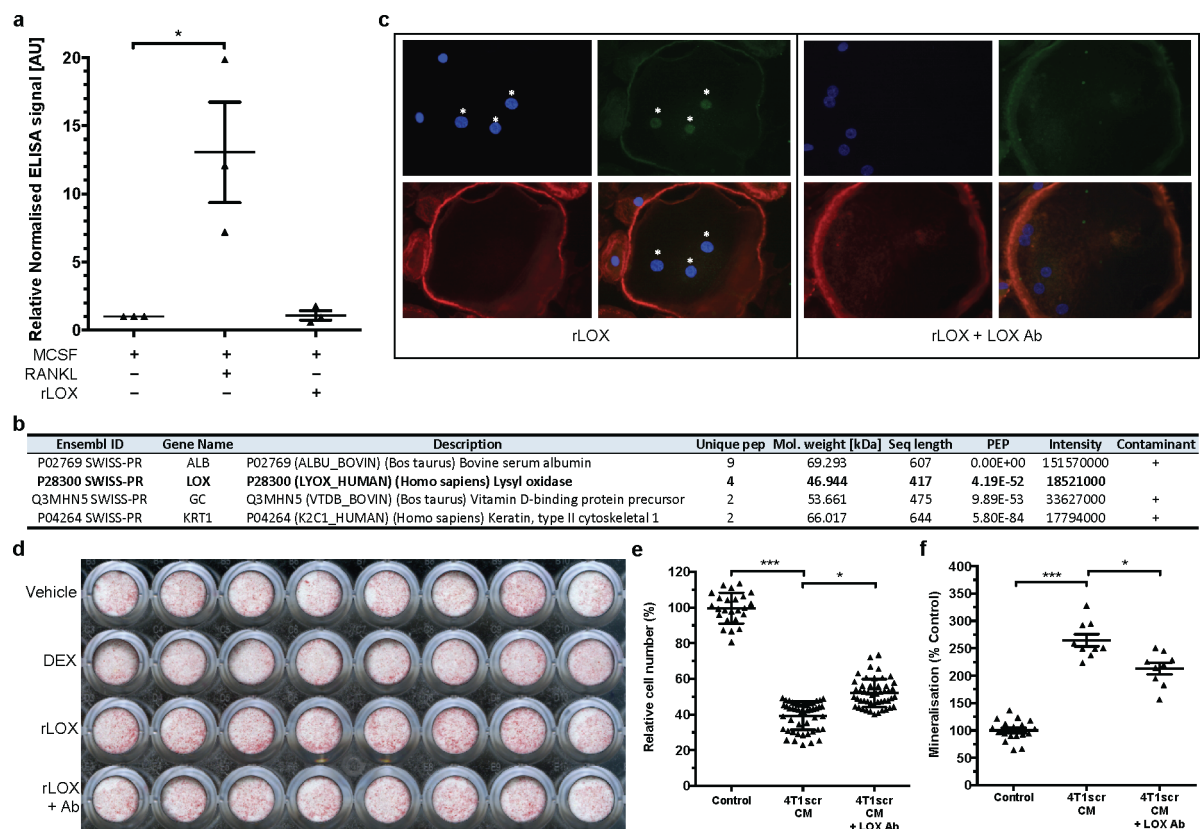
a, Immunoblotting of 4T1 mammary carcinoma line stably expressing either a scrambled (scr) or shLOX vector which leads to a significant decrease in levels of detectable LOX. Scans of original western blots available in Supplementary Information. **b**, Micro-CT scanning and reconstruction with structural analysis shows decreases in trabecular bone volume (as a percentage of total bone volume) ($n = 3$ mice per group). **c**, Decreases in trabecular number (per millimetre) ($n = 3$ mice per group) and **d**, decreases in trabecular thickness in tibiae of mice bearing 4T1scr mammary fatpad tumours over time ($n = 3$ mice per group). **e**, Micro-CT analysis of mouse tibiae shows increases in focal osteolytic lesions in 4T1scr tumour-bearing mice develop over time ($n = 3$ mice per group). * $P < 0.05$, ** $P < 0.01$, *** $P < 0.001$, unpaired parametric

one-tailed t -test. **f**, Representative immunohistochemical staining for pimonidazole (Hypoxyprobe) in 4 μ m section of 4T1 orthotopic mammary carcinoma, 3 weeks after implantation, shows hypoxia (brown staining) as a salient feature of tumours. Scale bar, 250 μ m. **g**, Bioluminescent imaging of luciferase signal 2 weeks after explant of samples taken from primary tumour, lung, bone marrow (tibia) and distant skin samples at 1–5 weeks after primary tumour implant. Selection was under 500 μ g ml⁻¹ zeocin for the luciferase expression cassette ($n = 3$ mice per time point). **h**, Quantification of **g** as a percentage of positive luciferase expressing explants from various sites after 4T1 tumour implant shows tumour cells do not begin to arrive in the bone until 3 weeks. **i**, qRT-PCR detection of luciferase expressing 4T1 tumour cells in secondary organs confirms explant culture experiments ($n = 3$ mice per time point).



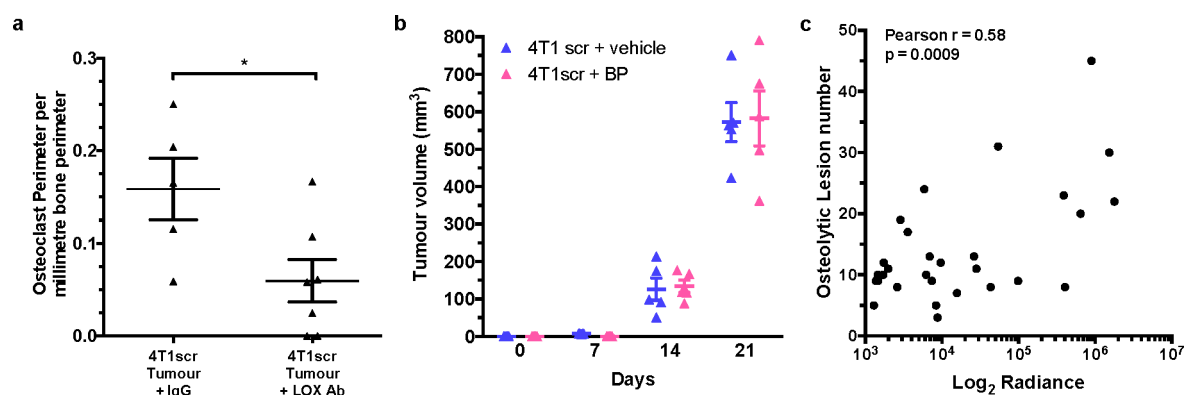
Extended Data Figure 5 | Effects of LOX modulation on circulating sera levels, primary tumour growth and osteolytic lesion formation. **a**, ELISA for LOX in the sera of 4T1scr and 4T1shLOX tumour-bearing mice (*n*: ELISA signal (arbitrary units) in mouse sera: 3 mice per group) shows decreased levels of circulating LOX upon genetic silencing at the primary tumour. **P* < 0.05, unpaired parametric two-tailed *t*-test. **b**, Growth curves as determined by calliper measurement for orthotopic 4T1scr and 4T1shLOX mammary tumours show no difference between primary tumour growth (*n*: mice; 3 per group). **c**, Injection of hypoxic CMs from SW480 human colorectal cancer cells stably expressing one of; empty vector control (EV), full-length LOX (+LOX),

or a catalytically inactive full-length LOX (+mutLOX) (K320A) confirms a LOX-dependent mechanism of focal osteolytic lesion generation in a second human model of cancer (*n*: mice; 8 per group). ***P* < 0.01, ****P* < 0.001, unpaired parametric two-tailed *t*-test. **d**, CTX ELISA (RatLaps) on sera of mice injected intraperitoneally twice a week with rLOX for 3 weeks. CTX is a telopeptide that can be used as a biomarker in the serum to measure the rate of bone turnover (*n*: nanograms per millilitre circulating CTX-I in mouse sera; 5 mice per group). All data are mean ± s.e.m. **P* < 0.05, ***P* < 0.01, ****P* < 0.001, unpaired parametric two-tailed *t*-test.



Extended Data Figure 6 | LOX modulates osteoclasts and osteoblast behaviour independently of RANKL. **a**, ELISA for RANKL in the CM of osteoclast cultures shows no detectable levels of RANKL in M-CSF alone (negative control) and rLOX cultures excluding the likelihood of autocrine production by cells in response to rLOX (n : ELISA signal (arbitrary units); data are from three independent experimental repeats in all groups). $*P < 0.05$, unpaired parametric two-tailed t -test. **b**, All proteins detected by mass spectrometry analysis in the rLOX preparations (based on MaxQuant 1.5 peptide identity score of 50 and a minimum of two unique MS peptide observations). **c**, Examples of nuclear localization of NFATc1 after addition of rLOX in the presence and absence of the LOX antibody (green, NFATc1; red, phalloidin; blue, DAPI). **d**, Representative alizarin red S plate showing mineralization ability (calcium deposits as detected by alizarin red S staining) of primary calvarial mouse osteoblasts after treatment with dexamethasone

(positive control) or rLOX \pm LOX ab; quantification shown in Fig. 3g. **e**, High-LOX-containing hypoxic 4T1scr CM significantly reduces cell proliferation of the human osteoblast-like SaOS-2 cell line, which can be partly blocked by treatment with anti-LOX antibody (n : normalized cell number per well; control 24 wells; 4T1scr CM 49 wells; 4T1scr CM + LOX Ab 51 wells). Data collected over three independent experimental repeats. $*P < 0.05$, $**P < 0.01$, $***P < 0.001$, unpaired parametric two-tailed t -test. **f**, Mineralization ability (calcium deposits as detected by alizarin red S staining) is increased in the human osteoblast-like SaOS-2 cell line in response to high-LOX-expressing hypoxic 4T1scr CM, the effects of which can be attenuated using the anti-LOX antibody (n : alizarin red S staining per well, data taken from three independent repeats; control 18 wells; 4T1scr CM 9 wells; 4T1scr CM + LOX Ab 9 wells). All data are mean \pm s.e.m. $*P < 0.05$, $**P < 0.01$, $***P < 0.001$, unpaired parametric two-tailed t -test.



Extended Data Figure 7 | Additional *in vivo* analysis of lesion formation and primary tumour growth. **a**, 4T1scr tumour-bearing mice treated with our LOX antibody show a decrease in osteoclast perimeter in tibial bones in support of LOX as a modulator of osteoclastogenesis shown in Fig. 3 (n : mice; 4T1scr Tumour + IgG 5, 4T1scr Tumour + LOX Ab 7). Data are mean \pm s.e.m. * $P < 0.05$, unpaired parametric two-tailed t -test. **b**, Weekly tumour volumetric measurements for 4T1scr tumour-bearing mice treated

with either zoledronic acid (0.6 mg kg⁻¹ intraperitoneally) or vehicle (PBS), show that, when administered alone, zoledronic acid does not affect primary 4T1scr primary tumour growth *in vivo* (n : mice; 4 in all groups). **c**, Pearson correlation shows a positive correlation between lesion number as determined by micro-CT analysis and luciferase signal (radiance (photons per second per square centimetre per steradian)) from 4T1Luc tumour cells within the bone ($r = 0.58$, 95% CI 0.2778–0.7834, $P = 0.0009$ (two-tailed)).

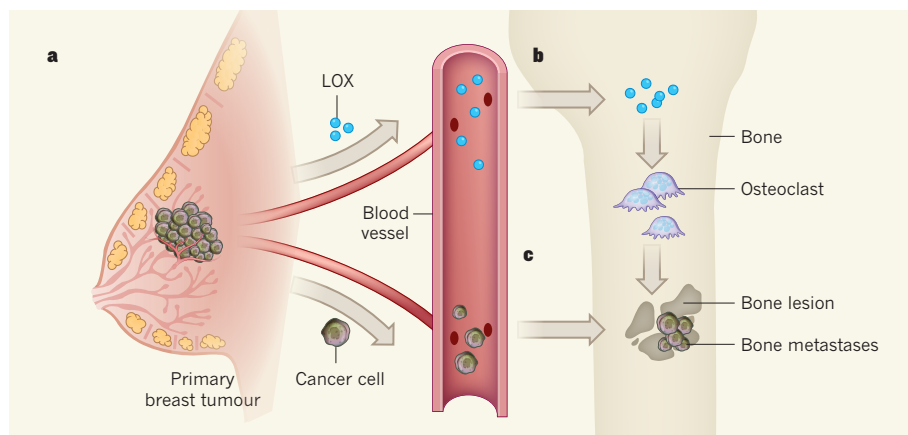


Figure 1 | Pre-metastatic niche formation in bone. **a**, Cox *et al.*² find that breast tumour cells that are exposed to hypoxic conditions secrete the enzyme lysyl oxidase (LOX) into the bloodstream. **b**, In bone, LOX activates cells called osteoclasts to enhance bone breakdown, resulting in the formation of bone lesions. **c**, These lesions create a pre-metastatic niche: breast cancer cells from the original tumour that are disseminated by the circulation are able to occupy this niche and form a metastatic tumour.

the authors demonstrate that such bone lesions can be created even in a tumour-free system: when they injected mice with factors secreted by hypoxic breast tumour cells, these soluble factors induced bone lesions that enhanced the formation of bone metastases by cancer cells circulating in the bloodstream. Thus, their study shows that systemic LOX, secreted by ER⁺ breast tumours, drives the formation of a pre-metastatic niche in bones, which precedes and facilitates the formation of metastases (Fig. 1).

The pre-metastatic niche concept suggests that a hospitable microenvironment is formed in target organs before the arrival of metastatic tumour cells and enables their invasion, survival and proliferation⁸. Although the notion of tumour cells as 'seeds' that require a fertile 'soil' for their growth was suggested more than a century ago^{9,10}, the mechanisms that enable this soil to be prepared have only emerged gradually over recent years. It was not clear whether the earliest changes in incipient metastatic niches are accomplished systemically, by soluble factors secreted from the primary tumour¹¹, or by the presence of a small number of disseminated tumour cells, or through both processes. Cox and colleagues' exciting discovery provides evidence supporting the systemic nature of pre-metastatic niche formation and contributes to our understanding of systemic regulation of cancer progression and metastasis.

The study is limited by its use of only one model of transplantable mammary tumour, rather than a genetically engineered model in which the breast tumour arises in the mouse. However, there is a lack of models in immune-competent mice in which such tumours spontaneously metastasize to bones. Another limitation is an interesting issue that remains unresolved: why is the secretion of LOX by hypoxic breast cancer cells predominantly linked with bone relapse in patients with ER⁺ breast cancer? Although hypoxia-related signalling was previously shown to drive breast

cancer metastasis⁵, a detailed dissection of the link between breast cancer subtype, hypoxia and tumour-cell attraction to bone is yet to be performed.

Elucidating the early interactions between disseminated tumour cells or their soluble products and their new microenvironment is an essential prerequisite for the development of effective targeted therapies. Target molecules are likely to be organ-specific, because the complex components and interactions of tissues vastly differ in different organs (such as bone versus brain). Adding to this complexity, this new study suggests that biomarkers that predict potential risk for organ-specific metastases are also specific

for different tumour subtypes.

Interestingly, several studies have indicated that drugs that prevent bone destruction (such as bisphosphonates and the monoclonal antibody denosumab) are efficient co-therapies for preventing bone metastasis^{1,12}. Therefore, the knowledge gained from Cox and colleagues' findings may open new horizons in the treatment of patients with breast cancer after removal of the primary tumour. Analysis of the expression of LOX may provide both a molecular tool to stratify patients by their propensity for bone metastasis and a target for preventive treatment for patients at a higher risk of bone metastasis. ■

Neta Erez is in the Department of Pathology, Sackler School of Medicine, Tel Aviv University, Tel Aviv, 69978 Israel.
e-mail: netaerez@post.tau.ac.il

1. Coleman, R. E., Gregory, W., Marshall, H., Wilson, C. & Holen, I. *Breast* **22** (Suppl. 2), S50–S56 (2013).
2. Cox, T. R. *et al.* *Nature* **522**, 106–110 (2015).
3. Joyce, J. A. & Pollard, J. W. *Nature Rev. Cancer* **9**, 239–252 (2009).
4. Erez, N. & Coussens, L. M. *Int. J. Cancer* **128**, 2536–2544 (2011).
5. Gilkes, D. M. & Semenza, G. L. *Future Oncol.* **9**, 1623–1636 (2013).
6. Barker, H. E., Cox, T. R. & Erler, J. T. *Nature Rev. Cancer* **12**, 540–552 (2012).
7. Erler, J. T. *et al.* *Cancer Cell* **15**, 35–44 (2009).
8. Kaplan, R. N., Rafii, S. & Lyden, D. *Cancer Res.* **66**, 11089–11093 (2006).
9. Paget, S. *Cancer Metast. Rev.* **8**, 98–101 (1989).
10. Witz, I. P. *Cancer Res.* **68**, 9–13 (2008).
11. McAllister, S. S. & Weinberg, R. A. *Nature Cell Biol.* **16**, 717–727 (2014).
12. Brown, J. E. & Coleman, R. E. *Nature Rev. Clin. Oncol.* **9**, 110–118 (2012).

This article was published online on 27 May 2015.

HIGH-ENERGY PHYSICS

Proton smasher spots rare particle decays

The extremely rare decays of particles known as neutral *B* mesons have been observed at CERN's Large Hadron Collider. The result may be a glimpse of physics beyond that of the standard model of particle physics. [SEE LETTER P.68](#)

DARIA ZIEMINSKA

For more than three decades, physicists have been looking for the decay of the 'strange *B* meson' particle into a pair of muons, the heavy cousins of electrons. The process is incredibly rare, and harder to find than the famous Higgs particle, the discovery of which at the Large Hadron Collider at CERN, near Geneva, Switzerland, was celebrated worldwide in 2012. The standard model of elementary particle physics¹ makes

an exact prediction of the number of particle-decay events researchers should observe in an experiment. Anything more than the predicted value means potential trouble for the standard model. On page 68 of this issue, researchers working on the CMS and LHCb collaborations² at the Large Hadron Collider describe a joint analysis of data from proton collisions that set the decay rate of the strange *B* meson at about three in one billion — in agreement with the standard-model prediction. However, they find that the decay rate of another type of

neutral B meson, the ‘non-strange’ B meson, is at odds with the expectation from the standard model.

The standard model is at a crossroads. It has been very successful in describing elementary particles and their interactions, but such particles comprise only 4% of the known Universe. The theory does not provide a candidate for the dark matter that binds galaxies together and makes up one-quarter of the cosmos. Nor does it accommodate dark energy, the remaining, unknown component of the Universe that is causing it to expand at an accelerated rate. It also does not explain the preponderance of matter over antimatter. Lastly, it makes a worrisome warning that the Universe is probably unstable, ready to collapse in a ‘big crunch’.

Many models have been proposed to solve some of these problems. One of the most compelling ideas for unknown physics beyond that of the standard model is supersymmetry³, affectionately called SUSY. Supersymmetry states that, for every known particle, there is a twin ‘superparticle’ of much higher mass. These superparticles could in principle be produced in colliders. They should quickly decay to lighter superparticles and ordinary particles, except for the lightest superparticle, which should be stable — and that is SUSY’s candidate particle for dark matter.

Physicists have been searching for SUSY superparticles for years, so far with no success. In the absence of direct observations, they watch for discrepancies of measurements of particle properties from standard-model predictions. The decay of neutral B mesons to muons (Fig. 1) is a sensitive test of the standard model because the model predicts the decay rate with good precision. B mesons are made up of one quark and a ‘bottom’ antiquark, the antimatter partner to the quark; quarks are the elementary building blocks of protons and neutrons, and come in six flavours (up, down, strange, charm, top and bottom). There are two kinds of neutral B meson, which have no charge. One type, the strange B meson (B_s^0), contains a bottom antiquark and a strange quark. The other, the non-strange B meson (B^0), has a bottom antiquark paired with a down quark. The decay of the neutral B mesons to a pair of muons would mean that the bottom antiquark and its quark partner annihilate, and that the energy released in the process is given to the muons.

But the standard model forbids the annihilation of quarks of different flavours, so it predicts the decay of the neutral B mesons into muons through an intermediate process that involves the exchange of a top quark between the quarks and the emission of two W bosons

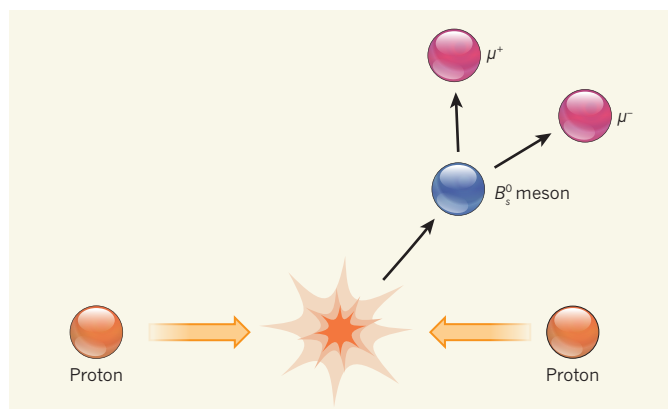


Figure 1 | The rare decay of neutral B mesons to muons. The CMS and LHCb collaborations² have accelerated and smashed together beams of protons travelling in opposite directions in the Large Hadron Collider at CERN, near Geneva, Switzerland, producing neutral B mesons, among many other particles. The authors observed the extremely rare decay of the strange neutral B meson (B_s^0) to two oppositely charged muons (μ^+ and μ^-) with high statistical significance.

(elementary particles that mediate the weak nuclear force). The decay of the strange B meson is expected to occur by this process in about four parts in one billion, and that of the non-strange B meson in about one part in ten billion. However, if yet-unknown SUSY superparticles are exchanged between the quarks in addition to the top-quark exchange, these decay rates will be greatly enhanced relative to the standard-model rate.

The decay rate of the strange B meson observed by the CMS and LHCb collaborations confirms the standard-model prediction. That is good news for the standard model, but not such good news for physics beyond it. However, the decay of the non-strange B meson, which the authors also observed, albeit with a lower statistical significance than obtained for the strange B meson, exceeded the standard-model expectation by almost fourfold — something to watch in the years to come.

CMS and LHCb are two of seven particle detectors at the Large Hadron Collider. Their designs follow different concepts. CMS is a large cylinder (21.6 metres long and 14.6 metres in diameter) in which two counter-propagating beams of protons collide and give rise to neutral B mesons, among many other particles. LHCb is specifically designed to study B mesons, which tend to stay close to the line of the beam pipe. Unlike the CMS detector, which surrounds the proton collision point, the LHCb detector is a stack of instruments stretching for 20 metres along the beam pipe on one side of the collision point. But the two teams adopted a similar strategy to analyse their data. Both groups selected particle events that involved two oppositely charged muons travelling from a common point, which is displaced by a few hundred micrometres from the point at which the protons collide. The events associated with the decay of a neutral B meson are a small fraction of initial candidates. The

rest are random pairs of muons originating from other, more common processes.

To separate the signal of the neutral B meson from background events, the teams each built a ‘decision tree’ — a sequence of binary splits of data into signal-like and background-like parts. The system ‘learns’ to distinguish between signal and background by ‘training’ on a simulated sample of the signal and on a sample of real data representing background events. For the selected signal-like events, the researchers deduced the mass of the parent particles using the momenta and directions of travel of the two muons. They then compared the spectrum of the deduced masses with that predicted for a sum of two bell-shaped curves corresponding to the two kinds of

neutral B meson, strange and non-strange, and a smooth background.

The two collaborations had previously performed this type of analysis, and each reported their results in separate publications^{4,5}. But it was only the combination of data from the two experiments that allowed the researchers to observe with high statistical significance the decay of the strange B meson. In the process, the researchers identified, and corrected, issues with the previous analyses. In particular, they isolated and subtracted a background from the decay of a particle called a bottom Lambda baryon that mimics the signal of a neutral B meson.

Studies of B -meson decays will continue in the coming years. The Large Hadron Collider has just restarted after a two-year break for upgrades, and will soon accelerate proton beams to an energy of 13 teraelectronvolts (TeV), increased from the 8-TeV level reached before the upgrades. The proton beams will also be more tightly focused and will collide at a higher rate than that achieved so far. Both experiments will collect a large number of rare events, and should eventually find which path away from the standard model nature has chosen. ■

Daria Zieminska is in the Physics Department, Indiana University, Bloomington, Indiana 47405, USA.
e-mail: daria@indiana.edu

1. <http://home.web.cern.ch/about/physics/standard-model>
2. The CMS and LHCb collaborations. *Nature* **522**, 68–72 (2015).
3. <http://home.web.cern.ch/about/physics/supersymmetry>
4. Chatrchyan, S. et al. (CMS Collaboration) *Phys. Rev. Lett.* **111**, 101804 (2013).
5. Aaij, R. et al. (LHCb Collaboration) *Phys. Rev. Lett.* **111**, 101805 (2013).

This article was published online on 13 May 2015.

in the presence of SA11, *P. multiseri* increases expression of genes associated with photosynthesis and carbon fixation, presumably to support the higher growth rates observed, as well as to provide organic carbon exudates for the bacterial partner.

But the emerging picture of a diatom–bacterium partnership is more complex than this simple resource swap. Amin *et al.* postulate that the exchanges between these free-living microbes are coordinated through cycling of the hormone indole-3-acetic acid (IAA) and the amino acid tryptophan. Best known for its use by terrestrial plants to direct developmental processes such as the growth of new shoots, IAA also has a role in signalling between soil bacteria and plants⁴. The researchers demonstrate that *P. multiseri* and *Sulfitobacter* SA11 secrete tryptophan and IAA, respectively. Moreover, they show that addition of synthetic IAA to cultures of *P. multiseri* stimulates the diatom's growth, but that the effect is significantly greater when the IAA-producing bacterium itself is present. This indicates that, although IAA promotes diatom cell division, additional unidentified factors are involved in the positive feedback loop that results in major diatom growth enhancement. The authors also detected IAA in water samples from five North Pacific sites and present transcriptomic evidence from field samples for multiple IAA biosynthesis pathways, each incorporating different precursor molecules. Thus, it seems that IAA signalling occurs across domains of life in both the terrestrial and marine biospheres and is probably an ancient mechanism of organismal communication.

Amin and colleagues' study represents a substantial step forward for understanding the complex network of interactions between phytoplankton and bacteria and provides a springboard for development of hypotheses on cross-talk between marine microbes. For example, the extreme interaction specificity observed suggests that the consortium of bacteria residing in a particular habitat may be a major force in structuring the local phytoplankton community, or vice versa. Moreover, it seems reasonable to speculate that, in addition to IAA and tryptophan, other signalling molecules participate in inter- or intradomain communication among marine microbes.

Perhaps the most pressing question we are left with is when and where such interactions occur. Symbioses between diatoms and nitrogen-gas-fixing cyanobacteria are known¹¹, and bacterial attachment to diatoms is often reported during algal blooms and in the bloom senescence phase^{12,13}. For decades, scientists have also speculated on the potential influence of microscale variability of resources in marine environments¹⁴ and on the significance of the phycosphere¹⁵ — a zone around algal cells considered analogous to the root zone of plants. Concentrations of algal secreted compounds are much higher in the

phycosphere than in nearby sea water, owing to the basic physics of the diffusive boundary layer surrounding the cell, thus promoting growth of bacteria in this layer^{13,15}.

Amin and colleagues' results suggest that the specific growth-enhancing interactions observed occur in the phycosphere, but the sampling methods and quantitation techniques needed to directly assess the physical nature of these associations are still lacking. Exciting times are ahead as scientists develop techniques to examine the physical intricacies of these mutualistic relationships, their prevalence and structuring roles in marine microbial communities, and how they might shift under environmental change. ■

Alexander J. Limardo and Alexandra Z. Worden are in the Department of Ocean Sciences, University of California, Santa Cruz, California 95064, USA, and at the Monterey Bay Aquarium Research Institute, Moss Landing, California. **A.Z.W.** is also at the Canadian Institute for Advanced Research,

Toronto, Canada.

e-mails: alimardo@mbari.org; azworden@mbari.org

1. Field, C. B., Behrenfeld, M. J., Randerson, J. T. & Falkowski, P. *Science* **281**, 237–240 (1998).
2. Worden, A. Z. *et al.* *Science* **347**, 1257594 (2015).
3. Thompson, J. A., Oliveira, R. A., Djukovic, A., Ubeda C. & Xavier, K. B. *Cell Reports* **10**, 1861–1871 (2015).
4. Sukumar, P. *et al.* *Plant Cell Environ.* **36**, 909–919 (2013).
5. Von Bodman, S. B., Bauer, W. D. & Coplin, D. L. *Annu. Rev. Phytopathol.* **41**, 455–482 (2003).
6. Amin, S. A. *et al.* *Nature* **522**, 98–101 (2015).
7. Bowler, C., Vardi, A. & Allen, A. E. *Ann. Rev. Mar. Sci.* **2**, 333–365 (2010).
8. Park, J. R. *et al.* *IJSEM* **57**, 692–695 (2007).
9. Stefels, J., Steinke, M., Turner, S., Malin, G. & Belviso, S. *Biogeochemistry* **83**, 245–275 (2007).
10. Czikzo, D. J. *et al.* *Science* **340**, 1320–1324 (2013).
11. Foster, R. A. *et al.* *ISME J.* **5**, 1484–1493 (2011).
12. Smith, D. C., Steward, G. F., Long, R. A. & Azam, F. *Deep-Sea Res. II* **42**, 75–97 (1995).
13. Amin, S. A., Parker, M. S. & Armbrust, E. V. *Microbiol. Mol. Biol. Rev.* **76**, 667–684 (2012).
14. Azam, F. *Science* **280**, 694–696 (1998).
15. Bell, W. & Mitchell, R. *Biol. Bull.* **143**, 265–277 (1972).

This article was published online on 27 May 2015.

DEVELOPMENTAL BIOLOGY

Diversity in the lymphatic vasculature

Two studies of the cells that give rise to lymphatic vessels reveal that precursors arise from unexpected sources, demonstrating that the origins of this vasculature are more diverse than anticipated. SEE ARTICLES P.56 & P.62

BENJAMIN M. HOGAN & BRIAN L. BLACK

The lymphatic vasculature is a specialized network that drains fluid from tissues and enables immune-cell trafficking and surveillance throughout the body. This major constituent of the circulatory system was long considered to be ancillary to the blood vasculature, and as such has received less attention than its counterpart. As a result, although the roles of lymphatic vessels in tissue maintenance and disease are now well appreciated^{1,2}, their origins have remained contentious for more than a century^{3,4}. Two studies^{5,6} in this issue provide insights into the origins of the lymphatic vasculature.

In vertebrate embryos, lymphatic vessels arise from two pre-existing veins⁷. Vascular endothelial cells that line the walls of these cardinal veins turn on genes that direct venous cells to become lymphatic endothelial cells (LECs), which leave the veins and form the lymphatic vessels. In this way, one vascular network gives rise to another. But precisely how and when a pool of LEC precursors is established in the cardinal veins, and whether

all cells in the early veins are identical, has remained unclear.

Zebrafish embryos are transparent, which makes them an ideal organism for visualizing cell movements. Nicenboim *et al.*⁵ (page 56) traced early LEC development in zebrafish and unexpectedly discovered that the cells on the dorsal (upper) and ventral (lower) walls of the cardinal veins are different. The researchers report that lymphatic precursors sprout from the dorsal wall, but that these cells actually originate in the ventral wall at an earlier developmental stage (Fig. 1).

By using fluorescence to track single cells, the authors found that precursor cells in the ventral wall divide, after which one of the two daughter cells migrates to the dorsal wall. These dorsal daughter cells can then give rise to LECs. Interestingly, the cells in the ventral wall also contribute to the intestinal blood vasculature, indicating that they can give rise to multiple types of endothelium. Nicenboim and colleagues showed that the fate of these nascent precursor cells is controlled by a signalling molecule, Wnt5b, which acts from tissues adjacent to the ventral

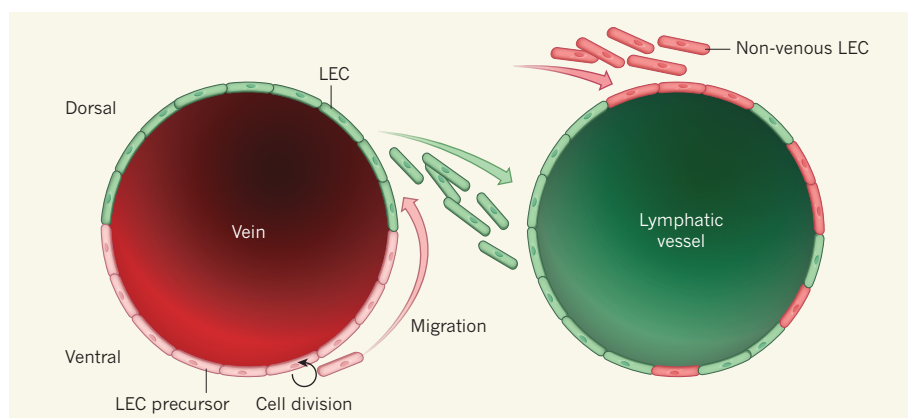


Figure 1 | Contributions to lymphatic-vessel development. Lymphatic endothelial cells (LECs), which derive primarily from veins in the early embryo, line lymphatic vessels. Nicenboim *et al.*⁵ report that LEC precursors from the ventral side of embryonic veins divide, before one of the two daughter cells migrates to the dorsal side of the vein. From there, these cells can differentiate into LECs and migrate to the site of forming lymphatic vessels. Klotz *et al.*⁶ found that the LECs that form lymphatic vessels in the heart originate both from embryonic veins and from other non-venous sources, including the yolk sac.

wall of the vein. This observation points to an unexpected instructive role for ventral tissues and Wnt signalling in driving cells to become LECs.

It is difficult to pinpoint the stage at which a cell becomes committed to its future identity, but Nicenboim and colleagues' observations should prompt us to revise our thinking about how cellular identity is acquired in vascular lineages. Their work suggests that changes in cellular identity are probably coupled to dynamic cell movements, rather than to step-wise changes in gene expression, as current dogma suggests. One attractive idea is that the range of cell types that undifferentiated precursors in the vasculature can become is restricted progressively at sequential locations during vessel development. Future analyses should test this and other models.

Klotz *et al.*⁶ (page 62) examined a later stage of development, when lymphatic vessels form in the heart, which, like all organs, uses the lymphatic system to maintain normal fluid levels and for immune-cell trafficking⁸. An understanding of how lymphatic vessels develop in individual organs, however, has been even more enigmatic than a definition of the origins of the system as a whole. Indeed, although the cardiac lymphatic system has previously been described⁹, its development, origins and functions have remained unclear.

These authors found that most of the cardiac lymphatic system in mice arises from embryonic veins located outside the heart. But unexpectedly, they show that many coronary LECs do not originate from veins at all (Fig. 1). By using various genetic 'fate-mapping' techniques to indelibly label cells, allowing cell movements and descendants to be traced, the authors observed that roughly 20% of LECs in the heart's lymphatic vasculature originate in the yolk sac that surrounds the developing embryo. The researchers suggest that these yolk-sac cells have a previously unappreciated

potential to give rise to LECs directly, in addition to their known roles in forming blood cells and vascular endothelial cells.

All fate-mapping experiments in mice must be interpreted cautiously, because the techniques used to label cells genetically can also label other cell types. Nonetheless, Klotz and colleagues' work indicates that cardiac LECs originate from different places: embryonic veins and at least one other source. Future studies that do not use genetic labelling should further clarify the origins of cardiac and other LECs in developing organs.

Klotz *et al.* also investigated the role of cardiac lymphatic vessels in repairing the heart after a heart attack. They found that the injuries sustained from a heart attack in mice stimulate the growth of new lymphatic vessels, which in turn promote cardiac repair. These are previously unknown functions for coronary lymphatic vessels, and the authors'

findings have implications for the treatment of cardiac conditions such as heart attack and atherosclerosis. They raise the possibility that the activation of LECs in the heart may be a way to promote cardiac repair.

These two studies provide fresh insight into our vascular drainage network. Taken together, they describe an early source of LEC precursors in embryonic cardinal veins, reveal an unexpected level of diversity in the signals that control early LEC development, and demonstrate that more cell types than previously appreciated contribute to the formation of cardiac lymphatic vessels. In the light of these observations, the molecular and cellular processes that control lymphatic-vessel formation seem to be much more diverse than was previously thought. The studies promise to invigorate future research into this enigmatic but vital vascular network. ■

Benjamin M. Hogan is at the Institute for Molecular Bioscience, University of Queensland, St Lucia 4072, Queensland, Australia. **Brian L. Black** is at the Cardiovascular Research Institute, University of California, San Francisco, San Francisco, California 94158, USA. e-mails: b.hogan@imb.uq.edu.au; brian.black@ucsf.edu

1. Stacker, S. A. *et al.* *Nature Rev. Cancer* **14**, 159–172 (2014).
2. Kutkut, I., Meens, M. J., McKee, T. A., Bochaton-Piallat, M.-L. & Kwak, B. R. *Eur. J. Clin. Invest.* **45**, 100–108 (2015).
3. Sabin, F. R. *Am. J. Anat.* **1**, 367–389 (1902).
4. Huntington, G. S. & McClure, C. F. W. *Am. J. Anat.* **10**, 177–312 (1910).
5. Nicenboim, J. *et al.* **522**, 56–61 (2015).
6. Klotz, L. *et al.* *Nature* **522**, 62–67 (2015).
7. Koltowska, K., Betterman, K. L., Harvey, N. L. & Hogan, B. M. *Development* **140**, 1857–1870 (2013).
8. Alitalo, K. *Nature Med.* **17**, 1371–1380 (2011).
9. Flaht, A. *et al.* *Dev. Dyn.* **241**, 1473–1486 (2012).

This article was published online on 20 May 2015.

CANCER

Precise control of localized signals

The tumour-suppressor protein PTEN is mostly found in the cell cytoplasm, tethered to endosome vesicles. This localization regulates the enzyme's activity towards specific lipids and influences its control of cell growth.

VUK STAMBOLIC

Loss of function of the PTEN tumour-suppressor protein is a common feature of many types of human cancer, including glioblastoma and prostate, kidney, thyroid and breast tumours¹. In addition to genetic

alterations occurring in sporadic tumours, germline mutations in the gene that encodes PTEN cause the group of disorders known as PTEN hamartoma tumour syndromes, which are characterized by benign tumours throughout the body and increased incidence of breast, thyroid and brain cancers¹. Since the

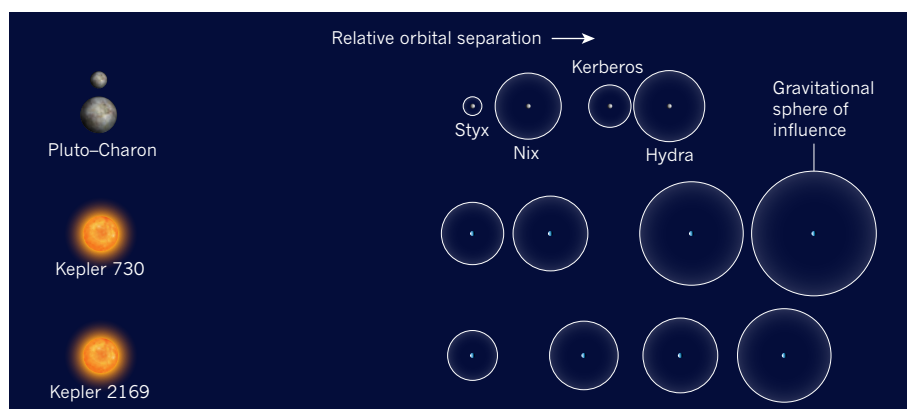


Figure 2 | Orbital architecture. The satellite system of Pluto–Charon resembles some of the exoplanet systems discovered by the Kepler space observatory. Pluto's small moons orbit the system's centre of mass clockwise; the exoplanets orbit their respective stars (Kepler 730 and Kepler 2169). For each system, the scale is set relative to the orbit of the innermost moon or planet (the relative scales vary across systems; the gap between Pluto and Charon is not on the same scale as the orbits of the moons). The dots indicate the relative positions of the moons or planets; the circles show their respective gravitational spheres of influence. Similarly to the exoplanets, the spheres of influence of Pluto's moons leave little space for other potential (as yet undiscovered) objects in intermediate orbits.

satellite formation^{5,7}. Large fragments that survived the giant impact, thought to have led to the creation of the system, might have irregular shapes; satellites grown from much smaller particles might be more rounded. The authors find that the ellipsoidal shapes of the two larger moons, Hydra and Nix, seem more consistent with grown satellites than with impact fragments. Their optical reflectivity, at 40%, is similar to Charon's (36–39%), but lower

than Pluto's (50–65%, which is comparable to the reflectivity of sea ice). With a reflectivity of only 4–6%, Kerberos is as dark as coal and seems out of place with such bright companions. Perhaps it is a dark fragment that was ejected during the giant impact.

It is hoped that NASA's New Horizons⁸ spacecraft, due to fly by Pluto in July, will throw yet more light on these questions. Close-up images taken by the spacecraft will further

constrain the sizes, shapes and reflectivities of Nix, Kerberos and Hydra, but not of Styx — it is too small to be resolved in the images. The mission's spectroscopic measurements of the relative abundances of various ices will probably yield a reflectivity for Styx, and allow comparison of the compositions of the satellites. If new satellites or rings of small particles are found, and their bulk properties established, this will provide additional information on the extent of the system. These much-anticipated observations will lead to improved theories of the formation and evolution of planets and their satellites. Linking all these results to ongoing observations of the growing population of known exoplanets will extend tiny Pluto's reach far beyond the Solar System. ■

Scott J. Kenyon is in the Department of Solar, Stellar and Planetary Physics, Smithsonian Astrophysical Observatory, Cambridge, Massachusetts 02138, USA.
e-mail: skenyon@cfa.harvard.edu

1. Youdin, A. N., Kratter, K. M. & Kenyon, S. J. *Astrophys. J.* **755**, 17 (2012).
2. Showalter, M. R. & Hamilton, D. P. *Nature* **522**, 45–49 (2015).
3. Fabrycky, D. C. et al. *Astrophys. J.* **790**, 146 (2014).
4. Canup, R. M. *Astron. J.* **141**, 35 (2011).
5. Kenyon, S. J. & Bromley, B. C. *Astron. J.* **147**, 8 (2015).
6. Cheng, W. H., Peale, S. J. & Lee, M. H. *Icarus* **241**, 180–189 (2014).
7. Desch, S. J. *Icarus* **246**, 37–47 (2015).
8. Stern, S. A. *Space Sci. Rev.* **140**, 3–21 (2008).

CANCER

Opening LOX to metastasis

New findings implicate the enzyme lysyl oxidase (LOX), secreted by oxygen-deprived breast cancer cells, in inducing bone lesions that precede and facilitate the spread of the cancer cells to the bone. SEE LETTER P.106

NETA EREZ

Despite extensive research, breast cancer remains one of the leading causes of cancer-related deaths in women, and mortality from breast cancer is almost exclusively a result of the tumour spreading to distant organs. Bones are the most common site of metastasis associated with breast cancer, affecting up to 80% of women with metastatic disease. Bone metastases are typically incurable and encompass severe disease features, including pain, bone destruction, hypercalcaemia and debilitating skeletal-related events¹. In this issue, Cox *et al.*² (page 106) establish a mechanistic link between bone metastasis of breast tumours and expression of the enzyme

lysyl oxidase (LOX) by breast cancer cells.

Metastases in bones and other organs are typically diagnosed months or years after the initial diagnosis and removal of the primary tumour. This temporal lag is, at least in part, due to the fact that although disseminated tumour cells have cell-intrinsic survival and proliferative programs, they must be able to manipulate tissue cells in the new and hostile microenvironment of the metastatic organ to support their growth^{3,4}. The early molecular changes at the metastatic niche are the rate-limiting step of metastasis, and understanding the mechanisms that facilitate the formation of a hospitable niche is a central challenge in cancer research.

Hypoxia (lack of an adequate oxygen supply) in the primary tumour is generally associated

with increased metastases⁵. However, when Cox and colleagues performed retrospective analyses of hypoxic breast tumours from humans, they found that hypoxia was correlated with increased bone metastases only in a subtype of breast tumour that does not express the receptor for oestrogen (ER[−] tumours). In an attempt to identify the factors underlying this specificity, Cox *et al.* analysed the proteins secreted by those breast cancer cells that were attracted to the bone and found that high levels of LOX were associated with bone metastases in ER[−] breast tumours. LOX belongs to a family of secreted proteins that crosslink collagen fibres in the extracellular matrix (ECM), which determines the strength and structural integrity of tissues⁶. LOX has been shown to contribute to metastasis of breast cancer to lungs by modifying the ECM at the metastatic niche^{6,7}, but it had not previously been implicated in regulating bone homeostasis.

Using a translatable mouse model of breast cancer that spontaneously metastasizes to bone, the authors demonstrate that LOX is secreted by hypoxic breast cancer cells and that it disrupts the balance between bone formation and destruction such that there is greater overall bone loss (resorption). These sites of damaged bone provide a favourable environment for disseminated breast cancer cells, thereby facilitating the formation of bone metastases. Moreover,

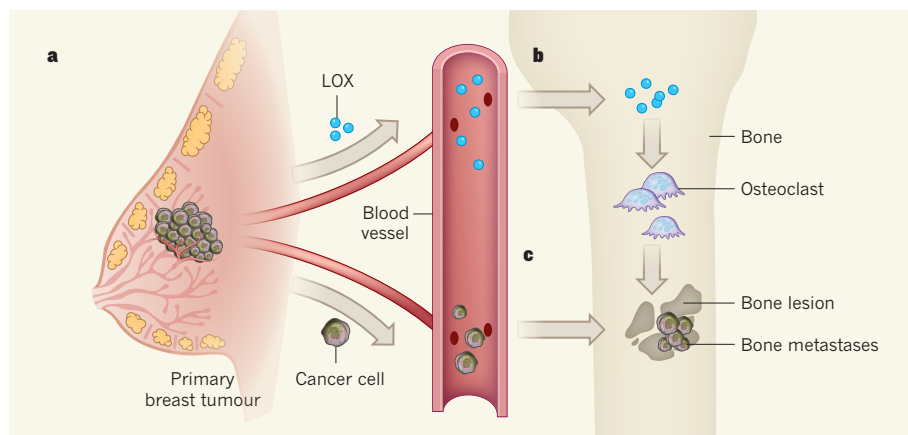


Figure 1 | Pre-metastatic niche formation in bone. **a**, Cox *et al.*² find that breast tumour cells that are exposed to hypoxic conditions secrete the enzyme lysyl oxidase (LOX) into the bloodstream. **b**, In bone, LOX activates cells called osteoclasts to enhance bone breakdown, resulting in the formation of bone lesions. **c**, These lesions create a pre-metastatic niche: breast cancer cells from the original tumour that are disseminated by the circulation are able to occupy this niche and form a metastatic tumour.

the authors demonstrate that such bone lesions can be created even in a tumour-free system: when they injected mice with factors secreted by hypoxic breast tumour cells, these soluble factors induced bone lesions that enhanced the formation of bone metastases by cancer cells circulating in the bloodstream. Thus, their study shows that systemic LOX, secreted by ER⁺ breast tumours, drives the formation of a pre-metastatic niche in bones, which precedes and facilitates the formation of metastases (Fig. 1).

The pre-metastatic niche concept suggests that a hospitable microenvironment is formed in target organs before the arrival of metastatic tumour cells and enables their invasion, survival and proliferation⁸. Although the notion of tumour cells as 'seeds' that require a fertile 'soil' for their growth was suggested more than a century ago^{9,10}, the mechanisms that enable this soil to be prepared have only emerged gradually over recent years. It was not clear whether the earliest changes in incipient metastatic niches are accomplished systemically, by soluble factors secreted from the primary tumour¹¹, or by the presence of a small number of disseminated tumour cells, or through both processes. Cox and colleagues' exciting discovery provides evidence supporting the systemic nature of pre-metastatic niche formation and contributes to our understanding of systemic regulation of cancer progression and metastasis.

The study is limited by its use of only one model of transplantable mammary tumour, rather than a genetically engineered model in which the breast tumour arises in the mouse. However, there is a lack of models in immune-competent mice in which such tumours spontaneously metastasize to bones. Another limitation is an interesting issue that remains unresolved: why is the secretion of LOX by hypoxic breast cancer cells predominantly linked with bone relapse in patients with ER⁺ breast cancer? Although hypoxia-related signalling was previously shown to drive breast

cancer metastasis⁵, a detailed dissection of the link between breast cancer subtype, hypoxia and tumour-cell attraction to bone is yet to be performed.

Elucidating the early interactions between disseminated tumour cells or their soluble products and their new microenvironment is an essential prerequisite for the development of effective targeted therapies. Target molecules are likely to be organ-specific, because the complex components and interactions of tissues vastly differ in different organs (such as bone versus brain). Adding to this complexity, this new study suggests that biomarkers that predict potential risk for organ-specific metastases are also specific

for different tumour subtypes.

Interestingly, several studies have indicated that drugs that prevent bone destruction (such as bisphosphonates and the monoclonal antibody denosumab) are efficient co-therapies for preventing bone metastasis^{1,12}. Therefore, the knowledge gained from Cox and colleagues' findings may open new horizons in the treatment of patients with breast cancer after removal of the primary tumour. Analysis of the expression of LOX may provide both a molecular tool to stratify patients by their propensity for bone metastasis and a target for preventive treatment for patients at a higher risk of bone metastasis. ■

Neta Erez is in the Department of Pathology, Sackler School of Medicine, Tel Aviv University, Tel Aviv, 69978 Israel.
e-mail: netaerez@post.tau.ac.il

1. Coleman, R. E., Gregory, W., Marshall, H., Wilson, C. & Holen, I. *Breast* **22** (Suppl. 2), S50–S56 (2013).
2. Cox, T. R. *et al.* *Nature* **522**, 106–110 (2015).
3. Joyce, J. A. & Pollard, J. W. *Nature Rev. Cancer* **9**, 239–252 (2009).
4. Erez, N. & Coussens, L. M. *Int. J. Cancer* **128**, 2536–2544 (2011).
5. Gilkes, D. M. & Semenza, G. L. *Future Oncol.* **9**, 1623–1636 (2013).
6. Barker, H. E., Cox, T. R. & Erler, J. T. *Nature Rev. Cancer* **12**, 540–552 (2012).
7. Erler, J. T. *et al.* *Cancer Cell* **15**, 35–44 (2009).
8. Kaplan, R. N., Rafii, S. & Lyden, D. *Cancer Res.* **66**, 11089–11093 (2006).
9. Paget, S. *Cancer Metast. Rev.* **8**, 98–101 (1989).
10. Witz, I. P. *Cancer Res.* **68**, 9–13 (2008).
11. McAllister, S. S. & Weinberg, R. A. *Nature Cell Biol.* **16**, 717–727 (2014).
12. Brown, J. E. & Coleman, R. E. *Nature Rev. Clin. Oncol.* **9**, 110–118 (2012).

This article was published online on 27 May 2015.

HIGH-ENERGY PHYSICS

Proton smasher spots rare particle decays

The extremely rare decays of particles known as neutral *B* mesons have been observed at CERN's Large Hadron Collider. The result may be a glimpse of physics beyond that of the standard model of particle physics. [SEE LETTER P.68](#)

DARIA ZIEMINSKA

For more than three decades, physicists have been looking for the decay of the 'strange *B* meson' particle into a pair of muons, the heavy cousins of electrons. The process is incredibly rare, and harder to find than the famous Higgs particle, the discovery of which at the Large Hadron Collider at CERN, near Geneva, Switzerland, was celebrated worldwide in 2012. The standard model of elementary particle physics¹ makes

an exact prediction of the number of particle-decay events researchers should observe in an experiment. Anything more than the predicted value means potential trouble for the standard model. On page 68 of this issue, researchers working on the CMS and LHCb collaborations² at the Large Hadron Collider describe a joint analysis of data from proton collisions that set the decay rate of the strange *B* meson at about three in one billion — in agreement with the standard-model prediction. However, they find that the decay rate of another type of

MICROBIOLOGY

Exclusive networks in the sea

The identification of an exchange of nutrients and signalling molecules between a planktonic alga and a bacterium demonstrates that targeted mutualistic interactions occur across domains of life in the oceans. [SEE LETTER P.98](#)

ALEXANDER J. LIMARDO &
ALEXANDRA Z. WORDEN

The sunlit surface waters of the ocean are inhabited by unicellular algae that perform approximately half of our planet's photosynthesis¹ and are crucial for sustaining Earth's atmosphere. These phytoplankton live in a complex milieu with other microorganisms, many of which rely on the products of algal photosynthesis for growth². Although chemical cross-talk between the microorganisms that inhabit the human body or the root zone of plants is well established^{3–5}, it is difficult to imagine similarly intimate interactions in dilute ocean environments. Indeed, an enduring mystery of marine ecology and carbon-cycle science is whether there are specific mutualistic relationships between ocean microbes or whether exchanges are largely the result of random encounters between released compounds and free-living cells. On page 98 of this issue, Amin *et al.*⁶ describe how a widespread free-living alga and a bacterium engage in a targeted exchange of nutrients and metabolites. This includes transfer of a hormone found in land plants, although neither organism is evolutionarily related to plants.

The diatoms are a group of eukaryotic algae that have important roles in primary production (the generation of organic carbon from carbon dioxide) and in marine food chains⁷. Amin *et al.* studied the diatom *Pseudo-nitzschia multiseries*, which has a complicated ecological role because, as well as being a primary producer, it can produce the neurotoxin domoic acid, which causes amnesic shellfish poisoning in humans and other consumers as its concentration is increased up the food chain. In the current report, the authors focus on how *P. multiseries* growth is affected by the activities of bacteria, the identities of bacteria that augment its growth, and how the alga or bacterium may manipulate the other to its own benefit.

To illuminate these interactions, Amin *et al.* used an impressive array of co-culturing experiments, genome sequencing, RNA-transcript analyses and metabolite profiling in studies extending from the laboratory into the wild. In characterizing algae–bacteria relationships, the researchers found that, among

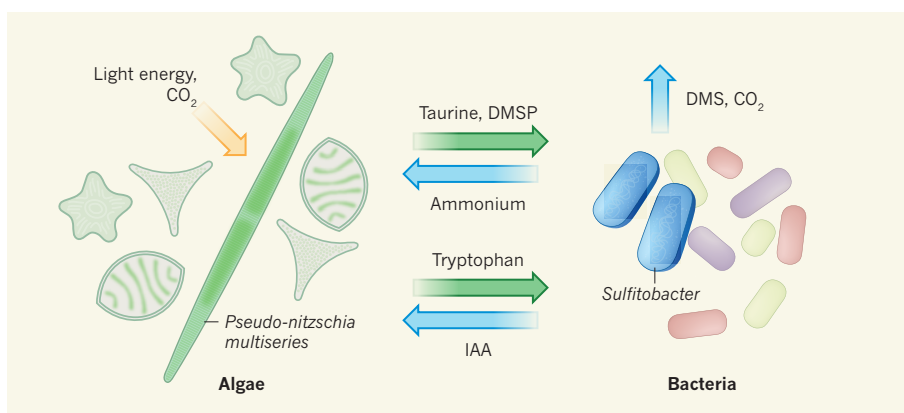


Figure 1 | Coordinated exchanges between a widespread marine alga and a bacterium. Photosynthetic algae such as diatoms coexist in the marine environment with many different bacteria. Amin *et al.*⁶ show that a specific mutualistic interaction occurs between the diatom *Pseudo-nitzschia multiseries* PC9 and the bacterium *Sulfitobacter* SA11. The diatom converts carbon dioxide to organic carbon, which the bacterium probably accesses in multiple forms, including excreted taurine and other organosulfur compounds such as dimethylsulfoniopropionate (DMSP); the latter is broken down by the bacterium to the gas DMS. The bacterium reduces nitrate to ammonium and provides other molecules, which together improve the growth efficiency of the diatom. The authors also show that *P. multiseries* produces tryptophan and *Sulfitobacter* produces indole-3-acetic acid (IAA), signalling molecules that apparently coordinate the metabolic activities of the two organisms.

49 bacterial strains isolated from *P. multiseries* cultures, members of the genus *Sulfitobacter* had the largest positive effect on the alga's growth. Further testing using *Sulfitobacter* strain SA11 showed algal growth enhancement occurred for just two of four *P. multiseries* strains examined, and there was no observable effect for another diatom genus. Perhaps more surprisingly, enhancement of bacterial growth was also highly specific, with only some strains of *P. multiseries* increasing the *Sulfitobacter*'s growth. Phytoplankton exude organic carbon molecules that are assimilated by bacteria, and themselves use nutrients remineralized by bacteria², but there is little evidence that greater specificity defines these exchanges. The findings presented unambiguously show that more nuanced interactions occur.

The authors characterized the mutualistic relationship between *P. multiseries* strain PC9 and *Sulfitobacter* strain SA11 in further detail (Fig. 1). Gene-expression analysis indicated that SA11 uses taurine, an organic compound excreted by the diatom, as a carbon source. The breakdown of taurine yields sulfite, which is notable because several *Sulfitobacter* strains oxidize sulfites as an energy source⁸. SA11

also responded to another diatom-derived organosulfur compound, dimethylsulfoniopropionate (DMSP), by upregulating a gene that degrades it. By this mechanism, SA11 presumably gains another carbon source, acrylate, while releasing the volatile gas dimethylsulfide (DMS). DMS is considered a climate-active gas because it is oxidized to sulfate particles around which water vapour can condense⁹, although its contribution to cloud formation is minor in the upper atmosphere where the largest cloud-related influences on climate occur¹⁰. Collectively, the study results suggest that compound exchanges and signalling such as those observed in this diatom–bacteria network represent an important link in global cycling of both carbon and sulfur.

Concurrent with its assimilation of diatom-derived organic carbon, SA11 secretes ammonium — a heavily scavenged commodity in low-nutrient marine settings because it is the most reduced form of nitrogen available. By outsourcing nitrate reduction to the bacterium and acquiring other molecules from it, the diatom can divert cellular resources towards other processes, such as growth. Indeed, the authors' transcriptome analyses indicate that,

in the presence of SA11, *P. multiseri* increases expression of genes associated with photosynthesis and carbon fixation, presumably to support the higher growth rates observed, as well as to provide organic carbon exudates for the bacterial partner.

But the emerging picture of a diatom–bacterium partnership is more complex than this simple resource swap. Amin *et al.* postulate that the exchanges between these free-living microbes are coordinated through cycling of the hormone indole-3-acetic acid (IAA) and the amino acid tryptophan. Best known for its use by terrestrial plants to direct developmental processes such as the growth of new shoots, IAA also has a role in signalling between soil bacteria and plants⁴. The researchers demonstrate that *P. multiseri* and *Sulfitobacter* SA11 secrete tryptophan and IAA, respectively. Moreover, they show that addition of synthetic IAA to cultures of *P. multiseri* stimulates the diatom's growth, but that the effect is significantly greater when the IAA-producing bacterium itself is present. This indicates that, although IAA promotes diatom cell division, additional unidentified factors are involved in the positive feedback loop that results in major diatom growth enhancement. The authors also detected IAA in water samples from five North Pacific sites and present transcriptomic evidence from field samples for multiple IAA biosynthesis pathways, each incorporating different precursor molecules. Thus, it seems that IAA signalling occurs across domains of life in both the terrestrial and marine biospheres and is probably an ancient mechanism of organismal communication.

Amin and colleagues' study represents a substantial step forward for understanding the complex network of interactions between phytoplankton and bacteria and provides a springboard for development of hypotheses on cross-talk between marine microbes. For example, the extreme interaction specificity observed suggests that the consortium of bacteria residing in a particular habitat may be a major force in structuring the local phytoplankton community, or vice versa. Moreover, it seems reasonable to speculate that, in addition to IAA and tryptophan, other signalling molecules participate in inter- or intradomain communication among marine microbes.

Perhaps the most pressing question we are left with is when and where such interactions occur. Symbioses between diatoms and nitrogen-gas-fixing cyanobacteria are known¹¹, and bacterial attachment to diatoms is often reported during algal blooms and in the bloom senescence phase^{12,13}. For decades, scientists have also speculated on the potential influence of microscale variability of resources in marine environments¹⁴ and on the significance of the phycosphere¹⁵ — a zone around algal cells considered analogous to the root zone of plants. Concentrations of algal secreted compounds are much higher in the

phycosphere than in nearby sea water, owing to the basic physics of the diffusive boundary layer surrounding the cell, thus promoting growth of bacteria in this layer^{13,15}.

Amin and colleagues' results suggest that the specific growth-enhancing interactions observed occur in the phycosphere, but the sampling methods and quantitation techniques needed to directly assess the physical nature of these associations are still lacking. Exciting times are ahead as scientists develop techniques to examine the physical intricacies of these mutualistic relationships, their prevalence and structuring roles in marine microbial communities, and how they might shift under environmental change. ■

Alexander J. Limardo and Alexandra Z. Worden are in the Department of Ocean Sciences, University of California, Santa Cruz, California 95064, USA, and at the Monterey Bay Aquarium Research Institute, Moss Landing, California. **A.Z.W.** is also at the Canadian Institute for Advanced Research,

Toronto, Canada.

e-mails: alimardo@mbari.org; azworden@mbari.org

1. Field, C. B., Behrenfeld, M. J., Randerson, J. T. & Falkowski, P. *Science* **281**, 237–240 (1998).
2. Worden, A. Z. *et al.* *Science* **347**, 1257594 (2015).
3. Thompson, J. A., Oliveira, R. A., Djukovic, A., Ubeda C. & Xavier, K. B. *Cell Reports* **10**, 1861–1871 (2015).
4. Sukumar, P. *et al.* *Plant Cell Environ.* **36**, 909–919 (2013).
5. Von Bodman, S. B., Bauer, W. D. & Coplin, D. L. *Annu. Rev. Phytopathol.* **41**, 455–482 (2003).
6. Amin, S. A. *et al.* *Nature* **522**, 98–101 (2015).
7. Bowler, C., Vardi, A. & Allen, A. E. *Ann. Rev. Mar. Sci.* **2**, 333–365 (2010).
8. Park, J. R. *et al.* *IJSEM* **57**, 692–695 (2007).
9. Stefels, J., Steinke, M., Turner, S., Malin, G. & Belviso, S. *Biogeochemistry* **83**, 245–275 (2007).
10. Czikzo, D. J. *et al.* *Science* **340**, 1320–1324 (2013).
11. Foster, R. A. *et al.* *ISME J.* **5**, 1484–1493 (2011).
12. Smith, D. C., Steward, G. F., Long, R. A. & Azam, F. *Deep-Sea Res. II* **42**, 75–97 (1995).
13. Amin, S. A., Parker, M. S. & Armbrust, E. V. *Microbiol. Mol. Biol. Rev.* **76**, 667–684 (2012).
14. Azam, F. *Science* **280**, 694–696 (1998).
15. Bell, W. & Mitchell, R. *Biol. Bull.* **143**, 265–277 (1972).

This article was published online on 27 May 2015.

DEVELOPMENTAL BIOLOGY

Diversity in the lymphatic vasculature

Two studies of the cells that give rise to lymphatic vessels reveal that precursors arise from unexpected sources, demonstrating that the origins of this vasculature are more diverse than anticipated. SEE ARTICLES P.56 & P.62

BENJAMIN M. HOGAN & BRIAN L. BLACK

The lymphatic vasculature is a specialized network that drains fluid from tissues and enables immune-cell trafficking and surveillance throughout the body. This major constituent of the circulatory system was long considered to be ancillary to the blood vasculature, and as such has received less attention than its counterpart. As a result, although the roles of lymphatic vessels in tissue maintenance and disease are now well appreciated^{1,2}, their origins have remained contentious for more than a century^{3,4}. Two studies^{5,6} in this issue provide insights into the origins of the lymphatic vasculature.

In vertebrate embryos, lymphatic vessels arise from two pre-existing veins⁷. Vascular endothelial cells that line the walls of these cardinal veins turn on genes that direct venous cells to become lymphatic endothelial cells (LECs), which leave the veins and form the lymphatic vessels. In this way, one vascular network gives rise to another. But precisely how and when a pool of LEC precursors is established in the cardinal veins, and whether

all cells in the early veins are identical, has remained unclear.

Zebrafish embryos are transparent, which makes them an ideal organism for visualizing cell movements. Nicenboim *et al.*⁵ (page 56) traced early LEC development in zebrafish and unexpectedly discovered that the cells on the dorsal (upper) and ventral (lower) walls of the cardinal veins are different. The researchers report that lymphatic precursors sprout from the dorsal wall, but that these cells actually originate in the ventral wall at an earlier developmental stage (Fig. 1).

By using fluorescence to track single cells, the authors found that precursor cells in the ventral wall divide, after which one of the two daughter cells migrates to the dorsal wall. These dorsal daughter cells can then give rise to LECs. Interestingly, the cells in the ventral wall also contribute to the intestinal blood vasculature, indicating that they can give rise to multiple types of endothelium. Nicenboim and colleagues showed that the fate of these nascent precursor cells is controlled by a signalling molecule, Wnt5b, which acts from tissues adjacent to the ventral

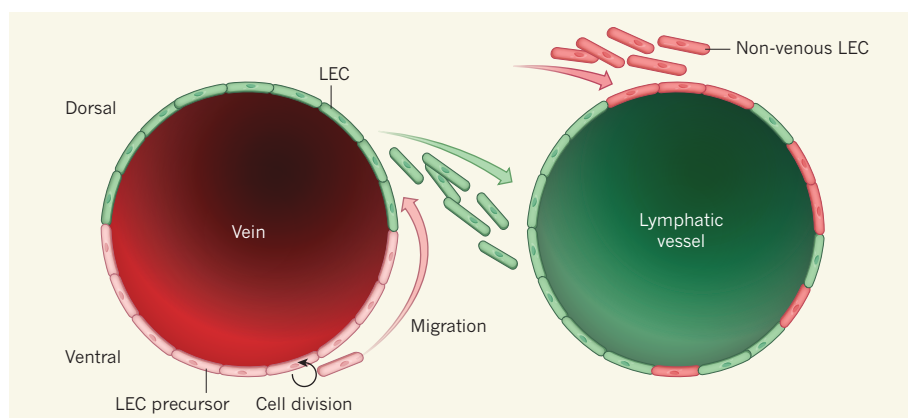


Figure 1 | Contributions to lymphatic-vessel development. Lymphatic endothelial cells (LECs), which derive primarily from veins in the early embryo, line lymphatic vessels. Nicenboim *et al.*⁵ report that LEC precursors from the ventral side of embryonic veins divide, before one of the two daughter cells migrates to the dorsal side of the vein. From there, these cells can differentiate into LECs and migrate to the site of forming lymphatic vessels. Klotz *et al.*⁶ found that the LECs that form lymphatic vessels in the heart originate both from embryonic veins and from other non-venous sources, including the yolk sac.

wall of the vein. This observation points to an unexpected instructive role for ventral tissues and Wnt signalling in driving cells to become LECs.

It is difficult to pinpoint the stage at which a cell becomes committed to its future identity, but Nicenboim and colleagues' observations should prompt us to revise our thinking about how cellular identity is acquired in vascular lineages. Their work suggests that changes in cellular identity are probably coupled to dynamic cell movements, rather than to step-wise changes in gene expression, as current dogma suggests. One attractive idea is that the range of cell types that undifferentiated precursors in the vasculature can become is restricted progressively at sequential locations during vessel development. Future analyses should test this and other models.

Klotz *et al.*⁶ (page 62) examined a later stage of development, when lymphatic vessels form in the heart, which, like all organs, uses the lymphatic system to maintain normal fluid levels and for immune-cell trafficking⁸. An understanding of how lymphatic vessels develop in individual organs, however, has been even more enigmatic than a definition of the origins of the system as a whole. Indeed, although the cardiac lymphatic system has previously been described⁹, its development, origins and functions have remained unclear.

These authors found that most of the cardiac lymphatic system in mice arises from embryonic veins located outside the heart. But unexpectedly, they show that many coronary LECs do not originate from veins at all (Fig. 1). By using various genetic 'fate-mapping' techniques to indelibly label cells, allowing cell movements and descendants to be traced, the authors observed that roughly 20% of LECs in the heart's lymphatic vasculature originate in the yolk sac that surrounds the developing embryo. The researchers suggest that these yolk-sac cells have a previously unappreciated

potential to give rise to LECs directly, in addition to their known roles in forming blood cells and vascular endothelial cells.

All fate-mapping experiments in mice must be interpreted cautiously, because the techniques used to label cells genetically can also label other cell types. Nonetheless, Klotz and colleagues' work indicates that cardiac LECs originate from different places: embryonic veins and at least one other source. Future studies that do not use genetic labelling should further clarify the origins of cardiac and other LECs in developing organs.

Klotz *et al.* also investigated the role of cardiac lymphatic vessels in repairing the heart after a heart attack. They found that the injuries sustained from a heart attack in mice stimulate the growth of new lymphatic vessels, which in turn promote cardiac repair. These are previously unknown functions for coronary lymphatic vessels, and the authors'

findings have implications for the treatment of cardiac conditions such as heart attack and atherosclerosis. They raise the possibility that the activation of LECs in the heart may be a way to promote cardiac repair.

These two studies provide fresh insight into our vascular drainage network. Taken together, they describe an early source of LEC precursors in embryonic cardinal veins, reveal an unexpected level of diversity in the signals that control early LEC development, and demonstrate that more cell types than previously appreciated contribute to the formation of cardiac lymphatic vessels. In the light of these observations, the molecular and cellular processes that control lymphatic-vessel formation seem to be much more diverse than was previously thought. The studies promise to invigorate future research into this enigmatic but vital vascular network. ■

Benjamin M. Hogan is at the Institute for Molecular Bioscience, University of Queensland, St Lucia 4072, Queensland, Australia. **Brian L. Black** is at the Cardiovascular Research Institute, University of California, San Francisco, San Francisco, California 94158, USA. e-mails: b.hogan@imb.uq.edu.au; brian.black@ucsf.edu

1. Stacker, S. A. *et al.* *Nature Rev. Cancer* **14**, 159–172 (2014).
2. Kutkut, I., Meens, M. J., McKee, T. A., Bochaton-Piallat, M.-L. & Kwak, B. R. *Eur. J. Clin. Invest.* **45**, 100–108 (2015).
3. Sabin, F. R. *Am. J. Anat.* **1**, 367–389 (1902).
4. Huntington, G. S. & McClure, C. F. W. *Am. J. Anat.* **10**, 177–312 (1910).
5. Nicenboim, J. *et al.* *522*, 56–61 (2015).
6. Klotz, L. *et al.* *Nature* **522**, 62–67 (2015).
7. Koltowska, K., Betterman, K. L., Harvey, N. L. & Hogan, B. M. *Development* **140**, 1857–1870 (2013).
8. Alitalo, K. *Nature Med.* **17**, 1371–1380 (2011).
9. Flaht, A. *et al.* *Dev. Dyn.* **241**, 1473–1486 (2012).

This article was published online on 20 May 2015.

CANCER

Precise control of localized signals

The tumour-suppressor protein PTEN is mostly found in the cell cytoplasm, tethered to endosome vesicles. This localization regulates the enzyme's activity towards specific lipids and influences its control of cell growth.

VUK STAMBOLIC

Loss of function of the PTEN tumour-suppressor protein is a common feature of many types of human cancer, including glioblastoma and prostate, kidney, thyroid and breast tumours¹. In addition to genetic

alterations occurring in sporadic tumours, germline mutations in the gene that encodes PTEN cause the group of disorders known as PTEN hamartoma tumour syndromes, which are characterized by benign tumours throughout the body and increased incidence of breast, thyroid and brain cancers¹. Since the

discovery of this protein, the subcellular localization of PTEN has been investigated as a plausible means for its regulation. Writing in *Molecular Cell*, Naguib *et al.*² examine the biology of the abundant PTEN pool in the cell cytoplasm.

Previous work has demonstrated that PTEN is found at the cell membrane, where it acts as a phosphatase enzyme to dephosphorylate phosphatidylinositol (3,4,5)-triphosphate (PIP3), a lipid molecule that is formed by the activity of the class I phosphatidylinositol-3-OH kinase (PI3K) enzymes^{3,4}. PIP3 dephosphorylation inhibits its activity in the cancer-promoting signalling pathway that is initiated by class I PI3K enzymes and that controls the enzymes protein kinase B (PKB; also known as Akt) and mammalian target of rapamycin complex 1 (mTORC1) (Fig. 1). Inhibition of this pathway is thought to be at the crux of PTEN's function as a tumour suppressor⁵, although more-recent evidence also points to PIP3-independent tumour-suppressive functions. PTEN is also subject to a complex mechanism of nuclear localization and retention, and it can exert its phosphatase activity in the nucleus to contribute to maintaining genome integrity⁶. And, remarkably, a secreted form of PTEN has also been discovered, enabling this tumour suppressor to function beyond the cells in which it is produced⁷.

Using high-resolution microscopy of fluorescently tagged PTEN, Naguib *et al.* show tight association of cytoplasmic PTEN with the endosomes (membrane-delineated intracellular vesicles originating from the cell membrane) assembled alongside the cellular microtubule network that forms part of the cytoskeleton. The endosomal localization of PTEN is ensured by the interaction of its CBR3 loop with phosphatidylinositol 3-phosphate (PI3P; not to be confused with PIP3), an endosomal phospholipid produced by the activity of the enzyme Vps34, which is a class III PI3K (ref. 8). Evolutionarily conserved among vertebrate species, the PTEN CBR3 loop has been shown to mediate general PTEN binding to other phosphoinositide molecules and cell membranes, and was found to be essential for the protein's growth-suppressing activity^{3,4}.

Using fluorescently tagged PTEN fusion proteins, Naguib and colleagues acquired data suggesting that CBR3-loop-mediated PTEN localization to endosomes plays a significant part in suppressing PKB signalling in cells. In support of this, they found that PTEN cytoplasmic organization was disrupted in Vps34-deficient mouse embryonic fibroblast cells, as was the localization of the pleckstrin homology domain of PKB that binds PIP3. It is worth noting that previous work in other cell systems⁹ found that disruption of Vps34 did

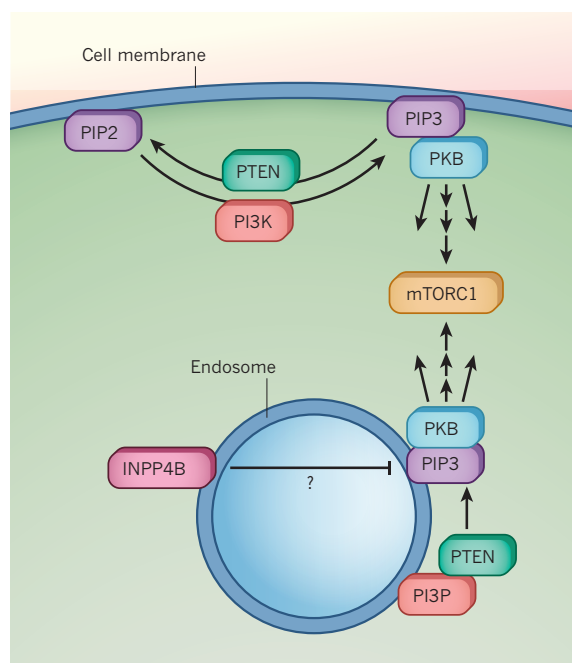


Figure 1 | Endosomal PTEN in PIP3 control. The PI3K signalling pathway, which controls cell proliferation, is triggered when the enzyme PI3K phosphorylates the cell-membrane phospholipid PIP2 to generate PIP3, which then activates protein kinase B (PKB), eventually leading to regulation of many of its downstream targets, including mTORC1. The tumour-suppressor protein PTEN, a lipid phosphatase enzyme, inhibits this pathway by dephosphorylating PIP3. Although PTEN transiently associates with the cell membrane, most PTEN resides in the cytoplasm. Naguib *et al.*² show that cytoplasmic PTEN is associated with endosomes, where it is attracted by direct binding to another phospholipid, PI3P, and dephosphorylates endosomal PIP3, contributing to downstream regulation of the PI3K pathway. Endosomes contain another lipid phosphatase, INPP4B, which under conditions of increased cellular PIP3 levels, may also dephosphorylate it to regulate PI3K signalling.

not affect steady-state or insulin-stimulated activity of PKB, possibly reflecting cell- or context-specific dependencies of the PI3K–PKB network on the endosomal PI3P state.

Considering that a proportion of the cell membrane is internalized through the process of endocytosis, Naguib *et al.* propose that PTEN association with PI3P favours dephosphorylation of endosomal PIP3, which is generated by PI3K activity on the cell membrane. Consistent with this idea, the authors found that liposomes (artificial vesicles with a phospholipid surface) containing both PIP3 and PI3P were more efficiently dephosphorylated by PTEN than the same vesicles containing only PIP3. Although PI3P may directly activate PTEN, it is more plausible that interaction between PTEN and PI3P increases the local concentration of PTEN, promoting its dephosphorylation of PIP3. Supporting such a view is the authors' demonstration that fusion to the PTEN amino terminus of an endosome-targeting FYVE domain (thus mimicking PI3P binding) confers an increase in PTEN activity towards the liposomes (containing both PIP3 and PI3P), even in the case of PTEN mutants with CBR3 loops that do not bind PI3P. Considering that

the FYVE-domain fusions were at the N terminus, a location physically distinct from the CBR3 loop, PTEN positioning towards the PIP3 substrate is probably not affected by PI3P binding.

Other moieties have been found to modulate PTEN's interaction with cellular membranes. For example, attachment of a SUMO protein at the lysine-266 amino-acid residue in the C2 domain of PTEN¹⁰ is thought to facilitate PTEN's association with the cell membrane; also, PTEN's N terminus contains a phosphatidylinositol (4,5)-bisphosphate (PIP2) binding sequence, which can further contribute to its membrane interactions¹¹. These mechanisms are expected to act in concert with CBR3 loop binding to PI3P to fine-tune PTEN localization. Moreover, dynamic changes in the carboxyl terminus of PTEN are also likely to influence its subcellular localization. This region of PTEN is thought to fold over the C2 domain, particularly when phosphorylated at a cluster of four serine or threonine residues (380–385 in human PTEN)⁵. This conformation renders PTEN inactive towards PIP3 (ref. 5). Other post-translational modifications, including other sites of phosphorylation, acetylation and binding of the PDZ-domain binding site at the extreme C terminus of PTEN, may further contribute to these interactions⁵.

It is conceivable that the newly discovered PI3P-dependent endosomal localization of PTEN coordinates a specific environment for its regulation, favouring control by specialized upstream inputs and allowing precise management of endosomal PIP3 by PTEN. Reflecting even further complexity in PIP3 management, recent evidence¹² reveals that endosomes also harbour another lipid phosphatase, INPP4B. Normally viewed as an enzyme that dephosphorylates phosphatidylinositol molecules at the 4' position of their inositol ring, INPP4B also displays limited activity towards the 3' position¹³, which could be particularly relevant in cells that lack PTEN and hence display increased abundance of PIP3. As our understanding of the mechanisms governing PTEN's subcellular localization increases, so does the realization that multiple, sometimes redundant mechanisms exist to control PIP3, with profound implications for downstream signalling. Such knowledge will be instrumental in the development of effective therapeutic options in cancers featuring loss of PTEN or activating mutations of the PI3Kα subunit, encoded by the *PIK3CA* gene. ■

Vuk Stambolic is at the Princess Margaret Cancer Centre, University Health Network,

and in the Department of Medical Biophysics,
University of Toronto, Toronto M5G 1L7,
Canada.
e-mail: vuks@uhnres.utoronto.ca

- Hollander, M. C., Blumenthal, G. M. & Dennis, P. A. *Nature Rev. Cancer* **11**, 289–301 (2011).
- Naguib, A. et al. *Mol. Cell* **58**, 255–268 (2015).
- Lee, J. O. et al. *Cell* **99**, 323–334 (1999).

- Georgescu, M. M. et al. *Cancer Res.* **60**, 7033–7038 (2000).
- Worby, C. A. & Dixon, J. E. *Annu. Rev. Biochem.* **83**, 641–669 (2014).
- Bassi, C. et al. *Science* **341**, 395–399 (2013).
- Hopkins, B. D. et al. *Science* **341**, 399–402 (2013).
- Backer, J. M. *Biochem. J.* **410**, 1–17 (2008).
- Byfield, M. P., Murray, J. T. & Backer, J. M. *J. Biol. Chem.* **280**, 33076–33082 (2005).

- Huang, J. et al. *Nature Commun.* **3**, 911 (2012).
- Iijima, M., Huang, Y. E., Luo, H. R., Vazquez, F. & Devreotes, P. N. *J. Biol. Chem.* **279**, 16606–16613 (2004).
- Chew, C. L. et al. *Cancer Discov.* <http://dx.doi.org/10.1158/2159-8290.CD-14-1347> (2015).
- Kofuji, S. et al. *Cancer Discov.* <http://dx.doi.org/10.1158/2159-8290.CD-14-1329> (2015).

This article was published online on 27 May 2015.

ASTRONOMY

Pluto leads the way in planet formation

Images from the Hubble Space Telescope cast new light on the orbits, shapes and sizes of Pluto's small satellites. The analysis comes just before a planned reconnaissance by the first spacecraft to visit them. [SEE ARTICLE P.45](#)

SCOTT J. KENYON

Pluto and its large moon Charon together make up the only 'binary planet' in the Solar System. With a mass roughly 11% that of Pluto, Charon orbits the binary system's centre of mass at a distance of 17,500 kilometres every 6.4 days. Over the past decade, images from the Hubble Space Telescope (HST) have revealed four circumbinary satellites with orbital periods of 20–40 days and masses roughly 0.001% (or less) of Pluto's (Fig. 1). Before the discovery of the innermost and least massive of these moons, Styx, dynamical studies¹ had suggested that the other three, Nix, Kerberos and Hydra, are packed as closely together as possible, with no room for other stable satellites between their orbits.

On page 45 of this issue, Showalter and Hamilton² present an analysis of all available HST images of the system, and derive new orbits and masses for the moons. They also derive limits on the moons' previously unknown shapes and reflectivities. As well as confirming that the moons are in extremely tight orbits, the authors infer new relationships between the orbital periods of satellite pairs. These results may help us to understand how planets and satellites form and remain on stable orbits for billions of years.

The architecture of Pluto's small satellites closely resembles that of several planetary systems discovered by the Kepler space observatory³ (Fig. 2). In these systems, every object has a gravitational sphere of influence that prevents other objects from orbiting nearby. The more massive the object, the larger its sphere of influence. When the gravitational spheres

of neighbouring objects nearly overlap, it is impossible to place other bodies on stable orbits between them. In tightly packed systems, the spheres of several (perhaps all) of the objects almost overlap. Small particles, such as interplanetary dust, might orbit in these intermediate regions, but large objects cannot.

These tightly packed systems place severe constraints on theories of planetary-system formation. According to current thinking, planets (and satellites) start as small seeds in a disk or ring surrounding the star (or planet) at the centre. These seeds grow by agglomerating other small solid objects along their orbits. Eventually, growing bodies feel the gravitational tugs of others in the system. Continued growth results in 'overpacking', whereby the

spheres of influence of many growing objects in orbit overlap. As the gravitational forces between these objects build, their orbital motions become chaotic, and further growth is promoted through mergers of objects. When only a few planets (or satellites) remain, they settle into nearly circular orbits and their spheres of influence do not overlap. How some systems end up with objects in closely packed orbits is an open question.

Current hypotheses^{4,5} on the formation of the Pluto–Charon system focus on a giant impact in which a proto-Charon collided with a proto-Pluto to form a binary planet surrounded by an expanding ring of debris. Pre-existing moons might have survived the impact and new moons may have grown out of small particles in the debris. As well as having ended up in tightly packed orbits, the four moons that are the end product of this process (Styx, Nix, Kerberos and Hydra) exist in orbits with orbital periods in an observed ratio of roughly 3:4:5:6 times that of Charon⁶, respectively. High-quality measurements of the orbits and masses of all the moons in the system are needed to understand how this process works.

To constrain these properties, Showalter and Hamilton measure precise positions of the moons on the HST images. Assuming that the four moons follow elliptical orbits around Pluto–Charon, the authors present detailed modelled fits to their positions that yield the period, orientation (the inclination of the orbital plane with respect to the orbital plane of Pluto–Charon) and ellipticity of each orbit. Variations in the brightness of the moons at different times along their orbits allowed the authors to derive estimates of their sizes, shapes, reflectivities and masses. They conclude that the moons have orbital-period ratios of 3.16:3.89:5.03:5.98 — close to, but not quite, integers. Curiously, the synodic period of Styx and Nix (the time interval between orbital phases when two moons line up on the same side of their planet) is almost exactly 1.5 times the synodic period of Nix and Hydra. How this 'three-body resonance' developed during the growth of the moons is unclear⁶.

The shapes and compositions of Pluto–Charon's four moons provide crucial tests of models of planet and

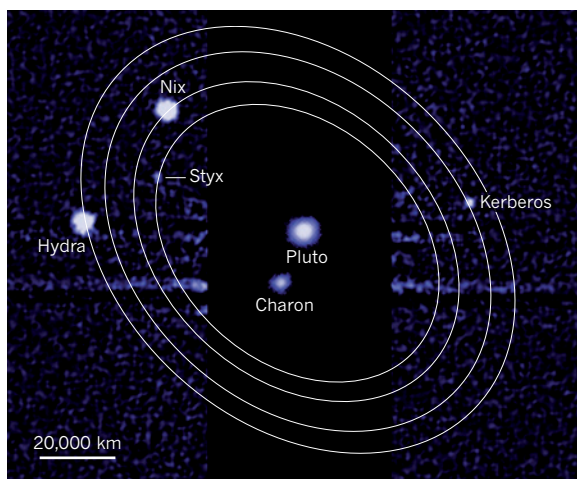


Figure 1 | Pluto and its satellites. This optical image, taken by the Hubble Space Telescope, depicts Pluto, its large moon Charon and four smaller moons Styx, Nix, Kerberos and Hydra. The image was taken in July 2012 when Styx was discovered. Showalter and Hamilton² have used such images to derive several properties of Styx, Nix, Kerberos and Hydra. The ellipses shown are illustrative paths of the moons around the centre of mass of the system.

NASA, ESA, M. SHOWALTER (SETI INST.)

CAREERS

TRADE TALK Moving from lab work to regulatory affairs **p.119**

PUBLIC SPEAKING How to plan a two-minute pitch go.nature.com/xhy3kb

BECOMING FACULTY Hurdles to expect and overcome go.nature.com/x3fwwc

JORG GREUEL/GETTY



RESEARCH CONTINUITY

Be prepared

When a key member of a team is lost, the work does not have to come to an end.

BY HANNAH HOAG

When Michael Pisaric was two years into his PhD, he travelled to Watson Lake in Canada with his supervisor, Julian Szeicz, and graduate student Tammy Karst-Riddoch, to collect sediment from several lakes in Yukon and in northern British Columbia. Szeicz was a geographer at Queen's University in Kingston, Canada, who worked on reconstructing ancient climates. The trio hoped that the samples would reveal how climate had influenced tree-line dynamics in the region over the past 10,000 years.

As they trudged through the snow and negotiated a series of switchbacks, a snow avalanche roared down the hill and covered them. When it cleared, Pisaric was buried up to his

shoulders and there was no sign of Szeicz. Karst-Riddoch dug Pisaric out and they ran down the hillside to call the Royal Canadian Mounted Police, who recovered Szeicz's body later that day.

These sorts of tragedies are rare, devastating and hard to deal with. The loss of a principal investigator owing to an accident or illness can not only set junior lab members adrift emotionally, it can also put their careers in jeopardy. But they can establish ways to keep their careers from becoming unhinged (see 'Set-back savers'). Collaborative networks can help to keep funding in place, and a hard look at the progress of their research and career path will help them to work out where to go next.

But first they must work through the emotional toll of the death or diagnosis. "You

have to take care of yourself, and that may mean moving away from your work for an extended period of time," says Pisaric, who did not return to research for six months after the event. "Come back when you are comfortable, not because of the pressure from other people." When Pisaric did return, he avoided his PhD research. Instead, he busied himself with data from his master's degree on changes to the Siberian tree line over the past 10,000 years, later publishing two papers^{1,2}. He found a new supervisor and a mentor and eventually returned to full speed.

When Tony Pawson, a cell biologist at the Lunenfeld-Tanenbaum Research Institute at Mount Sinai Hospital in Toronto, Canada, died unexpectedly in August 2013, his lab group consisted of about 30 people. "They ►



Nick Haddad says that his colleagues acted as a safety net when he had a debilitating accident.

► were in shock,” says Jim Woodgett, the institute’s director of research. They were referred to psychologists to address the grief and stress that they were experiencing; many had failed to recognize how dependent they were on this one person, he says.

It was stressful, recalls Greg Findlay, who now runs his own lab in embryonic stem-cell signalling at the University of Dundee, UK. “It was a terrible tragedy, yet we also had to think about, ‘Where did our lives go from here?’” Those who fared best were the ones who had already formed professional relationships with other scientists, mostly senior researchers at their own or other institutions, who gave them lab space, advocated for resources and fought on their behalf to ensure that they had enough time to recover emotionally. The same was true for Pisaric and others who benefited from a mentor who looked out for their emotional wellbeing and helped them to secure the financial resources and academic support they needed to continue their PhD work.

NETWORK BUILDERS

Graduate students and postdocs can become wrapped up in the race for results and publications, and often do not make building these networks a priority. But even their own health problems can stall the publications and experiments that are crucial to building a career. Establishing ties within an institute — and outside its walls — is important for career development. Connections made at conferences and online can turn into fruitful collaborations and job opportunities — and a much-needed safety net should their lab have

to shut down unexpectedly.

Nick Haddad, an ecologist at North Carolina State University in Raleigh, credits his collaborators for covering for him during the time that he was unable to work. He had just 4 days left to refine a paper with 25 co-authors when he had an accident that put him out of action for almost two months.

His collaborators contacted the journal editor and pulled together the pieces left dangling. The paper was eventually published in *Science Advances*³. Haddad sees the article as tangible evidence of his safety net. “I cannot remember being this excited about a paper, except maybe my first,” he says. “We like to think of ourselves as independent scientists and academics, except that it is not really true. We are a community of scholars, and my own success is not mine, but the success of a group of people who are interacting and collaborating.”

As well as collegial support, trainees need to ensure that their financial affairs are in order (see ‘Control your assets’). Graduate students, especially, tend to be supported by their supervisor’s funding. Pisaric, who is now a physical geographer at Brock University in St. Catharines, Canada, recalls that the initial response from the funding agency was to terminate Szeicz’s grant and claw back the unused money. It was an enormous blow on top of all the other emotional stress he was experiencing. “I was left wondering,” he says, “how do I finish my PhD with no funding?”

Research grants depend on the terms that the sponsor lays out in the funding agreement. Many of the grants from US and Canadian federal funding agencies are contracts between the agency and a laboratory’s principal investigator. The agency’s decision to support a

project therefore rests on the track record of the scientists leading it, not just on the idea, so the grant can be terminated if the recipient is no longer able to carry out the research or to meet other requirements. Like other agencies, the US National Science Foundation tries to be flexible when a grantee needs to step back from a project, says Dana Topousis, acting head of the foundation’s office of legislative and public

“These are human relationships, and there is always sympathy.”

affairs in Washington DC. In some cases, the project can be transferred to a co-principal investigator.

In the case of prolonged absence owing to illness, these agencies have provisions in place that allow the principal investigator to postpone or transfer the grant to a colleague. “I know of individuals who have put their grants on hold for chemotherapy or to care for someone in their family who is very ill,” says Judith Chadwick, assistant vice-president of research services at the University of Toronto. “These are human relationships, and there is always sympathy.”

In Pisaric’s case, his department encouraged him to draw up a budget that would allow him to complete crucial aspects of his research and cover conference expenses and lab costs, such as those related to sample analysis. The department then worked with the funding agency to secure some of the financial support he needed from Szeicz’s grant.

TIME FOR COMPROMISE

But other grants, including those for infrastructure, or support that comes from industry, may not be as flexible. When his supervisor passed away in the third year of his PhD at the Kennedy Institute of Rheumatology at the University of Oxford, UK, Adam Cribbs found that his own stipend remained intact, but other funding in the lab disappeared. That meant he was no longer able to do some planned experiments with a price tag of close to £10,000 (US\$15,654), but with a few compromises still managed to finish his PhD on time.

Unexpected disasters can also bring truths to the surface and give trainees a chance to re-evaluate the direction of their careers. They may choose to move into another area of research or even away from science.

Marc Chrétien was six years into his PhD in laboratory medicine at the University of Toronto when his supervisor died of cancer. Chrétien had been developing a method to study the intracellular response of endothelial cells to the stress created by blood flow. He says that instead of one person stepping in, five departmental scientists tried to achieve consensus on the direction of his research and his readiness to write up his thesis. “Emotionally, I was completely drained and exhausted,” he says. As a result, Chrétien decided to switch

SETBACK SAVERS

Beat the unexpected

Illness and death can catch people by surprise, but there are ways to mitigate some of the effects.

- Set up support networks. It is good to have advocates nearby, and connections outside your home turf are also important.
- Form good habits. Take detailed notes, scan them and, especially for field scientists, preserve an offsite copy.
- Know where all the data related to your research is stored — and establish access to it early on.
- Have conversations with colleagues about your research and your career goals.
- Remember to take care of your own emotional health. **H.H.**

SCIENTIFIC BEQUESTS

Control your assets

When a principal investigator (PI) has to leave his or her job suddenly, there can be squabbles over who gets the samples. But the effects are likely to be lessened and easier to circumnavigate if labs have carefully catalogued all the specimens, reagents and technologies, such as transgenic mouse lines or proprietary imaging tools.

In many cases, these resources are considered the property of the institution, so starting early in their employment, PIs should make sure that they manage them in such a way that would give the rest of the research community access to them in the event of the PI's absence.

Scientists who are not bound by intellectual-property policies should make a detailed inventory of the scientific assets they might wish to distribute, says Ron Weiss, a partner at the Massachusetts law firm Bulkley Richardson, who manages estates and estate planning for scientists and others. Ownership depends largely on the terms of the funding and on the investigator's contract, but some items may have been created or collected before the scientist joined the university or institute. "Understand the policies of your employment, and exactly what your relationship is. Usually you are an employee, but sometimes you are not. Scientists can leave a boatload of trouble if they don't adhere to the policies and someone else benefits at the expense of the institution that had the rights."

Scientists working at government

laboratories or with private companies are unlikely to own much of their data. But those who work independently and who have taken steps to protect their intellectual property will probably have assigned all the rights to an entity such as a limited-liability corporation, says Weiss. In the event of the scientist's death, the entity could then be sold to a pre-chosen buyer, and the research materials could be bequeathed through a memorandum referenced in a will.

Another approach to managing specimens is to distribute the goods up front. Josh Drew, a lecturer at Columbia University in New York, studies the evolution and conservation of coral-reef fish across the southwestern Pacific Ocean. For his fieldwork, he collects fish, clips a small segment of gill for DNA analysis and stores the fish in formalin. Once home, he donates the specimens to the American Museum of Natural History in New York so that others can study them long after he has left academia.

Drew admits that when he started the scheme he had not been thinking of what would happen to the specimens if he died suddenly or had to cope with a long-term illness. But he recognizes that his actions would help to cover his students and colleagues if that should happen. Drew has placed a two-year moratorium on access to the samples so that he has time to publish his research. "If I don't publish within two years, that's on me," he says. **H.H.**

TRADE TALK

Quality wrangler



After finishing her postdoc in chemical biology at Stanford University, California, Leslie Cruz took a job in regulatory affairs at Alexza Pharmaceuticals in Mountain View, California. She

explains how she continues to use the skills she learned in the laboratory.

What does it take to leave the bench?

The hardest thing for me was to realize that I wasn't happy. In graduate school, I would occasionally question my career path but was always led back to research in the laboratory.

What changed?

My postdoc adviser directed me to the university career office, which recommended *Career Opportunities in Biotechnology and Drug Development* (Harbor Laboratory, 2008). I read it cover to cover and took every quiz about how one's personality would be suited to different areas of the pharmaceutical industry. To my surprise, my results were the worst for discovery research and highest for regulatory affairs and project management.

Does your role use your scientific training?

I use it every day. I read a lot of 'quality documents' — regulatory submissions to establish that our pharmaceutical products are made using exacting procedures and have passed rigorous tests. I can see the trends in the data, read the graphs and methods and understand them.

What lessons did you learn from the lab?

It's not only what I learned but what I did: I wrote numerous grant applications. The important part of that was that I loved it, the reading and reviewing and documentation. That's what I do now, only with submission documents for regulatory agencies. The other part that I learned was working with people. At my job interview, people kept asking what I did outside of conducting experiments — they wanted to know that I had the skills to influence others. In my graduate programme, I was always the lab's contact for environmental-health and safety compliance, and worked with everyone to make sure that they were doing their training and paperwork. I had no idea that this would help me to get this job. I just did it because I enjoyed it. ■

INTERVIEW BY MONYA BAKER

This interview has been edited for length and clarity; see go.nature.com/vl1l9x for more.

tracks and applied to medical school. When he was accepted, he withdrew from the PhD programme and is now a second-year medical resident at McGill University in Montreal, Canada. He has already published a paper from his graduate work⁴ and aims to publish another in the future.

Cribbs, too, found a new direction. As he wrapped up his PhD research, he realized that he lacked the knowledge to properly analyse some of the data he was generating. After he finished his PhD, he applied for and got a UK Medical Research Council fellowship in bioinformatics, which is designed to train biologists in computational biology. Although his interest in bioinformatics was spurred by his supervisor, he says that he probably would not have changed course so dramatically and sought additional training had he not become much more independent than his peers. "I'm not sure I would have tried something new if I hadn't developed

this confidence," he says. "I collaborated with quite a few people and found out my strengths and weaknesses."

Such experiences are difficult and traumatic, but there can also be constructive outcomes. "It changed me, I grew up, it made me a better scientist," says Cribbs. "If you don't ask for help you don't get it — and that can make the difference between finishing and not finishing." ■

Hannah Hoag is a freelance writer in Toronto, Canada.

1. Pisaric, M. F. J., MacDonald, G. M., Cwynar, L. C. & Velichko, A. A. *Arctic Antarct. Alpine Res.* **33**, 19–27 (2001).
2. Pisaric, M. F. J., MacDonald, G. M., Velichko, A. A. & Cwynar, L. C. *Quaternary Sci. Rev.* **20**, 235–245 (2001).
3. Haddad, N. M. *et al. Sci. Adv.* **1**, e1500052 (2015).
4. Chrétien, M. L., Zhang, M., Jackson, M. R., Kapus, A. & Langille, B. L. *J. Cell. Physiol.* **224**, 352–361 (2010).

SCIENTIFIC BEQUESTS

Control your assets

When a principal investigator (PI) has to leave his or her job suddenly, there can be squabbles over who gets the samples. But the effects are likely to be lessened and easier to circumnavigate if labs have carefully catalogued all the specimens, reagents and technologies, such as transgenic mouse lines or proprietary imaging tools.

In many cases, these resources are considered the property of the institution, so starting early in their employment, PIs should make sure that they manage them in such a way that would give the rest of the research community access to them in the event of the PI's absence.

Scientists who are not bound by intellectual-property policies should make a detailed inventory of the scientific assets they might wish to distribute, says Ron Weiss, a partner at the Massachusetts law firm Bulkley Richardson, who manages estates and estate planning for scientists and others. Ownership depends largely on the terms of the funding and on the investigator's contract, but some items may have been created or collected before the scientist joined the university or institute. "Understand the policies of your employment, and exactly what your relationship is. Usually you are an employee, but sometimes you are not. Scientists can leave a boatload of trouble if they don't adhere to the policies and someone else benefits at the expense of the institution that had the rights."

Scientists working at government

laboratories or with private companies are unlikely to own much of their data. But those who work independently and who have taken steps to protect their intellectual property will probably have assigned all the rights to an entity such as a limited-liability corporation, says Weiss. In the event of the scientist's death, the entity could then be sold to a pre-chosen buyer, and the research materials could be bequeathed through a memorandum referenced in a will.

Another approach to managing specimens is to distribute the goods up front. Josh Drew, a lecturer at Columbia University in New York, studies the evolution and conservation of coral-reef fish across the southwestern Pacific Ocean. For his fieldwork, he collects fish, clips a small segment of gill for DNA analysis and stores the fish in formalin. Once home, he donates the specimens to the American Museum of Natural History in New York so that others can study them long after he has left academia.

Drew admits that when he started the scheme he had not been thinking of what would happen to the specimens if he died suddenly or had to cope with a long-term illness. But he recognizes that his actions would help to cover his students and colleagues if that should happen. Drew has placed a two-year moratorium on access to the samples so that he has time to publish his research. "If I don't publish within two years, that's on me," he says. **H.H.**

TRADE TALK

Quality wrangler



After finishing her postdoc in chemical biology at Stanford University, California, Leslie Cruz took a job in regulatory affairs at Alexza Pharmaceuticals in Mountain View, California. She

explains how she continues to use the skills she learned in the laboratory.

What does it take to leave the bench?

The hardest thing for me was to realize that I wasn't happy. In graduate school, I would occasionally question my career path but was always led back to research in the laboratory.

What changed?

My postdoc adviser directed me to the university career office, which recommended *Career Opportunities in Biotechnology and Drug Development* (Harbor Laboratory, 2008). I read it cover to cover and took every quiz about how one's personality would be suited to different areas of the pharmaceutical industry. To my surprise, my results were the worst for discovery research and highest for regulatory affairs and project management.

Does your role use your scientific training?

I use it every day. I read a lot of 'quality documents' — regulatory submissions to establish that our pharmaceutical products are made using exacting procedures and have passed rigorous tests. I can see the trends in the data, read the graphs and methods and understand them.

What lessons did you learn from the lab?

It's not only what I learned but what I did: I wrote numerous grant applications. The important part of that was that I loved it, the reading and reviewing and documentation. That's what I do now, only with submission documents for regulatory agencies. The other part that I learned was working with people. At my job interview, people kept asking what I did outside of conducting experiments — they wanted to know that I had the skills to influence others. In my graduate programme, I was always the lab's contact for environmental-health and safety compliance, and worked with everyone to make sure that they were doing their training and paperwork. I had no idea that this would help me to get this job. I just did it because I enjoyed it. ■

INTERVIEW BY MONYA BAKER

This interview has been edited for length and clarity; see go.nature.com/vl1l9x for more.

tracks and applied to medical school. When he was accepted, he withdrew from the PhD programme and is now a second-year medical resident at McGill University in Montreal, Canada. He has already published a paper from his graduate work⁴ and aims to publish another in the future.

Cribbs, too, found a new direction. As he wrapped up his PhD research, he realized that he lacked the knowledge to properly analyse some of the data he was generating. After he finished his PhD, he applied for and got a UK Medical Research Council fellowship in bioinformatics, which is designed to train biologists in computational biology. Although his interest in bioinformatics was spurred by his supervisor, he says that he probably would not have changed course so dramatically and sought additional training had he not become much more independent than his peers. "I'm not sure I would have tried something new if I hadn't developed

this confidence," he says. "I collaborated with quite a few people and found out my strengths and weaknesses."

Such experiences are difficult and traumatic, but there can also be constructive outcomes. "It changed me, I grew up, it made me a better scientist," says Cribbs. "If you don't ask for help you don't get it — and that can make the difference between finishing and not finishing." ■

Hannah Hoag is a freelance writer in Toronto, Canada.

1. Pisaric, M. F. J., MacDonald, G. M., Cwynar, L. C. & Velichko, A. A. *Arctic Antarct. Alpine Res.* **33**, 19–27 (2001).
2. Pisaric, M. F. J., MacDonald, G. M., Velichko, A. A. & Cwynar, L. C. *Quaternary Sci. Rev.* **20**, 235–245 (2001).
3. Haddad, N. M. *et al. Sci. Adv.* **1**, e1500052 (2015).
4. Chrétien, M. L., Zhang, M., Jackson, M. R., Kapus, A. & Langille, B. L. *J. Cell. Physiol.* **224**, 352–361 (2010).